

IMECHE CONFERENCE TRANSACTIONS



SEVENTH INTERNATIONAL CONFERENCE ON  
VIBRATIONS IN  
ROTATING MACHINERY



## **Vibrations in Rotating Machinery**



# Conference Organizing Committee

**M Brennan**

University of Southampton

**D Ewins**

Imperial College of Science, Technology, and Medicine

**C Fox**

University of Nottingham

**M Hall**

Consultant

**R Holmes** (Chairman)

University of Southampton

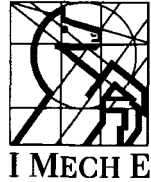
**A Parkinson**

The Open University

**R Wood**

University of Southampton

# IMechE Conference Transactions



---

Seventh International Conference on

## Vibrations in Rotating Machinery

12–14 September 2000  
University of Nottingham, UK

***Organized by***

The Tribology Group and The Machine Systems,  
Computing, and Control Group of the  
Institution of Mechanical Engineers (IMechE)

***Sponsored by***

Rolls-Royce

***Co-sponsored by***

JSME – Japan Society of Mechanical Engineers  
Vibration Institute  
KIVI – Koninklijk Instituut van Ingenieurs

**IMechE Conference Transactions 2000–6**



**Professional  
Engineering  
Publishing**

Published by Professional Engineering Publishing Limited for The Institution of  
Mechanical Engineers, Bury St Edmunds and London, UK.

**First Published 2000**

This publication is copyright under the Berne Convention and the International Copyright Convention. All rights reserved. Apart from any fair dealing for the purpose of private study, research, criticism or review, as permitted under the Copyright, Designs and Patents Act, 1988, no part may be reproduced, stored in a retrieval system, or transmitted in any form or by any means, electronic, electrical, chemical, mechanical, photocopying, recording or otherwise, without the prior permission of the copyright owners. *Unlicensed multiple copying of the contents of this publication is illegal.* Inquiries should be addressed to: The Publishing Editor, Professional Engineering Publishing Limited, Northgate Avenue, Bury St Edmunds, Suffolk, IP32 6BW, UK. Fax: +44 (0) 1284 705271.

© 2000 The Institution of Mechanical Engineers, unless otherwise stated.

ISSN 1356-1448  
ISBN 1 86058 273 7

A CIP catalogue record for this book is available from the British Library.

Printed and bound in Great Britain by Antony Rowe Limited, Chippenham, Wiltshire, UK.

The Publishers are not responsible for any statement made in this publication. Data, discussion, and conclusions developed by authors are for information only and are not intended for use without independent substantiating investigation on the part of potential users. Opinions expressed are those of the Author and are not necessarily those of the Institution of Mechanical Engineers or its Publishers.



# Contents

## Keynote Papers

C576/116/2000	<b>Active magnetic bearings – a step towards smart rotating machinery</b> R Nordmann, M Aenis, E Knopf, and S Straßburger	3
C576/115/2000	<b>Design guidelines for improved rotating machinery stability</b> R G Kirk	21
C576/010/2000	<b>The estimation of foundation parameters and unbalance</b> A W Lees, S Edwards, and M I Friswell	31

## Bladed Systems

C576/001/2000	<b>The effect of non linear damping on the resonant stresses in turbomachine LP rotor blades</b> J S Rao, C V Ramakrishnan, K Gupta, and A K Singh	45
C576/073/2000	<b>Travelling modes in turbine blades with compound periodic structure</b> E Saito and K Namura	55
C576/100/2000	<b>Optimal search for worst mistuning patterns in mistuned bladed discs based on large-scale finite element models</b> E P Petrov and D J Ewins	65
C576/111/2000	<b>A stochastic approach to turbine blade vibration and fatigue</b> D M Ghiocel and N F Rieger	77

## Balancing

C576/012/2000	<b>When to high-speed balance large turbine generator rotors</b> R G Herbert	93
C576/018/2000	<b>Exchangeability of rotor modules – a new balancing procedure for rotors in a flexible state</b> H Schneider	101
C576/021/2000	<b>‘The balancing act’ – balance for design, or design for balance?</b> S P Smith	109

C576/092/2000	<b>On the balancing of flexible rotors without trial runs</b> E Preciado and R H Bannister	121
C576/094/2000	<b>Experimental and predicted unbalance response of a rotary compressor crankshaft</b> F Sève, A Berlioz, R Dufour, and M Charreyron	131
C576/097/2000	<b>Min–max optimum flexible rotor balancing compared to weighted least squares</b> W C Foiles, P E Allaire, and E J Gunter	141
C576/098/2000	<b>Balancing a 1150 MW turbine-generator</b> E J Gunter, P E Allaire, and W C Foiles	149
<b>Case Studies</b>		
C576/004/2000	<b>Case histories of fatigue in compressor gas process pipework</b> J P Graham	167
C576/036/2000	<b>Rotor-bearing system design, analysis, and testing for exciter retrofit of a two-pole generator</b> H C Ha, C H Park, and S P Choi	181
C576/046/2000	<b>The lateral stability analysis of a large centrifugal compressor in propane service at an LNG plant</b> E A Memmott	187
<b>Surface Influences</b>		
C576/026/2000	<b>Dynamic characteristics of liquid annular seals with groove and hole pattern surface roughness</b> E Storteig and M F White	201
C576/007/2000	<b>Optimization of the rotor-dynamic behaviour of a balancing device using honeycomb profiles in high-pressure boiler feed pumps</b> C Trautmann and D-H Hellmann	213
C576/015/2000	<b>Dynamic behaviour of spiral bevel gears – rotational vibration of gears under running conditions</b> Y Uenishi, E Aoyama, Y Nakata, and T Hirogaki	223
<b>Rub</b>		
C576/027/2000	<b>Theoretical investigations on disc-brake squeal noise</b> I L M Ahmed, P S Leung, and P K Datta	235

C576/082/2000	<b>Spiral vibrations in rotors due to a rub</b> N Bachschmid, P Pennacchi, and P Venini	249
C576/093/2000	<b>Measurement of contact forces during blade rubbing</b> J Ahrens, H Ulbrich, and G Ahaus	259
C576/095/2000	<b>Rub-heated shafts in turbines</b> B Larsson	269
<b>Impacts and Rub</b>		
C576/033/2000	<b>Experimental investigation of partial rotor-rub against a non-rotating part</b> Y-S Choi	281
C576/062/2000	<b>Coupled bending and torsional vibrations due to rotor-to-stator contacts</b> X Deng, R Liebich, and R Gasch	291
C576/080/2000	<b>An experiment to measure the restitution coefficient for rotor-stator impacts</b> M L Adams, F Afshari, and M L Adams	301
<b>Identification</b>		
C576/076/2000	<b>On the identification of the foundation of a large turbogenerator unit by the analysis of transient vibrations</b> A Vania	313
C576/011/2000	<b>Estimating rotor unbalance from a single run-down</b> S Edwards, A W Lees, and M I Friswell	323
C576/029/2000	<b>Unbalance identification of flexible rotors based on experimental modal analysis</b> T Kreuzinger-Janik and H Irretier	335
<b>Active Control</b>		
C576/079/2000	<b>On-off control of HSF supported rotors</b> A El-Shafei and M El-Hakim	349
C576/101/2000	<b>Standardization of evaluation of stability margin for active magnetic bearing equipped rotors</b> O Matsushita, H Fujiwara, H Okubo, Y Kanemitsu, T Azuma, and R Herzog	361



C576/037/2000	<b>Active control of vibration in rotor/magnetic bearing systems with multiple design objectives</b> M O T Cole, P S Keogh, and C R Burrows	371
C576/110/2000	<b>Identification of the dynamic characteristics of turbulent journal bearings using active magnetic bearings</b> E Knopf and R Nordmann	381

### **Bearings and Rotors**

C576/103/2000	<b>Generalized stiffness and damping matrices of multi-DOF hydrodynamic lubrication films</b> H Springer	393
C576/084/2000	<b>Self-excited vibration of rotors in tilting-pad journal bearings</b> H Taura, M Tanaka, and K Suzuki	403
C576/050/2000	<b>A non-linear transfer matrix technique for statically indeterminate rotor bearing systems</b> A Liew, N S Feng, and E J Hahn	415
C576/041/2000	<b>Thermal distortion synchronous rotor instability</b> R G Kirk and A C Balbahadur	427

### **Bearings**

C576/072/2000	<b>Theoretical and experimental characterization of polyimide dry bushings</b> J-L Bozet, P Poysat, and P Mérot	439
C576/083/2000	<b>On 2xrev – vibration components in rotating machinery excited by journal ovalization and oil film non-linearity</b> N Bachschmid, B Pizzigoni, and E Tanzi	449
C576/028/2000	<b>Dynamic characteristics of oil-lubricated herringbone groove bearings</b> F P Wardle and C A Goat	459

### **Bearings and Seals**

C576/085/2000	<b>The stability characteristics of a journal bearing under starved lubrication</b> M Tanaka and K Suzuki	473
C576/071/2000	<b>Rotordynamics and leakage – measurements and calculations on labyrinth gas seals and their application to large turbomachinery</b> J Sobotzik, R Nordmann, F Hiß, and K Kwanka	485

C576/059/2000      **Vibration control of a flexible rotor with a slotted-ring sealed electro-rheological squeeze film damper**  
N-S Lee, D-H Choi, K-Y Seok, Y-B Lee, and C-H Kim      499

C576/104/2000      **Influence of various parameters on the non-linear behaviour of a flexible shaft incorporating an uncentralized squeeze-film damper**  
M C Levesley and R Holmes      509

### **Condition Monitoring and Cracked Rotors**

C576/108/2000      **Some strategies to achieve robust cepstral analysis**  
J Antoni and M El Badaoui      525

C576/031/2000      **Crack detection in rotating machinery by modal testing**  
C-W Lee and K-S Kwon      535

### **Condition Monitoring**

C576/003/2000      **Condition monitoring of rolling element bearings – a comparison of vibration-based techniques for incipient damage detection**  
A F Khan, E J Williams, and C H J Fox      547

C576/055/2000      **Diagnostic study of simulated faults on gears and bearings**  
C Breneur, J Mahfoudh, and D Play      561

C576/043/2000      **Model-based malfunction identification from bearing measurements**  
N Bachschmid and P Pennacchi      571

C576/025/2000      **Validation of online diagnostics of malfunctions in rotor systems**  
R Platz, R Markert, and M Seidler      581

C576/030/2000      **Failure root cause analysis applying vibrational diagnostics**  
U Südmersen, O Pietsch, W Reimche, and D Stegemann      591

C576/020/2000      **A measurement method for automotive creep groan induced vibration with data processing and analysis**  
M Bettella and R S Sharp      603

C576/006/2000      **Managing fatigue failure probability caused by misalignment and vibration in large turbine generators**  
A J Smalley, M J Roemer, and T H McCloskey      619

C576/065/2000	<b>Condition monitoring and diagnostics of constructive elements of rotor systems</b> V Volkovas	633
C576/096/2000	<b>Translational and rotational vibration measurements on rotors using laser vibrometry – advances in data interpretation</b> S J Rothberg and J R Bell	645
C576/106/2000	<b>Automated procedures for vibration monitoring of large rotating machinery in power plants</b> L Gregori, R Provasi, and G A Zanetta	657
C576/067/2000	<b>Processing of blade monitoring system data</b> M Balda	667

### **Theoretical Considerations**

C576/042/2000	<b>Rotordynamic interaction of a centrifugal pump impeller in an axial diffuser</b> E Torbergsen and M F White	679
C576/016/2000	<b>Approaches to numerical investigation of the character and stability of forced and self-excited vibration of flexible rotors with non-linear supports</b> J Zapoměl and E Malenovský	691
C576/053/2000	<b>Chaotic vibrations and internal resonance phenomena in a rotor system (twice the major critical speed)</b> T Inoue, Y Ishida, and T Murayama	701
C576/040/2000	<b>A helical transformation for rotating shafts allowing a simplified experimental procedure</b> I Bucher	711
C576/024/2000	<b>On the dynamics of windmilling in aero-engines</b> G von Groll and D J Ewins	721
C576/063/2000	<b>Levitron – an example of a purely permanent magnetic bearing of a rotor</b> R Gasch and M Lang	731
C576/077/2000	<b>Modelling the dynamic behaviour of a coupled rotor-foundation system by the mechanical impedance technique</b> P Bonello and M J Brennan	745

<b>Authors' Index</b>		757
-----------------------	--	-----



## Keynote Papers

*This page intentionally left blank*

# Active magnetic bearings – a step towards smart rotating machinery

R NORDMANN, M AENIS, E KNOFF, and S STRAßBURGER  
Darmstadt University of Technology, Germany

## 1 INTRODUCTION

In the field of rotating machinery the number of applications of rotating systems running in active magnetic bearings (AMB's) is increasing. In comparison to conventional bearings magnetic bearings are a typical mechatronic product consisting of mechanical, electrical and electronic components. Such systems have the ability to pick up changes in its environment by sensors and to react to the system or process by means of actuators after an appropriate information processing carried out in a microprocessor.

Nowadays, rotors in active magnetic bearings already offer a variety of advantages compared to conventional systems. Some of them are the tuning possibilities for stiffness and damping, the absence of friction and wear, the high running speeds, the vibration isolation and possible unbalance compensation. However, there is much more potential in such systems with respect to a smart behavior. With the mechatronic structure of a rotating machinery in AMB's consisting of built-in control, sensors, microprocessors, actuators and last but not least built-in software different novel features like identification, diagnosis, prognosis and correction can be realized. In this way it will be possible to design new machines with higher performance, higher reliability and a longer lifetime.

This paper particularly describes a Smart Machine Technology for rotating machines with AMB's and concentrates on the mentioned smart features of identification, diagnosis and correction. After a general description of the smart technology followed by a presentation of the necessary development tools three applications will show the usefulness of this new technology.

## 2 ACTIVE MAGNETIC BEARINGS (AMB'S)

### 2.1 Principle of Active Magnetic Bearings

Unlike conventional bearing systems, a rotor in magnetic bearings is carried by a magnetic field. This means, that sensors and controllers are necessary to stabilize the unstable suspension state of the rotor. Therefore, essential dynamic characteristics like stiffness and damping properties of

the whole system can be influenced by the controller (DSP-Board). For the following applications the rotor can be moved on almost arbitrarily chosen trajectories independently of the rotation, e.g. harmonic motions in one plane, forward or backward whirls. Additionally, an imbalance compensation can be performed.

A magnetic bearing system consists of four basic components: magnetic actuator, controller, power amplifier, and shaft position sensor (see Figure 1). To keep the rotor in the bearing center, the position sensor signal is used as input for a control circuit to adequately adjust the coil currents. The bearing configuration is composed of four horseshoe-shaped magnets (= 8 magnetic poles) and is operated in the so-called differential driving mode [1], where one magnet is driven with the sum of bias current  $i_0$  and control current  $i$ , and the other one with the difference.

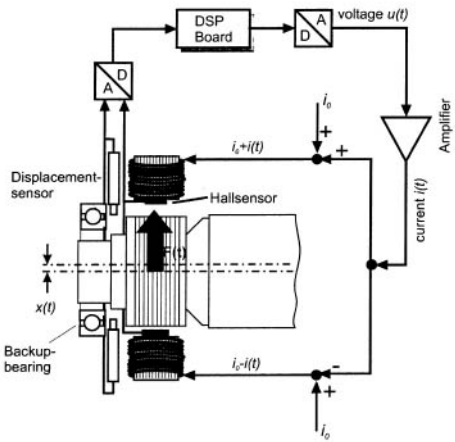


Figure 1: Principle of an AMB.

### 3 THE SMART MACHINE TECHNOLOGY

#### 3.1 The Mechatronic System

Typical for mechatronic systems, is the capability to measure physical quantities by means of sensor elements, to process these signals in a microprocessor and to control the static and dynamic behavior by means of actuators, which directly act on the mechanical process.

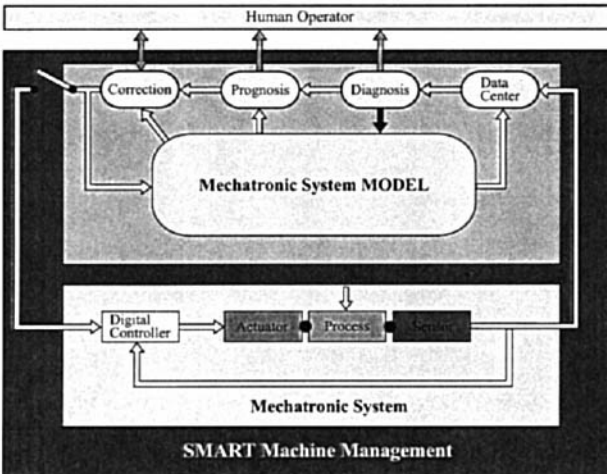


Figure 2: Smart Machine Technology

Figure 2 shows in the lower part a more generalized block diagram for such a mechatronic system. In our case this would be again the rotor of a machine tool or a turbomachine (process) running in active magnetic bearings (actuator), where displacement probes (sensors) measure the rotor position and after a feedback the digital controller (microprocessor) computes an output signal in order to control the process via the actuator.

Mechatronic systems already offer a variety of positive ef-

fects, as it was pointed out before. However, much more technical and economic benefits for industrial products and processes could be achieved with respect to higher performance (efficiency, power density, accuracy, speeds etc.) and higher reliability (reaction to failures, long maintenance intervals, robust operation etc.), if more *intelligence* would be added to the mechatronic system by well suited software and hardware components. This leads to the idea of the Smart Machine Technology, pointed out in Figure 2, which consists of three main parts: the real mechatronic system, its model and the smart machine management. The Smart Machine Technology has been realized in a European BRITE/EuRam research project and was briefly described in [2] [3].

### 3.2 The Mechatronic System Model

The mechatronic system model is a software representation of the actual real system consisting of all components. It is the core of the Smart Machine Technology. Besides the usual simulation capabilities it is important for additional features like identification, diagnosis, prognosis and correction. Furthermore, the model is used for the controller design.

Modelling is performed by application of the physical laws from different areas, e.g. Newtons mechanical equations, Maxwell equations, Navier-Stokes equations, but also by experimental methods. Due to the fact, that the quality requirements for the model are very high, the best suited tools have to be used in order to get a model representing the real system behavior in an economic way. The complete model has to be verified by comparison with the real system in a model updating procedure.

### 3.3 The Smart Machine Management

The Smart Machine Management indicates such additional functions, that are using the available information for a smart operation. In a data center information is collected from the sensors of the real mechatronic system and in parallel from the system model. Based on this data input an identification or a model based diagnosis of the systems actual state can be performed. Identification procedures allow a better insight into the system itself or into the actual process and from this point of view an optimization and reliability management is possible, for finding out failures in mechanical (rotor cracks, seal wear) or electrical components (sensors) and furthermore an optimized process. Based on the results of diagnosis a prognosis about the future behavior of the machine or about the need for corrective measures can be derived. Such corrections may be the compensation of an unbalance, special procedures for passing critical speeds, changing the feed of a machine tool during the manufacturing of delicate parts by taking into account the cutting forces or tool wear, or it may even lead to a self-tuning of the parameters of the actual control loop.

For rotating machinery the smart machine technology can be applied, if the above mentioned *smart* components of this technology are available. The next chapter concentrates on rotating systems with Active Magnetic Bearings and describes the ingredients for a successful application.

## 4 ADVANCED TOOLS FOR SMART ROTATING SYSTEMS WITH AMB'S

In order to use the possibilities of a rotor in Active Magnetic Bearings for the Smart Machine Technology some advanced tools are necessary. The most important ones are described in this chapter. In all of these tools software is a dominant part. It is necessary for the design of the overall mechatronic system, including the controller. Furthermore additional procedures in the Smart Machine Management, particularly the identification and diagnosis functions, are pro-

cessing data coming from the sensors and the system model with special software algorithms. New developed tools are also the software driven excitation of the rotor and the corresponding force measurement method.

#### 4.1 Modelling and Controller Design

The model of a rotating system in Active Magnetic Bearings consists of the following main components: the rotor with all important characteristics (stiffness, damping and inertia, gyroscopic effects, rotordynamic coefficients) and the active magnetic bearing system with the magnetic actuator, the amplifiers, the controller and the position sensors. Figure 3 shows the different parts and their integration in a MATLAB-platform.

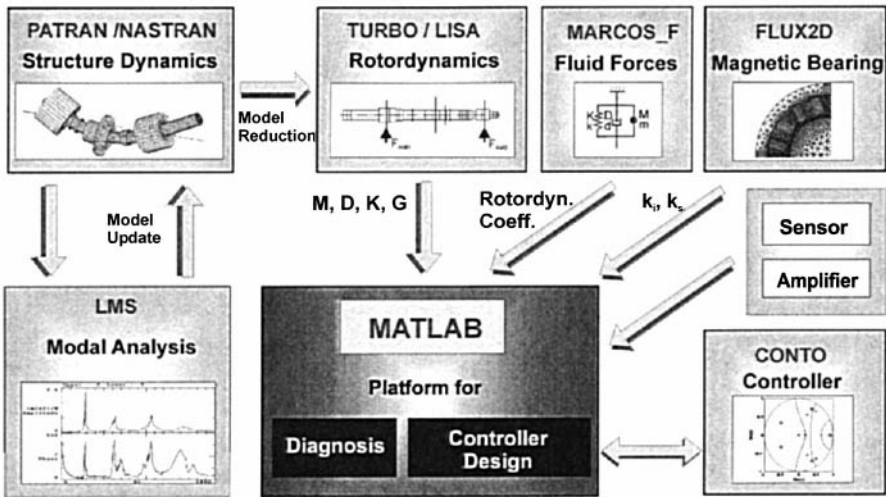


Figure 3: Integration of the mechatronic system components into the MATLAB platform

The rotor is usually modeled through a very detailed finite element model or a beam model, where a model update assures an accurate description of the reality. Special routines are available as finite difference codes for fluid structure interaction forces (pumps, compressors, turbines), expressed as rotordynamic coefficients. The AMB's are characterized by the two constants  $k_i$  and  $k_s$ , determined from calibration or magnetic field finite element codes. They relate the force in the bearing to the current and the displacement, respectively. The switching power amplifier used to drive the magnetic coils is simply modelled by a constant factor and the position sensors by a low pass filter ( $PT_2$  characteristic).

When all the above components are available at first the open loop plant is assembled to a cascade of the different subblocks shown in Figure 4. Then the continuous description of the system is discretized with the sampling frequency. The controller design to stabilize the unstable rigid body modes is based on the developed model and follows a PID-strategy with some additional filters accounting for the flexible modes (see also Figure 3)

For a validation of the entire model, compliance functions can be used. Figure 5 shows an example, pointing out the good agreement between the measured and the simulated compliance function of the closed loop. However, it should be mentioned that the remaining deviations of the simulated curve with respect to the measured one comes from the dynamics of a substructure.

ture, here the bearing housing, which was not included in the model and shows up with two additional resonance peaks in the measurement.

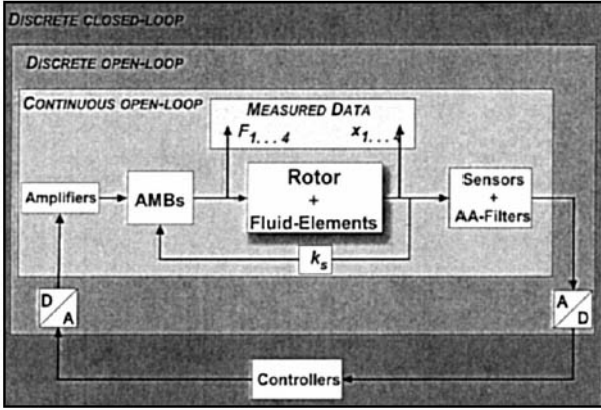


Figure 4: Block diagram of a Mechatronic system.

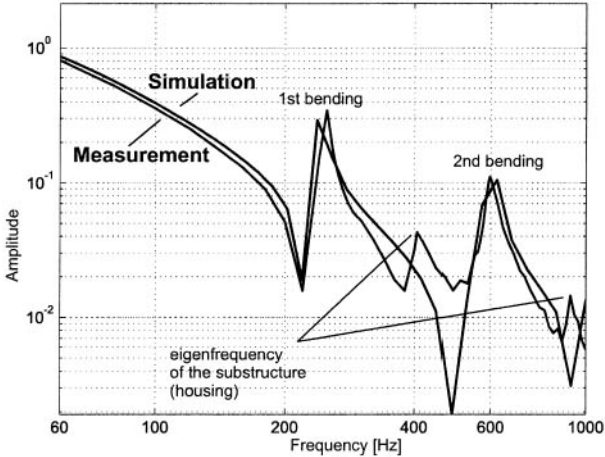


Figure 5: Comparison of simulation and measurement.

#### 4.2 Identification and Diagnosis

In the Smart Machine Management it was pointed out, that an identification and/or diagnosis procedure for the mechatronic system can be performed, based on the data coming from the system model and/or the sensor elements. By these procedures failures in the mechanical and/or electrical parts can be detected. This reliability management is applicable for the entire mechatronic system or for special components. In this paper we concentrate on the rotor itself, including those elements that are usually characterized by their rotordynamic coefficients, e.g. seals in pumps and compressors.

As mentioned before, a successful application of a model based identification and diagnosis for

rotating systems during operation depends on the accurate modelling of the rotordynamic system (for the diagnosis case with and without failures) and on the experimental determination of the dynamic behavior of the system. Eq. (1) shows the linear description for the dynamic behavior of a rotor with stiffness-, damping- and inertia characteristics, expressed by the matrices  $\mathbf{M}$ ,  $\mathbf{D}$  and  $\mathbf{K}$ . We assume, that the rotor matrices are time-invariant, but depend on the running speed and the actual operating condition.

$$\mathbf{M}\ddot{\mathbf{x}} + \mathbf{D}\dot{\mathbf{x}} + \mathbf{K}\mathbf{x} = \mathbf{F} \quad (1)$$

An identification of system parameters, that means parameters out of the matrices  $\mathbf{M}, \mathbf{D}, \mathbf{K}$ , is based on input-output relations, either in the time or in the frequency domain.

When input-output relations are considered in the frequency domain, the following complex frequency response functions are introduced

$$\hat{\mathbf{F}}(\Omega) = (\mathbf{K} - \Omega^2 \mathbf{M} + j\Omega \mathbf{D}) \hat{\mathbf{x}}(\Omega) = \bar{\mathbf{K}}(\Omega) \hat{\mathbf{x}}(\Omega) \quad (2)$$

$$\hat{\mathbf{x}}(\Omega) = (\mathbf{K} - \Omega^2 \mathbf{M} + j\Omega \mathbf{D})^{-1} \cdot \hat{\mathbf{F}}(\Omega) = \bar{\mathbf{H}}(\Omega) \cdot \hat{\mathbf{F}}(\Omega) \quad (3)$$

They can be subdivided into the compliance functions  $\bar{\mathbf{H}}_{kl}(\Omega)$  and the stiffness functions  $\bar{\mathbf{K}}_{kl}(\Omega)$ .  $\bar{\mathbf{H}}_{kl}(\Omega)$  is the system response (amplitude and phase) of the displacement  $\hat{x}_k$  due to a unit force excitation  $\hat{F}_l(\Omega)$ . In analogy  $\bar{\mathbf{K}}_{kl}(\Omega)$  is the necessary force  $\hat{F}_k(\Omega)$  when an isolated motion  $\hat{x}_l(\Omega)$  is excited without any other motion at any other degree of freedom.

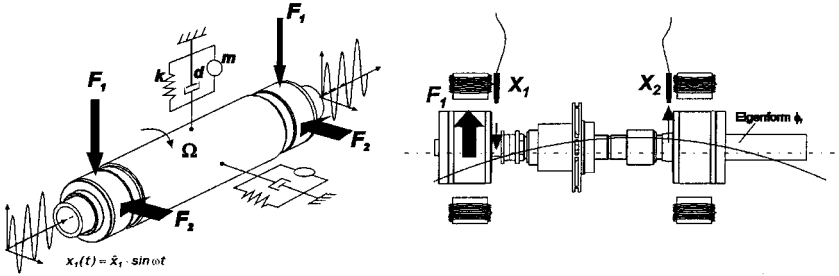
In the following applications (chapter 5) both of the frequency response functions will be used. In the first application of a rigid test rotor supported by a fluid film bearing (see chapter 5.1.), the rotordynamic coefficients of the fluid bearing will be identified. To determine the 2x2 coefficient matrices it is useful in this case to work with an excitation via displacements or motions, respectively. If, for example the rigid rotor is excited harmonically only in  $x_1$  direction, than both forces  $F_1$  and  $F_2$  are to be measured. With this information stiffness frequency response functions can easily be calculated and an extraction of the rotordynamic coefficients is possible. The basic principle of this identification procedure is shown in Figure 6 (left side).

For flexible rotor systems, it is much easier to use defined forces as an input and to measure the output displacements. This leads to the compliance functions. In a normal configuration with two radial magnetic bearings and one axial bearing, five linearly independent excitation patterns (2 radial degrees at each bearing, one axial degree) can be produced by the AMB's (see Figure 6, right side). For example, if the AMB produces a harmonic force in direction 1 and if the displacements of the rotor are measured in the degrees 1-5, one column of the transfer matrix can be determined. Again the system parameters (mass, damping, stiffness) are in some way part of these compliance functions and they have to be identified by curve fitting procedures.

For a model based fault diagnosis one can work with either one of the frequency response sets. In case of a failure the frequency response functions will usually change their characteristics and the model based diagnosis tries to find out the reason for this change, looking for the location, quality and size of a failure.

Besides the model based failure diagnosis it is also useful to consider a signal based procedure, especially when deviations in a special process have to be evaluated. Very often displacement signals are used for such a diagnosis. However, if force-signals are available, they allow a much better insight into the process behavior and its deviations. An example for this kind of failure diagnosis is given in chapter 5.3 for a machine tool grinding process.





$$\begin{bmatrix} \hat{F}_1 \\ \hat{F}_2 \end{bmatrix} = \begin{bmatrix} \hat{K}_{11} & \hat{K}_{12} \\ \hat{K}_{21} & \hat{K}_{22} \end{bmatrix} \begin{bmatrix} \hat{x}_1 \\ \hat{x}_2 \end{bmatrix}$$

$$\begin{bmatrix} \hat{x}_1 \\ \hat{x}_2 \\ \hat{x}_3 \\ \hat{x}_4 \\ \hat{x}_5 \end{bmatrix} = \begin{bmatrix} \hat{H}_{11} & \hat{H}_{12} & \hat{H}_{13} & \hat{H}_{14} & \hat{H}_{15} \\ \hat{H}_{21} & \hat{H}_{22} & \hat{H}_{23} & \hat{H}_{24} & \hat{H}_{25} \\ \hat{H}_{31} & \hat{H}_{32} & \hat{H}_{33} & \hat{H}_{34} & \hat{H}_{35} \\ \hat{H}_{41} & \hat{H}_{42} & \hat{H}_{43} & \hat{H}_{44} & \hat{H}_{45} \\ \hat{H}_{51} & \hat{H}_{52} & \hat{H}_{52} & \hat{H}_{54} & \hat{H}_{55} \end{bmatrix} \begin{bmatrix} \hat{F}_1 \\ \hat{F}_2 \\ \hat{F}_3 \\ \hat{F}_4 \\ \hat{F}_5 \end{bmatrix}$$

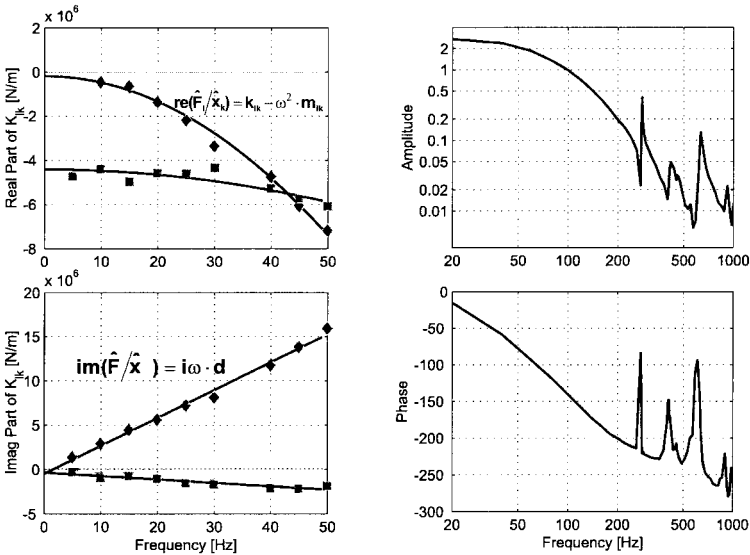


Figure 6: Identification of stiffness and compliance functions

### 4.3 Force Measurement

Basically, the magnetic bearing force can be computed from

$$\vec{F}_{AMB} = \frac{A_{pole}}{2\mu_0} \sum_{k=1}^8 \vec{B}_{pole,k}^2 \quad (4)$$

with  $A_{pole}$  the cross-section area of the poles and  $\mu_0$  the permeability of vacuum and  $\vec{B}_{pole}$  is the vector of the flux density.

The different force measurements in an AMB can be divided into two main groups. The first is based on the measurement of coil currents and rotor displacements ( $i$ - $s$ -method, reluctance network model) and the second method uses the direct measurement of the magnetic flux density  $B_{pole}$  with Hall sensors at each pole (Figure 7). The drawback of the latter method is, that the air gap has to be enlarged to integrate the Hall sensors resulting in a decrease of load capacity of the bearing. To partially overcome this problem, a modified force measurement was presented by Gähler, et al. [4], where only the north poles were equipped with Hall sensors, while the fluxes at the south poles were computed using an on-line approximation.

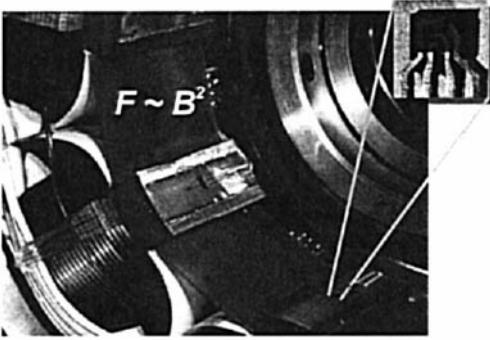


**Figure 7: Force measurements by means of Hall sensors**

If a direct measurement of the flux density is not possible or desired and if the AMB is driven in differential mode, eq. (4) can be linearized for small rotor displacements around the center

$$F_x = k_i i_x + k_s s_x \quad (5)$$

where  $i_x$  is the control current and  $s_x$  the rotor displacement in the  $x$ -direction. The constants  $k_i$ ,  $k_s$  depend on the chosen design point of the magnetic bearings (bias current  $i_0$  and air gap  $s_0$ ). A more advanced force measurement based on coil currents and rotor displacements is a reluctance network model. The linear network model used

here accounts much better for eccentric rotor positions and cross-coupling than the  $i$ - $s$ -method. Depending on the requirements, the model can further be extended to consider leakage and fringing effects, eddy currents, nonlinear material behavior, and hysteresis etc. as it is described, e.g. in Meeker, et al. [5] and Springer, et al. [6].

In the following, results of the four different force measurement techniques described above were applied to the AMBs. For each method the calibration was performed for an operating range of up to 25% of nominal bearing clearance and of a force level up to maximum bearing force.

Measured data was gained, while the rotor was floating in the AMBs and different external static forces  $F_{Ref}$  were applied. An external load cell was used to obtain the reference force  $F_{Ref}$ . More details about the calibration can be found in the work done by Förch, et al. [7] and Knopf, et al. [8].

Figure 8 shows the force error for the centric load case. The percentage values of the force errors are related to the maximum bearing force. It can be seen, that the force measurements of the flux based methods (using 4 respectively 8 Hall sensors) are clearly more accurate than the current-displacement based ones ( $i$ - $s$ -method, reluctance network). Analogues can be found for the eccentric case.

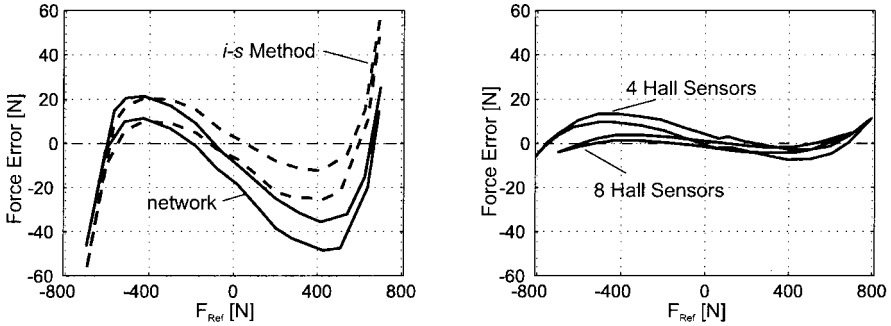


**Figure 8: Comparison of four different force measurements for the radial bearing.**

In summary, the advantages of the flux based methods are:

- they are clearly more accurate,
- influences of hysteresis and non-linearities of the magnetic material, power amplifier, etc. are diminished or completely eliminated,
- on-line implementation is possible (with some restrictions for the 4 Hall sensors method + approx.),

while the advantages for the current-displacement method are:

- no additional hardware is needed,
- *i-s*-method is the easiest one to implement in an on-line procedure (restricted applicable for the network).

## 5 APPLICATIONS FOR SMART ROTATING SYSTEMS

### 5.1 Identification of Rotordynamic Coefficients

In the first application, active magnetic bearings are used to gain knowledge about a special type of hydrodynamic journal bearings. The strategy of this research work is to use the possibilities of magnetic bearings to be operated as actuators and as sensor elements to isolate the dynamic behavior of the component under investigation and to identify its dynamic parameters.

In the field of chemical and environmental industry the demands on leakage free, so called hermetic pumps are getting more and more stringently. One possible way to realize this demands is to use medium lubricated journal bearings in combination with canned or wet motor pumps or magnetic drive pumps. The processing fluid has often a very low viscosity which causes turbulence in the lubricating film of the bearing. This effect changes the dynamic behavior of the bearings and consequently of the whole pump system. To estimate the influence of the journal bearing with respect to the whole pump system, a mathematical model of the journal bearing is necessary. In many cases basic equations can be gathered by applying the fundamental relations of fluid mechanics, which leads at least to the structure of the model, whereas it is often very difficult to estimate the system parameters. One possible way to overcome this, is to identify the system parameters experimentally in a testrig. This is often done using a-priori knowledge about

the structure of the model. In the case of turbulent journal bearings, the fluid forces can be expressed in a linearised form with stiffness-, damping- and inertia coefficients, as shown in Eq. (6)

$$\begin{bmatrix} F_1 \\ F_2 \end{bmatrix} = \begin{bmatrix} k_{11} & k_{12} \\ k_{21} & k_{22} \end{bmatrix} \cdot \begin{bmatrix} x_1 \\ x_2 \end{bmatrix} + \begin{bmatrix} d_{11} & d_{12} \\ d_{21} & d_{22} \end{bmatrix} \cdot \begin{bmatrix} \dot{x}_1 \\ \dot{x}_2 \end{bmatrix} + \begin{bmatrix} m_{11} & m_{12} \\ m_{21} & m_{22} \end{bmatrix} \cdot \begin{bmatrix} \ddot{x}_1 \\ \ddot{x}_2 \end{bmatrix} \quad (6)$$

A very straightforward way to identify these rotordynamic coefficients is to measure the complex stiffness frequency response functions as it is explained in chapter 4. 2. The testrig that allows such a procedure is shown in Figure 9. The tested bearing is located between two radial AMBs. The rotor is levitated by the magnetic bearings, its static position can be centered or off-centered in the journal bearing. Subsequently, a defined dynamic excitation can be enforced (e.g. small movements in one or two planes, forward or backward whirl, synchronous or non synchronous to rotational speed). This motion causes the above mentioned fluid-structure interactions. The rotor behaves dynamically stiff within the working range so that the displacements and the resulting forces inside the bearing can easily be computed from the displacements and forces measured by the AMB's. The force measurement of the AMB's is based on the Hall Sensor Method (see chapter 4. 3). The Hall sensors are integrated in each magnetic pole of the bearings. The rotor is controlled by a DSP. The actual data analysis and signal processing is performed on an external PC that is connected to the DSP via a serial link. The hydraulic part of the test rig is sealed up by two mechanical seals. The rotor is connected via a flexible membrane coupling to a servomotor. Both of these measures ensure that no additional stiffness or damping is added to the system which would affect the identification in a negative way.

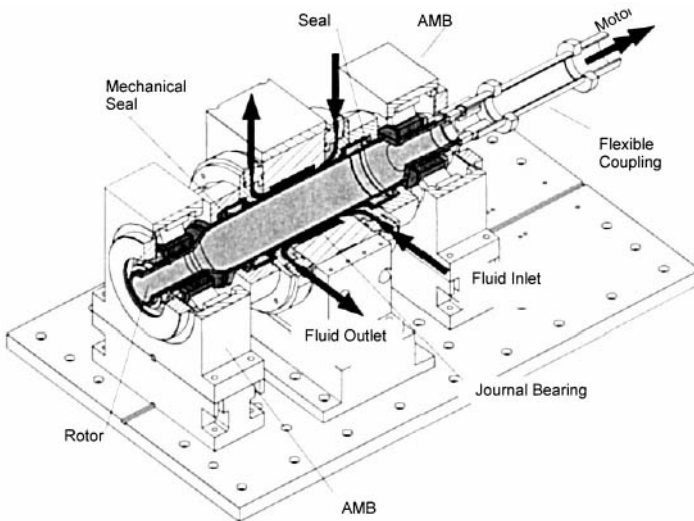


**Figure 9: Designed testrig**

### 5.1.1 Self alignment of the rotor /Auto adjustment

Prior to the actual measurements, the accurate force measurement is used to align the rotor precisely in the journal bearing. This procedure is necessary to compensate the machining tolerance and the temperature expansion of the rotor and the journal bearing housing. The alignment is done automatically. The software routine uses the contact forces, that are generated when the rotor is touching the journal bearing wall in standstill. The actual alignment of the rotor must be performed in four degrees of freedom (see Figure 10). If the rotor is tilted inside the journal bearing, the distances  $a$  and  $b$  are not equal and therefore the AMB forces are different. This difference is used for an iterative routine, whereby the rotor position is altered independently in the two bearing planes until the force difference is within a certain range. Typical contact forces are  $10\text{N} \pm 4\text{N}$ . This procedure is performed around the circumference and leads to measured clearances of the journal bearing. By applying a circle fit, the new nominal positions of the rotor in the AMBs, the actual bearing clearance and the deviation from the circular shape can be derived. The measured clearances and nominal positions are temperature dependent. Experiments showed, that the centre of the journal bearing changes only in vertical direction if the fluid temperature is rising. Both clearance and offset errors are compensated by a fast four point measurement of the journal bearing shape, prior to every new measurement.

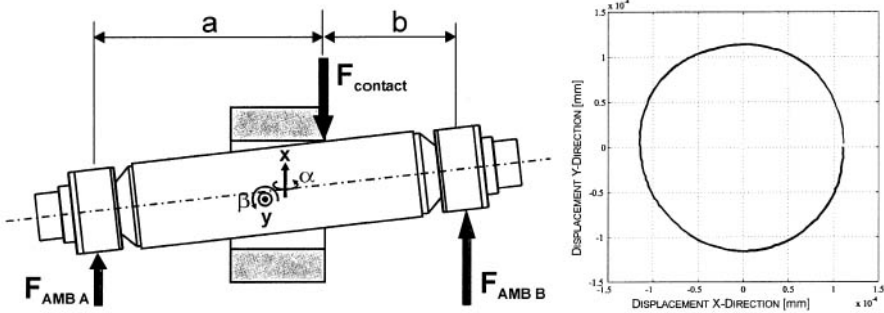
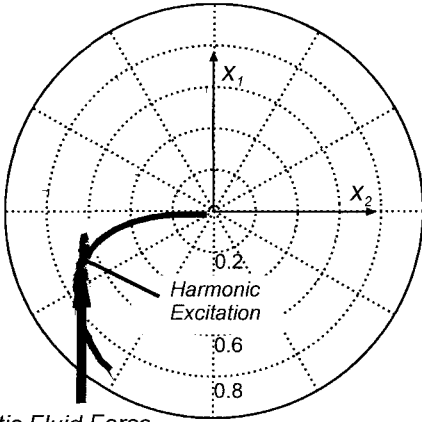


Figure 10: Automated rotor alignment

### 5.1.2 Identification of rotordynamic coefficients

For a given set of boundary conditions (rot. speed, geometry, fluid properties) the static and dynamic properties of the bearings depend mainly on the eccentric position of the rotor. This eccentric position is user defined. The eccentric position of the rotor in the journal bearing causes static hydrodynamic fluid forces, that are compensated by the magnetic bearing. Once the rotor has reached the defined static eccentricity  $\epsilon$ , linearly independent excitation vectors are computed. These harmonic excitations are generated by the AMB's in a stepped sine manner (see Figure 11) and adapted in phase and amplitude, until the measured harmonic displacements reach a certain tolerance [9].



static Fluid Force  
**Figure 11: Identification Technique**

The identification of the force and displacement amplitudes is done in the time domain by fitting artificial harmonic signals in a least square sense. This method has the advantage, that no leakage occurs, that no triggering or windowing is necessary and that it is also valid for very noisy signals. Due to the highly nonlinear static force displacement relation, the excitation amplitude has to be kept as small as possible. This is done by identifying the 1st and the 2nd harmonic of the excitation frequency. The excitation amplitude is automatically reduced if the amplitude of the higher harmonics reaches a defined limit. Typical excitation amplitudes are 3-5  $\mu\text{m}$  (= 2.5 to 4% bearing clearance). The force signals contain also the rotor mass, that can easily be subtracted. Unbalance vibrations do not disturb the measurements, because there is no correlation to the excitation signals.

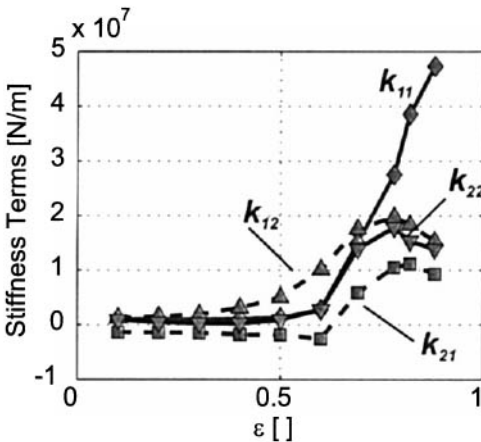


**Figure 12: Identified stiffness coefficients of a turbulent journal bearing (solid lines: diagonal elements, dashed lines: crosscoupled elements)**

With this method various measurements were performed. As an example, Figure 12 shows identified stiffness parameters in dependence of the relative eccentricity  $\epsilon$ . A complete set of rotordynamic coefficients can be found in [10]. For small eccentricities, the parameters remain almost constant. In this range of  $\epsilon$ , the cross coupled stiffnesses  $k_{12}$  and  $k_{21}$  are dominating over the direct stiffnesses  $k_{11}$  and  $k_{22}$ . This is in compliance with common seal theory, where it is assumed, that the certain parameters remain constant until a relative eccentricity of 50% of bearing clearance. For increasing  $\epsilon$ 's, there is a strong rise of the direct stiffness  $k_{11}$ , while  $k_{22}$  and the cross coupled stiffnesses decrease.

## 5.2 Diagnosis of a Centrifugal Pump

Today, monitoring systems are normally not an integral component of turbomachines. With these failure detection systems, the relative and/or absolute motions of the rotor are measured as output signals. After signal processing, certain features (threshold values, orbits, frequency spectra etc.) are created from the measured data. With the deviations of these features from a faultless initial state, the diagnosis attempts to recognize possible faults. The difficulty with these procedures is that the causes of the modifications of the output signals can not be detected clearly. The reason might either be a change of the process or a modification of the system itself.

An improvement of the existing diagnostic techniques can be achieved by using AMBs. They are well suited to operate contactless as actuator and sensor elements in rotating machinery (Figure 13). Consequently, frequency response functions (stiffness or compliance frequency responses) can be determined from the measured input and output signals, of which the physical parameters (mass, damping, stiffness) or modal parameters (natural frequencies, eigenmodes, modal damping) of the system are identified.

A magnetically suspended centrifugal pump (Figure 14) is used to validate and to demonstrate the performance of the developed model based diagnosis methods. The modular concept of the design enables an easy extension of the single-stage to a multi-stage pump system, both of which are subject for investigations.

Within this project several faults in the pump system will be identified. The aim of the project is to find out when a fault occurs and to determine the fault's type, location, and extend.

In general, the faults brought into the system are subdivided in two cases. Faults of type I (see Figure 15) are altering the system matrices. These are for example a crack in the rotor, the wear of the seals, loosening parts, etc. Faults of type II are caused by changing external loads like an increase of the imbalance, cavitation, etc.

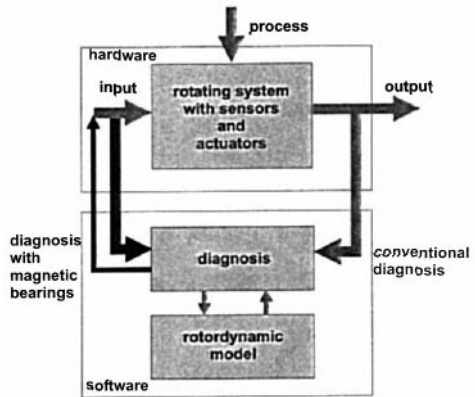


Figure 13: Failure diagnosis with AMB's

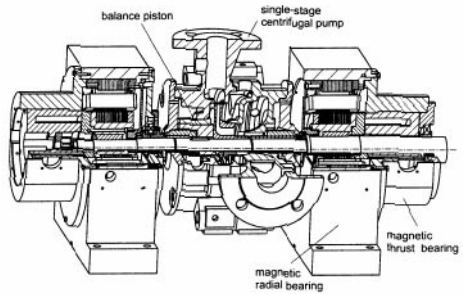


Figure 14: Test rig of the single-stage pump in AMBs.

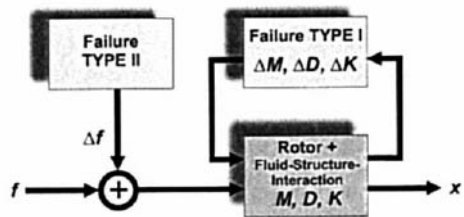
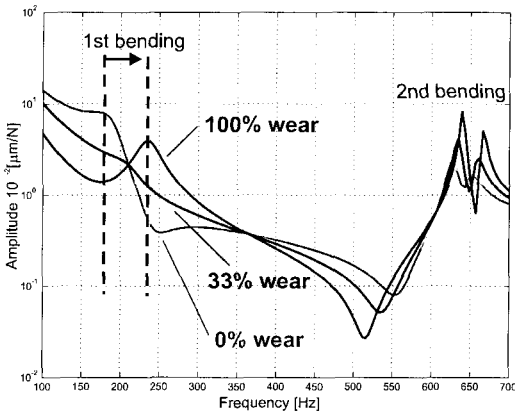


Figure 15: Scheme of the two different fault types being investigated



**Figure 16: Change of the compliance function  $H(\Omega)$  due to different wear states of the balance piston.**

### 5.3 Diagnosis of a High Speed Grinding Process

Internal grinding is applied on products such as outer rings of ball bearings or injection parts of combustion engines (Figure 17). The requirements for this process are very high and contradictory. On the one hand, very high shape and size accuracies as well as surface quality of the work-pieces are demanded. On the other hand short process cycles are wanted due to the mass production.

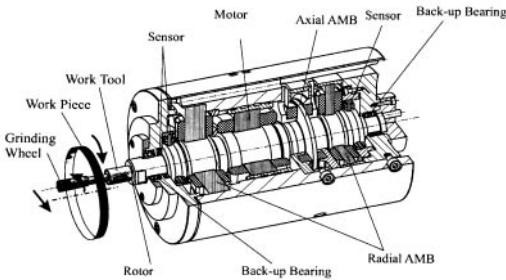


**Figure 17: Machine tool spindle for grinding**

The mean measures which can be taken to met these requirements are the improvement of the bearing system, the process monitoring and diagnosis as well as the process correction with regard of the process optimization [11] [12]. High speed grinding spindles in AMBs are best suited in order to carry out these measures.

Regarding the bearings system they allow high rotational speeds up to 180.000 rpm leading to a decreasing normal process force. The not existing mechanical friction within the bearings permits a long bearing life. Furthermore a high static spindle stiffness can be reached by an appropriate controller design. In Figure 18 a scheme is shown how the AMBs can be applied for the process diagnosis and correction. Using the measured displacement signals and the given control currents supplied by the AMB system the AMBs' forces are obtained and out of it the normal, tangential and axial process forces respectively. The normal process force is the essential quantity for the process diagnosis since it permits a direct conclusion to the process state. Based on the measured and calculated quantities the diagnosis algorithms are carried out to evaluate the process state, for instants with regard of chatter or a broken grinding wheel. Out of the diagnosis procedure or directly out of the signals correction procedures take place in order to optimize the grinding process. In this phase the AMBs are used as actuators to move the spindle to a required position.

Exemplarily, some simulation results of the pump with different worn out states of the balance piston are presented. The different states are a seal with a clearance of 0.2mm (new), 0.3mm (33% wear), and 0.5mm (100% wear). The corresponding mass, stiffness, and damping coefficients for the simulation are calculated using a finite difference program. Based on the models, it is possible to compute the resulting compliance functions  $H(\Omega)$  including the different seal states. Corresponding results are presented in Figure 16. The eigenfrequencies clearly increase with a wearing out piston due to decreasing inertia and damping forces in the seal.



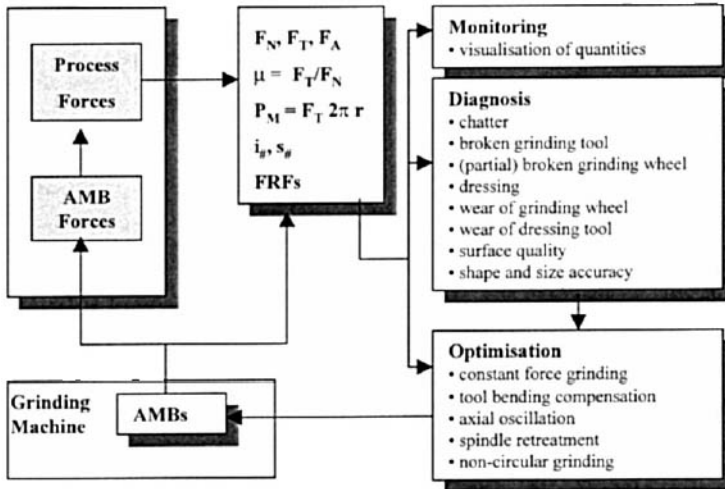


**Figure 18: Process Diagnosis and Correction for a Grinding Process**

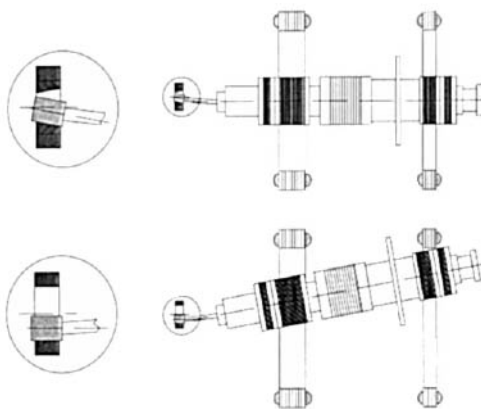


**Figure 19: Correction procedure with AMB's**

One correction procedure is shown in Figure 19. Due to its flexible property the work-tool is bent during grinding leading to a undesirable conical bore shape. By tilting the spindle within the bearings this effect does not take place.

The described concept is developed and tested on a AMB high speed grinding spindle test rig (Figure 17). The rotational speed of the work tool spindle is 120.000 rpm and of the work piece spindle from 1200 rpm up to 3600 rpm. The power of the spindle is 3kW. The maximal allowable grinding force is 110 N.

In the upper diagram of Figure 20 the measured normal process force is depicted. It shows the typical shape of a

grinding cycle. When the work-piece touches the work-tool the process forces begin to increase until it reaches a certain maximum. During this phase the tool is being bent due to its flexible property as shown in Figure 19. In the lower diagram of Figure 20 the curve is zoomed showing the dynamic force out of the out-of-round of the work piece. It decreases while grinding. Then the infeed is stopped to decrease the tool bending and to achieve a cylindrical shape of the bore (spark out phase). Finally, the work-piece is being quickly retreated.

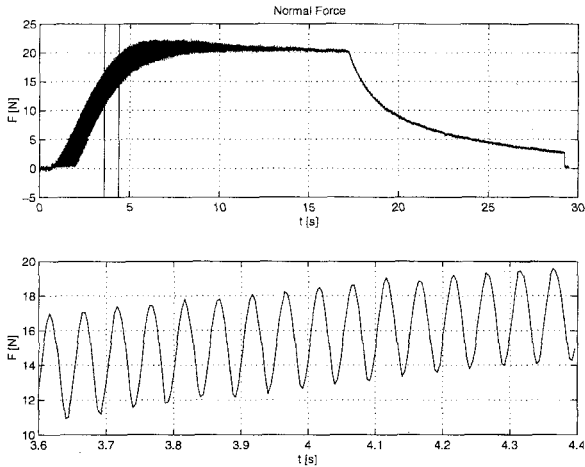


**Figure 20: Normal Process Force**

## 6 CONCLUSION AND OUTLOOK

In this paper a Smart Machine Technology has been presented for rotating machinery with active magnetic bearings. The technology uses parallel informations coming from the system sensors and the mechatronic system model in order to create additional smart features. With the developed tools for modelling, identification, diagnosis and correction it is possible to obtain smart machines with improved performance and higher reliability. The Smart Technology has been successfully applied in three cases of turbomachines and machine tools.

With new developments of hardware components, particularly in the field of microsystems (sensors and actuators) and additional software for new features, the Smart Machine Technology will be further improved and applied in practical rotating machinery.

## 7 ACKNOWLEDGEMENT

The presented paper results out of projects sponsored by the European Community under the Brite/EuRam programme (IMPACT Project No. BRPR-CT97-0544) and by the German Research Council (DFG).

## 8 REFERENCES

- [1] Schweitzer, G., Bleuler, H., Traxler, A.: Magnetlager. Springer Verlag, Berlin Heidelberg, 1994
- [2] Schweitzer G.: Magnetic Bearings as a Component of Smart Rotating Machinery. Proceedings of the Fifth International Conference on Rotor Dynamics IFToMM, Darmstadt, Germany, 1998.

- [3] Nordmann, R., Ewins, D., et al.: IMPACT - Improved Machinery Performance using Active Control Technology, BRITE/EuRam Project No. BRPR-CT97-0544, Start Jan. 1998.
- [4] Gähler, C., and Förch, P.: A Precise Magnetic Bearing Exciter for Rotordynamic Experiments, Fourth International Symposium on Magnetic Bearings, Zürich, Schweiz, 1994.
- [5] Meeker, D.C., Maslen, E.H., and Myounggyu, D.N.: A Wide Bandwidth Model For The Electrical Impedance of Magnetic Bearings, NASA conference publication No. 3336/PT2, 1996.
- [6] Springer, H., Schlager, G., and Platter, T.: A Nonlinear Simulation Model For Active Magnetic Bearing Actuators, Sixth International Symposium on Magnetic Bearings, Cambridge, USA, 1998.
- [7] Förch, P., Gähler, C.: AMB System for Rotordynamic Experiments: Calibration Results and Control, Fifth International Symposium on Magnetic Bearings, Kanazawa, Japan, 1996.
- [8] Knopf, E., and Nordmann, R.: Active Magnetic Bearings for the Identification of Dynamic Characteristics of Fluid Bearings, Sixth International Symposium on Magnetic Bearings, Cambridge, USA, 1998.
- [9] Gaehler, C.: Rotor Dynamic Testing and Control with Active Magnetic Bearings. Diss. Swiss Federal Institute of Technology Zürich. Zürich: 1998.
- [10] Knopf E., Nordmann R.: Identification of the Dynamic Characteristics of Turbulent Journal Bearings Using Active Magnetic Bearings. Proceedings of the 7th International Conference on Vibrations in Rotating Machinery, Nottingham, 2000.
- [11] Hörsemann W.: Hochgeschwindigkeitsschleifen mit aktiv magnetgelagerten Spindeln. Dissertation, Vulkan-Verlag, Essen 1992.
- [12] Ota M., Ando S., Oshima J.: Monitoring and Actuating Function of the Internal Grinding Spindle with Magnetic Bearings. 2nd International Symposium on Magnetic Bearings, Tokyo, Japan, 1990.

© 2000, With Author

*This page intentionally left blank*

# Design guidelines for improved rotating machinery stability

**R G KIRK**

Mechanical Engineering Department, Virginia Tech, Blacksburg, USA

## SYNOPSIS

The past quarter century has been a time of rapid growth in analytical capability for design evaluation of rotating machinery. This growth has been fueled by the power and speed of the personal computer in part, but even more so by the international growth of the field of rotor dynamics analysis. More recently, the speed and wide availability of the internet is giving an even faster mode of communication to discuss and solve problems. The Vibrations in Rotating Machinery conference, organized by the IMECHE, has played a key role in this growth by providing a timely international meeting every fourth year, since commencing in 1976. The opportunity to contribute to this field of study and to see and hear the many papers by other experts, has been an experience that will never be equaled in this field of study. The following discussion and information are a collection of guidelines based in part on information from the papers presented by the author at this and previous Vibrations in Rotating Machinery conferences. Personal experience is also a major factor in these proven guidelines.

## 1 INTRODUCTION

The evaluation of rotating machinery requires the command of several areas of engineering for most all types of machines. Some are more demanding than others. The basic split of machines is between aerospace and land based machinery. Both of these groups are then split into several subgroups. The author has experience in both jet aircraft engine dynamic analysis and land based turbo machinery, but with the majority of work experience and consulting in the turbo machinery branch. Prior to the early 1970's, the ability to compute the stability of multi-mass rotors was not possible as a design tool. Attempts at computing general multi-mass rotor eigenvalues had not been totally successful. The only computation available was the calculation of undamped critical speeds (1) and the elliptic forced response to rotating unbalance (2). Fluid film bearing characteristics were available for certain bearing

types in non-dimensional tables (3) and required hand preparation for use in the forced response analysis.

In the 1970's, the jet aircraft industry was looking at circular damped response to unbalance and was just starting to look at transient response due to blade loss. The damping in jet engines was and continues to come from oil film dampers at most radial roller bearing locations. The analysis of jet engines is complicated by the light weight and flexible supports that carry the rotors. Most engines are multiple rotor design. This adds a degree of difficulty when compared to the majority of land based turbo machinery. In jet engines, a labyrinth seal instability was one where the flexible stator structure of the seal ring would be excited and result in cracking and failure. Future research on labyrinth seal excited instability would address rotor instability in high pressure compressors.

By the early 1980's the bearing properties were being computed on-line from geometry descriptions. The majority of bearings used in high speed flexible rotor designs were tilting pad design radial bearings. By the late 1980's personal computers had advanced to the point that they were used in place of mainframe computers for rotor bearing analysis. A major contribution of the 70's and 80's was the documentation and extension of the analysis of fluid film seals, turbulent seals, and gas labyrinth seals. Another advance made in the 80's was Active Magnetic Bearing analysis and use in industrial machinery. In addition to controller instability, the user must be aware of rotor drop dynamics and the resulting potential high backup bearing loads and heat generation. Papers on most of these topics have been presented by the author of this paper over the past 24 years at the IMECHE Vibrations in Rotating Machinery conference (4 – 12).

The study of rotor instability is predominantly associated with self-excited nonsynchronous vibration. Motion is usually subsynchronous and closely matches the rotor first bending critical speed. The study of self-excited synchronous vibration has recently become of increasing interest in industrial turbomachinery. Synchronous instability resulting from rotor seal rubs or light rotor stator contact is well documented in the literature (13). The light rubbing can put excessive heat into a small sector of the shaft, resulting in a rotor thermal bow and either increasing or decreasing vibration, depending on the rub position, the rotor mode shape, and whether operation is above or below the dominant mode of vibration. These rubs are typically inboard of the main bearings and outward spiraling vibration occurs for operation below the critical speed and inward spiraling vibration for operation above the critical speed.

In 1933, D.M. Smith (14) reported on an investigation of stability of flexible rotors. In 1974, 41 years later, D.M. Smith (15) again reported on an investigation of stability problems but this time it was synchronous whirl in turbine and generator rotors. His theory of coupled blade, torsional, and lateral criticals was presented to explain how it may be possible for turbines to have this form of instability, but no answer was given that explained why the generators were also synchronously unstable. He did however, report that increasing the bearing clearance reduced or eliminated the synchronous instability in at least one case, when normally reducing the clearance was the fix for oil film instability.

Within the last decade much interest has been shown in the area of thermal bending in overhung rotors. Recent theoretical (16) and experimental (17,18) studies have focused on this problem. So far, most of the theoretical work has been done using complex analysis, and

almost no comparison between experimental and theoretical research has been made. This paper develops a simple model of rotor thermal bending without using complex analysis. This model is then compared with a more rigorous theoretical model and with an experimental study.

This phenomenon is primarily due to a temperature difference developing across the shaft. The temperature difference can either be caused by the rotor shaft rubbing against stationary components or by viscous shearing within the lubricant at a bearing or liquid seal location. The former mechanism was first noticed by Newkirk in 1926 and later analyzed by Dimarogonas (13). This mechanism is called the Newkirk Effect. The latter mechanism has recently been studied (16,17,18) and is often referred to as the Morton Effect.

Another form of self-excited transient response occurs under the condition of blade loss, or suddenly applied imbalance (12,19). The maximum transient response ratio to the steady-state conditions has an interesting characteristic. The accepted ratio of two occurs below the critical but a ratio of  $N/N_{cr}+1$  occurs for supercritical operation. The exact critical speed, however, does not experience any additional amplification.

The Morton Effect occurs when the journal is executing a synchronous orbit around the bearing center. This centered orbit causes one portion of the journal surface to always be at the minimum film thickness, while a diametrically opposite section of the journal surface is always at the maximum film thickness. Lower film thickness areas are generally associated with higher viscous shear stresses which produce higher temperatures. As a result, a hot spot will develop on the journal surface exposed to the minimum film thickness region and a cold spot will be formed on the surface at maximum film thickness. This leads to a temperature gradient developing across the journal. Such a gradient creates a thermal unbalance which is in the direction of the temperature gradient. Thermal bending will then occur if the resultant of the thermal unbalance and the overhung mechanical unbalance is adequate. Under these conditions the bent shaft will decrease the bearing clearance and elevate the thermal gradient. The increased temperature gradient will then initiate more thermal bending. These actions describe a positive feedback mechanism which will drive the system unstable. The response of a turbocharger undergoing the Morton Effect is shown in Fig. 1 ( taken from reference (18) ).

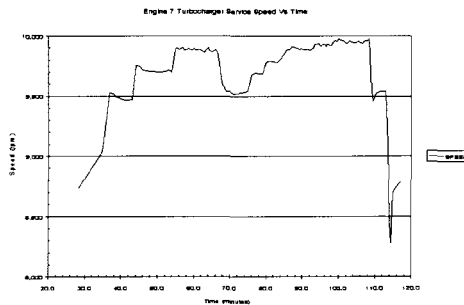


Fig. 1-a Measured Service Speed vs. Time for Modified Upgrade Turbine

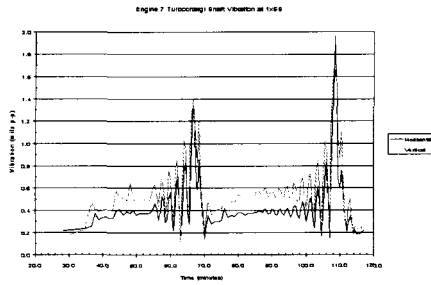


Fig. 1-b Measured Shaft Amplitude vs. Time for Modified Upgrade Turbine

## 2 GUIDELINES FOR ROTATING MACHINERY DESIGN

The design of machinery requires the cooperation of both mechanical and aerodynamic engineers to achieve an efficient and dynamically stable machine. The guidelines given below for stable design practice have evolved over the past 30 years and are a brief summary of things learned from applied industrial experience in rotor dynamics of rotating machinery. The guidelines are mostly relating to land base machinery.

### 2.1 Basic Rotor Construction

Rotors for compressors and multistage centrifugal pumps are usually built with stacked disk on shaft construction. Steam turbines are either disk on shaft or solid rotor construction. Power turbine and expander rotors can be center or multiple tie bolt design. Axial compressors are typically multiple tie bolt design. If the rotor stiffness is much less than the bearings, it should be clear that the damping will not be effective from the bearings. The general exception to this rule is multistage centrifugal pumps, where the eye wearing rings act like additional bearing supports due to the resulting turbulent seal stiffness and damping.

Impellers should be shrunk on the shaft with a differential fit to better insure that the shaft will not bow due to a hung fit on the impeller bore during transient operation. Fits should be relieved in the center and one tight and one loose or line to line fit applied. This usually requires a vertical stacking of the rotor. Similar caution applies to spacers, balance drums, and thrust collars.

Tie bolt attachment of turbine or expander disks requires a snap fit. Thrust pins or keys placed in the axial face can fight the primary fit and cause massive disk eccentricity and imbalance.

The rotor should be stack balanced adding no more than two components at a time, and final balanced in a high speed vacuum chamber if available. Solid rotor construction has many advantages in regard to rotor thermal stability for axial flow machinery.

Extreme caution is required for mid-span only, high speed balancing of flexible shaft rotors that have overhung elements such as thrust collars, trip bolt mechanisms, or coupling hubs.



## 2.2 Critical Speed Placement

The most basic analysis of rotating machinery is the undamped critical speed map. An example is shown in Figure 2.

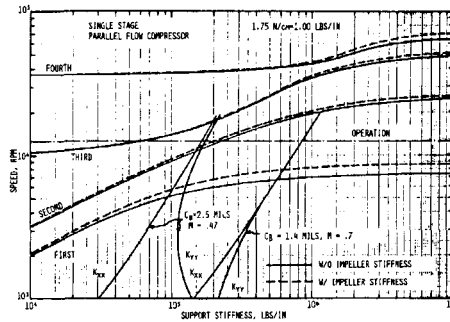


**Figure 2 Classical Critical Speed Map for Zero Damping**

**Table I Guidelines for Critical Speeds**

- cross 1-st  $N_{cr}$  at no more than 98% of  $N_{cr}$ -rigid
- cross 2-nd and 3-rd modes on the ramp portion of the critical speed map
- never cross any mode on a flat region of a mode
- max amplitude of a mode shape to bearing amplitude ratios of less than 10 is desirable and less than 5 would be even better
- consider both static stiffness and dynamic stiffness for the bearing characteristics
- degrade bearing stiffness for support stiffness influence

More advanced damped critical speed and stability calculations can be evaluated as a result of many advances in analysis and computers since 1972 ( 20 – 24).

## 2.3 Bearing Design

Rotors running below 6000 rpm could use a fixed geometry bearing design. Some form of stabilizing feature would be required in the higher end of the speed range. Taper land pockets are often used and offset halves are also popular. It is also true that small fast machinery for plant air service, are designed with fixed geometry bearings (25-26). In addition, small high speed turbochargers are designed with a floating bush bearing. A few basic guidelines are given in Table II for standard machinery bearing design.

**Table II Bearing Design; Fixed Geometry Inserts**

- taper land or double pocket recommended
  - preload of 50%, i.e., undercut equal to radial clearance
  - 90 % offset for 3 taper land design
  - clearance of 1.25 - 1.75 mils / inch of journal diameter
  - babbitt thickness of 40 - 60 mils
  - L / D ratios of 0.6 to 0.8 typical
- Note: 1 mil =  $25.4 \times 10^{-6}$  meter

For rotors running above 6000 rpm, a tilting pad design is usually preferred by the designer (27). In fact, many machines that could run on fixed geometry bearings are designed with tilting pads to satisfy customer specifications. Guidelines for tilting pad bearings are listed in Table III.

**Table III Bearing Design; Tilting Pads**

- 5 pad standard, 4 pad acceptable
- a pad preload of 40 - 60 % is recommended
- 55 - 60 % offset for cooler bearing and increased load capacity, but design is rotation sensitive
- clearance of  $((1 \text{ mil} / \text{inch}) + 1)$  mils on diameter with a tolerance of  $-1/2$  and  $+1 1/2$  mils
- babbitt thickness of 40 - 60 mils
- L / D ratios of 0.4 to 0.6 typical, square pad projected area is good !
- DO NOT ATTEMPT TO STABILIZE A MACHINE BY ONLY CHANGING THE BEARING PRELOAD BY A SMALL AMOUNT !!

## 2.4 Forced Response

A major analysis in design of rotating machinery is the forced response to imbalance. The sensitivity can be verified by test stand operation. Known imbalance weights can be applied, usually to the coupling flange. Basic guidelines are given in Table IV.

**Table IV Forced Response**

- keep peak response speeds at least 15% below and 20% above the design speed range.
- amplifications can be computed by the half power point method or the phase slope method
  - $A = Ncr / \Delta \omega$  at  $.707 \times$  peak amplitude
  - $A = (\pi / 360) \times (\Delta \Phi / \Delta N) \times Ncr$
- 0.1 g loading from  $(56,347 \times W / Nrpm^2)$  oz-in
- amplitude limit of  $\sqrt{12000 / Nrpm}$  in mils
- suggested limit of 1 mil for machines over 12000 rpm and less than 50000 rpm
- warning at 50 % of bearing clearance and shut down at 70 % of clearance

## 2.4 Seal Design

The design of centrifugal compressors usually requires either a gas or oil seal to seal the process gas. The standard floating ring seal is still used in many applications and must be designed with caution (28-29). Pump wear rings and balance drums are usually turbulent and require a special analysis (30-32). The suggested rules given in Table V are a starting point for oil seal designs.

The impeller labyrinths and the balance drum labyrinth seal are major contributors for compressor rotor instability (33-34). After the mid 1980's, the ability to add this important influence to compressor design allowed the designer to better predict the machine full load stability (see Table VI).

**Table V Oil Seals**

- use  $0.05 < L / D < 0.25$
- clearance of 1.0 - 1.5 mils / inch of diameter
- lapped face width of 0.1 - 0.25 radial
- use non-cavitated 360 deg journal bearing theory as an approximation with average temperature viscosity
- computer automated solution is recommended
- DO NOT over balance the axial pressure loading which will result in seal ring instability
- use adequate grooves in bore of seal ring for stability
- if speed ratio is less than  $2.2 \times N_{cr}$ , seals are your friend
- if speed ratio is over  $2.2 \times N_{cr}$ , expect instability

**Table VI Labyrinth Seals**

- use proven analysis to obtain Q-effective
- excitation will most always drive the rotor in forward whirl
- note for aerodynamic excitation
  - turbines --- forward whirl instability mechanism
  - compressors -- backward whirl instability mechanism
- tooth chamber volume, tip clearance, total length, and diameter are critical to good design
- entry swirl is key to proper prediction of stability
- balance piston and last stages are critical elements of a proper stability design evaluation for centrifugal compressors

## **2.5 Coupling Design Guidelines**

A suggested design procedure for preliminary selection of couplings is summarized as follows:

1. Size coupling for torque capacity requirements.
2. Check placement of spacer  $N_{cr}$ .
3. If the spacer is in the satisfactory region given in Figure 3 (Zones I and II, and the upper part of Zone III) for each of the adjoining machines journal reaction ratio,  $\frac{1}{2} W_{cplg}/W_{journal}$ , the design specifications need not require a train analysis.
4. If the design falls in the marginal region of Figure 3, a train or partial train analysis should be performed for test stand and field conditions if the spacer cannot be redesigned to move into the satisfactory region.
5. If the design falls in the unacceptable region the coupling spacer should be redesigned to move the calculated critical as far as possible toward the satisfactory zone, analysis being made as noted above.
6. Coupling designs that are below the marginal zone of Figure 3 should not be accepted for Turbomachinery application.
7. Coupling spacers should be designed to have a critical speed ratio of 2.0 or larger. Smaller ratios may be acceptable if adequate analysis is conducted to assure an insensitive design as outlined in this paper.
8. Design features of gear couplings should preclude the admission of oil into the spacer tube.
9. Gear couplings should be designed to have a minimum increase in mesh tip clearance at design speed and temperature.

10. Turbomachinery conditions having low horsepower requirements and utilizing gear couplings are particularly susceptible to larger than normal imbalance levels on the coupling due to spacer throwout.
11. Long spacer couplings having a critical speed ratio less than 2.0 should have at least three planes for balance correction.
12. Attention to proper material processing and heat treatment is essential in addition to the above considerations.

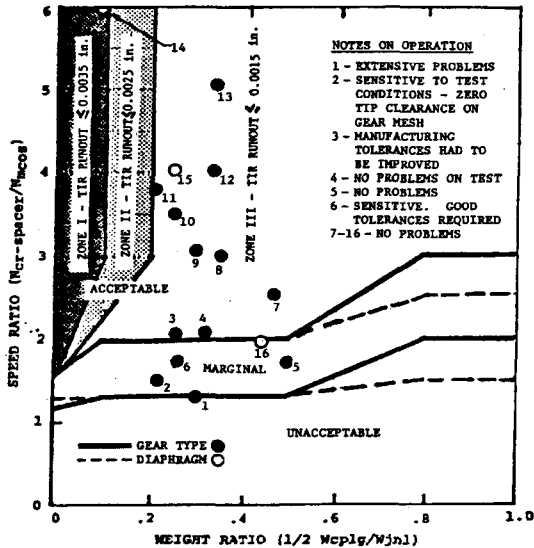


Fig. 3 Chart for coupling selection, showing degree of acceptability with overhung turbomachinery. Zones indicate runout level of balance bands relative to the mounting bore or rabbet fit. Experience over-plotted (taken from ref (35)).

### 3 CONCLUSIONS

The optimum design of rotating machinery is a complicated process and cannot be taught in a single technical paper or short course. The collection of personal experience of several engineers plus the latest state of the art computer analysis capabilities is an excellent starting point. Every machine is a new learning experience in almost every instance of the authors experience. The challenges are many, much is known, all the problems are not solved and the rewards are great for those that decide to accept rotating machinery as their expertise.

### REFERENCES

- 1 Prohl, M. A., "A General Method for Calculating Critical Speeds of Flexible Rotors," *Journal of Applied Mechanics, ASME*, Vol. 67, 1945, pp. A-142-A-148.

- 2 Lund, J.W., "Rotor-Bearing Dynamics Design Technology, Part V," Technical Report AFAPL-TR-65-45, Aero Propulsion Laboratory, Wright-Patterson Air Force Base, Ohio, May, 1965.
- 3 Lund, J.W., "Spring and Damping Coefficients for the Tilting-Pad Journal Bearing," ASLE Transactions, vol 7, no 4, pp 342-352, 1964.
- 4 Kirk, R. G., "The Impact of Rotor Dynamics Analysis on Advanced Turbo Compressor Design," I.Mech.E. Symposium, Vibration in Rotating Machinery, Churchill College, University of Cambridge, September 1976.
- 5 Kirk, R. G., and J. C. Nicholas, "Analysis of High Pressure Oil Seals for Optimum Turbo Compressor Dynamic Performance," Vibration in Rotating Machinery, I.Mech.E. Proceedings of Cambridge Conference, 1980.
- 6 Kirk, R. G., "Insights from Applied Field Balancing of Turbomachinery," Proceedings of I.Mech.E. Conference on Vibrations in Rotating Machinery, 1984.
- 7 Kirk, R. G., J. F. Hustak and K. A. Schoeneck, "Analysis and Test Results of Two Centrifugal Compressors Using Active Magnetic Bearings," Vibrations in Rotating Machinery, I. Mech. E. Proceedings of 4th International Conference, Edinburgh, Sept. 1988, pp. 93-100.
- 8 Kirk, R. G., "Evaluation of Liquid and Gas Seals for Improved Design of Turbomachinery," Vibrations in Rotating Machinery, I. Mech. E. Proceedings of 4th International Conference, Edinburgh, Sept. 1988, pp. 387-394.
- 9 Kirk, R. G., and E. E. Swanson, "Experimental Evaluation of Fluid-Film Bearings Using Electro-Magnetic Shaft Loading," International Conference on Vibration in Rotating Machinery, Bath, England, Sept 1992.
- 10 Kirk, R. G., and S. K. Baheti, "Analytical Evaluation of Taper Bore Grooved Liquid Ring Seals," IMechE International Conference on Vibrations in Rotating Machinery, Oxford, Sept. 9-12, 1996, pp 225-234.
- 11 Swanson, E.E., K.V.S. Raju, and R. G. Kirk, "Test Results and Numerical Simulation of AMB Rotor Drop," IMechE International Conference on Vibrations in Rotating Machinery, Oxford, Sept. 9-12, 1996, pp 119-132.
- 12 Kirk, R. G. and Avinash Balbahadur, "Thermal Distortion Synchronous Rotor Instability," accepted for presentation and publication, Proceedings of Vibrations in Rotating Machinery, IMECHE, University of Nottingham, Sept. 12-14, 2000.
- 13 Dimarogonas, A.D., 1973, "Newkirk Effect: Thermally Induced Dynamic Instability of High-Speed Rotors", ASME paper, 73-GT-26, p. 2-11.
- 14 Smith, D. M., "The Motion of a Rotor Carried by a Flexible Shaft in Flexible Bearings," Proceedings of Royal Society, Series A, Vol. 142, 1933, p. 92.
- 15 Smith, D.M., *Dynamics of Rotors*, Lyngby Symposium, Springer-Verlag, 1975, pp 524-545.
- 16 Keogh, P.S. and P.G. Morton, 1994, "The dynamic nature of rotor thermal bending due to unsteady lubricant shearing within bearing", *Proc. R. Soc. Lond. A*, 445, p. 273-290.
- 17 deJongh, F.M. and P.G. Morton, 1994, "The synchronous instability of a compressor rotor due to bearing journal differential heating", ASME paper, 94-GT-35, p. 1-13.
- 18 Faulkner, H.B., W.F. Strong and R.G. Kirk, 1997, "Thermally induced synchronous instability of a radial inflow overhung turbine, part II", DETC97/VIB-4174, Proceedings of DETC'97, 1997 ASME Design Engineering Technical Conferences, September 14-17, Sacramento, California, p. 1-5.
- 19 Kirk, R. G. and D. H. Hibner, "A Note on Blade Loss Dynamics of Rotor-Bearing Systems," *Trans ASME, J. Engrg. for Industry*, v98, 2, 1976, pp. 497-504.

- 20 Ruhl, R. L., and Booker, J. F., "A Finite Element Model for Distributed Parameter Turborotor Systems", *ASME, Journal of Engineering for Industry*, Series B, 1972, pp. 128-132.
- 21 Lund, J. W., "Stability and Damped Critical Speeds of a Flexible Rotor in Fluid-Film Bearings," *ASME Journal of Engineering for Industry*, Series B, Vol. 96, No. 2, 1974, pp. 509-517.
- 22 Bansal, P. N., and Kirk, R. G., "Stability and Damped Critical Speeds of Rotor-Bearing Systems," *ASME Journal of Engineering for Industry*, Vol. 97, No. B4, 1975, pp. 1325-1332.
- 23 Barrett, L. E., Gunter, E. J., Allaire, P. E., "Optimum Bearing and Support Damping for Unbalance Response and Stability of Rotating Machinery," *Trans. ASME, Journal of Engineering for Power*, Vol. 100, No. 1, 1978, pp. 89-94.
- 24 Kirk, R.G., "Stability and Damped Critical Speeds : How to Calculate and Interpret the Results," *CAGI Technical Digest*, Vol. 12, No. 2, 1980, pp. 375-383.
- 25 Nicholas, J. C., and R. G. Kirk, 1979, "Selection and Design of Tilting Pad and Fixed Lobe Journal Bearings for Optimum Turbo-Rotor Dynamics," Texas A&M Turbo-Machinery Symposium, Nov.
- 26 Nicholas, J. C., and R. G. Kirk, 1981, "Theory and Application of Multi-Pocket Bearings for Optimum Turbo Rotor Stability," *ASLE Transactions*, Vol. 24, No. 2, pp. 269-275.
- 27 Nicholas, J. C., Gunter, E. J., and Allaire, P. E., "Stiffness and Damping Coefficients for the Five Pad Tilting Pad Bearing," *ASLE Transactions*, 22(2), pp 112-124, 1979.
- 28 Miller, R. E. and R. G. Kirk, "The Influence of High Pressure Oil Seals on Turbo-Rotor Stability," *ASLE Transactions*, Vol. 22, No. 1, Jan., pp. 14-24, 1979.
- 29 Kirk, R. G. and S. K. Baheti, "Design of Liquid Seals for Centrifugal Compressors," *ASME Trans, Journal of Vibration and Acoustics* Vol. 121, 1, pp. 131-136, 1999.
- 30 Black, H. F., and Jenssen, D. H., "Dynamic Hybrid Bearing Characteristics of Annular Controlled Leakage Seals," *Proc. of the Inst. of Mech. Eng.*, 184, 3N, pp 92 – 100, 1970.
- 31 Childs, D. W., "Finite-Length Solutions for Rotordynamic Coefficients of Turbulent Annular Seals," *ASME Jour of Lubr. Tech.*, 105,3, pp 437-444, 1983.
- 32 Wilkes, K. W., R. G. Kirk, and D. A. Elrod, "Rotordynamics Analysis of Circumferentially Groomed Turbulent Seals: Theory and Comparison to Published Test Results," *STLE Tribology Transactions*, Vol. 36, No. 2, pp. 183-192, 1993.
- 33 Kirk, R. G., "Evaluation of Aerodynamic Instability Mechanisms for Centrifugal Compressors -- Part I: Current Theory," *ASME Journal of Vibration, Acoustics, Stress, and Reliability in Design*, Vol. 110, No. 2, April , pp. 201-206, 1988.
- 34 Kirk, R. G., "Evaluation of Aerodynamic Instability Mechanisms for Centrifugal Compressors--Part II: Advanced Analysis," *ASME Journal of Vibration, Acoustics, Stress, and Reliability in Design*, Vol. 110, No. 2, April, pp. 207-212, 1988.
- 35 Kirk, R.G., R. E. Mondy and R. C. Murphy, "Theory and Guidelines to Proper Coupling Design for Rotor Dynamics Considerations," *ASME Journal of Vibration, Acoustics, Stress and Reliability in Design*, Vol. 106, No. 1, Jan. 1984, pp. 129-138.

# The estimation of foundation parameters and unbalance

A W LEES, S EDWARDS, and M I FRISWELL

Department of Mechanical Engineering, University of Wales Swansea, UK

## ABSTRACT

*A blade loss on a large turbo-generator unit has been studied in order to validate an identification methodology incorporated in the program SIMFONE. The identification techniques use measured pedestal responses and models of the rotor and bearings to estimate a foundation model and unbalance force. The approach employed is described, and practical issues discussed. The change in unbalance between the two runs was identified and compared to the actual unbalance due to the blade loss. The position and magnitude of the unbalance were accurately predicted. The parameters obtained are physically reasonable and this gives confidence for the application of the approach.*

## 1 INTRODUCTION

The analysis of the vibrational behaviour of turbomachinery is a topic of great importance in most process industries and particularly in power generation. Apart from the need to design machinery to operate within acceptable limits, dynamic models are now used to great effect in the diagnosis of operational difficulties. With the high returns from modern plant there is an increasing need to develop reliable plant models for fault diagnosis, and, as reported by Lees and Simpson (1), the models are not yet developed to the stage of being applicable with confidence across a full range of plant problems.

A number of authors (2, 3, 4) have addressed this problem in recent years and the conclusion is that at present the supporting structure of a large turbine presents a significant problem, having a significant effect on the machine dynamics. Over the past 30 years there has been a strong trend towards the use of flexible steel supports for large turbines as this approach offers a number of practical advantages, not least the cost of fabrication. However this does highlight the importance of the supporting structure.

Lees and Simpson (1) discussed the modelling of this type of structure: in principle it should be possible to develop a suitable model from finite element techniques, but there are a number of practical difficulties. It is often found that similar units, built to the same drawings, display substantially different vibrational behaviour. The different vibrational behaviour is mainly due to small changes in a huge number of joints, that combine to give a substantial change in

stiffness of the structure. With these difficulties it is unlikely that the techniques of finite element model updating (5) could be used, as there are too many uncertain parameters in the joints. The most promising avenue is to identify a model of the foundations directly from measurements.

With these considerations in mind, it appears that substantial plant measurements are required to adequately characterise the dynamics of a foundations. Several exercises of this type have been carried out, for example Pons (6). However, such measurements are very costly in terms of time during which the generating plant is unavailable. Furthermore, the ideal state would be for the turbine to be fully assembled with casings but without the rotor - a state which is not normally available. It has not been considered a cost effective solution to the problem to carry out such trials on machines in the UK. Thus this paper considers the identification of the foundation properties of turbo-generators based on limited measurements on the fully assembled machine.

This paper summarises the issues involved in the identification approach, and demonstrates the method on a real machine. The theory and further examples are available in published papers, for example (7, 8, 9, 10).

## **2 RESPONSE MEASUREMENTS**

The response of the turbo generator mounted on the foundation may be measured using a range of transducers. For identification of the foundation model the general aim should be to measure as many variables as possible. All information is useful and may be used to reduce the uncertainty in the identified model. The minimum measurements should consist of the response at the pedestals, often measured using accelerometers. These measurements should be taken at a position close to the bearings, so that the data represents the response at the foundation side of the bearing housing. The identified model will then produce a dynamic stiffness of the foundation at the bearing housing. Ideally, the response in both the vertical and horizontal directions at all the bearings should be measured. If this is not possible, due to financial constraints, inaccessibility or transducer faults, then the measurements and the resulting foundation model will be incomplete.

The measurement of response data during run-downs is well established and equipment to generate the information in the frequency domain readily available. The important difference between the techniques used for run-downs and those used in general vibration analysis is the use of a variable sampling rate that is referenced to the shaft speed. Recently techniques using a constant sampling rate, and digital resampling of the resulting signals, have become practical. The total length of the sampling interval must be chosen as a compromise between the stationarity of the signal and the averaging of random noise. The analysis estimates the response assuming that the rotational speed is constant. Thus the sample time should be relatively short so that this assumption does not introduce large errors. A long sample time is required to average out the background broadband noise.

## **3 FORCING BY UNBALANCE**

The normal operation of a machine usually involves running at a single speed. Any unbalance, asymmetries or bearing non-linearities produce forces, and hence responses, at the rotational speed and the harmonics of this speed. Data from normal running may be used to identify foundation models at the running speed, and possibly its harmonics, but these data



will provide no useful information at other frequencies. Since applying external excitation is often impractical the unbalance response during either a run-down or a run-up is used. Any unbalance on the rotor, or known asymmetries, will provide forcing to the rotor causing the machine to respond. The major difficulty is estimating the unbalance force or the force produced by the asymmetry. During a balancing exercise known unbalance is placed on the rotor and run-downs performed. Given data from two run-downs, where the only difference is the addition of a known out of balance, then the responses may be subtracted to give the response to the known unbalance. This assumes that the machine behaves linearly, which is very likely to be justified for small mass additions. More serious is the assumption that the machine properties haven't changed between the two runs. Environmental factors, particularly temperature, would be difficult to control and may introduce large errors. There is also the problem that the response measurements are not taken at predetermined frequencies, but at frequencies determined by the rate of the run-down. The two run-downs would be at approximately the same rate, but they are unlikely to be equal. Thus interpolation would have to be used to generate sets of data at a common set of frequencies. The alternative is to estimate the unbalance force directly from the single run-down (9, 10).

#### 4 MODELLING

The aim is to model the foundation of the machine based on the response measurements. An initial assumption is that we have a good model of the rotor and an 'adequate' model of the bearings. Identification of the complete machine is possible, based on the excitation by a known force. By assuming we have models of the rotor and the bearings, the number of parameters to identify may be reduced, and thus the quality of the foundation model is improved. Also, to enable the location of faults in the rotor, it is desirable to separate the rotor/bearing model and the foundation model.

The rotor is relatively easy to model. Analysis packages are available to produce a model and to perform analysis and model reduction (11, 12). Experiments may be performed on the free-free rotor to validate the analytical model, or indeed provide an experimental modal model that may be used in the analysis. Such experiments performed on real rotors have produced natural frequency results with a 1-2% difference to those produced by analysis. These considerations lead to the conclusion that the rotor may be assumed to be modelled accurately, particularly when compared to the models of the bearings and foundations.

The models of the dynamics of journal bearing are much less accurate than the rotor models. Given the physical dimensions of the bearing, the properties of the oil and the load that the bearing carries, reasonable approximations for the linearised damping and stiffness coefficients may be calculated from the fluid dynamic equations (13). These coefficients are dependent on the rotational speed and this may cause significant problems for some procedures that try to identify the bearings and the foundation at the same time. The foundation will be approximated closely by a linear, reduced order model, either in terms of mass, damping and stiffness matrices, or in terms of a modal model or a frequency filter model. There is no guarantee that the bearing properties will be adequately represented by such a model, although recent work on replacing frequency dependent bearing models with higher order models with internal, fictitious degrees of freedom has shown some promise (14). Given an estimate of the bearing properties it is possible to apply the identification techniques to the foundation alone, but the estimated parameters should be robust with respect to errors in the bearing parameters. This is most important, as the combination of a relatively

inaccurate bearing model, and an uncertain static load, may lead to large errors in the assumed bearing properties.

## 5 THE IDENTIFICATION OF A FOUNDATION MODEL

The most attractive option to determine the foundation's dynamic properties is to estimate the total force that is applied to the foundation. If a known excitation is applied then this force arises from a combination of the known force and the force produced by the rotor and applied via the bearings. Although it is possible to estimate a complete dynamic model directly from the measured frequency response functions in this case, the effect of the rotor and bearings must be removed from the complete model to estimate the foundation model.

Lees (2) outlined a method to estimate the forces exerted on the foundation at the bearings, using the response of the foundation due to a known unbalance on the rotor. A complete analysis of this method was given by Lees and Friswell (9) and Smart *et al.* (7, 8), and is not repeated here. Given a model of the rotor and bearings, the force may be estimated given the set of measured pedestal responses. The sensitivity of this force estimate to uncertainties in the bearing stiffness has been studied by Lees and Friswell (15). When the bearing is substantially stiffer than the foundation, errors in the force estimate are restricted to a limited and predictable part of the frequency range. The problem frequencies are near the resonant frequencies of the rotor and bearing system mounted on rigid pedestals. Note that if the bearing parameters are speed dependent these resonant frequencies will change with speed, and these problems may not be encountered. Also the situations of greatest practical interest are those in which the foundation is very flexible compared to the bearing, thereby exerting a significant influence on the behaviour of the machine.

Once the force applied to the foundation through the bearings has been identified, a parameter based model of the foundations may be estimated. The dynamic stiffness cannot be estimated as a *frequency dependent matrix*, because a *complete set of independent forces applied at the bearing pedestals* is not available. The alternative method to obtain a model is to assume a *parametric representation of the foundation model* and to identify the unknown parameters. The basis of the measured data is the motion of the bearing pedestals, which is normally measured in only one direction. However the analysis is equally valid in either one or two dimensions.

The form of the foundation model may involve mass, damping and stiffness matrices, or alternatively a general frequency filter model. The latter is most useful when the number of modes of the foundation that are excited is much larger than the number of measured degrees of freedom. Feng and Hahn (4) solved this problem by splitting the frequency range, where each sub-range contained fewer modes of the foundation than the measured degrees of freedom. The situation with large turbo-generators is not so bad, as the number of measured degrees of freedom is quite high compared to the number of modes of the foundation that are excited. With frequency filter models the order of the model must be selected with care to ensure a robust estimated model (8). Smart *et al.* (8) also discuss the regularisation of the estimation procedure.

The alternative is to define the output residual, which is essentially the error between the pedestal response measurements and the predictions of these quantities from the model. This residual is a non-linear function of the parameters, however the penalty function is a direct measure of the quantities that are required to be reproduced. Also any degrees of freedom that are not measured are simply not compared in the residual, and so incompleteness can be dealt

with relatively simply. However the quality of the estimated parameters is considerably reduced if too few responses are measured. Any non-linear optimisation method may be used to estimate the parameters but the usual problems occur, namely the optimisation is computationally intensive (especially for models with a large number of bearings) and convergence to a global minimum is not guaranteed. A good estimate of the parameters from the linear estimation procedure is invaluable.

Both the linear and non-linear foundation model estimation algorithms, together with facilities for regularisation and order selection, have been implemented in MATLAB, as a package called SIMFONE. The unbalance force, in conjunction with a linear foundation model, may also be estimated. This software is described more fully, and demonstrated on a real machine, in the next section.

## **6 A PRACTICAL EXAMPLE USING SIMFONE**

During development of the SIMFONE package, several sets of both simulated and test-rig data were used in order to check the various features of the program. This allowed validation of the foundation and unbalance estimates, since these parameters were already known, and allowed quick calculations to be performed, due to the relatively small sizes of these models, and the corresponding amounts of data. It should also be noted that the model needed to represent a real machine's foundation is necessarily much more complicated than that used for a small test-rig: it was therefore felt that a calculation using real turbogenerator data would provide a demanding test of SIMFONE's ability to predict unbalance and foundation parameters. Such a calculation was recently made possible, with the provision of two sets of run-down data taken from a 250 MW turbogenerator, which suffered the sudden loss of several turbine blades. One run-down was performed shortly after this event, and another run-down some 5 months previous was also provided. The aim of this test was to estimate the flexible foundation model, and to predict the location, magnitude and phase angle of the change in unbalance in the shaft line.

### **6.1 Preparing the Data**

The turbogenerator rotor model supplied for the analysis contained a total of 10 measurement positions: front and rear bearings on the high-pressure turbine (HP), low-pressure turbines 1-3 (LP1, LP2 and LP3) and the generator (GEN). The bearing geometry and parameters were supplied together with the rotor model, and linearised speed-dependent bearing parameters were then automatically calculated by SIMFONE. Although 16 measurement channels were supplied in the run-down data, the bearing displacements measured on the exciter and governor, as well as the HP shaft eccentricities, were redundant in this case, since these items were not included in the rotor model. Had a more complete model of the shaft-line been made available, then use could have been made of these 6 extra channels. Measurements were only provided in the vertical direction (SIMFONE uses horizontal and/or vertical measurements). The main SIMFONE screen, showing the rotor/bearing model (upper window) and bearing displacements (lower window) is shown in Figure 1. This graphic-user-interface (GUI) allows viewing of all runs at all bearings, with either magnitude or phase measurements displayed. All other features of the program are also accessed via this window.

When importing data from ASCII format (as output by the industry-standard measurement systems) into SIMFONE, the user may select any number of runs for import. If the user chooses to specify one of these runs as a datum run, then this is the run from which all others are subtracted. In this case, run 2 (post-event) was selected as the datum run. The run 1

responses were then subtracted from those of run 2, leaving just one set of response data. The estimated unbalance due to this data was then just the additional unbalance for run 2. After import, the data are saved in a SIMFONE measurement file, negating the need for repeated import. The user may choose to estimate the foundation and/or unbalance over the whole frequency range, or to split the data into different frequency segments. The latter case introduces complications such as different estimates for the different frequency segments used, but may prove useful in cases where the data is of poor quality or has a high modal density (8). For the cases described here, the estimation routine was carried out over the complete run-down range, from 50 to 5 Hz.

Before performing the estimation, the user must input unbalance information. Unbalance planes are defined which, if the state of unbalance of the machine is known and only the foundation model is to be estimated, contain the mass, eccentricity and phase angle of the known unbalance at each plane. If, however, the unbalance is unknown and is to be estimated together with the foundation model, as done here, then only the axial locations of the unbalance planes are specified. Care must be taken in the unbalance plane specification, as problems may arise if the number of planes is over- or under-specified. For this work it was decided to perform the unbalance/foundation estimation routine for two different cases: *Case 1*: 1 unbalance plane per rotor (5 total), *Case 2*: 2 unbalance planes per rotor (10 total). For *Case 1*, the planes were defined near the centres of the 5 rotors. For *Case 2*, each rotor was defined with 2 planes, the ten planes being well spread out along the length of the shaft line.

## 6.2 The Estimation of the Foundation Model and Unbalance Force

During the parameter estimation stage, the user is given the option of using horizontal and/or vertical measurements, estimating unbalance in addition to the foundation model, and performing the estimation on any of the runs that have been imported into the program, as shown in Figure 2. In this work, vertical measurements were used and the unbalance was estimated. SIMFONE uses two estimation routines: linear and nonlinear, as outlined below.

*Linear*: This is used to provide an initial set of estimates. It is computationally inexpensive and typically only takes a few seconds for this size of calculation (depending on processing speed). Input and output polynomial parameters may be defined, and different model orders may be selected, with respect to inverse condition number and output error, though at the expense of increased computing time. Model order cannot be changed when estimating unbalance and the user is restricted to a mass, damping and stiffness model.

*Nonlinear*: A nonlinear estimator is used to improve upon the linearly-estimated parameters. The user may specify the relative change in parameters and/or function residual, and also the maximum number of iterations, below which the nonlinear estimation routine will return. The nonlinear estimator is computationally expensive, in comparison with the linear method. For the two cases discussed here, each calculation, which lasted around 10 minutes in total, terminated after the specified 10 iterations. The function residual, which is plotted for each iteration, decreased from 45% to 19% for *Case 1*, and from 58% to 19% for *Case 2*.

It should be noted that once the unbalance has been estimated, an improved foundation model might be obtained by selecting a different model order. Also, increasing the number of iterations used for the nonlinear estimation may also improve the foundation model. This is, however, at the cost of increased computational effort. Since this work is intended to be a demanding test on SIMFONE's ability, as would be performed by engineers in the field who cannot afford this extra time, no improved foundation model was attempted here.

### 6.3 Results

In order to check the quality of an estimated foundation model, SIMFONE combines the rotor/bearing model with the estimated unbalance and foundation parameters, and calculates estimated responses for those measurement positions used in the analysis. If the estimated foundation model is of high quality, then a good fit between measured and estimated responses will be seen. Figure 3 shows the measured and estimated responses for *Case 1*, at the HP turbine, and Figure 4 for *Case 2*, at the LP1 turbine. These cases and locations were simply chosen as examples, and are typical of the high quality of the other estimated responses. As can be seen from the two figures, there is a very good fit for both magnitude and phase. For the LP1 responses, there is some discrepancy in phase angle in the 0-25 Hz frequency range, although this does not give cause for concern, since the (unlikely) measured phase behaviour seen here is probably due to the low signal to noise ratio in this region. As soon as this ratio increases (above 25 Hz), the fit becomes accurate once again. Overall, the two estimated foundation models can therefore be said to be of high quality.

In order to verify the *estimated* unbalance parameters, the *actual* unbalance on the turbogenerator due to the blade loss was disclosed after the calculations had been completed: viewed from the steam end towards the electrical end of the shaft-line, with positive anti-clockwise rotation from bottom-dead-centre, the blade loss on the HP turbine caused an increase in unbalance of 1.392 kg.m @ 227°, at an axial distance of 1.905 m from the HP front bearing. The *estimated* unbalance parameters for the two cases are listed below.

**Table 1: Estimated unbalance parameters, Case 1**

Location	Magnitude (kg.m)	Phase Angle (degrees)
HP	1.7912	353
LP1	0.30281	284
LP2	0.077329	246
LP3	0.013228	284
GEN	0.062297	61

**Table 2: Estimated unbalance parameters, Case 2**

Location	Magnitude (kg.m)	Phase Angle (degrees)
HP Front	4.0044	327
HP Rear	2.6971	110
LP1 Front	0.51056	300
LP1 Rear	0.43599	243
LP2 Front	1.3279	266
LP2 Rear	1.1392	87.5
LP3 Front	0.48592	70
LP3 Rear	0.7703	252
GEN Front	0.53922	204
GEN Rear	0.65617	29

For *Case 1*, the balance plane at the HP was chosen at an axial length of 2.565 m from the HP front bearing, just 0.66 m from the actual axial position of the unbalance location (less than 9% of the total HP rotor length). One could therefore expect the estimated unbalance at this plane to be close to the value that would be obtained, had the actual axial location been used. Here, as would be the case in the field, this actual axial location was unknown before the

calculation was performed. The results shown in Table 1 are extremely encouraging. Taking just one look at the estimated additional unbalance for run 2, it is obvious that the change in unbalance occurred on the HP turbine. This additional unbalance magnitude is 6, 23, 135 and 29 times larger than the values estimated for the LP1, LP2, LP3 and GEN respectively (no unbalance changes other than the HP blade loss had been reported for the shaft line). Indeed, the error between the *actual* and *estimated* unbalance magnitudes for the HP is just 22% (remembering the 0.66 m difference in axial location). The error in phase angle of  $126^\circ$  does raise some concerns, and further work is necessary to investigate the underlying cause of this anomaly. Possible reasons include an undetected error in the measurement and/or angle declaration system(s), or a poor bearing model having been supplied with the turbogenerator rotor model. However, due to the high accuracy in estimated unbalance magnitudes along the shaft line, it is considered that the overall unbalance identification has been highly successful.

For *Case 2*, with two balance planes per rotor, one important point is first to be noted. For the LP2, LP3 and GEN estimates, the two unbalance magnitudes are all of similar size, and are  $178.5^\circ$ ,  $182^\circ$  and  $175^\circ$  apart, i.e. virtually out of phase. This has the effect, for the first mode of these individual rotors at least, of cancelling out the unbalance forcing. A small amount of resultant unbalance is apparent for the LP1 turbine. It is once again evident from the HP unbalance magnitude and phase estimates that it is indeed this turbine on which the major change in unbalance took place.

## 7 DISCUSSION AND CONCLUSIONS

This paper has given an overview of a method to estimate a foundation model for turbo machinery, and to estimate the unbalance force, from a single run-down. The software package SIMFONE has been written to implement the approach, and this has been demonstrated using data from a real machine before and after the sudden loss of several turbine blades. Taking into account the two unbalance estimation cases discussed above, it can be seen that the number of balance planes used for *Case 2* was most likely over-specified. This led to the  $180^\circ$  phase difference in estimated unbalance on the LP2, LP3 and GEN turbines. Further work would be necessary to draw some generic guidelines for the specification of unbalance planes, including an investigation of the effective modal unbalance of the shaft-line due to the estimated unbalances at the specified planes. Notwithstanding, if either the *Case 1* or *Case 2* calculations were performed in the field, the location of the unbalance change could be easily identified using SIMFONE, as has been proven here. Furthermore, the *Case 1* calculation provided a very accurate estimate of the unbalance magnitude due to the blade loss. In this sense, SIMFONE is able to provide a highly cost-effective tool for maintenance purposes. Once the turbogenerator had been run-down, the estimation could be performed, the problem shaft-line section identified, the covers removed and maintenance performed. This would prevent unnecessary, costly maintenance from being carried out. The estimated foundation model has also been shown to be of high quality, with measured and estimated responses matching very well overall. The availability of such a foundation model is important for analysis, design and maintenance purposes.

## 8 REFERENCES

1. Lees, A.W. and Simpson, I.C., 1983, The dynamics of turbo-alternator foundations, *IMechE Conference paper C6/83*.

2. Lees, A.W., 1988, The least square method applied to investigating rotor/foundation interactions, *IMechE Conference, Vibrations in Rotating Machinery*, Edinburgh, Paper C366/065.
3. Zanetta, G.A., 1992, Identification methods in the dynamics of turbogenerator rotors, *IMechE Conference, Vibrations in Rotating Machinery*, Bath, Paper C432/092.
4. Feng, N.S. and Hahn, E.J., 1994, Including foundation effects on the vibration behaviour of rotating machinery, *Mechanical Systems and Signal Processing*, Vol. 9, No. 3, pp. 243-256.
5. Friswell, M.I. and Mottershead, J.E., 1995, *Finite Element Model Updating in Structural Dynamics*, Kluwer Academic Publishers, 286 pp.
6. Pons, A., 1986, Experimental and numerical analysis on a large nuclear steam turbogenerator group, *IFTOMM International Conference on Rotordynamics*, Tokyo.
7. Smart, M.G., Friswell, M.I., Lees, A.W. and Prells, U., 1998, Estimating Turbo-Generator Foundation Parameters. *IMechE Journal of Engineering Science*, Vol. 212, No. C8, pp. 653-665.
8. Smart, M.G., Friswell, M.I. and Lees, A.W., 2000, Estimating Turbogenerator Foundation Parameters - Model Selection and Regularisation. *Proceedings of the Royal Society of London, Series A: Mathematical, Physical and Engineering Sciences*, in press.
9. Lees, A.W. and Friswell, M.I., 1997, The evaluation of rotor unbalance in flexibly mounted machines. *Journal of Sound and Vibration*, Vol. 208, No. 5, pp. 671-683.
10. Edwards, S., Lees, A.W. and Friswell, M.I., 2000, Experimental Identification of Excitation and Support Parameters of a Flexible Rotor-Bearings-Foundation System from a Single Run-Down, *Journal of Sound and Vibration*, Vol. 232, No. 5, pp. 963-992.
11. Nuclear Electric, 1994, *DYTSOS User Guide*.
12. Genta, G., 1995, *DYNROT 7.0 A Finite Element Code for Rotordynamic Analysis*, Dipartimento di Meccanica, Politecnico di Torino, Italy.
13. Smith, D.M., 1969, *Journal Bearings in Turbomachinery*, Chapman & Hall.
14. Friswell, M.I., Garvey, S.D., Penny, J.E.T. and Smart, M.G., 1998, Computing critical speeds for rotating machines with speed-dependent bearing properties, *Journal of Sound and Vibration*, Vol. 213, No. 1, pp. 139-158.
15. Lees, A.W. and Friswell, M.I., 1996, Estimation of forces exerted on machine foundations, *International Conference on Identification in Engineering Systems*, Swansea, March 1996, pp. 793-803.

## 9 ACKNOWLEDGEMENTS

The authors acknowledge the support and funding of BNFL (Magnox Generation) and British Energy plc, and of EPSRC through grant GR/M41629. Dr. Friswell gratefully acknowledges the support of the EPSRC through the award of an Advanced Fellowship. The authors acknowledge the technical input of Dr. Mark Smart, who was the principal author of the SIMFONE software while employed as a researcher at Swansea.

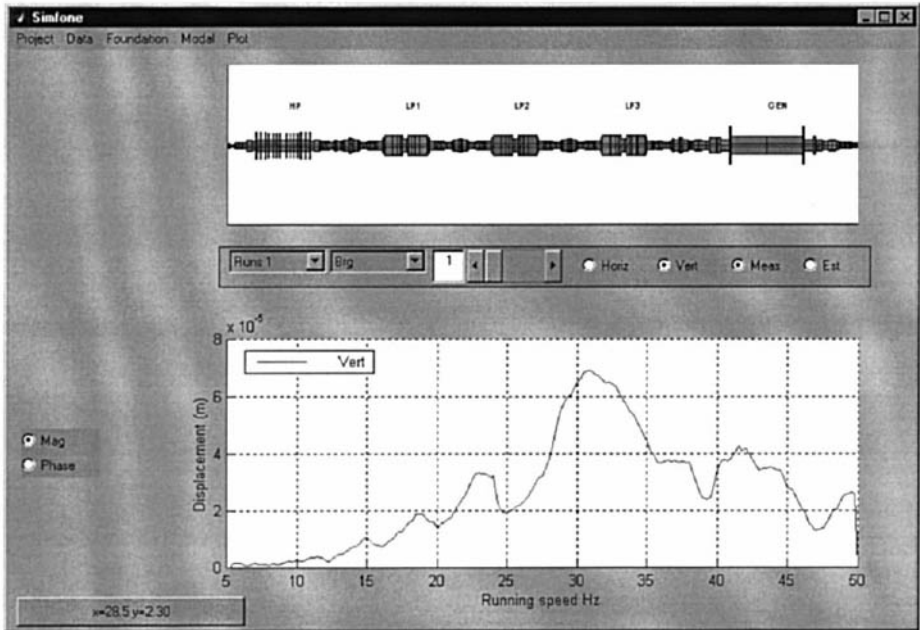


Figure 1: Main SIMFONE screen showing rotor model and run-down measurements

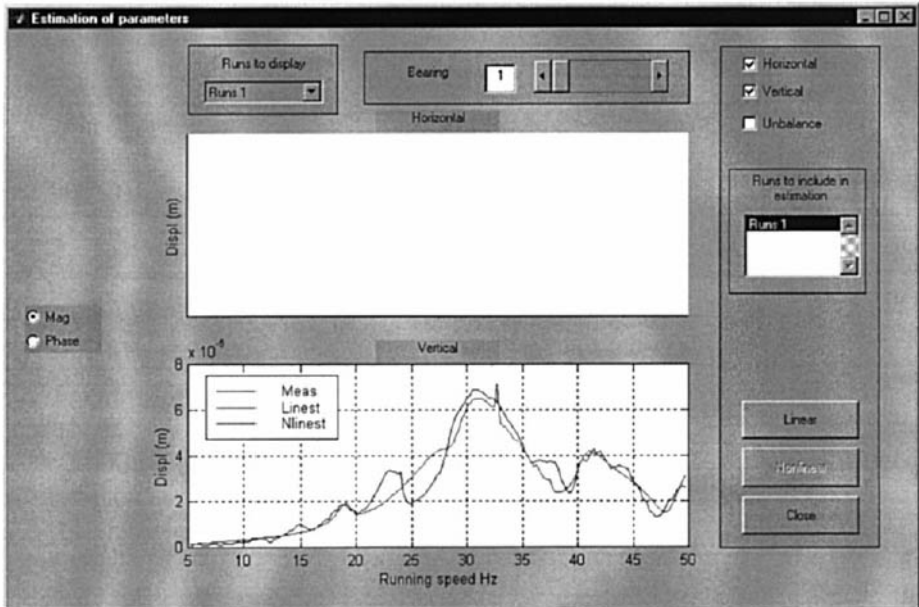
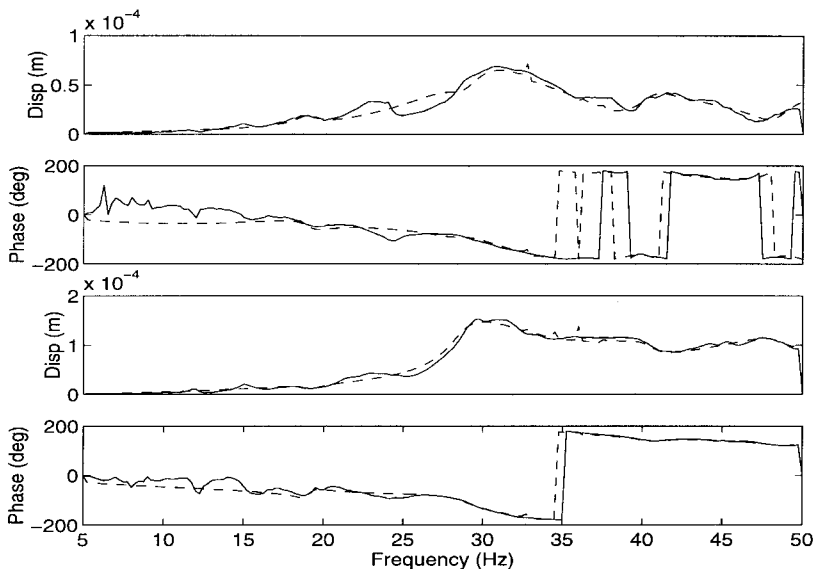
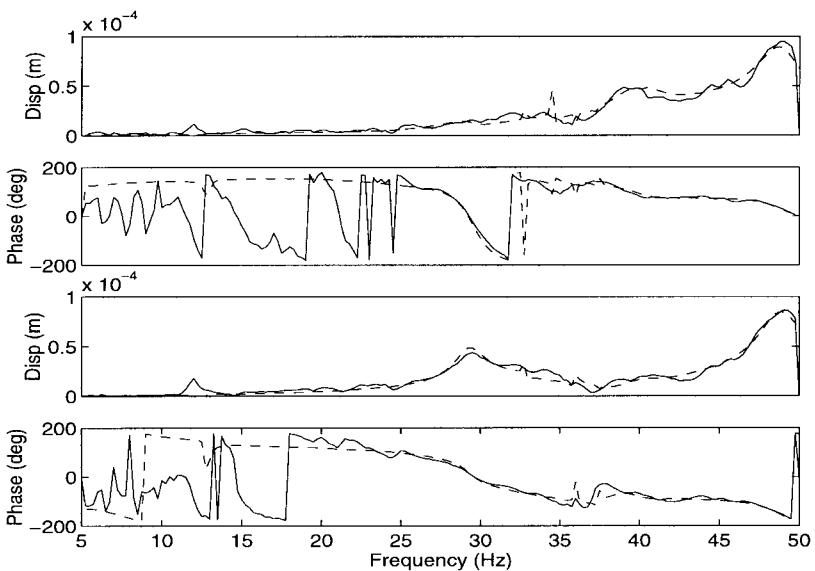


Figure 2: Unbalance/foundation parameter estimation window





**Figure 3: Measured (solid) and estimated (dashed) responses for HP front (top) and rear (bottom) bearings, Case 1**



**Figure 4: Measured (solid) and estimated (dashed) responses for LPI front (top) and rear (bottom) bearings, Case 2**

*This page intentionally left blank*

# Bladed Systems

*This page intentionally left blank*

# The effect of non linear damping on the resonant stresses in turbomachine LP rotor blades

J S RAO, C V RAMAKRISHNAN, and K GUPTA

Department of Mechanical Engineering, Indian Institute of Technology, New Delhi, India

A K SINGH

Bharat Heavy Electricals Limited, New Delhi, India

## ABSTRACT

Low pressure stage steam turbine blades in power plants are subjected to most severe mechanical stresses. The dynamic stress coupled with centrifugal and steady steam bending loads is responsible for fatigue-induced failures in these blades. The maximum stress occurs in the blade root junction. The dynamic stress is also affected by damping, which is generally non-linear in nature. This paper proposes a method of determining the dynamic stress at the root of a low pressure steam turbine blade with the help of CAE tools and 3-D FE model.

## 1. INTRODUCTION

The fundamental mode bending frequency of the last stage blades in the LP rotor is the lowest and falls typically in the region of 100 Hz. Therefore this stage of blades are subjected to several resonances during start-up and shutdown operations mainly arising from the per rev excitations. Around the operational speed, these blades are also likely to be subjected to resonance with 2 per rev excitation unless very tight control on the grid frequency is maintained. Therefore, it is not infrequent to find LP stage blade failures in steam turbines of power plants [1]. Hence, special attention has to be paid to the static and dynamic stresses in the blade root region to guarantee safe and reliable operation under all possible service conditions. It is a standard practice to calculate static stresses and natural frequencies in the centrifugal force field. Robertson and Walton [2] in their study found that efficiency and capital cost are dependent on the quality of the blade roots and they have analysed root system using classical stress analysis and finite element method.

Though design procedures for preventing fatigue-induced failures of turbine blading are practised, there is no indication that a satisfactory situation exists. Rao and Vyas [3] discussed various aspects involved in the life estimation analysis of turbomachine blading. The major hurdle faced in blade fatigue analysis has been a precise evaluation of the blade

dynamic stresses under forced vibration and resonant conditions and their dependence on excitation harmonics, vibrational modes and damping. Kramer and Plan [4] recently measured vibration of last stage blades using optical probes and showed peak resonances in the region of 3000 to 3600 rpm. Vyas [5] worked out fatigue strength parameters and employed Bagci's fatigue failure surface line and the concept of cumulative fatigue damage to work out life estimation of blades. However, he used a simple beam model to illustrate the procedure. Such an approach is not feasible for LP blades as maximum stresses occur in the root region.

Depending on the aspect ratio, the extent of pre-twist and complicated nature of root design, finite element method becomes handier. Bahree, Sharan and Rao [6] have used 20 noded curved solid element and determined the free vibration characteristics. MacBain [7] used 4 noded quadrilateral plate bending element of NASTRAN to evaluate the natural frequencies. Swaminadham, Soni, Stange and Reed [8] used NASTRAN program to determine the natural frequencies of a complex bladed-disc. Rao [9] described a mixed shell element to model a compressor blade.

Many investigators have studied material damping. Lazan [10] conducted comprehensive studies into the general nature of material damping and presented damping results for almost 2000 materials. Wagner [11] conducted damping tests on rotating steam turbine blades. Rao, Usmani and Ramakrishnan [12] investigated the damping due to Coulomb friction between the blade root junction surfaces. Peck, Johnson and House [13] conducted similar tests on long LP axial entry steam turbine blades and HP tangential entry steam turbine blades. Johnson [14] conducted studies on LP blades under high vibration and dynamic stress conditions. The results showed that the damping in steam turbine blades is primarily material damping due to high centrifugal force. Rao, Gupta and Vyas [15] obtained damping ratio as a function of strain in the blade and rotational speed for the first four modes. Average damping of these results has shown a distinct threshold speed beyond which the blade gets locked and the damping is then mainly due to material deformation. The stresses determined using this non-linear damping model have been found to be in better agreement with the experimental values when compared with an average viscous damping model.

In this paper a finite element model of a low-pressure last stage steam turbine blade is considered. The excitation is taken to be per rev excitation arising out of mechanical mounting errors of the diaphragms. A procedure to determine the dynamic stresses at the blade root is illustrated using SDRC I-DEAS CAE package. A damping model similar to that of Rao, Gupta and Vyas [15] is assumed in the calculation procedure.

## **2. FEM MODEL**

Here, a blade very closely resembling to the real life case of a 236 MW LP stage V is considered for the purpose of illustrating the resonant stress calculation using a non-linear damping model. The real life blade geometry and calculations are not reported here for obvious reasons. The 3-D CAD model is developed using SDRC I-DEAS Master Series 6.0. It has been developed in two stages. In the first stage, the blade form part has been developed. This has been obtained by first creating the blade sections at various heights drawn by feeding the co-ordinates of the points on the sections. The co-ordinates are joined by 3-D spline to obtain these sections. The blade part is then constructed by lofting through these sections. The fir-tree root and the bridge portion part have been constructed in the second

stage. This part has been created first by constructing the cross-section at mid point representing fir-tree root and the bridge portion by feeding the co-ordinates of the points on the mid plane cross-section. The root and the bridge part have then been obtained by revolving this cross-section along the curved path of the root section. The final blade 3-D CAD model has been obtained by joining these two parts namely the blade form part and the root and the bridge part. The CAD model thus developed is shown in Fig.1.

The blade form part has a height of 965.2 mm and the root and the bridge part has a height of 54.3868 mm. Thus the total height of the blade is 1019.5868 mm. The blade is a tapered blade with a minimum width of 8 mm and the maximum width of 23.6 mm. The angle of twist is  $89^\circ$ . The total mass of this blade is 25.43 Kg. There are 78 blades in this LP stage. This blade is placed on the LP disk by placing the bottom of the blade root at a radius of 790.1472 mm from rotor axis. There are 50 stationary guide blades in the stage. The blade is assumed to be of martensitic steel with an Ultimate Tensile Strength equal to 1120 MPa, the Modulus of Elasticity equal to  $2.068 \times 10^{11}$  N/m<sup>2</sup> and Poisson's Ratio equal to 0.284.



**Fig.1. 3-D CAD Model of Blade**



**Fig.2. Blade Model Showing the FE Mesh**

A 3-D FEM model is then developed using this CAD model. Using the mapped meshing option, a controlled 8 noded isoparametric solid element mesh is generated. The mesh thus obtained consists of 2720 nodes and 1682 solid elements. In root region, the maximum element length in the cross-sectional plane has been kept as 5 mm. Fig.2 gives a complete view of the meshed blade. Fig.3 shows a blow up of the root and the bridge portion.

The blade has been treated fixed at all the six root-landing positions in all three translational degrees of freedom. This 3-D FE model is used for frequency as well as the stress calculations.

### **3. FREQUENCY COMPUTAION**

The first four natural frequencies of the blade have been obtained at various rotational speeds using Structural Dynamics Research Corporation's program I-DEAS Master Series 6.0. Fig.4 gives the Campbell diagram for the blade with the six engine order excitations and first nozzle passing frequency interacting with the natural modes to give resonant rotor speeds.

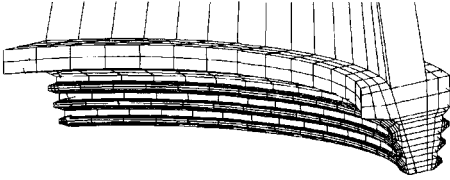


**Fig.3. Blow Up of the Root and the Bridge Portion**

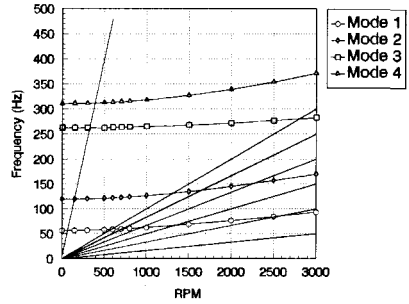


**Fig.4. Campbell Diagram**

Table 1 gives the resonant rotor speeds up to 3000 rpm, both for engine order excitations as well as for first nozzle passing harmonic.

Harmonic	Mode 1	Mode 2	Mode 3	Mode 4
1X				
2X	2550			
3X	1330			
4X	934	2260		
5X	714	1642		
6X	585	1315	2810	
NPF 1	70	145	317	376

It may be mentioned here that the I mode natural frequency determined at 3000 RPM for the real life LP stage V blade (whose data is not reported in this paper) obtained from the same program is 102 Hz. From experiments conducted on few of these blades in a balancing tunnel the I mode frequency is found to lie in between 99 to 101 Hz [16].

#### 4. DAMPING MODEL

The damping model is adopted from [15]. There it was recognised that the friction damping is dependent on centrifugal load, i.e. rotational speed, with the interfacial slip disappearing when the blade root gets locked in the disk. When the friction damping disappears, it is the material damping that fights the resonant conditions. Therefore, a non-linear damping model is developed through carefully conducted laboratory tests defining the damping to be a function of strain amplitude and the rotational speed for different modes of vibration. Fig.5 shows the average damping ratio taken as a function of rotor speed. This represents an average value of damping taken in the entire range of free vibration decay curve from the tests. The dependence of damping on the mode of vibration, rotational speed and the strain amplitude at the root of the blade is represented in the form of non-linear damping as defined in reference [15]. The damping values at the resonant speeds given in Table 1 are taken as a function of strain amplitude at the trailing edge of the bottom layer of the blade form and given in Figs.6 to 9.



At low speeds, the blade root remains somewhat loose in the disc slot. This looseness allows an interfacial slip between the blade and the disk and provides Coulomb friction damping. Usually this damping is of higher order when compared with the damping in the material of the blade. As the speed increases, the blade gets tightened in the root and the interfacial slip disappears. Then material damping is only available and it increases with the strain in the blade.

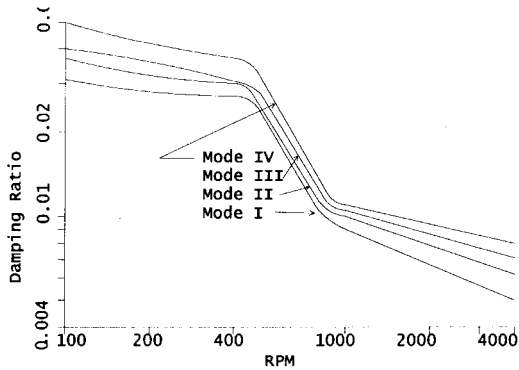


**Fig.5. Average Damping Ratio vs Rotor Speed**

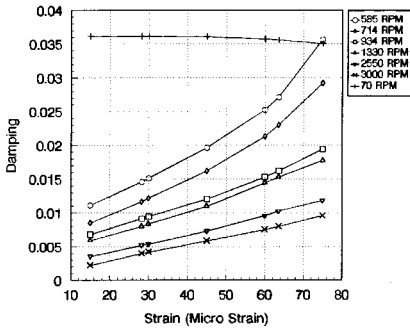


**Fig.6. Damping Ratio - Mode 1**

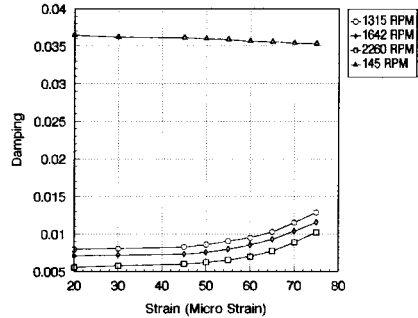


**Fig.7. Damping Ratio - Mode 2**

In Figs. 5 to 7, at low speeds, the damping remains almost constant and is independent of strain amplitude. The damping actually decreases with the strain amplitude in this region. This is also characterised by the initial high damping in Fig. 4 where the average damping values are presented. As the speed increases, the average damping values decrease with a rapid fall in the transition zone. Thereafter, the average damping decreases in a gradual manner as the speed increases and the damping here is entirely from the material deformation. Under material damping regime at high speeds the non-linear characteristic in Figs. 5 to 7 shows that the damping increases with strain amplitude. The damping characteristics defined in Figs. 4 to 8 are used in estimating the blade root stresses.

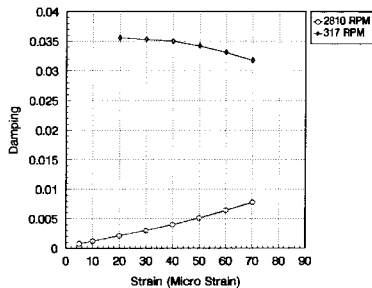


**Fig.8. Damping Ratio - Mode 3**

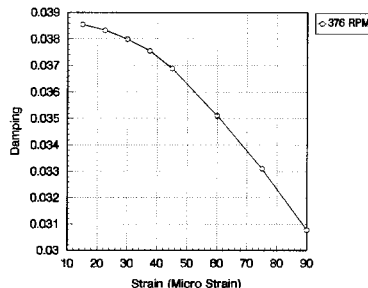


**Fig.9. Damping Ratio - Mode 4**

## 5. STEAM LOAD DATA

Steady state steam bending loads, both axial and tangential components, for this stage are given in Table 2, refer [17].

The per rev excitation for the first six harmonics is essentially due to mechanical mounting errors of the stator diaphragm blades. A mathematical simulation of these errors to determine the non-steady loads acting on the rotor blades is not feasible. Experimentally these non-steady loads are determined by Levin [18] and found to be  $\frac{1}{2}$  to 2% of steady loads for the first six harmonics. Since two per rev component is responsible for this resonance, the magnitude of the alternating load is taken to be 2% of the steady state steam bending load.

For aerodynamic excitation, the stage of a stator and rotor can be modelled using unsteady aerodynamic theories. Aerodynamic modelling and estimation of the stage non-steady forces is described by Rao [19]. He has shown that the aerodynamic load on the rotor blades lies in the range of 5 to 15% of the steady loads. In this work, the non-steady load is taken to be 10% of the steady state steam-bending load for nozzle passing excitation.

## 6. STRESS COMPUTATION

Campbell diagram for the blade, see Fig.4, shows that the present LP stage blade under consideration has nine per rev harmonic and four nozzle passing harmonic resonant speeds as summarised in Table 1. The stresses are computed at these resonant speeds, both with average damping as well as with non-linear damping values. I-DEAS is used to sweep the frequency around resonance to determine the stress response. The loads are applied on the pressure surface at appropriate heights by dividing them equally between all the nodes. To compute the stresses in the blade for non-linear damping, an iterative scheme is followed using the strain amplitude at the location of the trailing edge of the bottom layer of the blade form.

In the present scheme of iteration for non-linear damping, the first starting value of the strain has been assumed as that value of strain amplitude obtained from the case of average damping stress evaluation. Using this guess, corresponding modal damping is estimated. With this updated damping value, the resultant resonant stress and strain are computed once again. With the modified strain amplitude, corresponding modal damping is once again re-

estimated. With the new damping value thus determined, resultant resonant stress and strain are once again modified. This iteration is continued, till the convergence on the stress value is obtained. To illustrate the procedure, the result of iteration for the case of resonant speed corresponding to first mode and sixth per rev harmonic at 585 RPM are given in Table 3.

**Table 2**  
**Steady Steam Bending Load**

Blade Height (mm)	Steam Bending Load (N)	
	Axial Component	Tangential Component
907.399	28.002	34.025
970.264	31.603	34.134
1033.129	35.720	33.898
1095.994	40.666	33.216
1158.859	46.711	31.885
1221.724	53.989	30.183
1284.589	59.443	29.750
1347.454	60.558	31.805
1410.319	62.699	33.339
1473.184	70.884	31.305
1536.049	82.575	27.525
1598.914	93.165	24.251
1661.779	101.573	22.591
1724.644	108.094	22.333
1787.509	113.061	22.429

**Table 3**  
**Iteration Values at 585 RPM**

Starting Value		Resultant Value	
Micro Strain	Damping Ratio	Micro Strain	Stress (MPa)
24.572	0.013652358	27.897	14.907
27.897	0.014528759	26.215	14.008
26.215	0.014085552	27.038	14.449
27.038	0.014302413	26.629	14.230
26.629	0.014194641	26.832	14.338
26.832	0.014248132	26.731	14.284
26.731	0.014221518	26.781	14.311
26.781	0.014234693	26.756	14.297
26.756	0.014228106	26.769	14.304
26.769	0.014231531	26.762	14.301
26.762	0.014229687	26.766	14.303
26.766	0.014230741	26.764	14.302
26.765	0.014230214	26.765	14.302

Using this scheme, resonant stresses for all the harmonics have been obtained. The stress contours for both average and non-linear damping models revealed maximum values at the

root fixing location of the first landing. Fig.10 shows the stress contours for resonant stress case with non-linear damping corresponding to first mode and sixth per rev harmonic at 585 RPM. The maximum resonant stresses obtained in all the harmonics cases have been summarised in Table 4. The results are presented in the order of decreasing stresses.

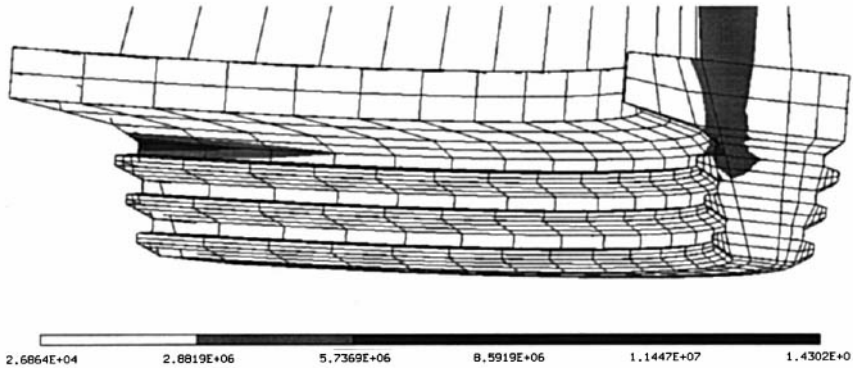


**Fig.10. Von Misses Stress Contours at 585 RPM, Mode 1, 6X**

**Table 4  
Maximum Resonant Stresses in Blade Root**

Critical Speed (RPM)	Average Damping Ratio	Average Stress (MPa)	Non Linear Damping Ratio	Non Linear Stress (MPa)	% Difference (1)	% Difference (2)
2550	0.00560	24.985	0.00637	21.949	-13.75	-13.83
1330	0.00760	23.930	0.00931	19.528	-22.50	-22.54
934	0.00954	20.393	0.01032	18.861	-8.18	-8.12
714	0.01225	16.371	0.01229	16.320	-0.33	-0.31
585	0.01550	13.131	0.01423	14.302	+8.19	+8.19
2260	0.00730	16.754	0.00579	21.556	+20.68	+22.28
1642	0.00818	16.358	0.00719	18.606	+12.10	+12.08
1315	0.00885	15.564	0.00804	17.140	+9.15	+6.43
2810	0.00745	0.828	0.00108	5.698	+85.50	+85.47
70	0.03750	5.602	0.03618	5.807	+3.52	+3.53
145	0.03450	4.196	0.03660	3.956	-6.09	-6.07
317	0.03250	0.105	0.03666	0.093	-12.80	-12.90
376	0.03700	0.292	0.03866	0.280	-4.49	-4.29

(1)  $100 \times (\text{Average Damping} - \text{Non-linear Damping}) / \text{Average Damping}$

(2)  $100 \times (\text{Stress with Non-linear Damping} - \text{Stress with Average Damping}) / \text{Stress with Non-linear Damping}$

The stress value obtained by the conventional average modal damping concept is compared with the stress value determined using the non-linear damping model. Column 7 in Table 4 shows this comparison by giving the percentage difference as  $100 \times (\text{Stress with Non-linear}$

Damping – Stress with Average Damping) / Stress with Non-linear Damping. To understand the relation between the stress and damping, consider the resonant stress  $\sigma$ , which can be written in terms of the quality factor  $1/2\xi$  as

$$\sigma = \sigma_{st}/2\xi$$

where  $\sigma_{st}$  is the steady state stress from steam bending. When the damping is changed, say by  $\Delta\xi$ , the corresponding resonant stress will be

$$\sigma + \Delta\sigma = \sigma_{st}/2(\xi + \Delta\xi)$$

Then it can be shown that

$$\Delta\sigma / (\Delta\sigma + \sigma) = -\Delta\xi/\xi$$

In view of the above relation, we can define the quantity  $100*(\text{Average Damping} - \text{Non-linear Damping}) / \text{Average Damping}$ , in Table 4 as given in column 6 and compare it with the quantity in column 7.

## 7. DISCUSSION

The results in Table 4 show that the maximum error is at 2810 RPM, which is the 3<sup>rd</sup> mode excited by 6<sup>th</sup> harmonic. Here the average damping value is equal to 0.00745 as given in Fig. 3 and Table 4. However the stress is very low, as a result the non-linear analysis shows a much lower equivalent damping ratio 0.00108 (see also Fig. 8) and hence the stress predicted is much higher than that of the average damping model. The interesting feature is that the differences calculated between the stresses and damping ratios in accordance to the relations given above are in good agreement with each other.

At the low speeds 70 to 317 RPM, the damping value is almost constant more as Coulomb damping rather than material damping, see Figs. 6 to 8, therefore, the influence of non-linearity is negligible. At 376 rpm in mode 4, see Fig. 9, the stress is very low and the average damping value turned about to be the same as the non-linear damping value, hence there is not much difference between the linear and non-linear analyses.

For speeds beyond 376 RPM, the present damping phenomena is more controlled by material damping as can be seen from Figs. 6 to 9 where the equivalent modal values increased with strain. Under these circumstances, the damping ratio depends on the final iterated stress value. If the damping value turns out to be much different from the average damping value, the stress results are also affected similarly. At speed 714 RPM it so turned out that the non-linear analysis resulted in a damping value closer to the average damping value and hence the difference in the stress results is negligible, otherwise the non-linearity in damping has significant influence in the determination of blade root stresses.

## 8. CONCLUSION

An iteration procedure is proposed to determine the dynamic stresses in a blade with non-linear damping using CAE tools and 3-D FE model. The non-linear damping is shown to be of significant importance in determining the dynamic stresses. Maximum errors in dynamic stress with average damping model have occurred when the blade is stressed relatively low. Under Coulomb damping at low speeds, the average and non-linear damping models have

differed very little even under low stress condition. The stress values are almost equal to each other whenever blade load resulted in a strain corresponding to average damping value.

## REFERENCES

1. Rao, J.S., Singh, A.K. and Sharma, K.V.B., "Blade and Rotor Dynamics in an Atomic Power Plant Accident", Proc. 9<sup>th</sup> World Cong. On the Theory of Machine and Mechanisms, Milan, Aug. 30-Sept. 2, 1998, Vol. II, p.1334.
2. Robertson, M.D. and Walton, D., "Design analysis of steam turbine blade roots under centrifugal loading", Journal of Strain Analysis for Engineering Design, v 25 n 3 July 1990, p.185-195.
3. Rao, J.S. and Vyas, N.S., "On Life Estimation of Turbine Blading", Proc. Rotor Dynamics Tech. Committee, 7th IFToMM Cong., Sevilla, Spain, 1987.
4. Kramer, E. and Plan, E., "Optical Vibration Measuring System for Long, free-standing LP Rotor Blades", ABB Review 5, 1997, p.4.
5. Vyas, N.S., "Vibratory Stress Analysis and Fatigue Life Estimation of Turbine Blade", Ph.D. Thesis, IIT, New Delhi, India, 1986.
6. Bahree, R., Sharan, A.M. and Rao, J.S., "The Design of Rotor Blades due to the Combined Effects of Vibratory and Thermal Loads", J. of Engg. Power and gas Turbines, Trans. ASME, 111, 1989, p.610.
7. MacBain, J.C., "Vibratory Behaviour of Twisted Cantilever Plates", J. Aircraft, 12, 1975, p343.
8. Swaminadham, M., Soni, M.L., Stange, W.A. and Reed, J.D., "On Model Generation and Nodal Analysis of Flexible Bladed-Disc Assemblies", Bladed-Disc Assemblies, 6, ASME Vibration Conf., Cambridge, MA, Sept. 27-30, 1987, p.49.
9. Rao, J. S., *Dynamics of Plates*, Marcel Dekker, 1999
10. Lazan, B.J., "Damping of Materials and Members in Structural Mechanics", Pergamon Press, New York, 1968.
11. Wagner, J.T., "Blade Damping Tests", Westinghouse Engg. Report, EC-401, May 1969.
12. Rao, J.S., Usmani, M.A.W. and Ramakrishnan, C.V., "Interface Damping in Blade Attachment Region", Proc. 3<sup>rd</sup> Intl. Conf. Rotor Dynamics, Lyon, Sept. 1990, p.185.
13. Peck, L.C., Johnson, P.J. and House, D.F., "Evaluation of Turbine Blade Root Design to Minimise Fatigue Failures", EPRI Project RP-1185-2, Palo Alto, California, 1981.
14. Johnson, P.J., "Evaluation of Damping in Free Standing Low Pressure Steam turbine Blades", EPRI Project RP-016-2, Palo Alto, California, 1982.
15. Rao, J.S., Gupta, K. and Vyas, N.S., "Blade Damping Measurement in a Spin Rig with Nozzle Passing Excitation Simulated by Electromagnets", Shock & Vibration Bull., 56, Part 2, 1986, p109.
16. BHEL Internal Report – Singh, A.K. and Nimbekar, P.K., Frequency Analysis of LP Stage-5 Blade and Disc for 235 MW Nuclear Turbine, Document No.: AE-83-O-CS, March 1998.
17. Rao, J. S., "Application of Fracture mechanics in the Failure Analysis of a last stage Steam Turbine Blade", Mechanism Machine Theory, Vol.33, No.5, 1998, p599.
18. Levin, A., *Moving Blades and Disks of Steam Turbines*, The State Power Engineering Publishers, Moscow, 1953 (In Russian)
19. Rao, J. S., *Turbomachine Unsteady Aerodynamics*, Wiley Eastern, 1991

# Travelling modes in turbine blades with compound periodic structure

E SAITO and K NAMURA

Hitachi Limited, Ibaraki, Japan

**Synopsis** This paper describes a theoretical investigation for a traveling mode phenomenon in compound periodic structures when subjected to engine order excitation. In addition, a series of experiments with a simple blade model are performed by simulating engine order excitation under non-rotating conditions. Ceramic oscillators are attached to all the blades. Each blade is excited by a sinusoidal wave with an inter-blade phase angle corresponding to the traveling mode. As a result, the traveling mode or irregularly traveling mode is observed to occur by giving slightly different exciting conditions.

## NOMENCLATURE

- $F, f$ : Exciting force  
 $K$ : A set of nodal diameters included in a natural mode  
 $N_G$ : Number of blades in a group  
 $M$ : Total blade number  
 $U, u$ : Energy supplied to the blades by exciting force  
 $W, w$ : Axial displacements  
 $a, b$ : Arbitrary mode function  
 $h$ : Harmonics order  
 $i$ : Blade number  
 $j$ : Mode index number  
 $k$ : Number of nodal diameter  
 $k_r$ : Representative number of nodal diameters  
 $n$ : Number of groups in a blade assembly  
 $r$ : Radial direction coordinate  
 $t$ : Time  
 $\Omega$ : Rotational speed  
 $\phi$ : Initial phase angle  
 $\theta$ : Circular direction coordinate  
 $\omega$ : Natural frequency

## 1 INTRODUCTION

Turbine blades are among the most important components which affect turbine efficiency and reliability. Sometime, for the purposes of increasing rigidity, adding damping and controlling the natural frequencies, turbine blades are interconnected by suitable connecting means.

Among the various blade structures, there exists a blade structure which includes both grouped and one-ringed blade structures in a turbine wheel to form a circumferential periodicity with a packet as a unit. This blade structure, which consists of more than two kinds of circumferentially periodic structures, may be called a compound periodic structure. It is well known that a mode of this structure is complex, being composed of plural nodal diameter components.

Ewins and Imregun<sup>(1)</sup> have investigated the vibration characteristics of a grouped bladed-disk, which has similar vibration characteristics to the compound periodic structure. Wagner and Griffin<sup>(2)</sup> have presented the harmonic response of a flexible disk having a number of groups of turbine blades on the theory of cyclically symmetric structures. The authors<sup>(3),(4)</sup> have shown the resonance condition of the compound periodic structure. The investigation by Wildheim<sup>(5)</sup> clarified that the vibration mode of the rotationally symmetric structure may behave like either a forward or backward traveling wave due to a rotating force. However, the traveling mode of the grouped bladed disk or the compound periodic structure has not been sufficiently studied. It is necessary to answer the question of how nodal diameter components in a natural mode behave when the natural mode is excited to resonance by engine order excitation.

This paper presents a theoretical investigation for the traveling mode of the compound periodic structure when subjected to engine order excitation. Then, the findings are confirmed in a series of experiments with a simple blade model by simulating engine order excitation under a non-rotating condition. By slightly changing the exciting conditions, two kinds of resonant response are observed. Their causes and features are also discussed.

## 2 MODE CHARACTERISTICS

In a bladed-disk system, the natural modes are characterized by nodal diameters. The compound periodic structure also has such natural modes, but each mode shape is rather complex because it is composed of plural nodal diameter components.  $K$ , a set of nodal diameters included in a natural mode, is given by the following equation<sup>(4)</sup>.

$$K = \ell n \pm j \quad \dots\dots\dots (1)$$

$\ell$ : integer ( $0 \leq \ell \leq N_G / 2$ ),  $j$ : integer ( $0 \leq j \leq n / 2$ )

The number  $j$  is defined as the mode index number and the numbers of nodal diameters included in a natural mode are obtained by giving each number of  $j$ . For example, with the blade assembly of  $N_G=4$  and  $n = 8$  (Fig.1),  $K=8\ell \pm j$  ( $\ell=0-2$ ,  $j=0-4$ ). When a number of  $j=3$  is given, a set of  $K$  which satisfies the equation is expressed as  $K=\{3, 5, 11, 13\}$ .

For convenience, a natural mode is generally labeled by the largest of the diametral components in its mode shape; for example, if the number of the largest diametral component is  $k_r$ , it is called the representative number of nodal diameters and used for the mode name.

## 3 THEORETICAL INVESTIGATION

Effective mode calculation of the compound periodic structure is associated with an understanding of the modal characteristics. In the beginning, as an example, a circular disk for a rotationally periodic structure is considered. The axial displacement of the disk can be described by



$$W(r, \theta, t) = \sum_{k=0}^{\infty} w_k(r) \{a_k(t) \cos k\theta + b_k(t) \sin k\theta\}. \quad \dots\dots\dots (2)$$

where  $r$  and  $\theta$  are polar coordinates,  $w_k$  is the radius mode shape corresponding to  $k$  nodal diameters, and  $a_k(t)$  and  $b_k(t)$  are arbitrary harmonic functions which include a natural frequency. From equation (2), it can be seen that the circumferential mode is expressed by a set of harmonic functions,  $\sin k\theta$  and  $\cos k\theta$ . This expression is especially useful for a rotationally periodic structure. In order to adapt equation (2) to the compound periodic structure, however, it is necessary to consider plural nodal numbers. Thus,  $W_i$  for a natural mode of the  $i$ -th blade with the compound periodic structure is as follows:

$$W_i(r, \theta, t) = \sum_K w_K(r) \{a_K(t) \cos K\alpha_i + b_K(t) \sin K\alpha_i\} \quad \dots\dots\dots (3)$$

where

$$\alpha_i = \frac{2\pi}{M}(i-1), \quad (i=1-M, \text{ integer}). \quad \dots\dots\dots (4)$$

And, arbitrary harmonic functions,  $a_K(t)$  and  $b_K(t)$  are assumed as follows:

$$a_K(t) = \sin(\omega t + \phi_{Ka}) \quad \dots\dots\dots (5)$$

$$b_K(t) = \sin(\omega t + \phi_{Kb}) \quad \dots\dots\dots (6)$$

Here, it should be noted that each nodal diameter component included in  $K$  has a same frequency  $\omega$  (i.e., a natural frequency) and its own initial phase angle  $\phi_{Ka}$ ,  $\phi_{Kb}$ .

As the blades move past the non-uniform flow around the circumference, they are subjected to a cyclic exciting force  $F$  which is composed of engine order components of rotational frequency.  $F$  is expressed as follows:

$$F = \sum_{h=1}^{\infty} f_h \cos(h\Omega t - h\alpha_i) \quad \dots\dots\dots (7)$$

where  $h$  is the harmonic excitation order,  $\Omega$  is rotational speed,  $f_h$  is the  $h$ -th exciting force. A common resonant condition for the blade assembly is that one of the natural frequencies coincides with exciting frequency of the  $h$ -th harmonic of rotational speed. That is

$$h\Omega = \omega. \quad \dots\dots\dots (8)$$

The  $i$ -th blade energy  $du_i$  supplied by exciting force is given below from equations (3)-(8).

$$\begin{aligned} du_i &= F \cdot \frac{dW_i}{dt} \cdot dt \\ &= f_h \sum_K w_K(r) \cos(\omega t - h\alpha_i) \{ \cos(\omega t + \phi_{Ka}) \cos K\alpha_i + \cos(\omega t + \phi_{Kb}) \sin K\alpha_i \} d(\omega t) \quad \dots (9) \end{aligned}$$

Thus, the  $i$ -th blade energy  $u_i$  is

$$u_i = \int d u_i = \int_0^{2\pi} d(\omega t) \\ = \pi f_h \sum_K w_K(r) \{ \cos K\alpha_i \cdot \cos(h\alpha_i + \phi_{Ka}) + \sin K\alpha_i \cdot \cos(h\alpha_i + \phi_{Kb}) \}. \dots\dots\dots (10)$$

Furthermore, the total energy supplied to all the blades by the exciting force is given as follows:

$$U = \sum_{i=1}^M u_i = \frac{\pi f_h}{2} \sum_{i=1}^M \sum_K w_K [ \cos\{(K+h)\alpha_i + \phi_{Ka}\} + \cos\{(K-h)\alpha_i - \phi_{Ka}\} \\ + \sin\{(K+h)\alpha_i + \phi_{Kb}\} + \sin\{(K-h)\alpha_i - \phi_{Kb}\} ]. \dots\dots\dots (11)$$

The total energy  $U$  takes a certain (i.e., non-zero) value only when the following condition is satisfied.

$$K \pm h = (\lambda - 1)M \dots\dots\dots (12)$$

where  $\lambda$  is a positive integer. Equation (12) is a resonant condition for a compound periodic structure<sup>(3),(4)</sup>. When  $K$  includes the nodal diameter component, which equals the order  $h$ ,  $U$  is rewritten as follows.

$$U = \frac{\pi M f}{2} \sum_K w_K (\cos \phi_{Ka} \pm \sin \phi_{Kb}) \dots\dots\dots (13)$$

Also, when subjected to the engine order excitation,  $U$  must be a maximum value at the resonance. So,  $\phi_{Ka}$  and  $\phi_{Kb}$  are given below.

$$\phi_{Ka} = 0, \quad \phi_{Kb} = \pm \frac{\pi}{2}. \dots\dots\dots (14)$$

Thus, the mode for the compound periodic structure when subjected to the engine order excitation can be given below from equations (3)-(6) and (14).

$$W_i(r, \theta, t) = \sum_K w_K(r) \{ \sin \omega t \cdot \cos K\alpha_i \pm \cos \omega t \cdot \sin K\alpha_i \} \\ = \sum_K w_K(r) \sin(\omega t \pm K\alpha_i) \dots\dots\dots (15)$$

Here + and - mean forward and backward directions in relation to the rotational direction, respectively. Again, it should be noted that the modes of nodal diameter components which are included in  $K$  have a same natural frequency  $\omega$ . Equation (15) shows a general traveling wave equation; it means that a mode for the compound periodic structure behaves like a traveling wave on the rotor wheel. Additionally, the modes of nodal diameter components, which are included in  $K$  and are not only related, but also unrelated to the harmonic excitation order  $h$ , can be observed for a traveling mode. This is the special feature for the compound periodic structure when subjected to engine order excitation.

## 4 EXPERIMENTAL METHOD

### 4.1 Model

Experiments were performed to check whether the theoretical investigation could express the traveling mode of a compound periodic structure correctly. The blade model is made of a plane steel disk, and includes the rectangular blade section and tie-wire components. Tie-wires are located at the top and middle of the blade height. The outer and the inner tie-wires compose the grouped structures ( $N_c=4$ ) and the one-ringed structure ( $M=32$ ), respectively. The specifications are given in Table 1 and the blade model is shown in Fig.2.

### 4.2 Excited traveling mode

As stated before, when the blades move past the non-uniform flow around the circumference, they are subjected to a cyclic exciting force. With the blade number defined as being numbered in the opposite direction for the rotation, exciting force is given as follows.

$$F_i = \sum_{h=1}^{\infty} f_h \cos(\omega t - h\alpha_i). \quad \dots\dots\dots (16)$$

Thus, each blade experiences an exciting force with its own peculiar phase angle  $h\alpha_i$  under rotation. In order to simulate the rotational excitation under a non-rotating condition, each blade of the model must be forced to oscillate by each cosine wave which includes the same exciting frequency and the inter-blade phase angle  $h\alpha_i$ .

Fig.3 shows the test equipment to simulate the rotational excitation. The test equipment is composed of the model, ceramic oscillators, a multi wave generator, a trigger generator, two FFTs, dynamic strain meters, strain gages, a data recorder and a computer. During operation, the computer calculates the excitation wave which includes harmonics number, exciting frequency and inter-blade phase angle for all the blades, and provides some digital wave signals of 4096 points per one period every blade. The digital wave signals are sent to the multi wave generator, and they are converted into excitation voltages. Excitation voltages, as from the trigger signal, are sent to the ceramic oscillators mounted on all the blades, and blade vibration occurs. The response signals of all the blades are measured by strain gages and the dynamic strain meter, and stored in the data recorder. During oscillation, excitation voltages and response signals are verified by each FFT.

## 5 EXPERIMENTAL RESULTS

According to the experimental findings, the mode shapes are observed for a mixture of fixed and traveling modes as to be expected. To find the cause of this modal phenomenon, the test model was investigated. As a result, it was revealed that there were two natural modes with slightly different natural frequencies to each other corresponding to a same nodal diameter  $k_n$ . The measured natural frequencies for the model are tabulated in Table 2. Here, the cause for this modal phenomenon is proved by a simple calculation. As the frequencies for sine and cosine terms in equation (15) are assumed as  $\omega + \delta\omega$  and  $\omega - \delta\omega$ , respectively,  $W_i$  can be written as follows:

$$\begin{aligned} W_i &= \sum_k w_k \{ \sin(\omega t + \delta\omega t) \cdot \cos K\theta \pm \cos(\omega t - \delta\omega t) \cdot \sin K\theta \} \\ &= \sum_k w_k [ \cos \delta\omega t \cdot \sin(\omega t \pm K\theta) + \sin \delta\omega t \cdot \cos(\omega t \mp K\theta) ]. \quad \dots\dots\dots (17) \end{aligned}$$

Thus, if  $\delta\omega$  is virtually zero,  $W_i$  is formed by only one traveling wave because the second terms is negligibly small. But, if  $\delta\omega$  has a certain value,  $W_i$  is formed by summing of two traveling waves which have various amplitudes, different traveling directions, and phase difference of  $90^\circ$ . Also, this model is highly sensitive to the resonant response. Even if  $\delta\omega$  is small, a traveling mode or an irregularly traveling mode is observed. Because the response of either upper or lower frequencies gets a large majority by giving slightly different exciting conditions. In order to excite the traveling mode in this model certainly, the exciting frequency must be given as the average of two natural frequencies.

### 5.1 Traveling mode

As an example for the traveling mode, the results of  $h = k_r = 3$  are shown in Figs.4(a) and (b) as the resonant responses of all the blades and the relative circumferential mode shapes respectively. Blade root stresses are indicated as their responses and mode shapes. In this case, the resonant responses of every blade form almost the same response pattern. The nodal points, namely, the points of zero amplitude move backward 3 wave lengths on one circuit of the model. The circumferential mode shapes are always a 3-nodal diameter mode, but it is not a pure sinusoidal wave.

The circumferential mode shapes in Fig.4(b) can be transformed to the relative response amplitude and the phase angle of nodal diameter components by discrete Fourier transform on the basis of total blade number  $M$ . In the response results of Fig. 5(a), the amplitude of  $k=3$  is remarkable and keeps about the same value. The amplitudes of other nodal components are small, but appeared clearly. On the other hand, in the phase angle results of Fig. 5(b), each result agrees fairly well with each sinusoidal approximate line. This means that not only  $k=3$  but also  $k=5, 11,$  and  $13$  components can form the traveling wave. This is the reason why the circumferential mode shapes are not a pure sinusoidal wave.

### 5.2 Irregularly traveling mode

Next, the results of  $h = k_r = 5$ , which is an example for the irregularly traveling mode, is shown in Figs.6(a) and (b). In this case, although the exciting frequency is given as the average of two natural frequencies, the irregularly traveling mode occurs because of the frequency difference of 2.4 Hz (Table 2), which is not small enough. If the model is machined with extreme accuracy and two natural frequencies corresponding to a nodal diameter are very close to each other, the response might show traveling mode. However, actual turbine blades have certain mistuning, which means that the two natural frequencies corresponding to a nodal diameter are not the same, so that the modes of the turbine blade with the compound periodic structure might behave as the irregularly traveling mode.

Figs. 7(a) and 7(b) show the discrete Fourier transform results. All response amplitudes do not keep the constant value because the circumferential mode appears like a fixed mode. However, all phase patterns agree fairly well with a sinusoidal approximate line. So this mode is not a fixed mode, and should be called an irregularly traveling mode.

### 5.3 Mode for $k_r \neq h$

Lastly, Figs.8 (a) and (b) show the circumferential mode shapes for  $k_r=3, h=5$  and  $k_r=5, h=3$ , respectively. Both show an irregularly traveling mode. In Fig.8 (a), the mode of  $k=3$  is remarkable, however, it can be excited by  $h=5$ . The reason why the traveling mode same as that shown in Fig.4 (b) is not exhibited has never been clear. In Fig.8 (b), the mode pattern is much the same as that of Fig.6 (b). The mode of  $k_r=5$  is also excited by  $h=3$ . As a result, it can be confirmed that the modes of the nodal diameter component, which is included in  $K$  and not only related but also unrelated to the harmonic excitation order  $h$ , can be observed for the traveling mode.

## 6 CONCLUSIONS

- (1) By the calculation considering the work done by the engine order excitation, the traveling mode of the compound periodic structure was investigated theoretically.
- (2) Traveling mode of the compound periodic structure was confirmed by a series of experiments with a simple blade model. The modes of nodal diameter components, which are included in a set of nodal diameters in a natural mode and not only related, but also unrelated to the harmonic excitation order, behave like the traveling mode.
- (3) The irregularly traveling mode could be observed in experiment because the mode has two slightly different natural frequencies corresponding to a nodal diameter.

## REFERENCES

- (1) Ewins, D. J. and Imregun, M., Vibration Modes of Packeted Bladed Disks, Trans. ASME, J. of Vibration, Acoustics, Stress and Reliability in Design, 1984, 175-180.
- (2) Wagner, L. F. and Griffin, J. H., Forced Harmonic Response of Grouped Blade Systems: Part 2-Application, Trans. ASME, J. of Eng. for Gas Turbines and Power, 1996, 137-145.
- (3) Namura, K. et al., Turbine Blade Assemblies and Their Vibration Characteristics, Proc. I Mech. E, 1992, 65-71
- (4) Saito, E. et al., Resonance Characteristics of Turbine Blades with Compound Periodic Structure, JSME, International J., Series B, Vol.41, 1998, 727-733.
- (5) Wildheim, J., Excitation of Rotating Circumferentially Periodic Structures, Trans. ASME, J. of Applied Mechanics, 1979, 878-882.

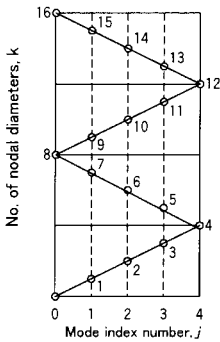


**Fig. 1 Mode chart**

**Table 1 Blade model specifications**

Blade		Tie-wires		
Number of Blades	32	—	Outer	Inner
Length	150 (mm)	Pitch	58.90 (mm)	44.18 (mm)
Thickness	4 (mm)	Thickness	4 (mm)	
Width	20 (mm)	Width	5 (mm)	
Material	Stainless Steel			
Young's Modulus	190 ( GPa )			

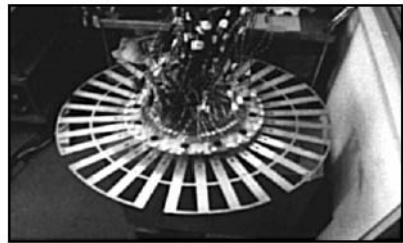


**Fig. 2 Blade model**

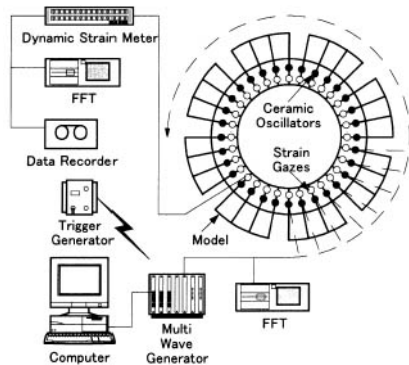


**Fig. 3 Test equipment**

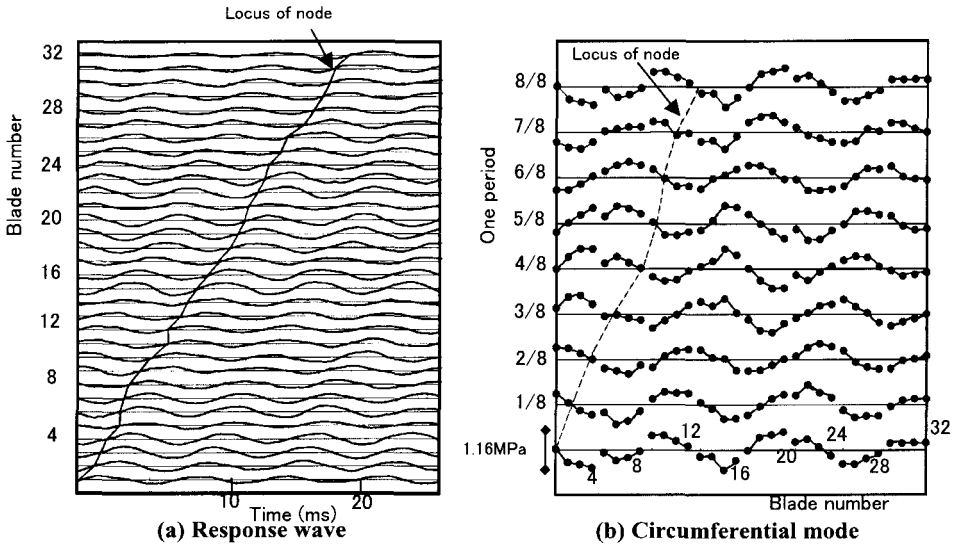
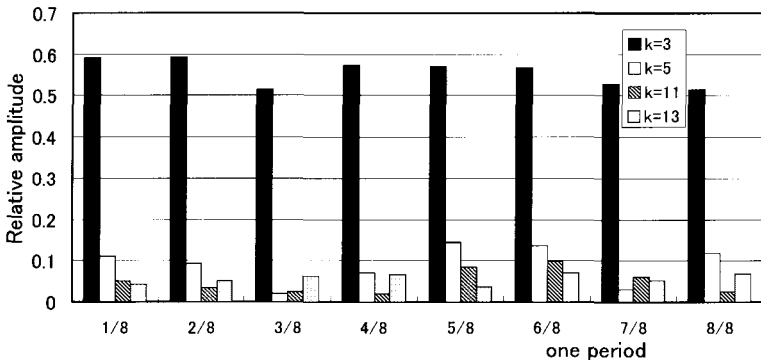
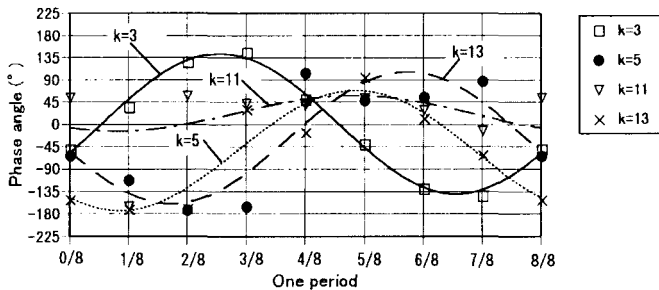


Fig.4 The case of  $k_r=3, h=3$



(a) Resonant response amplitude of each nodal diameter



(b) Phase of each nodal component

Fig.5 Fourier transform results of  $k_r=3, h=3$

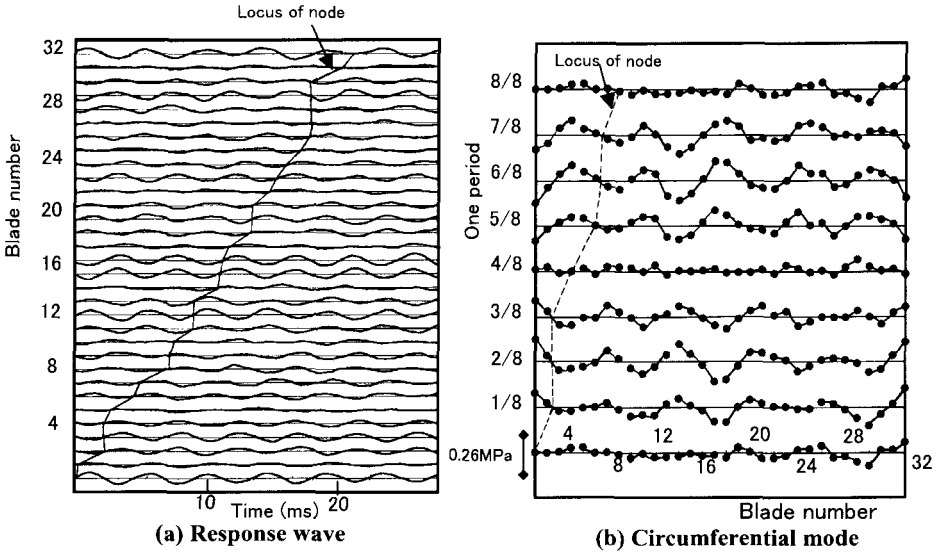


Fig.6 The case of  $k_r=5, h=5$

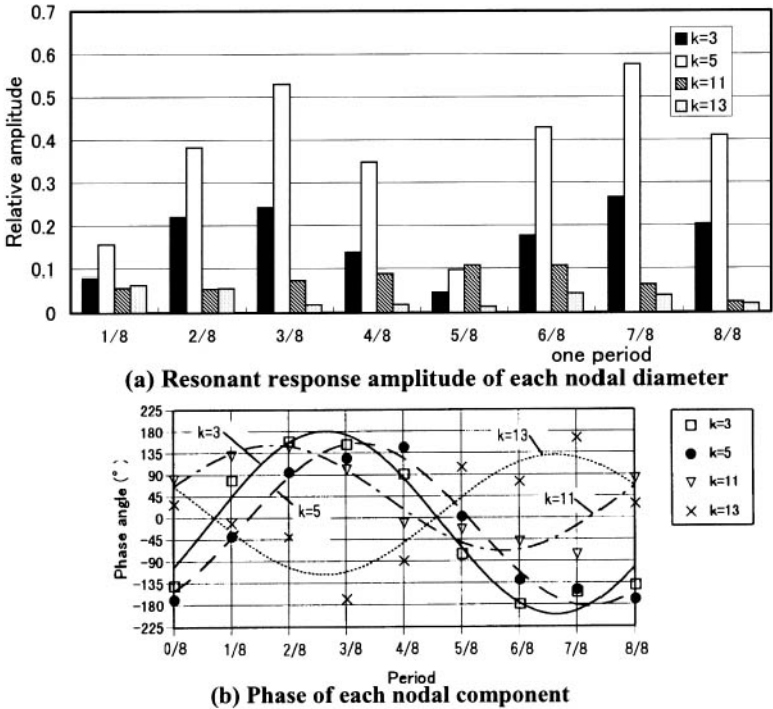
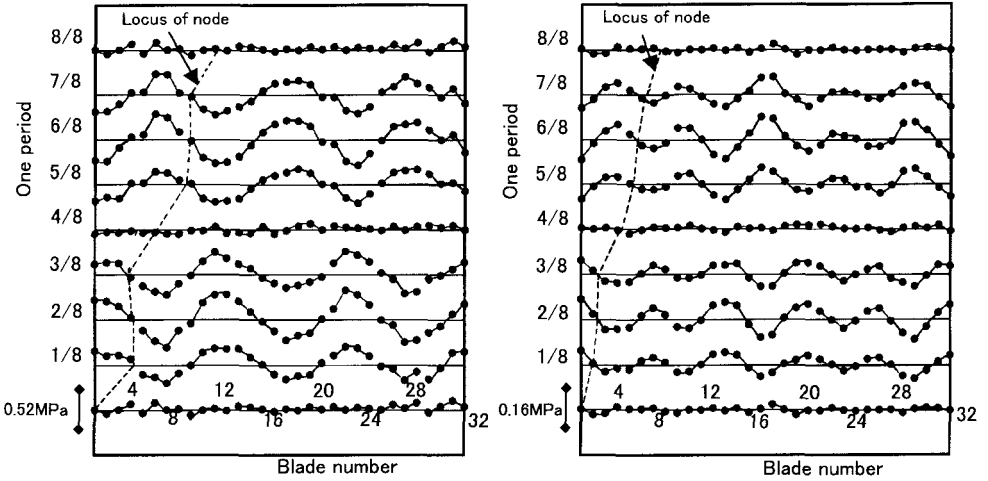


Fig.7 Fourier transform results of  $k_r=5, h=5$

**Table 2 Measured natural frequencies**

$kr$	$\omega_{upper}$	$\omega_{lower}$	$\omega_{difference}$	$\delta \omega$
0	116.8	114.2	2.6	1.31
1	121.4	119.4	2.0	1.00
2	135.2	134.0	1.2	0.60
3	156.8	156.2	0.6	0.30
4	173.9	173.5	0.4	0.20
4	219.8	219.5	0.3	0.15
5	246.3	243.9	2.4	1.20
6	291.7	289.2	2.5	1.25
7	340.9	338.1	2.8	1.40
8	366.2	364.5	1.7	0.85
8	507.0	505.6	1.4	0.7

Unit :Hz



(a) The case of  $k_r=3, h=5$

(b) The case of  $k_r=5, h=3$

**Fig.8 Circumferential mode for  $k_r \neq h$**



# Optimal search for worst mistuning patterns in mistuned bladed discs based on large-scale finite element models

**E P PETROV and D J EWINS**

Mechanical Engineering Department, Imperial College of Science, Technology, and Medicine, London, UK

## ABSTRACT

A method for searching for the worst frequency mistuning patterns (providing the highest response levels) in bladed disc assemblies is described. The method is intended for use with finite element models having a large number of degrees of freedom that could only be used currently for tuned bladed discs. The problem is formulated and solved as an optimization problem with the use of information about the sensitivity of maximum response levels with respect to mistuning variation. An effective analytical approach is developed to calculate the sensitivity coefficients without a significant increase in computational effort. Numerical studies are carried out for realistic finite element models of a bladed disc assembly to illustrate the method.

## 1 INTRODUCTION

Blade mistuning is inevitable in practical bladed discs and is usually caused by small imperfections in their manufacture and assembly process. Stress levels and vibration amplitude distributions are highly sensitive to mistuning variations even in the small ranges restricted by manufacture tolerances.

The problem assessing the mistuning worsening effect on resonance response levels has been studied so far mostly as a problem of analysis of response levels for some given mistuning patterns. These mistuning patterns are consciously chosen by the investigator, as was done in references (1)-(3) and (18) or are randomly generated, as in references (6),(7) and (13). In some references – (8),(9) and (15) – attempts are made to determine directly statistical characteristics of response levels variation in respect blade mistuning. More complete lists of references on studies of mistuned bladed discs can be found in references (4) and (16).

Although such results can give some estimate for the mistuning worsening effect, they do not guarantee that the trial mistuning patterns used are the worst (as in the case of deliberately chosen patterns) or they require generation and analysing a very large number of random mistuning patterns, which can be used only with very simplified models. Knowledge of the largest response level increase caused by the mistuning and of the arrangements of blades that are the most favourable, and those which are the most dangerous is very important for design practice. The answers can and should be obtained only for some specific bladed disc assemblies and under specific forcing conditions since it is very case-specific.

The problem of searching for the worst and best mistuning patterns has been formulated as an optimization problem first in paper (10), where blades of a mistuned bladed disc were modelled by pretwisted beams. Recently a new method for analysis of mistuned bladed discs has been developed (12), which allows use of detailed, realistic finite element models, such as were applied only for analysis of tuned bladed discs to date. The method is based on an exact relationship between the response of tuned and mistuned assemblies. It allows us to reduce exactly a large finite element model and to overcome excessive computational expense inherent usually to the analysis of mistuning.

In the present paper the problem of determining the worst mistuning patterns is formulated and solved as an optimization problem for large finite element models. Further development of the method is made to solve the optimization problem for such models. An effective method is developed for calculation of the sensitivity coefficients for maximum forced response with respect to blade mistuning. The effectiveness and accuracy of the sensitivity coefficient computations are based on an analytical derivation of the expressions for their calculation. Numerical studies are carried out for a finite element model of a realistic bladed disc.

## 2 THE PROBLEM FORMULATION

Usually, in service conditions, bladed discs are subjected to excitations of the so-called 'engine-order type', i.e. the amplitudes of vibration forces acting on different blades are identical but there is a fixed phase shift between forces on adjacent blades of the assembly.

A perfectly-tuned bladed disc subjected to such excitation generates the same amplitudes for all blades. Moreover, for such a bladed disc, the only modes that can be excited from a large variety of natural modes are those that have the same number of displacement waves around the circumference of the bladed disc as the engine order forcing.

Even small mistuning can change the vibration response characteristics of a bladed disc to a large extent. Amplitudes become different for the blades of a bladed disc and their distribution becomes very irregular. Many closely-spaced resonance peaks are excited. An example of the mistuning influence on the amplitudes of a bladed disc is shown in Fig. 1.

In the method proposed, the risk of a bladed disc failure is estimated from the maximum displacement amplitude level in the system, since effect of mistuning on stresses is supposed to be proportional to the effect on displacements. The maximum displacement response,  $\mathfrak{M}$ , is searched over all points of the bladed disc, over all excitation frequencies and over all time instants during a vibration period, which is represented by the following expression:

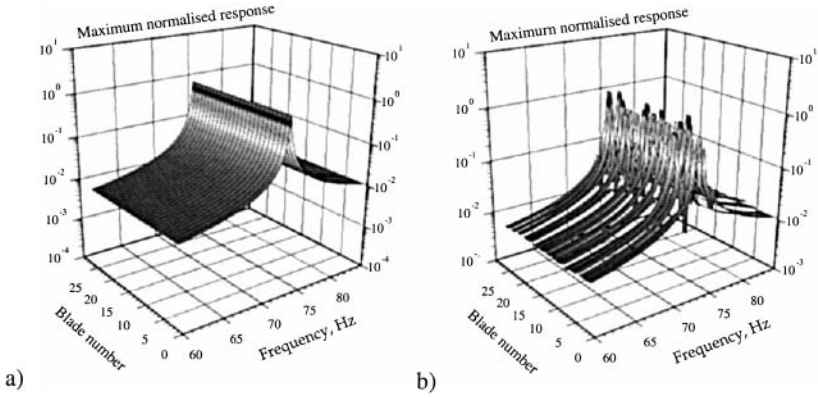


**Fig. 1** Forced response of each from 26 blades of the fan bladed disc:  
**a)** the case of tuned blades; **b)** the case of mistuned blades

$$\mathfrak{M} = \max_{\omega} \max_x \max_t \|\tilde{\mathbf{u}}(\omega, \mathbf{x}, t)\| \quad (1)$$

where  $\tilde{\mathbf{u}} = \{u_x, u_y, u_z\}^T$  is a vector of displacements at a considered point;  $\omega$  is the excitation frequency, which can admit values from a frequency range given, i.e.  $\omega \in [\omega^-, \omega^+]$ ;  $\mathbf{x} = \{x, y, z\}^T$  is a vector of co-ordinates of the point, which can be any point of the volume,  $V$ , occupied by the bladed assembly, i.e.  $\mathbf{x} \in V$ ;  $t$  is time, which can be considered over one period of vibration only, i.e.  $t \in [0, 2\pi/\omega]$ .

In practice, blade mistuning is usually measured by values of individual natural frequencies of the blades assembled into the bladed disc. We characterise a mistuning pattern by a vector of mistuning parameters,  $\mathbf{b}$ :

$$\mathbf{b} = \{b_1, b_2, \dots, b_{N_b}\}^T \quad (2)$$

where  $N_b$  is a total number of blades in the assembly. The  $j$ -th component of the vector is determined as the relative difference between the  $i$ -th natural frequency of the  $j$ -th blade,  $f_j^{(i)}$  and natural frequency of the perfectly-tuned, standard blade,  $f_0^{(i)}$ , i.e.

$$b_j = (f_j^{(i)} - f_0^{(i)}) / f_0^{(i)} \quad (3)$$

The choice of the particular mode used for the mistuning estimate is determined by the excitation frequency range of interest and the available experimental data.

The maximum displacement response is dependent on the mistuning pattern. In order to find the worst mistuning pattern (the one that provides the maximum displacement when acceptable mistuning is restricted by manufacture tolerances), the following constrained optimization problem is formulated:

$$\mathfrak{M}(\mathbf{b}) \rightarrow \max \quad (4)$$

with the bound constraints

$$\mathbf{b}^- \leq \mathbf{b} \leq \mathbf{b}^+ \quad (5)$$

### 3 CALCULATION OF THE MAXIMUM DISPLACEMENT

#### 3.1 Bladed-disc modelling and amplitude calculation

The equation of motion for forced vibration of a bladed disc can be written in the customary frequency domain form as:

$$(\mathbf{K} - \omega^2 \mathbf{M} + i\mathbf{D})\mathbf{q} = \mathbf{Z}(\omega)\mathbf{q} = \mathbf{f} \quad (6)$$

where  $\mathbf{q}$  is a vector of complex response amplitudes for nodal displacements along coordinate axes;  $\mathbf{f}$  is a vector of complex amplitudes of harmonic nodal loads;  $\mathbf{K}$ ,  $\mathbf{M}$  and  $\mathbf{D}$  are stiffness, mass and structural damping matrices of the system, respectively;  $\mathbf{Z}(\omega)$  is the dynamic stiffness matrix; and  $i = \sqrt{-1}$ . One can also include other terms representing gyroscopic and stiffening effects due to rotation in the dynamic stiffness matrix, if required.

For mistuned bladed discs, the matrices in Eq.(6) are too large to allow direct solution when a detailed enough finite element model is applied. Because of that, an effective method for calculation of vibration amplitudes of mistuned bladed discs has been developed in reference (12), which allows the use of large detailed finite element models that have previously been applied to the analysis of tuned bladed discs only. The method, together with a new technique for the analytical calculation of sensitivity coefficients of the maximum displacement with respect to mistuning (developed in Section 4), constitutes a basis for the optimization search of the worst mistuning pattern. The formulation given below for the method for amplitude calculation is modified to increase its efficiency for the optimization problem considered here.

In accordance with the method, the dynamic stiffness matrix for a mistuned system can be represented by a sum of the matrix for tuned system,  $\mathbf{Z}_0$ , and a mistuning matrix,  $\Delta\mathbf{Z}$ , characterising distinctions of the mistuned system from a tuned one, i.e.

$$\mathbf{Z} = \mathbf{Z}_0 + \Delta\mathbf{Z} \quad (7)$$

It can be shown that any mistuning matrix,  $\Delta\mathbf{Z}$ , can be expressed as the multiplication of two matrices,  $\mathbf{E}$  and  $\mathbf{V}$ , as follows:

$$\Delta\mathbf{Z} = \sum_{i,j=1}^N \Delta z_{ij} \mathbf{e}_i \mathbf{e}_j^T = \sum_{i=1}^N \mathbf{e}_i \left( \sum_{j=1}^N \Delta z_{ij} \mathbf{e}_j^T \right) = \underset{(N \times n)}{\mathbf{E}} \underset{(n \times N)}{\mathbf{V}} \quad (8)$$

where  $\mathbf{e}_i$  is a vector whose  $i$ -th component is equal to 1 and the others are equal 0;  $\mathbf{V}$  is a matrix, in which each row is constructed of the non-zero rows of the mistuning matrix,  $\Delta\mathbf{Z}$ ;  $\mathbf{E}$  is a matrix consisting of vectors  $\mathbf{e}_i$  corresponding to these non-zero rows;  $N$  is the number of degrees of freedom (DOFs) in the considered system and  $n$  is the number of non-zero rows in  $\Delta\mathbf{Z}$ .

Then, the complex amplitudes,  $\mathbf{q}$ , can be determined from Eqs.(6) and (8) by applying the Sherman-Morrison-Woodbury formula from references (14), (17) and we have the following expression for their determination:

$$\mathbf{q} = (\mathbf{Z}_0 + \Delta\mathbf{Z})^{-1} \mathbf{f} = \left[ \mathbf{A} - \mathbf{A}\mathbf{E}(\mathbf{I} + \mathbf{V}\mathbf{A}\mathbf{E})^{-1} \mathbf{V}\mathbf{A} \right] \mathbf{f} \quad (9)$$

where  $\mathbf{A} = \mathbf{Z}_0^{-1}$  is the FRF matrix of the tuned system; and  $\mathbf{I}(n \times n)$  is an identity matrix.

The main advantage of Eq.(9) is that it is exact and valid for any subset of the so-called 'active' nodes and DOFs selected. The active nodes are those where one wishes to determine

amplitude response levels and where mistuning is applied. The number of active nodes can be chosen to be small enough to enable effective calculations. Moreover, the FRF matrix of a tuned bladed disc used in (9) can be generated from the mode shapes and natural frequencies calculated from a finite element model of one its sector only, having taken into account the cyclic symmetry properties of the tuned assembly. The effective method for calculation of the FRF matrix for a tuned bladed disc is described in (12). An example of the finite element model for a bladed disc, its sector and active nodes chosen, is shown in Fig. 2.

Eq.(9) can be rewritten in the following set of two equations which are much more effective for computation:

$$\mathbf{q} = \mathbf{q}_0 - \mathbf{A}_E \mathbf{p} \quad (10)$$

where  $\mathbf{A}_E (N \times n) = \mathbf{A} (N \times N) \mathbf{E} (N \times n)$  is the FRF matrix of the tuned system with excluded columns corresponding to zero rows of matrix  $\Delta \mathbf{Z}$  and  $\mathbf{q}_0$  is vector of response amplitudes for the tuned bladed disc. An auxiliary vector,  $\mathbf{p} (n \times 1)$ , is determined from solution of the following equation:

$$(\mathbf{I} + \mathbf{V} \mathbf{A}_E) \mathbf{p} = \mathbf{V} \mathbf{q}_0 \quad (11)$$

The blade frequency mistuning is modelled by applying the mistuning matrix,  $\mathbf{V}_0 (n/N_B \times N/N_B)$ , of the same structure to each blade of the assembly. The differences in mistuning between blades are described by coefficients  $c(b_j)$ , which are used as a multiplier on matrix  $\mathbf{V}_0$ . Owing to this, the mistuning matrix for the whole bladed assembly,  $\mathbf{V}$ , can be expressed in the following, block-diagonal form:

$$\mathbf{V}(\mathbf{b}) = \text{diag} \{ c(b_1) \mathbf{V}_0, c(b_2) \mathbf{V}_0, \dots, c(b_{N_B}) \mathbf{V}_0 \} \quad (12)$$

The coefficient  $c(b_j)$  establishes correspondence between the mistuning parameters of the blade-alone natural frequencies defined in Eq.(3) and magnitudes of the components of the

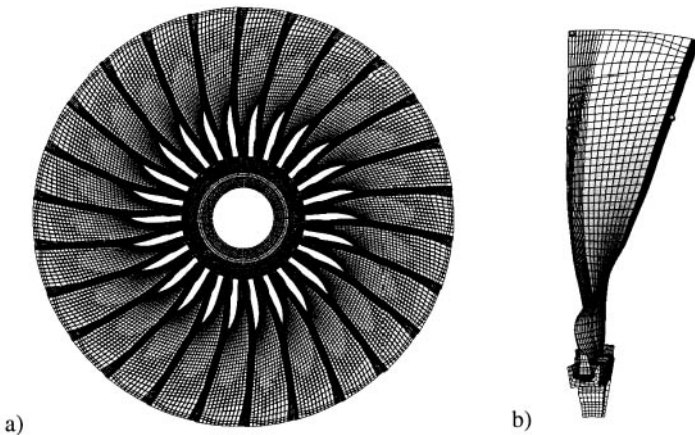


**Fig. 2 Finite element model and active nodes:**  
**a) a bladed disc; b) a sector of the bladed disc**

mistuning matrix. This coefficient is determined by calculating a chosen  $i$ -th resonance of a single blade,  $f^{(i)}$ , and hence the mistuning parameter  $b_j$  for a set of trial values  $c_j$ , ( $j = 1, n_c$ ). The spline approximation  $c(b)$  with respect to the introduced mistuning parameters,  $b$ , is then performed using the data calculated.

Although there is no restriction on the structure and values of components of the matrix  $V_0$ , it is useful to define some mistuning elements which have a physical interpretation and which help to form  $V_0$ . Simple examples of such elements can be: lumped masses, dampers or springs applied to nodes of the finite element model. In the case when the mistuning elements are applied to all active nodes,  $V_0$  is a diagonal matrix having non-zero components on its main diagonal. For this case Eq.(10) can be replaced by the following one:

$$\mathbf{q} = \mathbf{V}^{-1} \mathbf{p} \quad (13)$$

where, because of the diagonal structure of matrix  $V$ , its inverse is calculated by simple inversion of its diagonal components and, moreover, all matrix multiplications in Eqs. (11) and (13) can be performed very efficiently.

### 3.2 Maximum displacement over vibration period

Each component of the nodal displacement vector can have its own phase, which results in an elliptical in space orbit of a node during vibration. Because of that, the maximum displacement at a node cannot be obtained simply as the sum of the squares of the amplitude of all its co-ordinate components. The analytical formula has been derived in reference (11) to express the maximum displacements using complex amplitudes of co-ordinate displacements and it has the following form

$$\max_i \|\tilde{\mathbf{u}}_k\| = \max_i \|\operatorname{Re}(e^{i\omega t} \mathbf{u}_k)\| = \max_i \sqrt{\operatorname{Re}(e^{i\omega t} \mathbf{u}_k^T) \operatorname{Re}(e^{i\omega t} \mathbf{u}_k)} = \sqrt{\frac{1}{2} (\mathbf{u}_k^* \mathbf{u}_k + \mathbf{u}_k^T \mathbf{u}_k)} \quad (14)$$

where  $\mathbf{u}_k$  is a vector of complex amplitudes of co-ordinate components at the  $k$ -th node considered, and  $*$  represents the Hermitian conjugate.

### 3.3 Maximum displacement over a bladed disc assembly

The maximum displacement over all nodes of the system and the corresponding node number,  $k_{\text{opt}}$ , are determined by a simple comparison of  $\max_i \|\tilde{\mathbf{u}}_k\|$  at all nodes analysed.

### 3.4 Maximum displacement in a given excitation frequency range

Near resonance peaks, the amplitude levels of systems with small damping (which is typical of bladed discs) vary abruptly. Because of that, an accurate calculation of resonance amplitudes requires a very small excitation frequency step in order to locate the resonance frequencies precisely. Mistuned bladed discs have many resonance peaks, which are sometimes spread over a rather wide frequency range. To make the search for the maximum displacement,  $\mathfrak{M}$ , efficient, it is performed as the solution of an optimization problem with excitation frequency considered as an optimization parameter varied in a given range. Frequency stepping is applied to separate the resonance peaks and the step size can be chosen to be reasonable large for this goal. A combination of the golden section method and the inverse quadratic approximation method (see reference (5) ) is then used for precise determination of the resonance amplitudes. The displacements found at all resonance peaks

are compared and the largest value gives  $\mathfrak{M}$  and a value of the corresponding excitation frequency,  $\omega_{\mathfrak{M}}$ .

#### 4 SENSITIVITY COEFFICIENTS IN RESPECT TO MISTUNING

The number of variable parameters in the proposed optimization search of the worst mistuning patterns is equal to the number of blades in the assembly. This number is always large enough to make it necessary to use optimization methods based on the gradient of the maximum displacement with respect to the mistuning parameters. Because of this, determination of this gradient, where components are the sensitivity coefficients for the maximum displacement with respect to the mistuning parameters, is one of the most important tasks which determines the effectiveness of the method developed.

The sensitivity coefficients could be calculated using finite difference approximations for the derivatives. However, even the simplest first-order finite-difference formulas require calculating  $\mathfrak{M}(\mathbf{b} + \Delta b \mathbf{e}_j)$ , ( $j = 1, N_b$ ) at least  $N_b$  times for small increments,  $\Delta b$ . This is a very time-consuming process and makes this approach too expensive for the problem of analysing mistuned bladed discs, leaving apart inevitable approximation errors. The method proposed below for analytical determination of the sensitivity coefficients of the maximum displacement in a mistuned bladed disc with respect to the mistuning parameters provides a fast and exact calculation.

##### 4.1 Sensitivity coefficients for complex nodal amplitudes

Expressions for determination of the sensitivity coefficients for the complex nodal amplitudes can be obtained by differentiating Eqs.(10) and (11) with respect to the  $j$ -th mistuning parameter analysed:

$$\partial \mathbf{q} / \partial b_j = -\mathbf{A}_E \partial \mathbf{p} / \partial b_j \quad (15)$$

$$(\mathbf{I} + \mathbf{V} \mathbf{A}_E) \partial \mathbf{p} / \partial b_j = (\partial \mathbf{V} / \partial b_j) \mathbf{q} \quad (16)$$

where all matrices are calculated at the previously-found excitation frequency,  $\omega_{\mathfrak{M}}$ , corresponding to the maximum displacement, and the vector of complex amplitudes,  $\mathbf{q}$ , is determined from Eqs.(10) and (11). For the particular case of the diagonal matrix  $\mathbf{V}$ , specified in Section 3.1, the following, more efficient expression, can be used instead of Eq.(15):

$$\partial \mathbf{q} / \partial b_j = \mathbf{V}^{-1} (\partial \mathbf{p} / \partial b_j - (\partial \mathbf{V} / \partial b_j) \mathbf{q}) \quad (17)$$

Matrix  $\partial \mathbf{V} / \partial b_j$  is determined by differentiation of Eq.(12), which results in the following expression:

$$\partial \mathbf{V} / \partial b_j = \text{diag} \{ \mathbf{0}, \mathbf{0}, \dots, (\partial c / \partial b_j) \mathbf{V}_0, \dots, \mathbf{0} \} \quad (18)$$

where only the  $j$ -th block on the main diagonal of the matrix is non zero. The smooth character of the function,  $c(b)$ , and its spline approximation used, allow calculating derivatives  $\partial c / \partial b_j$  without difficulty and with high accuracy.

It should be noted that the calculation of the sensitivity coefficients for all the introduced mistuning parameters is not time-consuming, compared with the calculation of the maximum displacement, since all calculations are performed for only one excitation frequency,  $\omega_{\mathfrak{M}}$ .

Moreover, the matrix  $\mathbf{I} + \mathbf{V}\mathbf{A}_E$  in Eq.(16) is identical for derivatives with respect to all the mistuning parameters,  $b_j$  ( $j=1, N_B$ ). Taking this into account also allows us to save the computation time by decomposing the matrix in a Gauss elimination solution of Eq.(16) only once.

#### 4.2 Sensitivity coefficients for the maximum displacement

To use the derivatives of the complex amplitudes obtained in the previous section, we derive an expression for the sensitivity coefficients of the maximum displacement with respect to the mistuning parameters having taken into account the dependence of the maximum displacement on the real and imaginary parts of the complex amplitudes. This results in the following formula:

$$\frac{\partial \mathfrak{M}}{\partial b_j} = \left( \frac{\partial \mathfrak{M}}{\partial \mathbf{u}^{\text{Re}}} \right)^T \frac{\partial \mathbf{u}^{\text{Re}}}{\partial b_j} + \left( \frac{\partial \mathfrak{M}}{\partial \mathbf{u}^{\text{Im}}} \right)^T \frac{\partial \mathbf{u}^{\text{Im}}}{\partial b_j} = \text{Re} \left( \frac{\partial \mathbf{u}^*}{\partial b_j} \frac{\partial \mathfrak{M}}{\partial \mathbf{u}} \right) \quad (19)$$

where three components of the vector  $\partial \mathbf{u} / \partial b_j$  are selected from the vector of sensitivity coefficients for complex nodal amplitudes,  $\partial \mathbf{q} / \partial b_j$ , for the node,  $k_{\text{opt}}$ , where the maximum of displacements is achieved.

The complex vector,  $\partial \mathfrak{M} / \partial \mathbf{u}$ , is introduced in (19) to facilitate the use of derivatives of **complex** amplitudes with respect to the mistuning parameters. It is defined by the following expression:  $\partial \mathfrak{M} / \partial \mathbf{u} = \partial \mathfrak{M} / \partial \mathbf{u}^{\text{Re}} + i \partial \mathfrak{M} / \partial \mathbf{u}^{\text{Im}}$ . Having differentiated Eq.(14), this can be expressed through the complex amplitudes in the following form:

$$\frac{\partial \mathfrak{M}}{\partial \mathbf{u}} = \frac{1}{2\mathfrak{M}} \left( \mathbf{u} + \bar{\mathbf{u}} \frac{\mathbf{u}^T \mathbf{u}}{|\mathbf{u}^T \mathbf{u}|} \right) \quad (20)$$

where a bar above a symbol  $\mathbf{u}$  means a complex conjugate.

Expressions (19) and (20) are calculated jointly with Eqs.(15) and (16) for all mistuning parameters,  $b_j$ , to obtain all components of the vector of the sensitivity coefficients:

$$\nabla \mathfrak{M} = \left\{ \partial \mathfrak{M} / \partial b_1, \partial \mathfrak{M} / \partial b_2, \dots, \partial \mathfrak{M} / \partial b_{N_B} \right\}^T \quad (21)$$

The calculations are performed at the excitation frequency corresponding to maximum displacement,  $\omega_{\text{opt}}$ .

## 5 OPTIMIZATION SEARCH OF THE WORST MISTUNING PATTERN

The efficient method developed above for calculation of the sensitivity coefficients,  $\nabla \mathfrak{M}$ , and the objective function,  $\mathfrak{M}$ , allows us to make a search for the worst mistuning pattern using the derivatives. The most efficient optimization methods using the sensitivity coefficients belong to the family of quasi-Newton methods. An effective algorithm also based on quasi-Newton method has been developed and applied in reference (11) for the optimal search of worst and best mistuning patterns of bladed discs for the case when blades are modelled by pretwisted beams. The algorithm allows us to take into account the bound constraints imposed by manufacturing tolerances on mistuning variations. It has been used for the multi-degrees-



of-freedom finite element models of the bladed discs analysed here with some minor modifications.

## 6 NUMERICAL RESULTS

The presented method has been applied to the analysis of a bladed fan disc containing 26 blades, which is shown in Fig. 2. A detailed finite element model was used for determination of the FRF matrix of the tuned assembly. It contains above 120,000 DOFs in each sector of the finite element model and the full bladed disc comprises above 3,000,000 DOFs. Direct implementation of this model, comprising more than three million DOFs for the mistuned assembly, would be impractical for just response analysis, leaving apart the optimization search. Because of that, just 4 nodes were selected as the active nodes for each blade (see Fig. 2) and displacements were determined and controlled at these nodes. The number of DOFs analysed,  $n$ , in vector  $\mathbf{q}$  equals 468, which is quite acceptable for our purposes. The values of possible blade frequency mistuning were assumed to be located within the range [-5%...+5%].

### 6.1 Illustrative case: mistuning variation for two blades

The behaviour of the objective function in the developed optimization search is demonstrated on a relatively simple example, which can be visualised easily. In this example only two mistuning parameters are varied (namely:  $b_7$  and  $b_{22}$ ) and mistuning parameters for all the other blades are not varied and are assumed to be zero (i.e. these blades are tuned). The objective function normalised by its value for the perfectly tuned assembly,  $\mathfrak{M}(\theta)$ , i.e.  $\hat{\mathfrak{M}}(\mathbf{b}) = \mathfrak{M}(\mathbf{b})/\mathfrak{M}(\theta)$ , is shown in Fig. 3. It is evident that the objective function has a complex character with several local maxima. The points corresponding to sequential iterations of the optimization search are shown in this figure by circles. Initial values for the mistuning vector,  $\mathbf{b}$ , were close to the tuned values, where the objective function has a minimum ( $\hat{\mathfrak{M}}(\theta) = 1$ ). After 9 iterations the worst mistuning pattern was found, which for the considered case locates on the boundary of the area of acceptable mistuning, namely it has values  $b_7 = 5\%$ ,  $b_{22} = -5\%$  and the other 24 parameters are zero.

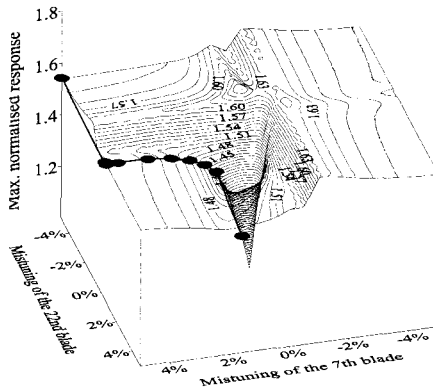
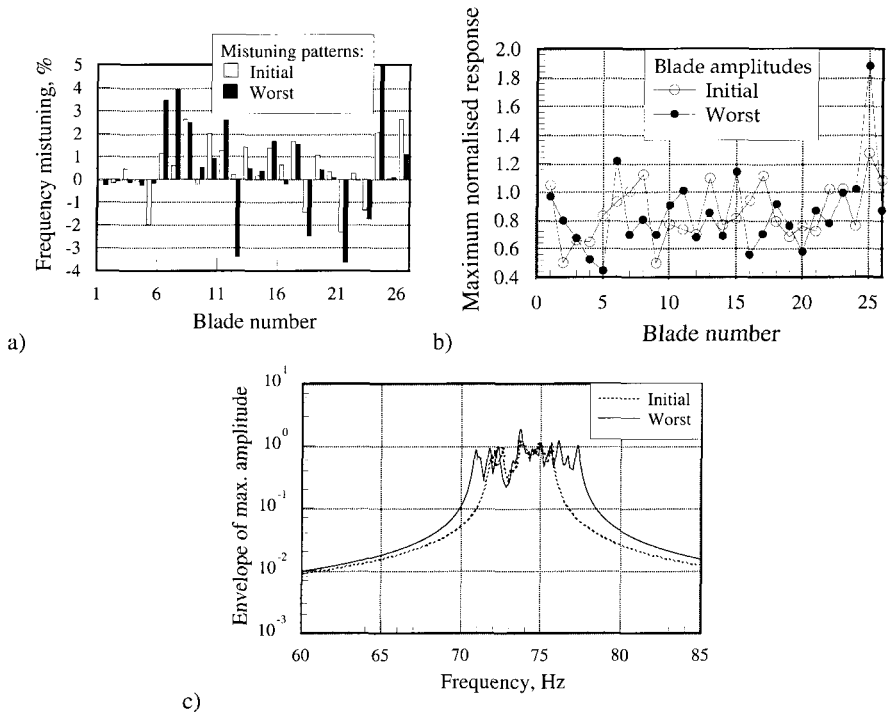


Fig. 3 Dependence the envelope of maximum response,  $\mathfrak{M}$  on mistuning parameter variation for two blades of the assembly

### 6.2 The realistic case: mistuning values for all blades are varied

Results for the case when mistuning values for all 26 blades are varied in the optimization search are shown in Fig. 4. The found worst mistuning patterns, maximum response levels for each of the blades and envelopes of maximum forced response function corresponding to the initial and worst patterns are compared in Fig. 4 with initial values. It is evident that the small changes in mistuning pattern can change many very important vibration characteristics of the bladed assembly, namely: (i) distribution of amplitudes over blades of the bladed assembly; (ii) range of resonance amplitudes; and (iii) maximum response levels.

The increase in the maximum response levels with the number of iterations when all 26 mistuning parameters are varied is shown in Fig.5. Results of the optimization search starting with four different initial values of the vector of mistuning parameters are shown. Starting the optimization search from different initial points can lead to different local maxima of the objective function,  $\hat{\mathcal{M}}$ . As one can see from the figure, that first iterations usually give a larger increase rate for  $\hat{\mathcal{M}}$  than later iterations. Furthermore, results of a search for the worst mistuning with the random (or called sometimes ‘statistical’) search are displayed. In the random search, the vector of mistuning parameters was generated randomly at each iteration and the corresponding value of  $\hat{\mathcal{M}}$  was calculated. Comparison of both methods demonstrates the superiority of the optimization search proposed in this paper.



**Fig. 4 Initial and found worst mistuning patterns, (a); maximum amplitude distributions corresponding to these patterns, (b); an envelope of maximum amplitudes calculated for the patterns, (c).**

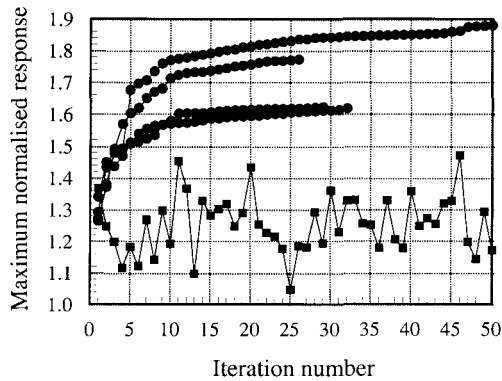


**Fig. 5 Increase of the maximum amplitude with the number of iteration for the optimization search starting from different initial configurations (—●—) and for random search (—■—).**

## 7 CONCLUDING REMARKS

A method has been developed to calculate the worst mistuning patterns for mistuned bladed discs which provide the highest response levels.

The method uses an optimization approach in a search for the worst mistuning pattern and is based on the developed effective algorithm for analytical calculation of the sensitivity coefficients for the maximum response level in respect to blade mistuning. It allows calculation of the sensitivity coefficients without a noticeable addition of computation time to the time of determination of the maximum response level.

The method is intended for use with finite element models having large number of degrees of freedom that could be used only for tuned bladed discs so far. It takes full advantage of the use of an exact condensation method based on the Sherman-Morrison-Woodbury formula for the finite element model.

Numerical investigations carried out for realistic finite element models of bladed disc assemblies have demonstrated the efficiency of the proposed method for searching the worst mistuning patterns and highest response levels that are possible in specific excitation conditions and design of bladed discs.

## 8 ACKNOWLEDGEMENT

The authors are grateful to Rolls-Royce plc. for providing the financial support for this project and for giving permission to publish this work.

## REFERENCES

- (1) Castanier, M.P., Óttarsson, G., and Pierre, C., (1999), "Reduced order modelling and vibration analysis of mistuned bladed disk assemblies with shrouds," *Trans. of ASME: J. of Eng. for Gas Turbines and Power*, Vol. 121, pp.515-522
- (2) Ewins, D.J., (1969), "Effect of detuning upon the forced vibration of bladed discs," *J. of Sound and Vibration*, Vol. 9, No.1, pp. 65-79
- (3) Ewins, D.J., and Han, Z.C., (1984), "Resonant vibration levels of a mistuned bladed disk," *Trans ASME, J. of Vibration, Acoustics, Stress and Reliability in Design*, Vol. 106, pp. 211-217
- (4) Ewins, D.J. (1991) "The effects of blade mistuning on vibration response – a survey". *IFTOMM 4th International Conference on Rotordynamics*, Prague, Czechoslovakia, 1991
- (5) Forsythe, G.E., Malcolm, M.A., (1977), "Computer methods for mathematical computations," Prentice-Hall Inc., Englewood Cliffs, N.Y.
- (6) Griffin, J.H. and Hoosac, T.M. (1984) "Model development and statistical investigation of turbine blade mistuning", *ASME J. of Vibr., acoustics, Stress and Reliability in Design*, Vol. 106, pp.204-210.
- (7) Griffin, J.H., (1992) "Optimizing instrumentation when measuring jet engine blade vibration", *ASME J. of Eng. for Gas Turbines and Power*, Vol. 114, pp.217-221
- (8) Mignolet, M.P. and Lin C.-C. (1993) "The combined closed form –perturbation approach to the analysis of mistuned bladed disks. *ASME J. of Turbomachinery*, Vol. 115, pp.771-780
- (9) Lin, C.-C., Mignolet, M.P. (1997) "An adaptive perturbation scheme for the analysis of mistuned bladed discs," *ASME J. of Eng. for Gas Turbines and Power*, Vol. 119, pp.153-160
- (10) Petrov, E.P., 'Optimization of perturbation parameters for forced vibration stress levels of turbomachine blade assemblies.' *Proc. of the IUTAM Symposium on Discrete Structural Optimization*, August 31 - September 2, 1993, Zakopane, Poland, pp. 108-117
- (11) Petrov, E.P., Iglin, S.P., 'Search of the worst and best mistuning patterns for vibration amplitudes of bladed disks by the optimization methods using sensitivity coefficients', *Proc. of 1st ASSMO UK Conf. 'Engineering Design Optimization'*, 8-9 July 1999, Ilkley, UK, pp. 303-310
- (12) Petrov, E.P., Sanliturk, K.Y., Ewins, D.J., A new method for dynamic analysis of mistuned bladed discs based on exact relationship between tuned and mistuned systems. (submitted to *Trans. ASME: J. of Eng. for Gas Turbines and Power*)
- (13) Sanliturk, K.Y, Imregun, M. and Ewins, D.J., (1992) "Statistical analysis of random mistuning of bladed assemblies". *Inst. Mech. Eng.* C432/110, pp. 51-57
- (14) Sherman, J., and Morrison, W.J., (1949), "Adjustment of an inverse matrix corresponding to changes in the elements of a given column or a given row of the original matrix," *Ann. Math. Statist.*, 20, p. 621.
- (15) Sinha, A., Chen, S., (1989) "A higher order technique to compute the statistics of forced response of a mistuned bladed disc assembly," *J. of Sound and Vibration*, Vol. 130, pp. 207-221
- (16) Slater, J.S., Minkiewicz G.R. and Blair A.J. (1999) "Forced response of bladed disk assemblies –A survey". *The Shock and Vibration Digest*, Vol.31, No. 1, pp.17-24
- (17) Woodbury, M. , (1950), "Inverting modified matrices," Memorandum Report 42, Statistical Research Group, Princeton University, Princeton, NJ
- (18) Yang, M.-T., Griffin, J.H. (1999), "A reduced order model of mistuning using a subset of nominal system modes," Presented at the ASME TURBO EXPO'99, Indianapolis, USA, ASME Paper 99-GT-288.

# A stochastic approach to turbine blade vibration and fatigue

D M GHIOCEL and N F RIEGER

STI Technologies Inc., Rochester, New York, USA

## ABSTRACT

The paper addresses the main aspects involved in probabilistic modeling of component fatigue life prediction for jet engine rotating components, specifically blades. Probabilistic high cycle/low cycle (HCF/LCF) life prediction of engine blades represents a difficult engineering problem involving multiple, complex random phenomena. The paper overviews key aspects of stochastic modeling of the HCF/LCF life prediction of engine blades. The paper highlights the need of the use of stochastic process and field models for including space-time varying random aspects which are important for modeling of flight profiles, operating environmental conditions, blade and dynamic stress/strain responses and material progressive damage process. The paper also addresses the stochastic modeling of highly nonlinear responses in multidimensional parameter spaces. Stochastic response surface techniques based on factorable stochastic fields or optimum stochastic models are suggested. An illustrative example of a typical blade is used for discussion and to show the consequences of different modeling assumptions.

## 1. INTRODUCTION

Probabilistic HCF/LCF life prediction for jet engine blades represents a difficult problem involving stochastic modeling of multiple, complex transient random phenomena. A key aspect for developing an advanced probabilistic HCF/LCF life prediction tool is to incorporate a refined stochastic modeling of space-time varying random phenomena such as those related to modeling of operating environment, material parameters and behavior, large nonlinear effects due to aero-elastic interactions, nonlinear damping effects, friction at contact interfaces, multi-site fatigue, progressive damage mechanism including damage interactions, etc. A major challenge of stochastic modeling of space-time varying and highly nonlinear effects consists of including a large number of elementary input random variables (also obtained by stochastic field factorization) in the probabilistic life prediction analysis. To handle a stochastic highly nonlinear multivariate-multidimensional problem such as HCF/LCF life prediction problem, innovative, efficient numerical techniques are needed. The level of sophistication for stochastic modeling in different parameter spaces depends on the significance of the randomness/uncertainty effects and also on the availability of statistical

data for describing the random phenomena. The number of random variables in a typical probabilistic HCF/LCF life prediction analysis may vary from a few to several tens of input random variables, depending drastically on the stochastic modeling refinement of space-time random phenomena.

In next sections, major uncertainties involved in blade fatigue life prediction are reviewed, making the appropriate stochastic modeling suggestions. It is the author's hope that these suggestions will help the engineering community to clarify specific stochastic modeling issues.

## 2. STOCHASTIC MODELING

In this section key stochastic variabilities associated to environmental and blade component conditions are addressed. Stochastic modeling of highly nonlinear stochastic responses is also discussed.

### 2.1 Flight Profiles

A severe flight speed profiles including a large number of pilot maneuvers is shown in Figure 1. This figure indicates that the speed profiles can be appropriately idealized by non-stationary pulse stochastic processes. It should be noted that depending on flight maneuvering, the pulse structure can vary in a continuous path or in discrete clusters that represent the periods of more intense maneuvers. Inside each cluster there is a short-length correlation between intensities of individual pulses indicating the pilot maneuvers are gradual rather than abrupt. Probability density of the operating speed profiles is extremely skewed, close to a shifted exponential distribution rather than a Gaussian distribution as shown in Figure 2.

Figure 3 shows the significance of stochastically modeling the speed profiles for typical aircraft flights. The illustrated life prediction comparative results are computed for the same blade (and material) performing a probabilistic damage accumulation analysis assuming a random sequence of different random flight speed profiles and a sequence of a repeated deterministic "representative" speed profiles, respectively. Figure 3 clearly indicates that the sequence of random speed profiles may be significantly severer for the HCF/LCF life than the sequence of deterministic "representative" speed profiles used for typical LCF verification. This happens due to the random occurrences of high vibratory stresses in the blade due to passing through multiple mode transient resonances. The random occurrences of these resonances are shown by vertical jumps in the damage accumulation curve of random flight sequence.

A simple model of a typical speed profile is the linear recursive pulse process model described by the sequence of realizations of two independent random variables  $Y$  and  $Z$  as follows:

$$X_k = Y_k X_{k-1} + (1 - Y_k) Z_k, k = 1, 2, \dots \quad (1)$$

where  $k$  is the step number in the random sequence. The  $Y$  variable is a binary random variable taking value 0 or 1 with probabilities  $1-p$  and  $p$ , respectively. The  $Z$  variable is an arbitrary distributed random variable with a cumulative distribution function denoted  $D(z)$ .

The pulse process is a non-Gaussian Markov discrete process as the current values are dependent only on the last step values. However, the recursive nature of the model ensures a larger memory. It can be shown that the asymptotic stationary covariance function of the Markov discrete process,  $X$ , is defined by:

$$C(X_k, X_{k+q}) = \sigma^2 p^q \quad (2)$$

where  $\sigma^2$  is the variance of distribution  $D(x)$  and  $q$  is the step lag. The asymptotic probability density of the Markov process,  $X$ , is given by:<sup>1</sup>

$$F(x) = \lim_{k \rightarrow \infty} (1-p)D(x) \sum_{i=1}^k p^{i-1} = D(x) \quad (3)$$

assuming that the starting point is zero.

As an alternate approach is to relate the non-Gaussian flight operational profile, denoted as a continuous process  $X(t)$ , to its Gaussian image, denoted by  $Z(t)$ , by a nonlinear memoryless monotonic transformation,  $g(\cdot)$ ,  $X(t) = g(Z(t))$ . This transformation can be further expressed by the relationship  $X(p, s) = F^{-1}(\Phi(Z(p, s)))$ , where  $F^{-1}(\cdot)$  is the inverse of marginal cumulative distribution function of  $X(t)$  and  $\Phi(Z)$  is the standard Gaussian cumulative distribution function of  $Z(t)$ . The pair correlation (an element of correlation matrix) of  $X(t)$ , denoted  $XX(t, t')$ , can be expressed in terms of the pair correlation of  $Z(t)$ , denoted  $ZZ(t, t')$ , by  $XX(t, t') = \int_{-\infty}^{\infty} \int_{-\infty}^{\infty} g(u)g(v) \Phi(u, v, ZZ(t, t')) du dv$ , where  $\Phi(\cdot)$  is the bivariate Gaussian density function. It should also be noted that the computed minimum value of the correlation coefficient function of the non-Gaussian process  $X(t)$  is not necessarily -1, as for a Gaussian process, but higher. This happens for a non-symmetric distribution.

To include the intensity dependence between pulse amplitudes a Gauss-Markov sequence model can be employed. This is a simple and flexible model to include dependence between pulse intensities. The intensity given occurrence are related by:

$$X_{k+1} = \rho X_k + \sqrt{1-\rho^2} Z_k \quad (4)$$

in which  $X_j$  = pulse intensity in step  $j$ .  $Z_k$  are independent normal variate with a mean of  $\mu_z = \sqrt{(1-\rho)/(1+\rho)} \mu_x$ , and a variance of  $\sigma_z = \sigma_x$ . The pulse intensity correlation is then given:

$$\rho_{X_j, X_k} = \rho^{|j-k|} \quad (5)$$

in which  $\rho_{X_j, X_k}$  is correlation coefficient between the pulse intensities in steps  $j$  and  $k$ .

If the pulse clustering effects is significant a modified double pulse process can be used. A macro-time scale pulse process is used to describe the occurrence and duration of pulse clusters. Then, a micro-time scale pulse process is employed to describe the pulse cluster structure. The second pulse processes is imbedded in the first pulse process. The correlation between cluster pulse intensities can be included as above discussed.

## 2.2 Aero-Loading and Blade Geometry

Aero-forcing and blade geometry deviations represent key factors for evaluating the blade fatigue life. The stochastic steady-state pressure profiles can be represented as a statistical function of the operating speed profiles as indicated in Figure 4. The random deviations from the regression curve are relatively homogeneous with respect to speed variation, but non-Gaussian. These random deviations are mainly due to transient effects. The unsteady aero-forcing represents the key parameter for an accurate HCF/LCF life prediction. Usually in engineering practice, the stimulus ratio is assumed to be a scalar variable and thus is modeled as a random variable. However, this is a crude assumption that may lead to a significant underestimation of modal stresses for high-order blade vibration modes that are major contributions to the HCF damage. Figure 5 shows the Interference Diagram for a typical engine blade. Few critical vibration modes produce the dominant HCF damage.

The unsteady pressure distribution amplitude near the blade tips may largely affect the dynamic behavior of the blade and magnitude of vibratory stresses. A more consistent approach that is to use stochastic fields for aero-pressure distribution for both the steady and unsteady components. Such an approach is discussed from mathematical modeling point of view in the next paragraphs in relation to the non-parametric stochastic modeling of airfoil geometry deviations.

An important aspect for HCF damage evaluation is the blade geometry deviation from nominal geometry due to manufacturing process, which can significantly influence the vibratory stresses. These geometry deviation effects can be important for the airfoil and attachment contact surfaces. The manufacturing geometry deviations can be idealized stochastic field models. Figure 6 illustrates a simulated airfoil geometry using a stochastic field model. Resonant stresses in a typical blade computed for an assumed nominal airfoil geometry, and for an airfoil with perturbed geometry including (assumed) manufacturing deviations, respectively, are shown in Figures 7 and 8.

From the mathematical modeling point of view, these stochastic fields are quite complex, being non-homogeneous, non-isotropic non-Gaussian vector fields. To handle these complex fields it is advantageous to represent them in terms of mutually orthogonal functions. This is an old idea in deterministic mathematical modeling. Examples are the Fourier type integrals and series, which depend on the orthogonality of elementary harmonic functions.

The same idea can be used in a stochastic context, by means of the theory of factorable random fields. It can be shown that under certain integrability conditions a stochastic function can be decomposed in an orthogonality structure in a probability measure space. Let assume that the random variables  $z_i$ ,  $i = 1, 2, \dots, m$  are defined on probability space  $(\Omega, F, P)$  and take values in the  $\sigma$ -field or Borel set  $(R, B)$  on  $R$ . Then, assume that  $u(z_1, \dots, z_m)$  is a function of  $L_2(R^m, P_z)$ , which means that it is a square integrable function with respect to a



probability measure  $P_z$  with its density defined by:

$$\frac{P_z(dz_1 \dots dz_m)}{dz_1 \dots dz_m} = f_z(z_1) \dots f_z(z_m) \quad (6)$$

It means that the following integral integral form has a finite value:

$$I_m = \int \dots \int_m u^2(z_1, \dots, z_m) f_z(z_1) \dots f_z(z_m) dz_1 \dots dz_m < \infty \quad (7)$$

where  $f_z(z_i)$ ,  $i = 1, 2, m$  are univariate probability densities. Then, if  $\{p_{i,k}(z_i)\}$ ,  $i = 1, 2, m$  are complete sets of random functions in  $L_2(\mathbb{R}, P_i)$  which are orthogonal with respect to the density  $P_i(dz_i)/dz_i = f_z(z_i)$ , in the sense that  $E[p_k(z_i)p_\lambda(z_i)] = 0$  for all  $k \neq \lambda = 0, 1$ , and  $i = 1, m$ . It follows that the function  $u(z_1, \dots, z_m)$  can be expanded in the following series:

$$u(z_1, \dots, z_m) = \sum_{k_1=0}^{\infty} \dots \sum_{k_m=0}^{\infty} u_{k_1 \dots k_m} p_{k_1}(z_1) \dots p_{k_m}(z_m) \quad (8)$$

where  $\{p_{k_1}(z_1), \dots, p_{k_m}(z_m)\}$ ,  $k_1, \dots, k_m = 0, 1, \dots$ , are complete sets of orthogonal random functions. The series coefficients are computed by solving the integral:

$$u_{k_1 \dots k_m} = \int \dots \int u(z_1, \dots, z_m) p_{k_1}(z_1) \dots p_{k_m}(z_m) u_1(z_1) \dots u_m(z_m) dz_1 \dots dz_m \quad (9)$$

The coefficients  $u_{k_1 \dots k_m}$  have a key minimizing property, specifically the integral difference:

$$D = \int \dots \int \left[ u(z_1, \dots, z_m) - \sum_{k_1=0}^{M_1} \dots \sum_{k_m=0}^{M_m} g_{k_1 \dots k_m} p_{k_1}(z_1) \dots p_{k_m}(z_m) \right]^2 \quad (10)$$

reaches its minimum only for  $g_{k_1 \dots k_m} p_{k_1} = u_{k_1 \dots k_m} p_{k_1}$ . The completeness relationship is:

$$I_m = \sum_{k_1=0}^{\infty} \dots \sum_{k_m=0}^{\infty} u_{k_1 \dots k_m}^2 = \int \dots \int_m u^2(z_1, \dots, z_m) f_z(z_1) \dots f_z(z_m) dz_1 \dots dz_m < \infty \quad (11)$$

which assures that the series expansion of  $g(z_1, \dots, z_m)$  converges to  $u(z_1, \dots, z_m)$ .

For general case, several techniques can be used for constructing factorable stochastic fields. For example, the use of the Pearson differential equation for defining different types of stochastic orthogonal polynomial series representations including Hermite, Legendre, Laguerre and Chebyshev polynomial series. One major application of theory of factorable stochastic fields is the spectral representation of stochastic fields.<sup>1,2</sup> The Karhunen-Loeve (KL) representation is usually associated with the case of Gaussian stochastic fields, for which the field can be decomposed in terms of a set of independent standard Gaussian random

variables (projections in multidimensional standard Gaussian space). The use of KL expansion assumes that the covariance function of the stochastic field is known which limits severely its area of applications.

The KL expansion of a stochastic field  $X(p)$  is based on spectral representation of covariance function,  $C(X(p), X(p'))$  as follows:<sup>3</sup>

$$C(X(p), X(p')) = \sum_{n=0}^{\infty} \lambda_n \Phi_n(p) \Phi_n(p') \quad (12)$$

where  $\lambda_n$  and  $\Phi_n(p)$  are the eigenvalue and the eigenvector of the covariance kernel, respectively. They are computed by solving the integral equation:

$$\int_D C(X(p), X(p')) \Phi_n(p) dp = \lambda_n \Phi_n(p') \quad (13)$$

The covariance function being symmetrical and positive definite has all its eigenfunctions mutually orthogonal, and they form a complete set spanning the function space that contains the field  $X(p)$ . It can be shown that if this deterministic set is used to represent the stochastic field, then the random coefficients used in the expansion are also orthogonal. The general form of the KL expansion is:

$$X(p) = \sum_{i=0}^n \sqrt{\lambda_i} \Phi_i(p) z_i \quad (14)$$

where set  $\{z_i\}$  represents a set of independent, standard Gaussian random variables. If the process being expanded is Gaussian, then the random variables  $\{z_i\}$  form an orthonormal Gaussian vector and the KL expansion is mean-square convergent irrespective of the correlation structure.

More generally, if the stochastic field  $X(p)$  is non-Gaussian and/or covariance function is known it can be formally expressed as a nonlinear functional of a set of standard Gaussian variables or in other words expanded in a set of random orthogonal random functions, denoted  $\{\psi_i\}$ . Herein, for exemplification, a stochastic expansion model based on a polynomial type series is suggested:

$$u(p) = \sum_{j=0}^p u_j(p) \psi_j \quad (15)$$

These polynomials should be orthogonal in the sense that their inner product  $E[\psi_j \psi_k]$  that is defined as the statistical average of their product is equal to zero if  $i$  is different than  $j$ . A given truncated series can be refined along the random dimension either by adding more random variables to the set  $\{z_i\}$  or by increasing the maximum order of polynomials included in the stochastic expansion. The first refinement takes into account higher frequency random fluctuations of the underlying stochastic process, while the second refinement captures strong

non-linear dependence of the solution process on this underlying process. Using the orthogonality property of polynomial chaoses, the coefficients of the stochastic expansion solution can be computed by:

$$u_k = \frac{E[\psi_k u]}{E[\psi_k^2]} \text{ for } k = 1, \dots, K \quad (16)$$

It should be noted at this point that the chaos expansion can be used to represent, in addition to the solution process, arbitrary non-Gaussian stochastic processes. Polynomial chaoses are orthogonal with respect to the normal probability measure,  $dP = \exp(-\frac{1}{2} \mathbf{z}^T \mathbf{z}) d\mathbf{z}$ , which makes them identical with the corresponding multidimensional Wiener-Hermite polynomials. The orthogonality relation between these random polynomials is expressed by the inner product in  $L_2$  sense with respect to Gaussian measure:

$$\int_{-\infty}^{\infty} \Gamma_n(z_{i1}, \dots, z_{in}) \Gamma_m(z_{i1}, \dots, z_{in}) \exp(-\frac{1}{2} \mathbf{z}^T \mathbf{z}) d\mathbf{z} = n! \sqrt{2\pi} \delta_{mn} \quad (17)$$

For an efficient numerical implementation, to increase the convergence, especially if the investigated problem is highly nonlinear in the original solution space, a transformed space polynomial chaos expansion representation can be also used. Transformation of logarithmic type can be appropriate for highly nonlinear problems that are not well represented by polynomial chaoses in the original space. This transformation is expressed mathematically by:

$$u = \exp \sum_{i=1}^n \frac{E[\ln u \psi_i]}{E[\psi_i^2]} \psi_i \quad (18)$$

### 2.3 Blade Stress/Strain Response

Typically the response surface method (RSM) is used to approximate the stochastic stresses/strains in blades. However, the accuracy of RSM has a limited accuracy for highly nonlinear systems. In RSM, the selection of sampling points for constructing the response surface using regression analysis is based on simple “rules” of design of experiment theory (Box-Benken, Central Composite designs) which may be more or less appropriate depending on the problem particularity. Moreover, the selection of “representative” solution points for the system response is based on an subjectively assumed “scale of variation” (arbitrarily selected to be one standard deviation, or two standard deviations, etc., based on the subjective judgments of the statistician). This may affect drastically the accuracy of classical response methodology. Its accuracy for highly nonlinear problems or for problems including correlated input variables is always being questionable. Also, it should be noted that for large number of variables RSM also becomes totally impractical due to an enormous computational effort involved, possibly, far larger than that of the direct Monte Carlo simulation (!). Therefore, at this time, an essential step for improving the efficiency of stochastic approaches for nonlinear problems consists of creating new computational efficient tools based on stochastic field modeling. The specialized literature on stochastic modeling issues has recognized in the last decade that stochastic field models represent a clear more accurate solution for stochastic

nonlinear problems.<sup>2,4,5</sup>

Herein a simple optimum stochastic field model is suggested for response surface modeling. Basically, this optimum stochastic estimation model assumes that a nonlinear response of a systems is modeled by a non-homogeneous stochastic field which is defined in such a way, so that the mean-square error with respect to the given data or solution points (assumed to be points of a realization of the stochastic field) is minimum. Using the optimum stochastic estimation models the correlation between values of a nonlinear response surface at short distances is explicitly taken into consideration. This remark also applies to values at data points, so that the “weight” of each point in a cluster is automatically reduced. Importantly, no homogeneity/stationary condition is needed. Conceptually, the response surface  $r(x)$  is divided into a trend and a random fluctuation:

$$r(x) = \bar{r}(x) + r'(x) \quad (19)$$

The distinction between the trend surface and random fluctuation is not clear-cut. Generally, we think of the trend a large-scale variation, regarded as fixed, and the fluctuation as a small-scale random process. Then  $C(x, x')$  is the covariance function of  $R'$  as well as of  $R$ . The importance of (19) is that shows that the two components can be predicted separately. For a smooth surface:

$$\hat{r}(x) = \hat{\bar{r}}(x) \quad (20)$$

whereas for stochastic interpolation the approximation is:

$$\hat{r}(x) = \hat{\bar{r}}(x) + \hat{r}'(x) \quad (21)$$

The theory for approximating a random process  $r(x)$  is precisely Wiener-Kolmogorov theory for a time series with a finite history used for forecasting.<sup>6</sup>

If the trend (mean) surface is assumed to be known then the stochastic response surface can be fully defined by the process  $w(x) = r'(x) = r(x) - \bar{r}(x)$ . A linear predictor of the form can be defined as:

$$\hat{w}(x) = \sum \lambda_i w(x_i) = \lambda^T w_N \quad (22)$$

which minimizes the mean-square functional:

$$E[w(x) - \hat{w}(x)]^2 = \text{var}(w(x)) - 2\sum \lambda_i C(x_i, x) + \sum \lambda_i \lambda_j C(x_i, x_j) = \sigma^2(x) - 2\lambda^T k(x) + \lambda^T K \lambda \quad (23)$$

where  $K_{ij} = C(x_i, x_j)$ ,  $k(x) = (C(x, x_i))$ ,  $\lambda$  is a function of  $x$ . Now equation (23) is a quadratic form in  $\lambda$  that can be minimized by finding its stationary point. Since the covariance matrix  $K$  is strictly positive definite and invertible there is no restriction in practice. The linear predictor equations can be expressed by:

$$\hat{w}(x) = [w_N^T K^{-1}]k(x) \quad (24)$$

$$\sigma_E^2(x) = \sigma^2(x) - k(x)^T K^{-1}k(x) \quad (25)$$

Thus, the optimum stochastic predictor is defined by the linear combination of the functions  $C(x, x_i)$  that passes through the data points.

## 2.4 Fatigue Life Prediction

Generally, stochastic dynamic stress response of a blade can be expressed by the matrix differential equation of motion:

$$\begin{aligned} \ddot{X}(t,s) &= g(X(t,s), E(t,s), D(t,s)) \\ \dot{D}(t,s) &= h(X(t,s), E(t,s), D(t,s)) \end{aligned} \quad (26)$$

where  $t$  is time and  $s$  is space coordinate. The stochastic stress-strain vector process,  $X(t, s)$ , the input environmental/material vector process, the  $E(t, s)$ , and the scalar damage parameter,  $D(t, s)$ , are fully coupled. Such an approach includes both changes in strength and constitutive model using damage parameter as an internal variable in the material constitutive model. The damage growth depends on stress amplitude and reciprocally the stress amplitude depends on damage level. However, currently in engineering practice the influence of damage on stresses is not considered. The damage accumulation models describe the damage evolution as a function of loading stress history, or more specifically as a function of closed stress-strain cycle sequence. The unclosed stress-strain cycles are not included. A key aspect is the cycle counting of the closed stress-strain cycles.

Using Rychlik's non-recursive definition, the rainflow counting procedure<sup>7</sup> can be described by a discrete Markov process of the min-max pair points, Pair  $(X_{\max}, X_{\min})$ , in a closed time interval,  $T$ :

$$X_{\min, T} \begin{cases} \max(X_{\min}^-, X_{\max}^+), t^+ < T \\ X_{\min}^-, \text{ otherwise} \end{cases} \quad (27)$$

$$X_{\max, T} \begin{cases} X_{\max}^+, t < T \end{cases} \quad (28)$$

The set of these pair points defines the rainflow cycle process,  $\text{rfc}(X)$ . Then, the counting distribution,  $N_T(X_{\min}, X_{\max})$  of the rainflow cycle process  $\text{rfc}(X)$  can be uniquely defined. The total cumulated damage due to cyclic stress loading can be directly computed by the convolution of the damage function with the cycle counting distribution:

$$D_T = \int_T d(t)dt = \sum_{i \text{ for } v \leq u} D(v_i, u_i) = - \iint_{v \leq u} N_T(v, u) \frac{\partial^2 D(v, u)}{\partial v \partial u} dv du + \int_R N_T(u, u) \frac{\partial D(u, u)}{\partial u} du \quad (29)$$

The total damage being defined by the sum of damages attached to all closed hysteresis. For Gaussian processes the turning point pairs in the cycle sequence can be idealized by an

irreducible discrete Markov process.

For non-Gaussian processes obtained by superposing a slow-varying non-Gaussian process and a fast-varying continuous Gaussian/non-Gaussian process, such as the case of superimposing the LCF and HCF components a possible practical solution is to employ hidden discrete Markov processes for describing the turning point random sequence.

A typical stress profile in a critical blade locations (stress cycle history) is shown in Figure 9. It shows the steady-state stress profile (LCF component) and vibratory stress profile (HCF component) for two different locations in the blade. The HCF component history (at the bottom of Figure 9) indicates a highly skew, non-Gaussian probability density of vibratory stress amplitudes.

For evaluating the stochastic crack initiation life, a local strain-life approach with a randomized strain-life curve is typically used. The notch root plasticity is introduced using Neuber's rule. The analytical expression of the stochastic strain-life transformation is:

$$\varepsilon_a = \frac{\sigma_f}{E} (2N_f)^b + \varepsilon_f' (2N_f)^c \quad (30)$$

where the equation parameters are random variables. The mean stress effect (including temperature, static, residual stresses from previous damages or processing, etc.) is included using weighted randomized Morrow and SWT correction schemes. An important aspect of using the strain-life curve is that it is possible to handle the random effects coming from surface finish, fretting effects, temperature effects, creep, etc.

The damage accumulation process is defined by the kinetic equation  $\frac{dD}{dN} = f(D, N(S_a, S_m), p)$  where  $D$  is the damage parameter and  $S_a$  and  $S_m$  are the alternating stress (half range of HCF component) and mean stress (LCF component). The letter  $p$  denotes the parameters of damage model. For an appropriate damage modeling, stress-dependent damage models are needed. They are capable of accurately including the HCF/LCF interactions and initial defects for predicting the crack initiation blade life. The damage curve approach (DCA) proposed by Halford, 1996,<sup>8</sup> can be simply constructed based on only two amplitude level experiments, i.e., LCF and HCF levels. These two levels should be appropriately selected to correspond to the extreme significant stress (or better life for constant amplitude) levels in the investigated component. For an arbitrary amplitude level, the DCA equation,  $D - N_f$ , represents a power-law function of the form  $D = (n / N_f)^{g(N_f)}$  where the exponent function  $g(N_f)$  is determined based on an experimental calibration. Typical stress-dependent DCA mean curves are shown in Figure 12. Such a nonlinear damage rule is required for obtaining an accurate evaluation of damage level at a given time. The linear damage rule (LDR), or Miner's rule, may give a crude estimate for such situations.<sup>5</sup> The greater the ratio between the (two) extreme life levels, the more severe HCF/LCF interaction or deviation from the linear damage rule is expected. The nonlinear DCA model is capable of including interactive effects from initial defects, FOD and fretting effects. An alternate is the Lemaitre-Caboche model that is analytically a more refined damage model.<sup>9</sup>

Stochastic damage models are typically described by diffusion process models driven by a non-white excitation (filter equations which transform the white-excitation in non-white excitation are included), which can be accurately handled using Ito stochastic calculus.<sup>10</sup>

Figures 9 through 11 illustrate computed results for random sequences of random flight profiles including also accidental damage. Figure 11 indicates that the HCF/LCF blade life is a highly uncertain variable. As shown, some rare, severe flight profiles affect drastically the blade life. Other blades may have very large lives well above the average (thus, it is not the most efficient economically to replace them based on pre-established scheduled replacement plan). Figures 12 and 13 show the probability distribution of predicted life without accidental damage and with accidental damage, respectively. It can be observed that accidental damage effects severely affect the blade life. The accidental damage effects were idealized as Poisson arrival processes with different mean occurrence rates, assumed to be functions of damage sizes.

### 3. CONCLUDING REMARKS

Probabilistic HCF/LCF life prediction for jet engine components represents an extremely difficult engineering problem involving stochastic modeling of multiple, complex random phenomena. The paper overviews key aspects of stochastic modeling of the life prediction for a typical engine blade.

The paper highlights the need of using stochastic process/field models for accurately capturing space-time variabilities in input parameters and also for approximating highly nonlinear stochastic responses. The paper suggests specific stochastic process/field models for flight operational profiles, blade aero-forcing, manufacturing geometric deviations and damage accumulation process.

### 4. REFERENCES

- (1) Grigoriu, M., *Applied Non-Gaussian Processes*, Prentice Hall, 1995.
- (2) Bogdanoff and Kozin, *Probabilistic Models of Cumulative Damage*, John Wiley Interscience Publication, 1985.
- (3) Loeve, M., *Probability Theory, 4th Edition*, Springer Verlag, 1977.
- (4) Ghiocel, D. M., *Stochastic High-Cycle Fatigue Life Prediction for Aircraft Jet Engines*, 13th ASCE Specialty Conference, Session on Stochastic FEM, Baltimore, June 13-16, 1999.
- (5) Ghiocel, D. M., and Rieger, N. F., *Specific Probabilistic Issues for Gas Turbine HCF Life Prediction*, the 3<sup>rd</sup> FAA/AFRL Workshop on Application of Probabilistic Design Methodologies to Gas Turbine Rotating Components, Phoenix, AZ, March 4-5, 1998.

- (6) Papoulis, A., *Probability, Random Variables and Stochastic Processes*, McGraw Hill, 1965.
- (7) Rychlik, I., *Rainflow Analysis: Markov Method*, Int. Journal of Fatigue, 15, No. 4, 1993.
- (8) Halford, G. A., *Cumulative Fatigue Damage Modeling – Crack Nucleation and Early Growth*, The 1<sup>st</sup> International Conference on Fatigue damage in Structural Materials, Hyannis, MA, September 22-27, 1996.
- (9) Lemaitre, M. and Caboche, R., *Mechanics of Solids*, Elsevier, 1998.
- (10) Bogdanoff and Kozin, *Probabilistic Models of Cumulative Damage*, John Wiley-Interscience Publication, 1985.

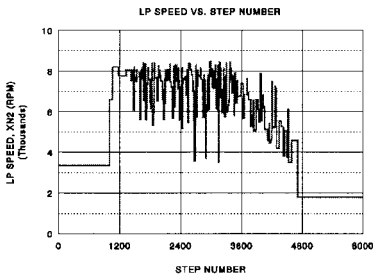


Figure 1. Speed Profile vs. Operational History

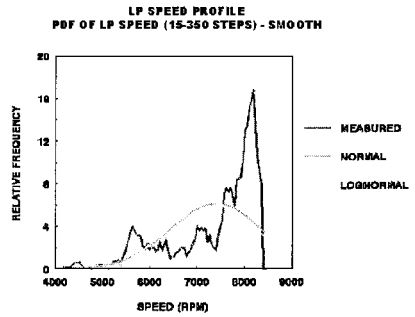


Figure 2. Probability Density of Speed

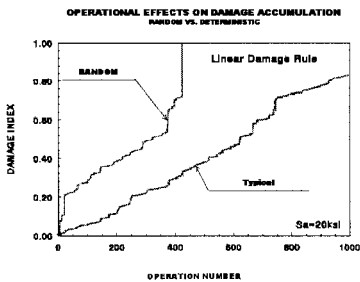


Figure 3. Flight Profile Variability Effect

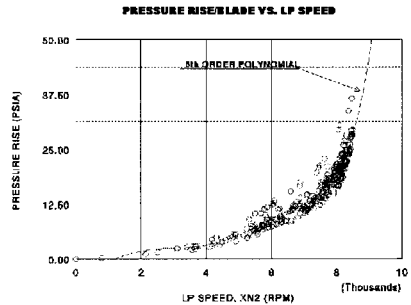


Figure 4. Blade Differential Pressure vs. Speed



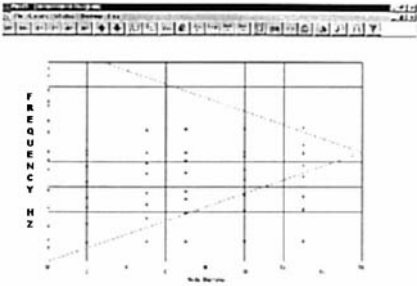


Figure 5. Inference Diagram

Blade Harmonic Distortion - Environmental - Job

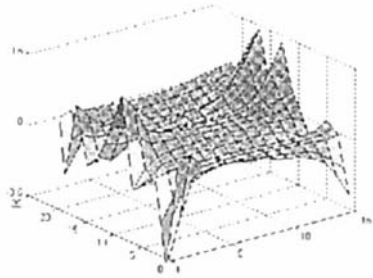


Figure 6. Characteristic Airfoil Geometry Deviation

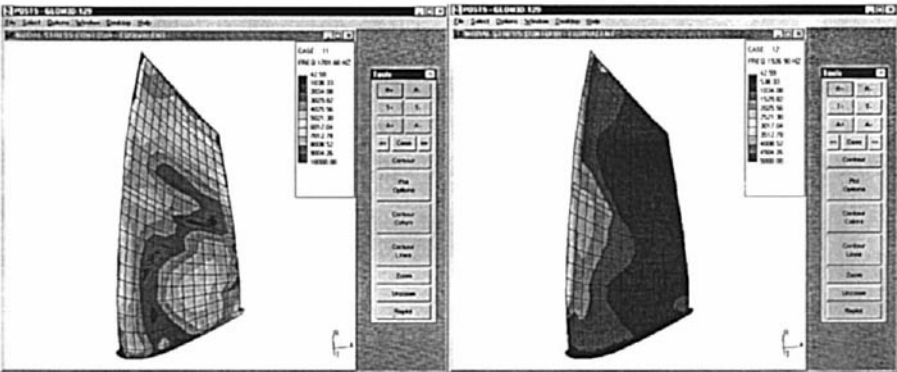


Figure 7. Resonant Stresses in Typical Blade with Assumed Nominal Airfoil Geometry

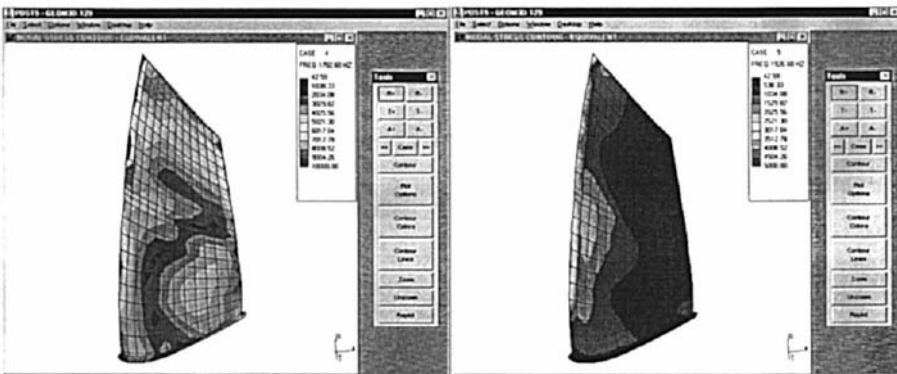


Figure 8. Resonant Stresses in Typical Blade with Assumed (Perturbed) Airfoil Geometry

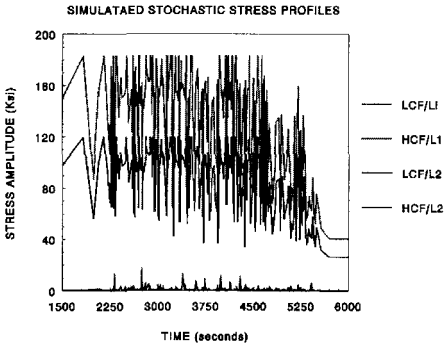


Figure 9. Steady State and Vibratory Stress

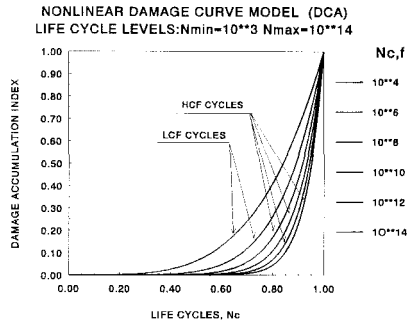


Figure 10. Nonlinear Damage Curves

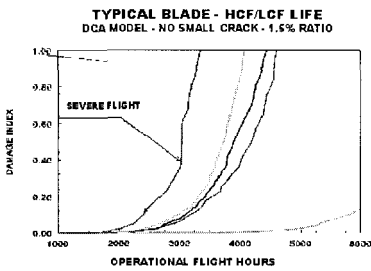


Figure 11. Predicted Life for Different Random Flight Sequences

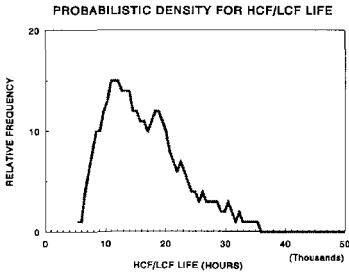
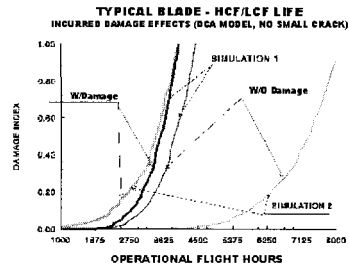


Figure 12. HCF/LCF Life PDF without Incurred Damage

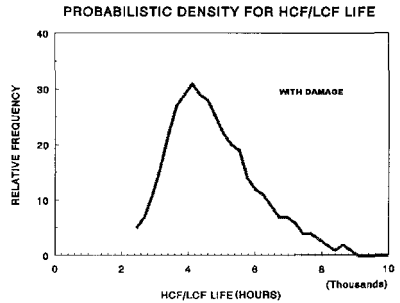


Figure 13. HCF/LCF Life PDF with Incurred Damage

Balancing

*This page intentionally left blank*

# When to high-speed balance large turbine generator rotors

**R G HERBERT**

National Power plc, Swindon, UK

## SYNOPSIS

Current international standards recommend that requirements for balancing depend on the flexibility of the rotor. In general terms rotors operating below their first critical speed can be balanced using rigid rotor procedures. Rotors operating close to or above their first critical speed are regarded as flexible and should be subjected to a high-speed balance procedure. However, there are many large turbine generators, with multiple rotors, that will pass through their shaft critical speeds where experience has shown these rotors can be safely low speed balanced. Calling for a high-speed balance, when it is not necessary can be costly in both down time and balancing fees and it could be prohibitive in many overseas locations. This paper suggests an alternative method to assess the need for high speed balancing, which considers the state of the rotor in terms of its flexibility and operating environment. A mathematical simulation of the rotor is simply based on its geometric design. This identifies the obvious flexible rotors, such as large generators and gas turbines. It is only in marginal cases where a qualitative understanding of the support structure is required. A number of large turbine generator rotors, in the range 350 to 660 MW, are considered and compared with maintenance experience.

## 1. INTRODUCTION

Most large flexible rotors are high-speed balanced by the original equipment manufacturer during the manufacturing process, since it guarantees the quality of the rotor and minimises potential problems during commissioning. Rotors will be in the high-speed pit for over speed testing and the additional work for the high-speed balance is minimal. A few large flexible rotors are only slow speed balanced but this does rely on a detailed sequence of balance runs as the rotor is assembled. The decision to use high-speed balance procedures on new rotors by the manufacturer

can be made with a full knowledge of the rotor design and usually within easy distance of a suitable balance pit.

Repair of older rotors poses more problems, particularly if the original manufacturer does not carry out the work. The rotor will have run for a number of years, its in-situ balance history may be unknown, extensive remedial work may have been carried out, detail design data may not be known and a high-speed balance pit is not usually readily available. In these situations the pressures to undertake only a low speed balance or no balance at all will be very strong. The potential risks of an in-situ balance during re-commissioning may be more attractive than the costs and extended down time that will result from the high-speed balance.

This paper presents a simple method to aid the decision, “when to use a high-speed balance procedure”. It is based on the analysis of the rotor’s flexibility relative to its support structure, and relates the results to experience of a fleet of rotors in the field.

## **2. RIGID AND FLEXIBLE ROTORS**

The environment in which the rotor operates dictates whether it can be considered as flexible or rigid. It is obviously necessary to consider the rotor’s flexibility but the environment will include the flexibility of the support structure and its normal speed range. In the power industry most pedestals are stiffness controlled but it may be necessary to consider mass controlled pedestals in other situations. Large industrial gas turbines have the weight of the casing on the pedestal, unlike steam turbines. However, most gas turbines above 100 MW operate as flexible rotors and are simply treated as flexible.

Rotors that are very stiff in relation to their support structures will be relatively unaffected by the environment and will operate as a free-free beam. The rigid body modes of “bounce” and “rock” will dominate at slower speeds and it will only be at higher speeds that the first true flexural mode will be excited. Provided the operating speed is well below the frequency of the first flexural mode the rotor can be safely low speed balanced. The well established standard ISO 1940-1 (1) is written for these rigid rotors and gives both the procedures for balancing and general guidelines on acceptable balance criteria.

Rotors that are weak in relationship to their support structures will operate as a pinned-pinned beam. The rotor’s motion will be dominated by its flexural modes and it will require high-speed balance procedures if it operates at speeds above or close to its first flexural frequency. ISO 11342 (2) outlines balancing procedures for the different classes of flexible rotors and methods to calculate acceptable levels on imbalance.

## **3. ROTORS THAT FALL BETWEEN FLEXIBLE AND RIGID**

Simple analysis of a rotor on flexible supports will show that as the support stiffness is increased the first natural frequency will change from the free-free rigid body bounce mode to a pinned-pinned first flexural mode. In the bounce mode all the motion is in the supports and in the

pinned-pinned mode all the motion is in the rotor. Figures 1-3 clearly show this behaviour. However, even when the support stiffness is equal to that of the rotor, figure 2, most of the motion is still within the supports and there is little bending of the rotor.



**Figure 1 Mode shape of a rotor supported on a weak structure**



**Figure 2 Mode shape of a rotor with equal stiffness to its supports**



**Figure 3 Mode shape of a rotor on stiff supports**

#### **4. ROTOR SUPPORT STIFFNESS MAPS**

Figures 4 and 5 show the shift in the shaft natural frequencies as the support stiffness is varied for a stiff HP (high-pressure) turbine and a flexible generator respectively. The natural frequencies are normalised relative to the rotational speed of the machine and the support stiffness is normalised relative to the stiffness of the rotor. Rotor stiffness is simply estimated from the first pinned-pinned natural frequency and the mass of the rotor.

$$\text{Rotor stiffness} = \text{Mass of rotor} \times (\text{First pinned-pinned natural frequency})^2$$

The first, second and third natural frequencies, as calculated by a computer simulation, are represented by the solid, dotted and dashed lines respectively. Due to the normal stiffness asymmetry of a supporting oil film and bearing structures these natural frequencies would normally be seen in pairs but to simplify the analysis here the supports are assumed to be symmetric. With low support stiffness the two lower modes are the “bounce” and “rock” rigid modes and the third is the first flexural mode. Rotors on stiff supports will only see the flexural modes

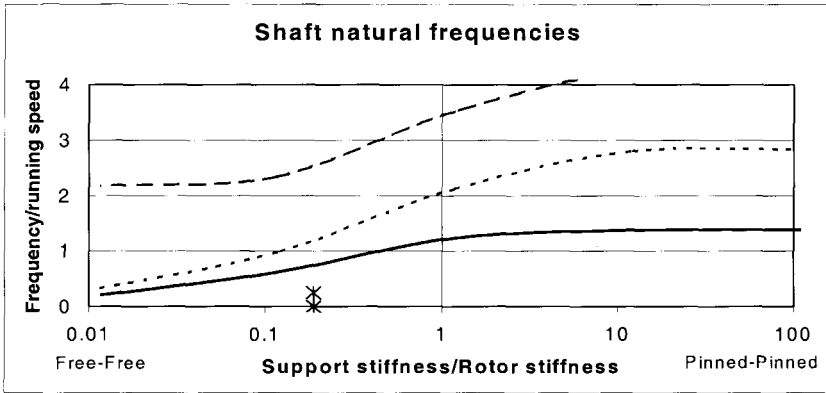


**Figure 4 A stiff HP rotor 350 MW**

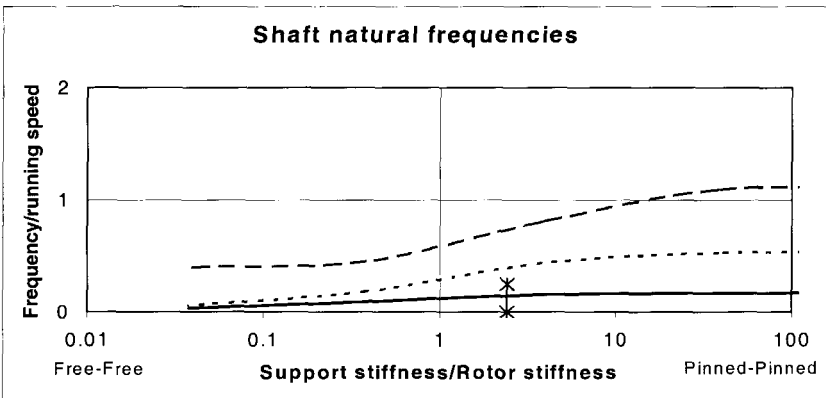


**Figure 5 A flexible generator rotor 660 MW**

The stiff rotor, figure 4, will always be rigid in this environment. Excitation of the first flexural mode will not take place at stiffness ratios below 1, the dashed line, since it is way above the operating speed. At stiffness ratios above 1, the rotor's first flexural mode, the solid line, is also above the operating speed and will not be excited. Indeed, when running this rotor in the machine it does have a critical speed within the operating speed range. However, the map shows that, if this occurs, there will be little bending in the shaft because the stiffness of the supports will need to be much less than that of the rotor.

For the flexible rotor, figure 5, the first flexural mode is always below the operating speed



LP rotors are in the intermediate range between rigid and flexible. Figure 6,7 and 8 show three such rotors.

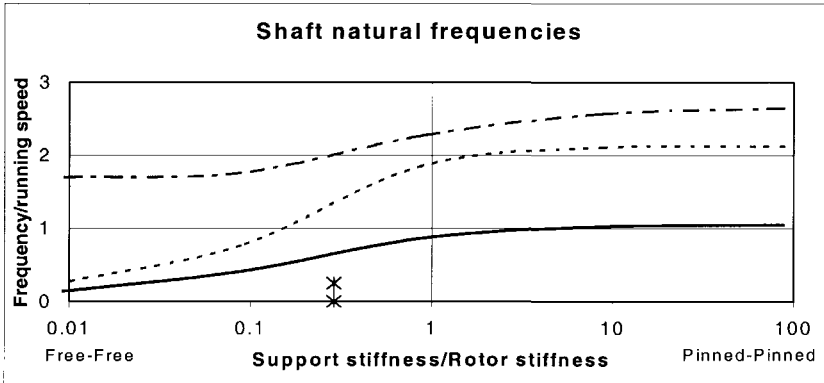


Figure 6 An intermediate stiffness LP rotor 660 MW

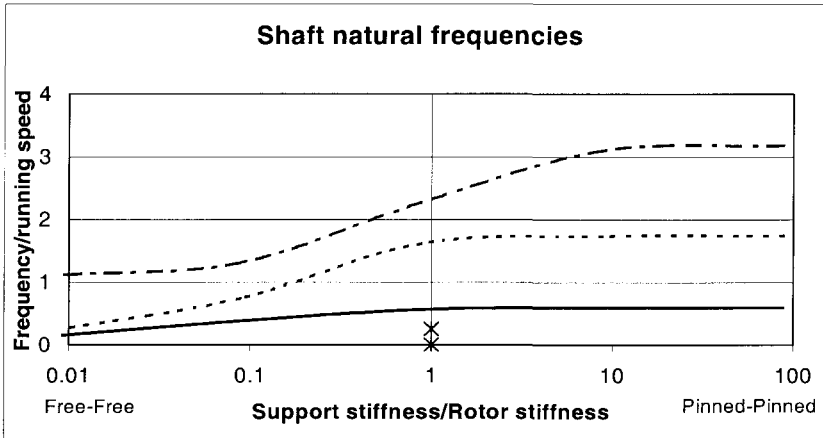


Figure 7 A flexible LP rotor 500 MW (a)

Figures 6 and 7 show that both these LP's will have their first flexural natural frequencies sufficiently close to running speed to warrant using high-speed balancing procedures. Figure 8 suggests that this rotor could be low speed balanced.

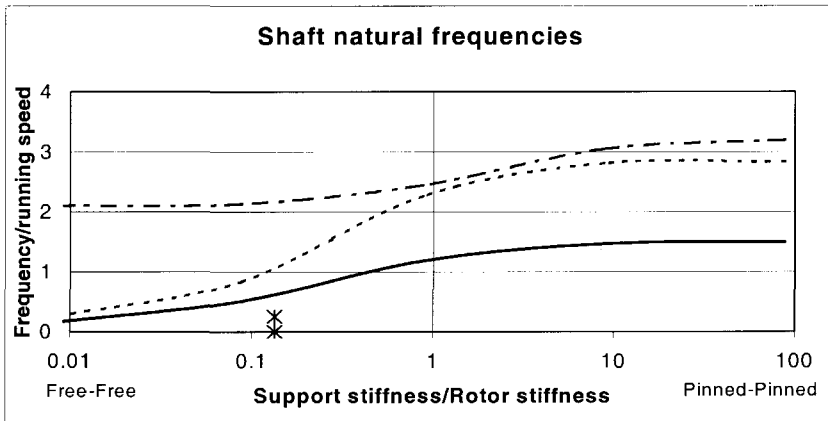


Figure 8 A relatively stiff LP rotor 500MW (b)

### 5. JOURNAL BEARING OIL FILM STIFFNESS

On each of these maps the “X” indicates an approximate value for the oil film stiffness at 50Hz which will ultimately limit that of the total support structure. These values are calculated using simple circular bearing theory and must be used with care. However, using this value will generally give a good estimate of the critical speeds observed on the total shaft lineout.

### 6. PINNED-PINNED NATURAL FREQUENCIES

Table 1 First pinned-pinned natural frequencies in Hz for a steam turbine generator set

Rotor	350 MW	500 MW (a)	500 MW (b)	660 MW
HP	69	67	38	56
IP	70	46	32	55
LP	65	75	30	52
Generator	22	12	21	8.5
Exciter	44	24	24	69

For the class of large rotors considered here, it can be seen from the stiffness maps that simply calculating the pinned-pinned natural frequency will give a quick estimate of the need to high or low speed balance. Analysis of the stiffness map is only necessary in marginal cases. Table 1

shows the values calculated for a range of 50Hz rotors and experience has shown that if the first pinned-pinned natural frequency is above running speed the rotor can be slow speed balanced. A small safety margin of about 10% should be used to allow for potential errors in the estimates calculated by the simulations.

The major exception to the above rule is the 500 MW (a) LP rotor with a pinned-pinned natural frequency of 75 Hz. However, this machine has suffered from a range of vibration related problems and the tradition to high-speed balance may have developed from a desire to minimise the influence of imbalance rather than a real need. The requirement for a high-speed balance of this rotor is now under review.

## **7. CONCLUSIONS**

A simple method has been presented which allows rotors that require high-speed balance procedures to be quickly identified. Confidence in the results can be obtained for marginal cases with a qualitative understanding of the support structures.

The method has only been compared with large, reasonably symmetric rotors used in the power generation industry and there is a need to consider its suitability when applied to a wider range of rotors.

## **8. REFERENCES**

1. ISO 1940-1 (1986-C1990) Mechanical vibration – Balance quality requirements of rigid rotors- Part 1 : Determination of permissible residual unbalance
2. ISO 11342 (1998) Mechanical vibration – Methods and criteria for the mechanical balancing of flexible rotors

## **9. ACKNOWLEDGEMENTS**

The author would like to thank National Power plc for the permission to publish this paper.

© 2000, National Power plc

*This page intentionally left blank*

# Exchangeability of rotor modules – a new balancing procedure for rotors in a flexible state

H SCHNEIDER

Schenck RóTec GmbH, Darmstadt, Germany

## ABSTRACT

Exchangeability of rotor parts or modules without the need for a subsequent balancing step is a goal in design and production throughout the industry. It is not easy to handle this properly for rotors in a rigid state, and it is even more complex in the case of rotors in a flexible state. The discussion bases on low speed balancing methods for rotors in a flexible state.

The new approach recommends some modal considerations to classical low speed balancing procedures of the individual parts, and adds a special balancing step in order to reduce the modal unbalance of the assembly. This step bases on the knowledge of the bending modes, the distribution of masses and moments of inertia along the rotor axis and on a separate measurement of the unbalance of each module.

The recommended procedure will maintain the goal of modular exchangeability and good unbalance condition at low speed, and will simultaneously reduce the modal unbalances and consequently the deflection of the assembled rotor at high speed.

## NOTATION

A, B	module A, B	$U_{Si}, U_{S\alpha}$	static unbalance of element $E_i$ , of assembly due to $\alpha$
$C_j$	correction in plane j for index balancing	$e_i$	eccentricity of centre of mass of $E_i$
$C_1, C_2, C_3$	modal unbalance correction in Planes 1, 2, 3	$m_i, m_A$	mass of element $E_i$ , of module A
$E_i$	rotor element $E_i$	r	radial coordinate of error
$J_{ai}, J_{pi}, J_{3A}$	axial, polar moment of inertia of element $E_i$ , of module A, module B	$z, z_i, z_A, z_B$	coordinate along the rotor axis, of centre of mass of element $E_i$ , of module A, of module B
$J_{pA}, J_{aB}, J_{pB}$	length of assembly, of module A, B	$\alpha, \beta$	angle error of module A, B in mating plane
$L, L_A, L_B$	length of assembly, of module A, B	$\gamma_A, \gamma_B$	inclination of main axis of module A, module B
$U_{Ci}, U_{C\alpha}$	couple unbalance of element $E_i$ , of assembly due to $\alpha$		
$U_n$	modal unbalance of $n^{\text{th}}$ mode		

$\Phi_n(z)$  mode function of  $n^{\text{th}}$  mode  
 $\frac{d\Phi_n(z_i)}{dz}$  inclination of mode function at coordinate  $z_i$

**Subscripts**

A, B related to module A, B  
 i designates rotor elements

j designates index correction planes  
 k designates modal correction planes  
 m number of index correction planes  
 n designates modes  
 p total number of rotor elements  
 1, 2, 3 related to modal correction planes on module A

## 1 INTRODUCTION

The International Standard ISO 11342<sup>1</sup> outlines procedures for low speed and high speed balancing of rotors in a flexible state. This document is well accepted all over the world. Recently, it has been revised to give even better guidance and entrance into this complex field. The latest edition starts from rotor configurations and characteristics of rotors in a flexible state and subsequently deducts recommended balancing procedures. Thus it emphasises two criteria – the locations where unbalances may occur and the modal nature of the flexible response.

## 2 CONFIGURATION AND CHARACTERISTICS OF ROTORS

Rotors with flexible behaviour may be very different. They range from some grams to some hundred tons in weight (figure 1, left), with service speeds between some hundred rpm to some hundred thousand rpm.

### 2.1 Characteristic elements

Each type of rotor can be reduced to three characteristic elements (figure 1, right), or a combination of them:

- a) flexible shaft without considerable unbalance,
- b) rigid disc or rigid section with unbalance,
- c) flexible section with unbalance.

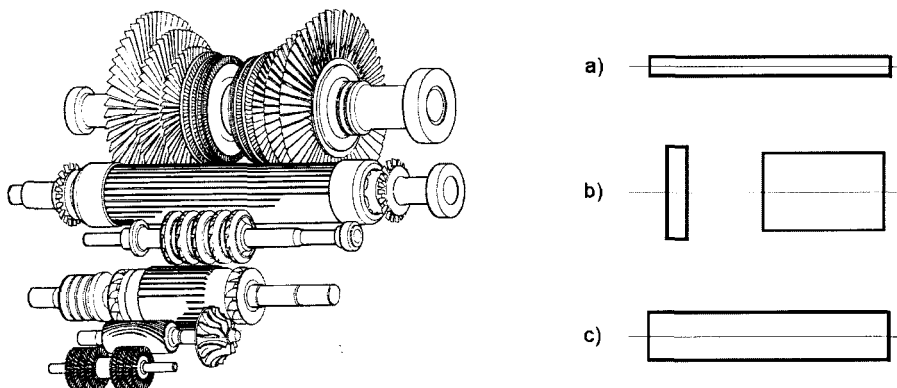


Figure 1. Various rotors with flexible behaviour (left), characteristic elements (right) to model such rotors

<sup>1</sup> ISO 11342 (1998): Mechanical vibration – Methods and criteria for the mechanical balancing of flexible rotors

## 2.2 Removable, integral

Only unbalances in up to two planes can be detected at low speed, i.e. this is sufficient for a single element type b) - rigid disc or section. A flexible rotor with more than one rigid element, connected by elements type a) flexible shafts in all probability will have more unbalance planes. In this case low speed balancing procedures are only applicable, if all elements (except one) are removable in order to correct for these unbalances individually, or in an step-by-step procedure.

An integral rotor – an element type c) alone, or a combination with other elements – definitely requires high speed balancing procedures. In this paper we concentrate on low speed balancing procedures.

## 3 MODAL ASPECTS

It is well known, that the sensitivity to unbalance is increasing with the *ordinate value* of the respective bending line: it is zero at a node and reaches its maximum at the antinode. This approach considers individual unbalance vectors only.

### 3.1 Static unbalance and couple unbalance

Each disc and each section of a real rotor will have a static unbalance, and a couple unbalance. The sensitivity to a couple unbalance increases with the *inclination* of the bending line<sup>2</sup>. The modal unbalance – using both kinds of unbalance – can be expressed as:

$$U_n = \sum_{i=1}^p \left[ U_{s_i} \phi_n(z_i) + U_{c_i} \frac{d\phi_n(z_i)}{dz} \right] \quad (1)$$

If we look into the different areas of the bending line we see:

- near to the nodes the couple unbalance dominates the rotor flexure,
- around the antinodes the static unbalance dominates the rotor flexure.

### 3.2 Balancing and assembly tolerances

This modal aspect – the different influences of static unbalances and couple unbalances – should be the basis to state balancing and fit tolerances:

- near to the nodes the couple unbalance needs a tighter tolerance than the static unbalance,  
*and*  
if the fit is controlled, axial runout of the disc(s) is more critical than eccentricity.
- around the antinodes the static unbalance needs a tighter tolerance than the couple unbalance,  
*and*
- if the fit is controlled, eccentricity is more critical than axial runout.

If more than one mode needs to be considered, tolerances may be derived for each mode individually. Out of the different sets always the smallest tolerance value per element and criteria applies.

---

<sup>2</sup> Bending line means the line(s) under service conditions.

## 4 EXCHANGEABILITY OF PARTS

Exchangeability of rotor parts or modules is a goal in design and production throughout the industry. Sometimes it is combined with the intention to avoid a subsequent balancing step.

### 4.1 Assembly errors

ISO 1940-2<sup>3</sup> distinguishes between systematic, randomly variable and scalar errors. All assembly errors together must be small enough not to upset the balance tolerance. If the errors are too large, special procedures to reduce systematic errors may be applied, such as index balancing and dummy balancing.

#### 4.1.1 Index balancing

Index balancing is a procedure developed for rotors in a rigid state. In fact, following this procedure, unbalances are corrected in planes different from their origin. This is acceptable, as long as this is done for individual parts in order to suppress tooling errors, or for rotors in a rigid state. Once this method is applied for rotors in a flexible state, only static and couple unbalances will be reduced. The modal unbalances are not controlled. They may remain unchanged, but typically they deteriorate, which may lead to an extensive flexure at high speeds.

#### 4.1.2 Dummy balancing

Balancing parts separately – e.g. an armature and a pulley – is a good idea in case one part (pulley) needs to be replaced from time to time. Systematic assembly errors can be taken into consideration, if the armature is balanced with a balanced pulley, or with a balanced dummy. A dummy is similar in its main data – mass, centre of mass, and difference in moments of inertia – to the part it replaces (e.g. the pulley). Sometimes index balancing and dummy balancing are combined.

## 5 ASSEMBLY

The problem with index balancing of rotors in a flexible state may be described on the basis of a simplified HP jet engine rotor (figure 2).

The geometrical errors at the mating interface of module A – for this configuration – may be expressed as an axial run-out (tilting angle  $\alpha$ ) of a certain amount at a certain angular location.

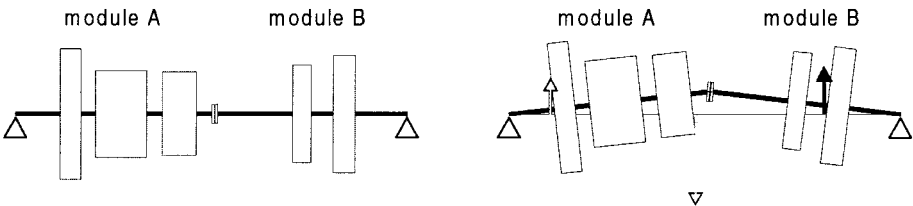


Figure 2: Simplified model of a flexible rotor with two modules and one bearing each, with: no error in mating plane (left), error  $\alpha$  in mating plane on module A (right)

<sup>3</sup> ISO 1940 (1997): Mechanical vibration – Balance quality requirements of rigid rotors. Part 2: Balance errors



Due to this axial run-out of module A, the axes of both modules will be inclined, forming a longitudinal plane governed by angle  $\alpha$ . All rotor elements will be displaced and tilted accordingly, thus creating static and couple unbalances. The same applies to errors at the mating interface on module B (tilting angle  $\beta$ ). Errors of both modules add up vectorially. The same holds true for the unbalances.

If these unbalances are within limits, which cause no vibration problems to the engine, no further step is needed. But if these unbalances are not acceptable, another balancing step – index balancing – is added.

By indexing module B relative to module A, all unbalances caused by module A are measured and corrected in module A:

- a) Unbalance of module A about its shaft axis,
- b) Unbalance occurring on module A due to error  $\alpha$ ,
- c) Unbalance occurring on module B due to error  $\alpha$ .

Each of the three unbalances needs a different approach:

The unbalance under a) was dealt with during the balancing procedure of module A (preferably in accordance with chapter 3).

Unbalances under b) occurring on module A due to error  $\alpha$  have to be corrected on module A. If the correction is properly distributed to the rotor components where the unbalances occur (due to displacement and tilt), it will not cause rotor bending.

The unbalances under c) are the problem. If the unbalance in module B (figure 2, right, black arrow) is corrected the usual way – with two correction planes on module A (figure 2, right, grey arrows) – it will create modal unbalances and thus cause a flexible rotor to bend at high speed.

What is stated for module A and error  $\alpha$  similarly holds true for module B and error  $\beta$ . The following description is based on error  $\alpha$ .

## 5.1 Calculations

Figure 3 shows all relevant data: the typical situation with an error  $\alpha$  in the longitudinal plane rz. The error  $\alpha$  is assumed to be very small<sup>4</sup>.

Inclination angle  $\gamma_A$  of module A axis and  $\gamma_B$  of module B axis are:

$$\gamma_A = -\frac{\alpha L_B}{L}; \quad \gamma_B = \frac{\alpha L_A}{L} \quad (2)$$

Equations for displacement  $e_i$  of element  $E_i$  are different for modules A and B:

$$e_i = -\gamma_A z_i = \frac{\alpha L_B}{L} z_i; \quad \text{for } 0 < z_i < L_A \quad (3)$$

$$e_i = \gamma_B (L - z_i) = \frac{\alpha L_A}{L} (L - z_i); \quad \text{for } L_A < z_i < L \quad (4)$$

<sup>4</sup> All physical quantities influenced by  $\alpha$  (e.g.:  $r$ ,  $\gamma_A$ ,  $\gamma_B$ ) normally have  $\alpha$  as a subscript. Since all calculations are based on error  $\alpha$ , this subscript has been deleted in the following explanation to improve legibility.

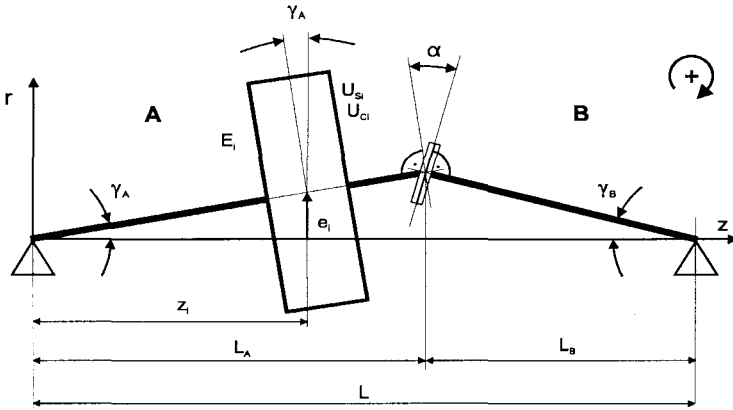


Figure 3. Model for calculations

The static unbalance  $U_{Si}$  of element  $E_i$  is:

$$U_{Si} = m_i e_i \quad (5)$$

The couple unbalance  $U_{Ci}$  of element  $E_i$  also is different for modules A and B:

$$U_{Ci} = \gamma_A (J_{ai} - J_{pi}) = -\alpha \frac{L_B}{L} (J_{ai} - J_{pi}); \quad \text{for } 0 < z_i < L \quad (6)$$

$$U_{Ci} = \gamma_B (J_{ai} - J_{pi}) = \alpha \frac{L_A}{L} (J_{ai} - J_{pi}); \quad \text{for } L_A < z_i < L \quad (7)$$

## 5.2 Modal Approach

The mode function  $\varnothing_n(z)$  describes the typical bending in the  $n^{\text{th}}$  mode. Calculations will be limited to the first mode. A possible rotor mode shape is assumed in Fig. 4.

The modal unbalance  $U_n$  of a rotor with  $p$  elements due to error  $\alpha$  (equ. 1) after the index balancing procedure (corrections  $C$  in  $j$  planes) is given by

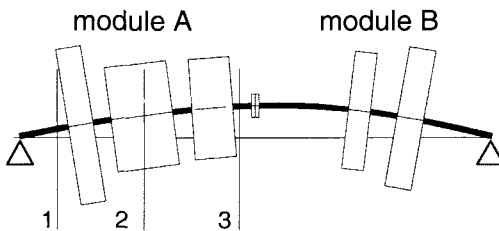


Figure 4. First bending mode with modal correction planes 1, 2, and 3 of module A

$$U_n = \sum_{i=1}^n \left[ U_{Si} \phi_n(z_i) + U_{Ci} \frac{d\phi_n(z_i)}{dz} \right] + \sum_{j=1}^m C_j \phi_{n_j} \quad (8)$$

and can be calculated on the basis of physical data, geometry, mode function and the distribution principle applied to the index balancing procedure.

### 5.3 Modal Correction

To correct the first modal unbalance without disturbing the unbalance of the rotor in its rigid state, three correction planes 1, 2 and 3 (figure 4) with unbalance corrections  $C_k$  ( $k = 1$  to 3) are required. The following equations apply:

$$\sum_{k=1}^3 C_k = 0; \quad \sum_{k=1}^3 C_k z_k = 0; \quad \sum_{k=1}^3 C_k \phi_k = -U_n \quad (9)$$

These equations are sufficient to calculate all modal corrections. If we look for the correction in plane 2, we find:

$$C_2 = \frac{-U_n}{-\phi_{n1} \frac{z_2 - z_3}{z_1 - z_3} + \phi_{n2} - \phi_{n3} \frac{z_1 - z_2}{z_1 - z_3}} \quad (10)$$

Once  $C_2$  is found, unbalance corrections  $C_1$  and  $C_3$  – using equations 9 – are:

$$C_1 = -C_2 \frac{z_2 - z_3}{z_1 - z_3}; \quad C_3 = -C_2 \frac{z_1 - z_2}{z_1 - z_3} \quad (11)$$

## 6 BALANCING PROCEDURE

The following provides a step by step procedure for modal balancing of the type of rotors discussed above. It is assumed that low speed balancing was performed properly (guided by chapter 2), and that each module is completely assembled.

### 6.1 Individual Module Balancing

Modules A and B each are balanced with a stub shaft. The goal is to eliminate error  $\alpha$  (and error  $\beta$ ) as far as possible from the relevant unbalance readings and thus from the unbalance corrections. The distance between the mating plane and the adjacent bearing should be as short as possible, ideally zero (0).

Unbalance corrections<sup>5</sup> are made according to the rules for low speed balancing of flexible rotors, using modal considerations (chapter 2).

### 6.2 Determination of Error $\alpha$ and Error $\beta$

Geometric measurements may be taken as usual, but utilising a balancing machine for this task may have some advantages, since balancing steps will follow anyway:

<sup>5</sup> These corrections may be only temporarily and later on consolidated with the modal correction (see 6.3)

<sup>6</sup> Within the error limits of the measurement of  $U_{S\alpha}$  and  $U_{C\alpha}$  and the rotor data used, both equations will lead to the same angle  $\alpha$ .

Mating modules A and B and using the indexing method, the unbalances for module A (and B) are obtained, e.g. in terms of static unbalance  $U_{S\alpha}$  and couple unbalance  $U_{C\alpha}$ . Based on the physical data and the geometry of the module,  $\alpha$  is calculated (a variation of equations 3 to 7), with  $z_A$  being the coordinate of the centre of mass of module A and  $z_B$  the coordinate of the centre of mass of module B<sup>6</sup>:

$$\alpha = U_{S\alpha} \frac{L}{L_B m_A z_A + L_A m_B (L - z_B)} \quad (12)$$

$$\alpha = U_{C\alpha} \frac{L}{L_A (J_{aB} - J_{pB}) - L_B (J_{aA} - J_{pA})} \quad (13)$$

Error  $\beta$  is derived similarly for module B.

### 6.3 Calculation of Corrections

Modal unbalance corrections C1, C2 and C3 for module A are calculated according to equations 10 and 11. Similar equations are used for module B for modal unbalance correction C4 to C6.

### 6.4 Performing Corrections

The calculated unbalance corrections are performed on both modules<sup>7</sup>.

Within the error limits of the measurement of  $U_{S\alpha}$ ,  $U_{C\alpha}$  and all rotor data used, both equations will lead to the same angle  $\alpha$  (amount and angular position).

## 7 OUTLOOK

Modal considerations may give some impulse to the balancing of flexible rotors at low speed; it may reduce the modal unbalances by a factor of 5 to 10, thus improving high-speed vibration condition. Especially in a field, where module exchange is of high importance (e.g. balancing of jet engine rotors), modal corrections at low speed may help to allow for module exchange, and also to keep vibration under service conditions in acceptable limits.

It is quite possible that this proposed procedure – focusing on an influence not considered up to now – will allow for coarser unbalance tolerances for the ‘classical’ balancing steps.

© 2000, H Schneider

---

<sup>7</sup> To reduce the total number of unbalance corrections (total amount of correction mass, number of locations), for the first balancing step (see 5.1), temporary corrections could be used. After having performed modal correction C2, these temporary corrections can be removed. Another balancing run vectorially adds the temporary corrections and the modal corrections C1 and C3, thus providing just one correction in each of the two planes.

# **‘The balancing act’ – balance for design, or design for balance?**

**S P SMITH**

Coventry Balancing Site Services, Oxford, UK

## **SYNOPSIS**

Some rotating machinery components frustrate the efforts of traditional balancing methods. The Dynamic Table approach can be used to resolve many of the problems. In this paper the proven method of Dynamic Table Tooling is explained. A range of examples is presented where the traditional balancing difficulties have been tackled and successfully overcome – but at the product acceptance stage. More cost effective results could be achieved by adopting a Balancing Strategy at the design stage. An informed strategy for balancing will greatly reduce the risk of discovering problems at the acceptance-testing phase, and can cut development and manufacturing costs. This paper and its referenced work relate only to rigid rotors.

## **1. INTRODUCTION**

Dynamic balancing is simply a procedure required to ensure a rotor or an assembly will rotate at its running speed without vibrating outside acceptable limits. All rotors will vibrate to some extent, because there is no perfect balance condition. Therefore the vibration level has to be given a limit, in order to manage the adverse effects of fatigue, noise, reduced efficiency and unwanted movement.

At the design stage a mathematical approach is simple to dictate, but sometimes proves difficult to implement. In practice the residual imbalance can rise to an unacceptable level due to fitting tolerances, system response or stability of the rotating assembly.

Careful consideration must be given not only to the desired balance tolerance, but also perhaps more importantly, to the means of effecting correction of the rotor to guarantee a vibration limit is met.

## 2. BACKGROUND

### 2.1 What is unbalance?

Unbalance is often defined as the unequal distribution of mass within a rotor about its rotating centreline. A condition of imbalance exists in a rotor, when vibration forces or motion is imparted to its bearings as a result of centrifugal forces.

### 2.2 Units of measurement

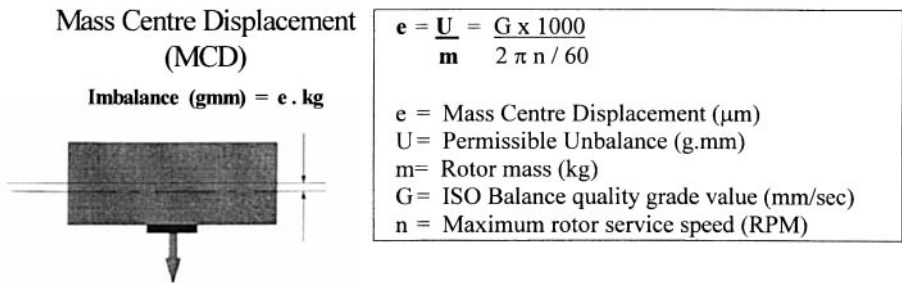
The amount of unbalance in a rotating body is normally expressed as the product of the residual unbalance mass and its distance from the rotating centreline. Therefore, the general units for expressing unbalance are gram-millimetres, (g.mm).

### 2.3 Balance tolerances to ISO 1940.

ISO 1940 (Balance quality requirements of rigid rotors), is one of the most widely used International guides for recommended balance quality grades. The standard categorises rotors, based on worldwide experience, according to their *type*, *mass* and *maximum service speed* into a quality grade (G). The number given (e.g. G0.4, G1, G2.5, G6.3, G16 etc.) relates to the allowable level of vibration (mm/sec) measured on the bearing housing at rotor service speed. It is the product of specific unbalance and the angular velocity of the rotor at maximum operating speed and is a constant for rotors of the same type. The quality grade determined by 'G' is related to permissible residual unbalance measured in g.mm and the allowable mass centre displacement (MCD) measured in micrometers, ( $\mu\text{m}$ ).

In general, the larger the rotor mass, the greater the permissible residual unbalance. It is therefore appropriate to relate the value of the permissible residual unbalance,  $U$ , to the rotor mass,  $m$ , in terms of permissible rotor mass centre displacement,  $e$  and equate this to maximum rotor service speed and the ISO quality grade,  $G$ . (ref fig 1)

Figure 1.



## 2.4 Force calculations

One important reason for balancing is that the forces created by unbalance are detrimental to the life of the machine, the rotor, the bearings, and the supporting structure. The amount of force created by unbalance depends on the speed of rotation and the amount of imbalance. Force (F) generated by imbalance can be calculated from the formula:

$$F \text{ (kg)} = 0.01 \times W \times R \times (\text{RPM} / 1000)^2$$

W = Imbalance mass in grams

R = Radius in centimetres

## 2.5 Influence of fitting tolerances

One of the most common causes of imbalance is the stack-up of fitting tolerances in the assembly of a machine. Murphy and Sod's law conspire together to guarantee the tolerances work against the finished quality levels.

Obviously, the heavier the rotor component is, the more critical the tolerance of fit becomes to its shaft for a given speed of rotation. If we consider a symmetrical rotor of weight 1000 Kg and having an offset on its shaft of 0.025mm.

Then at 1000 Rpm, F = 12.5 kg / Bearing and at 3000 Rpm, F = 112.5 kg / Bearing.

The following chart produced by the German Standards Institution (2), distinguishes between quality levels, rotor speed, bearing loads and acceptable eccentricity. It is useful in providing focus on machined fitting tolerances and the associated bearing loads. Whereas the majority of quality guidelines, relate to the vibratory motion produced by the residual imbalance level.

### Permissible Mass Centre Displacement and centrifugal force against rotor speed and quality grade (VDI 2060)

Quality class	Speed ranges rpm	Permissible centrifugal force as % of rotor weight	Residual eccentricity in $\mu\text{m}$
0	10,000	-	0.2
I	7,500 - 10,000	2.5	0.2...0.4
II	5,000 - 7,000	3	0.45...1.0
III	3,000 - 5,000	4	1.44...4.0
IV	1,500 - 3,000	5	5.0...20.0
V	750 - 1,500	6.5	25...100
VI	1,000	-	50...250

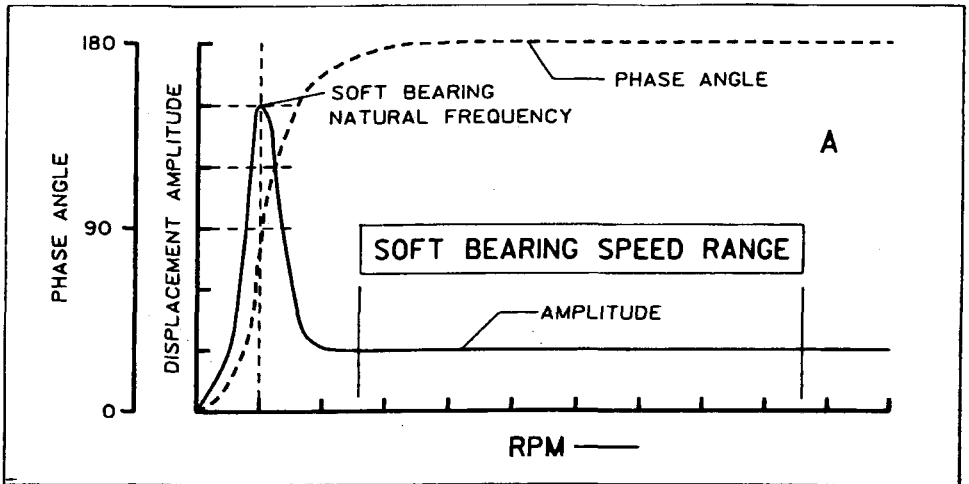
## 3. METHODS

### 3.1 The Traditional Approach

Most rotating assemblies or rotor component parts are dynamically balanced in a balancing machine. Balancing machines are generally divided into two types, that is the "soft" or flexible bearing machine and the "hard" or rigid bearing machine. The soft bearing balancing-

machine, derives its name from the fact that it supports the rotor to be balanced on bearings that are free to move in at least one direction. Usually, horizontally and perpendicular to the rotor axis. The resonance of the rotor and bearing system occurs at one half or less of the lowest balancing speed, (typically 250 rpm). By the time the balancing speed is reached, the measurements of vibration displacement, amplitude and phase have stabilised and can be measured with accuracy. The aim of the soft suspension is to provide a linear response above the minimum balancing speed. (ref fig 2) The suspension supports the rotor as if in free space, to provide unchallenged movement in the direction of displacement measurement. (ref fig 3)

**Figure 2.**



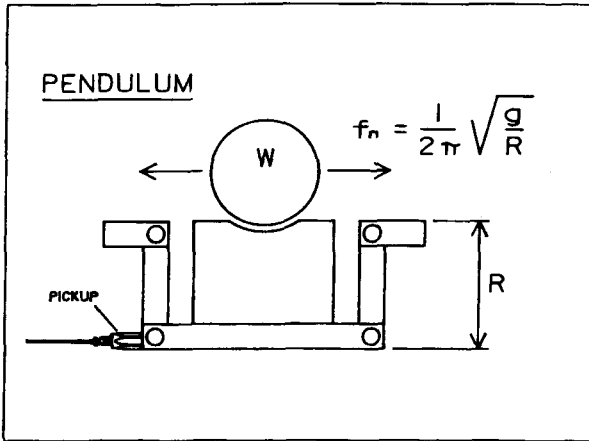
**Soft bearing suspensions provide a linear response from low balancing speeds**

### 3.2 Dynamic Table Tooling

The displacement measurement comes extremely close to the mass centre displacement (MCD) value derived in the balance tolerance calculations. Difficulty arises when the rotor cannot be supported in open rollers on the balancing suspensions without impeding this vitally important “free space” motion. For this reason special tooling has to be designed to support the rotor, allow it to spin and impart its “free” motion to the suspensions. The dynamic table is an arrangement that allows a complete or sub assembly to be mounted onto the suspensions. The design provides for completely free movement of the rotating assembly, regardless of how it is clamped or supported. The dynamic table is an invaluable tool to achieve balancing limits otherwise unachievable because of fitting tolerances, or awkward handling of component parts. The protected linear response of the suspension allows close and accurate scrutiny of the rotating assembly, knowing that the balancing machine is not influencing the motion. (ref fig 4)

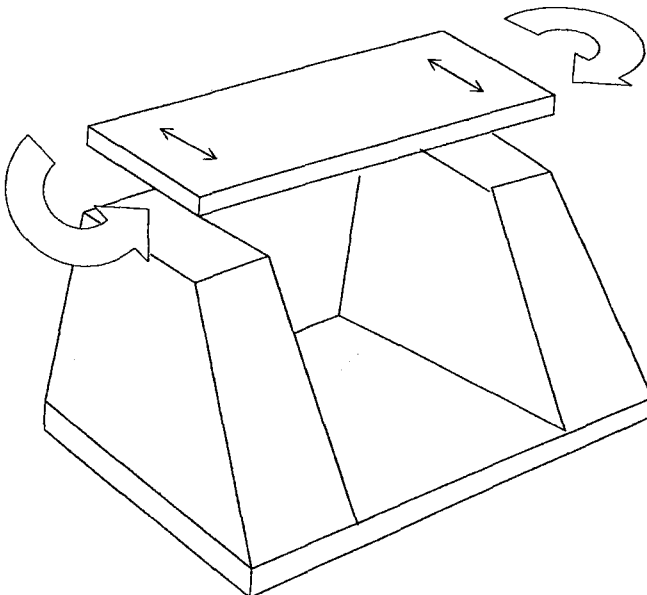


Figure 3.



Natural frequency of the pendulum suspension is not affected by the weight of the rotor

Figure 4.



Principle motions of the Dynamic Balancing Table

The following examples show 5 applications for the dynamic table and then discuss the reasoning behind the need to use this approach.

The examples discussed are: -

- A high-speed machine tool spindle (10,000 rpm) *Bridgeport Machines*
- A pancake motor driven vacuum pump (1500 rpm) *BOC Edwards High Vacuum*
- A Volvo 5 cylinder racing engine (8,500 rpm) *TWR Arrows F1*
- A low-speed research satellite (5 rpm) *DERA*
- A high-speed automobile supercharger (75,000 rpm) *Force One Superchargers*

## 4. RESULTS AND ANALYSIS

### 4.1 Example 1. CNC Machining Centre 10,000 rpm tool spindle

Bridgeport Machines Ltd are a global machine tool manufacturer, leading the market in CNC machining centres. They follow a programme of continuous approach towards improving their product and meeting customer needs. Spindle speeds have reached in excess of 10,000 rpm. These high spindle speeds require tighter balance tolerances to protect spindle life and achieve more challenging machining tolerances. Traditional balancing methods could not guarantee acceptable spindle vibration levels due to the accumulative effects from a stack up of fitting tolerances. It was not practical to refine manufacturing tolerances to such a degree as to protect final spindle vibration levels. The cost effective solution was to produce the precision high-speed spindle with externally accessible balancing planes and balance the whole assembly in a dynamic table tooled to cradle the spindle cartridge. This not only produced a superior spindle product, but also reduced manufacturing time and associated costs.

Spindle displacements measured at full speed following balancing were typically  $< 0.3\mu\text{m}$ .

### 4.2 Example 2. Pancake Motor Driven Vacuum Pump

A new vacuum pump, designed by Edwards High Vacuum to run at 1400 rpm, has broken new boundaries of design and function. However, it also had a particularly difficult set of balancing issues to conquer.

At first it seemed a straightforward requirement to reduce vibration-running levels to an acceptable 1.5 mm/sec RMS overall value.

The difficulties lay in the complex rotor design and the sensitivity of the assembly to couple imbalance. Conventional rotors are balanced about their respective journals. On this rotor however, the journal arrangement consisted of two back to back bearing races located mid way between the outboard balancing planes, at or close to the centre of gravity of the spin axis. The awkward shape of the rotor (due to its pumping requirements) meant that the bearings or journals would not see a true reflection of the imbalance loads imposed on them until all the component parts were assembled to the rotor.

The design consisted of a pancake motor providing drive at one end of the rotor assembly. The motor was supported in an overhanging fashion to the centrally located bearings. The

pump end of the assembly consisted of a large counterweight to balance an offset pump rotor. The pump rotor is unusual, as it is supported on an offset spigot about a bearing race. This is because it is attached to the pump casing by a set of bellows and therefore does not spin in a conventional way, but produces a rotating load to the rotor influenced by its mass centre and the resistance of the bellows.

For production requirements, balancing an almost assembled pump unit was not a viable proposition. Therefore a way had to be found to assess the influence of the pump rotor on the rotating assembly and a dummy mass produced to simulate the pump rotor.

The dynamic table rig first provided an ideal platform for vibration analysis, as there was no imposed influence on the vibration response measured. Secondly, the table was used to balance a complete pump unit, before replacing the pump rotor with a dummy mass and then correcting its balance influence to simulate the rotor it had replaced. Fortunately the pump rotor is a solid component, fully machined to very tight tolerances and therefore provides a consistent influence to the assembly.

The required vibration running levels of 1.5 mm/sec RMS overall, dictated the balance tolerance. The predominant vibration frequencies comprised of pump imbalance and electrical noise due to the pancake motor design. It was not commercially viable to improve the electrical properties of the pancake motor. Therefore, the residual levels of pump rotor imbalance had to be extremely low, so as not to influence the overall vibration running levels. The balance tolerance has been established at present at G1.5, relating to 50 g.mm and a typical measured displacement value on the balancing table of < 6.00  $\mu\text{m}$  pk-pk in each balancing plane.

It should be noted that in this application, the acceptable limit of couple imbalance could be as low as  $1/10^{\text{th}}$  of the permissible static tolerance.

#### **4.3 Example 3. Group II crankshaft balancing of assembled engines**

Crankshafts are often complex in shape, part machined and in part left as they were from forging. Inevitably, imbalance that is present generates centrifugal forces that are proportional to the square of the speed of rotation. From a force point of view, consider a crankshaft that has a typical 85mm stroke and a speed range to 6,500 rpm. If the imbalance condition relates to just 1 gram at the stroke radius, it will generate a detrimental cyclic force of 3.5 kilograms. The forces producing the vibrations are using energy, which would be better employed doing useful work rather than causing wear and tear. Reducing the vibration will increase power, acceleration and speed; engine parts can have their life extended by anything from 25% to 100%. The automotive industry have balance tolerances that vary from make to make, typically 70 g.mm to 300 g.mm is the allowance on a passenger car crankshaft. The motor racing industry tolerances are much lower, approximately  $1/10^{\text{th}}$  of that found in passenger cars.

In practice a mass produced crankshaft may attain a balanced standard of G6.3, relating to 2 grams at the crank throw. It follows that all the pistons and connecting rods must be match-weighted equally well; otherwise the balance tolerance will be lost. Not all crankshafts however are treated equally when it comes to balancing. Many IC engines use crankshafts, which are inherently out of balance. Their axis of inertia does not coincide with the axis of rotation and are classified as group II crankshafts.

These group II crankshafts rely on part of the reciprocating weight to balance the rotating masses. Traditionally, the crankshafts have bob-weights bolted onto their big end journals to simulate the percentage weight of the reciprocating parts. Then they would be balanced by traditional methods on open roller balancing machines. This approach is flawed by the percentage error in the calculated bob-weight. Additionally, the inherent fitting tolerances stack-up on engine components i.e. flywheel to crank, to pulley, etc. The resultant levels of vibration, noise, wear, and load attributed to imbalance can be significant. The high aims set in the motor racing industry is resulting in a new approach by top race teams. The TWR 1988 BTCC championship winning Volvo 5 cylinder engine is one such application.

The engine's typical balance levels were measured during dynamometer tests and found to be considerably higher than should be expected on a race built engine. Furthermore the resulting vibration movement of the crankcase was found to be exaggerated through critical speed ranges due to the aluminium block, which lacked inherent stiffness. Balancing the whole crankshaft assembly to more accurate and definitive levels, not only reduced power consumption, wear, vibration and noise, but also greatly improved system response throughout the critical speed ranges.

It should be noted that for this engine that rotates to 8.500 rpm, initial build would leave approximately between 500 and 800 g.mm of imbalance at each end of the crankshaft. Consequently, the respective bearing loads were increased by 40 – 60 kgs at full revs and crankcase movement varied between 70 – 100  $\mu\text{m}$  depending on the rpm.

Following a full assembly balance using the dynamic table approach, crankshaft bearing loads were reduced by up to 87 % and crankcase vibration displacements from dynamic unbalance were reduced to below 5 $\mu\text{m}$  at all speeds. The largest gains were noticed at speeds around 5000 rpm where critical crank case movement was reduced by 94 %, and produced power levels were measurably improved.

Other similar exercises carried out on race built 'V' engines, have shown initial unbalance levels typically to reach in excess of 3.4 kg.mm. This can only endorse the inaccuracy of common 'bob-weight' practice used for group 11 crankshaft balancing and highlight the difficulties of mass balancing con-rods accurately.

#### **4.4 Example 4. Research Satellites**

The Defence Evaluation and Research Agency Space Team at Farnborough (DERA) have had the demanding task of producing research satellites that spin while they are in orbit. Most satellites simply hold their station in a static attitude. The satellites weigh 102 kg and spin at 4 rpm; they will always assume their mass centre axis having no bearings to resist otherwise. The challenge was to balance the delicate and extremely valuable satellite flight models at a balancing speed not exceeding 100 rpm and at Farnborough within their clean rooms. The construction of the satellites meant they did not wish to accommodate centrifugal loads induced above this speed.

All conventional balancing machines balance at speeds in excess of 250 rpm. The second challenge was to support the satellite about its base on a mandrel arrangement tooled up for the dynamic table. The suspensions of the dynamic table are only linear from 250 rpm but the transducers are linear from 60 rpm. The instruments digital sampling, and converging filter,

meant very accurate readings of amplitude and phase could be obtained at lower balancing speeds. The problem lay with the critical speed ranges of the suspensions below 250 rpm. Even fractional changes of balancing speed below 100rpm greatly influenced balancing information, confusing calculations very easily.

Once the satellite flight model was loaded on to the dynamic table, the critical response of the suspensions was plotted to choose the optimum speed. This happened to be 95 rpm. Balancing runs were repeated to exact speeds and the two flight models were successfully balanced. One advantage of low - speed balancing using the dynamic table approach, is the systems ability to cope with very large initial imbalance levels. Typically the suspension displacements range from  $< 1.0\mu\text{m}$  to  $> 2900\ \mu\text{m}$ . To date, six satellite models have been successfully balanced in this manner.

The alternatives would have committed more time, more expense and with the considerable risks associated with transportation and handling.

#### **4.5 Example 5. Automotive Centrifugal Supercharger**

Balance quality grades are established against rotor weight and maximum rotor service speed. It follows that the permissible specific imbalance ( $e$ ) relates to residual unbalance ( $U$ ) per kg of rotor mass ( $m$ ), and is equivalent to the rotors (Mass Centre Displacement) at the centre of gravity. For rotors balanced within a specific quality grade, an allowable MCD exists for that speed range irrespective of rotor weight. To double the speed range would effectively half the allowable MCD. This imposes extremely tight fitting tolerances on high-speed rotors, such as the example given here with an automotive centrifugal supercharger.

A new design of centrifugal supercharger runs at speeds of up to 75,000 rpm, requiring tight balance tolerances to be met. Traditionally the majority of turbochargers produced, run in hydrostatic bearings to speeds in excess of 150,000rpm. The supercharger is by its very nature mechanically driven and has to run in ceramic rolling element bearings. This arrangement running at 75,000 rpm has a permissible specific imbalance ( $e$ ) of  $0.127\ \mu\text{m}$ . No machining tolerances however acute would protect the level of fitting accuracy required. An assembly balance was the only option available to guarantee finished product quality. Fortunately, since the compressor wheel and shaft were running in their own bearings, a small dynamic table easily supported the arrangement. The rotor balance tolerance was so sensitive to compressor wheel fit, that tests showed if the compressor wheel lock nut had to be re-torqued for any reason, the balance tolerance would be lost by a factor of 10.

Balancing the assembly on a dynamic table provided the finest balance tolerance achievable and proved its assembly status. The result was a very quiet, vibration free supercharger with longevity to match.

## **5. DISCUSSION**

The requirement for the dynamic table balancing approach was driven by the need to find a way out of production processes that were already underway and had followed traditional balancing routes, yet were in difficulty with no alternative plan of action. The table has proved to have a variety of uses. The ability to handle complete assemblies leads to many in-

service applications that save on costly strip-downs and rebuilds. This combined with linear response suspensions, allow for optimum balancing or dynamic assessment of the assembly.

There are many benefits: -

- It can provide a qualified balance unaffected by fitting tolerances.
- It may be the only way to balance an awkward rotor arrangement.
- Pre-production tooling costs can be kept to a minimum.
- It allows low speed balancing of an assembly.
- The finest balance tolerances can be achieved.
- It can be the most cost effective solution to a difficult task.

However, the underlying reason for its production need is brought about by a lack of timely attention to balance criteria, leading to focus on manufacturing tolerances with consequent costs to quality and value of the finished product. It would be better to allow the manufacturing process to dictate manufacturing tolerances and plan for final balancing of the prototype or production item after assembly. This strategy requires good provision for balancing efficiently and economically but has a better track record than chasing machined tolerances which may well turn out to be unnecessary. Attempting to balance components to limits that cannot be maintained in an assembly leads to expensive and time consuming rework in an attempt to chase balancing, vibration, noise and failure issues on the finished product.

It is common for balancing tolerances to be specified on a manufacturing drawing without due thought or for the wrong reason. Tolerances are frequently read across from other similar jobs or projects. Alternatively the balance tolerance is tightened up with the mistaken idea of producing a better product (with less noise and vibration). It does not necessarily follow that setting a tighter tolerance limit will achieve the objective; what really matters is the ability to achieve the limit consistently and as cost effectively as possible during the production run.

## 6. CONCLUSIONS

Balancing considerations should commence in the design office. It is therefore surprising how little attention is being paid to balancing at the design stage. Time and money could be saved in production if the compensating process, which must be carried out later, is addressed in the balancing strategy at the design stage. The act of balancing a component efficiently can only be carried out swiftly when the means of correction has been purposefully designed.

It is well known that measuring the magnitude and position of unbalance takes only a few seconds, whereas compensation frequently requires minutes or hours. However, with thought and planning compensation times can be achieved which only fractionally exceed the measuring time.

Specifications on drawings about the method and position of compensation and about the permissible final unbalance are frequently ambiguous and make it almost impossible for the balancing engineer to understand what is required. Advice from, or consultation with a balancing engineer will reap rewards at this stage.

All drawing specifications for balancing need to contain the following information;

- The number and position of the balancing planes.
- The method of mass compensation.
- The permissible residual unbalance  $U$  in g.mm or a quality grade  $G$  with associated rotor speed and weight.

If the component to be balanced is subsequently assembled into one unit with other parts, the fitting tolerances have to be taken into account. It would be futile to specify a permissible residual imbalance of  $e = 5\mu\text{m}$  for a fan rotor if the tolerance between bore and spindle is  $30\mu\text{m}$ . It is likewise pointless to specify a very fine balancing tolerance, if subsequently ball bearings with a permissible radial play of  $15\mu\text{m}$  are fitted.

In such cases imbalances can appear after assembly, which are larger than a multiple of tolerances, thus the time consuming procedure of fine balancing was wasted. It follows that balancing of the complete assembly is essential where high precision must be achieved and the designer must make the necessary provision for this.

The considerations for product vibration, noise and performance levels should incorporate balance criteria at the design stage and, not, as often is the case, be finalised once the manufacturing process has started. Early evaluation tests can conclude the influence that balance grades will have on finished product quality. Should a particular product or design benefit most from a final assembly balance, then this should be accounted for throughout the manufacturing process to reduce costs and qualify build quality. It is therefore necessary to consider the economics of each individual case taking into account its special characteristics.

## **7. ACKNOWLEDGEMENTS / REFERENCES**

**7.1.** ISO 1940/1-1986, "Balance Quality Requirements of Rigid Rotors." International Standards Organisation.

**7.2.** VDI 2060 – 1966, "Criteria for assessing the state of balance of rigid rotating bodies." German Standards Institute.

*This page intentionally left blank*



# On the balancing of flexible rotors without trial runs

**E PRECIADO**

Instituto de Investigaciones Eléctricas, Colonia Palmira, México

**R H BANNISTER**

School of Mechanical Engineering, Cranfield University, UK

## SYNOPSIS.

This paper analyses the data required to balance a flexible rotor without trial runs. The analysis shows that balancing without trial runs is only possible when the mode shapes are known. Considerations are also made in relation to the position of the vibration transducers. Trial runs will be necessary, however, when the residual vibration at normal operating speed is too high to allow continuous operation of the machine. A balancing procedure is verified using an experimental rotor rig.

## 1 INTRODUCTION.

The development of high speed rotating machinery has required the solution of a number of technical problems. These include the balancing of forces generated by a non-uniform distribution of mass around the shaft axis of rotation. The solution of this problem has been attempted following two different strategies, which resulted in the development of two families of balancing methods: the influence coefficient and the modal balancing methods.

The influence coefficient method assumes proportionality between the response of the rotor and the unbalance. This proportionality is represented by a matrix of influence coefficients, which are calculated by attaching one or several known masses in predefined balancing planes and measuring the rotor response in a series of trial runs. At least one trial run per balancing planes is required. The matrix is then used to determine a set of correction masses, which minimise the residual unbalance and the corresponding rotor vibration.

In the modal balancing method, on the other hand, the rotor unbalance and its corresponding response are represented in terms of the system mode shapes. From here, the unbalance forces are expressed as a series of modal unbalances, each one of them exciting only one mode of vibration. Similarly, each mode shape multiplied by a suitable scale factor contributes to the total deflection of the shaft. The unbalance is eliminated for each mode in turn using sets of

modal correction masses, which affect only the corresponding vibration mode, leaving other already corrected modes unaffected. At least one trial run is required per each mode corrected during the process.

Rotor balancing theory has been analysed by many researchers aiming to eliminate the required trial runs. Previous papers describing balancing techniques which require no trial runs are mostly based on modal analysis concepts, although there is at least one paper that proposes the use of a rotor computer model to calculate its influence coefficients, avoiding in this way the necessity of any trial run of the real rotor.

## **2 PREVIOUS ATTEMPTS TO ELIMINATE THE TRIAL RUNS.**

In 1966 Hundal and Harker (1) presented a method based on the dynamic response of the rotor in its normal modes. In this method the correction masses are determined by equating the modal components of the unbalance to the corresponding modal components of the correction masses. The procedure described in the paper requires the previous determination of the natural frequencies and the corresponding mode shapes. This procedure does not account for the presence of internal or external damping in the system.

The next paper was published by Palazzolo and Gunter (2) in 1977. In this paper, the authors considered a system with proportional damping and symmetric mass and stiffness matrices. Their procedure considers the natural frequencies to be well separated from each other, so that the mode shapes may be represented by the deflection of the rotor near the critical speeds. Therefore, the procedure is not suitable to balance a rotor with mixed modal behaviour. Another practical difficulty is that the determination of the unbalance force requires the slope of the phase angle versus frequency plot at the resonance, which is very difficult to estimate and affects the precision of the calculations.

Gash and Drechsler (3) proposed in 1978 a method that required the previous knowledge of the mode shapes and modal masses, as well as an initial estimate of damping and stiffness values. In this method the vibration response is measured in a speed range close to each critical speed. The method requires at least four measuring speeds and one measuring point for each mode. The generalised unbalances are identified by least-squares minimisation of data errors, which are considered to include the influence of lower and higher modes.

In a paper published in 1985, Morton (4) considered the deflection of a rotor to be made up of a number of flexural free modes, where the shaft is considered unconstrained, and a corresponding number of flexural rigid modes, where the shaft is considered to be rigidly supported at the bearings locations. The free modes allow unconstrained motion of the supports and the rigid modes contribute to the rotor flexure. Therefore, the support characteristics may be represented by frequency dependant impedances, which are generalised in terms of the free modes. Introducing these characteristics in the differential equations of motion produces two sets of forced equations: one set representing the bearing behaviour, which is discarded, and another set describing the vibration of the shaft, which is used to determine the rotor unbalance.

In 1986 Mecham, Brawley and Molis (5) proposed the use of a numerical model to calculate the rotor unbalance response. This means simulating the trial runs in the computer rather than

using the real machine. The accuracy of this method is limited by the reliability of the rotor model. In particular, the bearing characteristics are very difficult to estimate.

The latest paper on this subject was presented by Wiese (6) in 1992. This author, however, considered only the balancing of paper rolls with a normal operating speed no higher than 70% of the first natural frequency. Therefore, the procedure only considers the first flexural mode. This method requires modelling the system including the characteristics of the supports. No mention was made with respect to the determination of the system damping.

### 3 CONDITIONS REQUIRED TO ELIMINATE TRIAL RUNS.

The response of a flexible rotor may be expressed in terms of its characteristic functions as

$$v(z, t) = \sum_{r=1}^n v_r(z, t) = \sum_{r=1}^n q_r(t) \cdot \varphi_r(z) \quad (1)$$

where  $n$  is the number of vibration modes affecting the rotor response,  $q_r(t)$  represents the  $r$ th principal coordinate of the system,  $\varphi_r(z)$  is the  $r$ th characteristic function or mode shape for the free undamped vibrations and  $v_r(z, t)$  is the  $r$ th component of the vibration at the  $z$  coordinate. In a similar way, the eccentricity distribution may be expressed as

$$e(z) = \sum_{r=1}^n \epsilon_r \varphi_r(z) \quad (2)$$

where the elements  $\epsilon_r \varphi_r(z)$  represent the modal components of eccentricity. Each one of these modal components excites a single mode of vibration. Multiplying equation (2) by  $\rho A(z) \varphi_r(z)$  and integrating along the shaft gives

$$\epsilon_r = \frac{1}{m_r} \int \rho A(z) e(z) \varphi_r(z) dz \quad (3)$$

The modal mass,  $m_r$ , represents the equivalent mass of a single degree of freedom, which would generate a response similar to that observed in the  $r$ th mode of vibration. The characteristic function,  $\varphi_r(z)$ , represents the shape adopted by the shaft in its  $r$ th mode of vibration. This shape is defined as the ratio between the vibration values along the length of the shaft and a reference value, which is usually the vibration measured by one of the transducers. If the vibration measured by the transducer located at  $z = z_i$  were used as the reference value, the  $r$ th mode shape factor for to the axial position  $z = z_j$  would be

$$(\varphi_r)_{ji} = \frac{v_r(z_j, t)}{v_r(z_i, t)} \quad (4)$$

The relative nature of the mode shapes indicates that the modal eccentricity  $\varepsilon_r$  is a function of the reference deflection  $v_r(z_i, t)$ . Now, the vibration  $v_{ri}$  produced by the  $r$ th modal component of unbalance  $\varepsilon_{ri}$  at the position of the reference transducer is

$$v_{ri} = \frac{\Omega_r^2 \varepsilon_{ri}}{\sqrt{(1 - \Omega_r^2)^2 + (2 \zeta_r \Omega_r)^2}} = A_r(\omega) \varepsilon_{ri} \quad (5)$$

with a phase lag  $\phi_r$  with respect to the unbalance force given by

$$\phi_r = \tan^{-1} \left( \frac{2 \zeta_r \Omega_r}{1 - \Omega_r^2} \right) \quad (6)$$

where  $\Omega_r$  is the ratio between the rotation frequency and the  $r$ th natural frequency and  $\zeta_r$  is the  $r$ th damping ratio. The non-dimensional amplification factor  $A_r(\omega)$  is the same at any point along the shaft. To compensate the vibration given by equation (5), it is necessary to attach a mass  $U_{rj}$  to the balancing plane located at  $z = z_j$ , such that

$$U_{rj} \cdot R_j \cdot (\varphi_r)_{ji} = -m_{ri} \cdot \varepsilon_{ri} \quad (7)$$

where  $m_{ri}$  represents the modal mass as seen by an observer located at the reference transducer position and  $R_j$  is the radius of the balancing plane. From equation (7) we get

$$U_{rj} = -\frac{m_{ri} \cdot \varepsilon_{ri}}{R_j \cdot (\varphi_r)_{ji}} = -\left( \frac{m_{ri}}{R_j \cdot A_r(\omega) \cdot (\varphi_r)_{ji}} \right) \cdot v_{ri} \quad (8)$$

The procedure normally used to evaluate equation (8) is to attach a trial mass at the balancing plane in order to determine the global value of the terms between the parentheses in the right hand side of the equation. Thus, the correction mass required to eliminate the  $r$ th component of unbalance can only be found without trial runs if these terms can be determined by some other means. The negative sign considers that the correction mass has to be attached in antiphase with the unbalance force.

A common consideration when evaluating equation (8) is to consider a rotor speed equal to the natural frequency, for which the displacement response is  $90^\circ$  behind the unbalance force. Thus, the phase angle in the resonance defines the position of the unbalance and, therefore, the location of the correction mass. Considering  $\Omega = 1$  in equation (8) gives

$$U_{rj} = -\left( \frac{2 \cdot \zeta_r \cdot m_{ri}}{R_j \cdot (\varphi_r)_{ji}} \right) \cdot v_{ri} \quad (9)$$

It is important to mention that the use of a single mass excites all modes of vibration. Therefore, once the single correction mass has been found, it is necessary to transform it into

an equivalent set of masses, which produces the same effect on the corresponding unbalance component, but produces no effect on other modes.

#### 4 EFFECTS OF TRANSDUCER ORIENTATION.

According to modal theory, there is a phase lag of  $90^\circ$  of the displacement response with respect to the unbalance force in a rotor operating at its natural frequency. This also applies in the case of a rotor supported in asymmetric bearings, but only if the vibration transducer is located in the direction of one of the principal axes of stiffness. For any other direction the phase lag of the resonance vector is no longer  $90^\circ$  and errors are introduced when calculating the angular position of the correction masses (see reference (7)).

A principal axis of stiffness is the direction for which no cross coupling terms exist and the corresponding differential equation of motion uncouples from the other principal coordinate. There are two such axes for each mode of vibration, which means that the resonances are twice as many as in the case of symmetric bearings. The corresponding modes for these principal axes are usually known as horizontal and vertical modes of the shaft, even when the directions of the principal axes are not exactly horizontal or vertical. Practical experience shows that the transducers usually do not coincide with the principal axes, capturing for this reason the effect of the modes corresponding to both principal axes.

Consider two transducers located in the directions  $x$  and  $r$  and located also at the same axial position along the rotor. The angle between the two transducers ( $\tau$ ) is usually, but not necessarily, equal to  $90^\circ$ . Consider also another transducer located in the direction  $q$  located at  $\theta$  degrees from the  $x$  axis. Applying a coordinate transformation, it is demonstrated in reference (7) that the amplitude of vibration for the transducer in the  $q$  direction is given by

$$q = \frac{x \sin(\tau - \theta) + r \sin \theta}{\sin \tau} \quad (10)$$

which is a function of the displacements measured by the transducers in the  $x$  and  $r$  directions. Remembering from equation (9) that the correction mass is a function of the measured resonance vibration, it is clear that the magnitude of the correction mass will be affected by the angular position of the transducer. Now, the relative phase angle  $\phi_q$  is the value of  $\omega t$  for which the first derivative of equation (10) with respect to time vanishes. It can be shown that this angle is independent of the angular position of the transducer, see (7). This is a rather surprising fact, because the angle of the correction mass is a function of both, the transducer location and the relative phase angle for the resonance. That is to say

$$\chi = \phi + \theta + 90^\circ \quad (11)$$

where  $\chi$  is the angle required for the correction mass. The angles in equation (11) are measured on the shaft with respect to the fixed mark used for the generation of the reference pulse. The transducer of the pulse generator is assumed here to be in  $x$  direction. Equation (11) indicates that a change in the angular position of the transducer should be accompanied by a change in the relative phase angle, if the correction angle is to be maintained. Therefore, if the phase angle is independent of the transducer position, we have to accept the fact that only one

measuring direction provides the right angular location for the correction masses, this measuring direction being that of the principal axis of stiffness.

Of course, the above considerations are only relevant when trying to find the correction masses without trial runs. If trial runs are used as part of the balancing process, the correction masses are found by the principle of cause and effect and deviations of the rotor response from the theory of modal analysis, produced by improper alignment of vibration transducers, become irrelevant.

## **5 DESCRIPTION OF THE BALANCING PROCEDURE.**

Real rotors have an infinite number of degrees of freedom, but each one of them may be represented by a vibration mode with behaviour similar to that described by equations (5) and (6). This characteristic may be used to balance each mode of the rotor individually, but the procedure requires separating the modal components of vibration from the global response measured by the transducers. There is, however, no need to treat each mode separately. All modes may be corrected at the same time, equation (9) giving the correction mass required to compensate the  $r$ th modal unbalance. The procedure is as follows.

### **5.1 Development of a computer model for each rotor.**

This requires the geometry of the shafts and the physical properties of the material. No bearing, pedestal or foundation properties are required. Element sections should be placed at each measuring and correction positions. Each model may be verified exciting the rotors while hanging from the crane with a force hammer and measuring the free response with seismic transducers. Free-free mode shapes may then be obtained from the measured transfer functions and compared with predictions using the computer models.

### **5.2 Measurement of the synchronous vibration during run-up or run-down.**

Rotor vibration should be measured using two absolute displacement transducers per bearing to allow the determination of the principal axes of stiffness. It is recommended to measure in as many axial positions as possible to verify the mode shapes of the rotor sitting on its bearings. The vibrations measured in one of these axial positions will be used as the reference coordinate when determining the mode shapes. The reference coordinate may be different for each mode.

### **5.3 Extraction of modal parameters from the vibration signals.**

This includes amplitude and phase of each resonance vector, as well as the corresponding natural frequencies and modal damping ratios. It is best to use a computer tool specially designed to perform this task. If non-contact transducers are used to register the rotor vibration, it is important to subtract the slow-roll vectors produced by imperfections in the shaft. The resonance vectors may be used to draw a schematic representation of the mode shapes in order to identify the different modes of vibration.

### **5.4 Location of the principal axes of stiffness.**

The angular position of the principal axes,  $\alpha$  and  $\beta$ , corresponding to a pair of modes with natural frequencies  $\omega_1$  and  $\omega_2$  are given by the following expressions (see reference (7)):

$$\alpha = \tan^{-1} \left( \frac{x_2 \sin \rho}{x_2 \cos \rho - r_2} \right) \quad (12)$$

and

$$\beta = \tan^{-1} \left( \frac{x_1 \sin \rho}{x_1 \cos \rho - r_1} \right) \quad (13)$$

where the subscripts relate to the two resonances and  $\rho$  is the angle between the two transducers, which is usually  $90^\circ$ . There must be a set of axes for each pair of modes. Thus, this step should be applied to each pair of modes affecting the response of the rotor.

### 5.5 Calculation of the resonance vectors for the principal axes of stiffness.

The amplitude of each resonance vector for the direction of its principal axis may be calculated using equation (10). This is the parameter that has to be introduced in equation (9) to determine the correction mass required for each vibration mode.

### 5.6 Determination of mode shapes.

Use any computer program for determination of eigenvalues and characteristic functions. The stiffness values for the supports are assigned arbitrarily and modified until the natural frequency and mode shape factors at the measuring points coincide with the measured parameters. Note should be made of the mode shape factors at the location of the balancing planes, which are required for the decomposition of masses into modal sets.

### 5.7 Calculation of modal masses.

The rotor mass value required in equation (9) is the modal mass for each vibration mode, as observed from the position of the vibration transducer being used as reference. The modal mass is given by

$$m_{r_i} = \sum_{j=1}^m m_j \left[ (\varphi_r)_{ji} \right]^2 \quad (14)$$

which could be implemented in the computer program that calculates the natural frequencies and mode shapes.

### 5.8 Determination of individual correction masses.

Now it is possible to substitute the different parameters required in equation (9). This equation gives the magnitude of the mass. The angular position is given by equation (11). The result is a single correction mass for each mode. Each mass represents the correction required to compensate the unbalance of a given mode when attached at the same axial position as the mode shape factor included in the denominator of equation (9).

### 5.9 Calculation of correction modal mass sets.

In general, however, single masses affect all vibration modes. Thus, the single correction masses must be transformed into sets of modal masses that correct the original unbalance and do so without upsetting other modes of vibration. These two conditions are represented by the following system of equations.

$$\sum_{j=1}^n U_r(z_j) \cdot R_j \cdot (\varphi_s)_{j,i} = \begin{cases} 2 \zeta_r m_{r,i} v_{r,i} & \text{for } r = s \\ 0 & \text{for } r \neq s \end{cases} \quad (15)$$

where  $U_r(z_j)$  is the correction mass required at the balancing plane in  $z_j$  which forms part of the modal mass set necessary to compensate the unbalance in the  $r$ th vibration mode. Each set of modal masses has  $n$  elements. The number of balancing planes,  $n$ , is equal to the number of vibration modes considered during the balancing.

The procedure described should correct the unbalance in all modes considered during the analysis. However, this does not necessarily guarantee a low residual vibration at normal operating speed when the influence of higher modes is important, and a fine tuning balancing may be required.

## 6 BALANCING OF A ROTOR RIG.

This section describes the results obtained from the balancing of the experimental rotor rig shown in Figure 1. The rotor passes only one pair of modes before becoming unstable. Thus, only one balancing plane was necessary and no transformation of correction masses into modal sets was required. The measured critical speeds were 2056 and 2101 r/min. The vibration signals were measured in horizontal and vertical directions in order to identify the location of the principal axes of stiffness. The measuring position located near the free end bearing was selected as the reference point for the determination of mode shapes and modal masses. It was decided to use the central balancing plane.

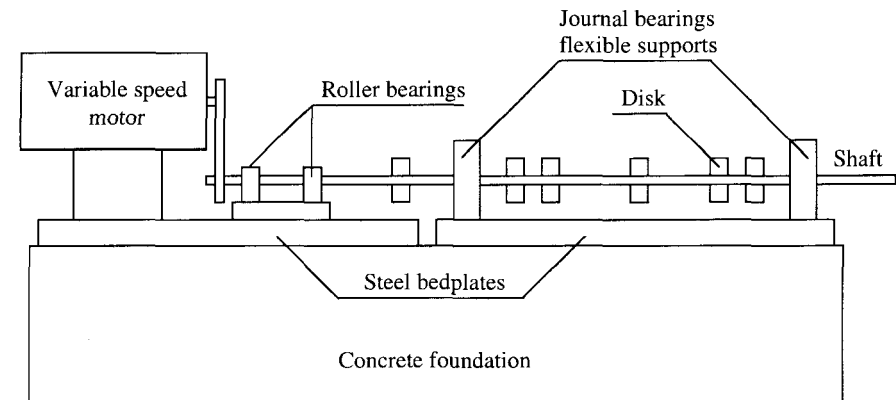


**Figure 1** Schematic representation of the experimental rotor rig used to validate the balancing procedure without trial runs.



The only known parameter in equation (9) was the radius of the balancing plane (100 mm). The rotor response was measured during run-down and a program for extraction of the modal parameters was applied to determine the principal axes of stiffness. From the data for the higher resonance, the angular location for the correction mass was calculated as  $182^\circ$  with respect to the reference mark, measured against shaft rotation. A computer program calculated the corresponding critical speed as 2101.32 r/min. The modal mass observed at the transducer position was then calculated as 499.58 kg, using equation (14) with the mode shape determined by the computer program. Introducing numerical values into equation (9) produced a correction mass of 12.9 g at the central balancing plane.

Thus, the correction mass required to balance this rotor was 12.9 grams at  $182^\circ$  from the reference mark on the shaft against the direction of rotation. There was no hole at that angular position in the balancing plane. Therefore, the correction mass was transformed into a pair of masses: 6.3 grams at  $150^\circ$  and 8.5 grams at  $210^\circ$ , which make a total of 12.86 grams at  $185^\circ$ .

Figure 2 shows the Bode diagram for the vertical direction in the free end, before and after the attachment of the correction mass. Unfortunately, due to the limited capacity of the rotor rig, the experiment considered only one pair of modes. Nevertheless, the experiment shows that the proposed procedure works in practice.

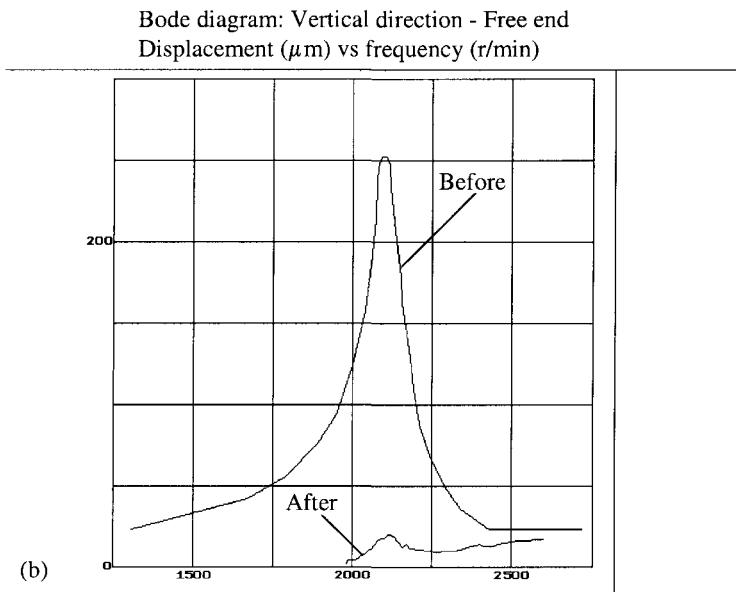


**Figure 2** Vibration recorded at the free end bearing before and after the balancing.

## 7 CONCLUSION.

The application of the procedure to the balancing of an experimental rotor shows that balancing without trial runs is not only a theoretical, but also a practical possibility. The dynamic characteristics of the rotor rig, however, did not cover all the situations possible to find in the field. Therefore, more work is required to verify the applicability of the proposed balancing procedure to rotors with more general characteristics.

## REFERENCES.

1. **Hundal, M. S., Harker, R. J., 1966.** Balancing of flexible rotors having arbitrary mass and stiffness distributions. *Transactions of the ASME, Journal of Engineering for Industry*, Vol. 88, No. 2, 217-233.
2. **Palazzolo, A. B., Gunter, E. J., 1977.** Modal balancing without trial weights by a modified Nyquist plot procedure. *Vibration Institute, Machinery Vibration Seminar*, Cherry Hill, New Jersey, USA, November.
3. **Gasch, R., Drechsler, J., 1978.** Modales ausgewuchter elastischer laufer ohne testgewichtssetzungen. *VDI Berichte*, No. 320, 45-54.
4. **Morton, P. G., 1985.** Modal balancing of flexible shafts without trial weights. *Proceedings of the Institution of Mechanical Engineers*, Vol. 199, No. C1, 71-78
5. **Meacham, W. L., Brawley, G. H., Molis, S. J., 1986.** Balancing of large steam turbine-generator using MoBal. *EPRI Rotating Machinery Dynamics, Bearings and Seals Symposium*, St. Louis, MO. September 9-11.
6. **Wiese, D., 1992.** Two new procedures to balance flexible rotors without test runs. *Institution of Mechanical Engineers, Proceedings of the 5<sup>th</sup> International Conference on Vibrations in Rotating Machinery*, Bath, England, 557-568.
7. **Preciado E., 1998.** Mixed modal balancing of flexible rotors without trial runs. *PhD Thesis, School of Mechanical Engineering, Cranfield University*, Cranfield, Bedford, U.K.

# Experimental and predicted unbalance response of a rotary compressor crankshaft

F SÈVE, A BERLIOZ, and R DUFOUR

Laboratoire de Mécanique des Structures, INSA de Lyon, Villeurbanne, France

M CHARREYRON

Tecumseh Europe, La Verpillère, France

## ABSTRACT

The Finite Element Method associated with the rotor-dynamics theory permits prediction of the unbalance response of a flexible rotor-crankshaft assembly of a rotary compressor. The speeds of rotation dependent characteristics of the fluid film bearings and the side-pull of the electric rotor are taken into account. The experimental set-up permits validation of the model: comparison of the predicted and experimental results concerning the bracket loads and the crankshaft orbit is satisfactory. This paper shows that the current unbalance combination induces an over-pronounced deflection of the crankshaft, with the rigid housing having no motion.

## 1- INTRODUCTION

Basically, a rotary compressor consists of a motor compressor set fixed by brackets inside a hermetic housing having external rubber mounts. The motor compressor set (see Fig.1) is composed of a rotor-crankshaft assembly mounted in the two fluid film bearings of the crankcase, which contains the mechanical parts of the pump. The counterweight masses located at the top and at the bottom of the electric rotor are designed to balance the eccentric masses of the pump.

Refrigerant rotary compressors are widely used today in air conditioning. Their operating speed depends on the frequency of their electricity supply (50 Hz or 60 Hz). Recent studies are in progress to eliminate start / stop cycles and to design a variable speed rotary compressor capable of variable BTU production. At the highest speeds of rotation, for example, above 6,000 rpm, mechanical problems can occur such as rotor-to-stator or bearing rub and failures at the weld spots of the brackets due to an over-pronounced unbalance response. Improving the unbalance response of such a machine requires a reliable model for installing counterweights suitable at low and high speeds of rotation.

This article focuses on the unbalance response of the flexible rotor-crankshaft assembly, which is investigated both numerically and experimentally.

Let the following assumptions be considered. The predicted mass unbalance response of the rotor dynamic system under study is performed at steady state within the 1,200 – 7,200 rpm speed range. The harmonic forces acting on the crankshaft due to the gas compression inside the cylinder is not considered (see [2]). The hermetic housing is assumed to have no motion and to be rigidly fixed on a rigid frame.

A finite element model is proposed, using the rotor-dynamics described in [1] and completing the models presented in [2] and [3]. Numerical results are concerned with orbits and bracket loads versus the speed of rotation. After the presentation of the experimental setup, measured and predicted results are compared to validate the model.

## 2- PREDICTED UNBALANCE RESPONSE

### 2-1 FE Model

The rotor-crankshaft assembly is modelled with two node beam elements (see Fig.2). The eccentric mass ( $m_{3r3}$ ) and the counterweight masses ( $m_{1r1}$ ) and ( $m_{2r2}$ ) have only one node. Particular attention is paid to the modelling of the lateral stiffness of the steel lamination set and the clamping point crankshaft/rotor. These particularities are updated by an experimental modal analysis.

The main bearing is split into two sub-bearings modelled by bearing elements located at nodes 5 and 26 and the outboard-bearing element is located at node 27. The calculation of the bearing characteristics (stiffness  $K_{ij}$ , damping  $C_{ij}$ ) is performed for each speed of rotation inside the 1,200-7,200 rpm speed range. All results are presented for a nominal bearing clearance.

In an induction motor, the magnetic field creates side-pull forces on the rotor [4]. The smaller the air gap, the greater these forces are. But they cancel themselves in the case of perfect rotor/stator concentricity. These non-negligible forces must be added to the model. It can be considered that the resultant force is a linear piece wise function of rotor eccentricity, so that it can be modelled by a stiffness element having a negative value. The compressor studied is equipped with a three-phase motor, where the negative stiffness valued at  $K_{RS} = 0.5 \cdot 10^6$  N/m is added at node 2 (see Fig.2) by way of matrix:

$$K_2 = \begin{bmatrix} -K_{RS} & 0 \\ 0 & -K_{RS} \end{bmatrix} \quad (1)$$

The mass unbalance response is predicted by solving the following equations:

$$M \ddot{X} + (C(\Omega) + C_1(\Omega)) \dot{X} + (K + K_1(\Omega) + K_2) X = F(\Omega) \quad (2)$$

with:  $X$ , the displacement vector containing all the DOF of the FE model,  $M, K$ , the classical mass and stiffness matrices,  $C(\Omega)$ , the non-symmetric gyroscopic matrix,  $C_1(\Omega), K_1(\Omega)$ , damping and stiffness matrices of the bearings,  $K_2$ , the anti-stiffness matrix due to the side-pull forces,  $F(\Omega)$ , the harmonic forces vector including the forces due to the unbalance masses  $m_{1r1}, m_{2r2}$  and  $m_{3r3}$ .

## 2-2 Rotor-crankshaft deflection

Equations (2) are solved for different speeds of rotation. The predicted unbalance response, versus the speed of rotation plotted in Figure 3, shows the deflection at the top of the rotor and at the middle of the three bearings. It can be noticed that there are no resonance phenomena within the speed range due to the damping. However the amplitude of the deflection increases with the speed of rotation and becomes over pronounced: the amplitude at the top of the rotor is higher than the air gap from 6,000 rpm and the amplitude at the main bearing is higher than the nominal clearance from 5,000 rpm.

The predicted rotor-crankshaft deflection at 7,200 rpm is presented in Figure 4.

The counterweight masses ( $m_1r_1$ ) and ( $m_2r_2$ ) and the flexibility of the crankshaft induce high deflection at the top of the rotor and at each part of the main bearing. The deflection at the outboard bearing is less pronounced.

## 2-3 Bearing Loads

Depending on the non-circular orbiting of the crankshaft and on the non-symmetric bearing characteristics, bearing loads due to the crankshaft deflection in bearings vary during a rotation period. Figure 5 presents the maximum load amplitudes along the X and Z axes versus the speed of rotation for the three bearings.

The predicted results shows that the main bearing (# 1 and # 2) is the most loaded and that bearing loads increase with the speed of rotation. These results agree with the unbalance response presented previously.

## 2-4 Bracket Loads

Lateral displacements  $U_i$ ,  $W_i$  and speeds  $\dot{U}_i$ ,  $\dot{W}_i$  along the X & Z axes respectively of the rotor at the  $i^{\text{th}}$  bearing are given by the following equations in the reference frame  $\mathfrak{R}(X,Y,Z)$ :

$$U_i(\Omega t) = U_i^{re} \cos(\Omega t) + U_i^{im} \sin(\Omega t) \quad (3)$$

$$W_i(\Omega t) = W_i^{re} \cos(\Omega t) + W_i^{im} \sin(\Omega t) \quad (4)$$

$$\dot{U}_i(\Omega t) = \frac{dU_i}{dt}, \quad \dot{W}_i(\Omega t) = \frac{dW_i}{dt} \quad (5)$$

with  $U_i^{re}$ ,  $W_i^{re}$ , the real parts and  $U_i^{im}$ ,  $W_i^{im}$  the imaginary parts of the lateral displacements,  $\Omega$  being the speed of rotation. Let  $P_i$  be the location of the axis of the rotor at time  $t=0$  (see Fig. 6). Thus, the bearing loads per cycle at the  $i^{\text{th}}$  bearing expressed in  $\mathfrak{R}(X,Y,Z)$  are:

$$\begin{pmatrix} F_{iX}(\Omega t) \\ F_{iZ}(\Omega t) \end{pmatrix} = - \begin{bmatrix} K_{iXX}(\Omega) & K_{iXZ}(\Omega) \\ K_{iZX}(\Omega) & K_{iZZ}(\Omega) \end{bmatrix} \cdot \begin{pmatrix} U_i(\Omega t) \\ W_i(\Omega t) \end{pmatrix} - \begin{bmatrix} C_{iXX}(\Omega) & C_{iXZ}(\Omega) \\ C_{iZX}(\Omega) & C_{iZZ}(\Omega) \end{bmatrix} \cdot \begin{pmatrix} \dot{U}_i(\Omega t) \\ \dot{W}_i(\Omega t) \end{pmatrix} \quad (6)$$

Let  $\mathfrak{R}_0(O,X_0,Y_0,Z_0)$  be fixed in the bracket plane as indicated in Figure 6.  $\theta$  is an experimental angle. Bearing loads in  $\mathfrak{R}_0$  are:

$$F_{iX_0} = F_{iX} \cos \theta - F_{iZ} \sin \theta \quad (7)$$

$$F_{iZ_0} = -F_{iX} \sin \theta - F_{iZ} \cos \theta \quad (8)$$

If the inertia and mass of the cylinder block are negligible, static balancing leads to:

$$\sum \vec{F}_{\gamma_0} = F_1 + F_2 + F_3 = 0 \quad (8)$$

$$\sum_{\text{Plane}(OY_0Z_0)} \vec{M}_0 = -F_2 \cdot a \frac{\sqrt{3}}{2} + F_3 \cdot a \frac{\sqrt{3}}{2} + F_{1Z_0} \cdot l_1 + F_{2Z_0} \cdot l_2 - F_{3Z_0} \cdot l_3 = 0 \quad (9)$$

$$\sum_{\text{Plane}(OX_0Z_0)} \vec{M}_0 = -F_1 \cdot a \cdot + (F_2 + F_3) \cdot \frac{a}{2} + F_{1x_0} \cdot l_1 + F_{2x_0} \cdot l_2 - F_{3x_0} \cdot l_3 = 0 \quad (10)$$

where  $a$ ,  $l_1$ ,  $l_2$  and  $l_3$  are geometric data depending on the compressor. Thus bracket loads  $F_1$ ,  $F_2$  and  $F_3$  can be calculated in  $\mathfrak{R}_0(O, X_0, Y_0, Z_0)$ . Figure 7 presents the predicted bracket loads during a revolution at 7,200 rpm.

### 3- EXPERIMENTAL INVESTIGATIONS

Figure 8(a) shows a front view of the compressor, drawn in Figure 8(b). The motor compressor set composed of bearings, cylinder block, crankshaft and rotor, is fixed by three adjustable brackets into the lower housing while the stator is fitted into the upper housing. The design of the two parts of the housing is such that the housing is assumed to have no flexibility and no motion (because it is screwed onto a rigid frame). Adjustable brackets permit adjusting the required air gap. The vane and the valve are removed for satisfying the no pressure assumption. Three piezoelectric load cells give the vertical bracket loads. A shaft extension is designed for measuring the orbit with two perpendicular proximity probes. A third identical sensor detects the top corresponding to the eccentric angular location.

### 4- EXPERIMENTAL VALIDATION

Measurement and numerical simulation are performed for different speeds of rotation within the [1,200-7,200] range. The characteristics of the extension shaft are added to the model and a node is created at the proximity probe location.

#### 4-1 Orbits

Figure 9 shows the experimental and numerical orbits at 3,600 rpm. Experimental and numerical signals, which correspond to the position of the rotor axis at  $t=0$ , are aligned to compare amplitudes and phases of these maximums. The maximum amplitudes of the orbit versus speeds of rotation are plotted in Figure 10. The experimental investigation cannot be carried out above 4,800 rpm because the shaft extension increases the deflection and rotor-to-stator rub occurs.

There is pretty good agreement between the measured and predicted response. The counterweight masses located at the top and the bottom of the rotor induce radial forces on the crankshaft, which bends exponentially with the speed of rotation.

#### 4-2 Bracket load

Figure 11 presents the top signal and the experimental bracket loads at 3,600 rpm.

Calculation of bracket loads is performed within the 1,200-7,200 rpm speed range. Due to the non-circular orbiting of the crankshaft in the bearings, the maximum loads are different at each bracket. Figure 12 compares numerical and experimental average maximum loads at the three brackets versus speed of rotation. The reliability of the model is shown.

## 5- CONCLUSION

An FE model simulation is performed to study the rotor dynamics of a variable speed rotary compressor. The rotor-dynamics of the rotating part of a rotary compressor has been investigated both experimentally and numerically, the hermetic housing having no motion.

The FE model takes into account in particular the fluid film bearing having speed of rotation dependant characteristics, the effect of the side-pull forces acting on the electric rotor and, of course, the flexibility of the rotor-crankshaft assembly.

The experimental set-up permits the measurement of orbits and bracket loads and the validation of the FE model.

It as been shown that the current unbalance mass combination induces an over-pronounced deflection: rotor-to-stator rub occurs from 6,000 rpm and crankshaft-to-bearing contact occurs from 5,000 rpm. A new unbalance combination must be calculated. This can be performed with the FE model proposed, and associated with balancing methods such as the modal balancing method or the influence coefficient method.

## ACKNOWLEDGEMENTS

The authors are indebted to Tecumseh Europe Co. for its support and permission to publish these works.

## REFERENCES

- [1] M. Lalanne, G. Ferraris, **Rotordynamics prediction in engineering**, 2<sup>nd</sup> edition, John Wiley & Sons, 1997.
- [2] R. Dufour, M. Gérard, M. Charreyron, *Dynamic analysis of a crankshaft in bending with an electric motor and non-linear fluid film bearing*, **IFTOMM, Fifth Intern. Conf. on Rotor dynamics**, 200-211, 1998.
- [3] R. Dufour, M. Charreyron, M. Gérard, *Dynamics prediction of refrigerant rotary compressor crankshaft*, **Proceedings Purdue Compressor Technology Conf.**, 281-286, 1998.
- [4] L. Marriot, *Finite element calculation of rotor sidepull forces in single-phase induction motors*, **Proceedings Purdue Compressor Technology Conf.**, 729-734, 1994.



**Figure 1:** Motor compressor set

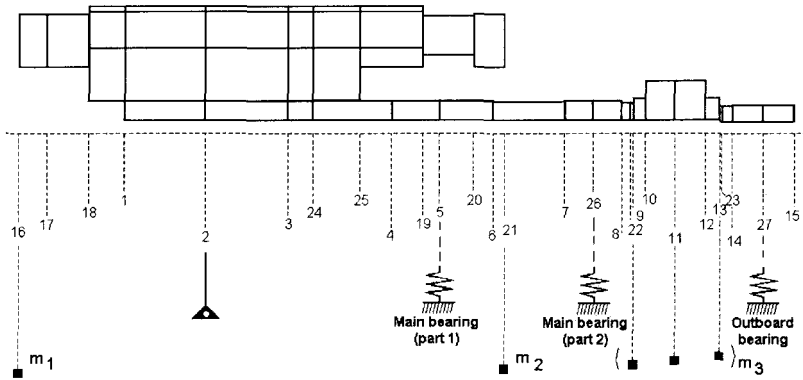


**Figure 2:** Finite Element Model of the rotor – crankshaft assembly

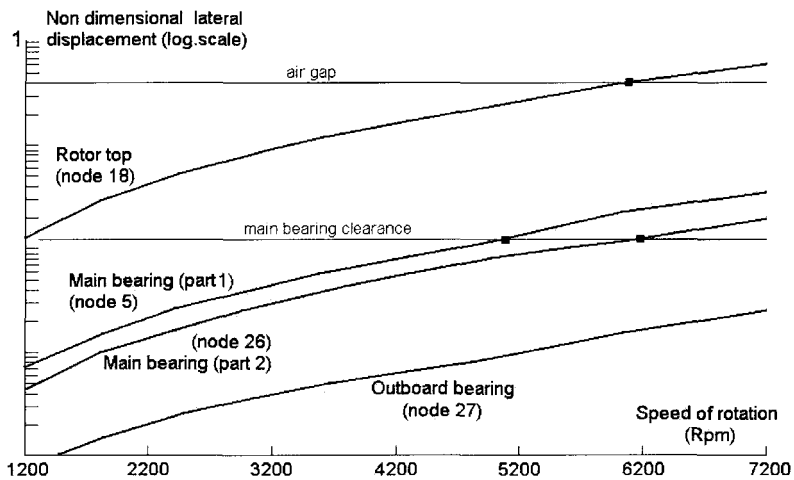


**Figure 3:** Mass unbalance response



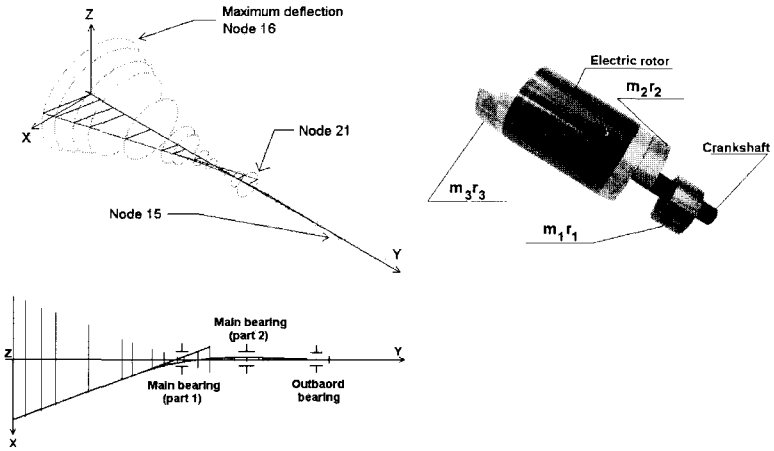


Figure 4: Rotor – crankshaft deflection at 7,200 rpm

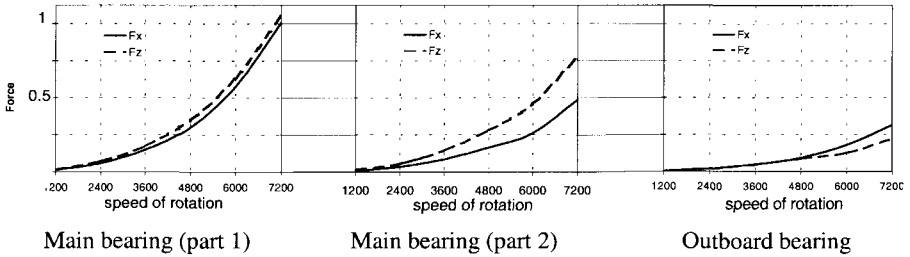


Figure 5: Non dimensional maximum bearings loads amplitude versus rotation speed

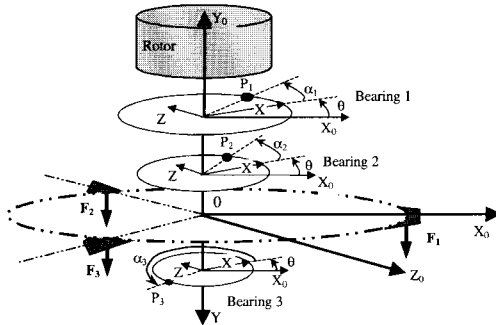
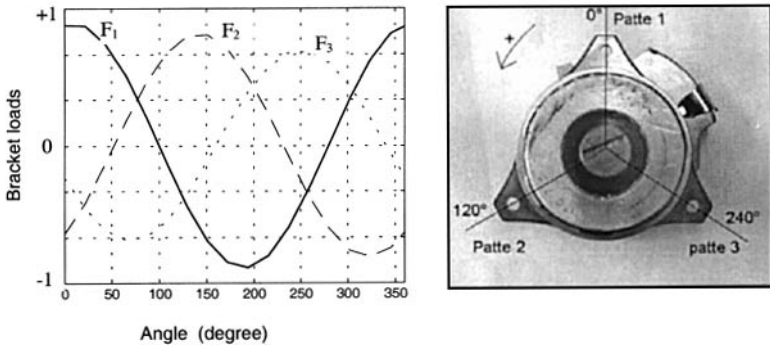
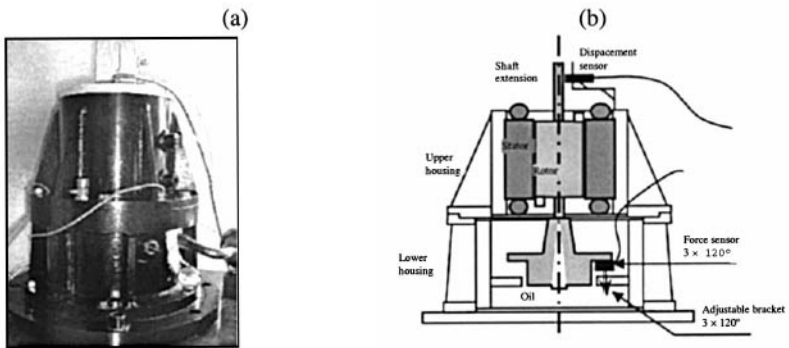


Figure 6: Reference frames for the calculation of the bracket forces



**Figure 7:** Non dimensional bracket loads



**Figure 8:** Experimental setup

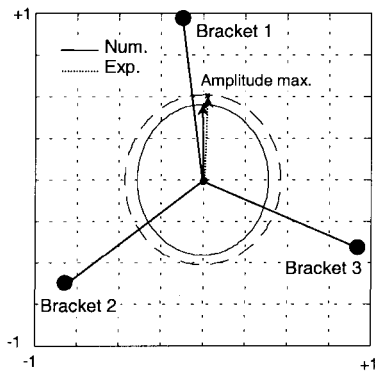


**Figure 9:** Non dimensional orbits at 3600 rpm

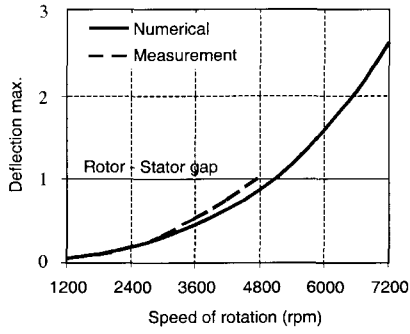


**Figure 10:** Non dimensional deflection versus speed of rotation

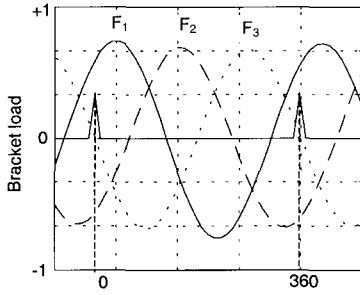


**Figure 11:** Non dimensional experimental bracket loads at 3600 rpm

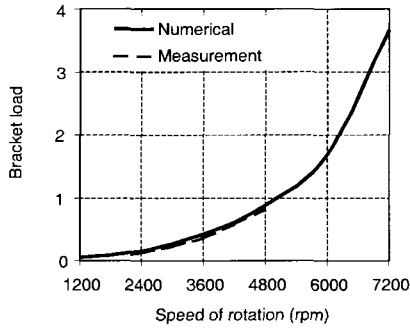


**Figure 12:** Non dimensional bracket load versus speed of rotation

*This page intentionally left blank*

## Min-max optimum flexible rotor balancing compared to weighted least squares

W C FOILES

General Electric, Atlanta, Georgia, USA

P E ALLAIRE and E J GUNTER

Mechanical and Aerospace Engineering, University of Virginia, Charlottesville, USA

### ABSTRACT

Balancing the rotors of rotating machines is a vital step in ensuring that the machines will operate reliably. Most rotor balancing today utilizes exact point (speed) or least squares balancing methods. An exact point balance solves for as many corrective balance weights as vibration measurements that are utilized and it has a unique solution. Least squares balancing involves using more measurements than balance planes available and is determined by minimizing the 2-norm of the final, post-balancing response vector. Weighting functions are sometimes used to improve the method when results are not satisfactory. The objective is then to minimize a performance index consisting of a weighted sum of the squares of the predicted final vibration. However, often least squares balancing and other methods of balancing produce a state of balance where a few locations along the rotor have vibrations which are rather high compared to the remaining locations. In other cases, the method may indicate that large balance weights are needed to balance rather small residual vibrations.

This paper presents the theoretical basis for a min-max optimum method of balancing with more measurements than balance planes using a set of experimentally determined influence coefficients. Often balance specifications require that the amplitude of rotor be less than a certain value at all measurement planes. The use of the min-max method allows for the optimum balancing of industrial rotors where the minimum value of the largest shaft vibration is obtained. The formulation of the method using real parameters and an inequality related to their projections onto the x and y axes is obtained suitable for a linear programming solution of the needed balance weights. A companion paper, entitled 'Balancing of a 1150 MW Turbine-Generator,' in this published work presents an application of the balancing method to a 1150 MW turbine generator. The results of the companion paper applied to the example turbine generator show a significant improvement in predicted balancing results using the min-max approach over the weighted least squares method.

## INTRODUCTION

Balancing a rotating machine generally consists of the addition or removal of relatively small weights at various axial and angular locations along the rotor that contribute rotating forces to the system. Various aspects relating to efficient balance strategies concern the size of the correction weights, modal excitation of weight distributions, optimal location of balance planes, and the number of balance planes required. Most rotor balancing is performed either utilizing a balancing machine or carried out in the normal bearings supporting the rotor. In the procedure of balancing, it should be noted that one is not actually searching for the imbalances in the rotor but for a set of balance weights which minimizes some measure of the residual vibrations. This said, it is always good balancing practice to look for obvious signs of material build-up, erosion, or damage such as missing blades.

An extensive literature review of balancing methods and results has just been published by the authors of this paper [Foiles, Allaire, Gunter, 1998] covering 166 references covering the last 100 years. This review covers influence coefficient methods, modal balancing, unified balancing, balancing using amplitude only, balancing using phase only, linear programming techniques, number of planes required to balance, bowed rotors, redundant balance planes, and other topics. Because this review has just been published, it is felt that this paper does not need a full literature summary - only particular relevant papers are discussed as needed.

The purpose of this paper is to describe a new method of balancing that has been developed to obtain a min-max optimum balance for flexible rotors. Today, most industrial balancing uses either an exact point or least squares procedure to compute the correction weights. The achievement of a very successful balancing is often more of an art than a science for difficult to balance rotors. Trial weight sets may consist of more than one weight to excite particular modes, as used in modal or unified balancing or 'static' and 'couple' balance weights as selected by the balancer. A conventional complex (including both magnitude and phase) rectangular influence coefficient matrix is developed where more measurements are taken than there are balance planes available. The new method provides the minimum value of the maximum vibration (called the min-max) optimum solution to the balancing problem. The method obtains the minimum of the largest value of shaft vibration. This paper develops the theoretical basis for this method while the companion paper provides the experimental verification of this method used in the balancing of a 1150 MW industrial turbine generator.

## BALANCING ASSUMPTIONS

Some common assumptions made in the normal practice of balancing are also made in this work. The first is linearity - the rotor response is linear for fixed system parameters such as rotor speed, operating temperature, process conditions, or external load (examples are gear loads in small machines and power generation in large generators). For fixed rotational speeds and operating conditions, a rotor system is called a linear time invariant (LTI) system. Early work by Rathbone [1929] showed that rotors respond linearly with both magnitude and angle of applied weights.

The second assumption is repeatability or invariance - if the state of the rotor is the same with regard to speed, operating temperature, process conditions, and load, the vibration response is the same. In some cases such as for a large turbine generator, it may take a long time for the rotor

to return to the same state and satisfy the repeatability requirement. If the balancer is not patient and takes data too soon, the balancing procedure may not be successful.

The third assumption is that imbalance excites only synchronous vibration at the running speed, resulting in both amplitude and phase at the 1x frequency component. Non 1x vibration components are not dealt with directly in the balancing of rotors.

## UNRESOLVED ISSUES IN BALANCING

Normally, balance requirements are stated in terms of a maximum response value at any available measurement point. With exact point methods, this is difficult to achieve with some rotors, sometimes requiring many balance runs with success being highly dependent upon the skill and experience of the individual performing the balance. A major improvement in balancing was introduced by Goodman [1964] with least squares balancing which allowed balancing to be done with fewer balance weight distributions than measurements. Usually this is employed as a relatively simple minimization of the 2-norm of the final vibration called least squares error balancing but a weighting matrix can also be employed to improve results by sophisticated balancers. However, while least squares balancing minimizes a weighted sum of the squares of the residual vibration at the measurement planes, it does not minimize the maximum of residual vibration (called min-max balancing). Often least squares balancing will leave a small number of measurement points with high vibrations relative to the rest of the vibration levels.

Another frequent complaint in balancing involves the calculation of large balance weights by least squares methods when the rotor unbalance is not large. Sometimes these calculated weights exceed the capacity of balance planes or cannot be applied for other reasons. This problem occurs when the influence coefficient matrix is ill-conditioned. Some of the columns of the influence coefficient matrix are or nearly are linearly independent. The least squares method is not well adapted to solve this problem. Pilkey and Bailey [1979] addressed the min-max balance method using a linear programming approach, separating their technique into time independent and time dependent algorithms. The linear programming method allows the magnitude of the balance weights to be constrained, but the method has not come into extensive industrial practice. Darlow [1989] developed a method to overcome the problem by reducing the number of balance planes.

Another problem which sometimes arises in least squares balancing is that adding balance planes worsens the final response rather than improving it. Adding additional information should always improve the resulting balance. However, when more balance planes are added in min-max balancing, the quality of balance always improves.

## INFLUENCE COEFFICIENTS

The key to industrial balancing methods is the influence coefficient matrix. Let  $m$  represent the number of measurement distributions and  $n$  represent the number of balance planes. Complex notation is employed because both magnitude and phase information are included in the associated matrices or vectors. The influence coefficients are developed from the equation

$$R_i = HB_i + R_o \quad (1)$$

where  $\mathbf{R}_t$  is the complex vibration response after a complex trial weight distribution vector  $\mathbf{B}_t$ ,  $\mathbf{H}$  is the  $m \times n$  complex influence coefficient matrix, and  $\mathbf{R}_o$  is the complex initial vibration response vector. The influence coefficient matrix is typically obtained by [Goodman, 1964]

$$\mathbf{H}^{(k)} = \frac{1}{\mathbf{B}_t^{(k)}} [\mathbf{R}_t^{(k)} - \mathbf{R}_o^{(k)}] \quad (2)$$

based upon the experimentally obtained values for all of the terms on the right hand side and applied on a column by column basis for each value of  $k$ .

## LEAST SQUARES ERROR BALANCING

In least squares error balancing, the balancing weight vector is given by

$$\mathbf{B}_b = -(\mathbf{H}^T \mathbf{H})^{-1} \mathbf{H}^T \mathbf{R}_o \quad (3)$$

[Goodman, 1964]. The final vibration response of the rotor at the measurement planes is

$$\mathbf{R}_f = \mathbf{R}_o + \mathbf{H} \mathbf{B}_b \quad (4)$$

with balance weights  $\mathbf{B}_b$ . This minimizes the 2-norm of the response vector

$$\min \|\mathbf{R}_f\|_2 = \min \left[ \sum_{i=1}^m (R_{fi})^2 \right] \quad (5)$$

for the optimum balance where the terms  $R_{fi}$  are the components of the final vibration response at each measurement point  $i$ . This method is called least squares error balancing and does not use a weighting matrix.

## LEAST SQUARES BALANCING WITH WEIGHTING MATRIX

In many cases, the residual response vector obtained with least squares error balancing is not acceptable. Some of the reasons were noted in the section on unresolved issues on balancing. A weighting matrix is used to improve the results. Let  $\mathbf{J}$  be defined as a performance matrix where

$$\mathbf{J} = \mathbf{R}_f^T \mathbf{W} \mathbf{R}_f \quad (6)$$

[Goodman, 1964]. The balance weight vector is given by

$$\mathbf{B}_b = -(\mathbf{H}^T \mathbf{W} \mathbf{H})^{-1} \mathbf{H}^T \mathbf{W} \mathbf{R}_o \quad (7)$$

It should be noted that the weighting matrix must be selected so that it is positive semi-definite but does not need to be diagonal. If the weighting matrix is the identity matrix, the balance weight vector reduces to the least squares error balancing. The selection of the weighting matrix



is left to the balancer; Goodman [1964] gives a methodology but his approach has no convergence guarantees insuring that the desired solution will be achieved. If a particular shaft mode or section of the rotor has larger than desired vibration, the weighting functions are adjusted accordingly to increase the weighted importance of those problem areas.

The function of weighting matrix scaling can be included in the initial response. The result is a somewhat modified expression for the balance weight vector is

$$\mathbf{B}_b = -(\overline{\mathbf{H}}^T \mathbf{H})^{-1} \overline{\mathbf{H}}^T \mathbf{W}^{1/2} \mathbf{R}_o \quad (8)$$

where the matrix  $\overline{\mathbf{H}}$  is defined as

$$\overline{\mathbf{H}} = \mathbf{H} \mathbf{W}^{1/2} \quad (9)$$

It may be noted that for any particular weighting matrix  $\mathbf{W}^{1/2}$  selected by the balancer, it is not necessary to actually multiply this weighting matrix times the computed influence coefficient matrix  $\mathbf{H}$ . Rather, if the vibration response vector is first multiplied by  $\mathbf{W}^{1/2}$  and then used to compute the influence coefficients, the weighting matrix will be included automatically.

## MIN-MAX BALANCING

Min-max balancing is carried out using a linear programming method for obtaining the balance weight vector. The influence coefficient matrix can be ill conditioned and should be conditioned using singular value decomposition. A real number version of the influence coefficients and rotor measured vibration response is used. The complex influence coefficient formulation is reformulated in terms of a real matrix form. The coefficient matrix  $\Phi(\mathbf{H})$  is given by

$$\Phi(\mathbf{H}) = \begin{bmatrix} \text{Re}(\mathbf{H}) & -\text{Im}(\mathbf{H}) \\ \text{Im}(\mathbf{H}) & \text{Re}(\mathbf{H}) \end{bmatrix} \quad (10)$$

The balance vector  $\mathbf{B}$  (either trial weight or final balance vector) and the vibration response vector  $\mathbf{R}$  (either trial weight or final response vector) are

$$\mathbf{B} = \begin{bmatrix} \text{Re}(\mathbf{B}) \\ \text{Im}(\mathbf{B}) \end{bmatrix}, \quad \mathbf{R} = \begin{bmatrix} \text{Re}(\mathbf{R}) \\ \text{Im}(\mathbf{R}) \end{bmatrix} \quad (11)$$

where only one column of each is required. Noting that the complex synchronous response and other terms in the balancing problem have the general sinusoidal form

$$z = x \cos \theta + iy \sin \theta \quad (12)$$

where  $x$  is the amplitude of vibration in the horizontal direction and  $y$  is the amplitude of vibration in the vertical direction while  $\theta$  is the phase angle relative to the  $x$  axis. The equations can be written in terms of the real cosine and sine terms in this manner.

The LTI real valued influence coefficient has the form

$$\Phi(H) = \begin{bmatrix} H_c & -H_s \\ H_s & H_c \end{bmatrix} \quad (13)$$

where the  $c$  and  $s$  subscripts indicate cosine and sine terms, corresponding to in-phase and quadrature components of the influence coefficient matrix. The particular values for the influence coefficient matrix are obtained from the real form of Eq. (2).

The final response equation following balancing is given by

$$\begin{bmatrix} R_{fc} \\ R_{fs} \end{bmatrix} = \begin{bmatrix} R_{oc} \\ R_{os} \end{bmatrix} + \begin{bmatrix} H_c & -H_s \\ H_s & H_c \end{bmatrix} \begin{bmatrix} B_{bc} \\ B_{bs} \end{bmatrix} \quad (14)$$

but the method of obtaining the balance weight vector is quite different than the least squares approach. The min-max objective of vibration is the minimization of the maximum residual vibration. This can be approximated by minimizing the maximum projection of the residual vibration onto the  $\pm x$  and  $\pm y$  axes and various rotations of the axis. The min-max algorithm uses a parameter  $\gamma$  that is greater than or equal to each of these projections. The min-max linear programming algorithm minimizes  $\gamma$  resulting in the minimization of the maximum residual vibration.

Let a row vector  $\Gamma$  of length  $2n$  be

$$\Gamma = [\gamma \quad \gamma \quad \dots \quad \gamma]^T \quad (15)$$

where  $n$  is the number of balance planes. The magnitude of  $\Gamma$  terms will be larger than any balanced response. Thus minimizing  $\Gamma$  will minimize the maximum residual response after balancing. The vector inequalities along the  $\pm x$  and  $\pm y$  axes are

$$\Gamma \geq \begin{bmatrix} \pm R_{fc} \\ \pm R_{fs} \end{bmatrix} \quad (16)$$

The linear inequalities become

$$\begin{bmatrix} \Gamma \\ \Gamma \end{bmatrix} \geq \begin{bmatrix} R_{fc} \\ R_{fs} \\ -R_{fc} \\ -R_{fs} \end{bmatrix} = \begin{bmatrix} R_{co} \\ R_{so} \\ -R_{co} \\ -R_{so} \end{bmatrix} + \begin{bmatrix} H_c & -H_s \\ H_s & H_c \\ -H_c & H_s \\ -H_s & -H_c \end{bmatrix} \begin{bmatrix} B_{bc} \\ B_{bs} \\ -B_{bc} \\ -B_{bs} \end{bmatrix} \quad (17)$$

This inequality must be satisfied for the implementation of min-max balancing.

This inequality Eq. (17) is converted to a form suitable for linear programming as

$$\begin{bmatrix} \mathbf{R}_{fc} \\ \mathbf{R}_{fs} \\ -\mathbf{R}_{fc} \\ -\mathbf{R}_{fs} \end{bmatrix} \geq \begin{bmatrix} -1 & H_c & -H_s \\ -1 & H_s & H_c \\ -1 & -H_c & H_s \\ -1 & -H_s & -H_c \end{bmatrix} \begin{bmatrix} \gamma \\ \mathbf{B}_{bc} \\ \mathbf{B}_{bs} \end{bmatrix} \quad (18)$$

In this inequality, the terms  $-1$  in the left hand column in the rectangular matrix on the right side of the inequality corresponds to  $2nx1$  vectors formed by  $\Gamma$ . These inequality terms only bound the projection of the vibration on the  $\pm x$  and  $\pm y$  axes. Instead of rotating the axes, the vibration response vectors can be rotated on projected onto the  $\pm x$  and  $\pm y$  axes. For an angle  $\theta$  relative to the  $x$  axis, the inequalities in Eq. (18) become

$$\begin{bmatrix} c\mathbf{R}_{fc} + s\mathbf{R}_{fs} \\ -s\mathbf{R}_{fs} + c\mathbf{R}_{fc} \\ -c\mathbf{R}_{fc} - s\mathbf{R}_{fs} \\ s\mathbf{R}_{fc} - c\mathbf{R}_{fs} \end{bmatrix} \geq \begin{bmatrix} -1 & cH_c + sH_s & sH_c - cH_s \\ -1 & -sH_c + cH_s & cH_c + sH_s \\ -1 & -cH_c - sH_s & -sH_c + cH_s \\ -1 & sH_c - cH_s & -cH_c - sH_s \end{bmatrix} \begin{bmatrix} \gamma \\ \mathbf{B}_{bc} \\ \mathbf{B}_{bs} \end{bmatrix} \quad (19)$$

where  $c = \cos\theta$  and  $s = \sin\theta$ . The linear programming balancing problem consists of satisfying Eqs. (18) and (19) for suitable choices of  $\theta$ . Good choices of  $\theta$  are given by

$$\theta = \frac{\pi}{2k}, \frac{\pi}{k}, \dots, \frac{(n-1)\pi}{2k} \quad (20)$$

The linear program has as its objective the minimization of  $\gamma$ . The results of the solution of the linear programming inequality is the corrective balance weight vector  $\mathbf{B}_b$  which minimizes  $\gamma$ . Since  $\gamma$  is greater than or equal to the projections of the residual vibration onto the axes, these balance weights approximately minimize the maximum residual vibration after balancing. The corrective balance weights computed a sub-optimal solution to the min-max ( $\infty$ -norm) balance. The actual evaluation of the final balancing solution is carried out by widely available calculation programs such as Matlab.

The final rotor response at the measurement planes is given by

$$\mathbf{R}_f = \mathbf{R}_o + \mathbf{H}\mathbf{B}_b \quad (21)$$

in complex form. This satisfies the min-max balancing relation

$$\min \|R_f\|_\infty = \min \left[ \max \|R_{fi}\| \right], i = 1, 2, \dots, m \quad (22)$$

where  $R_{fi}$  are the  $i$ th components of the final vibration response. The solution is obtained in a more directly scientific approach requiring little intuition on the part of the balancer. This is obviously quite different from the least squares minimization. An extensive example of the use of this method is discussed in the companion paper.

## CONCLUSIONS

A review of exact point and weighted least square balancing is given. While the least squares method is a major improvement over the exact point method, some significant problems with this method are still found: a small number of measurements may have large amplitudes of vibration following balancing and/or the method calculates rather large balance weights may be needed to balance small levels of unbalance if the influence matrix is ill-conditioned. The theoretical approach to min-max balancing method is developed in this paper. It is formulated as a real number linear optimization problem rather than as a complex minimization of least squares. A set of approximate inequality equations are formulated for the min-max approach. These are solved for the final balance weight vectors directly instead of using intuitively selected balance weight matrices in the weighted least squares method. A companion paper carries out an example predicted balancing scenario for a large 1150 MW industrial turbine generator illustrating the use of the least squares and min-max balancing procedures.

## REFERENCES

- Batia, R., 1997, Matrix Analysis, Graduate Texts in Mathematics, Springer-Verlag, New York.
- Darlow, M. S., 1989, Balancing of High-Speed Machinery, Mechanical Engineering Series, Springer-Verlag, New York.
- Foiles, W. C., Allaire, P. E., and Gunter, E. J., 1998, 'Review: Rotor Balancing,' *Shock and Vibration*, 5, pp. 325-336.
- Golub, G. H., and Van Loan, 1996, Matrix Computations, Johns Hopkins University Press, Baltimore, Third Ed.
- Goodman, T. P., 1964, 'A Least-Squares Method for Computing Balance Corrections,' *Journal of Engineering for Industry, Trans. ASME*, 86, pp. 273-279.
- Pilkey, W. D., and Bailey, J. T., 1979, 'Constrained Balancing Techniques for Flexible Rotors,' *Journal of Mechanical Design, Trans. ASME*, 101, pp. 304-308.
- Rathbone, T. C., 1929, 'Turbine Vibration and Balancing,' *Trans. ASME*, 51- Pt. 1, pp. 267-284.
- Udwadia, F. E., and Kalaba, R. E., 1996, Analytical Dynamics: A New Approach, Cambridge University Press, New York.
- Zhou, K., Doyle, J. C., and Glover, K., 1996, Robust and Optimal Control, Prentice Hall, New Jersey.

# Balancing a 1150 MW turbine-generator

**E J GUNTER** and **P E ALLAIRE**

Mechanical and Aerospace Engineering, University of Virginia, Charlottesville, USA

**W C FOILES**

General Electric Company, Atlanta, Georgia, USA

## ABSTRACT

Large turbine-generators have proven to be very difficult to field balance with the application of weights at only single or two planes. This paper represents a method of multi-plane balancing based on actual measured system influence coefficients and theoretically derived coefficients for an 1150 MW turbine-generator system. This class of turbine-generator cannot be balanced by the repeated application of single- or two-plane balancing. A simultaneous multi-plane balancing procedure is first presented using the weighted least squared error method. When using this method, however, it is necessary to assume weighting functions for some of the vibration measurements in order to produce a uniform balance level below a desired vibration level. The standard least squared error procedure tends to overbalance some planes, while leaving other planes under-balanced. The results of the least squared error method of balancing is compared with a MIN-MAX optimum flexible rotor balance procedure based on linear programming concepts. With this procedure, it is not necessary for the operator to include weighting functions and a more uniform balancing is obtained.

## 1 INTRODUCTION

This paper presents the dynamic analysis and balancing computations of a large 1150 MW, 11-bearing nuclear turbine-generator system. The complete unit weighs 727,300 Kg (1.6 million lb) and is 61.70 m (202 ft) long and operates at 1,800 RPM. The objective of the balancing investigation was to improve the field balancing procedure and minimize generator motion by application of balance weights on only the HP and LP turbines and exciter. The original balancing computations were by the weighted, least-squared error method.<sup>1,2,3</sup> This method requires the selection of measurement scaling factors for some stations in order to achieve an optimum value of balance. Balancing predictions using the Min-Max theory<sup>4</sup> produce a superior balance with fewer planes and also without the need for weighting functions.

## 2 CRITICAL SPEEDS OF TURBINE-GENERATOR COMPONENTS

As the first step in analyzing the dynamic characteristics of the 1150 MW turbine-generator set, the critical speeds and mode shapes were generated for each component of the system. The major component of the turbine-generator set consists of a high pressure turbine (HP) and three low pressure turbines connected to a generator, which in turn has an exciter attached.

### 2.1 High Pressure Turbine

Figure 1, for example, represents the first mode for the HP turbine. The turbines and generator were analyzed using the transfer matrix program *CRITSPD-PC*.<sup>5</sup> The HP turbine is approximately 380 in. (9.65 m) long and weighs over 150,000 lb (68,000 Kg). Figure 1 shows the first HP turbine critical speed to be approximately 1,200 RPM (120 Hz). For an assumed bearing stiffness of  $K_b = 4.0E6$  lb/in (7.0E8 N/m).

A reduced mass station model was next generated to match the original model's first three critical speeds. This step is necessary in the construction of the entire system from the components.

Figure 2 represents the HP second critical speed predicted to be at 1,710 RPM (28.5 Hz).

This value is very close to the operating speed of 1,800 RPM (30.0 Hz). Note that the coupling on the right is attached to the first low pressure turbine. Since this coupling has considerable amplitude and slope, it will be influenced by the stiffness of the low pressure turbine.

### 2.2 Low Pressure Turbine

There are three low pressure turbines attached to the right of the high pressure turbine. These turbines will be referred to as LP1, LP2, and LP3. The coupling connecting the HP turbine to LP1 will be referred to as C1 and the coupling connecting LP1 to LP2 will be referred to as C2. Coupling C3 connects LP2 to LP3. The LP turbines are approximately 425 in. long (10.8 m) and weigh 340,000 lb (154,000 Kg) each. The low pressure turbines are larger and have over twice the weight of the high pressure turbine. Therefore, the low pressure turbine first critical speed is lower. Figure 3 indicates that the third critical speed is 1,890 RPM (31.5 Hz) with an assumed bearing stiffness of  $2.0E6$  lb/in (7.9E7 N/m). The operating speed of 1,800 RPM is above the predicted second critical speed for the LP turbines. After the completion of the detached LP rotor model, a reduced LP model was generated with only one-half of the stations of the original LP model.

### 2.3 Generator

The generator is over 651 in long (54 feet) and weighs over 428,999 lb (214 tons). Since the generator has the longest span of any of the components and is the heaviest, it has the lowest first critical speed. Figure 4 represents the generator mode shape for the third critical speed at 2,062 RPM (34.4 Hz) for an assumed value of bearing stiffness of  $2E6$  lb/in.

Figure 5 represents the first four generator critical speeds as a function of bearing stiffness. At a high bearing stiffness of  $K_b = 7.0E6$  lb/in, the generator second critical speed will be at the operating speed. The operating speed on Figure 5 is shown as a dot-dash line.

It is seen that the generator may be operating near the second critical speed. The third critical speed is above the operating speed. The plot of the fourth critical speed is also shown on this plot. It is not desirable to have the rotor fourth critical speed to be exactly twice the operating speed. It is also undesirable to have a generator critical speed at exactly 60 Hz. Fine faults will cause 120 Hz excitation in a generator, which can excite the higher order torsional-lateral modes. The 120 Hz excitation has caused LP3 torsional blade vibration and subsequent blade loss in this class of turbine-generator.

## 2.4 Generator-Exciter

The generator was combined with the exciter to determine the combined generator-exciter modes. Figure 6, for example, represents an exciter mode at 1,452 RPM (24.3 Hz). This mode can be excited by unbalance at the exciter or by suddenly applied unbalance at the LP3 turbine due to blade loss.

There is no monitoring probe between the outboard generator and the exciter bearing to monitor the exciter behavior. This mode shows the importance of placing a vibration pickup between the 10th (generator outboard) and 11th bearings (exciter) to monitor exciter motion.

## 3 TURBINE-GENERATOR SYSTEM CRITICAL SPEEDS

It was determined that there are only minor gyroscopic effects involved with the turbines or the generator at or below 1,800 RPM. Finite element models were generated for each component which matched the transfer matrix models. Due to the speed of interest, the finite element program *MSC/pal2*<sup>6</sup> could be employed. The finite element model was also used to determine the static deflected mode shape of the system, as well as the combined dynamical modes of motion. Also, the finite element model could be used to determine the system forced response with unbalance and bearing stiffness and damping.

The first five modes of the system involve the component mass center of the generator and the various turbines. The first system critical speed is shown in Figure 7 at 496 RPM. This mode is the generator first critical speed, as would be expected, since it is the longest and heaviest of the components. Its natural frequency is relatively unaffected by the LP3 turbine. This mode is driven by unbalance at the generator mass center.

The next three turbine-generator modes involve the mass centers of the LP turbines. These modes occur within a narrow range of each other. When using the transfer matrix method to compute these modes, several modes were initially missed due to the frequency marching method and step increment used in the transfer matrix procedure. A great advantage of the *finite element method* is that it does not skip or miss modes. In Figure 8, which is the turbine-generator system second mode at 562 RPM, the motion of the three mass centers is in phase.

Figure 9 represents the third turbine-generator mode at 569 RPM. In this mode, the mass center of LP1 is out of phase to the mass center of LP3. The second and third system modes would be well controlled by the rigid rotor balancing of the LP rotors. Coupling alignment would have little influence on this mode.

The fourth turbine-generator mode at 585 RPM, as shown in Figure 10, shows that the LP1 and LP3 turbines are moving out of phase to the LP2 turbine. These three modes are similar to the behavior of a large three-mass rotor model.

The fifth system turbine-generator critical is identical to Figure 1 for the high pressure turbine at 1,182 RPM. The mode shape and first critical speed of the HP turbine is relatively unaffected by the LP turbines.

Figures 11 and 12 represent the turbine-generator sixth and seventh modes at 1,037 RPM and 1,162 RPM. These two modes are bifurcated modes of the generator second critical speed interacting with the turbines. The sixth mode at 1,037 RPM, as shown in Figure 11, corresponds with the original turbine-generator second critical speed.

In Figure 12, the slightly higher speed of the seventh mode (1,162 RPM) is caused by the interaction of the LP1 and LP2 turbines with the generator. Modes six and seven would probably appear as a single mode in the experimental test data.

Figure 13 is the ninth turbine-generator mode at 1,459 RPM and is essentially the first exciter mode. If there is no monitoring station between the 10th and 11th bearings, the exciter mode will not be observed. Also, blade loss at LP3 would cause a violent transient excitation of the turbine-generator eighth mode, with large exciter amplitude.

Figure 14 represents the 10th mode of the turbine-generator system at 1,673 RPM. Depending upon the assumptions of bearing stiffnesses, the 10th mode may be even closer to the operating speed at 1,800 RPM. This mode is of considerable importance from the standpoint of understanding multi-plane balancing of the turbine-generator. The motion at the ends of the HP and LP turbines is out of phase, with large response at couplings 1, 2, and 4.

After passing through the first five critical speeds, the turbine and generator mass centers became node points. This means that there is very little motion at the mass centers of the turbines and the generator. Figure 14 shows that there are 10 node points along the axis of the turbine-generator for the 10th mode. Theoretically, a minimum of 10 planes of balancing would be required to balance all 10 modes. Although coupling No. 1 between the HP and LP1 turbines has not been used as a balancing plane, Figure 14 shows that the first coupling location will have a considerable influence along the entire length of the turbine-generator.

#### **4 INFLUENCE COEFFICIENTS AND MULTI-PLANE BALANCING OF TURBINE-GENERATOR**

From the evaluation of the theoretical turbine-generator system critical speeds, much useful information on the balancing procedure for the 11-bearing turbine-generator is obtained. To perform an actual multi-plane balancing, influence coefficients of the turbine-generator to various balancing planes must be first experimentally determined. It is desirable to be able to balance the turbine-generator by the application of weights at the couplings and at the ends of the LP turbines. It is not desirable to apply field balance weights to the generator because of its operation in a hydrogen environment.



#### 4.1 Theoretical Coupling No. 1 Influence Coefficients

From the observation of Figure 14 of the system 10th mode, it can be seen that the first coupling location would provide an excellent balancing plane for trim balancing the turbine-generator at speed. In practice, however, only the second, third, and fourth coupling locations have been used. The influence coefficients for the first coupling, referred to as location C1, were generated analytically from the finite element program. A forcing function was placed at coupling location 1 and the forced response, including bearing damping, was computed for 1,800 RPM. Figure 15 represents the response of the rotor due to an unbalance force placed at the first coupling. The rotor response is a three-dimensional space curve because of the influence of bearing damping.

Figure 16 represents the in-plane and out-of-plane components of the response to unbalance at the No. 1 coupling. If there is no system or bearing damping, then the out-of-plane amplitude represented by the dotted line would be zero.

For example, at the critical speed for a single mass model, the out-of-plane response is lagging the forcing function by 90E. The in-plane and out-of-plane components of the influence coefficients are computed by multiplying the influence coefficient amplitude by the cosine or sine of the relative phase angle response to the unbalance vector.

In the actual system, measurements are made only at the 11 bearings. Figure 16 was generated by using only 11 amplitude and phase values computed for the bearings. A cubic spline curve fit was used to connect the points. The cubic spline curve fit identically matches beam theory. Thus, by using a cubic spline curve fit to only the bearing amplitudes, the amplitude at other sections may be accurately predicted, except at the exciter-generator region.

Note that the cubic spline curves pass through the mass centers of the LP turbines and the generator. By comparing Figures 15 and 16, it can be seen that the cubic spline curve fit does not match the shape of the rotor motion in the vicinity of the generator and exciter. To produce a more accurate curve in this vicinity, a measurement must be taken between the 10th and 11th bearings. Therefore, it is important to have a probe monitor the exciter motion when placing balancing weights along the shaft.

#### 4.2 Experimental Coupling Influence Coefficients

Experimental coupling influence coefficients have been obtained for weights placed on couplings 2, 3, and 4. The influence coefficients for a particular coupling location are obtained by subtracting the rotor response before and after the application of a trial weight and normalizing by the trial weight. Figure 17 represents the experimental turbine-generator response due to a weight placed at the No. 2 coupling between the LP1 and LP2 turbines. The response is given in terms of mils per 100 oz of applied unbalance at a 19.9 in. radius. Note that the C2 coupling shot causes a 90E response at that location and a large in-plane response at the sixth bearing near the third coupling.

An influence coefficient response plot similar to Figure 17 was generated by a trial weight placed at coupling No. 3. There is a large response at coupling No. 2 due to the trial weight placed at coupling No. 3. The in-plane components of the response due to the trial weight at coupling No. 3 causes very little excitation of the LP turbine mass centers. Therefore, the placement of an LP3 coupling weight should have minimal effect on the LP lower rotor

system critical speeds, which are essentially driven by LP rotor mass center unbalance. The No. 3 coupling balancing appears to have only a small influence on the exciter bearing motion. However, a probe should be placed between the No. 10 and 11 bearings to measure the exciter motion, which could be quite large.

#### 4.3 LP Turbine Static and Dynamic Influence Coefficients

Preliminary balancing calculations using the experimental influence coefficients for the couplings 2, 3, and 4 indicated that these planes alone would be insufficient to produce a satisfactory level of balance along the entire turbine-generator shaft. From the study of the turbine-generator 10th mode, as shown in Figure 14, it is apparent that the low-pressure turbines exhibit conical motion. That is, the motion at the ends of the turbine are out of phase to each other, while the turbine mass centers are node points. The prediction of conical turbine motion indicates that it would be highly desirable to use dynamic balancing shots on the turbines. In a dynamic or couple balance, two weights are placed on either end of the turbine shaft out of phase to each other.

In the actual balancing of the turbine-generator system, only balancing shots have been placed on the 3rd low-pressure turbine (LP3 turbine). A static balancing shot was employed in which the weights were placed in phase. Another combination balancing shot was later performed in which a weight of 64 oz. was placed at a single phase angle of 20E on the steam side and of the LP3 turbine and a second weight of 80 oz. was placed at 330E on the generator side of LP3. A large generator response obtained with this weight combination.

Figure 18 represents the vector diagram of the two balance weights  $U_s = 64 \text{ oz. @ } 20\text{E}$  and  $U_g = 80 \text{ oz. @ } 330\text{E}$  placed on the steam and generator ends, respectively. These two balance vectors may be resolved into static and dynamic components of balancing. The two weights can be replaced by a set of static balance weights of 62.3 oz. placed at 353E at both ends, and a dynamic couple of 33.5 oz. at 282E on the generator end and 33.5 oz. at 102E on the steam end of the LP3 rotor.

The computer program *ROTORBAL-PC*<sup>6</sup> was used to predict the rotor response due to the static unbalance of 64 oz. at 353E. The influence coefficients as shown in Figure 20 were used to perform the calculations. Using these values of predicted amplitude, it was then possible to compute the response of the rotor to a pure dynamic or couple balance set for the LP3 rotor. Figure 19 represents the computed response of the turbine-generator due to a couple unbalance on the LP3 turbine. Note the large response of the LP3 couple on the generator response. It is apparent that high generator response may be controlled by dynamic balance shots placed on the LP3 turbine.

Table 1 represents a summary table of the influence coefficients for the turbine-generator for 100 oz of unbalance per plane.

## 5 MULTI-PLANE BALANCING OF TURBINE-GENERATOR

The influence coefficients for the various coupling balance planes and the LP3 turbine static and dynamic balancing coefficients are shown in Table 1. The response is shown in mils of amplitude per 100 oz of unbalance at the various locations. These coefficients were used to generate the space curves, as shown in the previous figures.

By means of the influence coefficients, various balancing predictions were generated using the couplings by themselves and the addition of the couplings and a dynamic couple on the LP3 turbine. Table 2 represents various multi-plane balancing corrections generated for three planes of coupling, five planes using a dynamic balance on LP3, and six planes of balancing using the theoretical influence coefficients generated for the first coupling. Table 3 represents the initial amplitude and the final amplitude predicted with three, five, and six planes of balancing. In the first balance prediction, using couplings 2, 3, and 4, it was found that the rotor amplitude would increase at bearing locations 1, 3, 7, and 11. The increase in amplitude at these locations is shown with a plus. It is therefore apparent that with only three coupling locations used for a simultaneous balance, eight of the bearing amplitudes reduce, while three become larger. For example, the amplitude at probe 3 has increased to 5.25 mils. Also, it is desirable that the amplitude does not exceed 3 mils at the exciter. The amplitude at the exciter after three coupling balance shots have been added has increased to 3.42 mils, as shown in Table 3.

In the second balancing calculation, two planes on the LP3 turbine were used in addition to the three coupling locations. Although five physical planes are used in the balancing, from a computer standpoint this is a four-plane balance prediction, since a dynamic couple placed at the LP3 turbine is treated as one balancing entity. By applying the dynamic couple at the LP3 turbine, it is seen that all planes have been improved in amplitude. There has been a considerable reduction in the amplitude at bearing 3, from 5.25 to 2.16 mils. Also, the amplitude at the exciter is less than 3 mils. However, with the five planes of balancing, it is not possible to reduce all levels of vibration below 3 mils. For example, bearings 4, 5, and 8 have amplitudes above 3 mils.

In the six-plane balancing calculations, the first coupling location was used in addition to the other planes. The influence coefficients generated for the first coupling location are based on theoretical predictions. Therefore the calculations of the balance weights for these cases cannot be actually applied to the rotor until the actual influence coefficients for the No. 1 coupling are determined experimentally. However, this computation does illustrate the improvement in the overall balancing by employing the No. 1 coupling for additional balancing. In the first six-plane balance calculation, no weighting was applied to any of the vibration measurements. One of the advantages of a multi-plane balancing program is the ability to emphasize particular amplitudes of vibration for the purpose of balancing. In the first balancing calculation with six planes, as shown in Table 3, all vibration readings were treated with equal emphasis. In this case, very low levels of amplitude were obtained at bearings 1, 3, 5, 6, and 7. However, the amplitude at bearing 8 is 3.56 mils and the exciter has increased to 3.89 mils. This is considered to be undesirable. In the second six-plane calculation, weighting functions were employed at probes 3, 4, 8, and 11. The weighting function of .8 was used at bearing No. 3. This allowed the amplitude to increase. A weighting function of 1.5 was used at bearings 4, 8, and 11. The final theoretical six-plane balancing prediction demonstrates that the amplitude at all levels can be reduced below 3 mils.

## 6 MULTI-PLANE BALANCING BY MIN-MAX THEORY

The turbine generator may be well balanced by the use of the weighted least squared error balancing procedure. However, in order to achieve optimum balancing by this process, it is

necessary for the operator to iterate on the solution by the introduction of scale factors for various vibration measurements in order to achieve a uniform amplitude of motion after balancing. A superior balancing procedure has been developed by Foiles, as described in the preceding paper. The balancing is based upon the Moore-Penrose singular generalized inverse method and singular value decomposition (SVD) of the mHn rectangular influence coefficient matrix. Table 4 represents the predicted response and phase angles as computed by the least squared error balancing method without the application of weighting functions and the predicted turbine-generator vibrations using Min-max balancing theory.

The least squared error results are similar to those shown in Table 3, using five planes of balance. The slight difference in magnitude for some of the least squared predicted values occurs because, in Table 4, the least squared error balancing was re-computed using *MATLAB*<sup>7</sup>. Note that at probe locations 4, 5, and 8, the vibrations exceed the desired limit of 3 mils. With the Min-Max method of balancing, the largest amplitudes are 2.8 for probes 6, 8, and 9. Amplitudes below 3.0 mils could not be achieved with only five planes of balance, even with the use of weighting functions. As shown in Table 3, six planes are required with the weighted least squared error method to achieve a similar level of vibrations to that obtained with five balance planes using Min-Max theory. Table 5 shows the comparison between the balance weighting required for Min-Max balancing and the least squared error method.

## **7 SUMMARY AND CONCLUSIONS ON MULTI-PLANE TURBINE GENERATOR BALANCING**

The following are concepts of multi-plane balancing that have been developed from the computation of the theoretical rotor dynamical response and from the application of turbine-generator measured influence coefficients using least squared and Min-Max balancing.

1. The four coupling locations are inadequate to balance the entire turbine-generator system. This is because the turbine-generator operates through at least ten modes, so four balancing planes are insufficient.
2. The rotor requires at least six simultaneous planes of balancing to reduce the vibrations at all probes below 3 mils using least squared error balancing, but only five planes using Min-Max theory. The Min-Max procedure of balancing for large turbine-generators is clearly superior to the least squared error method, even with the use of weighting functions. Considerable skill by the operator must be used in selecting the weighting functions so as not to overbalance one section while under-balancing another section of the turbine-generator. The computation of the magnitude of the balance weights, on the average, by the Min-Max procedure appears to be lower than that predicted by least squared error. This is highly desirable.
3. Low-speed balancing of the individual turbines and generator on a balancing machine is recommended to balance out the rotor mass centers. The first five critical speeds encountered by the turbine-generator system are essentially excitations due to the mass centers of the various LP, HP, and generator rotors. By properly balancing the rotors on a balancing machine, the vibration of the lower modes will be minimized.

4. After the rotor passes through the first five critical speeds, the turbine and generator rotor mass centers become node points. This means that the mass centers have very little motion and most of the amplitude of a particular turbine component is a conical motion in which the ends are out of phase. No attempt should be made to place balancing weights at the turbine rotor centers to balance out amplitude at running speed, as this will cause excessive motion at the lower critical speeds.
5. The use of static balancing components on the turbines at running speed is to be discouraged. This is equivalent to adding mass center unbalance. This balancing weight distribution can cause large turbine response when passing through the lower turbine-generator critical speeds.

## REFERENCES

1. Goodman, T. P. 1964, "A Least-Squares Method for Computing Balance Corrections," *Journal of Engineering for Industry*, 86(3): 273–279.
2. Palazzolo, A. B., and E. J. Gunter, 1977, "Multimass Flexible Rotor Balancing by the Least Squares Error Method," Vibration Institute, Clarendon Hills, Ill.
3. Gunter, E., and C. Jackson, "Balancing of Rigid and Flexible Rotors," Chapter 3, *Handbook of Rotor Dynamics*, McGraw Hill, 1992.
4. Foiles, W., E. J. Gunter, and P. E. Allaire, "Theory of Min-Max Optimum Flexible Rotor Balancing With Generalized Inverse Methods," Submitted to 7th International Conference on Vibrations in Rotating Machinery, Nottingham, U.K., September 12–14, 2000.
5. "*CRITSPD-PC* User's Manual," Gunter, E. J., and G. Gaston, RODYN Vibration Analysis, Inc., Charlottesville, VA.
6. "*ROTORBAL-PC* User's Manual," Gunter, E. J., and G. Gaston, RODYN Vibration Analysis, Inc., Charlottesville, VA.
7. "*MATLAB* Version 5 User's Guide," Hanselman, D., and B. Littlefield, Prentice Hall, 1997.

Table 1 - Experimental Influence Coefficients for Turbine-Generator  
(Units - Mills/100 oz. Unbalance)

Probe	Probe Location	Balance Location									
		Coupling No. 2		Coupling No. 3		Coupling No. 4		LP3 Static		LP3 Dynamic	
		Mag	Phase	Mag	Phase	Mag	Phase	Mag	Phase	Mag	Phase
1	HPs	1.1	177°	1.9	124°	0.8	114°	2.3	29°	4.3	77°
2	HPg	0.3	43°	1.6	317°	0.5	213°	1.8	229°	1.6	270°
3	LP1s	1.4	323°	2.8	261°	1.7	158°	7.8	130°	3.3	238°
4	LP1g	2.5	92°	3.6	45°	2.6	315°	1.7	17°	3.1	210°
5	LP2s	2.9	94°	4.5	9°	2.8	330°	0.6	295°	3.8	213°
6	LP2g	4.5	355°	4.8	144°	3.3	61°	3.7	94°	7.3	322°

Table 2 - Multi-Plane Balancing Corrections

No. of Planes	Coupling No. 1*		Coupling No. 2		Coupling No. 3		Coupling No. 4		LP3 <sub>1</sub>		LP3 <sub>2</sub>	
	W, oz.	Phase	W, oz.	Phase	W, oz.	Phase	W, oz.	Phase	W, oz.	Phase	W, oz.	Phase
3			77.3	95°	32.7	341°	17	268°				
5			125	98°	109	351°	46	314°	68	124°	68	304°
6	164	358°	108	113°	79	17°	30	315°	40	148°	40	328°
6 <sup>**</sup>	154	93°	86	12°	56	308°	55	307°	86	162°	86	342°

\* Based on theoretically developed influence coefficients for coupling No. 1 unbalance

\*\* Probe weighting on 3, 4, 8, and 11

Table 3 - Initial and Predicted Rotor Response with Coupling Planes and LP3 Dynamic Couple Unbalance

Probe Location	Initial	3-Planes CPLS 2, 3, & 4	5 Planes CPLS 2, 3, 4, & LP3 Dynamic	6 Planes* CPLS 1-4, & LP3 Dynamic
1	2.17	2.37 (+)	1.68	0.8 .92 **
2	1.77	1.55	1.17	1.83 1.98
3	4.87	5.25 (+)	2.16	1.20 2.98
4	5.45	4.3	3.56	3.87 2.83
5	4.21	3.6	3.87	0.69 .86
6	3.55	1.0	2.57	0.91 1.13
7	2.27	2.99 (+)	1.35	0.72 2.09
8	4.26	2.15	3.26	3.56 2.62
9	3.47	1.48	2.55	1.95 2.32
10	2.19	1.12	2.15	0.89 .62
11	2.97	3.42 (+)	2.77	3.89 (+) 2.77

Based on theoretical coupling No. 1 influence coefficients \*\* Probe weighting factors on 3, 4, 8, & 11  
Bold = lowest amplitude

**Table 4 - Turbine-Generator Predicted Response Using Least Squared Error and Min-Max Balancing With 5 Balance Planes, Couplings 2-4, and a Couple Weight in Low Pressure Turbine 3**

Probe Location	Least Squared Balance 1 × mils	Min-Max Balance 1 × mils
1	1.71 Δ 352°	1.73 Δ 340°
2	1.18 Δ 186°	1.37 Δ 179°
3	2.17 Δ 28°	2.74 Δ 36°
4	3.56* Δ 7°	2.53 Δ 9°
5	3.87* Δ 332°	2.75 Δ 323°
6	2.59 Δ 151°	2.81 Δ 106°
7	1.32 Δ 3°	2.79 Δ 13°
8	3.23* Δ 99°	2.82 Δ 105°
9	2.58 Δ 251°	2.82 Δ 255°
10	2.18 Δ 103°	1.51 Δ 126°
11	2.77 Δ 126°	2.73 Δ 117°

\* Values above desired vibration

**Table 5 - Balance Weights Using Least Squared and Min-Max Balancing Couplings 2-4 and a Couple Weight on LP3**

Balance Plane	Min-Max Balance oz. Δθ°	Least Squared Balance oz. Δθ°
Coupling 2	125 Δ98°	159.9 Δ90°
Coupling 3	109 Δ351°	102.0 Δ351°
Coupling 4	46 Δ314°	58.4 Δ320°
LP3 Couple*	68 Δ304°	70.3 Δ304°

\* Phase angle measured at generator end

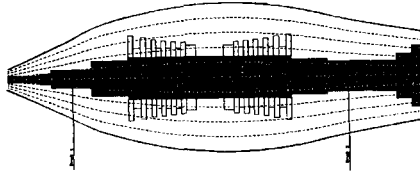


**Figure 1 - High Pressure Turbine 1st Critical Speed with  $K_s = 4.0E6$  lb/in (7.0E8 N/m)  
 $N1 = 1,200$  RPM (20 Hz)**

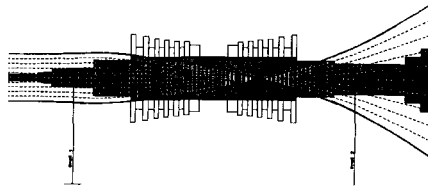


**Figure 2 - High Pressure Turbine 2nd Critical Speed with  $K_s = 4.0E6$  lb/in (7.0E8 N/m)  
 $N2 = 1,710$  RPM (28.5 Hz)**

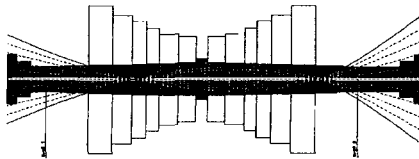


**Figure 3 - Low Pressure Turbine 3rd Mode at 1,888 RPM (31.5 Hz) with  
 $K_s = 2.0E6$  lb/in (3.5E8 N/m)**

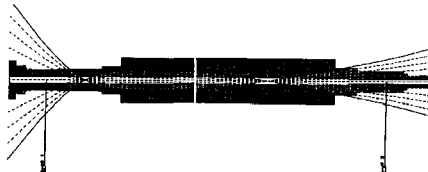


**Figure 4 - Generator 3rd Critical Speed with  $K_s = 2E6$  lb/in  
 $N3 = 2,062$  RPM (34.4 Hz)**



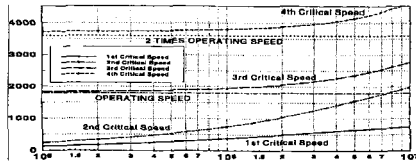


Figure 5 - Critical Speeds of Generator as a Function of Bearing Stiffness



Figure 6 - Exciter-Generator Critical Speed at 1,454 RPM (24.2 Hz)

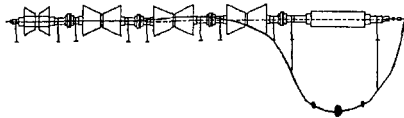


Figure 7 - First Turbine-Generator Mode  
Generator First Mode at 496 RPM

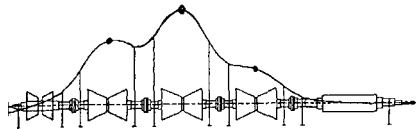
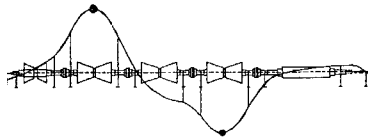
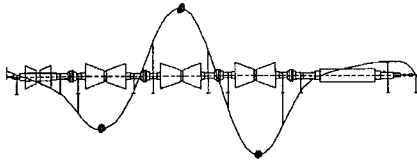


Figure 8 - 2nd Turbine-Generator Mode  
L.P Rotors in Phase at 562 RPM



**Figure 9 - 3rd Turbine-Generator Mode  
LP1 and LP3 out of Phase (569 RPM)**



**Figure 10 - 4th Turbine-Generator Mode - LP2  
out of phase to LP1 and LP3 (585 RPM)**

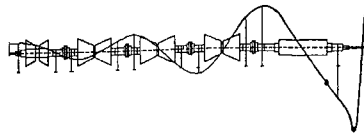


**Figure 11 - 6th Turbine-Generator Mode  
Generator Second Mode (1,037 RPM)**

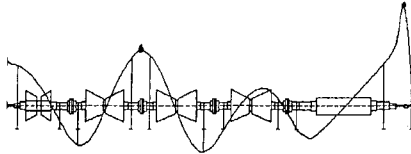


**Figure 12 - 7th Turbine-Generator Mode  
Generator 2nd Mode with LP  
Turbines (1,162 RPM)**

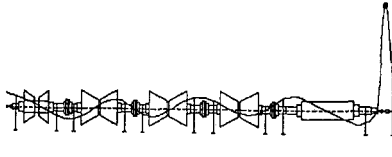


Figure 13 - 9th Turbine-Generator Mode  
Exciter 1st Mode (1,459 RPM)

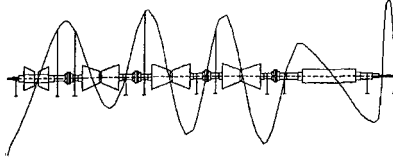


Figure 14 - 10th Turbine-Generator Mode at 1,073 RPM

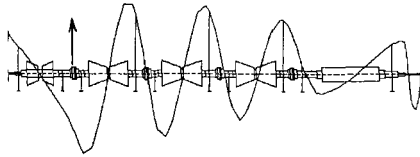


Figure 15 - Turbine-Generator Forced Response Mode  
Shape With Coupling No. 1 Unbalance at 1,800 RPM

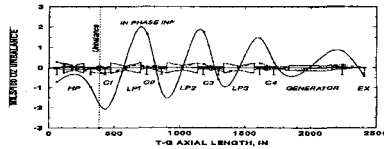


Figure 16 - Theoretical Turbine-Generator Influence  
Coefficients at 1,800 RPM Due to  
Coupling No. 1 Unbalance

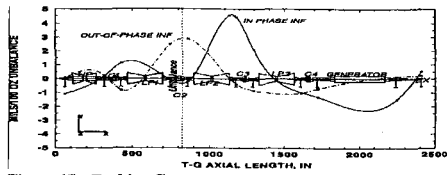


Figure 17 - Turbine-Generator Influence Coefficients at 1,800 RPM Due to Coupling No. 2 Unbalance

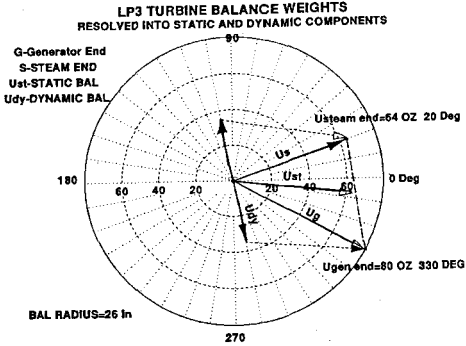


Figure 18 - Resolution of LP3 Turbine Balance Weights into Static and Dynamic Components

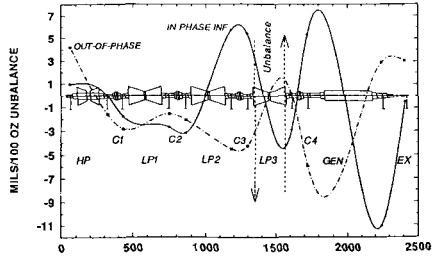


Figure 19 - Turbine-Generator Influence Coefficients at 1,800 RPM Due to LP3 Dynamic Unbalance

## Case Studies

*This page intentionally left blank*

## Case histories of fatigue in compressor gas process pipework

J P GRAHAM

Dynamics and Vibrations, Mitsui Babcock, Renfrew, UK

### ABSTRACT

Case histories of **reciprocating compressors** include problems due to incorrectly sized pulsation dampener bottles and resonance between the compressor and a flexible deck structure. A third example highlights a combination of design faults.

For **centrifugal compressors**, excitation due to rotating stall is examined and the use of high data acquisition techniques to determine the pulsation source is described.

The case histories indicate the compressor cylinder, valves and piping should be regarded as a dynamically coupled system, with the latter being particularly sensitive to problems originating within the compressor.

A methodology for monitoring the health of compressors, based on measurements of pipework pulsations and vibration is recommended. The method is cheap, risk based and is applicable to planned maintenance.

# 1 INTRODUCTION

Offshore gas and oil transport systems are subject to ever increasing pressure and temperature conditions. This has resulted in increased demands on compression units, i.e. high pressure gas injection, with resulting wear, stresses and fatigue on compressors and compressor components. The attached pipework of these units are easily excited and are particularly susceptible to fatigue. The use of Duplex and super Duplex pipework materials have exacerbated the problem.

Mitsui Babcock (MB) have been involved in the investigation and resolution of pipework fatigue problems associated with compressors in the British and Norwegian sectors of the North Sea, on refining plant and ships since 1985.

Typically, an investigation involves the installation of vibration, dynamic stress and pressure pulsation transducers. The signals are fed to a site-installed data acquisition and analysis system, varying between two and sixteen channels depending on the problem complexity. The analysis system has the capability to perform frequency analysis, modal and pulsation analysis, cycle counting and fatigue estimation.

Detailed below are a selection of investigations undertaken by MB.

## 2 CASE HISTORIES

### 2.1 Reciprocating compressors

#### 2.1.1 Incorrectly designed discharge dampener bottles

The discharge pipe work of a gas reciprocating compressor experienced high levels of vibration and several fatigue failures just downstream of the dampener bottle outlet, see Figure 1.

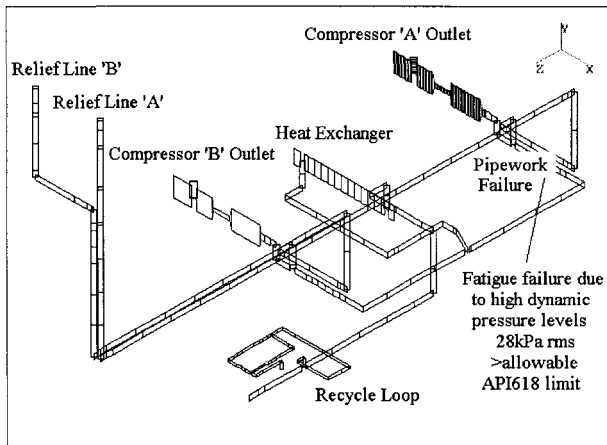


Figure 1 Acoustic model of compressor discharge pipework



Site measurements, using dynamic pressure transducers, established the pressure pulsation levels in the discharge pipework were well in excess of allowable levels as detailed in A.P.I. 618 (1). The high pulsation levels occurred at the compressor running frequency and 1<sup>st</sup> harmonic at 7 and 14 Hertz respectively.

An acoustic model of the pressure pulsation in the pipework was generated using “PULS”, a state-of-the-art pulsation modelling programme. The generated model was validated using the measured dynamic pressure levels. The assessment revealed that the pulsation dampener bottle had been incorrectly designed and in fact was producing pulsation amplifications in the pipework of approximately times two at both the 7 and 14 Hertz frequencies, see Figure 2. These high pulsation levels were driving the pipework, leading to high vibration.

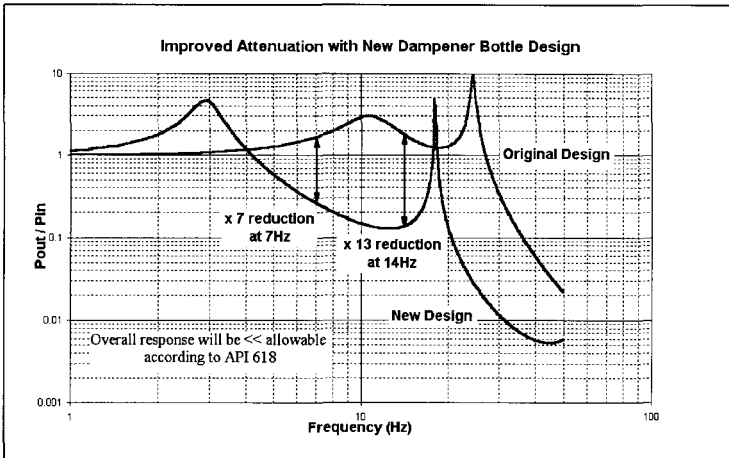


Figure 2 Improved attenuation with new dampener bottle design

The attenuation characteristic of the dampener bottle is determined by the volumes of the two sections of the bottle and the choke length between the volumes. These parameters were optimised to produce an attenuation characteristic resulting in an increased attenuation of times 7 and times 13 at the two dominant frequencies, see Figure 2.

The redesigned bottles were installed on the plant, after which pulsation measurements in the pipework confirmed reductions in line with prediction, see Figure 3. The vibration levels were reduced in proportion and fatigue of these lines was no longer a problem.

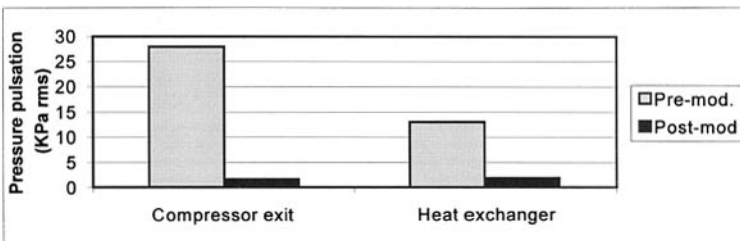


Figure 3 Pipework pressure pulsation pre and post Modification

### 2.1.2 Compressor Deck Resonance

Operation of two closely situated reciprocating compressors resulted in extremely high compressor, pipework and deck vibration. In addition to high gas pipework vibration, lubrication and cooling water pipework, mounted on a skid between the two compressors, repeatedly failed due to fatigue.

Velocity measurements of the deck structure, during operation, revealed extremely high levels of vibration in the region of the ancillary pipework skid at the compressor operating frequency, see Figure 4. This high skid movement in turn fatigued the attached pipework. The vibration of the compressors was an axial rocking motion, indicating very low vertical deck stiffness at the non drive end of the compressor, as indicated in Figure 5 (top right).

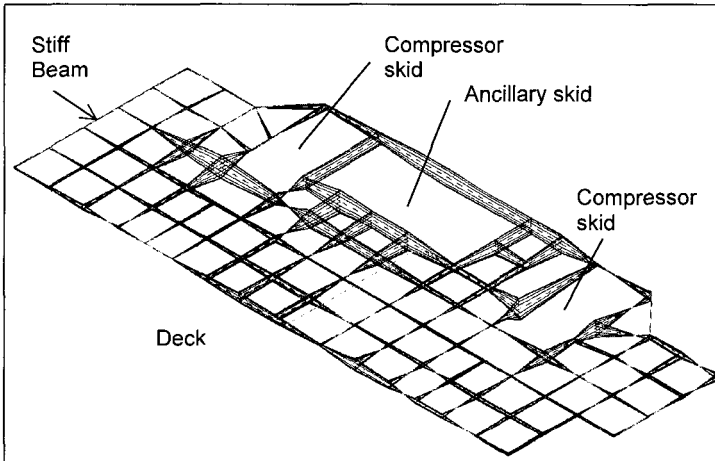


Figure 4 Deck vibrations at compressor running speed

Following the operational measurements, the compressors were shut down and a modal test of the compressor and deck structure carried out. This test comprised exciting the structure with a large hammer (with a force transducer installed in the tip) and measuring the structural responses on the deck and compressor at a large number of locations. The end result was the determination of the structural natural frequencies and corresponding mode shapes (or deflection patterns). This test revealed the 1<sup>st</sup> natural frequency of the compressor/deck system to be at 15 Hertz, see Figure 5 (unmodified) This frequency is coincident with the running frequency of the compressor, hence a resonance condition existed and was the reason for the high vibration levels.

From the modal test, an extremely accurate analytical model of the structure was generated and various modifications to move the structural natural frequency away from the running frequency were analysed.

Two of the modifications examined were as follows:

1. Extending the compressor support skid in the axial direction to encompass support from the very stiff beam, which is indicated in Figure 4. The modification is indicated in

Figure 5(right centre). This had the effect of changing the main structural natural frequency from 15 Hertz to approximately 21 Hertz, with the response at the compressor running frequency reduced by a factor of three, see Figure 5.

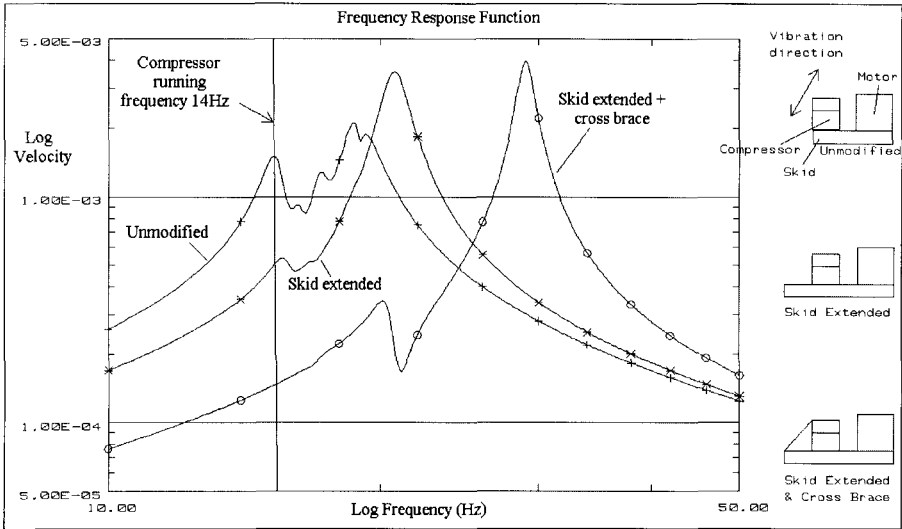


Figure 5 Effects of Modifications on Frequency Response

- Extending the compressor skid in the axial direction and adding a cross brace between the skid and the top of the compressor (see Figure 5, right bottom). This had the effect of moving the main structural natural frequency from 15 to 28 Hertz, with the response at the compressor running frequency reduced by a factor of nine from the original velocity, see Figure 5.

The modifications detailed in 2 above were carried out on the plant, after which the vibration was much reduced and no further problems were encountered during compressor operation.

The problem of foundation resonance is not uncommon if dynamic modelling is not carried out with the compressors attached to the deck.

### 2.1.3 Compressor Vibration on a Liquid Gas Carrying Vessel

The refrigeration system on a liquid gas carrying vessel employed four double acting reciprocating compressors. The liquid gas was stored in three spheres, with each refrigeration system essentially independent of the others. In each system, the vapourised gas was recompressed by one of the compressors, then condensed, expanded and stored in one of the spheres. The fourth compressor (standby) could be connected to any of the three systems by appropriate use of blanking spades and valves. The interconnecting pipework between the standby and the other compressors was, by necessity, complicated and resulted in long pipework runs, see Figure 6 (which details the discharge pipework). The compressors were

two stage, with the suction, interstage and discharge pressures approximately 3, 8 and 19 Bar respectively.

Fatigue failures had repeatedly occurred on the interstage and discharge pipework and vibration on all pipework stages was reported to be extremely high.

An investigation of the vibration problem was conducted on an eight day voyage in the Gulf of Mexico, during which vibration (velocity) and dynamic pressure pulsations in the pipework were recorded using a sixteen channel data acquisition and frequency analysis unit. In parallel, an analytical acoustic (pressure pulsation) model of the system was generated and correlated with the measured results. During turnaround, impact tests to determine natural frequencies of the pipework were carried out.

The main findings of the investigation were as follows:

- Pressure pulsations in the discharge pipework exceeded by a factor of four, the allowable pulsation levels as per A.P.I. 618 (1), at two times the running frequency of 20 Hertz (compressor speed 600 rpm). This frequency is always the most dominant in compressors with double acting cylinders. Pressure pulsations in the interstage pipework were at the allowable level. It should be noted there were no pulsation dampener bottles on any of the compressor stages and that shipping generally is not subjected to the same code requirements as land based and oil platform gas process pipework.
- Vibration and dynamic stress levels greatly exceeded the code values on the interstage and particularly the discharge pipework.
- From the impact test, the discharge pipework had a structural natural frequency very close to 20 Hertz.
- The analytical acoustic model indicated that pipework acoustic modes occurred in the region of 20 Hertz, due to the long pipework lengths associated with connection to the standby compressor ( $f_n = C*n/4L$ ,  $n=1,3,5\dots$ , where  $C$ = Velocity of sound,  $L$ =Pipe length).

The above indicated that to cure the vibration, a) the pressure pulsations had to be reduced, b) the discharge pipework structural natural frequency had to be increased and c) the low frequency acoustic modes had to be removed.

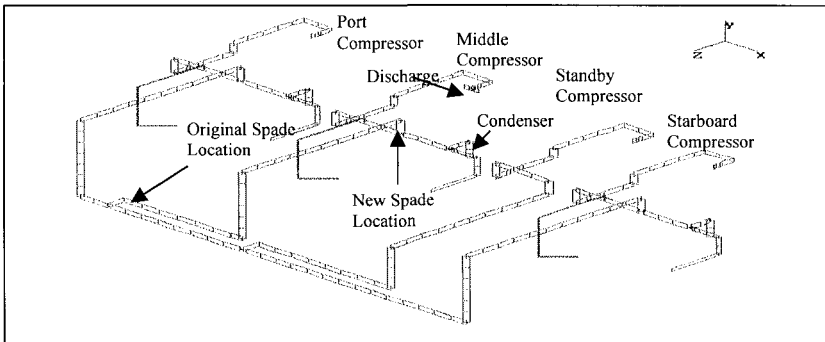


Figure 6 Compressor pipework layout

Pulsation dampener bottles were inserted in the discharge pipework of all four compressors. Orifice plates, that increase the damping in the compressor fluid, were installed in the suction and interstage pipework of the four compressors. These modifications reduced the pulsation in the discharge pipework by a factor of ten to twenty, depending on the operating conditions and reduced the suction and interstage pipework to below allowable levels.

Supports were added at key locations in the discharge pipework to move the problem dynamic structural mode to 10% above the excitation frequency.

The isolating spades were moved from their original locations to the positions indicated in Figure 6. This had the effect of considerably shortening the pipework acoustic lengths and consequently increasing the frequencies of the acoustic modes above the compressor excitation frequency.

The net result of these changes was to reduce the vibration and dynamic stresses within the pipework and machine to safe levels.

The above example indicates the benefits of examining both pulsation and vibration response to determine the most efficient solution.

## 2.2 Centrifugal Compressors

### 2.2.1 Rotating stall

Centrifugal compressors operating at low flow are sometimes subject to the phenomenon of rotating stall. At certain flowrates (see later), some local disturbance stalls one of the blades, the resulting breakdown in flow in the passage restricting the flow through the passage. In consequence the flow is diverted back and will affect the flow of the blade nearest to it so that in turn it stalls and in so doing has the effect of unstalling the initial passage, see Figure 7. In this way the stall cell or blocked passageway is propagated around the blade row and the stall will thus move around the rotor, see Pampreen (2).

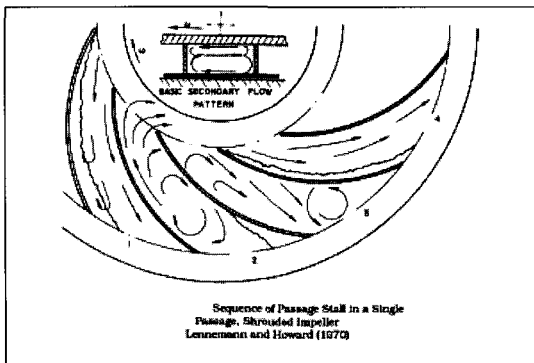


Figure 7 Rotating stall in a single passage

Rotating stall can occur in the impeller or diffuser section of the compressor. The stall pattern is different depending on whether it originates in the impeller or diffuser and whether the impeller is shrouded or unshrouded or the diffuser is vaned or unvaned.

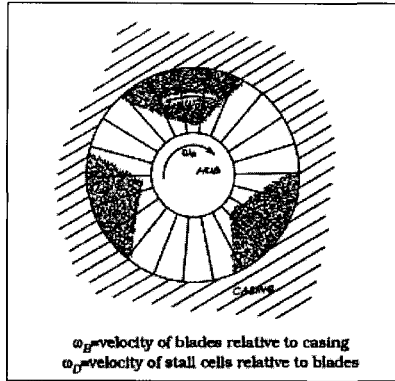


Figure 8 Three cell stall pattern

The rotating stall can be a single cell or cover a number of cells as shown in Figure 8. The stall frequency is always less than the machine frequency and the ratio of the stall frequency to the rotational frequency can point to the location of the stall mechanism, i.e. impeller or diffuser. The last section of a multistage machine is usually the most critical.

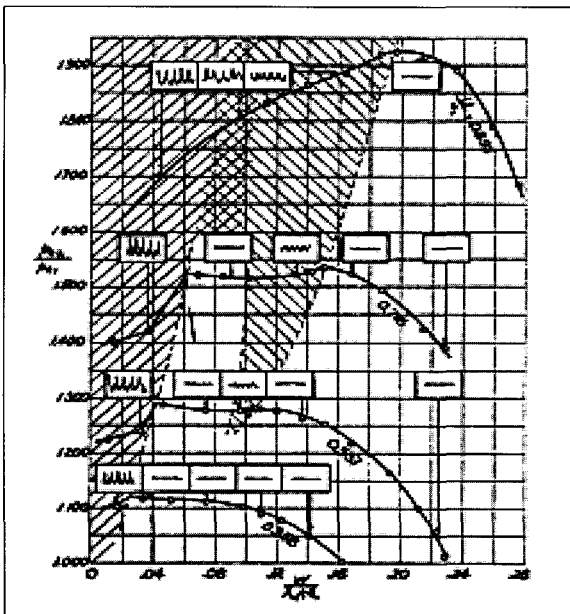


Figure 9 Compressor characteristic map

The performance characteristics of a typical variable speed centrifugal compressor are detailed in Figure 9. (The abscissa is normalised flow, the ordinate is discharge/suction pressure ratio and curves are plotted for four speeds normalised to design speed). Instability

regions (shaded) and pressure pulsation traces are superimposed on the curves. It is notable that pulsation occurs wherever the slope of the pressure ratio characteristic becomes positive. In the stable pulsation regime the slope is negative. In this regime a decrease in flow is accompanied by a rise in pressure, which tends to increase the flow back to its original value, hence producing stability. The opposite occurs with a positive slope resulting in instability and pulsation.

The violent pulsations at the left end of the curves, where there is a steep positive slope, are due to surge, which is very damaging and produces fluctuations through the entire compressor. The lesser pulsations (nevertheless serious) obvious in the two middle speed ratios are due to rotating stall. Rotating stall is therefore a possibility at any region of the compressor characteristic that is flat or slightly positive.

### 2.2.2 Diffuser rotating stall

Repeated fatigue failures occurred on the compressor 2<sup>nd</sup> stage discharge pipework in the gas process module of an offshore platform.

Investigation, utilising vibration, dynamic stress and pressure pulsation measurements, established that under certain operating conditions extremely high dynamic pressure pulsations were generated in the pipework, with consequent increase in vibration levels from 2 mm/sec rms to 140 mm/sec rms and dynamic stresses up to 111 N/mm<sup>2</sup> ptp at welds on the pipework. The dynamic stress corresponding to the fatigue limit for these types of welds was 35 N/mm<sup>2</sup> ptp. Excursions in and out of vibration occurred extremely suddenly, see Figure 10, with failure occurring after very short time periods.

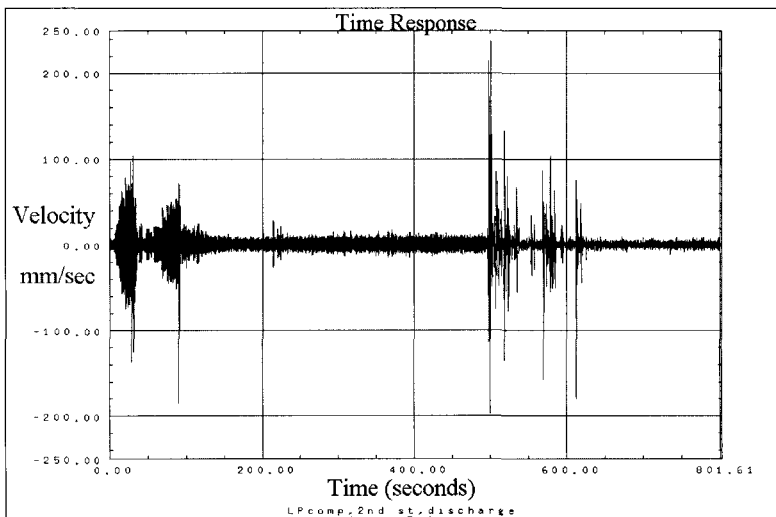


Figure 10 Pipework vibration response

During high vibration, the pressure pulsation levels at 20 Hertz increased by an order of magnitude, with significant increases also observed at 40 and 60 Hertz, see Figure 11. The frequency corresponding to the compressor speed was 139 Hertz, see Figure 12.

Measurements from the compressor monitoring system, on the most sensitive compressor bearing, indicated practically no change in the vibration of the compressor, see Figure 12.

The most likely causes of excitation were either flow induced excitation due to vortex shedding past branch pipework or rotating stall of the compressor. (Rotating stall occurs in a centrifugal compressor when laminar flow in the compressor internals breaks down due to undesirable pressure distribution and low flows).

Acoustic modelling and analysis of the conditions required to produce the excitation mechanisms concluded the cause of the problem was rotating stall in the last stage of the diffuser section. (This mechanism is typified by generation of pulsation frequencies at approximately 10 to 15% of the running frequency). Further confirmation was provided by correlating the flow with pulsation, which revealed high levels only occurred with low flows.

The problem was cured by ensuring the recycle valve remained a minimum of 10% open to prevent compressor flow decrease to the problem value. This cure did not affect platform operation and production.

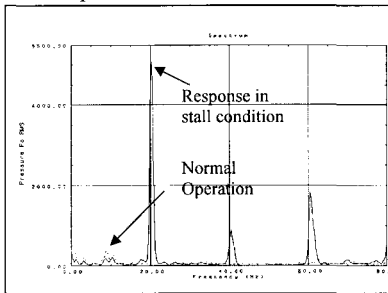


Figure: 11 Pipework Pulsation

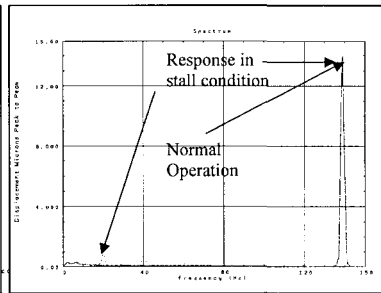


Figure: 12 Compressor Bearing Vibration

It should be noted the pipework (both fluid pulsation and pipe vibration) was extremely sensitive to the fault condition, even though the origin of the fault was in the compressor diffuser and was practically undetectable by the compressor monitoring system.

### 2.2.3 Impeller rotating stall

The discharge pipework (500 Bar) of a gas injection, variable speed, centrifugal compressor experienced unacceptable vibration levels over most of the compressor operating range. Measurement of the pulsation pressure in the discharge pipework established these pressure variations to be greatly in excess of API 618 (1).

There was disagreement between the compressor manufacturers and the pipework designers as to the cause the high pulsations. The compressor manufacturers postulated the high vibration was due to coincidence between the pipework natural frequencies and acoustic standing waves in the pipework at appropriate speed, temperature and pressure conditions. The pipework designers were of the opinion the root of the excitation was within the compressor.



Time history measurements of the compressor pressure pulsation, discharge pipework pressure pulsation and discharge pipework response using conventional data acquisition techniques shed little light on the cause of pulsation.

By installing dynamic pressure transducers in each of the five stages of the compressor and in the discharge pipework and utilising extremely fast data acquisition techniques ( 80,000 samples per second) it was possible to determine the source of the excitation was within the compressor. The first signs of increased pressure pulsation and vibration response in the pipework (top and bottom traces in Figure 13) occurred two milli-seconds after the disturbance initiation in the compressor (middle trace in Figure 13) with the pipework responses taking further time to achieve their maximum value.

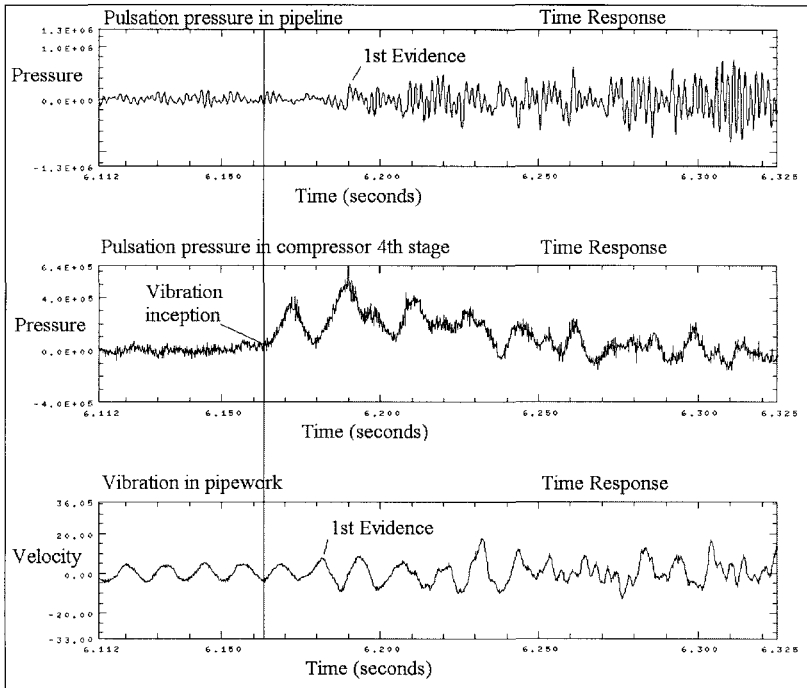


Figure 13 High speed data acquisition of compressor and pipework

Analysis of the high speed time histories revealed the source of the excitation to be in the 4<sup>th</sup> and 5<sup>th</sup> stages of the compressor. Further analysis of the data, including the finding that the main response frequency was in the region 74% of the compressor running speed (at all speed ranges), see Figure 14, confirmed the cause to be rotating stall in the impeller of the last stage. It was also noted stall initiation occurred on a very flat portion of the compressor characteristic curve.

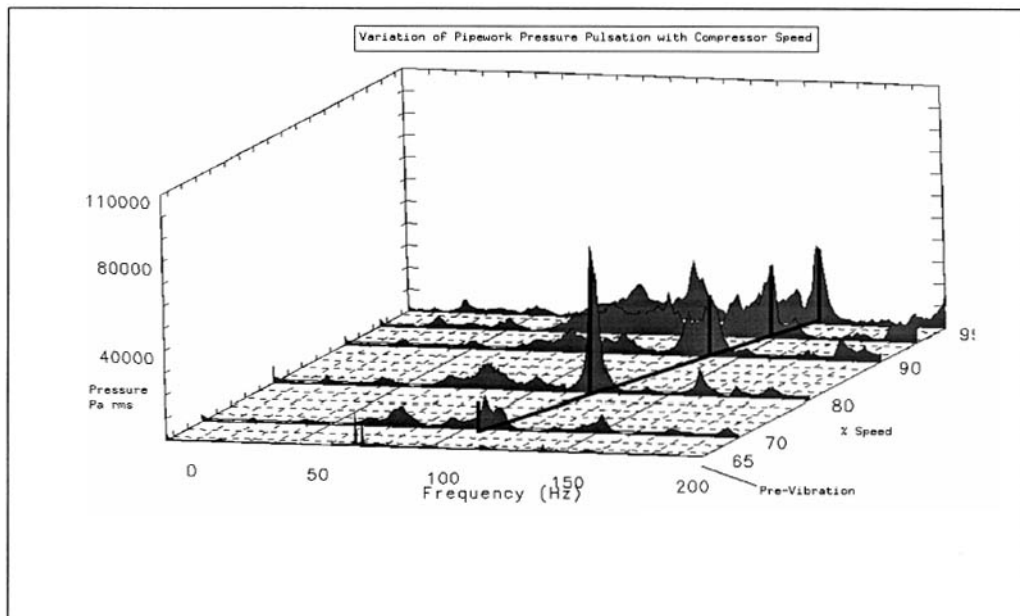


Figure 14 Pressure pulsation spectra for varying compressor speeds

The impeller was redesigned, resulting in an increased operational range free from the excessive vibration.

### 3 DISCUSSION

The above case histories have indicated a range of excitation mechanisms that can induce high vibration and fatigue in pipework systems (e.g. compressor/foundation resonance, incorrectly designed pulsation dampener bottles, impeller rotating stall, diffuser rotating stall). Also, in the majority of cases, it is the pipework that is the most likely to experience fatigue failure and not necessarily the generator of the excitation mechanism (e.g. compressor, pump, etc), which may not exhibit overt signs of malfunction. The suction and discharge pipework, therefore, are extremely sensitive monitors of compressor health. This is because a real compressor system does not behave as though the cylinder, valves and attached piping are non-interactive elements. The compressor cylinder valves and attached piping should be regarded as a dynamically coupled system and analysed as such, Ref (3).

Analysis of pressure pulsation spectra in suction and discharge pipework can determine other common faults in compressor operation. For example, a reciprocating compressor with fluttering valves will produce suction and discharge valve normalised displacements, a P-V diagram and pipework pulsation spectra as detailed in Figure 15. With the valve fluttering cured, the valve displacements and P-V diagram are steadier and the peak levels in the measured pulsation spectra in the pipework have decreased by a factor of three.

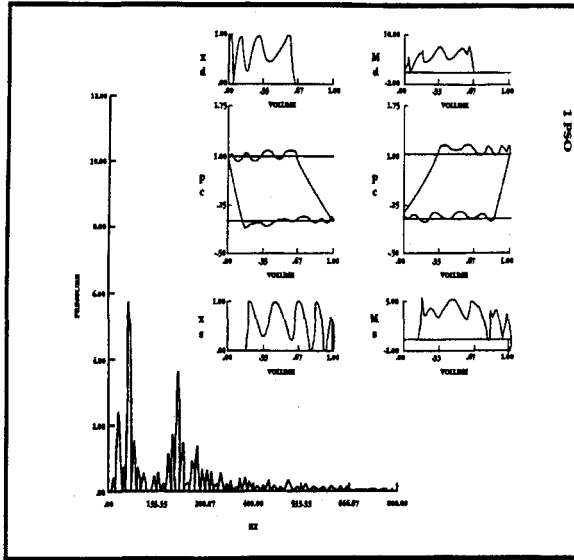


Figure 15 Pipework pulsation spectra for fluttering valves

Pulsation in the suction and discharge pipework can affect timely closures of suction and discharge valves, which will result in valve life reduction and deviation from specified flow through the valves.

All the faults detailed above will result in increased maintenance requirements, increased system pressure drops and loss of compressor performance.

The above measurements are easily obtained using dynamic pressure transducers (inserted into suction and discharge pipelines at a drain connection, instrument connection, etc) and accelerometers connected to a hand held data acquisition and analysis unit. The acquired data can be downloaded to more sophisticated analysis equipment.

The scope of the measurements can easily be extended to include vibration levels on the caps of all suction and discharge valves. The time histories of these measurements, when superimposed on the theoretical P-V diagrams of the corresponding cylinders will confirm correct (or otherwise) valve opening and closing sequences and vibration amplitude will determine valve problems and poorly performing valves. This information could be even more beneficial if a pressure transducer was installed in the relevant compressor cylinder.

Other areas that can be easily accessed and analysed are the compressor crosshead, the manifold bottles, cylinder ends and compressor foundation.

The above data can be collected extremely cheaply compared to many compressor monitoring systems. However, for a high quality assessment and diagnosis of the collected data, it is essential that experienced personnel be utilised. Vibration signatures and pattern recognition identify changes, but diagnosis of these changes is required to determine what faults have occurred and how to correct these faults within a planned maintenance scheme.

With improved data communications, transfer of the collected site data to an analysis centre is relatively straightforward. The analysis of data at one centre allows a database of common faults to be built up and hence increases the speed and accuracy of future assessments.

The envisaged system has been described for off-line monitoring. For critical plant, an on-line system can be installed and automatically transferred to the analysis centre. This option is more expensive but costs can be justified on the financial implications of the machine being out of service.

Based on pipework pulsation, pipework vibration and other easily accessible vibration monitoring locations, a low cost, highly sensitive, risk based monitoring system to increase compressor availability, decrease production losses and allow a planned maintenance strategy can be implemented.

#### 4 CONCLUSIONS AND RECOMMENDATIONS

Several case histories of vibration of compressor systems have been examined, where it has been established:

- The highest pressure pulsations and vibrations occurred in the compressor suction and discharge pipework, although the origins of excitation were within the compressor.
- The compressor monitoring equipment did not necessarily exhibit overt signs of compressor malfunction.

Analysis of suction and discharge pulsation spectra can determine faults within the compressor, i.e. valve malfunctions.

A monitoring system based on pipework pulsation, pipework vibration and other easily accessible vibration monitoring locations, can provide a low cost, highly sensitive, risk based monitoring system to increase compressor availability, decrease production losses and allow a planned maintenance strategy.

An increased diagnosis capability will result with data from all monitored sites fed to a central database, from which patterns relating to common faults can be established.

The monitoring capability is applicable to both on and off-line systems.

#### 5 REFERENCES

1. 'Reciprocating compressors for petroleum, chemical and gas industry services', API standard 618, 1995.
2. 'Compressor Surge and Stall' Pampreen, R C
3. 'Pulsation Control in Machinery and Piping' Southwest Research Institute, 1994.

# Rotor-bearing system design, analysis, and testing for exciter retrofit of a two-pole generator

H C HA, C H PARK, and S P CHOI

Hanjung – Korea Heavy Industries and Construction Co. Limited, Changwon, Korea

## ABSTRACT

This paper describes a case study gained from the retrofit of a generator excitation system, from an old one with an alternator to a new one without an alternator, for a 500 MW two-pole generator. Recently new excitation systems have been widely used for retrofit of existing old excitation systems because of their advantages, such as compactness, efficiency, convenience, and availability. In order to replace an old excitation system with a new one successfully, rotor dynamic characteristics, such as mode shape, critical speed, and unbalance response, were simulated with or without a steady bearing. Furthermore, verification testing of a field test was carried out to confirm the analytical results.

## 1. INTRODUCTION

Generator excitation systems have been used for supplying the field currents to generators. Many years ago most generators required alternators for the excitation system. Such excitation systems were so big, very complex and expensive. Nowadays, a new excitation system which does not require an alternator has been developed due to improved design technology in the generator excitation system. Advantages of the new one are compactness, efficiency, convenience, and availability. Therefore, new excitation systems have been replacing the existing old ones.

The rotor dynamic analysis is the most important item to increase the reliability of rotating machinery [1-5]. The dynamic characteristics of large rotating machinery are heavily dependent not only on the rotor itself, but also on the supporting conditions, such as bearing stiffness and damping, bearing bracket and foundation. In particular, the bearing stiffness and damping coefficients have a large influence on the rotor dynamic characteristics [2,3]. Therefore, in order to replace old excitation systems with new ones successfully, designers should consider carefully the dynamic characteristics of the rotor-bearing system from view points of how to eliminate the existing alternator rotor, whether or not a steady bearing is necessary, and what type of a steady bearing is optimum, etc. A steady bearing is an additional bearing required for supporting the end of collector shaft. The installation of the steady bearing is determined according to the results of rotor dynamic analysis.

This study describes an experience gained from the retrofit of a generator excitation system, from with an alternator to without an alternator, for a 500 MW two-pole generator that runs at

3,600 rpm. Rotor dynamic characteristics, such as mode shape, critical speed, and unbalance response, were simulated with or without a steady bearing, to design an appropriate modified rotating system. Both the bearing stiffness and damping coefficients were calculated. In addition, verification testing by the field test was carried out to confirm the analytical results

## 2. RETROFITS AND DESIGN CRITERIA

Figure 1 shows the existing generator excitation system with an additional generator, an alternator, which is coupled to the end of the generator rotor. In order to change the excitation system from the old one to the new one, first of all, the alternator rotor should be eliminated. The next must be considered how to modify the collector rotor system. Figure 2 shows the schematic view of a modified rotor system with a steady bearing and without a steady bearing. As mentioned above, the installation of the steady bearing is determined according to the results of rotor dynamic analysis since the dynamic characteristics of the rotating system are highly dependent on the bearing stiffness and damping coefficients.

In the present study, three kinds of design criteria were considered to decide the acceptability of the modified collector rotor system both statically and dynamically. The first criterion is based on the static stiffness of collector rotor overhang. If the stiffness is less than the design limit, a steady bearing should be installed at the end of collector rotor. This design limit was established several years ago and was deficient since excessive vibration problems were experienced on the collector rotor designed by this rule. The second criterion is to evaluate the sensitivity of the generator rotor near the resonance of the system. Shirake and Kanki [4] proposed this criterion based on operating experience and theoretical analysis for large turbine generator sets. The variable used to describe resonance sensitivity to unbalance is the Quality factor of resonance or Q-factor. This factor is commonly used to quantify the damping in order to predict the forced response and to evaluate system susceptibility due to forced excitation at a resonance. Thus, the Q-factor is determined based on the shape of the response curve. A highly damped response has a broad peak with low response value and yields a low Q-factor. Resonance with low damping has a sharp peak and yields a high Q-factor. Q-factor is determined at a particular resonance defined as  $Q = f_p / (f_2 - f_1)$ ; where  $f_p$  is the frequency at the resonance,  $f_1$  is the frequency less than  $f_p$  where the amplitude is 0.707 times the amplitude at  $f_p$ , and  $f_2$  is the frequency greater than  $f_p$  where the amplitude is 0.707 times the amplitude at  $f_p$ . Figure 3 shows an example of acceptable design criteria of Q-factor as a function of the ratio of critical speed to operating speed. This criterion indicates that design is acceptable when the Q-factor is below the limit line. The third criterion is that the vibration amplitude evaluated at the operating speed should be less than the limit value. The accurate vibration amplitude can be predicted because of improved rotor dynamics computer programs.

## 3. ANALYSIS AND MEASUREMENTS

There exist two requirements, i.e. theoretical analysis and measurement, for the successful retrofit. Theoretical analysis was performed to make a verification of a design criteria mentioned above. First of all, the shaft stiffness was calculated for the collector rotor overhang, as shown in Fig.2(a). It was found that the shaft stiffness was lower than the limit value so that a steady bearing was required. Rotor dynamic analysis was investigated by FEM

based on Timoshenko beam theory [1]. Figure 4 shows a vibration mode of the generator rotor system without a steady bearing at 3,758 rpm, which is the closest natural frequency to the operating speed (3,600 rpm). It can be seen that there exists a natural frequency near the operating speed and an overhang mode occurs. Figure 5 shows the unbalance response mode at 3,600 rpm. In order to obtain the unbalance response, it is assumed that 1,153 g-cm (1 pound-in) unbalance weight is placed at the end of the collector rotor. It can be seen that an excessive vibration amplitude as large as 1,271  $\mu\text{m}$  peak to peak, which is much larger than the design limit, occurs at the collector end. The Q-factor at 3,758 rpm is about 8.8, which is higher than the design limit. Therefore, it can be concluded that a steady bearing should be installed as shown in Fig.2(b).

In order to select an adequate steady bearing, three bearing types, cylindrical, elliptical, and tilting pad, were considered. It was found that any kind of bearing hardly changed the natural frequency near the operating speed but both the unbalance response and Q-factor were reduced drastically because of the steady bearing. However, both the cylindrical and elliptical bearing give a possibility of oil whirl and/or oil whip occurrence since the actual load acting on the bearing is so small [2,5]. In consequence, a six-pad tilting pad journal bearing was selected as a suitable steady bearing. Figure 6 shows the schematic view of the collector rotor system with a steady bearing, which is finally modified for the retrofit. Figures 7 and 8 show the vibration mode and the unbalance response, respectively. The modified system might be worried that the collector rotor would run near the resonance whose speed is about 3,715 rpm. However, because of the damping effect of the steady bearing, both the expected maximum unbalance response and Q-factor are very small; which are about 11  $\mu\text{m}$  peak to peak at 3,600 rpm and 1.78, respectively. Since these values are much smaller than the design limits, it is assured that this modified rotating system would run successfully during the operation.

Finally, verification testing by a field test was carried out to confirm analytical results. Figure 9 shows the vibration amplitude (peak to peak) measured at the collector end as a function of the rotational speed with or without a steady bearing. As shown in this figure, the vibration amplitude of one without a steady bearing increases sharply with speed and results in impossible operation over 2,500 rpm. On the other hand, the vibration amplitude of one with a steady bearing is very good in the whole range of operation. The measured vibration amplitude at the operating speed is as low as 30  $\mu\text{m}$  peak to peak but is larger than the expected value obtained by analysis. The reason is caused by the uncertainties such as unbalance weight and misalignment, etc. It can be concluded that the test results show good agreement with theoretical results. Consequently, the retrofit of the generator excitation system from with an alternator to without an alternator, for a 500 MW two-pole generator, was achieved successfully. Figure 10 shows a photograph of the newly modified collector rotor system.

#### 4. CONCLUSIONS

This case study was obtained from the successful retrofit experience of a generator excitation system from with an alternator to without an alternator, for a 500 MW two-pole generator. In order to modify and to design the collector rotor system, static and dynamic characteristics, such as shaft stiffness, natural frequency, mode shape, Q-factor, and unbalance response, were simulated by the analysis. Field test results show good agreement with theoretical results.

**REFERENCES**

- (1) Nelson, H. D., 1980, "A Finite Rotating Shaft Element Using Timoshenko Beam Theory", ASME Journal of Mechanical Design, Vol 102, pp.793-803
- (2) Nicholas, J. C. and Kirk, R. G., 1979, "Selection and Design of Tilting Pad and Fixed Lobe Journal Bearings for Optimum Turbo-rotor Dynamics", Proceedings of the 8<sup>th</sup> Turbomachinery Symposium, pp.43-57
- (3) Rao, J. S., 1983, Rotor Dynamics, New Age International Publishers.
- (4) Shiraki, K. and Kanki, H., 1979, "A New Vibration Criteria for High Speed Large Capacity Turbomachinery", Proceedings of the 8<sup>th</sup> Turbomachinery Symposium, pp.59-70.
- (5) Tonnesen, J. and Lund, J.W., 1978, "Some Experiments on Instability of Rotors Supported in Fluid-Film Bearing", ASME Journal of Mechanical Design, Vol 100, pp.147-155.

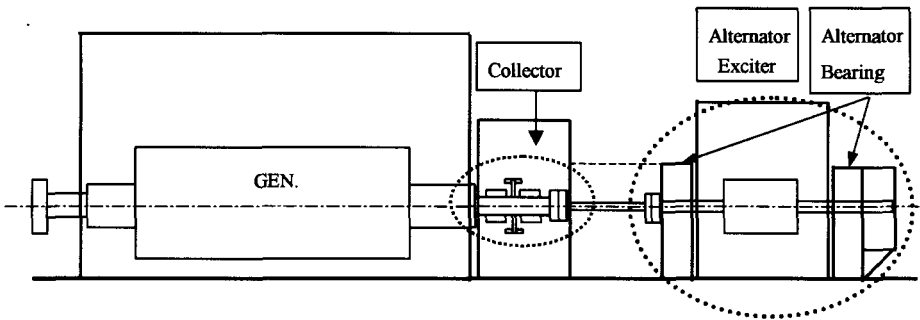


**Fig.1 Schematic view of old generator excitation system with an alternator**

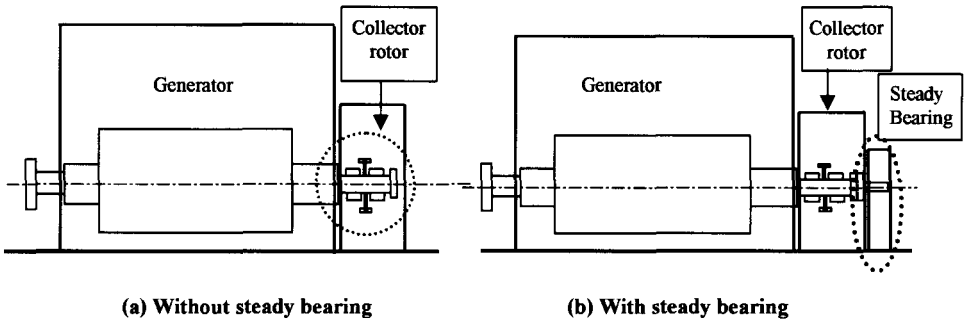


**Fig.2 Schematic view of new generator excitation system without an alternator**



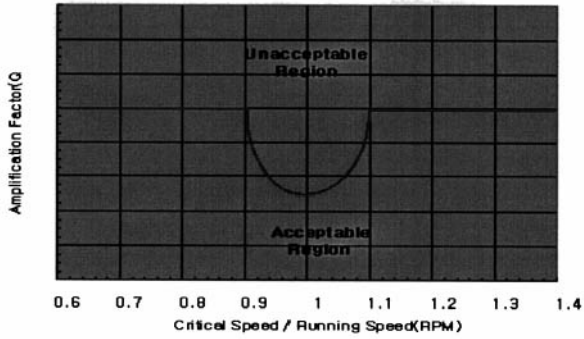


**Fig.3 An example of Q-factor criteria**

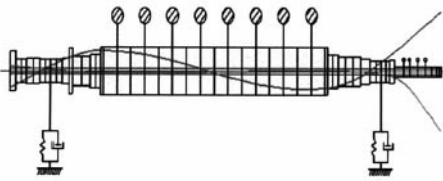


**Fig.4 Mode shape at 3,758 rpm  
(without steady bearing)**

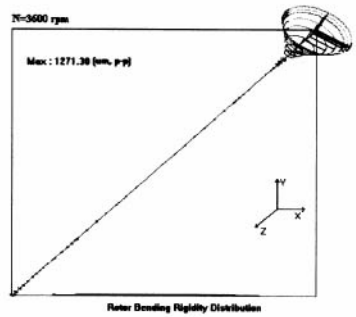


**Fig.5 Unbalance response at 3,600 rpm  
(without steady bearing)**

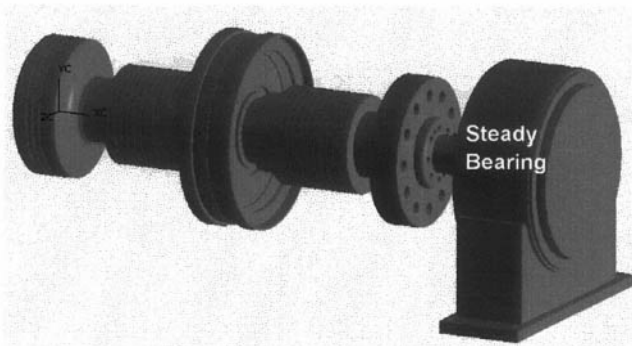


**Fig.6 Schematic view of modified collector rotor system with a steady bearing**

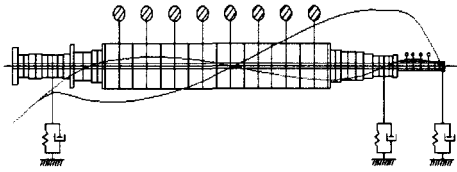


**Fig.7 Mode shape at 3,715 rpm  
(with steady bearing)**

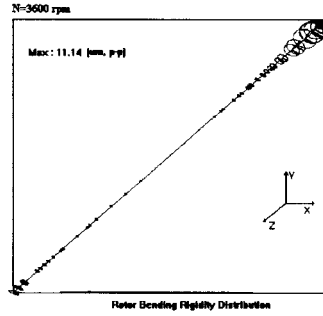


**Fig.8 Unbalance response at 3,600 rpm  
(with steady bearing)**

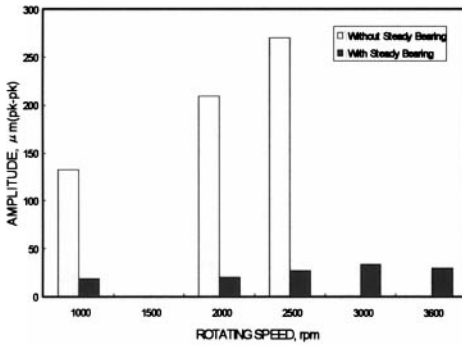


**Fig.9 Comparison of measured vibration amplitude between with and without steady bearing**

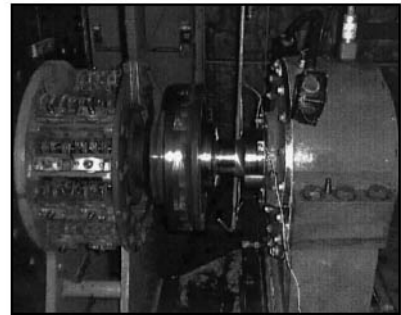


**Fig.10 A photograph of collector rotor system modified successfully**

# The lateral stability analysis of a large centrifugal compressor in propane service at an LNG plant

E A MEMMOTT

Rotor Dynamics Group, Dresser-Rand, Olean, New York, USA

## ABSTRACT

This paper discusses the lateral stability analysis, testing, and field operation of a large centrifugal compressor for propane service in a LNG plant. It has a high ratio of discharge density to inlet density, i.e. high volume reduction, it absorbs a large amount of horsepower, and the bearing span is long. It is a difficult application with five stages of compression and three sidestreams. The bearings are damper style, the breakdown seals are oil-film seals, and the labyrinths are of a pocketed design. A full load test on inert gas and field operation showed that any destabilizing forces are controlled by damper bearings and dampening type pocketed labyrinths with swirl brakes. It is shown that the cross-coupled stiffness in the balance piston labyrinth is not covered by the traditional load related formula for impeller/diffuser cross-coupled stiffness. The usage of this load related formula is discussed and a modification to it is recommended. An analytical approach to rotor dynamic design to achieve satisfactory lateral stability results is outlined.

## 1. ANALYTICAL & EMPIRICAL CONSIDERATIONS

### 1.1 Log Dec & Stiffness & Damping Coefficients

The damped eigenvalue program of Lund [1] is used to calculate the log dec of the first natural frequency of the compressor rotor. The higher the log dec the more likely the effect of unknown destabilizing forces can be minimized. Design changes are usually initiated if the log dec is under some minimum number. Various inputs of stiffness and damping coefficients are used in the damped eigenvalue program to account for destabilizing and stabilizing forces.

The stiffness and damping coefficients of bearings, oil-film seals, and labyrinths are calculated. Tilt pad bearings have negligible cross-coupled stiffness, as long as they are free to move at their pivot. Oil-film seals of the ring type can have high cross-coupled stiffness.

The stiffness and damping coefficients that are calculated for labyrinth seals are applied as an extra bearing station at that labyrinth. Toothed labyrinths may have high cross-coupled stiffness but have little direct damping. Damping type labyrinth seals such as honeycomb seals have been used [2-5]. For extensive references on labyrinth seals see [6].

An empirical estimate of cross-coupled stiffness related to load and impeller/diffuser geometry was given by Wachel [7]. The first natural frequency usually shows up only under load and is more severe as load is increased [2,3,5,7-16]. The sample propane compressor of this paper and results in [5] show that the empirical Wachel type estimate does not account for the destabilizing forces in the balance piston labyrinth nor in the division wall labyrinth.

## 1.2 Stability Threshold

A study of the effects of unknown excitations should be made. The damped eigenvalue program is used to plot the log dec of the first forward natural frequency vs. extra amounts of cross-coupled stiffness at the midspan. The stability threshold is the amount of extra cross-coupled stiffness needed to make the log dec equal zero. If a cross-coupled stiffness at the midspan has not been included in the damped eigenvalue input, then consideration is given to how high a safety factor is needed of the stability threshold over this stiffness. The log dec is calculated at the maximum continuous speed and not at the first peak response speed.

## 1.3 Damper Optimization

Damper bearings are used to provide improved stability. The range of values for the damping of the oil-film between the bearing cage and bearing housing should be considered, just as the range of journal bearing and oil-film seal clearances are considered. A plot of the stability threshold of the compressor vs. damping is beneficial. The damping can usually be optimized and it is typical to find a peak in the stability threshold that is much higher than for the non-damper case. A very high value of damping corresponds to the over-damped or non-damper case. A plot of the log dec vs. damping gives the same answers, but the sensitivity to unknown excitations is not evident, as it is on the plot of the stability threshold vs. damping.

## 1.4 Wachel Type Estimates

The Wachel formula [7] is  $K_{xy} = (\beta \times T) / (D \times h)$ , where  $K_{xy}$  is a cross-coupled stiffness,  $T$  is the torque,  $D$  is the impeller outside diameter, and  $h$  is the smaller of the impeller tip width or the diffuser width. Some have just used the impeller tip width.  $T = 63000 \times \text{HP}/\text{RPM}$  and  $\beta = (\text{MW} / 10) \times (\text{density out} / \text{density in})$ , where  $\text{MW} = \text{molecular weight}$  and  $\text{HP} = \text{horsepower}$ . Applying a large load in a small space increases the destabilizing forces in the compressor.

This compressor and the results discussed in [5] show that the Wachel formula should be applied on an impeller by impeller basis, i.e. that the density ratio at each impeller should be used, and that the smaller of the impeller tip width and the diffuser width should be used. Further, based on the results of [5], it is recommended to use  $\beta = 3 \times (\text{density out} / \text{density in})$  at each stage, i.e. 3 should replace  $\text{MW}/10$  in the Wachel formula. This is especially important and more conservative with lower MW gases such as ammonia syn gas. We will designate this adjusted Wachel number at the impeller as the PACC number, for predicted aerodynamic cross-coupling from the impeller diffuser interaction. The PACC number is  $30/\text{MW}$  times the Wachel number.

### 1.5 Modal Effects

The PACC and Wachel estimates are pure cross-coupled stiffness and a modal sum of the calculated cross-coupled stiffnesses at each impeller station can be made. We will call the modal sum of the PACC numbers the MPACC number. This modal sum can be applied at an extra bearing station at the midspan and the log dec calculated. Another method, which this author recommends, is to over plot the MPACC estimate on the plot of the log dec vs. cross-coupled stiffness at the midspan. The log dec from using the modal sum at the midspan is the same as applying the cross-coupled stiffness for each impeller at the impeller [11,14]. For any Wachel type estimate we will use the modal sum.

## 2. COMPRESSOR DESCRIPTION & HISTORY

In 1998 a large propane compressor, designated an 838B8-5, was full load full pressure tested on inert gas. This is a vertically split compressor with five impellers and three sidestreams. The sidestreams are located in front of the second, third, and fourth impellers. The compressor is driven on the intake end by a gas turbine through a gear and on the discharge end by a variable speed drive motor. The thrust disc is outboard of the journal bearing on the discharge end of the compressor. The train layout is diagrammed in Figure 1 and the compressor cross-section is shown in Figure 2. There are two identical trains with the same propane compressor for this LNG project.

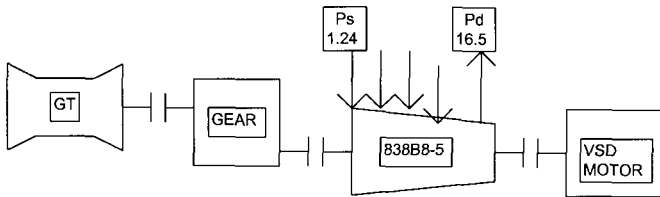


Figure 1 – Train Description

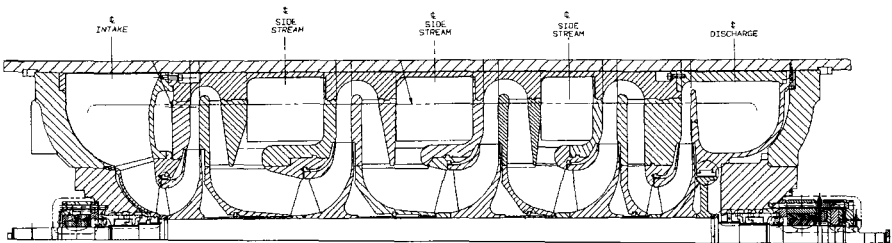
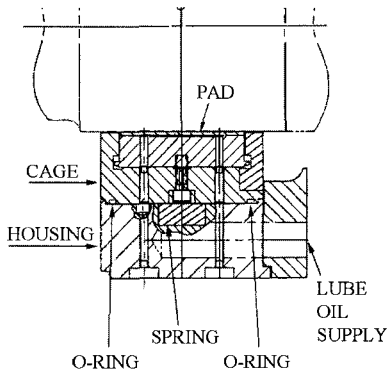


Figure 2 – Compressor Cross-Section

The inlet pressure is 1.24 bar (18 psia), the discharge pressure is 16.5 bar (239 psia), the MW = 44.1, and the compressor absorbs 39800 kW (53400 BHP). The maximum continuous speed is 3622 RPM. The bearing span/impeller bore is 13.70, the flexibility ratio, (the ratio of the maximum continuous speed divided by the first critical speed on rigid bearings), is 2.89, and the average gas density is 17.9 kg/m<sup>3</sup> (1.12 lb/ft<sup>3</sup>). The average gas density is not high, but the bearing span is relatively long and it is running at a high ratio times the first critical speed. As the average gas density rises it is prudent to have lower flexibility ratios [2,4,5,9,13,16]. The same applies for bearing span/impeller bore. This propane compressor has a very high ratio of density out of the compressor over density into the compressor of 11.7. The average density ratio at each impeller is 1.61.

The bearings are 5-shoe load on the pad tilt pad with L/D = length/diameter = .6 and dampers centered by springs. Damper bearings were chosen at the initial design phase before any analysis had been done. The seals are oil-film ring type seals with a sealing pressure of 1.48 bar (21.4 psig), sealed to the first side-stream. The damper bearings are shown in Figure 3 and the oil-film seals are shown in Figure 4.



**Figure 3 – Damper Bearing**

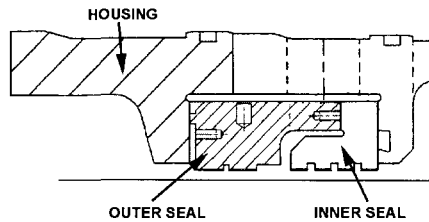


**Figure 4 – Oil-Film Seal**

Initial full load testing at speed indicated a reduction in the level of subsynchronous at the first natural frequency would enhance overall operation. Aerodynamic cross-coupled stiffness at the balance piston labyrinth was identified as the most probable root cause. The standard toothed labyrinth seal at the balance piston, which had no deswirling device, was replaced with a pocketed seal with swirl brakes. Other things were done, but they were believed to be secondary. For example, the impeller eye and interstage toothed labyrinths also were replaced with pocketed labyrinths with swirl brakes. A full load test was conducted and the amplitude of the first natural frequency was within the API617 specification for a mechanical test. The highest subsynchronous amplitude for a scan was 3.8 microns (.15 mils) and the peak hold for four hours at the subsynchronous was 6.4 microns (.25 mils). The effectiveness of the modifications, most importantly the pocketed labyrinth with swirl brakes at the balance piston, was demonstrated and the compressor was accepted for delivery.

The compressor was started in the field in 1999 and has been running well since. For example, Figures 5 and 6, vibration scans taken during normal operation, show 15 to 17 microns at the running speed and not much else. There is a similar compressor in similar service that has been running several years longer and also has been free of any significant levels of subsynchronous vibration. It has the same type damper bearings and is fitted with standard toothed labyrinths. The bearing span of that compressor is 5% shorter than the bearing span of the compressor analyzed in this paper.

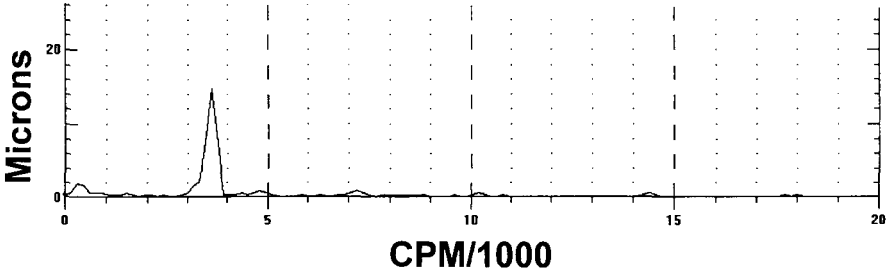


Figure 5 – Drive End Vibration Scan

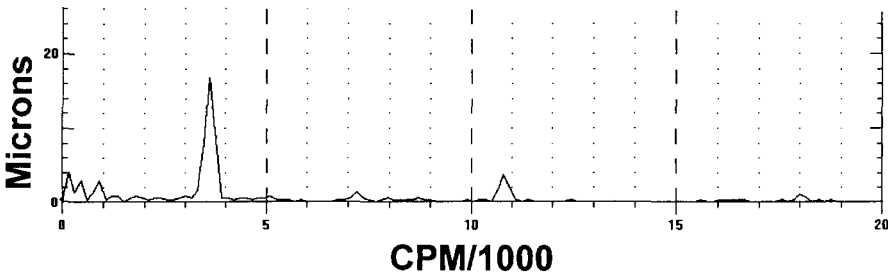


Figure 6 – Non-Drive End Vibration Scan

### 3. COMPRESSOR ROTOR DYNAMIC STABILITY ANALYSIS

#### 3.1 Damper bearing analysis

The damping of the oil-film between the bearing cage and bearing housing was calculated to be in the range  $2.10 \text{ E}+6$  to  $4.73 \text{ E}+6$  N-SEC/M (12,000 to 15,000 LB-SEC/IN). This is determined from the formula for a centered and non-cavitated, or 360 degree, oil-film damper [17]. The formula is  $\text{damping} = \mu \pi R (L/c)^3$ , where  $\mu$  is the viscosity,  $R$  is the radius,  $L$  is the sum of the lengths of the lands on each side of the feed groove, and  $c$  is the radial clearance. The lands have the same length. The damper film was assumed to be non-cavitated at the oil pressure of 1.38 BAR (20 PSIG). Early testing of dampers showed that for normal bearing inlet pressures a non-cavitated film is a good assumption [18,19]. Test experience where the oil pressure has been varied has confirmed this and the same conclusion has been reached from the analysis of another compressor with ring type oil-film seals.

It was assumed that there is no loss of pressure near the o-ring grooves. A full loss of pressure near the o-ring grooves would mean ¼ of this damping. Halfway in-between ¼ damping and full damping is about ½ of the non-cavitated, or the same as cavitated. Half of the damping as above is just about at the optimum damping value, as shown in Figure 8, whereas the full film assumption is to the right of it, so the full film assumption is conservative. The centered damping scales up by the factor  $(1/(1-\epsilon^2))^{1.5}$ , where  $\epsilon$  is the eccentricity ratio of the damper [17]. The eccentricity should be verified before the damper is installed and it should be within established limits. The maximum allowable eccentricity ratio was .29, which would result in an increase of only 14% in damping over the centered condition, nowhere near an overdamped case.

### 3.2 Oil-film ring seal analysis

For this low pressure application the oil-film ring seals have a minor effect on the rotor dynamics. The oil film seals were modeled as non-cavitated bearings with a radial load equal to a friction factor of .1 times the axial end load. The non-cavitated assumption for ring seals is conservative with regard to stability. Non-cavitated or cavitated makes little difference at this low pressure. The radial load used is a small fraction of the journal reaction, an indicator that the seals will not effect the rotor dynamics. There should be some load, otherwise the seal-housing interface might fret or low frequency vibration might occur.

### 3.3 MPACC & various Wachel estimates

TABLE 1 - WACHEL TYPE ESTIMATES

Widths	Last Diff	Each Diff	Each Diff	Each Imp		Each Diff
Density Ratio	Overall	Overall	Individual	Individual		Individual
Wachel (N/M)	5.58 E+7	4.07 E+7	5.66 E+6	3.56 E+6	MPACC	3.84 E+6
Wachel (LB/IN)	318,600	232,500	32,300	20,300	MPACC	21,900

There is an enormous difference between using the overall density ratio or the individual density ratios.  $232,500/32,300 = 7.2$ , which is approximately the overall density ratio divided by the average density ratio =  $11.7/1.61 = 7.3$ . Note that  $11.7^{1/5} = 1.64$  which is just about 1.61 and  $(11.7)^{(1-1/5)} = 7.2$  [5]. An alternative approach is to treat the compressor as four separate compressors, for the four inlets, with about equal horsepower in each, with density ratios of 11.7, 6.9, 4.1, and 2.5. This results in a modal sum of about  $2.57 \text{ E}+7 \text{ N/M}$  (147,000 LB/IN).

### 3.4 Labyrinth analysis

The toothed labyrinths were modeled by the program of Kirk [20], which he verified in a series of papers, which are listed in [21]. Two case studies are given in [2,14], which also verify its use. The pocketed labyrinths were modeled by using the honeycomb seal program of Scharrer & Pelletti [22]. The honeycomb seal program has given good agreement between analysis and the stable behavior seen with honeycomb seals [2,4,5,15]. The toothed labyrinths were not deswirled. The pocketed labyrinths were modeled as deswirled, as the pocket labyrinths were provided with swirl brakes. The teeth/pockets of the toothed/pocketed labyrinths were on the stator.



Effects that should be considered in a labyrinth analysis and design are: 1. Loss of clearance at a labyrinth due to centrifugal growth of the adjacent rotating part. 2. Loss of clearance due to the shrink fit of the adjacent rotating part. 3. Rotor sag – especially for compressors with low first critical speeds – rotor sag may be negated some by case sag – offset the labyrinths top and bottom if the relative sag is large. 4. Change of clearance in the axial direction of the balance piston labyrinth due to pressure effects from one side to the next and centrifugal growth. 5. Change of clearance in the axial direction of the impeller eye labyrinths due to tilt of the impeller eye surface under centrifugal growth. 6. Journal bearing and damper eccentricity. 7. Relative position of labyrinths vs. bearings from fits of parts.

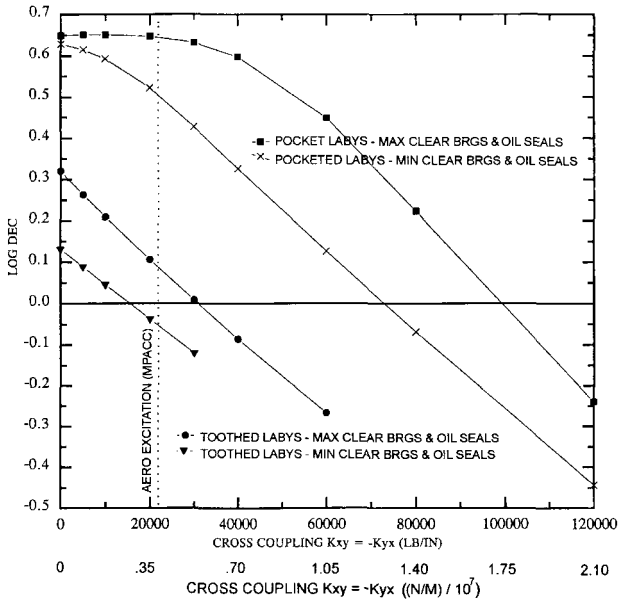
### 3.5 Stability analysis

Stability analyses was made with the inclusion of the coefficients of the balance piston, impeller eye, and interstage labyrinths and the results are described in Figures 7 and 8 and Table 2. Stability calculations were also made with inclusion of just the interstage labyrinths, just the impeller eye labyrinths, and just the balance piston labyrinth. The only labyrinth that was significant was the balance piston labyrinth. Just looking at the various coefficients would have been enough. The eye labyrinths could be significant in a high pressure compressor. Stability analyses showed that the effect of larger clearances on the pocket labyrinths did not produce instability. Two cases were studied, one with the pockets wiped to the root and the other wiped to throwaway with the pockets filled. For each of these it was assumed that the deswirl was lost. The stability was like the no labyrinths assumption.

Figure 7 is a plot of the log dec of the first natural frequency vs. arbitrary added cross-coupled stiffness at the midspan. This is for the maximum value of  $4.73 \text{ E}+6 \text{ N-SEC/M}$  ( $15,000 \text{ LB-SEC/IN}$ ) damping for the damper bearing. Figure 7 shows two cases, one with the standard toothed labyrinths and one with the pocketed labyrinths, and for each of these the effect of minimum and maximum clearance for the journal bearings and oil-film seals. The MPACC number is shown on this plot.

Figure 7 shows that the pocketed labyrinths provide a large stability improvement over that with the toothed labyrinths. With the toothed labyrinths and with the MPACC number instability is likely, as the stability threshold is just below the MPACC number for minimum clearance and just above it for maximum clearance. With the pocketed labyrinths and with the MPACC number stability is predicted, as the stability threshold is well above the MPACC number and the log dec is quite good. The application of the labyrinth stiffness and damping coefficients along with the MPACC number in the stability analysis provides good correlation with the test and field experience.

With either of the Wachel estimates using overall density ratio, or with the estimate from the alternative approach of using four separate but still high density ratios, instability is predicted with the pocketed labyrinths, as the excitation is well above the instability threshold. Yet the compressor is stable. These approaches to the Wachel estimate do not provide good correlation with the test and field experience.



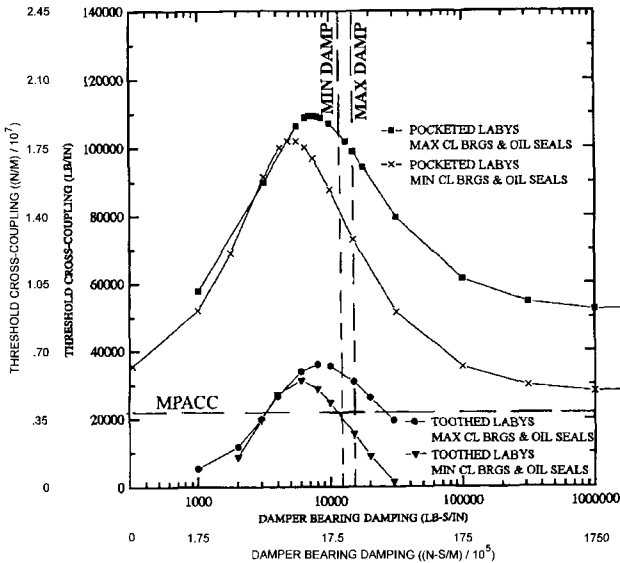
**Fig. 7 – Log Dec vs. Cross-Coupled Stiffness**

Figure 8 is a damper optimization plot. The horizontal axis is the damping of the oil-film between the bearing cage and the bearing housing. The curves on Figure 8 show the stability threshold, the amount of extra added cross-coupled stiffness needed at the midspan to bring about a log dec of zero. For a fixed amount of damping at the damper bearings, if there is more cross-coupled stiffness than on the curve, then the log dec will be negative and, if there is less than what appears on the curve, then the log dec will be positive.

Figure 8 shows that the damper bearings provide a large stability improvement over that with the non-damper bearings and that the pocketed labyrinths provide a large stability improvement over that with the toothed labyrinths. All the way to the right on Figure 8 is the non-damper bearing case. For non-damper bearings, with the toothed labyrinths, and without any added cross-coupling, except from the labyrinths, the compressor would be unstable for minimum clearance, as the stability threshold is negative and thus the log dec is negative. For non-damper bearings, toothed labyrinths, and the MPACC number added it is unstable for maximum clearance. The curves for the pocketed labyrinths in Figure 8 were similar to but better than curves made without the inclusion of labyrinths.

Figure 8 shows that the MPACC number and the Wachel estimates using individual diffuser or impeller widths and individual density ratios, all do a fine job of predicting that the stability with the pocket labyrinths and with the damper bearings would be acceptable and the stability with the toothed labyrinths and with damper bearings (or non-damper bearings) would not be acceptable. The application of the labyrinth stiffness and damping coefficients along with the MPACC number in the stability analysis provides good correlation with the test and field experience.

Figure 8 shows that either of the Wachel estimates using overall density ratio and the Wachel estimate from the alternative approach of using four separate but still high density ratios would say for any value of damping the compressor would be unstable with the pocketed labyrinth. Yet it is stable. These approaches to the Wachel estimate do not provide good correlation with the test and field experience.



**Fig. 8 – Stability Threshold v. Damper Bearing Damping**

The log dec of the first natural frequency for various assumptions about the bearings and labyrinth seals is shown in Table 2. The log dec with the damper bearings is calculated with the maximum damping of  $4.73 \text{ E}+6 \text{ N-SEC/M}$  ( $15,000 \text{ LB-SEC/IN}$ ) for the damper. The log dec with the MPACC number is calculated with this amount at the midspan.

Table 2 shows that the damper bearings provide a large stability improvement over that with the non-damper bearings and that the pocketed labyrinths provide a large stability improvement over that with the toothed labyrinths. The oil-film seals are not a big influence in this case, nor is the bearing clearance. It is very important to have the damper bearings, otherwise the log dec will be very low and instability is very possible. Without the inclusion of the labyrinth coefficients stability would be predicted with the damper bearings. But, with the toothed balance piston labyrinth and with the damper bearings the log dec is  $-.05$  to  $.09$  with the MPACC number. The MPACC number is needed, as without it and with the toothed labyrinths and with the damper bearings the log dec is positive. Stability is predicted with the pocketed labyrinth balance piston and with the dampers, and this is what happened.

A study was also made of the effect of changing to tilt pad oil film seals, which can have a big effect in high pressure compressors [2,4,8,10,12-16]. For these low pressure oil-film seals,

which could carry only a negligible amount of load, the effect on stability was small to change to tilt pad seals, so this was not done. Analysis of other propane and propylene compressors with large volume reductions showed that the density ratio of each impeller should be used in the MPACC estimate and not the overall density ratio.

TABLE 2 - LOG DEC

		Non-damper bearings		With damper bearings		Log dec Diff. Damp. – Non-damp.	
	Brg Clear.	W/O MPACC	WITH MPACC	W/O MPACC	WITH MPACC	W/O MPACC	WITH MPACC
No labyrinths	Min	.07	-.05	.49	.36	.42	.41
No oil seals	Max	.05	.01	.44	.41	.39	.40
No labyrinths	Min	.08	-.09	.48	.35	.40	.44
With oil seals	Max	.11	.04	.50	.49	.39	.45
With tooth labys	Min	-.13	-.30	.13	-.05	.26	.25
With oil seals	Max	.00	-.17	.32	.09	.32	.26
With pocket labys	Min	.20	.04	.63	.50	.43	.46
With oil seals	Max	.24	.17	.65	.64	.41	.47
Log dec Diff.							
Pocketed - toothed	Min	.33	.34	.50	.55		
	Max	.24	.34	.33	.55		

### 3. CONCLUSIONS

A large compressor in a high horsepower application is running successfully as predicted using the analytical techniques outlined in this paper. The effects of division walls and balance pistons should be included in the rotor dynamics modeling of compressors of even moderate densities. A dampening type pocketed labyrinth with swirl brakes at the balance piston appears to provide resistance to subsynchronous vibration. Further analysis and testing in a rig of the pocketed labyrinth is in process. The MPACC or Wachel estimate does not include the effects of division walls or balance pistons. The density ratio of each impeller should be used in the MPACC or Wachel estimate and not the overall density ratio. With consideration for division wall or balance piston effects and usage of the MPACC estimate surprises can be avoided at test and in the field. By appropriate analysis damper bearings and dampening type labyrinth seals can be selected early in the configuration of the machine and they are a sound engineered solution. An analytical approach to rotor dynamic design to achieve satisfactory lateral stability results has been outlined.

### 4. ACKNOWLEDGEMENTS

The author would like to acknowledge the wisdom and patience of Jim Southworth, the project manager for D-R of the LNG project, and the help received from Aubrey Nugara of KBR and Patrice Bardon of D-R, both of whom demanded the best of us. A special thanks goes to Del Hart, my first supervisor at Dresser-Clark, for guiding my development as an

engineer. Krish Ramesh of D-R has done an excellent job of automating the modeling of the labyrinth seals and the calculations of the labyrinth stiffness and damping coefficients. Ed Turner of D-R went to the site and obtained the field data. The author would like to thank Jim Shufelt for inserting the figures for publication.

## REFERENCES

- [1] Lund, J. W., 1974, "Stability and Damped Critical Speeds of a Flexible Rotor in Fluid-Film Bearings," *Trans. ASME, Journal of Engineering for Industry*, pp. 509-517, May.
- [2] Memmott, E. A., 1994, "Stability of a High Pressure Centrifugal Compressor Through Application of Shunt Holes and a Honeycomb Labyrinth," *CMVA, Proceedings of the 13th Machinery Dynamics Seminar*, pp. 211-233, Toronto, Sept. 12-13.
- [3] Gelin, A., Pugnet, J-M., Bolusset, D, and Friez, P., 1996, "Experience in Full Load Testing Natural Gas Centrifugal Compressors for Rotordynamics Improvements," *IGT & A C&E, Birmingham, UK, 96-GT-378*.
- [4] Memmott, E. A., 1998, "Stability Analysis and Testing of a Train of Centrifugal Compressors for High Pressure Gas Injection," *ASME Turbo Expo '98, ASME Paper 98-GT-378, Stockholm, June 2-5, Journal of Engineering for Gas Turbines and Power, July 1999, Vol. 121, pp. 509-514*.
- [5] Memmott, E. A., 2000, "Empirical Estimation of a Load Related Cross-Coupled Stiffness and The Lateral Stability Of Centrifugal Compressors," *CMVA, Proceedings of the 18th Machinery Dynamics Seminar*, pp. 9-20, Halifax, Apr. 26-28
- [6] Childs, D., 1993, *Turbomachinery Rotordynamics - Phenomena, Modeling, & Analysis*, New York, John Wiley and Sons, Inc., pages 227-354.
- [7] Wachel, J. C. and von Nimitz, W. W., 1981, "Ensuring the Reliability of Offshore Gas Compressor Systems," *Journal of Petroleum Technology*, pp. 2252-2260, Nov.
- [8] Coletti, N. J. and Crane, M. E., Jr., 1981, "Centrifugal Compression on the Arun High Pressure Injection Project," *Proceedings of the IMechE Conference on Fluid Machinery for the Oil, Petrochemical and Related Industries*, The Hague, Netherlands, pp. 63-70, March.
- [9] Fulton, J. W., 1984, "The Decision to Full Load Test a High Pressure Centrifugal Compressor in its Module Prior to Tow-Out," *IMEchE, 2nd European Congress on Fluid Machinery for the Oil, Petrochemical and Related Industries*, The Hague, The Netherlands, pp. 133-138, March.
- [10] Shemeld, D. E., 1986, "A History of Development in Rotordynamics - A Manufacturer's Perspective," *Rotordynamic Instability Problems in High Performance Turbomachinery*, NASA Conference Publication 2443, Texas A&M University, pp. 1-18, June 2-4.

- [11] Memmott, E. A., 1987, "Damper Bearings and Stability of a CO<sub>2</sub> Compressor," *Seventh Annual Rotating Machinery & Controls Industrial Research Conference*, San Diego, June
- [12] Memmott, E. A., 1990, "Tilt Pad Seal and Damper Bearing Applications to High Speed and High Density Centrifugal Compressors," IFToMM, *Proceedings of the 3rd International Conference on Rotordynamics*, Lyon, pp. 585-590, Sept. 10-12.
- [13] Memmott, E. A., 1992, "Stability of Centrifugal Compressors by Applications of Tilt Pad Seals, Damper Bearings, and Shunt Holes," IMechE, *5th International Conference on Vibrations in Rotating Machinery*, Bath, pp. 99-106, Sept. 7-10.
- [14] Marshall, D. F., Hustak, J. F., and Memmott, E. A., 1993, "Elimination of Subsynchronous Vibration Problems in a Centrifugal Compressor by the Application of Damper Bearings, Tilting Pad Seals, and Shunt Holes," NJIT-ASME-HI-STLE, *Rotating Machinery Conference and Exposition*, Somerset, New Jersey, Nov. 10-12.
- [15] Kuzdzal, M. J., Hustak, J. F., and Sorokes, J. M., 1994, "Identification and Resolution of Aerodynamically Induced Subsynchronous Vibration During Hydrocarbon Testing of a 34,000 HP Centrifugal Compressor," IFToMM, *Proceedings of the 4th International Conference on Rotordynamics*, Chicago, Sept. 7-9.
- [16] Memmott, E. A., 1996, "Stability of an Offshore Natural Gas Centrifugal Compressor," CMVA, *Proceedings of the 15th Machinery Dynamics Seminar*, pp. 11-20, Banff, Oct. 7-9.
- [17] Gunter, E J, Jr., Barrett, L. E., Allaire, P. E., 1975, "Design and Application of Squeeze Film Dampers for Turbomachinery Stabilization," *Proceedings of the Fourth Turbomachinery Symposium*, Turbomachinery Laboratory, Department of Mechanical Engineering, Texas A&M University, College Station, Texas, pp.31-45, Oct.
- [18] Tonnesen, J., 1976, "Experimental Parametric Study of a Squeeze Film Bearing," *Transactions of the ASME, Journal of Lubrication Technology*, pp. 206-213, April
- [19] Sharma, R. K. and Botman, M., 1978, "An Experimental Study of the Steady-State Response of Oil-Film Dampers," *Transactions of the ASME, Journal of Mechanical Design*, Vol. 100, pp. 216-221, April
- [20] Kirk, R. G., 1990, "Users Manual for the Program DYNPC28 - A Program for the Analysis of Labyrinth Seals," Negavib Research & Consulting Group, Virginia Tech, Blacksburg, VA, Jan.
- [21] Kirk, R. G., 1990, "A Method for Calculating Labyrinth Seal Inlet Swirl Inlet Velocity," *Trans. ASME, Journal of Vibration and Acoustics*, pp. 380-383, July.
- [22] Scharrer, J. K. and Pelletti, J. M., 1994-1995, "DCELL<sup>TM</sup> - A Computer Program for: Calculating Steady-State and Dynamic Characteristics of Honeycomb Annular Seals," *Rotordynamics-Seal-Research*, North Highlands, CA

## Surface Influences

*This page intentionally left blank*



# Dynamic characteristics of liquid annular seals with groove and hole pattern surface roughness

E STORTEIG and M F WHITE

Department of Marine Engineering, Norwegian University of Science and Technology, Trondheim, Norway

## ABSTRACT

In centrifugal pumps the rotordynamic coefficients of annular seals are important for predicting pump dynamic behaviour. Seal dynamics is greatly affected by the relationship between fluid flow and wall friction. Recently, friction factors have been published which relate the turbulent fluid flow in the seal to wall friction for seals with rectangular grooves and hole patterns. Based on these friction factors extensions were made to a theory for predicting dynamic characteristics of plain seals to deal with grooved and hole-patterned seals or a combination of both. The method does not require calibration with experimental data in order to give useful results. A parameter study indicated that for certain stator hole patterns the cross-coupled stiffness could be greatly reduced compared to that of a smooth seal. This means that self excited vibrations from the seal may be prevented, and the range of stable operation of the pump may be increased. Another extension of the theory accounts for angular stiffness, damping, and added mass moment of inertia for tapered seals.

## NOMENCLATURE

$a_1, b_2, b_3$	Moody friction factor constants: $a_1 = 1.375 \cdot 10^{-3}$ , $b_2 = 20000$ , and $b_3 = 10^6$
$a_{2r,s}, a_3$	Constants: $a_{2r,s} = b_2 e_{r,s} / (2\bar{C}_r)$ , $a_3 = b_3 / Re_z$
$b, d_{hr,s}$	Velocity ratio and hole diameter for hole pattern surfaces, $b = \frac{\omega R}{W}$
$\bar{C}_r, C_{in}, C_{ex}$	Average, inlet, and exit seal clearance
$e_{gr,s}, e_{hr,s}, e_{r,s}$	Groove depths, hole depths, and absolute machining roughness respectively
$f_{\theta gr,s}, f_{\theta r,s}$	Tangential friction factor for grooves and land/groove combination
$f_{z gr,s}, f_{z r,s}$	Axial friction factor for grooves and land/groove combination
$f_{hr,s}, f_{lr,s}$	Friction factor for hole portion, land portion of the seal surface
$F_{X,Y}, M_{X,Y}$	Reaction forces and moments on the rotor in the axial direction
$H, h$	Local clearance (excludes roughness depth) $H = (\bar{C}_r + \frac{\alpha L}{2}) - \alpha Z$ , $h = \frac{H}{\bar{C}_r}$
$H^*, h^*$	Film thickness including grooves, $H^* = H + H^+$ , $h^* = \frac{H^*}{\bar{C}_r}$
$H^+, h^+$	Total added film thickness for grooves, $H^+ = H_s^+ + H_r^+$ , $h^+ = \frac{H^+}{\bar{C}_r}$
$H_{r,s}^+, h_{r,s}^+$	Added film thicknesses for grooves $H_{r,s}^+ = \frac{e_{gr,s} L_{gr,s}}{L_{lr,s} + L_{gr,s}}$ , $h_{r,s}^+ = \frac{H_{r,s}^+}{\bar{C}_r}$
$K, C, M$	Direct translational stiffness, damping, and added mass respectively
$k, c, m$	Cross-coupled translational stiffness, damping, and added mass respectively
$K_{e\alpha}, C_{e\alpha}, M_{e\alpha}$	Rotational to translational stiffness, damping, and added mass
$k_{e\alpha}, c_{e\alpha}, m_{e\alpha}$	Rotational to translational stiffness, damping, and added mass
$K_{\alpha e}, C_{\alpha e}, M_{\alpha e}$	Translational to rotational stiffness, damping, and added mass moment of inertia
$k_{\alpha e}, c_{\alpha e}, m_{\alpha e}$	Translational to rotational stiffness, damping, and added mass moment of inertia
$L, L_{gr,s}, L_{lr,s}$	Seal length, groove width, and land width

$\bar{L}_{lr,s}, L_{in}, L_{ex}$	Average, inlet, and exit land width, $\bar{L}_{lr,s} = \frac{L_{in,r,s} + (N_{gr,s} - 1)L_{lr,s} + L_{ex,r,s}}{N_{gr,s}}$
$N_{gr,s}$	Number of grooves on rotor and/or stator
$U, W, u, w$	Tangential and axial bulk flow velocity, $u = \frac{U}{\omega R_r}, w = \frac{W}{\bar{W}}$
$U_r, u_r$	Bulk flow velocity relative to rotor, $U_r^2 = W^2 + (U - R\omega)^2, u_r^2 = 1 + b^2(u - 1)^2$
$U_s, u_s$	Bulk flow velocity relative to stator, $U_s^2 = W^2 + U^2, u_s^2 = 1 + b^2u^2$
$u_\infty, u_{\infty r,s}$	Fully developed bulk flows: tangential, relative to rotor and stator
$\bar{W}$	Average axial bulk flow velocity, $\bar{W} = \frac{\dot{Q}}{2\pi R C_r}$
$P, p$	Pressure and non-dimensional pressure, $p = \frac{P}{\rho \bar{W}^2}$
$P_s, P_e, p_s, p_e$	Inlet and exit chamber pressure, $p_s = \frac{P_s}{\rho \bar{W}^2}, p_e = \frac{P_e}{\rho \bar{W}^2}$
$Q, q$	Volumetric flow rate and non-dimensional seal taper angle, $q = \frac{\alpha L}{2C_r}$
$R_O, R_r, s$	Rotor orbit radius and rotor radii at rotor and stator land surfaces, $R_r \approx R_s = R$
$Re_z, Re_{r,s}$	Axial and relative rotor/stator Reynolds numbers, $Re_z = \frac{2\rho \bar{W} C_r}{\mu}, Re_{r,s} = \frac{2\rho U_{r,s} C}{\mu}$
$T, t, \tau$	Transition time through the seal, time and dimensionless time, $T = L/W, \tau = t/T$
$Z, Z_p, z, z_p$	Axial position and axial pivot position, $z = Z/L$ and $z_p = Z_p/L$
$\alpha, \alpha_X, \alpha_Y$	Seal taper angle and amplitude of angular perturbation about X- and Y-axes
$\chi_{\theta r,s}, \chi_{zlr,s}$	Land portion of grooved surfaces used for the tangential and axial friction factor
$\chi_{gr,s}, \chi_{hr,s}$	Relative portions of seals surfaces covered by grooves, holes
$F, \gamma_{r,s}$	Dimensionless whirl frequency, fraction of surface area covered by holes
$\mu, \rho, \Omega$	Dynamic viscosity, density, and angular speed of rotor orbital motion
$\tau_{zr,s}$	Axial wall shear stress for rotor and stator, $\tau_{zr,s} = f_{zr,s} \rho \frac{U_{r,s} W}{2}$
$\tau_{\theta r,s}$	Tangential wall shear stress, $\tau_{\theta s} = f_{\theta s} \rho \frac{U_s U}{2}, \tau_{\theta r} = f_{\theta r} \rho \frac{U_r (U - \omega R)}{2}$
$\theta, \xi, \xi_e$	Angular coordinate, viscous entrance and exit loss
$s, r, l, g, 0, 1$	Indices for rotor, stator, land, and groove variables, zeroth-, and first order variables

## 1 INTRODUCTION

Important aspects in the design of centrifugal pumps are efficiency, dynamic stability, and compactness. For given requirements of mass flow rate and pressure for a centrifugal pump it is often desirable to keep the dimensions of the pump as small as possible. To achieve this, the industry is trying to design pumps running at increased rotational speeds.

In this search for higher power density it is essential to quantify the forces acting on the rotor and housing during operation and to predict the rotor's dynamic behaviour. Previous studies have shown that the force on the rotor rotating around its own axis at a rotational speed,  $\omega$ , and at the same time precessing at a speed,  $\Omega$ , about the seal axis at a radius,  $R_O$ , (see Fig. 1) can be expressed as a quadratic function of the whirling speed,  $\Omega$ . The equation relating rotor reaction force and motion [2] can be given as

$$\begin{aligned}
 - \begin{Bmatrix} F_X \\ F_Y \\ M_Y \\ M_X \end{Bmatrix} &= \begin{bmatrix} K & k & K_{\epsilon\alpha} & -k_{\epsilon\alpha} \\ -k & K & -k_{\epsilon\alpha} & -K_{\epsilon\alpha} \\ K_{\alpha\epsilon} & k_{\alpha\epsilon} & K_\alpha & -k_\alpha \\ k_{\alpha\epsilon} & -K_{\epsilon\alpha} & k_\alpha & K_\alpha \end{bmatrix} \begin{Bmatrix} X \\ Y \\ \alpha_Y \\ \alpha_X \end{Bmatrix} \\
 + \begin{bmatrix} C & c & C_{\epsilon\alpha} & -c_{\epsilon\alpha} \\ -c & C & -c_{\epsilon\alpha} & -C_{\epsilon\alpha} \\ C_{\alpha\epsilon} & c_{\alpha\epsilon} & C_\alpha & -c_\alpha \\ c_{\alpha\epsilon} & -C_{\epsilon\alpha} & c_\alpha & C_\alpha \end{bmatrix} \begin{Bmatrix} \dot{X} \\ \dot{Y} \\ \dot{\alpha}_Y \\ \dot{\alpha}_X \end{Bmatrix} + \begin{bmatrix} M & m & M_{\epsilon\alpha} & -m_{\epsilon\alpha} \\ -m & M & -m_{\epsilon\alpha} & -M_{\epsilon\alpha} \\ M_{\alpha\epsilon} & m_{\alpha\epsilon} & M_\alpha & -m_\alpha \\ m_{\alpha\epsilon} & -M_{\epsilon\alpha} & m_\alpha & M_\alpha \end{bmatrix} \begin{Bmatrix} \ddot{X} \\ \ddot{Y} \\ \ddot{\alpha}_Y \\ \ddot{\alpha}_X \end{Bmatrix} \quad (1)
 \end{aligned}$$

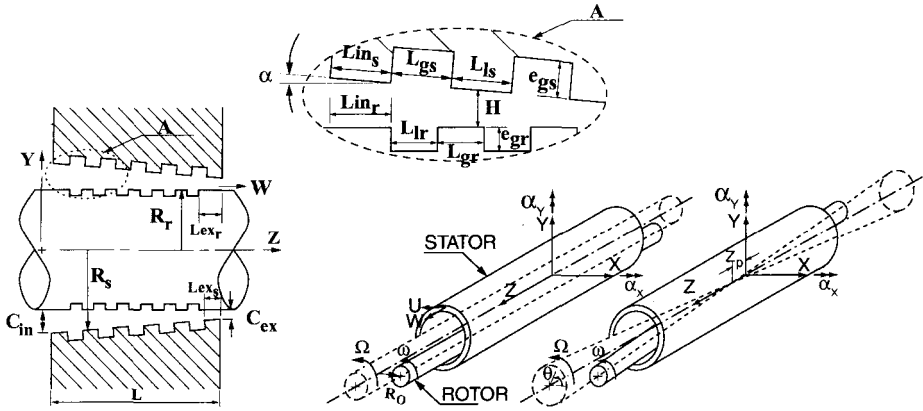


Figure 1: Left: Description of groove, rotor, and stator geometry. Right: Rotor orbits for perturbation analysis

## 2 BULK FLOW THEORY

In this paper a bulk flow theory and perturbation analysis are used to derive the rotordynamic coefficients in Eq. 1 from the seal pressure field. From Fig. 2 one can derive the continuity and momentum equations as used by [6], which includes the terms  $H^+ = H_s^+ + H_r^+$  and  $H^* = H + H^+$  (see Fig. 2) to take into account circumferential flow in the grooves. For hole pattern seals  $H^+ = 0$  and  $H^* = H$  as in the formulation by [2]. Note that in the current formulation, friction factors are related to the local land clearance,  $H$ , so  $H^+$  and  $H^*$  only appear in the first order solution of the equations below. By assuming an incompressible fluid and using the free body diagram of Fig. 2 continuity and momentum equations can be written as in [6]

$$\frac{\partial H}{\partial t} + \frac{1}{R} \frac{\partial (HU)}{\partial \theta} + \frac{\partial (HW)}{\partial Z} + \frac{H^+}{R} \frac{\partial U}{\partial \theta} = 0 \quad (2)$$

$$-H \frac{\partial P}{\partial Z} - (\tau_{zr} + \tau_{zs}) = \rho H \left[ \frac{\partial W}{\partial t} + \frac{U}{R} \frac{\partial W}{\partial \theta} + W \frac{\partial W}{\partial Z} \right] - \rho W \frac{H^+}{R} \frac{\partial U}{\partial \theta} \quad (3)$$

$$- \frac{H^*}{R} \frac{\partial P}{\partial \theta} - (\tau_{\theta r} + \tau_{\theta s}) = \rho H^* \left[ \frac{\partial U}{\partial t} + \frac{U}{R} \frac{\partial U}{\partial \theta} + W \frac{\partial U}{\partial Z} \right] - \rho W H^+ \frac{\partial U}{\partial Z} \quad (4)$$

Substituting shear stress expressions into the momentum equations and converting the continuity and momentum equations into non-dimensional form gives

$$-h \frac{\partial p}{\partial z} = \frac{w}{2} u_s f_{zs} \left( \frac{L}{C_r} \right) + \frac{w}{2} u_r f_{zr} \left( \frac{L}{C_r} \right) + h \left[ \frac{\partial w}{\partial \tau} + b \left( \frac{L}{R} \right) u \frac{\partial w}{\partial \theta} + w \frac{\partial w}{\partial z} \right] - h^+ b \left( \frac{L}{R} \right) w \frac{\partial u}{\partial \theta} \quad (5)$$

$$- \frac{h^*}{b} \frac{L}{R} \frac{\partial p}{\partial \theta} = \frac{u}{2} u_s f_{\theta s} \left( \frac{L}{C_r} \right) + \frac{(u-1)}{2} u_r f_{\theta r} \left( \frac{L}{C_r} \right) + h^* \left[ \frac{\partial u}{\partial \tau} + b \left( \frac{L}{R} \right) u \frac{\partial u}{\partial \theta} + w \frac{\partial u}{\partial z} \right] - h^+ w \frac{\partial u}{\partial z} \quad (6)$$

$$\frac{\partial h}{\partial \tau} + \left( b \frac{L}{R} \right) \left( \frac{\partial (hu)}{\partial \theta} + \frac{\partial (h^+u)}{\partial \theta} \right) + \frac{\partial (hw)}{\partial z} = 0 \quad (7)$$

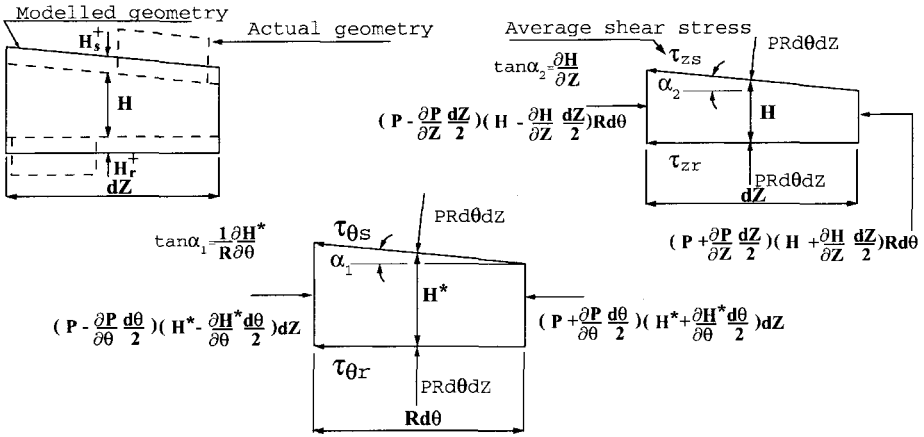


Figure 2: Forces acting on control volume. The shear stresses are averaged over the groove and land portion.

Throughout this article an index for the variable ending with 1 means first order perturbed value for the variable, while 0 means zeroth order solution for the variable. By introducing the zeroth and first order variables,  $h = h_0 + h_1$ ,  $u = u_0 + u_1$ ,  $p = p_0 + p_1$ , and  $w = w_0 + w_1$  and doing several manipulations the zeroth order equations may be written

$$h_0 w_0 = 1 \quad (8)$$

$$\frac{dp_0}{dz} = -\frac{1}{2h_0^2} (u_{s0}\sigma_{zs0} + u_{r0}\sigma_{zr0}) + \left[ \frac{1}{h_0^3} \frac{dh_0}{dz} \right] \quad (9)$$

$$\frac{du_0}{dz} = -\frac{1}{2} [u_0 u_{s0} \sigma_{\theta s0} + (u_0 - 1) u_{r0} \sigma_{\theta r0}] \quad (10)$$

where  $\sigma_{zs0} = f_{zs0} \left( \frac{L}{C_r} \right)$ ,  $\sigma_{\theta s0} = f_{\theta s0} \left( \frac{L}{C_r} \right)$ ,  $\sigma_{zr0} = f_{zr0} \left( \frac{L}{C_r} \right)$ , and  $\sigma_{\theta r0} = f_{\theta r0} \left( \frac{L}{C_r} \right)$ . The first order equations are given as

$$b \frac{L}{R} h_0^* \frac{\partial u_1}{\partial \theta} + \frac{\partial (h_0 w_1)}{\partial z} + \frac{\partial h_1}{\partial \tau} + \omega T u_0 \frac{\partial h_1}{\partial \theta} + w_0 \frac{\partial h_1}{\partial z} - \frac{h_1}{h_0^2} \frac{\partial h_0}{\partial z} = 0 \quad (11)$$

$$\frac{\partial p_1}{\partial z} + A_{2z} u_1 + A_{3z} w_1 + \left[ \frac{\partial w_1}{\partial \tau} + b \left( \frac{L}{R} \right) u_0 \frac{\partial w_1}{\partial \theta} + w_0 \frac{\partial w_1}{\partial z} \right] = A_{1z} h_1 + \frac{h^+}{h_0^2} b \left( \frac{L}{R} \right) \frac{\partial u_1}{\partial \theta} \quad (12)$$

$$\frac{L}{R} b \left( \frac{\partial p_1}{\partial \theta} \right) + A_{2\theta} u_1 + A_{3\theta} w_1 + \left[ \frac{\partial u_1}{\partial \tau} + b \left( \frac{L}{R} \right) u_0 \frac{\partial u_1}{\partial \theta} + \frac{1}{h_0^*} \frac{\partial u_1}{\partial z} \right] = A_{1\theta} h_1 \quad (13)$$

The expressions for  $A_{1\theta}$ ,  $A_{2\theta}$ ,  $A_{3\theta}$ ,  $A_{1z}$ ,  $A_{2z}$ ,  $A_{3z}$  are given in Appendix A. They contain the friction factors which are functions of the zeroth order solution. The format of the above equations is similar to that of [6] apart from the term  $\frac{\partial (h_0 w_1)}{\partial z}$  in Eq. 11, which is due to the angular whirling motion used for moment coefficients.

The clearance function for lateral and angular perturbations is given by Eq. 14 and the perturbed

land film thickness is given by Eq. 15

$$h = h_0 - [x + \alpha_y(z - z_p)] \cos\theta - [y - \alpha_x(z - z_p)] \sin\theta \quad (14)$$

$$h_1 = -[x(\tau) + \alpha_y(\tau)(z - z_p)] \cos\theta - [y(\tau) - \alpha_x(\tau)(z - z_p)] \sin\theta \quad (15)$$

where the dimensionless perturbation angles are  $\alpha_y = \alpha_Y \left(\frac{L}{C_r}\right)$ ,  $\alpha_x = \alpha_X \left(\frac{L}{C_r}\right)$ .  $z_p$  is the dimensionless axial coordinate of the pivot point, and  $\theta$  is the angular position around the rotor circumference. Assume a circular orbit and circular angular perturbation so that  $x_{max} = y_{max} = r_O$ , and  $\alpha_{x_{max}} = \alpha_{y_{max}} = \alpha_O$ . To simplify the derivation of the solvable ordinary differential equations, the perturbed film thickness is the real part of  $h_1$  where  $h_1 = -h_{1O}e^{j(\Omega T\tau - \theta)}$ ,  $h_{1O} = r_O + \alpha_O(z - z_p)$ , and  $r_O = \frac{h_{1O}}{C_r}$ . The assumed complex solutions are  $u_1 = \bar{u}_1 e^{j(\Omega T\tau - \theta)}$ ,  $w_1 = \bar{w}_1 e^{j(\Omega T\tau - \theta)}$ , and  $p_1 = \bar{p}_1 e^{j(\Omega T\tau - \theta)}$ .  $u_1$ ,  $w_1$ ,  $p_1$  are the complex first order tangential- and axial velocities and pressure relative to the stationary x, y, z coordinate system, and  $\bar{u}_1$ ,  $\bar{w}_1$ ,  $\bar{p}_1$  are the complex solutions relative to the rotating frame of reference. Note that the time,  $T$ , is the time it takes for a fluid particle to pass through the seal,  $\Omega$  is the frequency of orbital motion, which is a fraction,  $F$ , of the rotational speed,  $\omega$ , and hence  $T = \frac{L}{W}$ ,  $\Omega = F\omega$ , and  $\Omega \neq \frac{1}{T}$ .

By substituting the expression for the perturbed film thickness and the assumed form of the solution the complex equations to be solved are

$$\frac{d}{dz} \begin{Bmatrix} \bar{w}_1 \\ \bar{u}_1 \\ \bar{p}_1 \end{Bmatrix} + [A(z)] \begin{Bmatrix} \bar{w}_1 \\ \bar{u}_1 \\ \bar{p}_1 \end{Bmatrix} = r_O \begin{Bmatrix} g_1 \\ g_2 \\ g_3 \end{Bmatrix} + \alpha_O \begin{Bmatrix} g_4 \\ g_5 \\ g_6 \end{Bmatrix} \quad (16)$$

$$[A(z)] = \begin{bmatrix} \frac{1}{h_0} \frac{\partial h_0}{\partial z} & -j\omega T \frac{h_0^*}{h_0} & 0 \\ h_0^* A_{3\theta} & h_0^* (A_{2\theta} + j\Gamma T) & -jh_0^* \frac{1}{b} \left(\frac{L}{R}\right) \\ A_{3z} - \frac{1}{h_0^2} \frac{\partial h_0}{\partial z} + j\Gamma T & A_{2z} + j\frac{\omega T}{h_0^2} (h_0 + 2h^+) & 0 \end{bmatrix} \quad (17)$$

$$\begin{Bmatrix} g_1 \\ g_2 \\ g_3 \end{Bmatrix} = \begin{Bmatrix} \frac{1}{h_0} j\Gamma T - \frac{1}{h_0^3} \frac{\partial h_0}{\partial z} \\ -h_0^* A_{1\theta} \\ -\left(A_{1z} - \frac{1}{h_0^4} \frac{\partial h_0}{\partial z} + \frac{1}{h_0^2} j\Gamma T\right) \end{Bmatrix} \quad (18)$$

$$\begin{Bmatrix} g_4 \\ g_5 \\ g_6 \end{Bmatrix} = \begin{Bmatrix} \left(\frac{1}{h_0} j\Gamma T - \frac{1}{h_0^3} \frac{\partial h_0}{\partial z}\right) (z - z_p) + \frac{1}{h_0^2} \\ -h_0^* A_{1\theta} (z - z_p) \\ -\frac{1}{h_0^2} - \frac{1}{h_0^2} j\Gamma T (z - z_p) + \frac{1}{h_0^4} \frac{\partial h_0}{\partial z} (z - z_p) - A_{1z} (z - z_p) \end{Bmatrix} \quad (19)$$

where  $\Gamma = \Omega - u_0(z)\omega$ . The additional terms in this development compared to the combined previous work of [2] and [6] are found in  $g_4, g_5, g_6$  since the seal taper is included for the moment coefficients. For a seal with no taper  $h_0 = 1$  and the terms containing  $\frac{\partial h_0}{\partial z}$  vanish.

Unknowns for zeroth order equations are  $p_0(z)$ ,  $u_0(z)$ , and  $w_0(z)$ . Two boundary conditions can be derived from the Bernoulli equation and by assuming an inlet and outlet viscous pressure loss. The dimensional form of the boundary conditions is given in Eq. 20, the non-dimensional zeroth order form in Eq. 21, and the first order form in Eq. 22.

$$P_s - P(0, \theta, t) = \frac{\rho}{2} (1 + \xi) W^2(0, \theta, t) \text{ and } P(L, \theta, t) + \frac{\rho}{2} (1 + \xi_e) W^2(L, \theta, t) = P_e \quad (20)$$

$$p_s - p(0) = \frac{1}{2} (1 + \xi) w_0^2(0) \text{ and } p(1) - p_e = -\frac{1}{2} (1 + \xi_e) w_0^2(1) \quad (21)$$

$$\bar{p}_1(0) = -(1 + \xi)\bar{w}_1(0)/h_0(0), \bar{p}_1(1) = -(1 - \xi_e)\bar{w}_1(1)/h_0(1), \text{ and } \bar{u}_1(0) = 0 \quad (22)$$

The ordinary differential equation 8 was solved by a fourth order Runge Kutta method (see for example [7]), and a similar solution procedure was chosen for the complex equation 16. Since the boundary conditions are specified at both inlet and outlet, a linear shooting procedure was used. From the first order solution the forces acting on the rotor are derived in the same manner as in [2]. The rotor was perturbed in the radial and angular directions (see Fig. 1) and a least square fit of the data was performed to solve for the 24 coefficients. Five frequency ratios,  $f = \frac{\Omega}{\omega} = 0, 0.5, 1.0, 1.5, 2.0$  were used. Moment coefficients are calculated similarly based on the procedure by [1].

### 3 RESULTS

In [8] comparisons have been made between the results based on the theory presented in this article and experimental results. Since the comparisons made show that the theory is useful for predicting seal leakage and rotordynamic coefficients, the results in this article focus on how rotordynamic coefficients are affected by groove and hole pattern surfaces.

#### 3.1 Grooved seals

The focus for the parameter study is to see how different groove depths and widths will change the dynamic characteristics of an industrial seal. Hence, the minimum clearance of the seal, pressure difference, and fluid properties are kept constant throughout. The ratio between the groove width,  $L_{gs}$ , and average land width,  $\bar{L}_{ls}$ , is equal to 2.0 for all stators. For maximum leakage reduction the friction factor in Eq. 33 indicates that the land zone should approach zero, but this was an impractical choice due to wear considerations for the seal studied. The rotor is kept smooth for all cases analysed. Common seal parameters for the groove and hole pattern seal study are given as follows:  $\rho = 1000 \text{ kg/m}^3$ ,  $C_{in} = C_{ex} = 0.15 \text{ mm}$ ,  $\mu = 10^{-3} \text{ Pa} \cdot \text{s}$ ,  $e_s = e_r = 0.0$ ,  $u(0) = 0.5$ ,  $R = 72 \text{ mm}$ ,  $\xi = 0.25$ ,  $L = 56 \text{ mm}$ ,  $\xi_e = 1.0$ ,  $\omega = 15000 \text{ rpm}$ ,  $\Delta P = 10 \text{ MPa}$ ,  $z_p = 0.5$ , and  $h^+ = 1$ . For a seal with groove width to depth ratio,  $\frac{L_{gs}}{e_{gs}} = 6$  and groove depth to hydraulic diameter ratio,  $\frac{e_{gs}}{2C} = 1.067$  (near optimal groove geometry for leakage reduction [8]) the following coefficients were calculated:

$K = 5.541 \cdot 10^6 [\text{N/m}]$ ,  $k = 9.352 \cdot 10^7 [\text{N/m}]$ ,  $C = 1.115 \cdot 10^5 [\text{Ns/m}]$ ,  $c = 35404 [\text{Ns/m}]$ ,  $M = 25.23 [\text{kg}]$ ,  $m = -5.831 [\text{kg}]$ ,  $K_{\alpha\epsilon} = -272192 [\text{N}]$ ,  $k_{\alpha\epsilon} = -178720 [\text{N}]$ ,  $C_{\alpha\epsilon} = -222.1 [\text{Ns}]$ ,  $c_{\alpha\epsilon} = 25.83 [\text{Ns}]$ ,  $M_{\alpha\epsilon} = -1.644 \cdot 10^{-2} [\text{Ns}^2]$ ,  $m_{\alpha\epsilon} = 1.378 \cdot 10^{-2} [\text{Ns}^2]$ ,  $K_{\epsilon\alpha} = 5604247 [\text{N}]$ ,  $k_{\epsilon\alpha} = 921246 [\text{N}]$ ,  $C_{\epsilon\alpha} = 1556 [\text{Ns}]$ ,  $c_{\epsilon\alpha} = -142.9 [\text{Ns}]$ ,  $M_{\epsilon\alpha} = -0.1174 [\text{Ns}^2]$ ,  $m_{\epsilon\alpha} = 0.1042 [\text{Ns}^2]$ ,  $K_\alpha = -6281 [\text{Nm}]$ ,  $k_\alpha = 9719 [\text{Nm}]$ ,  $C_\alpha = 8.779 [\text{Nms}]$ ,  $c_\alpha = 1.707 [\text{Nms}]$ ,  $M_\alpha = 1.428 \cdot 10^{-3} [\text{Nms}^2]$ , and  $m_\alpha = -2.278 \cdot 10^{-4} [\text{Nms}^2]$ .

The translational coefficients  $K$ ,  $k$ , and  $C$  that vary most with groove geometry and the whirl frequency ratios are shown in Figures 3 and 4. The axial friction factor for the grooves (excluding the land portion) is independent of Reynolds number for fully turbulent flow, and identical to the hole friction factor in Fig. 6 when  $\frac{e_{gs}}{2C} = \frac{e_{hs}}{2C}$  and  $\frac{L_{gs}}{e_{gs}} = \frac{L_{hs}}{e_{hs}}$ . Leakage, based on average groove/land friction for the grooved seal is very similar to that of Fig. 6.

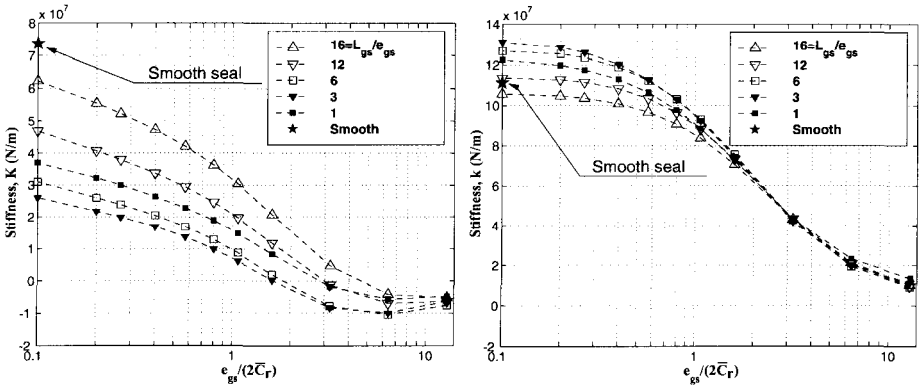


Figure 3: Grooved seal parameter study. Left figure: Direct stiffness. Right figure: Cross-coupled stiffness.

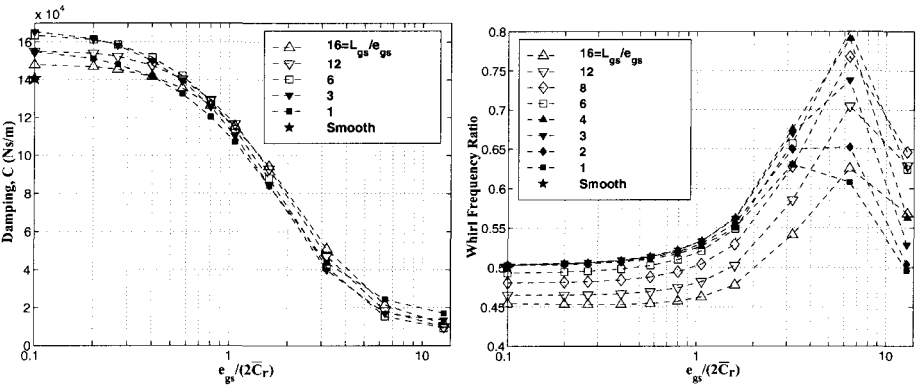


Figure 4: Grooved seal parameter study. Left figure: Direct damping. Right figure: Whirl frequency ratio.

### 3.2 Hole pattern seals

In this section the grooves of the seal are replaced by hole patterns where the hole diameter,  $d_{hs}$ , is two times the equivalent land length,  $\bar{L}_{ls}$ . Also the non-dimensional added film thickness,  $h^+ = 0$ .

For a seal with hole diameter to depth ratio,  $\frac{d_{hs}}{e_{hs}} = 6$  and groove depth to hydraulic diameter ratio,  $\frac{e_{hs}}{2C} = 1.067$  the following coefficients were calculated:

$K = 4.171 \cdot 10^7$ [N/m],  $k = -5.805 \cdot 10^7$ [N/m],  $C = 1.616 \cdot 10^5$ [Ns/m],  $c = 34433$ [Ns/m],  $M = 25.74$ [kg],  $m = -0.8909$ [kg],  $K_{\alpha\epsilon} = -416368$ [N],  $k_{\alpha\epsilon} = 51373$ [N],  $C_{\alpha\epsilon} = -344.9$ [Ns],  $c_{\alpha\epsilon} = 61.21$ [Ns],  $M_{\alpha\epsilon} = -3.331 \cdot 10^{-3}$ [Ns<sup>2</sup>],  $m_{\alpha\epsilon} = -2.859 \cdot 10^{-3}$ [Ns<sup>2</sup>],  $K_{\epsilon\alpha} = 8842105$ [N],  $k_{\epsilon\alpha} = 245919$ [N],  $C_{\epsilon\alpha} = 985.2$ [Ns],  $c_{\epsilon\alpha} = -147.8$ [Ns],  $M_{\epsilon\alpha} = -2.133 \cdot 10^{-2}$ [Ns<sup>2</sup>],  $m_{\epsilon\alpha} = 1.483 \cdot 10^{-2}$ [Ns<sup>2</sup>],  $K_{\alpha} = -8816$ [Nm],  $k_{\alpha} = 4907$ [Nm],  $C_{\alpha} = 10.61$ [Nms],  $c_{\alpha} = 1.268$ [Nms],  $M_{\alpha} = 1.334 \cdot 10^{-3}$ [Nm<sup>2</sup>], and  $m_{\alpha} = -1.002 \cdot 10^{-4}$ [Nm<sup>2</sup>].

Figures 5 and 6 show some of the key results that vary over the range of hole patterns studied.

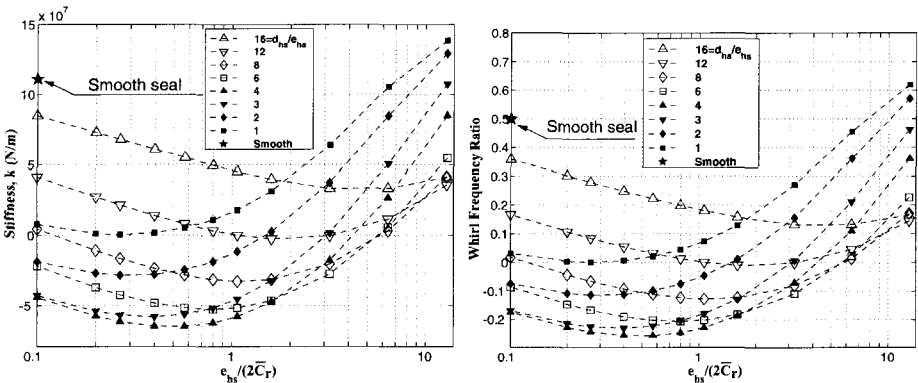


Figure 5: Parameter study of hole pattern seal. Left figure: Cross-coupled stiffness. Right figure: Whirl frequency ratio.

### 3.3 Discussion of results

For deep grooves there are substantial changes for several dynamic coefficients. The great reduction in direct stiffness,  $K$ , and direct damping,  $C$ , with increasing groove depth is supported by the experiment of [5]. The main reason for this reduction is the circumferential flow in the grooves ( $h^+ = 1$ ). However, the reduction in leakage also contributes to this effect. The reduction in stiffness may significantly reduce the first natural frequency of the system and the loss in direct damping may increase vibration levels. For groove depths of the same order of magnitude as the clearance or significantly smaller than the clearance, the loss in stiffness and damping are less dramatic, and it is more likely to find a solution with a compromise between leakage and dynamic characteristics. At an inlet swirl of 0.5 the cross-coupled stiffness is reduced at a slightly slower rate than direct damping as the groove depth to clearance ratio is increased. This means that the whirl frequency ratio (WFR) increases. One would have to decrease swirl at the inlet to reduce the WFR significantly as shown in [5].



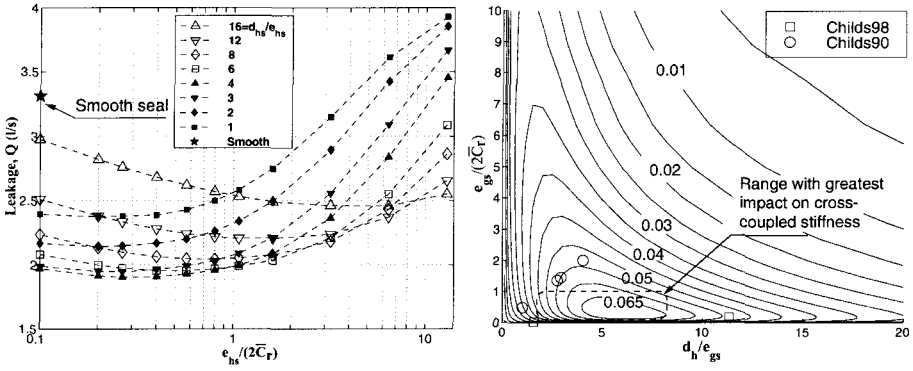


Figure 6: Parameter study of hole pattern seal. Left figure: Leakage. Right figure: Hole friction factor contours and geometries studied by [4] and [3].

For the hole pattern seals the most important trend in the above results is the large reduction in cross-coupled stiffness compared to that of a smooth seal. Fig. 5 actually indicates that the cross-coupled stiffness can be changed from a significantly from a value of about 11 MN/m for a smooth seal to zero or negative values for a range of hole-patterns. Whether negative values can be obtained in practice will require more experimental studies. Direct damping values are relatively constant and a few percent greater than the corresponding smooth seal damping. Based on the comparison between the results from the theory in this article and the experimental results by [3] it may be expected that direct damping is slightly over-predicted. Direct stiffness,  $K$ , is shown to be less for all choices of hole-patterns compared with a smooth seal. Added mass and cross-coupled damping do not change significantly for the whole range of hole patterns. Figure 6 indicates that the hole patterns can reduce the smooth seal leakage up to 40% in the range of hole geometries studied.

### 3.4 Conclusions

By introducing explicit friction factors for wide range of groove and hole pattern geometries, seal leakage and rotordynamic coefficients can be calculated by the theory presented. The results indicate that both leakage and rotordynamic coefficients are significantly affected by the choice of groove or hole pattern. A parameter study indicates which range of patterns are predicted to have the greatest influence on seal leakage and dynamic coefficients. Limited experimental data have been published in the literature for these roughness patterns.

## References

- [1] Dara W. Childs. Rotordynamic moment coefficients for finite-length turbulent seals. *Proceedings of the IFToMM Conference on Rotordynamic Problems in Power Plants*, pages 371–378, 1982. Rome, Italy.

- [2] Dara W. Childs. *Turbomachinery Rotordynamics; Phenomena, Modeling, and Analysis*. John Wiley & Sons, New York, 1993.
- [3] Dara W. Childs and Patrice Fayolle. Test results for liquid damper seals using a round-hole roughness pattern for the stators. In *ASME-STLE Joint Tribology Conference*, 1998.
- [4] Dara W. Childs, S. Nolan, and J. J. Kilgore. Additional test results for round-hole-pattern damper seals: Leakage, friction factors, and rotordynamic force coefficients. *Journal of Tribology*, 112:365–371, April 1990.
- [5] O. R. Marquette, D. W. Childs, and S. G. Phillips. Theory versus experiment for leakage and rotordynamic coefficients of circumferentially - grooved liquid annular seals with  $l/d$  of 0.45. In *ASME Fluids Engineering Division Summer Meeting FEDSM'97 June 22-26, FEDSM97-3333*. ASME, 1997.
- [6] R. Nordmann, F. J. Dietzen, W. Janson, A. Frei, and S. Florancic. Rotordynamic coefficients and leakage flow of parallel grooved seals and smooth seals. In *Proceedings of the workshop: Rotordynamic Instability Problems in High-Performance Turbomachinery - 1987*, NASA CP-2443, pages 129–153, Texas A & M University, 1987.
- [7] William H. Press, Saul A. Teukolsky, William T. Vetterling, and Brian P. Flannery. *Numerical Recipes in FORTRAN*. Cambridge University Press, 2. edition, 1992.
- [8] Eskild Storteig. *Dynamic characteristics and leakage performance of liquid annular seals*. Doctoral thesis, Norwegian University of Science and Technology, 2000.

## A FIRST ORDER PERTURBATION COEFFICIENTS

The coefficients listed below are used in Eq. 17.

$$A_{1z} = \frac{u_{s0}}{2h_0^2} \left( \frac{\sigma_{zs0}}{h_0} - \frac{\partial\sigma_{zs0}}{\partial h_0} \right) + \frac{u_{r0}}{2h_0^2} \left( \frac{\sigma_{zr0}}{h_0} - \frac{\partial\sigma_{zr0}}{\partial h_0} \right) \quad (23)$$

$$A_{2z} = \frac{b^2}{2h_0^2} \left[ u_0 \left( \frac{\partial\sigma_{zs0}}{\partial u_{s0}} + \frac{\sigma_{zs0}}{u_{s0}} \right) + (u_0 - 1) \left( \frac{\partial\sigma_{zr0}}{\partial u_{r0}} + \frac{\sigma_{zr0}}{u_{r0}} \right) \right] \quad (24)$$

$$A_{3z} = \frac{1}{2h_0^3} \left( \frac{\partial\sigma_{zs0}}{\partial u_{s0}} + \frac{\sigma_{zs0}}{u_{s0}} + \frac{\partial\sigma_{zr0}}{\partial u_{r0}} + \frac{\sigma_{zr0}}{u_{r0}} \right) - \frac{1}{h_0^2} \frac{\partial h_0}{\partial z} + \frac{u_{s0}\sigma_{zs0}}{2h_0} + \frac{u_{r0}\sigma_{zr0}}{2h_0} \quad (25)$$

$$A_{1\theta} = \frac{u_0 u_{s0}}{2h_0^*} \left( \frac{\sigma_{\theta s0}}{h_0} - \frac{\partial\sigma_{\theta s0}}{\partial h_0} \right) + \frac{u_{r0}(u_0 - 1)}{2h_0^*} \left( \frac{\sigma_{\theta r0}}{h_0} - \frac{\partial\sigma_{\theta r0}}{\partial h_0} \right) \quad (26)$$

$$A_{2\theta} = \frac{b^2 u_0^2}{2h_0^*} \left( \frac{\partial\sigma_{\theta s0}}{\partial u_{s0}} + \frac{\sigma_{\theta s0}}{u_{s0}} \right) + \frac{b^2 (u_0 - 1)^2}{2h_0^*} \left( \frac{\partial\sigma_{\theta r0}}{\partial u_{r0}} + \frac{\sigma_{\theta r0}}{u_{r0}} \right) + \frac{u_{s0}\sigma_{\theta s0}}{2h_0^*} + \frac{u_{r0}\sigma_{\theta r0}}{2h_0^*} \quad (27)$$

$$A_{3\theta} = \frac{u_0}{2h_0 h_0^*} \left( \frac{\partial\sigma_{\theta s0}}{\partial u_{s0}} - \frac{\sigma_{\theta s0}}{u_{s0}} \frac{b^2 u_0^2}{w_0^2} \right) + \frac{(u_0 - 1)}{2h_0 h_0^*} \left( \frac{\partial\sigma_{\theta r0}}{\partial u_{r0}} - \frac{\sigma_{\theta r0}}{u_{r0}} \frac{b^2 (u_0 - 1)^2}{w_0^2} \right) \quad (28)$$

where  $\sigma_{zs0} = f_{zs0} \left( \frac{l}{C_r} \right)$ ,  $\sigma_{\theta s0} = f_{\theta s0} \left( \frac{l}{C_r} \right)$ ,  $\sigma_{zr0} = f_{zr0} \left( \frac{l}{C_r} \right)$ ,  $\sigma_{\theta r0} = f_{\theta r0} \left( \frac{l}{C_r} \right)$ . In order to determine the above coefficients for groove- and hole pattern seals, the friction factors and their partial derivatives for each type of surface roughness are needed.

### A.1 Friction factor for smooth and machine roughness seals

For the land portion of the groove- and hole patterned seals the isotropic roughness Moody's friction formula is used where  $f_{lr,s} = a_1 \left[ 1 + \left( \frac{b_2 e_{r,s}}{2\bar{H}} + \frac{b_3}{Re_{r,s}} \right)^{\frac{1}{3}} \right]$ . The Reynolds number range is  $4000 < Re_{r,s} < 10^7$ . Partial differentiation of the non-dimensional Moody's equation yields:

$$\frac{\partial f_{lr,s0}}{\partial h_0} = \frac{1}{h_0} \frac{1}{3} (a_1 - f_{lr,s0}), \text{ and } \frac{\partial f_{lr,s0}}{\partial u_{r,s0}} = \frac{1}{u_{r,s0}} f_{lr,s0} b_{r,s} \quad (29)$$

$$\text{where } b_{r,s} = \left[ -\frac{1}{3} \frac{1}{\left( \frac{a_2 r_s}{h_0} + \frac{a_3}{h_0 u_{r,s0}} \right)} \left( 1 - \frac{a_1}{f_{lr,s0}} \right) \left( \frac{a_3}{u_{r,s0} h_0} \right) \right] \quad (30)$$

and  $f_{lr,s0}$  is Moody's friction factor from the zeroth order solution.

### A.2 Grooved seal friction factor

For grooved rotor and stator the friction factor consists of one part from the land portion and one from the grooved portion.  $f_{\theta r,s} = \chi_{\theta lr,s} f_{lr,s} + \chi_{gr,s} f_{\theta gr,s}$  and  $f_{zr,s} = \chi_{zlr,s} f_{lr,s} + \chi_{gr,s} \frac{w}{u_{r,s}} f_{zgr,s}$ . The reason for the terms  $w/u_{r,s}$  is that the axial friction factor for the grooves is related to the axial flow only, while the other friction factors are related to the total velocity relative to the rotor and stator.

$$\chi_{zlr,s} = \frac{\bar{L}_{lr,s} - 4\bar{C}_r}{\bar{L}_{lr,s} + L_{gr,s}}, \chi_{\theta lr,s} = \frac{\bar{L}_{lr,s}}{\bar{L}_{lr,s} + L_{gr,s}}, \text{ and } \chi_{gr,s} = \frac{N_{gr,s} L_{gr,s}}{L} \quad (31)$$

$$\bar{L}_{lr,s} = \frac{L \ln r_s + (N_{gr,s} - 1) L_{lr,s} + L e x_{r,s}}{N_{gr,s}} \quad (32)$$

If  $\chi_{zlr,s} < 0$  it is set equal to zero, so that all friction loss is due to the grooves. The relative portions of the seal  $\chi_{zlr,s}$  and  $\chi_{gr,s}$  covered by the land and groove zone are calculated based on the assumption that the same groove width and depth are used for all grooves on each surface and that the groove spacing is constant.

The details of the friction factors  $f_{\theta gr,s}$  and  $f_{zgr,s}$  for circumferential grooves are given below.

$$f_{zgr,s} = a_1 \left[ 1 + \left( \frac{b_2 a_{2zgr,s}}{h} e^{-(a_{r,s} \sqrt{\frac{a_{2zgr,s}}{h} + b_{r,s}})} \right)^{\frac{1}{3}} \right] \text{ and } f_{\theta gr,s} = a_1 \left[ 1 + \left( \frac{a_{2\theta gr,s}}{h} + \frac{b_3}{h u_{r,s}} \right)^{\frac{1}{3}} \right] \quad (33)$$

where

$$a_{r,s} = 3.8 \cdot \tanh(0.16 \cdot (L_{er,s} + 0.4)) + 0.25 \sqrt{L_{er,s} + 0.4} \quad (34)$$

$$b_{r,s} = 10.6 \cdot e^{-0.35 \cdot L_{er,s}} + 0.57 L_{er,s}^{-0.8} + 1.37 L_{er,s}^{0.54} - 10 \quad (35)$$

$$a_{2\theta gr,s} = \left( \left( \frac{u_{r\infty}}{u_{s\infty}} \right) \frac{(1 - u_{\infty})}{u_{\infty}} \cdot \left[ 1 + \left( a_{2gr,s} + \frac{a_3}{u_{r\infty}} \right)^{\frac{1}{3}} \right] - 1 \right) - \frac{a_3}{u_{s\infty}} \quad (36)$$

$$a_{2zgr,s} = \frac{e_{gr,s}}{2\bar{C}_r}, a_{2gr,s} = \frac{b_2 e_{r,s}}{2\bar{C}_r}, \text{ and } L_{er,s} = \frac{L_{gr,s}}{e_{gr,s}} \quad (37)$$

$$u_{r\infty} = \sqrt{1 + 4(u_{\infty} - 1)^2}, u_{s\infty} = \sqrt{1 + 4u_{\infty}^2}, \text{ and } u_{\infty} = 0.10(e^{-6L_{er,s}} - e^{-0.3L_{er,s}}) + 0.5 \quad (38)$$

Partial differentiation of the angular friction factor yields

$$\frac{\partial f_{\theta r,s0}}{\partial h_0} = \chi_{\theta lr,s} \frac{\partial f_{lr,s0}}{\partial h_0} + \chi_{gr,s} \frac{\partial f_{\theta gr,s0}}{\partial h_0} \quad \text{and} \quad \frac{\partial f_{\theta r,s0}}{\partial u_{r,s0}} = \chi_{\theta lr,s} \frac{\partial f_{lr,s0}}{\partial u_{r,s0}} + \chi_{gr,s} \frac{\partial f_{\theta gr,s0}}{\partial u_{r,s0}} \quad (39)$$

$$\frac{\partial f_{\theta gr,s0}}{\partial h_0} = \frac{1}{h_0} \frac{1}{3} (a_1 - f_{\theta gr,s0}) \quad \text{and} \quad \frac{\partial f_{\theta gr,s0}}{\partial u_{r,s0}} = \frac{1}{u_{r,s0}} f_{\theta gr,s0} b_{\theta gr,s0} \quad (40)$$

$$\text{where } b_{\theta gr,s0} = \left[ -\frac{1}{3} \frac{1}{\left( \frac{a_{2\theta gr,s}}{h_0} + \frac{a_3}{h_0 u_{r,s0}} \right)} \left( 1 - \frac{a_1}{f_{\theta gr,s0}} \right) \left( \frac{a_3}{u_{r,s0} h_0} \right) \right] \quad (41)$$

Partial differentiation of the axial friction factor yields

$$\frac{\partial f_{zr,s0}}{\partial h_0} = \chi_{zlr,s} \frac{\partial f_{lr,s0}}{\partial h_0} + \chi_{zgr,s} \frac{w_0}{u_{r,s0}} \frac{\partial f_{zgr,s0}}{\partial h_0} \quad \text{and} \quad \frac{\partial f_{zr,s0}}{\partial u_{r,s0}} = \chi_{zlr,s} \frac{\partial f_{lr,s0}}{\partial u_{r,s0}} + 0 \quad (42)$$

$$\text{where } \frac{\partial f_{zgr,s0}}{\partial h_0} = \left[ \frac{1}{3h_0} \left( \frac{a_{r,s}}{2h_0} \sqrt{\frac{a_{2zgr,s0}}{h_0}} - 1 \right) \right] \left( f_{zgr,s0} - \frac{a_1}{h_0 u_{r,s0}} \right) \quad \text{and} \quad \frac{\partial f_{zgr,s0}}{\partial u_{r,s0}} = 0 \quad (43)$$

### A.3 Hole pattern seal friction factor

$$f_{\theta r} = \chi_{lr} f_{lr} + \chi_{hr} \frac{u-1}{u_r} f_{hr}, \quad f_{\theta s} = \chi_{ls} f_{ls} + \chi_{hs} \frac{u}{u_s} f_{hs}, \quad \text{and} \quad f_{zr,s} = \chi_{lr,s} f_{lr,s} + \chi_{hr,s} \frac{w}{u_{r,s}} f_{hr,s} \quad (44)$$

The weighting factors, mean land length and hole area fraction are given by

$$\chi_{lr,s} = \frac{\bar{L}_{lr,s} - 4\bar{C}_r}{\bar{L}_{lr,s} + d_{hr,s}}, \quad \chi_{hr,s} = \frac{d_{hr,s}}{\bar{L}_{lr,s} + d_{hr,s}}, \quad \bar{L}_{lr,s} = d_{hr,s} \left( \frac{1 - \gamma_{r,s}}{\gamma_{r,s}} \right), \quad \text{and} \quad \gamma_{r,s} = \frac{\text{hole area } a_{r,s}}{\text{total area } a_{r,s}} \quad (45)$$

$d_{hr,s}$  are the diameters of holes on rotor and/or stator surface respectively. If  $\chi_{lr,s} \leq 0$  it is set equal to zero.

The hole pattern friction model for both tangential and axial direction is given by

$$f_{hr,s} = a_1 \left[ 1 + \left( \frac{b_2 a_{2hr,s}}{h} e^{-(a_{r,s} \sqrt{\frac{a_{2hr,s}}{h}} + b_{r,s})} \right)^{\frac{1}{3}} \right] \quad \text{where } a_{2hr,s} = \frac{e_{hr,s}}{2\bar{C}_r}, \quad L_{er,s} = \frac{d_{hr,s}}{e_{hr,s}} \quad (46)$$

$$a_{r,s} = 3.8 \cdot \tanh(0.16 \cdot (L_{er,s} + 0.4)) + 0.25 \sqrt{L_{er,s} + 0.4} \quad (47)$$

$$b_{r,s} = 10.6 \cdot e^{-0.35 \cdot L_{er,s}} + 0.57 L_{er,s}^{-0.8} + 1.37 L_{er,s}^{0.54} - 10 \quad (48)$$

$h$  is the non-dimensional film thickness,  $e_{hr,s}$  are hole depths for rotor and stator,  $d_{hr,s}$  are the hole diameters.  $\bar{C}_r$  is the minimum clearance for straight seals and average minimum clearance for tapered seals. The terms  $\frac{u-1}{u_r}$ ,  $\frac{u}{u_s}$ , and  $\frac{w}{u_{r,s}}$ , in Eq. 44 are needed since the friction factor for the holes in the tangential direction is related to the tangential flow only and the hole friction factor for the axial direction is related only to the axial flow. For holes on rotor and stator the friction factor is assumed to be isotropic. Partial derivatives are similar to those for the axial direction groove friction factor.

# Optimization of the rotor-dynamic behaviour of a balancing device using honeycomb profiles in high-pressure boiler feed pumps

C TRAUTMANN and D-H HELLMANN

Department of Mechanical Engineering, University of Kaiserslautern, Germany

## ABSTRACT

Rotor dynamic stability plays a crucial role in high-pressure boiler feed pumps because it directly affects availability. The major factor of influence are rotor gaps, e.g. those between impeller and pump casing, balancing device and casing as well as those of the journal bearings. They improve the damping characteristics and can therefore reduce the radial displacement of the shaft.

Particularly the long gap of the central balancing device can contribute to the instability of the rotor, e.g. if the fluid enter into the gap with swirl. In order to avoid this, so-called "swirl-brakes" can attached at the gap entrance. The rotor gaps doesn't influence only the rotor stability, but also the pump efficiency by changing the leakage flow. Thus a compromise between stability an efficiency has to be made.

In this paper the optimization of the rotor-dynamic stability of the rotor is described. Several honeycomb rings are installed in the balancing device of a high pressure boiler feed pump to improve stability an efficiency.

## INTRODUCTION

The development to even higher performance boiler feed pumps, e.g. by increasing the speed, the dynamic loads increase in a similar way. The vibrational behavior of a pump during operation characterises its loading, which is influenced by the appropriate selection of bearings and dimensioning of the gaps. Limiting values defined, such as those recommended in, among others, API 610 [1] have to be adhered to if the pump is to qualify for acceptance.

The displacement of the rotor shaft largely depends on the rotor gaps, such as: the gaps between impeller and pump casing, those between balancing device and casing, as well as the clearances of the journal bearings. Therefore, these must be developed in a way that they stabilize the rotor. The vortex destabilize the rotor, therefore this must be minimized. This can be achieved e.g. by the installation of swirl brakes or honeycomb profiles. The influence of honeycomb profiles on rotor dynamic, which are equipped in the balancing device is presented in the first part of this paper.

Besides the influence on the rotor dynamics, the balancing device compensate the axial thrust, which is caused by the pressure distributions along the impeller of each stage. The counteracting force is generated by a pressure drop along the balancing device. This pressure drop is only possible, if a gap flow exists. To keep overall efficiency high, this gap flow has to be minimized. This target can be achieved with different profiles. It has to be considered that some profiles can destabilize the rotor dynamic behavior [2,3,4].

In this investigation several honeycomb rings are mounted into the balancing device, simultaneously the balancing flow was measured. In the second part of this paper frequency measurements are presented, which show the influence of the honeycomb profiles on the rotor-dynamic behavior.

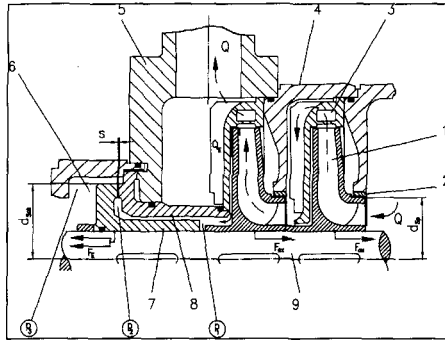


Fig. 1: Central balancing device in a multistage boiler feed pump  
 ① impeller, ② slit seal, ③ diffuser with return guide, ④ stage casing, ⑤ discharge casing, ⑥ balancing room, ⑦ balancing disc, ⑧ balancing counter disc, ⑨ shaft

## PUMP TEST RIG

All measurements were carried out on a seven-stage high-pressure ring-section pump. The investigation of the vibrational behavior is part of a project conducted at the Kaiserslautern University for identifying the excitation mechanisms of subsynchronous vibrations [5]. The pump is excited at the drive end. A shaker induces the oscillations into the bearing house, sweeping a frequency band from 30 to 100 Hz continuously in both the horizontal and vertical directions.

The main criterion for selecting this pump was the possibility it offered for measuring the rotor displacement directly in the hydraulic area. Access to the shaft was gained by replacing every second stage through a blind stage (Fig. 2) The pump has no impeller gaps in the blind stages. Therefore the stabilizing of the rotor is reduced. By selecting plain bearings and mechanical seals, it is ensured that the resulting rotor would be highly sensitive to vibrations. In addition to the measuring point in the middle of the bearings (shaft centre), the bearing housings were also equipped with two displacement sensors, in order to measure the radial shaft movement. The bearing house on the discharge side was also equipped with a displacement sensor for monitoring the axial shaft position. Furthermore, the balancing water flow is measured and likewise the pressure at the gap entry.

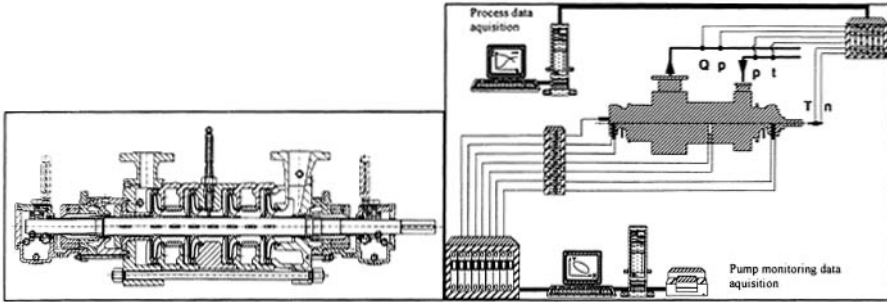


Fig. 2: Test pump,  $n_{\max} = 6500$  rpm;  $Q_{\text{opt}} = 132$  m<sup>3</sup>/h;  $H_{\text{opt}} = 2310$  m  
 Fig. 3: Sensor locations and data acquisition

The measured signals and the process parameters defining the operating point of the pump were transmitted to computers using data acquisition systems further processing (Fig. 3).

The boiler feed pump under investigation is currently installed in the pump condition monitoring test rig at the University of Kaiserslautern (Fig. 4). The dimensions of the test rig are such that it can accommodate any kind of vertical or horizontal pump with a drive rating of up to 85 kW at a pressure of up to 60 bar, a maximum temperature of 140 °C and a capacity in the range from 5 to 500 m<sup>3</sup>/h. The rig also qualifies for acceptance tests, as all sensor locations are in compliance with DIN 1944 and ISO 3555 requirements. With this setup it is possible to document the vibration response of high pressure multistage ring-section pumps as a function of the operating point.

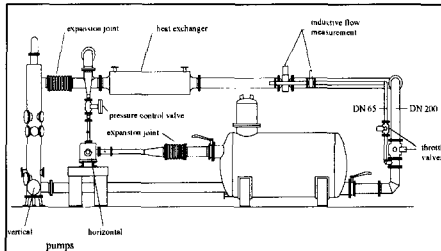


Fig. 4: Pump condition monitoring rig at Kaiserslautern University

## CHARACTERISTICS OF A MULTISTAGE RING-SECTION PUMP

Mechanical stress and design considerations limit the head per stage thus requiring the design of multistage pump. The maximum number of stages is limited by deflection and the admissible peak-to-peak vibration. The shift of the critical speed and the excitation forces must be considered, too.

In multistage high pressure boiler feed pumps axial forces of several tons can occur. For design reasons each individual impeller can't be discharged by the axial thrust. Therefore a central balancing device is added after the last stage, e.g. single piston, balancing disc or double piston. The balancing disc is divided into an axial throttle gap and a radial adjust gap (Fig. 6).

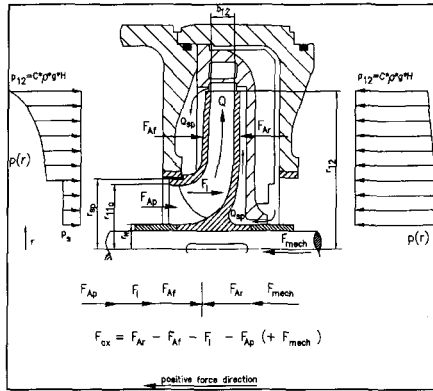


Fig. 5: Pressure distribution and force components in a multistage ring-section pump

For the calculation of the resulting axial thrust, the pressure distributions must be integrated and added for every single stage (Gl. 1-4).

$$F_{Ar} = 2\pi \cdot \rho \cdot \omega^2 \cdot \int_{r_N}^{r_{10}} \int_{r_N}^{r_{12}} k^2 \cdot r \cdot dr \cdot r \cdot dr \quad (1)$$

$$F_{Af} = 2\pi \cdot \rho \cdot \omega^2 \cdot \int_{r_N}^{r_{10}} \int_{r_N}^{r_{12}} k^2 \cdot r \cdot dr \cdot r \cdot dr \quad (2)$$

$$F_i = \rho \cdot c_{10}^2 \cdot \pi \cdot (r_{10}^2 - r_N^2) \quad (3)$$

$$F_{Ap} = p_{10} \cdot \pi \cdot (r_{3p}^2 - r_N^2) \quad (4)$$

Without any flow through the impeller side gaps, the ratio of angular velocity  $k$  is constant. It does not depend on the radius:

$$k = k_0 \quad (5)$$

As shown in figure 5, in multistage pumps the gap flow on the pressure side is directed to outer diameter of the impeller. The ratio of angular velocity  $k$  is in this case a function of the radius. Analytic solutions of the governing equations have not yet be found [6,7,8].

$$k = k(r) \neq k_0 \quad (6)$$

Forces in throttling gaps at the impeller and at the balancing device have a crucial influence on the vibration response of the pump rotor: they largely influence the eigenvalues and eigenmodes of the vibration, the amplitudes in case of forced vibrations and the stability limits.



In the literature only few publications deal with long throttling gaps ( $L/D > 0.75$ ), installed in balancing devices [3,4]. Childs [3] recommends two configurations, which are favorable for the stability rotor with long gaps. If honeycomb profiles are mounted into the central balancing device, the main damping  $D$  increases. The circumferential velocity, and thus the cross couple stiffness  $k$ , can not be reduced by honeycomb profiles. On the other hand labyrinth seals with swirl brakes can be mounted into the balancing device. The swirl brakes achieve a reduction of the cross couple stiffness  $k$ .

### HYDRAULIC MEASUREMENTS

First the balancing device of the boiler feed pump was converted in such a way that in the following investigations honeycomb rings can be integrated into the balancing counter disc (Fig. 6). The clearance gap width was adapted to the delivery status of the manufacturer and the shaping of the balancing disc was not changed.

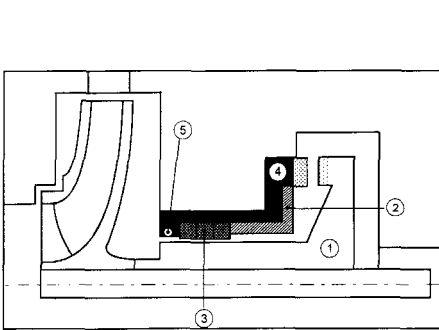


Fig. 6: Central balancing device with honeycomb rings  
 ① balancing disc, ② locking bushing,  
 ③ honeycomb rings, ④ balancing counter disc, ⑤ pressure probe

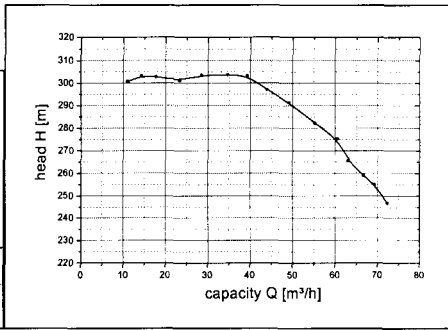


Fig. 7: Characteristic curve without honeycomb rings, n = 3000 rpm

The assembly described above was selected as reference measurement, but without any honeycomb profile. The rotor speed is  $n = 3000$  rpm. The boiler feed pump has its best efficiency point at  $Q = 60$  m³/h and  $H = 275$  m. Towards part load operation the gradient of the characteristic curve decreases compared to the design duty point (Fig. 7).

The balance water flow was measured in the return pipe (Fig. 8). The leakage was reduced up to a capacity of  $Q = 30$  m³/h by approx. 30 % and risen then again approx. 20 % with  $Q = 10$  m³/h.

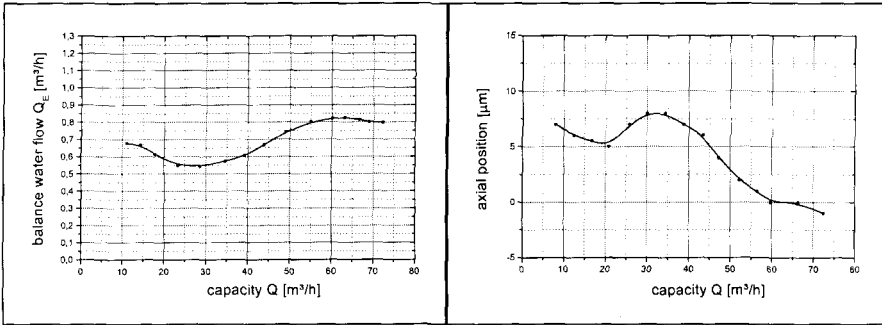


Fig. 8: Balance water flow without honeycomb rings,  $n = 3000$  rpm  
 Fig. 9: Axial rotor position without honeycomb rings,  $n = 3000$  rpm

The axial position of the rotor (Fig. 9) shifts to the suction side, starting from operating point to part-load. Up to the capacity of  $Q = 30$  m<sup>3</sup>/h, the rotor shifts to the suction side; between  $20$  m<sup>3</sup>/h  $< Q < 30$  m<sup>3</sup>/h to the discharge side and below  $Q < 20$  m<sup>3</sup>/h to the suction side again.

After the reference measurement without, honeycomb rings were inserted into the balancing counter disc. Only the balancing water flow (Fig. 10) is depicted as the characteristic curve and the axial position remain unchanged. The clearance gap width could be selected smaller at the honeycomb rings (0.1 mm), because they have better resistance to galling.

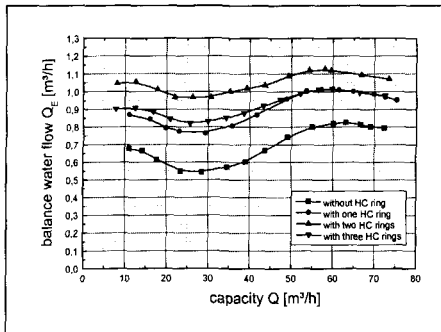


Fig. 10: Balance water flow with different honeycomb ring configurations,  $n = 3000$  rpm

The smaller clearance gap is not dominant - compared to the circumference velocity -, because the balance water flow increases in the configuration with two honeycomb rings. Only after the installation of three honeycomb rings, the balance water flow decreases again. Probably, now the circumference velocity was reduced, so the smaller clearance gap width has an influence again and the balance water flow also decreases.

## FREQUENCY MEASUREMENTS

Matz [5] investigated self-oscillating behaviour with double clearance gaps. As a result, three raised amplitudes were found in a stimulated frequency band from 50 Hz to 100 Hz. The amplitudes of these frequencies increased in comparison to their neighbouring frequencies. These can be used as possible natural frequencies of the

boiler feed pump. There are three „frequency-windows" in which the rotor shows high oscillation amplitudes. These frequency ranges are between 53...56 Hz, between 59...64 Hz and 67...74 Hz, with the natural frequencies at 55,4 Hz and 58,9 Hz. With double gap height yet another natural frequency was determined at 72,5 Hz. Within these ranges, frequency shifts which are caused by anisotropic oscillation behaviour can occur. Their extent depends e.g. on the variation by the assembly.

In this project the rotor's natural frequencies should be shifted and/or damped, as the honeycomb profiles are installed into the central balancing device.

Before the modification of the boiler feed pump the natural frequencies identified so far were reproduced [5]. The following frequencies were characterised by a amplitude increasing clearly to their side frequencies: 55,0 Hz, 59,7 Hz, 61,6 Hz and 70,6 Hz. These results are identical to those of [5].

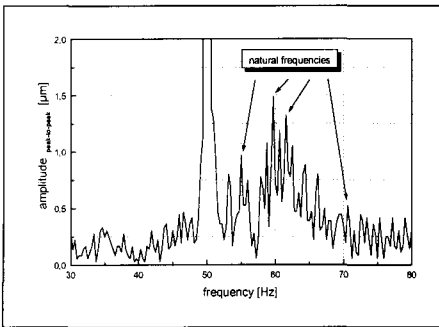


Fig. 11: Frequency spectrum before the modification

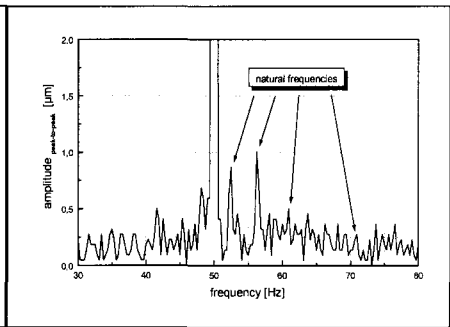


Fig. 12: Frequency spectrum without honeycomb ring

After the discharge housing was modified in such a way that a new balancing counter disk could be used, which could take up different locking bushings and honeycomb rings. The following gap geometry was selected:

*gap data:*  
 gap-diameter 75 mm  
 gap-length 84 mm  
 gap-height at smooth gap 0,15 mm  
 gap-height at honeycomb profile 0,1 mm  
 pressure-difference 24 bar

*honeycomb profile:*  
 cell-deep 3,5 mm  
 cell-width 1,59 mm (1/16")  
 width of one honeycomb ring 15 mm

Figure 12 shows the frequency spectrum after the modification, with which no honeycomb ring had been inserted. The measuring position "shaft center" is represented with this measuring point, because the rotor shows particularly large amplitude excursions. Additionally with the modification of the boiler feed pump this measuring position was not changed. Furthermore the balance of the machine remained unchanged.

*experimental parameters:*  
 rotor speed n = 3000 rpm  
 operating point Q = 1,0 \* Q<sub>opt</sub>  
 vibration excitation plane vertical  
 measure position shaft centre  
 measure plane Y-plane

In the first frequency window (53... 56 Hz), there are possible natural frequencies of 52,5 Hz and 56,3 Hz. It is remarkable that the frequency, that occurred in the second frequency window (59... 64 Hz) was strongly damped at 60 Hz. The amplitude was reduced by approx. 60 %, compared with the first configuration (Fig. 11). However two increased amplitudes occurred below 50 Hz. The reason for this could lie in the altered damping and stiffness characteristics, by the modification of the discharge housing and the balancing device. The natural frequency of 70,6 Hz, identified in the third window (67... 74 Hz), did not occur as expected, because this is to be assigned to the gap wear [5].

For the further changes, this measurement serves as a reference measurement, due to only the number of inserted honeycomb rings being varied in the following changes.

The inserted honeycomb ring has a width of 15 mm, which corresponds to 18 % of the length of the gap. In Fig. 13 the frequency spectrum of the measuring position „shaft center“ in Y-plane is represented.

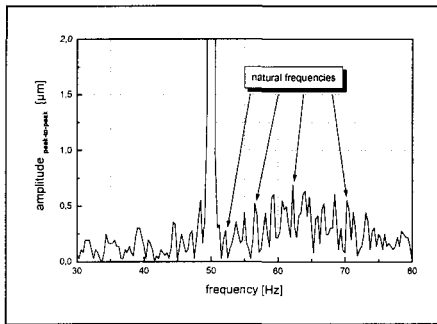


Fig. 13: Frequency spectrum with one honeycomb ring

On installation of one honeycomb ring the value of the main damping  $D$  increases, whereby the measured amplitudes are reduced at the natural frequencies of 52,5 Hz and 56,3 Hz by more than 50 %. An increasing of the amplitudes can be detected at 62 Hz and 70 Hz.

With the following change, two equal honeycomb rings are inserted into the balancing counter disk (Fig. 14). In the comparison to the reference measurement the amplitudes can be absorbed here with the natural frequencies of 52,5 Hz and 56,3 Hz by approx. 20 %. These values are however larger in relation to the measurement achieved with one honeycomb ring of approx. 30 %. Further increased amplitudes occur at 60 Hz. In the comparison to the measurement with one honeycomb ring these are substantially higher. The amplitude at 70 Hz, measured before, remains unchanged.

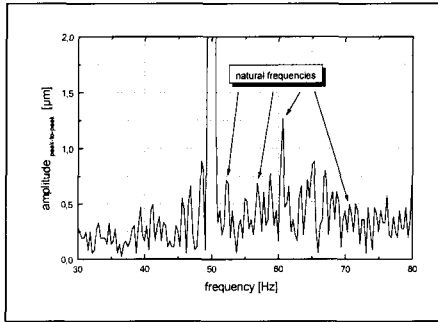


Fig. 14: Frequency spectrum with two honeycomb rings

The frequency spectrum (Fig. 15) in the comparison to the measurement with two honeycomb rings could be improved only slightly by the additional installation of a third honeycomb ring. The amplitude of the natural frequency at 61 Hz was reduced - related to the previous configuration - by approx. 30 %, while the amplitudes of the natural frequencies at 52,5 Hz and 56,3 Hz remained constant. The measured rise of the amplitude at 70 Hz is approx. 15 %, compared with the measurement with one honeycomb ring.

Obviously the damping characteristics can be not substantially improved by the application of two or three honeycomb rings. The lowest amplitudes were achieved with one honeycomb ring. This result should be verified with further attempts, where the profiled balancing disk is exchanged with a smooth one.

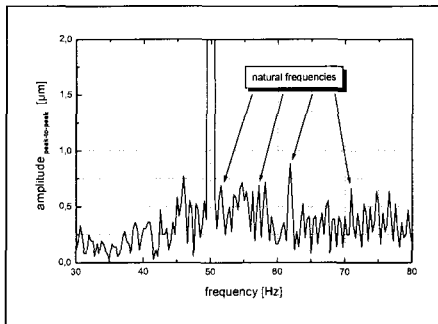


Fig. 15: Frequency spectrum with three honeycomb rings

## DISCUSSION OF THE MEASUREMENTS

The measurements presented in this paper show that the balance water flow is mainly determined by the radial gaps of the balancing disc. Throttling of the balancing water flow in the operating point, leads to an increase of the axial thrust and the rotor shifts to the suction side. Thus, the radial clearance of the balancing disc becomes closer and therefore also the balance water flow is reduced.

If honeycomb rings are mounted into the balancing counter disc, the flow resistance, due to the reduction of the circumferential velocity, is reduced and the balance water flow increases. If three honeycomb rings are inserted in the balancing counter disc, the balance water flow decreases again, remaining on the level with one honeycomb ring. Conclude from that, the increase of the leakage flow with one and with two honeycomb rings depends on the flow resistance. With three honeycomb rings the leakage flow is obviously influenced by the gap height and the length of gap.

The measurements of the frequency spectra resulted in, that the lowest amplitudes were measured in the configuration with one honeycomb ring.

## SUMMARY

In high pressure boiler feed pumps the central balancing device plays a crucial role for rotor-dynamical and hydraulic points of view. On the one hand, the axial thrust, which results from the pressure distribution at each impeller stage, must be compensated. This can only be carried out, if due to throttling an appropriate counter acting force is produced. The leakage flow occurring thereby, can be minimized by various gap profiles. On the other hand, the rotor can be stabilized or centered by the stiffness and damping characteristics of the balancing disc. Therefore the rotor-dynamic coefficients of the profiles must be selected in such a way that no instabilities can occur.

In this investigation honeycomb rings were mounted into the central balancing device. It was shown that a minimal leakage flow and a good stability of the rotor could not be achieved at the same time. Therefore a compromise must be found. Further investigations in this area will be necessary, because only some parameters influencing this behavior are known yet.

## LITERATURE

- [1] API Standard 610, 7th Edition, „Centrifugal Pumps for General Refinery Service“ American Petroleum Institute, Washington D. C., Feb. 1989
- [2] D.W. Childs et al., „Annular gas seals and rotordynamics of compressors an turbines“, Proc. of the 26<sup>th</sup> Turbomachinery Symp., pp. 201-220, Houston, Texas, 1997
- [3] D.W. Childs et al., „Annular honeycomb seals: test results for leakage and rotordynamic coefficients; comparsions to labyrinth an smooth configurations“, ASME Transactions, Journal fo Tribology, 111, pp. 293-301, April 1989
- [4] R. Nordmann et al., „Rotordynamic coefficients and leakage flow for smooth and grooved seals in turbopumps“, Proceedings IFToMM Meeting Tokyo, September 1986
- [5] B. Matz, „Experimentelle Untersuchungen der Rotordynamik einer Hochdruck-Gliederpumpe in diskreten Arbeitspunkten und bei Variation der Unwucht und der Spaltweiten“, Dissertation, Universität Kaiserslautern, Deutschland, Dezember 1996
- [6] U.K. Möhring, „Untersuchung des radialen Druckverlaufes und des Drehmomentes im Radseitenraum von Kreiselpumpen bei glatter, ebener Radseitenwand und bei Anwendung von Rückenschaufeln“, Dissertation, Universität Braunschweig, Deutschland, Januar 1976
- [7] B. Stampa, „Experimentelle Untersuchungen an axial durchströmten Ringspalten“, Dissertation, Universität Braunschweig, Deutschland, Januar 1971
- [8] F. Schubert, „Untersuchung der Druck- und Geschwindigkeitsverteilung in Radseitenräumen radialer Strömungsmaschinen“, Dissertation, Universität Braunschweig, Deutschland, Mai 1988

# Dynamic behaviour of spiral bevel gears – rotational vibration of gears under running conditions

**Y UENISHI**

Transmission Design Section, Mitsubishi Motors Company, Aichi, Japan

**E AOYAMA** and **Y NAKATA**

Faculty of Engineering, Doshisha University, Kyoto, Japan

**T HIROGAKI**

School of Engineering, University of Shiga Prefecture, Shiga, Japan

## ABSTRACT

In this study, the rotational acceleration of Oerikon-type spiral bevel gears and the vertical acceleration of the housing are measured under various conditions. At the same time, the root stresses are observed in order to assess the meshing condition of the gears. We conclude that it is important to estimate the rotational acceleration of spiral bevel gears in order to reduce the vibration of the gear housing. It is found that the rotational vibration of gears is related to the real contact ratio. In addition, we proposed use of the free vibration to model the rotational motion of spiral bevel gears by means of equivalent spur gears. Results calculated using this model are in good agreement with experimental ones.

Key words: Spiral bevel gears, Tooth root stresses, Rotational vibration, Tooth contact ratio

## 1. INTRODUCTION

In the case of parallel axis gears (for instance, spur gears or helical gears), it is clear that rotational vibrations of gears are mainly transmitted to the gear housing through gear shafts and bearings. Therefore it is necessary to improve them in order to reduce vibration of the gear housing. There have been many reports evaluating the dynamic behaviour of gear rotational vibration under running conditions (1)-(3). Many models for parallel shaft transmission have been presented in these reports.

On the other hand, spiral bevel gears have been widely used as low noise gears among bevel gears. Many studies have been done on the static transmission error, stress analysis and their reliability (4)-(8). However, in the case of spiral bevel gears, there have been few studies dealing with dynamic behaviour under running conditions (9), and little work has been done to clarify the mechanism of vibration of the gears to reduce vibrations of the gear housing. Moreover, the previous work has been limited to gear resonance failure. Therefore it is necessary to clarify the vibration characteristics of spiral bevel gears to reduce vibration of the gear housing.

In the present report, the rotational acceleration and the tooth root stresses of spiral bevel gears are measured to investigate the relationship between the tooth mesh and the vibration caused by a dynamic load under running conditions. Additionally, we present a single-degree-of-freedom model to simulate this rotational vibration.

**Table 1 Dimensions of spiral bevel gears (T type)**

	Drive gear	Driven gear
Tooth profile	Oerlikon	
Module	7.500	
Pressure angle (deg)	21	
Shaft angle (deg)	90	
Face width (mm)	21.4	
Helix angle (deg)	38.0	
Tooth depth (mm)	11.23	8.99
Addendum (mm)	5.35	2.40
Dedendum (mm)	5.88	6.59
Number of teeth	11	12
Reference diameter (mm)	82.50	90.00
Pitch angle (deg)	42.51	47.49
Material	SCM822	
Heat treatment	Carburized	

**Table 2 Dimensions of spiral bevel gears (H type)**

	Drive gear	Driven gear
Tooth profile	Oerlikon	
Module	3.750	
Pressure angle (deg)	21	
Shaft angle (deg)	90	
Face width (mm)	19.0	
Helix angle (deg)	38.0	
Tooth depth (mm)	5.62	5.62
Addendum (mm)	2.60	2.40
Dedendum (mm)	3.02	3.22
Number of teeth	22	24
Reference diameter (mm)	82.50	90.00
Pitch angle (deg)	42.51	47.49
Material	SCM822	
Heat treatment	Carburized	

## 2. EXPERIMENTAL METHOD

### 2.1 Dimensions of gears

Table 1 and Table 2 show the dimensions of the gears used. These are Oerlikon-type spiral bevel gears with uniform tooth depth along tooth width, which are generated by face hobbing. The material used is carbonized steel. Lapping of the tooth surfaces is carried out after the



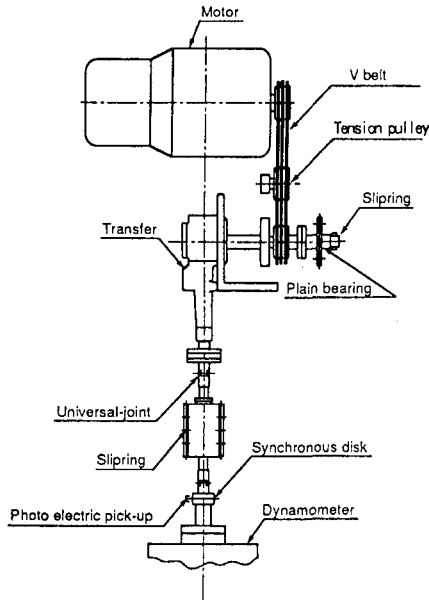


Figure 1 Experimental apparatus for running test

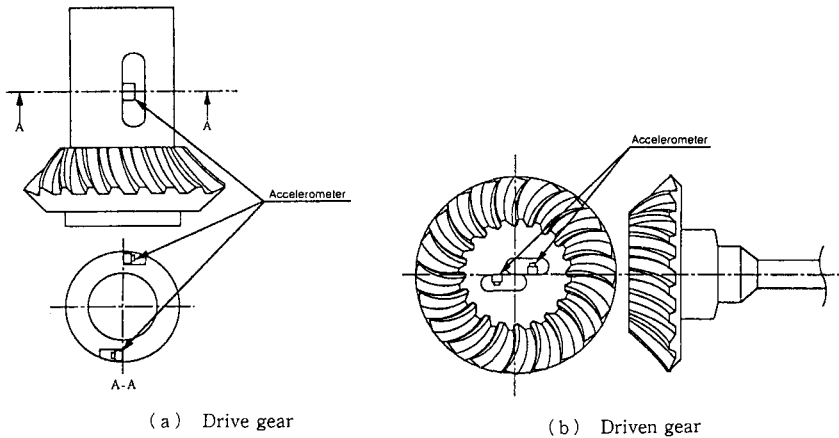


Figure 2 Positions of accelerometers

heat treatment processes.

Figure 1 shows the experimental apparatus for the running tests. Spiral bevel gears in the transfer housing are driven by an AC motor (maximum speed 7 000 rpm). Transmitted power is absorbed by a dynamometer.

Accelerometers are mounted on the gears, as shown in Fig. 2, in order to observe their

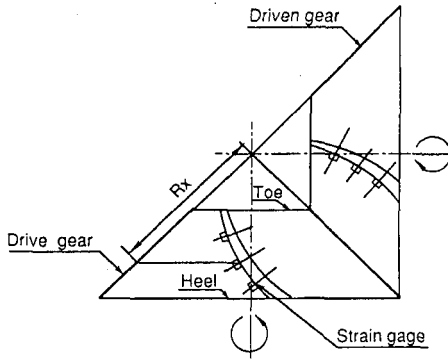
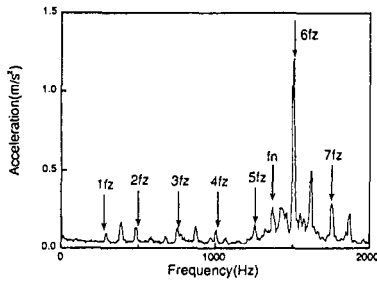
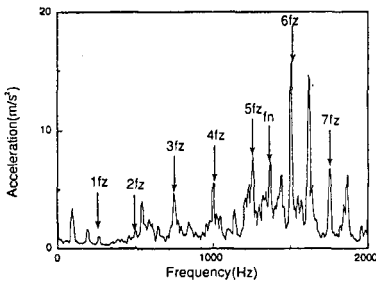


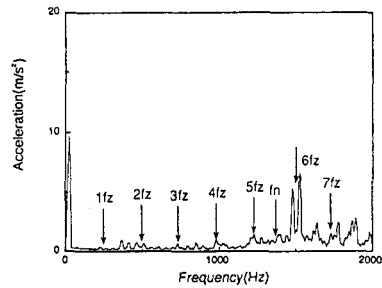
Figure 3 Positions of strain gages



(a) Acceleration of gear housing



(b) Rotational acceleration of drive gear



(c) Radial acceleration of drive gear

Figure 4 Relationship between acceleration and frequency  
(Mesh frequency=250 Hz, torque=46.8 Nm)

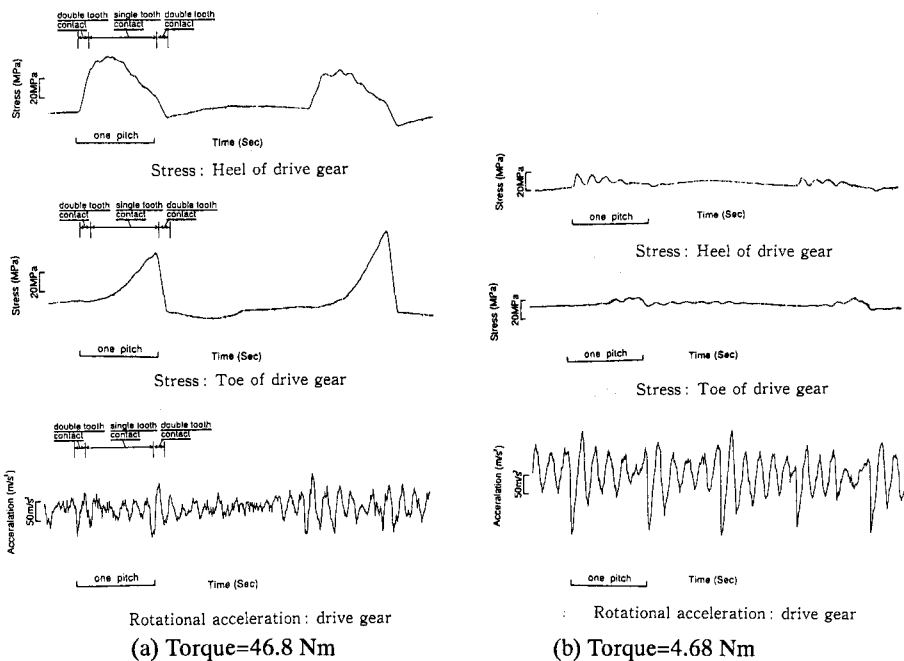


Figure 5 Tooth root stresses and rotational acceleration (Mesh frequency=250 Hz)

rotational vibrations under running conditions. It is feasible to obtain the rotational vibration and the radial vibration by operating (adding and subtracting) the signals from two sensors on each gear using an analog amplifier. The diameter between sensors on the drive gear is 38.5 mm, and on the driven gear 13.75 mm. The tooth root stresses are measured by a micro strain gage in order to estimate the meshing time. Figure 3 shows the measured positions of strains located at  $R_x=44.05$  mm (toe side),  $R_x=50.05$  mm (middle) and  $R_x=56.05$  mm (heel side). These signals are recorded through the slip rings shown in Fig. 1. Additionally, the vertical vibration on the gear housing near the bearing of the drive gear is also measured by an accelerometer.

The experimental conditions are 4.68 Nm – 46.8 Nm torque at the dynamometer and 684 – 2052 rpm motor speed. The tooth bearing patterns can be controlled by moving the axial relative position between gears. As shown in Fig. 3, the concave face of the drive gear tooth is meshed to the convex face of the driven gear in the running condition.

### 3. EXPERIMENTAL RESULTS AND DISCUSSION

#### 3.1 Vibration on the gear housing

Figure 4 (a), (b) and (c) show the relationship between acceleration and frequency in the running condition. The vertical acceleration on the housing, the rotational acceleration and the radial acceleration at the drive gear are shown in the respective figures. As for the rotational

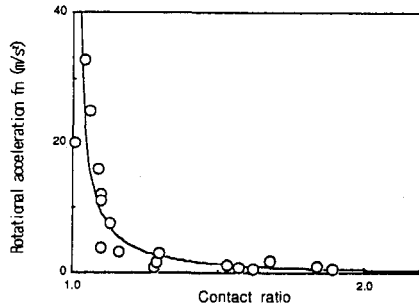


Figure 6 Relationship between rotational acceleration and real contact ratio  
(Mesh frequency=250 Hz)

vibration on the gear and the vertical vibration on the gear housing, the peak values can be seen at the mesh frequencies ( $1f_z$ ,  $2f_z$  and so on, as shown in Figures) as well as the rotational natural frequency ( $f_n$  as shown in the Figures). However, these vibrations disappeared in the radial direction of the gear. Thus, the rotational vibration caused by tooth meshing has a significant effect on the vibration of the gear housing in the case of spiral bevel gears.

### 3.2 Meshing and rotational vibration

Figure 5 (a) and (b) indicate the tooth root stresses and the rotational vibration of gear in running conditions. Looking at the tooth root stresses, it is found that the peak stress on each side appears at a different meshing time because of the spiral tooth trace along the tooth width. Furthermore, the meshing is started at the heel side of the tooth width, and is finished at the toe side. Here, we compare the meshing start point and the rotational vibration. The large vibration in rotation occurs at the initial meshing where the double tooth contact changes to a single tooth contact. In particular, the dynamic load can be seen at the tooth root stresses on the lower load, as shown in Figure (b). Moreover, it is also confirmed that there partly is no load on the tooth surface in meshing because no stress appears in the Figure. The separation of the gear teeth occurs in this time.

### 3.3 Influence of real contact ratio

There is a difference in the contact area on the tooth surface by the transmitted torque due to tooth crowning. Additionally, the area is also affected by the initial setting of the tooth bearing. So, we calculate the real contact ratio using the contact time of one tooth, the meshing time measured by the root stresses. It is defined as (meshing time) / (one pitch time of a tooth). Figure 6 shows the relationship between the real contact ratio and the  $f_n$  component of the rotational vibration at the same mesh frequency. In this figure, the results obtained using both H type gears and T type gears are plotted. Running conditions such as initial tooth bearing and transmitted torque are then changed. As a result, it is obvious that the rotational vibration caused by the spiral bevel gear meshing decreases as the real contact ratio increases. The dynamic load is significantly affected by this contact ratio. The increase in real contact ratio effectively decreases the rotational vibration of the spiral bevel gears.

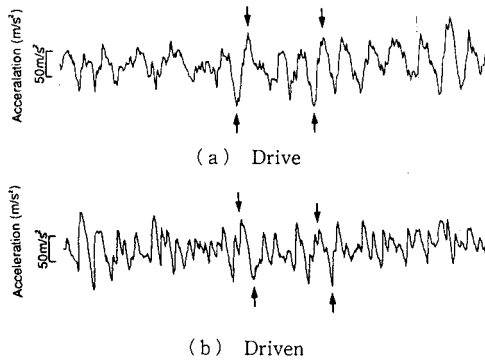


Figure 7 Rotational acceleration of drive and driven gear  
(Mesh frequency=500 Hz, torque=46.8 Nm)

### 3.4 Relative motion of drive and driven gears

Figure 7 shows the rotational accelerations of the drive and the driven gears when measured at the same time. A synchronous motion occurs, and the relative angular displacements between two gears indicate the coupled mode (as arrows show in the Figure), maintaining the constant rotating motion. Thus, it is considered that the equations of motion for the single degree-of-freedom, such as spur or helical gears, can also be established for spiral bevel gears.

## 4. MODELING AND ANALYSIS

### 4.1 Modeling

Rotational accelerations caused by the dynamic load of meshing are attracted attention in normal speed operations. As shown in Figure 5, the damping of vibration occurs sufficiently if the mesh frequency is sufficiently lower than the natural frequency. Thus, the equivalent equation of spiral bevel gears by means of cylindrical gears is indicated as Equation (1).

$$M\ddot{X} + C\dot{X} + KX = 0 \quad (1)$$

Here,

X: relative angular displacement between the drive gear and the driven gear.

C: damping between the meshing gear teeth

M: equivalent mass moment of inertia of the two mating gears

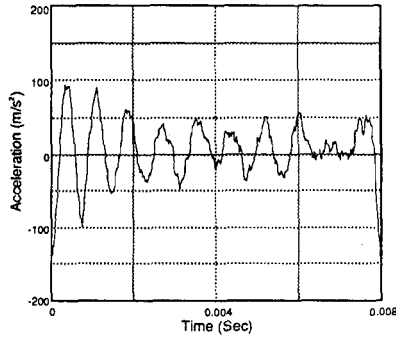
K: mesh stiffness

Then the stiffness for the axial tooth profile can be obtained by the finite elemental method. The mean value  $k_0$  is used for calculation, because the mesh stiffness is varied at each meshing point.

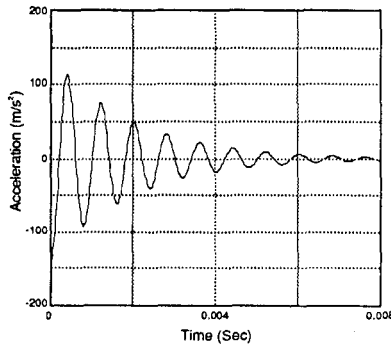
Here, the natural frequency ( $f_n$ ) based on the above model is presented by Equation (2)

$$f_n = (1/2\pi) \times \sqrt{k_0/M} \quad (2)$$

The frequency calculated with this model is 1400 Hz by this model. As can be seen in Fig. 4(b), 1350 Hz is considered the natural frequency of this gear system in experiments.



(a) Rotational acceleration



(b) Simulation

Figure 8 Comparison of experiment and simulation  
(Mesh frequency=125 Hz, torque=4.68 Nm)

Accordingly, it is found that the calculated values using this equivalent equation are in good agreement with the experimental ones.

#### 4.2 Analysis

In general, it is difficult to obtain the damping  $C$  by the theoretical method. Thus, we assume that the damping  $C$  is a logarithmic decrement such as Equation (3).

$$C = 2\zeta \times \sqrt{k/M} \quad (3)$$

Here,  $\zeta$  is the critical damping ratio, and  $\zeta$  is 0.065, because it is considered the same one of helical gears.

As can be seen in Fig. 5 (a), the large acceleration occurs at the initial point of single tooth contact, where double tooth contact varies to single tooth contact. The angular displacements at this are therefore used as the initial values of Equation (1).

Figure 8 (a) and (b) show the experimental and the calculated result, respectively. As regards the motion caused by the dynamic load of spiral bevel gears, they are good agreement. Thus, it is indicated that the application of the equivalent equation of cylindrical gears makes it feasible to predict the motion of spiral bevel gears.

## 5. CONCLUSION

1. The rotational vibration of the spiral bevel gears has a significant effect on the vertical vibration in the gear housing.
2. The large vibration in rotation occurs at the initial meshing where double tooth contact changes to single tooth contact.
3. The increase in the real contact ratio is effectively decreases the rotational vibration of spiral bevel gears.
4. It is possible to predict the rotational accelerations caused by the dynamic load of meshing in normal speed operations using the free vibration to model the rotational motion of spiral bevel gears by means of equivalent spur gears.

## REFERENCES

- (1) H-H. Lin, R. L. Huston and J. J. Coy, "On Dynamic Loads in Parallel Shaft Transmissions: Part 1 Modeling and Analysis", ASME Journal of Mechanisms, Transmissions, and Automating in Design, Vol. 110, June, 1988, p221
- (2) H-H. Lin, R. L. Huston and J. J. Coy, "On Dynamic Loads in Parallel Shaft Transmissions: Part 2 Parameter Study", ASME Journal of Mechanisms, Transmissions, and Automating in Design, Vol. 110, June, 1988, p226
- (3) A. S. Kumar, M. O. M. Osman and T. S. Sankar, "On Statistical Analysis of Gear Dynamic", ASME Journal of Vibration, Acoustics, Stress, and Reliability in Design, Vol. 108, July 1986, p362
- (4) W. D. Mark, "The Generalized Transmission Error of Spiral Bevel", ASME Journal of Mechanisms, Transmissions, and Automating in Design, Vol. 109, June 1987, p275
- (5) W. D. Mark, "The Generalized Transmission Error of Spiral Bevel", ASME Journal of Mechanisms, Transmissions, and Automating in Design, Vol. 109, June 1987, p275
- (6) Wells Coleman, "Effect of Mounting Displacements on Bevel and Hypoid Gear Tooth Strength", SAE Technical paper 750151, 1975
- (7) H. Winter and M. Paul, "Influence of Relative Displacements Between Pinion and Gear on Tooth Root Stresses of Spiral Bevel Gears", ASME Journal of Mechanisms, Transmissions, and Automating in Design, Vol. 107, March 1985, p43
- (8) G. D. Bibel, A. Kumar, S. Reddy and R. Handschuh, "Contact Stress Analysis of Spiral Bevel Gears Using Finite Element Analysis", ASME Journal of Mechanical Design, Vol. 117, June 1995, p235
- (9) R. J. Drago and F. W. Brown, "The Analytical and Experimental Evaluation of Resonant Response in High-Speed, Lightweight, Highly Loaded Gearing", ASME Journal of Mechanical Design, Vol. 103, April 1981, p346

*This page intentionally left blank*



Rub

*This page intentionally left blank*

# Theoretical investigations on disc-brake squeal noise

I L M AHMED, P S LEUNG, and P K DATTA

School of Engineering, University of Northumbria at Newcastle, UK

## ABSTRACT

The squeal noise of the brake is a significant problem in vehicles and it has not been solved satisfactorily until recently. It is well known that a squealing brake is more effective than the non-squealing one. However, decreasing this squeal noise during braking is very important for the comfort in driving. A multi-degree-of-freedom mathematical model has been developed to study the effect of different parameters on the brake squeal noise. The model has taken such factors as the distance between clamping bolts of the caliper, the width and thickness of the friction material, which were not included in previous work. The state-space equations developed have been solved using the program MATLAB. The program has been used in this study to calculate the complex eigenvalues, which indicate the natural frequencies and the instability of the system. It is evident from the analysis that squeal noise of the brake decreases with increasing distance between the clamping bolts of the caliper and with the increase in friction material thickness. However the squeal noise increases with increasing the width of the friction material.

## KEYWORDS:

Disc brake, brake squeal, friction material, instability, noise, friction, eigen frequency.

## 1 NOMENCLATURE

$r_i, r_o$	Inner and outer radius of the disc respectively.
$h$	Semi-thickness of the disc.
$\mu$	Coefficient of friction of the friction material.
$\rho, \rho_p$	Density of the disc and the pad respectively.
$E_d$	Young's modulus of the disc.

$M_d, M_p, M_c$	Mass of the disc, pad and the calliper respectively.
$I_d, I_p, I_c$	Moment of inertia of the disc, pad and the calliper respectively.
$x_d, x_p, x_c$	Displacements of the disc, pad and the calliper respectively.
$\theta_d, \theta_p, \theta_c$	Angles of rotation of the disc, pad and the calliper respectively.
$K_d, K_{L1}, K_{L2}$	Linear stiffness of the disc, the inner and the outer pad respectively.
$K_L$	Linear stiffness of the caliper.
$C_d, C_{L1}, C_{L2}$	Linear damping of the disc, the inner and the outer pad respectively.
$C_L$	Linear damping of the caliper.
$C_{Rd}, C_{R1}, C_{R2}$	Rotary damping of the disc, the inner and the outer pad respectively.
$C_R$	Rotary damping of the caliper.
$K_{Rd}, K_{R1}, K_{R2}$	Rotary stiffness of the disc, the inner and the outer pad respectively.
$K_R$	Rotary stiffness of the caliper.

## 2 INTRODUCTION

The theory of vehicle brake squeal noise attracted attention many years ago because of the complex dynamic problem during the duty of the brake. A number of issues have come to light to solve the problem of the brake squeal noise but it has not been solved yet. Moriaki (1) studied the low frequency brake groan that occurs due to the increase in the disc temperature. It was observed that the groan noise is an oscillatory phenomenon, which occurs from the effect of vibrations on the friction force between a disc and a pad during coupling of two rotational vibrations of a disc caliper. Nishiwaki (2) studied this squeal experimentally and theoretically by modifying the disc to eliminate brake squeal that occurred by self-excited vibration. The vibration modes during brake squeal generation at 6.32 kHz and 8.25kHz were visualized by Holographic Interferometry. However, the conventional disc vibrates at the maximum amplitude in the area excited artificially. Yasuaki (3) studied also the squeal of the disc brake experimentally by installing accelerometers on the back-plate of the pad. It was observed that the higher the coefficient of friction, the more the disc squeals. Bracken (4) used a brake dynamometer to study the same phenomena by knowing the intensity and duration of the squeal and also the frequency range of the squeal. Other variables to be controlled during the occurrence of the squeal like pressure, temperature, and speed ranges. Another point of view in dealing with the squeal was studied by Earles (5) who dealt with the squeal as not a serious problem considering that the squealing brake provides more effective braking than a non-squealing brake. A test rig was designed as an attempt to produce a system, which is more representative of a disc brake. It was concluded that increasing disc damping and allowing a decrease in disc stiffness would appear to produce the most benefit of decreasing the squeal noise generation. Millner (6) dealt with the squeal theoretically by studying the first eight disc mode instabilities for  $\mu$  (coefficient of friction) less than 0.5. The least value of linear stiffness of the caliper  $318 \text{ MNm}^{-1}$  to give instability was obtained at the third mode. The effect of negative friction-speed slope on the brake squeal was analyzed by Yongbin (7) who established a finite element model for the disc brake squeal. It was concluded that the brake squeal occurred due to the coupled vibrations of the brake system even if the negative  $\mu$ -speed slope doesn't exist. The squeal propensity increased with the friction level when the negative  $\mu$ -speed slope is absent. It was also that increasing the steel back-plate thickness and also lining thickness might reduce the squeal propensity.

In a separate piece of work a new system was developed to stop the squeals by Nishizawa (8). evaluating the electronic control canceling for the noise (ECCN) with the test vehicle. The

ECCN was installed in both front calipers of the test vehicle to stop the low frequency squeals (2-4KHz) by decreasing the rotor vibration electronically on both the noise dynamometer and the test vehicle. Thomas (9) studied the effect of the support stiffness and damping conditions on the measured modal parameters like frequencies and damping ratios. It was realized that the increase of the measured frequency of the supported system was related to the square of the frequency ratio of the rigid body mode and the elastic mode.

It is clear then from those issues that; there was no recommendation for reducing the squeal of the disc brake. The designed model has taken such factors as the distance between clamping bolts of the caliper width and thickness of the friction material, which were not included in the previous work. These factors might affect the disc brake squeal noise.

### 3 MATHEMATICAL MODEL OF THE DISC BRAKE SQUEAL NOISE.

It is well known for the floating caliper disc brake type that the piston of the caliper presses on the inner pad towards the rotor and the supporting bolts of the caliper push the outer pad towards the rotor as a reaction force. So, there is a lag between the two pads to press on the rotor and it is assumed that the forces occur at the same time and it is fully contact between the pads and the rotor during this application. A theoretical 8-degree of freedom mathematical model has been developed in this study depending on the theoretical model of North (10) and Millner (6). Other assumptions was made in the model including:

- 1- The disc has two degrees of freedom, one in the x-axis direction and the other around the y-axis direction.
- 2- The pads have two degrees of freedom, the first one in the x-axis direction and the other one around the y-axis direction.
- 3- The piston moves in the x-axis direction to the caliper.
- 4- The contact forces  $F1$  and  $F2$  are parallel to the face of the rotor and will be activated during the contact between the pads and the rotor.
- 5- It is also assumed that the rotor and the pads vibrate in the same mode.

Based on Newton's second law, the equations of motion of the disc brake in figure (1) can be written as:

$$M_d \cdot \ddot{x}_d + C_{L1} \cdot (\dot{x}_d - \dot{x}_{p1}) + K_{L1} \cdot (x_d - x_{p1}) + K_d \cdot x_d + C_d \cdot \dot{x}_d + C_{L2} \cdot (\dot{x}_d - \dot{x}_{p2}) + K_{L2} \cdot (x_d - x_{p2}) + F1 \cdot \theta_d + F2 \cdot \theta_d = 0 \quad (1)$$

$$I_d \cdot \ddot{\theta}_d + C_{R1} \cdot (\dot{\theta}_d - \dot{\theta}_{p1}) + K_{R1} \cdot (\theta_d - \theta_{p1}) + K_{Rd} \cdot \dot{\theta}_d + C_{Rd} \cdot \dot{\theta}_d + C_{R2} \cdot (\dot{\theta}_d - \dot{\theta}_{p2}) + K_{R2} \cdot (\theta_d - \theta_{p2}) + F2 \cdot h + F1 \cdot h = 0 \quad (2)$$

$$M_{p1} \cdot \ddot{x}_{p1} + C_{pL1} \cdot (\dot{x}_{p1} - \dot{x}_d) + K_{pL1} \cdot (x_{p1} - x_d) + C_{cL1} \cdot (\dot{x}_{p1} - \dot{x}_c) + K_{cL1} \cdot (x_{p1} - x_c) = 0 \quad (3)$$

$$I_{p1} \cdot \ddot{\theta}_{p1} + C_{R1} \cdot (\dot{\theta}_{p1} - \dot{\theta}_d) + K_{R1} \cdot (\theta_{p1} - \theta_d) + C_{R1} \cdot (\dot{\theta}_{p1} - \dot{\theta}_c) + K_{R1} \cdot (\theta_{p1} - \theta_c) - F1 \cdot d + F3 \cdot d = 0 \quad (4)$$

$$M_{p2} \cdot \ddot{x}_{p2} + C_{L2} \cdot (\dot{x}_{p2} - \dot{x}_d) + K_{L2} \cdot (x_{p2} - x_d) + C_L \cdot (\dot{x}_{p2} - \dot{x}_c) + K_L \cdot (x_{p2} - x_c) = 0 \quad (5)$$

$$I_{P2} \cdot \ddot{\theta}_{P2} + C_{R2} \cdot (\dot{\theta}_{P2} - \dot{\theta}_d) + K_{R2} \cdot (\theta_{P2} - \theta_d) + C_{R2} \cdot (\dot{\theta}_{P2} - \dot{\theta}_C) + K_{R2} \cdot (\theta_{P2} - \theta_C) + F2 \cdot d = 0 \quad (6)$$

$$M_C \cdot \ddot{x}_C + C_{L1} \cdot (\dot{x}_C - \dot{x}_{P1}) + K_{L1} \cdot (x_C - x_{P1}) + K_L \cdot x_C + C_L \cdot \dot{x}_C + C_{L2} \cdot (\dot{x}_C - \dot{x}_{P2}) + K_{L2} \cdot (x_C - x_{P2}) - F1 = 0 \quad (7)$$

$$I_C \cdot \ddot{\theta}_C + C_{R1} \cdot (\dot{\theta}_C - \dot{\theta}_{P1}) + K_{R1} \cdot (\theta_C - \theta_{P1}) + K_R \cdot \theta_C + C_R \cdot \dot{\theta}_C + F3 \cdot b = 0 \quad (8)$$

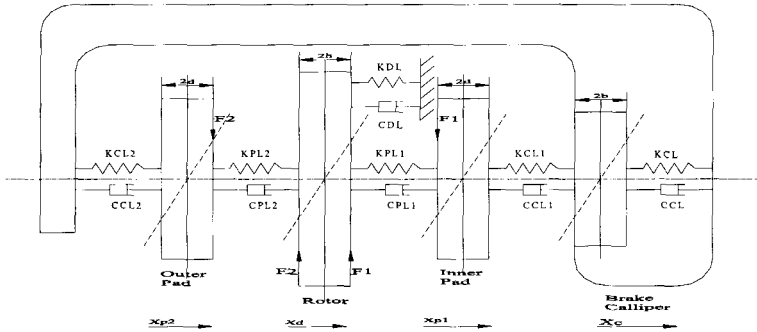


**Fig. (1) Theoretical 8-degree-of-freedom mathematical model**

Where  $F1 = \mu \cdot R1 = \mu \cdot [F_{st} + C_{L1} \cdot (\dot{x}_d - \dot{x}_{P1}) + K_{L1} \cdot (x_d - x_{P1})]$  (9)

$$F2 = \mu \cdot R2 = \mu \cdot [F_{st} + C_{L2} \cdot (\dot{x}_d - \dot{x}_{P2}) + K_{L2} \cdot (x_d - x_{P2})] \quad (10)$$

$$F3 = \mu \cdot R3 = \mu_b \cdot [F_{st} + C_{L1} \cdot (\dot{x}_C - \dot{x}_{P1}) + K_{L1} \cdot (x_C - x_{P1})] \quad (11)$$

The equations from (1) to (8) can be rewritten in the form of:

$$\ddot{x} + (c/m) \cdot \dot{x} + (k/m) \cdot x = 0 \quad (12)$$

$$\ddot{x} + 2 \cdot \zeta \cdot \omega_n \cdot \dot{x} + \omega_n^2 \cdot x = 0 \quad (13)$$

Where  $\omega_n$  is the natural frequency of the system.

$\zeta$  is the damping ratio or viscous damping factor and equal to  $\zeta = c/2 \cdot m \cdot \omega_n$

We assume the solutions of the form

$$x_d = A_d \cdot e^{\lambda t}$$

$$\theta_d = B_d \cdot e^{\lambda t}$$

$$x_{p1} = C_{p1} \cdot e^{\lambda t}$$

$$\theta_{p1} = D_{p1} \cdot e^{\lambda t}$$

$$x_{p2} = E_{p2} \cdot e^{\lambda t}$$

$$\theta_{p2} = F_{p2} \cdot e^{\lambda t}$$

$$x_c = G_c \cdot e^{\lambda t}$$

$$\theta_c = H_c \cdot e^{\lambda t}$$

And by substitution in the main equation, the characteristic equation can be expressed in the following form:

$$\lambda^2 + 2 \zeta \omega_n \lambda + \omega_n^2 = 0 \quad (14)$$

and the roots of this equation are

$$\lambda_1 = \omega_n \cdot (-\zeta + \sqrt{\zeta^2 - 1}) \quad \text{And} \quad \lambda_2 = \omega_n \cdot (-\zeta - \sqrt{\zeta^2 - 1})$$

and now, we have three categories of damped motion:

- 1- If  $\zeta > 1$  (over-damped) the roots will be negative real numbers and the system will decay without oscillation for a long period.
- 2- If  $\zeta = 1$  (critically damped) the roots will be negative real numbers equals to  $-\zeta\omega_n$  and the solution will be in the form  $x = (A_1 + A_2 t) \cdot e^{-\omega_n t}$ . The system will decay in relating long time and the motion will be non-periodic.
- 3- If  $\zeta < 1$  (under-damped) the system will decay in a short time and the solution will be in the form of  $x_d = A_d e^{-\zeta\omega_n t} \sin(\omega_d t + \psi)$  where  $\omega_d = \omega_n \cdot (1 - \zeta^2)^{1/2}$

#### 4 RESULTS

Generally, disc brake squeal is caused by the unstable vibrations of the brake system and to know if the brake system will squeal or not, it is possible to check the stability by applying a Matlab program. This program has the ability to carry out the eigenvalue analysis that can indicate the instability level and the natural frequency which the corresponding eigenvalue problem will be in the form of  $\det([A] - \lambda[I]) = 0$ . Each eigenvalue  $\lambda$  is a complex number that contains two parts. The first part is real and the second part is imaginary. If the real part is negative, this indicates that the mode is damped and stable but in some cases the real part will be positive, it means that the mode is not stable and the damping is negative.

From the eigenvalues, the instability levels and the eigenfrequencies are calculated. The instability level (degree of instability) is defined as the real part of the eigenvalue  $\alpha = \text{Re}[\lambda]$  and the eigenfrequency is defined as the imaginary part of the eigenvalue  $\omega = \text{Im}[\lambda]$  rad/sec. Some authors took the instability level as a squeal propensity and others don't. In this work the squeal propensity ( $\sigma$ ) that is the squeal index will be taken as  $\sigma = (\alpha^2 + \omega^2)^{1/4} \cdot \sin(\delta/2)$  as Millner's (6) assumption and the results agree with it. The eigen frequencies will be taken as  $\omega/2\pi$  Hz. Where  $\delta$  is the phase angle and equal to  $\arctan(\omega/\alpha)$ .

The data of the disc brake used in the numerical work is that:

	Mass (kg)	Density (kg/m <sup>3</sup> )	Outer radius (m)	Inner radius (m)	Poisson's ratio	Thickness (m)	Width (m)	$\mu$
Rotor	3.4	7800	0.107	0.063	0.27	0.012	-	-
Friction material	0.194	3000	-	-	0.23	0.0154	0.031	0.42

**Table (1) The disc brake data**

The equations of motion (1-8) can be rearranged into a matrix form as in the appendix and can be solved by using the state space method in the form of:

$$\dot{x} = Ax + Bu. \quad (15)$$

$$y = Cx + Du. \quad (16)$$

Where

$A$  is the System  $16 \times 16$  matrix (in the appendix).

$B$  is the Input  $16 \times 1$  matrix (in the appendix).

$C$  is the Output  $8 \times 16$  matrix (in the appendix).

$x$  is the System State  $16$ -vector.

$u$  is the Input vector.

## 5 DISCUSSION OF THE RESULTS

Figure (2A) indicates the effect of the Young's modulus of the rotor on brake squeal noise and degree of instability. The modulus of elasticity of the brake rotor was increased from 50 to 200 GN/m<sup>2</sup>. It can be noted from the figure that as the young's modulus of the rotor increases the squeal index decreases till a certain limit then increases again with the increase in the modulus of elasticity of the rotor to give the best value between 80 and 120 GN/m<sup>2</sup>. Further increase of Young's modulus to 200 GN/m<sup>2</sup> only increases the squeal index slightly. The maximum squeal 141 sec<sup>-1</sup> happened with a low modulus of elasticity and the best value of squeal was between 90 and 92 sec<sup>-1</sup> between 80 and 120 MN/m<sup>2</sup>. The maximum frequency reached in this case was 6308 Hz as indicated from (2B) with the maximum instability of 150 (Real Part) as in figure (2A). Figure (3A) indicates the effect of the Young's modulus (50-1200 MN/m<sup>2</sup>) of the friction material on brake squeal noise and degree of instability. The figure shows that as the young's modulus of the friction material increases the squeal index increases. The maximum squeal 243 sec<sup>-1</sup> occurred at a high modulus of elasticity of 1200 MN/m<sup>2</sup> and the best value of squeal was between 199 sec<sup>-1</sup> with a low modulus of elasticity of 50 MN/m<sup>2</sup>. The maximum frequency reached in this case was 10548 Hz as indicated in figure (3B) with the maximum instability of 64 (Real Part) as in figure (3A).

Figure (4A) indicates the effect of the caliper stiffness on brake squeal noise and degree of instability. The figure indicating that as the calliper stiffness increases the squeal index increases. The maximum squeal was 190 sec<sup>-1</sup> at a high caliper stiffness of 600 MN/m<sup>2</sup>. The maximum frequency reached in this case was 11531 Hz as indicated in figure (4B) with the maximum instability of 60 (Real Part) as in figure (4A). It is cleared from the figure also that the changing in the value of the squeal during the using of caliper stiffness between 200 and 400 MN/m<sup>2</sup> was small with respect to the value between 200 KN/m<sup>2</sup> and 200 MN/m<sup>2</sup>. When the semi-distance between the clamping bolts of the caliper increased from 30 to 70 mm figure (5A) the squeal index decreased to give the best value of the squeal at semi-distance between 50 and 70 mm. The minimum value of the squeal index was 222 sec<sup>-1</sup> at semi-distance Of 70 mm with a frequency of 2721 Hz. The problem in non-choosing the bigger semi-distance between the clamping bolts of the caliper that will affect the size of the caliper and the weight as well.

Figure (6A) shows that as the thickness of the rotor increases the squeal index decreases till a certain limit then increases again with the increase in thickness of the rotor to give the best value between 10 and 12 mm. The maximum squeal 140 sec<sup>-1</sup> happened with a thinner rotor of thickness 8mm. The maximum frequency reached in this case was 6337 Hz as indicated in



figure (6B) with the maximum instability of 130 (Real Part) as in figure (6A). It can be seen from figure (7A) that as the thickness of the friction material increases the squeal index decreases to give the best value at 11.5 mm. The maximum squeal was  $183 \text{ sec}^{-1}$  corresponding to a friction material of thickness 7.5 mm and the lowest squeal index was  $170 \text{ sec}^{-1}$  with a friction material thickness of 11.5 mm. The maximum frequency reached in this case was 4100 Hz as indicated in figure (7B) with the maximum instability of 45 (Real Part) as in figure (7A). The problem in controlling the thickness of the friction material is the size of the friction material itself and the weight as well plus the cost. Figure (8A) indicates that as the width of the friction material increases the squeal index increases. The best value of squeal was  $89 \text{ sec}^{-1}$  a friction material width between 20 and 30 mm and after this width it give unacceptable value of squeal. The maximum frequency reached in this case was 6925 Hz as indicated in figure (8B) with the maximum instability of 142 (Real Part) as in figure (8A).

It was realized from this theoretical analysis that there are some parameters, which affect the squeal index and degree of instability of the system. Choosing the appropriate specifications of the disc brake like mass, young's modulus, stiffness and dimensions of the brake might be useful to get the suitable squeal index and instability of the brake. For example, increasing the semi-distance between the clamping bolts of the calliper will improve the instability of the brake but on the other hand it will affect the calliper stiffness and also the mass of the calliper. Thickness of the friction material will decrease on the long term because of the wear and this will affect on the mass of the friction material and the also the stiffness as seen in figure (7). For the reason mentioned earlier, increasing the width of the friction material also will affect the mass of the pad and the volume of the brake; hence it will affect the cost of the brake. So, it is better to take the average of the parameters which achieve decrease of the instability and increase of the brake performance.

## 6 CONCLUSIONS

It is clear from this study that brake squeal noise is a big problem in the car particularly on the comfort of the passengers in the vehicle. Different parameters were used in this investigation to study the effect of changing of these parameters on the brake squeal like the Young's modulus of the rotor and the friction material and also the thickness of the rotor and the friction material as well. Different parameters were also taken into account in studying the squeal of the brake like the semi-distance between the clamping bolts of the caliper and the stiffness of the caliper as well and the conclusions of these investigations are:

- 1- Increasing the Young's modulus of the rotor will affect the system behavior and the best value of the Young's modulus between 80 and  $120 \text{ GN/m}^2$  that give the lowest value of the squeal noise and frequency.
- 2- Increasing the Young's modulus of the friction material will increase the squeal index noise of the brake system.
- 3- Increasing the semi-distance between the clamping bolts of the caliper will decrease the squeal index noise of the brake system and also will decrease the degree of instability of the brake system. The problem is, increasing this distance will increase the size of the caliper and the weight as well.
- 4- Increasing the thickness of the friction material will decrease the instabilities in the brake system. Decreasing of the friction material thickness will occur due to the wear resulting from the contact and friction with the rotor.

## 7 ACKNOWLEDGEMENTS

This work was carried out at School of Engineering, University of Northumbria at Newcastle, United Kingdom. We would like to thank our families during this work.

## 8 REFERENCES

- 1- Moriaki Gouya, and Massaki Nishiwaki "Study on Disc Brake Groan: SAE, No. 900007, pp 16-22, 1990.
- 2- Masaaki Nishiwaki, Hiroshi Harada, Hiromasa Okamura, and Takahiro Ikeuchi "Study on Disc Brake Squeal" SAE, No. 890864, pp 980-989, 1989.
- 3- Yasuaki Ichiba, and Yuji Nagasawa "Experimental Study on Disc Brake Squeal" SAE, No. 930802, pp 1227-1234, 1993.
- 4- William J. Bracken and Johnny K. Sakioka "A Method for the Quantification of Front Brake Squeal" SAE, No. 820037, pp 142-149, 1982.
- 5- Earles S.W., and Chambers P.W. "Disc Brake Squeal- some factors which influence its occurrence" IMechE, C454/88, pp 39-46, 1988.
- 6- Millner, N. "An Analysis of Disc Brake Squeal." SAE, No. 780332, 1978.
- 7- Yongbin Yuan "A Study of the Effects of Negative Friction-Speed Slope on Brake Squeal" ASME, DE-Vol. 84-1, Design Engineering Technical Conferences, Volume 3-Part A, 1995.
- 8- Yukio Nishizawa, Hironobu Saka, Shiro Nakajima, and Takeo Arakawa "Electronic Control Canceling System for a Disc Brake Noise" SAE, No. 971037, pp 83-88, 1997.
- 9- Thomas G. Carne, and Clark R. Dohrmann "Support Conditions, Their Effect on Measured Modal Parameters" Proceedings of the 16<sup>th</sup> International Modal Analysis Conference- Santa Barbara-California IMAC-1998 volume I.
- 10- North M.R. "Disc Brake Squeal- A Theoretical Model" MIRA Report, No. 1972/5.

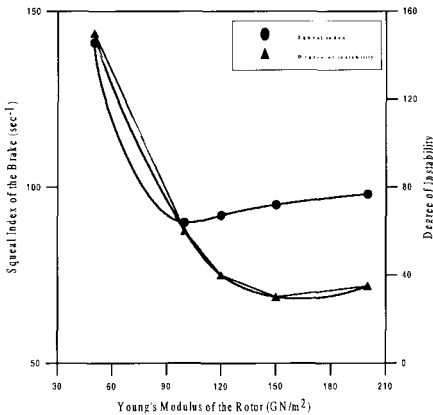


**Fig. (2A) Effect of Young's modulus of brake rotor on brake squeal noise and degree of instability.**

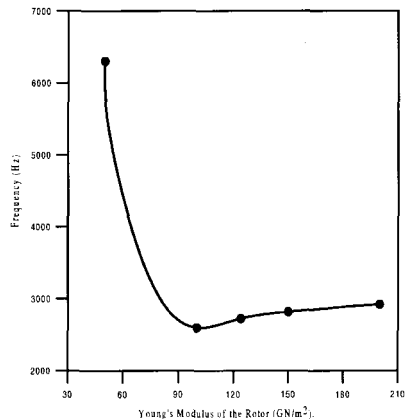


**Fig. (2B) Effect of Young's modulus of brake rotor on frequency of the brake.**

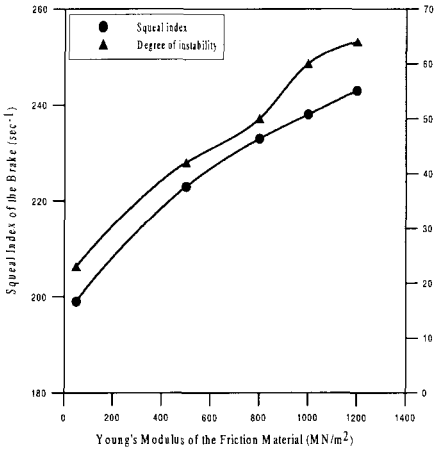


**Fig. (3A) Effect of Young's modulus of friction Material on brake squeal noise and degree of instability**

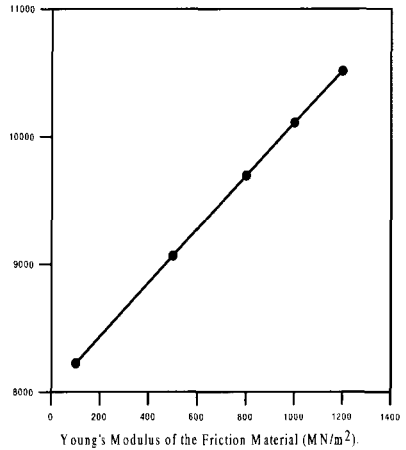


**Fig. (3B) Effect of Young's modulus of friction material on frequency of the brake.**

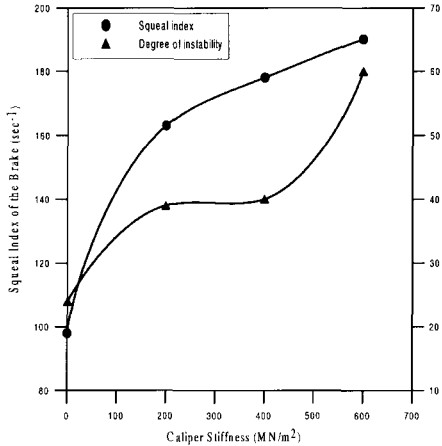


**Fig. (4A) Effect of caliper stiffness on brake squeal noise and degree of instability.**

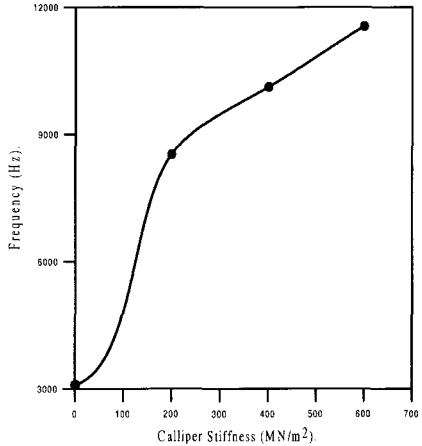


**Fig. (4B) Effect of caliper stiffness on frequency of the brake.**

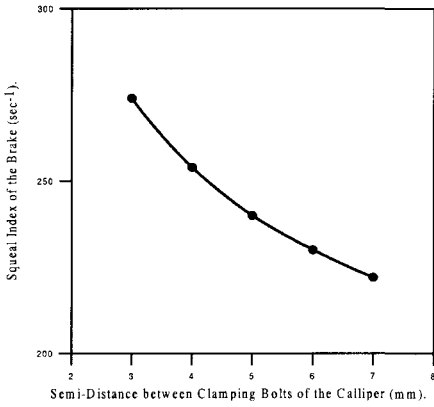


**Fig. (5A) Effect of semi-distance between clamping bolts of caliper on brake noise.**

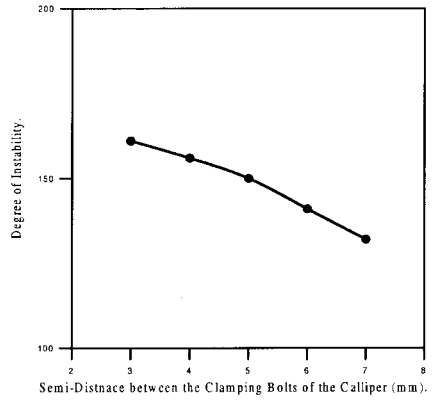


**Fig. (5B) Effect of semi-distance between clamping bolts of caliper on degree of instability.**

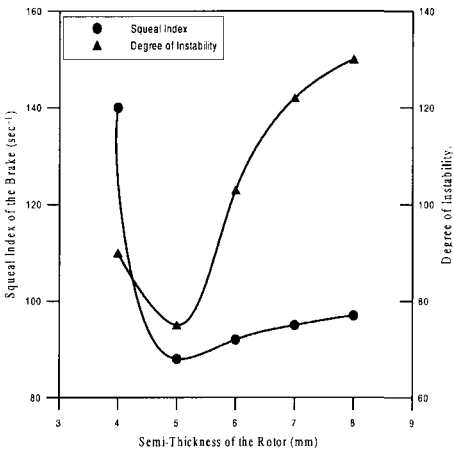


**Fig. (6A) Effect of semi- thickness of brake rotor on brake squeal noise and degree of instability.**

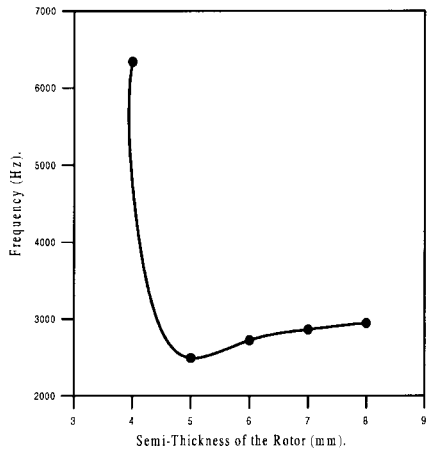


**Fig. (6B) Effect of semi-thickness of brake rotor on frequency of the brake.**

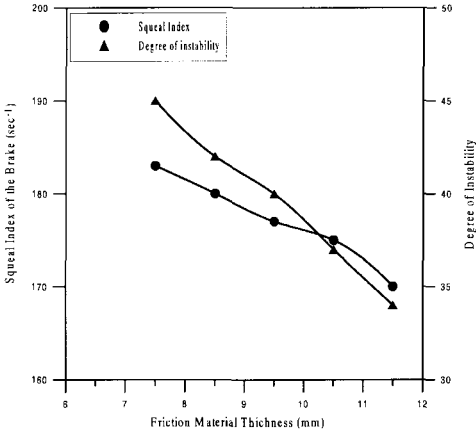


**Fig. (7A) Effect of friction material thickness on brake squeal noise and degree of instability.**

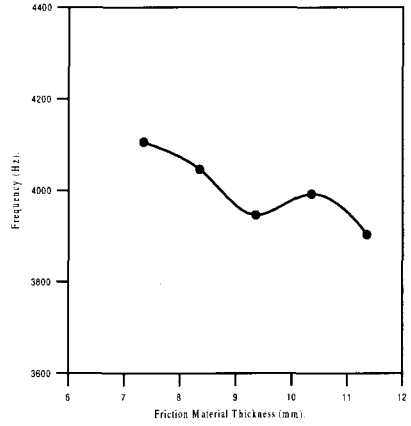


**Fig. (7B) Effect of friction material thickness on frequency of the brake.**

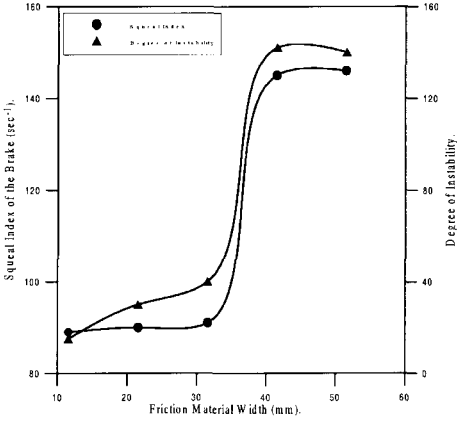


**Fig. (8A) Effect of friction material width on brake squeal noise and degree of instability.**

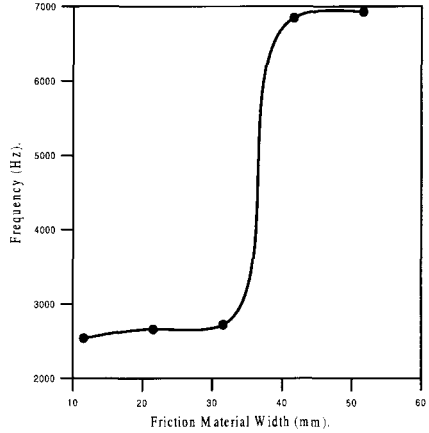


**Fig. (8C) Effect of friction material width on frequency of the brake.**

## APPENDIX (including MATLAB program)

```
% THE DISC BRAKE SQUEAL OF THE MATHEMATICAL MODEL.
MD=3.4; % mass of the disc in kg
MP1=0.1945; % mass of the inner pad in kg
MP2=0.1945; % mass of the outer pad in kg
MC=1.80; % mass of the calliper in kg
L=0.04675; % semi-length of the pad in m
b=0.03155; % width of the pad in m
t=0.01035; % thickness of the friction material in m
ro=0.107; % outer diameter of the disc in m
ri=0.063; % inner diameter of the disc in m
H=0.006; % semi-thickness of the disc in m
d=0.007675; % semi-thickness of the pad in m
u=0.0508; % semi-distance between clamping bolts of the calliper in m
up=0.27; % poisson Ratio
MU=0.42; % Coefficient of friction of the disc
MUB=0.35; % Coefficient of the friction at rubbing surface, backplate
n=3; % number of disc nodal diameter
p1=7800; % disc density in kg/m3
Ed=124e+09; % Youngs modulus of the disc in N/m2
Ep1=1e+09; % Youngs modulus of the inner pad in N/m2
Ep2=1e+09; % Youngs modulus of the outer pad in N/m2
FS=3000; % Steady state normal force acting on the the pad in N
F=1e+05; % pressure acting on the pad in N/m2
IC=(MC*u^2)/3; % Moment of inertia of the calliper
IP1=(MP1*L^2)/3; % Moment of inertia of the inner pad
IP2=(MP2*L^2)/3; % Moment of inertia of the outer pad
G1=(a*(MUB*b-a));
G2=(G1*MC)-IC;
G=(G2*IP1*MP1)-((a^2)*IC*MC*MP1)-(IP1*MC*IC); % Millner's constant.
a0=((ri^2*((ri/(3*ro))-1)^2)*(1-(n^2))^2); % Millner's constant.
a1=(2*ri*((ri/(3*ro))-1)*(1-(n^2))*(2*(1+up)-(n^2))); % Millner's constant.
a2=(1/2)*(((4-(n^2))^2)+((2*ri)/ro)*((ri/(3*ro))-1)*(1-(n^2))*(((n^2)/3)-3)-2*(1-up)*4-
(3*(n^2))-((2*ri)/ro)*((ri/(3*ro))-1)*(1-(n^2))); % Millner's constant.
a3=(2/3)*(((n^2/3)^3*(4*n^2)+(2*(1-up)*(3-(2*n^2)))); % Millner's constant.
a4=(1/4)*(((n^2/3)-3)^2+(4*(1-up)*(5*n^2/9)-1)); % Millner's constant.
k1=((ro^8)-(ri^8))/(72*(ro^2))-((2*(ro^7)-(ri^7))/(21*ro))+1-
(2*(ri/(3*ro))*((ri/(3*ro))-1))*((ro^6)-(ri^6))/6+(2*ri/5)*((ri/(3*ro))-1)*(ro^5)-
(ri^5))+((ri^2/4)*((ri/(3*ro))-1)^2)*((ro^4)-(ri^4)); % Millner's constant.
k2=(a4*(ro^4)-(ri^4))/(ro^2)+(a3*(ro^3)-(ri^3))/ro+(a2*(ro^2)-(ri^2))+a1*(ro-ri)+
(a0*log(ro/ri)); % Millner's constant.
DD=((Ed*H^3)/(3*(1-up^2))); % Flexural stiffness of the disc
wm=((DD*k2)/(p1*H*k1))^1/2; % natural frequency of the disc
KDL=(wm^2*MD); % Linear stiffness of the disc in N/m
ID=((ri+ro)^2*MD)/(4*n^2); % Moment of inertia of the disc about the axis parallel
to disc face in kg.m2
KDR=(wm^2*ID); % Rotary stiffness of the disc in N/m
KPL1=((2*Ep1*b*L)/t); % Linear stiffness of the inner pad in N/m
KPL2=((2*Ep2*b*L)/t); % Linear stiffness of the outer pad in N/m
KPL1=KPL2;
KPR1=((Ep1*b*L^2)/t); % Rotary stiffness of the inner pad in N/m
KPR2=((Ep2*b*L^2)/t); % Rotary stiffness of the outer pad in N/m
KPR1=KPR2;
KCL1=20e+03*20000; % Linear stiffness of the calliper in N/m
KCL2=20e+03*20000; % Linear stiffness of the calliper in N/m
KCL=20e+03*20000; % Linear stiffness of the calliper in N/m
KCL=KCL1;
KCL1=KCL2;
KCR=((u*KCL)/2); % Rotary stiffness of the calliper in N/m
KCR1=((u*KCL1)/2); % Rotary stiffness of the calliper in N/m
KCR2=((u*KCL2)/2); % Rotary stiffness of the calliper in N/m
KCR=KCR1;
KCR1=KCR2;
CDL=100; % Linear damping of the disc.
CDR=10; % Rotary damping of the disc.
CPL1=10; % Linear damping of the inner pad.
CPL2=10; % Linear damping of the outer pad.
CPL1=CPL2;
CPR1=(CPL1*L^2)/3; % Linear damping of the inner pad.
CPR2=(CPL2*L^2)/3; % Linear damping of the outer pad.
A2B1=-((KPL1+KPL2+KDL)/MD);
A2B2=-((CPL1+CPL2+CDL)/MD);
A2B3=-((2*MU*FS)/MD);
A2B5=KPL1/MD;
```



*This page intentionally left blank*



## Spiral vibrations in rotors due to a rub

**N BACHSCHMID** and **P PENNACCHI**

Dipartimento di Meccanica, Politecnico di Milano, Italy

**P VENINI**

Dipartimento di Meccanica Strutturale, Università degli studi di Pavia, Italy

### ABSTRACT

Spiral vibrations may develop in rotor systems when a full annular rub occurs. The rub on a stationary fixed thin seal ring is considered in this paper. A rather refined model for the thermal behaviour is presented, the thermal bow is calculated by an approximated method which has been validated by comparison with results of a 3D finite element model, and the vibrational behaviour of the rotor has been calculated by means of a traditional finite beam element model, in which the bow is represented by an equivalent bending moment distribution, and the contact force by a rotating external force. The normal contact force has been modelled in this first approach as a simple linear elastic force, due to the deformation of the seal, and the tangential force is simply the Coulomb friction force. The results allow to analyse deeper the stable and unstable behaviours of rubbing rotors, which are known from literature and field experience.

### 1 INTRODUCTION

A rub in rotating machinery occurs when the vibration amplitude in correspondence of a seal exceeds the clearance in the seal. The orbit of the shaft is then restricted within the clearance by the contact force with the seal. The rub may be a partial arc rub or a full annular rub. During partial arc rubs the contact force has a component of the impulse type and higher harmonic components may be generated in the vibration of the shaft and of the casing. Due to the change of the stiffness which is experienced by the shaft during one rotation when it is in contact with the casing or not, the rotor has variable stiffness parameters, and therefore also sub-harmonic components can arise.

When a full annular rub occurs, then the main symptom is the unsymmetrical heating of the shaft due to the friction force, which causes a bow to be superposed to the other exciting causes (such as unbalances a.s.o.), and consequently a change in the resulting vibration

vector. In a polar plot of the vibration vector one could see the extremity of the vibration vector moving slowly on a spiral path.

The vibration vector (which is usually measured in the bearings of the machine) rotates slowly generally in opposite direction with respect to the rotation of the shaft, and its amplitude increases or decreases, depending on the rotating speed of the shaft (with respect to the critical speeds) and on the value of the ratio of the rub introduced heat to the heat which is dissipated along the rotor.

In heavy machines like turbogenerators in power plants these spiral vibrations are the most common symptoms which are experienced during a rub.

Since more than 50 years the phenomenon of spiral vibrations has been observed and studied. A rather simple model was developed by Kellenberger (1), which derived two sets of coupled differential equations, one representing the thermal behaviour, which gives the time derivative of the bow as a function of the heat balance, and the other representing the dynamical behaviour of the rotor, modelled by a single degree of freedom system. Also the seal ring was represented as a single degree of freedom system, so that the contact force depends also from its dynamical behaviour. The coupling of the equations is represented by the fact that the severity of the rub (and therefore the introduced heat due to the contact force) is related also to the shaft vibration amplitude due to the developing thermal bow. As a solution of the equations the real eigenvalues indicate stable (decreasing) or unstable (increasing) spiral vibrations.

More recently other authors have analysed more deeply the behaviour of rubbing rotors, referring to Kellenberger's approach: in (2) the linear behaviour of real rotors with full annular rub is considered, and in (3) also the non-linear behaviour with partial rubs.

But the thermal behaviour is represented by an empirical relationship, which is probably unable to describe completely and exactly the transient development of the thermal bow. In (4) the complete heat equations are solved by Galerkin approximated method, by neglecting the heat conduction in axial direction, and the bow is then calculated by the temperature moment virtual work. But it seems that the axial heat flow is also important in determining the spiral vibration behaviour.

In this paper the thermal behaviour is described in detail by the complete 3D Fourier equations, which are integrated by a finite difference method, using a suitable time step. From the temperature distribution the thermal strains are calculated at each step, and therefrom the corresponding bow by means of an approximate approach which uses "equivalent" external bending moments. These rotating bending moments excite together with the original unbalance the vibrations of the rotor. The rotor is represented as usual by a finite beam element model. The influence of the developing bow on the rotor dynamic behaviour can be calculated in the frequency domain, at each time step, because the thermal transient has time constants which are several orders of magnitude higher than the time constants of the rotor vibrational transient.

## 2 DESCRIPTION OF THE METHOD AND OF THE CONTACT MODEL

The part of the rotor in which the heat is introduced and where it propagates is assumed to be cylindrical with constant diameter. The heat is introduced through nodes of the mesh, where the contact occurs, which form the so-called 'hot spot' (HS). The rubbing contact is assumed to develop in one cross section only, where a seal with a small clearance is placed, as shown in Figure 1. The temperature gradient in radial direction is very high and similarly in axial direction too. For a rather long time nothing noticeable happens at distances from the HS of

the same order of the radius, both in radial and in axial direction. This confirms that strain and stresses are high and concentrated in a small volume around the HS. A 'local bow' develops.

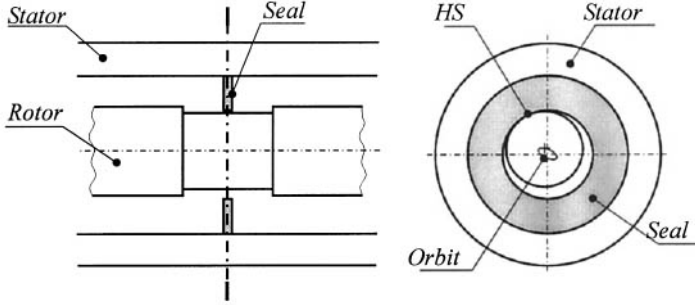


**Figure 1 Rubbing contact and hot spot (HS) position.**

Only after a rather long time, if the rotor continues rubbing, the gradient becomes lower and also the points that are not very close to the HS will be interested by a temperature transient. It should be also reminded that the HS migrates along the outer circumference, introducing heat from different points.

The heat developed in the seal (and in the stator) is not considered. The stator is considered as rigid and the seal as a spring of stiffness  $k_s$ , so that the normal contact force  $N$  is linearly dependent of the deflection  $\delta$  (deformation) of the seal. Also a non-linear contact force could easily be considered, if desired. The friction induced tangential force  $T$  is equal to  $\mu N$ , where  $\mu$  is the friction coefficient. The introduced heat in 1 second is:

$$W = \mu k_s \delta \frac{D}{2} \omega \quad (1)$$

where  $D$  is the diameter of the rotor in correspondence of the seal and  $\omega$  the rotational speed. Once the thermal behaviour has been studied, the bow and the equivalent bending moments can be calculated, which force the rotor to change its vibrations. The rotor is modelled as usual by means of finite elements. Close to the HS and symmetrically with respect to it, the same positions of the nodes in axial direction have been considered, in order to apply directly the equivalent bending moments.

The seal elastic deflection  $\delta$  is given by:

$$\delta = x_s - c \quad (2)$$

where  $x_s$  is the shaft vibration amplitude and  $c$  the clearance. If the orbit is elliptical, as in real machines due to ortotropic bearings, then  $x_s$  must be considered as a mean value between the major and the minor half axes which introduces the same heat in one revolution. In this application the harmonic components higher than the first are all neglected.

### 3 THE THERMAL BEHAVIOUR

Hereafter a few details are given on analytical and numerical issues regarding the treatment of the thermal part of the problem, leaving to upcoming sections a discussion on how thermal, mechanical and contact components merge together to fully define the rotor behaviour. The evolution of the temperature distribution clearly depends on the heat exchange modes

between the rotor and the surroundings as well as within the rotor itself. A widely accepted idealisation is as follows:

- pure heat conduction takes place in the interior of the rotor;
- the seal-rotor contact gives rise to a power generation that is modelled as a localised heat source for the rotor;
- convection takes place all over the skin of the rotor to account for interactions with the external environment.

By writing the Laplacian operator in cylindrical co-ordinates, one gets the well-known Fourier equation in the form:

$$\frac{\partial T}{\partial t} = \frac{K}{\rho \cdot C} \cdot \left( \frac{\partial^2 T}{\partial r^2} + \frac{\partial T}{r \cdot \partial r} + \frac{\partial^2 T}{r^2 \cdot \partial \vartheta^2} + \frac{\partial^2 T}{\partial z^2} \right) \quad (3)$$

where  $K$  is the thermal conductivity coefficient [W/m °C],  $\rho$  is the mass per unit volume [kg/m<sup>3</sup>],  $t$  the time [s],  $z$  the axial co-ordinate [m],  $r$  the radial co-ordinate [m],  $\vartheta$  the angular co-ordinate [rad],  $C$  is the specific heat [J/kg °C] and  $T$  [°C] is the temperature. An initial temperature distribution as well as boundary conditions as specified above should be coupled to the Fourier equation for the correctness of the problem.

The numerical solution of the Fourier PDE may be classically approached via well-consolidated finite-element schemes. For the purpose of this investigation, however, a finite-difference approach has been adopted, mainly to get an easier link to the other blocks of the simulating code. One should in fact recall that, for any given time instant, the Fourier equation is solved, the temperature gradients are used to derive the corresponding strains and eventually equivalent moments are computed that represent the input to a frequency-domain analysis providing amplitude and phase of the response, i.e. the rotor deflection.

Without entering details, it seems appropriate to show the discrete version of the Fourier equation that, after finite-differentiation and some algebra, reads:

$$\begin{aligned} T_n(r, \vartheta, z) = T_o(r, \vartheta, z) + D \cdot dt \cdot & \left[ \frac{T_o(r+1, \vartheta, z) - 2 \cdot T_o(r, \vartheta, z) + T_o(r-1, \vartheta, z)}{dr^2} + \right. \\ & + \frac{T_o(r+1, \vartheta, z) - T_o(r-1, \vartheta, z)}{r \cdot dr} + \frac{T_o(r, \vartheta+1, z) - 2 \cdot T_o(r, \vartheta, z) + T_o(r, \vartheta-1, z)}{r^2 \cdot d\vartheta^2} + \\ & \left. + \frac{T_o(r, \vartheta, z+1) - 2 \cdot T_o(r, \vartheta, z) + T_o(r, \vartheta, z-1)}{dz^2} \right] \end{aligned} \quad (4)$$

where  $D=K/\rho C$  is the thermal diffusivity coefficient,  $dt$  is the time step and  $T_n$  and  $T_o$  denote the new (unknown) and old (converged) values of the temperature respectively. Furthermore, notations such as  $r+1$  and similar denote the value of the relevant quantity (temperature) at an adjacent node. The discretised Fourier equation is written for all internal points of the rotor and coupled to the discrete boundary conditions giving rise to a linear system of equations having the current temperatures as unknowns.

Once the temperature distribution is evaluated, thanks to the isotropy of the rotor, standard thermo-mechanical relations are used to get the thermal strains as:

$$\begin{aligned} \varepsilon_r = \varepsilon_\vartheta = \varepsilon_z = \alpha \cdot (T - T_0) \\ \gamma_{xy} = \gamma_{yx} = \gamma_{zx} = 0 \end{aligned} \quad (5)$$

where  $\alpha$  is a material-dependent thermal expansion coefficient. Latter components of the strain tensor are then used to compute the stresses in the rotor by using standard isotropic elasticity relations as:

$$\begin{Bmatrix} \sigma_x \\ \sigma_y \\ \sigma_z \\ \tau_{xy} \\ \tau_{yz} \\ \tau_{zx} \end{Bmatrix} = \frac{E}{(1+\nu)(1-2\nu)} \begin{bmatrix} 1-\nu & \nu & \nu & 0 & 0 & 0 \\ & 1-\nu & \nu & 0 & 0 & 0 \\ & & 1-\nu & 0 & 0 & 0 \\ & & & \frac{1-2\nu}{2} & 0 & 0 \\ & & & & \frac{1-2\nu}{2} & 0 \\ & & & & & \frac{1-2\nu}{2} \end{bmatrix} \begin{Bmatrix} \epsilon_x \\ \epsilon_y \\ \epsilon_z \\ \gamma_{xy} \\ \gamma_{yz} \\ \gamma_{zx} \end{Bmatrix} \quad (6)$$

These are the stresses which would arise if appropriate constraints would prevent any elongation. The axial stress distribution allows to calculate an equivalent bending moment, which should generate similar strains and a similar overall deformation, as shown below.

The first step to determine the modulus  $M$  of that equivalent moment is to take into account the strains  $\epsilon$  given by eq. (5). A typical  $\epsilon_z$  axial strain distribution in the HS section is shown in Figure 2, in which also the generated bow and the radial elongations are emphasised. The axial strain distribution over the cross section is not linear and the cross sections subjected to the temperature gradient, due to the concentrated heating at the HS, are very much distorted.

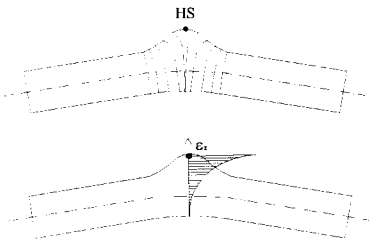


Figure 2 Strain  $\epsilon_z$  in the HS section.

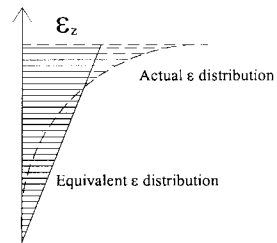


Figure 3 Equivalent  $\epsilon$  distribution.

This strain distribution, due to the thermal action, has to be modelled by mechanical loads, which should reproduce at least the resulting bow.

For the evaluation of the bow, the components  $M_x$  and  $M_y$  of the equivalent bending moment  $M$  are calculated separately, by considering the actual stress distribution over all the shaft sections:

$$\begin{aligned} M_x(z) &= \int_A \sigma_z \cdot b_x \cdot dA = \int_0^R \int_0^{2\pi} \sigma_z(r, \vartheta) r^2 \cdot \sin \vartheta \cdot dr \cdot d\vartheta \\ M_y(z) &= \int_A \sigma_z \cdot b_y \cdot dA = \int_0^R \int_0^{2\pi} \sigma_z(r, \vartheta) r^2 \cdot \cos \vartheta \cdot dr \cdot d\vartheta \end{aligned} \quad (7)$$

These bending moment components are applied to node  $z$  and the same components, with opposite sign, are applied to next node  $z + 1$ . The bending moment generates obviously a

linear stress and strain distribution (shown in Figure 3) over the cross section, which is not at all distorted. Since here an approximation has been made, the validation of this method with the results obtained with a 3D f.e. model, analysed with a commercial f.e. code, is required. First the temperature distribution was checked, and a very good agreement was found between the finite differences method and f.e. model, as shown in Figure 4. Secondly, stresses and deformations were calculated: Figure 5 shows the deformed (bowed) f.e. model of the cylinder, and Figure 6 shows the stress distribution, both calculated at the same time. The axial stress distribution, obtained with the f.e. model is compared with finite difference method results in Figure 8: again a good agreement is found. The bow, measured on the axis of the cylinder, obtained with the f.e. model, is then compared with the one calculated with the equivalent bending moments, and again a good agreement was found, as shown in Figure 7. These results confirm the validity of the proposed approach. The radial elongation increases the contact force, but has no influence on the rotor dynamical behaviour. The equivalent bending moments are used not only for simulating the statical bow, but also for being superposed to the unbalance and other exciting forces, in order to simulate the dynamical behaviour of the rotor. Note that the equivalent bending moments generate a vibration, which is the superposition of the statical rotating bow and of the dynamical vibration amplitude.

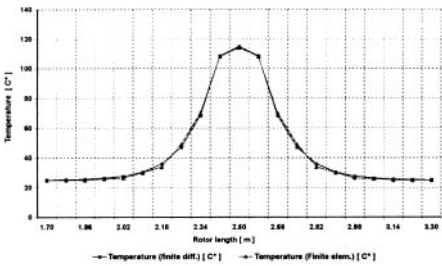


**Figure 4 Finite difference vs FEM solution. Temperature distribution in axial direction.**

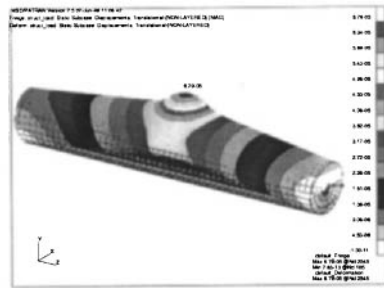


**Figure 5 FEM thermal deformed shape.**

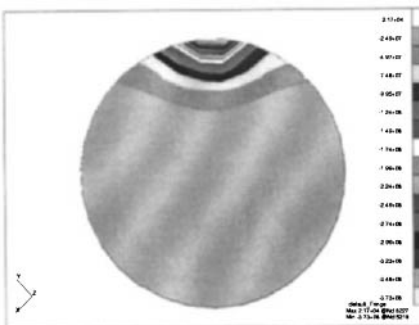


**Figure 6 FEM solution. Axial stress.**

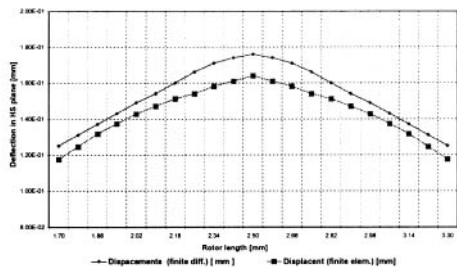


**Figure 7 Finite difference vs FEM solution. Thermal deflection.**

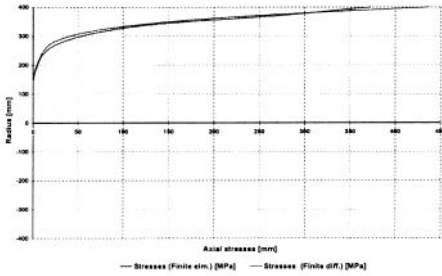


**Figure 8 Finite difference vs FEM solution. Axial stress.**

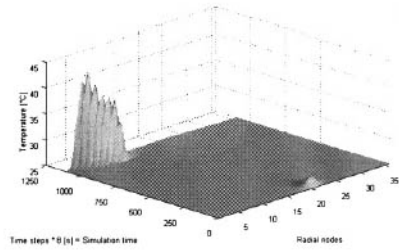


**Figure 9 Temperature distribution in the rotor surface in the seal.**

#### 4 THE MECHANICAL VIBRATIONAL BEHAVIOUR

If the rotor does not rub the seal, its vibrational behaviour is due to its natural unbalance  $F_{unb}$  (and permanent bow  $M_b$  if it is the case). Once the rotor comes into contact to the seal, the vibration vector has a phase lag with respect to the rotor unbalance, shown in Figure 11. The forcing system that modifies the vibrational behaviour of the rotor is composed by the contact force  $F$  (of components  $N$  and  $T$ ) and by several moments  $M$  simulating the thermal bow, whose components are given by eqs.(7). The bending moments are distributed over few nodes, in axial direction around the HS. Therefore the dynamical equation of the rotor system is

$$[M]\ddot{x} + [D]\dot{x} + [K]x = (F_{unb} + M_b + M + F) e^{i\Omega t} \quad (8)$$

The heat introduced by the rub creates a temperature difference between the diametrically opposite elements and the rotor starts bowing in an axial plane corresponding to the initial phase of the vibration vector. The bending moments, which model the bow, are vectors rotated by  $-90^\circ$  with respect to that plane.

At each time step the new value of  $x_s$  is determined by solving eq. (8) in the frequency domain. The vector  $x_s$  will be found rotated by a small angle due to the effect of the new exciting causes  $M$  and  $F$ . It is then checked if  $x_s$  is greater than the clearance  $c$ . In this case, the energy introduced by the rub is calculated, along with the new temperature distribution of the rotor (Figure 9) and the resulting bow moment  $M$ . This is introduced in eq. (8) along with the contact force  $F$  and the simulation loops. If  $x_s$  is smaller than the clearance  $c$ , then the new temperature distribution and the equivalent  $M$  are determined and eq. (8) is now solved without considering the contact force and the procedure loops.

#### 5 NUMERICAL RESULTS

The described method has been applied to the model of a typical HP-IP steam turbine of a 320 MW turbogroup, shown in Figure 10. The rubbing seal is assumed to be close to the middle of the rotor, in between the HP and the IP sections. Note that in the sealing zone the mesh has been thickened to apply the thermal model. The frequency response curve of the node in correspondence of the seal due to an unbalance is shown in Figure 11 as a Bode plot of amplitude and phase. The rotor is supposed to have the same axis of the stator (and of the

seal), which is certainly unrealistic, bearing in mind that the rotor has a static deflection due to its weight, that it is difficult to get exactly this condition during the alignment of the bearings, and that the oil film thickness is changing with speed and temperature. The unbalance is sufficient to deflect the shaft in correspondence of the seal by an amount which is slightly higher than the clearance: in this condition the calculation is started. The values of the different parameters are listed here below:

- seal stiffness  $k_s = 4 \cdot 10^6$  N/m
- seal clearance  $c = 0.1$  mm
- friction coefficient  $\mu = 0.2$
- convective heat coefficient (on the rotor surface)  $H = 35$  W/m<sup>2</sup>°C.

thermal conductivity, specific heat factor, heat conduction, density and thermal expansion coefficient have the standard values of alloy steel.

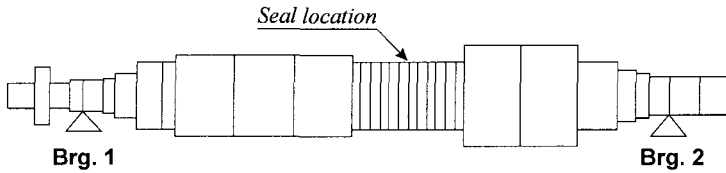


**Figure 10 HP-IP steam turbine of a 320 MW turbogroup.**

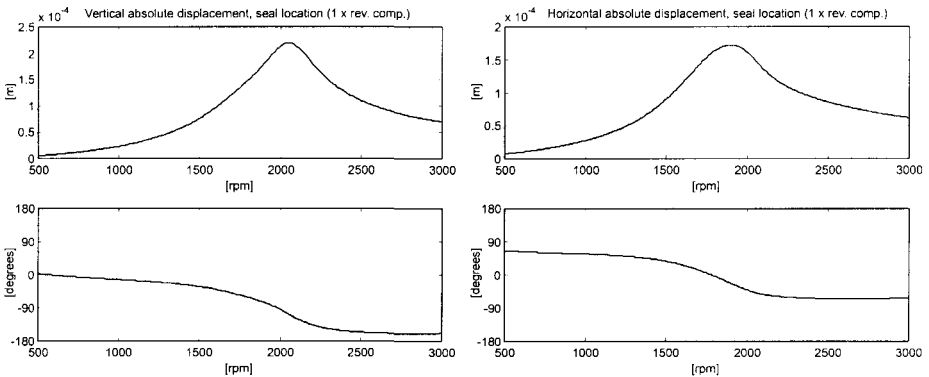
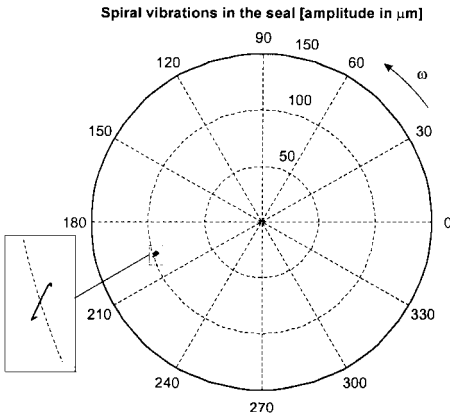


**Figure 11 Frequency response of the rotor model to an unbalance.**

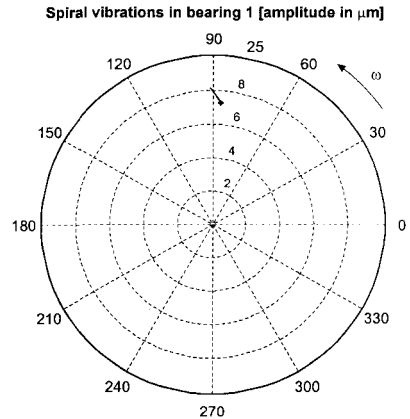
Two typical cases have been analysed: the first, at the normal operating speed of 3000 rpm, which is above the first critical speed, where the spiral vibrations are supposed to be “stable”, and a second one at 1700 rpm, which is just below the first critical speed, where the spiral vibrations are supposed to be “unstable”. In fact a rub may occur during the start-up of the machine: in this case the rub is likely to occur at a speed close to the critical speed, when the vibration amplitude is high due to the resonance effect.

Figure 12 shows the results at 3000 rpm in correspondence of the sealing. As soon as the rotor hits the seal, the developing bow lowers the vibration amplitude, so that the contact is soon lost and no heat is introduced anymore. The heat diffuses in the rotor body and the temperature on the skin lowers, the bow is reducing and, due to the unbalance, a new contact occurs in a position that is very close to the first one. In this position a steady state condition is achieved: the heat introduced by the light contact flows along the rotor without generating significant bows.





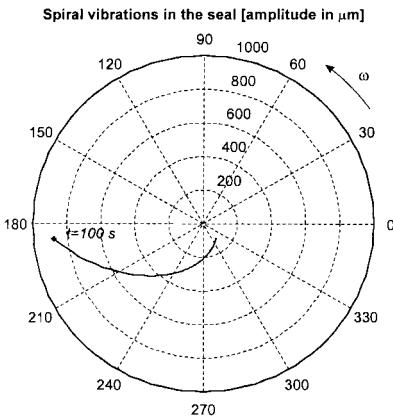
**Figure 12 Spiral vibration in the seal (3000 rpm).**



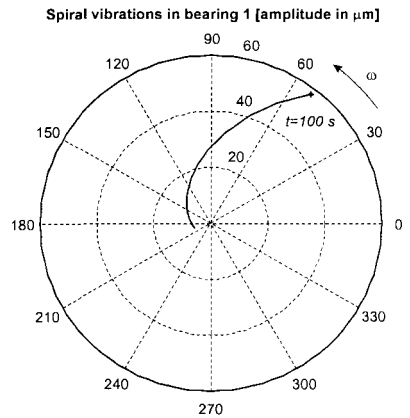
**Figure 13 Spiral vibration in bearing 1 (3000 rpm).**

Figure 13 shows the results in bearing 1. Even if Figure 12 can better show the phenomenon, Figure 13 is more significant from a diagnostics point of view, since the sensors (proximitors) in the actual machines for the monitoring of the dynamical behaviour are located in the bearings.

Figure 14 shows the results at 1700 rpm. Here the behaviour is clearly unstable, the vibration vector rotates and increases its amplitude. In this case the contact force increases strongly, as well as the introduced heat. The vibrations in the bearings can be seen in Figure 15, in which the vibration vector is shown in bearing 1. Note that the amplitude is increasing very fast.



**Figure 14 Spiral vibration in the seal (1700 rpm).**



**Figure 15 Spiral vibration in bearing 1 (1700 rpm).**

## 6 CONCLUSIONS

A method for calculating the behaviour of a rubbing rotor, with a rather refined model for the thermal behaviour, has been developed and some results have been validated with 3D f.e. calculations performed with commercial codes.

The numerical applications presented show that the transient behaviour can be evaluated with high accuracy, allowing to investigate the behaviour in different conditions. Experimental tests for the validation of the complete procedure have not been performed up to now.

## ACKNOWLEDGEMENTS

The grant of MURST Cofinanziamento "Identificazione di malfunzionamenti in sistemi meccanici" is gratefully acknowledged.

## REFERENCES

- (1) Kellenberger, W., "**Spiral vibrations due to the seal rings in turbogenerators thermally induced interaction between rotor and stator**", *Journal of Mechanical Design*, Vol. 2, 1980, pp. 177-184.
- (2) Liebich, R., Gasch, R., "**Spiral vibrations - modal treatment of a rotor-rub problem based on coupled structural/thermal equations**", paper C500/042, Proc.of *IMechE - 6<sup>th</sup> Conference Vibrations in rotating machinery*, 1996, pp 405-413.
- (3) Liebich, R., "**Rub induced non-linear vibrations considering the thermo-elastic effect**", Proc. of *5<sup>th</sup> IFToMM Int. Conference on Rotor Dynamics*, Darmstadt, 1998, pp. 802-815
- (4) Gruber, J., "**A contribution to the rotor-stator contact**", Proc. of *5<sup>th</sup> IFToMM Int. Conference on Rotor Dynamics*, Darmstadt, 1998, pp.768-779

# Measurement of contact forces during blade rubbing

J AHRENS and H ULBRICH

Institute of Mechanics, University of Essen, Germany

G AHAUS

Siemens AG Power Generation, Mülheim, Germany

## SYNOPSIS

The objective of this paper is the experimental investigation of the contact forces during blade rubbing against the casing. The emphasis of the investigation is the determination of the relation between the maximum of the normal contact force during one rub and the displacement of the blade tip in longitudinal direction. The time histories of the normal and tangential forces during the contact of the blade with the casing are measured. Furthermore, the influence of the contact force on the friction and the dependence on the rubbing speed are examined as well.

## NOTATION

$A$	cross-section area	$F_{QH}$	spectrum of $f_{QH}$
$c_K$	contact stiffness	$F_t$	tangential contact force
$EI$	bending stiffness	$H$	transfer function
$f_C$	contact force	$L$	blade length
$f_H$	impact force of the hammer	$n$	rotating speed
$f_{QC}$	quartz sensor response on $f_C$	$R$	disc radius
$f_{QH}$	quartz sensor response on $f_H$	$t$	time
$F_C$	spectrum of $f_C$	$\delta$	displacement at the blade tip
$F_H$	spectrum of $f_H$	$\mu$	friction coefficient
$F_n$	normal contact force	$\rho$	mass density
$F_{QC}$	spectrum of $f_{QC}$	$\Omega$	frequency/angular velocity

## 1 INTRODUCTION

In the recent years many theoretical studies have been carried out on the subject of contact between rotor and casing during operation. Several dynamic and kinematic models have been derived to determine the contact force, but it is noticeable that only a few of them were already proved by experiments. In most of the studies rotor rub has been modeled as contact between two concentric cylindrical surfaces which represent the rotor and the stator. The attention was focused on the qualitative aspects of the complex dynamical behavior induced by rubbing and, hence, simple models like linear springs have been used

to describe the relation between the normal contact force and the radial displacement of the rotor. Only a few investigations dealt with blade rubbing; a first theoretical study of the dynamics of a rotor during blade/casing interactions has been performed by Padovan and Choy (1). They considered the blade as an end loaded cantilever beam and derived a nonlinear force-deformation relation between the normal contact force and the displacement of the tip of the beam in longitudinal direction, which characterizes the contact law in radial direction. An extension of this model has been presented by the authors of this paper in (2) and has shown that the stiffening effect due to the rotation of the blade and variation change of the setting angle may significantly modify the contact forces in comparison to the model presented in (1). This subsequently leads to qualitatively different results in numerical simulations of the dynamics of the rubbing rotor. Still all of these models have the assumption in common that the contact process is quasi-static and therefore neglect elastic wave propagation in the impacting bodies. To verify this assumption and to give a recommendation which contact model fits best, it is necessary to observe the process of blade/casing rub in experiment.

In this paper the contact forces during blade rubbing are experimentally investigated. Therefore a test rig has been build which performs nearly realistic rubbing interactions of a rotating blade with the casing. In the following sections the experimental setup, the instrumentation, the applied measurement concepts and several results achieved are illustrated. However, at first a short outline of common contact laws in rotor rubbing is given.

## 2 RUB MODELS

When a rotor or a blade rubs at the casing the acting contact force can be split up into a normal force  $F_n$  and a tangential friction force  $F_t$ . According to the Coulomb friction law both force components are related by a single, possibly velocity dependent, coefficient  $\mu$ ,

$$F_t = \mu F_n, \quad (1)$$

where  $F_t$  acts in opposite direction to the rubbing velocity.

Many approaches take into account that the contact force in the normal direction is dependent on the radial distance  $\delta$  between rotor/blade and casing at the contact point and consequently allows a description with a contact stiffness  $c_K$ . Neglecting the influence of dissipation,  $F_n$  is then only a function of  $\delta$ . The most simple model is stated by the linear contact force relation

$$F_n = c_K \delta. \quad (2)$$

Also, models with nonlinear stiffness relations are often used. For instance, one method to describe the contact force between linear elastic bodies is the application of the following expression

$$F_n = c_K \delta^{3/2}, \quad (3)$$

where the exponent of  $3/2$  is according to the Hertzian theory.

A model for the rubbing of an straight elastic blade with no setting angle at a rigid casing

has been presented by Jiang et al. in (2). The normal contact force can be calculated by the following force-displacement relation as,

$$F_n = 2.5 \frac{EI}{L^2} \frac{1.549 \sqrt{\delta/L}}{\mu + 1.549 \sqrt{\delta/L}} + \frac{11}{56} \rho AL \Omega^2 \left( \frac{5}{22} L + \frac{35}{22} R \right) \frac{1.549 \sqrt{\delta/L}}{\mu + 1.549 \sqrt{\delta/L}}, \quad (4)$$

where  $L$  is the length,  $A$  the cross-section,  $\rho$  the mass density and  $EI$  the bending stiffness of the blade. The angular velocity is denoted by  $\Omega$  and the disc radius by  $R$ .

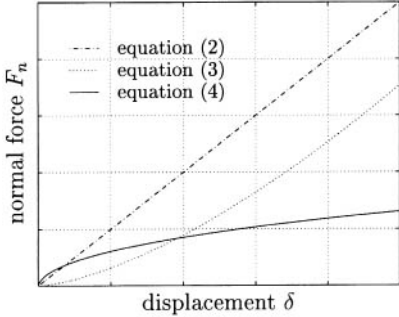


**Figure 1:** Relation between normal force and radial displacement for different rub models

Figure 1 shows a comparison between the contact stiffnesses determined by the three rub models. According to that the rubbing blade behaves as a softening spring, i. e. that for increasing radial displacement  $\delta$  the nonlinearity decreases the restoring normal force  $F_n$ . It should be pointed out here again that local inertia effects and wave propagation in the bodies are neglected. A detailed survey on further contact models is given in (3) by Markert and Wegener.

### 3 EXPERIMENTAL SETUP

The main objectives of this work are to examine the time history of the contact force during blade rubbing and to determine the normal contact stiffness in relation to the displacement of the blade tip in longitudinal direction. To this end, an appropriate test rig was built.

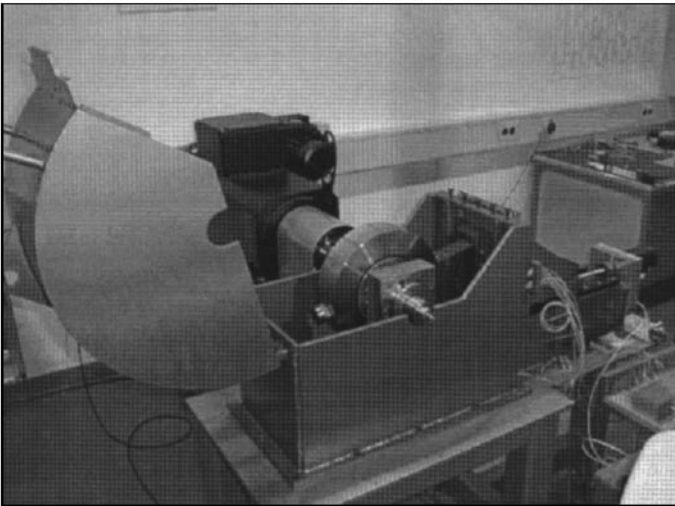


**Figure 2:** Picture of the test rig

As can be seen in Figure 2 the rotor consists of a shaft with high bending stiffness and a disk with a large polar moment of inertia, which ensures that the rotating speed is approximately kept constant during the rub process. The test blade is fixed to the disk and balanced with a counter-weight on the opposite side. The rotor is mounted in ball bearings and is driven by an asynchronous motor. To ensure a high level of safety, the complete assembly is placed into a massive steel housing. In order to explain the experimental setup more in detail a sketch of test rig and feeding device can be seen in the following Figure.

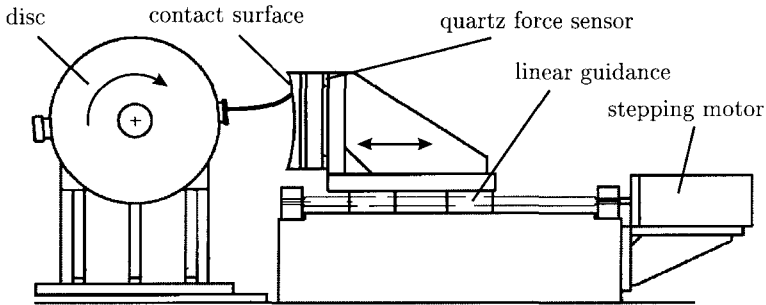


**Figure 3:** Principal sketch of test rig and feeding device

During the experiments a test blade rubs along a curved surface which can be driven by a stepping motor towards the rotating blade. The contact angle can amount up to  $30^\circ$  of the circumference and enable the simulation of partial rubs. The contact forces in the normal and the tangential direction at the blade tip are measured by means of quartz force sensors which are mounted between the contact surface and a supporting plate which is part of the feeding device. Contact surface, supporting plate and quartz sensors constitute the force measuring device. By adjusting the progress of the contact surface during the experiments the intensity of the blade rubbing is controlled. The movement of the feeding device or contact surface respectively is measured with an eddy-current sensor. It is assumed that no penetration of the contact surface by the blade tip occurs. The positioning of the contact surface via the stepping motor control enables the realization of different incursion patterns, e. g. ramp or stairs, and incursion rates.

Besides the maximum amplitudes and time histories of the forces, the contact duration is an important parameter in the derivation of a rub model. In order to obtain this quantity a voltage is applied to the contact surface which is electrically isolated from the rest of the test rig. Now, each time the grounded blade comes into contact with the surface an electric circuit is closed and the measured voltage drops down.

The experiments are conducted with constant rub speed, i. e. constant rotational speed, and with a special alloy steel as blade material and cast iron as contact surface material. This is in accordance with material combination used in existing turbomachinery. Also the geometrical dimensions of the blade are chosen in such way that the ratio of length to width and width to thickness corresponds with those of compressor blading in real gas turbines. The main dimensions of the disk, blade dummy and curvature of the contact surface can be taken from Table 1.

**Table 1:** Technical data of experimental setup

blade	length	100 mm
	width	44.4 mm
	thickness	3 mm
disk	diameter	300 mm
	thickness	75 mm
	moment of inertia	0.47 kg m <sup>2</sup>
	radius at the blade tip	267.5 mm
	radius of curvature of the rubbing surface	269.5 mm

The measurement of the short-time contact processes is realized with a data acquisition board plugged into a PC with a maximum sampling rate of 10240 Hz per channel, 16 bit resolution and 4 differential inputs.

#### 4 MEASUREMENT CONCEPTS

One problem that appears in the measurement of rubbing processes is the high excitation frequency due to the intermitting contact forces (impulse type). A result of this fact is that natural frequencies of the mechanical structure, e. g. the force measuring device, are excited by the contact forces and lead to an amplification and a phase distortion of the force signals supplied by the quartz force sensors. Now, this affection of the frequency characteristic of the measured signal has to be taken into account in the data analysis. A possibility to annulate this systematic error is inverse filtering in the frequency domain.

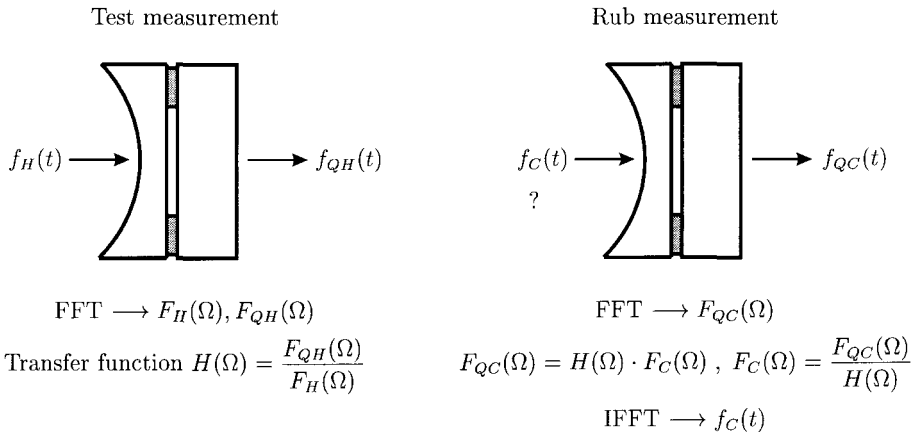


**Figure 4:** Procedure of inverse filtering

This method was successfully employed for contact interactions by Fumagalli in (4) and is illustrated in Figure 4. First, we apply a defined impact force  $f_H(t)$  with a modal hammer on the contact surface in a test measurement and measure the related signal  $f_{QH}(t)$  of the quartz force sensors. The impulse excitation of the structure generated by a hammer is similar to that of the contact force during blade rubbing. The transformation of both measured signals  $f_H(t)$  and  $f_{QH}(t)$  into the frequency domain by Fast Fourier Transform (FFT) provides  $F_H(\Omega)$  and  $F_{QH}(\Omega)$ . The transfer function  $H(\Omega)$  of the structure which characterizes the dynamic properties of the force measuring device (respectively the test rig) is then determined by simple division:  $H(\Omega) = F_{QH}(\Omega)/F_H(\Omega)$ . This procedure is performed for excitation and response in vertical and horizontal direction.

During the experimental investigations, the force  $f_{QC}(t)$  due to the rubbing of the blade along the contact surface is measured by the quartz force sensors and transformed into the frequency domain  $F_{QC}(\Omega)$ . To obtain the spectrum  $F_C(\Omega)$  of the unknown contact force, which directly acts at the contact surface,  $F_{QC}(\Omega)$  is divided by the transfer function  $H(\Omega)$  known from the test measurement. The time history of the contact force  $f_C(t)$  is then obtained from the Inverse Fast Fourier Transform (IFFT) of  $F_C(\Omega)$ .

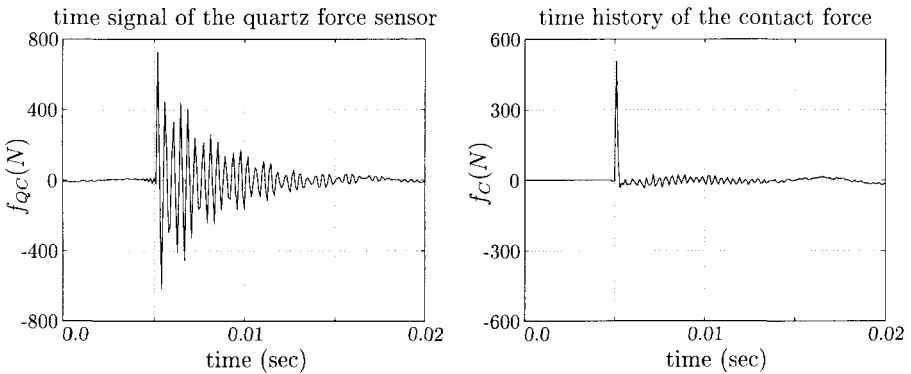


**Figure 5:** Force history before and after inverse filtering

Figure 5 shows the result of the inverse filtering of the signal of the normal force component given by the quartz force sensors for a blade rubbing at a flat contact surface. The time history of the corrected signal seems reasonable since the contact force can be represented by a half period of a sine function during the contact process. Thus, the technique of inverse filtering makes it possible to remove the inherent dynamics of the force sensing device from the measured signals.

## 5 EXPERIMENTAL INVESTIGATION OF RUBBING PROCESSES

In this section, the measurement of the time histories of the contact forces during the rubbing of the test blade along the casing and the relation between the normal and tangential force components determined by the coefficient of friction will be described.

The data acquisition is started, when the first bold contact occurs and, for that reason, the contact voltage drops below a given threshold value. The severity of the blade rub is determined by the radial position of the contact surface which itself is controlled by the



feed movement of the stepping motor. The experiments were performed for rotor speeds of 1200 rpm and 1800 rpm. Figure 6 shows the time histories of normal and tangential contact forces of one rubbing process and their duration represented by the dashed line of the voltage. The contact time is approximately 1.25 msec which is equivalent to a contact arc length of  $9^\circ$  of the complete circumference at a speed of 1200 rpm. Both components of the contact forces follows the shape of a half sine-wave with a maximum normal force of 448 N and a maximum friction force of 104 N. If we look at the time histories, the assumption that both forces are correlated by the coefficient of friction  $\mu$  seems to be reasonable although there are some remaining vibrations in the signal of the friction force. This means that the measurement concept used does not completely compensate the influence of the dynamics of the force measuring device.

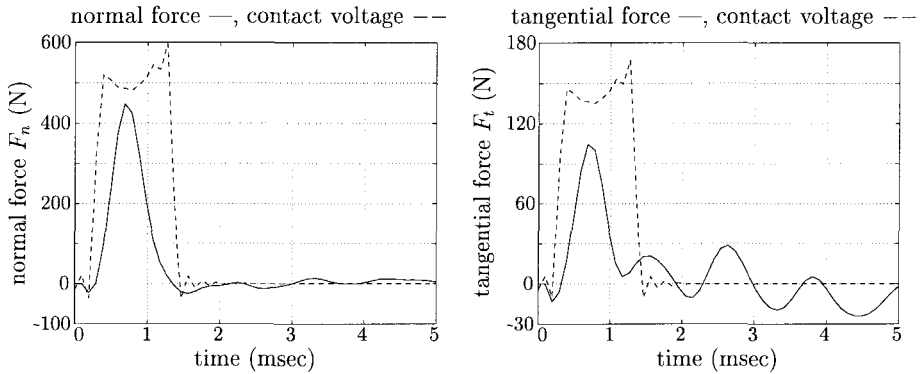


**Figure 6:** Measured normal and tangential contact force histories

Further experiments have been performed applying various displacements of the rubbing surface. After an initial contact the rubbing surface is driven into the rotating blade. Thereby, the displacement of the blade tip corresponds to the feed movement since the blade has to shorten or bend in order to pass. This procedure happens stepwise with a feed value of  $4\ \mu\text{m}$  each step and leads to an increasing blade tip load. The maximum displacement of the rubbing surface is given by a value of 0.025 mm. After one step the displacement is held constant for 10 sec and the contact time and forces are measured.

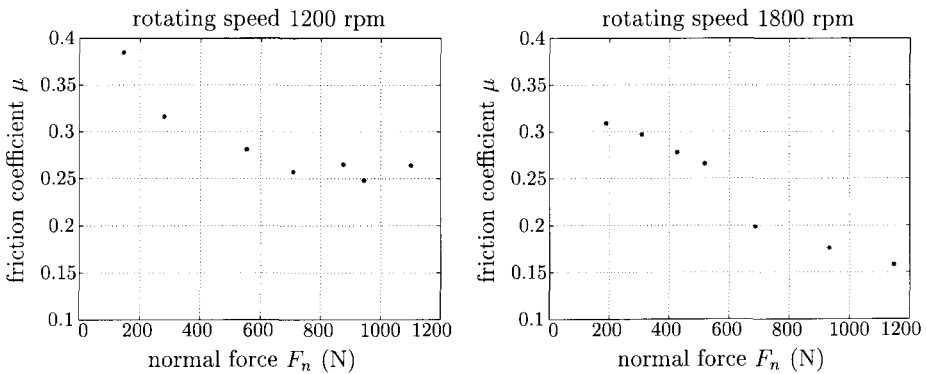


**Figure 7:** Load dependence of the friction coefficient  $\mu$  at different rotating speeds

To derive the coefficient of friction  $\mu$  the ratio of the amplitudes of the normal and the tangential contact force has been measured for rotating speeds of 1200 rpm and 1800 rpm. An average friction value of the occurring contacts at a distinct displacement has been determined and plotted against the normal force as shown in Figure 7. For both speeds it can be detected that the friction coefficient  $\mu$  obviously decreases with increasing magnitude of  $F_n$ . This observation is contradictory to the assumption of an load independent coefficient as it was made in the Coulombian theory.

**Table 2:** Friction coefficient for various rotating speeds

$n$	$\mu$
600 rpm	0.28
900 rpm	0.26
1200 rpm	0.27
1500 rpm	0.25
1800 rpm	0.23

Also, a slight decrease of the friction coefficient at higher sliding speeds can be detected (see Table 2). However, the exact knowledge of  $\mu$  is crucial for the analysis of rotor/stator rubbing. Kascak determines in (5) that small changes of the coefficient of friction can drive the rotor from stable forward whirling into the backward whirl instability, increasing the severity of the rubbing and possibly causing serious damage. Therefore, friction is one of the main parameter which is required to accurately predict the stability behaviour of rotor systems subjected to blade rubbing.

It should be pointed out that the exact determination of the load and speed dependence of the coefficient of friction is very difficult because of the permanent changes in the rubbing conditions due to wear, temperature changes and - most of all - transient dynamic effects.

Besides the coefficient of friction, the contact stiffness also is of large importance in the correct determination of the dynamics of rubbing rotors. Therefore, one of the objectives of the present study is also the identification of a corresponding contact stiffness. For this approach the relationship between the displacement  $\delta$  of the blade tip in the longitudinal direction and the normal contact force  $F_n$  is measured and compared with those given by the theoretical model of a rubbing blade represented by equation (4). Here, the load dependency of the friction coefficient is taken already into account.

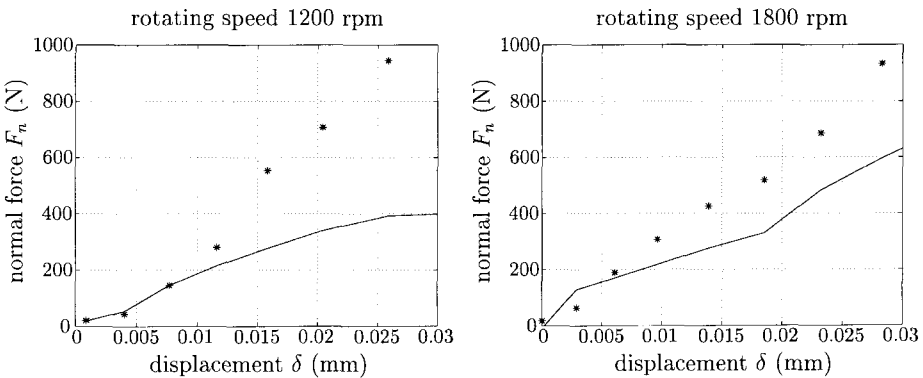


**Figure 8:** Force-displacement relationship, model(-) and measurement(\*)

The theoretical and measured contact stiffnesses characterized by the force-displacement relationship is shown in Figure 8 for 1200 rpm and 1800 rpm. For small displacements  $\delta$

of the blade tip up to 0.008 mm the theoretical and measured contact stiffnesses agree well for both speeds. This agreement deteriorates for increasing displacements and results in a rough theoretical underestimation of the measured data at large displacements. A possible explanation of this discrepancy is that vibrations of the blade lead to changing states at the beginning of the rubbing process. Light rubbing results only in a slight excitation of blade vibrations while for hard rubs the dynamics of the rubbing blade is strongly influenced. Thus, differences arise for increasing displacements. Depending on the vibrational state of the blade tip the contact starts under different initial conditions. This assumption is supported by the observation of a time dependent deviation of the contact force amplitudes at fixed displacements. Following the theory the maximal force should be constant in this case. One possibility to consider this effect is the measurement of the blade dynamics during the rubbing process via strain gauges and telemetry. A verification of this explanation and/or extension of the presented blade rub model would thus be possible.

It can be noticed that the lower speed results deviate much more from the theory than the higher speed results. This may be explained by the fact, that for lower rubbing speeds the contact time is long enough to allow blade vibrations during the rubbing process. Therefore, the influence of the blade dynamics is larger for lower than for higher speeds and hence also the discrepancy in the force-displacement relationship.

## 6 CONCLUSIONS AND OUTLOOK

An accurate prediction of the dynamics of rotor systems subjected to blade rubbing is strongly dependent on the contact model for the normal as well as the tangential force components. The selection of a suitable approach is difficult due to the number of available models. Also, there is a lack of experimental investigations of rubbing processes. In this work, measurements of contact force histories during blade rubbing have been carried out. The method of inverse filtering has been applied to eliminate the influence of the measurement device dynamics. Contact stiffness and the friction coefficient have been determined for various rotating speeds and compared with values given by the presented contact model.

The experimental investigations verify the assumption of a half sinusoidal time history of the contact forces, whereas the coefficient of friction seems not to be a constant parameter as suggested. The experimental data show that the friction coefficient depends not only on the sliding speed but also on the load. Further extensive measurements will be necessary to confirm the observations. Concerning the contact stiffness we can state that the values supplied by the theoretical model of the rubbing blade agree well for soft contacts but clearly underestimate the values at higher displacements (respectively harder contacts). As an explanation, it is assumed that the influence of the vibrational state of the blade at the beginning of the rubbing has a significant impact on the contact stiffness. To verify this assumption strain gauge measurements at the blade in combination with a telemetry system are in progress.

## REFERENCES

- (1) PADOVAN, J.; CHOY F. K.: *Nonlinear Dynamics of Rotor/Blade/Casing Interactions*. Journal of Turbomachinery, Vol. **109**, 1987, pp. 527-534.
- (2) JIANG, J.; AHRENS J.; ULBRICH, H.; SCHEIDELER, E. M.: *A Contact Model of a Rotating, Rubbing Blade*. Proceedings of the 5th International Conference on Rotor Dynamics, IFToMM, Darmstadt, 1998, pp. 478-489.
- (3) MARKERT, R.; WEGENER G.: *Transient Vibrations of Elastic Rotors in Retainer Bearings*. Proceedings of the 7th International Symposium of Transport Phenomena and Dynamics of Rotating Machinery, ISROMAC, Honolulu, 1998, pp. 764-774.
- (4) FUMAGALLI M. A.: *Modeling and measurement analysis of the contact interaction between a high speed rotor and its stator*. Ph.D. Thesis, Swiss Institute of Technology, ETH, Zürich, 1997.
- (5) KASCAK, A. F.: *The Response of Turbine Engine Rotors to Interference Rubs*. AVRADCOM Technical Report 80-C-14, NASA TM-81518, 1980.

## Rub-heated shafts in turbines

**B LARSSON**

Department of Mechanical Engineering, Linköping University, Sweden

### ABSTRACT

Heat generation in a friction contact between rotor and seal can be a source of shaft bow development. This will change the unbalance configuration, and can lead to severe vibration problems. The seals studied are of labyrinth type, against axial flow. The contact problem is strongly non-linear, as there is a gap between rotor and seal.

The closed loop from vibration to asymmetric heating to shaft bow back to vibration can be analysed by time integration. It has been observed that a limit cycle of the vibration amplitudes is often reached. Limit cycles can be expressed by their Fourier coefficients. This also leads to a direct frequency solution method.

Results are presented for a medium-sized steam turbine, in the form of time simulations, a frequency domain method and stability analysis. A case with multiple bows is analysed, and conditions for limit cycles are presented.

### 1 INTRODUCTION

Several observations of synchronous instability problems have been made in gas turbines and steam turbines, see (1), (2), (3). The problem has been studied for a long time and is often referred to as the Newkirk effect (4). Theoretical explanations have been presented, see (5) - (12). Still the implications of the non-linear relation between vibration and heat generation on the "spiralling" of the shaft need further attention. The aim of this paper is to present efficient theoretical models for the phenomena.

The contact between shaft and seal is distinct, near a relay characteristic. This is due to a preload of the seal supporting springs. Due to the limited preload force, the level of asymmetric heating is assumed to be limited in this model, implying a limit of the shaft bow and the vibrations. However, the level can be well beyond what is acceptable. In many cases with relatively high rotor response a limit cycle will develop. To fit the problem into a direct steady-state analysis (in the frequency domain) some model reduction regarding contact kinematics is performed.

## 2 NOMENCLATURE

$G$	gain = $R_b P$ (mm/W)
$P$	relation between friction heat and bow (rad/W)
$R_b, R_u$	rotor responses, referring to bow and mass unbalances (mm/rad and mm/kgm)
$e_{\text{shaft}}$	shaft eccentricity relative to seal (mm)
$s$	Laplace transform variable (1/s)
$t$	time (s)
$u_0$	mass unbalance (kgm)
$\beta$	complex bow angle (rad)
$\delta$	vibration amplitude (mm), complex
$\delta_i$	vibration amplitude (mm) at contact $i$ , complex
$\lambda$	rotor response coupling measure
$\theta$	friction heat input (W), complex
$\theta_i$	friction heat input (W) at contact $i$ , complex
$\omega$	frequency (rad/s)
$\Omega$	angular running speed frequency (rad/s)

## 3 CONFIGURATION

The method is not limited to specific configurations, but to emphasise some aspects a particular machine is chosen (a 120 MW steam turbine). See Fig. 1 and Table 1. The example of rotor response (major and minor ellipse radii) is at the first disc (node 2), due to an unbalance of 0.1 kgm at the first disc. At first resonance the middle seal package is most likely to give contact. At the next resonance, with a node in the middle, the two other seal packages are more likely to give contact. The real turbine has more than two discs. Typical tilting-pad bearings are used. The seals are of labyrinth type and they are segmented in the peripheral direction.

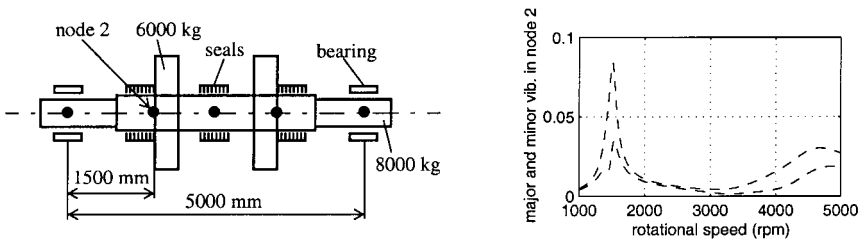


Figure 1: Rotor Model and Rotor Response.

Table 1: Rotor Data.

Parameter	Value	Parameter	Value
$e_{\text{shaft}}$	0.45 mm	$r_{\text{shaft}}$	300.0 mm
$m_{\text{rotor,tot}}$	20000 kg	$\theta_{\text{max, 3600 rpm}}$	1400 W
$r_{\text{seal}}$	300.5 mm	$n_{\text{nominal}}$	3600 rpm

## 4 MODEL CLASSIFICATIONS

We limit our attention to cases with seals that are preloaded in radial direction.

The kinematics of a contact between shaft and seal are investigated in (14). The general synchronous ellipse vibration needs a search to find the contact position with the seal.

In the case studied the friction heating  $\theta_i$  has a finite value, linear with running speed,  $\Omega r \mu F_{\max} \approx 1400 \text{ W}$  at nominal running speed (see (14) for a formal treatment), and a limit of maximum vibration can be estimated. This may correspond to unacceptably high vibration levels, but anyway it is an upper bound.

The rotor vibrations due to unbalances are fast and damped, steady state is reached in seconds for a given set of unbalances. We are interested in the relatively slow changes in unbalances, due to development of thermal bows in the shaft. In a time integration of this the rotor response can be seen as immediate. After a discretization into 5 nodes in the axial direction a finite element model is formulated. The equations of motion are solved for a particular running speed, and rotor response is deduced. See also (10), (12) and (13) regarding the responses  $R_u$  and  $R_b$ .

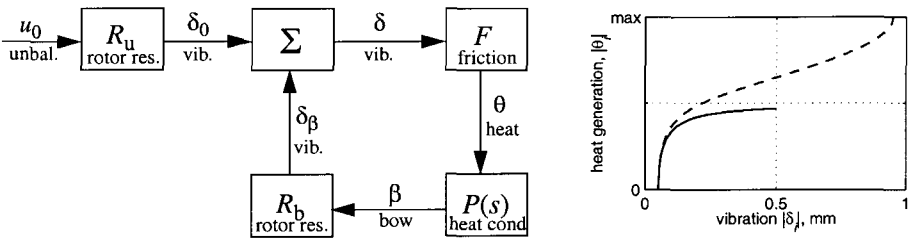


Figure 2: Left, Closed Loop. Right, Vibration-Heating Relation  $F$ .

The relation between thermal bow,  $\beta$ , and friction heating,  $\theta$ , can be approximated

$$P(s) = \frac{b_2 s^2 + b_3 s + b_4}{s^3 + a_2 s^2 + a_3 s + a_4} \quad (1)$$

for the one-bow case (with  $s$  the Laplace transform variable). The  $a$  and  $b$  coefficients follows after solution of heat conduction dynamics, see e. g. (6), (10), (12) and (14). In a two-bow case  $P(s)$  is a two-by-two matrix (diagonal).

In the simple case we only have shaft-seal contact at one seal package (a small axial distance relative to the whole rotor) and consequently one shaft bow. If further the level of initial mass unbalance is very low (nearly perfectly balanced) we have a case which gives clear and easily found solutions, see eq. 7. To initiate such a solution an appropriate heat state (bow) in the shaft has to be given. It is more realistic to include a mass unbalance, and let the following vibration initiate the heating.

In a more complicated case contact may be initiated at positions on the shaft, far apart. This leads to multiple bows, interacting with each other. See chapter 6 below.

The non linearity (in the rotor-seal contact) with saturation can in many cases give an unstable system at low vibration levels (provided contact is initiated), which augments the vibration level. The maximum friction heating will however stop the growth, so that the bow will be trapped in a certain region. In such cases that the closed loop has a phase delay, the bow will change phase and describe a limit cycle. A solution without phase delay gives a steady-state bow. A steady-state solution is also expected when asymmetric heating works in a direction to reduce the vibration level.

#### 4.1 Small-Vibration Approximation

In most situations the vibration level of the shaft is below 0.1 mm and compared to eccentricity (about 0.5 mm) and elliptic shape (also about 0.5 mm) this is small. If a contact is to occur the stationary gap between shaft and seal must be narrow. An actual contact will now occur near the position of minimum stationary gap. It is hence the vibration from rotor centre to minimum stationary gap (direction A in Fig. 3) that gives contact and the perpendicular vibration (B) just translates the shaft without giving any change in gap.

If the vibration is relatively small the small-vibration approximation can be used with fast calculations, because the position of the contact is known.

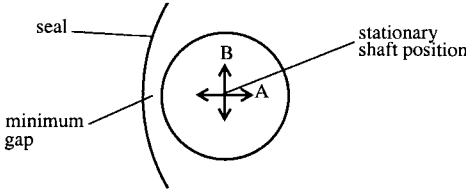


**Figure 3: Small-vibration approximation. Only the vibration marked A gives change in gap. The B vibration just translates the shaft over the surface.**

Since the orientation of the coordinate system is arbitrary we choose the direction coinciding with A in Fig. 3, and denote this  $\delta_i$ ,  $i$  indicating seal package number. This vibration amplitude is complex, as it carries phase information for the actual vibration.

In Fig. 2 (right) the relation between vibration  $\delta_i$  and asymmetric heating is presented, for our case with stationary gap 0.05 mm and  $\Delta r=0.05$  and without elliptic seal shape. The solid line is the *small-vibration approximation* used and the dashed line a forward circular whirl. The result is due to a gradually increasing relative contact time for partial annular rub up to full annular rub where maximum heat power is attained. This relation is direct, i. e. no phase delay exists, so  $\delta_i$  and  $\theta_i$  have the same phase.

#### 5 LIMIT CYCLE CASE

A limit cycle will result in many configurations, due to the degressive non-linearity (see Fig. 2, right). To reduce computation cost a frequency approach is sought. See also textbooks on harmonic balancing or describing functions, e. g. (15). The general vibration can now be expanded in its Fourier components:

$$\delta_1 \exp(i\Omega t) = (\delta_{\beta 1} + \delta_{01}) \exp(i\Omega t) = \left( \sum_{n=-\infty}^{\infty} c_n \exp(in\omega t) + \delta_{01} \right) \exp(i\Omega t) \quad (2)$$

where  $\delta_{01}$  could have been included in  $c_0$ , but we have chosen to expand just  $\delta_{\beta 1}$ .

Assume we have the vibration  $\delta_1$ , and thereby

$$\theta_1 = F(\delta_1)\delta_1 = \sum_{n=-\infty}^{\infty} e_n \exp(in\omega t) \quad (3)$$

with the nonlinear relation  $F$  a real positive function, as the heat generation corresponds to the contact spot on the shaft. Its Fourier expansion will also be used. The bow is

$$\beta_1 = P_{11}\theta_1 \quad (4)$$

and the resulting vibration response



$$\delta_{\beta 1} = R_{b11}\beta_1 = G_{11}\theta_1 = \sum_{n=-\infty}^{\infty} G_{11}(in\omega)e_n \exp(in\omega t) \quad (5)$$

there  $G_{11}$  is short notation for  $R_{b11}P_{11}$ .

Now if a limit cycle is to exist the same signal must appear after one cycle, so that

$$\delta_{\beta 1} = G_{11}F(\delta_1)(\delta_{\beta 1} + \delta_{01}) \quad (6)$$

If the mass unbalance is neglected  $\delta_{01}$  is zero and we have the *perfectly balanced case*, eq. 2 and eq. 5 give

$$\delta_{\beta 1} = \sum_{n=-\infty}^{\infty} c_n \exp(in\omega t) = \sum_{n=-\infty}^{\infty} G_{11}(in\omega)e_n \exp(in\omega t) \quad (7)$$

One solution to this is the circular orbit, or  $c_1 = G_{11}(i\omega)e_1$ , all other terms zero. This solution implies that the size of the vibration is constant and hence also the heat generation (the complex vibration amplitude and heating only change phase). The two unknowns  $\omega$  and  $c_1$  can be solved for from eq. 6.

## 6 MULTI-BOW CASE

With friction contact at different positions multiple bows will develop. The coupling between a bow at one position and a vibration at another contact is in most configurations strong, and the bows cannot be regarded one at a time. A number of transient time simulations show that in most cases a limit cycle with a common frequency will be reached, provided that the rotor response to bows adds to the vibration and does not reduce it and further that the initial condition initiates contact. Let us study a two-bow case and introduce the coupling measure

$$\lambda = \frac{|R_{b12}||R_{b21}|}{|R_{b11}||R_{b22}|} \quad (8)$$

Provided that the shaft bow responses differ from each other (a result of e.g. different shaft radii) and if the coupling is relatively weak ( $\lambda$  below about 0.01 in many different cases) the bow amplitude will never assume a constant value, see Fig. 4 (left). If the coupling is even weaker, each contact can give its own limit cycle, with different cycle times (not the same  $\omega$ ).

Often the coupling is strong enough to give limit cycles with a common frequency and the fluctuations as in Fig. 4 are indistinguishable.

As in the derivation of the one-bow model above (eq. 2) mass unbalance will be included. In the transient analysis an initial mass unbalance is easy to include, and simulations show that the circular limit cycles no longer exists (because the response to the mass unbalance will vary between adding and reducing the cyclic variation in response of the bow). See Fig. 4, right.

The frequency analysis becomes more elaborate as higher harmonics of  $\omega$  must be included. The angular speed of the limit cycle can vary a lot, see Fig. 4 (right), where the stars are equally distributed in time. This implies that higher harmonics than just the first must be included in a frequency analysis. One cycle is about two hours.

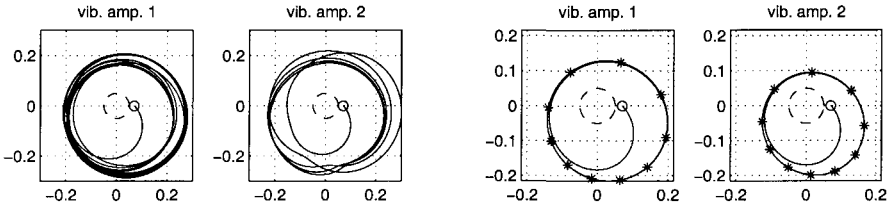


**Figure 4: Time transient of vibration amplitudes. Left, light coupling. Right, coupling of normal strength. Outside the dashed line we have contact, inside not.**

### 6.1 Frequency Analysis

Here it is assumed that the coupling (see eq. 8) is strong enough to give a common limit cycle frequency.

The one-bow case (eq. 3 to eq. 5) can be extended to two bows by introducing the vibration amplitudes  $\delta_{\beta 2}$  and  $\delta_{\beta 2}$  with

$$\delta_{\beta 2} = \sum_{n=-\infty}^{\infty} d_n \exp(in\omega t) \quad (9)$$

$d_n$  complex constants. Further the heating at contact 2 is denoted  $\theta_2$

$$\theta_2 = \sum_{n=-\infty}^{\infty} f_n \exp(in\omega t) \quad (10)$$

Asymmetric heating  $\theta_2$  also follows from  $\delta_2$  as  $\theta_1$  follows from  $\delta_1$ .

Another set of relations is that  $\delta_{\beta 1}$  and  $\delta_{\beta 2}$  must follow from the response:

$$\delta_{\beta 1} = G_{11}\theta_1 + G_{12}\theta_2 = \sum_{n=-\infty}^{\infty} (G_{11}(in\omega)e_n + G_{12}(in\omega)f_n) \exp(in\omega t) \quad (11)$$

$$\delta_{\beta 2} = G_{21}\theta_1 + G_{22}\theta_2 = \sum_{n=-\infty}^{\infty} (G_{21}(in\omega)e_n + G_{22}(in\omega)f_n) \exp(in\omega t) \quad (12)$$

It follows that

$$c_n = G_{11}(in\omega)e_n + G_{12}(in\omega)f_n \quad (13)$$

$$d_n = G_{21}(in\omega)e_n + G_{22}(in\omega)f_n \quad (14)$$

Truncating the series to  $-N \leq n \leq N$  and choosing  $t=0$  so that  $c_1$  becomes positive and real gives a set of  $4*(2N+1)-1$  real unknowns, but as  $\omega$  also is unknown we have  $4*(2N+1)$  real unknowns. The equation system is the real and imaginary parts of eq. 13 and eq. 14, which corresponds to  $4*(2N+1)$  real nonlinear equations. Multivalued solutions can exist, and to find the stable non-trivial ones it is suggested to use different starting solutions. In the simple cases the bows can be in phase or 180 deg out of phase with each other. To find both solutions, both in-phase and out-of-phase starting solutions should be used (this must also be done in the time simulation case). It is observed that  $N=5$  or higher can be needed, in cases of strong alteration of the speed along the cycle orbit. This gives a large equation system, but computation cost is low relative to time integration. Results are presented in Fig. 6.

Generalization to more than two bows follows easily but is omitted for clarity.

## 6.2 Stability

It is one thing to find a periodic solution, and another to determine if it is stable. With stability we actually mean asymptotic stability, that is if the disturbance vanishes the response to it also vanishes as time approaches infinity.

The response of the bow has been approximated with an ordinary differential equation of order three (the Laplace transform in eq. 1 can also be regarded as a differential operator in the time domain). Define  $x$  as the state vector of the shaft bows. The transformation of the ordinary differential equation into state space gives three states in each of the two bow directions (real form). As we have two contacts the total number of states is 12. The state space model is now:

$$\dot{x} = Ax + B\theta \quad (15)$$

$$\beta = Cx \quad (16)$$

with  $A$ ,  $B$  and  $C$  according to standard textbooks on control theory. Asymmetric heating vector  $\theta$  has dimension four on real form, and so has the bow vector  $\beta$ , in the two-contact case investigated. Denote the computed solution under investigation with index *nom* for nominal and the error or disturbance with *err*. The asymmetric heating  $\theta$  is  $F(\delta)\delta$ ,  $\delta = \delta_{nom} + \delta_{err}$ ,  $\delta_{nom} = \delta_0 + R_b\beta_{nom}$ ,  $\delta_{err} = R_b\beta_{err} = R_bCx_{err}$ . Further  $x = x_{nom} + x_{err}$ .

The assumption of small errors justifies the linearization

$$\dot{x}_{err} = Ax_{err} + B\theta_{err} = Ax_{err} + B \frac{\partial \theta(\delta_{nom} + \delta_{err})}{\partial \delta_{err}} \delta_{err} = A_{tot}(\omega t)x_{err} \quad (17)$$

The absolute value of the two derivatives corresponds to the slope in Fig. 2 at  $\delta_{nom1}$  and  $\delta_{nom2}$  respectively. The complex  $\theta_{err}$  must in eq. 17 be written on real form to fit in.

The matrix  $A_{tot}$  is periodic ( $T=2\pi/\omega$ ). Stability of such a system is decided with Floquet theory (see e. g. (16)). In short, a unit disturbance, at  $t=0$ , in each state is studied one at a time for one period. Each state vector  $x_{err}(T)$  is collected into a state matrix  $X_{err}(T)$ . Now the error is asymptotically stable if all eigenvalues  $\lambda_{X_{err}}$  of  $X_{err}$  are below 1 in absolute sense and unstable otherwise. Computing  $\max(|\lambda_{X_{err}}|)$  gives exactly unity (1.0), for known stable limit cycles and higher values for unstable solutions. Absolute stability accordingly is not satisfied for the linearized model. However limit cycles just inside the nominal limit cycle have  $\max(|\lambda_{X_{err}}|) > 1$ , and those just outside have  $\max(|\lambda_{X_{err}}|) < 1$ . Thus we let the set of nominal limit cycles belong to the stable group if they satisfy  $\max(|\lambda_{X_{err}}|) < 1+\epsilon$ , with  $\epsilon$  a small number (for numerical reasons). Typically  $\epsilon=0.05$ .

The presented stability analysis is not an exact and sharp method, because of the ambiguity of where to set the limit of stability (the choice of  $\epsilon$ ). A solution just on the border between stability and instability may be put in the wrong category. In the cases investigated, unstable solutions have  $\max(|\lambda_{X_{err}}|) > 2.0$  and we have found an useful engineering tool.

## 6.3 Approach to a Limit Cycle

After solution and confirmation of stability, a last question is if a particular limit cycle will ever be reached. What initial conditions are needed? A gradually developing bow implies that the limit cycle with the lowest amplitude (first Fourier harmonic) is the most likely to occur. In the two-bow case it is more likely that initial contact only exists at one of the seal packages. These results are the base for the analysis in the following chapter.

## 7 TWO-BOW EXAMPLE AT DIFFERENT RUNNING SPEEDS

Rotor responses are computed for different running speeds according to Table 2. Due to the symmetry in Fig. 1 and because the stationary shaft position has been chosen so that the A-direction in Fig. 3 corresponds to the horizontal direction (same for both contacts), the rotor response  $R_{u11}=R_{u22}$ ,  $R_{u12}=R_{u21}$ ,  $R_{b11}=R_{b22}$ ,  $R_{b12}=R_{b21}$ . It is not necessary to have the same

contact direction, and another choice would just change the rotor responses (asymmetric bearing properties).

**Table 2: Rotor responses at seals for mass unbalances and bows.**

rpm	$R_{u11}$	$R_{u12}$	$R_{b11} * 10^{-3}$	$R_{b12} * 10^{-3}$
1400	0.1799 - 0.3017i	0.1677 - 0.2996i	3.4642 - 4.2059i	2.8076 - 4.1948i
1700	-0.1663 - 0.0623i	-0.1854 - 0.0584i	-1.3575 - 0.8314i	-2.0481 - 0.8118i
3200	-0.0123 - 0.0376i	-0.1171 + 0.0313i	0.3951 - 0.2086i	-0.6971 + 0.1346i
3600	-0.0020 - 0.0780i	-0.1210 + 0.0730i	0.4678 - 0.3984i	-0.6802 + 0.3415i
4000	-0.0318 - 0.1167i	-0.0869 + 0.1124i	0.3369 - 0.5752i	-0.4894 + 0.5289i
5000	-0.1489 - 0.1137i	0.0364 + 0.1104i	-0.1957 - 0.5374i	0.1246 + 0.5035i

The stationary (maximum) values of  $P_1$  and  $P_2$  are  $0.161 * 10^{-6}$  rad/W, and with 1400 W at 3600 rpm the maximum bows are  $\beta_1 = \beta_2 = 0.000225$  rad.

### 7.1 Time Simulations

Results for vibration amplitudes are presented in Fig. 5 for different running speeds. In all cases a clearance of 0.05 mm and an initial vibration  $\delta_0 = 0.06$  mm (at contact 1, zero at contact 2) have been assumed.

The traditional problem with high vibration amplitudes below the first resonance is seen (the Newkirk effect). Just above the first critical speed the bow acts to reduce the initial unbalance. At the nominal running speed (3600 rpm) a limit cycle develops.

The result is sensitive to assumed parameters such as maximum friction heat, but nevertheless the chosen rotor configuration with a bearing at each end may experience considerable changes of vibrations due to asymmetric heating above the first critical speed. A slightly higher heating (e. g. a higher coefficient of friction) would imply vibrations beyond acceptable levels.

### 7.2 Frequency Solutions

Let us study the nominal running speed more thoroughly, and use the frequency method presented above. The approach used is to make a large amount of random starting solutions of low order ( $n = -1, 0, 1$  in the Fourier series) and compute a solution. All converged low order solutions are then used as different starting solutions for higher order models. In the specific case two solutions were found, according to Fig. 6. Computation of stability yields that the point solution is unstable ( $\max(|\lambda_{\text{Xerr}}|) = 20$ ) and that the limit cycle is stable, as  $\max(|\lambda_{\text{Xerr}}|) = 1.0$ . It is evident that the time simulation for 3600 rpm corresponds to the stable frequency solution at the same speed.

The highest degree of the Fourier expansions above that has been used with success is  $N = 7$ , corresponding to  $4 * (2 * 7 + 1) = 60$  equations and unknowns. The recommendation is however to use a lower order in the iterative search process.

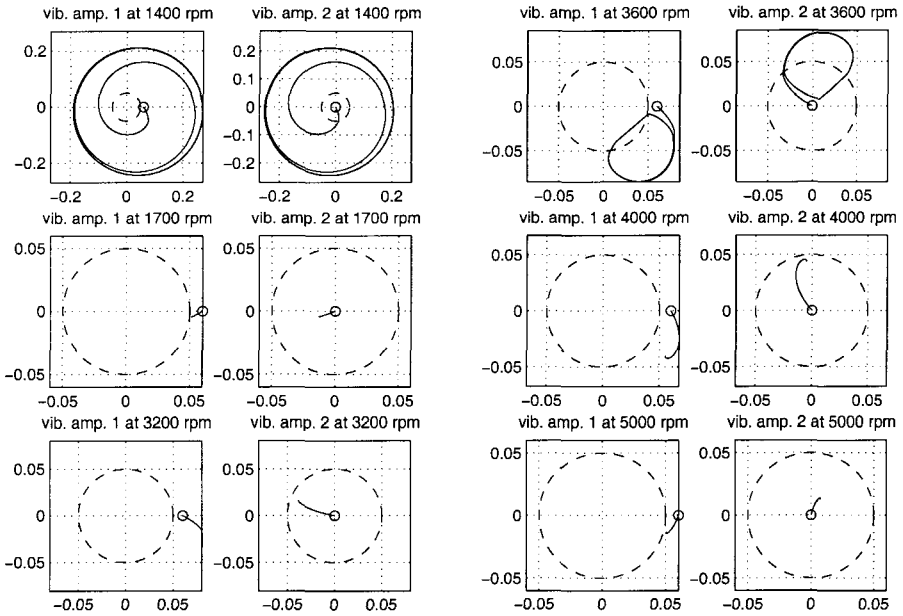


**Figure 5: Time simulation of rotor vibration. Vibration  $\delta$  in mm and circle indicate starting position.**

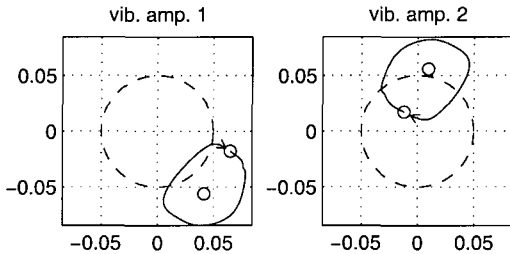


**Figure 6: Limit cycle at 3600 rpm. The circle inside the limit cycle is a point solution (constant in time). The circles indicate positions at  $t=0$ .**

## 8 CONCLUSIONS

Asymmetric frictional heating of a turbine rotor due to contact with a seal alters the dynamic response to an unbalance due to a closed loop, involving the temperature-dependent shaft bow. The time dependent response will in some cases assume a limit cycle (periodic change of the vibration). This is a result of the degressive rotor-seal contact to heat generation relation. It has been observed that the angular speed of the limit cycle may vary a lot, under certain circumstances.

The approach is well suited for multi-bow configurations (more than one bow in the axial direction), and the result for frictional contacts is presented for the first time. Further, a frequency-

domain solution is presented, and stability of computed limit cycles is decided with Floquet theory.

## 9 ACKNOWLEDGEMENT

The author wishes to thank his supervisor Karl-Olof Olsson for creative discussions and the Swedish Research Council for Engineering Sciences (TFR) for financial support.

## 10 REFERENCES

- (1) de Jongh, F. M. and Morton, P. G., *The Synchronous Instability of a Compressor Due to Bearing Journal Differential Heating*, ASME Journal of Eng. for Gas Turb. and Power, vol 118, 1996, pp 816-824.
- (2) Childs, D. W. and Jordan, L. T., *Clearance Effects on Spiral Vibrations Due to Rubbing*, ASME Design Engineering Technical Conference, Sep. 14-17, Sacramento, California, DETC97/VIB-4058, 1997.
- (3) Berot, F. and Dourlens, H. *On instability of overhung centrifugal compressors*, ASME Turbo Expo, 99-GT-202, Indianapolis, June 7-10, 1999.
- (4) Newkirk, B. L., *Shaft rubbing*, Mechanical Engineering, vol. 48 (1926), no. 8, pp 830-832.
- (5) Dimarogonas, A. D., *Analytical methods in rotor dynamics*, Applied Science Publishers Ltd., England 1983.
- (6) Dimarogonas, A. D., *An analytic study of the packing rub effect in rotating machinery*, Dissertation, Rensselaer Polytechnic Institute, Troy, N. Y., 1970.
- (7) Kellenberger, W., *Spiral vibrations due to the seal rings in turbogenerators. Thermally induced interaction between rotor and stator*, Journal of Mechanical Design, Jan 1980, vol. 102 pp. 177-184.
- (8) Schmied, J., *Spiral vibrations of rotors*, Rotating Machinery Dynamics, vol. two, Proceedings of the ASME Design Technology Conference, 1987, Boston, Massachusetts.
- (9) Muszynska, A., 1993, *Thermal/Mechanical Effect of Rotor-to-Stator Rubs in Rotating Machinery*, Vibration of Rotating Systems, ASME DE-vol. 60.
- (10) Keogh, P. S. and Morton, P. G., *The dynamic nature of rotor thermal bending due to unsteady lubricant shearing within a bearing*, Proceedings of the Royal Society of London, series A, vol. 445, May 1994, pp 273-290.
- (11) Larsson, B., *Journal Asymmetric Heating. Part I: Non-Stationary Bow*, ASME Journal of Tribology, vol. 121, 1999, pp 157-163.
- (12) Larsson, B., *Journal Asymmetric Heating. Part II: Alteration of Rotor Dynamic Properties*, ASME Journal of Tribology, vol. 121, 1999, pp 164-168.
- (13) Larsson, B., *Gas Turbine Rotor Exposed to the Newkirk Effect*, IFToMM's Fifth Inter. Conf. on Rotor Dynamics, Darmstadt, Sept. 7-10, 1998, pp 286-297.
- (14) Larsson, B., *Heat Separation in Frictional Rotor-Seal Contact*, submitted to ASME/STLE Tribology Conference, Seattle, 2000.
- (15) Cook, P. A., *Nonlinear Dynamical Systems*, Prentice Hall, 1994.
- (16) Farkas, M., *Periodic Motions*, Springer-Verlag, 1991.

## Impacts and Rub

*This page intentionally left blank*



# Experimental investigation of partial rotor-rub against a non-rotating part

Y-S CHOI

Department of Mechanical Engineering, Sungkyunkwan University, Kyunggi-do, Korea

## ABSTRACT

Rubbing occurs when a rotor contacts with a stator during the whirling motion of the rotor. Compared to a full annular rub, a partial rub against a nonrotating part is more common in practice. In this study, several partial rubbing phenomena of superharmonic and subharmonic vibrations, and jump phenomenon are demonstrated experimentally for the cases of light and heavy rub for a flexible rotor. The orbit patterns of forward or backward whirling are also calculated using directional spectrum analysis. The occurrence of subharmonic vibration during heavy rub is demonstrated as one impact per two rotations experimentally and numerically.

## 1. INTRODUCTION

The performance of rotating machinery such as a motor or a gas turbine can be maximized reducing the clearance between a rotation and nonrotating elements of the machine. During the whirling motion of a rotor, the rotor can contact with the stator of nonrotating elements. The contact between the rotor and stator during whirling motion is called a rubbing. The rubbing generated by some perturbation of normal operating conditions of the machine can maintain itself, and become more severe, leading to a higher vibration level. The rubbing can be one of the most damaging malfunction of rotating machinery.

Once rubbing occurs during the operation of rotating machinery, the runouts of the rotor and stator become large and the operation could be destructive. Because of this disastrous phenomenon, many researchers have been interested for the safe and reliable design of rotating machinery. Black[1] can be written as a notable contributor to this problem. He tried to explain the physics of rubbing using the polar receptance of the rotor and stator on a radial symmetric rotor. Ehrich[2] made a simple model and calculated the responses of the rotor

and stator numerically. Choi and Noah[3] treated this problem as a piecewise linear vibration problem, and proposed an algorithm to calculate the steady-state solution using FFT technique. The results showed that superharmonic and subharmonic responses could be found due to rubbing. Crandall and Lingener[4] showed a very specific pattern of whirling frequency responses during rubbing by an experiment, and developed a theory to explain backward rolling and backward slipping. Choi[5] demonstrated rubbing phenomenon which has different ways as increasing and decreasing the operating speed and explained the onset of backward whirling and the disappearance of backward slipping using the receptance of stator and rotor.

The study on a full annular rub has been done more than the study on a partial rub, since the circumferential homogeneity of the full annular rub makes the problem easy and simple. However, a partial rub is more common in practice. Intermittent impacts and friction during the partial rub make the phenomenon complex. In this respect, Beatty[6] provided a reliable rubbing detection methodology by relative harmonic frequency strength for the case of light rub. And Muszynska[7] demonstrated complex orbit patterns experimentally for a heavy rub and analyzed theoretically. However, the difference between the light and heavy rub is still not so clear, especially from the viewpoint of experimental demonstration.

In this study, several rubbing phenomena of super- and subharmonic vibrations, and jump phenomenon are demonstrated for the partial rub using an experimental apparatus. The experimental results are discussed by distinguishing between the light and heavy rub. The orbit patterns are calculated using the method of directional spectrum analysis to demonstrate the forward and backward components of the whirling motions. Also, the phenomenon of one impact per two rotations during heavy rub, which demonstrates the occurrence of subharmonic vibration, is discussed experimentally and numerically.

## 2. RUBBING PHENOMENON AND ITS ANALYTICAL MODEL

Destructive instability of rotors in high-speed and high efficiency rotating machinery with decreased clearance increases the possibility of rubbing due to thermal mismatch, rotor unbalance, aerodynamic and seal force, and misalignment at the minimum rotor/stator clearance locations, i.e., blade tips and seals. The occurrence of rubbing results in  $1X$ ,  $1/2X$ ,  $1/3X$  or  $2X$ ,  $3X$  components of vibration, high consumption of power, high levels of noise, and ultimately catastrophic failure of the machine itself.

Rubbing occurs in various ways depending on the design parameters and operation conditions of rotating machinery. Generally, rubbing has two types, a full annular rub and a partial rub. A partial rub involves intermittent contacts, whereas a full annular rub is continuous contact during whole whirling motion. The whirling direction may be the same as the rotor spin direction, forward whirling, or opposite, backward whirling. In the case of forward whirling, the whirling frequency is usually the same as the rotor speed, called forward synchronous whirling. Forward whirl always accompanies slipping. On the other hand, backward whirl goes with slipping or no slipping depending on the rotor speed. If there is no slipping at the contact surface, the rotor just rolls on the inner surface of the stator, called backward rolling. If slipping exists, it is called backward slipping [4,5].

The super- and subharmonic vibrations due to rubbing have been reported by numerical analysis [3] and experimental demonstrations [7,8]. The demonstrations were seen to be distinct in orbit pattern and Fourier spectrum. Subharmonic resonance is believed to be especially dangerous. The occurrence of superharmonic vibrations having higher harmonics can be deduced by the distortion of whirling orbits during rubbing. However, no other clear explanation on the occurrence of subharmonic response is still found.

Forward and backward whirl, super- and subharmonic vibrations have been reported to occur in both full annular and partial rub. For a full annular rub, only the friction force affects the whirling motion. However, for a partial rub, intermittent impact is added, which makes analysis more complicated.

For the analysis of a partial rub, Fig. 1 of an experimental apparatus was set-up in order to investigate the effect of contact position. The contact was supposed to occur at the middle of the shaft. The whirling motion was measured at both ends of the shaft using gap sensors in x and y directions. When the runout of the rotor due to the unbalance or bend of the shaft comes to the limit of the given clearance, the shaft comes into contact with a protrusion on the stator. The response of the rotor due to contact at a discrete protrusion would not be expected to be the same as contact at one point on a continuous circular stator. The contact between the rotor and stator causes the variation of stiffness of the rotor and the friction at the contact surface makes for complex whirling orbits. From the consideration of the effects of a partial rub, an analytical model of Fig. 2 is assumed. From the analytical model, the following equation of motion is derived.

$$M\ddot{z} + C\dot{z} + Kz + F(\omega t)[K_c|z| + N(1 + j\mu)]e^{j\beta} = Me\omega^2 e^{j(\omega t + \delta)} \quad \text{Eq. (1)}$$

where  $z = x + jy$

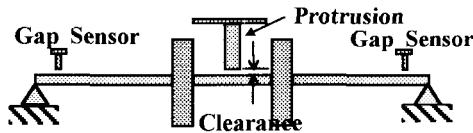


Fig. 1 Schematic diagram of experimental apparatus for partial rubbing

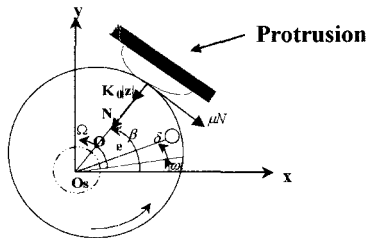


Fig. 2 Analytical model of partial rub

Where  $M$ ,  $C$ , and  $K$  are rotor mass, damping and stiffness coefficients,  $F(\omega t)$  is the function which indicates the contact, i.e., if the rotor contacts,  $F(\omega t)$  is unity, otherwise zero.  $K_c$ ,  $N$ ,  $\mu$ , and  $\beta$  are contact stiffness, normal force, friction coefficient, and the angle of contact position, respectively.  $e$  and  $\omega$  are eccentricity and exciting frequency, i.e., the rotor speed. The equation(1) can not be solved simply since the occurrence of contact can not be predicted, and the contact force and friction force are impossible to predict or calculate without further definition of the contact conditions. In this respect, experimental investigations on rubbing become meaningful and important.

### 3. EXPERIMENT

In this research, the RK-4 rotor kit, manufactured by Bently Nevada Co. was used to demonstrate various partial rubbing phenomena as shown in Fig. 3. The contact between the stator and rotor was accomplished by making a protrusion of brass screw bolt at the top of the stator. If the runout of the rotor exceeds the given clearance between the protrusion and shaft during the whirling motion of the rotor, the shaft becomes contact with the protrusion. The whirling orbit was measured using four gap sensors near the position of both bearing supports with x and y direction, respectively, as shown in Fig. 1. The running speed of the rotor was measured by a photo sensor with a spur gear having 60 teeth. A key phasor was set up to indicate the initial point of the whirling orbit. The signals measured by several sensors were stored in a computer through analog-to-digital conversion, and analyzed using MATLAB [8]. The position of partial rub was set to occur at the middle of the shaft. However, the measuring points for the whirling motion were near the bearing support. The difference can be corrected by considering the mode shape of the rotor. Fortunately the range of operation was much lower than the second natural frequency. Thus, only the first mode was considered.

The natural frequency and damping coefficient of the rotor system were measured from an impact test and a free run test. An impact was exerted on the center of the shaft, where the contact happens, and the response was measured at near the bearing position using gap sensors. The free run test means the running test for the rotor system by increasing and decreasing the speed of rotor. Since the tests were done after the cautious adjustment of the rotor system, which makes the orbit circular, the vertical and horizontal results show the same value. The stiffness of the rotor was found by static deflection test, which measures the static deflection of the shaft when a force is exerted on the center of the shaft. The mass of the rotor was calculated from the natural frequency and stiffness of the shaft. The system parameters of the rotor kit are shown in Table 1.

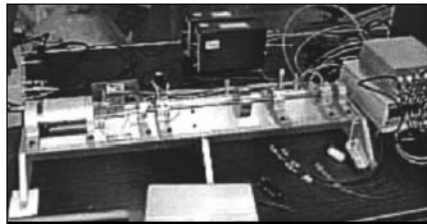


**Fig. 3 Experimental apparatus, RK-4 Rotor Kit**

Table 1 System parameters of the rotor kit

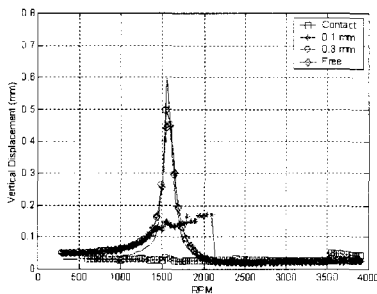
Mass, M	Viscous damping coefficient, C	Stiffness, K	Eccentricity, e
0.50 (kg)	2.60 (Ns/m)	14,100 (N/m)	0.125 mm

#### 4. FREQUENCY RESPONSE

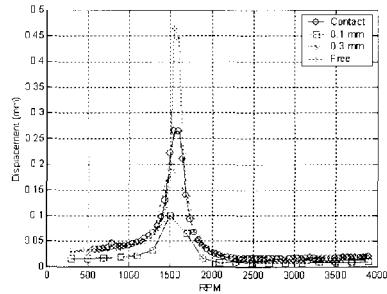
The runouts of the rotor were measured with varying clearance and rotor speed. Fig. 4 shows the vertical and horizontal displacements of the rotor. “Free” in the Fig. 4 means free response without any contact with the stator, “0.1 mm” and “0.3 mm” means the clearance size between the rotor and stator at the middle of the shaft, where the protrusion exists. “Contact” means zero clearance size, i.e., the shaft and protrusion are in contact with each other at the beginning of the rotor run.

The response of the free run shows a typical response of a single-degree-of-freedom rotor system. The response for 0.3 mm gap shows similar shape with the free run case. However, the response for 0.1 mm gap shows a very distorted response compared to the free run case. The vertical response for 0.1 mm gap especially shows a jump phenomenon. The responses of increasing speed are different from those of decreasing speed near the range of 2000 rpm. This is considered that the contact between the rotor and stator introduces nonlinearity due to hardening the stiffness of the rotor system.

The slight contact of 0.3 mm gap seems to be a light rub, and the deep contact of 0.1 mm gap seems to represent a heavy rub. As the speed increases, the vertical and horizontal responses with the variations of the gap size are almost similar. The horizontal response has little effect due to the protrusion for the case of 0.3 and 0.1 mm gap size. However, the horizontal responses for zero clearance are greater than for 0.3 mm clearance. This is because the orbit becomes flat as the duration of contact is longer in the case of zero gap. And, in the range of greater than 3000 rpm, the vertical responses of zero gap become larger as the irregularity of the orbit become larger.



(a) Vertical



(b) Horizontal

Fig. 4 Vibration levels for different clearances

## 5. WHIRLING ORBITS AND DIRECTIONAL SPECTRUM

Fig. 5 shows the whirling orbits during the partial rub for 0.1 mm and 0.3 mm gap near the range of the first critical speed. The orbit of 0.3 mm gap is almost a circle, like the response of the free case, however, the orbit of 0.1 mm gap is completely different from that of free case. Therefore, it can be said that the response of 0.3 mm gap represents a light rub and that of 0.1 mm gap represents a heavy rub. From these experimental results, a partial rub due to a protrusion attempts to maintain its orbit heavier during the whirling motion of the rotor for small interference, however, if the interference is not so small, the orbit becomes a completely different shape. The distortion of the orbit has the shape of a horizontally long irregular ellipse. The orbit of feature of 8 or star shape, which was demonstrated by Muszynska[7] was not found in this experiment. It is believed that the shape and material of the protrusion, the system parameters, and the operation speed have effects on the orbit shape.

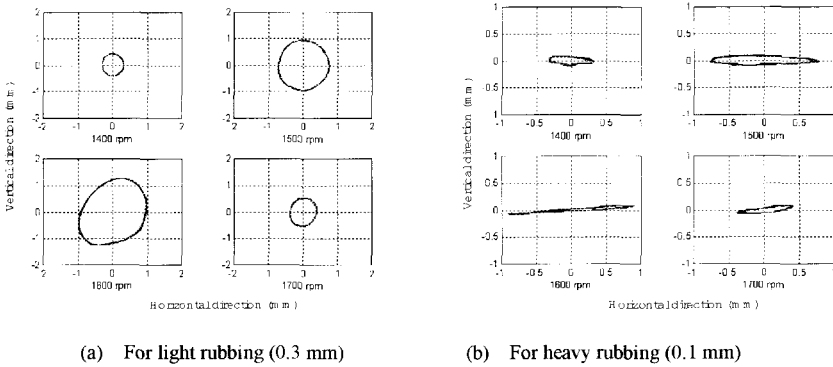


**Fig. 5 Orbits during rubbing**

The distorted orbits are generally the combination of forward and backward whirling motion with several higher modes. In this respect, the classification of forward and backward whirling motion is done using the directional spectrum analysis, which was developed by Lee [9].

$$w(t) = x(t) + jy(t) \quad \text{Eq. (2)}$$

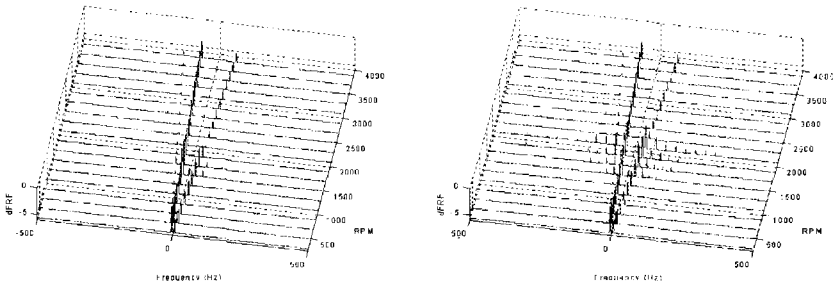
$$w(t) = r_f e^{j\omega t} + r_b e^{-j\omega t} \quad \text{Eq. (3)}$$

Where  $r_f$  and  $r_b$  are the complex amplitude of forward and backward whirling amplitudes, respectively.

The directional spectrum regards the x and y directional responses as a complex response as like the equation (3). The complex response is analyzed using FFT algorithm in the directional spectrum analysis. The results are shown in Fig. 6 as a waterfall diagram for the case of 0.3 mm and 0.1 mm gap, respectively.

As shown in Fig. 6 for the light rubbing of 0.3 mm gap, the backward components are

dominant after the contact and the second order superharmonic vibrations,  $2X$  are shown in the backward components. And for the heavy rubbing of 0.1 mm gap, the backward components are more dominant. Also, several higher harmonics are gathered near the first critical speed. This is believed that the strong nonlinear effects of impact and friction due to the contact between the rotor and stator make the complex orbits. Consequently the directional spectrum analysis on the response of partial rubbing shows the existence of the backward whirling components and higher harmonic terms. However, the existence of the subharmonic term, which is believed as a typical phenomenon of rotor rubbing, was not so clear in this directional spectrum analysis.



(a) For light rubbing (0.3 mm)

(b) For heavy rubbing (0.1 mm)

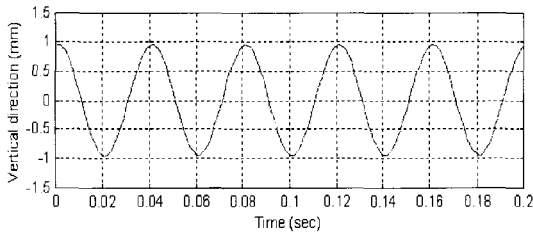
**Fig. 6 Directional Waterfall diagram**

## 6. SUBHARMONICS

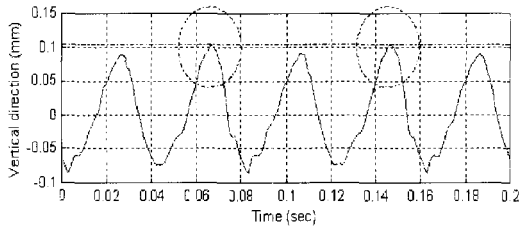
Fig. 7 shows the time response of vertical displacements of the whirling rotor during partial rubbing. As shown in Fig. 7(a) for the case of light rub, the time response is almost sinusoidal function without any large distortion due to the contact. However, for the case of heavy rub in Fig. 7(b), the time response shows a distorted shape from sinusoidal function, which is resulted from the inclusion of higher harmonics as shown in directional spectral analysis of Fig. 6. Also, the highest peak appears once per two revolutions of the whirling motion. This is shown more clearly in Fig. 7(c) of the whirling orbit, where the orbit is drawn for more than 10 revolutions. Nevertheless, the orbit is not completely overlaid. This is the experimental second order sub-harmonic response.

In order to verify the second order subharmonic vibration, i.e., one contact per two revolutions, an iterative numerical analysis for the equation of motion (1) was done using the system parameters of Table 1. Since the equation of motion (1) is a kind of nonlinear equation due to the contact, the steady-state response can be different depending on initial conditions. In this respect, to find all the steady-state responses is not so easy. The normal force and friction coefficient in the equation (1) can not be predicted. However, it is known that the displacement at the contact is the gap size, only the velocities of before and after contact are unknown. Here, the concept of the coefficient of restitution can be utilized. The initial displacement at the contact and an assumed initial velocity after the contact are input

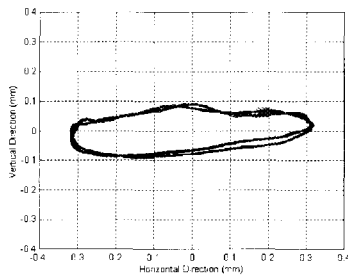
data for the free run condition. The displacement after one or two revolutions is then checked for the agreement with the original estimate. If not in agreement, the initially assumed velocity needs to be modified. Although the calculation can be done analytically, a fourth order Runge-Kutta method and shooting method for modifying the initial velocity were used. The numerical results for the light rubbing show only the 1X component, however, for the case of heavy rubbing as shown in Fig. 8(a), there is one contact only every two revolutions. Fig. 8(b) shows the velocities for the steady-state response. In this case, the coefficient of restitution was 0.76, which is the measured value from the experiment by checking the velocities of before and after the contact. Therefore, the analysis using this coefficient of restitution can be said to be valid. Consequently, the 1/2X component of subharmonic vibration during partial rubbing was found experimentally and was verified by mechanical analysis.



(a) For light rubbing (1500 rpm)



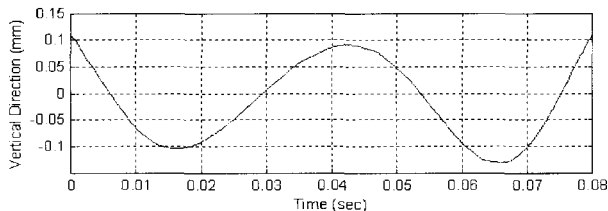
(b) For heavy rubbing (1500 rpm)



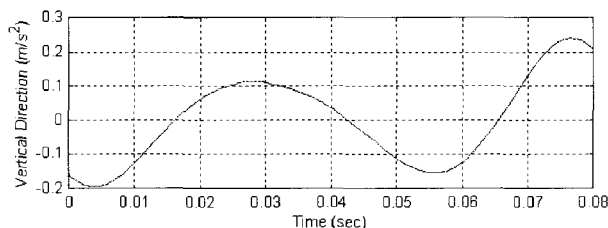
(c) Orbit of heavy rubbing (1500 rpm)

**Fig. 7 Time signals at impact**





(a) For heavy rubbing(displacement)



(b) For heavy rubbing (velocity)

**Fig. 8** Calculated time signals during rubbing

## 7. CONCLUSION

In this paper, a partial rub of a rotor due to contact with a nonrotating protrusion is investigated by an experiment for the clarifications of nonlinear characteristics, such as jump phenomenon, forward and backward whirling motion, and super- and subharmonic responses. The rubbing phenomena are demonstrated on the RK-4 rotor kit of Bently Nevada Co. The experiment shows the following results.

- 1) A partial rub characterizes the one kind of nonlinear phenomenon by showing the superharmonics, subharmonics, and jump phenomenon, which were demonstrated experimentally.
- 2) As long as the interference of the whirling shaft with a nonrotating part is not so large, the rotor shows a light rub with a similar response to the free run case. However, for the case in which the interference is large, the rotor demonstrates a heavy rub, giving a flat ellipse shaped orbit with distortions.
- 3) During the rub, impacts and friction generate a backward whirling motion, which was demonstrated by directional spectrum analysis.
- 4) The second order subharmonic response near the critical speed is due to the contact of once per two revolutions.
- 5) The coefficient of restitution can be utilized successfully to analyze the impact phenomenon of partial rub.

## ACKNOWLEDGEMENT

This work was supported by a grant from the Critical Technology 21 Project of the Ministry of Science and Technology, Korea.

## REFERENCE

- [1] Black, H. F., 1968, "Interaction of a Whirling Rotor with a Vibrating Stator across a Clearance Annulus," *J. of Mechanical Engineering Science*, 10, pp. 1-12.
- [2] Erich, F. F. and O'Connor, J. J., 1966, "Stator Whirl with Rotor in Bearing Clearance," ASME Paper 66. WA/MD-8.
- [3] Choi, Y. -S. and Noah, S. T., 1987, "Nonlinear Steady-State Response of a Rotor-Support System," *Journal of Vibration, Acoustics, Stress, and Reliability in Design*, Vol. 109, No. 4, pp. 225 ~ 261.
- [4] Crandall, S. H. and Lingener, A., 1990, "Experimental Investigation of reverse Whirl of a Flexible Rotor," in *Transactions, ITFoMM Third International Conference on Rotordynamics*, Lyon, France, pp. 13-18.
- [5] Choi, Y. -S., 1994, "Dynamics of Rotor Rub in Annular Clearance with Experimental Evaluation," *KSME Journal*, Vol. 8, No. 4, pp. 404-413.
- [6] Beatty, R. F., 1985, "Differentiating rotor response due to radial rubbing," *Journal of Vibration, Acoustics, Stress, and Reliability in Design*, Vol. 107, pp. 151-160.
- [7] Muszynska, A., 1984, "Partial lateral rotor to stator rubs," *ImechE C281/84*, pp. 327-335.
- [8] The MathWorks, 1996, "MATLAB User's Guide".
- [9] Lee, C.W., 1994, "Development of the Use of Directional Frequency Response Functions for the Diagnosis of Anisotropy and Asymmetry in Rotating Machinery:, Theory," *Mechanical Systems and Signal Processing*, Vol. 8, No.6, pp. 665-678.

# Coupled bending and torsional vibrations due to rotor-to-stator contacts

**X DENG**

Institute of Monitoring and Control for Rotating Machinery and Windturbines, Northwestern Polytechnical University, Xi'an, People's Republic of China

**R LIEBICH and R GASCH**

Aerospace Institute, Technical University of Berlin, Germany

## ABSTRACT

This paper presents the first calculations of a new Rotor-to-Stator contact model describing the coupled bending and torsional vibrations of a rotor and an elastic stator due to contacts. The numerical calculations lead to a variety of rotor orbit figures due to the different kinds of contacts and the big influence of all system parameters on the rotor behaviour. The model is able to describe full annular rubs, partial rubs and also the heavily destructive dry-friction-whip when the rotor rolls on the stator's inner surface.

## 1. INTRODUCTION

Rotor-stator-contact is a serious malfunction in rotating machinery. Rotor-stator-contact interaction inevitably affects the normal operation of the machine in the way of force and thermal unbalance, dynamic stiffness, and then changes the machine's motion. The malfunction due to rotor-stator-contact will directly lead to decreasing rotational speed, decreasing efficiency, and sometimes, catastrophic failure of the machine. The possibility of rotor-stator-contact in turbines has increased remarkably due to the rapid development in higher performance and its requirements such as closer clearances and bigger size.

Rotor-stator-contact is also a rather complex problem in rotating machinery due to its nonlinear dynamics characteristic. When a rotor-stator-contact related phenomenon happens, several dynamic phenomena occur such as friction, impact, coupling effect, stiffening effect, thermal effect and torsional effect. Many investigations have been done since the problem was first described by Newkirk in 1926. But as the numerical integration of stiff differential equations with many degrees of freedom was not possible until the late eighties, these analytical attempts were of very restricted value.

There is still a lot of work to do with this unwelcome problem which is encountered in modern industry. The authors present an investigation on the torsional vibration effect of rotor-stator-contact interaction, for which publications about this subject are presently rather rare. Ehrich (1) was one of the first who published a paper on rub influence on torsional vibrations.

Rotor-stator-contact problem involves many comprehensive nonlinear dynamics problems. In this paper, the torsional vibration effect of the rotor-stator-contact related problem is investigated. A complete rotor-stator-contact model with two discs is built in absolute coordinates. In this way, a multi-degree-freedom system is established. The presented rotor model describes the rotor and the stator vibration due to normal contact and the rubbing forces and the vibrations due to the coupling of bending and torsional vibration. The torsional vibrations are excited by the rubbing forces acting in a tangential direction at the rotor surface. Due to these forces the running speed is reduced for a short time. Higher friction coefficients often lead to dry-friction-whips. Multiple Contacts during one turn of the rotor lead to partial rubs. These partial rubs can be detected with the Fast-Fourier-Transformation (FFT) of the rotor vibration. First calculations are done using a stationary equation system which splits the torsional vibration into two parts: the stationary rotation and the vibration due to rub. This is necessary to understand more of the torsion influence on the rotor vibration. Future numerical calculations will consider instationary operations using a motor-moment acting in the torsional equation. With this future model it will be possible to focus on the rub's influence in torsional vibrations especially during run-ups and run-downs of turbines. So the present paper presents some first numerical calculations only.

At the end of the extensive investigation the authors hope to get some effective diagnosis criteria for rotor-stator-contact from numerical calculations and additional experimental investigations.

## 2. THE MECHANICAL MODEL

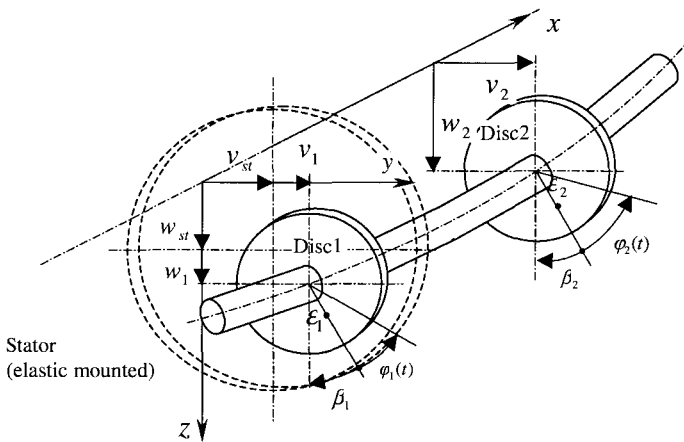


**Fig. 1: Rotor-stator-contact model**

The rotor-stator-contact model applied in this research is made up of a massless shaft, two discs and an elastic mounted stator, as shown in Fig. 1. The discs have some initial unbalances,





stationary part  $\Omega t$  (due to the constant rotational speed  $\Omega$ ) and a dynamic part  $\Delta\varphi$ . So we substitute in the following:  $\varphi_1 = \Omega t + \Delta\varphi_1$  and  $\varphi_2 = \Omega t + \Delta\varphi_2$ .

The torque moment and contact forces vectors are

$$\{f_{cor}\}^T = \{0 \ 0 \ 0 \ 0 \ M_1 \ M_2 \ 0 \ 0\}$$

and 
$$\{f_{con}\}^T = \{F_{z1}^* \ 0 \ F_{y1}^* \ 0 \ M_{T1}^* \ 0 \ -F_{z1}^* \ -F_{y1}^*\} \quad (9)$$

where both the motor and generator moments  $M_1$  and  $M_2$  are zero because of the non-stationary calculation.  $F_{z1}^*$ ,  $F_{y1}^*$  and  $M_{T1}^*$  are contact forces and moments which were described in the following.

### 3.1. Contact force

The same contact conditions from the paper of Liebich (2) were used. When the relative vibration of the rotor reaches the minimum of the radial clearance between rotor and stator, rotor-stator-contact interaction starts, and then the normal contact force and the tangential friction force inevitably generate at the point of contact. They act on both rotor and stator, but in an opposite way, shown in Fig. 2. The whole force generated by contact according to the established orthogonal coordinates is decomposed into the vertical component  $F_{y1}^*$  and the horizontal component  $F_{z1}^*$ . The torque moment  $M_{T1}^*$  is calculated in this way as well.

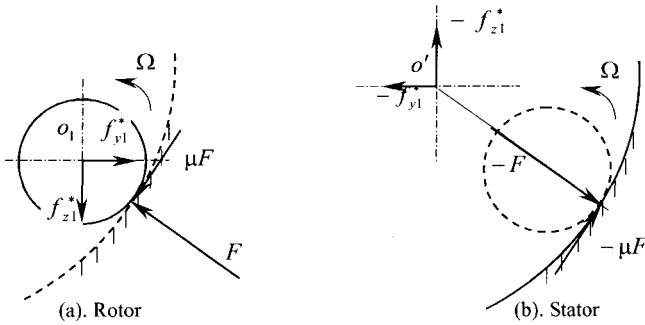


**Fig. 2: Contact force**

Here special attention should be paid to the direction of the tangential force, which is always opposite to the rotating direction. For forward whirl, the direction of tangential friction force is just what is shown in Fig. 2, but for backward whirl, it has to be turned through 180 degrees. Then  $F_{z1}^*$ ,  $F_{y1}^*$  and  $M_{T1}^*$  can be separately written as

$$\text{Forward whirl } (\dot{\varphi}_1 \geq 0), \quad F_{z1}^* = -|F|L_{c1} + \mu|F|L_{s1} \quad (10)$$

$$F_{y1}^* = -|F|L_{s1} - \mu|F|L_{c1} \quad (11)$$

$$M_{T1}^* = -|F|L_{c1} \cdot [\varepsilon_1 \sin(\beta_1 + \varphi_1) - r_1 L_{s1}] - |F|L_{s1} \cdot [r_1 L_{c1} - \varepsilon_1 \cos(\beta_1 + \varphi_1)] - \mu|F|L_{c1} \cdot [r_1 L_{c1} - \varepsilon_1 \cos(\beta_1 + \varphi_1)] + \mu|F|L_{s1} \cdot [\varepsilon_1 \sin(\beta_1 + \varphi_1) - r_1 L_{s1}] \quad (12)$$

and backward whirl ( $\dot{\varphi}_1 < 0$ ),  $F_{z1}^* = -|F|L_{c1} - \mu|F|L_{s1}$  (13)

$$F_{y1}^* = -|F|L_{s1} + \mu|F|L_{c1} \quad (14)$$

$$M_{T1}^* = -|F|L_{c1} \cdot [\varepsilon_1 \sin(\beta_1 + \varphi_1) - r_1 L_{s1}] - |F|L_{s1} \cdot [r_1 L_{c1} - \varepsilon_1 \cos(\beta_1 + \varphi_1)] + \mu|F|L_{c1} \cdot [r_1 L_{c1} - \varepsilon_1 \cos(\beta_1 + \varphi_1)] - \mu|F|L_{s1} \cdot [\varepsilon_1 \sin(\beta_1 + \varphi_1) - r_1 L_{s1}] \quad (15)$$

where

$$L_{s1} = \frac{v_{s1} - \varepsilon_1 \sin(\beta_1 + \varphi_1) - v_{st}}{\sqrt{[w_{s1} - \varepsilon_1 \cos(\beta_1 + \varphi_1) - w_{st}]^2 + [v_{s1} - \varepsilon_1 \sin(\beta_1 + \varphi_1) - v_{st}]^2}}$$

$$L_{c1} = \frac{w_{s1} - \varepsilon_1 \cos(\beta_1 + \varphi_1) - w_{st}}{\sqrt{[w_{s1} - \varepsilon_1 \cos(\beta_1 + \varphi_1) - w_{st}]^2 + [v_{s1} - \varepsilon_1 \sin(\beta_1 + \varphi_1) - v_{st}]^2}} \quad (16)$$

and the normal contact force is

$$|F| = s_{contact} \cdot \left[ \sqrt{[w_{s1} - \varepsilon_1 \cos(\beta_1 + \varphi_1) - w_{st}]^2 + [v_{s1} - \varepsilon_1 \sin(\beta_1 + \varphi_1) - v_{st}]^2} + r_1 - r_{st} \right] \quad (17)$$

which is valid only when

$$\sqrt{[w_{s1} - \varepsilon_1 \cos(\beta_1 + \varphi_1) - w_{st}]^2 + [v_{s1} - \varepsilon_1 \sin(\beta_1 + \varphi_1) - v_{st}]^2} + r_1 - r_{st} > 0 \quad (18)$$

Changing the 2<sup>nd</sup> order differential equation into a 1<sup>st</sup> order equation for the numerical treatment we get the state-space-equation of the rotor-to-stator contact model:

$$\{\dot{y}\} = -[A]^{-1}[B]\{y\} + [A]^{-1}\{p\} \quad (19)$$

where

$$\{y\} = \begin{Bmatrix} \dot{u} \\ u \end{Bmatrix}, [A] = \begin{bmatrix} M & 0 \\ 0 & -S \end{bmatrix}, [B] = \begin{bmatrix} D & S \\ S & 0 \end{bmatrix}$$

and

$$\{p\} = \begin{Bmatrix} f_{ub} \\ 0 \end{Bmatrix} + \begin{Bmatrix} f_{tor} \\ 0 \end{Bmatrix} + \begin{Bmatrix} f_{con} \\ 0 \end{Bmatrix}$$

#### 4. SOME RESULTS OF THE NUMERICAL CALCULATIONS

Applying the given data (see Notation and Data Table) of the model, we can precisely calculate the natural bending frequencies  $\omega_{B1} = 157.9$  rad/s,  $\omega_{B2} = 238.7$  rad/s and the torsional frequencies  $\omega_{T1} = 0$  rad/s,  $\omega_{T2} = 177.7$  rad/s. The rotor's data are chosen arbitrarily. Likely, a contact appears at the shaft. But the influence of rub on torsional vibrations becomes bigger with a larger radius. For this reason it is assumed in the first investigations that the rotor's contact with the stator takes place at disk 1 which has a larger radius than the shaft. The reason for contact in this model is an assumed sudden blade loss which indicates a sudden high unbalance. As was mentioned before these are the first results of the numerical investigation. Only a few examples will be presented to show the variety of the rotor response due to rub.



Fig. 3 shows the forward and backward FFT of the horizontal and vertical rotor response at disc 1 versus the rotor speed. Several subharmonics and superharmonics of the rotor's speed appear as well in forward direction as in backward direction. Childs (3), (4) investigated the influence of rub on 1/2 and 1/3 subharmonics in the frequency domain. His results demonstrated that 1/2 speed subharmonic motion can be explained as a stable nonlinear subharmonic motion. It is clearly shown in Fig. 3 that there are much more subharmonic and chiefly superharmonic motions as for example -1/2 or +2 speed harmonics. Two dashed lines in the figure mark travelling frequencies which are not fixed at special superharmonic ratios. These frequency ratios will vary versus the rotational speed. It is clear that there are more frequency ratios due to rub than 1/2 or 1/3 ratios we know from literature. Other rotor models will show obviously other ratios of subharmonic and superharmonic frequencies. The different appearing frequencies in back- and forward direction demonstrate the necessity to use the forward/backward FFT for rub detection as well.

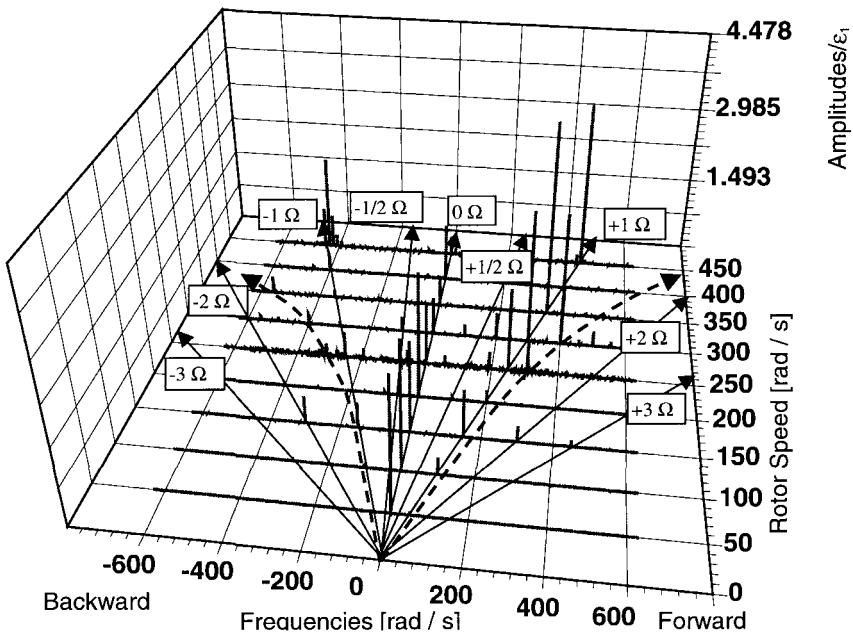


**Fig. 3: Forward/backward FFT of the the rotor orbit vs. rotor speed  $\Omega$**

Fig. 4 shows the FFT of the torsional vibration velocity of disk 1 versus the friction coefficient. The main frequency peak at the rotor speed frequency  $\Omega = 200$  rad/s appear even when there is no contact due to the coupling in the unbalance vector (see Eq. 6). Besides this rotor speed frequency ( $1\Omega$ ) several superharmonic frequencies mainly  $3/2\Omega$ ,  $2\Omega$  and  $5/2\Omega$  appear as well. Here, the influence of the friction coefficient is detectable in the torsional vibrations only. Looking at the Orbits at different friction conditions in Fig. 4 (insets) one can see that there is no difference in the vertical and horizontal rotor response due to a change in the friction coefficient.

Fig. 5 presents another example for the influence of friction on the torsional vibration. Here, the FFT of the torsional vibration velocity of disk 1 versus the friction coefficient is shown.

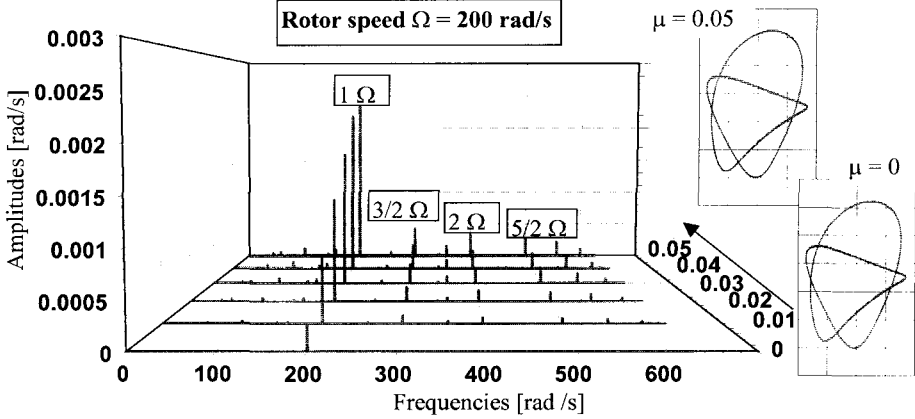


Fig. 4: FFT of torsional vibration's velocity  $\dot{\phi}_1$  vs. friction coefficient  $\mu$ , (Insets: some rotor orbits)

Besides the rotor speed frequency peak,  $1/3$  and  $2/3$  subharmonics and a smaller  $4/3$  superharmonic frequency were detectable. Different to the example before, in this case the main peak is not the rotor speed frequency peak but the  $2/3$  subharmonic peak followed by the  $1/3$  subharmonic peak. The rotors orbit remains nearly the same. As one can see there is a tendency to non-periodic motions in the higher friction domain.

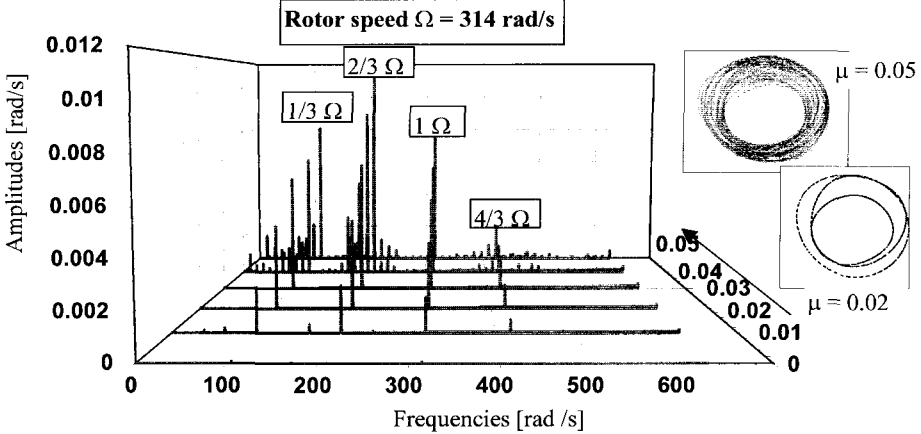


Fig. 5: FFT of torsional vibration's velocity  $\dot{\phi}_1$  vs. friction coefficient  $\mu$ , (Insets: some rotor orbits)

A friction coefficient of  $\mu = 0.05$  is relatively low. This means a well lubricated surface at the contact point. Usually a non-lubricated steel to steel contact should be described by higher friction coefficients up to  $\mu = 0.8$ . Further numerical calculations yield unstable behaviours of

the rotor due to higher friction coefficients. In most cases backward whirl orbits preceded these unstable behaviours. Here, the well-known dry-friction-whip took place which was described by Black (5).

## 5. FUTURE WORK

The next step of investigation is to use the non-stationary system of equations. For future general statements it is necessary to introduce dimensionless parameters to reduce the variety of calculation examples. The authors feel that there are strong and weak dimensionless parameters. So the authors hope to reduce the variety of important parameters to 4 or 5. With such a simple rotor-to-stator contact system it must be possible to understand and explain the whole rub problem and give hints for avoiding problematic turbine operations. Depending on the state of investigation the authors will present more interesting results at the conference.

## NOTATION AND DATA TABLE

$m_1 = m_2 = 124.05 \text{ kg}$	masses of disc1, disc2
$\varepsilon_1 = 6.7 \times 10^{-5} \text{ m}, \varepsilon_2 = 0$	eccentricities of disc1, disc2
$\beta_1 = \beta_2 = 0$	centrifugal angles of disc1, disc2
$r_1 = r_2 = 0.225 \text{ m}$	radii of disc1, disc2
$\Theta_1 = \Theta_2 = 3.14 \text{ kgm}^2$	rotation inertia of disc1, disc2
$M_1 = M_2 = 0,$	torque moments of disc1, disc2
$I_{a1} = I_{a2} = 3.068 \times 10^{-7} \text{ m}^4$	axle inertia moments of disc1, disc2
$I_{p1} = I_{p2} = 6.136 \times 10^{-7} \text{ m}^4$	polar inertia moments of disc1
$s_{11} = s_{22} = 5.081 \times 10^6 \text{ N/m}$	bending stiffnesses of system
$s_{12} = s_{21} = 1.988 \times 10^6 \text{ N/m}$	
$d_{11} = d_{22} = 7.83 \times 10^2 \text{ kg/s}$	bending dampings of system
$d_{12} = d_{21} = 0$	
$s_{T12} = s_{T21} = -4.956 \times 10^4 \text{ N}\cdot\text{m}$	torsional stiffnesses of system
$s_{T11} = s_{T22} = 4.956 \times 10^4 \text{ N}\cdot\text{m}$	
$d_{T11} = d_{T22} = 22.31 \text{ kg}\cdot\text{m/s}$	torsional dampings of system
$d_{T12} = d_{T21} = 0$	
$m_{st} = 372.15 \text{ kg}$	mass of stator
$s_{st} = 1.484 \times 10^8 \text{ N/m}$	stiffness of stator
$d_{st} = 1.41 \times 10^4 \text{ kg/s}$	damping of stator
$E, G$	Young's modulus (Steel), shear modulus of elasticity
$g, \rho$	acceleration of gravity, density of material (Steel)
$s_{contact} = 5.081 \times 10^7 \text{ N/m}$	contact stiffness coefficient between rotor and stator
$\mu$	friction coefficient
$F, \Omega$	contact force, steady running rotation speed

## REFERENCES

- (1) Ehrich, F.F. : Self-Excited Vibration, Shock and Vibration Handbook, 2<sup>nd</sup> Ed., Mc.Graw-Hill, 1976
- (2) Liebich, R. : Rub Induced Nonlinear Vibrations Considering the Thermo-Elastic Effect, Proc. of the 5<sup>th</sup> Int. Conf. on Rotor Dynamics, IFToMM, pp 802, 1998
- (3) Childs, D. : Rub Induced Parametric Excitation in Rotors, Journal of Mechanical Design, Transaction of the ASME, Vol. 101, pp 640-644, 1979
- (4) Childs, D. : Fractional-Frequency Rotor Motion Due to Nonsymmetric Clearance Effects, ASME Publ. 81-GT-145, Intl. Gas Turbine conf. Products Show, Engrg. Power, 1981
- (5) Black, H.F. : Interaction of a Whirling Rotor with a Vibrating Stator Across a Clearance Annulus, J. Mech. Engrg. Sci., Vol. 10 (1), pp 1-12, 1968

# An experiment to measure the restitution coefficient for rotor-stator impacts

M L ADAMS, F AFSHARI, and M L ADAMS

Department of Mechanical and Aerospace Engineering, Case Western Reserve University, Cleveland, Ohio, USA

## SYNOPSIS

An apparatus was devised to measure rotor-stator impact velocities with the objective to obtain restitution coefficient values to enable improved simulation accuracy of non-linear time-transient rotor vibration response computations. The apparatus provides accurate geometric control over rotor-stator line contact at the impact site and alternatively accurate setting of rotor-stator misalignment. Velocity and trajectory components through impact are measured using laser vibrometers and proximity probes, respectively. Restitution coefficient results compare favorably with published information from experiments on configurations which are not rotor-stator sets. The results exhibit the maximum coefficient-of-restitution values as impact velocity is reduced, and asymptotically approach a lower limit as impact velocity is increased. The results also indicate that rotor surface speed has a negligible effect on the coefficient-of-restitution values.

## 1 INTRODUCTION

The boiler feed pump illustration from Adams (1) in Figure 1 exemplifies the rotating machinery types that possess quite small internal annular radial clearance gaps. These small internal radial clearances are essential for efficient functioning of such machines and are among the most important reasons for the close attention paid to operating vibration levels in rotating machinery. This is because one of the deleterious effects of excessive rotor vibration is contact between rotor and stator at locations with small rotor-stator radial clearances. Such rotor-stator contact is of course undesirable but tolerable in most machines for brief periods during initial wear-in or operating transients. Persistent rotor-stator contact considerably accelerates the wearing open of the small rotor-stator clearance gaps, shortening considerably the time between machine repairs and major overhauls. Furthermore, persistent rotor-stator contact puts a machine in jeopardy of damage from large amplitude highly non-linear vibration.

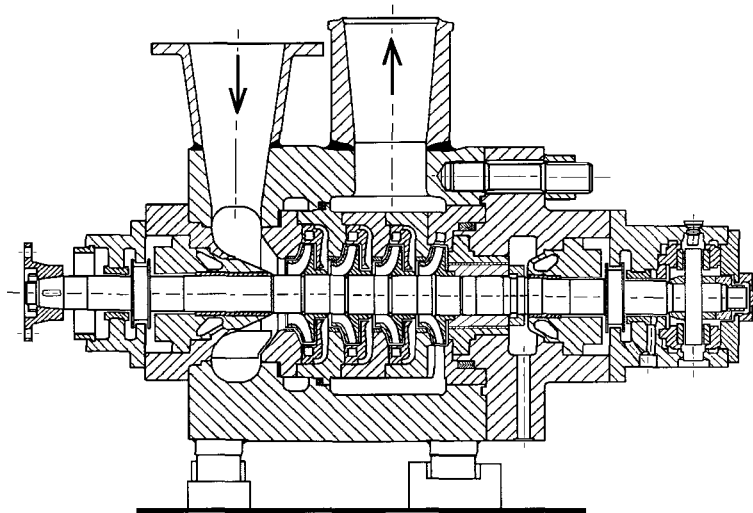


Figure 1. Boiler feed water pumps have small radial clearances at impeller rings, balance drum, end seals and bearings.

In the presence of significant rotor-stator rub-impact, the dynamic character of rotor vibration response is highly non-linear for a number of reasons. First, the sudden initiation of a rotor-stator interactive radial force at the start of contact is inherently quite nonlinear. Second, once rotor and stator are in contact, two additional non-linear effects come into play, (i) the Hertzian elastic contact radial stiffness and (ii) the rubbing tangential friction force. In quite strong rub-impact events, additional non-linear effects arise from local material yielding and fast-occurring wear at the rub-impact site(s).

In the modern era of rotating machinery vibration technology, several investigators have focused their attention on the quite important but highly complex problem of rotor-stator rubs and rub-impacts, as summarized by Muszynska (2). In a seminal work, Choy and Padovan (3) present several non-linear transient rotor vibration response simulation results, studying the influences of the assumed casing stiffness, rub friction coefficient, unbalance magnitude and system damping. The non-linear simulations of Adams and Abu-Mahfouz (4) show how the potential for dynamical chaos and routes to chaos in rotor-stator rub-impact-influenced vibration can provide indications and insight into the condition of a machine. Wu and Flowers (5,6) present two companion papers on their computational and experimental studies, respectively, for rotor-stator rub vibration phenomena with the influence of disk flexibility.

The primary motivation of the work reported in this paper is to improve the characterization and prediction accuracy of non-linear transient rotor vibration response computational simulations. This quest for improved simulation accuracy is driven primarily by the needs of an in-development model-based machinery condition monitoring and diagnostics system, as reported by Adams and Loparo (7). A common aspect of previous work on non-linear transient rotor vibration response simulation with rub-impact is the need to assume values for important inputs such as rub friction coefficient. As the results of Choy and Padovan (3) demonstrate, such simulations can show the influence of varying the important albeit elusive

input values, but are of questionable use for prediction of specific situations in an actual machine. Clearly, improvement to prediction accuracy requires serious experimental efforts to quantify the already identified important inputs as well as to uncover and evaluate previously unidentified important inputs. This paper is focused on one aspect of this quest for improved predictions, namely the evaluation of a previously unidentified important input, the rotor-stator impact restitution coefficient.

## 2 COMPARISONS BETWEEN FLEXIBLE-ROTOR TESTS AND SIMULATIONS

A precursor to the main experiments subsequently reported in this paper is a set of experiments conducted on the simple flexible rotor test rig illustrated in Figure 2. The complete unabridged documentation of those experiments is contained in the thesis of Michael Adams (8).

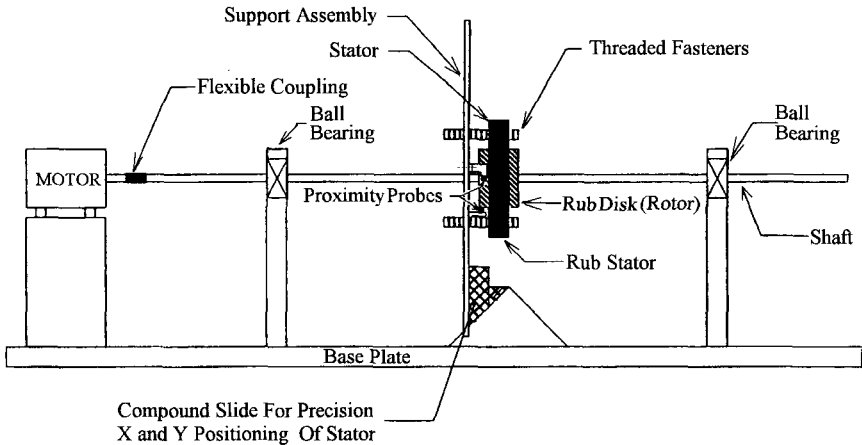


Figure 2. Simple flexible-rotor rub-impact test rig.

Non-linear transient simulations for the Figure 2 rotor rig were computed with now standard algorithms such as applied and presented twenty years ago by Adams (9). With rub-impact events, initial non-linear orbit simulations and corresponding measured orbits on this rig compared poorly. The simulation rotor orbits showed consistently more “bounce” in rotor-stator impacts than the measured orbits. This suggested that the energy lost through impacts was not negligible to the vibration orbits. The non-linear simulation algorithm was therefore modified to accommodate an impact restitution model within the Hertzian contact model. The computation for this employs the approach succinctly shown in Greenwood (10) wherein the total normal impact impulse  $\hat{F}$  is divided into two sequential parts, (i)  $\hat{F}_c$ , the compression impulse, and (ii)  $\hat{F}_r$ , the restitution impulse, as follows.

$$\hat{F} = \hat{F}_c + \hat{F}_r \quad (1)$$

The standard coefficient-of-restitution,  $e$ , can thereby be expressed as the ratio of the restitution impulse to the compression impulse, as follows.

$$e = \frac{\hat{F}_r}{\hat{F}_c} \quad (2)$$

For the non-linear simulations presented here, the compression impulse of a given rotor-stator impact is computed by integrating the Hertzian compression force against time during the compression portion of the impact. Then, per Eq. (2), the impact force time function during the restoration portion of the impact is computed by proportionally scaling down the Hertzian contact force during the impact rebound, consistent with the prescribed restitution coefficient value. Figure 3 shows simulations employing an assumed constant value of 0.8 for the restitution coefficient and corresponding test results for unbalance excitation of the Figure 2 rig. These simulation results show a more favorable comparison to corresponding measured orbits than earlier simulations that completely neglected energy loss through impact events. The Figure 3 comparisons serve to justify the task reported in this paper, i.e., the experimental determination of rotor-stator impact restitution coefficient values for actual conditions.

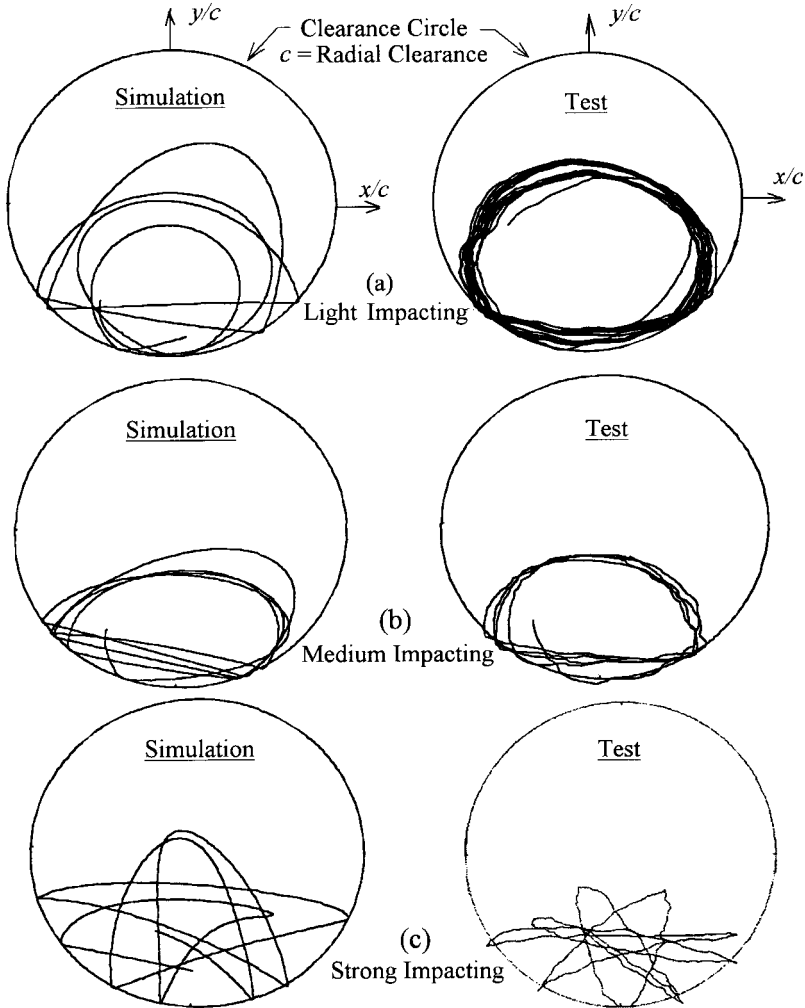


Figure 3. Comparisons between test and computer dynamic simulations for rub-impact cases.



### 3 TEST APPARATUS FOR IMPACT RESTITUION MEASUREMENT

The task of precision determination of rotor-stator impact restitution coefficients requires a quite elaborate experimental setup. The complete unabridged documentation of this task is contained in the thesis of Farhad Afshari (11). Several significant challenges were overcome to successfully perform this task. The two biggest challenges were (i) how to accurately measure  $X$  and  $Y$  orbital velocity signals simultaneously through an instrumented rotor-stator impact event, and (ii) how to experimentally produce a true line contact (and alternately a specified axial misalignment edge contact) between stator sleeve and journal at the moment of impact. To accurately measure orbital velocity changes through the very short time duration of a rotor-stator impact, two channels ( $X$  and  $Y$ ) of laser fiber optical vibrometers were employed. This laser device accurately measures velocity directly, and this can be well appreciated when one realizes the difficulties involved in the alternative of attempting to extract velocity measurements by numerically differentiating digitized displacement measurements. Each laser channel is comprised of components illustrated in Figure 4.

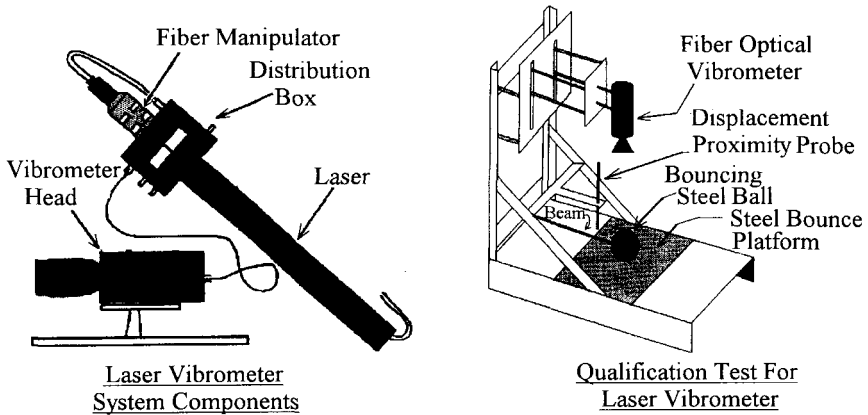


Figure 4. Laser Vibrometer.

To qualify the laser vibrometer for this application, a preliminary experiment was devised to compare motion taken with a proximity displacement probe and a vibrometer. This experiment is shown in Figure 4, and is comprised of a 2 inch diameter case hardened steel ball supported on a cantilever beam spring. The ball is manually raised above a steel bounce platform and released, causing a series of successive decaying impacts of the ball against the platform. For purposes of comparison, a velocity signal was processed from the numerically differentiated proximity probe displacement signal. A wavelet transform of this differentiated displacement signal was employed wherein "noise" was identified and removed in the wavelet transform domain followed by velocity signal reconstruction using the inverse wavelet transform. A surprisingly good match was obtained with the vibrometer directly measured velocity signal. Figure 5 is a comparison between reconstructed and directly measure velocity signals from one of these tests, and also shows the considerable numerical noise of the "raw" differentiated displacement signal before being de-noised using a wavelet transform. The results of the vibrometer qualification tests not only give assurance that the laser instrument is being properly used, but also yields a new approach (wavelet transform) for recovering reasonably accurate and noise-free rotor orbit velocity signals from proximity probe displacement signals, even

under the most demanding conditions, i.e., through an impact. This byproduct result can be exploited in industrial applications to extract accurate rotor orbit velocity signals from proximity probe displacement signals. This first use of the wavelet transform to extract velocity from proximity probe displacement signals could surely be further perfected, so it is highly likely that an even better agreement is achievable than in the comparison shown by Figure 5.

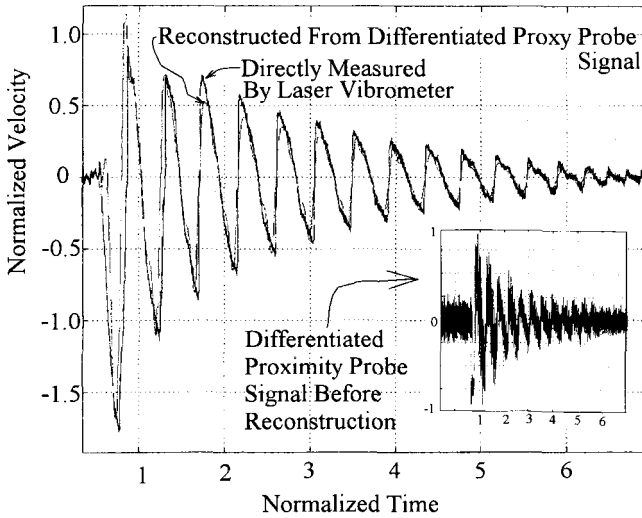


Figure 5. A typical result from laser vibrometer qualification tests.

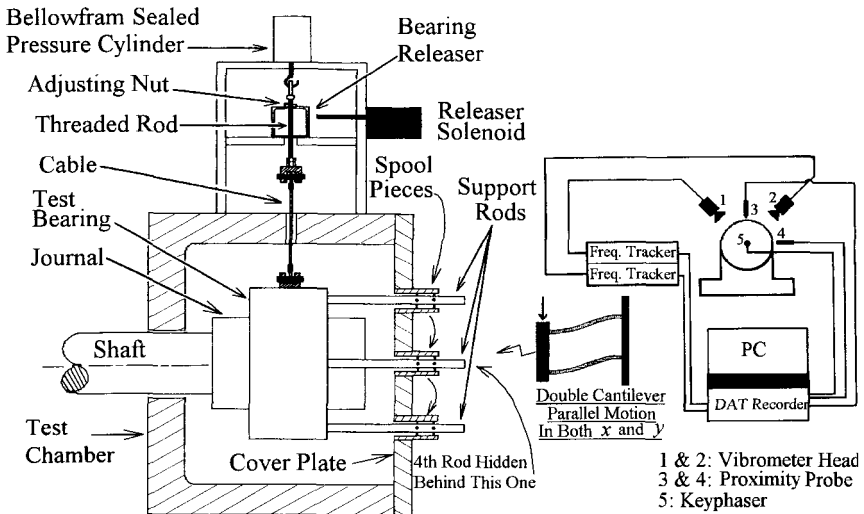


Figure 6. Impact test for rotor-stator restitution coefficient measurements.

The rotor-stator impact test apparatus is illustrated in Figure 6. The impact test bearing (stator) is supported off a test chamber front cover plate by four equal length and diameter double-cantilever beams (support rods) which are 90° apart and act collectively as a radial spring supporting the test bearing. Each rod is tightly secured into the test bearing by a strong shrink fit hole. The other end of each of the four support rods is tightly secured in a “spool piece” with eight set screws arranged at 90° angular intervals in two rows axially separated by approximately 1.5 inches (3.8 cm), as Figure 6 illustrates. Each rod is precisely tightened without moving its radial position with line contact (bearing resting on journal) or prescribed axial misalignment edge contact (using feeler gauge). During this assembly, each rod has two 0.1 mil (0.0025 mm) graduated dial indicators touching it in the horizontal and vertical directions respectively, to insure that the rod is not displaced by the set screws, and thus it is secured in its initial free-standing position. Once all four rods are secured to their respective spool pieces, the impact test bearing is constrained to move only in a parallel motion with no out-of-plane-rotation. This method for supporting the test bearing has proven very reliable in precisely setting and maintaining bearing-to-journal alignment or misalignment. Bearing and journal are constructed so different materials for bearing and journal can readily be tested.

#### 4 TEST RESULTS

Figure 7 shows an example of the measured and digitally recorded signals. The test setup is adjusted to have the vertically dropping bearing hit the journal with an impact velocity that is perpendicular to the horizontal impact surfaces. Oblique impact testing is part of future work with this apparatus. To extract an impact restitution coefficient from the measured signals, rotor and stator are characterized by their respective equivalent point masses, with the setup adjusted for the line of impact to pass through the rotor and stator geometric centers. Accordingly, the restitution coefficient is expressible as the ratio of the relative velocity of the two masses after impact to their relative velocity before impact, as in the following equation.

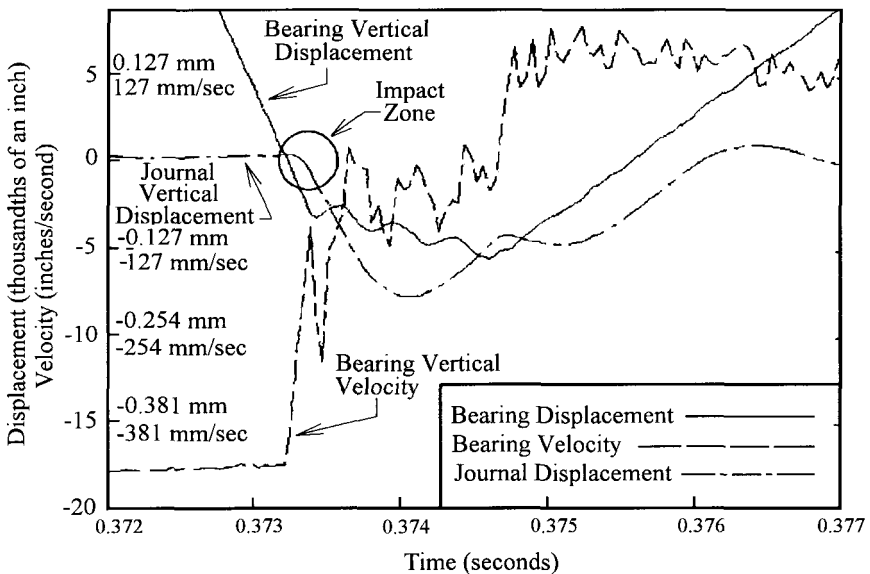


Figure 7. Measured signals from rotor-stator impact test apparatus.

$$e = \frac{V'_B - V'_R}{V_B - V_R} \quad (3)$$

Here,  $V_B$  and  $V_R$  are the bearing and rotor velocities respectively just before impact, whereas  $V'_B$  and  $V'_R$  are the bearing and rotor velocities respectively just after impact. The bearing velocity is measured directly with the  $X$  and  $Y$  vibrometers and the journal velocity is extracted from its  $X$  and  $Y$  proximity probe displacement measurements, as described in connection with Figure 5. As Figure 7 demonstrates, it is necessary to “zoom in” on the measured signals to extract the proper input velocities for Eq. (3).

The first series of tests have been performed for the aligned bearing case (line contact) with a bronze 180°-arc bearing liner insert and a steel journal specimen. The ground radial clearance between the bearing insert and journal is 0.010 inch (0.254 mm). Results for this test series are summarized in Figure 8 and show restitution coefficient values and a curve fit versus impact velocity typical for impact tests in general, e.g., see Goldsmith (12). Furthermore, the test results exhibit negligible effects of journal surface speed. The non-linear simulation cases shown in Figure 3 were made with an assumed restitution coefficient constant value of 0.8, and indeed show a bit more “bounce” than their corresponding tests. The restitution coefficient results shown in Figure 8 are significantly less than 0.8, with an asymptote of approximately 0.5, and therefore suggest that non-linear simulations should accommodate a variable restitution coefficient that is a function of the instantaneous rotor-to-stator impact velocity.

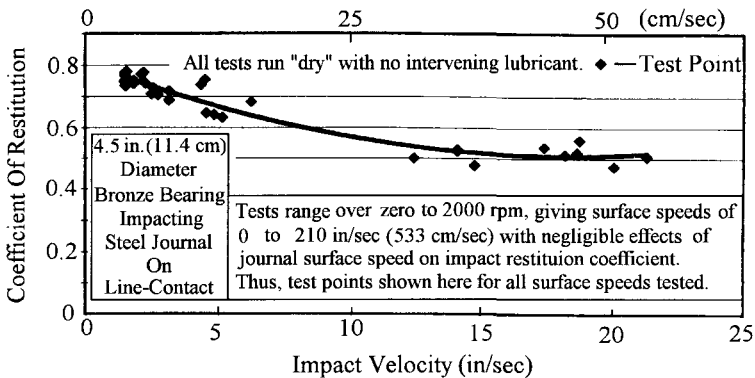


Figure 8. Bearing-on-journal impact restitution coefficient.

## 5 CONCLUSIONS

This work demonstrates a viable apparatus to study closely controlled rotor-stator impact events. The results thus far obtained with this apparatus yield restitution coefficient values consistent with comparisons between rotor orbital vibration simulations and corresponding measured test rig responses. The results suggest that rotational surface speed is of negligible importance to impact restitution. The apparatus is configured to conduct in-progress and future work to determine the influences on restitution coefficient from (i) different rotor-stator material combinations, (ii) interposing a lubricant between rotor and stator, (iii) rotor-to-stator axial misalignment, and (iv) oblique impact. It is difficult to imagine how this work could have been possible without the modern sensors and high-sampling-rate data acquisition systems used.

## REFERENCES

1. Adams, M. L., "*ROTATING MACHINERY VIBRATION-From Analysis To Trouble Shooting*", Marcel Dekker, New York 2000.
2. Muszynska, A., "*Rotor-To-Stator Element Rub-Related Vibration Phenomena In Rotating Machinery - Literature Review*", Shock and Vibration Digest, Vol. 21, 1989.
3. Choy, F. K. and Padovan, J., "*Non-Linear Transient Analysis of Rotor-Casing Rub Events*", Journal of Sound and Vibration, 113(3), 1987.
4. Adams, M. L. and Abu-Mahfouz, I., "*Exploratory Research on Chaos Concepts as Diagnostic Tools for Assessing Rotating Machinery Vibration Signatures*", Proceedings, IFTOMM 4<sup>th</sup> International Conference on Rotor Dynamics, September 1994, Chicago, IL.
5. Wu, F. and Flowers, G. T., "*A Study of the Influence of Rubbing on the Dynamics of a Flexible Disk Rotor System*", Proc., 38<sup>th</sup> International Gas Turbine Aeroengine Congress and Exposition, May 1993.
6. Wu, F. and Flowers, G. T., "*An Experimental Study of the Influence of Disk Flexible and Rubbing on the Rotordynamics*", Proc., 14<sup>th</sup> Biennial ASME Conference on Mechanical Vibration and Noise, Sept. 1993.
7. Adams, M. L. and Loparo, K. A., "*Model-Based Condition Monitoring from Rotating Machinery Vibration*", Final Report, Electric Power Research Institute (EPRI) Project WO3693-04, 1999.
8. Adams, Michael, "*Experiments and Calculations on Fundamental Nonlinear Rotordynamical Systems*", M.S. Thesis, Case Western Reserve University, 1996.
9. Adams, M. L., "*Non-Linear Dynamics of Flexible Multi-Bearing Rotors*," Journal of Sound and Vibration, 71(1), 1980.
10. Greenwood, D. T., "*Principles of Dynamics*", 2<sup>nd</sup> Ed., Prentice Hall, 1988.
11. Afshari, F., "*Design and Implementation of a Rotor-Stator Impact Experiment*", M.S. Thesis, Case Western Reserve University, 1998.
12. Goldsmith, W., "*Impact, The Theory and Physical Behavior of Colliding Solids*", Edward Arnold Publishers, Ltd., 1960.

*This page intentionally left blank*

# Identification

*This page intentionally left blank*



# On the identification of the foundation of a large turbogenerator unit by the analysis of transient vibrations

A VANIA

Dipartimento di Meccanica, Politecnico di Milano, Italy

## SYNOPSIS

This paper shows the results obtained with an identification method aimed to estimate the modal parameters of rotating machine foundations by analysing shaft and support vibration data collected with a condition monitoring system during rundowns and runups. This procedure allows modal analysis to be carried out at any time during the plant life; moreover, costly and complex usual modal tests can be avoided. The modal parameters of the foundation structure of a 320 MW steam turbogenerator have been estimated with the proposed identification method applied in the frequency domain. The results of this analysis have been validated using support vibrations measured in different unbalance conditions of the turbogenerator unit.

## 1 INTRODUCTION

The identification of the modal parameters of rotating machine foundations, carried out on the basis of the analysis of experimental data, can be very important to improve the accuracy of mathematical models used to simulate the machine dynamic behaviour. At this aim a modal testing should be carried out on the system obtained by removing the shafts from the fully assembled machine so that also the effects of the casings can be considered. Therefore, a common modal testing should require a long and costly outage. Moreover, in case of large foundations, a multiple excitation technique may be necessary. This should require the use of sophisticated and costly equipment.

In order to avoid the drawbacks of a common modal testing, an identification technique which allows the foundation modal parameters to be identified by the analysis of shaft and support vibration data collected with a condition monitoring system during rundowns and runups has been developed (1, 2, 3, 4). This technique is based on the Extended Kalman Filter algorithm (EKF) applied in the frequency domain. The main benefit of this method is the capability to

analyse the response of structures subjected to multiple excitations also in the case of fully correlated forces.

During transient operating conditions the foundation of a rotating machine is excited by the forces which act at the supports, that is the forces transmitted from the shafts through the bearings. When the non-linearity of the foundation is negligible the synchronous harmonic component (1X) of the support vibrations, due to the 1X forces acting at the connection points with the rotor train, can be analysed. Usually these forces, which are fully correlated, cannot be measured; however they can be evaluated using the shaft vibrations relative to the bearing housings and the stiffness and damping coefficients of the bearings. Therefore, only transient vibrations of shafts and supports, usually measured by monitoring systems, are required. If only the support vibrations are available the oil film forces can be estimated with techniques based on mathematical models of the system composed of the rotor train and the bearings (5). At first, this identification method was validated using theoretical data obtained with mathematical models which simulate the response of rotating machines (1, 2, 3) as well as experimental data obtained with a laboratory test rig (4). The identification method is herein only briefly described, while the paper is mainly focused on the results of an experimental investigation. The modal parameters of the foundation structure of a 320 MW steam turbogenerator have been estimated by the analysis of shaft and support vibrations measured during a machine rundown. The foundation was a large concrete structure composed of a top plate that was supported on pilasters connected to a base plate. As a usual modal testing of the foundation was impossible the results of this identification analysis have been validated using the vibrations measured in different unbalance conditions of the turbogenerator unit. That is, it has been shown that the modal parameters which had been identified using vibration data collected before balancing the turbogenerator could be used to fit the support vibrations measured during a rundown carried out after a balance procedure.

## 2 THE IDENTIFICATION METHOD

The modal parameters of a 320 MW steam turbogenerator foundation have been identified with a method that can be used to estimate the parameters of more general systems subjected to multiple excitations, fully correlated or not (3). This method is applied, in the frequency domain, to the system response due to known exciting forces contained in the vector  $F(\omega)$ . These forces can be external excitations obtained with shakers or the forces transmitted to a sub-system, at the connection points, by other components of a fully assembled system.

The frequency response of a linear structure evaluated at the  $i$ -th degree of freedom can be expressed in terms of the modal parameters in the following form:

$$z^i(\omega) = \left( \sum_{r=1}^N \psi_r^i \frac{\psi_r^T F(\omega)}{m_r(\omega_r^2 - \omega^2 + 2j\xi_r\omega_r\omega)} \right) \quad (1)$$

The term  $N$  is the number of normal modes,  $\psi_r$ , associated to the natural frequencies,  $\omega_r$ , contained in the frequency range of interest. The terms  $\xi_r$  and  $m_r$  are the damping ratios and the generalised masses, respectively. The normal modes  $\psi_r$  have been normalised by assigning a unity value to the  $r$ -th generalised mass. If the vector of the excitations  $F(\omega)$  is known and the system responses  $z^i(\omega)$  are measured at one or more points where the forces are applied, the modal parameters can be identified from Eq.(1) without the need to use the frequency response functions (FRF) of the system. It is important to emphasise that in case of

multiple fully correlated excitations the FRFs cannot be defined. In general, the vector  $F(\omega)$  contains the experimental data of the forces applied to the structure with shakers. Conversely, in case of rotating machine foundations the forces acting at the connection points during normal operating conditions (runups and rundowns) can be estimated by considering the bearing coefficients and the shaft vibrations relative to the bearing housings.

The unknown modal parameters contained in Eq.(1) can be estimated by using identification techniques applied in the frequency domain. In this investigation a technique based on the Extended Kalman Filter (EKF) has been used (3, 4). By applying the EKF approach to the modal parameter identification problem stated in Eq.(1) the state vector  $x$  can be defined as:

$$x = \{ \psi_1^T, \dots, \psi_r^T, \dots, \psi_N^T, \xi_1, \dots, \xi_r, \dots, \xi_N, \omega_1, \dots, \omega_r, \dots, \omega_N \}^T \quad (2)$$

As Eq.(1) describes the response of an ideal linear system the response  $z^i(\omega)$  evaluated at the  $i$ -th degree of freedom is supposed to depend on all the forces applied to the system: for large structures this can be a restriction. Anyhow, discrepancies between the real behaviour of the system and the ideal one can be considered with expressions obtained from Eq.(1).

### 3 CASE STUDY

The dynamic behaviour of a 320 MW steam turbogenerator has been analysed. The rotor train was composed of a high-intermediate pressure turbine, a low pressure turbine and a generator (Figure 1). The machine foundation was composed of a concrete top plate supported on eight pilasters which were connected to a base plate supported on the sub-soil. Spring elements were mounted between the top-plate and the pilasters. They significantly affected the dynamic behaviour of the foundation.

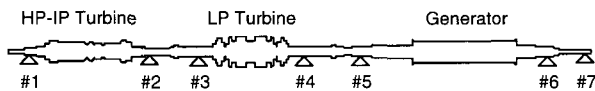


**Figure 1 Rotor train.**

Each journal bearing of the machine was equipped with a pair of radial (XY) proximity probes as well as with a pair of accelerometers located on the bearing housings in the same directions as the proximity probes. Therefore, both the foundation absolute vibrations at each support and the shaft vibrations relative to the bearing housings were measured. A condition based monitoring system continuously analysed the machine vibrations both in running state and during runups and rundowns.

In order to reduce the vibration levels of the generator a balance mass was mounted on the flange of the rigid coupling located between the LP turbine and the generator. In this investigation, the results of a tracking order analysis of the vibrations occurred during two rundowns carried out before and after the machine balancing, and in similar thermal conditions, have been analysed.

### 3.1 Flexural critical speed identification

The identification technique used to estimate the foundation modal parameters needs initial values of the parameters to be assigned in order to start the iterative process. In regard to the natural frequencies these initial guesses have been defined with a preliminary analysis of the experimental data. Conversely, the identification method is not too sensitive to the initial values of the damping ratios and the normal modes as a fast and good convergence of the parameter estimates is usually obtained. At first, the vibrations measured during a rundown carried out before balancing the turbogenerator have been considered. Figure 2 shows the Bodé plots of the 1 x revolution (1X) harmonic component of the absolute vibrations of the shaft and the foundation measured at the bearings #3 and #5 of the machine.

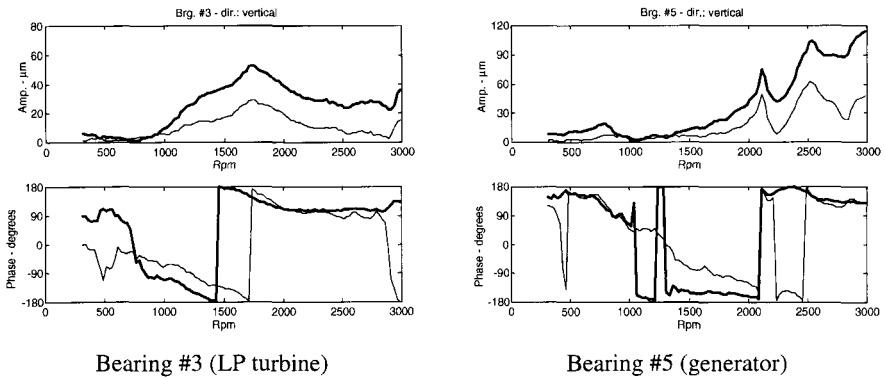


**Figure 2 Absolute vibrations (1X) measured in vertical direction at the bearings #3 (LP turbine) and #5 (generator). Solid line: shaft vibrations. Thin line: support vibrations.**

These diagrams show several peaks of the amplitude curves and significant changes in the phase curves which can be ascribed to resonances of the fully assembled machine. In order to recognise the peaks in the experimental vibrations due to flexural critical speeds of the rotors from those caused by natural frequencies of the foundation structure the theoretical response of the complete system has been simulated with a mathematical model in which a rigid foundation has been considered. As no information was available about the exciting forces really applied to the shafts (e.g. local or distributed unbalances) an arbitrary unbalance mass has been positioned on each shaft of the model of the fully assembled machine. The object of this preliminary analysis was only to identify the critical speeds of the shafts; therefore it was unimportant to obtain a good accord between the experimental vibration levels and those obtained with the model. Figure 3 shows the Bodé plots of the 1X shaft theoretical vibrations evaluated at the bearings #1, #3 and #5.

**Table 1 Flexural critical speeds of the turbogenerator rotors.**

	HP-IP Turbine	LP Turbine	Generator
First critical speed	26.1 Hz	19.2 Hz	14.2 Hz
Second critical speed	-	-	32.5 Hz
Third critical speed	-	-	43.3 Hz

By the analysis of these diagrams the flexural critical speeds of the rotors of the turbogenerator have been estimated. The results of this analysis, which are summarised in Table 1, are in a good accord with the experimental data. That is, the frequencies associated with the peaks of the theoretical vibrations correspond to those of some peaks in the diagrams of the experimental vibrations.

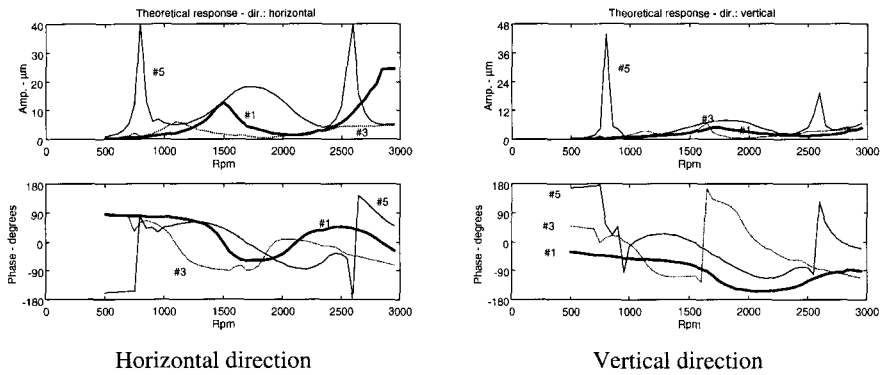


**Figure 3 Shaft theoretical vibrations (1X) evaluated at the bearings #1 (solid line), #3 (dotted line) and #5 (thin line).**

By analysing the 1X vibrations measured at the machine supports and considering the results shown in Table 1 it is possible to note that some peaks are caused by shaft resonances while other peaks of the support vibrations can be ascribed to natural frequencies of the foundation structure. Anyhow, it is important to remark that the spring elements located between the top-plate and the pilasters cause the foundation to be rather flexible. Owing to this, as well as to the values of the bearing oil-film coefficients, high shaft vibrations due to flexural critical speeds cause significant vibration levels of the machine supports.

### 3.2 Oil-film forces

In order to obtain further information about the foundation natural frequencies the oil-film forces transmitted from the shafts to the machine supports were analysed. As these forces were not measured their 1X harmonic component was estimated considering the bearing coefficients and the 1X experimental vibrations of the shafts relative to the bearing housings. Obviously, the care with which these forces are evaluated depends on the accuracy of the stiffness and damping coefficients of the oil-film. Figure 4 shows the Bodé plots of the 1X horizontal and vertical forces transmitted to the supports #3 and #5 during the rundown before balancing the turbogenerator. These force estimates have been used also to identify the modal parameters of the foundation.

By comparing the Bodé plots of the 1X oil-film forces to those of the 1X vibrations of the supports it was possible to note that over a wide frequency range the amplitude and phase curves of the foundation response evaluated at many of the degrees of freedom associated with the machine supports are quite similar to those of the exciting force acting at the same degrees of freedom. This behaviour was assumed to mainly be the effect of the vibrations, in the region of the rigid response of the structure, associated with natural frequencies which are contained in the range above the running speed of the turbogenerator (3000 rpm). In this case this effect is amplified by the significant flexibility of the foundation. Obviously, the

foundation response is the superposition of this contribution and the effect due to the foundation natural frequencies contained in the range below 3000 rpm.

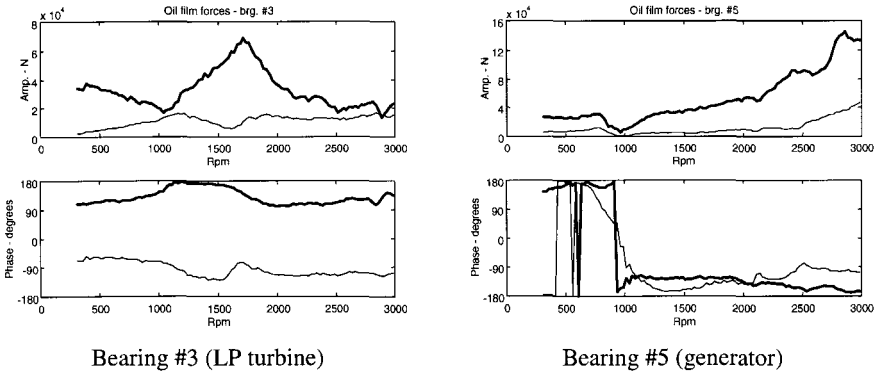


**Figure 4** Bode plots of the oil film forces (1X) acting at bearings #3 and #5. Solid line: vertical direction. Thin line: horizontal direction.

### 3.3 Identification of the foundation modal parameters

The modal parameters of the turbogenerator foundation have been estimated using an identification technique based on the Extended Kalman Filter (3, 4) briefly described in Section 2. The support 1X vibrations measured during a rundown occurring before balancing the machine have been analysed. Moreover, the 1X forces transmitted from the shaft to the foundation during the same rundown have been considered.

The number of normal modes to be identified and the initial values of the natural frequencies have been defined with a preliminary analysis, of the support vibrations, in which the effects of the flexural critical speeds of the shafts have been taken into account. As said above, the foundation response in the speed range below 3000 rpm is significantly affected by the contribution of the natural frequencies contained in the range above 3000 rpm. This effect has been considered by identifying a normal mode associated with a natural frequency to which an arbitrary value of 79.58 Hz (500 rad/s), significantly higher than the running speed, has been assigned. The natural frequencies and the damping ratios that have been identified are shown in Table 2.

**Table 2** Foundation natural frequencies and damping ratios.

	Mode n.1	Mode n.2	Mode n.3	Mode n.4	Mode n.5	Mode n.6
Natural frequency	7.74 Hz	16.27 Hz	22.23 Hz	35.49 Hz	43.29 Hz	79.58 Hz
Damping ratio	0.02700	0.03560	0.04323	0.01760	0.03485	0.0100

Eq.(1) describes the response of an ideal linear structure in terms of its modal parameters and correlated or uncorrelated exciting forces which are contained in the vector  $F(\omega)$ . In the case of rotormachinery foundations the response at each degree of freedom associated with a machine support should depend on all the forces applied at the connecting points between the rotor train and the foundation. For large structures this can be a serious restriction as the real contribution to the foundation response of the forces acting far from the considered  $i$ -th

degree of freedom can be less important than in the ideal case and sometimes it can be negligible. These discrepancies between the real dynamic behaviour and the ideal one could be taken into account by the following expression which is derived from Eq.(1):

$$z^i(\omega) = \left( \sum_{r=1}^N \psi_r^i \frac{\psi_r^T [w]^i F(\omega)}{m_r(\omega_r^2 - \omega^2 + 2j\xi_r\omega_r\omega)} \right) \quad (3)$$

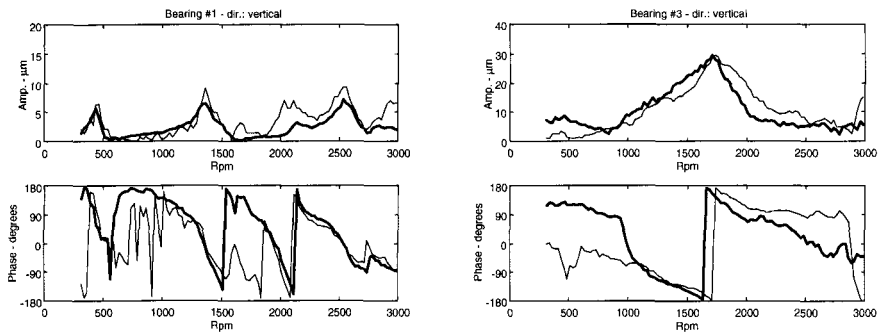
In Eq.(3) vector  $F(\omega)$  is multiplied by a weighting factor diagonal matrix,  $[w]^i$ , which depends on the  $i$ -th degree of freedom of the foundation response  $z^i(\omega)$ . The elements of the matrices  $[w]^i$  can be included in the state vector  $x$  (see Eq.(2)) so that they can be estimated with the identification technique together with the foundation modal parameters. If one or more of the parameters that must be identified is known it is possible to fix its value by setting its initial guess equal to the desired value and by assigning a zero value to the corresponding diagonal element of the error covariance matrix. In this investigation, a preliminary analysis of the 1X support vibrations and the 1X oil-film forces allowed some weighting factors to be fixed in advance as it was possible to presume that the contribution of some forces to the foundation response  $z^i(\omega)$  was negligible.

The foundation response measured at some degrees of freedom of the machine supports was mainly affected by the force acting at the same degree of freedom of the response or at least by the forces acting at some degrees of freedom located near the considered one. Therefore, the modal parameters have been identified by considering only some foundation responses at a time and by removing the contribution of undesired elements of vector  $F(\omega)$ . This has been obtained by assigning a zero value to some weighting factors. Table 3 shows the foundation normal modes identified with the EKF technique; they are associated with the natural frequencies reported in Table 2.

Figures 5 and 6 show some comparisons between the experimental 1X vibrations of the supports and the corresponding regenerated data obtained by substituting the identified modal parameters into Eq.(3). The curve fitting is very good over a wide range of the rotating speed.

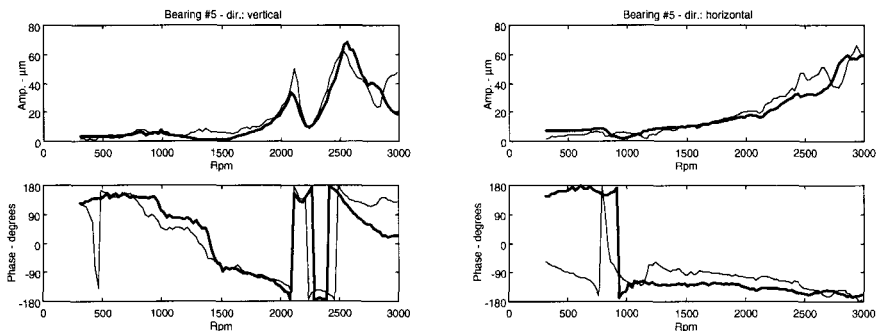
**Table 3 Foundation normal modes identified with the EKF technique.**

Bearing	Direction	Mode n.1	Mode n.2	Mode n.3	Mode n.4	Mode n.5	Mode n.6
1	Vertical	0.0000	0.0000	- 0.10622	0.0000	0.0000	6.2321
1	Horizontal	0.0000	0.0000	0.0000	0.0000	0.0000	0.0000
2	Vertical	0.0000	0.0000	8.6808	0.0000	0.0000	8.6788
2	Horizontal	0.0000	0.0000	0.0000	0.0000	0.0000	0.0000
3	Vertical	- 0.1200	0.3305	- 450.117	0.0000	0.2992	9.0155
3	Horizontal	0.0000	0.0000	0.0000	0.0000	0.0000	10.8902
4	Vertical	- 0.2700	- 0.4002	- 183.733	0.0000	- 1.3000	8.7000
4	Horizontal	0.0000	0.0000	0.0000	0.0000	0.0000	5.3331
5	Vertical	0.0000	0.9136	- 8.2269	0.9136	2.0063	1.9000
5	Horizontal	0.0000	0.0000	0.0000	0.0000	3.5117	15.6372
6	Vertical	0.0000	- 1.1977	- 0.2491	- 1.1977	- 0.9338	- 4.9300
6	Horizontal	0.0000	0.0000	0.0000	0.0000	0.0000	8.9195
7	Vertical	0.0000	0.0000	0.0000	0.0000	0.0000	- 11.7113
7	Horizontal	0.0000	0.0000	0.0000	0.0000	0.0000	- 19.9892



Bearing #1 (HP-IP turbine), vertical direction

Bearing #3 (LP turbine), vertical direction



Bearing #5 (generator), vertical direction

Bearing #5 (generator), horizontal direction

**Figure 5** Bode plots of the support vibrations (1X). Thin line: experimental data measured before the machine balancing. Solid line: regenerated data obtained with the identified modal parameters.

### 3.4 Modal parameter validation

The results of the identification analysis allow the regenerated data obtained with Eq.(3) to fit the experimental data with a fairly good accuracy. However, a good curve fitting could be obtained also with a suitable set of parameters different from the real ones. But, in this case, the identified parameters would hardly be able to fit the foundation responses due to different forces acting on the turbogenerator which, in turn, would cause different forces acting at the connection points between the shafts and the supporting structure. Unfortunately, it was impossible to carry out a common modal testing on the machine foundation; therefore reference values of the modal parameters could not be estimated.

However, in order to reduce the levels of the generator vibrations which occurred in the running state a balance mass was positioned on the flange of the rigid coupling located between the low pressure turbine and the generator. The vibrations of the shafts and the support measured during a rundown occurred after the machine balancing were analysed. Due to the effect of the balance mass the vibrations measured at the bearing #5, that is the generator bearing that was nearest to the balance plane, significantly decreased, especially in the speed range from 2000 rpm to 3000 rpm. Moreover, also the oil film forces transmitted to



the foundation structure at the bearings #4, #5 and #6, evaluated on the basis of the shaft vibrations relative to the bearing housings, significantly changed.

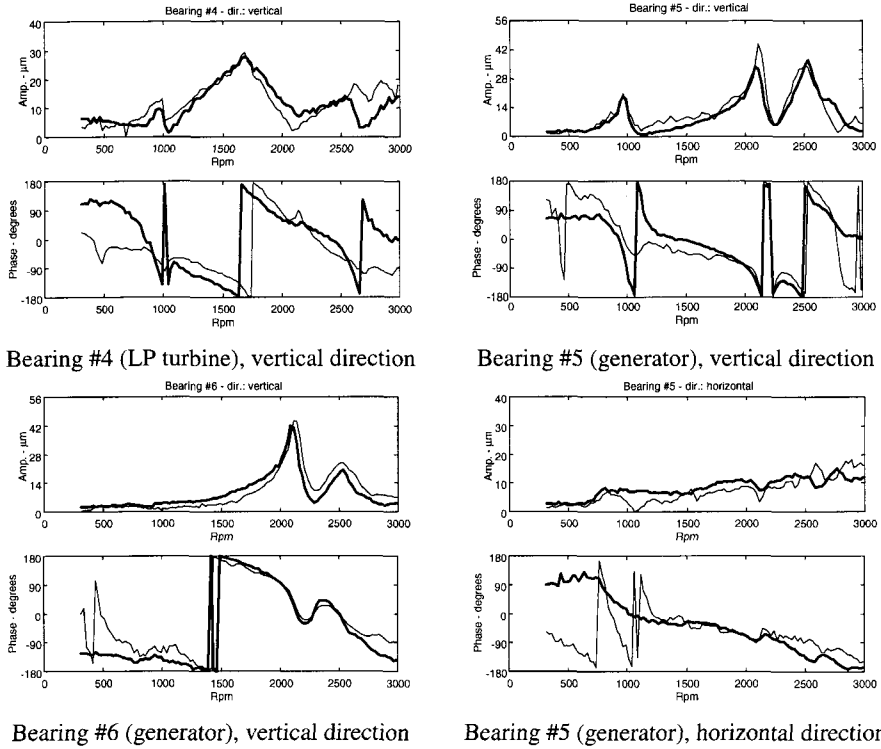


**Figure 6** Bode plots of the support vibrations (1X). Thin line: experimental data measured after the machine balancing. Solid line: regenerated data obtained with the modal parameters previously identified.

These forces have been substituted into Eq.(3) together with the modal parameters and the weighting factors that had been identified using the vibrations measured before the machine balancing. Then, the regenerated data obtained in this way have been compared to the support vibrations measured during the rundown after the machine balancing (Figure 6). Even if the balance mass had caused significant changes in the foundation response and the oil film forces in respect to the previous behaviour, the parameter estimates allowed the experimental curves to be fitted with a fairly good accuracy over a wide range of the rotating speed. Then, the good results obtained with this analysis allowed one to validate the foundation modal parameters estimated with the EKF identification technique although reference values were not available.

## 4 CONCLUSIONS

The need to carry out the identification of modal parameters of rotating machine foundations at any time, during the plant life, without requiring to do a complex and costly common modal testing induced the authors to develop an identification procedure by which only shaft and support vibrations measured during rundowns are analysed. This strategy implies the use of identification methods applied in the frequency domain. In this investigation a technique based on the Extended Kalman Filter has been used. Anyhow, other identification techniques like the Iterated Extended Kalman Filter or the Weighted Least Square method could be used to solve the identification problem. It is quite evident that the accuracy of the modal parameter estimates depends on the care with which the forces transmitted to the foundation are evaluated. The effect of errors in the evaluation of these forces can be reduced by analysing transient vibrations measured in different operating conditions which usually occur during the plant life (e.g. different balance conditions, thermal state, machine alignment).

The case study described in this paper has allowed the modal parameters of the foundation of a large turbogenerator unit to be identified. This analysis has emphasised some discrepancies between the real dynamic behaviour of the system and the ideal one which are rather usual for large concrete structures. This investigation has shown that it is possible to consider these nonlinear effects by multiplying the forces acting at the supports by suitable weighting factors that can be estimated together with the modal parameters with the proposed identification method. The analysis of quite different foundation responses measured before and after a machine balancing has allowed one to show that the identified modal parameters were able to fit all the experimental curves very well. As the modal parameters have been identified using the vibration data measured in only one balancing condition this analysis can be considered as a good test to evaluate the accuracy of the parameter estimates. Then, they can be used to improve the accuracy of mathematical models that simulate the dynamic response of fully assembled rotating machines. An accurate description of the response of these systems is very important to make model based diagnostic techniques more efficient.

## REFERENCES

- (1) Vania, A., «Identification of the modal parameters of rotating machine foundations», *Politecnico di Milano, Dept. of Mechanics, Internal Report*, 9-96, Milano (Italy), June 1996.
- (2) Curami, A., Vania, A., «Parameter Identification of Rotormachinery Supporting Structures», *IFTOMM 5<sup>th</sup> Int. Conference on Rotor Dynamics*, Darmstadt (D), September 1998.
- (3) Provasi, R., Zanetta, G.A., Vania, A., «Extended Kalman Filter for the Modal Model Identification of Mechanical Structures Excited by Correlated Sinusoidal Multi-Inputs», *3<sup>rd</sup> Int. Conf. on Acoustical and Vibratory Surveillance Methods and Diagnostic Techniques*, CETIM, Senlis (France), October 1998.
- (4) Vania, A., Pennacchi, P., Zanetta, G.A., Provasi, R., «Identification of structures excited with multiple fully correlated forces», *XIV National Congress AIMETA*, Como (Italy), October 1999.
- (5) Lees, A. W. And Friswell, M.I., «Estimation of forces exerted on machine foundations», *Int. Conf. on Identification in Engineering Systems*, Swansea, March 1996, 793-803.

# Estimating rotor unbalance from a single run-down

S EDWARDS, A W LEES, and M I FRISWELL

Department of Mechanical Engineering, University of Wales Swansea, UK

***ABSTRACT** A method, recently reported by the authors, is used to determine the state of unbalance of a rotating machine in the laboratory. This method allows the system to be balanced from a single run-down, which has obvious advantages for field balancing. In addition to excitation, the method also identifies the parameters of the machine's elastic support structure, which is a major consideration for the analysis of power station turbogenerators. The identification method is first presented, followed by the results obtained from an experimental rotor rig. A demanding set of experiments was performed and excellent results were achieved for both unbalance and support parameter identification. Using this single-shot balancing technique, vibration levels were successfully reduced by over ninety per-cent.*

## 1 INTRODUCTION

Traditional turbogenerator balancing techniques require at least two run-downs, with and without the use of trial weights respectively, to enable the machine's state of unbalance to be accurately calculated [1]. In addition, for turbogenerator analysis purposes, accurate models of the flexible steel foundations used in modern power stations must be available, which is seldom the case due to their complicated physical nature. Modelling techniques such as finite element analysis do not deliver acceptable results, and so direct estimation from measured response data has generally been accepted as the most promising technique [2]. It was shown [3] how it was possible to estimate both the flexible foundation parameters and the state of unbalance of a rotor, from a single set of vibration response data. This has obvious practical advantages for the efficient operation of turbomachinery. The only requirement of the method is a good rotor model, which is often available, or at least readily obtained using finite element modelling. In this paper, the experimental verification of that method is described.

## 2 THEORY

Consider the unbalanced rotor-bearings-foundation system shown in Figure 1. The system is written in terms of the dynamic stiffness matrices of its constituent components, as

$$\mathbf{Z}_R \mathbf{u}_R = \mathbf{f}_R \quad \text{for the rotor,} \quad (1)$$

$$\mathbf{Z}_B \mathbf{u}_B = \mathbf{f}_B \quad \text{for the bearings,} \quad (2)$$

$$\mathbf{Z}_F \mathbf{u}_F = \mathbf{f}_F \quad \text{for the foundations,} \quad (3)$$

where  $\mathbf{Z}$  is the subscript-dependent dynamic stiffness matrix of the local system component,  $\mathbf{u}$  is the subscript-dependent response vector and  $\mathbf{f}$  is the subscript-dependent force, due to some excitation of the rotor. Subscripts R, B and F relate to the rotor, bearings and foundations respectively. The individual dynamic stiffness matrices of each of these components are

$$\mathbf{Z}_R(\omega) = \mathbf{K}_R - \omega^2 \mathbf{M}_R \quad (4)$$

$$\mathbf{Z}_B(\omega) = \mathbf{K}_B = \mathbf{B} \quad (5)$$

$$\mathbf{Z}_F(\omega) = \mathbf{K}_F - \omega^2 \mathbf{M}_F + j\omega \mathbf{C}_F \quad (6)$$

where  $\mathbf{K}$  is the subscript-dependent stiffness matrix,  $\mathbf{M}$  is the subscript-dependent mass matrix,  $\mathbf{C}_F$  is the foundation damping matrix and  $\omega$  is the rotor running speed. In this instance, the bearing model is restricted to direct stiffness terms for the sake of clarity. A speed-dependent bearing model with damping could also be included if required, as detailed in [3].

### 2.1 Representing The System

The three substructures are partitioned into their internal and connected DoF, giving

$$\begin{bmatrix} \mathbf{Z}_{R,II} & \mathbf{Z}_{R,IB} \\ \mathbf{Z}_{R,BI} & \mathbf{Z}_{R,BB} \end{bmatrix} \begin{Bmatrix} \mathbf{u}_{R,I} \\ \mathbf{u}_{R,B} \end{Bmatrix} = \begin{Bmatrix} \mathbf{f}_{R,I} \\ -\mathbf{f}_{F,B} \end{Bmatrix} \quad (7)$$

$$\begin{bmatrix} \mathbf{K}_B & -\mathbf{K}_B \\ -\mathbf{K}_B & \mathbf{K}_B \end{bmatrix} \begin{Bmatrix} \mathbf{u}_{R,B} \\ \mathbf{u}_{F,B} \end{Bmatrix} = \begin{Bmatrix} \mathbf{f}_{F,B} \\ -\mathbf{f}_{F,B} \end{Bmatrix} \quad (8)$$

$$\begin{bmatrix} \mathbf{Z}_{F,BB} & \mathbf{Z}_{F,BI} \\ \mathbf{Z}_{F,IB} & \mathbf{Z}_{F,II} \end{bmatrix} \begin{Bmatrix} \mathbf{u}_{F,B} \\ \mathbf{u}_{F,I} \end{Bmatrix} = \begin{Bmatrix} \mathbf{f}_{F,B} \\ \mathbf{0} \end{Bmatrix} \quad (9)$$

The second subscript I represents the internal DoF of the rotor or foundations, depending on the first subscript, and the second subscript B represents the DoF of the bearings. It is assumed that the force needed to give a relative bearing deflection is due to the relative displacement of  $\mathbf{u}_{R,B} - \mathbf{u}_{F,B}$ , leading to the particular form of the bearing dynamic stiffness

matrix in equation (8). The  $\mathbf{f}_{R,I}$  term of equation (7) permits specification of an unbalance forcing in the system. The force acting on the rotor due to unbalance excitation is of the form  $\mathbf{f}_{R,I} = \mathbf{e}\omega^2$ , where  $\mathbf{e}$  is the vector of unbalance magnitudes, containing non-zero components corresponding to the locations of eccentric mass on the rotor, acting at specified unbalance planes. Combining equations (7) to (9) then leads to a general equation of motion for the global system:

$$\begin{bmatrix} \mathbf{Z}_{R,II} & \mathbf{Z}_{R,IB} & \mathbf{0} & \mathbf{0} \\ \mathbf{Z}_{R,BI} & \mathbf{Z}_{R,BB} + \mathbf{B} & -\mathbf{B} & \mathbf{0} \\ \mathbf{0} & -\mathbf{B} & \mathbf{B} + \mathbf{Z}_{F,BB} & \mathbf{Z}_{F,BI} \\ \mathbf{0} & \mathbf{0} & \mathbf{Z}_{F,IB} & \mathbf{Z}_{F,II} \end{bmatrix} \begin{Bmatrix} \mathbf{u}_{R,I} \\ \mathbf{u}_{R,B} \\ \mathbf{u}_{F,B} \\ \mathbf{u}_{F,I} \end{Bmatrix} = \begin{Bmatrix} \mathbf{f}_{R,I} \\ \mathbf{0} \\ \mathbf{0} \\ \mathbf{0} \end{Bmatrix} \quad (10)$$

or, in its simplest form

$$\mathbf{Z} \mathbf{u} = \mathbf{f} \quad (11)$$

Equation (10) represents the general equation of motion for a rotor-bearings-foundations system of this type. If further refinements, such as any particular gyroscopic or damping effects are to be included in the model then the only modifications that need to be made are in the specification of the individual dynamic stiffness matrices in equations (4) to (6). In the present study, the foundations are not specified as having any internal DoF, and the ball bearings used for the experimental rig are considered rigid (infinite stiffness), reducing equation (10) to

$$\begin{bmatrix} \mathbf{Z}_{R,II} & \mathbf{Z}_{R,IF} \\ \mathbf{Z}_{R,FI} & \mathbf{Z}_{R,FF} + \mathbf{Z}_F \end{bmatrix} \begin{Bmatrix} \mathbf{u}_{R,I} \\ \mathbf{u}_{R,F} \end{Bmatrix} = \begin{Bmatrix} \mathbf{f}_{R,I} \\ \mathbf{0} \end{Bmatrix} \quad (12)$$

Subscript F has now replaced subscript B, since the rotor now connects directly with the foundations, and the terms relating to the internal DoF of the foundations have been discarded, since these are no longer of interest.

## 2.2 Identifying The System

The top set of terms in equation (12) yields an expression for  $\mathbf{u}_{R,I}$ , which is then eliminated from the bottom set, allowing these terms to be re-written with the unknown and known terms grouped on the left and right hand sides respectively, giving

$$\mathbf{Z}_F \mathbf{u}_{R,F} + \mathbf{Z}_{R,FI} \mathbf{Z}_{R,II}^{-1} \mathbf{f}_{R,I} = [\mathbf{Z}_{R,FI} \mathbf{Z}_{R,II}^{-1} \mathbf{Z}_{R,IF} - \mathbf{Z}_{R,FF}] \mathbf{u}_{R,F} \quad (13)$$

Now let

$$[\mathbf{Z}_{R,FI} \mathbf{Z}_{R,II}^{-1} \mathbf{Z}_{R,IF} - \mathbf{Z}_{R,FF}] \mathbf{u}_{R,F} = \mathbf{P} \quad (14)$$

and

$$\mathbf{Z}_{R,FI} \mathbf{Z}_{R,II}^{-1} \mathbf{f}_{R,I} = \mathbf{Z}_{R,FI} \mathbf{Z}_{R,II}^{-1} \omega^2 \mathbf{e} = \mathbf{R} \mathbf{e} \quad (15)$$

where  $\mathbf{P}$  and  $\mathbf{R}$  contain terms collected at all measured frequencies. Substituting the unknown mass and stiffness parameters of equation (6) for  $\mathbf{Z}_F$  in equation (13) allows these desired elements to be estimated in a least squares sense. If the unknown parameters are grouped into a vector  $\mathbf{v}$ , and a corresponding matrix  $\mathbf{w}(\omega)$  containing the related response terms at each measured frequency is also defined (see [4, 5]), then we have

$$\mathbf{Z}_F(\omega) \mathbf{u}_{R,F}(\omega) = \mathbf{w}(\omega) \mathbf{v} \quad (16)$$

The parameters contained in  $\mathbf{v}$  depend on the form of the dynamic stiffness matrix specified for the foundations and the ordering of these parameters may be designated as desired. The foundation model used for these experiments was initially specified as diagonal mass, damping and stiffness matrices (i.e. with no cross-coupling present). This was considered a realistic representation of the physical system in question.

Equation (13) is now rewritten using equations (14) to (16) as

$$\mathbf{W} \mathbf{v} + \mathbf{R} \mathbf{e} = \mathbf{P} \quad (17)$$

Leading to the solution of

$$[\mathbf{W} \ \mathbf{R}] \begin{Bmatrix} \mathbf{v} \\ \mathbf{e} \end{Bmatrix} = \mathbf{P} \quad (18)$$

When solving for the unknown parameters,  $\mathbf{v}$  and  $\mathbf{e}$ , the condition of the matrix to be inverted in equation (18) should be taken into account, and the condition number may be improved by pre-conditioning or by scaling of parameters. In addition, if *a priori* knowledge of some terms exists, such as one or more of the foundation mass or stiffness terms, then this information may be included in the analysis. For further detail on both of these issues, see [3]. In the present study, solutions to equation (18) were obtained using the least squares method. Singular Value Decomposition (SVD) methods [6] may prove beneficial in cases where there is not enough information to sufficiently identify all desired parameters, although this was not necessary here. In practical cases,  $\mathbf{W}$  and  $\mathbf{P}$  will be complex, in which case these matrices must be separated into their real and complex parts, leading to a doubling of the order of these terms, although the parameters it is intended to identify remain real.

### 3 THE EXPERIMENTAL ROTOR RIG

The rotor rig, shown in Figure 2, included a solid steel shaft of length 750 mm and diameter 12 mm, along which 2 balance disks were placed. The rotor ran in ball bearings, assumed rigid for analysis purposes. The bearing pedestals were supported by springs, analogous to a turbogenerator's flexible foundations. These elastic foundations were considered highly desirable in such apparatus: most similar commercially available products use only rigid supports. The rotor was connected via a direct-drive flexible coupling to an electric motor (max. speed 3000 rpm). Various transducers were mounted on the rig: 4 low-mass, piezo-

electric accelerometers were attached to the bearing housings (2 bearings, 2 directions), to measure the response at these points (corresponding to the term  $\mathbf{u}_{R,F}$  in equation (14)), whilst a proximity switch provided a once-per-revolution pulse from a reference marker on the shaft, which allowed order tracking to be performed.

For the results presented in this paper, the system was configured in such a way that, measured from the coupling, disks A and B were at distances of 79 mm and 459 mm respectively, whilst bearings A and B were at distances of 234 mm and 733 mm. The corresponding model details are given in Table 1, where it can be seen that the rotor model consisted of five two-noded beam elements representing the shaft, each node having 2 translational and 2 rotational DoF. The two disks were modelled using additional mass and inertia terms at the disk locations. The free-free rotor model was verified by performing impact tests on the rotor supported in elastic slings. The first four measured and predicted (in brackets) natural frequencies were: 2 rigid body modes, 77.5 (77.5) and 211.3 (215.2) Hz. This error was not considered significant.

#### 4 EXPERIMENTAL RESULTS

Since this was the first time that the identification method had been tested experimentally, the potential of the rotor rig to quickly deliver reliable and repeatable results was utilised, and many run-downs were performed on which the identification method was carried out.

For the set of results described in this section, the unbalance configuration of the rotor was changed by adding extra mass to the disks. The rotor configuration described above remained the same throughout, and the reference speed range of 45-15 Hz was used for all run-downs. The state of unbalance of the rig for each run is given in Table 2, together with the identified unbalance parameters. Since the foundations were not changed in any way throughout the acquisition of these results, the estimated foundation parameters were expected to remain constant. The mean values and standard deviations of the estimated foundation parameters are given in Table 3, together with their measured values, for purposes of comparison. The values of unbalance mass used were of similar magnitude to the residual unbalance of the rotor. Note that the results for run 20 were not taken into account when calculating the mean values – the machine was so well-balanced in this case that there was insufficient forcing to allow reasonable estimates to be calculated. This particular case is discussed in more detail later.

Excellent accuracy in the identification of the unbalance parameters was achieved. The residual unbalance estimates for runs 1-2 and runs 3-7 are consistent, with no significant discrepancy in either unbalance magnitude or angle. The change in residual unbalance between runs 2 and 3 was due to the fact that the rotor was taken apart and put back together again at this point. This consistent identification highlights the robustness of the identification method for dealing with different data sets. The results for runs 3-20, with many variations in unbalance configuration, are also extremely encouraging. The most straightforward way to check the accuracy of the unbalance estimates was to calculate the error between the estimated additional unbalance (calculated using the estimated unbalance from two consecutive runs) and the actual additional unbalance. With the exception of run 12, where the maximum error in magnitude was 0.6 g for disk A, all other magnitude errors are no greater than 0.3 g, which is generally very low compared to the magnitude of the added

masses. The means and standard deviations of the estimated errors are both 0.1 g. Likewise, the errors in unbalance angle are also very small, with the mean error of  $17^\circ$  being less than 5%. These low errors in estimated unbalance are considered acceptable.

It should first be noted that (as stated above), the reason for the poor foundation estimates for run 20 was because the machine was so well-balanced in this case that there was insufficient forcing to allow reasonable estimates to be calculated. However, it should not be overlooked that the error in estimated added unbalance is still very low for this case. The maximum error in foundation stiffness estimation was just 6%, compared to the measured values, for the vertical direction at foundation A. The mass identification exhibits similar behaviour in terms of consistency, with the largest variation in estimates being for foundation A. Here, the mean estimated mass for foundation A is less accurate than for foundation B. Errors of 28% and 35% arise for the horizontal and vertical directions respectively, compared to just 3% and 0% for foundation B. The reason why the stiffness estimation is more robust than the mass estimation may be due to the fact that the identified mass terms are proportional to the square of the frequency, and so are weighted more towards higher frequencies, whilst the stiffness identification is equally weighted over all frequencies. However, the reason why the identification of foundation A suffers more than foundation B is less clear. The most probable cause is that foundation A is nearest the coupling, and any error in the modelling of the coupling is likely to have a much stronger influence on that foundation which is closest. In addition, if there are any dynamic effects due to the motor, which is not included in the rotor model, then these may also have a part to play. The accuracy of the estimated damping parameters is less straightforward to judge, since the actual foundation damping is unknown. However, the same trend of larger standard deviations for foundation A is evident, and the low magnitudes of the estimated damping coefficients (3.3%, -3.0%, 0.2% and 2.0% for  $A_x$ ,  $A_y$ ,  $B_x$ ,  $B_y$ ) would be expected for a structure of this type. The reason for the negative damping parameter for the vertical direction of foundation A may be due to some underlying physical cause or again due to some kind of modelling error. This does not, however, give cause for concern, as the magnitudes of the damping parameters are indeed very low.

Overall, both the foundation and the unbalance parameters have been estimated to high degrees of accuracy. The robustness of the method to changes in excitation has been shown by the consistently accurate foundation parameter identification and highly accurate unbalance identification, with various unbalance configurations being used. Although the estimates for foundation A are the least accurate, the estimates for foundation B and the unbalance estimates do not appear to suffer as a result. This shows great promise for the method in terms of application to real machines, where some kind of modelling error is normally inevitable. Robustness to this type of error, as seen in this instance, is therefore highly desirable.

A final check to be made on the estimated parameters was to combine them with the rotor model to obtain the estimated system responses, and to compare these estimated responses with those measured at the bearing housings, where a close fit between estimated and measured responses is indicative of a successful identification. This has been done in Figure 3, for the parameters identified from run 8. This particular set of data was simply chosen as an example and is typical of the estimated responses obtained for all other data sets considered here. As would be expected from the accurate parameter identification discussed above, there is excellent agreement between measured and estimated responses. The only discrepancy of any significance is found between the estimated and measured responses in the vertical



directions of both bearings, at the lower critical speed. The reason for this is most likely the negative damping coefficient identified in the vertical direction of bearing A.

Since one of the main goals of this work was to reduce vibration levels of rotating machinery by performing balancing using a single set of data, balancing was carried out using the identified parameters obtained from run 19. The identified unbalance masses were placed at positions opposite (as far as the disks would allow) the identified unbalance angle. The responses obtained for the two runs are shown in Figure 4. The responses are plotted using a linear scale as this allows a clearer comparison of the response magnitudes to be made. It can be seen from Figure 4 that the balancing procedure carried out on the machine was highly successful. Vibrational amplitude at the lower critical speed was reduced by up to 92%, whilst at the higher critical speed the amplitude was reduced by a maximum of 58%. The lowest measured reduction was 50%, for the higher critical speed in the vertical direction at both bearings. These large reductions in amplitude represent a very significant improvement in the machine's dynamic behaviour. The very low response amplitudes for run 20 are the reason why the estimated foundation parameters are of poor quality. Indeed, much of the measured response is low enough to be masked with noise.

The flexible support and unbalance identification method has thus far been applied to numerous sets of data obtained in experiment. The identified parameters were shown to be highly accurate and robust to changes in unbalance configuration and possible modelling error. Confidence acquired from the identification results was applied to perform balancing on the experimental rotor rig, whereby large reductions in vibrational amplitude were achieved after balancing from a single run-down. As far as field balancing is concerned, if it were possible to obtain such reductions in vibration from only a single run-down of a machine, as has been achieved here, then this would be a great benefit for machinery operation.

## 5 SUMMARY AND CONCLUSIONS

An identification method for estimating both the excitation and flexible support parameters of a rotor-bearings-foundation system has been presented. The method has great practical potential, since it allows balancing to be performed on a rotor using data obtained from just a single run-up or run-down of the machine, which has obvious benefits for the efficient operation of machinery in the field. Using this single-shot balancing technique, vibration levels of an experimental rotor rig were successfully reduced by as much as 92% of their original levels. The identification of flexible foundation parameters has been successfully achieved, with measured and estimated parameters matching very closely in most cases. The experimental results were very encouraging for the method and it is envisaged that the main thrust of future work on this topic should be the application of the identification method to larger, more complicated machines, and eventually to power station turbogenerators.

Due to the constraints imposed on article length, the authors were forced to omit a large portion of the experimental work carried out during the course of this research. A full coverage is given in references [4] and [5], where the identification of different rotor and foundation configurations has been investigated, together with the identification of concurrent rotor bend and unbalance excitation, and also the effect of specifying alternative foundation models on the system identification.

## ACKNOWLEDGEMENTS

The authors are pleased to acknowledge the support of BNFL (Magnox Generation) and the Engineering and Physical Sciences Research Council. Dr. Friswell gratefully acknowledges the support of the EPSRC through the award of an Advanced Fellowship.

## REFERENCES

- [1] A. G. Parkinson 1991 *Proceedings of the Institution of Mechanical Engineers Part C – Journal of Mechanical Engineering Science* **205**, 53-66. Balancing of Rotating Machinery.
- [2] A. W. Lees 1988 *Proceedings of the Institution of Mechanical Engineers - Vibrations in Rotating Machinery* Paper C306/88, 209-216. The Least Squares Method Applied to Identify Rotor/Foundation Parameters.
- [3] A. W. Lees and M. I. Friswell 1997 *Journal of Sound and Vibration* **208**, 671-683. The Evaluation of Rotor Unbalance in Flexibly Mounted Machines.
- [4] S. Edwards, A. W. Lees & M. I. Friswell 2000 *Journal of Sound and Vibration* **232(5)**, 963-992. Experimental Identification of Excitation and Support Parameters of a Flexible Rotor-Bearings-Foundation System from a Single Run-Down.
- [5] S. Edwards, Ph.D. Thesis 1999, University of Wales Swansea. An Investigation of Rub, Unbalance and Shaft Bow in Rotordynamic Systems.
- [6] A. Jennings and J. J. McKeown 1993, *Matrix Computation* (2nd Edition), Chichester; Wiley.

**Table 1: Details of rotor model**

Station	Distance from Coupling (mm)	Element Length (mm)
1 (coupling)	0	-
2 (disk A)	79	79
3 (bearing A)	234	155
4 (disk B)	459	225
5	596	137
6 (bearing B)	733	137

**Table 2: Actual and estimated unbalance parameters**

Run	Unbalance (Disk A; Disk B) (mass (g) @ phase angle (degrees))			
	Unbalance Configuration	Estimated Unbalance	Calculated Addition	Error
1	Residual	1.3@174		
	Residual	1.8@97		
2	Residual	1.3@173		
	Residual	1.8@96		
3	Residual	0.6@116		
	Residual	1.7@100		
4	Residual	0.6@121		
	Residual	1.7@99		
5	Residual	0.6@120		
	Residual	1.7@99		
6	Residual	0.6@120		
	Residual	1.7@99		
7	Residual	0.6@119		
	Residual	1.7@98		
8	0.8@120	1.5@122	0.9@127	0.1@7
	2.4@100	4.2@116	2.6@125	0.2@25
9	Residual	0.8@118	0.7@308	0.1@8
	Residual	1.7@97	2.6@308	0.2@28
10	Residual	0.9@114	0.1@81	-
	2.4@90	4.2@102	2.5@105	0.1@15
11	Residual	0.7@114	0.1@290	-
	Residual	1.8@97	2.5@285	0.1@15
12	2.0@312	1.9@-77	2.6@286	0.6@-26
	2.4@263	0.8@-44	2.5@289	0.1@26
13	Residual	1.2@-163	2.3@137	0.3@5
	Residual	1.8@97	2.6@109	0.2@26
14	2@281	2.3@-91	2.3@300	0.3@19
	2@281	1.0@6	2.1@306	0.1@25
15	Residual	1.4@-160	2.2@124	0.2@23
	Residual	1.8@95	2.1@124	0.1@23
16	2@349	1.0@-11	2.3@6	0.3@17
	2@259	0.2@-10	1.9@282	-0.1@23
17	Residual	1.2@-163	2.2@183	0.2@14
	Residual	1.8@94	1.9@101	-0.1@22
18	1.2@11	0.2@68	1.3@24	0.1@13
	1.8@281	0.9@26	1.7@304	-0.1@23
19	Residual	1.2@-162	1.3@205	0.1@14
	Residual	1.8@95	1.7@125	-0.1@24
20	1.2@11	0.2@86	1.3@25	0.1@14
	1.8@259	0.2@34	1.7@281	-0.1@22

**Table 3: Identified foundation parameters**

Estimated Parameter	Foundation/Direction (measured value)	Estimated Mean Value (std. dev.)	Error (%)
Stiffness (N/m)	Ax (17212)	17015 (538)	-1
	Ay (17707)	18797 (515)	6
	Bx (17277)	16691 (211)	-3
	By (17523)	16589 (148)	-5
Mass (kg)	Ax (0.356)	0.455 (0.012)	28
	Ay (0.356)	0.480 (0.013)	35
	Bx (0.352)	0.361 (0.005)	3
	By (0.352)	0.352 (0.005)	0
Damping (Ns/m)	Ax	5.89 (1.60)	-
	Ay	-5.77 (1.88)	-
	Bx	0.30 (0.82)	-
	By	3.02 (0.65)	-

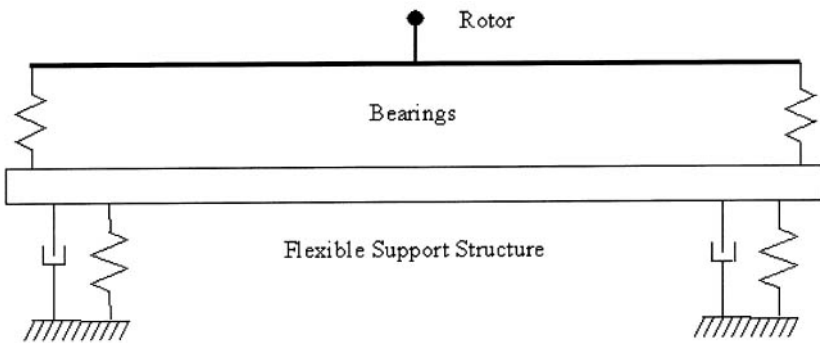


**Figure 1: Unbalanced rotor-bearings-foundation system**

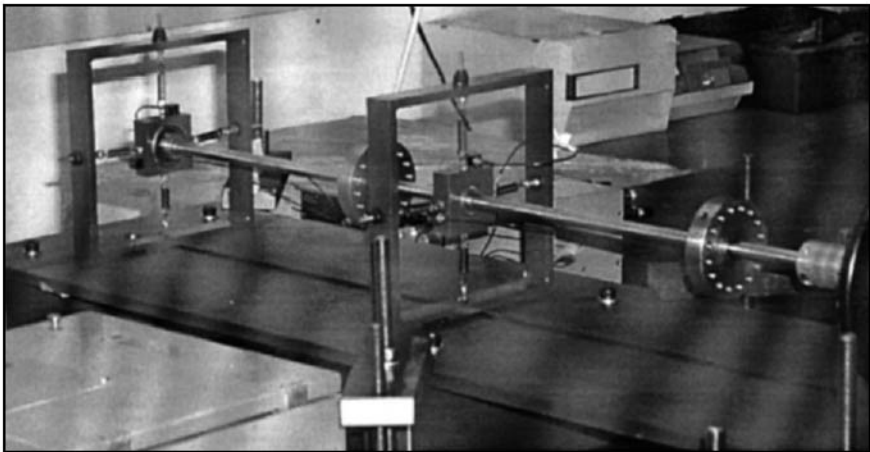


**Figure 2: General view of experimental rotor rig**

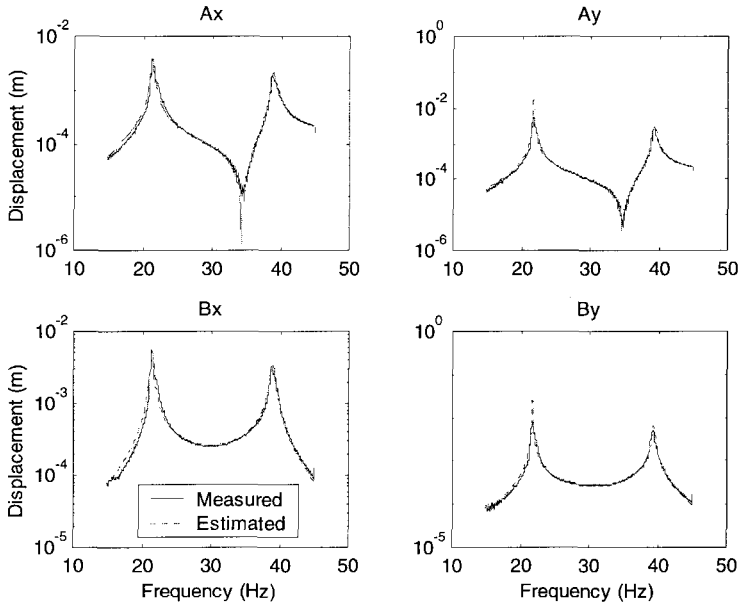


**Figure 3: Measured and estimated responses (pk-pk) for run 8**

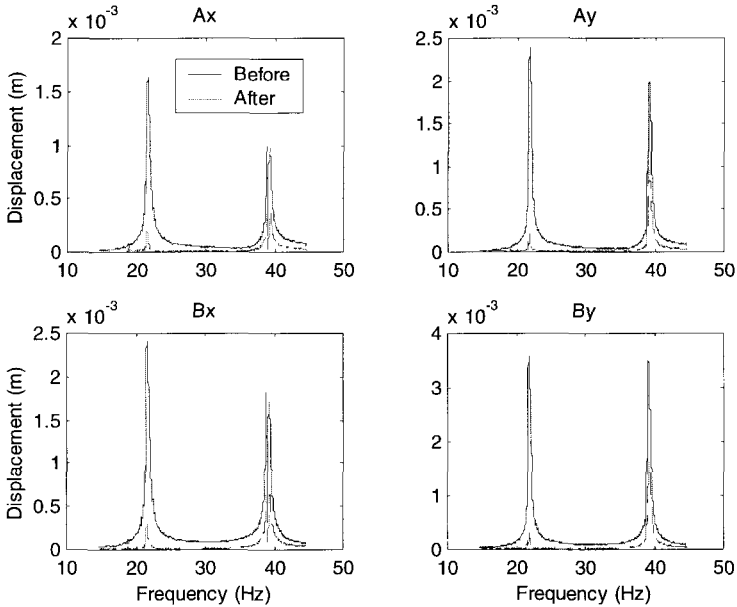


**Figure 4: Measured responses (pk-pk) before and after balancing**

*This page intentionally left blank*

## Unbalance identification of flexible rotors based on experimental modal analysis

T KREUZINGER-JANIK and H IRRETIER  
Institute of Mechanics, University of Kassel, Germany

### ABSTRACT

For the identification of the unbalance distribution of flexible rotors, a method was developed, which is based on the modal expansion of the frequency response functions. Basically, this expansion can be found either by a numerical calculation, which normally requires a model updating procedure for sufficient accuracy of the numerical model or by experimental results. In both cases, an appropriate modal testing technique is required for experimental modal analysis of the rotor.

A rotor test rig was designed for rotordynamic experiments, in particular for modal analysis and unbalance identification. The rotor is excited by a non-contact magnetic exciter which can be placed in various positions on the rotor shaft. The exciter includes two integrated laser sensors to realize driving-point displacement measurements in two directions and a piezoelectric force transducer for a direct measurement of the excitation force. The response of the rotor is detected by several non-contact laser sensors along the rotor. The frequency response functions are determined from the excitation and response data, and the modal parameters are extracted by the optimization technique of the Structural Dynamic Toolbox of E. Balmes (1). Some pre-tests to check both the linear behaviour and the quality of the measurement data as well as some FE-calculations will be shown. Experimental results of the modal tests and the unbalance identification will conclude the paper.

# 1 THEORY OF UNBALANCE IDENTIFICATION USING MODAL TESTING

The proposed method has the target to identify the unbalance distribution on the complete rotor. For that purpose, the spectrum of the unbalance response  $\bar{W}^U(\Omega_R) = \hat{W}^U e^{j\Omega_R}$  must be measured at constant angular speed  $\Omega_R$ . To describe the motion of the rotor, it is necessary to measure the displacement in each measurement plane in two perpendicular directions. Using a linear model, the spectrum of the unbalance response can be described by the unbalance force  $\bar{F}^U(\Omega_R) = \hat{F}^U e^{j\Omega_R}$  multiplied by the frequency response function matrix (FRFM)  $\bar{H}$

$$\hat{W}^U(\Omega_R) = \bar{H}(\Omega_R) \cdot \hat{F}^U(\Omega_R) . \quad (1)$$

Consequently, a pseudo inversion<sup>1</sup> of the generally incomplete FRFM  $\bar{H}$  leads to the unbalance force vector

$$\hat{F}^U(\Omega_R) = \bar{H}^+(\Omega_R) \cdot \hat{W}^U(\Omega_R) \quad (2)$$

and thus to the unbalance parameters combined in the vector  $\bar{\xi}$  ( $\bar{\Theta}$  including mass, geometry and transformation parameters (2), (3)) by

$$\bar{\xi} = \frac{1}{\Omega_R^2} \cdot \bar{\Theta}^+ \cdot \hat{F}^U(\Omega_R) . \quad (3)$$

In this way, it is possible to identify the origin of the unbalance forces as opposed to the common balancing methods. The knowledge of the unbalance distribution of the rotor enables:

- balancing for arbitrary speed ranges (depending on the numbers of balancing planes)
- trouble shooting systematically (for errors in technical design ...)
- on-line monitoring of the unbalance state

To apply the equations (1) to (3), three steps of consecutive identification procedures are required which are described in the following.

## 1.1 Identification of the Frequency Response Functions

The frequency response functions (FRFs) can be identified by an experimental modal analysis of the rotor at constant angular speed  $\Omega_R$ . The resulting FRFs  $\bar{H}_{rl}(\Omega_F)$  describe the relationship between the forced vibration at location  $r$  measured by non-contact laser sensors and the excitation force at location  $l$  using a self-developed magnetic exciter driven by several frequencies  $\Omega_F$ . One problem in modal testing of rotating structures is the bad signal to noise ratio and the disturbance from the rotating speed and its superharmonics. Thus a stepped sine excitation was used to get enough input energy into each frequency line, in particular for higher frequencies (up to 500 Hz). A spectral analysis of typical excitation signals has shown that these signals can be approximated very well using a

<sup>1</sup>pseudo inversion = +



harmonic series consisting of the exciter frequency and the rotating frequency and their first two superharmonics (for response signals in the same way) as described by

$$f(t) \approx \hat{F}_0^F + \sum_{q=R,F} \sum_{\nu=1}^3 \hat{F}_\nu(\Omega_q) \cos(\nu\Omega_q t + \alpha_\nu^F(\Omega_q)) \quad (4)$$

( $\Omega_F$  = excitation frequency,  $\Omega_R$  = rotation frequency). The superharmonics of  $\Omega_F$  result from the non-linear behaviour between the applied harmonic current signal

$$i(t) = \hat{i} \sin\left(\frac{\Omega_F}{2} t\right) \quad (5)$$

and the resulting force signal, whereas the superharmonics of  $\Omega_R$  come from the non-linearity in the rotor system, e.g. from the journal bearings.

To identify the amplitudes and phase angles of the force and response signals, for each excitation frequency a least squares approximation has been calculated. Regarding the amplitudes and phases of the excitation frequency  $\Omega_F$  ( $\nu = 1$ ) only, the modal parameters have been identified. For each frequency line  $\Omega_{F,m}$ , the values of the FRFs can be calculated by

$$\bar{H}_{rl}(\Omega_{F,m}) = \frac{\hat{W}_r(\Omega_{F,m})}{\hat{F}_l(\Omega_{F,m})} \cdot e^{j(\alpha_r^W(\Omega_{F,m}) - \alpha_l^F(\Omega_{F,m}))} \quad (6)$$

from the complex amplitudes

$$\hat{F}_l = \tilde{F}_l e^{j\alpha_l^F} \quad \text{and} \quad \hat{W}_r = \tilde{W}_r e^{j\alpha_r^W} \quad (7)$$

Next, the modal parameters of the rotor are determined from the FRF-measurements based on equation (6).

## 1.2 Identification of the Modal Parameters

The Structural Dynamic Toolbox (1) has been used to identify the residues  $\bar{R}_{rlk}(\Omega_F, \Omega_R)$  and the eigenvalues  $\bar{\lambda}_k(\Omega_R)$  from the measured FRFs according to equation (6).

Afterwards the eigenvectors have been calculated using the residues. Therefore an additional norm must be introduced, as, because of the non-symmetric system matrices, the eigenvectors must be partitioned into left- and right-hand eigenvectors  $\bar{\phi}_k^L$  and  $\bar{\phi}_k^R$ . The chosen norm leads to the identity of the components of the right- and left-hand eigenvector for each mode  $k$  at the driving-point.

The FRFM for the angular speed  $\Omega_R$  can be composed by using the identified left- and right-hand eigenvectors  $\bar{\phi}_k^L$  and  $\bar{\phi}_k^R$ , the eigenvalues  $\bar{\lambda}_k$  and by regarding the residual matrices  $\mathbf{E}$  and  $\mathbf{F}$  describing the influence of the out-of-band-modes by the equation<sup>2</sup>

$$\bar{\mathbf{H}}(\Omega_R) = \sum_{k=n_0}^{n_1} \left( \frac{\bar{\phi}_k^R \bar{\phi}_k^{LT}}{\alpha_k(j\Omega_R - \lambda_k)} + \frac{\bar{\phi}_k^{R*} \bar{\phi}_k^{LT*}}{\alpha_k(j\Omega_R - \lambda_k^*)} \right) + \mathbf{E} + \frac{\mathbf{F}}{\Omega_R^2}, \quad (8)$$

<sup>2\*</sup> = conjugate complex; <sup>T</sup> = transposed

where  $n_0$  describes the lowest and  $n_1$  describes the highest mode taken into account.

The advantages of composing over measuring the whole FRFM (for the rotation frequency only), are<sup>3</sup>

- the less number of combinations between excitation and response location; composing:  $n_c = 2n - 1$ , measuring:  $n_c = n \cdot n$
- possible considerations of locations which are not excitable (e.g. bearings, discs ...)
- a large number of data and therewith error reduction is well possible.

### 1.3 Identification of the Unbalance Forces

To compute equation (2), a pseudo inversion of the FRFM is required. For this, the singular value decomposition

$$\bar{\mathbf{H}}(\Omega_R) = \bar{\mathbf{U}} \bar{\mathbf{\Sigma}} \bar{\mathbf{V}}^{T*} \quad (9)$$

can be used. Regarding the incompleteness of the FRFM, a pseudo inversion has to be realized after a reduction of the matrices  $\bar{\mathbf{V}}$ ,  $\bar{\mathbf{\Sigma}}$  and  $\bar{\mathbf{U}}$  to the number of measured modes  $n_M = n_1 - n_0 + 1$

$$\bar{\mathbf{H}}^+(\Omega_R) = \bar{\mathbf{V}}_{n_M} \bar{\mathbf{\Sigma}}_{n_M}^{-1} \bar{\mathbf{U}}_{n_M}^{T*}. \quad (10)$$

Thus, by equation (2) and (3) the unbalance parameters can be found using only the measured unbalance response and the identified modal parameters completely based on measured data without any FE-calculations.

## 2 PREPARATION OF THE MODAL TESTS

To get sufficiently accurate results from an experimental modal analysis, it is necessary to make some preparations. For that purpose FE-calculations and pre-tests have been performed.

### 2.1 FE-Calculations

To determine the frequency range of the tests and the best exciter and measurement locations, a FE-model was used which describes the dynamic behaviour of the test rotor. The applied FE-program has been developed especially for rotating systems (2). The program considers the common mass and stiffness matrices and, additionally, the gyroscopic effects and the stiffness and damping properties of the journal bearings as described in (4).

Due to the non-symmetric system matrices of the rotor model, the left- and right-hand eigenvectors are different. The modes corresponding to the calculated and identified right-hand eigenvectors and the related eigenfrequencies are shown in figure 1 and 2 and discussed in section 3. Knowing the modes of the test rotor, the driving-point location was chosen half-way between the two bearings at the measurement plane number 1 in  $y$  direction (figure 3).

---

<sup>3</sup> $n$  describes the dimension of  $\bar{\mathbf{H}}$

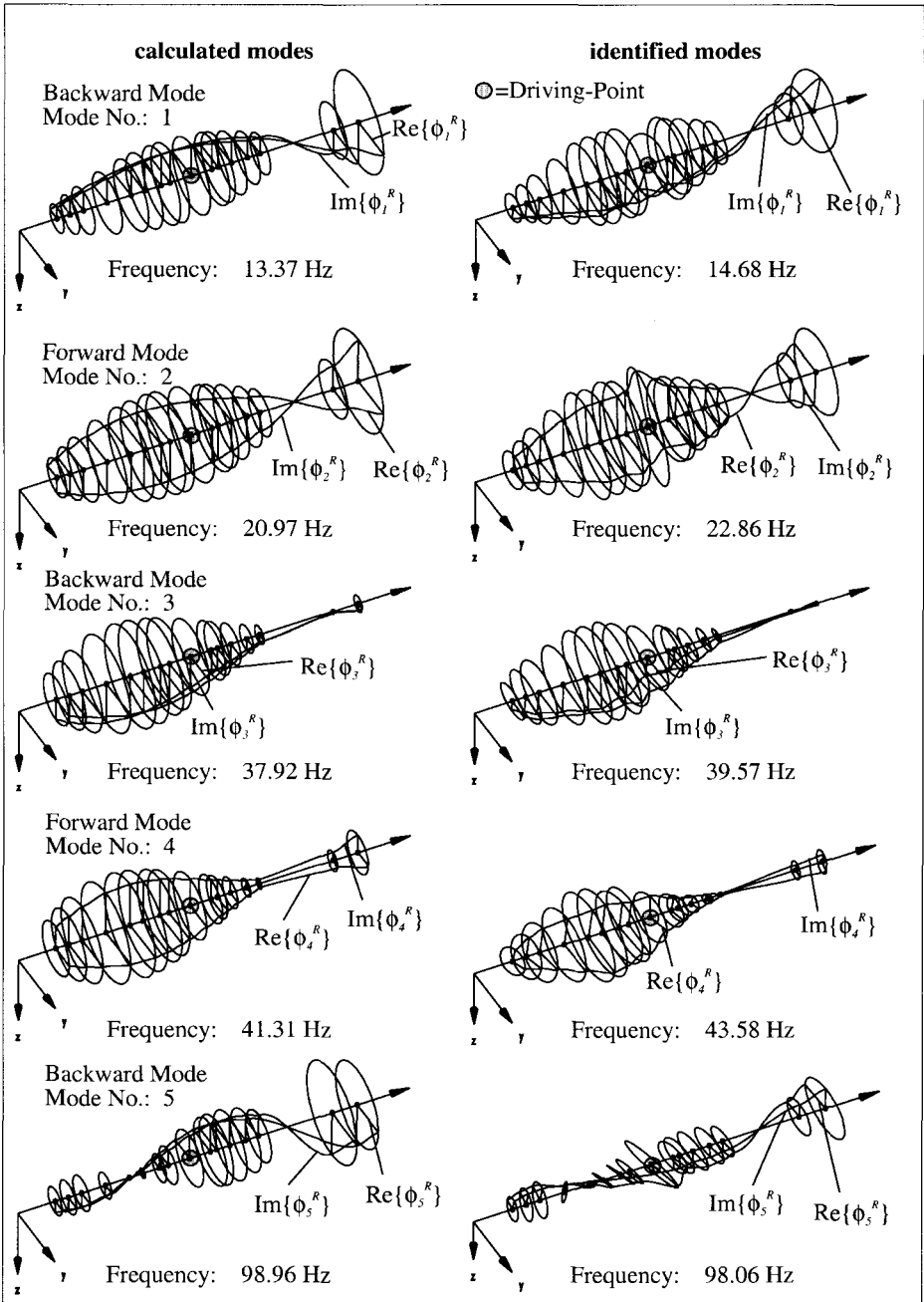


**Figure 1:** First to fifth calculated and identified eigenfrequencies and modes (right-hand eigenvectors) of the test rotor

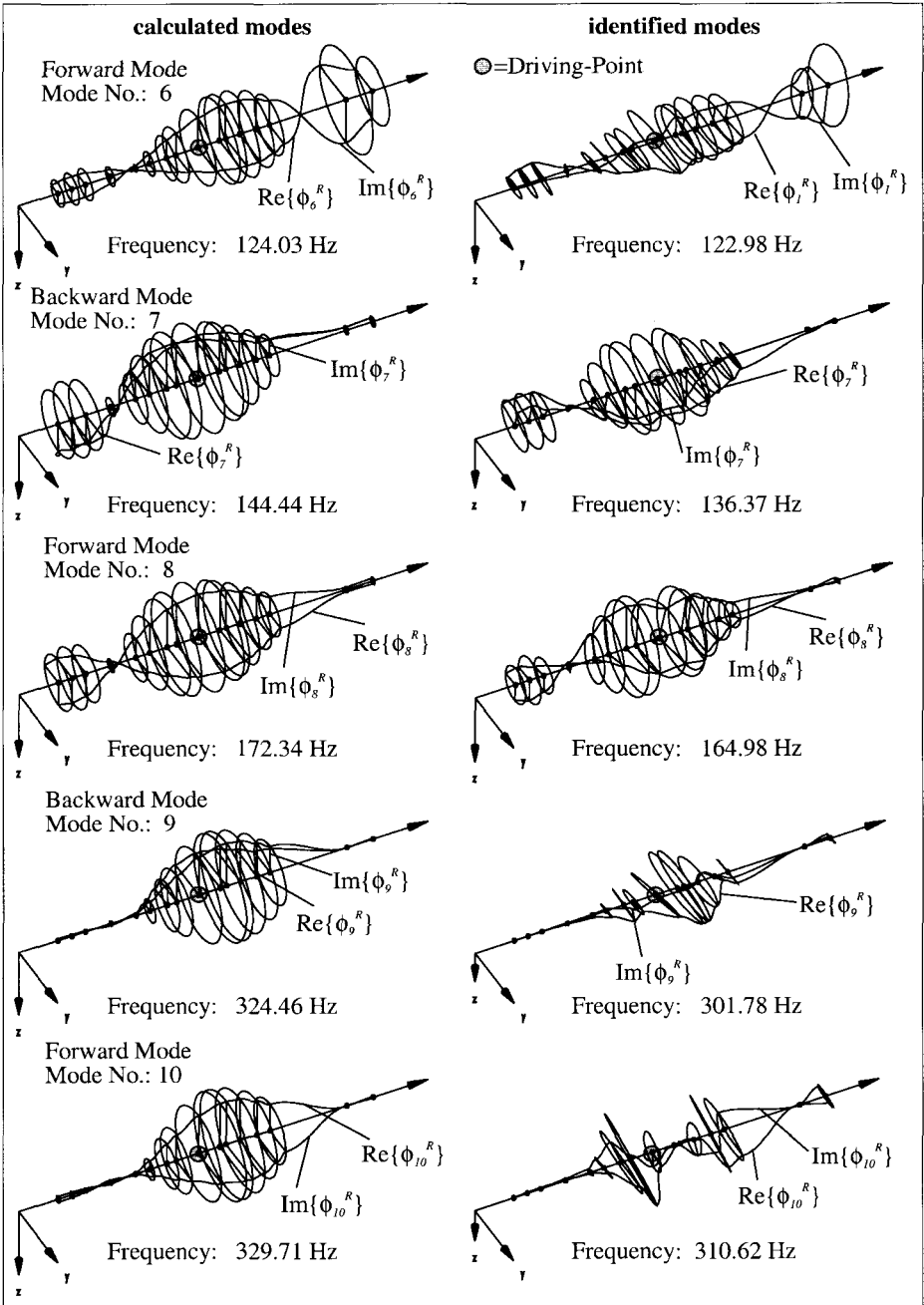
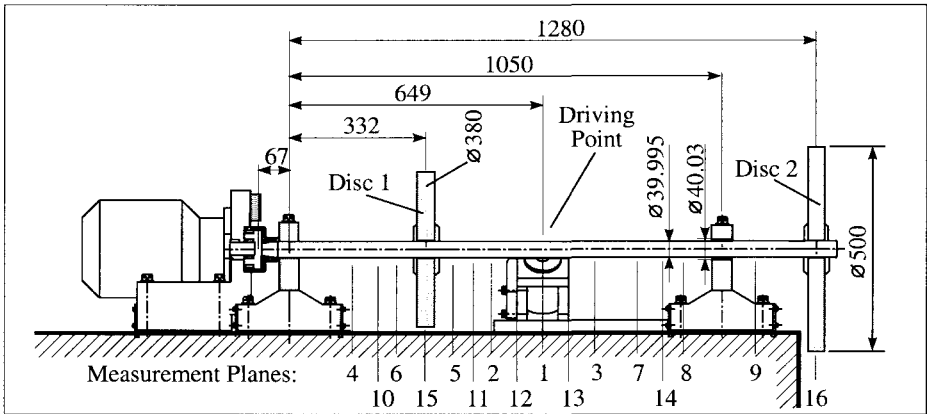


Figure 2: Sixth to tenth calculated and identified eigenfrequencies and modes (right-hand eigenvectors) of the test rotor



**Figure 3:** The measurement configuration of the test rotor

The unbalance response has been measured in the measurement planes 1 to 16 in  $y$  and  $z$  direction for each plane.

For the reconstruction of the non-symmetric FRFM, it is necessary to identify one column and one row of the FRFM. Accordingly, the locations of the laser sensors and the locations of the magnetic exciter have to be variable along the rotor shaft. It is impossible to excite the rotor at the disc locations (measurement planes 15 and 16). Therefore, the FRFs could be identified only for the measurement planes 1 to 14.

## 2.2 Pre-Tests to Check the Coherence and the Linearity

After the definition of the measurement planes and the exciter positions, pre-tests have been made to get information about the coherence between excitation and response and about the linearity behaviour of the rotor.

The FRFs for the modal analysis have been collected using stepped sine excitation. Accordingly, for each excitation frequency, a least-square approximation has been calculated to identify the amplitudes and phase angles of the excitation force and the response (see equation (4)). For that purpose, the coherence function has been calculated for each excitation frequency and is shown in figure 4 (for a better comparison the mobility has been plotted, too). It is seen, that in the vicinity of the eigenfrequencies the coherence function reaches acceptable values close to 1.

The linearity of the rotor has been proved by exciting the rotor close to some eigenfrequencies using several force amplitudes between 10 N and 220 N. In figure 5 the measured FRFs are shown. It can be seen, that the nonlinear behaviour of the rotor slightly shifts the eigenfrequencies around 23 and 136 Hz. Thus, the force level has been controlled to be constant over the whole frequency range during the modal tests. The non-linearity is caused by the journal bearings and the magnetic field of the exciter, which depends on the force level itself.

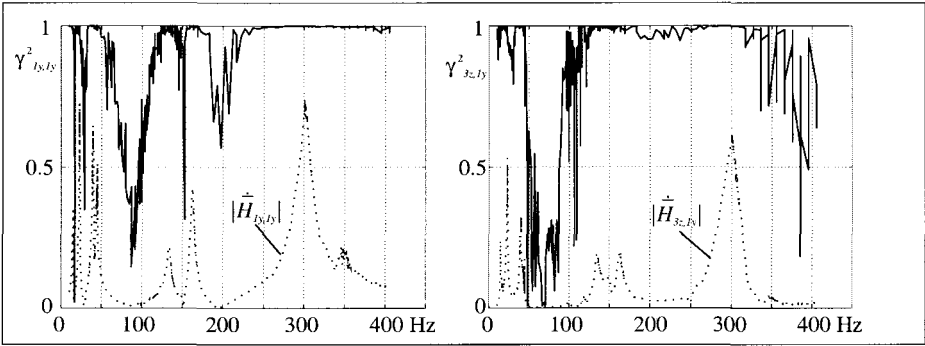


Figure 4: The coherence function for selected FRFs

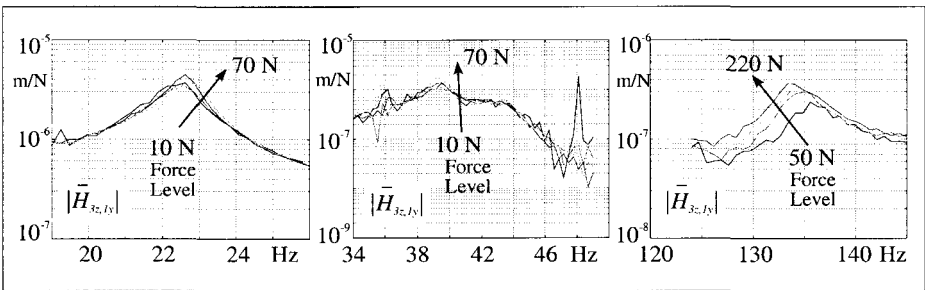


Figure 5: Measured FRFs excited by several force levels to check the linear behaviour of the rotor

### 3 RESULTS OF THE EXPERIMENTAL MODAL ANALYSIS

The rotor set-up and the realization of the experimental modal analysis is described in detail in (5) and (6).

In figure 6 some selected measured (dotted lines) and reconstructed FRFs are shown using both the right- and left-hand eigenvectors (dashed lines) and using only the right-hand eigenvectors (dashed-dotted lines), respectively.

In particular for the FRFs  $H_{1y,1z}$  and  $H_{1y,2y}$  from the variation of the exciter location, it is well visible that for this rotor with large gyroscopic effects due to the overhung position of disc 2 (see figure 3), the left-hand eigenvectors are required to describe the dynamic behaviour of the rotor.

Finally, the calculated and identified modal damping values and eigenfrequencies from the eigenvalues  $\bar{\lambda}_k = -D_k \omega_k + j \omega_k \sqrt{1 - D_k^2}$  are listed in table 1 and given in the figures 1 and 2, respectively. As the FE-model was not updated, there are sometimes considerable dif-

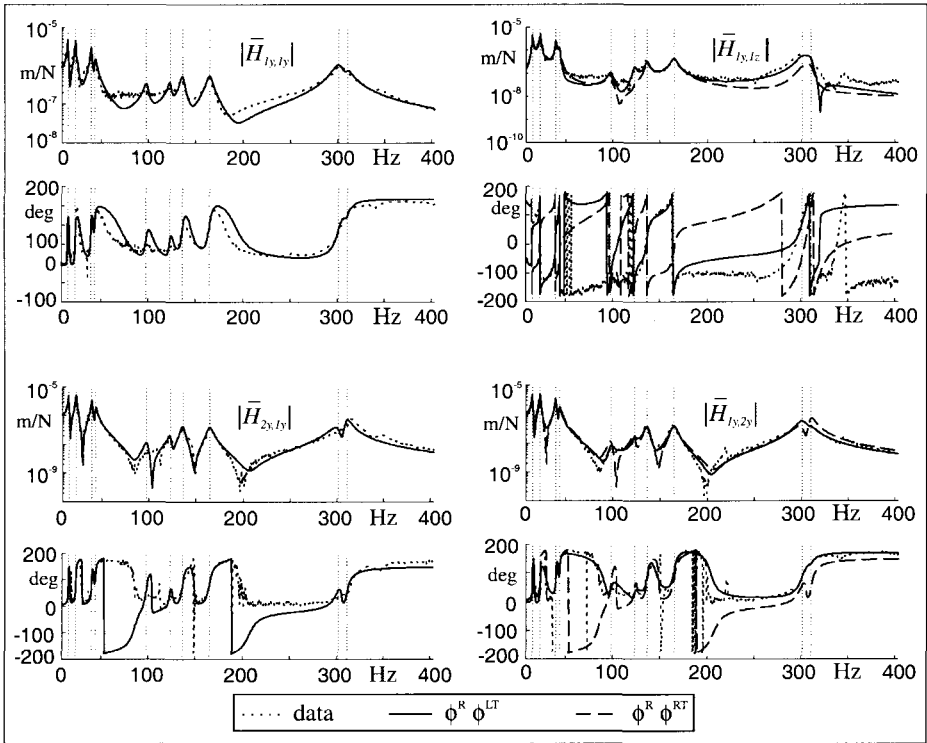


Figure 6: Measured and reconstructed FRFs

ferences in the numerical and experimental results. The agreement between the calculated and the identified modal damping parameters is very poor, due to the rough accuracy of the damping coefficients of the journal bearings and unknown additional damping sources in the rotor system, while the differences in the eigenfrequencies remain less than 10 % .

## 4 RESULTS OF THE UNBALANCE IDENTIFICATION

In the following section, at first simulated unbalance response data have been calculated, using the presented FE-model used for the identification, and afterwards some identification results are presented using the described test rotor.

The unbalance to be identified was attached to the test rotor by two grub screws in each disc. The unbalance of each disc described by its eccentricity  $\varepsilon^d$  and its mass  $m^d$  must be equal to the eccentricity of the grub screw  $\varepsilon^s$  and its mass  $m^s$

$$\vec{U} = U e^{j\alpha^U} = m^s \varepsilon^s e^{j\alpha^U} = m^d \varepsilon^d e^{j\alpha^U}, \quad (11)$$

Mode No.	identified	calculated
$k$	$D_k^d$	$D_k^{FE}$
1	0.0275	0.00030
2	0.0327	0.00074
3	0.0223	0.00054
4	0.0261	0.00132
5	0.0255	0.00145
6	0.0149	0.00092
7	0.0166	0.00045
8	0.0192	0.00044
9	0.0209	0.00063
10	0.0110	0.00063

**Table 1:** The identified and calculated modal damping values

which yields the eccentricity  $\varepsilon^d$  to be identified for given values  $m^s$ ,  $\varepsilon^s$  and  $m^d$  (see table 2).

Disc	grub screws		disc		unbalance	
	$m^s / \text{kg}$	$\varepsilon^s / \text{mm}$	$m^d / \text{kg}$	$\varepsilon^d / \text{mm}$	$U / \text{kg mm}$	$\alpha^U / \text{deg}$
1	$2 \cdot 4.83 \cdot 10^{-3}$	160	34.78	0.0444	1.545	-90
2	$2 \cdot 4.83 \cdot 10^{-3}$	220	60.92	0.0349	2.125	90

**Table 2:** Unbalances to be identified

#### 4.1 Simulation of the Unbalance Identification Using FE-Data

The unbalance response data and the modal parameters used for the identification procedure were calculated by the presented FE-model. Therewith, the unbalance identification was simulated to see the influence of first the neglected modes and second of a linear expansion of the eigenvectors for unmeasured locations (e.g. at the disc positions).

No. of modes $n_M$	disc 1			disc 2		
	$\varepsilon_1^d / \text{mm}$	$U_1 / \text{kg mm}$	$\alpha_1^U / \text{deg}$	$\varepsilon_2^d / \text{mm}$	$U_2 / \text{kg mm}$	$\alpha_2^U / \text{deg}$
20	0.0414	1.439	-90	0.0333	2.029	90
10	0.0414	1.439	-90	0.0333	2.029	90
4	0.0406	1.413	-90	0.0337	2.053	90

**Table 3:** Identified unbalances using FE-data

In table 3 the simulated identification results are listed in dependence of the number of modes used for the identification procedure. For the later identification using measured data, 10 identified modes can be used. The simulated results show that this is a sufficient



number to get enough accurate identification results.

No. of modes $n_M$	disc 1			disc 2		
	$\varepsilon_1^d / \text{mm}$	$U_1 / \text{kg mm}$	$\alpha_1^U / \text{deg}$	$\varepsilon_2^d / \text{mm}$	$U_2 / \text{kg mm}$	$\alpha_2^U / \text{deg}$
20	0.0281	0.977	-90	0.0434	2.644	90
10	0.0273	0.949	-90	0.0439	2.674	90
4	0.0198	0.689	-90	0.0484	2.949	90

**Table 4:** Identified unbalances using simulated unbalance response data and expanded FE mode shapes

Using the magnetic exciter, it is impossible to excite the rotor at the disc locations (measurement planes 15 and 16). Accordingly, the identified eigenvectors have to be expanded, to identify the unbalance at the locations of the discs. That has been done for the calculated FE-eigenvectors, too. As the identification results in table 4 show this expansion yields drastically worse results for the identified unbalance parameters.

## 4.2 Results of the Unbalance Identification Using Measured Data

As described above, the identified eigenvectors have to be expanded for the unmeasured locations of the discs. For that purpose, a linear interpolation for the disc 1 fixed on measurement plane 15 and a linear extrapolation for the disc 2 fixed on measurement plane 16, have been implemented for the real and imaginary parts of the eigenvectors. This leads to errors in the eigenvectors, in particular at the measurement plane 16 (see figures 1 and 2). However, the advantage of this expansion technique is that no FE-model is required for the identification procedure.

unbalance	disc 1			disc 2		
	$\varepsilon_1^d / \text{mm}$	$U_1 / \text{kg mm}$	$\alpha_1^U / \text{deg}$	$\varepsilon_2^d / \text{mm}$	$U_2 / \text{kg mm}$	$\alpha_2^U / \text{deg}$
complete	0.0981	3.412	-70.58	0.0727	4.429	-50.11
initial	0.0397	1.381	-43	0.0273	1.663	-22.89
grub screw	0.0654	2.275	-86	0.0500	3.046	-64

**Table 5:** Identified unbalances using measured response data and 10 identified and expanded mode shapes

Because the initial rotor was not exactly free of unbalances, the initial unbalances have been identified, too. Therefore, the unbalances introduced by the grub screws must be the difference of the complete unbalances and the initial unbalances as indicated in table 5. The identified eccentricities are acceptable for this first test of identification, but the identified phase angle for the disc 2 is very poor. Both facts are discussed in the conclusions.

## 5 CONCLUSIONS

In this paper, results of an experimental modal analysis on a rotor were presented to be used to identify the unbalance distributions of rotors. After a short description of the theory for the modal testing of rotating machines and the identification of the unbalance distribution some pre tests and identification results were presented.

The pre-tests have shown, that there exist some non-linearities in the test rotor, which have been considered by a constant force level for all frequencies. The signal conditions, quantified by the coherence function, led to acceptable values in the vicinity of the eigenfrequencies. Using a scanning laser vibrometer to detect the velocity, could lead to better signal to noise ratios. The accuracy of the unbalance identification depends on the number of considered modes which was shown by using simulated data. Furthermore it was shown, that using expanded modes (for the non-excited locations of the discs) the identification results have deteriorated. Finally, identification results have been presented using identified modal parameters and measured unbalance response data. The quality of the results is acceptable.

Concluding, the proposed unbalance identification technique using modal tests leads to acceptable results. The accuracy might be better by an improvement of the modal test using a laser vibrometer and by a further optimization of the excitation to increase the quality of the data base. Another disadvantage of the proposed method is the necessity to expand the eigenvectors to non-excited locations, e.g. the disc locations. Hence, the next goal is to be the unbalance identification using FE-eigenvectors calculated by an updated FE-model.

## REFERENCES

1. BALMES, E. : Experimental and Analytical Structural Dynamics Toolbox. Version 3, for use with MATLAB. Scientific Software Group, 1997.
2. BELZ, J. : Modalanalysegestützte Unwuchtidentifikation elastischer Rotoren. Dissertation. Berichte des Instituts für Mechanik (Bericht 4/1997), Uni-Gh Kassel, Germany.
3. BELZ, J., IRRETIER, H. : The Use of Modal Parameters for the Identification of the Unbalance Distribution of Elastic Rotors. IFToMM 5th. Fifth International Conference on Rotor Dynamics. Darmstadt Uni of Technology, Germany, Sept. 7-10, 1998. Proceedings pp. 679.
4. SOMEYA, T. : Journal-Bearing Databook. Springer-Verlag, Berlin, Heidelberg, New York, London, Paris, Tokyo, 1989.
5. KREUZINGER-JANIK, T., IRRETIER, H. : New Excitation and Response Measurement Techniques for Modal Testing of Flexible Rotors. IFToMM 5th. Fifth International Conference on Rotor Dynamics. Darmstadt Uni of Technology, Germany, Sept. 7-10, 1998. Proceedings pp. 695.
6. KREUZINGER-JANIK, T., IRRETIER, H. : Experimental Modal Analysis – A Tool for Unbalance Identification of Rotating Machines. ISROMAC-7. The 7th International Symposium on Transport Phenomina and Dynamics of Rotating Machinery. Honolulu, Hawaii, USA 22.26 Feb., 1998; Proceedings Vol. A, pp. 286

Active Control

*This page intentionally left blank*

## On-off control of HSFD supported rotors

**A EL-SHAFEI**

Department of Mechanical Design and Production, Cairo University, Egypt

**M EL-HAKIM**

Arab Organization for Industrialization Engine Factory, Helwan, Egypt

### ABSTRACT

This paper describes the theoretical and experimental application of on-off control to the Hybrid Squeeze Film Dampers (HSFDs). Two modes of operation are possible with an HSFD: a long damper mode with larger damping capability and a larger transmitted force, and a short damper mode with a smaller damping capability and a smaller force transmitted. The capabilities of HSFDs are described in detail as well as methods of designing the HSFD for the active control of rotors. The application of on-off control is presented as a means of passing critical speeds in the long damper mode, and alternatively sustaining operation at the short damper mode. Experimental application of the on-off control to a multi-mode rotor is presented. Excellent agreement between the theoretical and experimental results is obtained as well as evidence of the robustness of the on-off control, which is one of the best control algorithms for the HSFD (if designed properly), except for its disturbance rejection capabilities.

### 1. INTRODUCTION

Active Vibration Control (AVC) of rotating machines is sought after to improve the capability of a rotating machine to operate under varying and adverse conditions. Specifically, AVC is required to: improve the vibration isolation capability of the rotor support, reduce the amplitude of vibration of the rotor at all speeds, enhance the stability of the rotating machine, and allow the rotor to operate at high loads.

Burrows et al. (1) investigated the possibility of controlling rotating machinery vibration by controlling the pressure in a squeeze film damper (SFD). They pointed-out that control of rotors using active SFDs is much cheaper than using magnetic bearings, and is simpler and more reliable. This work was followed by several other investigators, including Adams and Zhloul (2) who studied the control of rotors by controlling the pressure in hydrostatic SFDs,

Mu et al. (3) who proposed an active SFD by using a movable conical damper ring, and El-Shafei (4) - (5), who proposed using Hybrid Squeeze Film Dampers (HSFDs) for active control of rotors. The basic idea is to control the flow rather than the pressure, which is much more effective in controlling SFDs.

Later, El-Shafei and Hathout (6) presented a complete model of the HSFD, as well as a bang-bang controller. Also, El-Shafei and El-Hakim (7) presented the first experimental results. The theoretical development of the adaptive control was presented by the same authors the following year (9). Hathout et al. (10) presented the application of the HSFD to the control multi-mode rotors, while El-Shafei and El-Hakim (11), presented the experimental results of the adaptive controller. They also presented the experimental results for PI control (12).

One of the basic conclusions of Burrows et al. (1) is that for most rotor systems only two levels of control are required to achieve the AVC requirements. Based on this idea, the on-off controller is investigated in this paper as an active control strategy for HSFDs. The flow is controlled in the damper to be axial to reduce the force at some speeds, or controlled to be circumferential to reduce the amplitude of vibration at other speeds, based on speed-scheduled instructions from the controller. Experimental results on a multi-mode test rig illustrate the concept. It is shown that the controller achieves its objectives in controlling the rotor, and is a possible application of on-off control to HSFD supported rotors.

## 2. BASIC THEORY OF THE HSFD

Most of the analyses of SFDs consider the short bearing approximation to Reynolds equation, which is justified if the damper is short in the axial direction such that the pressure induced flow in the damper is axial rather than circumferential. On the other hand, the long bearing approximation to Reynolds equation, which is justified if the damper is long in the axial direction such that the flow in the damper is circumferential, has attracted comparatively little attention (13-15). Usually open-ended dampers are considered short dampers and tightly sealed dampers are considered long dampers regardless of the actual physical length of the damper (which is usually short with respect to the diameter of the damper).

Short dampers and long dampers have very different characteristics (16). In general, long dampers are better at attenuating the amplitude response of the rotor, while short dampers are better at reducing the force transmitted to the support. Also it can be shown that the long damper provides more damping than a short damper. Thus if it is required to stabilize a rotor, then the long damper will remove more energy than the short damper. Also, because of the larger forces that are transmitted through a long damper, the long damper can be considered as a high load damper, i.e., it will be able to sustain high loads without executing large orbits (15), and thus the possibility of jump resonance is reduced. Table 1 summarizes the differences between short and long dampers.

If a squeeze film damper is designed to operate as a short damper when a small force transmitted to the support is desired, and to operate as a long damper when a small amplitude of vibration is desired, this would lead to a more effective squeeze film damper, and would allow rotors to operate safely at higher speeds. This can be accomplished by actively controlling the squeeze film damper to change its characteristics to either the long damper or the short damper. This implies that the control algorithm for such a hybrid damper would be

as simple as just switching from long to short dampers and vice versa. However, it may be required to obtain intermediate amounts of damping for better operation of the rotor.

**Table 1. Short versus long dampers**

	<b>Short Dampers</b>	<b>Long Dampers</b>
<b>Flow</b>	Axial	Circumferential
<b>Damping</b>	Low	High
<b>Amplitude Response</b>	Higher	Low at Critical Speed
<b>Transmissibility</b>	Low at Running Speed	Higher
<b>Fluid Inertia</b>	Minimal	Considerable
<b>Load</b>	Low	High
<b>Stability</b>	Fair	Better
<b>Jump Resonance</b>	Possible	Less Probable

This suggests that it is possible to develop an actively controlled hybrid squeeze film damper, which can operate as a long damper near critical speeds, such that it effectively attenuates the amplitude response of the rotor and avoids the possibility of a jump resonance, and it also can operate as a short damper at the operating speed region, such that it effectively reduces the force transmitted to the support. In addition, it can be used to provide intermediate amounts of damping. This is possible by designing the sealing on the damper, such that the damper becomes tightly sealed (i.e., long damper) or open-ended (i.e., short damper), or anything in between, according to the instructions of a controller. This is the Hybrid Squeeze Film Damper.

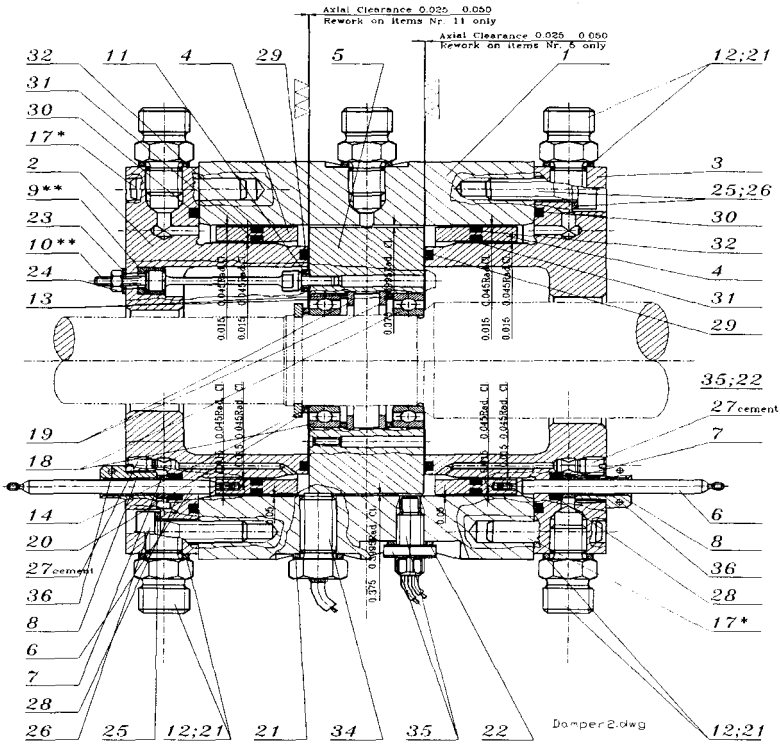
### 3. THE HYBRID SQUEEZE FILM DAMPER

Figure 1 shows the profile of the HSFD. Two movable sealing rings [4] with sliding fit both to the end caps and to the housing, one on each end of the damper as shown in Figure 1, are used as the controlling elements. The principle of the seals' operation is simple. The damper oil film and the hydraulically actuated seals are supplied from independently variable sources. In order for the damper to operate as a long damper, the pressure to the seal chambers [12] is elevated above the internal pressure of the damper [5]. The seal rings [4] will move in axially and seal the oil film inside the damper clearance. In order to return to the short damper configuration, the seal pressure is lowered until it is less than the internal pressure of the damper. This causes the seal rings [4] to return to their original positions.

It may be required to locate the sealing rings in intermediate positions, other than those for the short or long dampers, to provide for the required rotor control. Thus the sealing rings are connected to springs that would act to restrain their motion versus the applied pressure in the sealing chambers. As illustrated by the computer simulations of the system (17), this is quite an effective method of controlling the position of the sealing rings. To physically incorporate the springs in the design of the HSFD, 3 measuring rods [6] were connected to each sealing ring, and would protrude through the sealing chambers and the end caps, as shown in Figure 1. Springs, resting on the surfaces of the end caps, can be connected to the measuring rods to provide spring action restraining the motion of the sealing rings versus the applied pressure in the sealing chamber. The measuring rods have an additional benefit that they can be directly connected to a position transducer (e.g. an LVDT) to accurately measure the position of the sealing rings.

The spring rods [10] shown in Figure 1 allow for centering the journal in the damper, in addition to preventing the damper from rotation. The centering spring action provided by the spring rods [10] can be an important factor in the dynamics of the rotor bearing system (18).

The oil feed to the damper is provided by three feed holes distributed circumferentially at the center of the damper. The damper oil drain in the short damper mode is through the end caps. No damper drain is required in the long damper mode. The oil port for the seal chambers is located on the extended housing. This is the port connecting the seal chambers with the proportional pressure control valve (PPCV). This port provides for both the feed and drain to the seal chamber and is the only port required.



**Figure 1 Profile of manufactured HSF Damper**

#### 4. TEST ROTOR

The design criteria for the test rotor were set as follows:

- a - Three critical speeds to be attained in speed range.
- b - Speed range to be up to 15000 rpm.
- c - The HSF Damper to be located at a point of high modal activity.



A New shaft1 modified -which simulates 1mass4 Shaft- but with 3 Small Disks  
 Brg. Stiff. 1000000 Support Stiff. 6000  
 Three Mass thickness .5" (13 mm.) File :3mass919.dat  
 - SYNCHRONOUS ROTOR MODE SHAPES -

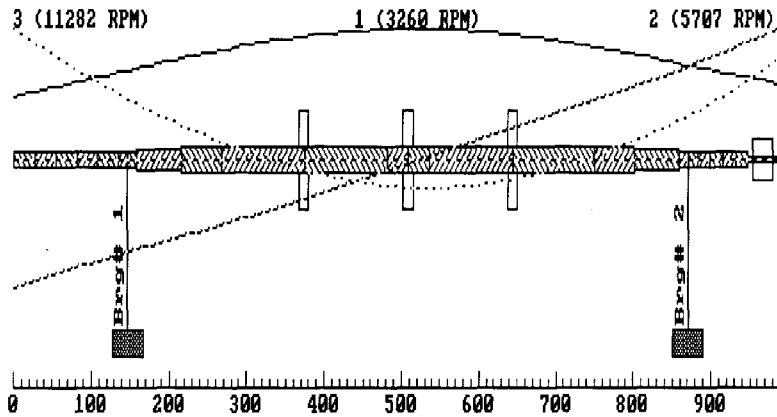


Figure 2 The test rotor and its mode shapes

The results of the extensive design effort (19) is illustrated in Figure 2, where a three mass rotor is selected. The three mass rotor exhibits three critical speeds at 3260 rpm, 5707rpm, and 11282 rpm. These critical speeds, as shown in Figure 2, can be classified as the bouncing mode, conical mode, and first bending mode, respectively.

Moreover, all three modes exhibit significant modal activity at the bearing location thus allowing the HSFD to adequately control all three modes. The first two modes can be classified as rigid modes, where most of the deflection (and thus potential energy) occurs in the support, while the third mode represents a flexible mode, where most of the deflection (and thus potential energy) occurs in the shaft.

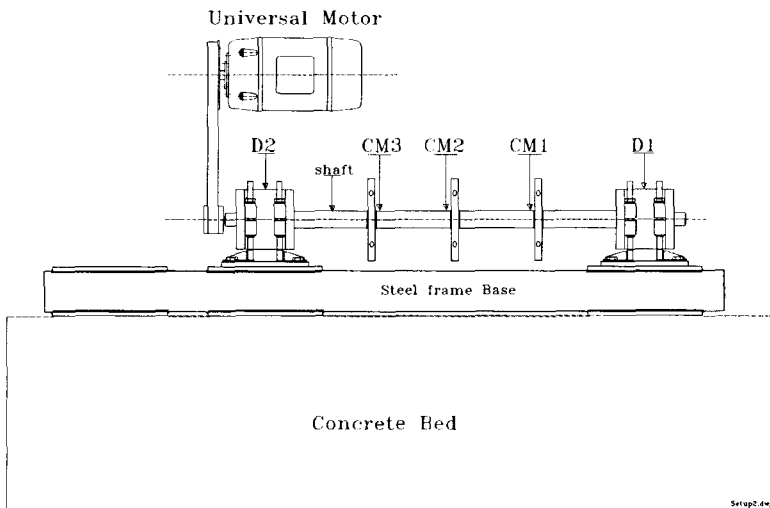


Figure 3 Set-up of test rotor

Figure 3 shows the set-up of the test rotor. A universal motor drives the rotor through a 2:1 belt drive. Two HSFDs, termed D1 and D2 support the rotor. The rotor is 985 mm long and weighs 13 kg. The measurement locations of the rotor vibration D1, D2, CM1, CM2 and CM3 are indicated in Figure 3. The complete details of the test rig can be found in previous papers by the authors (7), (11).

The HSFDs shown in the test rig of Figure 3, have the same cut-out as shown in Figure 1. The dimensions of the dampers are: clearance  $c=750 \mu\text{m}$ , length  $L=7.5 \text{ mm}$  and radius  $R=37.5 \text{ mm}$ . The oil chosen for the test rig is Shell Tellus 46 with viscosity  $\mu=0.014 \text{ Ns/m}^2$  at  $70^\circ\text{C}$  and oil density  $\rho=875 \text{ kg/m}^3$ .

## 5. CRITICAL SPEED TESTING

Critical speed testing is important before the application of the control algorithms because of the need to verify the behaviour of the test rig before controlling it. The procedure for critical speed testing was to run-up the rotor at above the third critical speed, and to manually remove the belt using a special tool, and to collect data (two channels at a time) using the tracking filter DVF3 during coast-down.

The results of the critical speed testing are illustrated in Table 2. The tests were repeatedly performed and the results indicated consistent repeatability of the critical speed data. Analysis of the coast-down data indicates that the critical speeds occur at 2950 rpm, 5400 rpm, and 11000 rpm. Table 1 represents a comparison between the theoretical critical speed data shown in Figure 2, and the experimental critical speed data. Good agreement is observed, and this experimental verification confirmed the suitability of the design of the rotor shown in Figure 2, for the application of the HSFD.

**Table 2 Comparison between Design & experimental critical speeds of new test rotor**

Critical Speed	Design Value (RPM)	Experimental Value (RPM)	Difference %
1 <sup>st</sup> Critical	3260	2950	9.5 %
2 <sup>nd</sup> Critical	5707	5400	5.4 %
3 <sup>rd</sup> Critical	11282	11000	2.5 %

## 6. OPEN-LOOP SYSTEM

The open-loop system consists of the control valve, the HSFD and the rotor. The system functions as follows: first a voltage is chosen from the PC controller and is supplied to the valve conditioning board. The board in turn supplies a current  $i$  which actuates the valve to output a controlled pressure  $p$  in the sealing chamber. The level of  $p$  positions the sealing ring between the short and long modes, and hence controls the amount of damping supplied to the rotor. This in turn controls the eccentricity ratio,  $\epsilon$ . Figure 4 shows the block diagram of the open-loop system. This is considered as the plant for the control development.

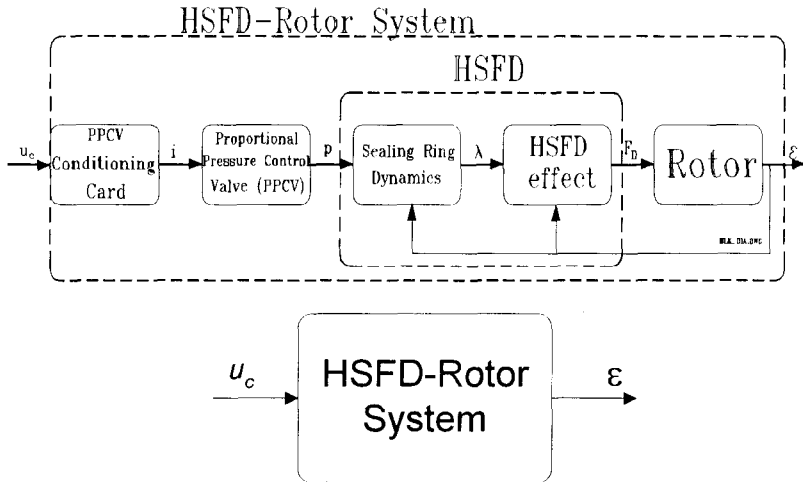


**Figure 4** Block diagram of open-loop system

Figure 5 shows the open-loop testing of the test rig in a coast-down test. Two curves are presented: one in the short damper mode where the pressure in the sealing chamber is minimum, and the other in the long damper mode, where the pressure in the sealing chamber is maximum. These tests illustrate the limits of the control of the HSFD on the rotor test rig. That is, any control effort can only locate the rotor in between the two limits illustrated in Figure 5. The purpose of the controller is to try to reduce the amplitude of vibration along the rotor, and simultaneously reduce the force transmitted to the support. The long bearing consistently shows smaller vibrations at the damper, but this is not necessarily the optimum damping value. Actually, the short bearing also consistently shows smaller vibrations at the centre location. This implies that the least deflection occurs with the short bearing. Moreover, previous theoretical and experimental results (5) indicate that the forces are much smaller in the short damper case. However, the long bearing provides much more damping which can be quite useful in crossing critical speeds and providing stability to the rotating machine. The controller thus should try to optimize the damping for varying operating objectives.

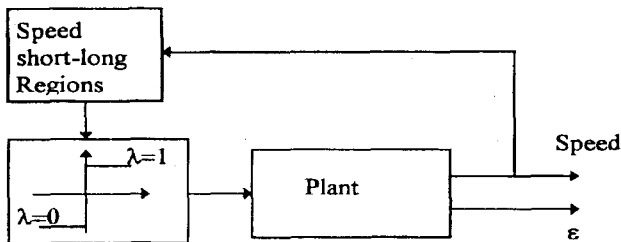


**Figure 6** On-Off Controller

## 7. ON-OFF CONTROL

The basic concept of the typical On-Off controller (see Figure 6) is to switch between two modes of operation based on the error signal, where  $\lambda$  indicates the position of the sealing ring. In the active vibration control of the rotor systems using HSFDs, the two modes of operations are the short and long damper modes. The criterion for tuning of the controller between its two modes is the major design implication. It is not quite straight forward to design the on-off controller based on the error signal. However, since the steady-state operation of the system in both the short and long modes is available at hand, a speed range can be chosen to be the switching criterion. This can easily be implemented as an on-off design. In summary, the controller is switched to either mode in a particular speed range as defined by the designer off-line. It was shown by Burrows et al. (1), that for some rotor systems only two levels of damping are required to control the behaviour of the rotor-bearing system. The same design principle was adopted by Hathout et al. (10), the on-off active controller is actuated at specific rotational speeds to achieve the desired damping level for particular speed ranges.

Neglecting the dynamics of the controller, which is composed of the servovalve and the sealing ring, one can assume that the HSFD attains any of the two modes instantaneously as requested by the control action. Thus, a particular mode can be achieved for a particular speed range. The selection of the switching instants was based on the operation in hand of the two modes as identified in Figure 5.

The speed range 2000 to 15500 rpm is divided into five regions. The criterion of using a short or a long damper in each region is based on the vibration amplitude of the bearing and the center mass. Table 3 lists the five regions constituting the speed range of operation with the desired mode of operation and the critical speed in each region if any exists. It is clear from the Table that the controller is to assume the long damper mode while passing through the first two critical speeds. This choice of the switching speeds is based on the fact that the long damper mode has smaller vibration amplitude at the critical speeds. However, the third mode is to be passed while in the short mode as this critical speed has the smallest amplitude. This is a selected schedule, but other schedules can be chosen based on system requirements.

**Table 3 Speed ranges for the on-off controller**

Speed Range in rpm	Damper Mode	Critical Speed
rest to 3000	Short	None
3000 to 5800	Long	First critical speed
5800 to 9000	Short	None
9000 - 9400	Long	Second critical speed
9400 - 15500	Short	Third critical speed

Figure 7 shows the experimental results of implementing the on-off controller. It is clear from the figures that the controller succeeded in attaining the desired mode of operation in the given speed region. Switching between the two modes is not instantaneous and a time delay is observed in the response. However, this is not significant as the switching is designed off-line, and as a result one can include the delay in the design of the different regions.

Comparison of the theoretical results with the experimental results indicated the capability of both modes of operation in controlling the rotor vibrations. However, switching between the modes is slower in the experimental than in the theoretical studies. This was expected based on the delay characterization discussed in (19) and (20), which can be included in the design of the controller.

The reasoning for choosing the above schedule for speed control is as follows:

- 1- In the short damper mode a smaller force is transmitted to the support, thus it is advantageous to operate the rotor as much as possible in this mode of smaller force.
- 2- The long damper provides more damping, thus it is advantageous to operate in the long damper mode at the critical speeds.
- 3- Notice that in the long damper mode in Figure 7 (a) and (b), the deflection at the rotor centre CM2 is larger than in the short damper mode, thus it may be advantageous that in the bending mode of the rotor (the third mode) to try to minimize the deflection between the damper D2 and the centre of the rotor CM2. Comparison of Figures 7 (a) and (b) indicates that at high speeds operating in the short damper mode allows only a deflection of about 50  $\mu\text{m}$  between D2 and CM2 although the third critical exhibits a node between CM2 and D2. Thus depending on the objective one can operate around the third critical either in the short damper mode to reduce deflection as in Figures 7 (a) and (b), or in the long damper mode to reduce the amplitude of vibration.

## 8. CONCLUSIONS

This paper presented the application of on-off control to the HSF supported rotors. The hybrid squeeze film damper lends itself readily to the application of on-off control between its limits of short damper and long damper modes. The basic principle of operation and the experimental design and validation of the on-off control were presented based on a speed-scheduled implementation. It is clear that the on-off controller achieves the required design performance, with some delay. However, this delay can be easily included in the design of the speed schedule.

Although the on-off control was quite successful in controlling the rotor system through a run-up or coast-down, it has the deficiency of not being able to accommodate varying operating conditions, or disturbances, such as sudden unbalance, because of no feedback on the rotor system. This disadvantage should not distract from the more important advantages of a well-behaved controller, which responds precisely as the designer wishes and performs experimentally as theoretically predicted.

## REFERENCES

- (1) Burrows, C.R., Sahinkaya, M.N., and Turkay, O.S., "An Adaptive Squeeze-Film Bearing", ASME Paper No. 83-Lub-23, 1983.
- (2) Adams, M.L., and Zahloul, H., "Attenuation of Rotor Vibration Using Controlled-Pressure Hydrostatic Squeeze-Film Dampers", presented at the Eleventh Biennial ASME Vibrations Conference, Boston, MA, September 1987.
- (3) Mu, C., Darling, J., and Burrows, R., "An Appraisal of a Proposed Active Squeeze Film Damper", Journal of Tribology, Trans. ASME, Vol. 113, No. 4, pp. 750-754, 1991.

- (4) El-Shafei, A., "Hybrid Squeeze film Damper for Active Control of Rotors", U.S. Patent number 5,058,452, October 1991.
- (5) El-Shafei, A., "Experimental and Analytical Investigation of Hybrid Squeeze Film Dampers", *Journal of Engineering for Gas Turbine and Power Trans. ASME*, Vol.115, No.2, pp.353-359, 1993.
- (6) El-Shafei, A., and Hathout, J.P., "Modeling and Control of HSFs for Active Control of Rotor-Bearing Systems", *ASME Journal of Engineering for Gas Turbine and Power*, Vol.117, No.4, pp.757-766, 1995.
- (7) El-Shafei, A., and El-Hakim, M., "Development of a Test Rig and Experimental Verification of the Performance of HSFs for Active Control of Rotors", presented at the International Gas Turbine and Aeroengine Congress and Exposition, Houston, Texas- June 5-8, 1995, ASME paper 95-GT-256, 1995.
- (8) Hathout, J-P, and El-Shafei, A., "Adaptive Control of Rotor-Bearing Systems Using Hybrid Squeeze Film Dampers", *Proceedings of Sixth Int. Conf. On Vibration in Rotating Machinery*, Oxford, England, I. Mech. E., pp.671-690, 1996.
- (9) Hathout, J.P., and El-Shafei, A., "PI Control of HSFs for Active Control of Rotor-Bearing Systems", *ASME Journal of Engineering for Gas Turbine and Power*, Vol. 119, No. 3, pp.658-667, 1997.
- (10) Hathout, J.P., El-Shafei, A, and Youssef, R., "Active Control of Multi-Mode Rotor-Bearing Systems Using HSFs", *ASME Journal Tribology*, Vol. 119, No. 1, pp. 49-56, 1997.
- (11) El-Shafei, A., and El-Hakim, M., "Experimental Investigation of Adaptive Control Applied to HSF Supported Rotors", presented at the International Gas Turbine and Aeroengine Congress and Exposition, Indianapolis, June 7-10, 1999, ASME paper 99-GT-176. Accepted for publication in the *Trans. of ASME*, 1999.
- (12) El-Shafei, A., and El-Hakim, M., "Experimental PID Control of HSF Supported Rotors", submitted to the *Journal of Dynamic Systems, Measurement and Control*, *Trans of ASME*, 2000.
- (13) Feder, E., Bansal, P.N., and Blanco, A., "Investigation of Squeeze Film Damper Forces Produced by Circular Centered Orbits", *Journal of Engineering for Power, Trans. ASME*, Vol.100, pp.15-21, 1978.
- (14) Holmes, R., and Dogan, M., "The Performance of a Sealed Squeeze-Film Bearing in a Flexible Support Structure", *Proc. I. Mech. E.*, Vol.199, No. Cl, 1985.
- (15) El-Shafei, A., "Unbalance Response of Jeffcott Rotor Incorporating Long Squeeze Film Dampers", *Journal of Vibration and Acoustics Trans. ASME*, Vol.113, No.1, pp.85-94, 1991.
- (16) El-Shafei, A., "Long and Short Bearing Approximations for Squeeze Film Dampers", *Proceedings of the Vibration Institute*, pp.145-151, 1989.
- (17) El-Shafei, A., El-Hakim, M.M., and Hathout, J-P, "Control of Rotor Vibrations Using Hybrid Squeeze Film Dampers", Report No. MDP-EOARD-1/93, Cairo University, 1993.
- (18) El-Shafei, A., "Unbalance Response of a Jeffcott Rotor Incorporating Short Squeeze Film Dampers", *Journal of Engineering for Gas Turbine and Power, Trans. ASME*, Vol.112, No.4, pp.445-453, 1990.
- (19) El-Shafei, A., Massoud, A. T., El-Hakim, M., Hathout, J.-P., Youssef, R., "Control of Rotor Vibrations Using Hybrid Squeeze Film Dampers", Report MDP-EOARD-1/97, Cairo University, 1997.
- (20) El-Shafei, A., "Active Control Algorithms for the Control of Rotor Vibrations Using HSFs", presented at IGTI Turbo Expo, Munich, Germany, May, 2000, ASME paper 2000-GT-564.

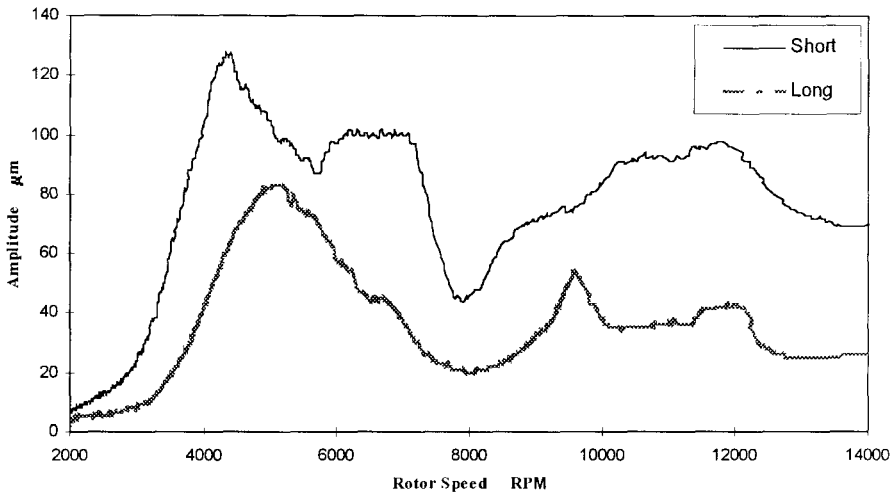


Figure 5 (a) Experimental response of rotor at damper 2 for short and long damper modes

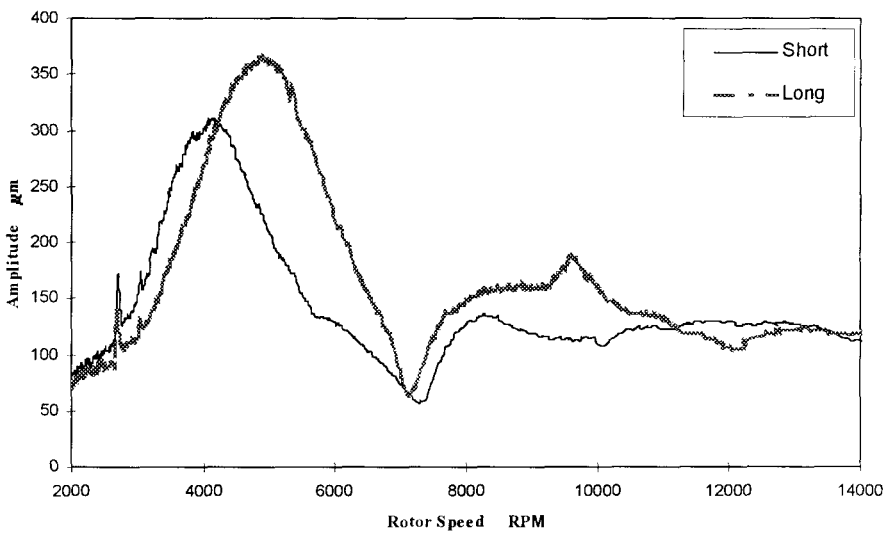
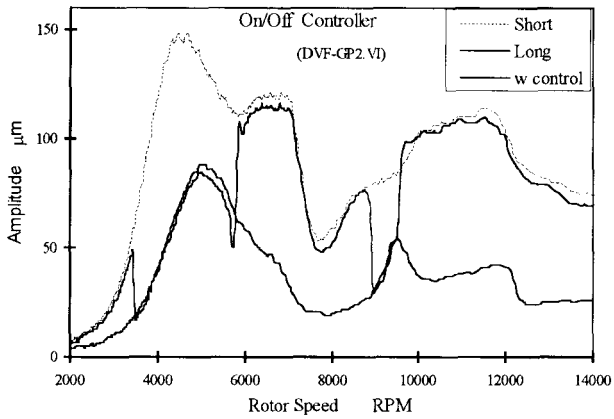
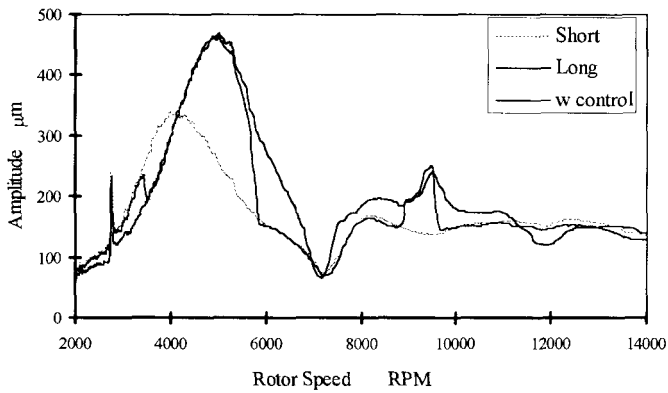


Figure 5 (a) Experimental response of rotor at damper 2 for short and long damper modes



**Figure 7 (a) Experimental response of rotor at damper 2 for On/Off Controller**



**Figure 7 (b) Experimental response of rotor at CM2 for ON/Off Controller**

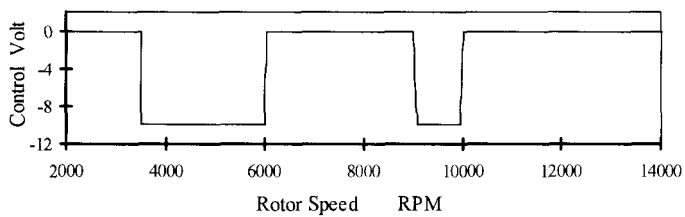


**Figure 7 (c) Actuating signal for ON/Off Controller**



# Standardization of evaluation of stability margin for active magnetic bearing equipped rotors

O MATSUSHITA, H FUJIWARA, and H OKUBO

Mechanical Engineering Department, National Defense Academy, Yokosuka, Japan

Y KANEMITSU

Faculty of Engineering, Kyushu University, Fukuoka, Japan

T AZUMA

Ishikawashima Noise Control Limited, Tokyo, Japan

R HERZOG

MECOS Traxler AG, Winterthur, Switzerland

**ABSTRACT** In addition to the conventional types of ball and oil bearings, active magnetic bearings (AMB) are a new type of bearing element in the market of rotating machines. The system consists of a mechanical part of the rotor and an electronic part of the controller. Besides the evaluation of the vibration level, the stability margin, called the spill over problem, concerning the combined controller-rotor system is then required for standardization of these technologies.

In this paper, the stability margin against the spill over instability is evaluated by several methods; total gain method, Q-factor, Nyquist plot and sensitivity function. The relationship between these methods is explained. For the evaluation, a new Nyquist plot on a log scale chart is recommended, including an example of the test data. A proposal for an ISO standard is finally summarized with the zone limit value relative to the evaluation of the stability margin. The control robustness is also discussed with the simulation.

## 1. INTRODUCTION

Active magnetic bearings (AMB) support a rotor without mechanical contact, as shown in Fig.1. The bearing force levitating the rotor is generated by electro-magnets so that the force is reacted by a servo feedback control law, e.g., the PID control. The AMB reacting force is then determined by the control loop transfer function from the sensor to the magnetic force.

Compared with the rotors supported by ball bearings or oil film lubricated bearings, the AMB features a soft support. An example of the comparison is shown in a critical speed map in Fig.2, in which the soft support is described on the left side and the stiff support is on the

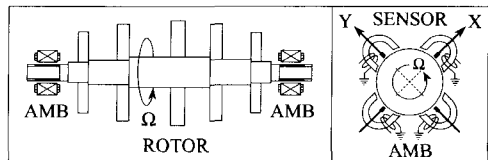


Fig. 1 Active magnetic bearing equipped rotor

right side. To compensate the soft support stiffness, the AMB must be placed at vibrating portions of each eigen mode. Therefore, the AMB rotor is inevitably in a large vibration level region, but it is quite normal. However, existing standards requiring low level vibration, e.g., ISO standard 7919/1-5<sup>[1]</sup> and API 617 edition<sup>[2]</sup>, are very strict for AMB turbo rotors. Instead, the ISO vibration evaluation should be reconsidered from the point of view of the AMB dynamics, in order to accept the comparably large vibration level for the AMB rotors.

In addition to the vibration level, the AMB rotor should be evaluated with respect to the stability margin, determined by the sophisticated controller transfer function. The stability margin of the usual control theory is well known as the gain and phase margin, but it is applicable only to simple rotors having low natural frequency modes. These natural frequencies are called critical speeds and the corresponding damping ratios (phase margins) are regulated by the Q-value evaluation of ISO 10814<sup>[4]</sup>. Our standardization is to evaluate the stability margin of high frequency bending modes, called spill over instability.

Spill over instability is caused mainly by the phase lag of the controllers. The controller phase lag is equivalent to the negative damping of mechanical systems. For the evaluation of this stability margin, we have to estimate the balance of material positive damping of the rotor and the controller negative damping. One of the means to measure the stability margin is to directly increase the total gain of the controller. Another mean is to make the comparison of both Q-factors between the open and closed loop responses. The Nyquist plot and the sensitivity function also provide good information on the stability margin. The relationship between these methods should be explained. A log scale Nyquist plot is recommended and included in our test data of an AMB equipped flexible rotor. Finally, we propose to the ISO a zone limit table for evaluating the stability margin to be applied to actual rotors. The robustness of the control system is also discussed with the simulation results.

## 2. DESCRIPTION OF ROTOR SYSTEM

### 2.1 Modelling of rotor system

The equation of motion of a rotor-bearing system, as shown in Fig.1, is generally described as follows:

$$M\ddot{z} + D\dot{z} + Kz = U \tag{1}$$

where,  $z$ = complex displacement vector ( $Z=X+jY$  form)  $\equiv [z_{11} \ z_{12} \ z_2]$ ,

$M$ = mass matrix,  $D$ = damping matrix,  $K$ = stiffness matrix and  $U$ = input vector.

The AMB force is taken into account by  $U$ . This displacement vector includes the journal

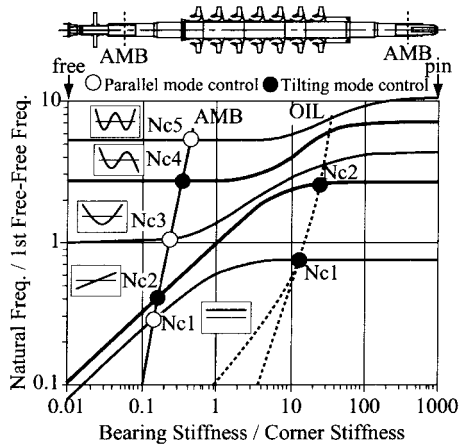


Fig. 2 A typical critical speed map of a LP rotor

movements of the bearing portion at both ends, noted by  $z_{11}$  and  $z_{12}$ , and the vibration displacement of the rotor, noted by  $z_2$ . We only consider the vibration control of the parallel modes. As shown on the left side of a typical critical speed map in Fig.2 obtained from an AMB turbo compressor, the parallel control engages the parallel rigid mode Nc1 and the free-free bending modes of Nc3 and Nc5. The vertical axis is normalized by the natural frequency of the first free-free mode, e.g., by about 100 Hz of the AMB turbo compressor.

## 2.2 Transfer function of rotor system

According to the modal synthesis technique<sup>[3]</sup>, a reduced order model is obtained, having three degrees of freedom:

$$M_3 \ddot{z}_3 + D_3 \dot{z}_3 + K_3 z_3 = -B u \quad (2)$$

$$y = C z_3$$

where,  $M_3$  = mass,  $D_3$  = damping and

$$K_3 = \text{stiffness matrices}, z_3 = [z_1 \quad \eta_1 \quad \eta_2]^T =$$

displacement vector,  $B$  = input matrix =  $[1 \quad 0 \quad 0]^T$ ,

$C$  = output matrix =  $[1 \quad 0 \quad 0]$  and  $y$  = displacement

sensor =  $z_1 \approx (z_{11} + z_{12})/2$

The displacement vector  $z_3$  indicates the three elements of  $z_1$ ,  $\eta_1$  and  $\eta_2$  corresponding to the parallel rigid motion Nc1 and the two bending modes of Nc3 and Nc5, respectively. In order to discuss the practical engineering applications, we consider the following matrices:

$$M_3 = \begin{bmatrix} 1 & 0.89 & 0.32 \\ 0.89 & 1 & 0 \\ 0.32 & 0 & 1 \end{bmatrix}, D_3 = \begin{bmatrix} 0 & 0 & 0 \\ 0 & 2\sqrt{5}\zeta_m & 0 \\ 0 & 0 & 2 \times 20\zeta_m \end{bmatrix}, K_3 = \begin{bmatrix} 0 & 0 & 0 \\ 0 & 5 & 0 \\ 0 & 0 & 400 \end{bmatrix}, z_3 = \begin{bmatrix} z_1 \\ \eta_1 \\ \eta_2 \end{bmatrix} \quad (3)$$

The corresponding 3 dof system is described in Fig. 3. The total mass is set by unit and the first natural frequency will be normalized by  $\omega_1 \approx 1$ , in order to maintain the generality of the discussion. The second and third natural frequencies will be Nc3=4.95 and Nc5=28.6. The mass distribution of 10%, 80% and 10% is assumed to simulate the rigid mode and the two bending modes, respectively. These values are generally typical for actual turbo rotors.

The damping ratio  $\zeta_m$  indicates the material damping. This value will be treated as a parameter for the survey of system stability. Rotor material damping is well known to be a source of instability in rotating systems. However, the damping loss due to the rotation is neglected here, since the natural frequency Nc5 to be discussed is higher than the rotational speed.

The transfer function  $G_p(s)$  of the control plant is calculated by the relationship between the input  $u$  and the output  $y$ , i.e.,

$$G_p(s) \equiv \frac{y}{u} = \frac{[(s/\omega_{p1})^2 + 2\zeta_{p1}(s/\omega_{p1}) + 1][(s/\omega_{p2})^2 + 2\zeta_{p2}(s/\omega_{p2})s + 1]}{ms^2[(s/\omega_{f1})^2 + 2\zeta_{f1}(s/\omega_{f1}) + 1][(s/\omega_{f2})^2 + 2\zeta_{f2}(s/\omega_{f2}) + 1]} \quad (4)$$

where:  $m=1$ ,  $\omega_{p1}=\sqrt{5}=2.23$ ,  $\omega_{p2}=20$ ,  $\omega_{f1}=4.95 \approx \text{Nc3}$ ,  $\omega_{f2}=28.6 \approx \text{Nc5}$ ,

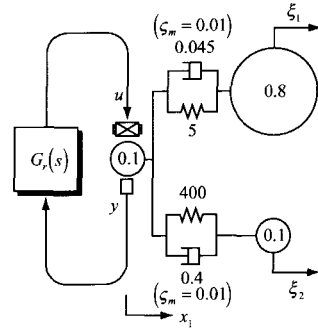


Fig. 3 Quasi-modal model

$$\zeta_{p1} = \zeta_{p1} = \zeta_m, \quad \zeta_{f1} = 2.16\zeta_m, \quad \zeta_{f2} = 1.73\zeta_m$$

The denominator of the plant transfer function indicates the array of eigen frequencies under the free-free condition, i.e., 0 Hz rigid mode and two free-free bending modes of  $\omega_k$  ( $k=1,2$ ). The numerator includes the array of eigen frequencies under the pin-pin boundary condition, noted by  $\omega_{pk}$  ( $k=1,2$ ). These free-free and pin-pin bending eigen frequencies correspond to the frequencies located at the left and right sides of the critical speed map in Fig.2, respectively. The Bode plot of the control plant is shown in Fig.4. The peak resonance frequencies correspond to the free-free eigen frequencies, while the anti resonance frequencies indicate the pin-pin eigen frequencies.

### 2.3 Modal model

The plant transfer function of Eq.(4) is decomposed by factor expansion with each free-free eigen frequency.

$$G_p(s) \approx \frac{1}{ms^2} + \frac{1}{m_{f1}(s^2 + 2\zeta_{f1}\omega_{f1}s + \omega_{f1}^2)} + \frac{1}{m_{f2}(s^2 + 2\zeta_{f2}\omega_{f2}s + \omega_{f2}^2)} \quad (5)$$

where  $m_{f1}=1/3.57$ ,  $m_{f2}=1/5.25$  for each modal mass

The rated rotational speed is assumed to be between  $\omega_1 \approx Nc3$  and  $\omega_2 \approx Nc5$ , in order to consider flexible rotors. Therefore, the rigid mode critical speed  $Nc1 \approx 1$  and the first bending mode critical speed  $\omega_1 \approx Nc3$  must be placed in the operational speed range and these resonance vibrations should be controlled with well damped conditions so as to satisfy the Q factor criterion prepared by ISO 10814<sup>[41]</sup>. This is outside of the scope of this paper. The higher eigen frequencies, represented here by  $\omega_2 \approx Nc5$ , are generally close to system instability.

## 3. DESCRIPTION OF ROTOR-AMB GLOBAL SYSTEM

### 3.1 AMB control loop transfer function

To simulate an actual PID Bode plot for the AMB turbo compressor of Fig.2, the following transfer function of the control loop was prepared in a simplified way:

$$G_r(s) \equiv \frac{u}{y} = 0.84 \frac{1+s}{1+\alpha s} \frac{1}{1+s/33} \quad (\alpha=0.16) \quad (6)$$

The first part of the transfer function of Eq.(6) is a typical example of the phase lead controller. The second one indicates the 1<sup>st</sup> order LPF (low pass filter) having the phase lag of power amplifiers and/or actuators. The corresponding Bode plot of this controller is described in Fig.4. Since the border between the phase lead and lag regions, about  $\omega = 12.9$ , appears between  $\omega_1=4.95$  and  $\omega_2=28.6$ , the controller provides negative damping to the second bending mode  $\omega_2$ .

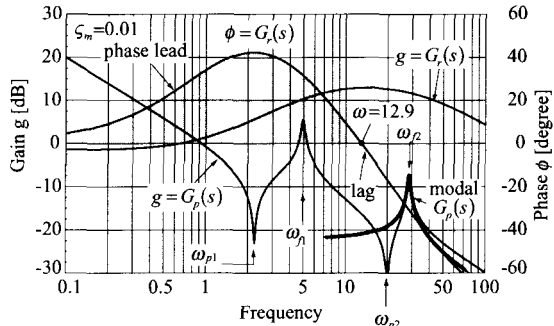


Fig. 4 Transfer function of plant and controller

### 3.2 Open loop transfer function

The open loop transfer function  $G_o(s)$  is defined as the following formula:

$$G_o(s) \equiv G_r(s)G_p(s) \quad (7)$$

It is well known that the crossover frequency  $\omega_g$  and the phase margin  $\phi_m$  are very important parameters for the closed system identification, as defined by the following forms:

$$\left|G_o(j\omega_g)\right| \equiv \left|G_r(j\omega_g)G_p(j\omega_g)\right| \equiv 1 = 0\text{dB} \quad \phi_m \equiv \angle G_o(j\omega_g) \equiv \angle G_r(j\omega_g)G_p(j\omega_g) \quad (8)$$

According to the Bode plot of the open loop  $G_o(j\omega)$  in Fig.5, the intersections of these gain curves, noted by  $\omega_{\kappa_1} \approx 1$  and  $\omega_{\kappa_2} \approx 6$ , indicate the gain crossover frequencies, i.e., approximate natural frequencies of the closed loop. We know each phase margin, noted by  $\phi_{m_1} \approx +32^\circ$  and  $\phi_{m_2} \approx +28^\circ$ . Although this paper concerns only the third intersection of the possible unstable mode, no crossover frequency was found.

### 3.3 Open loop analysis by modal model

Around the third eigen frequency  $\omega \approx \omega_{f_2}$ , we can use the modal model of 1 dof system as shown in Fig.4. The controller transfer function is replaced by both the spring  $K_a$  and damper  $C_a$  elements as shown in the following relations:

$$G_r(j\omega) \equiv g(\omega)e^{j\theta(\omega)} = K_a + j\omega C_a \quad \text{for } \omega \approx \omega_{f_2} \quad (9)$$

$$\text{where } G_r(j\omega_{f_2}) \equiv g_a e^{j\theta_a} = 11.8\text{dB} \angle -32^\circ = 3.88 \angle -32^\circ \equiv K_a + j\omega_{f_2} C_a$$

From the modal model of the third term of Eq.(5), we can estimate the controller damping ratio  $\zeta_a$ , which is negative because of the phase lag, as follows:

$$\zeta_a \equiv \frac{C_a}{2\omega_{f_2} m_{f_2}} = \frac{g_a \sin \theta_a}{2m_{f_2} \omega_{f_2}} = -0.012 \sin \theta_a = -0.0063 \quad (10)$$

As a result of the equivalent replacement of the controller by the spring and damper elements, the total damping ratio  $\zeta_3$  of the closed system is then predicted by the sum of the positive damping ratio  $\zeta_2$  of the material and the negative damping ratio due to the controller:

$$\zeta_3 = \zeta_{f_2} - \zeta_a = 1.73\zeta_m - 0.0063 = 0.011 \quad (\text{if } \zeta_m = 0.01) \quad (11)$$

This system is stable. In this way, the open loop can predict the complex eigenvalue,  $\lambda = \{\text{natural frequency, damping ratio}\}$ , of the closed system as follows:

$$\lambda_3 = \{\zeta_3 \quad \omega_3\} = \{0.011 \quad 28.9\} \quad (12)$$

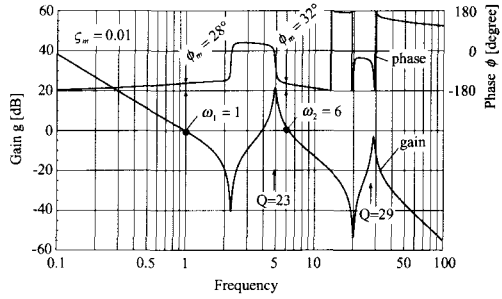


Fig. 5 Open loop

### 3.4 Closed loop transfer function

The closed loop transfer function  $G_c(s)$  is obtained as follows:

$$G_c(s) = \frac{G_o(s)}{1 + G_o(s)} \quad (13)$$

The corresponding Bode plot is shown in Fig.6. The rigid critical mode ( $\omega_1 \approx 1$ ) and the first bending critical mode ( $\omega_2 \approx 6$ ) are well damped. The second bending critical mode ( $\omega_3 \approx 30$ ) is still sensitive, but stable. In fact, the eigenvalue analysis on the closed system provides eigen solution  $\lambda_3 = -0.308 \pm j29 = \{0.011, 29\}$ , which coincides with the prediction of Eq.(12).

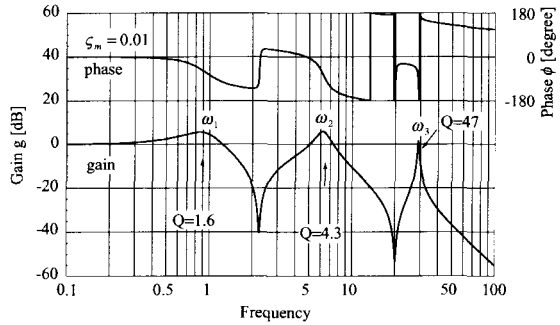


Fig. 6 Closed loop

## 4. MEASUREMENT METHODS FOR STABILITY MARGIN

### 4.1 Stability margin evaluation by directly increasing total gain

To find the stability limit, we can directly increase the total gain to just before the onset of instability. In this case, since the increase of the total gain induces the increase of the negative damping, the total gain margin  $T$  will be obtained:

$$T = \zeta_f / \zeta_a = 0.0173 / 0.0063 = 2.8 \quad (\text{if } \zeta_m = 0.01) \quad (14)$$

This way is the simplest, but is hazardous in a practical sense.

### 4.2 Stability margin evaluation by Q-factors

When discussing the partial zone around the second bending frequency  $\omega \approx \omega_2$ , the open loop transfer function and the corresponding closed loop transfer function indicate each Q-factor noted  $Q_o$  and  $Q_c$ , respectively, as follows:

$$Q_o = \frac{1}{2\zeta_f} \quad \text{and} \quad Q_c = \frac{1}{2(\zeta_f - \zeta_a)} \quad (15)$$

Note that the controller damping is included in the closed loop and excluded in the open loop. Then, we can find the stability margin by the ratio  $R$  between these two Q-factors:

$$R \equiv \frac{Q_o}{Q_c} = 1 - \frac{1}{T} \quad (16)$$

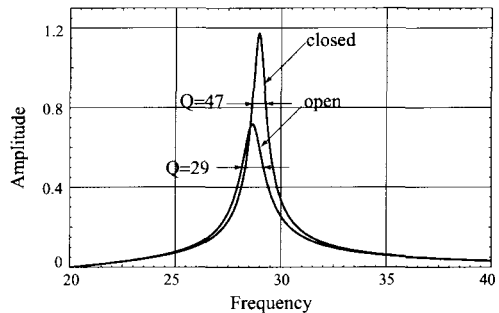


Fig. 7 Q-factors of open and closed loops

For instance, the closed and open loop response curves are shown in Fig.6 and Fig.5, and the corresponding resonance curve around  $\omega_2$  is detailed in the linear chart of Fig.7. The Q-factors are  $Q_c=47$  and  $Q_o=29$ , respectively, and then the gain margin=2.6 was obtained in agreement with Eq.(14). However, the Q-factor of the high frequency mode is too high to measure it accurately.

### 4.3 Stability margin evaluation by Nyquist plot of open loop response

The Nyquist plot is usually described in the linear chart, so that the overview of the plot locus will be easily out of the measurement range. Instead, we recommend the Nyquist plot on the log scale chart. This paper refers to it as the “dB” Nyquist plot. This dB Nyquist plot is shown in Fig.8, with the parameter of the material damping  $\zeta_m$ . As shown in the dB Nyquist plots, we can see global behaviour of the locus of all eigen modes. The distance from the critical point  $(-1,0)$ , i.e.,  $(0\text{dB} \angle 180^\circ)$  is measured. The intersection between the real axis and the Nyquist plot curve is seen at  $-8\text{dB}$  in Fig.8(1). This distance on the real axis, noted by  $D$ , dB, presents the total gain margin as follows:

$$D_r \text{ dB} = \zeta_{f_2} / \zeta_a = T \quad (17)$$

For example, we see that the intersection of  $-8\text{dB} \angle 180^\circ$  and this real axis distance indicates the total gain margin  $D_r=+8\text{dB} = 2.51$ , as agreed with Eq.(14).

### 4.4 Stability evaluation by sensitivity function

The stability margin evaluation stated in the previous section 4.3 concerns only on the gain margin. However, we need to take into account the phase margin. If the distance is measured in any direction to find the shortest distance from the critical point to the plot curve, we can regulate the gain margin and phase margin at the same time. The distance from the critical point is defined by  $|1 + G_o(j\omega)|$ . Therefore, the following function, called the sensitivity function<sup>5)</sup>, is more convenient for this measurement:

$$G_s(s) = 1/(1 + G_o(s)) \quad (18)$$

As shown in the Bode plot of this sensitivity function of Fig.9, we can

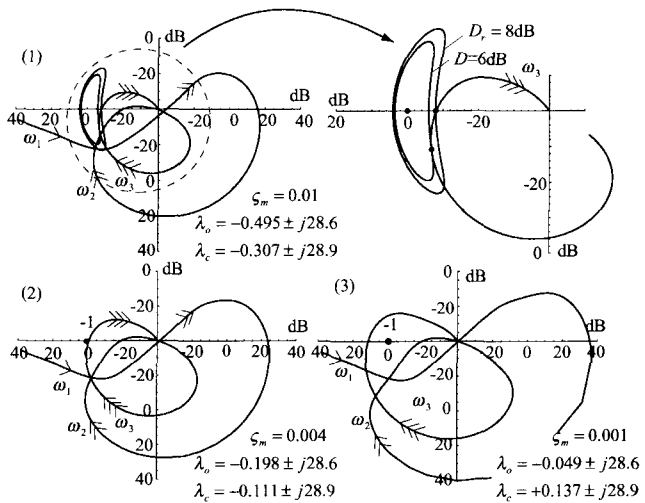


Fig. 8 Nyquist plot

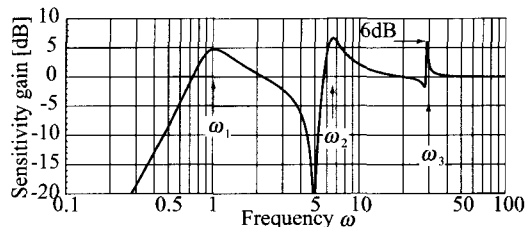


Fig. 9 Sensitivity function

see the peak value of +6dB around  $\omega \approx \omega_2$ . In fact, the shortest distance is also measured by  $D=6\text{dB}$  in the dB Nyquist plot shown in Fig.8(1). This value  $D$  is a little smaller than the value of  $D_r$  mentioned above.

#### 4.5 Parameter survey

We prepared case studies for five values of the material damping ratio,  $\zeta_m=0.02-0.001$ . In each case, the controller is the same, as defined by the above Eq.(6). Several examples of the dB Nyquist plot are shown in Fig.8. The stability limit of the material damping is  $\zeta_m \approx 0.004$ . In these figures, the complex eigenvalues of the open loop system (free-free eigen mode) and the complex eigenvalues of the closed loop system are listed, in order to compare how much negative damping is provided by the controller. In all cases, the natural frequency of the closed system is identical, even with and without the control. However, the stability, i.e., the real part of the complex eigenvalue decreases due to the negative damping of the controller.

The evaluation results of the stability margin are shown in Table 1, depending upon each method. Though the total gain method, Q-factor method and the real axis distance  $D_r$  should be theoretically identical, they differ slightly. The difference is caused by the measuring error. The sensitivity margin, i.e., the shortest distance  $D$ , is a little less than the total gain margin.

Table 1: Parameter Survey on Stability Margin

No.	Material		AMB	Total gain	Q-factors			Real Axis Distance		The Shortest Distance	
	$\zeta_m$	$\zeta_{f2}$			$\zeta_a$	$T = Q_c / (Q_c - Q_o)$	$Q_o$	$Q_c$	$T$	$D_r$ dB	$D_r$
1	0.02	0.0357	-0.00636	5.53	14	18	4.5	12.8	4.37	12	4
2	0.01	0.0173	-0.00636	2.72	29	47	2.6	8.0	2.51	6	2
3	0.007	0.0122	-0.00636	1.92	41	91	1.8	3.8	1.55	1.6	1.2
4	0.004	0.0069	-0.00636	1.08	72	1318	1.05	0.3	1.03	0	1.0
5	0.001	0.0017	-0.00636								

#### 4.6 Robustness measurement requirement

Any standard is not perfect. One of the exception is considered here for improving the proposal. The calculation assumes the same controller of Eq.(6) and the material damping  $\zeta_m=0.004$  set as a stable limit. Since the system is a stable limit in these parameters, as shown in Fig.8(2), we add a notch filter or a zero-pole cancelling filter, as shown in the following formulas:

$$\text{notch filter } G_E(s) = \frac{s^2 + \omega_e^2}{s^2 + 2\zeta_e \omega_e s + \omega_e^2} \quad (19)$$

$$(\omega_e = \omega_{f2}, \zeta_e = 0.1)$$

$$\text{Z-P filter } G_{ZP}(s) = \frac{s^2 + \omega_z^2}{s^2 + 2\zeta_p \omega_p s + \omega_p^2} \frac{\omega_p^2}{\omega_z^2} \quad (20)$$

$$(\omega_p = \omega_{p2}=20, \omega_z = \omega_{f2}=28.6, \zeta_p = 0.1)$$

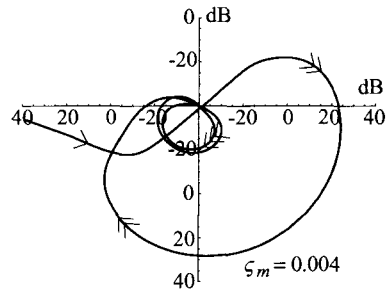


Fig. 10 Stabilization with notch filter

Since the Nyquist plot of the open loop including these filters is modified to be very far from the critical point  $(-1,0)$ , as shown in Fig.10 and 11, the system stability is improved



greatly. To check the robustness, we assume an error of frequencies by upward of 10%. This mistake causes the instability for the notch filter controller. However, the zero-pole filter is still stable. The latter is more robust than the former. This requires another way to measure it.

#### 4.7 Case studies

The present marketing instruments are not sufficient to execute every method for evaluating the stability margin, e.g., dB Nyquist plot. We are developing the instrumentation procedures to obtain indexes for this evaluation, but this has just started. Test data obtained from a flexible rotor is displayed in Fig.12. An example of the open loop Bode plot is shown in (1) of Fig.12. It is measured by a typical FFT analyzer. In this open loop gain curve, many peaks of bending eigen frequencies appear. This Bode plot data is rearranged, and then redrawn in the dB Nyquist plot (2). The detail plot around 645Hz is shown in (3). In the case of the addition of the zero-pole filter, the Bode plot is measured and the corresponding dB Nyquist plot is rearranged, as shown in (4). As a result of the zero-pole filter, the distance margin is increased. In the future, we need more measurement data of the stability margin obtained by real machines.

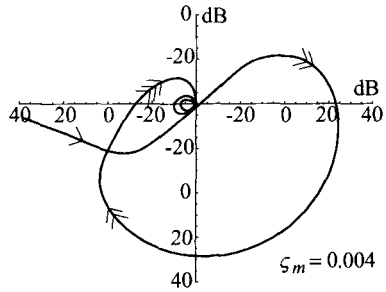


Fig. 11 Stabilization with z-p filter

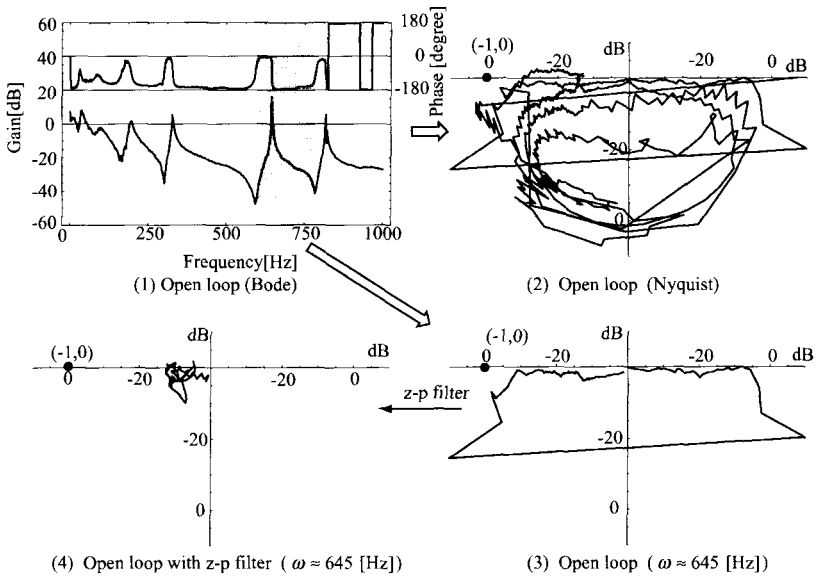


Fig. 12 Nyquist plot of a test rotor

### 5. PROPOSAL FOR ISO ZONE LIMIT

ISO TC10//SC2/WG7 is developing the standard for the vibration level and stability

margin for AMB rotors. As a summarization of this paper, the following zone limits of Table 2 are prepared for the ISO proposal. The definition of each zone is as follows:  
 Zone A: newly commissioned machines would normally fall within this zone.  
 Zone B: normally considered acceptable for unrestricted long-term continuous operation.  
 Zone C: normally considered unsatisfactory for long-term continuous operation.  
 Zone D: normally considered to be sufficiently severe to cause damage to the machine.

Table 2: Proposed Criteria of Zone limits

Zone	Clearance Margin	Power Supply Margin		Stability Margin		
	Vibration $Z_{max}$	Current $I_m$	Voltage $V_m$	Total gain $T$	Q-factor ratio : $R$	Sensitivity Gain : $D$
A	$\leq 0.2 \times C_{min}$	$\leq 0.7 \times I_c$	$\leq 0.4 \times V_c$	$>200\%$	$<0.5$	$<6dB$
B	$\leq 0.3 \times C_{min}$	$\leq 0.8 \times I_c$	$\leq 0.6 \times V_c$	$>142\%$	$<0.3$	$<3dB$
C	$\leq 0.4 \times C_{min}$	$\leq 0.9 \times I_c$	$\leq 0.8 \times V_c$	$>125\%$	$<0.2$	$<2dB$
D	$> 0.4 \times C_{min}$	$> 0.9 \times I_c$	$> 0.8 \times V_c$	$<125\%$	$>0.2\%$	$>2dB$

where  $C_{min}$  is minimum radial clearance between rotor and stator.  $I_c$  and  $V_c$  are maximum capacities of the current and the voltage of power amplifiers and DC power sources.

## 6. CONCLUSIONS

- (1) In order to develop the ISO standard concerning the stability margin of AMB equipped rotors, a suitable reduced model is provided for easy comprehension without losing generality. Several indexes related to system stability are numerically examined with this model.
- (2) The indexes of total gain method, Q-factor method and the real axis distance of a Nyquist plot indicate only the gain margin. Finally, it is recommended that the sensitivity margin, being equivalent to the shortest distance on the Nyquist plot from the critical point, is the most reliable index, because it includes the evaluation of gain and phase margins at the same time.
- (3) The discussion on the stability evaluation is summarized for the proposal of the zone limit table for the ISO standard. Though the robustness is numerically demonstrated, the measurement still remains a problem.

## REFERENCES

- [1] ISO7917-1-5 ; Mechanical vibration of non-reciprocating machine, (ISO TC108/SC2/WG1), (1996)
- [2] API-617/6; Centrifugal compressor for general refinery service , (1995)
- [3] O. Matsushita, M. Ida and R. Takahashi; Application of quasi-modal concept to rotational ratio response analysis, IMechE C319/84, (1984), pp.427-437
- [4] Shiraki, K. and Kanki, H.; A new vibration criteria for high speed /large capacity turbo machinery, Proceeding of Eighth Turbomachinery Symposium, pp.59-70, (1979)
- [5] B. Shahian and M, Hassul; Control System Design using MATLAB, Prentice Hall (1993), pp.398-400

# Active control of vibration in rotor/magnetic bearing systems with multiple design objectives

M O T COLE, P S KEOGH, and C R BURROWS

Department of Mechanical Engineering, University of Bath, UK

## SYNOPSIS

In rotor dynamic systems containing active elements such as magnetic bearings there is considerable potential to reduce system vibration. However, the objectives in vibration control may include a range of different performance measures. For example, rotor orbit magnitudes, rotor/bearing displacements, transmitted forces and stator accelerations are all usefully minimised. These will arise from direct forcing, base motion, rotor-stator interaction and other secondary sources. Much of the work in the open literature has focused on single performance objectives in the design of vibration controllers and, in particular, the control of unbalance induced vibration. A shortcoming of this type of approach is that the performance of the system may be unacceptably poor when operating with unexpected conditions or disturbances. Multiple objectives may be considered in the controller design to reduce this problem, but will usually involve a trade-off between individual objectives to give an optimised overall performance. A typical example of this is the compromise between reducing rotor orbit size and transmitted force magnitude. In this paper, techniques are investigated for achieving multiple objectives in the design of vibration control strategies for a flexible rotor/magnetic bearing system. Model based controller design methods are used to produce state-space controllers that achieve the specified objectives. To validate the methods a selection of these controllers are implemented, tested and compared on an experimental system.

## 1 INTRODUCTION

Optimal controller design will usually involve satisfying a combination of design objectives. For example, specifications in classical controller design can relate to both the tracking response and disturbance rejection of the closed loop system. Robust controller design will additionally incorporate stipulations that ensure robustness to model uncertainty or plant variations, for example, in terms of gain or phase margins.

Advances in multivariable control theory, and the associated numerical tools, now enable similar multiple performance and robustness objectives to be used in the design of high order centralised controllers for plants with one or more inputs and outputs. Such techniques often involve frequency domain specifications such as bounds on the maximum RMS gain ( $H_\infty$  norm) or the RMS response to white noise ( $H_2$  norm) for the closed loop system.

Recently, techniques have been developed that take advantage of the fact that many types of controller design can be formulated as convex optimisation problems (1). In such a framework, multiple design objectives can be combined without altering the convex nature of the problem. In particular, a large range of closed loop specifications can be formulated as linear matrix inequalities (LMI's) that can be combined and solved to derive a state space controller (2) that satisfies a range of specifications.

Techniques for the optimal control of vibration have usually been applied to rotating machinery to develop controllers that satisfy a single type of performance objective, particularly for unbalance vibration control. For example, the use of notch filters to extract the synchronous vibration component has been investigated by Herzog *et al.* (3). Alternatively, some researchers have exploited a digital controller implementation for calculation of the synchronous components and appropriate feedback, both adaptively (4) and with dynamic feedback for enhanced transient vibration control (5). Multi-variable controller design has also been considered using mixed  $H_2/H_\infty$  objectives. For example, Nonami *et al.* (6) used such a method to achieve specified performance and robustness in vibration control of a rigid rotor. Other robust controller design techniques that have been applied to rotor/magnetic bearing systems include  $\mu$  synthesis (7),  $H_\infty$  design (8) and gain scheduled design (9). However, there is often a wide range of performance considerations that are important in this class of problem. Two of these were considered by Cole *et al.* (10), who applied  $H_\infty$  controller design techniques to the problem of combined direct rotor forcing and base motion disturbance rejection in a flexible rotor/magnetic bearing system. In this paper, multi-objective controller design is further extended through the consideration of transmitted vibration levels.

## 2 ROTOR/MAGNETIC BEARING SYSTEMS

Rotor systems that include active magnetic bearings can be broadly classified according to whether the rotors are flexible or effectively rigid, and whether they are completely levitated or supported additionally by passive (hydrodynamic or rolling element) bearings. From a control aspect, the most useful case for consideration is that of a completely levitated flexible rotor as it is then straightforward to modify the modelling and design for consideration of the other cases.

### 2.1 Experimental system

The experimental system (figure 1) considered in this study is a flexible rotor (mass 100kg, length 2m) supported by two radial magnetic bearings. The predicted natural frequencies of the first three flexural modes for the free rotor are 170, 420 and 1000 rad/s, the first two of which are below the designed maximum rotational speed of 628 rad/s. The rotor is driven directly by a motor through a flexible coupling at one end of the shaft, the other end free. Eight displacement transducers measure the rotor displacement in four planes and all eight signals are available for control feedback. Each magnetic bearing has two opposing pole pairs arranged

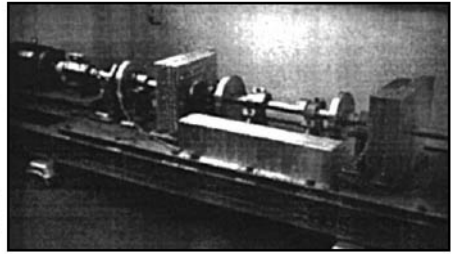
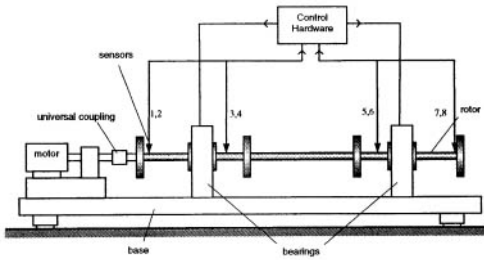


Figure 1 Experimental system (schematic/photograph)

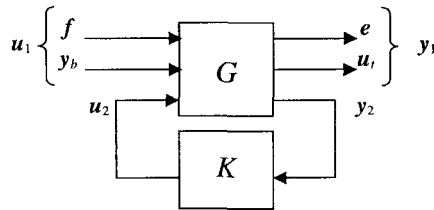


Figure 2 Closed loop system

orthogonally at  $45^\circ$  to the vertical, giving force control in the  $x$ - $y$  plane. The bearings are mounted on a stiff base (supported by isolators) and are capable of delivering radial control forces up to 1000 N at frequencies within the bandwidth of 650 rad/s.

## 2.2 Vibration control problem

The system considered for controller design is shown in figure 2, having disturbance/control inputs  $u_1/u_2$  and error/measurement outputs  $y_1/y_2$ . Controllers will be synthesised that give closed loop frequency responses, from components of  $u_1$  to components of  $y_1$ , having magnitudes (as measured by the  $H_\infty$  or  $H_2$  norm) that are limited by suitable bounds. Additional specifications will be given that will restrict the closed loop system poles to prescribed regions of the complex plane. It will be seen that a wide range of practical requirements, in terms of controller performance, stability and robustness, for the closed loop system can be achieved with this set of criteria.

## 2.3 System modelling

For a flexible rotor supported by magnetic bearings a general state space description of the system will have the form

$$\begin{aligned}
 \dot{x} &= \mathbf{A}x + \mathbf{B}_u u_i + \mathbf{B}_f f \\
 y_s &= \mathbf{C}_y x + \mathbf{D}_y y_b \\
 e &= \mathbf{C}_e x + \mathbf{D}_e y_b
 \end{aligned} \tag{1}$$

where  $x$  is the vector of rotor states (translatory and rotational displacements and velocities),  $u_i$  the vector of forces applied by the bearings,  $f$  the vector of direct forces acting on the rotor,  $y_b$  the vector of base displacements at the bearing locations and  $y_s$  the measured rotor

displacement (relative to the base). For the present problem, the signal  $e$  will comprise of the relative rotor to base displacements at the auxiliary bearing locations, as this signal should be limited if auxiliary bearing contact is to be avoided. The system matrices can be derived from a flexible rotor finite element model (10). For magnetic bearings operating in an opposing pole pair configuration, with constant bias currents and differential driving mode, the bearing force can be written as

$$\mathbf{u}_t = \mathbf{u}_c + K_z \mathbf{y}_t \quad (2)$$

where  $\mathbf{u}_c$  is the bearing control force due to the control current and  $K_z$  is the negative stiffness of the bearing. If the rotor displacement at the bearings  $\mathbf{y}_t$  is measured, then proportional feedback can be applied to give zero bearing stiffness. The transmitted force  $\mathbf{u}_t$  is then equal to any additional control feedback applied.

For control synthesis, the system must be arranged to have the form of the open loop system ( $G$ ) given in section 2.2. The exact constitution of the signals  $\mathbf{u}_1$  and  $\mathbf{y}_1$  will depend on the control problem being considered, but in practice  $\mathbf{u}_1$  can be constructed from any combination of disturbance and reference signals acting on the system and  $\mathbf{y}_1$  constructed from any combination of input signals and system states.

The closed loop transfer function matrix from  $\mathbf{u}_1$  to  $\mathbf{y}_1$  relates the Laplace transform ( $\mathcal{L}$ ) of the two signals according to:

$$\mathbf{Y}_1 = P(G, K)\mathbf{U}_1 \quad (3)$$

where

$$\mathbf{Y}_1 = \mathcal{L} \begin{bmatrix} \mathbf{e} \\ \mathbf{u}_t \end{bmatrix}, P = \begin{bmatrix} T_{ey_b} & T_{ey_b} \\ T_{u_b y_b} & T_{u_b f} \end{bmatrix}, \mathbf{U}_1 = \mathcal{L} \begin{bmatrix} \mathbf{y}_b \\ \mathbf{f} \end{bmatrix} \quad (4)$$

Here  $P$ , a linear fractional transformation on  $G$  and  $K$ , has been partitioned into sub-matrices  $T_{ab}$  according to the components of  $\mathbf{U}_1$  and  $\mathbf{Y}_1$ . The signals of interest for the subsequent controller design are the system disturbances  $\mathbf{y}_b$  and  $\mathbf{f}$  and the system outputs  $\mathbf{u}_t$  and  $\mathbf{e}$ .

### 3 CONTROLLER DESIGN OBJECTIVES

For the system described in section 2, a variety of controller performance specifications can be considered as outlined in sections 3.1-3.3.

#### 3.1 Direct rotor forcing response

This is the most commonly considered disturbance type, usually in the form of unbalance disturbance, synchronous with the running speed. Direct rotor forcing is modelled (equation (2)) by an appropriate disturbance vector  $\mathbf{f}$ .

##### 3.1.1 Synchronous disturbance

The synchronous unbalance excitation of the system at a single running speed can be minimised using loop shaping techniques. That is, by minimising the  $H_\infty$  norm of the weighted transfer function matrix  $T_{ef}$  from the unbalance force vector  $\mathbf{f}$  to rotor vibration signal  $\mathbf{e}$ :

$$\|w(s)T_{ef}(s)\|_\infty \leq \gamma \quad (5)$$

where  $w$  is a stable transfer function chosen with lightly damped poles at the rotational frequency in order to give high gain around this frequency. This transfer function is often referred to as a loop shaping filter as it shapes the frequency response of the closed loop system. Any closed loop transfer function satisfying equation (5) will have a frequency response satisfying

$$\bar{\sigma}(T_{ef}(j\omega)) \leq \gamma |w(j\omega)|^{-1} \quad (6)$$

where  $\bar{\sigma}$  denote the maximum singular value. In many applications the run-up and run-down vibration levels of the rotor may also be important, particularly at critical speeds where peak amplitudes occur when forcing is synchronous with the rotor natural frequencies. In these circumstances,  $w$  can be chosen to weight the frequency response matrix  $T_{ef}(j\omega)$  over a wider frequency range and thereby place a bound on the peak magnitudes at all the critical speeds within the running speed range. If gyroscopic effects are significant then implementation of such a strategy will require scheduling of controllers or linear parameter varying (LPV) controller design techniques (11).

Use of the  $H_\infty$  norm will minimise the response (RMS vibration amplitude) due to the worst case unbalance vector. However, it is also valid to minimise the  $H_2$  norm of  $T_{ef}$ , which relates to the RMS response averaged over all possible disturbance frequencies and amplitude vectors  $f = Fe^{j\omega t}$ . Pole placement techniques may also be used to ensure acceptable damping levels for the rotor modes. A minimum damping ratio ( $\zeta_n > \zeta_{\min}$ ) for the closed loop system poles may be specified, thereby requiring that poles are confined to a conic sector in the left half complex plane. The control force levels (and hence controller gain) required to achieve a specified damping ratio increase with natural frequency, and so high damping of high order flexural modes may be impossible or impractical to achieve. An alternative specification is a maximum decay time for the closed loop modes. This corresponds to a pole placement region of a semi-infinite left half plane so that  $\text{Re}(p_n) < -\delta$  for all closed loop poles  $p_n$ .

### 3.1.2 Transient disturbance

Direct transient forcing of the rotor may arise from impact of the rotor with the stator, from mass loss type events and rotor-fluid or rotor-stator interaction forces. The expected spectral content of the forcing should be reflected in the choice of weighting function used for the loop shaping method. If the nature of any transient disturbance is known to have a broad bandwidth then an appropriate  $H_2$  criterion is likely to be most suitable. However, for narrow bandwidths an  $H_\infty$  criterion will allow optimal shaping of the frequency response.

### 3.2 Vibration transmission minimisation

In applications where the transmission of synchronous vibration through the bearings to external locations is a problem, the transfer function from direct rotor forces to bearing force  $T_{u,f}$  should be minimised at the desired frequency using a suitable weighted  $H_\infty$  criterion. To achieve this, the weighting function used will have a lightly damped pole with natural frequency identical to the rotational frequency at which force transmission is to be minimised.

### 3.3 Base motion disturbance rejection

The system base or stator on which the bearings are mounted is never completely immobile and motion can occur due to external excitation. For example, in transport applications or when seismic activity can occur, it is important that the rotor moves with the bearings so that contact is prevented or minimised. In many situations base motion will be low frequency in character

(high frequency excitation can usually be prevented by mounting on isolators). A suitable objective for many applications is to minimise the transfer function from base displacement to rotor displacement at bearing locations  $T_{ey_b}$  over a low frequency range. This can be achieved using a suitably weighted  $H_\infty$  bound, similar to equation (5). In some applications, base motion can be induced by a short direct impulse (e.g. impact) to the base or stator. In the Laplace domain, the rotor to base motion will be described by the impulse response of the system, which is simply the closed loop transfer function from  $y_b$  to  $e$ :

$$e(t) = \mathcal{L}^{-1}(T_{ey_b}) \quad (7)$$

Therefore, minimising the peak signal component of  $e$  (i.e. the  $L_\infty$  norm of  $e$ ) will be a suitable objective.

**Table 1 Controller design specifications**

Controller	Design specifications				
	Direct forcing response	Base motion	Force transmission	Pole placement	Solver
K1	minimised over 0-100 rad/s ( $H_\infty$ spec.)	none	none	$\text{Re}(p) < 0/s$	Ricatti based
K2	none	low freq weighted ( $H_\infty$ spec.)	minimised at 20Hz ( $H_\infty$ spec.)	$\text{Re}(p) < 0/s$	Ricatti based
K3	none	low freq weighted ( $H_\infty$ spec.)	none	$\text{Re}(p) < 50/s$	Ricatti/ LMI based
K4	minimised over 0-100 rad/s ( $H_\infty$ spec.)	low freq weighted ( $H_\infty$ spec.)	minimised at 20Hz ( $H_\infty$ spec.)	$\text{Re}(p) < 0/s$	Ricatti based
K5	minimised over 0-100 rad/s ( $H_\infty$ spec.)	low freq weighted ( $H_\infty$ spec.)	none	$\text{Re}(p) < 0/s$	Ricatti based
K6	minimised over 0-100 rad/s ( $H_2$ spec)	low freq weighted ( $H_\infty$ spec.)	none	$\text{Re}(p) < 0/s$	LMI based

## 4 CONTROLLER DESIGN

The most general form of the closed loop plant has outputs and inputs  $y_1 = [e^T \ u_b^T]^T$  and  $u_1 = [y_b^T \ f^T]^T$ , where  $e$  is a combination of rotor to stator displacements at critical locations. Controllers are designed using a combination of specifications on the closed loop transfer functions with additional pole placement criteria, as summarised in table 1. For all controllers, a frequency dependent limit is placed on the control force magnitude to give similar controller gains for all controllers and ensure a sufficient level of robustness to modelling errors (particularly at high frequencies).

### 4.1 Design specifications

The controllers designed with direct rotor forcing response specifications (table 1, K1, K4, K5) have an upper bound on the  $H_\infty$  norm of the weighted transfer function  $T_{ef}$  (as in equation (6)). The shaping filter has been chosen to give a bound on the maximum response of the first two flexural rotor modes. For K3, rather than using a frequency response specification, the response has been influenced by specifying a pole placement region that ensures all closed loop poles have real parts less than  $-\delta/s$ . To solve this problem a LMI based algorithm is used that allows



a combination of pole placement and  $H_\infty$  criteria. An important consideration when combining  $H_\infty$  criteria with pole placement constraints is that any shaping filter used must already satisfy the pole placement criterion, as its poles will remain unaffected by the control feedback. Possible problems with this restriction can be overcome through forcing a shift in the closed loop plant poles by first shifting the eigenvalues of the  $\mathbf{A}$  matrix of the unweighted plant. This is achieved by shifting all the plant poles  $p_o \rightarrow p_o + \delta$  by changing  $\mathbf{A}$  to  $\mathbf{A} + \delta \mathbf{I}$ . The controller that stabilises the modified plant can then be applied to the original plant if the controller  $\mathbf{A}$  matrix poles are first shifted  $\mathbf{A} \rightarrow \mathbf{A} - \delta \mathbf{I}$ . The closed loop plant will then have poles satisfying  $\text{Re}(p_c) < -\delta$ , although synthesis was performed to give poles satisfying  $\text{Re}(p_c) < 0$ . This method can succeed as a pole placement method in itself without any need to explicitly specify a pole placement region other than the default for stability  $\text{Re}(p_c) < 0$ . For the controller K6 a mixed  $H_\infty/H_2$  objective has been used for which the direct rotor forcing response has been optimised through minimisation of the  $H_2$  norm of the relevant transfer function.

Transmitted vibration has been minimised for some controllers (K2 and K4) close to a frequency of 126 rad/s. Specifications take the form of an upper bound on the  $H_\infty$  norm of the weighted closed loop transfer function matrix  $T_{uf}$ . The weighting is chosen with lightly damped poles at the desired frequency (126 rad/s). Synthesis produces controllers which cancel the poles of the weighting function with zeros with the same natural frequency, ensuring the controller has minimal gain and force transmission at this frequency. This particular frequency has been chosen for purposes of validation: the experimental system has a flexible structure mounted on the base with a resonant frequency close to 126 rad/s, amplifying the effect of vibrations transmitted at this frequency. This allows the vibration to be measured easily with an accelerometer mounted on the structure, without the need for sensitive vibration measurement equipment.

Base motion response specifications (K2 - K6) take the form of an upper bound on the  $H_\infty$  norm of the weighted closed loop transfer function  $T_{ey}$ . In all these cases, the weighting minimises the peak response over a low frequency range of disturbances (0-100 rad/s). The weighting function used has been restricted to a second order transfer function. Higher orders could be used, but will result in increased controller order. In practice, this is restricted by the performance (speed) of the computational hardware.

#### 4.2 Controller performance with nominal plant

The predicted closed loop performance of each controller with the nominal plant is derived from the closed loop transfer function matrix  $T_{y,u}$ . Figure 3 shows the RMS rotor displacement signal, as a function of rotational speed, due to the worst case unbalance distribution with overall magnitude 0.001 kgm. The lack of direct forcing specification in the derivation of controller K2 has resulted in a poor synchronous response compared with the other controllers. The response for K3 shows that, although the resonance at 300 rad/s is well damped, the peak response is comparable with K2. This suggests that a pole placement design criteria may not be suitable if minimal peak synchronous vibration is required. Figure 4 shows the transmitted force as a function of rotational speed for a selection of controllers. The specification for the minimisation of bearing force imposed for controllers K2 and K4 has resulted in a minimised transmitted force at the desired frequency of 126 rad/s. Figure 5 shows the RMS response of the rotor to a worst case base motion of RMS magnitude 1mm. It can be seen that the response for controller K1 is significantly higher than the other controllers over the frequency range of importance 0 - 100 rad/s, indicating that rotor-stator impact will occur more easily during low frequency base motion.

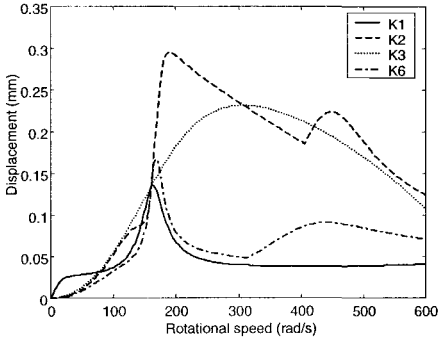


**Figure 3 RMS synchronous response of all rotor displacement signals due to worst case unbalance distribution**

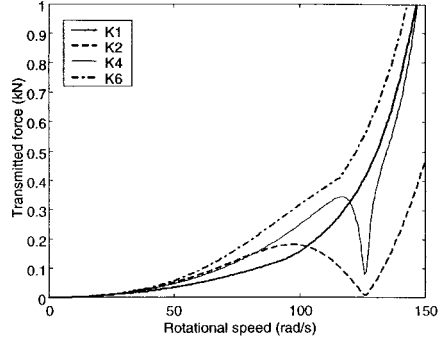


**Figure 4 RMS transmitted bearing force due to worst case unbalance distribution**

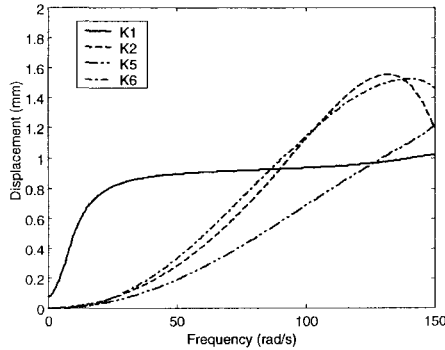


**Figure 5 RMS response of rotor-base displacement signals due to worst case base motion**

## 5 EXPERIMENTAL PERFORMANCE

Controllers of the types given in table 1 were implemented and tested on the experimental system described in section 2.1. A significant problem for some of the controllers derived is that they are not always well conditioned for implementation. One particular problem is that the controller poles may not be desirably placed, either because they are too fast or are unstable. Controller robustness is also difficult to guarantee for the type of modelling errors occurring with flexible rotor systems. The use of structured uncertainty models in the controller design (7) is one method of resolving this problem, although the complexity of the controller synthesis problem will increase correspondingly and the multiple objective techniques applied here may no longer be feasible. Of course, the alternative to improving

controller robustness is to improve the system model, for example, through system identification techniques.

### 5.1 Synchronous response

Figure 6 shows the mean orbit amplitude measured by the displacement sensors over a running speed range of 0–250 rad/s. The response with the PID controller clearly shows three resonant peaks at the critical speeds corresponding to the two rigid body modes and first bending mode of the rotor at 70, 110 and 180 rad/s. The response with controller K1, designed to minimise the peak direct rotor forcing response over the running speed range, shows a fairly constant level of synchronous vibration around 0.2mm. The controller K2 has been designed for optimal base motion response only and clearly results in a large synchronous response at 200 rad/s due to insufficient damping of the first rotor bending mode. The controller K5 has been designed with consideration of both base motion and direct rotor forcing and the peak synchronous response is comparable with K1, although the low frequency response is reduced. This is a secondary result of the controller having higher low frequency gain, required for attenuated base motion response.

### 5.2 Transmitted vibration

The measured acceleration at a location on the base is shown in figure 7 for four controllers (PID, K1, K4 and K5). The main component of the vibration is at the rotational frequency of 126 rad/s. It can be seen that the transmitted vibration with the PID controller is significantly higher than with the other three. The synchronous response of the PID controller (figure 6) shows that a resonance occurs close to this frequency (110 rad/s) and this results in a large transmitted force also. All the state space controllers result in a reduced level of vibration, the relative rms acceleration for K1, K4 and K5 being 1:0.6:0.83 respectively. The inclusion of the appropriate design specification has reduced the force transmitted by the bearings for controller K4, although not as much as predicted. Reasons for this include possible modelling errors, particularly inaccurate estimation of the bearing static characteristics (negative stiffness and current gain). Non-collocation of sensors and bearings also means that zero bearing stiffness, as previously specified for the open loop plant, can only be approximated with local feedback at each bearing.

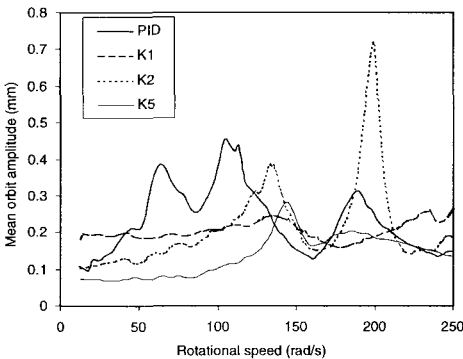


Figure 6 Measured synchronous response

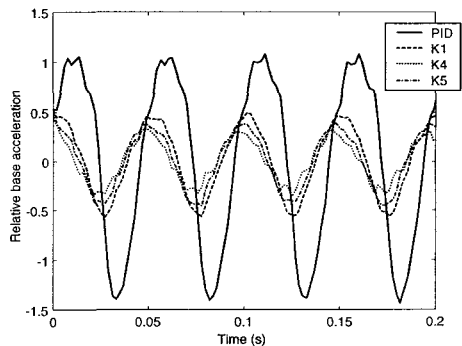


Figure 7 Transmitted vibration (running speed 126 rad/s)

## 6 CONCLUSIONS

In this paper design methodologies have been presented for controllers in a flexible rotor/magnetic bearing system using multiple design objectives. A range of possible design considerations has been addressed and reasons for their importance outlined, including those of direct rotor forcing, transmitted vibration and base motion disturbance. Controllers were synthesised using both Ricatti equation based and LMI based algorithms. The performance of these controllers was analysed both by simulation and experimental implementation and testing. The methods used for the design and derivation of controllers can be successfully applied for the purpose of optimising a number of important measures in the performance of rotor/magnetic bearing systems.

## ACKNOWLEDGEMENT

The authors acknowledge the support of the Engineering and Physical Sciences Research Council under Grant GR/L62238.

## REFERENCES

- 1 Boyd, S.P. and Barrat, C.H. 1991 *Linear controller design, limits of performance*, Prentice Hall, 1991, pp.156-167.
- 2 Iwasaki, T., and Skelton, R.E., "All controllers for the general  $H_\infty$  control problem: LMI existence conditions and statespace formulas", *Automatica*, vol. 30, 1994, pp1307-1317
- 3 Herzog, R., Bühler, P., Gahler, C., and Larssonneur, R., "Unbalance compensation using generalised notch filters in the multivariable feedback of magnetic bearings", *IEEE Transactions on control system technology*, 1996, Vol. 4, No. 5, pp. 580-586.
- 4 Knospe C.R. Lindlau, J.D and Hope, R.W., "Synthesis techniques for robust adaptive vibration control", *6<sup>th</sup> International Symposium on Magnetic Bearings, Proceedings*, Boston, MA. 1998, pp. 683-692.
- 5 Keogh, P.S., Burrows, C.R., and Berry, T., 1996, "On-line controller implementation for attenuation of synchronous and transient rotor vibration," *ASME Journal of Dynamic Systems, Measurement, and Control*, Vol. 118, pp. 315-321.
- 6 Nonami, K., Sivrioglu, S. and Ueyama, H. "Active magnetic bearing systems by means of LMI-based  $H_\infty$  control and mixed  $H_2/H_\infty$  control", *Transactions of JSME*, 1996, vol. 62, no. 600, pp. 3159-3167.
- 7 Losch, F., Gahler, C. and Herzog, R. " $\mu$ -synthesis controller design for a 3MW pump running in AMBs", 6th International Symposium on Magnetic Bearings, MIT, Cambridge MA. August 1998, pp. 415-428.
- 8 Shiau, T.N., Sheu, G.J. and Yang, C.D. "Vibration and control of a flexible rotor in magnetic bearings using hybrid method and  $H^\infty$  control theory", *ASME Journal of Engineering for Gas Turbines and Power*, 1997, Vol. 119, pp. 178-185.
- 9 Mason, S., Tsiotras, P. and Allaire, P. "Linear Parameter Varying Controllers for Flexible Rotors Supported on Magnetic Bearings", 6th International Symposium on Magnetic Bearings, MIT, Cambridge MA. August 1998, pp. 341-351
- 10 Cole, M.O.T., Keogh P.S., and Burrows, C.R. "Vibration control of a flexible rotor/magnetic bearing system subject to direct forcing and base motion disturbances", *IMechE, Proceedings Journal (Part C)*, Vol. 212, pp. 535-546.
- 11 Apkarian, P., Gahinet, P. and Becker, G. "Self-scheduled  $H_\infty$  control of linear parameter-varying systems: a design example", *Automatica*, vol. 31, no. 9, September 1995, pp. 1251-1261

# Identification of the dynamic characteristics of turbulent journal bearings using active magnetic bearings

E KNOPF and R NORDMANN

Department of Mechatronics, Darmstadt University of Technology, Germany

## 1 ABSTRACT

In the field of chemical and environmental industry the demands on leakage free, so called hermetic pumps are becoming more and more stringent. One possible way to realise this demands is to use process fluid lubricated journal bearings in combination with canned or wet motor pumps or magnetic drive pumps (horizontal and vertical type). The processing fluid has often a very low viscosity which causes turbulence in the lubricating film of the bearing. The turbulence in the lubricating film changes the static and dynamic behaviour of the bearing and therefore of the whole pump system. Up to now, calculation tools for the design of turbulent bearings are not state of the art.

In the presence of a sufficient static preload (e.g. horizontal machines), the dynamics of the journal bearing can be linearised around a equilibrium point /Someya88/. The description of the dynamic characteristics is done using rotordynamic coefficients. When the lubricating film becomes turbulent, the stiffness and damping coefficients differ strongly from these of laminar bearings, and moreover, inertia coefficients can no longer be neglected.

Within the presented research project, active magnetic bearings (AMBs) are used to identify the dynamic characteristic of hydrodynamic, turbulent journal bearings. The AMBs represent a mechatronic tool to levitate and to position a test rotor without any mechanical contact, to generate relative motions of the rotor inside the journal bearing and to measure the generated displacements and forces during rotation in a very accurate way. The paper describes the experimental technique and typical results of the static and dynamic behaviour of a cylindrical journal bearing operated in the turbulent regime are presented.

## 2 EXPERIMENTAL METHOD

Figure 2.1 shows the basic design of the testrig. In normal operation the rotor is supported by two magnetic bearings. The journal bearing is located between the two AMBs. The rotor is connected to a synchronous motor via a flexible coupling (low stiffness in radial direction, high

stiffness in torsional direction). The whole unit is mounted on a rigid foundation and vibrationally isolated to the ground. For the evaluation of linear journal bearing dynamics, the rotor is set to defined offset positions. These eccentric positions cause static fluid forces in the journal bearing due to hydrodynamic effects. Subsequently, an additional defined displacement excitation around the operating point is enforced. The journal bearing reacts with dynamic forces caused by Fluid-Structure-Interactions which can be described by stiffness, damping and inertia coefficients (*linear dynamics*). The rotor can be considered as dynamically stiff in the working range (1. elastic eigenfrequency: 1079 Hz), and therefore, the displacements and forces acting in the journal bearing can easily be computed with the forces and displacements measured with the AMBs. The forces are computed on-line on the DSP-board from the magnetic flux densities measured by the Hall sensors, that are integrated directly in the airgap between the rotor and the stator part of the magnetic bearing. The testrig is digitally controlled. Due to the large uncertainties of the journal bearing characteristics (the dynamic properties are unknown prior to identification and are changing with the operating point), it was very practical to use the  $H_\infty$  method for controller design (actual controller: 12th order). The signal processing and data analysis is performed off-line using standard CAE- Software. The test rig is designed in a modular way. Fig. 2.2 shows the realized testrig in the configuration with cylindrical journal bearing. The journal bearing is axially supplied with the lubricant and sealed up against atmosphere by two mechanical seals (low stiffness in radial direction). The rotor consists of a hollow shaft with two laminated radial bearing units shrink fitted to the shaft.

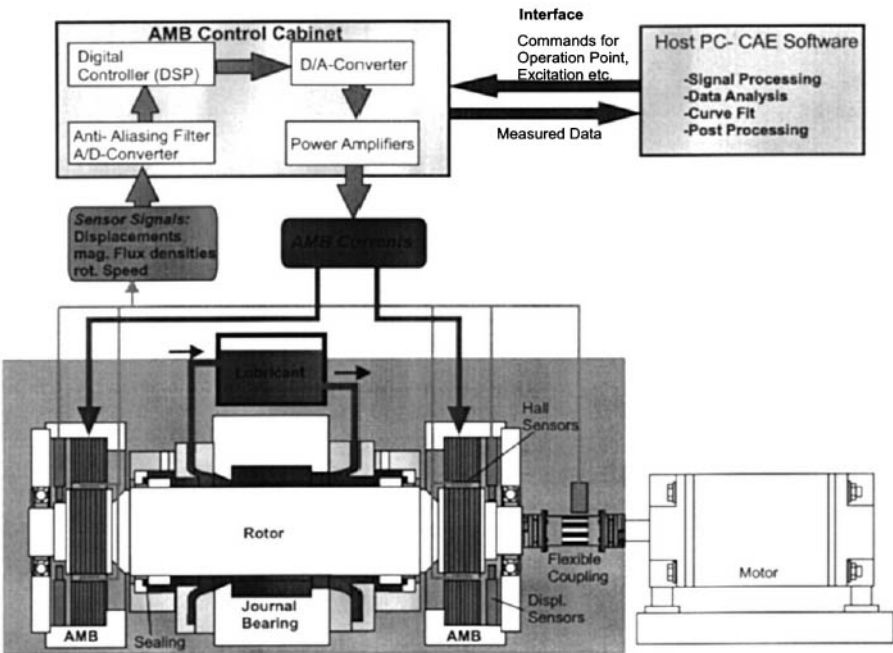
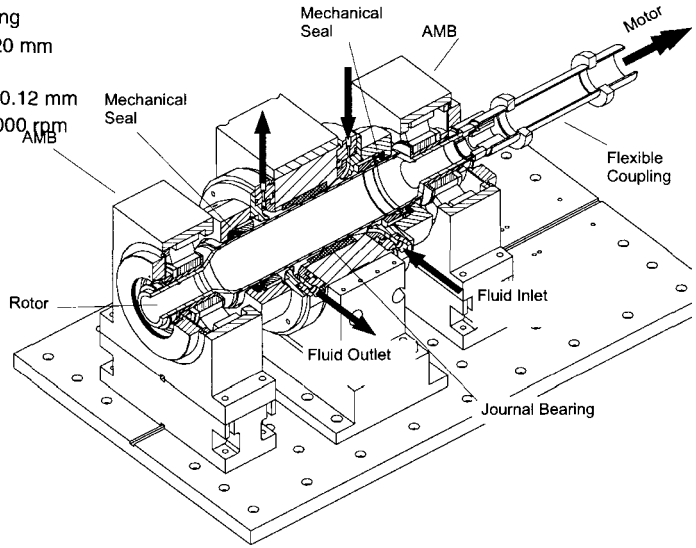


Figure 2.1: Scheme of experimental setup

**Technical data:**

Maximum AMB-Force:  
750 N per axis per bearing  
Main Rotor Diameter: 120 mm  
Airgap AMB :0.4 mm  
Airgap Journal Bearing: 0.12 mm  
Max. Rotation Speed: 6000 rpm



**Figure 2.2: Designed test rig**

**2.1 Active Magnetic Bearings**

Figure 2.3 shows the principle structure of an active magnetic bearing. A displacement sensor measures contactless the rotor position. After an A/D conversion the displacement signal is compared to a reference signal. The controller computes an output voltage  $u(t)$  outgoing from

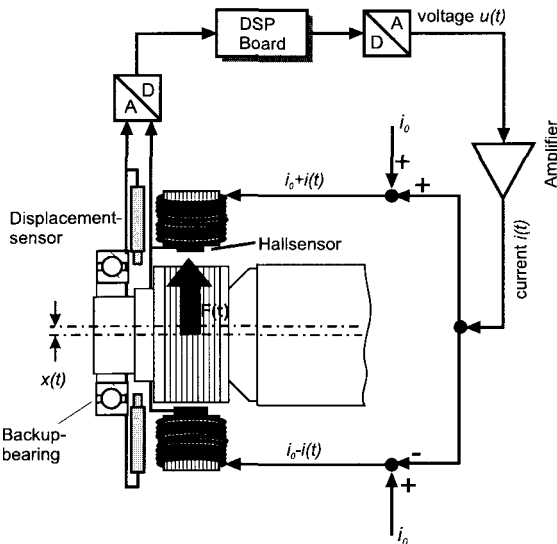


**Figure 2.3: Principle of a active magnetic bearing**

the difference and according to the implemented control law. The amplifier converts the controller voltage  $u(t)$  into the current  $i(t)$ . In Figure 2.3 the typical differential configuration of AMB systems can be seen, which means that all coils are supplied with a pre-magnetisation current  $i_0$ . For every two opposite coils, the current  $i(t)$  is superimposed once positive and the other side negative. The maximum bearing force is reached if for one coil the resulting current is equal to zero.

The presented testrig is additionally equipped with Hall sensor elements for the measurement of the magnetic forces

directly in the airgap between the rotor and the stator part of the bearing. The described setup allows a number of possibilities which are new for rotordynamic experiments, including:

- Arbitrary choice of the static operating point of the rotor in the bearing.
- Measurement of the effective forces acting on the rotor allows to obtain the frequency response function of the free rotor including possible fluid structure coupling elements, like journal bearings.
- Contact free excitation allows experiments independent from the rotational speed.
- Stepped sine excitation yields data with a high signal-to-noise ratio.
- Arbitrary choice of excitation amplitudes, phases and frequency allows selective excitation of a single degree of freedom of the rotating part.

### 3 FORCE MEASUREMENT TECHNIQUE USING HALL SENSORS

The precision of the identification procedure depends on the precision of the force measurement. Due to the static and dynamic characteristics of journal bearings, the following requirements for the force measurement method have to be fulfilled:

- The force measurement has to be accurate in the whole range of possible AMB forces, particularly in the area of amplifier saturation and for small dynamic force amplitudes.
- The measurement must be valid for all possible rotor positions, especially for eccentric positions.
- Hysteresis effects should be neglectable.

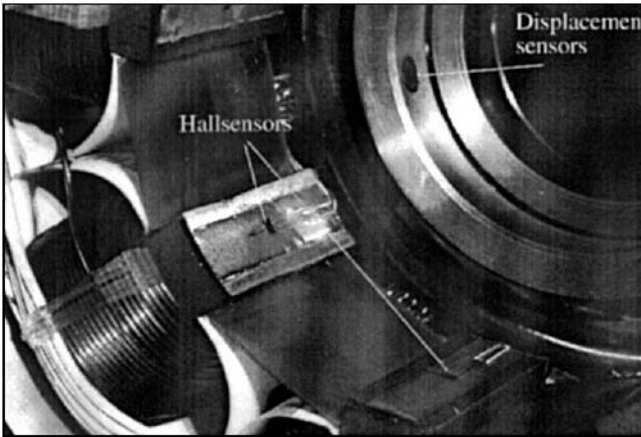


Figure 3.1: Magnetic bearing with Hall Sensors

One common method for the force measurement with AMB's is the so called *i-s-method*, where the force is calculated using a linearised current-displacement relationship /Schweitzer88/. This method neglects saturation and hysteresis effects (accuracy at maximum AMB-force about 15%), but is good for moderate magnetic forces. The presented test rig is often operated in the area above 80% of maximum mag-

netic force, so that a more accurate method was implemented. The magnetic force of one pole can be calculated from the flux density  $B_G$  using Eq. (3.1), the total force of one radial magnetic bearing results from the vectorial sum of the individual pole forces:

$$F_{Pole} = \frac{A_G}{\mu_0} \cdot B_G^2, \quad \vec{F}_{total} = \sum \vec{F}_{Pole} \quad (3.1)$$



The flux density is measured with hall sensors, that are integrated in the air gap between rotor and stator part. With this method static force errors of 1% at maximum AMB force are achieved. A more detailed description can be found in /Knopf98/.

#### 4 IDENTIFICATION METHOD

In laminar theory the description of the linear dynamic characteristics of journal bearings is defined via spring and damping coefficients. If the lubricating film becomes turbulent, additional inertia forces take effect, so that the dynamic force displacement relations are described by 2x2 mass-damper-spring elements. For a given set of boundary conditions (rotating speed, geometry, fluid properties) the static and dynamic properties of the bearings depend mainly on the eccentric position (and therefore on the Sommerfeld number) of the rotor. For small motions  $x_1$  and  $x_2$  around a operating point the dynamic equilibrium of forces leads to Eq. (4.1) /Nordmann98/. Generally, the  $k$ ,  $d$ ,  $m$  matrices are cross coupled and show no symmetrical characteristics. This means, that contrary to e.g. annular seals, every element of the  $K$ ,  $D$ ,  $M$  matrices has to be identified.

$$\begin{bmatrix} F_1 \\ F_2 \end{bmatrix} = \begin{bmatrix} k_{11} & k_{12} \\ k_{21} & k_{22} \end{bmatrix} \cdot \begin{bmatrix} x_1 \\ x_2 \end{bmatrix} + \begin{bmatrix} d_{11} & d_{12} \\ d_{21} & d_{22} \end{bmatrix} \cdot \begin{bmatrix} \dot{x}_1 \\ \dot{x}_2 \end{bmatrix} + \begin{bmatrix} m_{11} & m_{12} \\ m_{21} & m_{22} \end{bmatrix} \cdot \begin{bmatrix} \ddot{x}_1 \\ \ddot{x}_2 \end{bmatrix} \quad (4.1)$$

For harmonic excitations at discrete frequencies  $\omega$ , Eq. (4.1) can be rewritten as:

$$\begin{bmatrix} \hat{F}_1 \\ \hat{F}_2 \end{bmatrix} = \underbrace{\begin{bmatrix} k_{11} + i\omega d_{11} - \omega^2 m_{11} & k_{12} + i\omega d_{12} - \omega^2 m_{12} \\ k_{21} + i\omega d_{21} - \omega^2 m_{21} & k_{22} + i\omega d_{22} - \omega^2 m_{22} \end{bmatrix}}_{[K(\omega)]} \cdot \begin{bmatrix} \hat{x}_1 \\ \hat{x}_2 \end{bmatrix} \quad (4.2)$$

$$re([K_{lk}(\omega)]) = [k_{lk} - \omega^2 m_{lk}] , \quad im([K_{lk}(\omega)]) = [-i\omega d_{lk}] \quad (4.3)$$

The four frequency response functions  $[K_{lk}(\omega)]$  ( $l, k=1,2$ ) contain the rotordynamic parameters in a linear manner. They can be extracted after a decomposing into real- and imaginary parts (see Eq. (4.3) and Fig. 4.2). To achieve this purpose experimentally, 2 linearly independent excitation patterns are necessary. In our case, each translational DOF  $x_1$ , resp.  $x_2$  is excited separately during rotation (see Fig. 4.1). For example, an excitation in  $x_1$  direction and the measurement of the forces  $F_1$  and  $F_2$  leads to the identification of the first column of the transfer matrix (see Eq. (4.2)). Once the rotor has reached the defined static eccentricity  $\epsilon$ , excitation vectors are computed, one in the direction of the fluid force (= DOF  $x_1$ ) and one perpendicular to the fluid force (= DOF  $x_2$ ). These harmonic excitations are generated by the AMBs in a stepped sine manner and adapted in phase and amplitude, until the measured harmonic displacements reach a certain tolerance /Gähler94/. The identification of the force and displacement amplitudes is carried out in the time domain by fitting artificial harmonic signals in a least squares sense. This method has the advantage, that no leakage occurs, that no triggering or windowing is necessary and that it is also valid for very noisy signals. Due to the highly non linear static force displacement relation, the excitation amplitude has to be kept as small as possible. This is done by identifying the 1st and the 2nd harmonic of the excitation frequency. The presence of higher harmonic frequencies is an indicator for nonlinear behaviour. The excitation amplitude is automatically reduced if the amplitude of the higher harmonics reaches a defined limit. Typical excitation

amplitudes are 3-5  $\mu\text{m}$  ( $\approx 2.5$  to 4% bearing clearance). The force signals contain also the rotor mass, that can easily be subtracted. The frequencies of the displacement excitations are chosen independently from the rotational speed. Therefore unbalance signals do not disturb the identification procedure, because there is no correlation between these signals.

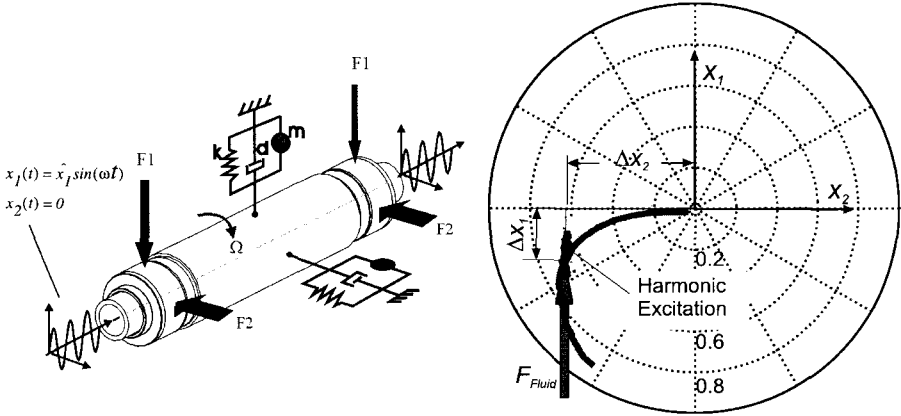


Figure 4.1: Principle of the identification procedure and measured excitation

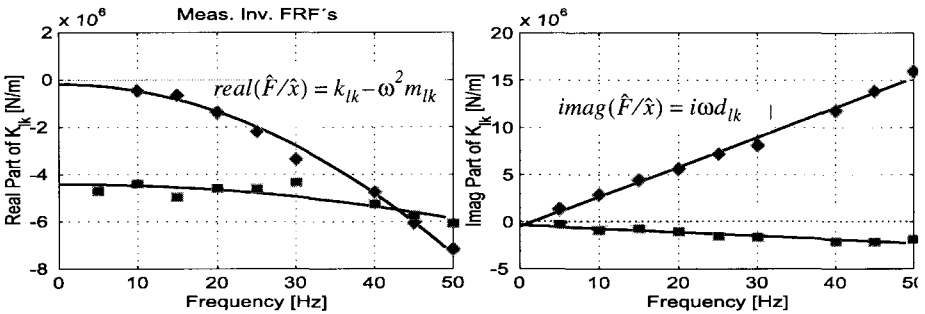


Figure 4.2: Measured stiffness functions ( $\hat{x}_1=4\mu\text{m}$ ,  $\varepsilon=0.1$ )

## 5 EXPERIMENTAL RESULTS

### 5.1 Static Behaviour

The evaluation of the static behaviour of laminar journal bearings is standardized /DIN83/ and well known. One characterising function is the Sommerfeld number  $So$ :

$$So = \frac{F\Psi^2}{LD\eta\Omega} \quad (5.1)$$

To derive a relation between  $So$  and the relative eccentricity  $\varepsilon$ , polynomial function can be used which are based on approximations to numerical data /DIN83/ ( $a_{1,2}=f(L/D)$ ):

$$So = \left(\frac{L}{D}\right)^2 \frac{\varepsilon}{2(1-\varepsilon^2)^2} \sqrt{\pi^2(1-\varepsilon^2) + 16\varepsilon^2 \frac{a_1(\varepsilon-1)}{a_2+\varepsilon}} \quad \text{with } \varepsilon = \frac{|\Delta x_1 + \Delta x_2|}{C} \quad (5.2)$$

Eq. (5.1) and Eq. (5.2) are valid for Reynolds numbers  $Re$  smaller than the critical Reynolds number  $Re_{crit}$ :

$$Re = \frac{(\Omega r C \rho)}{\eta} < 41,2 \sqrt{\frac{C}{r}} \quad (5.3)$$

For higher Reynolds numbers, the static turbulent force can be calculated by an empirical relation based on /Constantinescu59/:

$$F_{turb}/F_{lam} = 1 + \frac{7}{600}(1 + \epsilon)^{0,725} Re^{0,725} \quad (5.4)$$

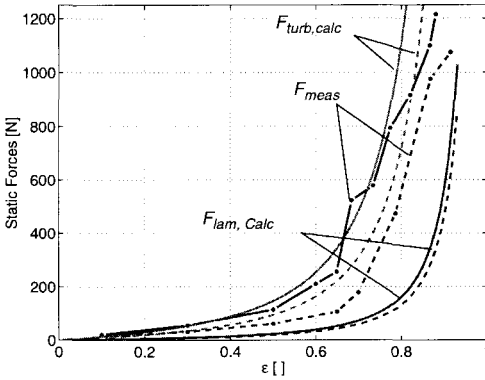


**Figure 5.1:** Comparison of static forces (dashed lines:  $Re=2000$ , solid lines:  $Re=3000$ ,  $Re_{crit}=980$ ). Calculated forces derived from Eq. (5.2) and Eq. (5.4)

In Fig. 5.1 results from static measurements are shown for  $Re=2000$  and  $Re=3000$ . Eq. (5.3) shows that higher Reynolds numbers can either be achieved by a decrease of  $\eta$  or an increase of  $\Omega$ . Both variations lead to higher Reynolds numbers  $Re$  and therefore to higher turbulent forces  $F_{turb}$  (see Eq. (5.3) and Eq. (5.4)). Regarding the laminar force  $F_{lam}$ , these two measures (decreasing  $\eta$  and increasing  $\Omega$ ) tend to compensate each other (see Eq. (5.1)), so that  $F_{lam}$  remains almost unchanged (see Fig. 5.1). The measured forces  $F_{meas}$  are up to 4 times higher than the calculated  $F_{lam}$  and correspond good with the calculated  $F_{turb}$ .

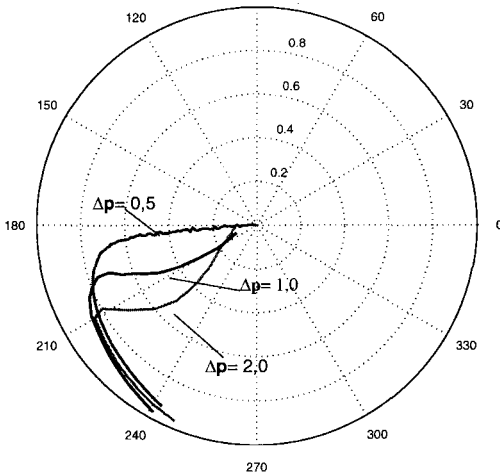


**Figure 5.2:** Journal centre loci for different axial pressure drops ( $Re=2000$ ,  $L/D=0,3$ ,  $p_{in}=3 \cdot 10^5 \text{ N/m}^2$ )

Figure 5.2 shows measured journal centre loci for different axial pressure drops. The rotor was charged with a vertical load produced by the AMB's. Because of the ambient static entrance pressure of  $3 \cdot 10^5 \text{ [N/m}^2]$ , the journal centre loci differ from the well known semicircular shape even for small axial pressure drops which is typical for cylindrical bearings. For small eccentricities, the rotor deviates almost horizontally to the vertical load. In this area, the hydrodynamic pressure is smaller than the ambient pressure. With increasing eccentricities the hydrodynamic pressure gets larger and consequently, the influence of the static pressure vanishes. For  $\epsilon < 0,8$  there is also a significant dependency to  $\Delta p$ . The

static cross coupling for higher  $\Delta p$ 's is smaller, the journal bearing here shows characteristics which are also known for annular seals. For  $\epsilon > 0,8$ , the hydrodynamic pressure in the circumferential direction becomes dominant and the dependency on the axial pressure drop vanishes. All the cases now show typical journal bearing behaviour.

### 5.2 Rotordynamic Coefficients

In the following, the typical dynamic behaviour of the examined cylindrical journal bearings is explained. Fig. 5.3 shows measured mass, damping and stiffness coefficients and the corresponding measured Sommerfeld numbers of the test bearing in dependence of the relative eccentricity  $\epsilon$ . The trend of the curves is typical for all measurements that were performed, though the absolute values may change. Until a relative eccentricity of about 0.5, the different rotordynamic coefficients remain almost constant (with some restriction for  $d_{22}$ ). This proves the rule-of-thumb for annular seals, where it is assumed that the dynamic properties remain unchanged up to 50% of seal clearance. Regarding the direct masses  $m_{11}$  and  $m_{22}$ , they show significant values of about 37 kg. If the eccentricity is increased  $m_{22}$  drops down negative values of -45 kg. This declension is reproducible and accompanied by a strong rise of the damping  $d_{22}$ . Furthermore, in this range of  $\epsilon$ , the cross coupled stiffnesses are dominating over the direct stiffnesses. For further increasing  $\epsilon$ 's, there is a strong rise of the direct stiffness  $k_{11}$  while  $k_{22}$  and the cross coupled stiffnesses decrease. For  $\epsilon > 0,8$ , the mass term  $m_{22}$  again reaches positive values that are comparable to small  $\epsilon$ 's,  $m_{11}$  tends to zero.

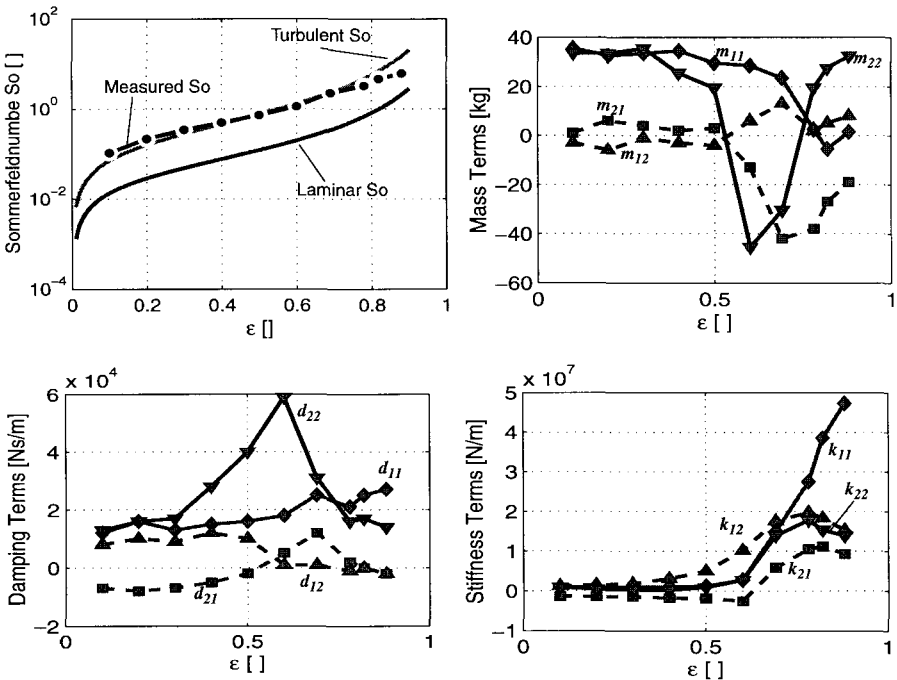


Figure 5.3: Measured rotordynamic coefficients and according Sommerfeldnumbers ( $Re=3000, L/D=0,3, p_{in}=3, \Delta p=2 [N/m^2]$ )

### 5.3 Stability Behaviour

Unlike laminar journal bearings, where only stiffness and damping properties are relevant, the turbulent journal bearings themselves represent an oscillatory system, with inertia, stiffness and damping coefficients. Consequently, standard stability evaluation tools like eigenvalue analysis can be used. The eigenvalues of a damped system are either real or pairwise conjugated complex /Craig81/:

$$\lambda_k = -\delta_k \pm i\omega_{d,k} \quad (5.5)$$

The real part represents the damping properties, negative real parts (=positive  $\delta_k$ 's) are stable. In Fig. 5.4 the damping constants are plotted in dependence of  $\epsilon$  on the left side. The right picture shows the eigenvalues of the bearing in the complex plane. The journal bearing was operated at  $Re=3000$ ,  $p_{im}=1$ ,  $\Delta p=0.5 [10^5 \text{ N/m}^2]$ .

The journal bearing remains stable over a wide range. Between  $\epsilon=0.6$  and  $\epsilon=0.8$ , this is the area where  $m_{22}$  becomes negative. The negative inertia coefficients lead to positive real eigenvalues (see Fig. 5.4). In this case, the system is monotonic unstable. For  $\epsilon>0.8$  the journal bearing again reaches positive damping constant and remains stable.

It should be mentioned that this is no sufficient evidence, that the total rotor system becomes unstable. The conclusion is vice versa. Mechanical systems such as rotors are always stable (if there are no other destabilizing forces are acting). If this rotor is supported in turbulent journal bearings and the bearings are stable, the whole system is stable (if there are no other destabilizing forces acting). On the other hand, if the journal bearing is unstable, the residual structure has to compensate this instability to ensure a safe operation of the machine.

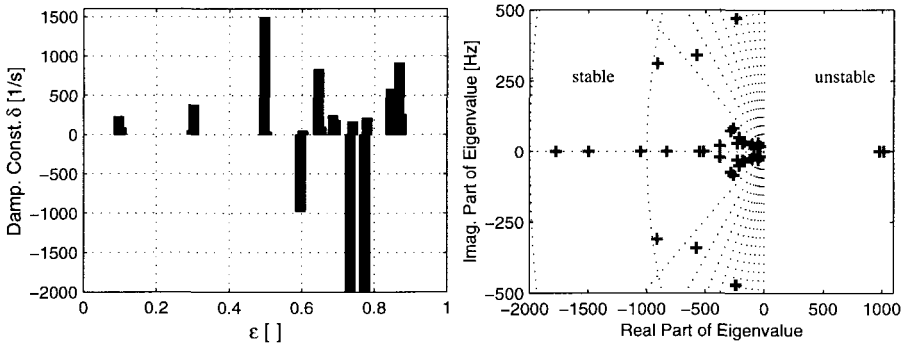


**Figure 5.4: Damping constant  $\delta$  for different eccentricities  $\epsilon$  and poles of the journal bearing in the complex plane ( $Re=3000$ ,  $p=1$ ,  $\Delta p=0.5 [10^5 \text{ N/m}^2]$ ).**

## 6 CONCLUSION AND OUTLOOK

In this paper a novel designed AMB-test rig for the identification of turbulent journal bearings was presented. The use of active magnetic bearings offers the advantage of a great flexibility, concerning motion or force generation and data acquisition.

It has been shown, that the turbulence in the lubricating film of the journal bearing has a large impact on the static and dynamic behaviour. Consequently, the effect of the turbulence has to be taken into account if a bearing is operated in the turbulent region. The inertia effect cannot be

neglected like it is valid for laminar bearings. In the future, the measurements will be extended towards higher Reynolds numbers and the nonlinear dynamic behaviour of the bearing will be investigated.

## 7 ACKNOWLEDGMENT

The presented paper is a result from research work sponsored by the German Research Council (DFG). Special thanks also to MECOS who manufactured the AMBs.

## 8 NOMENCLATURE

$a_1$	$= 1,1642 - 1,9456\beta + 7,1161\beta^2 - 10,1073\beta^3 + 5,0141\beta^4$	$\beta$	$= L/D$
$a_2$	$= -1,000026 - 0,02363\beta - 0,4215\beta^2 - 0,038817\beta^3 - 0,090551\beta^4$	$p_{in}$	Entrance pressure
$A_G$	Airgap area	$\delta$	Damping constant
$B_G$	Flux density in the airgap	$\Delta p$	ax. pressure drop
$F$	Force	$\varepsilon$	rel. eccentricity
$f$	excit. frequency	$\lambda$	Eigenvalue
$i$	complex unit	$\eta$	dyn. viscosity
$K$	Stiffness function	$\mu_0$	Permeability of air
$L$	Bearing length	$\rho$	fluid density
$n$	rot. Speed	$\Omega$	$= 2\pi n$
$D$	Diameter	$\omega$	$= 2\pi f$
$r$	Shaft radius	$\psi$	$= 2C/D$ , Clearance ratio
$C$	Bearing Clearance		

## 9 REFERENCES

- /Constantinescu59/** Constantinescu, R.: On Turbulent Lubrication, *Proc. Instn Mech. Engrs.*, Vol. 173, Nr. 38, p. 881, 1959
- /Craig83/** Craig, Roy R., Structural Dynamics, Jon Wiley & Sons, New York
- /DIN83/** German Industrial Standard, Nr. 31652, Part 1 & 2, Berlin 1983
- /Gähler94/** C. Gähler, P.Förch: A Precise Magnetic Bearing Exciter for Rotordynamic Experiments, *4th Int. Symposium on Magnetic Bearings*, Zurich, Switzerland, 1994
- /Knopf98/** Knopf, E.: Active Magnetic Bearings for the Identification of Dynamic Characteristics of Fluid Bearings-Calibration Results, *6th Int. Symposium. on Magnetic Bearings*, Cambridge, USA, 1998
- /Nordmann98/** Nordmann, R.: New Identification Techniques in Rotordynamics using Force and Motion Control, *4th Int. Conference on Motion and Vibration Control*, Zurich, Switzerland
- /Schweitzer88/** Schweitzer G., Bleuler H., Traxler A.: Active Magnetic Bearings, Springer Verlag, Berlin Heidelberg, 1994
- /Someya88/** Someya, T. (Editor): Journal Bearing Databook, Springer Verlag, Berlin Heidelberg, 1988

# Bearings and Rotors

*This page intentionally left blank*



# Generalized stiffness and damping matrices of multi-DOF hydrodynamic lubrication films

H SPRINGER

Department of Mechanical Engineering, Vienna University of Technology, Austria

## SYNOPSIS

In this paper a general matrix calculus is developed to compute stiffness and damping matrices of dimension  $(n \times n)$  corresponding to a given number of  $n$  degrees of freedom of the structural surfaces enclosing a thin lubrication film. Small disturbance displacements and velocities of the lubricated surfaces are represented by an  $n$ -dimensional generalized displacement vector. The lubrication stiffness and damping characteristics are determined from Reynolds' equation by introducing a truncated series expansion. Structural stiffness and damping effects can be superimposed to the lubrication characteristics by applying the principle of virtual work. A numerical example of an elastically supported tilt-pad thrust bearing with six degrees of freedom is presented.

## NOTATION

$\left. \begin{matrix} C_p \\ C_\tau \\ C_s \end{matrix} \right\}$	damping matrices due to lubrication pressure $p$ , lubrication shear stress $\tau$ , and structural suspension forces, respectively,
$\partial$	$(2 \times 1)$ -matrix differential operator,
$\epsilon \ll 1$	average film thickness to length ratio,
$h(x, z, t)$	film thickness function of the lubricant between structural surfaces $S_1$ and $S_2$ ,
$\left. \begin{matrix} K_p \\ K_\tau \\ K_s \end{matrix} \right\}$	stiffness matrices due to lubrication pressure $p$ , lubrication shear stress $\tau$ , and structural suspension forces, respectively,
$L$	characteristic length of the lubrication area $A$ ,
$\mu$	dynamic viscosity of the lubricant,
$m$	number of independent pressure shape functions within the vector $\psi$ ,
$n$	number of degrees of freedom of the structural surfaces $S_1$ and $S_2$ ,
$n_j$	$(3 \times 1)$ -normal vector in a point $P_j$ of the structural surface $S_j$ , $(j = 1, 2)$ ,
$N(x, z)$	geometric distribution matrix for the perturbation velocities of the structural surfaces $S_1$ and $S_2$ ,

$N^\pm(x, z)$	} geometric distribution submatrices composed from $N$ ,
$N_v(x, z)$	
$N_h(x, z)$	
$p(x, z, t)$	pressure stress distribution within the lubricant,
$\Delta p(x, z, t)$	perturbation pressure distribution due to surface displacements $\mathbf{q}(t)$ ,
$\psi(x, z)$	$(m \times 1)$ —pressure shape function vector to solve Reynolds' equation,
$\mathbf{q}(t)$	$(n \times 1)$ —generalized displacement vector of structural surfaces $S1$ and $S2$ ,
$S1, S2$	structural surfaces enclosing the lubricant,
$\boldsymbol{\tau}(x, y, z)$	$(2 \times 1)$ —shear stress distribution vector within the lubricant,
$\boldsymbol{\tau}_S(x, z, t)$	$(4 \times 1)$ —shear stress distribution vector at surfaces $S1$ and $S2$ ,
$\Delta \boldsymbol{\tau}_S(x, z, t)$	$(4 \times 1)$ —shear stress distribution vector at surfaces $S1$ and $S2$ due to surface displacements $\mathbf{q}(t)$ ,
$\mathbf{t}_{jx,z}$	$(3 \times 1)$ —tangential vector in a point $P_j$ of the structural surface $S_j$ in $x$ - and $z$ -direction, respectively, $(j = 1, 2)$ ,
$u_j, v_j, w_j$	components of $\mathbf{v}_j$ , $(j = 1, 2)$ ,
$\mathbf{v}_1, \mathbf{v}_2$	$(3 \times 1)$ —lubrication velocity vectors at structural surfaces $S1, S2$ , respectively,
$\mathbf{v}^+, \mathbf{v}^-$	$(2 \times 1)$ —surface velocity vectors, composed from $\mathbf{v}_1, \mathbf{v}_2$ .

## 1 INTRODUCTION

Stiffness and damping characteristics of hydrodynamic lubrication films can be determined from Reynolds' pressure equation, see [1], for example. Lund, [2], first determined stiffness and damping characteristics of journal bearings from Reynolds' equation by calculating a perturbation pressure distribution of the bearing due to small displacements of the shaft. Glienicke, [3], and Nordmann, [4], experimentally identified  $(2 \times 2)$ -stiffness and damping matrices of journal bearings. The agreement between experiments and calculations, however, is not very good, in general. Ollson, [5], showed that the damping matrix of a thin hydrodynamic lubrication film is always symmetric.

When calculating stiffness and damping characteristics of hydrodynamic bearings, a usual assumption is to consider the structural surfaces (which enclose the thin lubrication film) to be rigid. For example, the shaft and the sleeve of a journal bearing usually are considered to be undeformable. If the bearing sleeve is stationary, then, in the planar case, the shaft has two translational degrees of freedom (DOF) of the shaft-center displacements within the bearing sleeve. In addition, two angular displacements of the shaft axis may be considered. In the case of a cylindrical radial tilt-pad journal bearing the number of DOF is  $p + 2$  where  $p$  is the number of tilt-pads of the bearing. In addition to the angular pad displacement, radial and tangential displacements of each pad may be introduced, resulting in  $2p$  more DOF of the overall bearing. In this paper a generalized method is presented that allows to calculate multi-dimensional dynamic characteristics of a hydrodynamic bearing directly from a perturbation approach applied to Reynolds' pressure equation. From the principle of virtual work stiffness and damping matrices are obtained including pressure and shear stress effects of the lubrication film as well as stiffness and damping effects of the structural bearing components.

## 2 REYNOLDS' EQUATION AND THE LUBRICATION STATE

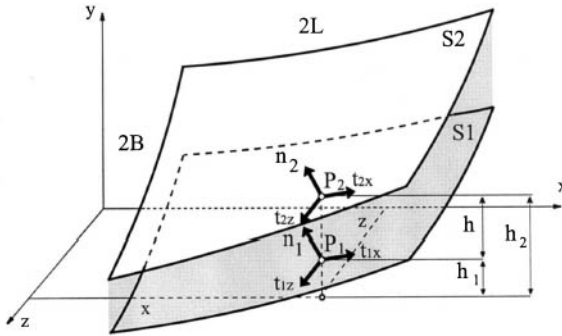


Figure 1: Lubrication film enclosed between structural surfaces  $S1$  and  $S2$ .

Figure 1 shows a thin lubrication film enclosed between two structural surfaces  $S1$  and  $S2$ . The film thickness between two opposite points  $P1$  and  $P2$  at the surfaces is given by  $h(x, z, t) = h_2(x, z, t) - h_1(x, z, t)$ . Usually  $S1$  is considered as a plane reference surface, and for a stationary lubrication state, indicated by "0", this plane coincides with the  $x$ - $z$ -plane of the absolute  $x$ - $y$ - $z$  coordinate system. Then, without losing generality,  $h_{01}(x, z) \equiv 0$  and  $h_0(x, z) = h_{02}(x, z)$  holds.

The nonstationary pressure distribution  $p(x, z, t)$  between the moving surfaces  $S1$  and  $S2$  can be determined from Reynolds' differential equation in matrix form

$$\partial^T \left( \frac{h^3}{\mu} \partial p \right) = 12(v_2 - v_1) + 6\mathbf{v}^{-T}(\partial h) + 6h(\partial^T \mathbf{v}^+), \quad (1)$$

see Ref.[1], for example. On the left hand side of Eq.(1) the  $(2 \times 1)$ -matrix differential operator  $\partial$  is defined by

$$\partial \triangleq \{ \partial / \partial x \quad \partial / \partial z \}^T. \quad (2)$$

On the right hand side of Eq.(1) tangential velocity vectors

$$\mathbf{v}^\pm(x, z, t) = \{ u_1(x, z, t) \pm u_2(x, z, t) \quad w_1(x, z, t) \pm w_2(x, z, t) \}^T \quad (3)$$

along with the normal velocity term  $v_2(x, z, t) - v_1(x, z, t)$  appear. The  $(6 \times 1)$ -vector

$$\mathbf{v}(x, z, t) = \left\{ \begin{array}{l} \{ u_1(x, z, t) \quad v_1(x, z, t) \quad w_1(x, z, t) \}^T \\ \{ u_2(x, z, t) \quad v_2(x, z, t) \quad w_2(x, z, t) \}^T \end{array} \right\} \quad (4)$$

contains the  $x$ -,  $y$ - and  $z$ -velocity components  $\{u_{1,2} \quad v_{1,2} \quad w_{1,2}\}$  of two opposite points  $P1$  and  $P2$  of the moving surfaces  $S1$  and  $S2$ , respectively. After the pressure distribution  $p(x, z, t)$  for given boundary conditions  $p(\mathbf{B}) = 0$  is calculated from Eq.(1), the shear stress vector within the lubricant  $x$ - $z$ -plane can be determined from

$$\boldsymbol{\tau}(x, y, z, t) = \left\{ \begin{array}{l} \tau_x(x, z, t) \\ \tau_z(x, z, t) \end{array} \right\} = \frac{2y - h(x, z, t)}{2} (\partial p(x, z, t)) - \frac{\mu}{h(x, z, t)} \mathbf{v}^-(x, z, t), \quad (5)$$

where  $\mu$  denotes the lubricant's dynamic viscosity, see Ref.[1], for example. The shear stresses acting on the surfaces  $S1, S2$ , respectively, are determined from Eq.(5) and summarized in the  $(4 \times 1)$ -vector

$$\boldsymbol{\tau}_S(x, z, t) = \begin{Bmatrix} \tau(x, y = 0, z, t) \\ -\tau(x, y = h, z, t) \end{Bmatrix} = \begin{Bmatrix} -h(\boldsymbol{\partial} p)/2 - \mu \mathbf{v}^-/h \\ -h(\boldsymbol{\partial} p)/2 + \mu \mathbf{v}^-/h \end{Bmatrix}. \quad (6)$$

Corresponding to the self-adjoint differential equation (1), a variational principle of the form

$$J = \iint_A \left[ \frac{h^3}{\mu} (\boldsymbol{\partial}^T p)(\boldsymbol{\partial} p) + 24p(v_2 - v_1) + 12p\mathbf{v}^{-T}(\boldsymbol{\partial} h) + 12ph(\boldsymbol{\partial}^T \mathbf{v}^+) \right] dA \Rightarrow \text{Extremum}, \quad (7)$$

can be established, where  $A$  denotes the area of positive pressure  $p(x, z, t) > 0$ .

In most bearing applications the lubrication state of a thin film is composed of a time independent, stationary part indicated by "0" and a time variant, non-stationary part. Then, the pressure and shear stress states can be written, respectively,

$$p(x, z, t) = p_0(x, z) + \Delta p(x, z, t), \quad (8)$$

$$\boldsymbol{\tau}_S(x, z, t) = \boldsymbol{\tau}_{0S}(x, z) + \boldsymbol{\Delta} \boldsymbol{\tau}_S(x, z, t). \quad (9)$$

The velocity state of the structural surfaces  $S1$  and  $S2$  can be composed of

$$\mathbf{v}(x, z, t) = \mathbf{v}_0(x, z) + \mathbf{N}(x, z)\dot{\mathbf{q}}(t), \quad (10)$$

where

$$\mathbf{q}(t) = \{\mathbf{q}_1^T(t) \quad \mathbf{q}_2^T(t)\}^T \quad (11)$$

is a  $(n \times 1)$ -generalized displacement vector which represents  $n_1$  and  $n_2$  translational and rotational independent displacements (degrees of freedom, DOF) of the structural surfaces  $S1$  and  $S2$ , respectively. The matrix

$$\mathbf{N}(x, z) = \begin{bmatrix} \mathbf{N}_{u1}^T(x, z) & \mathbf{N}_{v1}^T(x, z) & \mathbf{N}_{w1}^T(x, z) & \mathbf{0} & \mathbf{0} & \mathbf{0} \\ \mathbf{0} & \mathbf{0} & \mathbf{0} & \mathbf{N}_{u2}^T(x, z) & \mathbf{N}_{v2}^T(x, z) & \mathbf{N}_{w2}^T(x, z) \end{bmatrix}^T, \quad (12)$$

is of dimension  $(6 \times n)$ , with  $n = n_1 + n_2$  being the number of the overall DOF of both surfaces  $S1$  and  $S2$ .  $\mathbf{N}(x, z)$  can be calculated from the geometric properties of the surfaces, see example in section 5. Furthermore, the velocity state in Eq.(1) is given by

$$\mathbf{v}^\pm(x, z, t) = \mathbf{v}_0^\pm(x, z) + \mathbf{N}^\pm(x, z)\dot{\mathbf{q}}(t), \quad (13)$$

$$v_2 - v_1 = [(v_{02}(x, z) - v_{01}(x, z))] + \mathbf{N}_v(x, z)\dot{\mathbf{q}}(t), \quad (14)$$

with the geometric matrices

$$\mathbf{N}^\pm(x, z) = \begin{bmatrix} \mathbf{N}_{u1}(x, z) & \pm \mathbf{N}_{u2}(x, z) \\ \mathbf{N}_{w1}(x, z) & \pm \mathbf{N}_{w2}(x, z) \end{bmatrix}, \quad (15)$$

$$\mathbf{N}_v(x, z) = \begin{bmatrix} -\mathbf{N}_{v1}(x, z) & \mathbf{N}_{v2}(x, z) \end{bmatrix}, \quad (16)$$

to be composed from matrix  $\mathbf{N}(x, z)$  in Eq.(12). The film thickness state is described by

$$h(x, z, t) = h_0(x, z) + \mathbf{N}_h(x, z)\mathbf{q}(t), \quad (17)$$

where  $\mathbf{N}_h(x, z)$  is of dimension  $(1 \times n)$  and is determined from the geometry of the surfaces  $S1$  and  $S2$ .

### 3 PERTURBATION PRESSURE AND SHEAR STRESSES

If Eqs.(8), (13), (14), (17) are substituted into Eq.(1) and a linearization is carried out with respect to  $\Delta p$ ,  $\mathbf{q}$  and  $\dot{\mathbf{q}}$ , the stationary pressure distribution  $p_0(x, z)$  can be calculated from

$$\partial^T \left( \frac{h_0^3}{\mu} \partial p_0 \right) = 12(v_{02} - v_{01}) + 6\mathbf{v}_0^{-T} (\partial h_0) + 6h_0 (\partial^T \mathbf{v}_0^+), \quad (18)$$

and the perturbation pressure distribution  $\Delta p(x, z, t)$  is determined by the differential equation

$$\partial^T \left( \frac{h_0^3}{\mu} \partial \Delta p \right) = \mathbf{s}(x, z) \mathbf{q}(t) + \mathbf{d}(x, z) \dot{\mathbf{q}}(t), \quad (19)$$

with

$$\begin{aligned} \mathbf{s}(x, z) &= 6[\mathbf{v}_0^{-T} (\partial \mathbf{N}_h) + (\partial^T \mathbf{v}_0^+) \mathbf{N}_h] - \partial^T \left[ \frac{3h_0^2}{\mu} (\partial p_0) \mathbf{N}_h \right], \\ \mathbf{d}(x, z) &= 12\mathbf{N}_v + 6[(\partial^T h_0) \mathbf{N}^- + h_0 (\partial^T \mathbf{N}^+)]. \end{aligned} \quad (20)$$

Various methods are available in the literature to solve the partial differential equation (18) for the stationary pressure distribution  $p_0(x, z)$  for given boundary conditions  $p_0(\mathbf{B}) = 0$ , see Ref.[1], for example. Further, the corresponding variational principle Eq.(7) may be used to obtain approximate solutions for  $p_0(x, z)$ , for example, see Ref.[7].

Applying the same boundary conditions for  $\Delta p(x, z, t)$  as for  $p_0(x, z)$ , a truncated series expansion of the form

$$\Delta p(x, z) = \boldsymbol{\psi}^T(x, z) \mathbf{r}(t) \quad (21)$$

is applied to Eq.(19), where  $\boldsymbol{\psi}(x, z)$  is a  $(m \times 1)$ -dimensional vector of  $m$  independent functions  $\psi_j(x, z)$ ,  $j = 1 \dots m$ , which fulfill the boundary conditions  $\boldsymbol{\psi}(\mathbf{B}) = \mathbf{0}$ , see Ref.[7], for example. Then, from the variational principle that corresponds to Eq.(19), the coefficient vector  $\mathbf{r}(t)$  can be obtained from  $\partial J / \partial \mathbf{r} = \mathbf{0}$ , see Eq.(7), and the solution for the perturbation pressure is obtained in the form

$$\Delta p(x, z, t) = \boldsymbol{\psi}^T(x, z) \mathbf{R}^{-1} \mathbf{S} \mathbf{q}(t) + \boldsymbol{\psi}^T(x, z) \mathbf{R}^{-1} \mathbf{S} \dot{\mathbf{q}}(t), \quad (22)$$

where

$$\mathbf{R} = \iint_A (\partial \boldsymbol{\psi}^T)^T \frac{h_0^3}{\mu} (\partial \boldsymbol{\psi}^T) dx dz, \quad (23)$$

$$\mathbf{S} = - \iint_A \boldsymbol{\psi}(x, z) \mathbf{s}(x, z) dx dz, \quad \mathbf{D} = - \iint_A \boldsymbol{\psi}(x, z) \mathbf{d}(x, z) dx dz \quad (24)$$

holds, with  $A$  being the area of positive pressure  $p(x, z, t) > 0$ . If Eqs.(8), (9), (13), (17) and (21) are substituted into Eq.(6) and a linearization is carried out with respect to  $\Delta p$ ,  $\mathbf{q}$  and  $\dot{\mathbf{q}}$ , the stationary shear stress vector is obtained as

$$\boldsymbol{\tau}_{0S} = \left\{ \begin{array}{l} -h_0 (\partial p_0) / 2 - \mu \mathbf{v}^- / h_0 \\ -h_0 (\partial p_0) / 2 + \mu \mathbf{v}^+ / h_0 \end{array} \right\}. \quad (25)$$

Further, the perturbation shear stress vector becomes

$$\Delta \boldsymbol{\tau}_s = -[\boldsymbol{\chi}^T \mathbf{R}^{-1} \mathbf{S} + \mathbf{f}] \mathbf{q} - [\boldsymbol{\chi}^T \mathbf{R}^{-1} \mathbf{D} + \mathbf{g}] \dot{\mathbf{q}}, \quad (26)$$

where

$$\boldsymbol{\chi}^T(x, z) = \frac{h_0(x, z)}{2} \begin{bmatrix} \boldsymbol{\partial} \boldsymbol{\psi}^T(x, z) \\ \boldsymbol{\partial} \boldsymbol{\psi}^T(x, z) \end{bmatrix}, \quad (27)$$

$$\mathbf{f}(x, z) = \left\{ \begin{array}{l} \boldsymbol{\partial} p_0(x, z)/2 - \mu \mathbf{v}_0^-(x, z)/h_0^2(x, z) \\ \boldsymbol{\partial} p_0(x, z)/2 + \mu \mathbf{v}_0^-(x, z)/h_0^2(x, z) \end{array} \right\} \mathbf{N}_h(x, z), \quad (28)$$

$$\mathbf{g}(x, z) = \frac{\mu}{h_0(x, z)} \begin{bmatrix} \mathbf{N}^-(x, z) \\ -\mathbf{N}^-(x, z) \end{bmatrix}. \quad (29)$$

#### 4 LUBRICATION AND STRUCTURAL STIFFNESS AND DAMPING MATRICES

Pressure and shear stresses, respectively, act perpendicular and tangentially to the structural surfaces, see Figure 2. Therefore, the direction of the pressure forces acting upon surfaces  $S1$  and  $S2$ , respectively, is given by  $-\mathbf{n}_1 = \{0 \quad -1 \quad 0\}^T$  and  $\mathbf{n}_2 = \{-\partial h/\partial x \quad -\partial h/\partial z\}$ . The directions of the shear forces acting upon  $S1$  and  $S2$ , respectively, are given by  $\mathbf{t}_{1x} = \{1 \quad 0 \quad 0\}^T$ ,  $\mathbf{t}_{1z} = \{0 \quad 0 \quad 1\}$  and  $\mathbf{t}_{2x} = \{1 \quad \partial h/\partial x \quad 0\}^T$ ,  $\mathbf{t}_{2z} = \{0 \quad \partial h/\partial z \quad 1\}^T$ . Virtual small displacements  $\delta \mathbf{x}$  of two opposite points on the surfaces  $S1$  and  $S2$  can be expressed from Eq.(10) by the generalized displacement vector  $\mathbf{q}$  in the form  $\delta \mathbf{x} = \mathbf{N} \delta \mathbf{q}$ . The virtual work of the lubrication and structural forces can be determined from

$$\delta W = \delta W_p + \delta W_\tau + \delta W_s = \iint_A \delta \mathbf{q}^T \mathbf{N}^T \mathbf{n} (p_0 + \Delta p) + \mathbf{t} (\boldsymbol{\tau}_{0S} + \Delta \boldsymbol{\tau}_S) dx \quad dz + \delta W_s, \quad (30)$$

with

$$\mathbf{n} = \{-\mathbf{n}_1^T \quad \mathbf{n}_2^T\}^T = \mathbf{n}_0 + \Delta \mathbf{n},$$

$$\mathbf{t} = \begin{bmatrix} \mathbf{t}_{1x} & \mathbf{t}_{1z} & \mathbf{0} & \mathbf{0} \\ \mathbf{0} & \mathbf{0} & \mathbf{t}_{2x} & \mathbf{t}_{2z} \end{bmatrix} = \mathbf{t}_0 + \Delta \mathbf{t}. \quad (31)$$

The stationary equilibrium state of the surfaces  $S1$  and  $S2$  cancels out in Eq.(30). If lubrication and structural prestress effects due to terms  $\Delta \mathbf{n} p_0$ ,  $\Delta \mathbf{t} \boldsymbol{\tau}_{0S}$ , etc., are neglected in Eq.(30), the stiffness and damping matrices corresponding to lubrication and structural forces are approximately obtained from

$$\iint_A \delta \mathbf{q}^T \mathbf{N}^T (\mathbf{n}_0 \Delta p + \mathbf{t}_0 \Delta \boldsymbol{\tau}_S) dx \quad dz + \delta (\Delta W_s) =$$

$$\cong -\delta \mathbf{q}^T (\mathbf{K}_p + \mathbf{K}_\tau + \mathbf{K}_s) \mathbf{q} - \delta \mathbf{q}^T (\mathbf{C}_p + \mathbf{C}_\tau + \mathbf{C}_s) \dot{\mathbf{q}}. \quad (32)$$

Substituting Eqs.(22), (26) into (32) leads to

$$\mathbf{K}_p = \mathbf{E}_p^T \mathbf{R}^{-1} \mathbf{S}, \quad \mathbf{K}_\tau = \mathbf{E}_\tau^T \mathbf{R}^{-1} \mathbf{S} + \mathbf{F} \quad (33)$$

for the stiffness matrices due to lubrication pressure and shear, respectively, and

$$\mathbf{C}_p = \mathbf{E}_p^T \mathbf{R}^{-1} \mathbf{D}, \quad \mathbf{C}_\tau = \mathbf{E}_\tau^T \mathbf{R}^{-1} \mathbf{D} + \mathbf{G} \quad (34)$$

for the damping matrices due to lubrication pressure and shear, respectively, where

$$\mathbf{E}_p^T = - \iint_A \mathbf{N}^T \mathbf{n}_0 \boldsymbol{\psi}^T dx \quad dz, \quad \mathbf{E}_\tau^T = \iint_A \mathbf{N}^T \mathbf{t}_0 \boldsymbol{\chi}^T dx \quad dz, \quad (35)$$

$$\mathbf{F} = \iint_A \mathbf{N}^T \mathbf{t}_0 \mathbf{f} \, dx \, dz, \quad \mathbf{G} = \iint_A \mathbf{N}^T \mathbf{t}_0 \mathbf{g} \, dx \, dz. \quad (36)$$

The structural stiffness and damping matrices  $\mathbf{K}_s$  and  $\mathbf{C}_s$ , respectively, of the surfaces  $S1$  and  $S2$  are calculated in the usual way from the stiffness and damping properties of the bearing structure, see example in the following section.

## 5 EXAMPLE: PLANAR THRUST BEARING WITH ELASTIC SUSPENSION

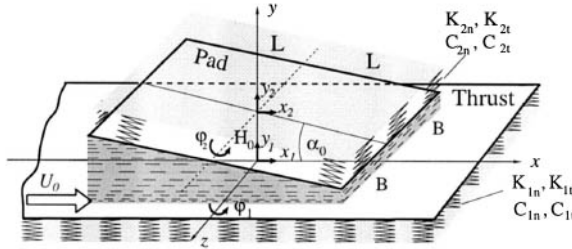


Figure 2: Planar tilt-pad thrust bearing with elastic suspension and six degrees of freedom

Figure 2 shows a single pad of a planar thrust bearing. Both the pad and the thrust are rigid bodies with a distributed visco-elastic suspension, as indicated by the springs in Figure 2. In the two-dimensional planar case the thrust and the pad have three degrees of freedom each. Therefore, the generalized displacement vector is defined in the form

$$\mathbf{q} = \{x_1/L \quad y_1/L \quad \varphi_1 \quad x_2/L \quad y_2/L \quad \varphi_2\}^T. \quad (37)$$

In the following, dimensionless coordinates  $X = x/L, Z = z/B$  are introduced, where  $2L$  is the length and  $2B$  is the width of the pad, see Figure 2. In the stationary equilibrium state of the pad-thrust bearing, the average film thickness is  $H_0$  and the wedge angle is  $\alpha_0 = H_0/2L = \epsilon/2$ , with  $\epsilon = H_0/L \ll 1$  being a small parameter. From Ref.[8] the stationary bearing state is determined by the following.

Film thickness:  $h_0(X, Z) = H_0(1 - X/2)$ ,

velocities:  $\mathbf{v}_{01} = \{U_0 \quad 0 \quad 0\}^T, \mathbf{v}_{02} = \{0 \quad 0 \quad 0\}^T, \mathbf{v}^+ = \mathbf{v}^- = \{U_0 \quad 0\}^T$ ,

pressure (approximate solution, see Ref.[7]):

$$p_0(X, Z) \cong 0.43 \frac{U_0 L \mu}{H_0^2} (1 + 0.98X)(1 - X^2)(1 - Z^2).$$

The geometric distribution matrices as introduced in Eqs.(9), (12), (13), and (14) are linearized with respect to the small parameter  $\epsilon$  and obtained in the form

$$\mathbf{N}(X) \doteq \begin{bmatrix} 1 & 0 & 0 & 0 & 0 & 0 \\ 0 & 1 & X & 0 & 0 & 0 \\ 0 & 0 & 0 & 0 & 0 & 0 \\ 0 & 0 & 0 & 1 & 0 & \epsilon X/2 \\ 0 & 0 & 0 & 0 & 1 & X \\ 0 & 0 & 0 & 0 & 0 & 0 \end{bmatrix}, \quad \begin{aligned} \mathbf{N}^\pm(X) &\doteq \begin{bmatrix} 1 & 0 & 0 & \pm 1 & 0 & \pm \epsilon X/2 \\ 0 & 0 & 0 & 0 & 0 & 0 \end{bmatrix}, \\ \mathbf{N}_v(X) &\doteq \begin{bmatrix} 0 & -1 & -X & 0 & 1 & X \end{bmatrix}, \\ \mathbf{N}_h(X) &\doteq \begin{bmatrix} 0 & -1 & -X & 0 & 1 & X \end{bmatrix}. \end{aligned} \quad (38)$$

From Ref.[7] a truncated polynomial series ( $m = 2$ )

$$\psi(X, Z) = \{(1 - X^2)(1 - Z^2) \quad X(1 - X^2)(1 - Z^2)\}^T \quad (39)$$

is applied to Eq.(21) in order to solve Eq.(19) for the perturbation pressure distribution  $\Delta p(x, z)$ ; see Eqs.(22) to (24). From Eqs.(23), (24) and Eqs.(33) to (36) the lubrication stiffness and damping matrices can be calculated and linearized with respect to the small parameter  $\epsilon = H_0/L$ . The result for the stiffness matrix is

$$\mathbf{K} = \mathbf{K}_p + \mathbf{K}_\tau + \mathbf{K}_s \doteq \mathbf{K}_{0p} + \mathbf{K}_{0s} + \epsilon(\mathbf{K}_{1p} + \mathbf{K}_{1\tau} + \mathbf{K}_{1s}) \quad (40)$$

with

$$\mathbf{K}_{0p} = \frac{\mu U_0 L^5}{H_0^3} \begin{bmatrix} 0 & 0 & 0 & 0 & 0 & 0 \\ 0 & 1.529 & 1.515 & 0 & -1.529 & -1.515 \\ 0 & 0.495 & 0.546 & 0 & -0.495 & -0.546 \\ 0 & 0 & 0 & 0 & 0 & 0 \\ 0 & -1.529 & -1.515 & 0 & 1.529 & 1.515 \\ 0 & -0.495 & -0.546 & 0 & 0.495 & 0.546 \end{bmatrix},$$

$$\mathbf{K}_{1p} = \frac{\mu U_0 L^5}{H_0^3} \begin{bmatrix} 0 & 0 & 0 & 0 & 0 & 0 \\ 0 & 0 & 0 & 0 & 0 & 0 \\ 0 & 0 & 0 & 0 & 0 & 0 \\ 0 & -0.764 & -0.757 & 0 & 0.764 & 0.757 \\ 0 & 0 & 0 & 0 & 0 & 0 \\ 0 & 0 & 0 & 0 & 0 & 0 \end{bmatrix},$$

$$\mathbf{K}_{1\tau} = \frac{\mu U_0 L^5}{H_0^3} \begin{bmatrix} 0 & 3.334 & 1.579 & 0 & -3.334 & -1.579 \\ 0 & 0 & 0 & 0 & 0 & 0 \\ 0 & 0 & 0 & 0 & 0 & 0 \\ 0 & -1.999 & -0.299 & 0 & 1.999 & 0.299 \\ 0 & 0 & 0 & 0 & 0 & 0 \\ 0 & 0 & 0 & 0 & 0 & 0 \end{bmatrix}. \quad (41)$$

The distributed pad (1) and thrust (2) suspension stiffnesses per unit area are indicated by  $K_{1,2n}$  in the normal directions and  $K_{1,2t}$  in the tangential directions of the corresponding bearing surfaces  $S1$  and  $S2$ , see Figure 2. Then the structural suspension stiffness matrix  $\mathbf{K}_s$  is composed of  $\mathbf{K}_s \doteq \mathbf{K}_{0s} + \epsilon \mathbf{K}_{1s}$ , where

$$\mathbf{K}_{0s} = \text{diag} [A_1 L^2 K_{1t} \quad A_1 L^2 K_{1n} \quad J_{1z} K_{1n} \quad 4BL^3 K_{2t} \quad 4BL^3 K_{2n} \quad \frac{4}{3}BL^3 K_{2n}],$$

$$\mathbf{K}_{1s} = \begin{bmatrix} \mathbf{0} & \vdots & \mathbf{0} \\ \dots & \vdots & \dots & \dots & \dots \\ & \vdots & 0 & k_{45} & 0 \\ \mathbf{0} & \vdots & k_{54} & 0 & 0 \\ & \vdots & 0 & 0 & 0 \end{bmatrix},$$

$$k_{45} = k_{54} = 2BL^3(K_{1n} - K_{1t}). \quad (42)$$

In the structural stiffness matrix  $\mathbf{K}_{0s}$ ,  $A_1$  indicates the area and  $J_{1z}$  indicates the area moment of inertia with respect to the z-axis of the distributed thrust suspension stiffness.



Note that  $\mathbf{K}_{1s}$  holds for the pad wedge angle  $\alpha_0 = \epsilon/2$  in this example. If the thrust carries more than one pad, then the dimension of the generalized displacement vector  $\mathbf{q}$  in Eq.(37) has to be extended to a corresponding higher number of degrees of freedom.

The result for the damping matrix is

$$\mathbf{C} = \mathbf{C}_p + \mathbf{C}_\tau + \mathbf{C}_s = \mathbf{C}_{0p} + \mathbf{C}_{0s} + \epsilon(\mathbf{C}_{1p} + \mathbf{C}_{1\tau} + \mathbf{C}_{1s}) \quad (43)$$

with

$$\mathbf{C}_{0p} = \frac{\mu L^6}{H_0^3} \begin{bmatrix} 0 & 0 & 0 & 0 & 0 & 0 \\ 0 & 1.522 & 0.299 & 0 & -1.522 & -0.299 \\ 0 & 0.299 & 0.231 & 0 & -0.299 & -0.231 \\ 0 & 0 & 0 & 0 & 0 & 0 \\ 0 & -1.522 & -0.299 & 0 & 1.522 & 0.299 \\ 0 & -0.299 & -0.231 & 0 & 0.299 & 0.231 \end{bmatrix},$$

$$\mathbf{C}_{1p} = \frac{\mu L^6}{H_0^3} \begin{bmatrix} 0 & 0 & 0 & 0 & 0 & 0 \\ 0.381 & 0 & 0 & -0.381 & 0 & 0 \\ 0.075 & 0 & 0 & -0.075 & 0 & 0 \\ 0 & -0.762 & -0.150 & 0 & 0.762 & 0.150 \\ -0.381 & 0 & 0 & 0.381 & 0 & 0 \\ -0.075 & 0 & 0 & 0.075 & 0 & 0 \end{bmatrix},$$

$$\mathbf{C}_{1\tau} = \frac{\mu L^6}{H_0^3} \begin{bmatrix} 0 & 0.381 & 0.075 & 0 & -0.381 & -0.075 \\ 0 & 0 & 0 & 0 & 0 & 0 \\ 0 & 0 & 0 & 0 & 0 & 0 \\ 0 & 0.381 & 0.075 & 0 & -0.381 & -0.075 \\ 0 & 0 & 0 & 0 & 0 & 0 \\ 0 & 0 & 0 & 0 & 0 & 0 \end{bmatrix}. \quad (44)$$

Analog to the distributed suspension stiffness matrix of the pad and the thrust, the distributed suspension visco-damping matrix  $\mathbf{C}_s$  can be established in the linearized form  $\mathbf{C}_s = \mathbf{C}_{0s} + \epsilon\mathbf{C}_{1s}$ , with

$$\mathbf{C}_{0s} = \mathbf{diag} [A_1 L^2 C_{1t} \quad A_1 L^2 C_{1n} \quad J_{1z} C_{1n} \quad 4BL^3 C_{2t} \quad 4BL^3 C_{2n} \quad \frac{4}{3} BL^3 C_{2n}],$$

$$\mathbf{C}_{1s} = \begin{bmatrix} \mathbf{0} & \vdots & \mathbf{0} \\ \dots & \vdots & \dots & \dots & \dots \\ & \vdots & 0 & c_{45} & 0 \\ \mathbf{0} & \vdots & c_{54} & 0 & 0 \\ & \vdots & 0 & 0 & 0 \end{bmatrix},$$

$$c_{45} = c_{54} = 2BL^3(C_{1n} - C_{1t}). \quad (45)$$

Note that the zero-order stiffness matrix  $\mathbf{K}_{0p}$  due to pressure in the lubricant is not symmetric, which is a general property of any lubrication film. Further, two non-symmetric first order stiffness matrices  $\epsilon\mathbf{K}_{1p}$ ,  $\epsilon\mathbf{K}_{1\tau}$  due to pressure and shear, respectively, in the lubricant appear, which are one order of magnitude smaller than  $\mathbf{K}_{0p}$  and therefore neglected in most practical calculations. The zero-order lubrication damping matrix  $\mathbf{C}_{0p}$  due to pressure turns out to be symmetric, which is a general property, see Ref.[5]. Further, two non-symmetric damping matrices  $\epsilon\mathbf{C}_{1p}$ ,  $\epsilon\mathbf{C}_{1\tau}$ , respectively, due to pressure and

shear in the lubricant appear, which are one order of magnitude smaller than  $C_{0p}$  and therefore neglected in most practical calculations. It is interesting to note that the sum  $\epsilon(C_{1p} + C_{1r})$  is symmetric, although  $C_{1p}$  and  $C_{1r}$  are not symmetric. Therefore, the total lubrication damping matrix, including zero- and first-order terms, is still symmetric.

The structural suspension stiffness and damping matrices are symmetric as usual. Note that there are first order cross-coupling terms  $K_{1s}$  and  $C_{1s}$  in stiffness and damping, respectively, which are caused by the pad wedge angle  $\alpha_0 = \epsilon/2$  in this example.

## 6 CONCLUSION

A general matrix calculus is developed in this paper to calculate multi-dimensional stiffness and damping matrices of thin lubrication films of hydrodynamic bearings. Structural stiffness and damping of the lubricated boundary surfaces of the bearing can be incorporated into the analysis for an arbitrary number of degrees of freedom. Lubrication stiffness and lubrication damping matrices of zero order and first order are obtained showing non-symmetry of stiffness in both orders and symmetry of the total damping matrix.

## DEDICATION

This paper is dedicated to Professor Dr. Aleš Tondl (Prague) on the occasion of his 75th birthday.

## REFERENCES

- [1] Constantinescu, V. N., A. Nica, M. D. Pascovici, G. Ceptureanu, & S. Nedelcu, 1985. *Sliding Bearings*. New York: Allerton Press, Inc.
- [2] Lund, J.W., 1964. Spring and Damping Coefficients for the Tilting Pad Journal Bearings. *SALE-Transactions* 7: 342-352.
- [3] Glienicke, J., 1970. Experimentelle Ermittlung der statischen und dynamischen Eigenschaften von Gleitlagern für schnellaufende Wellen. *Fortschritts-Berichte VDI 1-22*. Düsseldorf: Verein Deutscher Ingenieure.
- [4] Nordmann, R., 1984. Identification of Stiffness and Damping Coefficients of Journal Bearings by Means of the Impact Method. *CISM-Courses and Lectures No. 273, Dynamics of Rotors: Stability and System Identification*: 395-409.
- [5] Ollson, K.O., 1996. Some Fundamental Aspects on the Dynamic Properties of Journal Bearings. *IMECHE-Conference Publication C 500/020*: 31-40.
- [6] Finlayson, B.A., 1972. *The Method of Weighted Residuals and Variational Principles*. London: Academic Press.
- [7] Springer, H., 1978. Zur Berechnung hydrodynamischer Lager mit Hilfe von Tschebyscheff-Polynomen. *Forschung im Ingenieurwesen*, 44, No.4: 126-134.
- [8] Springer, H., 2000. Lubrication to Structure Interactions in Thin Hydrodynamic Films. *Proceedings of 7th International Conf. on Flow Induced Vibrations, 19-21 June, 2000, Luzern*: To be published.

# Self-excited vibration of rotors in tilting-pad journal bearings

H TAURA, M TANAKA, and K SUZUKI

Department of Mechanical Engineering, University of Tokyo, Japan

## SYNOPSIS

This paper studies the stability characteristics of a rigid rotor supported in tilting-pad journal bearings theoretically. Stability charts for a rigid rotor supported in tilting-pad journal bearings are obtained with a full set of linear rotordynamic coefficients, and the effects of preload factor, pad inertia and load direction on the stability are discussed. Tilting-pad journal bearings with low preload factor are found to cause oil whip even if pad inertia is negligibly small. Pad inertia lowers the stability threshold, and load direction affects the shape of the unstable operation regions in the stability charts.

## NOTATION

$C_b$  bearing clearance

$C_p$  pad clearance

$C_{jk} = C_p \omega c_{jk} / W$ ,  $C_{j\tilde{\alpha}} = C_p \omega c_{j\tilde{\alpha}} / (W R_p)$ ,  $C_{\tilde{\alpha}k} = C_p \omega c_{\tilde{\alpha}k} / (W R_p)$ ,  $C_{\tilde{\delta}\tilde{\delta}} = C_p \omega c_{\tilde{\delta}\tilde{\delta}} / (W R_p^2)$

$\Delta F_x, \Delta F_y$  increment oil film force applied to journal in  $x, y$  direction

$\Delta F_{\tilde{\xi}_i}, \Delta F_{\tilde{\eta}_i}$  increment oil film force applied to journal in  $\tilde{\xi}_i, \tilde{\eta}_i$  direction

$I$  moment of inertia of pad around pivot

$K_{jk} = C_p k_{jk} / W$ ,  $K_{j\tilde{\alpha}} = C_p k_{j\tilde{\alpha}} / (W R_p)$ ,  $K_{\tilde{\alpha}k} = C_p k_{\tilde{\alpha}k} / (W R_p)$ ,  $K_{\tilde{\delta}\tilde{\delta}} = C_p k_{\tilde{\delta}\tilde{\delta}} / (W R_p^2)$

$\Delta M_i$  increment of oil film moment acting on the  $i$ th pad

$R$  bearing radius

$R_p$	distance between the pivot point and the centre of curvature of the pad
$W$	bearing load
$X$	$= \Delta x / C_b$
$Y$	$= \Delta y / C_b$
$c_{\xi\xi_i}, c_{\xi\eta_i}, c_{\eta\xi_i}, c_{\eta\eta_i}$	fixed-pad damping coefficients of oil film of the $i$ th pad
$c_{jk}, c_{j\delta}, c_{\delta ik}, c_{\delta\delta i}$	global damping coefficients of oil film
$k_{\xi\xi_i}, k_{\xi\eta_i}, k_{\eta\xi_i}, k_{\eta\eta_i}$	fixed-pad spring coefficients of oil film of the $i$ th pad
$k_{jk}, k_{j\delta}, k_{\delta ik}, k_{\delta\delta i}$	global spring coefficients of oil film
$m$	half of rotor mass
$m_p$	preload factor
$n$	total number of pad
$\Delta x, \Delta y$	small displacement of journal centre in the vertical and the horizontal directions
$\Delta\delta_i$	small angular displacement of the $i$ th pad
$\gamma_i$	pivot position angle of the $i$ th pad
$\delta_i$	tilt angle of the $i$ th pad
$\psi_i$	$= \Delta\delta_i R_p / C_b$
$\iota$	$= I / (m R_p^2)$ dimensionless moment of inertia of pad
$\lambda$	$= \mu LR (R / C_p)^2 (g / C_p)^{1/2} / (\pi W)$ bearing modulus
$\mu$	lubricant viscosity
$\nu$	$= \omega / (g / C_p)^{1/2}$ dimensionless shaft speed
$\nu_c$	dimensionless stability threshold shaft speed
$\tau$	$= \omega t$ dimensionless time
$\omega$	shaft speed

#### Superscripts

( $\cdot$ )	differential with respect to $t$
( $\cdot$ ) $'$	differential with respect to $\tau$

#### Subscripts

$i$	ordinal number of pad
$j, k$	$x$ or $y$

## 1. INTRODUCTION

Tilting pad journal bearings are widely used in high speed rotating machinery because the bearings are superior to other journal bearings in the capability of suppressing oil whip which often occurs at high shaft speeds, though a large moment of inertia of bearing pad is known to cause oil whip at very high shaft speeds. The bearings, however, have been occasionally reported to cause oil whip [1-6], even if the moment of inertia of bearing pad is small. These reports show that oil whip can occur when the bearings with low preloaded pads are operated at high shaft speeds and under low bearing loads. Consequently the highly preloaded bearings can be a practical solution for rotating machinery operated under such conditions, though the mechanism of the oil whip of tilting pad journal bearing has not been fully explained, based

on theoretical analysis.

On the other hand, the highly preloaded bearings are known to cause higher  $Q$  values, that is, the higher vibration response of rotor at critical speeds. Thus pad preload is trade-off for suppressing oil whip and decreasing the sensitivity to unbalance excitation for high speed rotating machinery equipped with tilting pad journal bearings.

As newly designed rotating machinery is expected to satisfy both stable operation at higher shaft speeds and reasonably low  $Q$  values, design engineers need to understand the effect of pad preload on the stability behaviour of the journal bearing much more qualitatively and quantitatively.

The linear spring and damping coefficients of bearing oil film are a main factor that dominates oil whip stability of rotating machinery equipped with journal bearings, and the cross-coupling spring coefficients are known to reduce stability. However no cross-coupling spring and damping coefficients are obtained for tilting-pad journal bearings if calculation is carried out in the same way as ordinary fixed-bore journal bearings.

On the other hand, Lund [7] obtained four cross-coupling coefficients of spring and damping as well as four direct spring and damping coefficients of the bearing with pad inertia being included, and suggested that the bearing could be unstable if pad inertia was incorporated.

Allaire *et al.*[8] presented a method to calculate a full set of the spring and damping coefficients of tilting pad journal bearing. Each number of the spring or the damping coefficients is  $5n+4$  respectively. However they did not show the results of the application of this method to the unstable vibration of tilting pad journal bearing.

Parsell *et al.* [9] obtained eight rotordynamic coefficients of the bearing from the  $(5n+4)$  coefficients of Allaire *et al.* [8], assuming that the journal and the pads are oscillating at subsynchronous frequencies. They obtained negative direct terms of damping coefficient with the effect of pad inertia being neglected in the case of high Sommerfeld number and also low preloaded pad, and they suggested that tilting pad journal bearing could be unstable even if the effect of pad inertia was neglected.

## 2. THEORETICAL ANALYSIS

### 2.1 A full set of rotordynamic coefficients

The authors use a full set of rotordynamic coefficients presented by Allaire *et al.*[8] to analyse the stability of the rotor-bearing systems, but use a method which is different from their method in obtaining the rotordynamic coefficients.

Figure 1 shows a schematic of a five-pad tilting-pad journal bearing with a rotating journal at its static equilibrium.  $x$  and  $y$  are the vertical and the horizontal coordinates on the cross section of the bearing respectively. It is assumed that each pad is constrained on its pivot and

has a single degree of freedom of tilting around the pivot. The tilt angle  $\delta_i$  of the  $i$ th pad is defined as the angle between  $\overline{O_B P_i}$  and  $\overline{O_{P_i} P_i}$  where  $O_B$  is the centre of the bearing,  $O_{P_i}$  the centre of pad curvature and  $P_i$ , the pivot point.  $\xi_i$  and  $\eta_i$  represent the local orthogonal coordinates of the  $i$ th pad with the origin at  $O_{P_i}$ .

When the journal and each pad are perturbed at the static equilibrium, the vertical and the horizontal components of incremental oil film forces acting on the journal and the incremental oil film moment acting on each pad are assumed to be expressed in the following linear form:

$$\Delta F_x = c_{xx} \Delta \dot{x} + c_{xy} \Delta \dot{y} + k_{xx} \Delta x + k_{xy} \Delta y + \sum_{i=1}^5 (c_{x\delta_i} \Delta \dot{\delta}_i + k_{x\delta_i} \Delta \delta_i), \quad (1)$$

$$\Delta F_y = c_{yx} \Delta \dot{x} + c_{yy} \Delta \dot{y} + k_{yx} \Delta x + k_{yy} \Delta y + \sum_{i=1}^5 (c_{y\delta_i} \Delta \dot{\delta}_i + k_{y\delta_i} \Delta \delta_i), \quad (2)$$

$$\Delta M_i = c_{\delta x} \Delta \dot{x} + c_{\delta y} \Delta \dot{y} + k_{\delta x} \Delta x + k_{\delta y} \Delta y + c_{\delta \delta_i} \Delta \dot{\delta}_i + k_{\delta \delta_i} \Delta \delta_i, \quad i=1, \dots, 5. \quad (3)$$

where  $\Delta x$ ,  $\Delta y$  are small displacements of the journal centre, and  $\Delta \delta_i$  is a small angular displacement of the  $i$ th pad, and  $\Delta \dot{x}$ ,  $\Delta \dot{y}$  are small velocities of the journal centre and  $\Delta \dot{\delta}_i$ , a small angular velocity of the  $i$ th pad. The numbers of spring coefficients or damping coefficients are  $n+2$  in each of Eqs. (1) and (2), and  $3n$  in Eq. (3), in total,  $5n+4$ . These coefficients are called a full set of rotordynamic coefficients.

When the journal moves from its equilibrium by  $\Delta \xi_i$  or  $\Delta \eta_i$  in the local coordinate system with the tilt angle of each pad being fixed at equilibrium, the four components of the incremental oil film force are divided by  $\Delta \xi_i$  or  $\Delta \eta_i$ . Then, the four fixed-pad spring coefficients, that is,  $k_{\xi \xi_i}$ ,  $k_{\xi \eta_i}$ ,  $k_{\eta \xi_i}$ ,  $k_{\eta \eta_i}$ , are obtained in the local coordinate system for each pad.

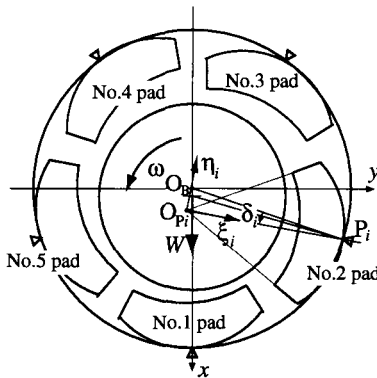


Fig. 1 A schematic of 5 pad tilting-pad journal bearing

Next, each pad is assumed to have the incremental tilt angle  $\Delta \delta_i$  from its equilibrium with the journal centre remaining at its equilibrium to obtain the rotordynamic coefficients for the pad

tilt motion. Allaire *et al.* [8] actually calculated and obtained the coefficients. However, the authors of this paper adopt another approach as follows: The tilt motion  $\Delta\delta_i$  of each pad moves the centre of pad curvature  $O_{pi}$  by  $R_p \Delta\delta_i$  along an arc, which can be regarded a linear motion in the  $\eta_i$  direction, because  $\Delta\delta_i$  is very small. Alternatively, this pad motion is equivalent to the linear motion  $R_p \Delta\delta_i$  of the journal centre in the opposite direction with the pad fixed at its equilibrium. Consequently, the rotordynamic coefficients for pad tilt motion need not be calculated independently, but two of the fixed-pad coefficients,  $\kappa_{\xi\eta_i}$  and  $\kappa_{\eta\eta_i}$  can be appropriated for.

Then, Eq. (4) shows the incremental components of oil film spring force in the local coordinate system with the original and the additional journal motion being considered.

$$\begin{pmatrix} \Delta F_{\xi_i} \\ \Delta F_{\eta_i} \end{pmatrix}_{spring} = \begin{pmatrix} k_{\xi\xi_i} & k_{\xi\eta_i} \\ k_{\eta\xi_i} & k_{\eta\eta_i} \end{pmatrix} \begin{pmatrix} \Delta\xi_i \\ \Delta\eta_i + R_p \Delta\delta_i \end{pmatrix}. \quad (4)$$

These two components are expressed in the global coordinate system as follows:

$$\begin{pmatrix} \Delta F_{x_i} \\ \Delta F_{y_i} \end{pmatrix}_{spring} = \begin{pmatrix} \cos\gamma_i & -\sin\gamma_i \\ \sin\gamma_i & \cos\gamma_i \end{pmatrix} \begin{pmatrix} \Delta F_{\xi_i} \\ \Delta F_{\eta_i} \end{pmatrix}_{spring}. \quad (5)$$

The coordinate transformation from the  $x$ - $y$  system to the  $\xi_i$ - $\eta_i$  system is expressed as follows:

$$\begin{pmatrix} \Delta\xi_i \\ \Delta\eta_i \end{pmatrix} = \begin{pmatrix} \cos\gamma_i & \sin\gamma_i \\ -\sin\gamma_i & \cos\gamma_i \end{pmatrix} \begin{pmatrix} \Delta x \\ \Delta y \end{pmatrix}. \quad (6)$$

Substituting Eq. (6) into Eq. (4), then Eq. (4) into Eq. (5), Eq. (7) is obtained as follows

$$\begin{aligned} \begin{pmatrix} \Delta F_{x_i} \\ \Delta F_{y_i} \end{pmatrix}_{spring} &= \begin{pmatrix} \cos\gamma_i & -\sin\gamma_i \\ \sin\gamma_i & \cos\gamma_i \end{pmatrix} \begin{pmatrix} k_{\xi\xi_i} & k_{\xi\eta_i} \\ k_{\eta\xi_i} & k_{\eta\eta_i} \end{pmatrix} \begin{pmatrix} \cos\gamma_i & \sin\gamma_i \\ -\sin\gamma_i & \cos\gamma_i \end{pmatrix} \begin{pmatrix} \Delta x \\ \Delta y \end{pmatrix} \\ &+ R_p \begin{pmatrix} \cos\gamma_i & \sin\gamma_i \\ -\sin\gamma_i & \cos\gamma_i \end{pmatrix} \begin{pmatrix} k_{\xi\eta_i} \\ k_{\eta\eta_i} \end{pmatrix} \Delta\delta_i. \end{aligned} \quad (7)$$

Equation (7) gives the incremental components of oil film spring force under a pad in the global system when the journal is given a small displacement and also the pad is given a small increment of tilt angle at equilibrium, respectively.

Similarly, the incremental components of oil film damping force under a pad are expressed in the global system with the four fixed-pad damping coefficients of the pad as follows:

$$\begin{pmatrix} \Delta F_{xi} \\ \Delta F_{yi} \end{pmatrix}_{damping} = \begin{pmatrix} \cos \gamma_i & -\sin \gamma_i \\ \sin \gamma_i & \cos \gamma_i \end{pmatrix} \begin{pmatrix} c_{\xi\xi_i} & c_{\xi\eta_i} \\ c_{\eta\xi_i} & c_{\eta\eta_i} \end{pmatrix} \begin{pmatrix} \cos \gamma_i & \sin \gamma_i \\ -\sin \gamma_i & \cos \gamma_i \end{pmatrix} \begin{pmatrix} \Delta \dot{x} \\ \Delta \dot{y} \end{pmatrix} \\ + R_p \begin{pmatrix} \cos \gamma_i & \sin \gamma_i \\ -\sin \gamma_i & \cos \gamma_i \end{pmatrix} \begin{pmatrix} c_{\xi\eta_i} \\ c_{\eta\eta_i} \end{pmatrix} \Delta \hat{\delta}_i. \quad (8)$$

The sum of Eqs. (7) and (8) gives the contribution of a pad to the spring and damping components of the incremental oil film forces expressed in the global coordinate system. Furthermore the forces are summed up with respect to all the pads, and the  $x$  component and also the  $y$  component of the oil film force are obtained in the global coordinate system.

Each side of the expression of the  $x$  or  $y$  component is compared with that of Eq. (1) or (2), respectively. Then, Eqs. (9) to (12) are obtained as follows:

$$\begin{pmatrix} k_{xx} & k_{xy} \\ k_{yx} & k_{yy} \end{pmatrix} = \sum_{i=1}^5 \begin{pmatrix} \cos \gamma_i & -\sin \gamma_i \\ \sin \gamma_i & \cos \gamma_i \end{pmatrix} \begin{pmatrix} k_{\xi\xi_i} & k_{\xi\eta_i} \\ k_{\eta\xi_i} & k_{\eta\eta_i} \end{pmatrix} \begin{pmatrix} \cos \gamma_i & \sin \gamma_i \\ -\sin \gamma_i & \cos \gamma_i \end{pmatrix}, \quad (9)$$

$$\begin{pmatrix} k_{x\delta_i} \\ k_{y\delta_i} \end{pmatrix} = R_p \begin{pmatrix} \cos \gamma_i & \sin \gamma_i \\ -\sin \gamma_i & \cos \gamma_i \end{pmatrix} \begin{pmatrix} k_{\xi\eta_i} \\ k_{\eta\eta_i} \end{pmatrix} \quad i=1, \dots, 5, \quad (10)$$

$$\begin{pmatrix} c_{xx} & c_{xy} \\ c_{yx} & c_{yy} \end{pmatrix} = \sum_{i=1}^5 \begin{pmatrix} \cos \gamma_i & -\sin \gamma_i \\ \sin \gamma_i & \cos \gamma_i \end{pmatrix} \begin{pmatrix} c_{\xi\xi_i} & c_{\xi\eta_i} \\ c_{\eta\xi_i} & c_{\eta\eta_i} \end{pmatrix} \begin{pmatrix} \cos \gamma_i & \sin \gamma_i \\ -\sin \gamma_i & \cos \gamma_i \end{pmatrix}, \quad (11)$$

$$\begin{pmatrix} c_{x\delta_i} \\ c_{y\delta_i} \end{pmatrix} = R_p \begin{pmatrix} \cos \gamma_i & \sin \gamma_i \\ -\sin \gamma_i & \cos \gamma_i \end{pmatrix} \begin{pmatrix} c_{\xi\eta_i} \\ c_{\eta\eta_i} \end{pmatrix} \quad i=1, \dots, 5. \quad (12)$$

Thus the  $(2n+4)$  elements of global spring coefficients and also the  $(2n+4)$  elements of global damping coefficients shown in Eqs. (1) and (2) are now available.

Then the remaining  $3n$  elements of spring or damping coefficients shown in Eq. (3) will be obtained as follows: The frictional torque acting on each pad surface is assumed to be negligibly small. Then the moment  $\Delta M_i$  of oil film force acting on the pad is expressed in the local coordinate system as shown in Eq. (13) because  $\Delta F_{\xi}$  has no contribution to the moment which is calculated with respect to the pivot point.

$$\Delta M_i = R_p \Delta F_{\eta_i}. \quad (13)$$

First, the spring component  $\Delta F_{\eta_i \text{ spring}}$  of  $\Delta F_{\eta_i}$  shown in Eq. (4) is considered. Equation (6) is substituted into Eq. (4), and then Eq. (4) into Eq. (13), resulting in Eq. (14) which gives the spring component of the incremental oil film moment under the  $i$ th pad as follows:

$$\Delta M_{i \text{ spring}} = R_p \begin{pmatrix} k_{\eta\xi_i} & k_{\eta\eta_i} \end{pmatrix} \begin{pmatrix} \cos \gamma_i & -\sin \gamma_i \\ \sin \gamma_i & \cos \gamma_i \end{pmatrix} \begin{pmatrix} \Delta x \\ \Delta y \end{pmatrix} + R_p^2 k_{\eta\eta_i} \Delta \delta_i. \quad (14)$$

Similarly, the damping component of the incremental oil film moment under the  $i$ th pad is given as follows:



$$\Delta M_{idamping} = R_p \begin{pmatrix} c_{\eta\zeta i} & c_{\eta\eta i} \end{pmatrix} \begin{pmatrix} \cos \gamma_i & -\sin \gamma_i \\ \sin \gamma_i & \cos \gamma_i \end{pmatrix} \begin{pmatrix} \Delta \dot{x} \\ \Delta \dot{y} \end{pmatrix} + R_p^2 c_{\eta\eta i} \Delta \dot{\delta}_i, \quad (15)$$

The sum of Eqs. (14) and (15) gives the contribution of a pad to the spring and damping components of the incremental oil film moments expressed in the global coordinate system. Furthermore the components are summed up with respect to all the pads, and the oil film moment are obtained.

Each side of the expression of the moment is compared with that of Eq. (3). Then, Eqs. (16) to (19) are obtained as follows:

$$\begin{pmatrix} k_{\delta\delta x} \\ k_{\delta\delta y} \end{pmatrix} = R_p \begin{pmatrix} k_{\eta\zeta i} & k_{\eta\eta i} \end{pmatrix} \begin{pmatrix} \cos \gamma_i & -\sin \gamma_i \\ \sin \gamma_i & \cos \gamma_i \end{pmatrix} \quad i=1, \dots, 5, \quad (16)$$

$$k_{\delta\delta i} = R_p^2 k_{\eta\eta i} \Delta \delta_i \quad i=1, \dots, 5, \quad (17)$$

$$\begin{pmatrix} c_{\delta\delta x} \\ c_{\delta\delta y} \end{pmatrix} = R_p \begin{pmatrix} c_{\eta\zeta i} & c_{\eta\eta i} \end{pmatrix} \begin{pmatrix} \cos \gamma_i & -\sin \gamma_i \\ \sin \gamma_i & \cos \gamma_i \end{pmatrix} \quad i=1, \dots, 5, \quad (18)$$

$$c_{\delta\delta i} = R_p^2 c_{\eta\eta i} \Delta \delta_i \quad i=1, \dots, 5. \quad (19)$$

As the  $3n$  spring and the  $3n$  damping coefficients are obtained, all the elements of the full set of linear spring and damping coefficients of the tilting-pad journal bearing are now available from Eqs. (9) to (12), and Eqs. (16) to (19), once the eight fixed-pad rotordynamic coefficients are calculated for each pad at equilibrium. It should be noted that these coefficients are independent of pad inertia and vibration frequency. The values of the coefficients obtained by means of the present method were confirmed to be equal to those obtained by means of the method of Allaire *et al* [8].

## 2.2 Stability analysis

A rigid Jeffcott rotor is assumed to rotate in two identical tilting-pad journal bearings at both ends. With the full set of spring and damping coefficients obtained in the last section, the dimensionless equations of motion of the rotor and the pads are expressed as follows:

$$v^2 X'' + C_{xx} X' + C_{yy} Y' + K_{xx} X + K_{yy} Y + \sum_{i=1}^5 (C_{x\delta i} \psi_i' + K_{x\delta i} \psi_i) = 0 \quad (20)$$

$$v^2 Y'' + C_{yx} X' + C_{yy} Y' + K_{yx} X + K_{yy} Y + \sum_{i=1}^5 (C_{y\delta i} \psi_i' + K_{y\delta i} \psi_i) = 0 \quad (21)$$

$$i v^2 \psi_i'' + C_{\delta x} X' + C_{\delta y} Y' + K_{\delta x} X + K_{\delta y} Y + C_{\delta\delta i} \psi_i' + K_{\delta\delta i} \psi_i = 0 \quad i=1, \dots, 5, \quad (22)$$

The first two equations represent the translational motions of the rotor in the vertical and the horizontal directions, and the third one, the tilt motion of the  $i$ th pad with respect to its pivot point.

The linear stability of the rotor-bearing system is determined as follows: A characteristic

equation of the system is derived from Eqs. (20) to (22), and numerically solved for complex eigenvalues for a specific operating condition by means of the QR method. The system is stable if the maximum real part is negative, and unstable if positive. Consequently the stable-unstable boundary is searched for numerically with the shaft speed being swept, and is obtained where the maximum real part changes its sign. This calculation is conducted over a wide range of  $\lambda$ , and a stability chart is obtained for a specific rotor-bearing system.

Table 1 shows the specification of the bearing used in the calculation. The values of pad number,  $L/D$  and pad angle are fixed. The effect of the load directions, LOP and LBP is examined. Preload factor covers a wide range from 0 to 0.6. The dimensionless pad inertia covers a wide range of order of magnitude, and the practical value of  $t$  is known to be about  $10^{-4}$  for actual bearing pads.

The laminar isoviscous Reynolds equation is numerically solved for the hydrodynamic pressure in the oil film, and a full set of the rotordynamic coefficients are calculated. If the equilibrium of a pad can not be determined for a given eccentricity ratio of the journal because of no hydrodynamic pressure under the pad, which often occurs with upper pads, the pads are assumed to have no contribution to the rotordynamic coefficients of the bearing.

Table 1 Bearing specification for calculation

Total number of pad	5
Load direction	Load-On-Pad (LOP) Load-Between-Pads(LBP)
$L/D$	0.4
Pad angle	60°
Pivot position	Center pad
Preload factor $m_p$	0, 0.05, 0.1, 0.15, 0.3, 0.6
Dimensionless pad inertia $t$	$10^{-5}$ , $10^{-4}$ , $10^{-3}$

### 3. RESULTS AND DISCUSSIONS

Figures 2 through 5 show the stability charts obtained. The horizontal coordinate  $\lambda$  represents the bearing modulus, and the vertical one  $v$ , the dimensionless shaft speed. Both coordinates are scaled logarithmically.  $\lambda$  looks like the Sommerfeld number as shown in NOTATION, but it should be noted that the term of shaft speed is not included. The lines shown in each figure correspond to the boundaries between stable and unstable regions of operation of the rotor-bearing system, and the system can be in stable operation in the region below the lines, while it is unstable in the region above them.

Figure 2 (a) corresponds to the case of  $m_p=0$  and LOP, while Fig. 2 (b), to the case of  $m_p=0$  and LBP. In both charts, the stability threshold  $v_c$  is found to decrease monotonically with increasing  $\lambda$ , and levels off eventually. Both pad inertia and load direction are found to have little effect on the stability threshold in the calculated range of  $\lambda$ . Consequently tilting-pad journal bearings with zero preload factor can be unstable at high shaft speeds, which is not

caused by large pad inertia. The threshold speed can be very low for large  $\lambda$ . Consequently small  $\lambda$  must be selected to keep the rotor-bearing system stable up to high shaft speeds.

Figure 3 (a) corresponds to the case of  $m_p=0.1$  and LOP. The stability threshold decreases with increasing  $\lambda$  up to around 0.7 and is affected little by pad inertia, which is similar to the case of  $m_p=0$  shown in Fig. 2 (a). On the contrary, the stability threshold increases with increasing  $\lambda$  above around 0.7, and is affected greatly by pad inertia. The larger the pad inertia, the lower the threshold speed.

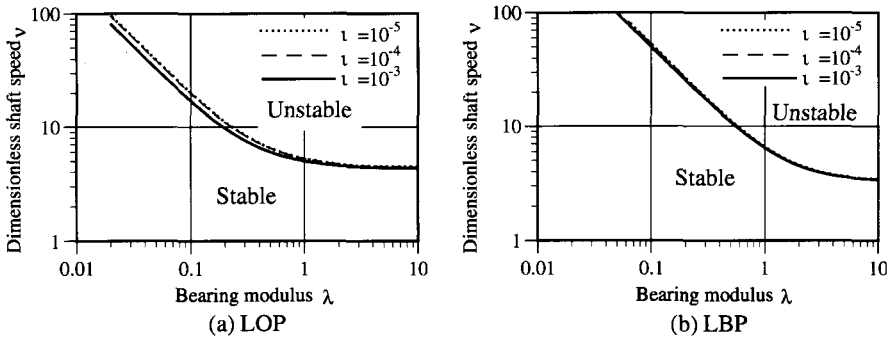


Fig. 2 Stability charts ( $m_p=0$ )

Figure 3 (b) corresponds to the case of  $m_p=0.1$  and LBP. The stability threshold decreases with increasing  $\lambda$  up to 0.3 and increases sharply beyond  $\lambda=0.6$ , which is similar to the case shown in Fig. 3 (a). However, for  $\lambda$  between 0.3 and 0.6, the boundary lines bend sharply, making peaks.

In both charts, Sommerfeld number was found to be constant on each of the boundary lines slanting to the right in the range of lower  $\lambda$ . Furthermore the anti-load side pads were found to develop hydrodynamic pressure only in the region above the slanting boundary lines. Consequently in the range of lower  $\lambda$ , the rotor-bearing system turns unstable above a shaft speed due to the anti-load side pads that become active above the shaft speed. Because of that, pad inertia does not affect the stability of the system much in this region of lower  $\lambda$ . Furthermore this result implies that the system can remain stable even at higher shaft speeds in this region, if anti-load side pads are removed.

In the case of LOP, two anti-load side pads are arranged in a symmetrical position with respect to the static load line. Consequently the critical Sommerfeld number corresponding to the development of hydrodynamic pressure is the same for the two pads because the journal comes up vertically along the load line in the bearing clearance, and the two pads become active at the same time. On the other hand, in the case of LBP, there are one top pad and two neighbouring pads positioned slightly downward of the former on the anti-load side of the bearing. Consequently the critical Sommerfeld number for the top pad is reached later than that for the two neighbouring pads with increasing shaft speed, and after the two neighbouring

pads become active, the top pad becomes active. This explains the difference of the stability behaviour between LOP and LBP around the bottom of the threshold.

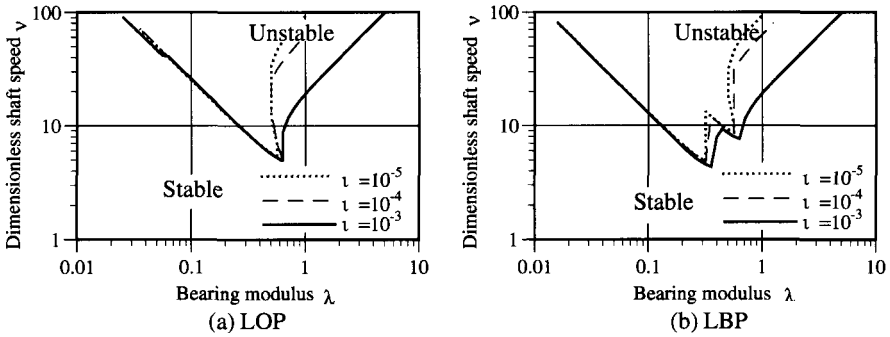


Fig. 3 Stability charts ( $m_p=0.1$ )

Figure 4 (a) corresponds to the case of  $m_p=0.15$  and LOP. The stability boundary in the case of  $\tau=10^{-3}$  is similar to that in the case of  $m_p=0.1$  and LOP, shown in Fig. 3 (a). On the other hand, in the cases of  $\tau=10^{-4}$  and  $10^{-5}$ , the region of unstable operation is drastically reduced to the slanting narrow 'island' surrounded by the upper and lower boundary lines. Consequently, the system with smaller pad inertia becomes once unstable with increasing shaft speed in the region of lower  $\lambda$ , but it reverts to stable operation with further increase in shaft speed.

Figure 4 (b) corresponds to the case of  $m_p=0.15$  and LBP. The unstable operation region splits into two parts in the case of lower pad inertia, and the rotor-bearing system repeats the stable-unstable conversion four times with increasing shaft speed.

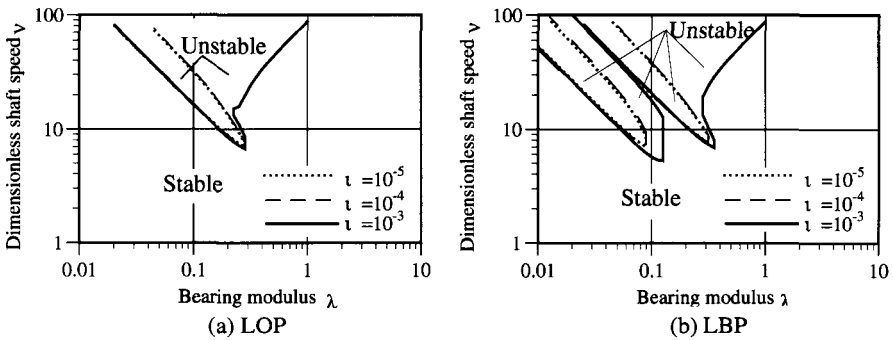


Fig. 4 Stability charts ( $m_p=0.15$ )

Figure 5 (a) and (b) show the effects of preload factor  $m_p$  in the case of  $\tau=10^{-4}$ , a standard value of inertia of pad in practical use. Increasing preload factor improves stability of tilting-pad journal bearing drastically in the region of higher  $\lambda$ , while, in the region of lower  $\lambda$ , the unstable operation region gradually reduces, though the threshold speed, if any, is not affected much. As a whole, the higher the prelaod factor, the larger the stable operation region. This

agrees at least qualitatively with the results obtained in test rigs [1], [2] or in an actual machine[4].

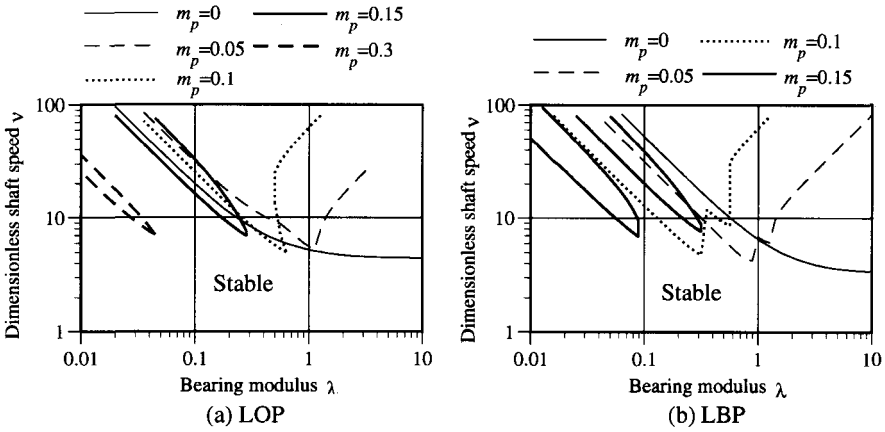


Fig. 5 Variation of preload factor ( $\epsilon=10^{-4}$ )

#### 4. CONCLUSIONS

The linear stability of a rigid rotor supported in tilting-pad journal bearing was analyzed theoretically with a full set of linear spring and damping coefficients for a wide range of operating and geometric conditions. Some stability charts were obtained and discussion followed. The following conclusions are derived.

1. Tilting-pad journal bearings with low preload factor can cause oil whip even if pad inertia is negligibly small.
2. Increasing preload factor improves stability of tilting-pad journal bearing drastically in the region of higher bearing modulus, while the region of unstable operation gradually reduces with increasing preload factor in the region of lower bearing modulus. As a whole, the higher the prelaod factor, the larger the stable operation region.
3. Pad inertia has a great effect on the stability threshold in the case of lower preload factor in the region of higher bearing modulus and lowers the stability threshold, but it has little effect in the region of lower bearing modulus.
4. Load direction has little effect on the stability behaviour in the region of higher bearing modulus, but in the region of lower bearing modulus, the unstable operation region changes its shape, depending on load direction.

The present theoretical model can explain the unstable vibration of rotor in tilting-pad journal bearings observed in test rigs or in actual machine.

## ACKNOWLEDGEMENT

This research project was partially supported by Grant-in-Aid for Scientific Research No. 11-09849 from the Ministry of Education, Science, Sports and Culture of Japan.

## REFERENCES

- 1 **Orcutt, F. K.**, The Steady State and Dynamic Characteristics of the Tilting-pad Journal Bearing in Laminar and Turbulent Flow Regimes, *Trans. ASME, Ser. J*, 1967, Vol. 89, pp. 392-404.
- 2 **Saito, S.**, *Trans. Jpn. Soc. Mech. Eng. (C)*, 1981, Vol. 47, No. 413, pp. 30-37.
- 3 **Flack, R. D.** and **Zuck, C. J.**, Experiments on the Stability of Two Flexible Rotors in Tilting Pad Bearings, *Tribology Trans.*, 1988, Vol. 31, pp. 251-257.
- 4 **Lie, Y., Xie Y. B., Jun, Z.** and **Damou, Q.**, Experiments on the destabilizing factor in tilting-pad bearings, *Tribology International*, 1989, Vol. 22, pp.329-334.
- 5 Text of Course, 1991, *Jpn. Soc. Mech. Eng*, No. 920-17, Vol.1, pp. 100-101.
- 6 Text of Course, 1995, *Jpn. Soc. Mech. Eng*, No. 95-I-8, pp. 20-21.
- 7 **Lund, J. W.**, Spring and Damping Coefficients for the Tilting-pad Journal Bearing, *ASLE Trans.*, 1965, Vol. 7, pp. 342-352.
- 8 **Allaire, P. E., Parsell, J. K.** and **Barrett, L. E.**, A Pad Perturbation Method for the Dynamic Coefficients of Tilting-Pad Journal Bearings, *Wear*, 1981, Vol. 72, pp. 29-44.
- 9 **Parsell, J. K., Allaire, P. E.** and **Barrett, L. E.** Frequency Effects in Tilting-pad Journal Bearing Dynamic Coefficients, *ASLE Trans.*, 1983, Vol. 26, pp. 222-227.

# **A non-linear transfer matrix technique for statically indeterminate rotor bearing systems**

**A LIEW, N S FENG, and E J HAHN**

School of Mechanical and Manufacturing Engineering, University of New South Wales, Australia

## **ABSTRACT**

Transfer matrix methods have long been used to obtain the vibration behaviour of linearised rotor bearing systems. Recently the technique has been enhanced to find the unbalance response of statically determinate systems with hydrodynamic bearing type non-linearities. This paper further extends the non-linear approach to statically indeterminate systems, enabling application to practical rotating machinery. The technique is illustrated on simple unbalanced rotor bearing systems with two and four bearings. It is shown that in statically indeterminate systems, unbalance may affect not only the orbit size and shape but also the load distribution between the bearings, and hence the system response.

## **1. INTRODUCTION**

Transfer matrix (TM) methods have long been used as a quick and efficient way of obtaining solutions to the vibration behaviour of linearised rotor bearing systems (1). Rao (2) summarises the basic methodology of the TM method for both torsional and transverse vibrations. A problem with the traditional TM method is that it is limited to linearised systems whereas bearing forces frequently cannot be adequately represented by linear combinations of journal displacement and velocity (3). In linear systems, unbalance responses must be stable and synchronous with the respective excitation frequencies, whereas in systems with non-linear bearing forces, one can also obtain significant non-synchronous components.

A common way of dealing with non-linear bearing forces is to use transient analysis. Such methods are very powerful in solving rotor dynamics problems but, in the experience of the authors, require excessive computer resources for parametric studies. A more practical technique for evaluating the steady state unbalance response of non-linear rotor bearing systems is harmonic balance (4). Using harmonic balance concepts, Yamauchi (5) extended

the TM approach to determine periodic type unbalance responses of rotor bearing systems with non-linear elements, assuming a cubic function type non-linearity; and Liew et al (6) applied the TM technique to obtain unbalance responses of flexible rotor bearing systems with squeeze film damper and/or hydrodynamic bearing type non-linearity. Both of these non-linear extensions were limited to statically determinate systems.

In statically indeterminate systems, where rotors are supported on three or more bearings (there are eleven or more bearings in some practical turbogenerator systems where the rotors of the various stages are rigidly coupled) the configuration state (i.e. the relative locations of the bearings) can play a significant role in the vibration behaviour of the rotating machinery (7-10). This paper shows how TM techniques can be used to evaluate the unbalance response of such more realistic multiple bearing machines, using as illustration the effect of alignment change in machines with more than three bearings. Note that this paper is only concerned with unbalance response and all references to TMs are restricted to this context. Also, only transverse vibrations are considered here, though the theory could be applied equally well to torsional vibrations.

## 2. NOMENCLATURE

- C,D,L = Bearing clearance, diameter and length respectively. [m]  
E = Young's Modulus. [Pa]  
e = Journal eccentricity [m];  $\varepsilon$  = eccentricity ratio =  $e/C$ .  
 $e_{yi,zi}^a$  = Aligned eccentricity component in the y and z directions for bearing i. [m]  
 $e_{yi,zi}^m$  = Misaligned eccentricity component in the y and z directions for bearing i. [m]  
 $f_{r,s}$  = Fluid film forces acting on the journal in the radial and tangential directions. [N]  
 $\mathbf{G}$  = A type of shaft flexibility matrix. [ $\text{m N}^{-1}$ ]  
I = Second moment of area of shaft segment. [ $\text{m}^4$ ]  
 $I_{d,p}$  = Diametral and polar moments of inertia respectively. [ $\text{kg m}^2$ ]  
 $\mathbf{K}$  = A type of shaft stiffness matrix =  $\mathbf{G}^{-1}$ . [ $\text{N m}^{-1}$ ]  
 $L_i$  = Axial distance from the first bearing to the i'th bearing. [N]  
 $l_m$  = Axial distance from the first bearing to the left side of the m'th shaft segment. [m]  
 $M_{fy}$  = Bending moments in the y direction due to support reaction force variations. [Nm]  
 $M_{ui}$  = Bending moment due to a unit load applied to the rotor at bearing i. [N m]  
 $m_{yi,zi}$  = Misalignment of the i'th bearing housing in the y and z directions. [m]  
n = Number of bearings in the rotor bearing system.  
 $n_j$  = Index of shaft segment to the right of the j'th bearing.  
t = Time [s];  $\tau$  = dimensionless time =  $\omega t$ .  
x = Distance along the rotor from the first bearing support. [m]  
y, z = Displacements transverse to the rotor. Here y is vertical. [m]  
 $\delta_{yi,zi}$  = Change in position between the aligned rotor centre and the misaligned rotor centre at bearing i in the vertical and horizontal directions. [m]  
 $\Delta_{y,z}$  = Vector of the change in deflection shape of the rotor due to  $\Delta F_y$  and  $\Delta F_z$  in the vertical and horizontal directions [m];  $\Delta_{yi,zi}$  = element of  $\Delta_{y,z}$  corresponding to bearing i. [m]



- $\Delta \mathbf{F}_{y,z}$  = Vector of the change in mean or static bearing force component between the aligned and misaligned configurations in the vertical and horizontal directions [N];  $\Delta F_{y_i,z_i}$  = element of  $\Delta \mathbf{F}_{y,z}$  corresponding to bearing  $i$ . [N]
- $\mu$  = Absolute viscosity of bearing fluid. [Pa s]
- $\theta$  = Angular coordinate along the bearing surface measured from the point of maximum film thickness. [rad]
- $\theta_1$  = Value of  $\theta$  at which the pressure region becomes positive. [rad]
- $\rho$  = Material density. [ $\text{kg m}^{-3}$ ]
- $\omega$  = Rotor speed. [ $\text{rad s}^{-1}$ ]
- $\Omega$  = Fundamental frequency. [ $\text{rad s}^{-1}$ ]
- $\psi$  = Angular position of the line of centres with respect to the  $y$ -axis. [rad]
- $\dot{\phantom{x}}, \phantom{x}'$  = Differentiation with respect to  $t$  and  $\tau$ .

### 3. THEORY

#### 3.1 Statically determinate systems

Since the application of the TM technique to determine the unbalance response of statically determinate rotor bearing systems with hydrodynamic bearing type non-linearity is described in detail in (6), a brief summary of the procedure should suffice. The basic principle is that between non-linear elements, TMs can be formulated for all the linear elements (rotor segments) and multiplied together to form TMs between the rotor ends and the non-linear elements. For example, a system with 4 non-linear elements would have 5 TMs, two at the ends of the rotor and three between the non-linear elements. All the degrees of freedom (i.e. the displacements and rotations) at the non-linear elements, the so-called “non-linear degrees of freedom”, are the unknowns of the problem.

Assuming periodic solutions, the non-linear degrees of freedom and their time derivatives are defined in terms of harmonic components. Correspondingly, a set of TMs as described above is used for each harmonic of interest. For a guessed periodic solution (displacements and rotations), all forces are calculated using the appropriate non-linear functions, which relate the system motions to the forces. Since the resulting force expressions are necessarily periodic, their harmonic components, which will be functions of the guessed problem unknowns, can be applied to the appropriate TMs, which are used to calculate the non-linear degrees of freedom (displacements and rotations). By comparing the results with the guessed solution and iterating until convergence via a non-linear equation solver, an equilibrium solution is obtained. Upon solution for the non-linear degrees of freedom, the remaining degrees of freedom can be easily obtained by using element TMs. A flow diagram of the method is shown in Fig. 1.

Note that in common with the harmonic balance technique, only equilibrium periodic solutions can be found via this approach, and these depend on the initial guess. There is, therefore, no guarantee that all possible equilibrium solutions have been found. Also, the solution period has to be assumed right from the start. This is usually taken to be that corresponding to synchronous vibration, but if half frequency whirl were suspected, the logical choice would be twice that period. Finally, note that solution stability is not tested here. One could use methods such as presented in (4) or alternatively, one could use the solution as initial conditions to a transient program and see if the solution varies with time.

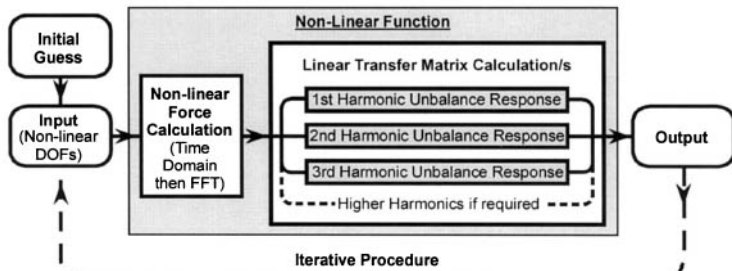


**Figure 1: The non-linear transfer matrix concept**

### 3.2 Statically indeterminate systems

For statically indeterminate rotor bearing systems, i.e. for systems with  $n$  support bearings where  $n \geq 3$ , the bearing reaction forces and hence the static deflection line of the rotor depend on the design of the bearings, the configuration state and the operating conditions; and the mean or static components of the bearing reaction forces are not known a priori. Practical turbogenerators, where individual rotors are rigidly coupled to form a single overall rotor supported on as many as eleven or more bearings, are examples of such systems.

In common with (7), we define the aligned state at some given speed to be that configuration state which, for a balanced rotor, results in no shear forces and bending moments at the rigid couplings. Before coupling the individual rotors together, they are either supported by two bearings, in which case they are statically determinate with static deflection lines determined by the reaction forces and journal eccentricities; or when they are supported by three bearings, two of the bearings are arbitrarily selected to be load carrying, thereby defining the static deflection line for such individual rotors as well. The aligned state then consists of the static deflection lines of the individual rotors, so joined that the positions and slopes are matched at the couplings; and with all the journals at eccentricities dictated by the corresponding reaction forces. In practice, this aligned state is referred to as quasi-catenary alignment (7). For convenience, positions are defined relative to the line joining the two centres of the end bearings. Note that because journal bearing eccentricities change with speed, the aligned state will generally be different at different speeds. Hence even if the actual configuration state agrees with the so defined aligned state, this will generally be at one speed only; at other speeds the configuration state will differ from the aligned state. At any speed, this difference between the configuration state and the aligned state corresponding to that speed is termed the misalignment at that speed. Note that only lateral misalignments are considered here. Any effects of angular misalignment are assumed to be negligible.

On positioning the misaligned rotor so that its static deflection line coincides with that of the aligned rotor at the first and last bearing, so that  $\Delta_{z1} = \Delta_{y1} = 0$  and  $\Delta_{zn} = \Delta_{yn} = 0$ , one can use shaft bending theory (11) to find the change in deflection shape between the aligned rotor and the misaligned rotor at the other  $n-2$  bearing locations, as a function of the change in the bearing reaction forces that result from the misalignment. Thus, the change in deflection shape is given by (as shown in the Appendix):

$$\Delta_{y_i} = \sum_{j=1}^{n-1} \sum_{m=n_j}^{n_{j+1}-1} \frac{l_{m+1} - l_m}{6E_m I_m} \left\{ \begin{aligned} & \left[ \left( \xi + l_m \frac{L_i}{L_n} \right) \sum_{k=1}^j \Delta F_{y_k} (2l_m + l_{m+1} - 3L_k) \right] \\ & + \left[ \left( \zeta + l_{m+1} \frac{L_i}{L_n} \right) \sum_{k=1}^j \Delta F_{y_k} (l_m + 2l_{m+1} - 3L_k) \right] \end{aligned} \right\} \quad (1)$$

$i = 2, 3, \dots, n-1,$

where

$$\xi = \begin{cases} -l_m & \text{for } l_m < L_i \\ -L_i & \text{for } l_m \geq L_i \end{cases} \quad \text{and} \quad \zeta = \begin{cases} -l_{m+1} & \text{for } l_{m+1} < L_i \\ -L_i & \text{for } l_{m+1} \geq L_i \end{cases}.$$

Additionally the equations of motion require that:

$$\sum_{i=1}^n \Delta F_{y_i} = 0 \quad \text{and} \quad \sum_{i=2}^n \Delta F_{y_i} L_i = 0. \quad (2)$$

The above equations may be written in matrix form as:

$$\Delta_y = G \times \Delta F_y \quad \text{or} \quad \Delta F_y = K \times \Delta_y. \quad (3)$$

Note that in the above  $y$  can be replaced by  $z$ .

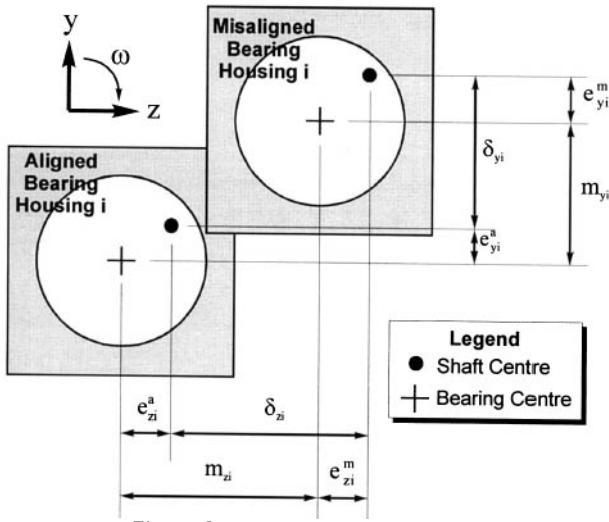


**Figure 2: Misalignment parameters**

Referring to Fig. 2, the differences between the position of the aligned rotor and the misaligned rotor ( $\delta_{y_i}$  and  $\delta_{z_i}$ ) are given by:

$$\delta_{y_i, z_i} = m_{y_i, z_i} - e_{y_i, z_i}^a + e_{y_i, z_i}^m \quad \text{for } i = 1, 2, \dots, n, \quad (4)$$

from which  $\Delta_y$  and  $\Delta_z$  can be calculated by simply shifting the misaligned rotor so that at  $i = 1$  and  $n$ , aligned and misaligned journal centres coincide. Thus:

$$\Delta_{y_i, z_i} = \delta_{y_i, z_i} - \delta_{y_1, z_1} - \frac{L_i}{L_n} (\delta_{y_n, z_n} - \delta_{y_1, z_1}) \quad \text{for } i = 1, 2, \dots, n. \quad (5)$$

Pre-multiplication of  $\Delta_y$  and  $\Delta_z$  by  $\mathbf{K}$  yields  $\Delta\mathbf{F}_y$  and  $\Delta\mathbf{F}_z$ . Adding these to the reaction forces acting on the aligned rotor yields the reaction forces acting on the misaligned rotor. Since the eccentricity components  $e_{y_i}^m$  and  $e_{z_i}^m$  (in equation 4) are not initially known and are non-linearly related to the reaction forces  $F_{y_i}$  and  $F_{z_i}$ , iteration is required. For assumed values of  $e_{y_i}^m$  and  $e_{z_i}^m$ , the above calculation procedure gives a force distribution which can be compared with that obtained from the fluid film force calculations. Under unbalance conditions this static calculation is combined with the dynamic TM calculations to form the non-linear problem, which is here solved using the Levenburg-Marquardt non-linear least squares approach.

#### 4. NUMERICAL EXAMPLES

The following assumptions apply to all examples:

- External excitation is solely from unbalance.
- The short bearing approximation (SBA) to Reynolds equation (with constant fluid properties) is valid.
- The pressures at the ends of the journal bearing are atmospheric.
- Only positive pressures contribute to the fluid film forces (ie.  $\pi$  film).
- The motion of the rotor within the bearing is periodic with shaft speed.
- The bearing housings are rigid.

Note that the examples presented here are purely for verification of the solution technique. For real situations the SBA may be inappropriate and a more costly bearing force function such as a finite difference solution to Reynolds equation may need to be used. Speeds in the following examples are chosen arbitrarily; they are near critical speeds but are well within the linear stability threshold. The forces exerted by the bearings on the rotor may then be written as (12):

$$\begin{bmatrix} f_r \\ f_s \end{bmatrix} = -\frac{\mu RL^3 \omega}{C^2} \left( \varepsilon (\psi' - \frac{1}{2}) \begin{bmatrix} I_{11} \\ I_{20} \end{bmatrix} + \varepsilon' \begin{bmatrix} I_{02} \\ I_{11} \end{bmatrix} \right), \quad (6)$$

$$\text{where: } I_{mn} = \int_{\theta_1}^{\theta_1 + \pi} \frac{\sin^m \theta \cos^n \theta d\theta}{(1 + \varepsilon \cos \theta)^3}, \quad \text{and } \theta_1 = \tan^{-1} \left( \frac{\varepsilon'}{\varepsilon (\psi' - \frac{1}{2})} \right).$$

##### 4.1 Statically determinate rotor bearing system

This example, although somewhat unrealistic, serves to illustrate some of the salient features of the non-linear TM technique and its capability for solving highly non-linear problems. Figure 3 is a schematic for the unbalanced statically determinate rotor with an unbalance of  $1 \times 10^{-4}$  kg-m at the central mass. Rapid convergence was obtained by first assuming a single

harmonic and then increasing the number of harmonics, each time using the previous solution as the initial guess. The solution was considered accurate when adding a harmonic no longer changed the orbit.

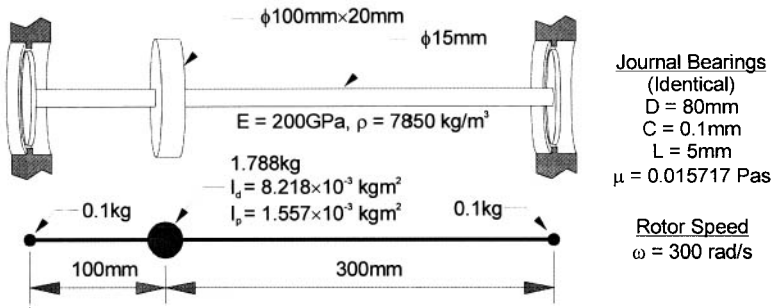


**Figure 3: Statically determinate rotor model**

Figure 4 compares the non-linear TM solution with the steady state solution obtained using a constant step size fourth order Runge-Kutta transient technique. For the transient solution the time steps were successively reduced until there was no change in the force evaluations. Note the perfect agreement between these solutions. Nine harmonics were used to obtain an accurate solution, necessitating the solution of a set of non-linear equations in seventy-six unknowns (viz. the Fourier coefficients defining the orbits in both bearings). Also shown is the orbit corresponding to the linearised bearing force solution. Here, the linearised solution predicts incorrect static displacements and impossible orbits.

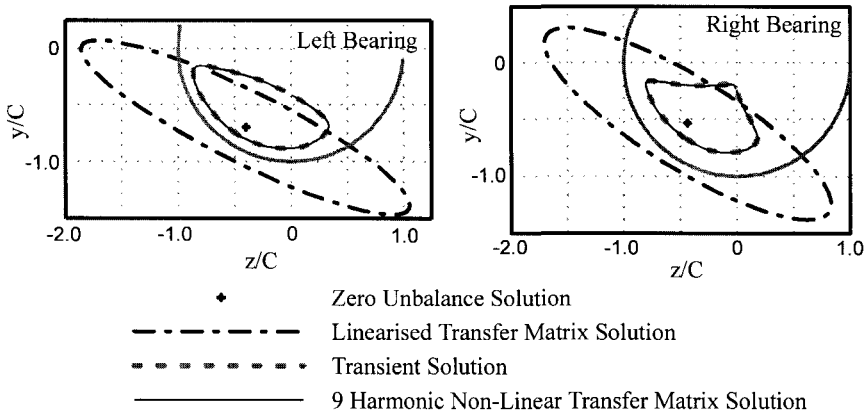


**Figure 4: Statically determinate rotor solution comparison**

#### 4.2 Statically indeterminate rotor bearing system

For statically indeterminate systems, the four bearing system shown in Fig. 5 (Rotor B coupled with Rotor A in (7)) was selected to illustrate the capabilities of the non-linear TM approach and the solution differences between it and the linearised approach. Table 1 contains the pertinent input data. A relatively simple lumped mass model was adopted to keep the calculation manageable for the transient analysis software used for checking solution

accuracy. For the non-linear solutions the linearised solutions were used as initial guesses. Transient analysis confirmed that all non-linear solutions were accurate.

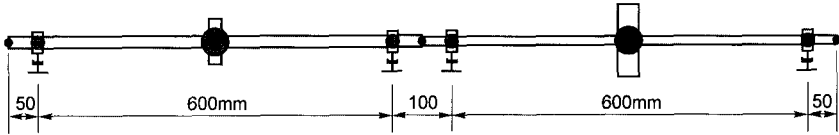


Figure 5: Statically indeterminate rotor dimensions

Table 1: Input data for statically indeterminate rotor bearing model

Mass #	Mass (kg)	Bearing Data				Shaft Data	
		L (m)	D (m)	C (m)	$\mu$ (Pa·s)	Length	Diameter
1	0.061654						
2	0.531011	0.018	0.036	$9 \times 10^{-5}$	$14 \times 10^{-3}$	0.05	0.02
3	5.939850					0.3	0.02
4	0.531011	0.018	0.036	$9 \times 10^{-5}$	$14 \times 10^{-3}$	0.3	0.02
5	0.096334					0.05	0.02
6	0.361618	0.018	0.036	$9 \times 10^{-5}$	$14 \times 10^{-3}$	0.05	0.015
7	9.616160					0.3	0.015
8	0.361618	0.018	0.036	$9 \times 10^{-5}$	$14 \times 10^{-3}$	0.3	0.015
9	0.034680					0.05	0.015

$I_p = I_d = 0.01 \text{ kg}\cdot\text{m}^2$  at masses 3 and 7;  $I_p = I_d = 0$  elsewhere.

$E = 200 \text{ GPa}$ ;  $\rho = 7850 \text{ kg}/\text{m}^3$ ; Unbalance:  $1 \times 10^{-3} \text{ kg}\cdot\text{m}$  at mass #7; Rotor Speed: 200 rad/s

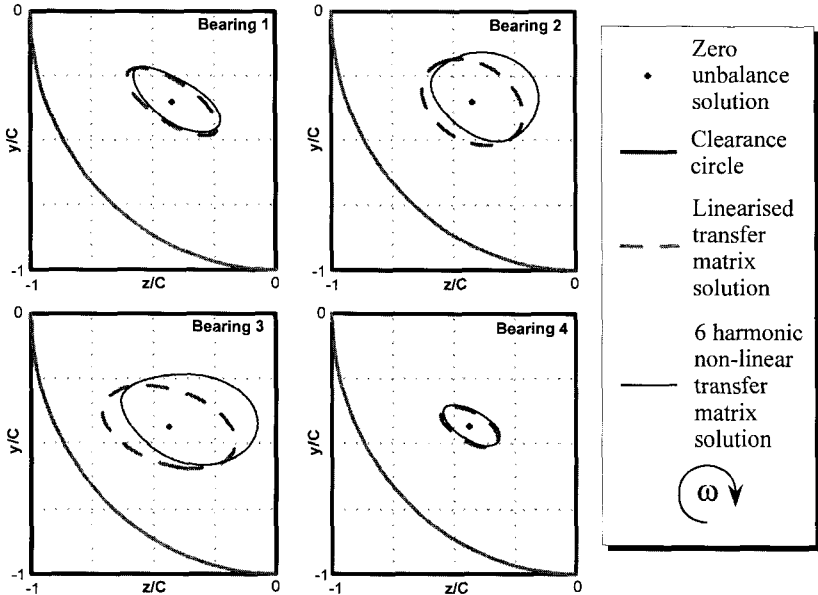
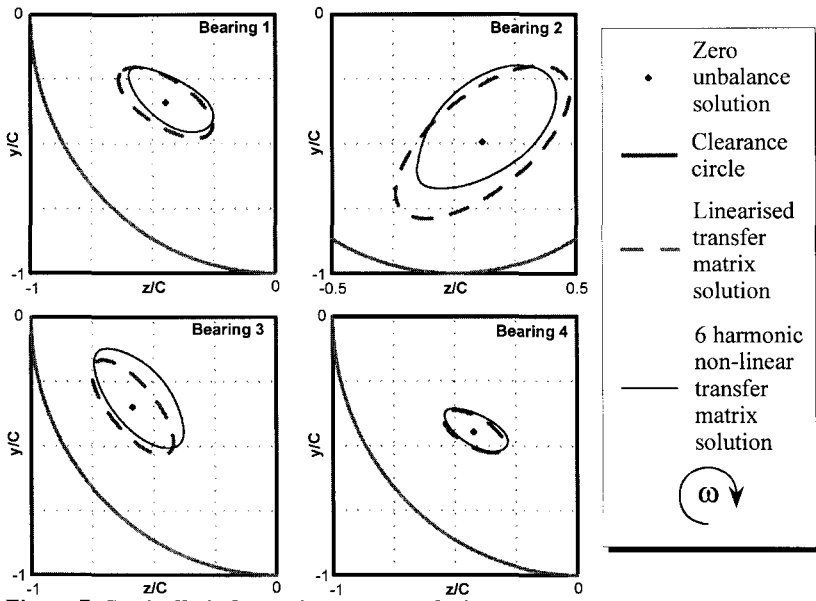


Figure 6: Statically indeterminate rotor solution comparison for the aligned configuration

Figure 6 compares the linearised and non-linear solutions with zero and finite unbalance for the aligned rotor (aligned at 200 rad/s). The zero unbalance solutions coincide, consisting only of static values; all reaction forces are vertical and there are zero shear forces and bending moments at the coupling. With an unbalance of  $1 \times 10^{-3}$  kg-m at the right hand disk, six harmonics were needed to represent the correct solution. There is a significant orbit shift and change in orbit shape at bearings 2 and 3 between the non-linear and linearised solutions. The reaction forces are no longer exactly vertical. There are now static horizontal bearing force components of about 1N (still an order of magnitude below the static vertical bearing force components) at bearings 2 and 3. The static shear forces and bending moments at the coupling are also no longer zero. With six harmonics, the non-linear approach involved the solution of a set of non-linear equations in 104 unknowns whereas the linearised approach, if static determinacy inherent to the aligned state were not assumed, would have involved a solution set of only 8 unknowns, viz. those to obtain the reaction force components.



**Figure 7: Statically indeterminate rotor solution comparison for the horizontally misaligned configuration**

Figure 7 compares the linearised and non-linear solutions with zero and finite unbalance if the 3<sup>rd</sup> bearing is misaligned by its radial clearance ( $9 \times 10^{-5}$  m) in the positive z direction. Again the zero unbalance solutions coincide; and again with the same unbalance as for the aligned case, six harmonics were needed to obtain the correct solution. The shifts in journal orbits and changes in orbit shape between the linearised and non-linear solutions are more pronounced than in the aligned case. The dynamic response of the system is also significantly altered as a result of the misalignment, as evidenced by the shift of the zero unbalance journal position in bearing 2, indicating a significant difference in reaction load distribution between the aligned and misaligned rotors.

Concerning computational efficiency, for the above misaligned statically indeterminate example, as implemented on Matlab™, the non-linear TM solution was approximately an order of magnitude faster than the transient approach. However, this can only be regarded as at best indicative, since comparing the efficiency of the numerical solutions is difficult and very approximate as there are many variables influencing the computation times of solutions (algorithms, platform, tolerance, programming style etc.).

## 5. CONCLUSIONS

The non-linear TM approach for finding periodic solutions has been successfully extended to statically indeterminate unbalanced rotor bearing systems with hydrodynamic bearing type non-linearity.

In statically indeterminate rotor bearing systems, the mean reaction load distribution, and hence the form of the dynamic response, is influenced not only by the configuration state, but also by the magnitude of the unbalance excitation.

Though only applied to a four bearing rotor system, the approach is applicable to practical turbogenerator systems, which may have many more bearings supporting the rotor.

## 7. ACKNOWLEDGEMENTS

This work was supported by the Australian Research Council and by the Aeronautical and Maritime Research Laboratories DSTO (Australia).

## REFERENCES

- (1) Lund, J. W., "Stability and Damped Critical Speeds of a Flexible Rotor in Fluid Film Bearings", *Trans ASME, Journal of Engineering for Industry*, May 1974, pp. 509-517.
- (2) Rao, J.S., *Rotor Dynamics*, 3rd Edition, New Age International (P) Ltd, New Delhi, 1996.
- (3) Bachschmid, N., Dellupi, R., "Non Linear Behaviour of Oil Film Bearings and its relevance in Force Identification Procedures", ASME Paper No. 97-GT-70, pp. 2457-2464.
- (4) Hahn, E.J. and Chen, P.Y.P., "Harmonic Balance of General Squeeze Film Damped Multi-Degree of Freedom Rotor Bearing Systems", *Trans ASME, Journal of Tribology*, Vol. 116, No. 3, 1994, pp. 499-507.
- (5) Yamauchi, S., "The Nonlinear Vibration of Flexible Rotors (1<sup>st</sup> Report)", *Trans. JSME*, Vol. 49, No. 446, Series C, Oct. 1983, pp. 1862-1868, (in Japanese).
- (6) Liew, A., Feng, N. S., Hahn, E. J., "Application of Transfer Matrices to Non-linear Rotor Bearing Systems", Proc. of ASME Design Engineering Technical Conference: 17th



Biennial Conference on Mechanical Vibration and Noise, Sept. 12-15, 1999, Las Vegas, paper no. DETC99/VIB-8263, 9pp.

- (7) Hori, Y. and Uematsu, R., "Influence of Misalignment of Support Journal Bearings on Stability of a Multi-rotor System", *Tribology International*, Oct. 1980, pp. 249-252.
- (8) Feng N. S. and Hahn E. J., "Vibration Analysis of Statically Indeterminate Rotors With Hydrodynamic Bearings", *Trans ASME, Journal of Tribology*, Vol. 120, No. 4, Oct. 1998, pp. 781-788.
- (9) Ding, J., and Krodkiewski, J. M., "Inclusion of Static Indetermination in the Mathematical Model for Nonlinear Dynamic Analysis of Multi-bearing Rotor Systems", *Journal of Sound and Vibration*, vol. 164, no. 2, June 1993, pp. 267-280.
- (10) Nikolajsen, J. L., "The Effect of Misalignment on Rotor Vibrations", *Trans ASME, Journal of Engineering for Gas Turbines and Power*, Vol. 120, July 1998, pp. 635-640.
- (11) Gere, J. M. and Timoshenko, S. P., "Mechanics of Materials", 3<sup>rd</sup> SI Ed, Chapman and Hall, UK, 1991.
- (12) Pinkus, O. and Sternlicht, B., "Theory of Hydrodynamic Lubrication", McGraw Hill, NY, 1961.

## APPENDIX

Consider the deflection of the rotor in the y direction. To define the position of the rotor in space  $\Delta_{y1} = 0$  and  $\Delta_{yn} = 0$ . Using the unit load method the other relative displacements are:

$$\Delta\delta_{yi} = \int_{L_1}^{L_n} \frac{M_{ui}M_{iy}}{EI} dx \quad i = 2, 3, \dots, n-1, \quad (A1)$$

where (see Figure A1)

$$M_{ui} = \begin{cases} -x + x \frac{L_i}{L_n} & \text{for } x \leq L_i \\ -L_i + x \frac{L_i}{L_n} & \text{for } x \geq L_i \end{cases}, \quad (A2)$$

and (see Figure A2)

$$M_{iy} = \sum_{k=1}^j \Delta F_{yk} (x - L_k) \quad \text{for } L_j \leq x \leq L_{j+1}. \quad (A3)$$

Substituting equations A2 and A3 into equation A1 and separating the integral span by span give:

$$\Delta\delta_{yi} = \sum_{j=1}^{n-1} \sum_{m=n_j}^{n_{j+1}-1} \int_{L_m}^{L_{m+1}} \frac{1}{E_m I_m} \left( \frac{-x}{-L_i} + x \frac{L_i}{L_n} \right) \sum_{k=1}^j \Delta F_{yk} (x - L_k) dx, \quad (A4)$$

which upon integration and manipulation yields equation 1. A similar equation for the z direction is obtained by replacing y with z.

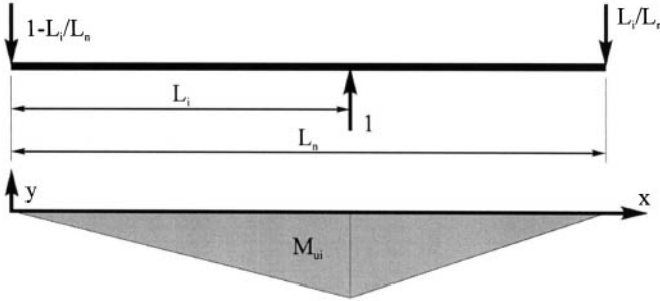


Figure A1: Bending moments due to a unit load at bearing i

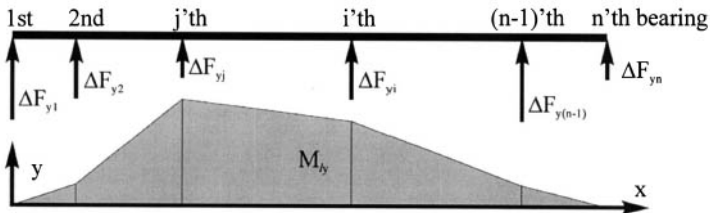


Figure A2: Bending moments due to the support reactions

# Thermal distortion synchronous rotor instability

R G KIRK and A C BALBAHADUR

Mechanical Engineering Department, Virginia Tech, Blacksburg, USA

## SYNOPSIS

The occurrence of synchronous vibration is typically considered, and correctly so, to be related to a poor state of balance of the rotating components. This has prompted many suppliers to provide at speed balancing of critical machinery. High or excessive synchronous excitation can be produced by operation on or near a critical speed, by operating under conditions of a suddenly applied rotating imbalance, or by the creation of a rotor imbalance through a mechanical or fluid effective rub condition. Standards have been written to assure that operation on or near critical speeds will be minimized. The sudden loss of balance, such as a blade loss in a jet engine or land based gas turbine has been documented in the early seventies but a recent revisit of this condition has produced interesting results. The occurrence of thermal instability is of great interest to many users due to the identification of this phenomenon as a cause or likely cause of ever increasing numbers of machinery vibration problems. An approximate model for thermal bending caused by viscous lubricant shearing in overhung rotors has been developed. This model has been tested against a published theoretical model and an experimental study. It was found that the current model agrees well with both the other theoretical model and the experimental data.

## NOTATION

$c_l$ = lubricant specific heat capacity [J/kg $^{\circ}$ C]	$W$ = rotor weight [N]
$C_b$ = radial bearing clearance [m]	$W_b$ = bearing load [N]
$E$ = Young's Modulus [Pa]	$h$ = film thickness [m]
$\dot{E}_b$ = rate of energy transfer to bearing [W]	$m_d$ = disk mass [kg]
$\dot{E}_j$ = rate of energy transfer to journal [W]	$y_d$ = thermal disk deflection [m]
$\dot{E}_{lub}$ = rate of energy storage in lubricant [W]	$z$ = axial dimension [m]
$\dot{E}_{visc}$ = rate of visc. energy dissipation [W]	$y_d$ = thermal conductivity of the journal [ $^{\circ}$ C $^{-1}$ ]
$H$ = heat transfer coefficient [W/m $^2$ $^{\circ}$ C]	$\beta$ = thermoviscosity coefficient [ $^{\circ}$ C $^{-1}$ ]
$I$ = area moment of inertia [m $^4$ ]	$\epsilon$ = eccentricity ratio (dim)

$L$ = bearing length [m]	$\theta$ = circumferential coordinate [rad]
$L_d$ = disk overhang length [m]	$\mu$ = lubricant viscosity [Pa s]
$R_j$ = journal radius [m]	$\mu_0$ = supply lubricant viscosity [Pa s]
$T$ = circumferential journal temperature [ $^{\circ}$ C]	$\phi$ = angle between th. and mech. unb. [rad]
$T_{amb}$ = ambient temperature [ $^{\circ}$ C]	$\rho$ = lubricant density [ $\text{kg/m}^3$ ]
$T_0$ = lubricant supply temperature [ $^{\circ}$ C]	$\tau$ = shear stress [Pa]
$U$ = resultant imbalance [kg m]	$\varphi$ = bend angle [rad]
$U_{thr}$ = threshold imbalance [kg m]	$\omega$ = journal speed [rad/s]

## 1 INTRODUCTION

The study of rotor instability is predominantly associated with self-excited nonsynchronous vibration. Motion is usually subsynchronous and closely matches the rotor first bending critical speed. The study of self-excited synchronous vibration has recently become of increasing interest in industrial turbomachinery. Synchronous instability resulting from rotor seal rubs or light rotor stator contact is well documented in the literature (1). The light rubbing can put excessive heat into a small sector of the shaft, resulting in a rotor thermal bow and either increasing or decreasing vibration, depending on the rub position, the rotor mode shape, and whether operation is above or below the dominant mode of vibration. These rubs are typically inboard of the main bearings and outward spiraling vibration occurs for operation below the critical speed and inward spiraling vibration for operation above the critical speed. In 1974, D. M. Smith (2) reported on an investigation of synchronous whirl in turbine and generator rotors. His theory of coupled blade, torsional, and lateral critical speeds was presented to explain how it may be possible for turbines to have this form of instability, but no answer was given that explained why the generators were synchronously unstable. He reported that increasing the bearing clearance reduced or eliminated the synchronous instability in at least one case, when normally reducing the clearance was the fix for oil film instability.

Another form of self-excited transient response occurs under the condition of blade loss, or suddenly applied imbalance (3). The maximum transient response ratio to the steady-state conditions has the interesting characteristic shown in Figure 1, where the lines are for varying amounts of critical damping ratio,  $\zeta = \text{damping} / \text{critical damping}$ . The accepted ratio of two occurs below the critical but a ratio of  $N/N_{cr}+1$  occurs for supercritical operation. The exact critical speed, however, does not experience any amplification.

Within the last decade much interest has been shown in the area of thermal bending in overhung rotors. Recent theoretical (4) and experimental (5,6) studies have focused on this problem. So far, most of the theoretical work has been done using complex analysis, and almost no comparison between experimental and theoretical research has been made. This paper develops a simple model of rotor thermal bending without using complex analysis. This model is then compared with a more rigorous theoretical model and with an experimental study. Rotor thermal bending is a complicated phenomenon that can lead to unstable spiral vibration (7). This phenomenon is primarily due to a temperature difference developing across the shaft. The temperature difference can either be caused by the rotor shaft rubbing against stationary components or by viscous shearing within the lubricant at a bearing or liquid seal location. The former mechanism was first noticed by Newkirk in 1926 and later analyzed by Dimarogonas (1). This mechanism is called the Newkirk Effect. The latter mechanism has recently been studied

(4,5,6) and is often referred to as the Morton Effect. This paper concentrates on the Morton Effect.

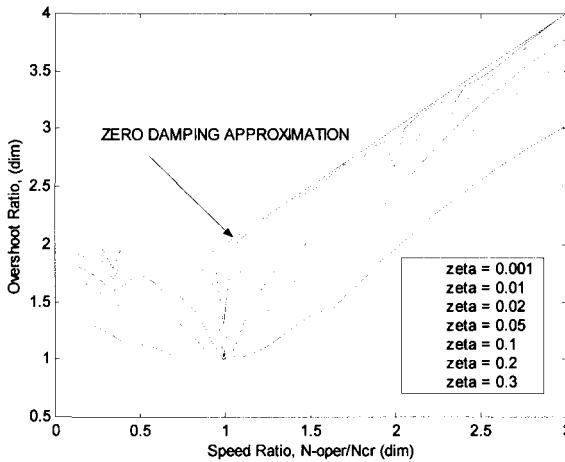


**Figure 1 Blade Loss Transient Response Overshoot versus Critical Speed Ratio**

The Morton Effect occurs when the journal is executing a synchronous orbit around the bearing center. This centered orbit causes one portion of the journal surface to always be at the minimum film thickness, while a diametrically opposite section of the journal surface is always at the maximum film thickness. Lower film thickness areas are generally associated with higher viscous shear stresses which produce higher temperatures. As a result, a hot spot will develop on the journal surface exposed to the minimum film thickness region and a cold spot will be formed on the surface at maximum film thickness. This leads to a temperature gradient developing across the journal. Such a gradient creates a thermal imbalance that is in the direction of the temperature gradient. Thermal bending will then occur if the resultant of the thermal imbalance and the overhung mechanical imbalance is adequate. Under these conditions the bent shaft will decrease the bearing clearance and elevate the thermal gradient. The increased temperature gradient will then initiate more thermal bending. These actions describe a positive feedback mechanism which will drive the system unstable.

In this paper, it is assumed that the journal is in a synchronous, centered orbit and is subjected to a known overhung imbalance. The thermal imbalance will then be calculated and the resultant imbalance will be compared with a threshold imbalance.

## 2 THERMAL BENDING MODEL

The thermal bending model involves solving the energy equation for the circumferential temperature distribution around the journal within the bearing. This temperature distribution is then used to calculate the deflection of the overhung disk. A thermal imbalance is then computed from this deflection and the resultant of the thermal and mechanical imbalances is compared with a threshold imbalance. The threshold imbalance was chosen to be the imbalance produced by a force equal to 35% of the total rotor weight. It was assumed that instability will

occur if the thermal imbalance is greater than the threshold imbalance. Another key assumption in this model is that the static equilibrium position of the journal represents an average of the dynamic positions of the journal. As a result, the average journal temperature distribution can be obtained by considering only the static equilibrium journal position.

### 2.1 Temperature distribution

Figure 2 shows the energy flow in a portion of a plain journal bearing.  $\dot{E}_{lub}$  represents the rate of energy advection by the lubricant,  $\dot{E}_j$  is the rate of energy transfer to the journal,  $\dot{E}_b$  is the rate of energy transfer to the bearing housing and  $\dot{E}_{visc}$  is the rate of viscous energy dissipation. An energy balance for the bearing can now be written

$$\dot{E}_{visc} = \dot{E}_{lub}|_{\theta+d\theta} - \dot{E}_{lub}|_{\theta} + \dot{E}_j + \dot{E}_b \quad [1]$$

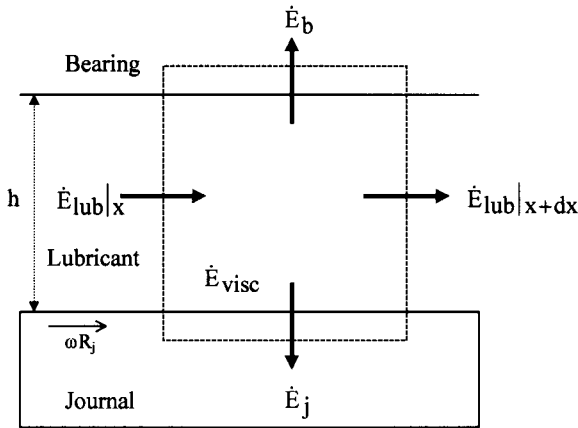


**Figure 2** Energy flow in a plain journal bearing

Substituting for the terms in [1] yields

$$\omega R_j \tau dx dz = \rho_l h dz \frac{\omega R_j}{2} c_l \left( T + \frac{dT}{dx} dx \right) - \rho_l h dz \frac{\omega R_j}{2} c_l T + f H dx dz (T - T_{amb}) + (1-f) H dx dz (T - T_{amb}) \quad [2]$$

The rate of viscous energy dissipation,  $\dot{E}_{visc}$ , depends on the speed of the journal surface,  $\omega R_j$ , and the viscous shear stress,  $\tau$ , which acts over an area  $dx dz$  ( $z =$  axial dimension). This energy source term heats up the advecting lubricant that has a density of  $\rho_l$  and a specific heat capacity of  $c_l$ . A fraction,  $f$ , of the remaining heat is transferred to the journal while the rest is assumed to be lost in the bearing housing and surroundings. It is assumed that the total heat loss is equal to  $H dx dz (T - T_{amb})$ , where  $T_{amb} =$  average journal temperature = average bearing temperature. After simplification, the equation [2] reduces to

$$\omega R_j \tau = \rho_l h \frac{\omega R_j}{2} c_l \frac{dT}{dx} + H (T - T_{amb}) \quad [3]$$

If the lubricant is Newtonian, then the shear stress will be given by,  $\tau = \mu du/dy$ . Furthermore, a linear Petroff-type velocity profile can be assumed, which means that the shear strain rate  $du/dy = \omega R_j/h$ . The viscosity in the shear stress expression is a function of temperature, and, according to Reynolds, it may be approximated as

$$\mu = \mu_0 e^{-\beta(T-T_0)} \quad [4]$$

It should be noted that since  $h \ll R_j$ ,  $x \sim R_j\theta$ , where  $\theta$  = circumferential angle measured from the line joining the bearing and the journal centers. Also, the temperature rise above the ambient temperature can be defined as  $\tilde{T} = (T - T_{amb})$ , and likewise,  $\tilde{T}_0 = (T_0 - T_{amb})$ . Substituting all of these into the equation [3] and rearranging yields

$$\frac{d\tilde{T}}{d\theta} + \frac{2H}{\rho_1 c_1 \omega h} \tilde{T} - \frac{2\mu_0 \omega R_j^2}{\rho_1 c_1 h^2} e^{-\beta(\tilde{T}-\tilde{T}_0)} = 0 \quad [5]$$

The plain journal bearing film thickness expression is  $h = C_b(1 + \varepsilon \cos\theta)$ . If this formula is incorporated into equation [5] the following result is obtained

$$\frac{d\tilde{T}}{d\theta} + \frac{2H}{\rho_1 c_1 \omega C_b} \frac{\tilde{T}}{(1 + \varepsilon \cos\theta)} - \frac{2\mu_0 \omega R_j^2}{\rho_1 c_1 C_b^2} \frac{e^{-\beta(\tilde{T}-\tilde{T}_0)}}{(1 + \varepsilon \cos\theta)^2} = 0 \quad [6]$$

The eccentricity ratio can be extracted from the load versus eccentricity equation, which has been derived in detail by Cameron (8). After solving for the eccentricity ratio  $\varepsilon$ , equation [6] can be solved numerically to obtain the temperature distribution around the circumference of the journal. The required boundary condition sets the temperature at maximum film thickness (the lowest temperature) to the value of the lubricant supply.

## 2.2 Thermal imbalance

The static bending moment ( $M$ ) in the journal can be expressed as

$$M = EI \frac{d\psi}{dz} \quad [7]$$

The maximum stress ( $\sigma_{max}$ ) in the shaft can be written as

$$\sigma_{max} = \frac{R_j M}{I} \quad [8]$$

If this maximum stress is primarily caused by thermal effects, then:

$$\sigma_{max} = E\alpha\Delta T \quad [9]$$

where  $\Delta T = (\tilde{T}_{max} - \tilde{T}_{min}) = \tilde{T}(\theta = \pi) - \tilde{T}(\theta = 0)$ . Equation [7] can be substituted into [8], and [8] and [9] can be equated to give

$$\frac{d\psi}{dz} = \frac{\alpha\Delta T}{R_j} \quad [10]$$

For a given journal speed, the right hand side of equation [10] is essentially constant. Therefore, equation [10] can be integrated between the middle of the bearing, where it is assumed that the bend angle is zero, and some arbitrary axial distance,  $z$ , to give

$$\psi = \frac{dy}{dz} = \frac{\alpha\Delta T}{R_j} z \quad [11]$$

where  $y$  = deflection of journal. If there is zero deflection at the bearing middle, equation [11] can be integrated between the bearing and the overhung disk, which is at  $z = L_d$ , to obtain

$$y_d = \frac{1}{2} \frac{\alpha\Delta T}{R_j} L_d^2 \quad [12]$$

Equation [12] gives us the thermal deflection of the overhung disk. This deflection can be converted into a thermal imbalance,  $U_t$  given by

$$U_t = m_d y_d \quad [13]$$

### 2.3 Mechanical imbalance

It is very difficult to accurately describe an arbitrary mechanical imbalance for every rotor. Therefore, a nominal imbalance of 0.72 kg mm (1 oz in.), acting at an angle of zero degrees with respect to a coordinate system fixed to the rotor, was assumed to be present on the overhung disk. This information and other relevant rotor properties were input into VT-FAST (Virginia Tech - Front-end Automated Simulation of Turbomachinery) which is a rotordynamics software package that is currently used in both the classroom and industry. Results from the model enabled the angle ( $\phi$ ), between the mechanical imbalance and the response at the bearing, to be calculated. The induced bearing response coincides with the minimum film thickness region that is responsible for the highest journal circumferential temperature. This hot spot gives rise to the thermal deflection and the subsequent thermal imbalance. Hence,  $\phi$  is the angle between the mechanical ( $U_m$ ) and thermal ( $U_t$ ) imbalances.

### 2.4 Instability criterion

The mechanical and thermal imbalances can be added vectorially to produce a resultant imbalance ( $U$ ) that can be represented as

$$U = \sqrt{U_t^2 + U_m^2 - 2U_t U_m \cos(\pi - \phi)} \quad [14]$$

Next, a threshold imbalance ( $U_{thr}$ ) for synchronous thermal instability can be defined as the imbalance caused by a force equal to 35% of the rotor weight. This threshold imbalance is

$$U_{thr} = \frac{0.35W}{\omega^2} \quad [15]$$

Whenever  $U$  exceeds  $U_{thr}$ , the rotor will be unstable. As a result, the threshold speed for instability ( $\omega_{thr}$ ) occurs when  $U = U_{thr}$ . This critical speed can be obtained graphically from the intersection of the  $U$  vs.  $\omega$  and the  $U_{thr}$  vs.  $\omega$  curves.

## 3 COMPARISON WITH OTHER RESEARCH



### 3.1 Keogh and Morton

In their paper (4), Keogh and Morton present a theoretical analysis of a symmetric rotor that is shown in Figure 3. This rotor consists of a shaft with a step variation in diameter. The shaft is supported by two identical plain journal bearings and a disk of constant mass is placed, at an overhung position, on either shaft end. The pertinent data for this rotor is summarized in table 1.

The Keogh and Morton model examined the stability of a complex rotor thermal bend angle. From this complex analysis, they were able to calculate the eigenvalues of the rotor system and determine the corresponding growth factors ( $\sigma$ ). Since the system response depends on  $e^{\sigma t}$ , a positive growth factor would indicate a theoretical instability.

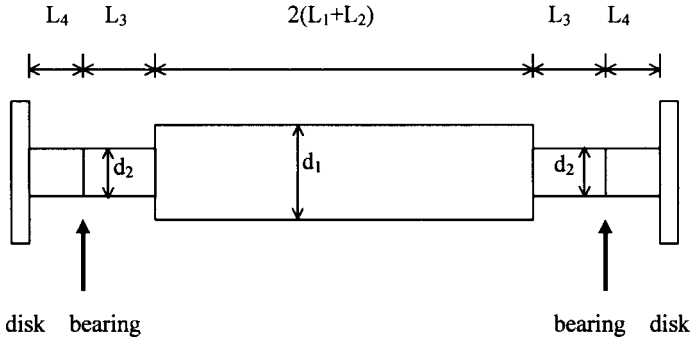


**Figure 3 Schematic diagram of the Keogh and Morton symmetric rotor**  
 $L_1 = L_2 = 19.7$  in(0.5 m),  $L_3 = 11.8$  in(0.3 m),  $L_4 = 7.87$  in(0.2 m),  
 $d_1 = 7.09$  in(0.18 m),  $d_2 = 3.94$  in (0.1 m)

**Table 1 Data for Keogh and Morton rotor**

Parameter	SI Units	Symm. Rotor	EG Units	Symm. Rotor
<u>Lubricant Properties</u>				
Density	$\rho_l$ kg/m <sup>3</sup>	850	lbm/in <sup>3</sup>	0.031
Specific heat capacity	$c_l$ J/kg/°C	2000	Btu/lbm/°F	0.478
Supply temperature	$T_0$ °C	45.0	°F	113
Supply viscosity	$\mu_0$ Pa s	0.0061-0.0091	µreyn	0.885-1.32
Thermovisc. coeff.	$\beta$ °C <sup>-1</sup>	0.049	°F <sup>-1</sup>	0.027
<u>Bearing Properties</u>				
Length	L m	0.035	in	1.38
Radial clearance	$C_b$ m	1.00E-04	mils	3.94
Heat transfer coeff.	H W/m <sup>2</sup> /°C	50	hp/ft <sup>2</sup> /°F	0.0035
Bearing load	$W_b$ N	2500	lbf	562
<u>Journal Properties</u>				
Radius	$R_j$ m	0.050	in	1.97
Heat transfer coeff.	H W/m <sup>2</sup> /°C	50	hp/ft <sup>2</sup> /°F	0.0035
Coeff. of Thermal Exp.	$\alpha$ °C <sup>-1</sup>	1.10E-05	°F <sup>-1</sup>	6.11E-06
Angular speed	$\omega$ rad/s	500-1300	RPM	4775-12414
<u>Rotor Properties</u>				
Rotor weight	W N	4524	lbf	1017
Disk mass	$m_d$ kg	20	oz	705
Disk overhang	$L_d$ m	0.20	in	7.87

From their analysis, Keogh and Morton concluded that the critical speed range, in which rotor thermal bending can occur, is between 1023 rad/s (9769 RPM) and 1086 rad/s (10371 RPM). The current analysis used the data in table 1 to predict a synchronous thermal threshold speed range from 1024 rad/s (9781 RPM) to 1290 rad/s (12320 RPM) which encompasses the Keogh and Morton range. This threshold speed of thermal bending was obtained from the intersection of the resultant imbalance and threshold imbalance curves shown in Figure 4.

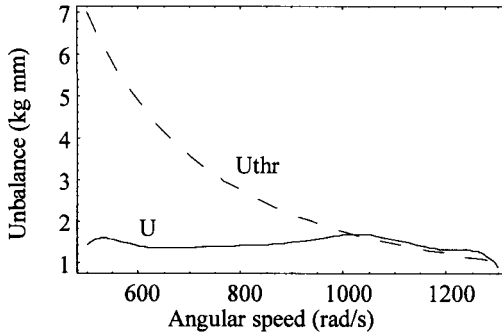


**Figure 4 Imbalance curves from current analysis of Keogh and Morton rotor**

### 3.2 Faulkner, Strong and Kirk

Faulkner, Strong and Kirk (3) did an experimental study of a large turbocharger that is schematically shown in Figure 5. The turbocharger had a centrifugal compressor impeller at one end and a radial inflow turbine disk at the other end. Relevant data for this turbocharger is shown in table 2. During operation, it was observed that the turbocharger became unstable near 10,000 RPM (1047 rad/sec). Faulkner, Strong and Kirk initially thought that the instability was due to the turbine wheel becoming loose at the high operation speeds. However, a careful inspection of the turbine wheel position, before and after operation, indicated that the wheel did not move while the turbocharger was running. Furthermore, a damped critical speed analysis failed to justify the existence of a lateral critical speed near 10,000 RPM (1047 rad/sec). It was finally concluded that the source of the instability was the thermal bowing of the rotor shaft near the turbine end of the turbocharger. The current thermal instability model was used to analyze the turbocharger. It was found that the thermal threshold was predicted to be 990 rad/s (9459 RPM) near the turbine end of the turbocharger (Figure 6a) while the compressor end had a predicted threshold speed of about 1436 rad/s (13716 RPM) (Figure 6b). From these results, it can be concluded that the turbine end would be the most likely to cause the thermal bowing of the turbocharger near 10,000 RPM. The calculated critical speed of the compressor end is too high to have been a problem around 10,000 RPM. These conclusions are in agreement with the observations.

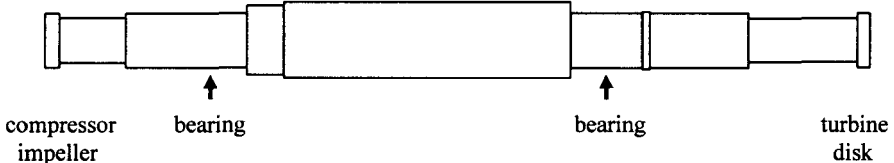


**Figure 5 Schematic diagram of the turbocharger studied by Faulkner, Strong and Kirk**

**Table 2 Data for Faulkner, Strong and Kirk turbocharger**

Parameter	SI Units	Turbine	Compressor	EG Units	Turbine	Compressor	
<u>Lubricant Prop.</u>							
<u>Properties</u>							
Spec. ht. Cap.	$\rho_l$	kg/m <sup>3</sup>	850	850	lbm/in <sup>3</sup>	0.031	0.031
Supply temp.	$c_l$	J/kg <sup>o</sup> C	2000	2000	Btu/lbm <sup>o</sup>	0.478	0.478
Supply viscosity	$T_0$	<sup>o</sup> C	87.8	87.8	<sup>o</sup> F	190	190
Thermovisc. coeff.	$\mu_0$	Pa s	0.0072	0.0072	$\mu$ reyn	1.89	1.89
	$\beta$	<sup>o</sup> C <sup>-1</sup>	0.278	0.278	<sup>o</sup> F <sup>-1</sup>	0.154	0.154
<u>Bearing Properties</u>							
Length	L	m	0.057	0.067	in	2.25	2.63
Radial clearance	$C_b$	m	6.35E-05	7.62E-05	mils	2.5	3
Heat trans. coeff.	H	W/m <sup>2</sup> <sup>o</sup> C	50	50	hp/ft <sup>2</sup> <sup>o</sup> F	0.0035	0.0035
Bearing load	$W_b$	N	921	956	lbf	207	215
<u>Journal Properties</u>							
Radius	$R_j$	m	0.041	0.041	in	1.63	1.63
Heat trans. coeff.	H	W/m <sup>2</sup> <sup>o</sup> C	50	50	hp/ft <sup>2</sup> <sup>o</sup> F	0.0035	0.0035
Coeff. of th. exp.	$\alpha$	<sup>o</sup> C <sup>-1</sup>	1.10E-05	1.10E-05	<sup>o</sup> F <sup>-1</sup>	6.11E-06	6.11E-06
Angular speed	$\omega$	rad/s	524-1571	524-1571	kRPM	5-15	5-15
<u>Rotor Properties</u>							
Rotor weight	W	N	1877	1877	lbf	422	422
Disk mass	$m_d$	kg	51	60	oz	1808	2102
Disk overhang	$L_d$	m	0.20	0.16	in	8.06	6.35

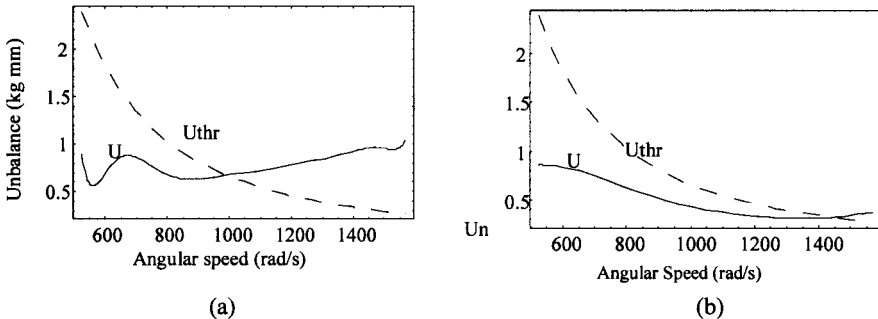


**Figure 6 Imbalance curves from current analysis of the (a) turbocharger turbine end and (b) turbocharger compressor end**

#### 4 SOLUTION SENSITIVITY TO THE THRESHOLD UNBALANCE FORCE

The threshold unbalance force in the two cases studied above was 35% of the rotor weight. Table 3 shows the effect on the calculated instability speeds if different threshold unbalance force magnitudes were chosen. It appears that a change of only 5% in the threshold unbalance force can change the calculated instability speed by several hundred RPM. The solution is therefore sensitive to the choice threshold unbalance force. From the data shown in table 3, the optimum threshold unbalance force seems to be 35% of the rotor weight. This choice of unbalance force is

the one that gives data that most corresponds with the Keogh and Morton instability range. In addition, this force magnitude predicts an instability speed that lies close to the observed thermal instability speed at the turbine end of the Faulkner, Strong and Kirk turbocharger.

**Table 3 Instability speed values (RPM) for different threshold unbalance forces**

Unbalance Force (% of rotor weight)	Keogh & Morton - Symmetric Rotor	Faulkner, Strong & Kirk - Turbine	Faulkner, Strong & Kirk - Compressor
25	8713-12479	8221	11290
30	9231-12414	8913	12850
35	9781-12320	9459	13716
40	11870-12094	9950	14254
45	stable	10385	14701

## 5 CONCLUSIONS

An approximate model of thermal bending caused by viscous lubricant shearing in overhung rotors has been developed. This model agrees with the results from another theoretical model and with the data from an experimental study. An unbalance force of 35% of the rotor weight seemed to be the best choice for a threshold criterion for the rotors evaluated to date. The results from the current model are promising, but this model needs to be further tested against more experimental data and theoretical analyses as soon as they become available. Future work will also deal with the consequences of deviating from the centered synchronous orbit assumption.

## 6 REFERENCES

- (1) Dimarogonas, A.D., 1973, "Newkirk Effect: Thermally Induced Dynamic Instability of High-Speed Rotors", ASME paper, 73-GT-26, p. 2-11.
- (2) Smith, D.M., *Dynamics of Rotors*, Lyngby Symposium, Springer-Verlag, 1975, pp 524-545.
- (3) Kirk, R. G. and D. H. Hibner, "A Note on Blade Loss Dynamics of Rotor-Bearing Systems," *Trans ASME, J. Engrg. for Industry*, v98, 2, 1976, pp. 497-504.
- (4) Keogh, P.S. and P.G. Morton, 1994, "The dynamic nature of rotor thermal bending due to unsteady lubricant shearing within bearing", *Proc. R. Soc. Lond. A*, 445, p. 273-290.
- (5) deJongh, F.M. and P.G. Morton, 1994, "The synchronous instability of a compressor rotor due to bearing journal differential heating", ASME paper, 94-GT-35, p. 1-13.
- (6) Faulkner, H.B., W.F. Strong and R.G. Kirk, 1997, "Thermally induced synchronous instability of a radial inflow overhung turbine, part II", DETC97/VIB-4174, Proceedings of DETC'97, 1997 ASME Design Engineering Technical Conferences, September 14-17, Sacramento, California, p. 1-5.
- (7) Schmied, J., 1987, "Spiral Vibrations of Rotors", *Rotating Machinery Dynamics*, Vol. 2, ASME Design Technology Conference, Boston, September 1987.
- (8) Cameron, A., 1966, *The Principles of Lubrication*, p. 292.

Bearings

*This page intentionally left blank*

# Theoretical and experimental characterization of polyimide dry bushings

**J-L BOZET** and **P POYSAT**

Institut de Mécanique, Université de Liège, Belgium

**P MÉROT**

Du Pont de Nemours, Mechelen, Belgium

## ABSTRACT

In electrical motors of small size, there is a will to use bushings running dry like bushings made of polyimide.

Nevertheless, specific problems like vibration and noise are faced.

Theoretical investigations have been performed by using a Jeffcott rotor model. This model taught us that for a fixed type of bushing material, geometry and clearance, one can often experience instability above a critical rotational speed of the shaft. This instability corresponds to backward whirl and shocks producing normal impact force and then noise. Conditions of appearance and full description of these phenomena are detailed.

In parallel, an experimental program has been set up in order, first, to better understand and quantify the phenomena then, in a second step, to validate the theoretical model. Good correlation has been obtained.

Experimental information has been provided by a test bench equipped with speed and position sensors allowing the construction of the shaft trajectory. In addition, a high speed camera has been used to effectively visualise the whirl movement of the shaft.

## 1. INTRODUCTION

In electrical motors of small size corresponding to a maximum power of 2 kW, there is a trend at least at the research stage to use bushings running dry like bushings made of VESPEL\* polyimide. Compared to a classical solution like ball bearing or lubricated bronze bushing

such a solution allows mainly ease in assembly, reduced length of bearings and consequently reduced dimension of the whole motor.

Nevertheless, the use of this material in permanent conditions in bearings of high speed electrical motor running in different position between horizontality and verticality can be accompanied by noise and vibration.

Indeed, in real conditions it has been noticed that the rotor can show unacceptable vibration followed by a dramatic decrease of its own rotational speed. To remedy to this situation, both theoretical and experimental investigations lead us to identify technical solutions where stiffness of the system must be decreased to limit the contact force between the bushing and the shaft while its damping must be increased to dissipate the energy of the rebounds which follow the contact.

In fact, noise and vibration are associated to instability phenomena appearing above a critical rotational speed for given configuration.

## **2. EXPERIMENTAL INSTALLATION**

The instability phenomena have been underscored by using a BENTLY NEVADA rotor kit test bench (Fig.1) (1). It could be configured in such a way it was very close to the configuration met on real electrical motor of small size. In fact, the coil and the shaft of the electrical motor has been replaced by a disk of similar mass. The nominal diameter of the shaft was 10 mm while the distance between the two bearings was set at 80 mm. The rotor mass wheel of the bench was in the middle of this distance.

The movement of the shaft inside the clearance of the bearings was measured by proximity sensors (two at each bearing) placed 90° apart from each other in a plane perpendicular to the shaft. The recording of the signal delivered by the pair of sensors located at one bearing allowed the construction of the shaft trajectory inside the clearance. The data corresponding to the position of the shaft were collected by a data acquisition system fitted in a PC. Then the ADRE software (2) developed by BENTLY NEVADA allowed analysis with different tools like FFT, time response of both displacements, waterfalls.

In addition, noise measurements were done with a microphone placed close to the bearing and a high speed camera (40000 images/sec) has been used to effectively visualise the whirl movement of the shaft. Moreover, the bench was mounted on a platform whose position could be adjusted between horizontality and verticality.

## **3. MECHANICAL BEHAVIOUR OF THE ROTOR**

In some real applications, the motor was subject to bothering noise and vibration accompanied by a drop of the rotational speed. These phenomena, proofs of instability, were appearing mainly if the motor endured external perturbations or was in vertical position.

The exact nature and the origin of this behaviour could be found and explained by experiments on the bench.



In fact, it could be noted that instability was associated with backward whirl where the shaft was rolling in the bushing in a sense opposite to the one corresponding to its own rotational speed.

The three following captures of trajectories (fig. 2 to 4) correspond to the running of the shaft in VESPEL\* polyimide bushings fitted in steel rings at increasing rotational speed. The clearance between shaft and bushing was 80  $\mu\text{m}$ . The bench was horizontal.

In figure 2, the motion of the shaft is located at the bottom of the bushing. The amplitude is small and the orbits have a good repeatability. This behaviour is very soft and silent.

In figure 3, the amplitude becomes larger and the orbits lose their gentle movement along the bottom of the bushing. In fact, the shaft leaves the surface of the bushing and falls heavily. An impact force is added to the gravity force. The movement of the shaft evolves toward a backward whirl situation. In fact, when a radial contact takes place between a moving surface and a surface at rest, the Coulomb friction introduces a tangential force opposite to the sliding speed, here on the rotor. This tangential force initiates a backward whirl motion which in its turn produces a larger centrifugal force on the rotor. The rise of this force increases the radial contact force and consequently the tangential force responsible for the backward whirl. Appearing for a given rotational speed of the rotor, there is instability in the running of the device.

In figure 4, the shaft endures a backward whirl. There is instability involving noise and vibration.

Direct visualisation has been done with a high speed camera. The result is presented at figure 5. In this case, looking at pictures from left to right and top to bottom, one can see the evolution of the clearance between shaft and bushing. Corresponding to a quarter of a clockwise revolution of the shaft (follow small black line on the shaft), one has an anticlockwise evolution of the clearance and presence of impact of the shaft against the bushing. The clearance was 0.1 mm, the shaft was running at 2700 rpm and the platform of the bench was inclined at 45°. Computed from the pictures the backward whirl speed was 4800 rpm.

#### **4. EXPERIMENTAL PROCEDURE AND TEST PROGRAMS**

An experimental configuration was characterised by several parameters. These were type of VESPEL\* polyimide for the bushing, clearance between shaft and bushing, degree of unbalance of the disk and position of the platform on which the bench was attached. At this stage, the VESPEL\* bushing is circled by a steel ring without any kind of improvement

For a given configuration, with an acceleration rate fixed at 2500 rpm/min for any test, the rotational speed of the bench was increased till 6000 rpm if instability was not met before. For a configuration several runs were made in order to characterise the repeatability of the appearance of instability during the test. In fact, the phenomena are repeatable inside a band of rotational speed. The width of this band was increasing with the clearance while the degree of unbalance had little influence. Appearance of instability was detected and quantified by

notably recording the level of noise taken by a microphone placed close to the disk of the bench but more surely by noting the drop in rotational speed. As to the position of the bench, it has been demonstrated that instability starts sooner when inclining the bench from horizontality to verticality. This is due to the fact that the stabilising effect of the gravity on the rotor plays any more role when the bench is in a vertical position.

The lack of repeatability of the phenomena disallowed to establish a stability criterion. Moreover, it must be noted that external perturbations like shocks induced almost systematically instability that is to say unacceptable noise and vibration. Nevertheless, maps dividing the space into stability region and instability region for a given set of parameters were drawn.

The use of these maps is not sufficient to guarantee the wanted unnoisy behavior of the system. So, several technical solutions were investigated like on the one hand the use of a trilob form for the bushing and on the other hand the coating of the shaft with a low friction varnish.

This second solution shows improvement and confirmed the fact that a smooth running is in fact a compromise between friction and damping in the system. This confirmation is strengthened by the association of the best behavior with the type of VESPEL\* which has the best internal damping.

## 5. NUMERICAL FORMULATION

Following hypothesis have been made :

- the equations are related to one bearing ;
- the shaft is considered as infinitely rigid and the rotor (shaft + coil) is represented at one bearing by a single mass point which is equivalent to the half mass of the whole rotor ;
- gyroscopical effects are neglected.

Development of the model is based on the works of F.F. Ehrich (3) and Y.B.Kim associated with S.T.Noah (4). Being in cartesian coordinates (X,Y) whose origin is attached at the centre of the bearing (see figure 6), one can write according to Newton's second law :

$$M \frac{d^2 X}{dt^2} = ME \omega^2 \cos(\omega t) - (F'_s + F'_d) \cos \psi + s F'_f \cos(\psi - \frac{\pi}{2}) - K_c X - C_c \frac{dY}{dt}$$

$$M \frac{d^2 Y}{dt^2} = ME \omega^2 \sin(\omega t) - (F'_s + F'_d) \sin \psi + s F'_f \sin(\psi - \frac{\pi}{2}) - K_c Y - C_c \frac{dY}{dt} - Mg$$

where M is the mass, E the eccentricity that is to say the distance between geometrical centre and centre of gravity of the rotor,  $\omega$  the rotational speed of the shaft and s the signature of the sliding speed.

The influence of the clearance on stiffness, damping or friction has been taken into account by introducing for each parameter a set of two values (see figure 7) (3). Running inside the clearance corresponds to stiffness  $K_c$  and damping  $C_c$  while contact between shaft and

bushing corresponds to the existence of forces  $F_s$  and  $F_d$ . The choice between these situations is made according to the existence of contact or not between the shaft and the bushing.

To ease the comparison between several type of rotor, converting the two former equations in a non dimensional form is highly recommended.

One obtain

$$x'' = \cos(\theta) - 2 \frac{\zeta}{\omega} x' - \frac{1}{4\omega^2} \left(1 + \frac{1}{\sqrt{\alpha}}\right)^2 x - \phi F_{non-linear}$$

$$y'' = \sin(\theta) - \frac{\lambda}{\omega^2} - 2 \frac{\zeta}{\omega} y' - \frac{1}{4\omega^2} \left(1 + \frac{1}{\sqrt{\alpha}}\right)^2 y - \phi F_{non-linear}$$

where :

$$F_{non-linear}^x = \left[ 2 \frac{\zeta_B}{\omega} \left( \frac{x'x + y'y}{r^*} \right) \frac{x}{r^*} + \frac{1}{4\omega^2} \left(1 + \sqrt{\alpha}\right)^2 x \left(1 - \frac{\delta^*}{r^*}\right) - \mu \frac{1}{4\omega^2} \left(1 + \sqrt{\alpha}\right)^2 y \left(1 - \frac{\delta^*}{r^*}\right) \right]$$

$$F_{non-linear}^y = \left[ 2 \frac{\zeta_B}{\omega} \left( \frac{x'x + y'y}{r^*} \right) \frac{y}{r^*} + \frac{1}{4\omega^2} \left(1 + \sqrt{\alpha}\right)^2 y \left(1 - \frac{\delta^*}{r^*}\right) - \mu \frac{1}{4\omega^2} \left(1 + \sqrt{\alpha}\right)^2 x \left(1 - \frac{\delta^*}{r^*}\right) \right]$$

with

$$x = X/E; y = Y/E; \theta = \omega t; \lambda = \frac{d}{d\theta}; \zeta = C_c / 2\sqrt{KM}; K = \frac{4K_B K_C}{(\sqrt{K_B} + \sqrt{K_C})^2}; \alpha = \sqrt{K_B / K_C}$$

$$\lambda = g/E\omega_n^2; \zeta_B = C_B / 2\sqrt{KM}; \omega_n = K/M; r^* = R/E; \delta^* = \Delta/E$$

$\phi = 1$  if shaft and bushing are contacting

$\phi = 0$  if shaft and bushing are not contacting

## 6. CONFRONTATION BETWEEN EXPERIMENTAL AND THEORETICAL APPROACHES

The equations describing the behavior of the rotor have been solved in a MATLAB-SIMULINK software environment.

The conditions corresponding to the description of the backward whirl phenomena made in chapter 3 have been used for illustrating the model. As a reminder, the conditions were 80 $\mu$ m for the clearance and an eccentricity of 8 $\mu$ m.

Figures 8 to 10 correspond to the start of the backward whirl. They show in a non dimensional way the trajectory of the shaft inside the clearance zone, the contact force and the backward whirl speed. The rotational speed of the shaft associated to figures 8 to 10 is respectively 4200 rpm, 4230 rpm and 4300 rpm.

On figure 8, the displacement of the rotor is clearly located at the bottom of the bushing. The contact force is low and periodic. The whirl speed indicates a gentle oscillation between a position high and a position low.

On figure 9, the amplitude as well as the contact force become larger. The whirl speed becomes negative.

On the figure 10, instability is almost built.

So, simulation gives a start of backward whirl between 4200 and 4300 rpm compared to 4400 rpm in real tests (see figure 3). This comparison shows a good correlation between simulation and experiment. This correlation is also noticeable on figure 11 where for the simulation curve each point is the mean of 5 measures of the rotational speed.

## 7. CONCLUSION

Potential instability phenomena appearing in high speed electrical motor of small size have been detailed in an experimental way as well as in a theoretical way. The appearance of instability is associated with a backward whirl of the shaft accompanied with shocks producing noise.

It has been shown that the instability develops sooner when increasing the clearance and inclining the bench till verticality is reached.

Technical solutions were developed but it appeared that a trustable one is linked to a fine tune balance between friction and damping. New investigations based on the compromise between friction and damping are underway and early results give us a very good confidence in a near future success associated to an adapted technical solution.

## REFERENCES

- (1) BENTLY NEVADA Rotor Kit RK4, 1997, BENTLY NEVADA Corp.
- (2) ADRE for Windows, Guide, BENTLY NEVADA.
- (3) Ehrich, F.F., January 1988, « High Order Subharmonic Response of High Speed Rotors in Bearing Clearance », ASME Journal of Vibration, Acoustics, Stress and Reliability in Design, Vol.110, pp 9-16.
- (4) Kim, Y.B., Noah, S.T., 1996, « Quasi-periodic Response and Stability Analysis for a non Linear Jeffcott Rotor ».

(\* ) VESPEL is a registered trademark of Du Pont de Nemours.

## ACKNOWLEDGMENT

The authors wish to thank Professor J.C. Golinval for fruitful comments provided during the research program.

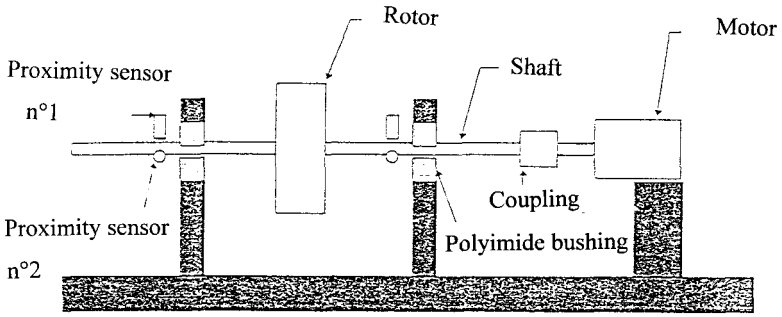


Figure 1-Sketch of the test bench

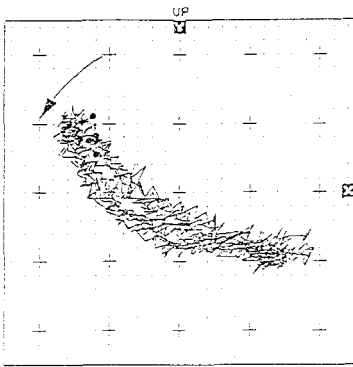


Figure 2-Experimental trajectory of shaft ( $\omega=3779$  rpm)

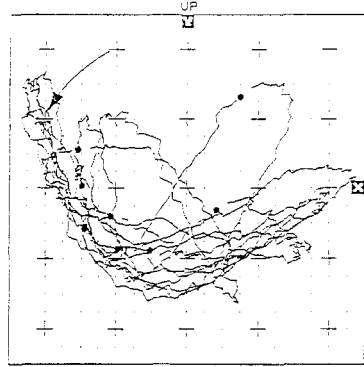


Figure 3- Experimental trajectory of shaft ( $\omega=4417$  rpm)

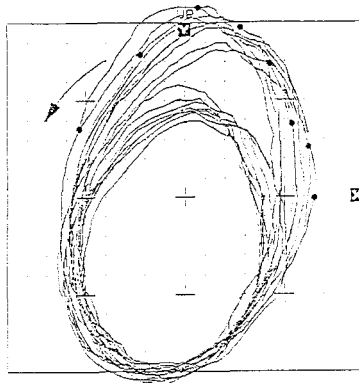
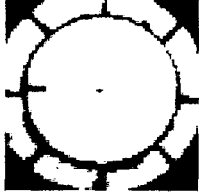
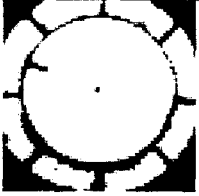



Figure 4- Experimental trajectory of shaft ( $\omega=5243$  rpm)

					
Frame n°	14401		14451		14501
Time	0.35555556		0.35679012		0.35802469




					
Frame n°	14551		14601		14651
Time	0.35925926		0.36049383		0.36172839

Figure 5-Visualisation of backward whirl

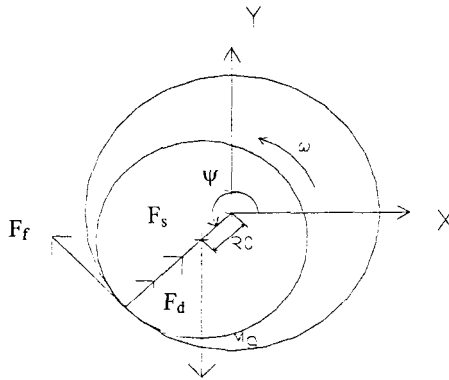


Figure 6-Acting forces on the system

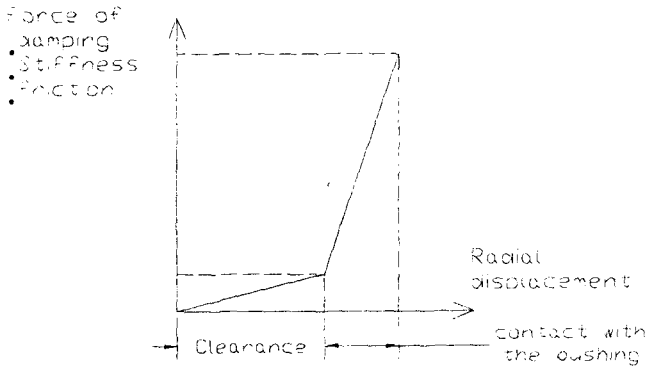


Figure 7-Evolution of contact parameters

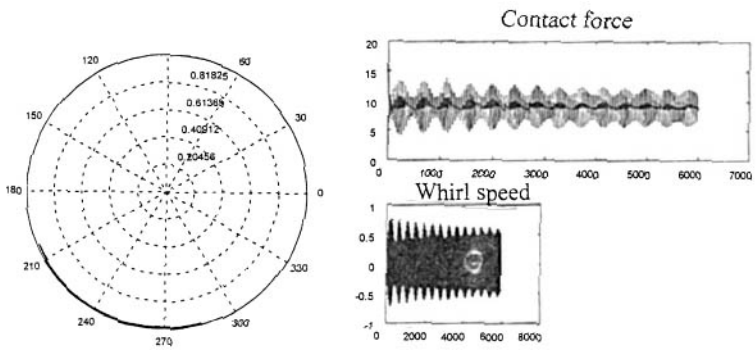


Figure 8-Modeled trajectory of shaft ( $\omega=4200$  rpm)

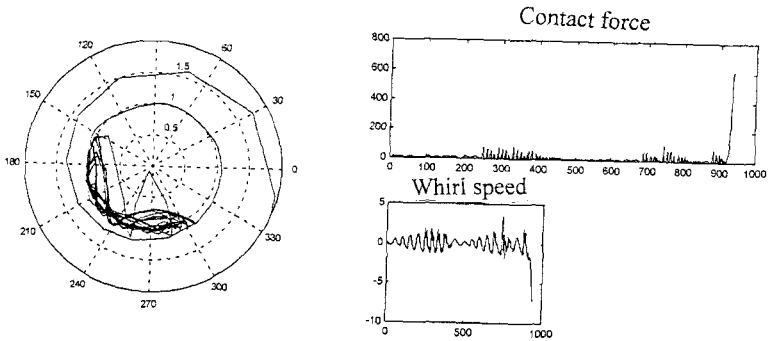


Figure 9-Modeled trajectory of shaft ( $\omega=4230$  rpm)

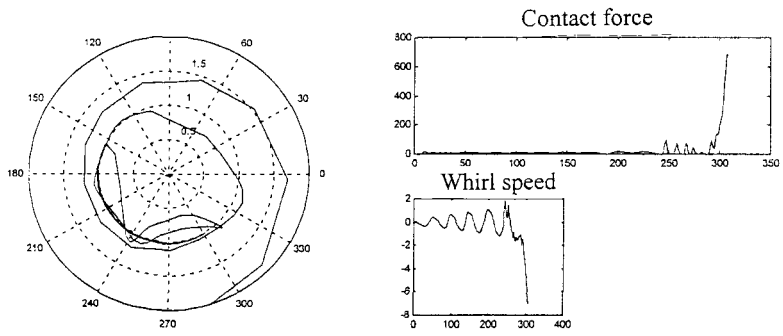


Figure 10-Modeled trajectory of shaft ( $\omega=4300$  rpm)

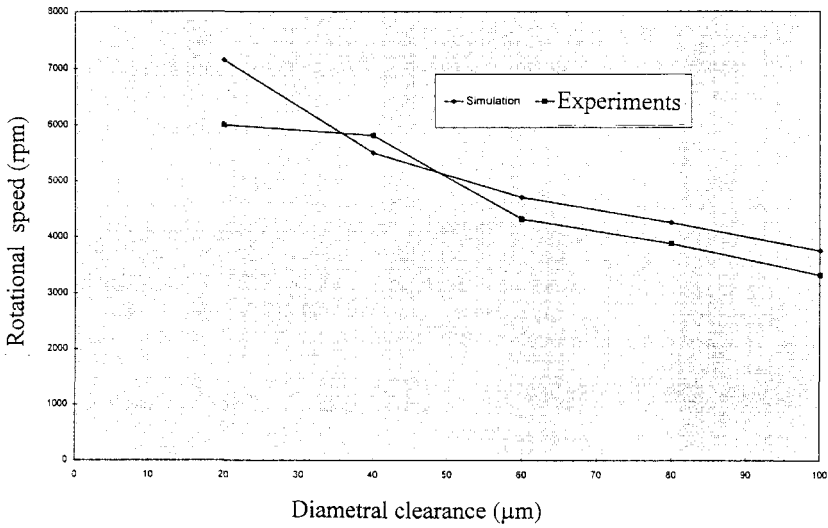


Figure 11-Comparison between theory and experiment

(Evolution of stability with clearance)



# On 2xrev – vibration components in rotating machinery excited by journal ovalization and oil film non-linearity

**N BACHSCHMID, B PIZZIGONI, and E TANZI**  
Dpartimento di Meccanica, Politecnico di Milano, Italy

## ABSTRACT

The presence of a twice-per-revolution component in vibration signals detected during the monitoring of rotating machinery is symptomatic of various possible malfunctions. This paper specifically describes characteristics allowing for the distinction of 2xrev. effects associated with geometrical errors in shaft journals, and the non-linearity of the oil-film force-displacement law in lubricated oil film bearings.

## 1. INTRODUCTION

A variety of malfunctions can cause twice-per-revolution vibration effects in rotating machinery: axial asymmetries, transverse cracks, journal ovalization and oil-film non-linearities in lubricated bearings. Certain characteristics, however, noticeable at working (or very low) speed - more so during a rotating-speed transient (i.e. running-up or coasting-down) - may help to distinguish one exciting cause from another. In this respect, studies have been carried out on typical behaviours relating to different excitation causes. This may be very helpful for diagnostic purposes, when it is necessary to identify the impending malfunction from vibration measurements normally performed on the bearings.

This paper considers two exciting causes associated with lubricated bearings, namely i) errors in journal geometric profile (journal ovalization), and ii) non-linear oil-film behaviour. Models of these two exciting causes are illustrated herein, and some interesting conclusions are drawn from the results of several simulations performed through their use. Orbits of an oil-film bearing journal were generated for different load conditions by means of a non-linear model; these were subsequently analysed to extrapolate any common behavioural peculiarities. The vibrations of a rotor measured on a test rig in conditions of high unbalance, or high bearing misalignment (both ought to highlight non-linear effects), are shown and compared in the theoretical analysis.

The behaviour of an ovalized bearing journal was also analysed by calculating oil-film forces and associated equilibrium positions of the ovalized journal during its rotation at a constant speed. This was repeated at several different speeds. A simplified model was also developed and tested for simulating such behaviour. In this case, too, the calculated results are compared with experimental results obtained on the test rig where one shaft revealed both journals as having consistent ovalization errors. All calculations and experimental results refer to a two-lobe lemon-shaped bearing with a given geometry; as a result of this, similar analyses ought to be carried out for other bearing types - in order to ascertain whether such conclusions have a more general validity.

## 2. TEST BEARINGS

The test rig available at the Politecnico di Milano - Dipartimento di Meccanica set up in compliance with the European MODIAROT (1) project was used. This includes a rotor train consisting of two shafts with a rigid coupling, supported by four identical lubricated bearings of the two-lobe type. The test rig and the bearing are represented in Fig. 1 The main geometric characteristics of this two-lobed bearing are:

Journal radius	$R_0 = 50.0 \text{ mm}$	Vertical positions of centre lobes
Bearing width.	$L = 40.0 \text{ mm}$	Lobe 1 $X_C^{(1)} = -0.15 \text{ mm}$
Radial clearance	$\delta = 0.30 \text{ mm}$	Lobe 2 $X_C^{(2)} = +0.15 \text{ mm}$
Angular lobe amp.	$\beta^{(1)} = \beta^{(2)} = 140^\circ$	

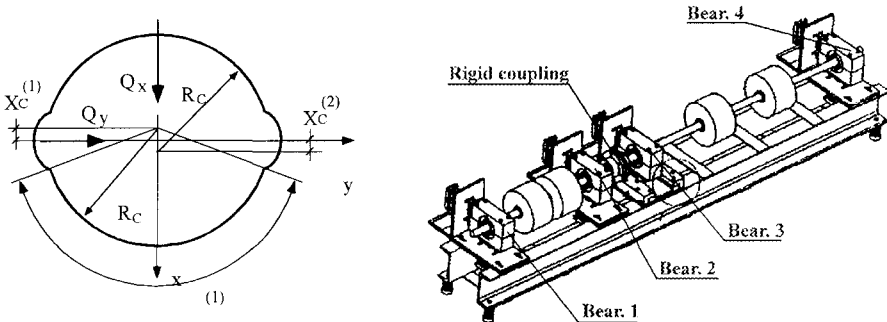
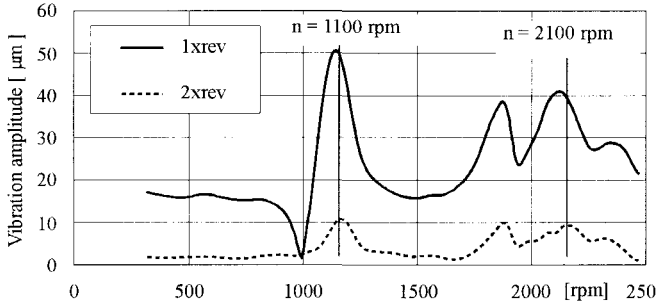


Figure 1. Two-lobe bearing geometry (left) and test-rig (right)

## 3. NON-LINEAR BEHAVIOUR ORBITS

From literature and field experience it is known that big-sized journal orbits in oil film bearings - which occur, for example, in passing through a critical speed - show 2xrev. components in its vibration spectra ; these may be attributed to oil film non-linear behaviour. With reference to tests performed on the test rig, Fig. 2 shows a 1xrev. and 2xrev. shaft vibration trend detected in correspondence of bearing 2 during a speed transient, with an unbalanced rotor. As may be noted, during the passage of the first critical speed (around 1100 rpm) there is a strong increase of the 2xrev. vibration component, and the same happens at higher speed (around

2000 rpm) when high 1xrev. components are measured due to a supporting structure resonance.



**Figure 2. 1xrev. and 2xrev. harmonics in a speed transient**

It has also been pointed out that, in the presence of high bearing misalignment, the journal orbit is “squeezed” and becomes “banana-shaped”. In this case too, a 2xrev. component appears. Fig. 3 shows a number of orbits measured in bearing 2, in different operating conditions: the small orbits refer to a well balanced rotor, and the big sized ones to an unbalanced rotor, both for two speeds (1100 rpm and 2100 rpm) where high vibrations are measured, as shown in previous Fig. 2. Also the effect of bearing misalignment is shown: the orbits in the middle of the figure are related to 0 misalignment, those on the r.h. side are related to -0.3 mm horizontal misalignment of bearing 3, and those on the l.h. side to +0.3 misalignment of the same bearing. The non linear effects, in terms of “squeezed” orbits, and presence of 2xrev. components are emphasised by the high unbalance (mainly at 1100rpm) and by the bearing misalignment (mainly at 2100 rpm).

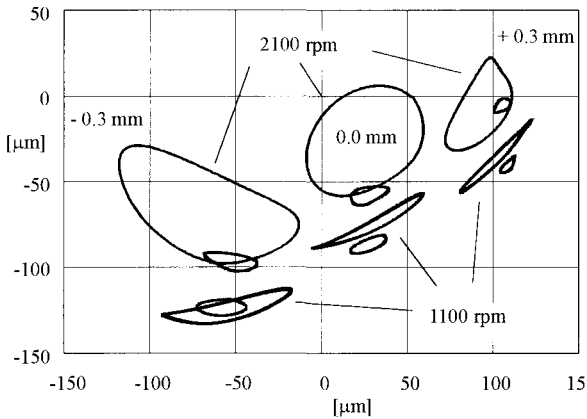


**Figure 3. Orbits measured experimentally in relation to two rotating speeds, different unbalances and different bearing alignment conditions.**

### 3.1 - Mathematical model

In the part that follows, so-called "non-linear orbits", traced by the journal centre in the clearance space of a lubricated bearing, are calculated and analysed. To determine the effects of a high static and dynamic loads on the dynamic behaviour of a journal, a model, consisting of a rigid rotor (of mass  $2m$ ) with a horizontal axis, symmetrically supported by two identical lubricated bearings and subjected to a  $2Q$  load assigned and applied in the centre line, was used. The size and direction of the load were assigned in order to obtain, each time, the desired equilibrium positions of the journal centre. A rotating load, simulating a known unbalance, was then applied to this system. In a suitably chosen reference system, non-linear dynamic equilibrium equations, during symmetric rotor translation, become:

$$\begin{cases} m\ddot{x} + F_x(x, y, \dot{x}, \dot{y}, \Omega) = Q_x + m\Omega^2 e \cos(\Omega t) \\ m\ddot{y} + F_y(x, y, \dot{x}, \dot{y}, \Omega) = Q_y + m\Omega^2 e \sin(\Omega t) \end{cases} \quad (3.1)$$

in which the components  $F_x(x, y, \dot{x}, \dot{y}, \Omega)$  and  $F_y(x, y, \dot{x}, \dot{y}, \Omega)$  of the oil film forces are obtained by integrating Reynolds' oil film equation according to the method outlined in (2). System (3.1) integration takes place subsequently in the time domain. Fig. 4 shows the orbits obtained in a situation of constant static load and increasing unbalance, resulting in orbits which gradually increase in size: two groups are related to the bearing loaded vertically only at two different speeds (1000 rpm and 3000 rpm), and the other two are related to the bearing loaded also horizontally.

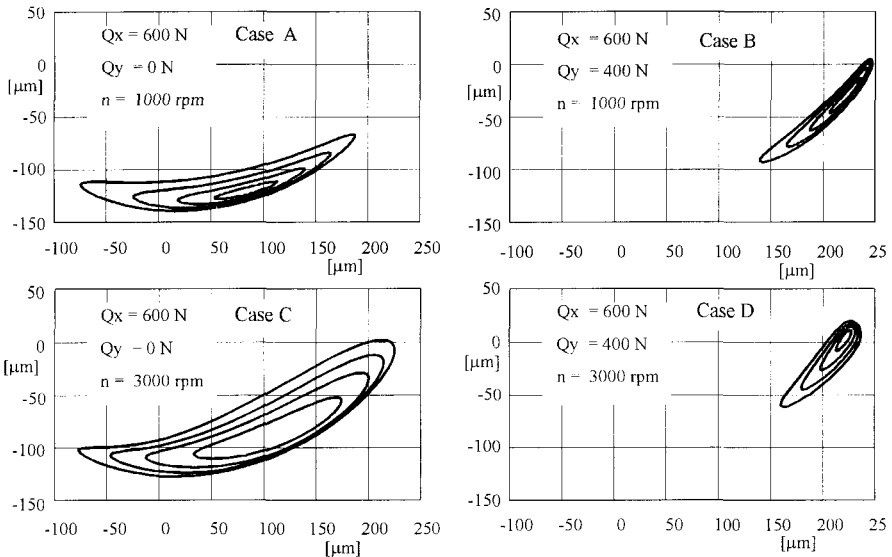


**Figure 4. Orbits obtained with constant load + increasing unbalance**

The results, in terms of the amplitude of a  $2x$ rev. component referring to that of the  $1x$ rev. and  $2x$ rev. component phase evaluated with respect to the initial position of rotating unbalance, for

the same rotation speeds, are shown in Fig. 5. As expected, the 2xrev. component increases as the orbit size increases, but amplitude and phase do not vary significantly.

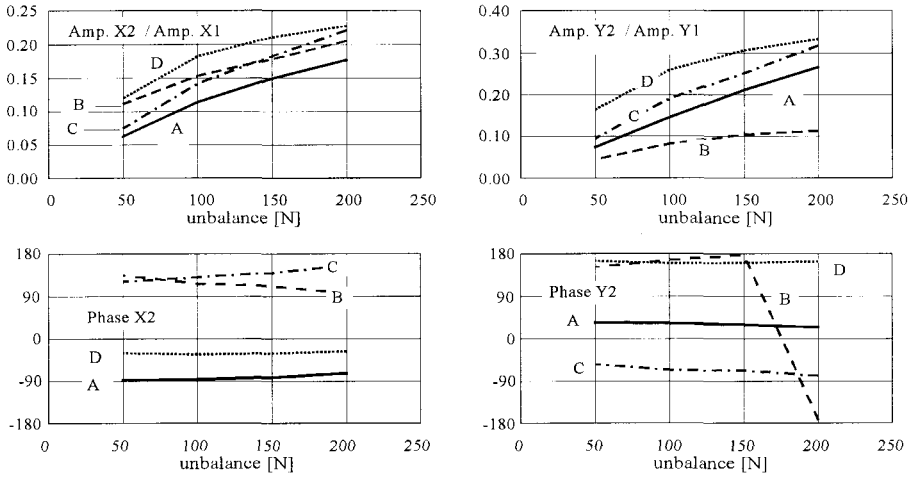


**Figure 5. 2xrev component amplitude (referring to that of the 1xrev component) and related phase**

Fig. 6 shows some orbits obtained with constant unbalance ( $m\epsilon\Omega^2 = 100\text{N}$ ) as the static load increases: the effect of oil film stiffness increase due to load increase can be seen.

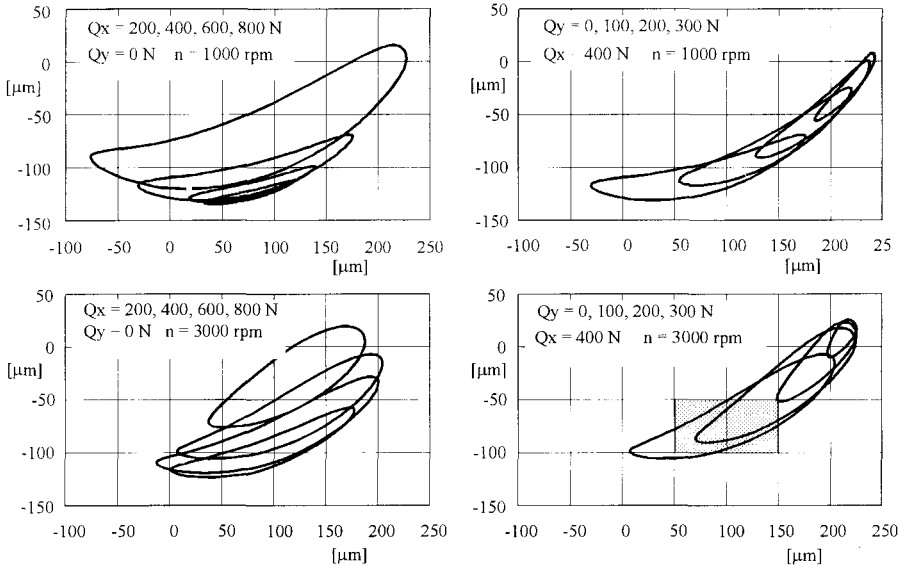


**Figure 6. Orbits computed for variable load+constant unbalance: displacements in  $\mu\text{m}$ . (The grey region shows the grid within which a deeper analysis has been made).**

These results show that the 2xrev. component constitutes a small percentage of the 1xrev. component, decreasing even further (together with the latter) as the load increases and oil film stiffness subsequently increases. On the contrary, as orbit size increases, a slight percentage increase of the 2xrev. component is registered.

In order to analyse the system behaviour with an orbit that remains small as the load increases, reference can be made to the analytical calculation shown in (4) which, without resorting to time domain integration, allows for evaluation of the effects of non-linearity in each journal static equilibrium position. The results - in terms of 2xrev. component amplitudes referring to 1x rev. component amplitude as the journal position changes within the grid shown in Fig. 6 - are shown in Fig. 7. At a constant speed, different loads correspond to different journal positions; the vertical and horizontal loads corresponding to the speed of 1000 rpm are indicated in Fig. 8. The 2xrev. component is rather small and decreases as the load increases, while the phase itself has a very variable trend, at least the phase of the vertical component.

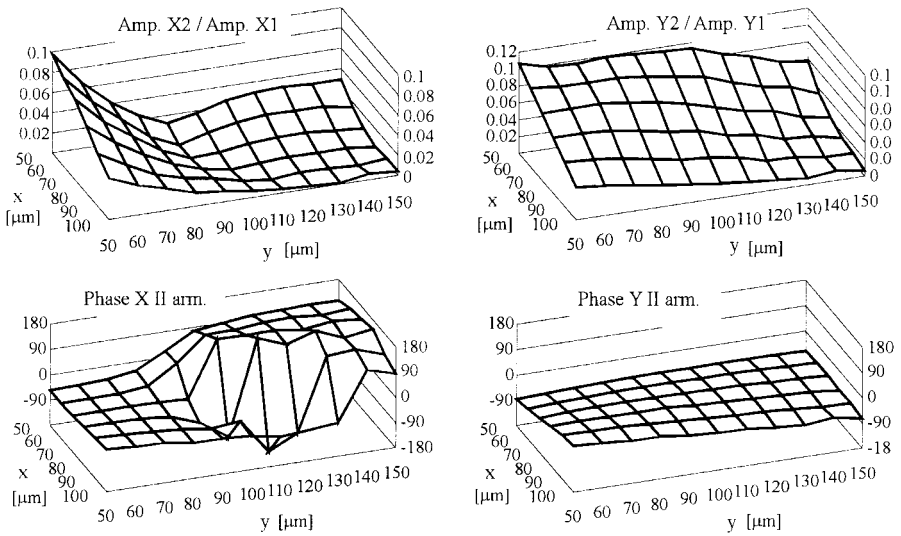


**Figure 7. 2xrev. component amplitude (referring to that of the 1xrev. component) and related phase**

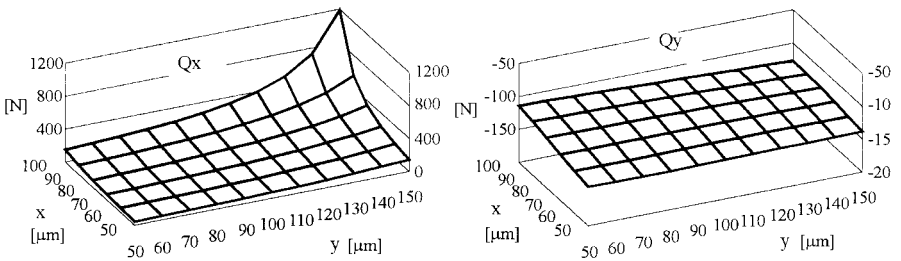


**Figure 8. Vertical and horizontal loads (in N) in different journal positions (1000 rpm)**

#### 4. EFFECTS OF GEOMETRIC JOURNAL IRREGULARITIES

Under ideal conditions, a shaft journal has a cylindrical surface with a constant circular section and an axis that coincides with the rotation axis of the rotor itself. The actual geometry of this component inevitably differs from the ideal one, both in terms of axial as well as circumferential direction due to a functional irregularity. As shown in (3), these irregularities are the cause of journal vibration excitation.

##### 4.1 Mathematical model

Having assumed a polar coordinate system whose origin lies in the rotation axis, the real journal profile may be represented by means of a  $R = R(\varphi)$  function. This paper only takes the 2xrev. irregularity component into consideration given by:

$$R(\varphi) \cong R_0 + R_2 \cos(2\varphi + \psi_2) \quad (4.1)$$

in which  $R_2$  is the circularity error, i.e. the so-called journal "ovalization", and  $\varphi$  represents the circumferential coordinate for the journal. The thickness expression  $h$  of the oil film to be included in Reynolds' equation assumes the following form:

$$h = \delta - R_2 \cos(2(\vartheta - \beta) + \psi_2) + y \cos \vartheta - x \sin \vartheta \quad (4.2)$$

where:  $\varphi = (\vartheta - \beta)$ ,  $\vartheta$  is the circumferential coordinate for the bearing,  $\beta$  identifies the journal reference axis position with respect to reference  $(x, y)$ , with  $\beta = \Omega t$  at steady state conditions and  $\delta$  is the radial clearance. The dynamic non-linear equilibrium eq. (3.1) become:

$$\begin{cases} m\ddot{x} + F_x(x, y, \dot{x}, \dot{y}, \Omega) = Q_x \\ m\ddot{y} + F_y(x, y, \dot{x}, \dot{y}, \Omega) = 0 \end{cases} \quad (4.3)$$

in which calculation of the components  $F_x(x, y, \dot{x}, \dot{y}, \Omega)$  and  $F_y(x, y, \dot{x}, \dot{y}, \Omega)$  of the oil film force is performed by integrating Reynolds' equation by using expression (4.2) for the oil film thickness and its derivatives. In this case too, system integration (4.3) should be performed in the time domain. The effects of ovalization can be shown somewhat approximately with a (4.3) linearized model. Depending on the external load and rotor rotation speed  $\Omega$ , the static equilibrium position of the journal is identified, and the stiffness [K] and damping [C] matrices equivalent to the oil film are calculated, (allowing for rotor equilibrium under an assigned  $2Q$  load, and the absence of journal defects). Ovalization of the journal may be represented by a vector  $\vec{s}_0$  of module  $R_2$  rotating at a  $2\Omega$  speed:

$$\vec{s}_0 = R_2 \exp i(2\Omega t + \psi_2) \quad (4.4)$$

The dynamic action caused by journal ovalization are estimated as follows:

$$\vec{F}_0 = [K]\vec{s}_0 + [C]\dot{\vec{s}}_0 = R_2 [K] \exp i(2\Omega t + \psi_2) + i2\Omega R_2 [C] \exp i(2\Omega t + \psi_2) \quad (4.5)$$

Relative vibration amplitudes  $\{x_0\}$  caused by journal ovalization can therefore easily be calculated according to the linear system:

$$[M]\{\ddot{x}_0\} + [C]\{\dot{x}_0\} + [K]\{x_0\} = \{F_0(R_2, \Omega)\} \quad (4.6)$$

where  $[M]$  is the rotor mass matrix.

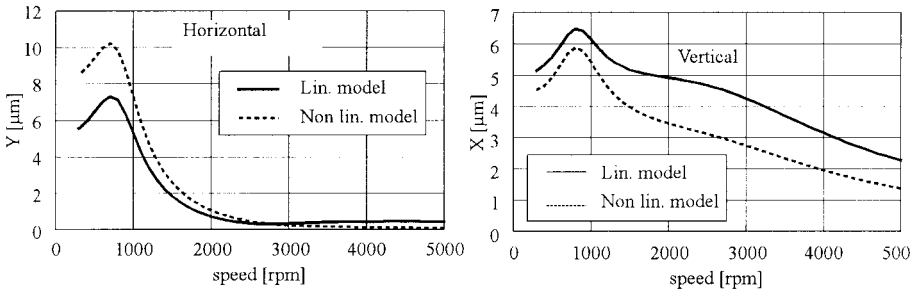


**Figure 9. Frequency response: 2xrev. vibration components**

In order to evaluate the degree of approximation of the linear model (4.6), figure 9 shows the 2xrev component trend of the frequency response in direct comparison to that obtained using the non-linear model (4.3) taken from (3). As may be seen, the linear model overestimates the vertical component in the entire speed range, while the horizontal one is overestimated at high speed only.

#### 4.2 - Experimental results

Measuring journal relative vibrations on the test rig by means of two radial proximity probes, mounted on the bearing housing in two positions at an angular distance of  $90^\circ$  (as in turbomachinery) at a very low speed, the phase of the 2xrev vibration induced by axial asymmetry or a crack measured in one direction is  $90^\circ$  out of phase with respect to the 2xrev vibration detected in the other direction. In fact, by representing the vibration using a rotating vector, it has an angular speed  $2\Omega$  double that of the shaft; its passage under the second proximitor situated at a  $\alpha = \pi/2$  angle with respect to the first, takes place after a time  $\tau = \alpha/2\Omega = \pi/4\Omega$  equal to one fourth of the  $\pi/\Omega$  period of the second harmonic, thus determining the angular phase lag indicated.

The phase lag of vibrations induced by a journal ovalization, meanwhile, is  $180^\circ$ . Journal ovalization, detected improperly as a vibration, can in fact be represented e.g. by two  $180^\circ$  vectors rotating at the same angular speed  $\Omega$  as the journal. The passage of the same vector relative to the second pick-up situated at  $\alpha = \pi/2$  angle with respect to the first takes place after a time  $\tau = \alpha/\Omega = \pi/2\Omega$  equal to half of the  $\pi/\Omega$  period of the second harmonic. It must be recalled that, in this instance, since the proximity probes are measuring the distance to the journal surface and not a displacement of the journal axis, the displacements measured are apparent vibrations. In two absolute x,y measurement directions with a  $90^\circ$  angle between them, this apparent low revolution vibration may be indicated, for example, as follows:

$$\begin{aligned} x &= R_2 \cos(2\Omega t) \\ y &= R_2 \cos(2\Omega t - \pi) \end{aligned} \quad (4.7)$$

The locus with these coordinates is the straight line  $y = -x$ . By assuming that (4.7) is the result of an actual vibration, this straight line would be interpreted as the trajectory of the



centre of the journal. By transforming the values measured in order to apply them to a system rotated at  $45^\circ$  with respect to the x,y measurement example, an amplitude vibration  $R_2\sqrt{2}$  would be obtained in one direction, and “nil” vibration at  $90^\circ$  in the other. This operation sequence is normally used to monitor rotating machinery, the aim being to identify the site traced from the journal centre using proximity couples which, when mounted on bearing housings, have a  $90^\circ$  angle between them - but at  $\pm 45^\circ$  with respect to the vertical. However, it is not uncommon for these findings to be transformed in order to apply them to the horizontal and vertical directions. By monitoring the vibrations of a rotating machine journal at high speeds the vibrations of the journal axis are detected by the proximity sensors as the superposition of a geometrical error with generated vibrations. As a consequence of this fact, during a run-down transient the 2xrev. signals induced by journal ovalization would show a rather constant trend of phase and amplitude due to the superposition of the constant value ovalization error, as shown in Fig. 10 where the measured 2xrev. components in bearing 3 in  $\pm 45^\circ$  directions are represented. From the dimension measurements performed, the journal of this bearing showed a  $R_2 = 5.8 \mu\text{m}$  ovalization. The phase shift between the 2 sensors is  $\sim \pi$ .

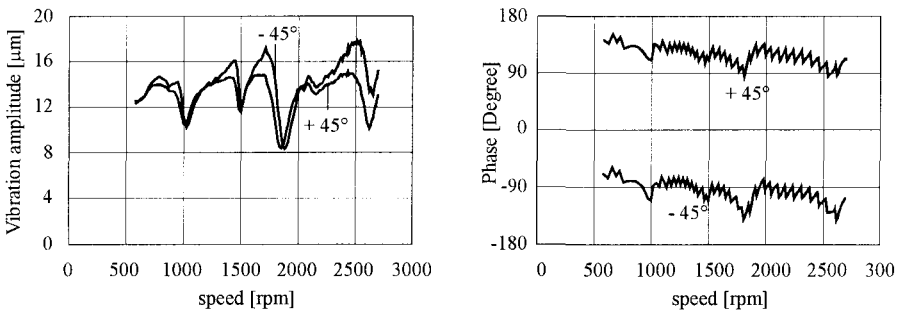


**Figure10. Experimental findings of the 2xrev. component in  $\pm 45^\circ$  directions**

In Fig.11, for comparison with the results obtained by the linear model (4.6) they are transformed to be referred to vertical and horizontal directions.

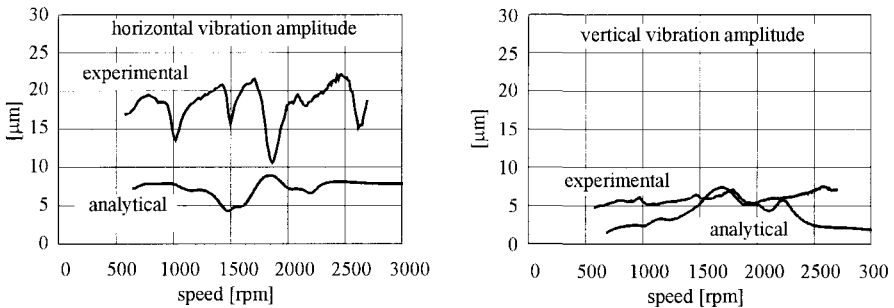


**Figure 11. Analytical-experimental comparison of the 2xrev. component in vertical and horizontal directions**

The previously described apparent vibration is clearly recognisable in horizontal direction, both in the measured and in the calculated diagrams. The overall agreement is not very good: the mean horizontal amplitude is much lower than the measured one and some positive or negative peaks in the respectively vertical and horizontal diagrams are not reproduced by the linear model. This latter effect is due to oil film non-linearities which, when passing through a critical speed (around 1100 rpm and 1800 - 2100 rpm), amplify the 2xrev. components not accounted for in the linear model employed.

## 5. CONCLUSIONS

The characteristic features of 2xrev. effects in orbits traced by journals of “lemon-shaped” two-lobe lubricated bearings were analysed using suitable models. A number of experimental results have also been presented. The following conclusions can be drawn:

- 2xrev. components due to oil film non linearity are related to the orbit size rather than to bearing loads;
  - its amplitude is (quasi linearly) related to the corresponding 1xrev. component;
  - its phase changes with the load but is independent of the unbalance or of the size of the orbit;
- 2xrev. components due to journal ovalization are recognisable because affected by an “apparent” vibration component which is generally higher than the true vibration.

It is therefore possible to distinguish both analysed components from those caused by axial unsymmetry or transverse cracks, due to different relationships between horizontal and vertical components and their phase.

## ACKNOWLEDGMENTS

The MURST Cofinanziamento grant “Progettazione funzionale e sperimentazione di supporti e tenute innovativi per il macchinario rotante” is gratefully acknowledged.

## REFERENCES

- (1) Bachschmid N., Dellupi R., *Experimental validation of unbalance identification methods*, Proc. V IFToMM Int. Conf. on Rotordynamics, Darmstadt, pp. 709-721, September 1998
- (2) Ruggieri G., *Un metodo approssimato per la risoluzione dell'equazione di Reynolds*, L'Energia Elettrica, n. 2, pp. 86-95, 1976
- (3) Bachschmid N., Pizzigoni B., Tanzi E., *Effetti di irregolarità geometriche del perno sul comportamento della coppia portante lubrificata*, Proc. V Convegno di Tribologia, Varenna, pp.313-323, 1998
- (4) Pizzigoni B., Tanzi E., *Un metodo approssimato per lo studio del comportamento non lineare di cuscinetti lubrificati*, Proc. XIII Congresso AIMETA, Siena, 1997

# Dynamic characteristics of oil-lubricated herringbone groove bearings

F P WARDLE and C A GOAT  
Loadpoint Limited, Swindon, UK

## Synopsis

Herringbone grooves machined into fluid film journal bearings have the effect of eliminating the half speed whirl phenomenon normally associated with plain journal bearings. Coupled with the recent development of cost effective manufacturing techniques such bearings may well compete in a wider range of precision or high speed rotor dynamic applications than has so far been possible. In this paper experimental measurements of the dynamic characteristics of an oil lubricated herringbone groove journal bearing are presented and compared to those of a plain journal bearing of the same geometry. The measurements confirm that the herringbone groove bearing is not prone to instability and that it exhibits a high accuracy of rotation and high dynamic stiffness.

## Introduction

In this paper Herringbone Groove Bearing (HGB) is the term used to describe a fluid film journal bearing which contains a series of helical grooves symmetrically disposed about the bearing centreline as shown in fig 1. This type of bearing belongs to a family of bearings generally referred to as spiral groove bearings which embrace cylindrical, spherical, conical and flat annular bearing geometry's. Grooves may be machined into the rotating or stationary bearing component and may extend part way or completely across the bearing surface depending upon the operating characteristics required. Such bearings may be liquid or gas lubricated but in this paper attention is confined to oil lubrication. Spiral groove bearings have been known for more than half a century, the first published analysis being attributed to Whipple in 1949 (1). Since then there have been several notable developments in the understanding of grooved bearings (2 – 4). However the most comprehensive work on oil lubricated grooved bearings was published in

1975 by Bootsma (5). This covered the theoretical analysis of all types of spiral groove bearing and experimental work validating the theory and evaluating different modes of lubricant supply and sealing. Two principle advantages of grooved bearings over plain bearings are apparent from Bootsma's work. Firstly that they are not prone to half speed whirl and secondly that they can operate without the need for a continuous feed of lubricant. The grooves were also found to affect bearing load capacity and stiffness. At low eccentricities Bootsma found that grooved bearings had a similar stiffness to plain bearings however at high eccentricities the plain bearing exhibited a significantly higher load carrying capacity.

The above advantages of grooved bearings make them a potential choice in applications where accuracy of rotation and/or high speed is important. There are many such applications however HGB's have not yet found widespread use. Much of the early research was directed at domestic recording equipment and some video recorders are reported to have grooved bearings. More recently research has been directed at the computer hard disc drive (6-10) where the superior running accuracy of HGB's compared to ball bearings enable data tracks on the discs to be more closely spaced thereby increasing disc capacity. Such disc drives are only just becoming commercially available (11). The slow take up of HGB's, particularly in high volume applications has been partly due to the time to develop cost effective manufacturing equipment. Grooves have proved difficult to machine to the required tolerances and only now are cost effective methods being introduced (12).

In the potential applications for the HGB the bearing parameters of particular interest are stability, rotational accuracy, static stiffness and damping. Although the stability of the HGB has been analysed and verified by past research and its rotational accuracy determined in individual applications, no data appears to have been published regarding its dynamic stiffness. In this paper an overall assessment of the dynamic characteristics of an oil lubricated HGB is made. Dynamic flexibility measured by an impulse technique is used to assess the stability, stiffness and damping of a bearing – shaft system incorporating HGB's and measurements of shaft displacement are used to assess accuracy of rotation. The results are discussed and compared with measurements taken on the same system fitted with an equivalent plain bearing.

## **Experimental Arrangement**

The test bearings were built into a spindle cartridge mounted on a massive vibration isolation platform and driven by an inline motorised air spindle via a flexible coupling as shown in fig 2. This drive arrangement enables speeds of up to 20 000 rpm to be obtained with a minimum of extraneous vibration. Running accuracy of the air spindle was better than 5  $\mu\text{m}$  and its balance better than 0.1 gm cm. Finally an oil pump and reservoir provided a means of continuously feeding the bearings with oil.

The preferred bearing arrangement was as shown in fig 3. This comprised of the two test journal bearings of 25.4 mm in diameter spaced 120 mm apart and a double sided thrust bearing to provide axial location. Not only is this arrangement stable and common to many types of precision machine but its simplicity allows a rigid construction and accurate machining of the critical bearing surfaces. The housing comprised of an 80 mm diameter, 20 mm wall thickness

stainless steel tube into which was interference fitted two lead bronze bushes. These defined the length of the test journal bearings and were through bored in a single operation to ensure negligible misalignment and accurate diameter control. Before fitting the bushes an oil feed arrangement was machined into them offset 5 mm from the bearing centre. Two shafts were manufactured, one with a plain outside diameter, the other identical except for the addition of herringbone grooves. Again the simple shaft geometry permitted accurate machining. The shaft surface containing the bearing seatings was machined in a single operation and was extended beyond the end of the cartridge to provide an accurate surface for displacement measurement. The thrust bearing was an inward pumping spiral groove design and was made as a separate disc so that its axial position on the shaft could be adjusted by the use of spacers. This allowed offset of the herringbone groove in the bearing journal to be investigated in later studies.

Measurements of dynamic stiffness at the spindle nose were taken using an impulse response technique. An ADE Technologies capacitance type of displacement sensor was rigidly clamped to the bearing housing and positioned so as to pick up radial movements of the shaft close to the front journal bearing. This sensor had a measurement range of +/- 100 um, a resolution of 0.01 um and a frequency response of 0 – 5 000 Hz. An impulsive force in a radial direction was applied to the shaft via a small single row radial ball bearing mounted on the end of the shaft. The ball bearing was used to minimise a friction component of force which would otherwise be generated by impacting with a moving surface. A Dytran 1050v3 force gauge with a range of 0 – 400 N and a resolution of 0.01 N was used to measure the applied impact force. Force and displacement signals were fed via amplifiers to a PC based two channel frequency analyser which automatically generated transfer function and coherence.

Static loads and deflections were measured by hanging a dead weight through the centre of the ball bearing and using the capacitance sensor to monitor deflections. The sensor could be moved through 90 degrees to measure X and Y components of deflection.

Finally temperature of the front journal bearing was monitored by a thermocouple attached to the end face of the lead bronze bush 2 mm from the shaft.

### **Bearing Design**

The dimensions of the journal bearing were diameter - 25.4 mm and length - 15 mm. Diametral clearance was 50 um for both plain and herringbone grooved bearings. Machining time was approximately 4s. A fully grooved bearing design was chosen for good stability. The groove design was not optimised in any way but the parameter values are typical of bearings designed for maximum stability. Groove parameters were:-

Groove depth	-	25 um
Groove angle	-	30 degrees
Groove/land width ratio	-	0.8
Number of grooves	-	12

Grooves were machined using an electrochemical micromachining technique as described in ref. 12. Machining time was approximately 4s. The axial length of the grooves was made 20 mm compared to the bearing width of 15 mm so that they could be offset relative to the bearing centre line.

Bearing materials were journals – LB4 lead bronze, shaft – 440C stainless steel heat treated to 58 HRc. The bearings were lubricated with Shell Tellus T10 mineral oil having a viscosity of 10 cSt at 34 degrees Centigrade.

## Spindle Characteristics

The characteristics of the spindle at a position overhung from the front journal bearing is relevant to many precision bearing applications. In this investigation the small amplitude response of the shaft about the no load equilibrium position is of particular interest.

### Motion Errors

The accuracy of rotation of the shaft was measured in a radial plane using the displacement sensor mounted at the spindle nose as shown in fig. 2. Measurements are displayed as amplitude spectra in figs. 4 and 5 for the shaft supported by grooved and plain bearings respectively. Motion errors appear as discrete frequencies harmonic of the rotational speed of 130 Hz (7 800 rpm). For the grooved bearing, fig 4, the largest harmonic corresponds to rotational speed and has an amplitude of 0.15  $\mu\text{m}$  RMS, higher order harmonics are significantly lower at 0.05  $\mu\text{m}$  maximum. For the plain bearing all harmonics are similar in amplitude at 0.05  $\mu\text{m}$  RMS. It should be noted that the motion errors shown in figs. 4 and 5 contain errors due to out of round of the shaft and out of balance. For both types of bearing the shaft was precision machined but not balanced. The machining resulted in out of round at the measurement position of 0.19 and 0.20  $\mu\text{m}$  pk-pk for the grooved and plain bearings respectively.

### Static Stiffness

Fig. 6 shows examples of the radial load – deflection relationships for the spindles with plain and grooved bearings rotating at a speed of 7 800 rpm. In this figure deflection is the resultant displacement of the shaft which is the root mean square of displacements in line and perpendicular to the direction of the applied load. The spindle with grooved bearings exhibits a linear load – deflection relationship at all eccentricities up to the limit measured whereas the spindle with plain bearings only has a linear load – deflection relationship at low eccentricities. Furthermore the spindle with plain bearings exhibited a higher stiffness than the spindle with grooved bearings. Based upon resultant displacement, stiffness of the former was found to be 7.41 N/ $\mu\text{m}$  compared to 4.64 N/ $\mu\text{m}$  for the latter. The most marked difference between spindles with grooved and plain bearings is the phase of the displacements with respect to the direction of the applied load, fig. 7. For plain bearings the phase was observed to decrease with increasing eccentricity from 85 degrees at  $e = 0.05$  to 46 degrees at  $e = 0.33$  whereas for grooved bearings the phase remained low at approximately 30 degrees for eccentricities between 0.05 and 0.37.

**Dynamic Stiffness**

Figs 8 and 9 show examples of the dynamic flexibility of the spindle with grooved and plain bearings, at a rotational speed of 7 800 rpm. These measurements are for shaft displacements inline with the applied force. Similar measurements were taken for shaft displacements perpendicular to the direction of the applied force and for a range of rotational speeds. The spindle with plain bearings exhibited a high flexibility at a frequency of 65 Hz which corresponds to half running speed and is therefore due to the half speed whirl phenomenon well known on this type of bearing. The local maxima in the response curve at frequencies harmonic of 130 Hz are due to shaft motion error or out of round picked up by the displacement sensor. Local to these frequencies, coherence was low whereas generally it was better than 0.99. Within the 0 – 1000 Hz frequency range considered, the dynamic flexibility of the spindle with grooved bearings exhibits an almost ideal characteristic with flexibility generally reducing with increasing frequency. The maximum dynamic flexibility occurs at 65 Hz which again is the half speed whirl frequency, however the magnitude of the flexibility is only 50% higher than the static flexibility.

**Dynamic Characteristics of the Bearings**

The dynamic characteristics of fluid film bearings are generally defined in terms of four stiffness and four damping coefficients (13):-

$$\begin{matrix} K_{xx} & K_{xy} \\ K_{yx} & K_{yy} \end{matrix} \quad \text{and} \quad \begin{matrix} C_{xx} & C_{xy} \\ C_{yx} & C_{yy} \end{matrix}$$

Where K refers to stiffness, C to damping and the subscripts x and y refer to orthogonal directions in the plain of the bearing. For small amplitude bearing motions about the no load position:-

$$K_{xx} = K_{yy} \quad K_{xy} = K_{yx} \quad C_{xx} = C_{yy} \quad \text{and} \quad C_{xy} = C_{yx}$$

Thus the bearing’s dynamic stiffness is defined by the four parameters  $K_{xx}$ ,  $K_{xy}$ ,  $C_{xx}$ , and  $C_{yy}$ .

**Stiffness Coefficients**

The no load stiffness coefficients of the grooved and plain bearings can be determined from experimental load - deflection measurements of the spindle. A number of assumptions are first necessary: that shaft bending deflections are small compared to bearing deflections; bearing load – deflection relationships are linear and that the phase of the bearing deflection is independent of amplitude. The assumptions are justified by theoretical estimates of shaft bending stiffness and experimental observation of shaft load – deflection relationships. If F is the load applied to the shaft and d is the resultant shaft deflection at phase 0, then given the bearing spacing and the overhang of the applied force from the first bearing, the resultant stiffness of this bearing was estimated to be  $K_f =$

1.96 F/d at phase angle 0. The second bearing has the same resultant stiffness but is displaced 180 degrees in phase.

Resultant stiffness  $K_r$  and phase  $\theta$  for both grooved and plain bearings are shown in figs. 10 and 11. The experimental results are also compared with theoretical calculations based upon the analysis of Ref. 5. For stiffness  $K_r$ , the agreement between theory and experiment is good at low speeds but as speed increases the differences between theory and experiment diverge. Agreement between theory and experiment in respect of phase is reasonable over the speed range investigated.

Stiffness coefficients  $K_{xx}$  and  $K_{xy}$  are related to  $K_r$  and as follows:-

$$K_{xx} = K_r / \cos \theta \quad K_{xy} = K_r / \sin \theta$$

and can therefore be determined from the data presented in figs. 10 and 11.

### Damping Coefficients

Damping coefficients were determined from the transfer function measurements. At the first resonant frequency of the bearing – shaft system the magnitude of the dynamic flexibility is dependent only on damping which in this case is predominantly due to the bearings. At resonance, the magnitude of the dynamic flexibility is related to frequency and damping coefficient by:-

$$= 1 / c$$

The direct and cross coupled damping coefficients were determined for both grooved and plain bearing types and are shown in normalised form as functions of bearing speed, fig. 12. Over most part of the speed range investigated the grooved bearing exhibited significantly higher damping than the plain bearing.

### Discussion

Although the experimental results presented in this paper are for one size of bearing operating over a limited range of conditions the results are considered significant and relevant to a number of precision rotor dynamic applications.

Motion error measurements shown in figs. 4 and 5 are artificially high due to residual imbalance of the shaft and out of round of the measured surface yet they show harmonics of rotational speed to be generally less than 0.05  $\mu\text{m}$  RMS for both grooved and plain bearing types. These are comparable with motion errors of bearings used in high precision machining applications.

Static load – deflection characteristics of the bearings summarised in figs. 6 and 10 show the plain bearing to have a higher resultant stiffness than the grooved bearing and therefore higher load carrying capacity. In this case the grooved bearing has about 67 % of the stiffness of the



plain bearing. It should be noted that the basis of the comparison is bearings of the same minimum clearance. The grooved bearing has a higher average clearance than the plain bearing and exhibits lower running temperatures and friction torque. Compared on the basis of the same friction level (or average clearance) then the grooved bearing stiffness is 84% of that of the plain bearing. At low speeds, experimental measurements compare reasonably well with predictions from an analytical model based on Ref. 5 but for higher speeds the predictions over estimate load capacity and stiffness.. The differences between theory and experiment are attributed mainly to thermal effects and a limitation of the theoretical model. Whilst the effect of bearing temperature on oil viscosity was included in the comparison, the effect of temperature on bearing clearance was neglected. Furthermore the implementation of the model used to generate theoretical predictions assumed a full Somerfeld boundary condition which in practice tends to over estimate bearing loads. Nonetheless agreement is sufficient to enable the model to be used to examine a wider range of bearing variables and the observation of grooved bearing stiffness being less than or equal to that of a plain bearing applies to a wide range of bearing designs.

The phase of the bearing deflection with respect to the direction of the applied load shown in figs. 7 and 11 highlight a major difference between grooved and plain bearing types at the low eccentricities considered in this investigation. Grooved bearings exhibit a much lower phase than plain bearings and this must assist its stability under dynamic load conditions. Again theoretical - experimental comparisons were made and reasonable agreement achieved.

A number of important observations can be made from the measurements of dynamic flexibility of the bearing – shaft system, figs. 8 and 9. The plain bearing clearly exhibits half speed whirl when excited by an impulse and this severely limits the system's minimum dynamic stiffness. In fig. 9 whirl corresponds to a minimum dynamic stiffness of 0.13 N/um which is very low compared to the bearing's static stiffness of 6.56 N/um. For the grooved bearing an increase in dynamic flexibility at the half speed whirl frequency can also be observed, fig. 8 and this also determines the system's minimum dynamic stiffness. However the effect is small and minimum dynamic stiffness is 2.07 N/um compared to a static stiffness of 3.29 N/um. Thus although the grooved bearing results in a system with half the static stiffness of that for a plain bearing, the dynamic stiffness is a factor of 16 higher. At frequencies above the half speed whirl frequency the dynamic flexibility of the system with the grooved bearings (fig. 8) is generally less than that of the system with plain bearings (fig. 9) which indicates that the grooved bearings generally have higher damping.

Damping is further quantified by the experimental results of fig. 12. Compared to other bearing types both the grooved and the plain bearings exhibit high damping coefficients. However over most of the speed range considered the grooved bearing exhibits significantly higher damping than the plain bearing.

## Conclusions

Oil lubricated herringbone groove bearings exhibit good running accuracy, high dynamic stiffness and excellent stability characteristics. Their main advantages over plain bearings of the same size and clearance are stability and dynamic stiffness. However their improved dynamic performance is accompanied by lower static stiffness and load carrying capacity.

## Acknowledgements

The authors would like to thank J. F. W. Sweet, the Managing Director of Loadpoint for supporting this investigation, Tony Snow and Dave Gilham of Loadpoint Bearings for the supply of test rig components and Alistaire Tonkin and Pete Rickards for assistance with the experimental work.

## References

- 1) Whipple R. T. P.  
Herringbone pattern thrust bearing, AERE, T M 29. 1949
- 2) Hirs G. G.  
The load capacity and stability characteristics of hydrodynamic grooved journal bearings. ASLE Trans. 8, 296 – 305, 1965.
- 3) Muiderman E. A.  
New possibilities for the solution of bearing problems by means of the spiral groove principle. Proc. I. Mech. E. 180, 174 – 183, 1965/1966.
- 4) Muiderman E. A.  
Spiral Groove Bearings, Macmillan, London, 1966.
- 5) Bootsma J.  
Liquid lubricated spiral-groove bearings, Ph. D. Thesis, Technological University of Delft, 1975.
- 6) Ku C-P. R.  
Dynamic characteristics of spindle motors supported by hydrodynamic bearings. Proceedings of the 24<sup>th</sup> Incremental Motion Control System & Devices Conference, 6-8 June, San Jose, California, 1995.
- 7) Leuthold H., Jennings D  
Spindle motors with hydrodynamic bearings and high inertial load. Proceedings of the 24<sup>th</sup> IMCSD, 6-8 June, San Jose, California, 1995.

- 8) Leuthold H., Murphy S.  
Impact testing of spindle motors with hydrodynamic bearings. Proceedings of the 25<sup>th</sup> IMCSD, 11-14 June, San Jose, California, 1996.
- 9) Rahman M., Leuthold H.  
Computer simulation of a coupled journal and thrust hydrodynamic bearing using a finite element method. Proceedings of the 25<sup>th</sup> IMCSD, 11-14 June, San Jose, California, 1996.
- 10) Zhu J., Ono K.  
A comparison study on the performance of four types of oil lubricated hydrodynamic bearings for hard disc drive spindles. Trans. ASME. Vol. 121, pp 114-120, 1999.
- 11) Ku C-P. R., Parsonault S., Leuthold H.  
Hydrodynamic motors trim disk drive run out. Data Storage, January 1998.
- 12) Wardle F. P.  
Electrochemical micromachining of mass produced fluid film bearings. Proceedings of Euspen 1<sup>st</sup> International Conference, Bremen, May 31 - June 4. 1999.
- 13) Rao J. S.  
Rotor Dynamics, second edition, John Wiley and Sons, New Delhi, 1991.

© 2000, Loadpoint Ltd

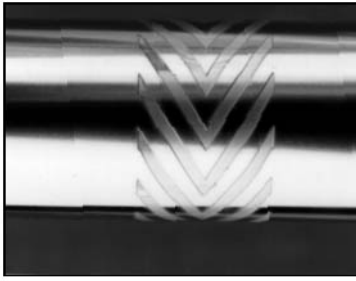


Fig 1 Herringbone Groove Journal Bearing

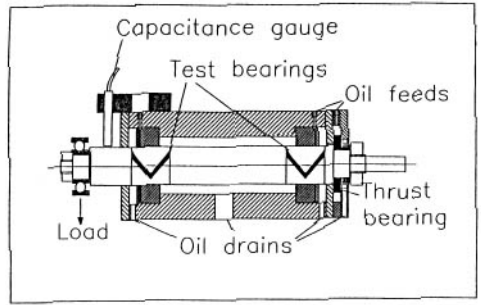


Fig 2 Schematic Rig Layout

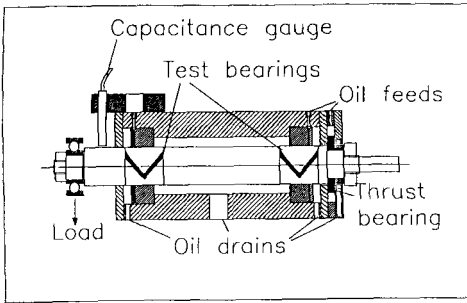


Fig 3 Test Bearing Arrangement

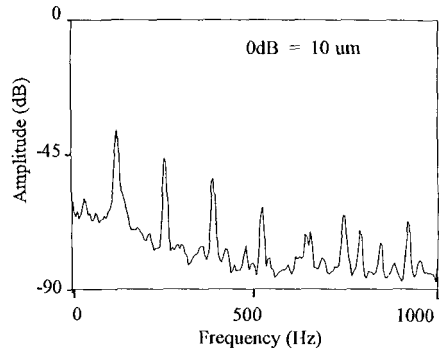


Fig 4 Spindle Motion Error with Grooved Bearings

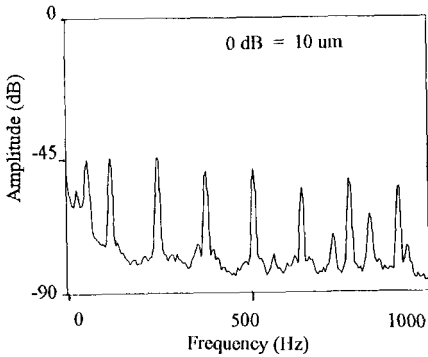


Fig 5 Spindle Motion Error with Plain Bearings

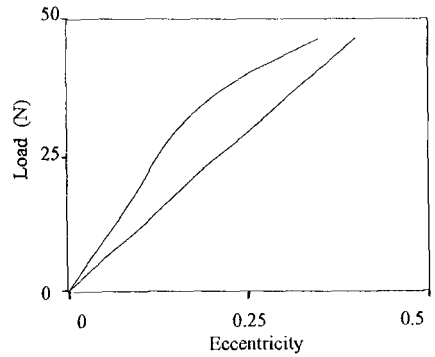


Fig 6 Spindle Load-Deflection Relationship

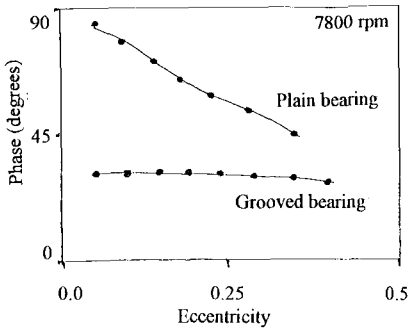


Fig 7 Phase of Spindle Deflection

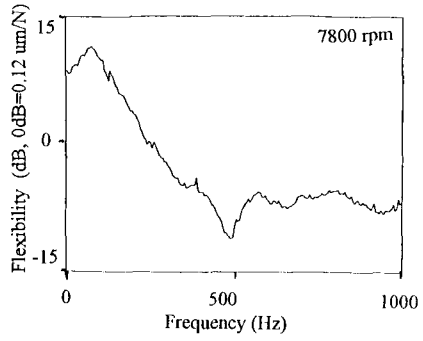


Fig 8 Dynamic Flexibility of Spindle with Grooved Bearings

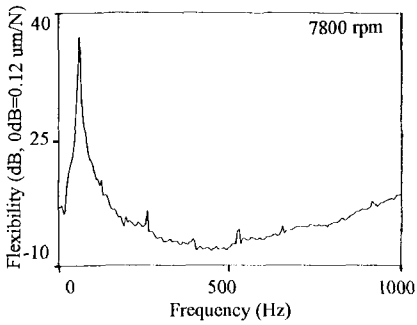


Fig 9 Dynamic Flexibility of Spindle with Plain Bearings

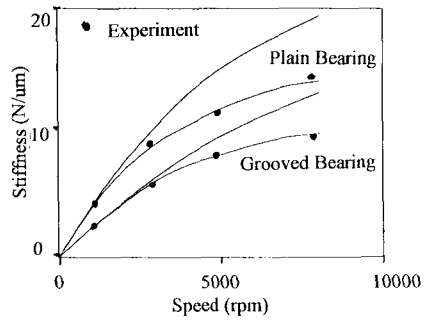


Fig 10 Bearing Stiffness v Speed

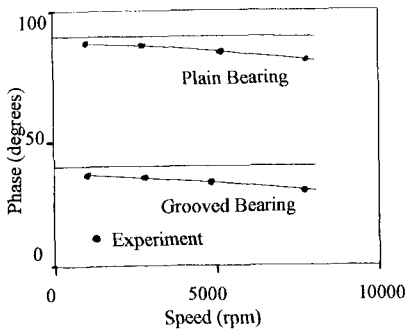


Fig 11 Phase v Speed

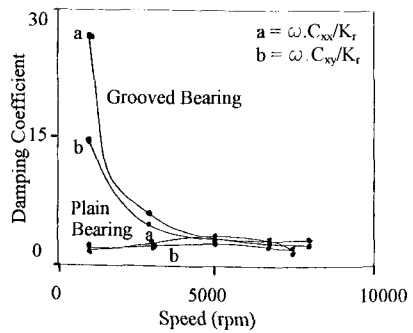


Fig 12 Damping Coefficients v Speed

*This page intentionally left blank*

## Bearings and Seals

*This page intentionally left blank*



# The stability characteristics of a journal bearing under starved lubrication

M TANAKA and K SUZUKI

Department of Mechanical Engineering and Engineering Synthesis, University of Tokyo, Japan

## SYNOPSIS

The hydrodynamic oil film in a journal bearing operating at a constant load and speed is found experimentally to reduce its area and thickness when the flow rate of lubricant oil to the bearing decreases beyond the limit that can maintain flooded lubrication condition. This observed result gives a theoretical model of the formation and rupture of bearing oil film under starved lubrication condition. Then the static and dynamic performance of the journal bearing is calculated, based on this model. Next, the stability characteristics of a Jeffcott rotor is studied theoretically and experimentally when the rotor is supported in journal bearings operated under starved lubrication conditions. Starved lubrication conditions are concluded to reduce the threshold speed of the unstable vibration of the rotor.

## NOTATION

$C$	mean radial clearance of bearing
$C_{xx}, C_{xy}, C_{yx}, C_{yy}$	dimensionless damping coefficients of oil film
$D$	bearing diameter
$K_{xx}, K_{xy}, K_{yx}, K_{yy}$	dimensionless spring coefficients of oil film
$L$	bearing width
$N$	rotational speed, rpm
$Q$	supply oil flow rate
$U$	journal surface velocity
$W$	bearing load

$f_x, f_y$	oil film force in the vertical and horizontal directions respectively
$g$	acceleration of gravity
$h$	oil film thickness
$k_s$	bending stiffness of shaft
$m$	mass of rotor
$p$	oil film pressure
$q$	circumferential oil flow rate
$q_{out}$	axial oil flow rate
$u, v, w$	oil film velocities in the $x, y, z$ directions of oil film
$x, y, z$	circumferential( $x$ ), radial( $y$ ) and axial( $z$ ) coordinates of oil film, or vertical( $x$ ) and horizontal( $y$ ) displacements of journal centre from its equilibrium
$x_R, y_R$	vertical and horizontal displacements of rotor centre from its equilibrium
$\alpha$	rotor flexibility index $mg/(k_s \cdot C)$
$\mu$	viscosity of lubricant
$v_c$	dimensionless stability threshold speed $\omega_c / (g/C)^{1/2}$
$\theta$	circumferential angle from oil groove position
$\theta_b$	angle of starting position of axially complete oil film
$\theta_{cav}$	angle where oil film ruptures

## 1 INTRODUCTION

Journal bearings are usually operated under fully flooded lubrication conditions. Consequently the hydrodynamic lubrication model is usually derived with the assumption that lubricant is supplied to the film inlet at a sufficient flow rate.

However some bearings may have to be operated under starved lubrication conditions. One of the possible reasons is malfunctioning of the lubricating system which would decrease oil flow rate due to clogging up of the oil filter, an oil leak from a loosened pipe joint and partial loss of oil pump capacity.

The other reason is the new introduction of spot lubrication into high-speed tilting-pad journal bearings. Conventional bearings of this type are usually operated under fully flooded lubrication because the pad chamber is full of pressurised oil by means of the ring seals at both ends of the chamber. This configuration guarantees high service reliability in operation, but with increase in shaft speed, the pad surface temperature tends to increase dangerously because hot oil does not flow out of the chamber rapidly but stays inside longer, increasing pad surface temperature. Consequently spot lubrication is applied to high-speed tilting-pad journal bearings to decrease operating temperatures of bearing pads and to gain some safety margin against bearing seizure.

Spot lubrication is achieved by removing the ring seals and feeding lubricant under pressure through nozzles placed in the spaces between adjacent pads. Cold new lubricant can reach the hot surface of the moving journal directly, and hot oil discharged from under the pads can flow out of the pad chamber freely without any restriction. This method was shown to make a large contribution to decreasing pad surface temperature and increasing the safety margin of high-speed tilting-pad journal bearing (1).

However this method has one shortcoming; only part of the lubricant discharged from the trailing edge of each pad re-circulates and comes into the clearance of the next pad, and a considerable part of the discharged oil flows out of the chamber. On the other hand, the oil flow rate needed for flooded lubrication increases with increased shaft speed. Eventually the flow rate needed exceeds the supplied rate. Consequently such bearings have to be operated under starved lubrication conditions, and design engineers need to know the static and dynamic performance of a starved journal bearing.

Some theoretical work (2, 3) was reported on starved lubrication, but to the best knowledge of the authors, its effect on the stability of rotor in journal bearings has not been reported.

This paper gives the behaviour of oil film observed in a transparent journal bearing and also a theoretical model of oil film formation under starved lubrication conditions. Based on the model, the rotordynamic coefficients of a starved journal bearing are calculated. Then the linear stability analysis is carried out to obtain the threshold speed of unstable vibration (oil whip) of a flexible rotor in the bearings. The calculated threshold speeds are compared with measurements in a test rig.

## **2 THEORETICAL ANALYSIS**

### **2.1 Starved oil film model**

Figure 1 shows the schematic of the formation and rupture of oil film on a developed lubricating plane of a full circular journal bearing operating under starved lubrication conditions (4).

This figure was obtained from the oil film behaviour observed in a circular bearing made of transparent plastics. Lubricant oil was supplied into the oil groove at the top of the bearing at controlled flow rates. Static loads were applied to the bearing by means of dead weights. The behaviour of the oil film in the clearance was recorded by means of a video-camera recording system and analysed.

Under flooded conditions, an axially complete oil film is found to start from the oil groove position ( $\theta = 0$ ). However oil film cannot cover the full bearing width at the groove position when oil flow rate is insufficient, and the bearing is starved of lubricant. Specifically, the oil film at  $\theta = 0$  is found to consist of three separate streams, that is, a stream of new oil from the

groove at the midwidth of the bearing and two streams of re-circulating oil at both sides of the groove. Two cavities are formed between the central stream and two adjacent side streams. Each of the three streams increases its width gradually in the circumferential direction and the two cavities decrease in area because of the decreasing film thickness. Eventually these three streams merge into one complete film at and beyond  $\theta = \theta_b$ , downstream of the maximum bearing clearance position. Oil film ruptures at  $\theta = \theta_{cav}$  and beyond this point, two side streams of oil film are separated by a cavity.

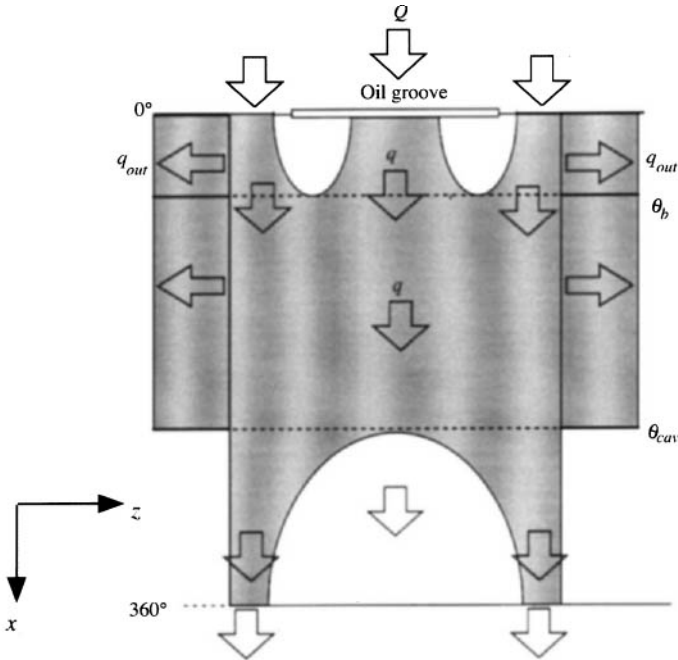


Fig. 1 Oil Film Model

Compared with flooded lubrication, the hydrodynamic oil film becomes thinner and also covers less area of the lubricating plane, resulting in a higher journal eccentricity ratio under a constant load and shaft speed. Consequently the static and dynamic characteristics of the oil film is different from that under flooded lubrication conditions.

## 2.2 Basic equations

The laminar, iso-viscous Reynolds Equation (Eq. (1)) is assumed to be applicable to the oil film.

$$\frac{\partial}{\partial x} \left( \frac{h^3}{\mu} \frac{\partial p}{\partial x} \right) + \frac{\partial}{\partial z} \left( \frac{h^3}{\mu} \frac{\partial p}{\partial z} \right) = 6U \frac{\partial h}{\partial x} \quad (1)$$

where  $x$  and  $z$  are the coordinates of the lubricating plane,  $h$  is oil film thickness,  $U$  is journal

surface speed,  $\mu$  is lubricant viscosity and  $p$  is oil film pressure.

This equation is made discrete by means of the finite difference method, and is solved numerically for the pressure.

Equations (2) & (3) give the oil film velocities in the circumferential and axial directions respectively.

$$u = U \frac{y}{h} - \frac{y(h-y)}{2\mu} \frac{\partial p}{\partial x} \quad (2)$$

$$w = -\frac{y(h-y)}{2\mu} \frac{\partial p}{\partial z} \quad (3)$$

where  $y$  is the coordinate for the film thickness direction.

Equation (2) is integrated with respect to  $y$  from 0 to  $h$  and also with respect to  $z$  across the width where oil film exists, then the oil flow rate in the circumferential direction is given as follows.

$$q(x) = 2 \int_0^h \int_0^h u dy dz = \int \left( \frac{Uh}{2} - \frac{h^3}{12\mu} \frac{\partial p}{\partial x} \right) dz \quad (4)$$

Equation (3) is integrated with respect to  $y$  from 0 to  $h$  and also with respect to  $x$  along the circumferential length where positive oil film pressure exists, then the axial oil flow rate is given as follows.

$$q_{out}(x) = 2 \int_0^h -w|_{z=0} dy dx = \int \frac{h^3}{6\mu} \frac{\partial p}{\partial z} |_{z=0} dx \quad (5)$$

### 2.3 Equilibrium under starved lubrication

Under flooded lubrication conditions, the eccentricity ratio and the attitude angle of the journal at equilibrium can be numerically obtained by solving Eq. (1) repeatedly for a given bearing load and a given journal speed, and the equilibrium is independent of oil flow rate. On the other hand, under starved lubrication conditions, oil film forces are dependent on the supplied oil flow rate and also on the shape of the oil film formed in the clearance. Consequently the equilibrium need to be obtained by coupling Eqs. (1), (4) and (5).

The following assumptions are adopted in the calculations.

- (1) The oil film is symmetric with respect to the centreline of the bearing.
- (2) No side leakage takes place downstream of the circumferential position  $\theta = \theta_{cav}$ , where oil film rupture takes place, and the oil re-circulates to the groove position.
- (3) Re-circulating oil flows near the side ends of the bearing, and newly supplied oil spreads out from the central part of the bearing.

Equilibrium can be determined to be reached when the oil film shape, the journal eccentricity ratio and the attitude angle are calculated to obtain the oil film force vectorially equal to a given load for a given shaft speed and a given oil flow rate.

### 2.4 Stability analysis

When equilibrium is obtained for a given starved lubrication condition, the eight rotordynamic coefficients of the bearing can be calculated by perturbing the journal at the equilibrium. Figure 2 shows an elastic shaft with a single mass at its mid-span horizontally supported in identical journal bearings at both ends. Eq. (6) gives the equations of motion of the rotor-bearing system in the rotating plane and also the equations of force balance.

$$\left. \begin{aligned} m\ddot{x}_R + k_s(x_R - x) &= 0 \\ m\ddot{y}_R + k_s(y_R - y) &= 0 \\ k_s(x_R - x) &= 2f_x \\ k_s(y_R - y) &= 2f_y \end{aligned} \right\} \quad (6)$$

where  $f_x$  and  $f_y$  are expressed in the form of linear summation of spring and damping terms given by the eight rotordynamic coefficients.

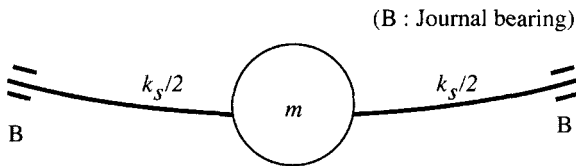


Fig. 2 Schematic model of rotor-bearing system

The Routh-Hurwitz criterion is applied to the characteristic equation derived from Eq. (6), and the threshold speed  $v_c$  of the unstable vibration (oil whip) is obtained as follows.

$$v_c = \sqrt{\frac{A_1 A_3 A_5^2}{(A_1^2 + A_2 A_5^2 - A_1 A_4 A_5)(A_5 + \alpha A_1)}} \quad (7)$$

where

$$A_1 = K_{xx} C_{yy} - K_{xy} C_{yx} - K_{yx} C_{xy} + K_{yy} C_{xx}$$

$$A_2 = K_{xx} K_{yy} - K_{xy} K_{yx}$$

$$A_3 = C_{xx} C_{yy} - C_{xy} C_{yx}$$

$$A_4 = K_{xx} + K_{yy}$$

$$A_5 = C_{xx} + C_{yy}$$

## 3 RESULTS AND DISCUSSION

### 3.1 Oil film formation

Figures 3 and 4 show the examples of calculated two-dimensional oil film formation with

constant load ( $W=49$  N) and constant oil supply rate ( $Q=100$  ml/min) and also with journal speeds  $N=1000$  rpm and  $2000$  rpm respectively. Both the diameter and the width of the bearing are  $40$  mm, and the mean radial clearance is  $94$   $\mu\text{m}$ . The axial groove length is  $32$  mm. For a higher shaft speed (Fig. 4), the oil film streams are more stretched in the circumferential direction, and the starting point angle of the axially complete oil film region,  $\theta_b$  increases and the terminating point angle  $\theta_{cav}$  decreases. Thus the circumferential region of the complete oil film is found to decrease with increasing shaft speed.

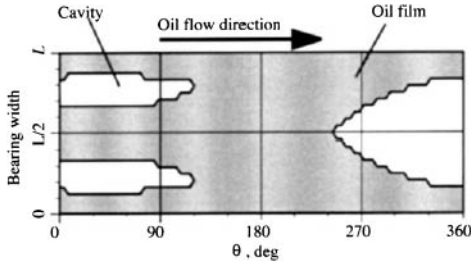


Fig. 3 Oil film formation (Calculated,  $Q=100$ ml/min,  $N=1000$ rpm,  $W=49$ N,  $L/D=1.0$ )

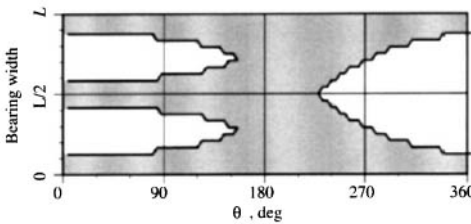


Fig. 4 Oil film formation (Calculated,  $Q=100$ ml/min,  $N=2000$ rpm,  $W=49$ N,  $L/D=1.0$ )

Figure 5 shows the measured variation of  $\theta_b$  with shaft speed for various oil flow rates at a constant load  $W=49$  N. The axially complete oil film is found to start further downstream with increase in shaft speed and also with decrease in oil flow rate.

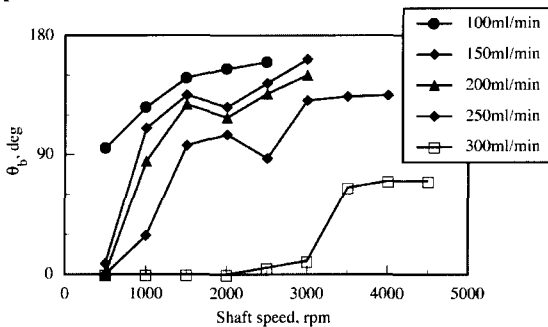


Fig. 5 Variation of  $\theta_b$  with shaft speed (measured,  $W=49$ N,  $L/D=1.0$ )

Figure 6 shows the comparison of measured and predicted variations of  $\theta_b$  with oil flow rate at a constant shaft speed  $N=2500$  rpm and at a load  $W=49$  N. Predictions are in good agreement with measurements.

Thus the oil film formation model presented here is proved to be applicable to the journal bearings operating under starved lubrication conditions.

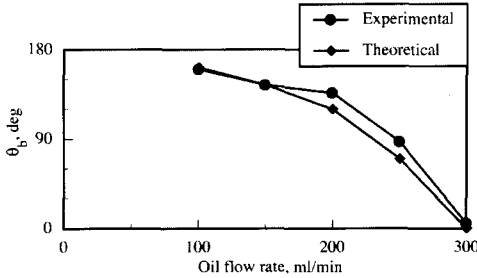


Fig. 6 Variation of  $\theta_b$  with oil flow rate ( $N=2500$ rpm,  $W=49$ N,  $L/D=1.0$ )

### 3.2 Journal centre loci

Figure 7 shows calculated journal centre loci in a journal bearing of a mean radial clearance  $80 \mu\text{m}$  for various oil flow rates. The journal eccentricity ratios decrease and the attitude angles increase along the loci with increasing shaft speed. A single locus is obtained for a given operating condition under flooded lubrication conditions, but under starved lubrication conditions different journal centre loci are obtained, depending on the oil flow rate. Namely a locus peels off the normal locus corresponding to flooded lubrication condition at a journal eccentricity ratio where starved lubrication condition starts, depending on a given oil flow rate. The lower the flow rate, the higher the journal eccentricity ratio. When the eccentricity ratio is reached, the decrease in the eccentricity ratio and the increase in the attitude angle are killed, and even pushed back for further increase in shaft speed.

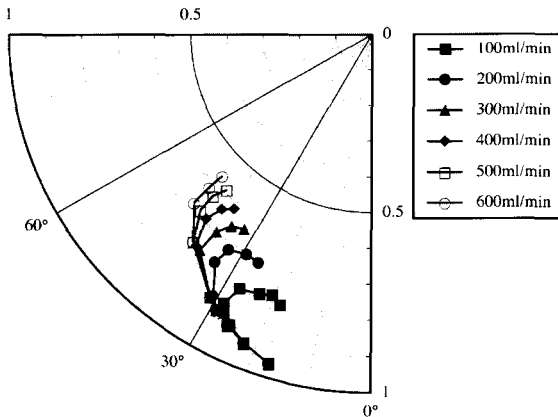


Fig. 7 Journal centre loci (calculated,  $L/D=1.0$ )



Figure 8 shows a similar result corresponding to a bearing of  $L/D=0.6$ , and the same discussion as in the case of Fig. 7 is presented.

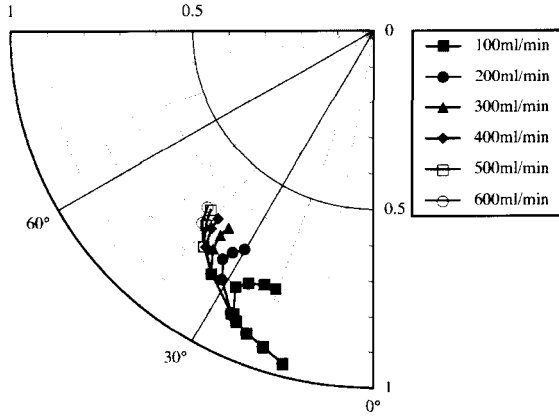


Fig. 8 Journal centre loci (calculated,  $L/D=0.6$ )

### 3.3 Threshold speed of unstable vibration

Experiments were carried out to investigate the effect of oil flow rate on the threshold speed of unstable vibration of rotor supported in journal bearings. An elastic rotor is supported in a journal bearing at one end and in a rolling element bearing at the other end. The bearing diameter is 40 mm, and the mean radial clearance is 80  $\mu\text{m}$ . Two journal bearings of  $L/D=0.6$  and 1.0 are tested. The first critical speed of the shaft bending mode is 1450 rpm, and the corresponding  $\alpha$  is 5.7. The dynamic viscosity of the lubricant used is 4.3 mPa·s at 40 degree in centigrade. The displacement of the vibrating rotor is detected by means of gap sensor, and the FFT analysis is conducted to determine the stability threshold speed.

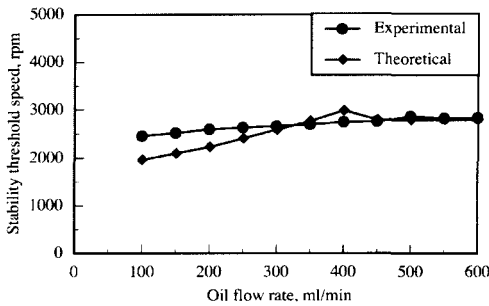


Fig. 9 Variation of stability threshold speed with oil flow rate ( $L/D=1.0$ )

Figure 9 shows the measured and calculated variation of the stability threshold speed with oil flow rate for the bearing of  $L/D=1.0$ . Here the bearing is operated under starved lubrication condition for the oil flow rates under 500 ml/min. The stability threshold speed is shown to

decrease with decreasing oil flow rate, and the measurements are in fairly good agreement with the prediction qualitatively and quantitatively.

Figure 10 shows a similar result for the bearing of  $L/D=0.6$ . Here the bearing is operated under starved lubrication condition for all the oil flow rates tested. The stability threshold speed is also shown to decrease with decreasing oil flow rate, but the quantitative agreement is not so good, compared to the case shown in Fig. 9.

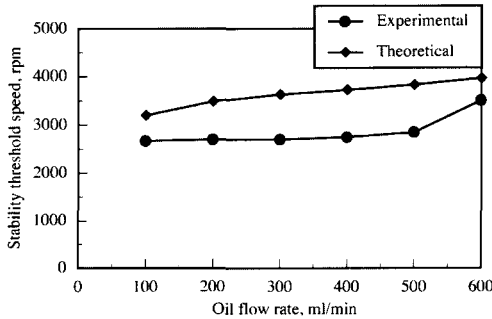


Fig. 10 Variation of stability threshold speed with oil flow rate ( $L/D=0.6$ )

## 4 CONCLUSIONS

Oil film formation in a full circular journal bearing was analysed theoretically and experimentally under starved lubrication conditions, and then the effect of starved operation on the stability threshold speed of rotor-bearing system was investigated theoretically and experimentally. The following conclusions are derived.

(1) Under starved lubrication conditions, the oil film cannot cover the full bearing width at the inlet of the convergent clearance, and the axially complete oil film starts downstream of this point.

(2) The axially complete oil film decreases in area and thickness with the decrease of oil flow rate and the increase in journal speed and bearing load. Consequently, the journal eccentricity ratio and the attitude angle at equilibrium are different from those for flooded lubrication conditions, which inevitably affects the static and dynamic characteristics of the oil film.

(3) Under starved lubrication conditions, the stability threshold speed decreases with decreasing oil flow rate, and the measurements are in fairly good agreement with the prediction qualitatively and quantitatively in the case of the bearing of  $L/D=1.0$ .

The thermo-hydrodynamic analysis is needed to elucidate the behaviour of bearing performance under starved lubrication conditions more precisely.

## References

1. TANAKA, M., "Thermohydrodynamic Performance of a Tilting Pad Journal Bearing With Spot Lubrication", July 1991, ASME Trans. J. of Tribology, Vol.113, No.3, 615-619.
2. ARTILES, A. and Heshmat, H., "Analysis of Starved Journal Bearings Including Temperature and Cavitation Effects", Jan. 1985, ASME Trans. J. of Tribology, Vol.107, No.1, 1-13.
3. Bonneau, D. and Frene, J., "Film Formation and Flow Characteristics at the Inlet of a Starved Contact - Theoretical Study", April 1982, ASME Trans., J. of Lubrication Technology, Vol.105, No.2, 173-186.
4. Tanaka, M., "Journal bearing performance under starved lubrication", Tribology International (in printing)

*This page intentionally left blank*

# Rotordynamics and leakage – measurements and calculations on labyrinth gas seals and their application to large turbomachinery

J SOBOTZIK and R NORDMANN

Department of Mechatronic Systems, Technische Universität Darmstadt, Germany

F HIB

Siemens Power Generation, Mülheim, Germany

K KWANKA

Technische Universität München, Germany

## ABSTRACT

The flow in labyrinth gas seals can cause self-excited vibrations of the rotor. An exact prediction of these forces in the blueprint stage is necessary to estimate the dynamic behaviour of the rotor with the target to avoid such a vibration regime. In the past, a series of systematic experimental investigations of labyrinth seals with different geometries using a new identification approach has been published. Computational Fluid Dynamics using Finite-Difference-Techniques allow the calculation of complex flow problems and deliver both leakage flow rate and rotordynamic coefficients. They consider optional laminar and turbulent flow conditions and fluid compressibility characteristics.

This paper presents experimental rotordynamic coefficients and leakage rates of labyrinth gas seals of different shapes in comparison to values calculated by a finite-difference method. This validation should represent a further step on the way to possible improvements in the design of labyrinth seals.

The importance of considering the stiffness as well as the damping coefficients in a rotordynamic design process is demonstrated for a large supercritical turbogenerator.

## NOMENCLATURE

$a$	Amplitude of the vibrational mode		limit
$C, E, K$	Direct damping, inertia, stiffness coefficients	$r_i$	Shaft radius
$c, e, k$	Cross damping, inertia, stiffness coefficients	$x, y$	Coordinates of displacement
$c_{u0}$	Entry swirl	$\omega$	Rotational speed
$F_r$	Lateral force	$\Omega$	Whirling frequency
$F_x, F_y$	Pressure force in x and y-direction	$TOS2i$	Nomenclature of the look-through labyrinth (tooth on stator, $i$ cavities)
$\Delta h_s$	Isentropic static specific enthalpy difference of the stage	NCi	Number of nodes in the chamber in $i$ -direction
	$\Delta h_s = h_{s,0} - h_{s,2}$	NGi	Number of nodes in the gap in $i$ -direction
$\Delta r$	Change in direct stiffness of the magnetic bearing	NZ	Number of nodes on the circumference
$p$	Calculated pressure	$v_0$	Specific volume of steam before stationary blade seal
$p_0$	Pressure before stationary blade seal	$v_1$	Specific volume of steam before rotating blade seal
$p_1$	Pressure before rotating blade seal	$z'$	Number of seal strips of stationary blade seal
$p_2$	Pressure behind rotating blade seal	$z''$	Number of seal strips of rotating blade seal
$\Delta p$	Pressure difference		
$\Delta q$	Change in magnetic excitation at the stability		

## INTRODUCTION

The motion-dependent interaction forces between fluid and rotor can be described by the linear, skew symmetric equation of motion given in eq. 1. The typical matrices for gas seals contain direct and cross-coupled stiffness and damping terms, the so-called rotordynamic coefficients. In complement to fluid seals, the added-mass terms  $E$  and  $e$  are usually negligible (see, e.g. Childs [1993]).

$$\vec{F} = - \begin{pmatrix} K & k \\ -k & K \end{pmatrix} \begin{pmatrix} x \\ y \end{pmatrix} - \begin{pmatrix} C & c \\ -c & C \end{pmatrix} \begin{pmatrix} \dot{x} \\ \dot{y} \end{pmatrix} - \begin{pmatrix} E & e \\ -e & E \end{pmatrix} \begin{pmatrix} \ddot{x} \\ \ddot{y} \end{pmatrix} \quad (1)$$

Eq. 1 may be applied on systems, where small rotor displacements around the centred equilibrium position can be assumed. To introduce the rotordynamic influence of labyrinth seals, their rotordynamic coefficients have to be identified experimentally and/or numerically.

A wide variety of experimental setups to generate the required relative displacement between rotor and stator has been introduced. First steps with static arrangements (e.g. Benkert and Wachter [1980], Leong and Brown [1984]) have been followed by dynamic measurements with external shakers (Childs et.al. [1986], Childs [1993], Wright [1983]) or by shaft-in-shaft arrangements (Millsaps and Martinez-Sanchez [1993]). During the past years, set-ups with active magnetic bearings were employed to measure forces of liquid seals (Matros, Neumer, Nordmann [1994]) and of gas seals Wagner and Steff [1996]), where magnetic bearings carry a relatively heavy test rotor and are also used as a measurement device for the flow-induced forces.

Nevertheless there is a lack of systematic experimental identified dynamic coefficients. In most cases bulk flow models are frequently applied to determine the coefficients of eq. 1. They lead to good results and economic processing times, if the regard is focussed on simple seal geometries. But the bulk flow theory, originally employed with straight pump (Childs [1982]) and gas seals (Nelson [1985]), presumes many simplifications. For advanced seal geometries, finite difference techniques seem to be a more adequate choice. There have been some publications about these techniques in the past, e.g. (Dietzen and Nordmann [1988], Nordmann and Weiser [1988], Nordmann, Dietzen and Weiser [1989]). In discussions, their demand of computer hardware and execution time and the lack of comparisons with test results have been criticized. To validate the code's performance, systematic tests of different labyrinth are needed. Not only the labyrinth shapes have to be varied, but the parameters which may be influenced in real machinery, e.g. the inlet swirl, the seal's length, etc.. The availability of such systematic parameter variations would enable the verification of the derived leakage flow rates and rotordynamic coefficients and lead to points of interest for future advancements.

Results of experimental and numerical approaches are needed to predict the rotordynamic behaviour of highly optimised turbomachinery. It is obvious, that not only stiffness values but the whole set of rotordynamic coefficients have to be taken into account.

## EXPERIMENTAL APPROACH

Usually the fluid generated forces are measured directly by using heavy and stiff rotors which are performing a rotating and a whirling motion at the same time. Since the forces in gas seals are small in comparison to seals with incompressible fluids, it turns out to be difficult to measure the unsteady forces in amplitude and phase accurately. An overview of the few existing experimental set-ups with the used procedures is given by Childs [1993].

The fundamentally new identification procedure uses the same phenomena for identification purposes which occurs in the real turbomachinery (Kwanka [1995a]). The influence of the

rotor-fluid interaction on the rotordynamic behaviour is used for identification purposes. The procedure employs a flexible rotor with two major excitation sources. In a first step both sources are placed at midspan position. First, a test seal with unknown dynamic coefficients and secondly, a magnetic bearing with an adjustable dynamic behaviour which is known due to a previous dynamic calibration. The magnetic bearing is not used in the traditional sense as a bearing but as an exciting and/or stiffening device. The actual use of a magnetic bearing was inspired by Ulbrich [1988]. The magnetic bearing exerts displacement-dependent direct and cross-coupled forces on the rotor. The rotor can be excited magnetically up to the stability limit or stiffened/weakened to realise a specific change in the whirling frequency.

The basic idea is to find the change in the dynamic behaviour of the flexible rotor in terms of stability and whirling frequency caused by the flow through the test seal. The stability limit without flow through the test seal gives the original information about the dynamic behaviour of the rotor. The stability limit is mainly determined by the dynamic characteristics (damping and excitation) of the journal bearings which carries the rotor and the amplitude at that specific axial position. At the stability limit the magnetic excitation corresponds to  $q_0$ . The whirling frequency of the unstable rotor is approximately equal to the excited natural frequency of the rotor  $\Omega$ .

With flow through the test-seal both, the magnetic excitation necessary to destabilise the rotor and the whirling frequency of the unstable rotor are varied. The change in whirling frequency can be compensated with a known magnetic stiffness  $\Delta r$ . Simultaneously, the forward excitation of the seal reduces the magnetic excitation at the stability limit from  $q_0$  to  $q$ . This change equals to  $\Delta q$ .

Assuming a circular whirling orbit a relation between the measured variation of direct and cross-coupled magnetic stiffness and the unknown dynamic coefficients of eq. (1) of the test seal can be found.

$$\Delta r = -K - c\Omega + E\Omega^2 \quad (2)$$

$$\Delta q = q - q_0 = k - C\Omega - e\Omega^2 \quad (3)$$

By repeating the measurement for at least three whirling frequencies  $\Omega$  all unknown dynamic coefficients can be calculated. The quadratic curves fitted out of the measured points contain the desired information. In contrast to liquid seals the inertia coefficients can be neglected with seals for compressible fluids. As a consequence the information about the remaining four dynamic coefficients is now contained in a straight line. The intersection with the ordinate gives the stiffness coefficients and the slope the damping values (see fig. 1).

The quality of the identified coefficients can be improved considerably due to a more reliable curve fitting when backward whirling frequencies are investigated additionally. The stability limit of the backward mode is increased when a forward aerodynamic excitation acts into the test seal.

A conversion procedure becomes necessary in case that the test seal and the magnetic bearing are not located at the same axial position. The nonconservative  $\Delta q$  can be converted by assuming that the energy input with a circular whirling orbit is the same for both positions. The conversion of the conservative  $\Delta r$  is based on the assumption that the conservative forces have the same influence in central position regardless of their working point. Both experimentally validated conversions are working with the amplitude ratios of the calculated bending mode (Kwanka [1995b]).

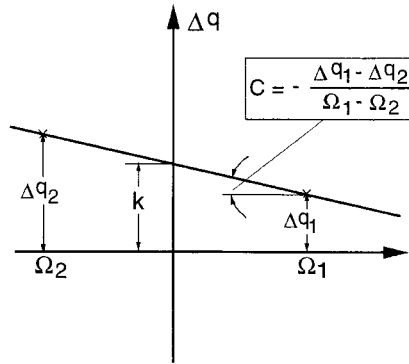


Fig. 1: Identification of the nonconservative coefficients

The test rig used for the identification of the dynamic coefficients is displayed in fig 2. The test seal is located in the central axial position of the flexible rotor with a diameter of 23 mm. The whirling frequency is varied from 26 to 35 Hz by modifying the span between the bearings. The test seal section consists of two identical labyrinth seals which are arranged symmetrically to the inflow. Before entering the seals the flow passes a guide vane ring which is generating the entry swirl. The entry swirl is of outstanding importance for the occurrence and magnitude of the exciting mechanism. The symmetrical arrangement helps to double and average the forces. The seals and the guide vane can easily be removed and changed to other geometries or guide angles.

The magnetic bearing is positioned as close as possible to one side of the test seal outside the midspan location. The auxiliary bearings help to limit the vibrations with high amplitudes in the unstable vibration regime. The rotor is carried in hydrodynamic journal bearings. The axial position of the rotor is fixed via a flexible rod which couples the shaft to a variable speed motor. No axial load occurs because of the symmetric arrangement which is permanently monitored.

The compressed air entering the seals is metered with an orifice and expands to ambient conditions at the exit of the seals. The measured mass flow corresponds to the leakage through the seals. Additionally, the entry swirl is estimated out of the leakage flow and the nozzle area and angle. The adjusted pressure difference is controlled with an electro-pneumatic valve

The precise identification of the stability limit and the whirling frequency is essential for the procedure. The stability limit can be recognised on the monitor of an oscilloscope due to a sudden and distinct change of the vibration orbit in amplitude and shape. Simultaneously the unstable whirling frequency appears in addition to the frequency of rotation on the monitor of the signal analyser. In the majority of cases, the stability limit can be determined within  $\pm 1-2$  N/mm. The resolving limit of the signal analyser restricts the accuracy of the measured whirling frequencies. Least square fitted identification lines, see Fig. 1, are the result of five measurements with forward and backward whirling direction respectively. The mean relative deviation from the best fitted line is usually below 1.5%. Finally, the excellent reproducibility of the identified coefficients indicates that the influence of the bearing alignment is negligible (Kwanka and Nagel [1997]).



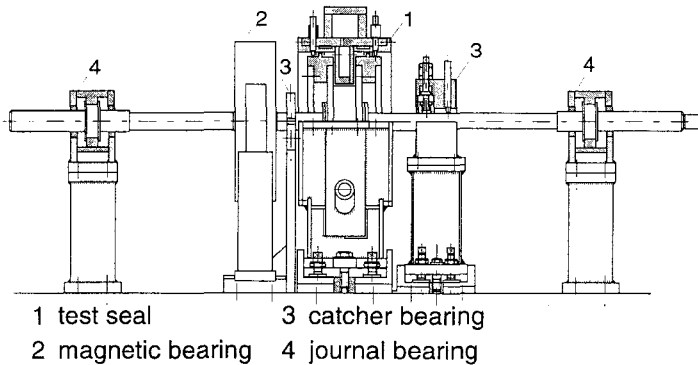


Fig. 2: Test rig with main components

### CALCULATION OF THE ROTORDYNAMIC COEFFICIENTS

The principles of the used procedure to calculate leakage flow rates and rotordynamic coefficients of arbitrary labyrinth geometries have been presented years ago (Dietzen and Nordmann [1988]). Compared with bulk flow calculations, these procedures require adequate working memory and processing time (see Table 1). Requirements in terms of computer hardware and computing time has delayed the verification of their results with an adequate number of test results.

Geometry	n [rpm] / p [bar] / entry swirl ratio [-]	RAM-Memory [MByte]	processing time [min]
TOS22	750 / 1 / 25.7	195	302

Table 1: required working memory and processing time for a TOS22 calculation

Different labyrinth shapes may be modelled and examined without the necessity to adjust parameters to available measurements. The turbulent flow through the seal is described by the help of Navier-Stokes equations in combination with the continuity equation and an  $k-\epsilon$  turbulence model. To calculate the effective viscosity  $\mu_e$  of the turbulent fluid flow, the laminar viscosity  $\mu_l$  and a turbulent viscosity  $\mu_t$  are summed. It is assumed that the shaft is whirling on a circular orbit with a precession frequency around the stator's centre. This time dependant problem is circumvented by the introduction of a rotating coordinate system, fixed at the shaft's centre. In this coordinate system, the flow distribution is calculated by a full 3-dimensional finite-difference procedure. The variables are calculated at the nodes of a grid, used to discretize the labyrinth's geometry. First, the equations are solved for a centred shaft position, delivering the values for the case of a symmetric flow through the seal. Among other flow characteristics, the leakage flow rate is calculated in this step. Subsequently, the 3-dimensional system of equations has to be solved for several shaft precession frequencies. As solver the SIP- (Strongly-Implicit-Procedure) Algorithm is applied. The system of equations is solved by respect of the boundary conditions. Actually the adaptation of more sophisticated solvers for the arising sparse matrices is in progress. Their successful execution will lead to shortened computation times.

The modelling starts at the beginning of the gap below the first tooth. No influence of the flow in the chamber in front of this gap is considered with exception of the circumferential velocity rate. On the left side of Fig. 3 the calculated pressure distribution is plotted over the seal length and the seal height for TOS22 labyrinth (TOS=Tooth On Stator). The right

picture shows the velocity vectors resulting of the calculated axial and radial velocities for the same geometry. It has to be noticed that both pressure and velocity distributions are displayed with a highly distorted scale. The grid independence of the calculated  $k$  and  $D$  values is demonstrated for the TOS22 labyrinth in table 1.

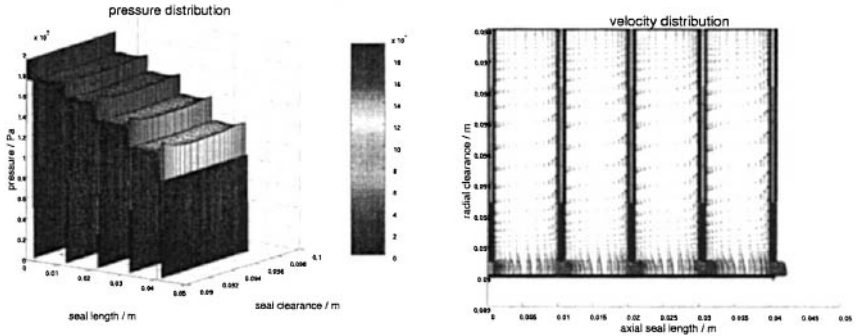


Fig. 3: pressure distribution and velocity distribution for a TOS24 seal (distorted scale!)

NCx	NCy	NGx	NGy	Nz	k [N/m]	C [Ns/m]
14	16	5	5	48	0.384E5	0.330E2
16	20	7	7	48	0.381E5	0.339E2
26	30	10	10	48	0.390E5	0.331E2

Table 2: Grid independence testing, TOS22

The pressure is determined by the use of the PISO (Benodekar [1985]) algorithm. The calculation was stopped when magnitude of the largest residual was less than 0,001. After the pressure distribution is obtained, the forces acting on the rotor are derived by a pressure integration on the rotor surface.

$$F_x = - \int_0^L \int_0^{2\pi} p \cdot \cos \theta \cdot r_i d\theta dz \quad (4)$$

$$F_y = - \int_0^L \int_0^{2\pi} p \cdot \sin \theta \cdot r_i d\theta dz \quad (5)$$

Having calculated the forces  $F_x$  and  $F_y$ , the stiffness and damping coefficients may be derived easily by solving the following equations for at least 2 different precession frequencies.

$$F_x = K + \Omega c \quad (6)$$

for the direct stiffness  $K$  and cross-coupled damping  $c$  and

$$F_y = -k + \Omega C \quad (7)$$

for cross-coupled stiffness  $k$  and direct damping  $C$ . In principle, in addition to the stiffness and damping coefficients of eq. 1, the mass term may be calculated by solving the equations

for a third precession frequency. Typically, in gas seals, only negligible added-mass terms are developed (Childs [1993]) and therefore their determination has been omitted to restrain computation time.

## RESULTS AND COMPARISON

Labyrinth seals always permit a certain leakage flow with the orientation of the pressure drop. In some applications a predefined leakage flow rate is required, e.g. for cooling needs, in other applications the leakage flow rate just reduces the efficiency of the machine. The knowledge of the leakage rate belonging to a certain seal design and its dependence on design modifications is always useful. Both the experimental work and the numerical approach allow the determination of the leakage flow rate. In fig. 5 the flow rates for a TOS22 and a TOS62 look through labyrinth are compared. Both seals are tested at a shaft speed of 750 rpm and with a pressure drop of 1 bar. The experimental values and the calculations show that the leakage rate of the TOS62 seal is about 10 % below the value of the TOS22 seal.

This figure also shows for a TOS22 and a TOS24 seal, look through labyrinths with 2 and 4 cavities, the influence of a positive and negative entry swirl on the leakage rate.

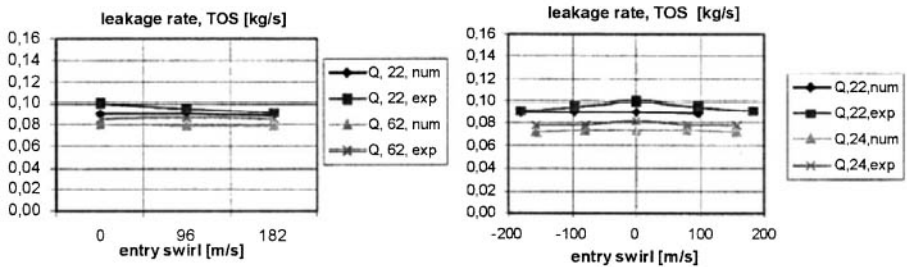


Fig. 5: Leakage rates of different look through labyrinth designs

In experiment and in calculation, the leakage flow rate is slightly higher at zero entry swirl. The two labyrinths have been investigated under identical conditions, shaft speed 750 rpm and pressure drop 1 bar. As expected, the sealing efficiency of the TOS24 labyrinth is higher than that of the TOS22 labyrinth.

Changes in the shape of the labyrinth cavities also have an influence on the leakage rate of a seal. In fig. 6 three labyrinths with different cavity heights, shown in Table 3 are compared. The maximum leakage occurs, similar to the geometries in Fig. 5, at zero entry swirl. With medium entry swirl, the TOS24 seal has a leakage rate which surmounts the rates of the TOS44 and TOS54 seal.

	TOS44	TOS24	TOS54	TOS22	TOS62
cavity height [mm]	3.75	7.50	11.25	7.50	7.50
cavity pitch [mm]	9.20	9.20	9.20	9.20	18.40
tooth width [mm]	0.80	0.80	0.80	0.80	0.80
radial clearance[mm]	0.50	0.50	0.50	0.50	0.50
rotor radius [mm]	90.0	90.0	90.0	90.00	90.00
number of cavities	4	4	4	2	2

Table 3: geometry data for different teeth on stator seals, pressure drop 1 bar

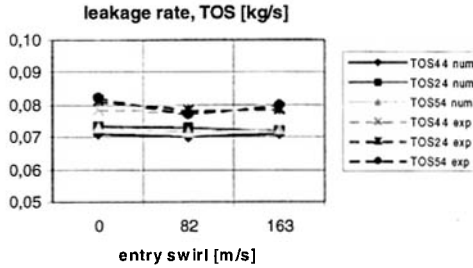


Fig. 6: Leakage flow rate of teeth on stator seals with different cavity heights

All three diagrams show that the dependency of leakage rates on geometrical and process parameters is obviously identified in experiments and as well as in calculations. In all cases, the calculated values are about 10 % below the measured ones. This offset may be caused by geometrical deviations of the seal inlet region between the real seal and the assumptions in the calculation. Despite this static offset, all changes of the leakage rate in dependence of the parameter variations are displayed.

Leakage is not the only criterion to select a seal for a certain application. Beside the restrictions belonging to the available installation space, its influence on the rotordynamic behaviour of the machines shaft has to be taken into account. The rotordynamic coefficients, see eq.1, are displayed in fig. 7.

The magnitude of the direct stiffness  $K$  of gas seals has generally low absolute values. At zero entry swirl, the absolute stiffness values of the three labyrinth geometries are close to each other. They increase and diverge slightly with increasing inlet swirl. In comparison to the other ones TOS44 geometry produces the highest stiffness values in both experiment and calculation.

Cross coupled stiffness  $k$  is minimal for an axial directed inlet flow and increases linear with the entry swirl value. Its value increases with decreasing cavity height of the labyrinth. The calculated gradients are slightly higher for all three cavity shapes. Direct Damping  $C$  increases nearly linear with the circumferential inlet velocity, it is already present with axial inlet flow. TOS54 geometry produces the lowest direct damping values in both experiment and calculation. The calculated values are always higher as the measured ones, the best consistence may be found for the TOS24 geometry, the one with the medium cavity height. Compared with the direct damping, the values of the cross coupled damping are very low. They seem increase linear with the entry swirl.

Most interesting trait of a gas seal is its stability behaviour from a rotordynamic point of view. Stabilising and destabilising forces acting on a whirling rotor are produced by the cross coupled stiffness and the counteracting direct damping. To count up their influence, Childs (Childs [1993]) proposes the so called whirl frequency ratio  $\Omega_w$ . He calculates its value, see eq. 8, at the shaft running speed  $\omega$ . This allows the comparison of different seal designs by means of destabilisation, the higher the value of  $\Omega_w$  the higher is the destabilising influence of the seal.

$$\Omega_w = \frac{k}{\omega D} \quad (8)$$

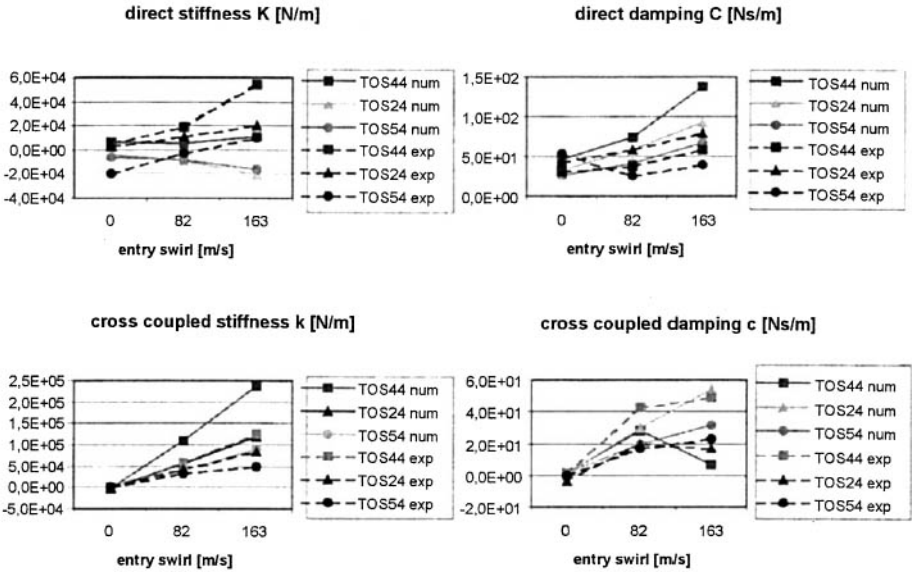


Fig. 7: Rotordynamic coefficients of TOS44, TOS24 and TOS54 seals

For the TOS seals with variation of the cavity height (TOS44\_TOS24\_TOS54) and the cavity pitch (TOS22-TOS62) the calculated whirl frequency ratios are shown in Fig. 8. The whirl frequency ratio starts at zero for axial inlet flows and increases with the entry swirl. Its gradient seems to decline at higher entry swirl values. The TOS44 geometry produces the highest whirl frequencies ratios relative to the geometries with higher cavities. TOS62 geometry, with twice the cavity pitch, generates a higher whirl frequency ratio than the TOS22 labyrinth. TOS22, with two cavities, shows nearly identical values as the TOS24 seal with 4 cavities.

Whirl frequency ratio is only a number to compare different seals by means of destabilising forces, calculated assuming that the rotors whirl frequency is identical with its rotating speed. To calculate the destabilising forces for a certain rotor, the whirl frequency ratio has to be calculated at its whirl frequencies which depend on its eigenfrequencies.

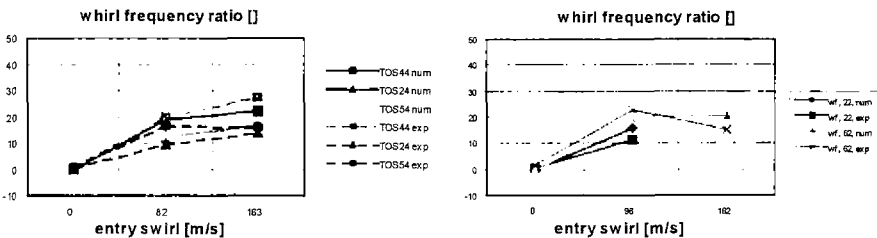


Fig. 8: Whirl frequency ratios for different teeth on stator seal geometries

## PRACTICAL APPLICATION

The results of the first two sections are used for practical stability calculations of large supercritical turbo-generator sets which consist of a high-pressure turbine, a medium-pressure turbine, two low-pressure turbines and a generator, see Fig. 9.

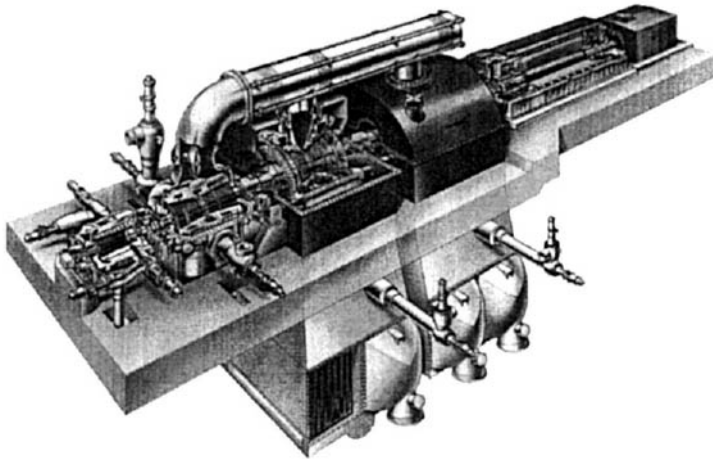


Fig. 9: Supercritical turbo-generator set

The aim of the investigation is to assess the stability characteristics of several bearing types for the high-pressure turbine. Two rotor models which reflect the uncertainties inherent in seal modelling are checked for stability.

The rotor is supported by journal bearings and the elastic foundation. The seals are the source of two destabilising effects: (1) The unsymmetrical circumferential pressure distribution and (2) the unbalanced torque forces due to the varying radial clearance of the seals.

The unsymmetrical pressure distribution is modelled with the help of the seal coefficients obtained from measurements and computations as described in the first sections of this paper.

The unbalanced torque forces  $F_x$ ,  $F_y$  of each stage are computed according to the formula

$$\begin{pmatrix} F_x \\ F_y \end{pmatrix} = \frac{\pi \Delta h_s}{\omega} H \begin{pmatrix} 0 & -1 \\ 1 & 0 \end{pmatrix} \begin{pmatrix} x \\ y \end{pmatrix} = \begin{pmatrix} 0 & c_{23} \\ c_{32} & 0 \end{pmatrix} \begin{pmatrix} x \\ y \end{pmatrix} \quad (9)$$

which is a function of the isentropic static specific enthalpy difference of the stage, the rotor speed and the constant  $H$ .  $H$  is a constant which is a function of the pressures, the specific volumes and the number of seal strips of the stage.  $c_{23}$  and  $c_{32}$  denote the cross-coupling coefficients and  $x$  and  $y$  are the displacements of the rotor. Similar formulas were established by Thomas (Thomas [1978]).

The seals of the high-pressure (HP) turbine are included in the rotor model in the following ways: In model 1 only the cross-coupling stiffness coefficient  $k_1$  due to the unsymmetrical pressure distribution for each seal and the cross-coupling stiffness  $k_2$  due to the unbalanced torque force for each stage are included. The second model includes all coefficients (stiffness  $K$  and  $k$ , damping  $C$  and  $c$ ) due to the unsymmetrical pressure distribution for each seal and due to the unbalanced torque force for each stage. This is the model closest to reality.

The stability of the rotor is assessed with the following approach: Every change of parameters of the rotor-bearing-system is supposed to only result in a shift of the shaft centre on the path.

The shift of the shaft centre on the path can equally be achieved by changing the rotor speed  $\Omega$  (and the Sommerfeld number  $S_o$ ). Each change in the rotor speed will change the frequency and the damping of each eigenform of the rotor-bearing-system.

The HP modes are prone to go unstable hence the damping of one or more modes goes negative at a rotor speed, the so-called limit speed. A high damping at nominal speed (from a practical point of view above 1,5%) and a high limit speed (from a practical point of view above 30% of nominal speed) are desirable. The damping and also the corresponding frequency are influenced by the dynamic properties of the seals and the bearings.

Altogether four modes with HP turbine participation must be taken into account for the stability analysis. They are shown in Fig. 10.

For the two models under consideration the amount of damping of each of the four critical modes of the high pressure turbine was calculated for the nominal speed of 50 1/s and for a speed of 30% above the nominal speed by means of the machine dynamics code MADYN (Klement [1993]). The analysis was carried out for six different types of bearing #1 and bearing #2 of the high-pressure turbine, see table 4.

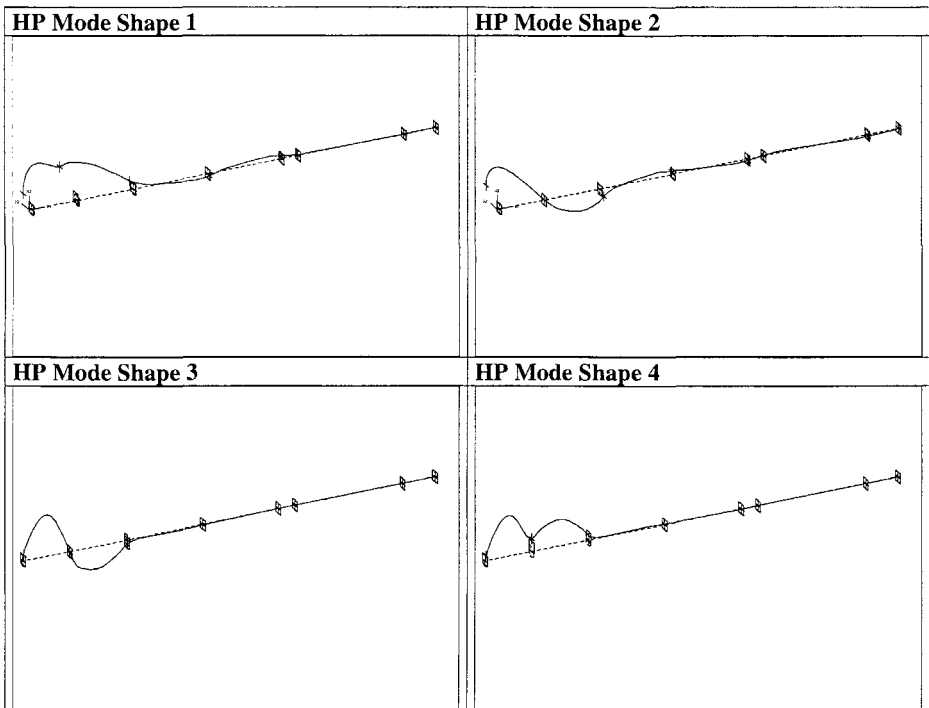


**Fig. 10: Modeshapes of the regarded system**

B1	Two-lobe bearing	B4	Modified tilting-pad bearing
B2	Modified two-lobe bearing	B5	Offset-half bearing
B3	Tilting-pad bearing	B6	Three-lobe bearing

**Table 4: Regarded Bearing types**

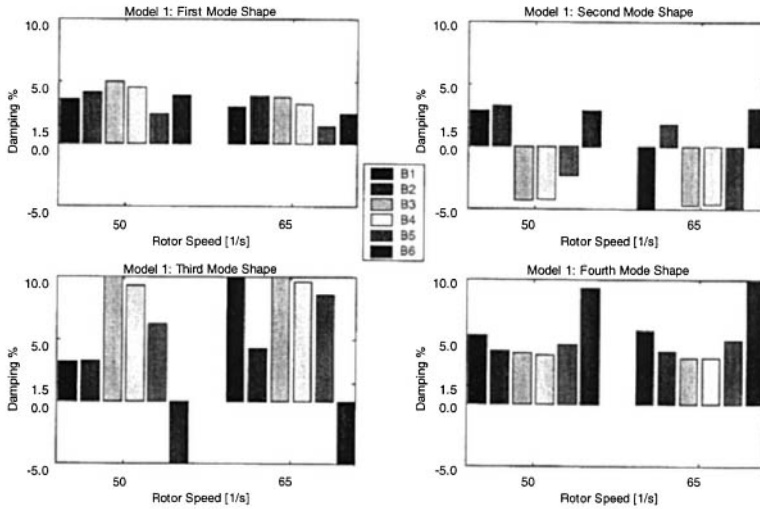


**Fig. 11: Damping Coefficients calculated with Model 1**

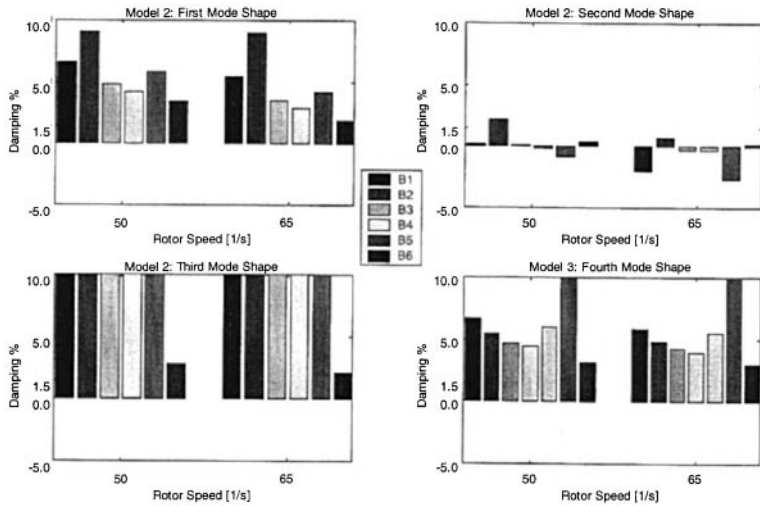


**Fig. 12: Bearing Coefficients calculated with Model 2**

The second mode (horizontal mode) is the most critical in terms of damping. The modified two-lobe bearing (B2) and the three-lobe bearing (B6) provide the biggest amount of damping for the rotor system. The inclusion of direct damping in model 2 leads to a higher modal damping of the first, second and fourth mode. The damping of the second mode is reduced. The tilting-pad bearing, the modified tilting-pad bearing and the offset-half bearing are not suitable to provide a high modal damping. Only the modified two-lobe bearing B2 fulfils the



stability condition. The analysis demonstrates that it is very important to include the damping effects of the seals to arrive at reasonable forecasts of rotor stability.

### **SUMMARY AND OUTLOOK**

This paper presents an easy to handle experimental approach to determine the rotordynamic coefficients and the leakage of labyrinth gas seal. By the help of Finite-Difference Techniques, similar values have been calculated. Leakage, rotordynamic coefficients with inclusion of the damping values and whirl-frequency ratios are compared under variation of process and geometrical parameters. All comparisons show a satisfactory agreement. The experimental and the numerical approach display qualitatively a comparable sensitivity to slight modifications of the seal systems.

Efforts to accelerate the computation algorithms are in progress. In addition it is scheduled to measure the velocity distributions in labyrinth gas seals and compare these values to the calculations.

The application part of this paper demonstrates the necessity to integrate not only the stiffness, but also the damping coefficients in the rotordynamic calculation of turbomachinery.

## REFERENCES

- Benckert H., Wachter J., 1980. "Flow Induced Spring Coefficients of Labyrinth Seals for Application in Rotordynamics", NASA Conference Publication 2133, Proceedings of a workshop held at Texas A&M University, pp. 1-17.
- Benodekar, R. W., Goddard, A.J.H., Gosman, A.D., Issu, R.I., 1985, "Numerical prediction of turbulent flow over surfacemounted ribs", AIAA Journal Vol. 23, No. 3
- Childs D. W., 1982, "Finite Length Solutions for Rotordynamic Coefficients of Turbulent Annular Seals", Journal of Lubrication Technology, ASME-Paper, No. 82, Lub. 42
- Childs D. W., 1993. "Turbomachinery Rotordynamics", John Wiley & Sons, Inc.
- Childs D. W., Nelson C. E., Nicks C., Scharrer J., Elrod D., Hale K., 1986. "Theory Versus Experiment for the Rotordynamic Coefficients of Annular Gas Seals: Part 1 - Test Facility and Apparatus", Trans. ASME, J. of Tribology, Vol. 108, pp. 426-432.
- Dietzen, F.-J. and Nordmann, R., 1988, "A 3-Dimensional Finite Difference Method for Calculating the Dynamic Coefficients of Seals", Proceedings of the Rotordynamic Instability Workshop, Texas A&M University, Texas, USA, pp. 211-227
- Klement, H.-D., 1993, "Berechnung der Eigenfrequenzen und Stabilität von Rotoren mit MADYN", VDI-Report 1082, pp. 37-46.
- Kwanka K., Mair R., 1995. "Identification of Gas Seal Dynamic Coefficients Based on the Stability Behaviour of a Rotor", Proceedings of the 1st. European Conference of Turbomachinery - Fluid Dynamic and Thermodynamic Aspects, March 1-3, Erlangen-Nürnberg, Germany, VDI-Report 1186, pp. 297-309.
- Kwanka K., 1995a: „Ein neues Identifikationsverfahren für dynamische Koeffizienten von Labyrinthdichtungen“, SIRM III, Irretier H., Nordmann R., Springer H. (Hrsg.), Vieweg Verlag, pp. 216-224.
- Kwanka K., 1995b: „Variation of Fluid Flow Forces in Seals with Rotor Bending“, DE-Vol. 84-2, 1995 Design Eng. Technical Conference., Vol. 3 - Part B, ASME 1995, pp. 1277-1282.
- Kwanka K., Nagel M., 1997. "Experimental Rotordynamic Coefficients of Short Labyrinth Gas Seals", NASA Conference Publication 3344, Proceedings of a workshop held at Texas A&M University, May 6-8, 1996, pp. 135-144.
- Krämer, E., Wohlrab, R., 1994: "Lagerungseinflüsse bei Dampfturbinenrotoren mit Spaltanregung", VDI-Berichte 92, pp. 109-125
- Kwanka K., 1995: "Variation of Fluid Flow Forces in Seals with Rotor Bending", DE-Vol. 84-2, 1995 Design Eng. Technical Conf., Vol. 3 - Part B, ASME 1995, pp. 1277-1282.
- Kwanka K., 1997. "Rotordynamic Impact of Swirl Brakes on Labyrinth Seals with Smooth or Honeycomb Stators", ASME Paper No. 97-GT-232, ASME Turbo Expo '97, Orlando, Florida.
- Kwanka K., 1998. "Influence of Labyrinth Seal Geometry on Rotordynamic Coefficients", Proceedings of the Fifth International Conference on Rotor Dynamics (IFTOMM), H. Irretier and R. Nordmann (Ed.), Vieweg Verlag, pp. 241-251.
- Leong Y. M. M. S., Brown R. D., 1984: "Experimental Investigations of Lateral Forces Induced Through Model Labyrinth Glands", NASA CP 3239, pp. 187-196.
- Matros M., Neumer T., Nordmann R., 1994. "Identification of Rotordynamic Coefficients of Centrifugal Pump Components Using Magnetic Bearings", Preprints of the Fifth International Symposium on Transport Phenomena and Dynamics of Rotating Machinery (ISROMAC-5), May 8-11, 1994, Kaanapali, Hawaii, USA, pp. 55-72.
- Millsaps K. T., Martinez-Sanches M., 1993. "Rotordynamic Forces in Labyrinth Seals: Theory and Experiment", NASA Conference Publication 3239, Proceedings of a workshop held at Texas A&M University, pp. 179-207.
- Nordmann, R., Dietzen, F.-J., Weiser, H.P., 1989, "Calculation of Rotordynamic Coefficients and Leakage for Annular Gas Seals by Means of Finite Difference Techniques", Journal of Tribology, July 1989, Vol. 111/545
- Nordmann, R., Weiser, H.P., 1988, "Rotordynamic Coefficients for Labyrinth Seals Calculated by Means of a Finite Difference Technique, Proceedings of the Rotordynamic Instability Workshop, Texas A&M University, Texas, USA, pp. 161-175
- Ulbrich H., 1988: "New Test Techniques Using Magnetic Bearings", Magnetic Bearings Proceedings of the First International Symposium, ETH Zürich, G. Schweitzer (Editor), Springer Verlag, pp. 281-288.
- Thomas, H.-J., 1978: "Zur Laufstabilität einfacher Turborotoren besonders bei Spaltanregung", Konstruktion 30, Vol. 9, pp. 339-344
- Wagner N. G., Steff K., 1996: "Dynamic Labyrinth Coefficients from a High-Pressure Full-Scale Test Rig Using Magnetic Bearings", NASA Conference Publication to be published, Proceedings of a workshop held at Texas A&M University, May 6-8, pp. 95-111.
- Wright D. V., 1983. "Labyrinth Seal Forces on a Whirling Rotor", ASME Applied Mechanics Division, Proceedings of a Symposium on Rotor Dynamical Instability, Adams M. L. Jr. (Editor), ASME Book-Vol. 55, pp. 19-31.

# Vibration control of a flexible rotor with a slotted-ring sealed electro-rheological squeeze film damper

N-S LEE and D-H CHOI

Hanyang University, Seoul, Korea

K-Y SEOK, Y-B LEE, and C-H KIM

Korea Institute of Science and Technology, Seoul, South Korea

## Abstract

High speed flexible rotors supported by electro-rheological squeeze film damper (ER-SFD) experience highly nonlinear dynamic characteristics and electric discharge problems at large amplitudes. Therefore, controlling the vibration amplitudes at the critical speeds is not a simple task.

In this paper, a deliberately machined slotted ring design of squeeze film damper which has a predetermined clearance at leakage sides is used to inherently eliminate the electric discharge problems. A fuzzy algorithm was also applied for reducing vibration amplitudes of a flexible rotor supported by the discharge-free slotted-ring sealed ER-SFD. Results showed that optimum values of yield shear stress of ER fluids exist for minimizing vibrations at the SFD and at the overhung rotor, controlled by a fuzzy set. Also, a fuzzy controller could be applied to the nonlinear rotating system.

## 1. INTRODUCTION

The remarkable effect of electro-rheological fluids has been reported and several successful applications of ER fluids to mechanical elements have been accomplished at laboratory level. Wide and reversible variation of the yield shear stress and fast activation are among the merits of ER fluids when the electric field is applied. The behavior of ER fluids can be idealized by a Bingham model which is often used for grease lubrication modeling. The property of ER fluid depends on its initial yield shear stress ( $\tau_0$ ). Almost all ER fluids activate like Bingham plastic fluids. The most outstanding properties of the Bingham fluid are the initial yield stress and the initial viscosity of the electro-rheological fluid. Especially, in the case of ER fluid as a fluid for the ER-SFD, the yield shear stress  $\tau_0$  can be modeled by

$$\tau_0 = \alpha \left( \frac{V}{h} \right)^\beta$$

where  $V$  is the applied voltage at ER.  $h$  is the film thickness at the squeeze film damper clearance and  $\alpha, \beta$  are experimentally-determined constants [1]. In this paper,  $\alpha, \beta$  values are 397.96 and 0.961134, respectively.

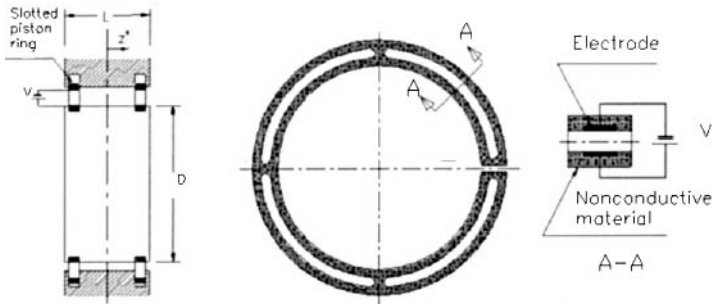


**Fig. 1 Slotted ring ER-SFD**

The initial viscosity ( $\mu_0$ ) of ER fluid is very important because it determines the range of system controllability. Recently, the applications of ER fluids to fluid film bearings such as journal bearings, step bearings and squeeze film dampers have also been initiated.

Tichy[2,3] developed and solved a modified Reynolds equation obtained by applying a Bingham model to a one dimensional journal bearing and squeeze film damper. The ER effect is significant and beneficial in the squeeze film damper in which the flow is mainly Poiseuille flow. However, it is not as remarkable in the journal bearing where the flow is mainly Couette. Kim et al. [4] studied the rotor vibration control supported by the ER-SFD with end seal and without end seal cases for a rigid rotor system. The influence of the end seal is more effective for the control of the high-speed rotor system supported by an ER-SFD. However, in the conventional ER squeeze film dampers, the clearance between the bearing(housing) and damper(journal) surfaces is used as a gap of electrodes so that electric discharge can occur at the position of the minimum film thickness when the eccentricity ratio is high. Thus, the conventional ER squeeze film dampers might be impossible to be used directly in the rotor bearing system, despite the high increase in their damping capacity. In this paper, a deliberately machined slotted ring design of squeeze film damper which has a predetermined clearance at its leakage sides is used to eliminate the electric discharge problems. As shown in figure 1, since the cross section of the ring is mechanically slotted into a constant gap where electrodes are inserted, a newly proposed ER squeeze film damper, called a slotted ER-SFD in this paper, has a merit of eliminating the electric discharge problem. In the slotted ER-SFD, ER fluids are unexcited in a squeezed annular region behaving as a Newtonian fluid, while ER fluids are excited by an external electric field at the slot of the ring behaving as a Bingham fluid. Thus, controlling the strength of an electric field applied to the slotted rings, the local end leakage can be varied, which affects the fluid film pressure field inside squeezed annular region and its damping force can be controlled subsequently. Lee and et al.[5] applied this concept to a flexible rotor system. They showed that the slotted ring ER-SFD can be used as a controllable active damper in the high speed rotating system for reducing vibration. Supply voltage control showed the best performance over the entire speed range. On the other hand, the optimum value with supply pressure and surface area of the electrode showed a somewhat smaller effect in some speed ranges.

Morishita et al.[6] studied the effect of the application of ER fluid to a squeeze film damper. They showed that rotor vibration could be reduced remarkably over a wide range of rotating speed and there existed an optimum damping for every vibration mode.

Nikolajsen et al.[7] suggested that the ER damper may also easily be incorporated in a feedback control loop using a shaft displacement or housing acceleration signal.

The central purpose of this paper is to propose an effective fuzzy controller for reducing the vibration amplitude of a flexible rotor system supported by the slotted ER-SFD where the combination of supply voltage and supply pressure is applied for providing the control of shear strength inside the squeeze film damper clearance. Moreover the fuzzy controller is applied to the nonlinear rotating system.

## **2. TEST RIG; SLOTTED ER-SFD**

### **2.1 Description of Overall Slotted ER-SFD**

The overall rotor system supported by a slotted ring ER-SFD is shown in figure 2. It consists of a damper mass, a SFD housing, 0.1 Hp variable speed DC motor with a maximum speed of 10,000 rpm. The flexible rotor shaft with a self-aligned radial ball bearing at one end for pivot support is supported by a slotted ER-SFD at the other end to move freely. The journal of the squeeze film damper has an electric insulation to prevent electrical shock. The slotted ER-SFD located at the center of the shaft has six flexible bars to prevent rotation as well as providing partial support stiffness of the SFD. This arrangement is very sensitive to the total system motion. Therefore, it should not limit radial vibration and should not generate unnecessary pre-load. Length from the left self-aligning ball bearing to the center of the slotted ER-SFD is 135 mm, while length from the ball bearing to the rotor is 320 mm. The centering spring span ( $r_k$ ) is 300 mm and centering spring stiffness is about 12,000 N/m. For the purpose of investigating unbalance response, 2.2 grams of large unbalance mass at a location of 37.5 mm radius from the center of the rotor was attached to the pre-balanced rotor. Radius, length, and clearance of the SFD journal are 50mm, 15mm, and 1.0mm, respectively.

### **2.2 Measurement and data processing scheme**

The overall data processing system for measurement and data acquisition of test data for the slotted ER-SFD rotor system is shown in figure 3. To measure the vibrations in x and y directions, two eddy-current type displacement sensors were installed at the SFD housing, 90 degrees apart. They have sensitivity of 7.087 V/mm. For measuring the supply pressure, a strain-gauge type pressure sensor, PT1, was used. The supply pressure of the slotted ER-SFD was controlled by a proportion valve which has a maximum pressure range of 2,500 kPa, and a flow rate range of 31 l/min. To obtain effective results of supply pressure control, a controllable P-Q valve was used with on-line computer control by a 12 bit D/A. To measure the temperature of the lubricant, two K type thermo-couple sensors were used and the operating temperature was fixed at 35 degrees Celcius.

A high-voltage amplifier was made for the ER-SFD in controlling the supply voltage to the ER-fluid. Voltages of the computer D/A operate in 0~5 Vdc range and voltage amplification through the amplifier was made for achieving up to 5 kV with very low current at 10 mA. It has a safety fuse to protect the test apparatus from high voltage shock. All data were processed by a A/D and D/A 12 bit converter, and preserved on the computer hard disk. This rotor system has a maximum speed of 10,000 rpm and the rotating speed was detected by a pulse-counter type proximity probe.

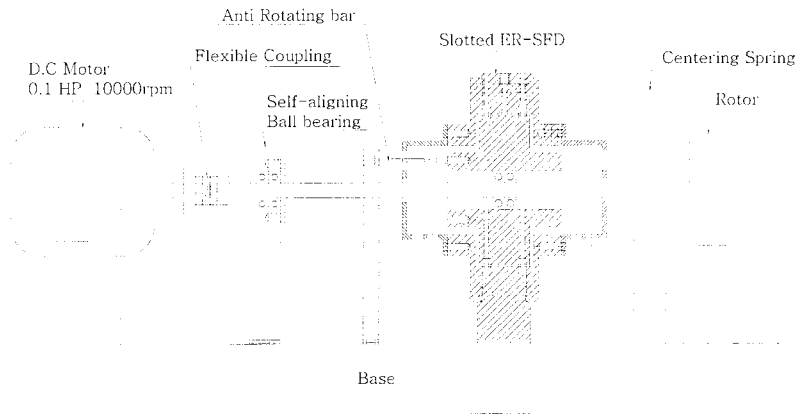


**Fig. 2 Flexible rotor system supported by slotted ring ER-SFD**

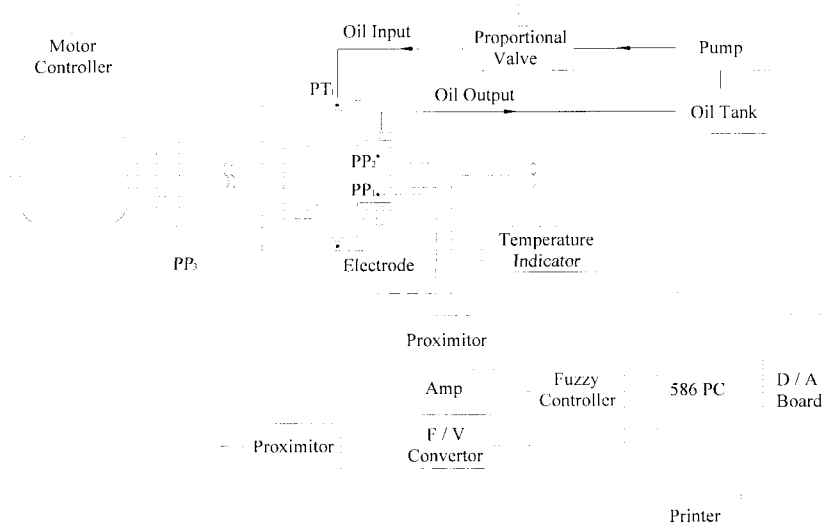


**Fig. 3 Schematic diagram for slotted ring ER-SFD system**

### 3. DESIGN OF FUZZY CONTROLLER

Generally, fuzzy inference systems have been successfully applied in a wide variety of control fields such as automatic control, data classification, decision analysis, expert systems, and computer vision. As an alternative to classical control theory, it allows the resolution of imprecise or uncertain information. Due to the nonlinear characteristic of the flexible rotor system supported by the slotted ER-SFD, fuzzy logic (generally justified for both linear and nonlinear systems) was used to select the optimum applied voltage.

Mamdani's implication method is adopted here in the fuzzy inference scheme to combine the membership values for each rule, with the center of gravity (COG) defuzzification to obtain the output value. Membership functions are determined by trial and error procedures because of the independence of the mathematical model based on error. Each fuzzy logic controller has the amplitude  $\varepsilon$  and the rotational speed  $\omega$  as input parameters.

$$\omega = \{LF, F, M, S, GS\},$$

$$\varepsilon = \{VS, MS, M, ML, VL\}$$

The describable values of Fuzzy variables are not evaluated by numbers but by a fuzzy set. Triangular and trapezoidal membership functions are used for the fuzzy input/output subsets. The fuzzy input subsets are  $LF$ = Less than First critical speed,  $F$ =First critical speed,  $M$ =Medium,  $S$ =Second critical speed,  $GS$ =Greater than Second critical speed for the rotational speed and  $VS$ =Very Small,  $MS$ =Moderate Small,  $M$ =Medium,  $ML$ =Moderate Large,  $VL$ =Very Large values for the amplitude.  $AV$  is the applied output voltage.

$$R : \omega \times \varepsilon \rightarrow AV$$

Membership functions are represented in figure 4 and 5 as an antecedent and a consequent, respectively. And the adopted inference control rules are summarized in table 1.

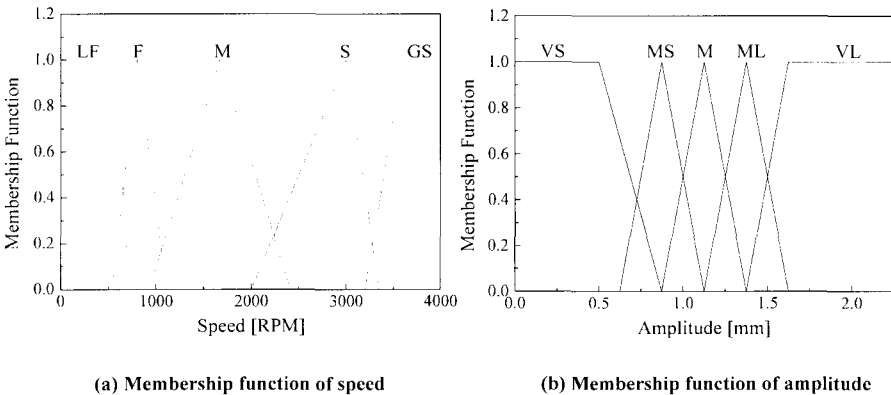


**Fig. 4 Map of membership function (input)**

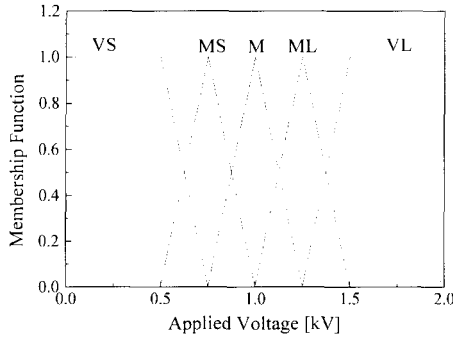


**Fig. 5 Map of membership function (output)**

**Table 1. Fuzzy control rules**

Speed \ Amplitude	Amplitude				
	VS	MS	M	ML	VL
LF	VS	MS	MS	MS	M
F	VS	M	M	M	ML
M	VS	VS	VS	VS	VS
S	VS	MS	M	ML	VL
GS	VS	M	M	VL	VL

#### **4. RESULTS AND DISCUSSION OF FLEXIBLE ROTOR SYSTEM SUPPORTED BY SLOTTED ER-SFD**

As mentioned above in section 1, the slotted ER-SFD has a merit of eliminating the electric discharge problem since the cross section of a ring is mechanically slotted into a constant gap where electrodes are inserted. However, over voltage can still be applied to induce discharge problems at the slotted rings. Therefore, it is still important to select optimum supply voltage at the slotted rings, even though there are no electric discharge problems at the damper clearance as in the conventional ER-SFD.

In this section, the investigation of the optimally applied supply voltages at the slotted ER-SFD for the vibration control at different rotating speeds are presented. In this rotor system with a selected centering spring, the first critical speed was measured at about 750 rpm with a rigid translatory mode. The bending mode of the flexible rotor occurs at about 2,900 rpm. The influence of supply voltage with increasing speed until the second critical speed was investigated. The range of supply voltage up to 2.0 kV was selected to investigate how the rotor with slotted ER-SFD will behave at the first and second critical speeds. Figure 6 and 7 show the amplitudes of the flexible rotor supported by the slotted ER-SFD at the ER-SFD and at the overhung rotor. The effective surface area ratio of the electrode is 0.94, and external supply pressure is 10 kPa. Experimental influence of supply



voltage for vibration control with different speeds was investigated. The effective surface area ratio 0.94 means that the electrode surface area has 94% of the total circumferential area. Without electrical field (0.0kV), the viscosity of ER fluid is similar to Newtonian fluid with nominal viscosity. Applied to the slotted rings of the ER-SFD, the amplitudes of the ER-SFD and rotor vibrations were decreased at the first and second critical speeds by both constant supply voltage (2.0kV) and fuzzy control. Control of vibration amplitude in the fuzzy application at the ER-SFD in the first critical speed range is easier than that at the overhung rotor. Also the same amplitude of 2kV results were showed at the second critical speed, for fuzzy and constant high voltage, arriving at the conclusion that the system proved the controllability with a discharge free ER-SFD.

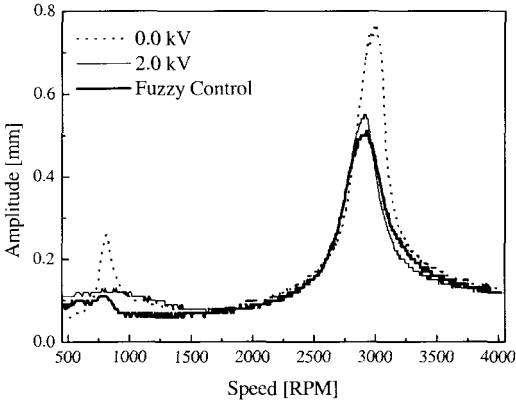


**Fig. 6 Comparison of unbalance response amplitude with constant supply voltage and optimal fuzzy control voltage at slotted ER-SFD**

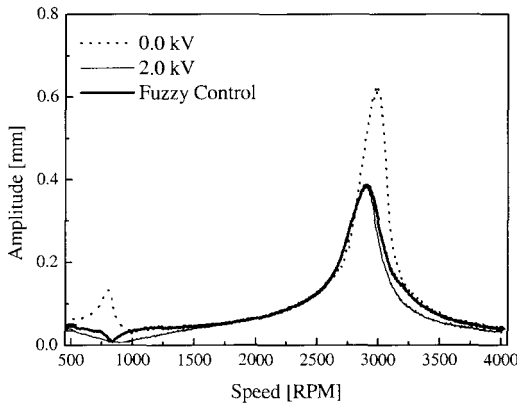


**Fig. 7 Comparison of unbalance response amplitude with constant supply voltage and optimal fuzzy control voltage at overhung rotor**

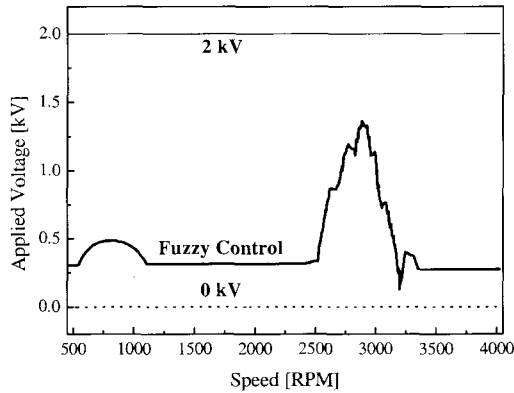


**Fig. 8 Comparison of constant supply voltage and optimal fuzzy control voltage at slotted ER-SFD**

The effectiveness of the constant supply voltage and fuzzy control are compared, as shown in figure 8. Fuzzy control algorithm is more beneficial from the energy saving viewpoint. When the supply voltage was applied to the system, the vibration amplitudes with the fuzzy control algorithm were nearly identical with the constant supply voltage case in the entire speed range. However gross consumed power with fuzzy control for reducing vibration amplitudes of the ER-SFD were much less than with constant supply voltage, as shown in figure 8.

## 5. CONCLUSIONS

In this paper, the vibration of the rotor system supported by slotted ER-SFD can be effectively reduced by using fuzzy algorithms. The maximum output voltage is about 0.5 kV at the first critical speed and 1.4 kV at the second critical speed.

With fuzzy algorithms, the vibration amplitude reduction is almost the same as with constant voltage at the ER-SFD with overhung rotor. Even though the overall applied voltage is much less than 2kV, the damping capacity of the system controlled by fuzzy algorithm is comparable to that of the system applied by constant voltage (2 kV). It shows that an efficient voltage can be selected to reduce the vibration amplitude with a fuzzy algorithm.

## ACKNOWLEDGMENTS

This work was supported by a grant from the Critical Technology 21 Project of the Ministry of Science and Technology, Korea.

## References

- (1) Kim, C. H. *et al.*, "Vibration Control of a Pressurized, Sealed, ER Fluid SFD supported rotor", 7th ISROMAC Conference, pp.238~247, Feb., 1998
- (2) Tichy, J. A., "Hydrodynamic Lubrication Theory for the Bingham Plastic Flow Model", *J. of Rheology*, Vol. 35, No. 4, pp. 477-496, 1991
- (3) Tichy, J. A., "Behavior of a Squeeze Film Damper with an Electro-rheological Fluid", *STLE Tribology Trans.* Vol. 36, No. 1, pp. 127-133, 1993
- (4) Kim, C. H. *et al.*, "Test results for vibration control of an overhung rigid rotor supported by a sealed and electro-rheological fluid squeeze film damper", *International Conference on the Integration of Dynamics, Monitoring and Control*, Sept. 1999
- (5) Lee, Y.B. *et al.*, "Test Results for Vibration Control of an Overhung Flexible Rotor Supported by a Discharge Free Slot Electro-rheological Squeeze Film Damper", *Asia-Pacific Vibration Conference '99*, pp.484~489, Dec. 1999
- (6) Morishita, S. *et al.*, "Controllable squeeze-film damper: an application of electro-rheological fluid", *ASME J Vibrations and Acoustics*, Vol. 114, pp.354-357
- (7) Nikolsjsen, J. L. *et al.*, "An electroviscous damper for rotor applications", *ASME J Vibrations and Acoustics*, Vol. 112, pp.440-443

© 2000, With Author

*This page intentionally left blank*

# **Influence of various parameters on the non-linear behaviour of a flexible shaft incorporating an uncentralized squeeze-film damper**

**M C LEVESLEY**

*School of Mechanical Engineering, University of Leeds, UK*

**R HOLMES**

*Department of Mechanical Engineering, University of Southampton, UK*

## **SYNOPSIS**

This paper presents experimental results on the vibration response of a rotating assembly comprising a rotor, bearing housing and an uncentralised squeeze film damper. The physical size and configuration of rotor assembly used in this study are comparable with that of a current small to medium sized turbofan aero-engine. Unlike previous experimental studies, the operating speed range of 0 to 12000 rpm is more representative of actual aero-engine rotor speeds. At these elevated speeds the rotor exhibits significant amounts of flexure. The uncentralised configuration of the squeeze film coupled with the oil film's susceptibility to cavitation, has produced some significant non-linear characteristics. The experimental data are compared with preliminary theoretical predictions in which both the rotor and bearing supports are considered to be flexible. The paper concludes that there are significant performance advantages to be gained in supplying oil above a certain threshold but relatively little gain in further increases in supply pressure. The flexible nature of the rotor at high speeds highlights the problem of locating the squeeze-film damper at an optimum position to attenuate vibration levels arising from both rigid body and flexural modes of vibration.

## **1 INTRODUCTION**

Over the last thirty years the use of squeeze-film dampers (S.F.D's) in rotor support structures has increased to the point where they are now regarded as standard. In the aero engine industry advances in material technology coupled with economic pressures, have placed increased emphasis on the development of larger and lighter gas turbine engines. Inevitably structures have become more flexible, containing very little inherent damping. As with most rotating machinery, the principal form of vibration is due to a residual amount of rotor unbalance. Efforts to reduce this inherent unbalance will undoubtedly bring benefits but a point is soon reached at which the cost of reducing the residual unbalance will far outweigh

the benefits. By careful design of the squeeze-film dampers a significant amount of damping can be introduced into these structures, reducing rotor vibrations, mechanical fatigue and aircraft cabin noise levels. However it must be stressed that too much damping which can result in the damper acting as a rigid link can be as undesirable as too little (1). Previous experimental studies (2,3) have shown that the oil supply pressure, the amount of unbalance, the location of the supply groove, the type of end-seals used etc., all have a significant influence on the performance of the squeeze-film damper. The purpose of this current research program is to examine the behaviour of a squeeze-film damper under dynamic load using a variety of experimental parameters. The research extends that described in a previous paper (4), in particular by increasing the speed range of the same test facility to speeds more representative of typical commercial aero-engine gas turbines, typically 12,000 rpm.

## **2 EXPERIMENTAL TEST FACILITY**

### **2.1 General description**

The experimental rig is described in reference (2). Modifications to this test rig have been carried out and the current arrangement is shown in figure 1. It consists of a heavy rotor (1) driven at the left hand end by an electric motor via a flexible coupling. At this end a deep groove self aligning bearing (2) rigidly supports the rotor, providing both axial location and a point about which the rotor can pivot. At the right hand end the rotor accommodates an aero engine roller bearing assembly (3) shown in more detail in figure 1b. The rotor/bearing assembly was balanced to British Standard BS6861 G2.5 suitable for running at a speed of 200 rev/s (12,000 rpm). Unbalance masses (4) are subsequently fitted to the right hand end of the rotor to produce a rotating out of balance force of known magnitude.

A liner (5) is held within a steel housing ring (6) which is located axially by four slender bars (7) and is rigidly supported heavy steel supports (not shown). Circularity plots of the internal surface of the liner and of the external surface of the roller bearing race (8) show peak deviations from a mean value of  $\pm 4 \mu\text{m}$  and  $\pm 0.9 \mu\text{m}$  respectively, which are well within specification. It is these components which form the boundaries of the squeeze-film.

Oil is supplied to the damper by an oil pump fitted with a cooler and accumulator to ensure a stable supply at pressures up to 8 bar at a constant temperature of  $27^\circ\text{C}$  ( $\pm 1^\circ\text{C}$ ). Oil temperature is monitored both in the oil supply reservoir which gives the temperature at entry to the squeeze-film, and directly under the squeeze-film damper bearing assembly just before the oil is scavenged back to the oil supply reservoir. Due to high oil flow rates at high pressures, a combination of an oil thrower ring (9), various oil baffles (10) and compressed air jets are necessary to prevent oil entering the space between the capacitance displacement transducer and the rotor. These transducers are located so as to measure the rotor displacement in horizontal and vertical axes both at a location close to the squeeze-film and also midway between the two supporting bearings (see following section for more detail). A photo diode is used to measure the rotational position relative to the unbalance mass and the speed of the rotor, all of which provide signals from which the rotor response may be recorded and analysed.

## 2.2 Rotor and squeeze film damper dimensions

Figure 2 shows a schematic representation of the rotor giving details of the dimensions of the shaft at various positions. An additional mass of 598.9 g is added at the centre of section 3 to account for the mass of a ground steel ring used to measure displacement of the rotor at a mid rotor location. An additional mass of 2.380 kg is added at the centre of section 7 to account for the mass of the roller bearing assembly plus locking ring. The rotor is supported at the centre of section 7 and at a position 25.41 mm from the left hand edge of section 1. Unbalance masses of 12.5, 25.0 and 50.0 grammes are attached at a radius of 49.1 mm from the rotor centre and at a position 8 mm from the right hand edge of section 11. Displacements are recorded in both vertical and horizontal axes at positions 12 mm from the right hand edge of section 3 (referred to as *Mid Rotor Probe* location) and 30.5 mm from the right hand edge of section 11 (referred to as *SFD Probe* location). The rotor is made of mild steel with a density of 7860 kg/m<sup>3</sup> and modulus of elasticity of 200 GPa.

The squeeze film damper has land lengths of 18.2 mm ( $\pm 0.1$  mm) and 1.7 mm with a non central supply groove of width 5 mm and a single oil feed to the groove. The squeeze-film radial clearance was measured at 0.121 mm and it has a radius of 80.0 mm. The oil has an average viscosity of 0.0049 kg m<sup>-1</sup> s<sup>-1</sup> at its operating temperature of 27°C. The damper is sealed at each end using piston rings. These geometric and sealing requirements were a feature of the actual engine SFD for which the present test rig provided an experimental assessment.

## 2.3 Bearing support stiffness

In figure 3 an impact test response measured with no squeeze-film damping in the vertical axis at the mid-rotor position shows a resonance at a frequency of 161 Hz. With infinitely stiff bearing supports theoretical modelling predicts the first resonance peak at 180 Hz. This lower than predicted peak indicating a certain degree of flexibility in the bearing supports. Further simulation suggests a stiffness value of 100 MN/m to be appropriate at the bearing supports.

## 3 EXPERIMENTAL RESULTS

Figures 4 and 5 show the response of the rotor at the squeeze-film damper probe location and at the mid rotor probe location respectively in a) vertical and b) horizontal axes when subjected to unbalance masses of 12.5, 25 and 50g and oil supply pressures of 1,2,4 and 8 bar.

From figure 4 (squeeze-film damper probe location), at 12.5g of unbalance it clear to see that changes in supply pressure from 1 to 8 bar has very little effect on the amplitudes of vibration, particularly in the vertical axis. In the horizontal axis differences are more pronounced but remain relatively small. At 25g of unbalance differences produced by changes in oil supply pressure are clearly visible, particularly in the vertical axis. For example, a supply pressure of 1 bar results in a sharp rise in vibration amplitude between 140 and 160 rev/s. Increasing the supply pressure to 2 and then 4 bar delays the onset of this increase to between 150 and 170 rev/s and reduces its amplitude. A further increase to 8 bar reduces the amplitude of vibration still further and produces a trough at 170 rev/s. Though slightly less clear, these trends are reflected also in the horizontal axis response with higher supply pressures in general producing lower amplitudes of vibration. For 50 g of unbalance,

increasing the supply pressure again reduces amplitudes of vibration. In the vertical axis amplitudes of vibration are reduced between rotor speeds of 120 and 170 rev/s as the supply pressure rises from 1 to 4 bar. A further increase to 8 bar has very little additional effect. Similarly in the horizontal axis, increasing the supply pressure from 1 to 2 and then to 4 bar reduces amplitudes of vibration between rotor speeds of 110 and 140 rev/s. Again a further increase to 8 bar has little additional effect in the horizontal axis. At this level of unbalance, increasing the oil supply pressure from 1 to 8 bar also has a positive effect in reducing the amplitudes of vibration in both axes at the highest rotor speed of 190 rev/s. In the horizontal axis in particular it can be seen to have been reduced by approximately 50%.

In figure 5 (mid rotor probe location) at 12.5g of unbalance it is again clear to see that changes in supply pressure (1 to 8 bar) have very little effect on the amplitudes of vibration. With 25 g of unbalance, changes in supply pressure from 1 to 2 and then 4 bar result in a general increase in vibration amplitude, an opposite effect to that seen at the squeeze film location. A further increase to 8 bar lowers the speed at which the resonance peak occurs in the horizontal axis from 170 to 150 rev/s, while increasing it in the vertical axis from 150 to 180 rev/s. At 50 g of unbalance this trend is reversed with an increase in supply pressure attenuating amplitudes of vibration in the vertical axis and increasing slightly the speed at which the peak amplitudes occur. In the horizontal axis increasing the supply pressure from 1 to 2 bar again causes an increase in vibration amplitude and an increase in the speed at which the peak amplitude occurs. Further increases from 2 to 4 and finally 8 bar have little further effect on vibration amplitude.

From the experimental data the following general comments can thus be made on the effects of oil supply pressure and unbalance.

In general, increasing the supply pressure appears to increase the amount of damping produced by the squeeze-film, however at low unbalance the effect is small, while at high unbalance it is more pronounced. This increase in damping is most probably due to changes in the amount of cavitated oil within the squeeze-film annulus.

Between speeds of 150 and 170 rev/s and for low oil supply pressures, the amplitudes of vibration in the vertical axis for an unbalance mass of 50.0 g are lower than for an unbalance mass of 25.0 g (figure 4a). This is confirmed by corresponding rotor-centre orbits shown in figures 6a and 6b. A possible explanation for this is the extent of the region of cavitated oil within the squeeze film. It is possible that the between 160 and 170 rev/s oil cavitation occurs at 25.0 g unbalance but is suppressed at 50.0 g due to small differences in the histories of speed increases between the tests. Cavitation of the oil film greatly effects its properties, reducing the damping force generated and introducing a stiffness force, which could account for this unexpected result. Either side of this limited speed range, amplitudes of vibration are considerably greater for the 50.0 g unbalance than for the 25.0 g unbalance. This result highlights problems in predicting exact conditions that will produce oil film rupture.

In general both supply pressure and unbalance have little influence on the frequency contents of the vibration signals. However, it should be noted that as the unbalance increases and hence also the strength of the synchronous vibration signal increases, relative noise levels are reduced and hence appropriate waterfall diagrams appear 'cleaner'. This can be seen in figures 7a and 7b. Apart from a dominant first excitation order signal, 1.5, 2 and 3 times



excitation order signals can be seen along with faint 1/6, 1/3, 1/2, 2/3 and 5/6 sub-synchronous signals.

#### 4 LINEAR ANALYSIS

Figure 8 shows a schematic diagram of the theoretical model used in the linear analysis of the rotor response in the vertical axis. The rotor was modelled using 32 lumped masses and stiffnesses derived from the rotor dimensions given in 2.2. The bearing supports  $k_2$  and  $k_3$  are represented as a linear stiffness using the value determined in 2.3. The deep groove self aligning bearing at the left hand end of the rotor is represented as a rigid link by using a very high linear stiffness ( $k_1=100 \times 10^{12}$  N/m). Damping introduced via the squeeze film is included using a linear damping coefficient,  $C$ . Linear responses were produced for an unbalance mass of 50 grammes both at the at the SFD probe location (Figure 9) and mid rotor probe location (figure 10) using a transfer matrix method of solution. Amounts of assumed squeeze film damping equal to 2, 20 and 200 kNs/m are used to illustrate the effects of changes in damping on the predicted response.

From the data generated by the linear model the following general comments can be made regarding the effects of damping.

For low levels of damping at the SFD Probe location, predicted amplitudes of vibration show a resonance peak at 70 rev/s followed by a trough at 160 rev/s before a further increase in amplitude as rotor speed increases. At the Mid Rotor location, low levels of damping produce a resonance peak at 220 rev/s.

Increasing damping generally results in a reduction in amplitudes of vibration across much of the frequency range. At the SFD Probe location the first resonance peak (seen at around 70 rev/s) is attenuated and migrates to a higher rotor speeds as damping is increased, while at the at the Mid Rotor location this trend is reversed with the resonance peak migrating to lower rotor speeds with increased damping.

At the SFD Probe location and over a limited range of speeds (142-162 rev/s), very high levels of damping result in an increase in vibration amplitude. At the Mid Rotor location this trend is echoed, here however very high levels of damping result in an increase in vibration amplitude over a more limited speed range (centred on 160 rev/s). At these elevated levels the SFD begins to act as a *rigid link*, with flexure of the rotor acting in conjunction with the support stiffness produces a the resonance peak at 160 Hz, confirming the results presented in 2.3.

#### 5 COMPARISON OF LINEAR ANALYSIS WITH EXPERIMENTAL DATA

It should be stressed that although the analysis is for a linear damper only, the trends seen in the data in figures 9 and 10 bear a marked similarity to some of the trends seen in experimental data presented earlier. To further illustrate this, comparison is made between the data given in figures 9 and 10 and the solid line (50 g of unbalance) in figures 4a and 5a respectively.

Comparing theoretical and experimental data at the vertical SFD probe location suggest that for higher oil supply pressures (4 and 8 bar) a linear damping coefficient of between 2 and 20 kNs/m would result in reasonably close agreement. At this level of damping the frequency response (both experimental and theoretical) would exhibit a steady increase in vibration amplitude up to a value of around 0.04mm followed by a trough at around 160 rev/s before amplitudes rise steeply as the rotor speed further increases up to its maximum values.

In section 4 it was suggested that the increase in experimental vibration amplitude seen between rotor speeds of 120 and 170 rev/s at low oil supply pressures (1 and 2 bar) may be as a result of oil film cavitation. The theoretical data confirms that a drop in damping resulting from cavitation would in fact result in higher levels of vibration over this range.

Comparing theoretical and experimental data at the vertical mid rotor probe location again suggests a damping coefficient of between 2 and 20 kNs/m would result in reasonably close agreement for higher oil supply pressures (4 and 8 bar). The theoretical data again confirms that a reduction in damping due to cavitation may explain the increased levels of vibration seen for the lowest oil supply pressure at rotor speeds of between 120 and 170 rev/s.

## 6 CONCLUSION

The experimental behaviour of the SFD has demonstrated some interesting non-linear squeeze-film behaviour. Due to its uncentralised design, responses in vertical and horizontal axes are markedly different.

The effects of oil supply pressure and out of balance on the response of the rotor have been found to be closely linked. Increasing the oil supply pressure at low levels of unbalance has little effect while at high levels of unbalance the effect is much more pronounced.

At low oil supply pressures (1-2 bar) the response of the rotor is more sensitive to unbalance. Changes in unbalance can cause large changes in the amplitudes of vibration. This is probably due to the damper's susceptibility to oil-film cavitation at low supply pressure. These changes in amplitude are particularly noticeable close to the squeeze-film.

At higher oil supply pressures (4-8 bar) the rotor is less sensitive to changes in unbalance. This is probably due to a more stable cavitation regime and it is probable that at these elevated pressures oil-film cavitation may be almost entirely suppressed.

In general, increasing the supply pressure appears to improve the damping capacity of the squeeze-film. This increase in the amount of damping produced is probably due to a reduction in the extent of oil cavitation within the squeeze-film annulus.

The frequency content of the vibration signals is only marginally effected by oil-supply pressure and rotor unbalance. Apart from a strong first excitation order signal, 1.5 2 and 3 times exception order signals were recorded along with faint 1/6, 1/3, 1/2, 2/3 and 5/6 sub-synchronous components.

At low oil supply pressures and for a limited range of speeds, amplitudes of vibration were found to be lower for an unbalance of 50.0 g than for a 25.0 g unbalance. This unusual result is probably explained by differences in cavitation regimes.

The linear model shows that in general increasing the amount of damping reduces levels of rotor vibration. However at very high levels of damping and over a limited frequency range the reverse is true. This is explained by excessive damping eliminating motion across the SFD. This in conjunction with the flexibility of the rotor and its supports effectively results in an undamped resonance at a rotor speed of 160 rev/s.

Changing the amount of damping can change the speed at which resonance peaks are predicted to occur. This is apparent both at the SFD probe and mid-rotor location.

Although the analysis is for a linear damper only, trends seen in the predicted response show a marked similarity to some of the trends seen in experimental data.

## REFERENCES

- 1) Levesley, M.C. and Holmes, R. The efficient computation of the vibration response of an aero-engine rotor-damper assembly. Proc. Instn. Mech. Engrs, Part G, 1994, 208, 41-51.
- 2) Levesley, M.C. and Holmes, R. The effects of oil supply and sealing arrangements on the performance of squeeze-film dampers: an experimental study. Proc. Instn. Mech. Engrs, Part J, 1996, 210, 221-232.
- 3) Levesley, M.C. and Holmes, R. Experimental investigation into the vibration response of an aero-engine rotor-damper assembly. Proc. Instn. Mech. Engrs, Part G, 1994, 208, 52-66.
- 4) Holmes, R. and Dogan, M. Investigation of a rotor bearing assembly incorporating a squeeze-film damper bearing. Proc. Instn. Mech. Engrs, J. Mech. Engrg. Sci. 1982, 24, 129-137

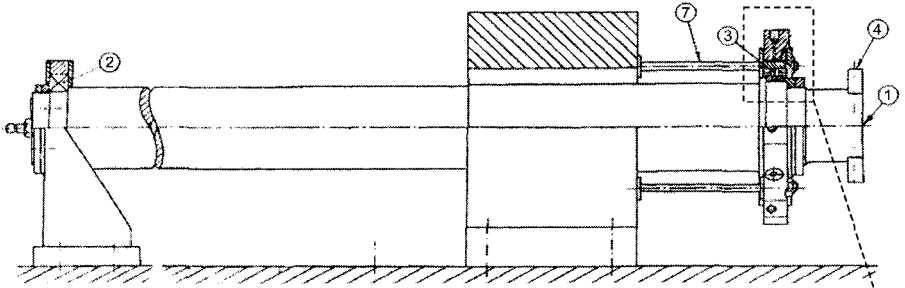


Figure 1a Experimental test facility

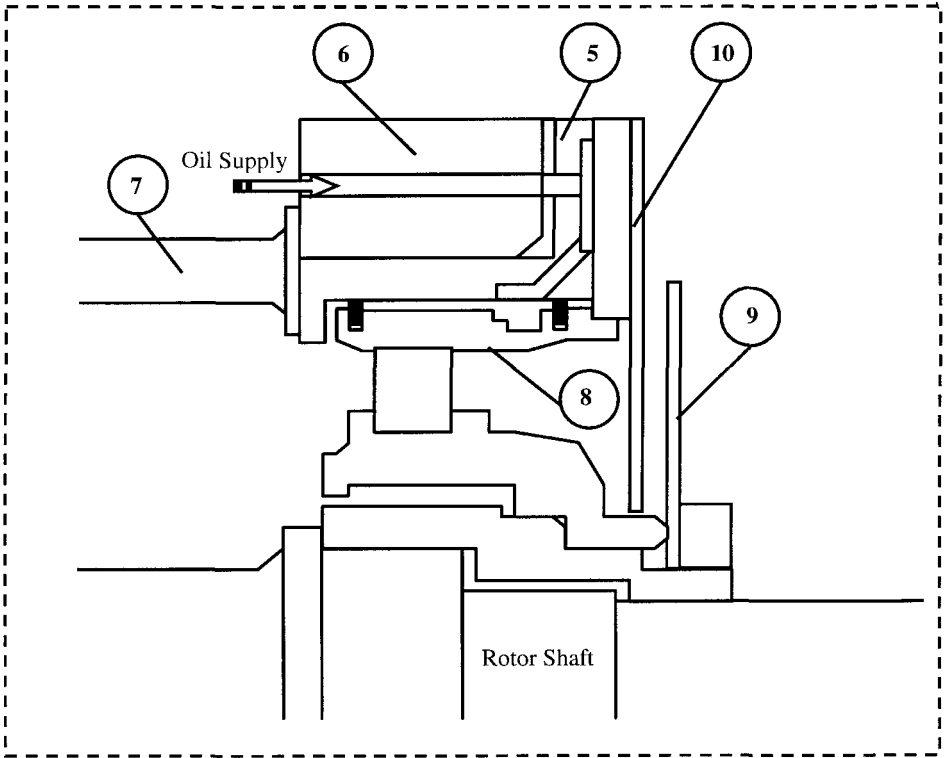
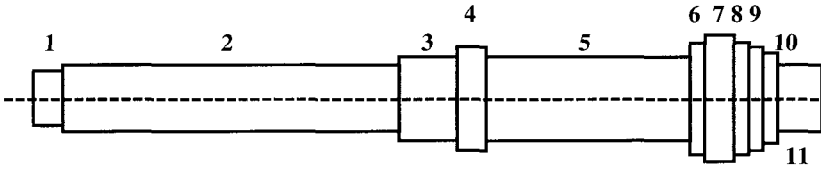


Figure 1b Squeeze film damper bearing detail



Section Number	Length of Section (m)	Diameter of Section (m)
1	0.0349	0.0762
2	0.5628	0.0860
3	0.0420	0.0950
4	0.0060	0.1040
5	0.3132	0.0921
6	0.0060	0.1016
7	0.0252	0.1120
8	0.0088	0.1030
9	0.0104	0.0936
10	0.0091	0.0900
11	0.0452	0.0762

Figure 2 Rotor Dimensions

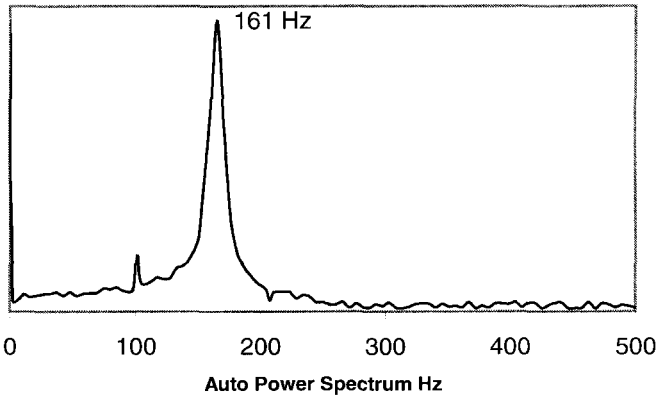
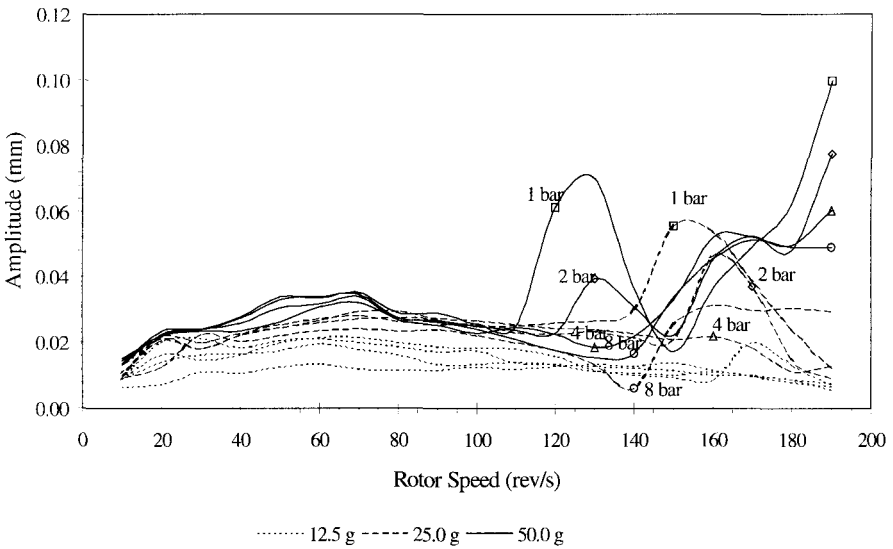
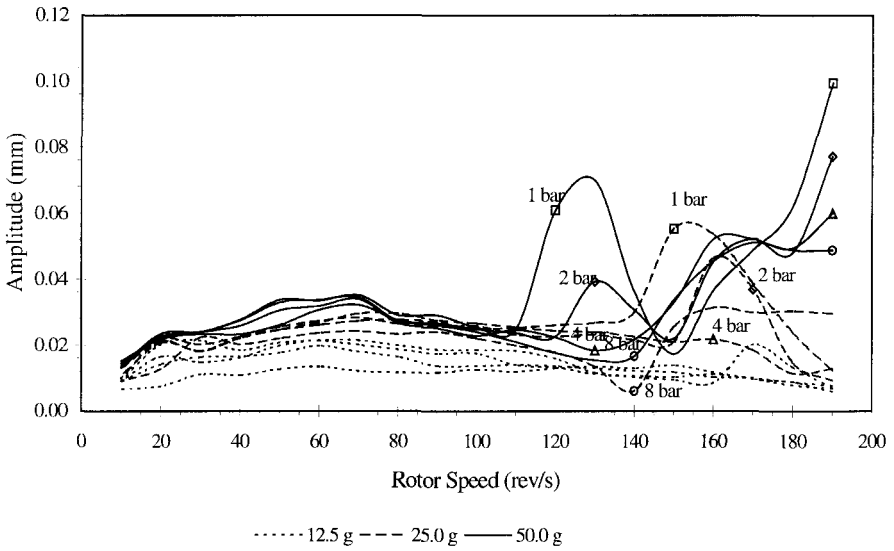
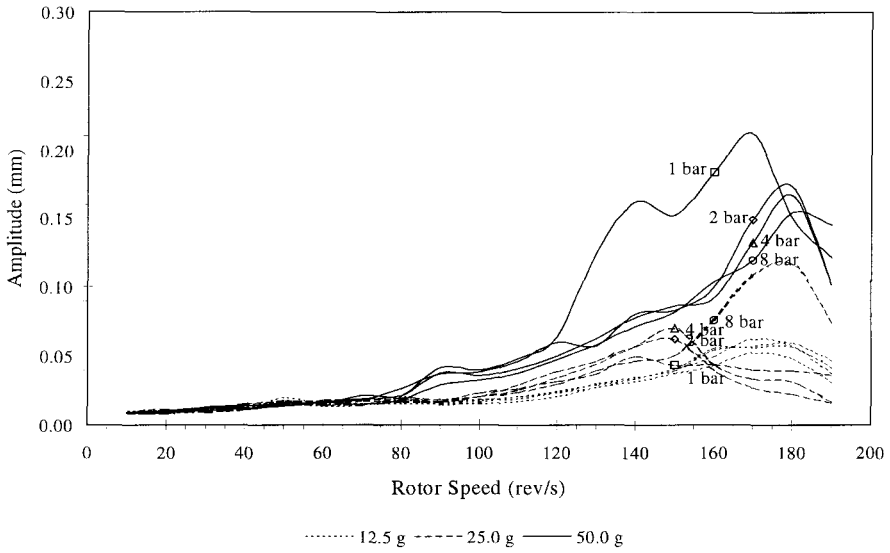
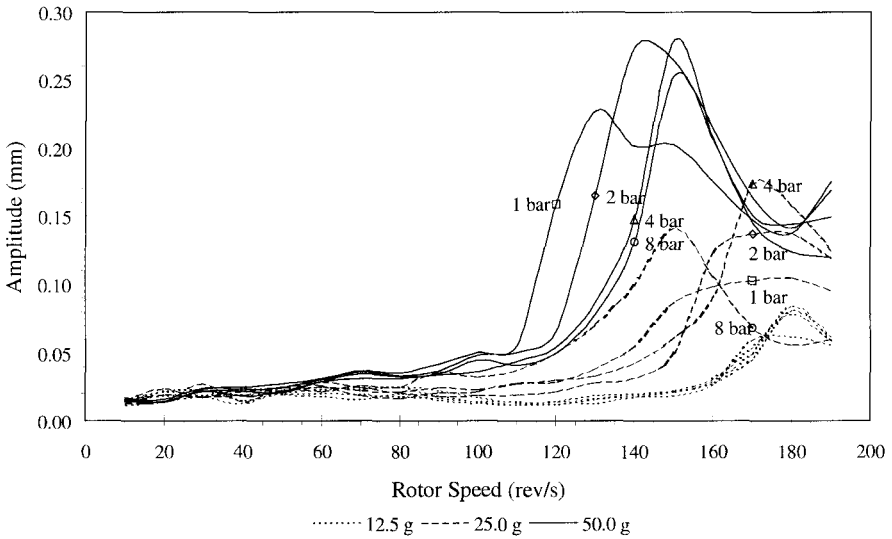


Figure 3 Impact test (vertical axis)





**Figure 5a) Vertical experimental mid rotor probe response**



**Figure 5b) Horizontal experimental mid rotor probe response**

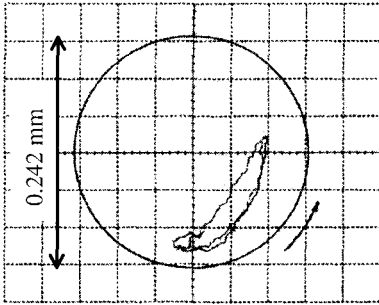


**Figure 6a) Rotor-centre orbit at 25.0 grammes unbalance (SFD probe, oil supply pressure 1 bar, rotor speed 160-170 rev/s,)**

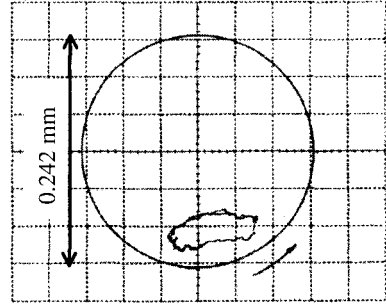


**Figure 6b) Rotor-centre orbit at 50.0 grammes unbalance (SFD probe, oil supply pressure 1 bar, rotor speed 160-170 rev/s,)**

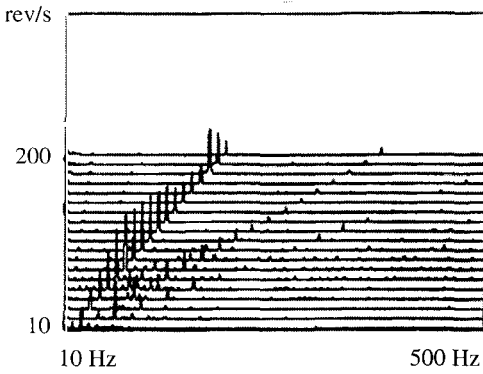


**Figure 7a) Waterfall diagram for 12.5 gramme unbalance (Oil supply pressure 1 Bar)**

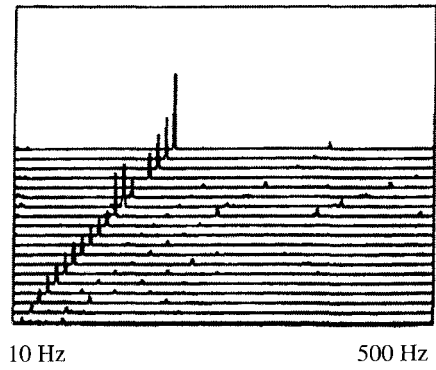


**Figure 7b) Waterfall diagram for 50.0 gramme unbalance (Oil supply pressure 1 Bar)**

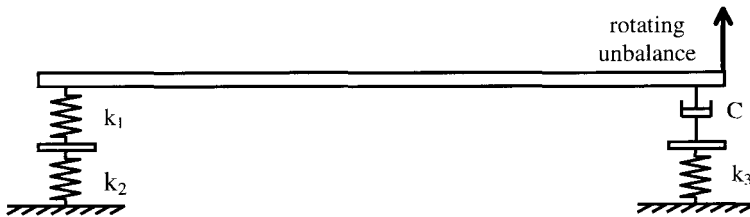


**Figure 8) Schematic diagram of linear model**



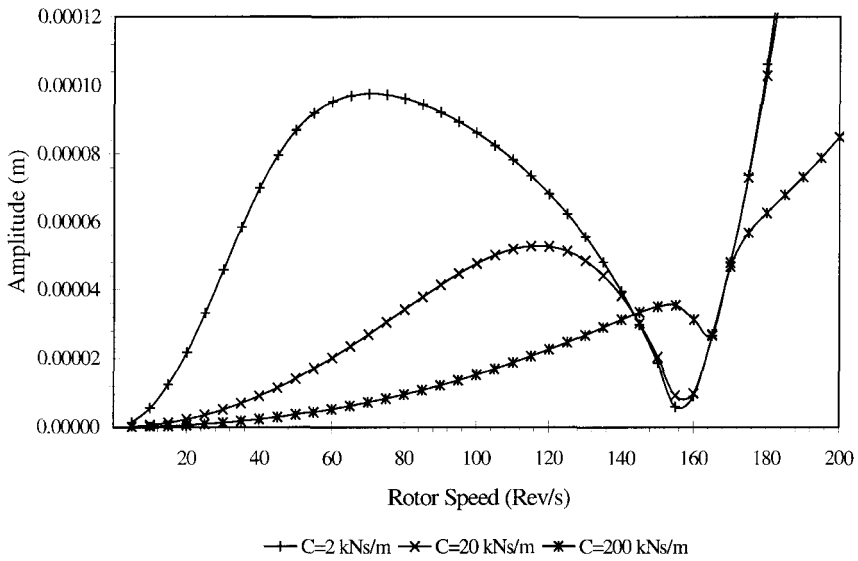


**Figure 9 Theoretical SFD probe response (50 g mass unbalance)**

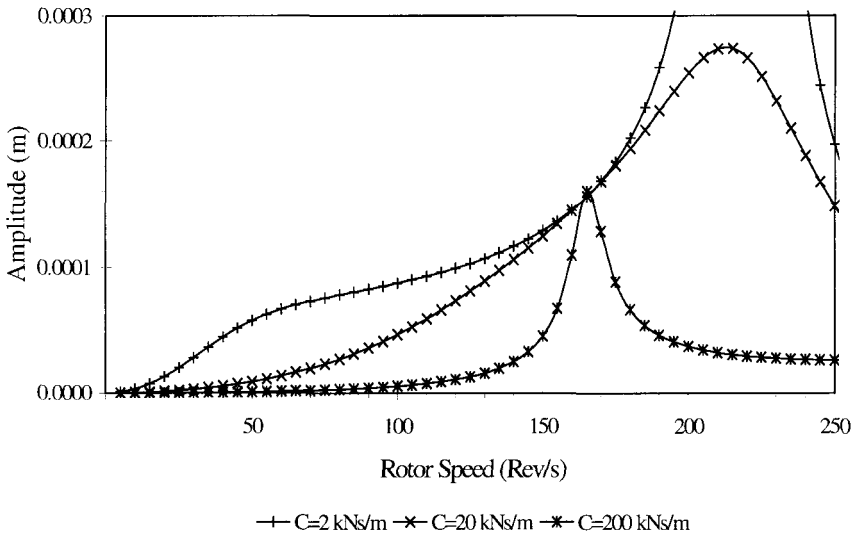


**Figure 10 Theoretical mid rotor probe response (50 g mass unbalance)**

*This page intentionally left blank*

# Condition Monitoring and Cracked Rotors

*This page intentionally left blank*

# Some strategies to achieve robust cepstral analysis

J ANTONI and M EL BADAoui

Laboratoire d'Analyse des Signaux et des Processus Industriels, Roanne, France

## ABSTRACT

Cepstral analysis has long been used to detect repetitive patterns in structural vibration signals. However the technique is very sensitive to small speed fluctuations and to additive noise. In this paper we discuss some strategies to bypass these drawbacks. This is ideally achieved though the use of angular sampling and synchronous averaging. Yet, there are many instances where this strategy is not possible. In such cases, we propose to use a modified cepstrum based on higher order moments of the signal and which is shown to be robust to additive noise. Performance of the robust cepstrum is assessed in detail.

## 1. INTRODUCTION

The effectiveness of cepstral analysis for structural vibrations was demonstrated as early as 1975 by R.B. Randall on gear systems [1]. However, development of the technique has been restrained by two major issues: the high sensitivity of the cepstrum to small speed fluctuations and to additive noise.

We recently showed that the first issue could be efficiently overcome by coupling cepstral analysis with angular sampling [3,4], that is with an acquisition mode that is phase-locked with the angular speed of the system to be analysed. Alternatively, this methodology opened new ways to tackle the second issue, especially through the use of synchronous averaging.

Because of their importance, angular sampling and synchronous averaging are discussed in detail in sections 3 and 4 of this paper. Some useful results for the analysis of gear systems derived in [3,4] are presented herein, as well as some guidelines for their practical implementation in the industrial world.

Section 5 presents an alternative cepstrum analysis to tackle the issue of additive noise, when synchronous averaging is not possible. The proposed strategy, called robust cepstral analysis, is recommended when only one measurement is available. It is based on the observation that strong immunity to noise is achieved by computing the cepstrum on higher order moments instead of the raw signal. The technique is first discussed from the theoretical viewpoint of higher order statistics and its relationship to simple convolution operations on the power density spectrum is then introduced.

Performance of the proposed robust cepstrum is assessed on synthesised signals. Comparisons are made with the power cepstrum and limitations are discussed. Finally, examples are given of applications to real structural vibration signals measured on gearboxes.

## 2. CEPSTRAL ANALYSIS

The power cepstrum is a non-linear operator initially used in the detection of echoes [2] and later introduced in vibration monitoring of rotating machinery [1]. Its mathematical definition is:

$$p(t) = F^{-1} \left\{ \ln |X_T(\nu)| \right\} \quad (1)$$

where  $F^{-1}$  denotes the inverse Fourier transformation and  $X_T(\nu)$  is the Fourier transform of signal  $x(t)$  over duration  $T$ .

The power cepstrum has very interesting properties. Firstly, it is highly sensitive to repetitive patterns such as those generated by local tooth faults in gear systems. Secondly, it transforms a convolution product into an addition and finally only its value for  $t=0$  depends on the original signal amplitude. It can be shown [3] that the power cepstrum of vibration signals from a pinion-gear pair in mesh is made up of two discrete distributions of decreasing positive peaks and whose periods are those of the pinion and the gear respectively. The following properties have been established: (i) the area of the first peak in each distribution is proportional to the square root of the signal energy emitted during one rotational period of the pinion or the gear, (ii) the sum of the first two peaks is constant and depends only on the signal to noise ratio (the noise includes all those contributions which are statistically independent of the meshing process). These properties suggest that tooth defects could be effectively detected in the power cepstrum by analysing the evolutions of the two first peaks which are related to each rotating part.

## 3. ANGULAR SAMPLING

There are two methods for data acquisition. The first one is the temporal acquisition which is the most prevalent. It consists in acquiring the data by using a constant clock period  $T_s$ . This is advantageous in the sense that it is simple to set, but it is not always the best method in the case of rotating machinery analysis. The second method is the angular acquisition with a constant angle sampling  $\theta_s$  which is more suited to our tasks. Angular sampling presents two main benefits :

- (i) Occurrences of cyclic phenomena always take place at the same angular position in the vibration signal. Possible dispersions due to mechanical backlashes can be further reduced by loading the machine with a brake device.
- (ii) The vibration signals are rendered periodic so that Fourier analysis performed on an integer number of rotations is exempted from leakage effects. This allows us to have an optimum frequency resolution.

In practice, the most efficient way to achieve angular sampling is obtained by fastening an incremental optical encoder on the primary shaft. This optical encoder generates an electrical signal which controls the acquisition panel and the anti-aliasing filter with respect to the rotation speed. The advantage of using an optical encoder over other devices such as magnetic pickups is that it can provide a very large number of pulses per revolution, thus avoiding any post-resampling of the signal.

## 4. SYNCHRONOUS AVERAGING

In the previous section, we highlighted the fact that a signal acquired under angular sampling is periodic, with a period  $T_0$  depending on the kinematics of the machine. Synchronous averaging consists in dividing the signal into sections with duration equal to the period  $T_0$  and averaging them. This processing is constructive for any phenomena being synchronous with the machine cycle. On the other hand, any phenomena that are asynchronous are destroyed. It can be shown [8] that synchronous averaging consists of a comb filter in the frequency domain, all harmonics of the basic frequency  $1/T_0$  being set to a unit gain and the other frequencies being set to zero.

## 5. AN ALTERNATIVE ROBUST CEPSTRUM

As mentioned in the introduction, classical cepstral analysis doesn't always give the expected results. The two main reasons are the high sensitivity of the cepstrum to speed variations during acquisition and to extraneous additive noise. It was shown in the previous sections that angular sampling and synchronous averaging are good solutions to alleviate these issues. However, there are some instances when these solutions are not possible. For example it may not be possible to fasten an optical encoder device on the machine. Then there is no alternative than time sampling. Even with angular sampling, there may be cases when the time required to run the full common period of two shafts is so long that only a few periods may be recorded, but not enough for averaging.

In either case, when the synchronous average is not available, it would be useful to have a technique based on cepstrum analysis but which is more robust than the usual approach. In the sequel, we propose to use the spectrum of higher order moments of the signal - specifically of the squared autocorrelation function - instead of the classical power cepstrum to alleviate the issue of additive noise. In order to legitimise this approach, we first introduce it from a theoretical viewpoint and then explain its effectiveness with more empirical considerations.

### 5.1. Integrated Polyspectra

During the last decades, considerable attention has been paid to the use of higher-order statistics in signal processing. Higher-order statistics bring many advantages compared to the second-order case which is restricted to the analysis of the mean and the autocorrelation function of a given signal. In particular, it has been verified that higher-order moments and their Fourier transforms, the higher-order spectra or polyspectra, can gain high immunity from additive noise [5,6]. We will make use of this property in the particular case of repetitive deterministic signals corrupted by additive random noise, such as gear mesh vibration signals. For a stationary real signal, say  $x(t)$ , the third and fourth moments are given by

$$\begin{cases} M_3^x(\tau_1, \tau_2) = E\{x(t)x(t+\tau_1)x(t+\tau_2)\} \\ M_4^x(\tau_1, \tau_2, \tau_3) = E\{x(t)x(t+\tau_1)x(t+\tau_2)x(t+\tau_3)\} \end{cases} \quad (2)$$

The corresponding bispectrum and trispectrum are given by

$$\begin{cases} S_3^x(\nu_1, \nu_2) = F2\{M_3^x(\tau_1, \tau_2)\} = \lim_{T \rightarrow \infty} \frac{1}{T} E\{X_T(\nu_1)X_T(\nu_2)X_T(\nu_1 + \nu_2)^*\} \\ S_4^x(\nu_1, \nu_2, \nu_3) = F3\{M_4^x(\tau_1, \tau_2, \tau_3)\} = \lim_{T \rightarrow \infty} \frac{1}{T} E\{X_T(\nu_1)X_T(\nu_2)X_T(\nu_3)X_T(\nu_1 + \nu_2 + \nu_3)^*\} \end{cases} \quad (3)$$

where  $F2$  and  $F3$  denote the double and the triple Fourier transforms and where  $X_T(\nu)$  is the short-time Fourier transform of signal  $x(t)$  over an interval of length  $T$ . Now, upon changes of variables

$$\begin{cases} \nu_1 = \nu + \alpha/2 \\ \nu_2 = -\nu + \alpha/2 \end{cases} \quad (4.a) \quad \text{and} \quad \begin{cases} \nu_1 = \nu + \alpha/2 \\ \nu_2 = -\nu + \alpha/2 \\ \nu_3 = -\nu - \alpha/2 \end{cases} \quad (4.b)$$

Equations (3) become

$$\begin{cases} S_3^x(\alpha, \nu) = \lim_{T \rightarrow \infty} \frac{1}{T} E\{X_T(\alpha)^* X_T(\nu + \alpha/2)X_T(\nu - \alpha/2)^*\} \\ S_4^x(\alpha, \nu) = \lim_{T \rightarrow \infty} \frac{1}{T} E\{|X_T(\nu - \alpha/2)X_T(\nu + \alpha/2)^*|^2\} \end{cases} \quad (5)$$

Inspection of these formulae shows that the bispectrum measures the interaction between the harmonic  $X_T(\alpha)$  at frequency  $\alpha$  and the couple of harmonics  $X_T(\nu - \alpha/2)X_T(\nu + \alpha/2)^*$  separated by a frequency range  $\alpha$ . Similarly the trispectrum measures the interaction between the harmonic moduli  $|X_T(\nu - \alpha/2)|^2$  and  $|X_T(\nu + \alpha/2)|^2$ . The important point is that for a periodic signal with period  $T$ , the bispectrum and trispectrum are non zero only for  $\{\nu = 2k\pi/T, \alpha = 2l\pi/T, (k, l) \in \mathbb{Z}^2\}$ . A detailed proof can be found in [6]. Figure (1.a) depicts the structure of  $S_3^x(\alpha, \nu)$  for such a signal, which is similar to a two-dimension train of delta functions. This kind of pattern has been named a “bed of nails” in the scientific literature.

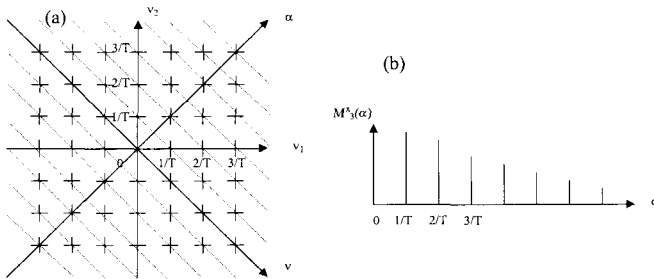


**Figure 1 :** (a) The bispectrum of a periodic signal with period  $T$ . (b) The integrated bispectrum (over  $\nu$ ).

Now if some additive noise was present in the signal, it would be transformed into a constant level background into the bispectrum, and obviously this wouldn't affect the “bed of nails” structure. Furthermore, a natural idea when the estimation of  $E\{. \}$  is poor – or non-existent - would be to integrate out the bispectrum over frequency  $\nu$ , that is along the dashed lines



inclined at 45° clockwise in Figure (1.a). It can be proved that this integration process gives rise to a new spectrum  $M_3^x(\alpha)$  such that

$$M_3^x(\alpha) = \int_{\mathbb{R}} M_2^x(\alpha, \nu) d\nu = F\{R_{x,x}^2(\tau)\} \quad (6)$$

In other words, the integrated bispectrum forms a Fourier pair with the cross-correlation  $R_{x,x}(\tau)$  of the squared signal with itself. Figure (1.b) depicts the typical shape of the integrated bispectrum.

The bispectrum was useful to interpret the steps involved in our approach. However, it may yield difficulties in practice because it has complex values and requires the existence of the harmonic  $X_T(\alpha)$  in the low frequency part of the spectrum, which is a rather restrictive condition. Alternatively, the integrated trispectrum is always real positive and doesn't require the existence of the harmonic  $X_T(\alpha)$ . It can be proved that

$$M_4^x(\alpha) = \int_{\mathbb{R}} M_3^x(\alpha, \nu) d\nu = F\{R_{xx}^2(\tau)\} \quad (7)$$

where  $R_{xx}^2(\tau)$  stands for the squared autocorrelation of the signal. We are now ready to propose a definition for a robust cepstrum, say  $p_R(\tau)$  :

$$p_R(\tau) = F^{-1}\{\ln F\{R_{xx}^2(\tau)\}\} \quad (8)$$

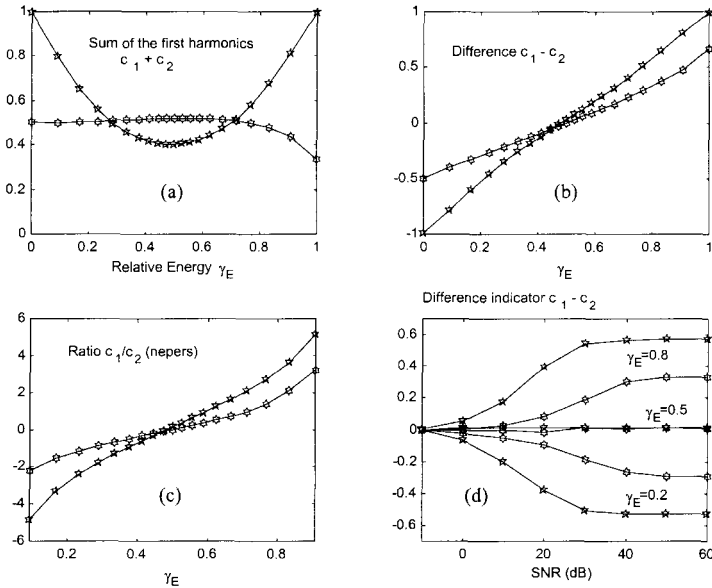
## 5.2. Empirical Interpretation

The theory beyond the robust cepstrum is all right, but it is better understood from simple empirical considerations. Let us consider still the same deterministic signal  $x(t)$  imbedded in random additive noise. A first convolution of the reversed signal with itself yields the autocorrelation function  $R_{xx}(\tau)$ . It is obvious that the convolution product preserves the repetitive structure of the signal – although phase relationships are lost – while achieving a first step to reduce the non-coherent noise. The next operation is to square  $R_{xx}(\tau)$  or, equivalently, to convolve the power spectrum with itself. This again preserves the periodic structure in the power spectrum while achieving a second step in the reduction of non-coherent noise in the frequency domain.

These operations make sense with respect to our objectives. Yet they are highly non-linear and unfortunately fail to reproduce some results given in section 2.

## 5.3. Performance Analysis

In order to compare the performances of the robust cepstrum with those of the classical power cepstrum, we synthesised a simple gearbox vibration signal from two trains of delta functions, each with the periodicity of a wheel. The relative energy (amplitude) of the trains was tuned to simulate the occurrence of a defect on either the first wheel or the second wheel. For example, two trains with equal amplitudes featured a defect-free gearbox. On the other hand, a train substantially higher than the other featured an advanced defect on the related wheel. Details of the modelling can be found in [3]. For each relative energy level denoted by  $\gamma_E$ , the cepstra were computed and the first of the cepstral harmonics – called rharmonics –  $c_1$  and  $c_2$  corresponding to wheels N°1 and N°2 were detected. Figure (2.a) depicts the sum  $c_1 + c_2$  of



the amplitudes of the rhamonics, Figure (2.b) their difference  $c_1 - c_2$  and Figure (2.c) their ratio  $c_1 / c_2$  on a logarithmic scale for various values of  $\gamma_E$ .

**Figure 2 :** Performance analysis of the robust cepstrum (pentagram) compared with the power cepstrum (hexagram).

It was first checked that the property of the power cepstrum to preserve a (almost) constant sum for the first rhamonics was no longer true for the proposed robust cepstrum. Indeed, Figure (2.a) rather showed an evolving sum ranging between 0.4 and 1.0 depending on the value of  $\gamma_E$ . This fact was put on account of the interferences resulting from the non-linear operations involved in the definition of the robust cepstrum. On the other hand, the proposed robust cepstrum shows better performance to detect the occurrence of a defect as can be observed in Figure (2.b) and (2.c). The relative contrast between amplitudes of the cepstral rhamonics was emphasised.

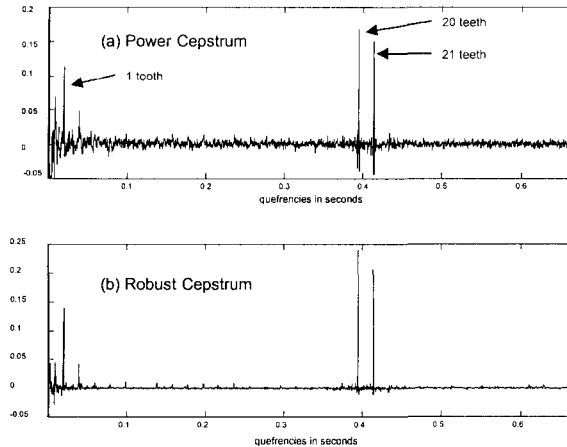
Next we verified this was especially true when some random white (Gaussian) noise was added to the synthesised structural vibration signal.

Figure (2.d) displays the behaviour of the difference indicator  $c_1 - c_2$  for three different values of the relative energy ratio ( $\gamma_E = 0.2$ ,  $\gamma_E = 0.5$ ,  $\gamma_E = 0.8$ ) versus various signal to noise ratios (SNR) in dB. The differential indicator can be used as a threshold to test for a defect on wheel N°1 ( $\gamma_E = 0.2$ ), for no defect ( $\gamma_E = 0.5$ ) or for a defect on wheel N°2 ( $\gamma_E = 0.8$ ). It was computed respectively for the classical power cepstrum and the proposed robust cepstrum. The experiment corroborated the theoretical results found in section 4 and showed evidence of the robustness of the proposed cepstrum. Indeed, the difference indicator for the robust cepstrum was divided by 2 for a SNR of approximately 15 dB compared to 30 dB for the classical power cepstrum.

#### 5.4. Applications to real Data

In order to illustrate the use of the robust cepstrum, we present some results obtained on real structural vibration signals from a two shaft gearbox. The first wheel had 20 teeth, the second

21 and the system was run at 1000 *rpm*. The vibration signal was recorded with an accelerometer and sampled with a frequency of 3 *kHz* during 20 seconds. This enabled us to record little more than 2 common periods of wheels N°1 and N°2. The experiment was a typical case where computing a statistically significant synchronous average was not possible. Therefore we computed the proposed robust cepstrum to reduce the effect of additive noise as well as the classical power cepstrum for comparison. Figure (3) depicts the two cepstra. One can observe that the SNR was quite good so that the two power cepstra showed nice rhamonics at the locations of the two wheel periodicities. But as can be checked for Figure (3.b), the robust cepstrum showed very clear rhamonics and a good overall SNR. When looking carefully at the lower queffrency range, one could distinguish the small rhamonics due to the meshing.



**Figure 3 :** (a) power cepstrum and (b) robust cepstrum for the same vibration signal recorded on a gearbox - 1<sup>st</sup> experiment.

The second experiment also gave evidence of the robustness of the proposed cepstrum against additive extraneous noise. Here again, we were concerned with the analysis of a simple gearbox. The first wheel had 15 teeth and the second 56. The system was run at 700 *rpm* at full load to reproduce an accelerated fatigue test. The vibration signal was recorded with an accelerometer and sampled with a frequency of 6.4 *kHz* during 10 seconds. Use was made of an external tachometer to resample the signal synchronously with the shaft speed. This processing gave access to 8 common synchronous periods of the two wheels, however this was still rather short to reach good statistical significance when computing the synchronous average. Actually, even after averaging, the signal was found to be noisy. Figure (4) displays the two cepstra computed on the vibration signal and its squared autocorrelation function. One can ascertain the decline of the rhamonics due to noise in the power cepstrum and the better clarity in the robust cepstrum which still displays a multitude of peaks, even though some of them, in the lower queffrency range, may be due to interferences.

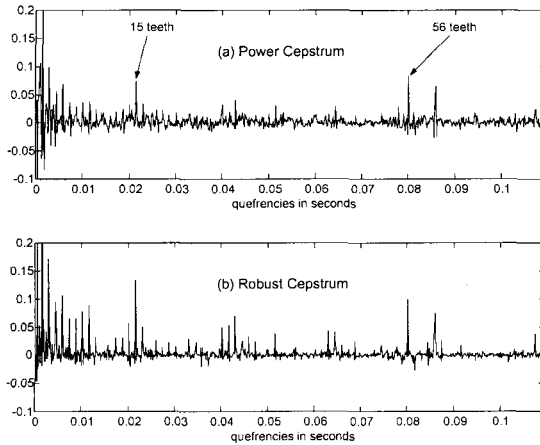


**Figure 4 :** (a) power cepstrum and (b) robust cepstrum for the same vibration signal recorded on a gearbox – 2<sup>nd</sup> experiment.

The same measurements were repeated fifteen times to track the evolution of a defect during the fatigue test. Time history of the normalised differential indicator  $(c_1 - c_2)/(c_1 + c_2)$  [3] is displayed in Figure (5) for both the classical power cepstrum and the proposed robust cepstrum. One can observe the occurrence of a defect on the tenth measurement and its development until the twelve measurement. The indicator computed with the robust cepstrum gave the best sensitivity and reached a critical value of 1 despite the additive noise. These results on real data corroborated the results obtained from simulations in the previous section. Please note that in this case, both the robust cepstrum and the power cepstrum identified the defect on the 10<sup>th</sup> measurement, yet the robust cepstrum showed a greater sensitivity to the evolution of the malfunction.

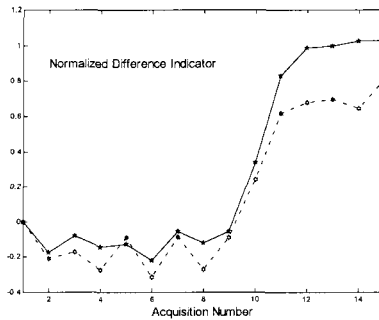


**Figure 5 :** Tracking of a defect with the Normalised Difference Indicator. Dashed line : power cepstrum. Solid line : robust cepstrum.

## 6. CONCLUSION

Important issues in cepstral analysis of structural vibrations are high sensitivity of the power cepstrum to speed fluctuations and additive noise. We discussed angular sampling and synchronous averaging as a very satisfactory solution to render the cepstrum more insensitive. However this methodology requires restrictive preparations which cannot always be met in practice. Therefore we proposed an alternative robust cepstrum which has better immunity to additive noise than the power cepstrum. The definition was first studied from a theoretical point of view and then discussed in terms of simple convolution operations. The effectiveness of the robust cepstrum was checked both on synthesised signals and on real data. In all cases, it showed better clarity than the classical power cepstrum even though it yielded some artefacts due to interferences. Therefore we would recommend to use it jointly with rather than instead of the power cepstrum.

## NOMENCLATURE

$R_{xx}(\tau)$	<i>autocorrelation function of <math>x(t)</math></i>
$X_T(\nu)$	<i>short-time Fourier transform of <math>x(t)</math></i>
$p(t)$	<i>power cepstrum</i>
$p_R(\tau)$	<i>robust cepstrum</i>
$M_3^x(\tau_1, \tau_2)$	<i>third order moment of <math>x(t)</math></i>
$M_4^x(\tau_1, \tau_2, \tau_3)$	<i>fourth order moment of <math>x(t)</math></i>
$S_3^x(\nu_1, \nu_2)$	<i>bispectrum of <math>x(t)</math></i>
$S_4^x(\nu_1, \nu_2, \nu_3)$	<i>trispectrum of <math>x(t)</math></i>
$M_3^x(\alpha)$	<i>integrated bispectrum of <math>x(t)</math></i>
$M_4^x(\alpha)$	<i>integrated trispectrum of <math>x(t)</math></i>

## REFERENCES

- [1] R.B. Randall "Gearbox Fault Diagnosis Using Cepstrum Analysis", *Proc. 5<sup>th</sup> World Congr. Theory of Machines and Mechanisms, I.Mech.E., London*, Vol.1, 1975, pp. 169-174.
- [2] B.P. Bogert, M.J.R. Healy, J.W. Tukey, "The Quefrency Analysis of Time Series of Echoes: Cepstrum, Pseudo-Autocovariance, Cross-Cepstrum and Saphe Cracking", *Proc. Symp. Time Series Analysis*, M. Rosenblat (ed.), New-York, Wiley 1963, pp. 209-243.
- [3] M. El Badaoui "Contribution au Diagnostic Vibratoire des Réducteurs Complexes à Engrenages par l'Analyse Cepstrale", PhD dissertation, Université de Saint-Etienne Jean Monnet, Saint-Etienne, France, 1999.
- [4] M. El Badaoui *et al.* "Monitoring of Complex Gear System by Synchronous Cepstral Analysis", *Traitement du Signal*, Vol.16, N°5, 1999, pp. 371-381.
- [5] C.L. Nikias, M.R. Raghuvveer "Bispectrum Estimation : a Digital Signal Processing Framework", *Proc. IEEE*, Vol.75, N°7, 1987, pp. 869-891.
- [6] J.W.A. Fackrell, P.R. White, J.K. Hammond, R.J. Pimington, A.T. Parsons "The Interpretation of the Bispectra of Vibration Signals – I Theory", *Mechanical Systems and Signal Processing*, Vol.9, N°3, 1995, pp. 257-266.
- [7] J.W.A. Fackrell, P.R. White, J.K. Hammond, R.J. Pimington, A.T. Parsons "The Interpretation of the Bispectra of Vibration Signals – II Experimental Results and Applications", *Mechanical Systems and Signal Processing*, Vol.9, N°3, 1995, pp. 267-274.
- [8] S. Braun "Mechanical Signature Analysis : Theory and Applications", Academic Press, 1986.

*This page intentionally left blank*

# Crack detection in rotating machinery by modal testing

C-W LEE

Department of Mechanical Engineering, KAIST, Taejeon, South Korea

K-S KWON

LG Electronics Inc, Seoul, South Korea

It is shown that the crack development in a rotor can be effectively detected by employing the complex modal testing method. In particular, the reverse directional frequency response function (dFRF) defined between the rotation frequency-modulated input and output of asymmetric rotor is used to accurately identify the stiffness asymmetry due to a crack in a shaft. The reverse dFRF for an asymmetric rotor requires a simple estimation technique, using the vibration signal from a single sensor and the force signal from a single exciter. The magnitude and phase of the estimated reverse dFRF indicate not only the presence and severity but also the circumferential location of a crack.

## 1. INTRODUCTION

Current trends towards high speed, high power and lightweight in rotating machinery design and operation often impose severe stress and environmental conditions upon rotors. High torsional and radial loads, together with a complex pattern of rotor motion, can create severe mechanical stress conditions that may eventually lead to development of a crack in the shaft. The rotor crack is one of the most serious faults in high-speed rotating machinery. Obviously, a cracked rotor must be replaced or repaired to prevent equipment from possible damage. If a crack is detected at an early stage, the rotor may be economically repaired at a relatively low cost and within a short period of time. Therefore the detection of rotor cracks at early stages is critical for safe and efficient operation of rotors.

A lot of effort has been put to find effective methods to detect the development of transverse crack in shafts because of the great danger of such types of faults in rotor systems [1,2,3,4,5,6,7]. In order to diagnose the rotor crack, some special flaw detection techniques, such as those using supersonic waves or infrared rays, have been tried although they are much limited in applications to revolving rotors. On the other hand, the vibration signature analysis technique has drawn much attention in recent years. When a transverse crack occurs on a rotor shaft, the stiffness of the shaft is certain to change which affects the vibration behavior of the

rotor. Through continuous vibration monitoring, the weak crack information may then be extracted from vibration signals. It has been well known that a crack, which may open and close during a revolution of shaft, causes the vibrations with multiple harmonics of higher order [5]. But the main problem of crack detection methods based on using the multiple harmonics is that the same harmonics can be generated in uncracked rotor systems with, for example, non-linearity of supports or misalignment. Furthermore, it is very complicated to recognize the source of additional harmonics. In an attempt to overcome this limitation, additional excitation forces were added to rotors and their responses were measured [6]. On the other hand, model based identification of crack has been tried [7], but it may be difficult to obtain exact mathematical models of many practical rotors. To identify the cracked rotor system, the classical modal testing method has also been attempted for rotors [3]. However, it has some limitations in gaining valuable knowledge of rotor dynamics, because it lacks the important information such as the directivity and asymmetric properties of a rotor system. The complex modal testing, which has been developed particularly for identification of rotating machinery, uses the directional frequency response functions (dFRFs) which account for the directivity as well as the asymmetric properties of the rotor system [8,9,10]. A rotor system with a cracked shaft can be modeled as a stiffness asymmetric rotor that features a time varying stiffness in accordance with the rotor revolution. On the other hand, a stiffness asymmetric rotor can be well identified by the reverse dFRF, which is defined by the modulated input excitation and output response [8,9,10].

This work is to detect a crack in a rotor based on the modal testing method while the rotor system is operating at its running speed. To identify the crack, modal testing method using reverse dFRF is used. Thus, the main objective of the present work is to provide a method for an accurate detection and diagnosis of a cracked rotor without interrupting the operation of the rotating machinery by use of the reverse dFRF. Another objective of the work is to provide a simple measurement and excitation technique, which requires only one vibration sensor and one exciter to estimate the reverse dFRF.

## 2. DIRECTIONAL FREQUENCY RESPONSE FUNCTIONS

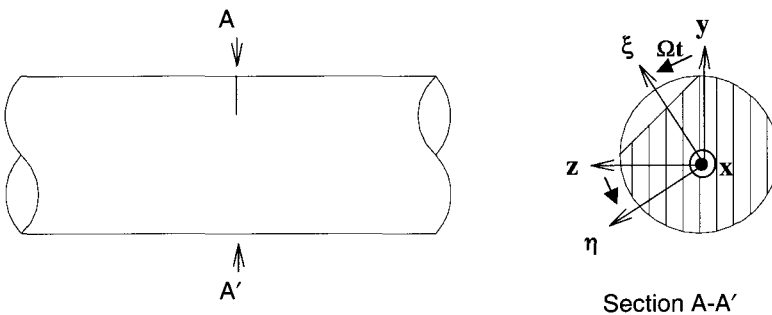


**Figure 1. Partially cut-away sketch of a crack in a shaft of rotor**

The presence of an open transverse crack in a rotating machine causes the bending stiffness of the rotor shaft to vary with its angular position, introducing a stiffness asymmetry. An open cracked rotor can be modeled as an asymmetric rotor system whose equation of motion can be



conveniently written in the complex form, using the stationary co-ordinate system,  $xyz$ , shown in Figure 1, as [8,9,10]

$$\mathbf{M}\dot{\mathbf{p}}(t) + \mathbf{C}\dot{\mathbf{p}}(t) + \mathbf{K}_f \mathbf{p}(t) + \mathbf{K}_r e^{j2\Omega t} \bar{\mathbf{p}}(t) = \mathbf{g}(t) \quad (1)$$

where the  $N \times 1$  complex response and input vectors,  $\mathbf{p}(t)$  and  $\mathbf{g}(t)$ , defined by the real response vectors,  $\mathbf{y}(t)$  and  $\mathbf{z}(t)$ , and the real input vectors,  $\mathbf{f}_y(t)$  and  $\mathbf{f}_z(t)$ , respectively, are

$$\mathbf{p}(t) = \mathbf{y}(t) + j\mathbf{z}(t), \quad \bar{\mathbf{p}}(t) = \mathbf{y}(t) - j\mathbf{z}(t),$$

$$\mathbf{g}(t) = \mathbf{f}_y(t) + j\mathbf{f}_z(t), \quad \bar{\mathbf{g}}(t) = \mathbf{f}_y(t) - j\mathbf{f}_z(t). \quad (2)$$

For simplicity, it is assumed, without loss of generality, that the stationary parts, including the bearings and foundations, have axi-symmetric property. Here  $j$  means the imaginary number;  $\Omega$  is the rotational speed; the bar denotes the complex conjugate;  $\mathbf{M}$ ,  $\mathbf{C}$  and  $\mathbf{K}$  are the  $N \times N$  complex matrices representing the generalized mass, damping and stiffness, respectively; and the subscript  $f$  and  $r$  refer to the symmetric and asymmetric properties, respectively. Note that  $\mathbf{K}_r$  is the  $N \times N$  complex sparse matrix of which norm is a direct measure of crack development. It will prove convenient to rewrite equation (1) with the periodically time-varying stiffness matrix, along with its complex conjugate form, as

$$\begin{bmatrix} \mathbf{M} & \mathbf{0} \\ \mathbf{0} & \bar{\mathbf{M}} \end{bmatrix} \begin{bmatrix} \dot{\mathbf{p}}(t) \\ \dot{\bar{\mathbf{p}}}(t)e^{j2\Omega t} \end{bmatrix} + \begin{bmatrix} \mathbf{C} & \mathbf{0} \\ \mathbf{0} & \bar{\mathbf{C}} \end{bmatrix} \begin{bmatrix} \dot{\mathbf{p}}(t) \\ \dot{\bar{\mathbf{p}}}(t)e^{j2\Omega t} \end{bmatrix} + \begin{bmatrix} \mathbf{K}_f & \mathbf{K}_r \\ \bar{\mathbf{K}}_r & \bar{\mathbf{K}}_f \end{bmatrix} \begin{bmatrix} \mathbf{p}(t) \\ \bar{\mathbf{p}}(t)e^{j2\Omega t} \end{bmatrix} = \begin{bmatrix} \mathbf{g}(t) \\ \bar{\mathbf{g}}(t)e^{j2\Omega t} \end{bmatrix}. \quad (3)$$

Note that the newly defined stiffness matrix now becomes constant, at the expense of modulating the response vector by the frequency of  $2\Omega$ . Taking the Fourier transform of equation (3), we easily obtain

$$\begin{bmatrix} \mathbf{D}_f(j\omega) & \mathbf{D}_r\{j(\omega - 2\Omega)\} \\ \hat{\mathbf{D}}_r(j\omega) & \hat{\mathbf{D}}_f\{j(\omega - 2\Omega)\} \end{bmatrix} \begin{bmatrix} \mathbf{P}(j\omega) \\ \hat{\mathbf{P}}\{j(\omega - 2\Omega)\} \end{bmatrix} = \begin{bmatrix} \mathbf{G}(j\omega) \\ \hat{\mathbf{G}}\{j(\omega - 2\Omega)\} \end{bmatrix}, \quad (4)$$

where  $\mathbf{P}(j\omega)$ ,  $\hat{\mathbf{P}}(j\omega)$ ,  $\mathbf{G}(j\omega)$  and  $\hat{\mathbf{G}}(j\omega)$  are the Fourier transforms of  $\mathbf{p}(t)$ ,  $\bar{\mathbf{p}}(t)$ ,  $\mathbf{g}(t)$  and  $\bar{\mathbf{g}}(t)$ , respectively, and the partitioned dynamic stiffness matrices are given by

$$\begin{aligned} \mathbf{D}_f(j\omega) &= \mathbf{K}_f - \omega^2 \mathbf{M} + j\omega \mathbf{C}, \quad \mathbf{D}_r\{j(\omega - 2\Omega)\} = \mathbf{K}_r, \quad \hat{\mathbf{D}}_r(j\omega) = \bar{\mathbf{K}}_r, \\ \hat{\mathbf{D}}_f\{j(\omega - 2\Omega)\} &= \bar{\mathbf{K}}_f - (\omega - 2\Omega)^2 \bar{\mathbf{M}} + j(\omega - 2\Omega) \bar{\mathbf{C}}. \end{aligned}$$

From equation (4), the two-sided directional frequency response matrices (dFRMs) can be defined in the stationary co-ordinate system as [10]

$$\begin{bmatrix} \mathbf{P}(j\omega) \\ \hat{\mathbf{P}}\{j(\omega - 2\Omega)\} \end{bmatrix} = \begin{bmatrix} \mathbf{H}_{gp}(j\omega) & \mathbf{H}_{\tilde{g}p}(j\omega) \\ \mathbf{H}_{g\tilde{p}}(j\omega) & \mathbf{H}_{\tilde{g}\tilde{p}}(j\omega) \end{bmatrix} \begin{bmatrix} \mathbf{G}(j\omega) \\ \hat{\mathbf{G}}\{j(\omega - 2\Omega)\} \end{bmatrix}, \quad (5)$$

where

$$\begin{aligned} \mathbf{H}_{gp}(j\omega) &= \left[ \mathbf{D}_f(j\omega) - \mathbf{D}_r\{j(\omega - 2\Omega)\} \hat{\mathbf{D}}_f\{j(\omega - 2\Omega)\}^{-1} \hat{\mathbf{D}}_r(j\omega) \right]^{-1}, \\ \mathbf{H}_{\bar{g}p}(j\omega) &= - \left[ \mathbf{D}_f(j\omega) - \mathbf{D}_r\{j(\omega - 2\Omega)\} \hat{\mathbf{D}}_f\{j(\omega - 2\Omega)\}^{-1} \hat{\mathbf{D}}_r(j\omega) \right]^{-1} \\ &\quad \times \mathbf{D}_r\{j(\omega - 2\Omega)\} \hat{\mathbf{D}}_f\{j(\omega - 2\Omega)\}^{-1} \\ \mathbf{H}_{\bar{g}\bar{p}}(j\omega) &= \bar{\mathbf{H}}_{\bar{g}p}\{-j(\omega - 2\Omega)\}, \quad \mathbf{H}_{\bar{g}\bar{p}}(j\omega) = \bar{\mathbf{H}}_{gp}\{-j(\omega - 2\Omega)\}. \end{aligned}$$

Here  $\mathbf{H}_{gp}(j\omega)$  and  $\mathbf{H}_{\bar{g}\bar{p}}(j\omega)$  are referred to as the *normal* dFRMs, whereas  $\mathbf{H}_{\bar{g}p}(j\omega)$  and  $\mathbf{H}_{gp}(j\omega)$  are referred to as the *reverse* dFRMs of asymmetric rotor, and it is assumed, without loss of generality, that all inverse matrices exist. In order to completely define the dFRMs, it is now sufficient to consider two dFRMs, i.e.

$$\mathbf{P}(j\omega) = \begin{bmatrix} \mathbf{H}_{gp}(j\omega) & \mathbf{H}_{\bar{g}p}(j\omega) \end{bmatrix} \begin{bmatrix} \mathbf{G}(j\omega) \\ \tilde{\mathbf{G}}(j\omega) \end{bmatrix}, \quad (6)$$

where  $\tilde{\mathbf{G}}(j\omega) = \hat{\mathbf{G}}\{j(\omega - 2\Omega)\}$  is the Fourier transform of  $\tilde{\mathbf{g}}(t) = \bar{\mathbf{g}}(t)e^{j2\Omega t}$ . It can be easily shown that the reverse dFRF in equation (5) can be approximated, for  $\|\mathbf{K}_r\|^2 \ll \|\hat{\mathbf{D}}_f\{j(\omega - 2\Omega)\}\|$ , as

$$\mathbf{H}_{\bar{g}p}(j\omega) \cong -[\mathbf{D}_f(j\omega)]^{-1} \mathbf{K}_r [\hat{\mathbf{D}}_f\{j(\omega - 2\Omega)\}]^{-1} \quad (7)$$

Note that, for  $\omega$  and  $\Omega$  given,  $\mathbf{H}_{\bar{g}p}(j\omega)$  is proportional to the non-zero complex elements of the sparse matrix  $\mathbf{K}_r$ , which indicates the circumferential location as well as the strength of crack development. It holds naturally that, for isotropic (symmetric, or equivalently, uncracked) rotor systems,  $\mathbf{H}_{\bar{g}p}(j\omega) = \mathbf{H}_{gp}(j\omega) = \mathbf{0}$  [8,9], since  $\mathbf{K}_r = \mathbf{0}$ . For the case when the shaft stiffness of a rotor is changed due to development of a crack in the shaft and so is  $\mathbf{K}_r$ , the magnitude of each reverse (normal) dFRF,  $\mathbf{H}_{\bar{g}p}(j\omega)$  ( $\mathbf{H}_{gp}(j\omega)$ ), reflects the deviated (mean) shaft stiffness, whereas the corresponding phase strongly depends upon the crack opening and location. Therefore, the reverse dFRF is a good diagnostic tool for crack development in a rotor system. In other words, the presence and degree of a crack, and the circumferential location of the crack can be determined from the magnitude and phase of reverse dFRF as in equation (7).

### 3. ONE-EXCITER/ONE-SENSOR METHOD FOR IDENTIFICATION OF CRACKED ROTOR

Using the two-complex input/single-complex output model shown in Figure 2, the input and output spectral relationships for asymmetric rotor have been extensively discussed in [10], developing the two effective estimation methods of dFRFs such as the two-exciter/two-vibration sensor method and the one-exciter/two-vibration sensor method.

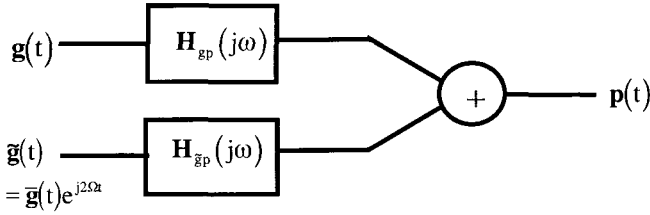


**Figure 2. Two-complex input/single-complex output model for asymmetric rotor**

In this section, estimation of the reverse dFRF using a simpler method requiring only one exciter and one (vibration) sensor is newly discussed. If the rotor response is measured along one direction, say the y-axis, the measured response  $y(t)$  can be expressed in terms of the complex response,  $p(t)$ , and its complex conjugate response  $\bar{p}(t)$  as

$$y(t) = \frac{p(t)}{2} + \frac{\bar{p}(t)}{2}. \quad (8)$$

Taking the Fourier transform of equation (8) and using equation (5), we can obtain

$$\begin{aligned} Y(j\omega) &= \frac{P(j\omega)}{2} + \frac{\hat{P}(j\omega)}{2} \\ &= \frac{H_{gp}(j\omega)}{2}G(j\omega) + \frac{H_{\tilde{g}p}(j\omega)}{2}\tilde{G}(j\omega) + \frac{H_{\hat{g}p}(j\omega)}{2}\hat{G}(j\omega) + \frac{H_{\tilde{\hat{g}}p}(j\omega)}{2}\tilde{\hat{G}}(j\omega), \end{aligned} \quad (9)$$

where  $Y(j\omega)$  is the Fourier transform of  $y(t)$ . In addition to the Fourier transforms,  $G(j\omega)$  and  $\tilde{G}(j\omega)$  of  $g(t)$  and  $\tilde{g}(t) = \bar{g}(t)e^{j2\Omega t}$ , respectively, there also appear  $\hat{G}(j\omega)$  and  $\tilde{\hat{G}}(j\omega)$ , which are the Fourier transforms of  $\hat{g}(t)$  and  $\tilde{\hat{g}}(t) = g(t)e^{-j2\Omega t}$ , respectively. The dFRFs such as  $H_{gp}(j\omega)$  and  $H_{\tilde{g}p}(j\omega)$  appear simply due to lack of the z directional response information in the uni-directional measurement,  $y(t)$ . On the other hand, when only one exciter is used to generate a real excitation force, say  $g(t)=f_y(t)$  or  $g(t)=jf_z(t)$ , then the corresponding complex input  $g(t)$  and its complex conjugate signal  $\bar{g}(t)$  are fully correlated so that it holds

$$\hat{G}(j\omega) = \kappa G(j\omega), \quad (10)$$

where  $\kappa=1$  for  $g(t)=y(t)$ ,  $\kappa=-1$  for  $g(t)=jf_z(t)$ . By substituting equation (10) into equation (9), the relationship between the complex input and output signals, when one sensor and one exciter are available, can be obtained as

$$Y(j\omega) = H'_{gp}(j\omega)G(j\omega) + \frac{H_{\tilde{g}p}(j\omega)}{2}\tilde{G}(j\omega) + \frac{H_{\tilde{\hat{g}}p}(j\omega)}{2}\tilde{\hat{G}}(j\omega), \quad (11)$$

where

$$H'_{gp}(j\omega) = \frac{H_{gp}(j\omega)}{2} + \kappa \frac{H_{\tilde{g}p}(j\omega)}{2}.$$

Unless the complex input signals,  $g(t)$ ,  $\tilde{g}(t)$ , and  $\tilde{\hat{g}}(t)$  are fully coherent, equation (11) becomes

$$\begin{bmatrix} \frac{H'_{gp}(j\omega)}{2} \\ \frac{H_{\tilde{g}p}(j\omega)}{2} \\ \frac{H_{\hat{g}p}(j\omega)}{2} \end{bmatrix} = \begin{bmatrix} S_{gg}(j\omega) & S_{g\tilde{g}}(j\omega) & S_{g\hat{g}}(j\omega) \\ S_{\tilde{g}g}(j\omega) & S_{\tilde{g}\tilde{g}}(j\omega) & S_{\tilde{g}\hat{g}}(j\omega) \\ S_{\hat{g}g}(j\omega) & S_{\hat{g}\tilde{g}}(j\omega) & S_{\hat{g}\hat{g}}(j\omega) \end{bmatrix}^{-1} \begin{bmatrix} S_{gy}(j\omega) \\ S_{\tilde{g}y}(j\omega) \\ S_{\hat{g}y}(j\omega) \end{bmatrix}, \quad (12)$$

where  $S_{ik}(j\omega)$ ,  $i, k = g, \tilde{g}, \hat{g}, y$ , is the spectral density function. Since  $\bar{g}(t)$  is fully correlated to  $g(t)$ , the normal dFRF,  $H_{gp}(j\omega)$ , cannot be separated from the estimated  $H'_{gp}(j\omega)$ . According to the results in [11,12],  $S_{ik}(j\omega)$  become zero, for  $i, k = g, \tilde{g}, \hat{g}$  and  $i \neq k$ , with the increase in the number of averagings. Then, equation (12) reduces to the usual relation for the single-input/single-output model given as

$$H_{\tilde{g}p}(j\omega) = 2 \frac{S_{\tilde{g}y}(j\omega)}{S_{\tilde{g}\tilde{g}}(j\omega)}. \quad (13)$$

From equation (12) or (13), the reverse dFRF of an asymmetric rotor, which is known to be indicative of presence of a crack, can be well identified by a simple technique requiring only a single exciter and a single sensor.

#### 4. NUMERICAL EXAMPLE

In this section, effectiveness of the proposed identification method of the reverse dFRF for an open cracked rotor is demonstrated with a theoretical model: a simple rotor with shaft stiffness asymmetry, whose equation of motion in the stationary co-ordinates is given by [12,13]

$$m\ddot{r}(t) - j\Omega_p \dot{r}(t) + cr(t) - \Delta k e^{j2\theta} e^{j2\Omega t} \bar{r}(t) + kr(t) = g(t) \quad (14)$$

where  $m$ ,  $c$  and  $\Omega_p$  indicate the mass, damping and gyroscopic effect, respectively, and  $k$  and  $\Delta k$  correspond to the mean and deviatoric stiffnesses, the latter indicating the degree of stiffness asymmetry. Here,  $\theta$  represents the circumferential location of the crack from the reference angle. The normal and reverse dFRFs associated with equation (14) can be derived theoretically, from equation (5), as

$$\begin{aligned} H_{gp}(j\omega) &= \frac{\hat{D}_r\{j(\omega - 2\Omega)\}}{\hat{D}_r\{j(\omega - 2\Omega)\}D_r(j\omega) - D_r\{j(\omega - 2\Omega)\}\hat{D}_r(j\omega)}, \\ H_{\tilde{g}p}(j\omega) &= \frac{-D_r\{j(\omega - 2\Omega)\}}{\hat{D}_r\{j(\omega - 2\Omega)\}D_r(j\omega) - D_r\{j(\omega - 2\Omega)\}\hat{D}_r(j\omega)} = D(\omega, \Omega)\Delta k e^{j2\theta}, \end{aligned} \quad (15)$$

where

$$\begin{aligned} D_r(j\omega) &= -\omega^2 m + \omega(jc + \Omega_p) + k, \\ D_r\{j(\omega - 2\Omega)\} &= -\Delta k e^{j2\theta}, \quad \hat{D}_r(j\omega) = -\Delta k e^{-j2\theta}, \\ \hat{D}_r\{j(\omega - 2\Omega)\} &= -(\omega - 2\Omega)^2 m + (\omega - 2\Omega)(jc - \Omega_p) + k \end{aligned}$$

$$D(\omega, \Omega) = \frac{1}{\hat{D}_r \{j(\omega - 2\Omega)\} \hat{D}_r(j\omega) - D_r \{j(\omega - 2\Omega)\} \hat{D}_r(j\omega)}$$

From equation (15), we obtain

$$\left| H_{\hat{r}p}(j\omega) \right| \propto \Delta k, \quad \angle H_{\hat{r}p}(j\omega) = \angle D(\omega, \Omega) + 2\theta$$

implying that the magnitude of the reverse dFRF is directly proportional to the deviated shaft stiffness due to development of an open crack and the corresponding phase is shifted by twice the crack opening angular position. In the simulations, the following numerical values were used:  $m = 4 \text{ kg}$ ,  $c = 50 \text{ N}\cdot\text{s/m}$ ,  $k = 2 \times 10^5 \text{ N/m}$ ,  $\Omega_p = 300 \text{ N}\cdot\text{s/m}$  and  $\Omega = 100 \text{ rad/s} = 15.9 \text{ rps}$ .

To simulate the excitation input force using one exciter,  $g(t) = f_y(t)$ , a sequence of real data  $f_y(t)$  was generated from a Gaussian random process with zero mean. Then the equation of motion was numerically integrated with the time interval of 2.0 ms using the Runge-Kutta integration method to compute the complex response,  $p(t) = y(t) + jz(t)$ . For the unidirectional vibration measurement, only one directional response, say  $y(t)$ , was taken from the calculated complex response to estimate the dFRFs. Throughout the simulations, reverse dFRFs were estimated using equation (12) with 200 ensemble averaging of the 2048-point FFT using the Hanning window and then compared with the theoretical ones given in equation (15).

Figure 3 illustrates the effects of crack growth on the reverse dFRF of the cracked rotor. Figures 3(a1), (b1), (c1) and (d1) are the magnitude plots of the reverse dFRFs when the ratio of the deviation to mean stiffness takes the values of 5, 10, 20, and 30%, respectively. Figures 3(a2), (b2), (c2) and (d2) are the corresponding phase plots for the crack opening angle of 0, 22.5, 45, and 90 degrees from the reference angle. The results confirm that the magnitude of the reverse dFRF increases proportional to the crack growth and the phase is shifted by twice the crack opening angular position.

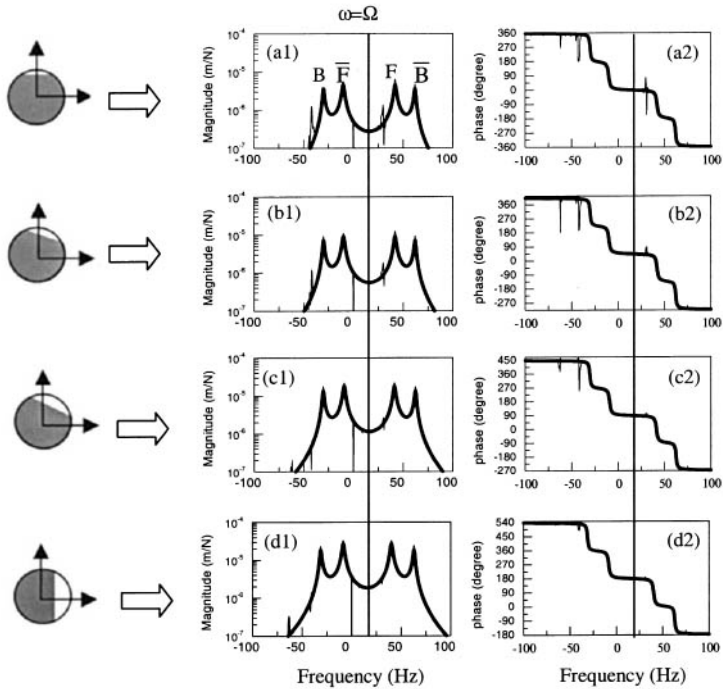


**Figure 3. Magnitudes and phases of reverse dFRFs for cracked rotors**

The resonant peak amplitudes appearing in the magnitude plot of dFRF are normally sensitive to the damping as well as the crack size. Thus it becomes impractical to compare the change in the resonant peak amplitudes for identification of the crack growth. On the other hand, the magnitude of dFRF near the rotation frequency ( $\omega \approx \Omega$ ), which is called the stiffness line, can be well estimated using the almost symmetric property of the reverse dFRF with respect to  $\omega = \Omega$ , although the stiffness line is locally affected by the unbalance response.

Note here that the asymmetric property can be clearly identified in the reverse dFRF: the conjugate modes (marked  $\bar{F}$  and  $\bar{B}$ ) as well as the forward and backward modes (marked  $F$  and  $B$ ) appear in the frequency domain symmetrically with respect to the rotation frequency of  $\Omega/2\pi$  ( $=15.9$ rps), instead of zero frequency for anisotropic rotor systems.

From the simulation of a simple rotor, it can be easily understood that the reverse dFRF can be well estimated by a simple method requiring a single exciter and a single vibration sensor. The reverse dFRF of a cracked rotor represents the crack development and its location. A further study on general flexible rotor models with a crack is in progress. However, it is expected that the knowledge gained from the study of a simple cracked rotor can be easily extended to general rotors without any difficulties, since the cracked rotor model (1) treated in section 2 represents the most general cases.

## 5. CONCLUSIONS

The complex modal testing is proposed for effective crack detection in a rotor. In particular, use of the reverse dFRF is recommended to identify not only the presence and severity but also the circumferential location of a crack in rotors. Although the simulation was limited to a simple analytical cracked rotor model, the technique can be similarly extended to more general cases.

## REFERENCES

- (1) Imam, "Method of On-line detection of incipient cracks in turbine-generator rotors," U.S. Patent, No. 4408298, 1983.
- (2) Shiohata, et al, "Method of and Apparatus for Detecting Crack Conditions," U.S. Patent, No. 4635210, 1987.
- (3) Miller, et al, "Shaft Crack Detection Method," U.S. Patent, No. 4975855, 1990.
- (4) Imam, et al, "System and Method for Detecting the Occurrence, Location and Depth of Cracks in Turbine-generator Rotors," U.S. Patent, No. 5258923, 1993.
- (5) Ehrich, F.F., Handbook of Rotor Dynamics, McGraw-Hill Inc., 1992.
- (6) Iwatsubo, T., Arii, S. and Oks, A., "Detection of a transverse crack in a rotor shaft by adding external force", ImechE conference, C432/093,1992, pp. 275-282.
- (7) Ratan, S., Baruh, H. and Rodriguez, J. "On-line Identification and Location of Rotor Cracks", Journal of Sound and Vibration, Vol. 194, No.1, 1996, pp.67-82
- (8) Joh, C.Y. and Lee, C.W., "Use of dFRFs for Diagnosis of Asymmetric/Anisotropic Properties in Rotor-Bearing System", Transactions of the ASME, Journal of Vibration and Acoustics, Vol. 118, 1996, pp. 64-69.
- (9) Lee, C.W., and Joh, C.Y., "Development of the Use of Directional Frequency Response Functions for Diagnosis of Anisotropy and Asymmetry in Rotating Machinery: Theory," Mechanical Systems and Signal Processing, Vol. 8, No. 6, 1994, pp. 665-678.
- (10) Lee, C.W. and Lee, S.K., "An Efficient Complex Modal Testing Theory for Asymmetric Rotor System : Use of Unidirectional Excitation Method", Journal of Sound and Vibration, Vol. 206, No. 3, 1997, pp. 327-338.
- (11) Bendat, J.S., and Piersol, A.G., *Random Data : Analysis and Measurement Procedures*, John Wiley & Sons, second edition, 1986.
- (12) Lee, C.W., and Kwon, K.S., "Identification of rotating asymmetry in rotating machines by using reverse dFRF," ASME, Design Technical Conference, Las Vegas, NV, September, 1999, DETC99/VIB-8267.
- (13) Lee, C.W., *Vibration Analysis of Rotors*, Kluwer Academic Publishers, 1993.

*This page intentionally left blank*



# Condition Monitoring

*This page intentionally left blank*

# Condition monitoring of rolling element bearings – a comparison of vibration-based techniques for incipient damage detection

**A F KHAN**

Condition Monitoring and Diagnostic Group, Rawalpindi, Pakistan

**E J WILLIAMS** and **C H J FOX**

School of Mechanical, Materials, Manufacturing Engineering, and Management, University of Nottingham, UK

## SYNOPSIS

Rig tests were carried out on seven roller bearings to evaluate a number of vibration-based techniques in an attempt to develop a reliable and effective damage detection method. The choice of frequency band was important and the band containing high frequency structural resonances was found to be most sensitive to incipient damage. The techniques vary in their ability to detect damage, but by using a combination of the information each one provides, an effective detection strategy has been proposed.

## 1 INTRODUCTION

In this era of highly competitive regional and global markets, business managers have more than their share of worries. It is axiomatic, that for industries to thrive and succeed, they must minimise expenditure, a large proportion of which is consumed by machine maintenance costs. Apart from these, machine failures and the resulting production losses are a major detriment to the economic viability of industrial plants. Ultimately, the desire is to ensure that the plant operates smoothly and gives an optimum level of productivity. Hence, it is imperative that industries now adhere to novel, innovative and revolutionary methods of plant maintenance. The primitive methods of periodic overhaul, or the highly inefficient breakdown-servicing philosophy, must be relegated to engineering history. In today's world of precision tools, high-tech software and diagnostic equipment, condition monitoring of plant machines is the most efficient, cost effective and reliable method of plant maintenance. Condition monitoring leading to predictive maintenance allows maintenance activities to be planned in advance and undertaken only when necessary. Catastrophic failures and production losses are virtually eliminated.

A large proportion of rotating industrial machinery uses rolling element bearings. These seldom fail due to simple fatigue, but due to defects such as imbalance, misalignment, bent shafts, mechanical looseness, oil contamination and poor lubrication. The end result is the growth of defects on either the raceways or the rolling elements. If not properly monitored and repaired in time, this can lead to major breakdowns.

Vibration-based condition monitoring techniques can provide an effective means of detecting defects in rolling element bearings. An undamaged bearing typically generates broadband random vibration, which changes in amplitude and/or shape with the initiation of damage. The peak and root-mean-square (RMS) of the vibration signal quantify changes in its level, while crest factor and kurtosis (see section 3.2) give information on the changing shape. These single-number parameters have been used previously for detecting damage [1,2,3], but with variable success.

The determination of the location of damage is important, particularly if there are several bearings in close proximity. Under some circumstances, this can be done by observing the time waveform and recovering approximate recurrence timings [4]. However, this technique is of little use when the signals are complex or exhibit poor signal-to-noise ratio. Spectral analysis may be an answer in the case of a complex vibration signal [4], but there are problems in the direct comparison of the spectra when small speed fluctuations are present [5]. Techniques vary in their ability to detect incipient damage under different situations and it may be concluded that it would be unwise to rely solely on one technique. The purpose of the present study is, therefore, to explore the individual capabilities of these techniques and, in particular, the possibility of using them in combination.

## 2 EQUIPMENT AND TEST CONDITIONS

The test rig (Fig.1) consisted of a shaft, located radially and axially in a housing by two support bearings and driven at one end by a variable-speed DC motor via a toothed belt drive. The roller bearings tested (Type NU 204) were mounted at the other end of the shaft and carried a constant radial load, applied by a loading arm and dead weights (not shown). An oil mist system provided lubrication to all three bearings. Vibration measurements were made using a piezoelectric accelerometer (Endevco Type 213E) attached to the bearing housing. A charge amplifier (B&K Type2635) conditioned the signal and a combination of high and low-pass filters (Fern Developments EF5-02 & EF5-01) was used to select different analysis bandwidths. Subsequent signal processing and storage was carried out on a Hewlett Packard HP5451C Fourier analyzer.

The test bearings were run at 6000 rev/min, with a radial load of 4590 N. The combination was within the design envelope, but chosen at the high end of the permitted range in order to accelerate the rate of the damage. It gave an  $L_{10}$  life of 157 hours. This is the period within which 10% of a large group of nominally identical bearings would be expected to fail. The bearings were run for at least four hours before beginning observations. Normally, the data was captured twice in a day (one-twelfth of the  $L_{10}$ ), although more frequent measurements were made if changes in the bearing behaviour warranted it.

For fault detection and diagnosis purposes, the acceleration signal was processed to give the peak, RMS, crest factor, kurtosis and spectrum by averaging forty 2048-sample data blocks for a range of passbands up to 40 kHz. The 0-1.25 kHz band was chosen to analyse the velocity

level and the 0-5 kHz band was selected to highlight lower-order defect-related harmonics. Preliminary spectral mapping prior to the appearance of damage indicated that there were a number of structural resonances between 7 kHz to 25 kHz (Fig. 2), but that there was very little of significance below 7 kHz. Two passbands (5-12.5 kHz and 12.5-25 kHz) were chosen to highlight any changes occurring at the structural resonances and the 27-35 kHz frequency band detected changes in the response associated with the transducer resonant frequency (32 kHz). The techniques developed are described more fully in reference 6.

### 3 RESULTS AND DISCUSSION

The results from the 12.5–25 kHz frequency band are not discussed, since they were similar to those for the 5-12.5 kHz band and the latter provided better frequency resolution without the need for zoom processing. Also, limiting the maximum frequency to 12.5 kHz doubles the sampling period and accommodates more shaft cycles per sample period, which was advantageous when looking for amplitude modulation effects. Finally, the RMS velocity was measured in the 60-1250 Hz frequency band instead of 0-1250 Hz to prevent vibration of the loading arm from influencing the overall level [6].

#### 3.1 Undamaged Bearing

Several roller bearings were tested and produced instances of damage on each of the three main elements; the raceways and the rollers. As a baseline for comparison, Fig 3 shows the time waveform (5-12.5 kHz) along with the corresponding spectrum for a typical undamaged bearing. The time waveform reveals a constant noise level, occasionally disrupted by random bursts of energy such as those caused by *micro-slip* or *small wear particles in the oil*. The spectrum has broadband characteristics with no identifiable pattern to the individual peaks.

#### 3.2 Incipient Damage

The level and “shape” of the vibration signal changes with the initiation of damage in a way that depends on the nature and location (inner or outer raceway, or roller) of the damage. Figures 4, 5 and 6 show time waveforms and the corresponding spectra for incipient damage at each of the three locations. The changes in the signal can be characterised as follows.

As an inner race defect comes into contact with the rollers, it generates impulsive transients recurring at a frequency  $f_i$  (Fig. 4a). The waveform exhibits amplitude modulation at the shaft frequency,  $f_s$ , as the defect moves in and out of the loaded region. In the frequency domain (Fig. 4b), this produces spectral lines at harmonic multiples,  $mf_i$ , along with sidebands at  $\pm nf_s$  due to the amplitude modulation (where  $m$  and  $n$  are integers).

The time waveform due to a defective roller (Fig. 5a) is characterised by transients at a frequency,  $f_b$ . This is double the roller’s spin frequency, since the defect strikes both inner and outer races each revolution. The signal is also amplitude modulated as the defective roller rotates through the loaded region at the cage frequency,  $f_c$ . In the frequency domain (Fig. 5b), this produces spectral lines at frequency  $mf_b$ , accompanied by the side bands at frequency  $\pm nf_c$ , due to the amplitude modulation.

A defective outer race (Fig. 6a) exhibits a time waveform signal with regular impact transients occurring at frequency,  $f_o$ , corresponding to the roller-passing frequency. This generates spectral lines at frequencies  $mf_o$  in the frequency domain (Fig.6b).

The change in the level of the vibration signal can be quantified by measuring the overall level across a broad band of frequencies or in narrow bands from dc upwards. In both cases, this can be done either by recording the highest peak value, or by computing the RMS value. The changing shape of the signal can be quantified by calculating the dimensionless parameters crest factor and kurtosis. Crest factor is the ratio of peak to RMS levels of a signal, while the kurtosis value for a waveform  $x(t)$  of length  $T$  seconds is given by:

$$\text{Kurtosis, } k = \frac{\frac{1}{T} \int_0^T x^4(t) dt}{\text{RMS}^4}$$

### 3.3 Single Number Parameters

Table 1 shows the variation in the single-number parameters peak, RMS, crest factor and kurtosis for a number of test bearings at different stages of the endurance test. The levels are normalized with respect to the undamaged level and are thus presented as gains (the undamaged levels are also quoted for completeness). The incipient damage condition was defined by the appearance of a noticeable change in the level and/or shape of the signal (see figures 4a, 5a and 6a). The pre-damage *I* and *II* represent the two observations prior to detection of incipient damage and for which neither the time waveform nor the spectrum (not shown) had shown a significant change in shape.

The peak and RMS values in the structural frequency band (5-12.5 kHz) registered a statistically significant rise, corresponding to a gain of 1.5, at the incipient damage stage in all the bearing cases, except bearing 24. In this bearing, the gain was lower.

The RMS acceleration in the transducer resonance frequency band (27-35 kHz) showed obvious rises in the case of bearings 20, 22 and 24. The main advantage of using this band is its pre-defined location. However, the results are not consistent with other bearings.

The RMS velocity in the 60-1250 Hz frequency band only registered a significant increase for bearings 23 and 24, as shown in Figs. 7a & 7b. However, it was later discovered that the high values were due to a loose test-bearing seat rather than to a defective bearing. When the bearing was refitted, the RMS velocity settled back to its normal level again. This suggests that measuring the velocity level is very effective for tracking down shaft-related problems. Crest factor and kurtosis did not change sufficiently to provide a clear indication of incipient damage in almost all the bearing cases.

Although the level rises in the structural resonance band gave a consistent indication for detecting incipient damage, they should not be used alone as conclusive evidence of the presence of damage. They can, however, be used as a preliminary tool to monitor general bearing condition and can be obtained with minimum effort and complexity. Following a certain level rise, which can be set by experience, a more complex analysis can be performed utilizing the diagnostic capabilities of time waveform pattern and spectral analyses.

The question of whether the peak or RMS value is better suited to detecting incipient damage depends on the site of the damage. This work has found that the peak level rises more for signals exhibiting amplitude modulation, as in case of defective inner races and rolling elements (bearings 20, 24, 23 and 25). On the other hand, the reverse is true for signals containing more impact transients, such as for defective outer races (bearings 21 and 22). They are, therefore, both important for the detection of incipient damage.

### 3.4 Diagnostic Parameters

As discussed above, an initial indication of damage can be obtained from the level measurements in the structural and the transducer resonance frequency bands. Detection, however, must be complemented by diagnostic techniques such as time waveform pattern and spectral analyses to confirm the presence of damage. Time waveform pattern analysis was found very suitable for detecting amplitude modulation in cases of defective rollers or inner races (Figs. 4a & 5a), while the spectra exhibited a complex picture due to the amplitude modulation (Figs 4b & 5b). Individual transients due to the impact of the rolling elements on an outer race defect were not clearly discernible in the time domain (Fig. 6a), although the spectrum (Fig. 6b) displayed easily distinguishable frequency lines. Therefore, both time waveform pattern and spectral analyses are vital, depending on the site of the damage.

Care must be exercised in interpreting the time waveforms and the spectra. In one case (bearing 25), frequency lines characteristic of an outer race defect appeared after 91 hours (frequency band 5-12.5 kHz, Fig. 8a). The gains in the peak and RMS levels (1.51 and 1.64 respectively) also indicated possible damage. However, the outer race impact transients were not discernible in the time waveform (not shown) and the bearing was allowed to run further without inspection. The bearing eventually failed after 974 hours due to a roller defect that was detected at 916 hours with the help of amplitude modulation in the time waveform of 5-12.5 kHz (Fig.8b). When the bearing was examined for evidence of outer race damage, only minor signs of debris denting were noticed on the load side. Thus, although the level measurement and the spectral analysis were sufficiently sensitive to detect a minor defect in the bearing, they provided misleading information about its overall state. The information from the time waveform pattern analysis was vital in this case for demonstrating that the outer race was not spalled.

## 4 CONCLUDING COMMENTS

There are many techniques that can be used to detect and diagnose incipient damage in rolling element bearings. However, experience gained by testing roller bearings in an endurance test rig suggests that it would be unwise to rely exclusively on any one technique to detect bearing damage. Pass band level measurement at the structural resonance frequency band is a good indicator for detecting incipient damage and can be used for preliminary investigations. Once it shows a prescribed increase in level, it must be complemented by time waveform pattern and spectral analyses to confirm the presence of damage and identify its location. Velocity level measurement complemented by spectral analysis proved very helpful in detecting shaft-related problems. Industrial experience has revealed that most premature bearing failures can be prevented if imbalance, bent shafts or misalignment are corrected in time. By using the combined evidence of the different techniques, confidence in incipient damage detection can be improved.

## 5 REFERENCES

1. Hampson, L.G. *Diagnostic Checks for Rolling Bearings*. Proceedings of Seminar on Rolling Element Bearings, IMechE, London, 1983, 17-22.

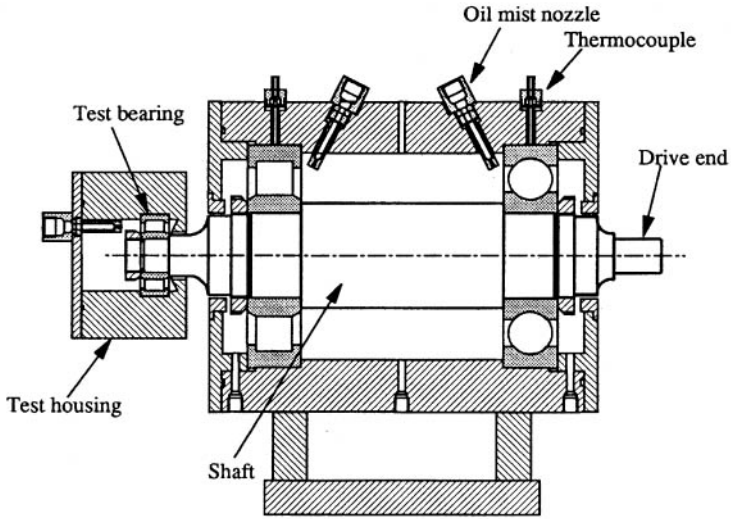
2. Henry, T. *Advances in Monitoring Bearings*, Conference on Bearings: Searching for Longer Life, Chartered Mechanical Engineering, 1984, 54-60.
3. Alfredson, R.J. *Time Domain Methods for Monitoring the Condition of Rolling Element Bearings*” Mechanical Engineering Transactions, 1985, 102-107
4. Igarashi, T. *Studies of the Vibration and Sound of Defective Rolling Bearings*, Bulletin of JSME, 1982, Vol. 25, No. 204, 994-1001.
5. Randall, R.B. *Effective Machine Monitoring Using A Calculator-Based System*, First Conference on Condition Monitoring in the Process Industries, Manchester, 1979, 3.1-3.9
6. Khan, A.F. *Condition Monitoring of Rolling Element Bearings-A Comparative Study of Vibration Based Techniques*, Ph.D. Thesis, 1991, University of Nottingham.

© 2000, With Author



Bearing & Damage site	Single-Number Parameter	Undamaged Level	Gain		
			Pre-damage II	Pre-damage I	Incipient Damage Detected
Data collected at ⇒			<b>45.5 Hrs</b>	<b>54 Hrs</b>	<b>70 Hrs</b>
#20 Inner Race	peak (5-12.5 kHz)	7.35 ±0.48 m/s <sup>2</sup>	1.29 ±0.09	1.25 ±0.09	2.9 ±0.2
	RMS (5-12.5 kHz)	1.53 ±0.03 m/s <sup>2</sup>	1.47 ±0.04	1.43 ±0.03	2.3 ±0.06
	RMS (60-1250 kHz)	1.98 mm/s	1.11	1.14	1.21
	RMS (27-35 kHz)	10.76 m/s <sup>2</sup>	3.1	1.58	3.2
	c.f. (5-12.5 kHz)	4.8 ±0.29	0.88 ±0.04	0.87 ±0.04	1.26 ±0.06
	k (5-12.5 kHz)	4.2 ±0.47	0.85 ±0.02	0.83 ±0.07	1.52 ±0.09
Data collected at ⇒			<b>43.5 Hrs</b>	<b>54 Hrs</b>	<b>68 Hrs</b>
#21 Outer Race	peak (5-12.5 kHz)	10.2 ±0.19 m/s <sup>2</sup>	1.54 ±0.06	1.63 ±0.06	1.66 ±0.06
	RMS (5-12.5 kHz)	2.7 ±0.03 m/s <sup>2</sup>	1.42 ±0.03	1.56 ±0.03	1.71 ±0.03
	RMS (27-35 kHz)	14.84 m/s <sup>2</sup>	1.13	1.19	1.23
	c.f.(5-12.5 kHz)	3.77 ±0.07	1.08 ±0.05	1.04 ±0.04	.97 ±0.04
	k(5-12.5 kHz)	3.36 ±0.06	1.02 ±0.03	1.0 ±0.03	.94 ±0.02
	Data collected at ⇒			<b>35 Hrs</b>	<b>50 Hrs</b>
#22 Outer Race	peak (5-12.5 kHz)	6.9 ±0.23 m/s <sup>2</sup>	1.15 ±0.05	1.4 ±0.06	1.44 ±0.07
	RMS (5-12.5 kHz)	1.6 ±0.02 m/s <sup>2</sup>	1.18 ±0.03	1.51 ±0.03	1.57 ±0.03
	RMS (60-1250kHz)	3.0 mm/s	0.97	0.95	0.93
	RMS (27-35 kHz)	7.0 m/s <sup>2</sup>	1.32	1.76	1.74
	c.f. (5-12.5 kHz)	4.32 ±0.14	0.97 ±0.04	0.93 ±0.04	0.92 ±0.04
	k (5-12.5 kHz)	3.82 ±0.09	0.97 ±0.03	0.88 ±0.02	0.87 ±0.03
Data collected at ⇒			<b>50 Hrs</b>	<b>61 Hrs</b>	<b>74.5 Hrs</b>
#23 Roller	peak (5-12.5 kHz)	10.0 ±0.34 m/s <sup>2</sup>	1.34 ±0.06	1.35 ±0.06	1.66 ±0.08
	RMS (5-12.5 kHz)	2.54 ±0.03 m/s <sup>2</sup>	1.28 ±0.02	1.31 ±0.02	1.478 ±0.03
	RMS (60-1250 kHz)	2.4 mm/s	1.26	1.46	1.57
	RMS (27-35 kHz)	12.2 m/s <sup>2</sup>	1.2	1.2	1.27
	c.f.(5-12.5 kHz)	3.9 ±0.12	1.05 ±0.04	1.03 ±0.04	1.12 ±0.05
	k (5-12.5 kHz)	3.4 ±0.07	1.05 ±0.02	1.03 ±0.02	1.16 ±0.04
Data collected at ⇒			<b>70.5 Hrs</b>	<b>77 Hrs</b>	<b>91 Hrs</b>
#24 inner race	peak (5-12.5 kHz)	7.04 ±0.27 m/s <sup>2</sup>	0.91 ±0.05	0.96 ±0.05	1.31 ±0.08
	RMS (5-12.5 kHz)	1.71 ±0.02 m/s <sup>2</sup>	0.94 ±0.02	0.97 ±0.02	1.16 ±0.02
	RMS (60-1250 kHz)	3.3 mm/s	1.2	1.3	1.5
	RMS (27-35 kHz)	1.3 m/s <sup>2</sup>	1.42	1.6	3.3
	c.f. (5-12.5 kHz)	3.7 ±0.15	0.99 ±0.05	0.95 ±0.04	0.92 ±0.04
	k (5-12.5 kHz)	3.2 ±0.13	0.99 ±0.05	0.97 ±0.04	0.96 ±0.04
Data collected at ⇒			<b>868 Hrs</b>	<b>892 Hrs</b>	<b>916 Hrs</b>
#25 Roller	peak (5-12.5 kHz)	6.64 ±0.28 m/s <sup>2</sup>	2.31 ±0.05	2.66 ±0.05	6.26 ±0.02
	RMS (5-12.5 kHz)	1.56 ±0.03 m/s <sup>2</sup>	2.62 ±0.03	2.75 ±0.03	5.38 ±0.06
	c.f. (5-12.5 kHz)	4.25 ±0.16	0.88 ±0.03	0.97 ±0.05	1.15 ±0.07
	k (5-12.5 kHz)	3.6 ±0.1	0.89 ±0.03	0.95 ±0.03	1.23 ±0.07

Table 1: Changes in Single-number Parameters at Different Stages of Damage



Note: Load direction on the test bearing is applied perpendicular to the plain of the diagram

Figure 1 Test Rig

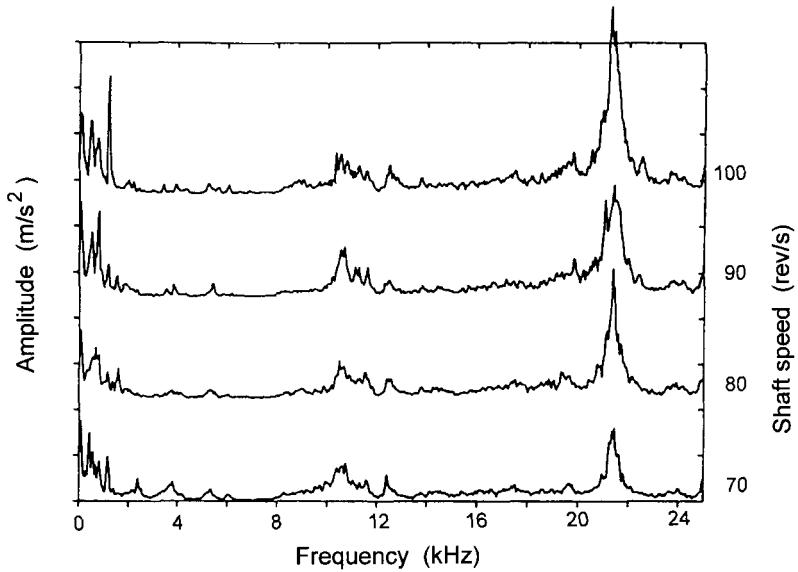


Figure 2 Spectral Plot at Four Shaft Speeds at a Load of 4590 N

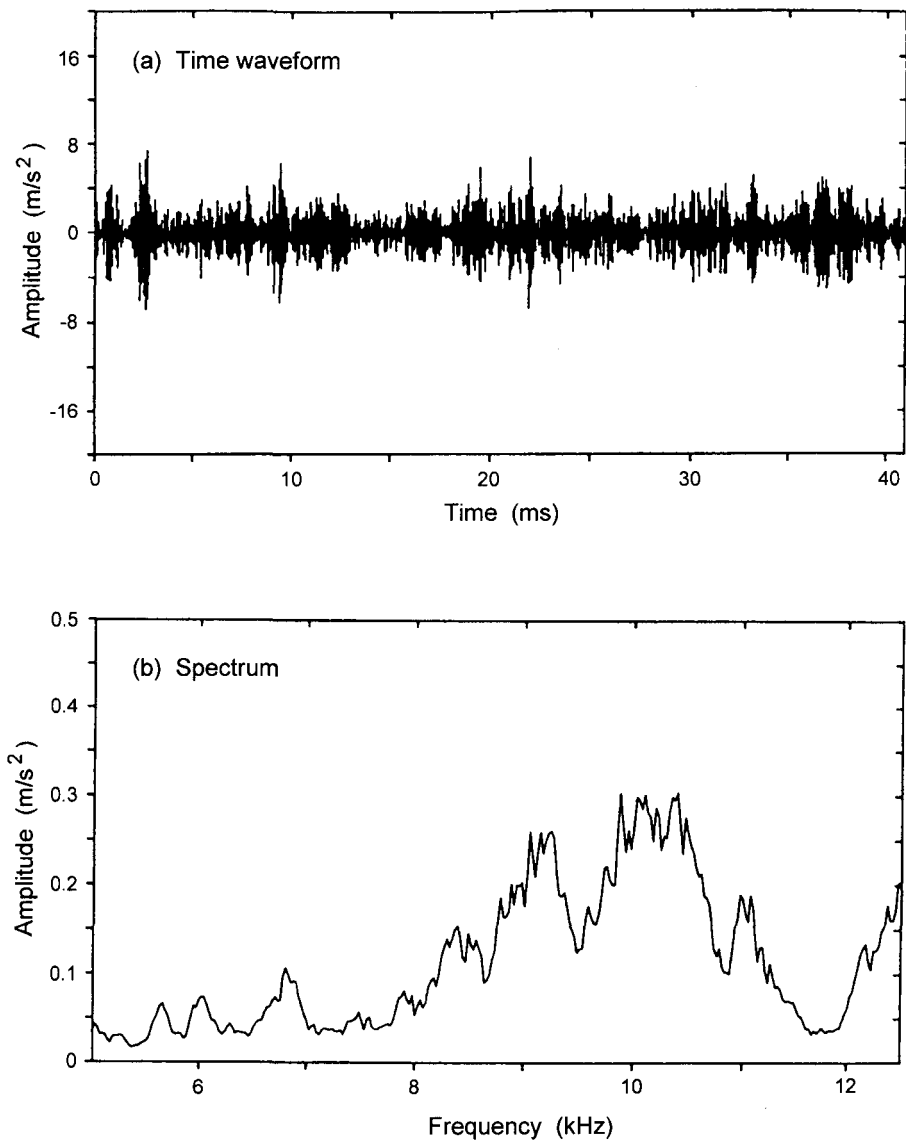


Figure 3 Measurements from an Undamaged Bearing (5 - 12.5 kHz)

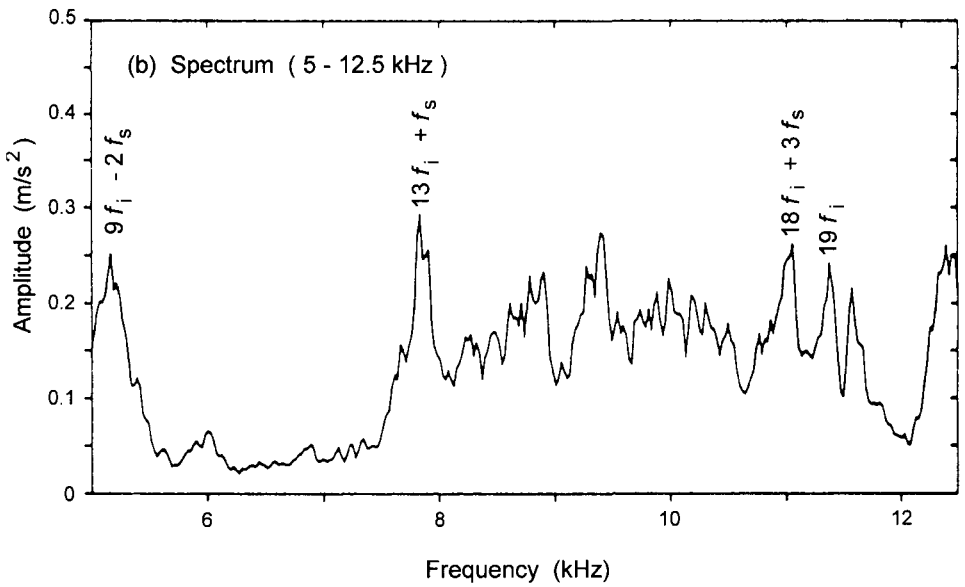
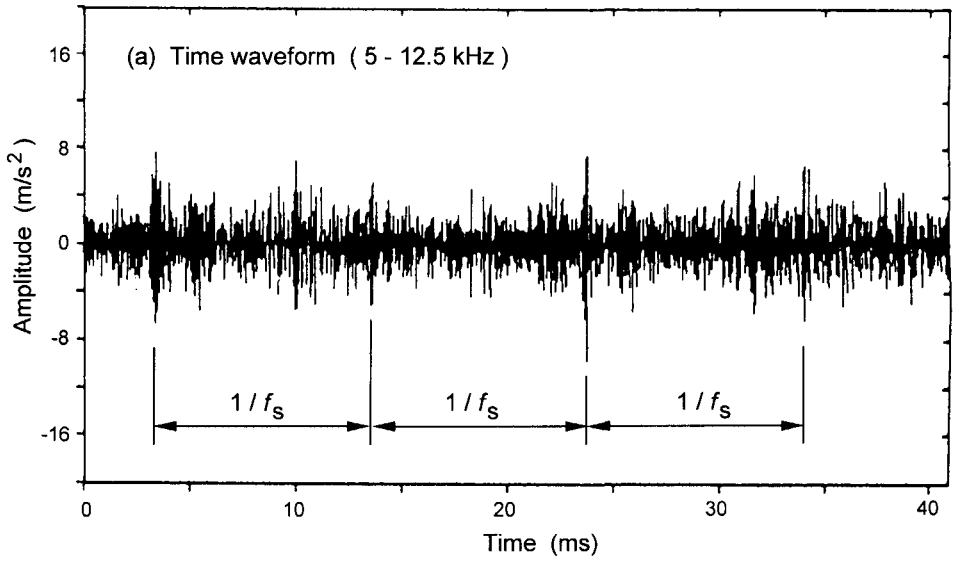


Figure 4 Inner Race Damage after 91 hours (Bearing 24)

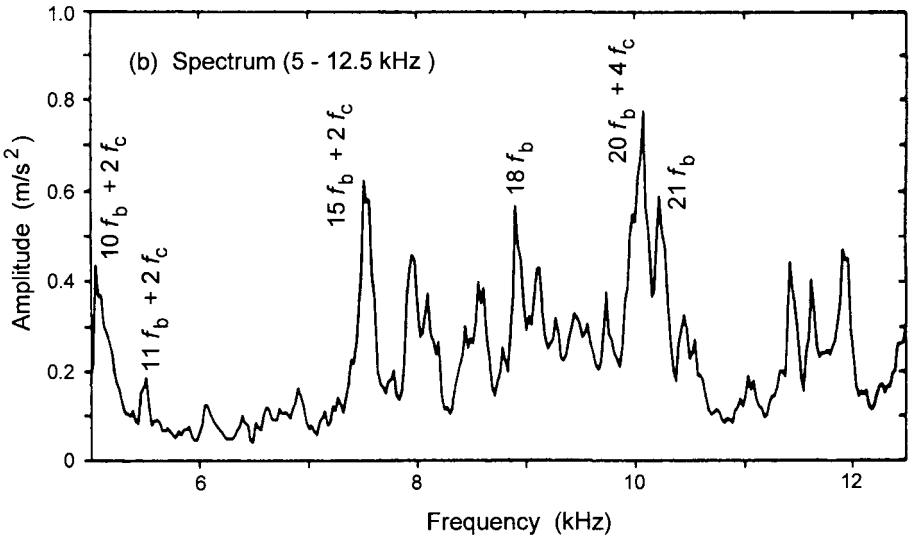
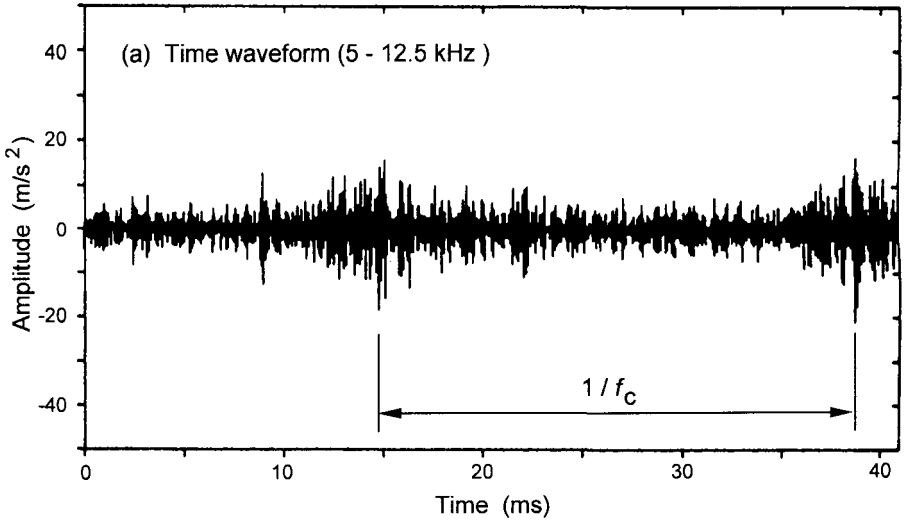


Figure 5 Roller Damage after 74.5 hours (Bearing 23)

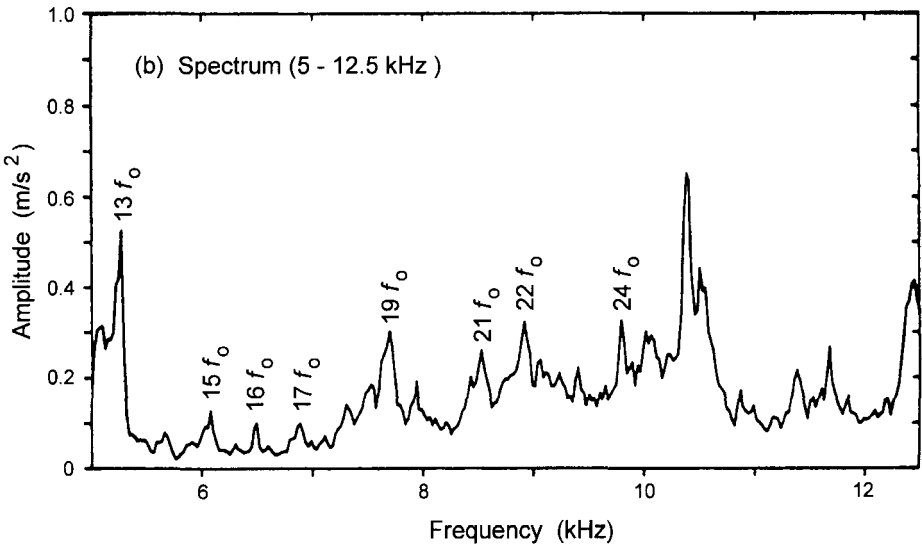
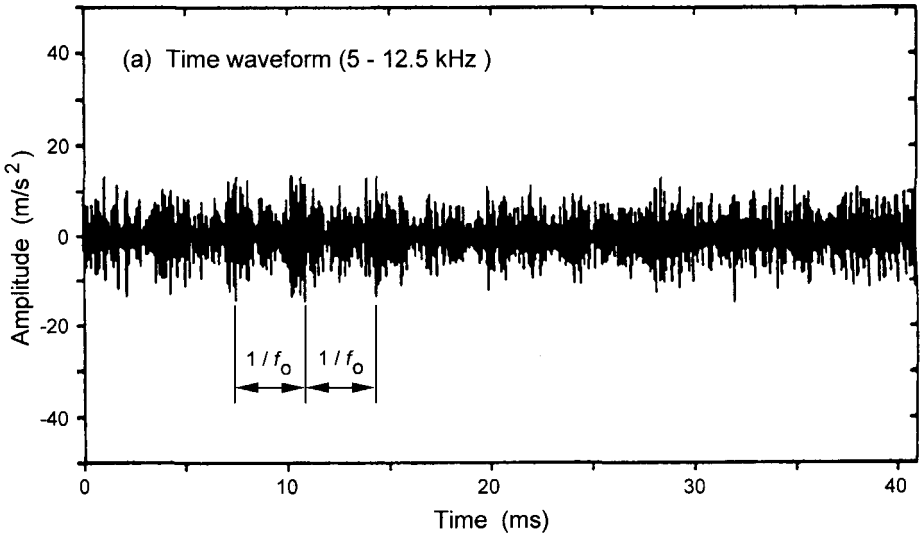


Figure 6 Outer Race Damage after 57 hours (Bearing 22)

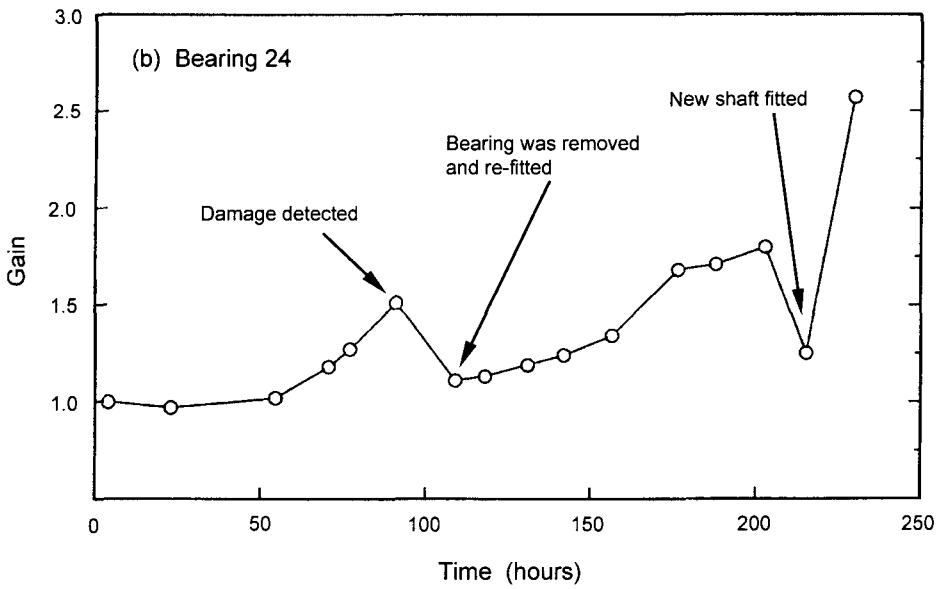
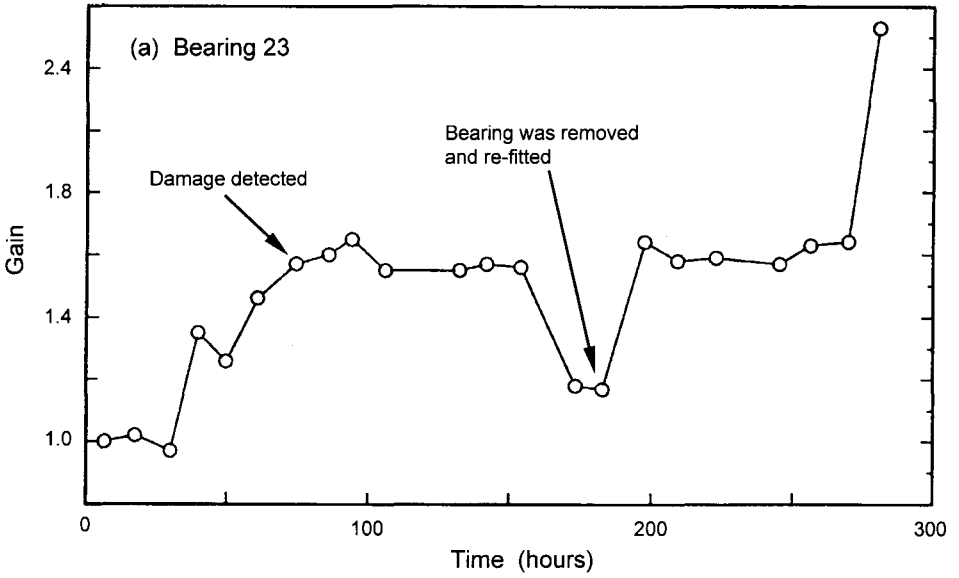


Figure 7 Gain in RMS Velocity Level ( 60 – 1250 Hz )

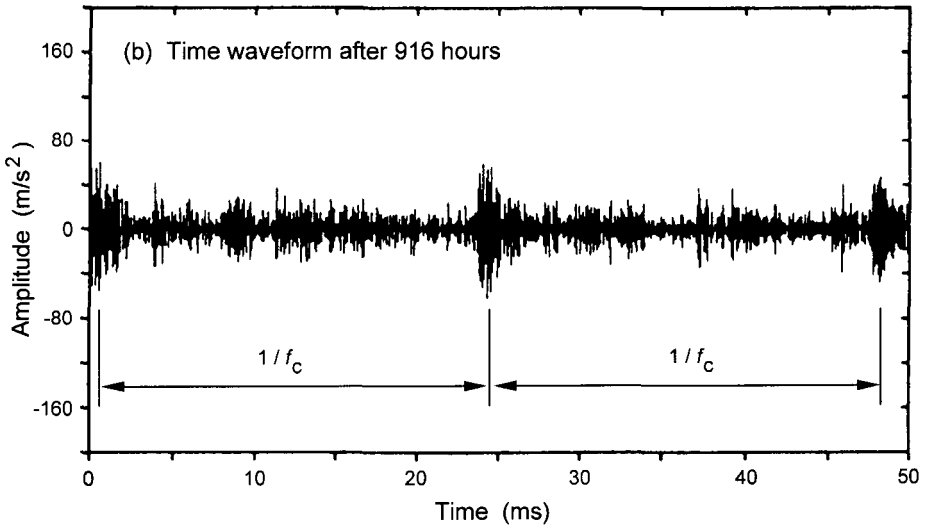
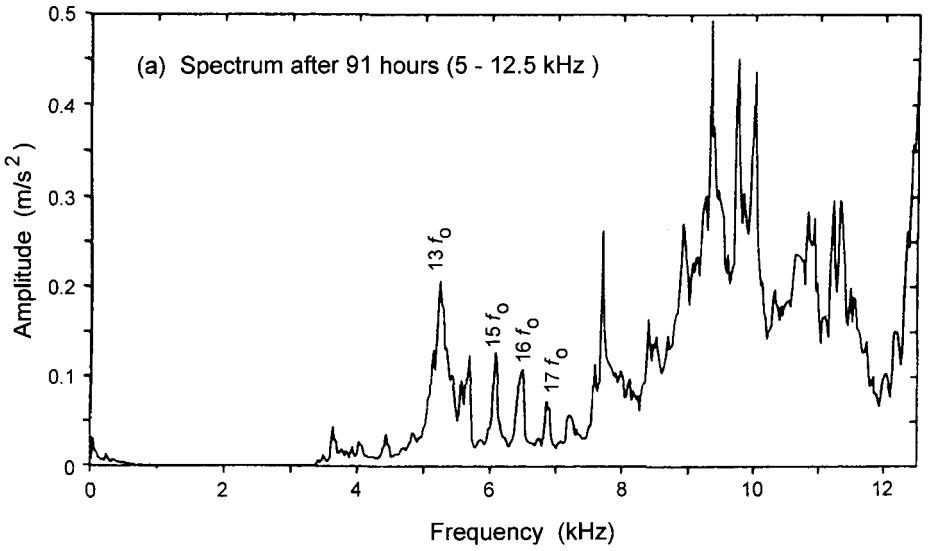


Figure 8 Bearing 25 (5 - 12.5 kHz)



## **Diagnostic study of simulated faults on gears and bearings**

**C BRENEUR, J MAHFOUDH, and D PLAY**  
Laboratoire CASM-INSA de Lyon, Villebanne, France

### **ABSTRACT**

This experimental study was carried out on a single stage geared system, the aim is to provide measurements and process of analysis which enable the detection and the identification of simultaneous faults on gears and bearings.

Local metal removal from the inner race of ball and roller bearings and uniformly distributed fault (scuffing) for gears have been considered. Accelerations are measured on the bearing housing using piezoelectric accelerometers. These responses predominately provide information about bearings, while the gear transmission error measured with optical encoders supplies the essential information about gear condition. Signals are processed in spectrum and cepstrum domains.

The combined measurements and the applied procedures provide a powerful tool for the detection and the identification of simultaneous faults.

## 1. INTRODUCTION

The increase of machine performance using higher speeds with lighter structures enhances vibration problems. For financial reasons, down time has to be reduced and also optimised, and above all, these machines have to operate in a safe working environment. Monitoring Based Maintenance thus seems to provide a suitable tool, many studies were performed in this field (1), (2) and (3). The general procedures are almost the same, only the applied techniques change due to the nature of the studied system, the main operations are to :

- detect the presence of a fault,
- qualify its nature and its origin,
- quantify its effects,
- and, finally, define thresholds.

This study is a step in a research program for the definition of analysis procedures and indicators for the diagnostic of gearbox. The studied mechanism is a simple stage geared system. The analysis of fault modes and effects show that the major defects appear on gears and bearings. Several studies were carried out for the detection of gear faults (4, 5, 6, ...). Depending on their natures, fault effects can be detected more or less easily using vibration, gear transmission error or noise measurements. Each defect has its specific signature that can be identified by processing the system response in different analysis domains. Spectrum analysis are widely applied in this field, and in order to point out periodicity in spectra, signals were processed in the cepstrum domain (7). Several models were proposed for the monitoring of bearing faults (8, 9, 10, 11, ...). Accelerations measured on bearing housing describe closely the dynamic behaviour of bearings, the identification of faults occur through the analysis of system response in spectrum and cepstrum domains.

The presence of simultaneous faults induces modifications on the system response. The established procedures in the case of lonely fault may be insufficient especially when defects have similar dynamic behaviours. In this work, simultaneous faults were simulated on gears and bearings. The aim is to extract the suitable indicators. Gear transmission error and acceleration measured on bearing housings were the considered system response since it contain essential information about defective elements. Signals were processed in spectrum and cepstrum domains.

## 2. EXPERIMENTAL PROCEDURE

### 2.1. Experimental rig

The test bench (Figure 1) is constituted of two shafts of 60 mm in diameter, mounted on two bearings and coupled with gears. The test bench was designed and used for high loaded bearings and gears studies. The input shaft is driven by a 120 kW DC motor. The output shaft is braked by a DC motor. Rotating speed can be varied between 0 and 6000 rpm and is feedback controlled. The resistant torque can be applied independently from 0 to 150 Nm.

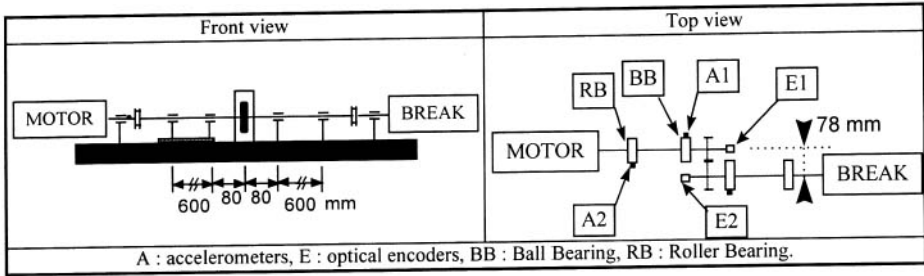


**Figure 1 Schematic arrangement of the test gear apparatus**

Test gears are 36/38 toothed with an initial AGMA 12 quality, a contact ratio of 1.3 and a pitch module of 2 mm, their centre-distances are 78 mm. Test bearings were SKF type 6012 for ball-bearings and SKF type NU1013 for roller bearings.

## 2.2. Simulated faults

Three faults were simulated : uniformly distributed fault on gear and local faults on the inner race of bearings. Uniformly distributed fault on gear was induced by scuffing, it was created by gradually removing lubrication, after 40 hours run at 3500 rpm and 90 Nm. Local faults on ball (BB) and roller bearings (RB) were created as a strip metal removal from the inner race using a grinding wheel, fault on RB was 0.088 mm of depth and 1.7 mm of width (figure 2), fault on BB was not measured due to the access difficulties, fault dimensions are smaller than those of roller bearing fault.

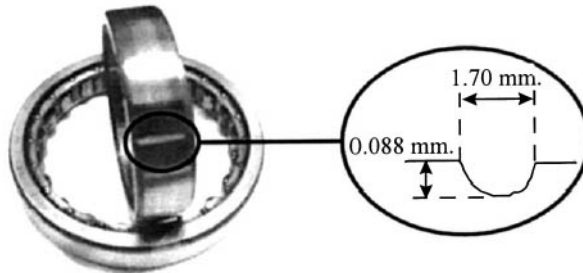


**Figure 2 Local fault on roller bearing.**

## 2.3. Measurements and analysis

System response must contain enough information to allow fault identification. Acceleration measurements provide suitable information about bearing health, while gear transmission errors describe accurately the dynamic behaviour of gears.

Bearing accelerations were measured using piezoelectric accelerometers A1 and A2. Accelerometers were placed near each defective element. Signals were recorded after filtration

(20 kHz) using a data acquisition microcomputer module. The sampling frequency (50 kHz) takes into account the whole studied phenomena.

Gear transmission error is measured using ‘through shaft’ optical encoders (E1 and E2) mounted at each shaft end. Acquisition is performed by dissociating the angular sampling data provided by encoders from the precision performance issued from a 100 MHz timer (12). The evolution of the angular position of each shaft can be calculated and the simultaneous analyses of the two encoder signals leads to the gear transmission error. The theoretical precision for a speed of 2300 rpm is 0.5 second of arc. Of course, increasing of speed would decrease the theoretical precision.

Signals (acceleration and transmission error) are processed in spectrum and cepstrum domains. The operating conditions were two speeds (1300 and 2300 rpm) and two loads (60 and 120 Nm).

**Table 1 Definition of fault configurations on gears and bearings**

	S0	S1	S2	S3	S4	S5	S6	S7
DG		X		X		X		X
LBB					X	X	X	X
LRB			X	X			X	X

Indicators were established by comparing signatures issued from the analysis domains with and without faults. Several configurations were considered (Table 1) in relation with the studied faults (Distributed fault on Gear : DG ; Local fault on Ball Bearing : LBB and Local fault on Roller Bearing : LRB ) and their combinations. The state S0 corresponds to the studied system without faults and S7 when all three fault types were monitored at the same time.

The evolution of the observed indicators were studied for the all operating conditions, levels of the studied parameters increase with respect to the input speed. On the other hand, the load has no significant effects. In this work, the obtained results for 2300 rpm and 60 Nm will be presented, the same trends were observed for the other operating conditions.

### 3.RESULTS

Signals were processed in spectrum and cepstrum domains, the aim is to establish suitable indicators for the detection and identification of the simulated faults. Only final results are presented in this paper. It can be noted that :

- transmission error is the suitable system response which enables gear fault identification,
- acceleration is the suitable response for bearing fault identification.

#### 3.1.Transmission error

The presence of gear fault leads to an increase in signal amplitude (Figure 3), especially for high order gear meshing harmonics (H1, H2, ...).

In addition, around the meshing harmonics, the presence of peaks separated by the meshing frequency can be noted. This observation can be pointed out more easily in the cepstrum domain, where the presence of the gear fault leads to an increase of the meshing rhamonics (R1, R2, ...).

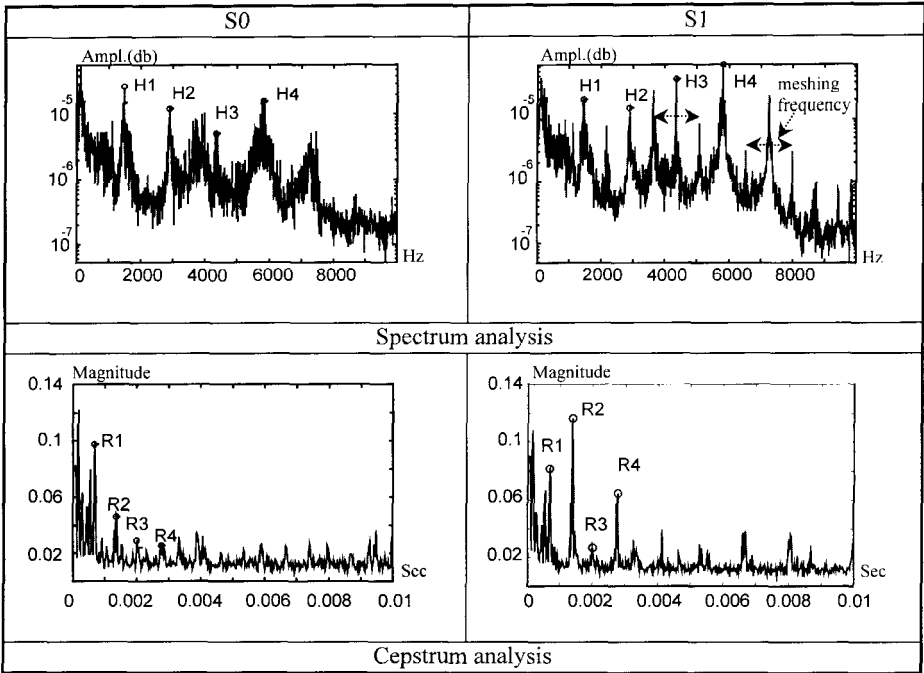


**Figure 3 Transmission error (2300 rpm, 60 Nm)**

In order to quantify gear fault effect, the sum of the first four meshing rhamonics was chosen as indicator (Table 2). The percentage increase in comparison with the signature without fault (S0) provides an efficient diagnostic. Signatures S1, S3, S5 and S7 correspond to the different combinations with gear fault, the percentage increase is greater than 40%.

**Table 2 Comparison of the sum of the first four gear mesh rhamonics**

	S0	S1	S2	S3	S4	S5	S6	S7
$\Sigma R$	0.182	0.275	0.172	0.261	0.201	0.256	0.169	0.295
% increase / S0		51.0	-5.5	43.4	10.4	40.6	-7.1	62.0

### 3.2. Accelerations

The effect of bearing local fault in the spectrum domain is characterised by the presence of sidebands around the meshing frequencies and its harmonics spaced by the corresponding

frequency of the bearing fault. It leads also to a slight amplitude level increase at the meshing frequency and its harmonics. The bearing fault frequencies are calculated depending on the rotational speed, the geometrical characteristics of the bearing and the type of fault.

In the case of a single fault bearing (either ball or roller bearing) this behaviour can be observed easily using measurement obtained from one accelerometer (either A1 or A2). On the other hand, the presence of combined faults induces a significant ‘perturbation’ in the signals. The signal obtained from the accelerometer nearest the defect was found to contain less perturbations. Thus, accelerometer A1 has been dedicated for the detection of the ball-bearing fault and accelerometer A2 for the roller bearing fault.

### 3.2.1. Ball bearing

The effect of bearing fault can be clearly pointed out in the cepstrum domain (Figure 4). The presence of the fault leads to a magnitude increase of bearing queffreny and its rhamonics (LBBR1 and LBBR2). As the defective bearing is mounted on the input shaft, the presence of fault produces a magnitude increase of the input shaft queffreny and its rhamonics (ISR1 and ISR2).

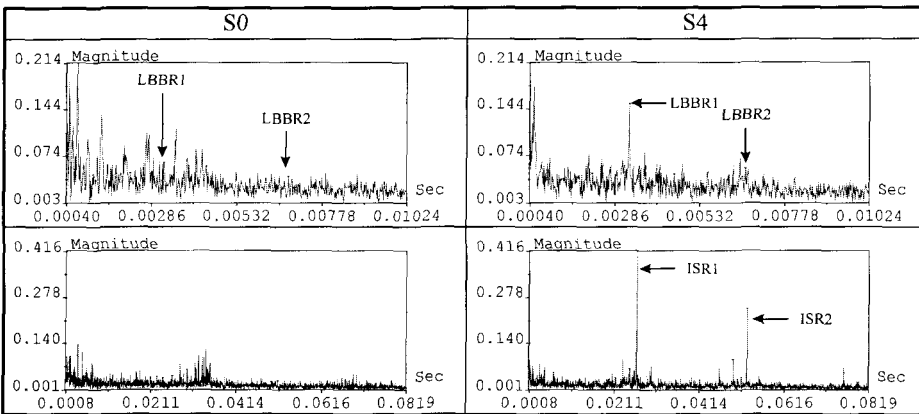


Figure 4 Acceleration-A1-cepstrum analysis (2300 rpm, 60 Nm)

In order to quantify fault effect, the magnitude sum of the first two rhamonics of the ball bearing fault and the input shaft were chosen as indicators (Table 3). The comparison of percentage increase with respect to the signature without fault leads to the identification of the fault for the different studied configurations.

Table 3 Comparison of the magnitude sum of the first two rhamonics of LBB & IS-A1

	S0	S1	S2	S3	S4	S5	S6	S7
$\Sigma$ LBBR	0.1044	0.1080	0.1227	0.1311	0.1814	0.1883	0.1616	0.1508
% increase / S0		3.5	17.5	25.5	73.7	80.4	54.8	44.4
$\Sigma$ ISR	0.1472	0.2023	0.1888	0.2646	0.6880	0.7862	0.7440	0.7641
% increase / S0		37.4	28.2	79.7	367.3	434.0	405.4	419.0

### 3.2.2. Roller bearing

A local fault on the roller bearing produces the same dynamic behaviour. In this case, measurements obtained from accelerometer A2 were processed and the indicators were the magnitude sum of the first two rhamonics of input shaft quefreny and roller bearing fault quefreny (LRBR).

**Table 4 Comparison of the magnitude sum of the first two rhamonics of LRB & IS-A2**

	S0	S1	S2	S3	S4	S5	S6	S7
$\Sigma$ LRBR	0.1132	0.0960	0.2320	0.2999	0.0981	0.1284	0.3207	0.2942
% increase / S0		-15.2	104.9	164.9	-13.4	13.4	183.2	159.8
$\Sigma$ ISR	0.0678	0.1456	0.3704	0.3180	0.0988	0.0994	0.2801	0.2485
% increase / S0		114.6	446.2	368.9	45.7	46.5	313.0	266.4

The identification of faults can be easily carried out by comparing the increase percentage with respect to the signature without fault (Table 4). The comparison of bearing fault quefreny levels in both cases : ball bearing and roller bearing, shows that the percentage increase depends on the importance of fault dimensions. The use of input shaft rhamonics as indicator provides supplementary criteria which are necessary, especially for small dimension faults.

## 4.DISCUSSION

Generally in the case of separated faults, the acceleration measurements contain enough information for the detection and the identification of the simulated faults. This is not the case when combined faults were considered.

The presence of distributed faults on gears leads, in spectrum domain, to an amplitude increase at the meshing frequency and the associated harmonic, this is due to the fact that the fault excitation occurs for each tooth passage which is the meshing frequency. On the other hand, the presence of bearing local fault, beside sidebands around meshing harmonics, produces a similar behaviour. In the presence of combined faults, the diagnosis of gear faults using acceleration measurements becomes a delicate task especially for low speed and torque operating conditions. The gear transmission error measurements have the advantage in containing the majority of the information about the gears and to be less sensitive to bearing faults.

The use of two accelerometers was necessary for the identification of bearing faults. In the case of only one local fault, it can be detected using one measurement point, either A1 or A2. The local fault on the roller bearing can be identified using measurements issued from accelerometer A1 (Table 5). Fault effect can be quantified even with the presence of gear faults (signature S3). The identification becomes difficult with the presence of ball-bearing fault (signatures S6 and S7).

**Table 5 Comparison of the magnitude sum of the first two rhamonics of LRB-A1**

	S0	S1	S2	S3	S4	S5	S6	S7
$\Sigma$ LRBR	0.1178	0.1498	0.1738	0.1744	0.0965	0.1204	0.1054	0.1030
% increase / S0		27.2	47.6	48.1	-18.1	2.2	-10.5	-12.5

Fault Modes, Effects and Criticality Analysis of the studied system enable the isolation of critical elements and their associated defects. Each defect has a signature which can be identified using suitable indicators. Suitable sensors placed in the vicinity of critical elements provide responses which contain the majority of the information about eventual defects and are still less sensitive to perturbations.

## CONCLUSION

The purpose of this work was to establish the procedures of measurements and analysis for the detection and the identification of combined faults. The aim is to acquire required skill which enables automatic monitoring of gearboxes.

A uniformly distributed fault (scuffing) on gears and local fault on the inner race of ball and roller bearings have been simulated. The indicator definition requires the use of signals that contain the majority of information about the defective element with a *minimum sensitivity* to perturbations induced by the other elements. The transmission error is the suitable system response that describes closely the dynamic behaviour of gears and provides the required information about gear condition. Measurements obtained from accelerometers placed on bearing housings contain the predominant indicators about bearing conditions.

Signals were processed in spectrum and cepstrum domains. The quantification of the effects of simulated faults can easily be done in the cepstrum domain. The chosen indicators were :

- the magnitude sum of the first four rhamonics of the meshing quefrequency for gears,
- for bearing, the magnitude sum of the first two rhamonics of bearing fault quefrequency. As the defective bearings were mounted on the input shaft, the level of the first two rhamonics of input shaft quefrequency provides supplementary indications, especially in the case of small fault dimensions.

The chosen indicators enable an efficient identification of the simulated faults. This study will be extended for further fault type such as pitting on the bearing outer race, wear and cracks.

## ACKNOWLEDGMENTS

The authors would like to thank P. Soleilhac, assistant engineer, for his invaluable help during the entire experimental program.



## REFERENCES

- [1] MATHEW J., 1989, " Monitoring the vibrations of rotating machine elements- An Overview", The 1989 ASME Design Technical Conference on Mechanical Vibration and Noise, Montreal- Canada, pp. 15-22.
- [2] MONK R., 1979, " Machine health monitoring - Some common defects.", J. Noise control vibration, Vol. 10, N° 1, pp. 24-26.
- [3] WALSH C. T., 1992, " Condition monitoring of machine systems for the 1990 s and Beyond", J. Machine vibration, vol. 1, pp. 203-210.
- [4] STEWART R.M., 1980, "The Specification and Development of A Standard for Gearbox Monitoring", Proc. Instr. Mech. Eng., pp 353-358.
- [5] RANDALL R. B., 1982, "A New Method of Modeling Gear Faults", J. Mechanical Design, ASME, 104, pp 259-267.
- [6] MAHFOUDH J., BARD C., AL- ATTASS M. and PLAY D.,1995," Simulation of gearbox dynamic behaviour with gear faults" Second International Conference on Gearbox Noise, Vibration and Diagnostics, IMECHE, London, pp. 91-100.
- [7] RANDALL R.B., 1980, "Advances in the application of cepstrum analysis to gearbox diagnosis", Second International Conference, IMECHE, pp.169 - 174.
- [8] MATHEW J. and ALFREDSON R. J., 1984, "The condition monitoring of rolling element bearing analysis" J. Vibration, Acoustic, Stress, and reliability design, Vol. 106, pp. 447 - 453.
- [9] SHIROISHI J., LI Y., LIANG S., KURFESS T., DANYLUK S., 1997, "Bearing condition diagnostics via vibration and acoustic emission measurements", Mechanical Systems and Signal Processing, Vol. 11, N° 5, pp. 693-705.
- [10] TANDON N., NAKRA B.C., 1993, "Detection of defects in rolling element bearings by vibration monitoring", Journal of the Institution of Engineers (India)- Mechanical Engineering Division, vol. 73, pp. 271 - 282.
- [11] IGARASHI T. and HIROYOSHI H, 1982, " Studies on the vibration and sound of defective roller bearings." Bulletin of the JSME, Vol. 25, N° 204, pp. 994 - 1001.
- [12] BARD C., REMOND D. and PLAY D., 1994, "New Transmission Error Measurement for Heavy Load Gears", 1994 International Gearing Conference, 7-9 September, Newcastle, England, pp.393-399.

*This page intentionally left blank*

# Model-based malfunction identification from bearing measurements

N BACHSCHMID and P PENNACCHI

Dipartimento di Meccanica, Politecnico di Milano, Italy

## ABSTRACT

Some results of a model based malfunction identification procedure, which uses the vibration measurements taken in the bearings only of a rotor system, are presented.

The procedure has been applied to experimental results obtained on a 4 oil film bearing, 2 rigidly coupled shafts test rig, on which several different malfunctions have been applied. The 1x rev. vibration components are related to 1x rev. excitations (unbalance, bow and coupling misalignment) and the 2x rev. vibration components to 2x rev. excitations (transverse crack, journal ovalization, axial unsymmetry).

The results allow to evaluate the accuracy of the method and the capability of distinguishing among different faults which generate similar effects, and its sensitivity to measuring or modelling errors.

## 1 INTRODUCTION

In recent years, different types of model based methods have been developed for the study of the dynamical behaviour of rotating machines (1). A model based malfunction identification procedure, based on a least square fitting approach in the frequency domain (briefly LSFADF), has been developed by the authors in the European Community funded project MODIAROT (2). Besides of the definition of the rotor, bearing and supporting structure models, also the model of the faults have to be defined for the identification procedure (2). An effective identification procedure has to distinguish among different faults which generate similar effects: unbalance, bow and coupling misalignment produce 1x rev. excitations, while transverse crack, journal ovalization, axial unsymmetry produce 2x rev. excitations. The capability of LSFADF in distinguishing the faults is analysed in this paper by means of experimental tests. Test results related to a known malfunction are fed to the identification procedure: for each different fault and for each possible location of the fault along the rotor, the "residual" is calculated, which is a measure of the quality of the fitting between (model based) calculated results and experimental results. The location in which the residual has a minimum is the most probable location of the fault; the lowest value of the minima related to the different faults identifies the most probable type of fault.

## 2 TEST-RIG DESCRIPTION

The PdM test-rig (see Figure 1) is made by a rotor composed by two rigidly coupled shafts, connected to a foundation frame by means of four lemon shaped oil film bearings. The shafts diameter is 25 mm and the total length of the two rigid coupled shafts is about 2 m, the total mass is less than 100 kg. Two shrink-fitted disks are mounted on each shaft.

As in many real industrial machines, each one of the four lemon shaped oil film bearings is equipped with two eddy current proximity probes, which allow to measure the relative journal-bearing displacements in two directions at  $90^\circ$  between each other (at  $\pm 45^\circ$  from the vertical axis), so that it is possible to describe the journal orbit inside of the bearing.

Each bearing housing is equipped with two accelerometers, in order to measure their transversal absolute accelerations in horizontal and vertical direction.

The absolute shaft displacement is then obtained by adding to the relative displacements, measured by the proximity probes and rotated by  $45^\circ$  in order to have horizontal and vertical displacements, the bearing housing displacements, obtained by integrating twice the accelerations measured by the accelerometers. The heavy processing of the measured data may introduce some errors.

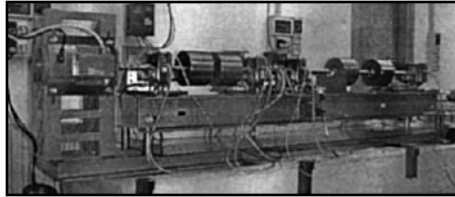


Figure 1 PdM test-rig and sensor arrangement.

## 3 IDENTIFICATION PROCEDURE AND MODEL OF THE FAULTS

It can be shown that almost all faults which can effect a rotor system can be represented by a set of equivalent external forces.

If the system is supposed to be linear, it is possible to consider only the part  $\mathbf{x}$  of displacements of the rotor connected with the developing fault in the identification procedure. The component  $\mathbf{x}$  may be obtained by calculating the vector differences of the actual vibrations (due to weight, original unbalance and fault) minus the original vibrations (due to original unbalance and weight) measured in the same operating conditions before the fault was developing. So the following equation holds:

$$[\mathbf{M}]\ddot{\mathbf{x}} + [\mathbf{D}]\dot{\mathbf{x}} + [\mathbf{K}]\mathbf{x} = \mathbf{F}_f(t) \quad (1)$$

in which the faults are represented by an external force system  $\mathbf{F}_f(t)$ .

If a steady-state situation is considered, which is generally the case during the operation of the machine, all time dependent quantities,  $\mathbf{x}$  and  $\mathbf{F}_f(t)$ , in eq. (1) are periodical and it is possible to switch from time domain to the frequency domain by means of the Fourier analysis. Assuming linearity of the system and applying the harmonic balance criteria the eqs. (2) are obtained for each harmonic component,

$$\left[ -(n\Omega)^2[\mathbf{M}] + i n \Omega [\mathbf{D}] + [\mathbf{K}] \right] \mathbf{X}_n = \mathbf{F}_{f_n} \quad (2)$$

The problem of fault identification is then reduced to a force identification procedure.

Some faults considered here, unbalance, bow and coupling misalignment, generate mainly 1x rev. components in the response of the system, therefore it is interesting to consider them together and to test the capability of the identification methods to discriminate among the different faults.

Other faults generate mainly 2x rev. components: among these transverse cracks, journal ovalization and general rotor axial unsymmetry are considered. The presence of 2x rev. components due to oil film non linearity, which are emphasised by high 1x rev. components and/or by high loads in the bearings, has been disregarded in this linear approach.

The problem of fault identification may be seen under a double aspect:

1. the localisation of the defect along the rotor;
2. the quantitative determination of the fault.

As regards these aspects, vector  $\mathbf{F}_j(t)$  has many null-elements since the analysed faults give a force fault system extended to not more than 2 nodes of the rotor model as shown in the following, therefore the force vector can be expressed as:

$$\mathbf{F}_{f_j} = [\mathbf{F}_L] \alpha \quad (3)$$

where  $[\mathbf{F}_L]$  is the localisation vector which has all null-elements except for the d.o.f. to which the forcing system is applied and  $\alpha$  is the complex vector of the identified defects. The vector  $[\mathbf{F}_L]$  does not give just the assumed position of the defect but also expresses the link between the force fault system and the modulus and phase of the identified fault that produce it.

### 3.1 Unbalance fault model

The complex vector of the fault force system  $\mathbf{F}_{f_j}$  becomes in case of unbalance:

$$\mathbf{F}_{f_j} = [0 \quad \vdots \quad 1 \quad 0 \quad i \quad 0 \quad \vdots \quad 0]^T \cdot m r \Omega^2 e^{i\varphi} = [\mathbf{F}_L] \alpha \quad (4)$$

where the only elements different from zero are the ones relative to the horizontal and vertical d.o.f. of the node  $j$ , where the unbalance is supposed to be applied.

### 3.2 Bow and rigid coupling misalignment fault models

The thermal or permanent bow and the rigid coupling misalignment are analysed together, because both faults generate an asymmetrical axial strain distribution which deflects the rotor. In fact a (rotating) thermal bow of a rotor is due to an asymmetrical heating or cooling of the symmetrical rotor, or to a symmetrical heating of an asymmetrical rotor, which both cause an asymmetrical axial strain distribution on the cross section of the shaft. The asymmetrical heating can be localised when it is due to a full annular rub (local bow), or can be extended to a certain length of the rotor, as in a generator when a cooling duct is obstructed (extended bow). A similar asymmetrical strain distribution is caused by a radial or angular misalignment of a rigid coupling between two rotors of a shaft line. The rigid coupling misalignment can be due to manufacturing errors of the two surfaces of the flanges, assembling errors (different tightening forces in the connecting bolts) or corrosion. This strain distribution does not influence the system parameters and may be considered as created by an external system of

forces, provided that the associated vibrations in the bearings are small enough to consider the system as linear.

The bow can be simulated, generally in a fairly accurate way, by imposing on the rotor, in only two nodes of the f.e. model, a suitable system of rotating moments (or bending couples), which generates the same (polarly asymmetrical) strains and therefore the same static deflection. Therefore in each one of the two nodes of the f.e. model (the extremity nodes of the part of the rotor which is interested by the bow) only one rotating moment is applied, in order to have an easier identification procedure.

A similar situation holds also for the coupling misalignment fault: this can be simulated by suitable rotating moments and forces. The nodes where the fault force system is applied are the extremity nodes of the flanges of the coupling where the misalignment occurs: also this malfunction can be considered as a local bow.

Therefore for the identification procedure both these faults are given by a rotating, speed independent, force system that generates, statically, the deflection and, dynamically, at the operating speed, the total vibration of the shaft.

The complex vector of the fault force system  $\mathbf{F}_f$ , which simulates the bow, and the corresponding  $[\mathbf{F}_L]$  and  $\alpha$  become:

$$[\mathbf{F}_L] = [0 \quad \vdots \quad 0 \quad i \quad 0 \quad 1 \quad \vdots \quad 0 \quad \vdots \quad 0 \quad -i \quad 0 \quad -1 \quad \vdots \quad 0]^T \quad \alpha = Me^{i\varphi} \quad (5)$$

where the only elements different from zero are the ones relative to the horizontal and vertical rotational d.o.f. of two nodes.

The rigid coupling misalignment is simulated by a balanced force system, independent from rotating speed, applied to the coupling flanges. This force system produces a deformation of the finite beam elements that schematise the coupling, which reproduces the angular and radial deflection of the nodes  $j-1$  and  $j+1$  of the flanges and makes the rotor assume the static deflection due to this defect (Figure 2).

The corresponding localisation matrix  $[\mathbf{F}_L]$  and the parameters vector  $\alpha$  are, in case of angular and radial misalignment:

$$[\mathbf{F}_L] = [0 \quad \dots \quad K_{R,j-1} \quad K_{R,j+1} \quad \dots \quad 0]^T \cdot \begin{bmatrix} 1 & 0 \\ 0 & i \\ i & 0 \\ 0 & 1 \end{bmatrix}, \quad \alpha = \begin{bmatrix} \Delta x_R + \Delta x_L \\ \Delta \phi_R + \Delta \phi_L \end{bmatrix} \quad (6)$$

where  $K_{R,j-1}$  and  $K_{R,j+1}$  are the stiffnesses of the rotor system reduced to the coupling extremity nodes.

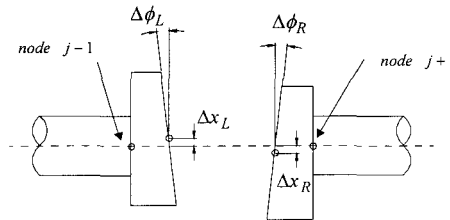


**Figure 2 Representation of the angular and radial misalignment of the two flanges of the coupling.**

### 3.3 Transverse crack and axial unsymmetry fault models

It has been shown (3) that a crack can be modelled by a suitable system of external forces or couples, which depend on the depth of the crack and of the bending moment which is applied to the rotor in the cracked section. These forces are 1x rev., 2x rev. and 3x rev. However, since the 1x rev. component is generally masked by other effects (unbalance, bow), and the 3x rev. is generally very small, only the 2x rev. component will be used in the identification procedure. The localisation vector  $[F_L]$  and  $\alpha$  have the following expressions:

$$[F_L] = [0 \quad ; \quad 0 \quad i \quad 0 \quad 1 \quad 0 \quad -i \quad 0 \quad -1 \quad ; \quad 0]^T \quad \alpha = Me^{i2\varphi} \quad (7)$$

Therefore, the crack is considered as a 2x rev. local bow in the identification procedure. It can further be shown that an axial unsymmetry can be represented again by a set of 2x rev. external couples: this fault is then considered as an 2x rev. extended bow and the localisation vector  $[F_L]$  has the same expression of eq. (5) and  $\alpha$  the same of eq. (7).

### 3.4 Journal ovalization fault model

When the rotating journal in an oil film bearing presents ovalization errors, then the rotor is forced through the oil film by a 2x rev. force, which depends on oil film stiffness and damping coefficients and on the ovalization error. Therefore the model of the journal ovalization error is composed by two 2x rev. external forces in each bearing, whose amplitude generally decreases with the speed (4). Here a 2x rev. rotating, constant amplitude force is considered for the sake of simplicity.

## 4 UNBALANCE IDENTIFICATION

In order to obtain the experimental results with the test rig described above, the unbalance has been imposed through a known unbalancing mass ( $3.6 \cdot 10^{-4}$  kgm at  $-90^\circ$ ) placed on one of the balancing planes. Two different cases were taken into account:

- unbalance on the short shaft: balancing plane 2 in Figure 3;
- unbalance on the long shaft: balancing plane 7 in Figure 3.

The experimental data of the vibrations on both the short and the long shaft are grouped into the vectors  $X_i$  (displacements), which are used in eq. (2) (considering the first harmonic component only). These vectors are referred to a single speed, but, as the measures are available in the range between 500 and 2700 rpm, it is possible to use more speeds for the identification procedure. The speeds used in the unbalance identification are in the range from 600 to 2700 rpm with a step of 300 rpm, as shown for example in Figure 4, where the amplitude of the experimental absolute journal displacements, in case of unbalance on the long shaft, are presented (the asterisks show the speeds which have been used for the identification procedure) for the bearing 1, as an example.

Using these speeds for the identification procedure, the relative identification residual can be calculated for each possible node of application of the unbalance, changing in an opportune way the localisation matrix  $[F_L]$ . The most probable location of the unbalance is where the residual reaches its minimum; the corresponding identified value of  $\alpha$  furnishes amplitude and phase of the fault. The results are shown in Figure 5, where the trend of the residual and of the identified unbalance are presented.

The localisation of unbalance on the shaft line is very good for both cases, with a minimum residual always about in the node where the unbalance is applied. Its quantitative determination is also good.

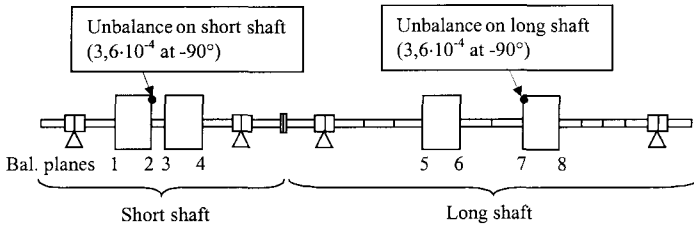


**Figure 3 Unbalances on the short and the long shaft of the rotor.**

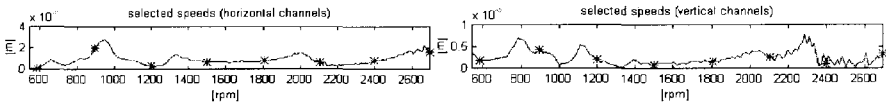


**Figure 4 Unbalance response curves in bearing 1.**

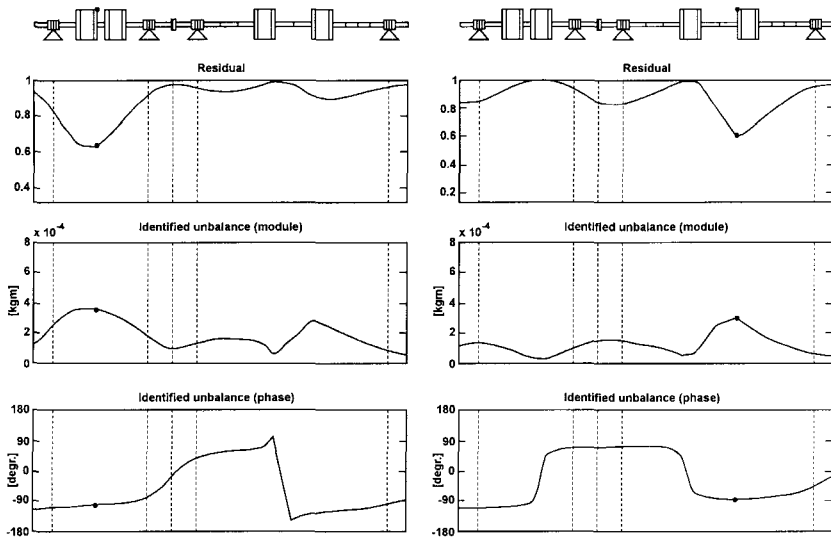


**Figure 5 Unbalance identification on the short and the long shaft of the rotor.**

In order to check if the identification method is able to distinguish the actual malfunction among the other candidates, the same experimental data are used with other malfunction models which generate mainly 1x rev. components: these are a coupling angular misalignment or a local bow and an extended bow on the long shaft and an extended bow on the short shaft. The residual corresponding to the extended bow is marked by a symbol at midspan.

The results are shown in Figure 6, where the diagram of the identification residuals obtained with the unbalance data are presented.

In both cases, the unbalance is identified as the most probable fault, but other candidates, such as the local bow, are not far away.



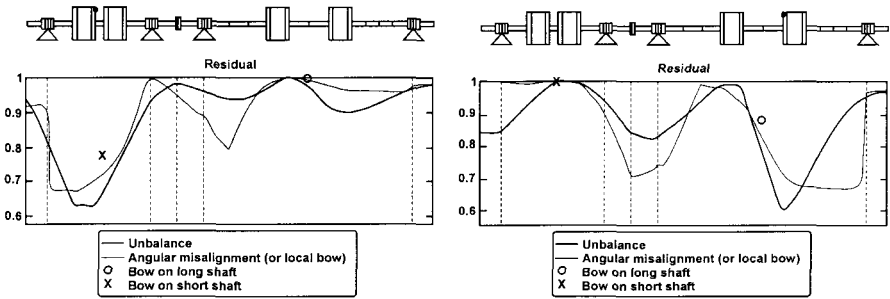


**Figure 6** Relative residuals with the experimental data of unbalance on the short shaft: (left) and long shaft (right).

### 5 BOW IDENTIFICATION

Since the rotor used in the PdM test rig has a permanent bow (Figure 7) with a maximum deflection of about 0.17 mm in the middle of the long shaft and 0.05 mm in the middle of the short shaft (see the stars in Figure 9), the reference situation, i.e. the experimental data of the rotor without bow, is not available. For this reason, the experimental data used, are obtained after the balancing and by subtracting the effect of the known balancing masses: this way, the experimental data due to the bow alone are obtained, assuming the original unbalance negligible.

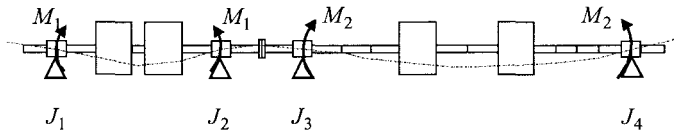


**Figure 7** Representation of the couples that schematise the original bow of the rotor.

Following the procedure exposed in paragraph 3, the experimental data used for the bow identification are also used to test the capability of the method to distinguish the bow among the other possible faults which give a similar effect. The results obtained by means of the model identification are shown in Figure 8.

The best results are obtained when a permanent bow on both shafts is considered, which is identified with a residual of less than 0.4. The next candidate has a minimum which is far away from that one of a bow on both shafts. Therefore, the true candidate is identified with a high degree of confidence. The identified couples  $M_1$  and  $M_2$  deflect the shafts as shown with solid line in Figure 9. The agreement between experimental and measured bows seems acceptable, bearing in mind that vibrations are measured always only in the bearings.

### 6 RIGID COUPLING MISALIGNMENT IDENTIFICATION

A tapered spacer with an angle of 0.545 mrad and a phase of  $-120^\circ$  has been inserted between the two halves of the coupling, in order to generate a coupling misalignment.

The capability of distinguishing the rigid coupling misalignment from other faults generating a similar effect, is considered. The considered faults are unbalance, angular misalignment, angular and radial misalignment, bow on the long shaft and bow on the short shaft. The identification speed sets are the same used in the previous cases. The results are shown in Figure 10.

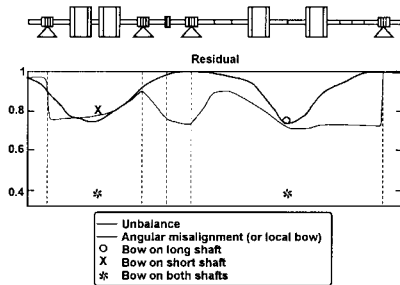


Figure 8 Relative residuals with the bow experimental data.

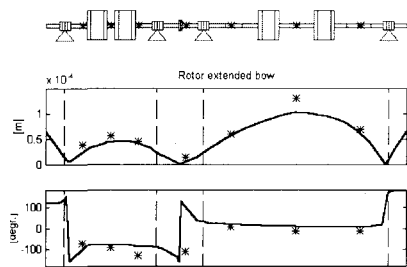


Figure 9 Comparison of the experimental and analytical bow calculated with the identified moments.

From the analysis of the identification results, the best results are obtained when both types of coupling misalignment are identified: the angular and radial misalignment and the angular misalignment only. The identified values are:  $4.5 \cdot 10^{-4}$  rad,  $-111^\circ$  (angular) and  $1.82 \cdot 10^{-5}$  m,  $85^\circ$  (radial) in the first case and  $4.42 \cdot 10^{-4}$  rad,  $-112^\circ$  (angular) in the second case. Both values are rather close to the actual introduced misalignment.

## 7 TRANSVERSE CRACK IDENTIFICATION

A crack of a relative depth of 25÷30% of the diameter, has been generated in the middle of the long shaft. The change in 2x rev. vibrations in the bearings (with respect to the uncracked shaft) have been calculated and considered for the crack identification procedure.

Figure 11 shows the results, compared with the residuals obtained with other candidates: extended bow or axial unsymmetry along all the shaft and journal ovalization.

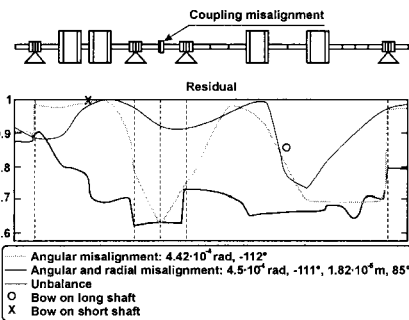


Figure 10 Relative residuals with the angular misalignment experimental data.

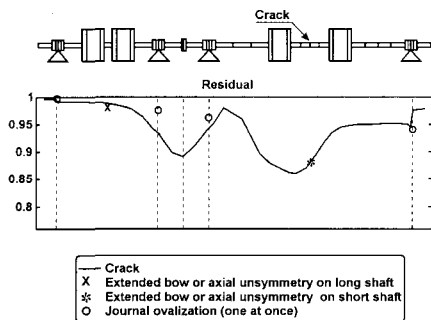


Figure 11 Relative residuals with the cracked rotor experimental data.

The crack results as the best, or most probable candidate. From the identified  $\alpha$ , also the crack depth can be derived (3). The identified value was in this case 39%, which is not far from the true value.

## 8 JOURNAL OVALIZATION IDENTIFICATION

From beginning the long rotor had an ovalization error of roughly  $10 \mu\text{m}$  on the journal of bearing 3 and roughly  $5 \mu\text{m}$  on the journal of bearing 4. Smaller ovalization errors were measured on the journals of the short shaft.

The 2x rev. measurements were taken to check if the model based identification procedure would be able to distinguish this fault from the other 2x rev. faults. In order to make a more effective identification, the journal ovalization has been first calculated separately for each bearing at once and then simultaneously for the bearing 3 and 4. The results are shown in Figure 12 compared with other 2x rev. candidates: extended bow or axial unsymmetry and crack. The journal ovalization on both the bearings of the long shaft results as the most probable candidate.

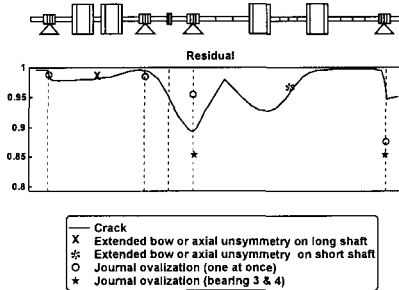


Figure 12 Relative residuals with the reference experimental data.

## 9 MEASURING ERRORS AND MODELLING ERRORS

Due to the level of accuracy in the data acquisition system (which was a 8-channel spectrum analyser in tracking filter modality), and in the necessary data processing (in order to extract the supporting structure displacements from measured accelerations, and the vertical and horizontal journal relative displacements from  $\pm 45^\circ$  directions of the proximity probes and also to obtain the vector differences, which are needed to extract the effect of one fault only), which resulted not very high, the measured data are affected by errors which are certainly not negligible. Further, also several modelling errors are present: it has been shown that the oil film parameters were very inaccurate due to a wrong estimate of the actual geometry and of the actual oil flow rate, and also the estimated model of the rigid coupling between the two shafts seems to be inaccurate.

The model based identification relies on a comparison of calculated results with measured experimental results: in this comparison it is difficult to distinguish measuring errors from modelling errors. In order to show how much these errors affect the fitting of calculated and measured results, as an example, Figure 13 shows the comparison of calculated results (obtained with the real unbalance) and measured results. The fitting is rather inaccurate, and this will obviously be reflected also in the value of the residual in the identification process, which is rather high. In almost all applications shown, the residual is higher than 0.6, which

means rather poor agreement between experimental and calculated data. Nevertheless the actual malfunction is always identified among other candidates. This confirms the validity and the robustness of the proposed model based approach in the frequency domain.

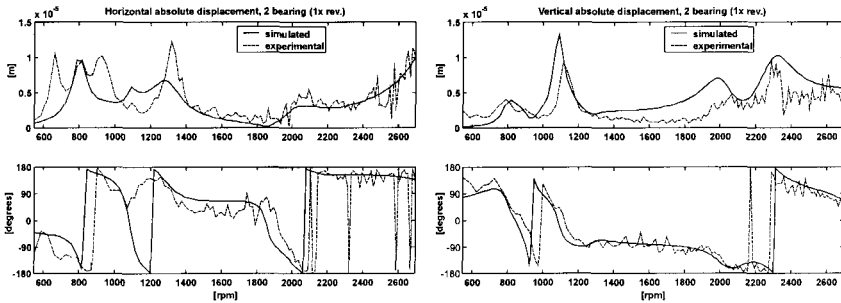


Figure 13 Comparison between calculated (with the fault actual value) and experimental data in bearing 2.

## 10 CONCLUSIONS

Several results in model based identification of malfunctions in a rotor system of a test rig are presented. Although the accuracy of the models is not very high and the fitting of experimental and calculated results is rather poor, due to measuring and modelling errors, the true malfunction is always identified among other candidates which cause similar effects. This proves that the proposed method should be applicable to industrial machines in an industrial environment, for which often the available models are not very accurate or reliable due to lack of informations about the actual geometry of the bearings and about the supporting structure dynamical behaviour.

## ACKNOWLEDGEMENTS

The financial support of Brite-Euram Contract BRPR-CT95-0022 MODIAROT is gratefully acknowledged.

## REFERENCES

- (1) Mayes I. and Penny J.E.T., “**Model based diagnostics of faults in rotating machines**”, Proc. of *12th International Congress on Condition Monitoring and Diagnostic Engineering Management-COMADEM 99*, Sunderland, July 1999, pp. 431-440, ISBN 1-901892-13-1.
- (2) Bachschmid N., Vania A., Tanzi E. e Pennacchi P., “**Identification and Simulation of Faults in Rotor Systems: Experimental Results**”, Proc. of *EURO DINAME 99 - Dynamic Problems in Mechanics and Mechatronics*, Wissenschaftszentrum Schloß Reisenburg der Universität Ulm, 11-16 July 1999, Günzburg, Germany, pp. 3-11.
- (3) Bachschmid N., Pennacchi P., Tanzi E. and Audebert S., “**Identification of Transverse Cracks in Rotors Systems**”, Proc. of *ISROMAC-8 Conference*, 26-30 March 2000, Honolulu, Hawaii, pp.1065-1072, ISBN 0-9652469-9-X.
- (4) Bachschmid N., Pizzigoni B. and Tanzi E., “**Effetti di irregolarità geometriche del perno sul comportamento della coppia portante lubrificata**”, Proc. of *V Convegno AIMETA di Tribologia*, 8-9 ottobre 1998, Varenna, Italy, pp. 313-323.

# Validation of online diagnostics of malfunctions in rotor systems

R PLATZ, R MARKERT, and M SEIDLER

Department of Applied Mechanics II, Darmstadt University of Technology, Germany

## SYNOPSIS

An identification algorithm in time domain for the model based diagnosis of faults in rotor systems has been developed and validated. Within the new diagnostic method the faults of rotor machinery are represented by fictitious equivalent loads acting on the undamaged rotor system.

To verify the concept, the identification method is tested numerically on a simple rotor-stator system. Moreover, various influences existing in practical applications, like defective sensors, noise in measured vibration signals or short sample length, affect the identification results. All these influences are examined independently by executing a lot of numerical tests on a simple rotor-stator system. Beyond that, the identification method was also tested experimentally on two real test rigs.

## 1 INTRODUCTION

The dynamical behaviour of a rotor-stator system may change due to malfunctions like unbalance, rubbing, misalignment or cracks. Vibration sensors at various locations of a rotor continuously provide information about the state of a machine during operation.

On the one hand, signal based monitoring methods are widely used but give only limited qualitative information about type, location and magnitude of faults, [1], [2] and [3]. On the other hand, model based monitoring systems allow to use information contained in the on-line recorded data more precise. Faults are detected by continuously comparing data during the operation of the rotor system with simulated output from the mathematical model using computational methods.

As the result of the BRITE-EURAM project MODIAROT, different model based identification methods for early detection of malfunctions in rotor systems of power plants have been developed, [4], [5] and [6]. These methods work either in the time or in the frequency domain

depending on the malfunction type and the operating state for which the measured vibration data is available. In [7] a new time domain identification method has been presented based on least squares fitting, which is to be validated in the present paper.

## 2 IDENTIFICATION METHOD

The identification method is based on the idea that system faults can be represented by virtual loads  $\Delta\mathbf{F}$  that act on the linear undamaged system model. Equivalent loads are fictitious forces and moments which generate the same dynamic behaviour as the real non-linear damaged system does. This method enables to maintain linear, so that fast linear analysis can be carried out to identify faults while the machines is still running.

### 2.1 Mathematical Description

Generally, vibration changes  $\Delta\mathbf{r}(t)$  caused by a fault, represented by additional forces  $\Delta\mathbf{F}(\boldsymbol{\beta}, t)$ , can be described by the equation of motion

$$\mathbf{M}_0\Delta\ddot{\mathbf{r}}(t) + \mathbf{B}_0\Delta\dot{\mathbf{r}}(t) + \mathbf{K}_0\Delta\mathbf{r}(t) = \Delta\mathbf{F}(\boldsymbol{\beta}, t). \quad (1)$$

The fault-induced change of the dynamic behaviour depends on the malfunction type, position and severity, [12]. These fault parameters are put together in the fault parameter vector  $\boldsymbol{\beta}$ .

Principally, equation (1) relates the residual vibrations  $\Delta\mathbf{r}(t)$  as difference between the damaged vibrational state and normal vibrations of the undamaged rotor directly to the equivalent forces of the faults present in the system [7]. During the real operation of a rotor system, the equivalent load  $\Delta\tilde{\mathbf{F}}(t)$ , representing the fault, is calculated by simply putting the measured residual vibrations  $\Delta\tilde{\mathbf{r}}(t)$ ,  $\Delta\dot{\tilde{\mathbf{r}}}(t)$  and  $\Delta\ddot{\tilde{\mathbf{r}}}(t)$  into equation (1).

### 2.2 Determination of Equivalent Loads

#### 2.2.1 Signal Processing

On the one hand, measured vibration data for both the undamaged and the damaged rotor system have to be available for the same operating conditions to obtain residual vibrations. Usually, directly matching data are not available, therefore signal processing needs to be carried out. For example, small differences in rotor speed can be compensated by adjusting the time scale of the recorded normal vibrations to the time scale of the current measurement.

If, for example, only acceleration signals are measured, velocities and displacements need to be determined by integration to put all three types of signals into equation (1), eventually. This can be done either in the time domain or via FFT in the frequency domain.

#### 2.2.2 Modal Expansion

For the calculation of the equivalent loads from the mathematical model of the rotor system by equation (1), measured residual rotor deflections  $\Delta\tilde{\mathbf{r}}(t)$ , residual velocities  $\Delta\dot{\tilde{\mathbf{r}}}(t)$  and residual accelerations  $\Delta\ddot{\tilde{\mathbf{r}}}(t)$  must be available at all nodes of the model. In practice, vibration transducers are installed only at a few positions of the rotating machinery, mainly at bearing locations. Therefore, the residual vibrations need to be reconstructed via modal expansion from the directly measured vibrations  $\Delta\tilde{\mathbf{r}}_M(t)$ ,  $\Delta\dot{\tilde{\mathbf{r}}}_M(t)$  and  $\Delta\ddot{\tilde{\mathbf{r}}}_M(t)$  at the measuring positions. This technique is based on the approximation of the residual vibration by a linear combination of

only a few eigenvectors. The full vibrational state of the model at all degrees of freedom is estimated by using least squares. This leads to a linear relation

$$\Delta \tilde{\mathbf{r}}(t) = \mathbf{Q} \Delta \tilde{\mathbf{r}}_M(t), \quad (2)$$

see [7] for further details.

### 2.2.3 Equivalent Loads

The equivalent force  $\Delta \tilde{\mathbf{F}}(t)$  characterising the unknown fault is calculated by putting the residual vibrations of the full vibrational state into equation (1),

$$\Delta \tilde{\mathbf{F}}(t) = \mathbf{M}_0 \mathbf{Q} \Delta \ddot{\tilde{\mathbf{r}}}_M(t) + \mathbf{B}_0 \mathbf{Q} \Delta \dot{\tilde{\mathbf{r}}}_M(t) + \mathbf{K}_0 \mathbf{Q} \Delta \tilde{\mathbf{r}}_M(t). \quad (3)$$

Only simple matrix multiplications and additions have to be carried out on-line.

## 2.3 Fault models

Generally, each fault is represented by a mathematical model describing the relation between the fault parameters  $\boldsymbol{\beta}$  and the equivalent force  $\Delta \tilde{\mathbf{F}}(t)$ . Hence,  $\Delta \mathbf{F}(\boldsymbol{\beta}, t)$  is a mathematical expression for the time history of the forces acting on the individual degrees of freedom of the model. The fault vector  $\boldsymbol{\beta}$  contains information about the type, position and the magnitude of the fault. A selection of different fault models is briefly presented in the following.

### 2.3.1 Unbalance

A single unbalance  $u_n$  with the phase angle  $\delta_n$  acting on the rotor at position number  $n$  is replaced by the equivalent forces

$$\Delta F_{nh}(\boldsymbol{\beta}, t) = \Omega^2 u_n \sin(\Omega t + \delta_n) \quad (4)$$

$$\Delta F_{nv}(\boldsymbol{\beta}, t) = \Omega^2 u_n \cos(\Omega t + \delta_n) \quad (5)$$

at node  $n$  in horizontal and vertical direction respectively [8]. The equivalent forces on all other nodes are zero. Therefore, the fault parameters of the single unbalance are given by

$$\boldsymbol{\beta}_{unb} = [n, u_n, \delta_n]^T. \quad (6)$$

### 2.3.2 Rotor-Stator Rub

The main characteristic of rotor to stator rub is from NEWTONS law *action = reaction*, which means that during contact at any time the force the stator exerts on the rotor is equal to the force the rotor exerts on the stator. A simple fault model is therefore

$$\Delta F_i(\boldsymbol{\beta}, t) = -\Delta F_j(\boldsymbol{\beta}, t), \quad (7)$$

with  $i$  and  $j$  being the two node numbers of rotor and stator that are in contact. In [9] it has been shown that the forces between rotor and stator consist mostly of harmonics with 1/3, 1/2, 1 and 2 times the rotor speed. The equivalent forces are therefore approximated by

$$\begin{aligned} \Delta F_i(\boldsymbol{\beta}, t) &= A_{1/3} \sin(\tfrac{1}{3}\Omega t + \delta_{1/3}) + A_{1/2} \sin(\tfrac{1}{2}\Omega t + \delta_{1/2}) \\ &\quad + A_1 \sin(\Omega t + \delta_1) + A_2 \sin(2\Omega t + \delta_2) \\ \Delta F_j(\boldsymbol{\beta}, t) &= -\{A_{1/3} \sin(\tfrac{1}{3}\Omega t + \delta_{1/3}) + A_{1/2} \sin(\tfrac{1}{2}\Omega t + \delta_{1/2}) \\ &\quad + A_1 \sin(\Omega t + \delta_1) + A_2 \sin(2\Omega t + \delta_2)\} \end{aligned} \quad (8)$$

with the fault vector

$$\beta_{rub} = [i, j, A_{1/3}, \delta_{1/3}, A_{1/2}, \delta_{1/2}, \dots] \quad (9)$$

containing the number of d.o.f. being in contact as well as the amplitudes  $A_n$  and the phases  $\delta_n$  of the contact force.

### 2.3.3 Rigid Coupling Misalignment

In [10] it is shown that rigid coupling misalignment can be represented by equivalent loads (forces and moments) acting on the two neighbouring nodes of the misaligned coupling. Similar to unbalance the equivalent loads are rotating with the rotor shaft. A system of linear equations calculates the equivalent moments out of the misalignment geometry and vice versa. The fault vector

$$\beta_{mis} = [C, \hat{F}, \delta_F, \hat{M}, \delta_M] \quad (10)$$

contains information about the coupling node  $C$  and the absolute values  $\hat{F}$  and  $\hat{M}$  and phases  $\delta_F$  and  $\delta_M$  of forces and moments caused by the coupling misalignment.

### 2.3.4 Transverse Crack

The basic idea to model a transverse crack in a shaft is to consider the change of the cracked element's stiffness. For a breathing crack the change  $\Delta\mathbf{K}(t)$  of the rotor stiffness matrix depends on time or rotation angle, describing opening and closing the crack, [11]. The changed stiffness matrix of the cracked element is multiplied with the displacement vector  $\mathbf{r}(t)$  which yields in the equivalent force

$$\Delta\mathbf{F}_{cr}(\beta, t) = \Delta\mathbf{K} \mathbf{r}(t). \quad (11)$$

For estimating the crack depth  $a$ , the identified equivalent load  $\Delta\mathbf{F}_{cr}$  is approximated by a Fourier series,

$$\Delta\mathbf{F}_{cr} = \sum_{m=0}^3 \mathbf{c}_m \cos(m\Omega t) + \mathbf{s}_m \sin(m\Omega t). \quad (12)$$

The Fourier coefficients  $\mathbf{c}_m$  and  $\mathbf{s}_m$  depend on the crack depth  $a$  and properties of the undamaged system, [12]. The fault vector is given by

$$\beta_{cr} = [I, a, \mathbf{c}_m, \mathbf{s}_m] \quad (13)$$

with the indicator  $I$  determining the crack position, [13].

## 2.4 Least Squares Fitting in the time domain

A least squares algorithm is used to achieve the best fit between the measured equivalent forces  $\Delta\tilde{\mathbf{F}}(t)$  and the theoretical ones  $\Delta\mathbf{F}_i(\beta_i, t)$  produced by the fault models by adjusting the fault parameters  $\beta_i$  for all faults taken into account,

$$\int \left| \sum_i \Delta\mathbf{F}_i(\beta_i, t) - \Delta\tilde{\mathbf{F}}(t) \right|^2 dt = \text{Min}. \quad (14)$$

Starting from an initial guess, the least squares algorithm varies the fault parameters  $\beta_i$  of each fault model until the deviation is minimum.



## 2.5 Probability Measures

In [7] two probability measures have been introduced. The first probability measure  $p_1$  is the normalised correlation of the identified equivalent forces of a particular fault with the total of the measured equivalent forces for lag  $\tau = 0$ . It takes values between  $-1 \leq p_1 \leq 1$ , where  $p_1 = 1$  means that the particular equivalent force matches the total of measured equivalent forces perfectly.

The second probability measure  $p_2$  is an intensity that measures the contribution of the particular fault to the total of measured equivalent forces. The intensity measure takes values in the interval  $0 \leq p_2 \leq 1$ , where  $p_2 = 1$  signifies that the identified fault is the only one present in the rotor system.

## 2.6 Summary

Figure 1 shows the whole identification process. The measured vibration signals  $\tilde{\mathbf{r}}_M(t)$  are the input and the fault parameters  $\beta_i$  for each fault type are the output.

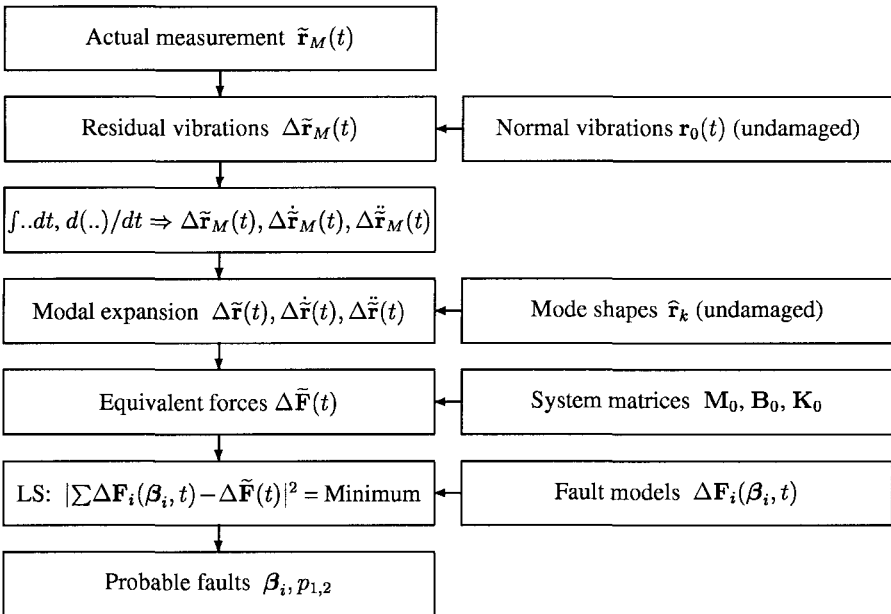


Figure 1: Flow Chart of the Identification Method

## 3 Validation

The effects of different modelling, measuring and identification parameters as well as disturbances and errors in the measuring signals on the identification results have been investigated by means of numeric experiments with a simple rotor system. In addition, the method has been applied on two real test rigs.

### 3.1 Numeric Experiments

The simple rotor system consists of a rigid foundation body and a flexible rotor carrying four rigid disks (figure 2). The foundation as well as the rotor are supported by linear springs and dampers. Gyroscopic effects as well as cross coupling terms between the two radial directions are neglected, so that the dynamic behaviour is characterised by only six degrees of freedom all being in the same direction, two for the foundation and four for the rotor.

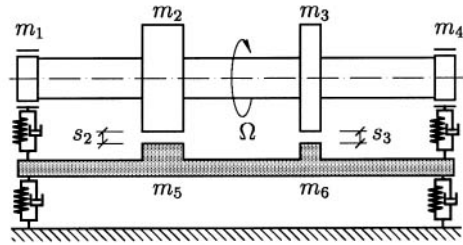


Figure 2: Simple Test System

The first mode shapes as well as the the corresponding natural frequencies and modal damping coefficients are shown in figure 3. The rotor speed was 9.5 Hz, which is between the second rigid body mode (mode 2) and the first bending mode (mode 3). During normal operation of the undamaged system two residual unbalances  $|u_{02}| = 50$  gmm and  $|u_{03}| = 100$  gmm excite the rotor at the middle disks  $m_2$  and  $m_3$ . Two faults were shown here exemplarily: additional unbalances at disks  $m_2$  and  $m_3$  and rubbing between disk  $m_2$  and foundation  $m_5$ . For these fault types, studies of different cases of various parameters effecting the identification process in the time domain are examined independently. The time window of the stationary measurements covers about 5 rotor revolutions.

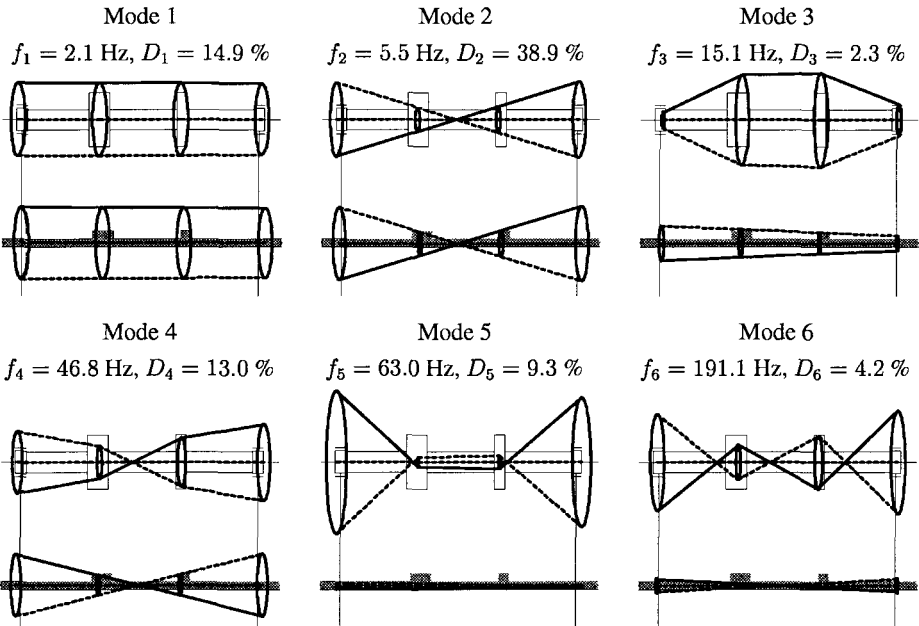


Figure 3: Mode Shapes and Modal Parameters

### 3.1.1 Identification of Unbalances

The additional unbalances  $|u_2| = 30$  gmm at  $70^\circ$  and  $|u_3| = 600$  gmm at  $230^\circ$  represent the additional faults at disk  $m_2$  and  $m_3$  which has to be identified by the described algorithm. The identified unbalances  $\tilde{u}_k$ , the corresponding probability measures  $p_j(u_k)$  as well as the relative errors  $\varepsilon_k$ , combining deviations relative to the dominating unbalance, are listed in table 1.

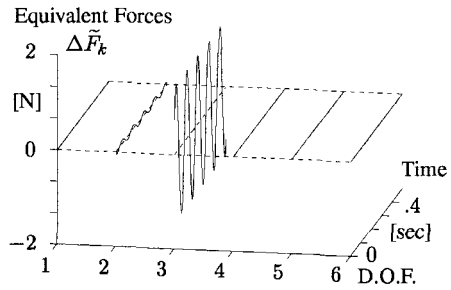


Figure 4: Equivalent Forces (Unbalance)

Test case 1: The time-histories of displacements, velocities and accelerations were exactly measured at all six degrees of freedom of the rotor-stator system; therefore modal expansion was not necessary. The identification algorithm was constrained to search only for unbalances at the correct positions at the two middle disks. Figure 4 shows the equivalent forces at all six degrees of freedom. The unbalances were identified exactly and the estimated equivalent forces match the two additional unbalances which exert on the rotor in reality.

Test case 2: Faults were searched for at all possible positions of the rotor system, even at the stator where no unbalances are expected to be identified. No effect on the results occurred.

Test case 3: The two fault types unbalance and rubbing were searched for simultaneously, although no rubbing existed. No effect on the results occurred.

Test case 4: The sample length of approximately 5 revolutions was reduced to a half a revolution. No effect on the results occurred.

Test case 5: The forced vibrations excited by unbalances were superimposed by free oscillations decaying with time. No effect on the results occurred.

Table 1: Results for Unbalance Identification

Nr.	Test Case Description	Identified Unbalances in gmm		Errors in %		Probability Measures in %			
		$ u_2 $	$ u_3 $	$ \varepsilon_2 $	$ \varepsilon_3 $	$p_1(u_2)$	$p_1(u_3)$	$p_2(u_2)$	$p_2(u_3)$
1	Reference Case	30	600	0	0	5.0	99.9	0.25	99.8
2	Searching at all Pos.	30	600	0	0	5.0	99.9	0.25	99.8
3	Searching diff. Faults	30	600	0	0	5.0	99.9	0.25	99.8
4	Short Sample Length	30	600	0	0	5.0	99.9	0.25	99.7
5	Transient Vibrations	30	600	0	0	5.0	99.9	0.25	99.8
6	Noisy Signals	29	600	0.01	0	4.9	99.8	0.11	99.9
7	Calibration Error	45	596	2.6	0.1	7.6	99.7	0.58	99.4
8	5 Sensors, 5 Modes	30	600	0	0	3.2	64.5	0.25	99.8
9	5 Sensors, 4 Modes	48	570	9.0	7.6	5.6	67.2	0.68	99.3
10	5 Sensors, 3 Modes	286	254	> 50	> 50	53.9	48.1	55.7	44.3
11	3 Sensors, 3 Modes	393	320	> 50	46.7	62.6	51.1	60.0	40.0
12	3 Sensors, 2 Modes	142	131	27.6	> 50	35.5	32.0	53.7	46.3

Test case 6: All measuring signals were falsified by band-limited noise. The standard deviation of the disturbances was about 2 % of the amplitude of the correct signal. Both unbalances were identified correctly.

Test case 7: A calibration error of 10 % at  $m_2$  and  $m_3$  was simulated. The dominating unbalance at  $m_3$  was identified correctly.

Test case 8: The accelerations were measured at five positions only. Modal expansion was applied to estimate the full vibrational state with the first five modes. The unbalances were identified exactly. However, forces at other positions were detected which lead to low probability measures.

Test case 9: The accelerations were measured at five positions only. Modal expansion was applied with the first four modes. The dominating unbalance at  $m_3$  was identified sufficiently.

Test case 10: The accelerations were measured at five positions only. Modal expansion was applied with the first three modes. The results became more inaccurate due to the low number of modes used for modal expansion.

Test case 11 and 12: The accelerations were measured at three positions only. Modal expansion was applied with the first three modes and with mode 2 & 3, respectively.

### 3.1.2 Identification of Rubbing

Between the disk  $m_2$  and the foundation  $m_5$ , the gap  $s_2$  was reduced. With the initial unbalance  $|u_{02}|$ , partial rubbing at this position occurred. Figure 5 shows that the equivalent forces fulfilling NEWTON'S law *action = reaction*. Studies were carried out for similar test cases as examined in chapter 3.1.1. Throughout the different test cases, the algorithm always searched at the only two possible contact locations at  $m_2/m_5$  and  $m_3/m_6$ .

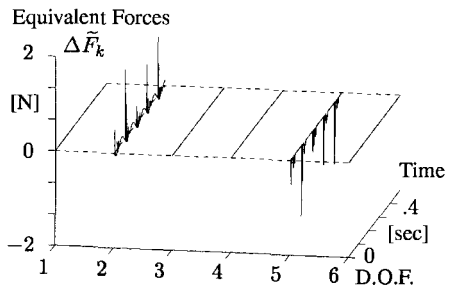


Figure 5: Equivalent Forces (Rubbing)

Table 2: Results for Rubbing Identification

Test Case		Max. Contact Force in N		Probability Measures in %			
Nr.	Description	$F_{2,5}$	$F_{3,6}$	$p_1(F_{2,5})$	$p_1(F_{3,6})$	$p_2(F_{2,5})$	$p_2(F_{3,6})$
1	Reference Case	0.056	0.000	18.1	0	100	0
3	Searching diff. Faults	0.056	0.000	18.1	0	100	0
5	Transient Vibrations	0.047	0.000	16.7	0	100	0
6	Noisy Signals	0.056	0.006	17.9	1.9	98.8	1.2
7	Calibration Error	0.057	0.001	17.8	0.3	100	0
8	5 Sensors, 5 Modes	0.039	0.022	1.4	0.7	79.0	21.0
9	5 Sensors, 4 Modes	0.033	0.017	2.8	1.1	86.3	13.7
10	5 Sensors, 3 Modes	0.019	0.029	4.6	4.8	48.3	51.7
11	3 Sensors, 3 Modes	0.029	0.030	0.8	0.7	51.2	48.8
12	3 Sensors, 2 Modes	0.033	0.042	12.6	12.6	50.1	49.9

### 3.1.3 Identification of Unbalance and Rubbing Simultaneously

Finally, the method was tested for identifying the faults unbalances and rubbing acting on the rotor system simultaneously. The gap  $s_2$  between the disk  $m_2$  and the foundation  $m_5$  was reduced. Additionally, the two unbalances  $|u_2|$  and  $|u_3|$  were applied. The algorithm searched on all possible locations for the two faults. Figure 6 shows the equivalent forces.

The dominating unbalance  $|u_3|$  was identified correctly. Rubbing only at  $m_2/m_5$  could be identified.

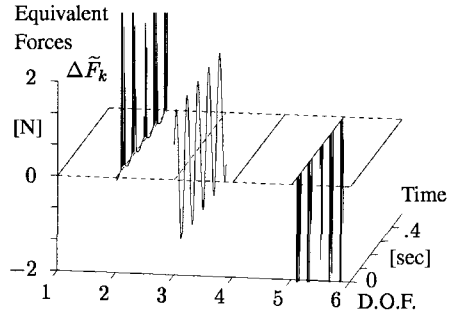


**Figure 6: Equivalent Forces (Unbalance & Rubbing)**

## 3.2 Application to Real Rotor Systems

The identification method was tested experimentally on two different test rigs which were built by POLITECNICO DI MILANO and DARMSTADT UNIVERSITY OF TECHNOLOGY within the Brite Euram project MODIAROT [14]. As an example, the investigated fault was an unbalance.

The identification method determined correctly the location of the fault at both test rigs by finding the largest equivalent force at the position where the fault was applied in reality. However, the identified magnitude of the unbalances differed from the actual applied unbalance due to the estimation via modal expansion. Small equivalent forces were estimated for other nodes not directly affected by the faults.

As for the test rig of the POLITECNICO DI MILANO, the equivalent forces were smeared over the entire system as a consequence of the approximation of the full vibrational state, which is represented by 188 degrees of freedom. However, only eight measuring positions and therefore a maximum amount of eight modes only could be used for modal expansion.

## 3.3 Conclusion

The model based identification method for rotor systems is able to determine the type and amount of the fault and to localize the position of the fault.

Generally, the reliability of the identification results highly depends on the properties of the mathematical model and of the measuring conditions of the rotor system. That means, on the one hand, the model needs to be very accurate. This can be achieved by a large number of degrees of freedom, because the identification algorithm avoids time-consuming numerical integrations and nonlinearities do not occur.

On the other hand, a sufficient number of measurement locations is essential for a successful identification of faults. As the validation shows, the higher the amount of measurement locations, the more accurate the estimation of the full vibrational state can be done. Using the vibrational state of all degrees of freedom of the rotor system without estimation via modal expansion, the identification process is able to identify the fault error-free.

## ACKNOWLEDGEMENT

The research project MODIAROT was partially funded by the European Community (Brite Euram III, BE 95 - 2015, Contract BRPR-CT 95-0022). The authors gratefully acknowledge Mr. Pedersen from the EC as well as the Partners in this project: N. Bachschmid (PDM, I), A. Zanetta (ENEL, I), J. Penny (Aston U, GB), I. Mayes (PowerGen, GB), M. White (NTU Trondheim, N) and S. Audebert (EDF, F) and their co-workers.

## REFERENCES

- [1] BRUEL & KJAER: Machine Condition Monitoring Using Vibration Analysis, A Case Study from a Petrochemical Plant. *Application notes BO 0163-11*.
- [2] BRUEL & KJAER: Permanent Vibration-Monitoring. *Application notes BG 0250-11*.
- [3] GLENDENNING, A., PENNY, J.E.T. and GARVEY, S.: Model-Based Condition Monitoring and Diagnosis in Turbo-Machinery. *Proc. of the 150th Anniversary Meeting*. IMechE, Birmingham, UK.
- [4] PENNY, J.E.T.: Model Based Diagnostics of Rotor Systems in Power Plants. *Project Program of the Brite Euram Project MODIAROT*, Be 95 - 2015.
- [5] MAYES, I. and PENNY, J.E.T.: Model Based Diagnostics of Faults in Rotating Machines. *Proc. 12th Int. Congress on Condition Monitoring and Diagnostic Engineering Management*. Sunderland, UK, pp. 431 - 440.
- [6] BACHSCHMID, N. and DELLUPI, R.: Model based diagnosis of rotor systems in power plants – A research program funded by the European Community. *Proc. 6th Int. Conf. on Vibrations in Rotating Machinery*. IMechE, Oxford, UK, pp. 50-55.
- [7] MARKERT, R., PLATZ, R. and SEIDLER, M.: Model Based Fault Identification in Rotor Systems by Least Squares Fitting. *ISROMAC-8*, Honolulu, Hawaii, March 2000.
- [8] BACHSCHMID, N. and DELLUPI, R.: Sub-task 4.1: Fault Representation: Unbalance. *Final Report of Brite Euram Project MODIAROT*, Be 95 - 2015.
- [9] BACH, H., MARKERT, R. and WEGENER, G.: Sub-task 4.8: Rotor to Stator Rub. *Final Report of Brite Euram Project MODIAROT*, Be 95 - 2015.
- [10] BACHSCHMID, N. and ZANETTA, G.: Sub-task 4.3: Rigid Coupling Misalignment. *Final Report of Brite Euram Project MODIAROT*, Be 95 - 2015.
- [11] AUDEBERT, S. and BACHSCHMID, N.: Sub-task 4.7: Model Transverse Crack. *Final Report of Brite Euram Project MODIAROT*, Be 95 - 2015.
- [12] BACH, H., BORK, H. and MARKERT, R.: Fault Determination for the Example of a Cracked Rotor. *ZAMM* 78, Sppl.1, pp. 241 - 242.
- [13] BACH, H. and MARKERT, R.: Determination of the Fault Position in Rotors for the Example of a Transverse Crack. *Structural Health Monitoring*, Edited by Fu-Kuo Chang, Technomic Publ. Lancaster/Basel (1997), pp. 325-335.
- [14] MARKERT, R., SEIDLER, M., BACH, H. and PLATZ, R.: Sub-task 7.1.1: Least Squares Fitting in Time domain. *Final Report of Brite Euram Project MODIAROT*, Be 95 - 2015.

# Failure root cause analysis applying vibrational diagnostics

U SÜDMERSEN, O PIETSCH, W REIMCHE, and D STEGEMANN

Institute for Nuclear Engineering and Non Destructive Testing, University of Hannover, Germany

## ABSTRACT

Slight changes of operational parameters, reconditioning or structural modifications to increase the efficiency of turbo machines can lead to unexpected effects in operation. In these cases the vibration levels often increase with non-stationary or non-linear behaviour and can even lead to unexpected shut-downs for reasons ranging from excessive wear up to severe system damage. The presented case studies demonstrate systematic approaches for monitoring vibration signatures that can be used to identify the root cause of failures, supporting the fast solution of operational problems and proving the success of preventative measures.

## 1 INTRODUCTION

Due to the liberation of international markets the economic success of companies in power generation and process industries depends on the availability, reliability and the efficiency of turbo-machines and related key components like pumps, fans, mills, etc. Therefore, most of them are equipped with condition monitoring systems that identify irregularities in the operational conditions by using vibration measurements. State of art is the threshold comparison of overall vibration levels in time domain and the limiting values of amplitude information at the harmonics of the rotating frequency (e.g. gear mesh frequencies, blade rotation sounds, balance and misalignment condition at 1<sup>st</sup> and 2<sup>nd</sup> harmonic of rotation), or certain machine specific mechanical and flow induced resonances (1, 2). Using the information from the complex vibration signals as an input to a computerized diagnostic system, the contents can be extracted more efficiently by analytical methods. The increased capacity of digital data acquisition and processing in combination with extended analysis techniques in time and frequency domain guaranty the transient, nearly on-line, evaluation of the vibration signatures even with fast operation changes. The combination of simplified models and actual vibration signatures as a tool of failure root cause analysis allows faults and unfavourable operation conditions to be identified

and verified at an early stage, while correlation with process parameters (e.g. temperature, flow, pressure, etc.) hints to the possibility of process optimization. Used as basic information and input to the plant managing system unnecessary inspections or unplanned shut-downs can be avoided. The visualisation of the actual vibrational conditions is of fundamental importance for the measurement technique and its results to be accepted by the technical and operational staff. This has often been neglected when implementing new features to supervision systems.

## 2 DATA ACQUISITION AND EVALUATION

For transient and stable operation conditions the vibrational signatures of the turbo-machines are determined by using the signals from the vibrational standard instrumentation with relative and absolute displacement as well as velocity pick-ups, extended by additional accelerometers in combination with adapted analysis techniques in time and frequency domain. Up to 64 channels with maximum sample rates of 50 kHz can be processed in parallel to determine high frequency flow or burst excitations, the signatures at the blade rotation sounds with their modulations, as well as low frequency resonances and rotor speed harmonics.

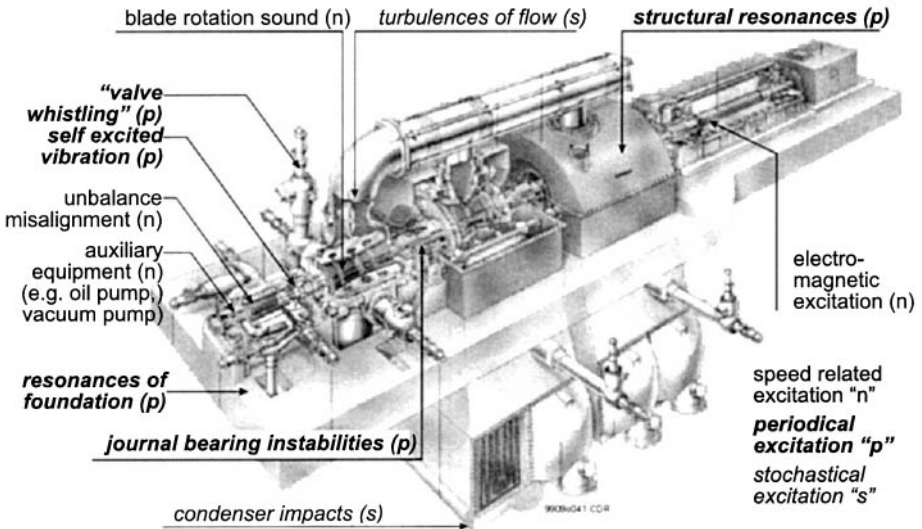


**Fig. 1:** General sources of excitation

The vibration signals in time domain are described by several statistical values, which quantify general information about intensities (e.g. standard deviation, variance), the signal's shape (e.g. kurtosis-, form-, crest-factor), as well as by the probability functions which fix the signal distribution. Using the trendsetting of these values and the correlation coefficient to determine similarities and their time dependent or operational related changes first hints to the necessity of extended investigations are obtained. Spectral functions, like the Power-Spectral-Density and the phase spectrum, classify the signal components by amplitude and phase relations describing the different excitation sources. Correlation analysis using the transfer function and coherence gives information about the signal transmission path related to the interaction of different machine parts, while cepstra and coherence analysis quantify the periodical information of spectra and coherence data by inverse Fourier transformation (3, 4). The correlation of the measured vibra-



tional characteristics with structural modelling allows the specification of single frequency components as well as the proof of excitation sources, while the parallel processed thermo-hydraulic parameters indicate the influence of operation control. Additionally, the phase information shows the interaction between single machine components, e.g. turbine, generator, foundation, auxiliary equipment, which generally can be subdivided by speed related excitations, periodically excited resonances of structure and flow, as well as stochastic components like mechanical and flow related friction (fig.1).

The following case studies should show examples of the use of vibration diagnostic techniques in combination with simplified analytical models to monitor machines in operation and for failure source localization. Attention should be given to the aimed visualization of measurement results to describe the actual condition of the machine, especially referring to the acceptance of the diagnostic technique by the plant's operational staff to get support based on their experiences and notifications during permanent operation.

### **3 EXCEEDED NOISE EXCITATION AT CONDENSER**

The presented case study shows one example of the efficiency of high frequency acceleration measurements for fast failure source localisation using standard analysis techniques in time and frequency domain. Due to change of law the fresh water pumps of a nuclear power plant had to be changed for operation with higher mass flow to reduce the maximum difference between fresh water inlet and outlet temperature. After the restart an increased noise level at one of the six condensers (K1-2) was detected at higher flow rates. As drawn in the fig.2 all condensers are supplied by one common pipe. Vibration measurements using additional accelerometers at different measurement positions should prove whether it was mechanically or flow induced and, hence, the source. Overall 16 sensors were fixed at the condensers themselves as well as on the outlet pipe system. Installed pressure transducers in the outlet tubes should determine pressure fluctuations.

Sample rates up to 50 kHz allow the separation of the excited frequency components during transient operation with different load changes, proving highest frequency pulse excitation inside the middle part of the outlet pipe of condenser K1-2. This could be concluded comparing the absolute values and shape of the acceleration signals at the housings and the outlet tubes. Visually, the acceleration signals in fig.2 show a relationship between the higher flow rate and the amount and amplitude of pulses in the acceleration signals, only obtained at the outlet tube of condenser K1-2. Spectra comparisons show additional broad banded peaks of structural resonances at frequency ranges up to 5 kHz, also during operation with lower mass flow. Increasing the flow rate the intensity of all broad banded peaks as well as the signal ground level at K1-2 raises significantly, while the spectra of acceleration for all other condensers (in fig.2 pointed out for K1-1) show only a broad banded increase of the signal ground level between 0.5 and 3 kHz related to the increased flow friction. If air is injected into the water at the single condenser inlets, the pulse excitation in the outlet pipe of condenser K1-2 decreases. The broad banded resonances disappear in the spectra. The signals ground level drops even below the condition at lower flow rates, which hints to cavitation in the outlet pipe of condenser K1-2.

Due to the fact that the absolute pressure values of all condensers are quite similar, and all outlet pipes are connected to a common cooling water discharge chamber, only higher velocity of the water within condenser K1-2 can be the reason for cavitation. The formation of vapour bub-

bles can only occur at the outlet of the condenser bundle or due to the sharp bend of the outlet pipe. Inside this pipe the pressure level increases and the steam bubbles collapse exciting the high frequent structural resonances as visible in the acceleration signals by high frequent pulse excitation in the middle and lower part of the outlet pipe. The measurement results exclude loose condenser parts as an excitation source as supposed first and proved by correlation analysis which show significant common signal information between the acceleration signals at the middle and lower measurement position at the outlet pipes. No common information is obtained between the acceleration signals on the condenser side walls and the outlet. For all frequency components the coherence values are zero.

Assuming that all condensers were just cleaned the resistance of flow should be equal. Therefore, the reason for different flow rates must be related to the design of the condenser arrangement as schematically drawn in the upper part of fig.2. The fresh water supply is achieved by one common pipe with a 90° bend just in front of condenser K1-1 and K1-2 (less than five times the tube diameter). The inlet pipe of condenser K1-1 is within the dead wa-

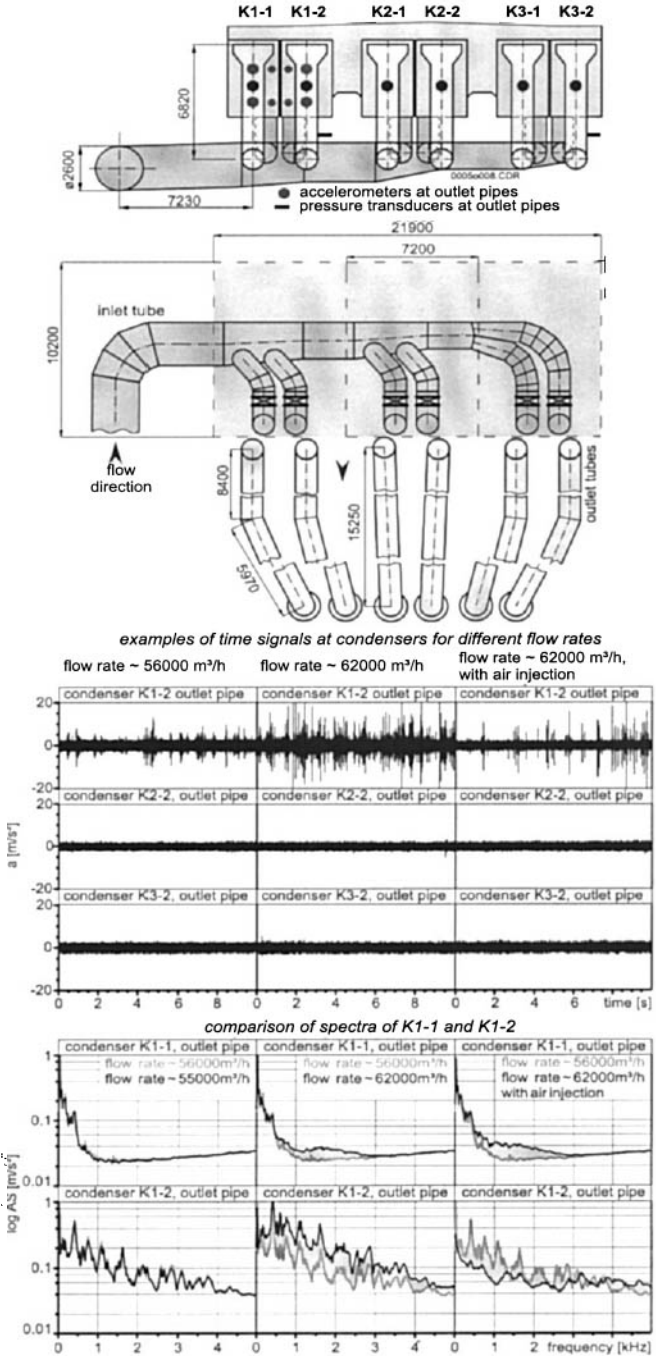


Fig. 2: Cavitation in condenser arrangement

ter area behind the 90° bend. Additionally the reduced diameter of the supply pipe behind the inlet of condenser K1-2 increases the flow resistance at this position. Later FE-simulations of the pressure fluctuation and the corresponding local flow velocities as well as the vector field of flow within the inlet tube prove the result derived from the vibrational behaviour. The local velocity fields show quite well the difference between condenser K1-1 and K1-2 as well as for condenser K2-1/K2-2 related to the undesirable geometrical properties of the condenser inlet, just visible for the smaller flow rates. If the flow rate increases, the effect is emphasized, and dependent on the temperature conditions of the fresh water also the condenser K2-2 can reach operation conditions similar to that ones of K1-2. As a result of the abrasive consequence of the collapsing bubbles the protective coating has to be inspected more frequently. Concluding that maximum flow occurs through condenser with less turbulence in the inlet area, i.e. through condenser K1-2 rather than K1-1, K2-2 rather than K2-1, this effect can be avoided by straightening the flow pattern after the bend by using additional baffle blades.

Further case studies are available using aimed acceleration measurements for failure source localisation at fans and pumps where rolling element bearings showed wear far before reaching their nominal life time (5). The comparison of the vibrational behaviour at several identical units supports to implement condition-based maintenance programmes (6), while measurements at new machines shortly after start-up prove design and operational problems (7).

#### 4 MECHANICAL AND THERMAL MISALIGNMENT

The extension of analysis and visualisation tools using already installed vibration sensors, additional implementing time synchronous multi plane data acquisition and processing, often fit to determine the influences of reconditioning and operational changes as demonstrated by the following example. After maintenance, new alignment, and increasing the efficiency by changing the LP-parts of a 920 MW steam turbine the  $S_{\max}$ -values of relative shaft displacement showed quite high levels, with additional load and time dependencies. Related to the requirements of electrical consumption the operation is characterized by a large number of shut-downs and start-ups during which the vibration amplitudes at the bearing blocks at critical speeds were quite unstable, often reaching values far above the shut-down criteria. Balancing the HP-, IP-, and LP-parts as well as the generator did neither fix nor solve the problem. In one case, after balancing the LP-parts, the condition got even worse, and the machine could not start-up, until the additional weights were removed again. Balancing the generator with weights of more than 1 kg showed no effect to the rotor speed harmonic component, but became visible at increased higher harmonics.

An additionally installed vibration monitoring system allows the multi-channel parallel processing of all shaft and bearing vibration signals, extended by accelerometers at certain measurement positions to detect rubbing events (7). The complex behaviour of the rotor system should be described, looking for indications of the source of the machine's extraordinary operating conditions. The relative shaft displacement and the corresponding bearing block vibration at nominal load condition are presented in fig.3. For visualization of the dynamical rotor behaviour the kinetic wave paths are drawn as 3D-diagrams with an imaginary rotor axis. Connecting the synchronous points of the orbits the dynamical rotor displacement is obtained, which in combination with the shaft sweep give hints to the alignment condition. The parallel data processing allows to assess the phase relation of the rotor excitation and the mechanical response of the bearings.

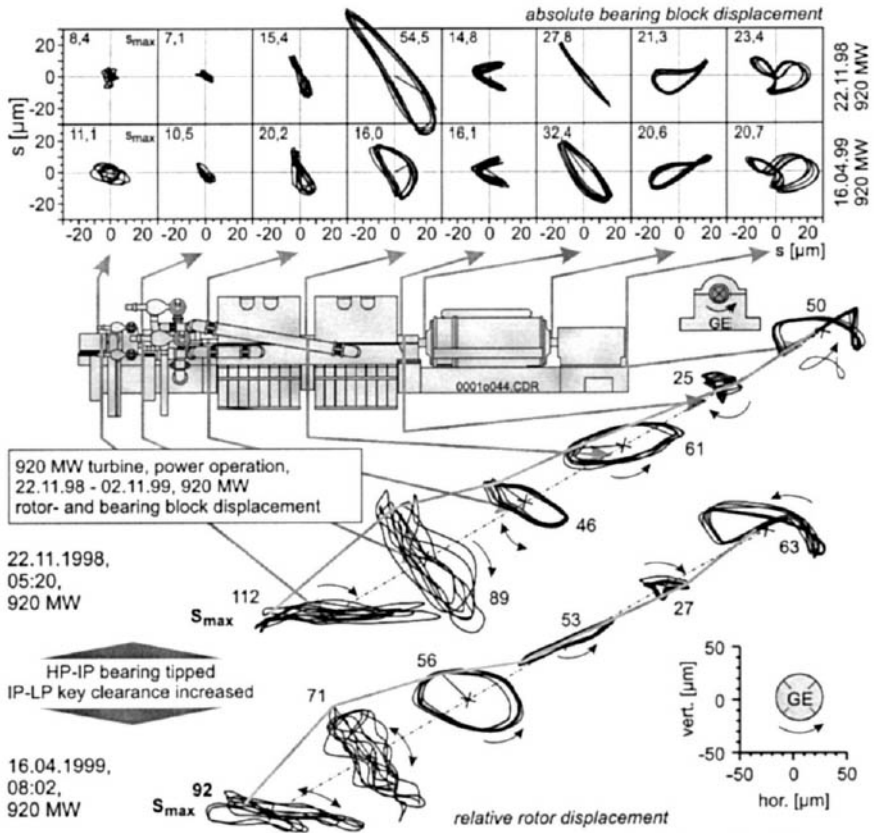


**Fig. 3:** Orbits and kinetic wave paths at power operation of a 920 MW turbine

Directly after start-up and at low loads all shaft displacements show elliptical kinetic wave paths, with nearly 90° compounding maximum values at HP-, HP-IP-, and IP-LP1-bearing and counter rotation of rotor sweeps inside the HP-IP-bearing hinting to some alignment problems. Similar vibration signatures are obtained at the LP2- and GE-bearing. Due to at that time missing displacement pick-ups in the two GE-bearings the non ideal alignment between turbine and generator is concluded by observing the form and phase angle of absolute bearing displacement to the corresponding neighbours. At increased load the phase angle of the  $S_{max}$ -values stay stable, while the elliptical kinetic wave paths within the first three bearings collapse with superimposed stochastic excitations in direction of  $S_{max}$ .

Additional to alignment problems this signature hints to thermal related compulsive forces inside the first three bearings, which also influence the bearing vibration between the LP1-LP2-part. The reactive moment of increased axial forces tipped the concrete key of the IP-LP1-bearing, which is the turbine's fixing point. Installed accelerometers at the turbine parts and the bearings showed high frequency pulse excitations with speed related modulations in the axial direction. The additional axial forces became also visible at increased wear on the mutually displaced pair of keys, which fix the axial bearing between HP- and IP-part. The flat kinetic wave path as well as the orbital bearing vibration between LP1-LP2 hints even here to forced circular

tion and unexpected shaft bending. The sensibility and instability of the complex rotor system to small changes of operational parameters become also visible comparing the vibrational signatures during several shut-downs. The tightly constrained condition of the rotor within the first three bearings is proved by the dynamical behaviour of the rotor system during shut-down, where the curve of wave paths inside the HP-bearing show extreme sweep curves with only one main deviation as well as for the absolute LP1-LP2-bearing vibration. The instability of the system becomes visible comparing different shut-downs with only slight differences in temperature conditions (shut-down from full and partial loads) with changes of maximum values at critical speed of more than 100%. At the turbine's fixing point, the IP-LP1-bearing, in certain cases maximum bearing vibrations above values of  $200\mu\text{m}$  were measured at critical speed of 1085 rpm, while the corresponding shaft vibrations collapse to a slim line with a sudden phase jump, hinting to rubbing events (fig.4, right side). To classify single events, combined visualisation of the complete shut-down process with all critical speeds as well as „single rotations“ and the actual rotor position inside the bearings are required as exemplarily presented in fig.4.

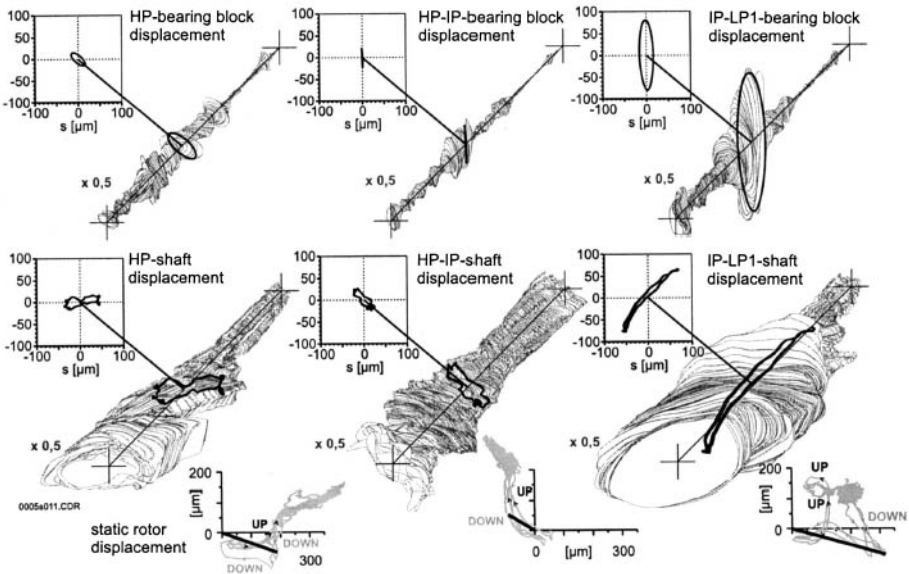


**Fig. 4:** Vibrational behaviour during transient operation and critical speed (1085 rpm)

The absolute values of misalignment can be estimated by the stationary shaft displacement within the bearings, fixed by the DC-values of the displacement pick-ups as drawn in the bottom of fig.4 and in fig.5 for one start-up, followed by one week of load operation, and one shut-down. As made visible, the rotor inside the HP-bearing moves with increased speed to the right side, in the HP-IP-bearing to the left-hand side, and inside the IP-LP1-bearing again to the right-hand side proving alignment problems of the system. After five days of operation the stationary rotor displacement during shut down dropped down to the same level as at start-up. Due to the fact that the absolute position of the shaft inside the bearings cannot be determined exactly using the DC-values of the displacement pick-ups, the measurement must be calibrated by fixing the zero position. In the case of fig.5 the slow motion during turn drive with a pre-heated turbine is compared with that one with cold turbine parts. The misalignment between the first three bearings became visible, too.

The temperature related shift of the zero position for each bearing hints to the influences on the vibrational behaviour by the foundation. While for most bearings a vertical dislocation can be stated, the HP-IP-bearing shows mainly a horizontal one, related to a horizontal tipping of the concrete key as proved later on by mechanical measurements with dial gauges. By tipping the HP-IP-bearing to reduce the misalignment in combination with increasing the gap of the radial keys at the IP-LP1-bearing, which is the turbine's fixing point, the absolute vibration levels in the HP- and HP-IP-bearing dropped down slightly visible at the orbits in fig.3. The sensitivity of the system against alignment changes becomes obvious by the reduction of the maximum LP1-LP2-bearing vibration from 55 to 16  $\mu\text{m}$ . Further investigations at the HP-IP-bearing are required to solve the operational problem, related to a plant shut down of several weeks. The complex measurement results implicate several excitation sources which influence the actual condition of the machine.

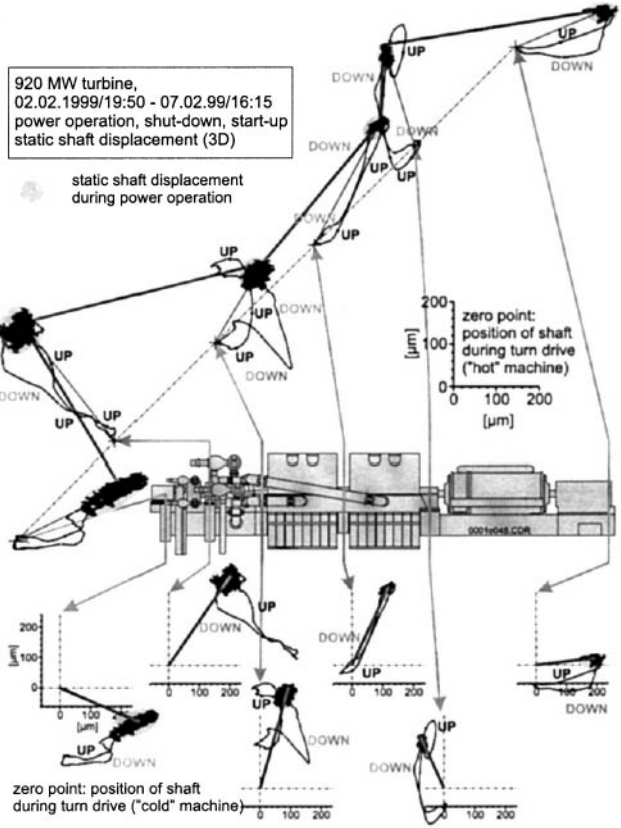


**Fig. 5:** DC-components of shaft vibration (3D)

Easily to perform statistical evaluation of vibration signatures and the correlation with related operational parameters like electrical power, exciter current, certain temperature conditions of structure elements (7), and the steam parameters often hint to excitation sources, too. One example is presented in fig.6, where the maximum values of rotor displacement and velocity at the bearings are drawn as function of exciter current. Near to the determination of load dependencies within the single measurement planes, including threshold comparison of the absolute vibration values to the standards, the parabolic behaviour of the maximum rotor displacement in the exciter bearing hints to superimposed mechanical and thermal unbalance. The increase of the exciter bearing vibration with a squared proportionality to the exciter current supports the statement that the excitation source is related to unsymmetrical heat dissipation. Levels of relative shaft vibration up to 150  $\mu\text{m}$  in the generator bearings are not tolerable for permanent operation. The nearly linear behaviour with only slight dependencies on the exciter current and frequency analysis proving the unbalance component as main excitation source shows the re-

quirement of further generator balancing. By using the installed vibration pick-ups with advanced data visualisation the success of investigations to increase the security and range of efficiency in operation could be tested directly, also giving hints to further requirements.

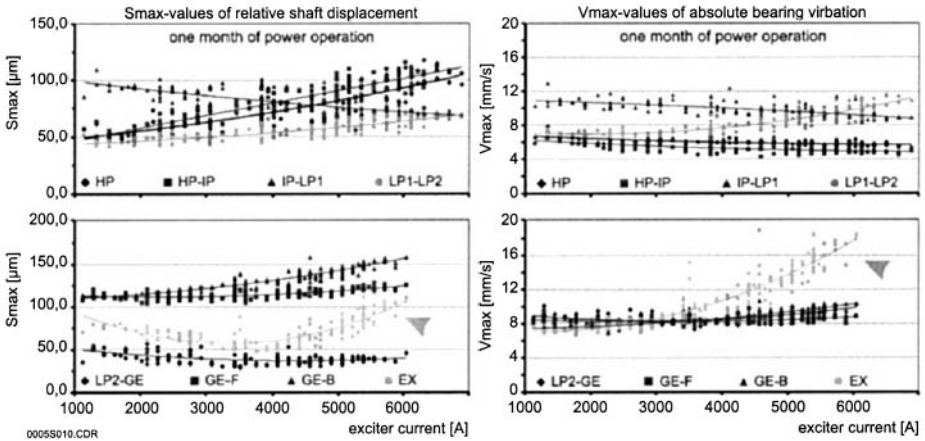


Fig. 6: Relation between exciter current and maximum vibration values

## 5 SPARKING OF A BRUSH HOLDER AT THE EXCITER

Failures or unfortunate conditions of rotating machine components or mechanical parts in contact to them, can be characterised by the intensity and amount of higher harmonics of the rotating frequency in the vibration signals. For classification purposes this information has to be quantified in single values, calculated by the cepstrum for a single vibration signal and by the coherence looking for common periodical components in two signals for source localisation as presented in the next example. After reconditioning the brush holder P at the exciter of a 350 MW steam turbine generator showed increased sparking. Regrinding the relevant rotor areas as well as additional pre-load of the brush led only to short time improvement.

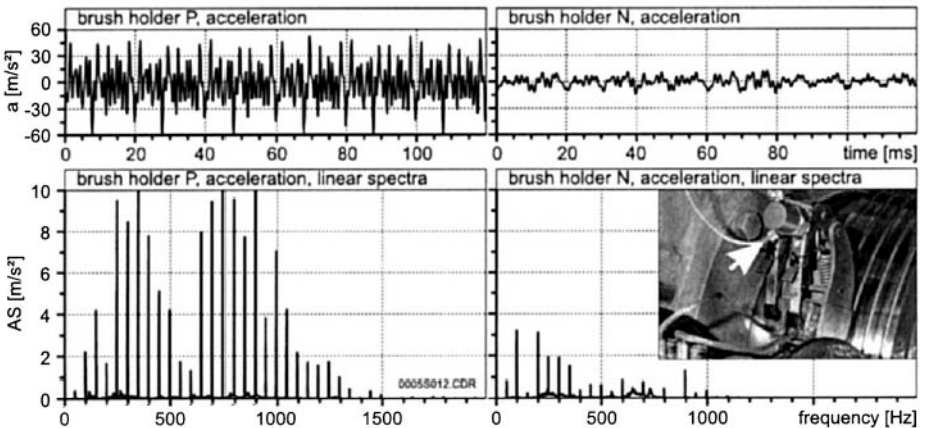
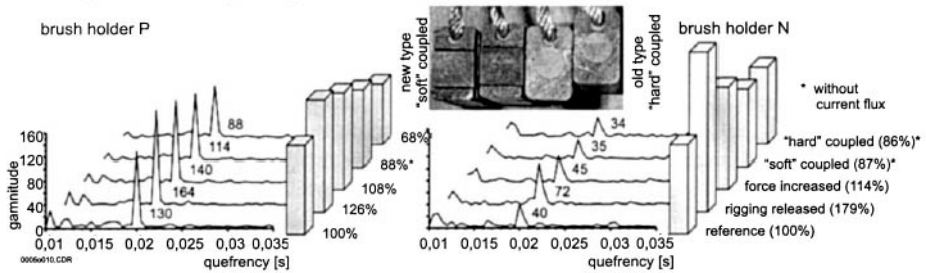


Fig. 7: Acceleration signatures at the brush holders

Unambiguous dependencies between the spark development and different operation conditions was not proven. Therefore, additional accelerometers were installed on the brush holders which should give an indication of the influences of electrical load changes, variation of additional pre-load, and changes of brush stiffness due to mechanical rigging. Correlation analysis of the vibrational behaviour of the structural components nearby, the rotational excitation of the rotor itself, and the related bearing block should prove excitation sources and describe the signal transmission paths. The comparison of the time signals in fig.7 shows clearly increased high frequent acceleration at the brush P, proved as mainly speed related excitation by the narrow banded peaks of the high frequent linear amplitude spectra.



**Fig. 8:** Cepstrum gamnitudes at different operation conditions

The broad banded peaks of the low frequency logarithmic spectra in fig.9 describe structural resonances, which are superimposed by the narrow banded rotational components. In cases of these interferences slight changes of operational conditions, e.g. the alignment condition, the run-in-effect of new brushes, etc., could lead to considerable amplitude modulation initiating brush sparking. Correlation analysis hints to axial resonances of the exciter casing where the brush holders are welded.

For automatic supervision the visual impression of the acceleration time signals and the spectral intensities has to be quantified by single values. With standard deviations of 30 to 6.6 m/s<sup>2</sup> the integrated dynamical components are ~ 4.5 times higher at the P-brush than at the N-brush. The quotient 3.25 of cepstrum gamnitudes at the rotating quefrequency (20 ms) in fig.8 classify the information as mainly speed related. Comprehensively the single investigation of changing the operational parameters like the increased pre-load, the brush type, and load changes showed mainly slight influences to the vibrational behaviour, as quantified by the cepstrum gamnitudes. Main influences are obtained by additional rigging of the exciter casing, as shown in the photo of fig.9.

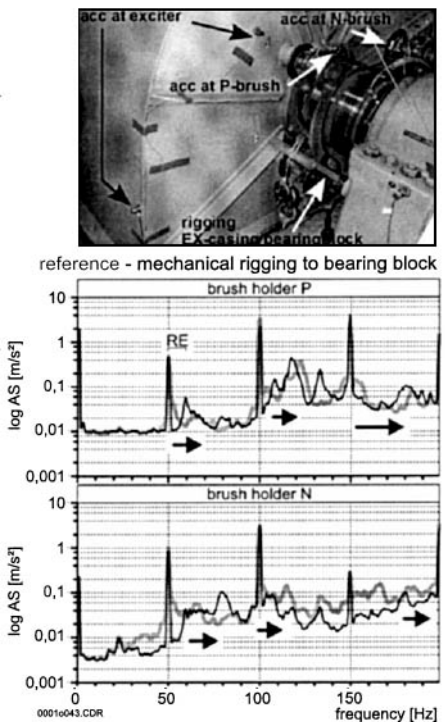


**Fig. 9:** Frequency shift of resonances

The stiffening of the mechanical system by axial rigging the exciter to the bearing block leads to a postponement of the structural resonances



which are superimposed with rotational harmonics, shifting from frequency ranges of 50 to 60 Hz, from 100 to 105 Hz, and from 150 to 180 Hz (see amplitude spectra fig.9 at brush P). Here-with it concerns obviously mainly axial excitation sources, proved visually through retroactively installed accelerometers at the exciter casing and coherence analysis, quantified by the corresponding coherences. A structural stiffening at the axial part of the exciter housing is recommended therefore. Up to the next shut-down permanent monitoring of the acceleration levels and the spectral components should avoid unexpected sparking.

## 6 SUMMARY

The experiences obtained by monitoring several machine arrangements in power plants as well as production industries prove the successful use of aimed vibration monitoring for fast failure source localization and process optimization at machines in operation. Most installed vibration monitoring systems serve for threshold comparison and alarm monitoring. To get the alarm is state of art, to quantify and classify the obtained information is the second step implemented in modern process control systems (2, 3). To fix the excitation source and to develop reaction strategies with short time delay proving the success of actions still requires certain expert knowledge. As proved by several industrial projects the interlink between vibration analysis with the process parameters realises a fast and reliable tool for condition-based description of machines in operation.

Aim of all investigations is to realize a partial share for the economic/ecologic production within an optimized production process and high performance availability. Therewith, the plant management system, the possibilities of supervision and the condition-based maintenance must be interlinked, combining the tools of advanced data processing, evaluation, documentation and data visualization as one of the most important point of view for system acceptance by the operational staff.

## REFERENCES

- 1 N.N., VM 600 - An Integrated Condition Monitoring System for Turbomachinery, VibroMeter SA, Fribourg, Switzerland
- 2 N.N., Vibrocam 5000 - Methods, Application and Solution for Conventional and Vibration Diagnostic Condition Monitoring of Turbo-Sets in Power Stations and Industrial Plants, Carl Schenk AG, Darmstadt, Germany
- 3 Randall, R.B., 1987, Frequency Analysis, Brüel & Kjaer, Denmark
- 4 Silvia, D.S., 1996, Data Analysis, A Bayesian Tutorial, Rutherford Appleton Laboratory and St. Catherine's College Clarendon Press, Oxford, U.K.
- 5 Schüler, J., Südmersen, U., Runkel, J., 1994, Failure Diagnostics by Vibration Analysis at Fresh-Water Pumps, CETIM, Senlis, France
- 6 Südmersen, U., Stegemann, D., Camerini, C., 1992, Vibration Analysis in Predictive Maintenance of Oilpumps, 13<sup>th</sup> WCNDT, Sao Paulo, Brasil
- 7 Südmersen, U., Liu, Y., et.al., 1998, Vibrational Diagnostic of Rotating Machinery in Power Plants, ISROMAC-7, Honolulu, USA

*This page intentionally left blank*

# A measurement method for automotive creep groan induced vibration with data processing and analysis

M BETTELLA and R S SHARP

School of Mechanical Engineering, Cranfield University, UK

## ABSTRACT.

The automotive creep groan phenomenon is described. The occurrence of creep groan in a luxury saloon car has been studied in detail. Running conditions have been varied widely to determine the effects. A measurement and recording system devised specifically for the work is described and results are processed to yield frequency data and orbital motions. The results represent a substantial advance in knowledge of the detailed nature of the phenomenon and of the participation of component parts of the system. They have been applied to the design of a laboratory rig, which is currently under construction and which will allow better access and control than possible on the test car.

## 1. INTRODUCTION.

Creep groan specifically refers to unpleasant vibrations, generated by road vehicle braking systems, occurring at very low speeds. No clear and definitive explanation for it has yet been given and now it is of commercial significance, since the loss of refinement and acoustic comfort introduces substantial risk of customer dissatisfaction. This is an issue with many modern cars, but in particular is relevant to luxury cars, where automatic transmission is a common feature and customer expectations, especially about noise and vibration quality levels, are very high. Creep groan is a vibration phenomenon that may arise whenever there is the need to keep the car steady and – at the same time - some forces are acting on it. The typical picture is a traffic light or queue situation faced by an automatic transmission car, in which engine and driving wheels are not completely disconnected through the clutch, but always coupled by the hydraulic torque converter. Whenever the driver is applying only a light pressure on the brake pedal, a vibration cycle, involving brake components (such as caliper and pad) and the suspension may take place. Unpleasant sound emitted by conventional brake pads can be classified into three types, depending on their frequency, as in table 1 (Mibe [9], Nack [3] and Lee [8]). The one known as creep groan is the first in the table, occurring during starting and stopping manoeuvres (0-2 km/h). This low pitch (base frequency most often less than 100 Hz, but sometimes up to 300 Hz) “groaning” sound, whose resonance system is the suspension, is generated by self-excited vibration arising on

the friction surface between brake pads and the rotor. According to the low frequency range involved in creep groan, brake components are supposed to behave as rigid bodies.

**Table 1: Classification of brake noise**

Noise Type	“Groan”	“Moan”	“Squeal”
Frequency	Around 100 Hz	Around 100 Hz	2 to 20 kHz
Car Speed [km/h]	0 to 2	10 to 30	> 10
Condition	Starting/Stopping	Deceleration	Deceleration
Source	Pad and Rotor	Pad and Rotor	Pad and Rotor
Resonance System	Suspension	Suspension	Brake Components

The vibration cycle has been monitored through accelerometers and a sound pressure level meter. Creep groan tests were run in several configurations; pulling the car through its own engine or placing it on an inclined surface and letting it move under gravity; groan events were recorded with the car on its own four wheels or jacking up one rear suspension and braking the free hub (without any wheel or tyre). The measurement environment was aimed at understanding the nature of this kind of self-excited vibration, the motion of the system components and which ones are prone to groan noise generation. Front and rear suspensions behave somewhat differently and the contributions of tyre torsional stiffness and inertia have been appreciated. The creep groan cycle is not sensitive to car motion direction and no differences can be recognised between vibration occurring throughout recorded events with the automatic transmission set to “Drive” or “Reverse” state. Two different phases in the phenomenon were distinguished; an earlier and chaotic one, in which the phenomenon is friction-driven, followed by a period where some system natural frequencies are excited. The paper will describe the measurement system, the data processing and the results, drawing conclusions about the creep groan vibration cycle.

Creep groan can occur at either front or rear axle, driving the car through its engine power or during an attempt to stop the car on an inclined surface. This implies that the power train is not contributing or affecting noise generation. The estimate of the braking torque value involved in the creep groan phenomenon leads to the same picture considering either the engine-driven or the slope-driven case. In the first situation, with the engine pulling the vehicle:

Idle torque (engine)	$t_{eng}$	43 to 67 Nm
Ratio (1 <sup>st</sup> gear)	$\tau_1$	3.571
Ratio (axle)	$\tau_a$	3.06
Idle torque (rear axle)	$t_{ra} = \tau_1 \tau_a t_{eng}$	470 to 730 Nm

The driving torque ( $t_{ra}$ ) pulls the car through the rear axle and, whilst brake pressure is applied, brake torque acts on each of the four brake discs. Symbols  $t_{groan\_f}$  and  $t_{groan\_r}$  refer to brake torque applied to a single disc (front or rear axle respectively) during groan noise emission. A braking effort distribution of 60% on the front wheels is assumed.

$$t_{groan\_f} = \frac{1}{2} 0.6 t_{ra} \approx 140 + 220 \text{ Nm}$$

$$t_{groan\_r} = \frac{1}{2} 0.4 t_{ra} \approx 100 + 150 \text{ Nm}$$

Imagining the car on a  $5^\circ$  slope, the driving torque  $t_{ra}^*$  (star symbol for the gravitation effect due to the inclined plane) can be estimated as:

$$t_{ra}^* = m g h \sin \alpha \approx 770 \text{ Nm}$$

where  $m = 1800 \text{ kg}$ ,  $g = 9.81 \text{ ms}^{-2}$ ,  $\alpha = 5^\circ$  and the height of the centre of mass is  $h = 0.5 \text{ m}$ . Hence the relationship  $t_{ra}^* \approx t_{ra}$  (the torque due to gravitation on a  $5^\circ$  slope is similar to the torque pulling the car with the engine in idle condition). This allows to estimate the brake torque applied on a single brake disc, while creep groan vibration is generated, in the range of 100 to 200 Nm.

## 2. DATA ACQUISITION ENVIRONMENT.

The aim of the acquisition system has been focused on measuring acceleration levels of brake and suspension components and includes a sound pressure level meter located at the driver's ear position. The system is based on a notebook computer connected to a 16-channel digital acquisition system including anti-aliasing low-pass filters. The transducer set presently includes four triaxial piezo-accelerometers, three single axis piezo-accelerometers and one microphone, as illustrated below.

Analog to digital converter: IOTECH Daqbook/200

A/D resolution: 16 bit

Signal conditioners: 4 x IOTECH DBK18 Low-Pass Filter Cards

Input Connections: 4 BNC connectors per card.

Voltage Input Range: 0 to  $\pm 5 \text{ V DC}$

Low-Pass Filter: 3-pole active Butterworth, 1 kHz (-3 dB)

Single Axis Piezo-Accelerometers:

Endevco 61A-100, Sensitivity: 100 mV/g, Range:  $\pm 50 \text{ g}$ , Frequency Response ( $\pm 5\%$ ): 1 to 2000 Hz; Quantity: 2

Endevco 2256A-100, Sensitivity: 100 mV/g, Range:  $\pm 50 \text{ g}$ , Frequency Response ( $\pm 5\%$ ): 1 to 10000 Hz; Quantity: 1

Triaxial Piezo-Accelerometers:

Endevco 63A-500, Sensitivity: 500 mV/g, Range:  $\pm 10 \text{ g}$ , Frequency Response ( $\pm 5\%$ ): 1 to 2000 Hz; Quantity: 1

Endevco 63B-100, Sensitivity: 100 mV/g, Range:  $\pm 50 \text{ g}$ , Frequency Response ( $\pm 5\%$ ):

1 to 2000 Hz; Quantity: 1

Endevco 63A-100, Sensitivity: 100 mV/g, Range:  $\pm 50$  g, Frequency Response ( $\pm 5\%$ ):

1 to 2000 Hz; Quantity: 2

Microphone: Bruel&Kjaer sound pressure level meter.

### 3. ANALYSIS OF A CREEP GROAN EVENT.

#### 3.1 Rear Suspension.

Standard equipment for the rear wheel drive saloon car are steel single piston floating calipers. One part of the caliper is bolted to the hub-carrier, the second one is allowed to translate horizontally and parallel to the wheel rotation axis (y axis in Fig. 1), guided by two steel pins coated with rubber insulation. When hydraulic pressure is applied, the inner pad is pushed against the internal side of the brake disc while the caliper floating component pushes the outer pad toward the external side of the disc.

Fig. 1 illustrates the location of the sensors on the rear suspension components: piezo-accelerometers are located on outer pad, brake caliper and hub carrier. The microphone was located inside the cockpit, at the driver's ear position. The car was operated by its own engine on a flat surface, with automatic gear in "Drive" state. It was allowed to creep forwards by releasing slightly the pressure on the brake pedal. With the car in this condition it was not very difficult to obtain the generation of a continuous groan noise lasting up to two seconds. Whenever the driver increases or reduces the force on the pedal, the car comes to a complete stop or it is allowed to move faster and the creep groan noise ceases. In normal conditions, without tuning the foot pressure on the brake pedal in order to intentionally sustain the noise production and make the vibrations last longer, at the end of the groaning phase the car has advanced only about one quarter of a full wheel revolution. No considerable differences were appreciated in the backward motion of the car, occurring exactly in the same way but with the automatic transmission set to "Reverse".

Data were recorded at a sampling rate of 3 kHz and filtered with the IOTECH on board anti-aliasing low pass filters set to 1 kHz (-3 dB). Figs 2a, 2b, 2c and 2d represent the time domain plots of the acceleration measured on the brake pad (horizontal direction), caliper (horizontal and vertical) and hub-carrier (vertical) respectively. The distinction between the creep groan phase and the rest period is very clear; acceleration levels suddenly increase from the very low amplitudes caused by the running engine perturbation and, after about 1.5 second, dramatically drop. Less than a second later another creep groan event has been recorded: it is easy to note that in the first and the second cases, acceleration amplitudes reach very similar levels. Table 2 summarises acceleration peak levels on each transducer and root mean square velocity (high-pass filtered above 5 Hz) as well. The power radiated by a vibrating surface (Cremer [2]) is  $P = \rho c S \tilde{v}^2$ , where  $\tilde{v}$  is the root mean square velocity. Figs 3 and 4 respectively show the frequency domain analyses and coherence function estimate; the signals were divided into sections 512 samples long (resulting in 0.17 second time intervals). Each was detrended and then the average was calculated. Coherence diagrams were evaluated between each channel already plotted in the time domain, Fig. 2, with the sound pressure level meter output taken as reference. Engine idle revolution velocity (that keeps almost a constant rate during the generation of the brake groan vibration) is around 800 rpm

(corresponding to 13.3 Hz) and the base V8 four stroke cycle frequency is 53 Hz. Hence, the harmonics that will be discussed further are not related to engine effects. Fourier analyses of brake components highlights the presence of a peak at 126 Hz, that is distinctive throughout the four plots (Fig. 3), from the pad to the hub-carrier. Caliper diagrams indicate the occurrence of multiple tones of this base frequency (Figs 3b and 3c, 252 and 378 Hz). Coherence plots (Fig. 4) show the correlation between component accelerations and the noise. Coherence between hub-carrier and the sound is high in the low frequency range of the spectrum and shows reasonable peaks in correspondence of 126 Hz (already noted in the power spectral density function) and at half of it, 63 Hz. The same analysis on the pad motion returns very similar results; on the contrary, correlation between caliper vibration and the recorded sound does not reach high values, except for some very small frequency ranges, including the already mentioned 126 Hz line.

**Table 2- Rear suspension measured vibration levels.**

<b>Location and direction</b>	<b>peak-peak acceleration [ms<sup>-2</sup>]</b>	<b>acceleration rms [ms<sup>-2</sup>]</b>	<b>velocity rms [mm s<sup>-1</sup>]</b>
Pad-y	35	3.5	4.8
Hub carrier-z	24	2.0	2.3
Caliper[CAL1]-x	35	3.5	2.2
Caliper[CAL1]-y	30	4.2	3.0
Caliper[CAL1]-z	90	11.0	7.5
Caliper[CAL2]-x	15	2.0	1.3
Caliper[CAL2]-y	40	4.8	4.9
Caliper[CAL2]-z	80	9.2	8.3

The present overview and table 2, which illustrates mean square velocity levels of the components, lead to the concept that friction interaction between brake pad and caliper is the source for the vibrations. The relevant frequency band for our investigation is around 100 Hz and radiation efficiency makes large surfaces much more prone to low pitch sound emission. This implies that noise emission is mainly due to suspension arms and possibly the disc, and only a minor contribution is arising from the brake caliper (according to coherence estimate). Coherence and Power Spectral Density highlight a system behaviour which concentrates energy in a few narrow frequency bands; but this is true only during the centre interval of the creep groan event, when some structural natural modes are being excited. Fig. 5 below illustrates how the system evolves during the slow speed brake manoeuvre. The sliding-FFT plot (waterfall) shows the evolution of the vertical acceleration of the hub-carrier, whose time history is in Fig. 2d. The phenomenon begins at 2.5 second with a chaotic phase, driven by the friction interaction between pads and rotor. Half a second later (Centre of FFT window at 3 seconds) the second phase replaces the chaotic one and only a few spikes in the frequency domain can be identified at previously mentioned values. When full pressure is applied again by the driver's foot, the system suddenly comes to a complete rest. The implication of this system behaviour is that the chaotic nature of the friction forces between the sliding surfaces, that is rich in a wide band of the frequency domain is prone to easily excite the structural modes of the suspension.

### 3.2 Front Suspension.

There are some fundamental differences between front suspension components of this car and the above analysed rear one. They are both double wishbone structures, but the rear one has the feature to include the driving axle as upper wishbone. Brake system components differ in size too. The measurement investigation (and this paper as well) focused more thoroughly on the rear side of the car because of the possibility of running the free hub only, the vehicle being a rear wheel drive one. This situation was suitable to have an easier access on components and to locate easily the acceleration transducers. Only a brief overview of the front suspension will be given here. Vibration levels are reported in table 3. Pad and caliper acceleration levels are lower compared to the rear suspension, but acceleration on the lower wishbone is still in the  $15 \text{ ms}^{-2}$  peak-to-peak range, as above. A peak in correspondence of 65 Hz has been found and one at 130 Hz as well, very close to the previously identified 126 Hz one.

**Table 3. Front suspension vibration levels.**

<b>Location and direction</b>	<b>peak-peak acceleration [<math>\text{ms}^{-2}</math>]</b>	<b>acceleration rms [<math>\text{ms}^{-2}</math>]</b>	<b>velocity rms [<math>\text{mm s}^{-1}</math>]</b>
Pad-y	8	0.70	0.8
Caliper[CAL1]-x	20	1.90	6.4
Caliper[CAL1]-y	15	1.30	1.3
Caliper[CAL1]-z	25	2.90	2.7
Hub carrier-z	10	0.80	1.0
Lower Wishbone-x	15	1.60	5.4
Lower Wishbone-y	12	1.00	2.0
Lower Wishbone-z	15	1.50	1.8

### 3.3 Body Panels Acceleration Levels.

**Table 4. Body measured vibration levels.**

<b>Location and direction</b>	<b>peak-peak acceleration [<math>\text{ms}^{-2}</math>]</b>	<b>acceleration rms [<math>\text{ms}^{-2}</math>]</b>	<b>velocity rms [<math>\text{mm s}^{-1}</math>]</b>
B-Post-y	0.8	0.15	0.5
Rear Screen z	1.5	0.23	0.5
Rear Lateral Wing-y	1.0	0.15	0.2
Rear Boot-z	1.2	0.23	0.4
Rear Mudguard-y	1.5	0.22	0.3

A key issue in facing the creep groan study is the proper identification of the bodies whose vibrations contribute most to the unpleasant noise generation. Acceleration levels of body panels and windscreens were investigated as well (Table 4) and values obtained indicate no relevant role in the generation of the creep groan noise. Triaxial acceleration transducers were located on B-post (the vertical beam of the car body frame between the front and the rear doors), rear windscreen and one on the wheel rim to correlate vibration of the car body with a channel very close to the source of the phenomenon. Single axis accelerometers were placed on the rear boot, the rear wing and one inside the mudguard, on the panel that could be



supposed to be part of the resonance box able to amplify the noise generated by suspension components. Coherence results (not included in the present paper) between accelerations recorded from body panels transducers and accelerometers on brake pad or caliper did not show any relevant correlation. The same conclusion arose from coherence plots between body panel accelerations and the microphone signal. A hammer test to investigate natural frequencies for the car body panels where transducers were placed did not allow to discover modes very close to the frequency lines involved in creep groan for the present car and above illustrated, such as 63 or 126 Hz. All this implies that the boundary for the creep groan phenomenon is constituted by suspension sub-frames.

### **3.4 Car jacked up.**

Jacking up the car on one side at the rear and clamping the wheel resting on the ground allowed testing the groan occurrence in new conditions. The suspended free wheel was driven by the engine, setting the transmission in the "Drive" state. Time and frequency domain results are plotted in Figs 6 and 7 respectively. The main difference between the standard case (car with four wheels on the ground) and the present one is the difficulty that the driver meets to achieve the generation of the unpleasant vibration; some skill in tuning the foot pressure on the brake pedal has to be developed. The wheel rotation speed is a crucial parameter in the friction interaction, and without tyre/ground interaction forces, the wheel is prone to spin fast, immediately after the brake pedal is released. The very low revolution speed condition, typical of creep groan, may be passed through without any noisy side effect. The time history of the signal tells how the vibrations come in several bursts lasting each up to two tenths of a second, but able to reach acceleration levels compared to the wheel-on-ground case. The following plots (Fig. 7), reporting the frequency analyses denote how the region where the energy is concentrated has shifted to a higher band (with respect to the standard case) and the relevant peak in the hub-carrier plot is at 170 Hz, which was never seen before. This agrees with the human perception that the noise during the groan noise emission was higher in pitch. The present case was obviously not taking into account tyre torsional stiffness and was run with the suspension in full rebound.

### **3.5 Car jacked up, one wheel removed.**

To appreciate the role of the wheel inertia a set of tests in the hub free condition has been run. Only the wheel belonging to the lifted suspension has been removed. Figs 8 and 9 illustrate present results. Creep groan was easy to obtain and it was sustained for one or two seconds continuously. This can be explained considering that the free hub is storing much less kinetic energy than the wheel (previous case) and so it is easier for the brake components to slow down the rotor and match the creep groan slow speed conditions. The present phenomenon is different from the noise in the standard car condition and the sound pitch is of a diverse nature, as witnessed by the frequency plots in Fig 9. Torque necessary to brake the free hub is reduced and components whose motion is directly governed by the brake momentum are affected by this change. Power spectral density functions related to pad and caliper have a completely new shape.

## **4. COMPONENT MOTION ORBITS.**

The present analysis refers to the centre interval in the creep groan event, when the cycle has already settled to a stable regime, after the beginning chaotic transient phase. This study could be carried out only on the rear axle in the free hub case because of the necessity to place

several transducers on the brake caliper, which was impossible with the car wheel in place, because of the little clearance between brake components and the wheel rim. Triaxial acceleration signals related to caliper and pad were integrated twice and band-pass filtered between 10 and 200 Hz. In this case a solid state rate gyroscope was located on the hub to measure the axle rotation speed. The gyroscope has a working range that goes from DC to 60 Hz and was fundamental to monitor hub rotation. (Piezo-electric sensors used on the brake components are not able to detect down to DC vibrations). Fig. 10 allows comparing the brake disc motion (rate gyroscope once integrated signal) with vertical displacement of either caliper or brake pad. It is hardly possible to distinguish the curves related to caliper and pad (constrained to shift together by their shape). The gyroscope line allows to recognise the intermittent motion carried out by the brake disc and to distinguish the time in which the disc is rotating forwards from the period of rest (constant intervals in displacement curve). The calipers on the rear axle in the presently tested car are in front of the brake discs. When the disc rotates forwards it drags the pad and the caliper downwards, the components move in full contact relationship and their relative velocity is null ("C" mark in figure). Later forces do not allow the caliper to move anymore and it springs upwards simultaneously with the pad ("S" to identify the sliding phase in the figure). The transition from slip to stick denotes a double inversion of velocity direction and is different from the beginning of a new sliding phase. This behaviour is mirrored when the revolution direction of the wheel is inverted, setting the automatic to "Reverse".

Fig. 11 illustrates the orbits, projected on the vertical yz plane, described by caliper and pad. It was obtained by integrating twice accelerations in y and z directions recorded from three triaxial accelerometers located on the caliper front surface and the pad, as in Fig. 1. They move almost together with a quasi-translation and a slight rocking effect. Only one cycle has been plotted for simplicity but, when the system reaches the regime phase, the behaviour is not chaotic at all and the orbit pattern can be identified not only along the same creep groan event, but in every occurrence of the creep groan vibration, with high reproducibility. Every single cycle describing the plotted orbits has a duration less than 0.04 s, corresponding to a base frequency of about 30 Hz. The access to components is difficult in presence of the wheel and inhibited the complete proof, but the first cause of the stick-slip occurrence is supposed to be this 30 Hz cycle. Tyre and wheel (inertia, torsional stiffness and damping) make the fully assembled system behave somewhat differently, but the orbit frequency (30 Hz) is close to the half of the 63 Hz measured on the car in standard configuration.

## 5. CONCLUSIONS.

The present investigation regarding the creep groan phenomenon on road vehicles identifies acceleration levels of brake and suspension components and car body panels. Frequency analysis and coherence functions between accelerations recorded very close to the source and remote parts and coherence estimated between accelerations and acoustic noise suggest that the unpleasant noise is radiated mainly by suspension arms and brake components of relevant size, such as the calipers. The nature of the event is friction driven at the beginning, during the transient phase, where a wide range of frequency components is present. It is then very difficult to characterise and reproduce, being different from one event to the next. After this first chaotic phase, the system natural modes swell, giving to the noise its typical pitch, that in the case of the presently analysed car corresponds to a base frequency of 63 Hz and its double at 126 Hz evident in acceleration and sound pressure signals. The post-processing phase of

the study, with double integration of the acceleration signals, gave brake component displacements. Comparisons with the solid state rate gyroscope output (located on the hub) allowed to highlight the rotor intermittent movement and its synchronous advancement with the pad and caliper, followed by the spring-back action. This definitely takes the creep groan induced vibration into the stick-slip friction driven phenomenon category. Acceleration levels on body panels, associated with the low coherence with the microphone signal imply that the boundary for the creep groaning investigation is the car suspension, not the whole car. The role of tyre torsional stiffness and wheel inertia has been appreciated as well.

At Cranfield University a laboratory rig focused on further experimental study has been designed and it is expected to be working soon. It will present the full front suspension sub-frame and run the brake disc through an electric motor (driven by an inverter able to accurately control very low revolution velocity and torque output). Body inertia will be simulated by a flywheel. The rig will include a transducer to monitor hydraulic pressure and a torque sensor as well. The torque sensor selected has also the feature to match closely the tyre torsional stiffness, whose role is supposed to be fundamental to properly reproduce the creep groan vibration. A mathematical model is being developed in order to simulate laboratory rig behaviour and will be focused to parameter identification analysis.

#### **ACKNOWLEDGEMENTS.**

The authors are pleased to acknowledge technical contribution made to the project by Jaguar Cars Ltd and Federal-Mogul Corporation and financial support from EPSRC in the form of grant number GR/L36642.

#### **REFERENCES.**

1. Pierce, A. D., *Acoustics - An Introduction to its Physical Principles and Applications*, New York, McGraw-Hill, 1981
2. Cremer, L. and Heckl, M., *Structure-Borne Sound*, Springer-Verlag, Berlin, 1973
3. Nack, N. V. and Joshi, A. M., *Friction Induced Vibration: Brake Moan*, SAE-951095, 1995
4. Gouya, M. and Nishiwaki, M., *Study on Disc Brake Moan*, SAE-900007, 1990
5. Liang, C. and Inui S., *Dynamic Analysis of Structures Involving Coulomb Friction using a Dynamic Compliance Technique*, Washington, DC, AIAA-95/1179, 1995.
6. Abdelhamid, M. K., *Creep Groan of Disc Brakes*, SAE-951282, 1995
7. Ibrahim, R. A., *Friction-Induced Vibration, Chatter, Squeal, and Chaos, Part I and II*, in *Friction-Induced Vibration, Chatter, Squeal, and Chaos*, Ibrahim, R. A. and Soom, A. eds, New York, ASME, 1992.
8. Lee, A. and Sheridan, D.C., *Diagnosis of Noise and Vibration Problems during Braking*, General Motors Corporation, USA, ISATA Magazine, pp. 8-10, January 1997
9. Mibe, T., *Friction Characteristics Analysis of Brake-Pad Material at Low Speeds*, Nissan Motor Co. Ltd, Technical Center, JSAE-881020, 1988

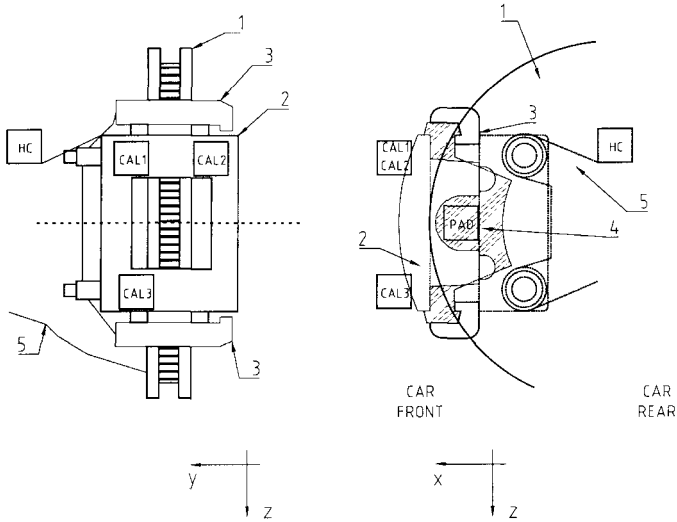


**Figure 1: Rear suspension transducer layout and adopted reference system.**

1) Brake disc; 2) caliper floating part; 3) caliper fixed part; 4) outer pad; 5) hub-carrier. Location of accelerometers on the caliper floating part [CAL1, CAL2, CAL3], pad [PAD] and hub-carrier [HC].

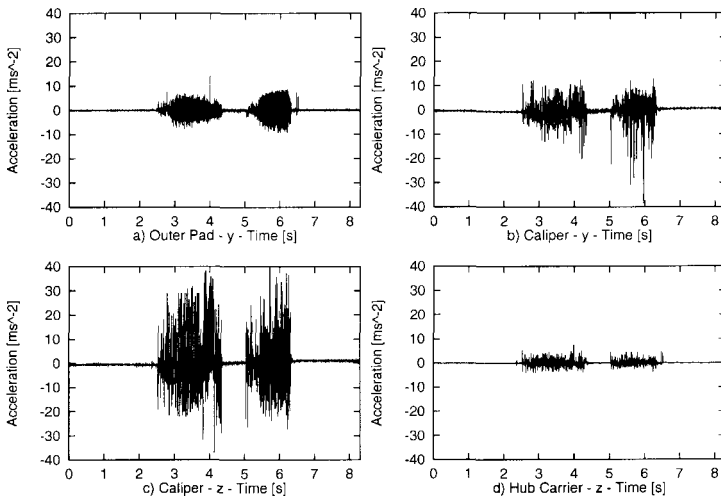


**Figure 2: Rear suspension - Time domain accelerations.**

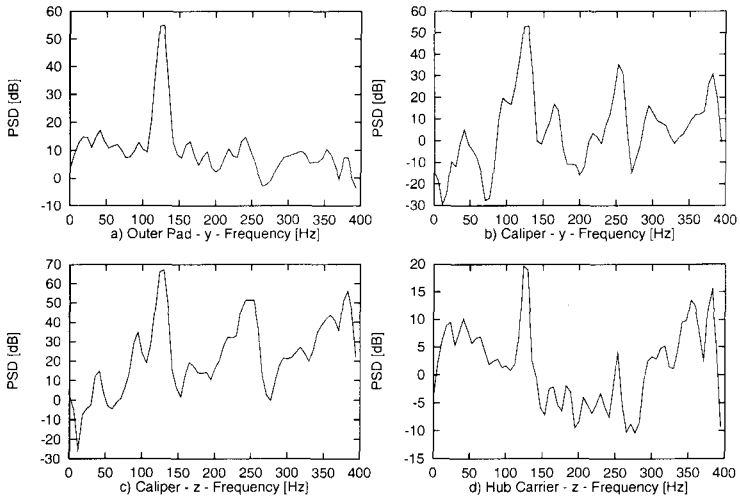


**Figure 3: Rear suspension - Power spectral density function. (Base  $1 \text{ ms}^{-2}$ )**

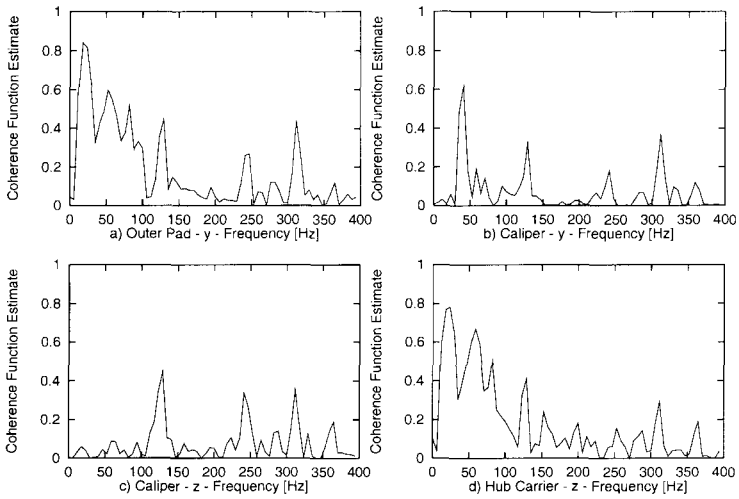


**Figure 4: Rear suspension - Coherence function estimate with sound pressure level meter. (48 averages).**

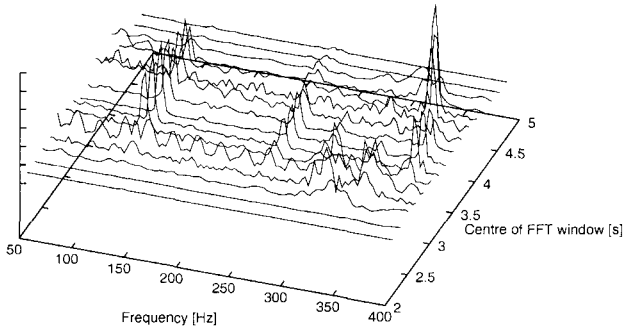


**Figure 5: Rear suspension - Hub carrier y – Acceleration FFT - Waterfall diagram.**

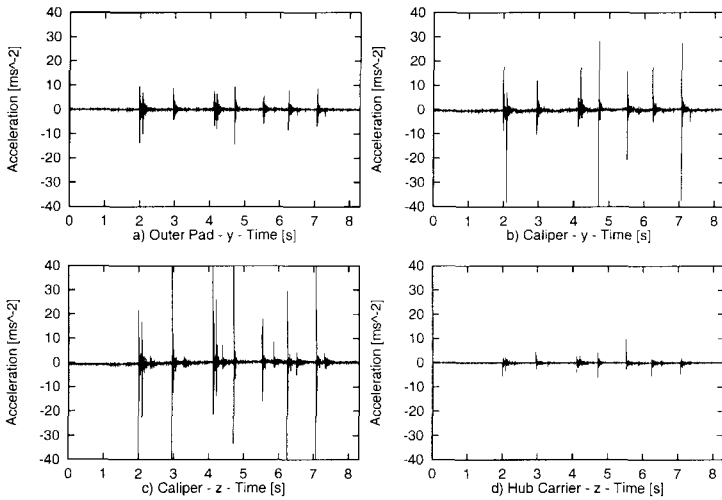


**Figure 6: Rear suspension, car jacked up - Time domain acceleration.**

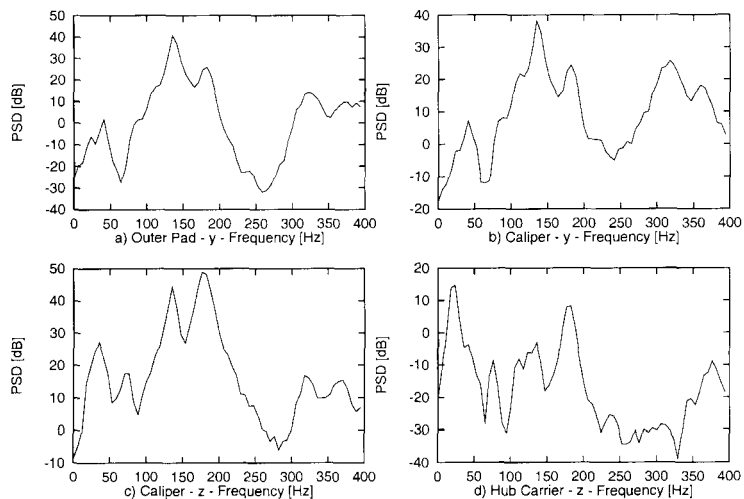


**Figure 7: Rear suspension, car jacked up - Power spectral density function. (Base  $1 \text{ ms}^{-2}$ )**

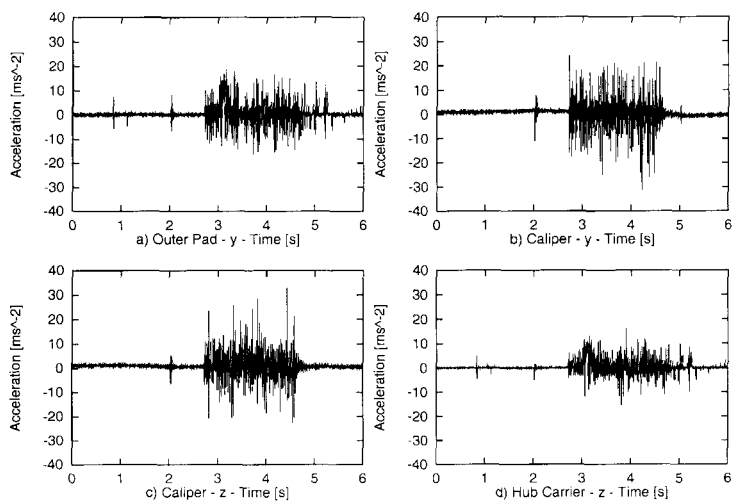


**Figure 8: Rear suspension, car jacked up, free hub - Time domain acceleration.**

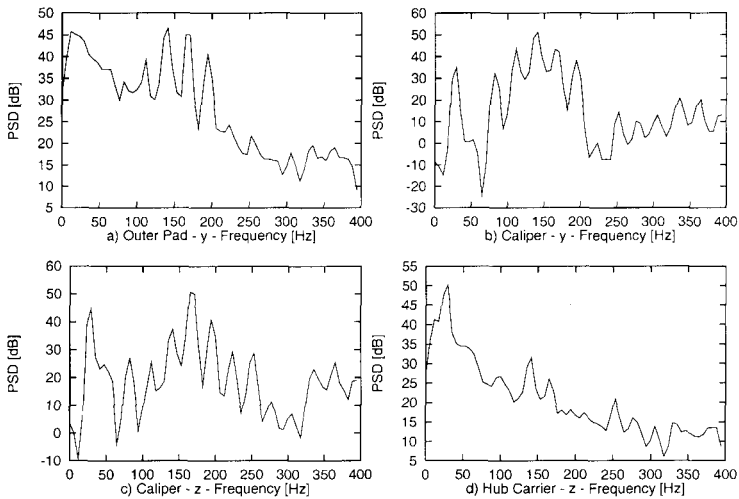


**Figure 9: Rear suspension, car jacked up, free hub - Power spectral density function. (Base  $1 \text{ ms}^{-2}$ )**

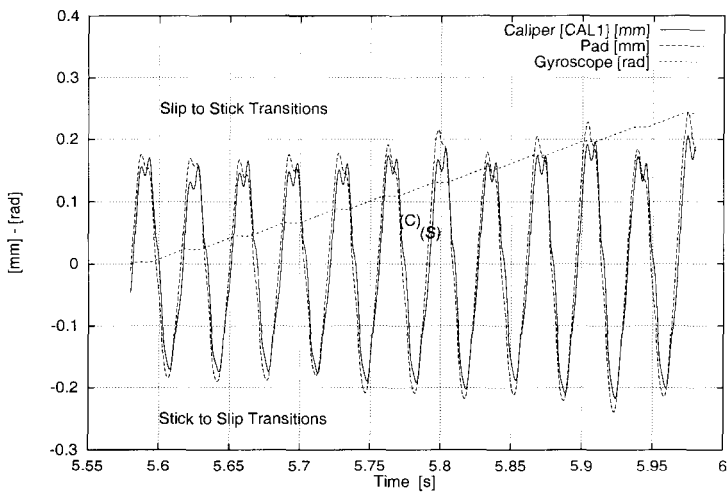


**Figure 10: Rear suspension, car jacked up, free hub - Comparison between caliper, pad and brake disc motion. (C) full contact phase. (S) relative sliding phase.**



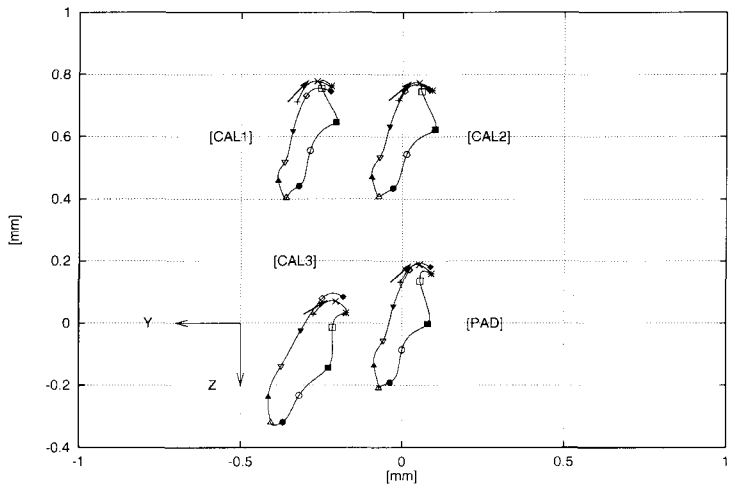


**Figure 11: Rear suspension, car jacked up, free hub - Orbit of caliper and pad projected on vertical yz plane.**

*This page intentionally left blank*

# Managing fatigue failure probability caused by misalignment and vibration in large turbine generators

**A J SMALLEY**

Southwest Research Institute, San Antonio, Texas, USA

**M J ROEMER**

Impact Technologies, Rochester, New York, USA

**T H McCLOSKEY**

Electric Power Research Institute, Palo Alto, California, USA

## SYNOPSIS

This paper develops and illustrates a model-based method to predict probability of fatigue failure in the bearings or shaft of a large steam generator rotor subjected to vibration and misalignment. The model uses hydrodynamic bearing analysis to find static and dynamic forces from measured shaft position and vibration, and from these determines dynamic stresses in shaft and bearing. The model accumulates fatigue damage; it uses Monte Carlo simulation to handle uncertainty, and predict failure probability versus future time. Probability of failure versus time, failure consequence cost, and maintenance cost, when combined, enable calculation of optimum time to balance and align.

## NOTATION

$\phi$	=	attitude angle from shaft displacement vector to vector opposite fluid film resultant force on shaft.
$\omega$	=	shaft rotational speed (radians per second).
$\psi$	=	angle from X-axis to the shaft displacement vector.
$\Delta\xi_K, \Delta\eta_K$	=	measured changes in displacement relative to probes.
$\Delta\xi'_K, \Delta\eta'_K$	=	vibratory displacements along probe axes (bearing K).
$\sigma, M, C, I$	=	components of shaft stress calculation (stress, bending moment, half section dimension, transverse moment of area).
$\theta_1, \theta_2,$	=	angular position of probes relative to upwards vertical.
$\phi_{1K}, \phi_{2K}$	=	vibration phase angles for probes 1 and 2 at bearing K.
$\sigma_I^*$	=	intensified maximum stress at Station I.
$\Delta T$	=	time interval for prevailing conditions of speed, etc.
$\Delta X, \Delta Y$	=	changes in shaft displacement, based on probe measurement.
$\sigma_{XI}, \sigma_{YI}$	=	stresses at Station I acting in X and Y planes due to bending.
$C_d$	=	bearing diametrial clearance.

$D$	=	bearing diameter.
$D_F$	=	fraction of life consumed in time $\Delta T$ .
$D_{OI}$	=	shaft outer diameter at Station I.
$e$	=	magnitude of shaft displacement from center of bearing.
$F_K$	=	total or resultant fluid film force acting on the shaft.
$F_{MX1}, F_{MX2}$	=	X-forces at master bearings 1 and 2, which equilibrate all <u>other</u> forces acting on the shaft.
$F_{MY1}, F_{MY2}$	=	Y-forces at master bearings 1 and 2, which equilibrate all <u>other</u> forces acting on the shaft.
$F_{PAXI}, F_{PAYI}$	=	partial arc forces acting on the shaft in X and Y directions.
$F_{SXI}, F_{SYI}$	=	station forces due to weight near Station I.
$F_{WI}$	=	downwards force due to shaft weight in the vicinity of Station I, not including any additional weights.
$F_{XI}, F_{YI}$	=	I <sup>th</sup> bearing forces acting on shaft in X and Y directions.
$F_{XK}, F_{YK}$	=	fluid film forces on shaft in the positive X and Y directions.
$F_{XNETI}, F_{YNETI}$	=	total forces acting on shaft in X and Y direction at Station I.
$F_{XTOTAL}, F_{YTOTAL}$	=	sum of slave bearing, weight, and partial arc forces.
$G'_{1K}, G'_{2K}$	=	amplitudes of dynamic motion in line with two probes.
$I_I$	=	shaft transient second moment of area at Station I.
$K_{TI}$	=	stress concentration factor at Station I.
$L$	=	bearing length.
$L_I$	=	length from Station 1 to Station I.
$L_{M1}, L_{M2}$	=	lengths from Station 1 to master bearings 1 and 2.
$M_{XI}, M_{YI}$	=	bending moments acting at Station I in X and Y planes.
$M_{XTOTAL}, M_{YTOTAL}$	=	moments about Station I by all, but master bearing forces.
$N_{BRG}$	=	number of bearings.
$N_C$	=	number of cycles to failure at prevailing stress.
$N_J, S_J$	=	pairs defining stress versus cycles to failure for shaft.
RPM	=	rotor speed in revolutions per minute.
$t$	=	time, seconds.
$V_{XI}, V_{YI}$	=	shear forces acting in field between Station I and Station I+1.
$W_{AD-I}$	=	added weight at Station I (e.g., disk or turbine wheel).
$W_I$	=	weight of shaft section between Stations I and I+1.
$X'_K(t), Y'_K(t)$	=	instantaneous shaft displacement from geometric center.
$X_0, Y_0$	=	shaft position at known reference condition.
$X_K(t), Y_K(t)$	=	shaft positions from bearing center vertically downwards (X), and horizontally (Y - 90° from X with shaft rotation).

## 1 INTRODUCTION

In the competitive power market, turbine generators must operate profitably. Performing maintenance on a machine reduces revenue and adds cost. In a regulated environment, prudent cost of shutting down to correct “high vibration” could be passed on to the consumer. In a competitive environment, high vibration criteria need closer scrutiny.

Smalley, et al [1] conclude existing criteria represent consensus guidelines, and do not support machine specific tradeoffs between expected cost of failure and cost of corrective action. Smalley, et al [1] introduced risk-based criteria, calculating damage potential from

measurement and inferential models, and enabling the desired economic tradeoff. McHugh [2] anticipated the model-based concept by estimating severity of bearing vibrations from inferred dynamic pressure.

Calculating and optimizing net value has become increasingly popular in major overhaul timing; it requires the expected cost avoided by maintenance action, from which is subtracted the cost of maintenance action (including any lost revenue). As Smalley and Mauney [3] show, expected cost equals the product of failure probability and failure cost. Predicting failure probability presents the biggest technical challenge in this calculation.

This paper expands on and illustrates the concepts of Smalley, et al [1]; its top down approach identifies the components of analysis and data required for “end-to-end” application. It implements each component to the extent that available measurements and data allow, invoking analyses, assumptions, and uncertainty management consistent with available precision. This approach helps identify technical areas with the strongest need for further investigation.

The paper addresses two illustrative failure causes: bearing fatigue and shaft fatigue. The two failure mechanisms are closely related; in particular, misalignment contributes to the mean bearing load upon which is superimposed to vibration load.

## 2 CONFIGURATION UNDER CONSIDERATION

Figure 1 shows schematically a large steam turbine system with six bearings. The No. 1 bearing on the HP/IP is a tilting pad (load on pad) and the next five are sleeve bearings. Table 1 lists bearing, length, diameter, clearance, and nominal load. Figure 2 presents a rotor flexibility model.

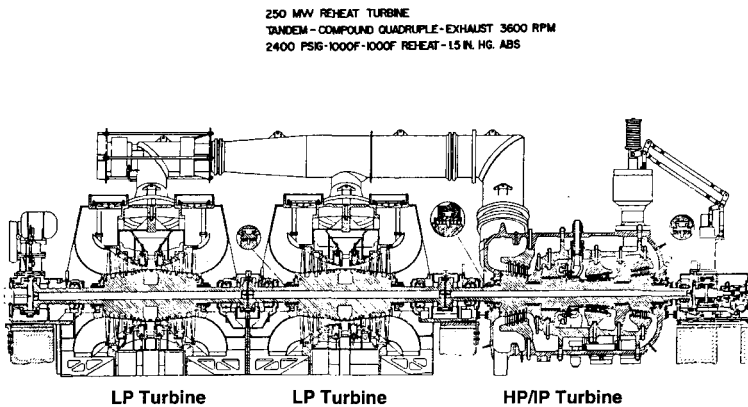


**Fig. 1 Schematic for HP-IP/LP/LP Large Steam Turbine under Consideration**

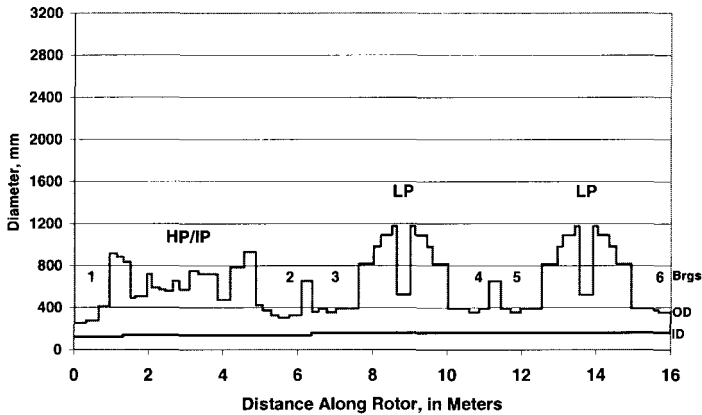


**Fig. 2 Rotor Model Diameter versus length from OB End of HP/IP**

**Table 1 List of Bearings**

No.	Type	Length (L) mm	Diameter (D) mm	Clearance (C <sub>d</sub> ) microns	Nominal Load Newtons
1	Tilt-Pad	234	254	558.8	82,394
2	Sleeve	305	305	596.9	82,394
3	Sleeve	287	356	698.5	89,075
4	Sleeve	287	356	749.3	89,075
5	Sleeve	287	356	698.5	89,075
6	Sleeve	287	356	690.9	89,075

Figure 3 overviews the logic to calculate nominal shaft stresses and bearing pressures versus time (historical data), and to imbed this historical data in a probabilistic analysis. This diagram provides context for the subsequent analysis. Two inputs define the conditions imposed on the rotor bearing system: 1) measured vibration, and 2) measured DC journal position as a function of time. Measured position drives a bearing static model, which uses bearing geometry, speed, and viscosity to calculate static forces on the shaft. With partial arc and rotor weight forces, these determine the shear force, bending moment, and stress distributions. Rotating through this static stress distribution causes stress reversal and (if severe enough) fatigue damage.

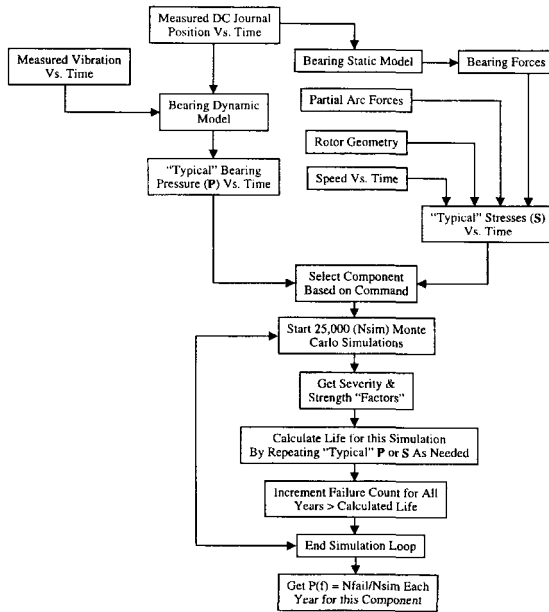


**Fig. 3 Bearing and Rotor Bending Module**

Measured shaft position and measured vibration drive the bearing dynamic model to produce bearing dynamic loads and associated bearing pressure. Based on the distribution of uncertainty in the measurements and material strength, a sufficient number of Monte Carlo simulations will generate a representative distribution of failures and survivals in each time period of interest for any selected shaft or bearing. Dividing each failure count by the simulation count creates failure probability as a function of time. The following analysis develops these methods.

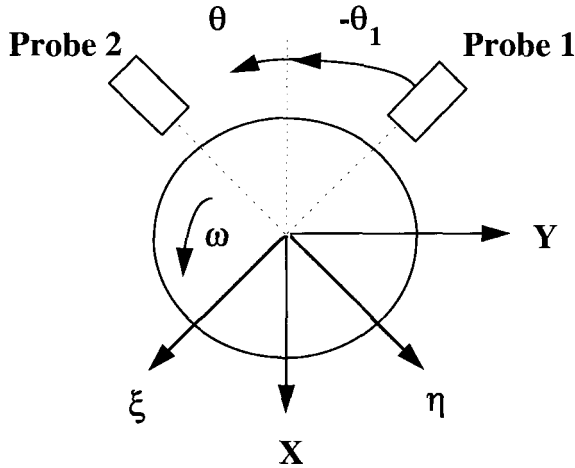
### 3 BEARING STATIC ANALYSIS

Figure 4 shows a shaft with position and vibration monitored by orthogonal probes. The probe displacements give shaft position relative to the bearing geometric center as follows for bearing number K:

$$X_K(t) = X_0 + \Delta X = X_0 + \Delta \xi \cos \theta_1 + \Delta \eta \sin \theta_1 \quad (1)$$

$$Y_K(t) = Y_0 + \Delta Y = Y_0 - \Delta \xi \sin \theta_1 + \Delta \eta \cos \theta_1 \quad (2)$$

Subscript zero implies a reference condition – normally the shaft sitting down in the bearing;  $\Delta X$ ,  $\Delta Y$ ,  $\Delta \xi_K$ , and  $\Delta \eta_K$  represent measured change with time from this reference. With a single vertical probe,  $\theta_1 = 0$ , so  $\Delta X = \Delta \xi_K$  and  $\Delta Y$  is unknown, requiring some assumption about shaft horizontal position in the bearing.



**Fig. 4 Definition of Shaft and Probe Parameters at Bearings**

In general, for a sleeve bearing, from solution to the Reynolds equation:  $F_{XK} = -F_K \cos(\phi - \psi)$ ;  $F_{YK} = +F_K \sin(\phi - \psi)$ . Where  $F_K$  and  $\phi$  are the dimensional fluid film force acting on the journal and the associated attitude angle, at eccentricity  $e = \sqrt{(X_K(t))^2 + (Y_K(t))^2}$ ;  $\tan \psi = \frac{Y_K(t)}{X_K(t)}$ .

With a single vertical probe, the horizontal bearing force has been assumed zero (other assumptions are possible). A tabular data set can be generated defining  $F_{XK}$  and  $Y_K$  as a function of  $X_K$  with  $F_{YK} = 0$ . For a given vertical shaft deflection within any sleeve bearing, this table yields interpolated values for vertical force and horizontal deflection.

It is possible to compute tilting pad bearing forces by solving the Reynolds equation for any journal position relative to the pads; however, with only a vertical probe, the horizontal bearing force has again been assumed zero. The corresponding vertical force versus deflection data can be readily generated since this is the standard load on pad condition.

#### 4 SHAFT EQUILIBRIUM ANALYSIS

In addition to bearing forces, the shaft has a distribution of weight forces. The shaft is subdivided into stations and acting at each station, the vertical force  $F_{W1} = (W_{1-1} + W_1)/2 + W_{AD-1}$ .

The bearing set consists of two master bearings and  $(N_{BRG} - 2)$  slave bearings. Only with more than two bearings can forces from bearing offset be calculated. For this rotor, bearings 1 and 6 are chosen as master bearings, and bearings 2, 3, 4, and 5 as slave bearings. Slave bearing forces are determined from the measured shaft position; master bearing forces equilibrate all other forces.



At any station:

$$F_{SX1} = F_{W1} + F_{X1} + F_{PAX1} \text{ and } F_{SY1} = F_{Y1} + F_{PAY1} \quad (3)$$

The vertical and horizontal reaction forces at the master bearing are then calculated as follows:

$$F_{MX1} = - \left[ \frac{L_{M2} F_{XTOTAL}}{(L_{M1} - L_{M1})} - \frac{M_{XTOTAL}}{(L_{M2} - L_{M1})} \right] \quad F_{MX2} = - \left[ \frac{M_{XTOTAL}}{(L_{M2} - L_{M1})} - \frac{L_{M1} F_{XTOTAL}}{(L_{M2} - L_{M1})} \right] \quad (4)$$

$$F_{MY1} = - \left[ \frac{L_{M2} F_{YTOTAL}}{(L_{M2} - L_{M1})} - \frac{M_{YTOTAL}}{(L_{M2} - L_{M1})} \right] \quad F_{MY2} = - \left[ \frac{M_{YTOTAL}}{(L_{M2} - L_{M1})} - \frac{L_{M1} F_{YTOTAL}}{(L_{M2} - L_{M1})} \right] \quad (5)$$

$$F_{XTOTAL} = \sum_{I=1}^{NSTA} F_{SX1} \quad F_{YTOTAL} = \sum_{I=1}^{NSTA} F_{SY1} \quad (6)$$

$$M_{XTOTAL} = \sum_{I=1}^{NSTA} F_{SX1} * L_I \quad M_{YTOTAL} = \sum_{I=1}^{NSTA} F_{SY1} * L_I \quad (7)$$

Defining  $F_{XNET1}$  and  $F_{YNET1}$  as the net forces at Station I (combining master bearing, slave bearing, partial arc, and shaft weight forces, whichever applies at that station), their distribution maintain the entire shaft in equilibrium. Shear and bending moments are then recursively related:

$$V_{X1} = V_{X1-1} + F_{XNET1} \quad V_{Y1} = V_{Y1-1} + F_{YNET1} \quad (8)$$

$$M_{X1} = M_{X1-1} + V_{X1-1} \Delta L_{1-1} \quad M_{Y1} = M_{Y1-1} + V_{Y1-1} \Delta L_{1-1} \quad (9)$$

and:

$$V_{X1} = F_{XNet1}; \quad V_{Y1} = F_{YNet1}; \quad M_{X1} = 0; \quad M_{Y1} = 0 \quad (10)$$

Shear forces are constant within each field (fields lie between stations); bending moments change linearly over each field.

#### 4.1 Determination of Stress

Applying the formula ( $\sigma = MC/I$ ) at each station yields:

$$\sigma_{X1} = \text{MAX} (M_{X1}, M_{X1+1}) D_{O1}/(2I_1) \quad \sigma_{Y1} = \text{MAX} (M_{Y1}, M_{Y1+1}) D_{O1}/2I_1 \quad (11)$$

Giving maximum stress for the cross section:

$$\sigma_1^* = K_{TI} (\sigma_{X1}^2 + \sigma_{Y1}^2)^{1/2} \quad (12)$$

$K_{TI}$  is a stress concentration factor. Peterson [4] provides stress concentration factor as a function of fillet radius and diameters at each section change.

## 4.2 Calculation of Damage

A linear damage approach gives  $D_F$ , the fraction of life consumed in the time interval of length  $\Delta T$ , in terms of the number of cycles to failure at the prevailing stress,  $\sigma^*$ :

$$D_F = \text{RPM } \Delta T / (60 N_c) \quad (13)$$

Four SN pairs define straight-line segments on a log-log plot so that, by linear interpolation between these SN pairs, the number of cycles to failure can be calculated, as shown in equation (14). Table 3 will define the four SN pairs for the different turbine materials.

$$N_c = \exp [\log N_J + (\log N_{J+1} - \log N_J) * (\log \sigma^* - \log S_J) / (\log S_{J+1} - \log S_J)] \quad (14)$$

$$\text{If } S_{J+1} < \sigma^* < S_J \text{ or } \sigma^* < S_{J+1} \text{ and } J = 3 \quad N_c = 1 \text{ if } S_1 < \sigma^* \quad (15)$$

## 4.3 Bearing Dynamic Model

The following equations yield instantaneous shaft position within bearing K:

$$X'_K(t) = X_K(t) + \Delta \xi'_K \text{ Cos } \theta_1 + \Delta \eta'_K \text{ Sin } \theta_1 \quad Y'_K(t) = Y_K(t) - \Delta \xi'_K \text{ Sin } \theta_1 + \Delta \eta'_K \text{ Cos } \theta_1 \quad (16)$$

where:

$$\Delta \xi'_K(t) = G'_K \text{ Cos } (\omega t - \phi_{1K}) \quad (\Delta \eta'_K(t) = G_{2K}' \text{ Cos } (\omega t - \phi_{2K}) \quad (17)$$

With a single vertical probe, a circular orbit is assumed. We are only interested in amplitudes and can set  $\phi_1$  to zero and  $\phi_2$  to  $\phi_1 - \pi/2$ .

For sleeve bearings, Equations (1) and (2) determine instantaneous values for vertical and horizontal force. Solving the Reynolds equation for squeeze film effects would yield damping forces; while more comprehensive, the present analysis does not attempt this; it is expected that the maximum forces will occur at, or near, the extremes of motion.

For the tilting pad bearing, two sets of tabular data are used in the non-equilibrium analysis: one for the shaft displaced (and loaded) symmetrically between the pads, and one for shaft displaced (and loaded) towards the pivot point. The instantaneous shaft displacements define a non-equilibrium shaft eccentricity vector direction. By assuming shaft deflection stays aligned with the load and deflection varies sinusoidally between the two directions, it is possible to construct a table of displacement versus force for this particular non-equilibrium vector direction. Interpolating from this table yields the instantaneous force.

Thus, the vibration superimposed on steady-state displacement yields maximum and minimum force values for each bearing, and from these, maximum and minimum average pressure values.

## 4.4 Bearing Fatigue Analysis

These maximum and minimum average pressure extremes provide a basis for applying the data of Gyde [5], who performed fatigue tests on a large number of bearings. Gyde's data can be organized as in Figure 5, to show number of failures within  $10^7$  cycles versus bearing pressure.

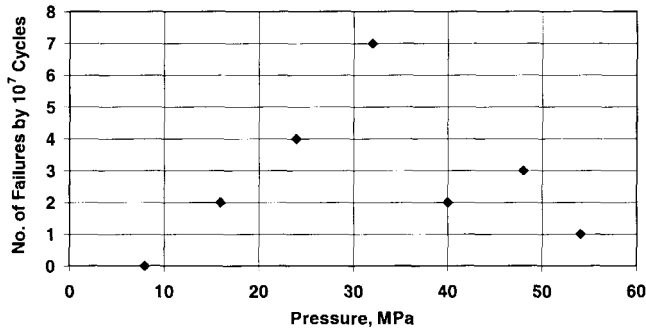


**Fig. 5 Cumulative Probability of Failure versus Maximum Instantaneous Value of Mean Pressure (Load/Area); Data from Gyde (5)**

Figure 5 closely approximates a triangular distribution with minimum of 8 MPa, maximum of 56 MPa, and mode of 32 MPa. For more general applications, if we know the mode, these results give us multipliers with which to determine the minimum and maximum values, which define the triangular distribution (multipliers of 0.25, 1, 1.8, for minimum, mode, and maximum). Such a distribution could be used directly in Monte Carlo simulation; however, it represents only high cycle fatigue information - not the sloping low cycle fatigue behavior applicable to higher pressures. Yahraus [6] provides typical curves of bearing peak pressure versus cycles to failure. Yahraus' data shows the number of cycles to failure reduces when stress increases by a factor of 3.16. We assume that Yahraus' data defines the slope of the low cycle fatigue portion of the pressure versus cycles to failure (PN) curve, which applies between 1000 and  $10^7$  cycles to failure; and that below 1000 cycles to failure and above  $10^7$  cycles to failure, the PN curve has near flat variation; four PN pairs have been generated (see Table 2). These pairs define the mode of the cycles to failure as a function of bearing mean dynamic pressure. For use in Monte Carlo simulation, the triangular distribution is assumed to have the same shape, defined by multipliers, as extracted from Figure 5.

**Table 2 Constructed PN Data for Bearing Fatigue Based on Mean Effective Pressure**

P, MPa	N
101.4	1
101.1	2.5E6
32	1E7
31.7	1E12

We then apply a triangular probability function, based on Gyde's data, to any nominal pressure value, such that the low end of the triangular distribution is one-quarter, and the high end is 1.8 times the mode value interpolated from Table 2 (adapting Equations (14) and (15) to the PN data).

#### 4.5 Probability Distribution for SN Data

A triangular distribution has been created, with guidance, from available tensile strength and endurance limit data for representative shaft materials (Table 3). From the observed variance, a triangular distribution with low end 0.707 times the mode and high end 1.414 times the mode is applied to values interpolated.

**Table 3 SN Data for Shaft Materials**

LP Turbine		HP-IP Turbine	
No. of Cycles, N	S, MPa	No. of Cycles, N	S, MPa
1	671	1	746
$10^3$	670	$10^3$	739
$3 \times 10^6$	387	$10^6$	373
$10^{12}$	380	$10^{12}$	366

### 5 PROBABILISTIC ANALYSIS

For each casing, the station with the highest stress at any point in the time history is used to track cumulative damage and calculate probability of failure versus time as shown in the flow chart of Figure 6 (implicitly assuming that the highest stress point will incur the highest damage). A similar procedure is followed for bearing fatigue probabilistic analysis.

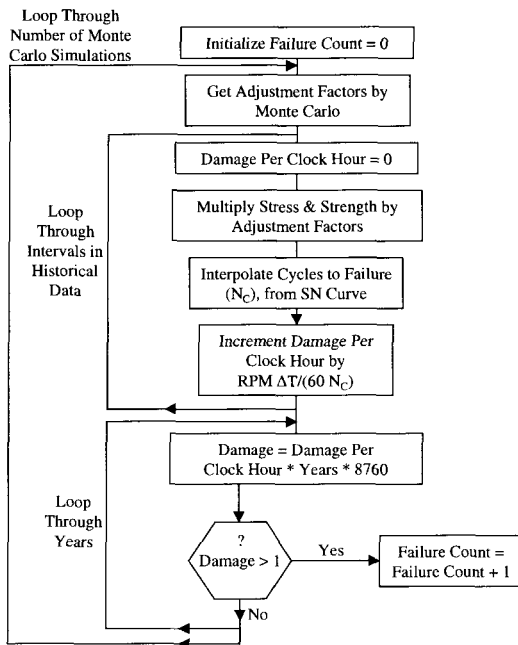


**Fig 6 Flow Chart for Failure Probability Calculation**

## 6 RESULTS

The following provides typical predictions for the turbine of Figure 1, which has a single, vertical non-contact probe at each bearing. The turbine currently has capability to record vibration during startup and steady operation, as shown in Figure 7, but as yet, not static position data. Figure 7 shows recorded vibrations in microns peak-to-peak as a function of time during startup and during steady-state operation. This figure also includes the speed variation during startup. The six bearings referred to can be located on Figure 2. The peaks in the vibration curves represent transition through critical speed for the different casings.

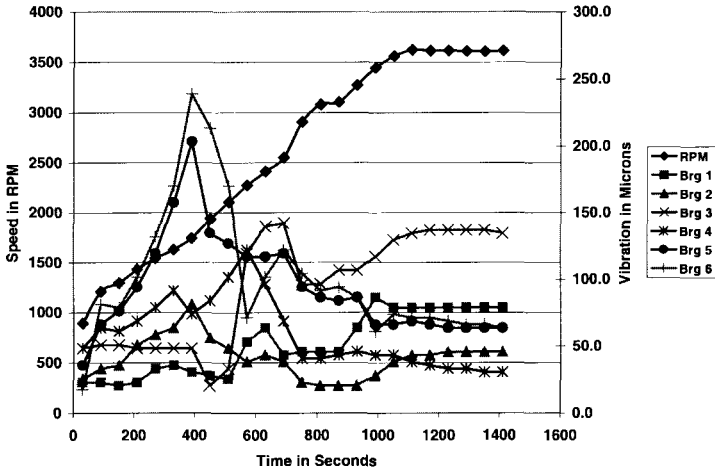


**Fig 7 Vibration and Speed as a Function of Time during Startup**

To demonstrate the methodology (with measured shaft static position unavailable), shaft position versus speed was predicted for the nominal load on each bearing, and then with one bearing (No. 3) overloaded and an adjacent bearing (No. 2) underloaded to simulate a condition with enough misalignment to create a finite probability of shaft fatigue failure in the second LP turbine. The existing vibration data was used for bearings No. 1 through No. 4, and for bearing No. 6. For bearing No. 5, vibration at the critical speed was exaggerated to simulate a condition of excessive unbalance - sufficient to create a finite probability of bearing fatigue failure.

The highest stress in the shaft and the highest dynamic pressure in the bearing occur during startup in this example, so that over the years repeated startups will cause an accumulation of damage. The Monte Carlo simulation process, described in the flow chart of Figure 6, generates the probability curves shown in Figure 8. The highest curve in this figure shows the probability of shaft fatigue failure for the LP 2 casing, predicted as a result of the simulated misalignment. The next highest curve in Figure 8 shows the probability of fatigue failure in the No. 5 bearing, predicted as a result of high vibration.

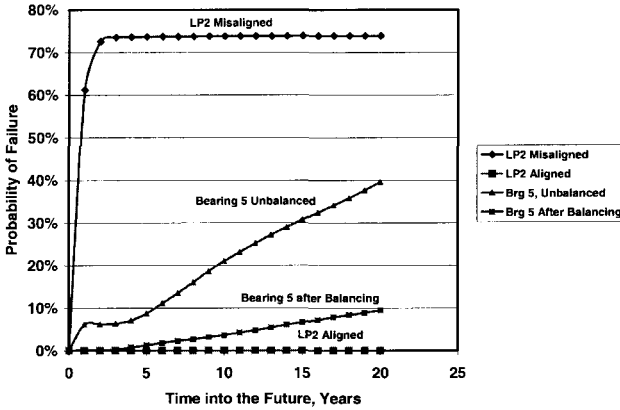


**Fig 8 Probability of failure for LP2 and bearing No. 5 before and after balancing and alignment**

The analysis also predicts the result of corrective maintenance action, and allows assessment of the extent of the corrective action (alignment and balancing) necessary in terms of the reduction in probability of failure which they achieve. For this example, the analysis assessed how probability of failure would reduce as a result of aligning to reduce bearing overload by a factor of two, and as a result of balancing to reduce vibration level by a factor of two. Figure 8 shows that the alignment action reduced the probability shaft fatigue failure to zero, and that the balancing reduced the probability of bearing fatigue failure by a factor of four.

Figure 9 shows illustrative distributions of shaft bending stress and bearing peak dynamic pressure at one interval during the startup. The value of this information, in general, is to provide detail on the cause of high failure probability of failure. At this interval, the highest stresses are in the central casing, and both bearings No. 5 and No. 6 show the highest dynamic stress. However, the conditions at other intervals may be more severe.

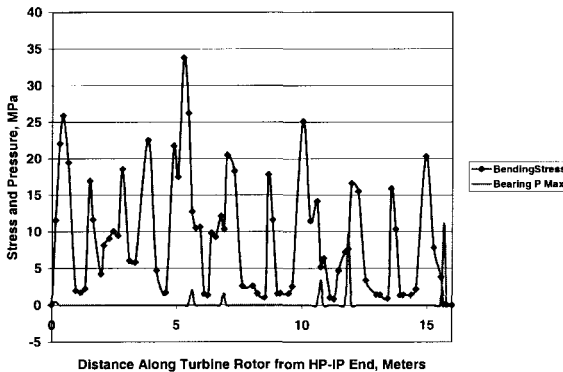


**Fig 9 Typical distributions of shaft bending stress and bearing peak dynamic pressure at one interval during startup**

To use these results in overhaul decision-making, the failure probability curve must be multiplied by financial consequence of failure, and the net present value reduced by the overhaul cost. The effect of overhaul timing at any time in the future is addressed by sliding the after-overhaul curve to the right. It should be recognized that reducing vibration or misalignment without component replacement does not zero out previous damage; the starting point for future accumulation differs according to whether or not the component is replaced at overhaul time. While it is relatively inexpensive to replace a bearing, shaft replacement is an unlikely option. Thus the potential for permanent damage must be recognized for a shaft, which has operated in the past with excessive misalignment.

## 7 DISCUSSION

Quantitative information on failure probability will enable engineers to quantify the significance of “high” vibration and misalignment in business terms. This paper shows a way to calculate failure probability for a large power-generating turbine. The inferential process starts with measurements of time varying shaft position in each bearing, transforms these through a bearing model into static and superimposed dynamic forces, and uses standard relationships to calculate distributions of shaft stress and bearing dynamic pressures. The potential for failure depends on comparing stress and pressure with component fatigue limits. Using linear fatigue theory damage increases with time, but because no fatigue data is “crisp” and because the inferential analysis involves a number of idealizations, both severity and strength levels contain uncertainty. Uncertainty is handled by repeating the damage rate calculation many times with uncertain variables satisfying an imposed probability distribution. Since each simulation leads to either survival or failure in a given period, dividing the number of failures by the number of simulations yields a curve showing how failure probability varies with time.

The paper shows an end-to-end working process, but a number of elements in this process would benefit from improved data and models, including availability of both horizontal and vertical shaft displacement data, more extensive low and high cycle bearing fatigue data, and more realistic bearing force inferential models for arbitrary dynamic position.

In implementing the bearing analysis, it became clear that, with high vibrations, nonlinearity of the bearing’s force displacement relationships has an influence and reduces the validity of separating static and dynamic behavior. The mean static force applied by the shaft to a bearing is reacted by a time varying force which will not vary sinusoidally (even for sinusoidal motions) when such motions are large. An improved approach would start with a dynamic bearing analysis and calculate a time averaged static equilibrium position.

The value of the total signal from non-contact displacement probes demonstrated in the paper needs to be recognized, together with the need for accuracy in this signal. Accuracy is influenced by calibration, gap setting, temperature effects on the calibration curve, mounting methods, and effects of thermal growth. A number of articles in *Orbit* magazine (Muszynska; [7]) have emphasized the importance of the DC probe signal for diagnostic and condition monitoring purposes, but for model-based applications the accuracy demands become much higher.

The time scale to which the model is applied deserves discussion. The immediate interest in the vibration and misalignment module (for the EPRI TurboX package; Roemer, et al [8]), was to contribute to decisions on major overhauls with typical choices in years. The potential failures relevant to such time scales generally involve “low cycle” fatigue, where vibration

and misalignment cause damage during transient excursion (startup, shutdown, and loading). Such is the case for the examples in this paper. During steady operation, large numbers (tens of millions) of rotational cycles accumulate within weeks. If misalignment or vibration is continuously excessive during steady operation, the time scale for the failures discussed here will tend to be days or weeks, rather than years.

The concepts demonstrated here, therefore, have the potential for further enhancement and wide application in both short and long term maintenance decisions, as discussed above.

## 8 CONCLUSIONS

The increasingly competitive environments in which machinery is operated demand criteria for actions to enhance mechanical integrity which balance operational needs of the business with the potential for machinery damage.

This paper has demonstrated an end-to-end working method for calculating probability of failure from high vibration and misalignment as a function of time, which can form an essential input to such new criteria.

The areas of bearing fatigue, bearing inferential models for force as a function of displacement, and shaft total displacement measurement require enhancement for such methods to achieve full value and wide application.

Although applied here to long term decisions, the method presented with the enhancements discussed, also has potential for wide application in short term decisions to balance and realign.

## 9 REFERENCES

1. Smalley, A. J., Baldwin, R. M., Mauney, D. A., Millwater, H. R., "Towards Risk Based Criteria for Rotor Vibration," IMechE 1996, Paper No. C500/081/96.
2. McHugh, J. D., "Estimating the Severity of Synchronous and Subsynchronous Shaft Vibration Within Fluid-Film Journal Bearings," *Vibrations*, 1(1), June 1985, pp. 4-8.
3. Smalley, A. J. and Mauney, D. A., "Risk-Based Maintenance of Turbomachinery," *Proceedings of the 26<sup>th</sup> Turbomachinery Symposium*, Texas A&M University, September 16-18, 1997, Houston, Texas.
4. Peterson, R. E., Stress Concentration Design Factors, John Wiley & Sons, 1953.
5. Gyde, N., "Fatigue Fractures in Babbitt Lined Journal Bearings," Thesis 1969, Laboratory of Internal Combustion Engines, Technical University of Denmark, Copenhagen.
6. Yahraus, W. A., "Rating Sleeve Bearing Material Fatigue Life in Terms of Peak Oil Film Pressure," 1988 Society of Automotive Engineers, Inc., No. 871685.
7. Muszynska, A., "Shaft Vibration Versus Shaft Stress," *Orbit*, Vol. 10, No. 3, December 1989, pp. 4-7.
8. Roemer, M. J., Dewey, R. P., Atkinson, B. C., McCloskey, T. H., "Turbine Generator Maintenance Outage Optimization: Probability/Risk Assessment of Net Present Value," 1997 ASME Joint Power Generation Conference, Dallas, Texas.



# Condition monitoring and diagnostics of constructive elements of rotor systems

V VOLKOVAS

Research Laboratory of Vibrodiagnostics, Kaunas University of Technology, Lithuania

## ABSTRACT

Using the numerical modelling of mechanical systems with distributed parameters and identification procedures there are investigated dynamical interaction of damaged constructive element with mobile and immobile oscillating elements, connected to the diagnostical object processing algorithms identifying the technical state of supporting elements, with various types of bearing.

The results are connected with the creation of new diagnostic methods of elements for rotor systems.

## 1 INTRODUCTION

Failure of rotor systems very often causes different accidents in industry. Therefore, problems of increasing operating reliability, diagnostics of the technical state and condition monitoring are always of great importance. Operating reliability of different objects depends upon many factors and each of them has an influence upon the general level of technical provision for normal functioning of the object. The latter includes such concepts as safety, efficiency, economic optimum, etc.

One of the ways to increase the reliability of mechanical systems is to provide them with monitoring and diagnostic equipment based on the analysis of a vibroacoustical process.

For the implementation of diagnostics and monitoring, scientists concentrated their efforts on the solution of the following problems: theoretical basis of the identification methods for defects and their analysis in a qualitative relation to the location of the damage and its importance; analytical basis for the mathematical simulation of structural elements and of

their dynamic behaviour at stiffness reducing damage; development of novel techniques for the state diagnosis of mechanical systems.

The identification of defects in the various constructive elements (assembly of bearings, rotors, wheels with blades and others) of rotor systems requires the creating of systematic diagnostic methods, universal approaches in selection and analysis of diagnostical parameters, formation of the rules to accept the diagnostical calculations which minimize the errors of diagnosis. This led to optimizing diagnostical systems, realizing their design and at the same time, with a newly developed rotor system or to choose optimal methods and applications of the diagnostics to already existing objects.

Elaboration of the techniques of diagnostics and a common approach to this problem should be based on dynamic models and on the identification of mechanical systems containing the defects like reduction of stiffness, for instance. Some results of condition monitoring and diagnostics development of the elements of rotor system are presented below.

## 2 DIAGNOSTICS AND CONDITION MONITORING TECHNIQUES OF OBLONG CONSTRUCTIVE ELEMENTS

Dynamics of various rotor systems' constructive elements such as rotors, blades and supported elements can be described by the generalized matrix-vector equation

$$M\{\ddot{x}\} + C\{\dot{x}\} + K\{x\} = \{f\} \quad (1)$$

where M, C, K are mass, damping and stiffness matrices, respectively; {f}- vector of excitation forces;  $\{\ddot{x}\}$ ,  $\{\dot{x}\}$ ,  $\{x\}$  - vectors of the parameters of the dynamic state.

Once the model structure of a conservative or a quasi-conservative weakly-damped system is determined, the parameter identification of their unknown factors may be performed on the basis of the frequency equation. Its solution with resonance frequencies  $\Omega_j$  leads to an expression such as

$$E_j = \Delta(\Omega_j, \bar{p}) \approx 0, \quad j = \overline{1, n} \quad (2)$$

where  $\Delta$  operator,  $\bar{p} = (p_1, p_2, \dots, p_k)$  - vector of unknown parameters.

For  $n=k$ , Taylor expansion of this expression with respect to the initial parameters estimates  $\bar{p}^*$ , truncated by linear terms of the series and by constrains  $E_j \rightarrow 0$  eventually yields the unknown parameters of the model. This is a fairly general approach as, let's say, the frequency equation may be found by the finite element technique for an arbitrary mechanical system or its part.

It is known that, when a mechanical system is damaged, its constructive parameters change and as a result natural frequencies of the system also changed [1].

So, if we have a vector  $\{x\}$  from the model (1), we should make the following functions of sensitivity

$$U_{ij} = \frac{\partial x_j}{\partial p_i}, \quad (3)$$

which represent a changing vibrational signal that depends upon different features of the defect. This approach gives us the possibility to investigate the influence of different aspects of defects (place, geometrical parameters, changes of mechanical parameters, etc.) on vibrational processes.

There are two possibilities in the latter approach: vibration measuring may be used for condition monitoring as the determination of the moment of defect initiation; measured vibration analysis may be used for the diagnostics as the procedure for the defect determination, its place and characteristics (geometrical, physical and mechanical).

The general monitoring procedure may be expressed as follows,

$$U_x(t) = |\{x^*\} - \{x_t\}| \leq \{\delta_x\}; \quad U_p(t) = |\{p^*\} - \{p_t\}| \leq \{\delta_p\}, \quad (4)$$

where  $\{x^*$  and  $\{x_t$  are state vectors of the system in an initial condition and at time  $t$ , respectively;  $\{p^*$  and  $\{p_t$  are system parameters at normal conditions and are identified at time  $t$ ;  $\{\delta_x$  and  $\{\delta_p$  are tolerances of the prior assigned state vectors and parameters, respectively.

In the case of a defect we have  $\Delta p_i \Rightarrow \Delta x$  and the conditions of a defect initiation may be

$$\left( \frac{\partial U_x(t)}{\partial t} \right)_{\delta_x} \neq 0, \quad \left( \frac{\partial U_p(t)}{\partial t} \right)_{\delta_p} \neq 0 \quad (5)$$

where  $( )_{\delta}$  denotes that the measurements must be done with the accuracy admitted in  $\delta$  area.

Dynamic simulation of damaged mechanical systems opens the way to a number of techniques for tests and condition monitoring of oblong structures based on the frequencies and modes of vibration, as well as interactions of the structures with the added dynamical elements (mass or piezo-electric elements).

## 2.1 Diagnostics based on frequencies and modes

By including the technique of finite elements it is possible to develop a versatile procedure of analysis for defects on construction parts using the simulation of defects (place and characteristics). Any damage that reduces stiffness is described in terms of the parameter changes of the finite elements, or disruptions of links between the corresponding finite elements, when auxiliary nodes for cracks are introduced. The stiffness matrix consists of stiffness matrices for the finite elements  $[K_{ij}]$ , and includes the locations of nodes for the defects [2]. After the analysis of the defected constructive element has been made, with the

help of a structure model (1) we obtain theoretical contact between the parameters of the defect and dynamic characteristics of the element. These results are the theoretical basis of diagnostical methods.

They were used in developing a technique and a computer algorithm for locating defects in oblong structures like shafts or long rotors, which may be modeled as a beam. They simulate changes of, say, natural frequency, dependent on the location, so that a matrix of features can be built

$$B = [b_{n,m}] , \quad (6)$$

where  $b$  is a weight factor related to the change of natural frequency,  $n$  the number of natural frequencies covered,  $m$  the number of location sites along the beam.

With the concept of quasi-harmonic forced oscillations of damaged parts, we can now develop a vector of specifications for the damage in terms of the resonance frequencies of the structure

$$\{v\} = \{b_n^* \} \quad (7)$$

This is compared to every column in matrix  $B$ , when the corresponding column of matrix  $B$ , for instance  $\{b_{n,j}\} = \{b_n^*\}$ , that shows the co-ordinate  $x = \Delta x \cdot j$  of the damage in the beam.

The suggested technique generalises the well known method [3].

## 2.2 Methods based on the interactions of the structures and added elements

**Controlled added elements.** The techniques of crack diagnosis in oblong structures of rotor systems, such as shafts or long turbine rotors without blades, whose dynamics are similar to a beam's dynamics are based on the interaction between the structure and the added element moving along the structure during the test.

A current location of the added element by a control device is reflected in the co-ordinate system of the structure. Then the dynamic behavior of a reference mechanical system, (Fig.1) can be compared to the co-ordinates of the added element and of the damage. By the control of the added element we mean both their modes of motion and the ensurance of specific interactions of the structural parts, when local changes of stiffness are reflected by the parameters of oscillation of the reference mechanical system.

The transverse vibration of the defective oblong constructive element is described by the beam's general differential equation

$$EI \frac{\partial^4 y(x,t)}{\partial x^4} + \rho F \frac{\partial^2 y(x,t)}{\partial t^2} = \sum_{i=1}^2 M_i \delta(x-x_i) + P(t) \delta(x-x_1) + F_2 \delta(x-x_2), \quad (8)$$

where  $E, I, \rho, F$  - stand for Young's modulus, moment of inertia, density and cross-sectional area, respectively;  $y(x,t)$  - are current cross-sections  $x$ ;  $M_i$  ( $i=1,2$ ) - flexion moment at the

beam ends,  $\delta$  - the Dirac delta function;  $P(t)$  - force of the added dynamic element of the beam;  $F_2$  - its interaction with the local element of stiffness  $K_2 < K^{(j)}$ .

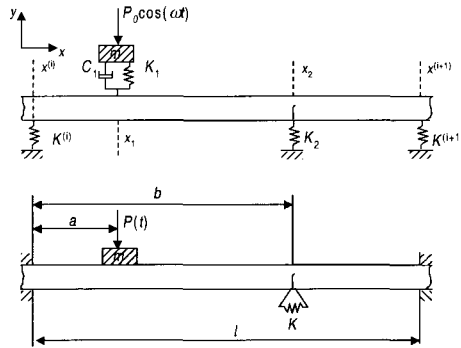


**Figure 1. A general dynamical model of a mechanical system: stiff beam, added dynamic element and co-ordinate system for the mathematical description of a separate section of a damaged beam.**

The relation of  $P(t)$  for a simple dynamic element of mass  $m$  added to a construction part, including stiffness factor  $K_1 \neq 0$  and damping factor  $C_1 = 0$ , is

$$P(t) = \frac{\omega^2 m(x_1) + P_0}{1 - \omega^2 m / K_1} \cos \omega t \quad (9)$$

and at least two controls of forced oscillation are possible:

- a)  $P_0 = const$ ,  $Y = y(x_i) = var$ ;
- b)  $Y_0 = y(x_i) = const$ ,  $P_0 = var$ .

It is possible to suggest the bending moment as a parameter of integrity of the defect. In the region of the latter it is

$$M = K \left( \frac{\partial y(x, t)}{\partial x} \Big|_{b+0} - \frac{\partial y(x, t)}{\partial x} \Big|_{b-0} \right), \quad (10)$$

where  $b$  is the co-ordinate of the defect in Fig.1;  $K$  the flexion stiffness in the region of the defect.

In that case for describing the dynamics of a constructive element we have three equations of the damaged beam and twelve boundary condition equations. The suggested mathematical model has revealed several specific features of oscillations in the mechanical systems studied. The frequency-amplitude relations have been found and depend on the co-ordinates of the

defects, on the values of  $K$ ,  $m$  and  $P_0$ . Specific minima and maxima were observed at the coordinates of the defect (see Fig. 2).

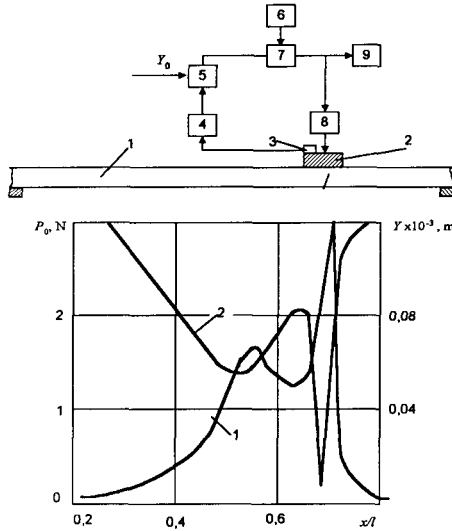


**Figure 2.** The behavior of amplitudes  $Y(1)$  of added mass and of the exciting force  $P_0(2)$  for different distances from the damage ( $b/l=0,7$ ) in the different control case a) or b); 1 - beam, 2 - added mass, 3 - transducer, 4 - amplifier, 5 - reference unit, 6 - generator, 7 - controlled amplifier, 8 - oscillator, 9 - control signal recorder.

It was found that the quantity  $D$  of defect of same simple constructive elements, (e.g. thin shafts) for determined  $m$  and  $\omega$  may be estimated from the experimental measurements by the following expression:

$$D = 1,4 \times 10^{-3} \frac{\Delta y / y}{1 + \Delta y / y}, \quad (12)$$

where  $\Delta y$  is the change of amplitude of vibration in the defect region of the testing element;  $y$  is the amplitude of vibration of an element far from the defect.

**Mechanical energy converting elements.** The operation of rotor systems is accompanied by vibration processes, the analysis and the transformation, which make it possible to inspect vibrationally the technical state of the system using autonomous built-in devices working on the conversion of the mechanical energy of vibration into electrical energy, applying for this reason piezoelectric matrices connected to the mechanical system. They can be made of piezoceramics or piezofilm and can work reliably enough by being placed directly in the objects to be inspected. Both the absence of electronic devices and the power supply source and the ability to transmit the understored converted energy from different elements of mechanical systems including rotating elements to the motionless parts with the least disturbances make these devices the most preferable. Relative precision and abilities of the

energy transformation for the diagnostic problem can be evaluated by simulating the dynamics of a general model according to the technical state of a mechanical system [4].

The theory of a conversion model of the mechanical energy into electrical energy is based on the Lagrange equations of the second order describing elastic oscillations of mechanical systems, on the equations of the conversion effect and on the equations of dissipation or withdrawal of the converted electrical energy. It means that the whole system consists of three sub-systems: mechanical, conversional and electrical. A general model of the whole vibrational system enables us to analyse the parameters of the converted energy according to different parameters assigned by both physical and mechanical properties of the inspected system and disturbances. This model also allows us to optimize the parameters of converting and withdrawing the converted electrical energy from the sub-systems taking into account the reason of the conversion process. By seeking to convert the maximum sensitivity of the autonomous inspection unit to some defects of the mechanical system (crack, loosening fixture, change of the vibration frequency spectrum, etc.) considering the imposed constraints, it is possible to obtain an optimal conversion of a sub-system of the whole vibrational system mentioned above.

The numerical analysis of a mathematical model has indicated that such defects of the structural element as crack, loosening fixture, change of the vibrational parameters, etc. are obtained. Built-in inspection is available practically when the power of a separate spectral component of the vibration is not less than 0.12 W.

### **2.3 Crack diagnostics by means of acoustic emission.**

In modern diagnostics the method of acoustic emission is well-known. Its wider use in practice is limited by different problems that are sometimes technically difficult to solve, e.g. signal stability in a wide range of temperature changes, separation of a signal from other kinds of noise, selection of informative parameters, etc. Trying to get maximum sensitivity, we have carried out a mathematical simulation of the monocrystal LiNbO<sub>3</sub> with the purpose of establishing the indicators of piezomodules in different directions and to select optimal sections of the crystal in the sense of signal reception.

When the numerical experiment has been carried out, types of crystal sections were determined, the best sections in the sense of sensitivity for the registration of the waves of a certain type. In the case of acoustic emission, the most frequently important is not the registration of the waves of a certain type, but the maximum sensitivity of any waves propagating from a defect in general. Therefore, such a direction of the crystal section was chosen that allowed one to obtain maximum sensitivity while registering quasi-longitudinal wave oscillations.

This result was very important when creating transducers for acoustic emission for special monitoring systems of rocket turbines ("Buran" project).

## **3 CONDITION MONITORING OF ROTATING ELEMENTS**

The spectrum of diagnostics of rotating constructive elements is very wide, but it is possible to distinguish two aspects that are very important which concern reliability: registration of

rotating constructive elements during the process of their break down and identification of the technical condition of support elements (bearings).

### 3.1 Crack monitoring of rotating constructive elements

Cracks in rotating elements generate acoustic signals, which usually vanish among other noises or become very weak and they cannot be registered reliably enough by a measurement system. In such a case the defect, e.g. break of a turbine blade is noticed only when the increased vibration occurs because of unbalance.

Diagnostics of cracks on the grounds of acoustic emission has many unused reserves. As was mentioned, the application of this method in the case of rotating constructive elements is very interesting. It is also necessary to evaluate the low power of the signals of high frequency and as a rule the great damping of the acoustic canal. In solving these problems there was taken a mathematical model, which describes elastic oscillations of the mechanical sub-system in the zone of the converted element, transformation of the oscillation energy into electric energy, change and transformation of electric voltage shapes from the rotating constructive element (rotor) into the stationary element (stator), where the load (indicator or other measurement means) is situated. Such a modelling has allowed the creation of a device for crack diagnostics in a rotating element of the turbine, shown in Fig. 3.

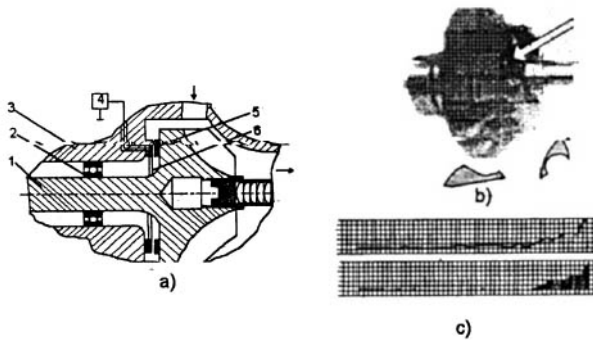


**Figure 3. A device for crack monitoring in the turbine (a): 1-rotor; 2-bearing; 3-stator; 4-indicator; 5-plate of the monocrystal; 6-metal ring dielectrically fastened on a stator. The rotor of the turbine with the blades torn away (b). Change of the peak value and intensity of the acoustic emission during the experiment (c).**

Applying the above mentioned means (increase of the informativeness of the method of acoustic emission, designing of special transducers, receiving only these signals, which frequency is more than 1 MHz, widening of the range of operating temperatures, etc.) and corresponding technologies of measurement, there were carried out a series of experiments that have confirmed the suppositions being accepted in the stage of creation and the expected results. As it is seen from the Fig. 3 a crack of a rotor blade in the rocket turbine at high speed was reliably registered for more than 20s (a turbine blade was 80% cut near the base). It was possible to achieve this only because the element of great sensitivity for tension waves of high frequency is fixed in the place of a possible defect and because there aren't any intermediate elements, bringing some noise (transmitter and amplifier, etc.) and because geometric



parameters as well as electric ones while modeling have been carefully chosen. Creation of the presented devices is especially urgent and effective for rotating constructions of a limited resource and reliability is one of the most important features.

### 3.2 Identification of the condition of the bearings

In modern scientific technical literature different methods of evaluation of the condition of bearings are analysed. It is possible to determine the condition of bearings according to the level of noise and its change in the course of time, with reference to the noise it has raised in comparison with the standard ones, using special nomograms for the condition change of bearings, according to the change of statistical parameters of the bearing noise, etc.

The quantity of noise the bearing produces depends on the type of the bearing and on its operating conditions. Therefore, the condition diagrams and the quantities being determined according to them differ. To increase the reliability of the results of diagnostics, there was analysed the dependency of the noise the bearing produces on the type of bearing (roller, ball, thrust, etc.), on its size and operating conditions (number of revolutions, size of the acting loads).

There has been carried out special experimental research to determine the dependencies of the noise level of the parameters HR (signal level that corresponds ~1000 imp/s, is expressed in decibels) and of the parameters LR (signal level that corresponds ~50 imp/s, is expressed in decibels) on the type of bearings and their operating conditions, using the SPM technique.

Nomograms of individual types of bearing in corresponding operating conditions were the result of experimental research. This means that for practical monitoring systems it is necessary to create new nomograms corresponding to the bearing condition change from the experimental nomograms of the same type of bearings we have already obtained.

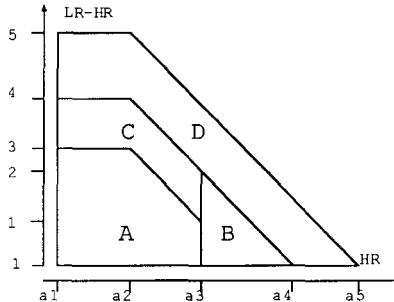


**Figure 4. A Generalized diagram. Zones: A - good condition of the bearing; B - deteriorated condition of the bearing (bad lubrication); C - deteriorated condition of the bearing (disturbance of rolling elements); D - inadmissible condition of the bearings (it is necessary to change the bearing).**

In case we could approximate the form of the nomogram zones, its location and change of location depending on operating conditions of bearings, at first it was necessary to describe mathematically the nomogram itself and its characteristic zones. The description of the nomograms has been made according to the generalized diagram presented in Fig. 4 ( $a_1 \div a_5$

points of a sudden change of the diagram in the abscissa axis (HR),  $b1 \div b5$ - in the ordinate axis ( $\Delta=LR-HR$ ). For the approximation there were used polynomial equations of the 3rd degree. The error of different operating conditions of bearings that has been received in the interval from 30 to 60 did not exceed  $\pm 1$  dB. That is quite accurate enough, because the error of the measuring parameters is  $\pm 2$  dB.

There were determined the dependencies of the variable quantities  $a(i)$  and  $b(i)$  on the operating conditions of bearings individually for each type of bearing. The programme of diagnostics was also created, which determines the condition of bearings (A, B, C or D) of a real rotor system, according to the calculated operating conditions of bearings and according to the measured parameters of HR and LR.

#### 4 CONCLUSIONS

Creation of the dynamic models and evaluation of the technical state of oblong constructions by the identification of mechanical systems with distributed and lumped parameters is effective and universal enough for the mathematical simulation of the dynamics of damaged constructions, for the analysis of the defect influence and for the search of informative diagnostic parameters.

*A number of methods for crack testing in oblong constructions based on the analysis of quasi-harmonic processes and phenomena of the interaction in damaged constructions with added elements have been theoretically found.*

Theoretical description and the method of vibrodiagnostics of different defects, in particular cracks, based on the dynamic model of the conversion of the mechanical energy into electrical energy by means of piezoelements covering the construction are suggested.

The method for the condition identification of different types of bearings are devised. The evaluation frames of the technical condition of bearings for different parameters of the acoustic signals are determined and the approximation programme for the evaluation frame is also made. This allows one to get a proper technical condition of the evaluation frame for any different operation condition of the bearing. According to this the diagnosis is made automatically.

#### REFERENCES

- (1) Adams, R.D. & Coppendale, J. Measurement of the elastic module of structural adhesives by a resonant bar technique, *Journal of Mechanical Engineering Science*, 18, Nr.3, pp. 93-100, 1976.
- (2) Volkovas, V., Klumbys, A. & Ragulskis, K. Mathematical Simulation and Vibrodiagnostics of Fault States in Mechanical Systems, "SEECO-82", *Environ. Eng. Today. Proc. Pap. Sym. Soc. Environ. Eng., London*, 13-15, July, Vol.1. Buntingford, pp.7-25, 1982.
- (3) Cawley, P. Non-destructive testing of mass-produced components by natural frequency measurement, *Proc. of the Institute of Mechanical Eng.* Vol.199, Nr.B3, pp. 161-168, 1985.

- (4) Volkovas, V. Some Theoretical Problems in Modern Techniques of Diagnostics in Mechanical Systems, Proc. Intern. AMSE Conf. "Systems Analysis, Control and Design", Lyon, July 4-6, Vol.3, pp. 205-212, 1994.

*This page intentionally left blank*

# Translational and rotational vibration measurements on rotors using laser vibrometry – advances in data interpretation

S J ROTHBERG and J R BELL

Department of Mechanical Engineering, Loughborough University, UK

## ABSTRACT

Laser Doppler Vibrometry is now a well established experimental technique and commercially available instruments are gaining in popularity. This paper sets out a comprehensive model of the velocity sensed by both a single laser beam and by a pair of parallel beams incident on a rotating shaft requiring three translational and three rotational coordinates to describe its vibratory motion fully. While the intention is to measure the six vibration components, the model reveals how it is instead only possible to measure six vibration “sets”, each inseparable combinations of more than one of the vibration components. Arrangements for isolation of each “set” are detailed and an essential post-processing technique to resolve translational and rotational vibration components is demonstrated in a measurement of crankshaft bending vibration.

## 1. INTRODUCTION

The non-contact nature of Laser Vibrometers (1) offers significant advantages over traditional contacting vibration transducers and measurements on hot, light or rotating components are often cited as important applications. On rotating machines, it is most common to measure the vibration transmitted into a non-rotating part of the machine using a contacting transducer such as an accelerometer but low vibration transmission can make this unreliable, especially for rotor torsional vibrations. For translational or rotational vibrations, non-contact transducers capable of measuring directly from any location on a structure but especially directly from the rotor itself would be valuable assets and LDV offers this possibility.

30 years ago, one of the first reported LDV applications was for axial vibration measurement directly from a rotating turbine blade (2). Investigations of magnetic discs (3, 4), bladed discs (5, 6) and modal analysis on rotating discs (7) are typical and more recent examples of measurements that can be made using a single probe laser beam. Parallel beam arrangements

have also been developed, first for torsional vibration measurement on rotors (8) and more recently for angular vibration measurement on non-rotating structures (9). Such devices have also been used recently for assessment of crankshaft bending vibration (10).

Previous experience with LDV measurements on rotors has highlighted a cross-sensitivity to vibration components perpendicular to the component it is intended to measure. A feature of much previous work has been prediction of acceptable performance but only in the presence of a single vibration component, neglecting the effects of other components present in the more complex motions likely to be encountered in practice. Previous studies have acknowledged cross-sensitivities (10, 11) but these have merely been special cases of the totally general case. This paper summarises an analysis of the velocity sensed when laser beams are incident in an arbitrary direction on a target that is of substantial interest in engineering – a rotating shaft requiring three translational and three rotational co-ordinates to describe its vibratory motion fully. To demonstrate the type of cross-sensitivities encountered, measurements are made on the crankshaft of a running diesel engine with the intention of resolving pitch and yaw vibration from simultaneous measurements which individually show cross-sensitivity to pitch in an intended yaw measurement and *vice-versa*. This resolution uses a post-processing technique, also suitable for radial vibration measurements (12).

## 2. VELOCITY MEASURED BY A SINGLE LASER BEAM INCIDENT ON A ROTOR

The case considered is that of a rotating shaft, which can have arbitrary shape, undergoing an arbitrary vibration requiring three translational and three rotational co-ordinates for description. (The resulting theory, however, will be equally applicable to any non-rotating, vibrating structure). As shown in Figure 1, the origin of the translating reference frame  $xyz$  is fixed to a point on the centre line of the shaft with the undeflected shaft rotation axis defining the direction and position of the  $z$ -axis. The time dependent unit vector  $\hat{z}_R$  defines the changing direction of the shaft rotation axis, which deviates from the  $z$ -axis as the shaft tilts. P is the instantaneous point of incidence of the laser beam on the shaft and is identified by the position vector  $\vec{r}_p$ . Provided that the illuminated axial element of the shaft can be assumed to be rigid, the velocity of P,  $\vec{V}_p$ , is the sum of the translational velocity of origin O and the velocity of P relative to O as a result of rotation about an instantaneous rotation axis passing through O.  $\vec{V}_p$  can be expanded as:

$$\vec{V}_p = (\dot{x}\hat{x} + \dot{y}\hat{y} + \dot{z}\hat{z}) + \dot{\theta}_x(\hat{x} \times \vec{r}_p) + \dot{\theta}_y(\hat{y} \times \vec{r}_p) + \dot{\theta}_z(\hat{z} \times \vec{r}_p) + \Omega(\hat{z}_R \times \vec{r}_p) \quad (1)$$

where  $\dot{x}$ ,  $\dot{y}$  and  $\dot{z}$  are the translational vibration velocities of the origin O in the  $x$ ,  $y$  and  $z$  directions (defined by the unit vectors  $\hat{x}$ ,  $\hat{y}$  and  $\hat{z}$ ),  $\Omega$  is the total rotation speed of the axial shaft element (combining rotation speed with any torsional vibration) and  $\dot{\theta}_x$ ,  $\dot{\theta}_y$  and  $\dot{\theta}_z$  are the angular vibration velocities of the shaft around the  $x$ ,  $y$  and  $z$  axes (pitch, yaw and roll).

In the usual configuration, a laser vibrometer measures target velocity at the point of incidence in the direction of the probe laser beam given by the unit vector  $\hat{b}$ . As the shaft vibrates and rotates, however, the position of this point, both on the target and in space, changes continuously, particularly if the shaft is not cylindrical. While the point of incidence does change position in space, it will always lie somewhere along the line of the beam itself

and, by this means, an important feature of operation can be demonstrated. The velocity sensed by a laser beam is insensitive to the shape of the target (13), even when the incident beam changes axial and radial position on the target shaft quite dramatically.

The velocity measured by the laser vibrometer,  $U_m$ , is the component of the velocity of the point of incidence in the direction of the incident beam. With the incident beam oriented according to the angles  $\alpha$  and  $\beta$  (refer to Figure 2a), this velocity is given by (13):

$$\begin{aligned}
 U_m = & \cos \beta \cos \alpha \left[ \dot{x} + (\dot{\theta}_z + \Omega)y - (\dot{\theta}_y - \Omega\theta_x)z \right] \\
 & + \cos \beta \sin \alpha \left[ \dot{y} - (\dot{\theta}_z + \Omega)x + (\dot{\theta}_x + \Omega\theta_y)z \right] \\
 & - \sin \beta \left[ \dot{z} - (\dot{\theta}_x + \Omega\theta_y)y + (\dot{\theta}_y - \Omega\theta_x)x \right] \\
 & - (y_0 \sin \beta + z_0 \cos \beta \sin \alpha) \left[ \dot{\theta}_x + \Omega\theta_y \right] \\
 & + (z_0 \cos \beta \cos \alpha + x_0 \sin \beta) \left[ \dot{\theta}_y - \Omega\theta_x \right] \\
 & + (x_0 \cos \beta \sin \alpha - y_0 \cos \beta \cos \alpha) \left[ \dot{\theta}_z + \Omega \right]
 \end{aligned} \tag{2}$$

Equation (2) allows the vibration engineer to be sure of vibration component sensitivity for any laser beam arrangement on any target. It shows that the measured velocity is the sum of six terms, each the product of a combination of geometric parameters and a combination of motion parameters - the "vibration sets". The six vibration sets, in square brackets, are inseparable combinations of different motion parameters and, no matter how a laser beam is aligned, only the sets can be measured directly. The six vibration sets in equation (2) are referred to by the vibration parameter that might be regarded as the intended measurement. These are, in the order presented, the  $x$  radial,  $y$  radial, axial, pitch and yaw vibration sets and the rotation speed set which includes torsional vibration. Equation (2) can be simplified by setting  $z_0 = 0$  so that the plane of the origin of the  $xyz$  axes and the "measurement plane" are coincident, since this is just a matter of definition.

A previous description of this cross-sensitivity in radial vibration measurements (11) demonstrated how the "error terms" in the measured velocity, principally  $(\dot{\theta}_z + \Omega)x$  and  $(\dot{\theta}_z + \Omega)y$  in equation (2), could be of sufficient magnitude to mask the intended radial vibration measurement. A particular problem in the measurement of synchronous radial vibrations was also highlighted. Since the first description of this problem, there has been discussion about whether a particular arrangement of laser beams or a particular variation of the arrangement, for example by scanning the laser beams, might enable resolution of individual motion components. Equation (2) shows that direct measurement of pure radial, axial or bending vibration is not possible because the measurement will always be sensitive to other motion components. It may be possible to assume the effects of additional shaft motions are negligible, enabling direct measurement. For example, if the amplitudes of the vibration components are known to be similar then the intended measurement dominates at frequencies much higher than rotation frequency. In a general case, however, reliable estimation of components requires post-processing as set out in section 4. In contrast, unambiguous measurement of the axial element's time-resolved rotation speed appears possible, accepting that the torsional vibration and roll motion of the shaft are indistinguishable. Isolation of any one of the six sets requires appropriate choice of values for  $\alpha$ ,  $\beta$ ,  $x_0$ , and  $y_0$ . A radial and an axial vibration measurement are shown below as examples.

To measure the  $x$  radial vibration set requires alignment of the laser beam so that it passes through the centre of the shaft and along the  $x$ -axis making  $\alpha = \beta = 0^\circ$  and  $y_0 = 0$ :

$$U_m = [\dot{x} + (\dot{\theta}_z + \Omega)y - (\dot{\theta}_y - \Omega\theta_x)z] \quad (3)$$

Similarly,  $\alpha = 90^\circ$ ,  $\beta = 0^\circ$  and  $x_0 = 0$  enable the  $y$  radial vibration set to be isolated. Equation (3) shows agreement with previous two dimensional theory for radial vibration measurements (11) which was validated experimentally over a range of vibration amplitudes, frequencies and shaft rotation speeds, including speed fluctuations. This equation, however, extends the theory to include motion of the shaft in all six degrees-of-freedom, revealing a third term in the measured velocity,  $(\dot{\theta}_y - \Omega\theta_x)z$ . Attempts to resolve  $x$  and  $y$  radial motions by post-processing (12) currently rely on the assumption that this third term is an order of magnitude smaller than the first two.

To measure the axial vibration set, aligning the laser beam so that it is parallel to the shaft rotation axis ( $\beta = 90^\circ$ ), makes the measured velocity equal to:

$$U_m = [\dot{z} - (\dot{\theta}_x + \Omega\theta_y)y + (\dot{\theta}_y - \Omega\theta_x)x] + y_0[\dot{\theta}_x + \Omega\theta_y] - x_0[\dot{\theta}_y - \Omega\theta_x] \quad (4)$$

Alignment such that  $x_0$  and  $y_0$  are zero simplifies the measurement.

### 3. MEASURING ROTATIONAL VIBRATION SETS WITH PARALLEL BEAMS

While values for the geometric coefficients in equation (2) can be found that enable the radial and axial vibration sets to be isolated, isolation of the rotational vibration sets requires the geometric coefficients of the three translational vibration sets to equal zero i.e.  $\cos\beta\cos\alpha = \cos\beta\sin\alpha = \sin\beta = 0$ , to which there is no solution. This means that none of the rotational vibration sets can be isolated using a single laser beam. Repeated application of equation (2) for two beams indicates that isolation of each rotational vibration set requires use of parallel beams. In an interferometer, the difference velocity,  $\Delta U_m$ , is obtained conveniently. For rotation,  $\vec{\omega}$ , about an instantaneous axis passing through O,  $\Delta U_m$  can be written concisely as (14):

$$\Delta U_m = \vec{\omega} \cdot (\vec{d} \times \hat{b}) \quad (5)$$

where  $\vec{d}$  is a vector in the plane of the beams perpendicular to the beam direction  $\hat{b}$  and of magnitude equal to the perpendicular separation of the beams,  $d$ . Figure 2a shows the laser beam orientated according to the angles  $\alpha$  and  $\beta$  from which  $\hat{b}$  can be expanded into Cartesian components. For  $\vec{d}$ , consider an initial position in the  $yz$  plane inclined at an angle,  $\gamma$ , to  $\hat{z}$  as shown in Figure 2b. After finite rotations first by  $\beta$  and then by  $\alpha$ , the projection of  $\vec{d}$  into each direction can be found. Finally, expanding  $\vec{\omega}$  in the manner of equation (1), equation (5) can be written as:

$$\Delta U_m = d [ (\sin\gamma \sin\beta \cos\alpha - \cos\gamma \sin\alpha) [\dot{\theta}_x + \Omega\theta_y] + (\sin\gamma \sin\beta \sin\alpha + \cos\gamma \cos\alpha) [\dot{\theta}_y - \Omega\theta_x] + \sin\gamma \cos\beta [\dot{\theta}_z + \Omega] ] \quad (6)$$



The following table summarises the configurations enabling isolation of each of the rotational vibration sets. Where considerations such as limited access do not allow the necessary alignment, consideration must be given to the influence of other motions on the intended measurement. A previous study (15) highlighted the sensitivity to angular vibrations of rotation speed set measurements made with the Laser Torsional Vibrometer (LTV) when  $\beta \neq 0$ . A maximum of  $20^\circ$  was recommended.

Desired measurement	$\alpha$	$\beta$	$\gamma$	Side / End of shaft?
Pitch set, $d(\dot{\theta}_x + \Omega\theta_y)$	0	$\pm \pi/2$	$\pi/2$	End
	$\pi/2$	$\beta$	0	Side
Yaw set, $d(\dot{\theta}_y - \Omega\theta_x)$	$\pi/2$	$\pm \pi/2$	$\pi/2$	End
	0	$\beta$	0	Side
Rotation speed set, $d(\dot{\theta}_z + \Omega)$	$\alpha$	0	$\pi/2$	Side

Note the sensitivity to both pitch and yaw in the pitch and yaw sets. This is an important problem that can only be addressed by post-processing as described in section 4.

### 3.1 Measurement using twin pairs of parallel laser beams

In many practical situations access to the shaft is restricted and it is not physically possible to align the beams at the angles set out in the previous section to isolate the required vibration set. The requirement for just one or two distinct values of  $\alpha$  or  $\beta$ , rather than the possibility to measure at any orientation is very restrictive. For example, with this restriction, measurement of unambiguous rotation speed cannot be achieved from the end face of a shaft which is often the only area of access. An alternative optical arrangement capable of measuring the shaft rotation speed, pitch vibration and yaw vibration sets from a variety of angles is desirable. The geometric values required to measure the vibration sets using two pairs of parallel beams are summarised in the following table and depicted in Figures 3a-c.

Desired measurement	Signal	$\alpha_1$	$\alpha_2$	$\beta_1$	$\beta_2$	$\gamma_1 = \gamma_2$	Side / End of shaft?	Figure
$\dot{\theta}_x + \Omega\theta_y$	$\Delta(\Delta U)$	0	0	$\beta$	$-\beta$	$\pi/2$	Side	3a
	$\Sigma(\Delta U)$	0	0	$\beta$	$\pi - \beta$	$\pi/2$	End	3a
	$\Delta(\Delta U)$	$\alpha$	$-\alpha$	0	0	0	Side	3c
	$\Sigma(\Delta U)$	$\alpha$	$\pi - \alpha$	0	0	0	Side	3c
$\dot{\theta}_y - \Omega\theta_x$	$\Delta(\Delta U)$	$\pi/2$	$\pi/2$	$\beta$	$-\beta$	$\pi/2$	Side	3b
	$\Sigma(\Delta U)$	$\pi/2$	$\pi/2$	$\beta$	$\pi - \beta$	$\pi/2$	End	3b
	$\Sigma(\Delta U)$	$\alpha$	$-\alpha$	0	0	0	Side	3c
	$\Delta(\Delta U)$	$\alpha$	$\pi - \alpha$	0	0	0	Side	3c
$\dot{\theta}_z + \Omega$	$\Sigma(\Delta U)$	$\alpha$	$\alpha$	$\beta$	$-\beta$	$\pi/2$	Side	3a&b
	$\Delta(\Delta U)$	$\alpha$	$\alpha$	$\beta$	$\pi - \beta$	$\pi/2$	End	3a&b

Three basic beam configurations exist; in the first, the beams are incident on the side of the shaft while, in the second, the beams are incident on the end face of the shaft. As shown in Figures 3a-c, the desired angular vibration set is selected by choosing the appropriate value for  $\alpha$ , while measurement of the rotation speed set can be achieved with any value of  $\alpha_1 = \alpha_2 = \alpha$ . This means that, for the same physical arrangement, measurements of the rotation speed set and one of the angular vibration sets can be obtained simultaneously simply by choosing to take both the sum,  $\Sigma(\Delta U)$ , and the difference,  $\Delta(\Delta U)$ , in the velocities measured by each individual pair of beams. In the third configuration, the beams are incident on the side of the shaft at different axial locations. This arrangement enables simultaneous measurement of the pitch and yaw vibration sets by taking both the sum and the difference in the velocities measured by each individual pair of beams.

#### 4. POST-PROCESSING FOR RESOLUTION OF VIBRATION COMPONENTS

This post-processing technique is equally applicable to radial and angular vibration measurements. It is written in angular terms to support the crankshaft pitch and yaw measurements that follow. The pitch,  $\dot{\Theta}_x(t)$ , and yaw,  $\dot{\Theta}_y(t)$ , vibration sets can be written:

$$\dot{\Theta}_x(t) = \dot{\theta}_x + \Omega\theta_y \quad (7a)$$

$$\dot{\Theta}_y(t) = \dot{\theta}_y - \Omega\theta_x \quad (7b)$$

It is possible to manipulate equations (7a&b) to give the genuine angular vibration velocities,  $\dot{\theta}_x$  and  $\dot{\theta}_y$ , on a frequency-by-frequency basis in terms of the measurable quantities  $\dot{\Theta}_x(t)$ ,  $\dot{\Theta}_y(t)$  and  $\Omega$ . Evaluating for the  $m^{\text{th}}$  component i.e. at  $\omega = \omega_m$  gives:

$$\dot{\theta}_{y_m} = W(\omega_m) \left( \dot{\Theta}_y(t) + \Omega \int \dot{\Theta}_x(t) dt \right) \Big|_{\omega=\omega_m} \quad (8a)$$

where  $W(\omega_m) = (\omega_m^2 / \omega_m^2 - \Omega^2)$ . Similarly, considering the pitch vibration:

$$\dot{\theta}_{x_m} = W(\omega_m) \left( \dot{\Theta}_x(t) - \Omega \int \dot{\Theta}_y(t) dt \right) \Big|_{\omega=\omega_m} \quad (8b)$$

Therefore, the genuine vibration velocity components can be resolved by evaluating the bracketed terms of equations (8a&b) and then weighting by  $W(\omega_m)$ . Inspection of equations (8a&b) shows that the weighting term is infinite and the bracketed term is zero for synchronous vibrations, i.e.  $\omega_m = \Omega$ , which makes this technique unsuitable for synchronous vibration measurement. This leads to a gap in the resolved data at the synchronous frequency and a velocity-time trace cannot be reconstructed. This is not a limitation of the post-processing technique but a limitation on the use of LDV for both translational and rotational vibration measurements on rotors. At synchronous frequency, equations (7a&b) are no longer independent and cannot be solved as simultaneous equations. A measured synchronous component can only be considered as a conservative estimate of the sum of the two (either angular or radial) velocities.

## 5 DIESEL ENGINE CRANKSHAFT VIBRATION MEASUREMENT

For measurements of pitch and yaw vibration, a novel optical configuration was devised providing three parallel laser beams aligned as shown in Figure 4. Combination of beams 1 and 2 gives the pitch vibration set and combination of beams 1 and 3 gives the yaw vibration set. The beams were aligned parallel to the crankshaft rotation axis of a four cylinder two litre diesel engine and incident on the end face of the crankshaft pulley to provide simultaneous measurements of the pitch and yaw vibration sets. A Laser Torsional Vibrometer (LTV) was used to measure the crankshaft rotation speed with its beams aligned, within access constraints, to minimise the sensitivity to bending vibration.

Both pitch and yaw vibrations were resolved in the manner set out in section 4 and Figure 5 shows waterfall plots of the resolved crankshaft pitch and yaw vibrations across a range of engine speeds. The broad peak around 450Hz, especially apparent in the pitch vibration, corresponds to the first bending mode of the crankshaft confirmed using modal testing of the stationary crankshaft (10). These are the first known resolved measurements of crankshaft pitch and yaw to be taken on a running engine by non-contact means and without modification to the crankshaft.

## 6. CONCLUSIONS

This paper has summarised theory describing the velocity sensed by laser beams incident on a rotating structure requiring three translational and three rotational co-ordinates to describe its vibratory motion fully. The theory is equally applicable to measurements on targets with simpler motions, such as non-rotating targets, allowing the vibration engineer to determine the vibration component sensitivity of any measurement with any laser beam orientation.

Six separate vibration sets, each a combination of motion parameters, appear in the full expression for the vibration velocity sensitivity using a single laser beam. The  $x$  radial,  $y$  radial, and axial sets can be isolated by appropriate geometric set-up of the laser beam while the pitch and yaw vibration sets and the rotation speed set can be eliminated but not isolated with a single laser beam. Parallel beam arrangements can isolate the rotational vibration sets, offering insensitivity to the translational vibration sets. A full range of versatile arrangements using two pairs of parallel beams was also presented as an alternative means to measure the pitch, yaw and rotation speed sets. All measurements demonstrate insensitivity to target shape.

Previous analyses have predicted satisfactory application when only single vibration components have been considered. For a rotating shaft undergoing arbitrary motion, direct measurement of radial or axial vibration is not possible because the measurement will always be sensitive to other motion components. Resolution of individual motion components within each set has been shown not to be possible by any geometric arrangement of the laser beam or by introduction of additional laser beams. An approximate solution to resolve steady-state, non-synchronous, vibrations was applied to the assessment of pitch and yaw vibration of the crankshaft of a running diesel engine enabling identification of the first natural frequency in bending. As the first such non-contact measurements, the potential of laser technology for machinery diagnostics under challenging conditions is, once again, emphasised.

## ACKNOWLEDGEMENTS

J.R. Bell acknowledges the support of the Engineering and Physical Sciences Research Council.

## REFERENCES

1. D.C. WILLIAMS (ed.) 1993 *Optical methods in engineering metrology* Chapman & Hall, London, Chapter 6.
2. Q.V. DAVIS and W.K. KULCZYK 1969 *Nature* **222**, 475-476. Vibrations of turbine blades measured by means of a laser.
3. T.A. RIENER, A.C. GODING and F.E. TALKE 1988 *IEEE Transactions on Magnetics* **24(6)**, 2745-2747. Measurement of head/disc spacing modulation using a two channel fiber optic laser Doppler vibrometer.
4. R.W. WLEZEIN, D.K. MIU and V. KIBENS 1984 *Optical Engineering* **24(4)**, 436-442. Characterization of rotating flexible disks using a laser Doppler vibrometer.
5. R.A. COOKSON and P. BANDYOPADHYAY 1980 *Transactions of the ASME Journal of Engineering for Power* **102**, 607-612. A fiber-optics laser Doppler probe for vibration analysis of rotating machines.
6. A.K. REINHARDT, J.R. KADAMBI and R.D. QUINN 1995 *Transactions of the ASME Journal of Engineering for Gas Turbines and Power* **117**, 484-488. Laser vibrometry measurements on rotating blade vibrations.
7. A.B. STANBRIDGE and D.J. EWINS 1995 *Proceedings of ASME Design Engineering Technical Conference, Boston, USA* **3(B)**, 1207-1213. Modal testing of rotating discs using a scanning LDV.
8. N.A. HALLIWELL, C.J.D. PICKERING and P.G. EASTWOOD 1984 *J. Sound and Vibration* **93(4)**, 588-592. The laser torsional vibrometer: a new instrument.
9. N.A. HALLIWELL, A. HOCKNELL and S.J. ROTHBERG 1997, *J. Sound and Vibration* **208(3)** 497-500. On the measurement of angular vibration displacements: a laser tiltmeter.
10. T.J. MILES, M. LUCAS, N.A. HALLIWELL and S.J. ROTHBERG 1999 *Journal of Sound and Vibration* **226(3)**, 441-467. Torsional and bending vibration measurement on rotors using laser technology.
11. S.J. ROTHBERG and N.A. HALLIWELL 1994 *Transactions of the ASME Journal of Vibration and Acoustics* **116(3)**, 326-331. Vibration measurements on rotating machinery using laser Doppler velocimetry.
12. J.R. BELL and S.J. ROTHBERG 1998 *Proceedings of SPIE - 3rd International Conference on Vibration Measurements by Laser Techniques: Advances and Applications, Ancona, Italy* **3411**, 14-22. Radial vibration measurements on rotors using laser vibrometry: a first practical solution to the cross-sensitivity problem.
13. J.R. BELL and S.J. ROTHBERG 1999 *submitted to Journal of Sound and Vibration*. Laser vibrometers and contacting transducers, target rotation and 6 degree-of-freedom vibration: what do we really measure?
14. J.R. BELL and S.J. ROTHBERG 1999 *submitted to Journal of Sound and Vibration*. Rotational vibration measurements using laser vibrometry: comprehensive theory and practical application.
15. T.J. MILES, M. LUCAS and S.J. ROTHBERG 1995 *Proceedings of the 15th ASME Biennial Conference on Vibration and Noise, Boston, USA*, **84-3(C)** 1451-1460. The laser torsional vibrometer: successful operation during lateral vibrations.

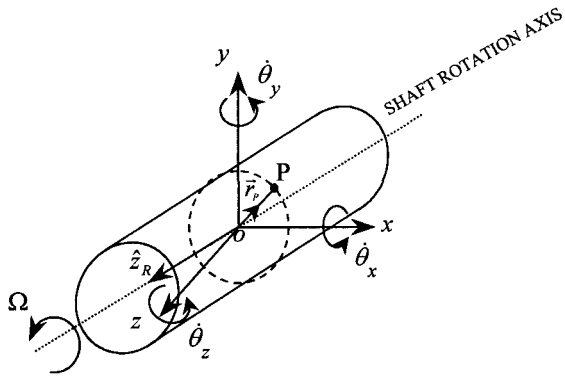


**Figure 1. Definition of a point P on a vibrating and rotating component undergoing arbitrary vibration.**

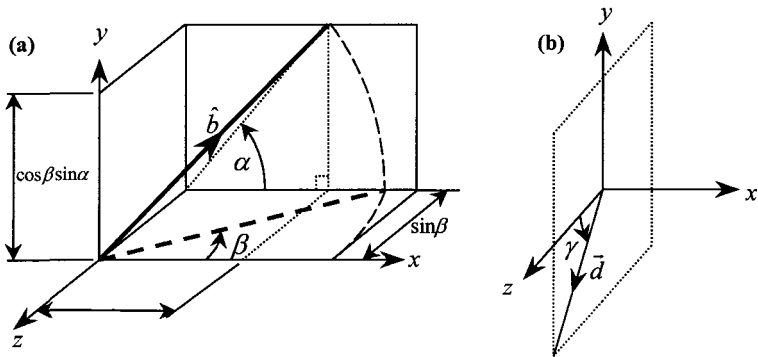


**Figure 2. Laser beam orientations, defining angles  $\alpha$ ,  $\beta$  and  $\gamma$**

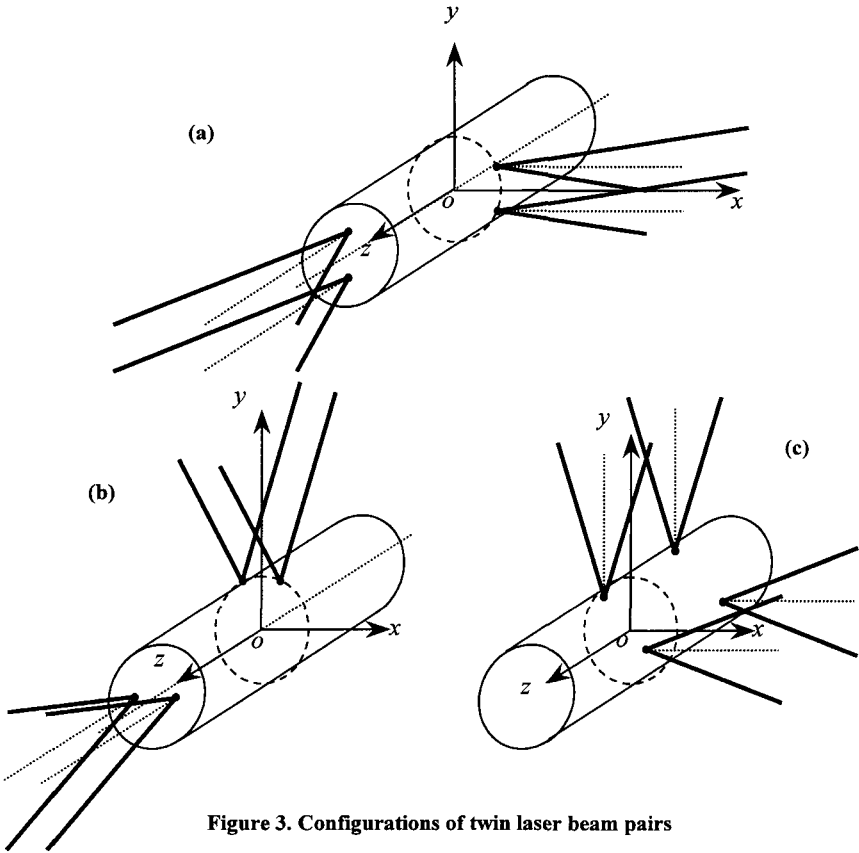


Figure 3. Configurations of twin laser beam pairs

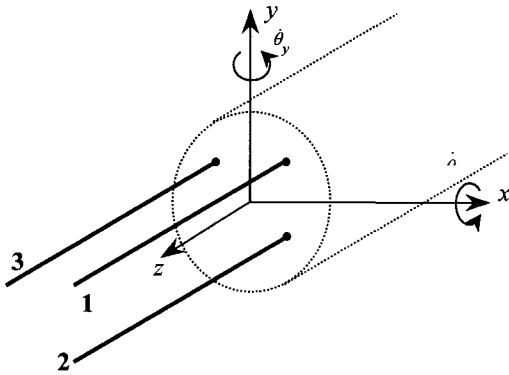
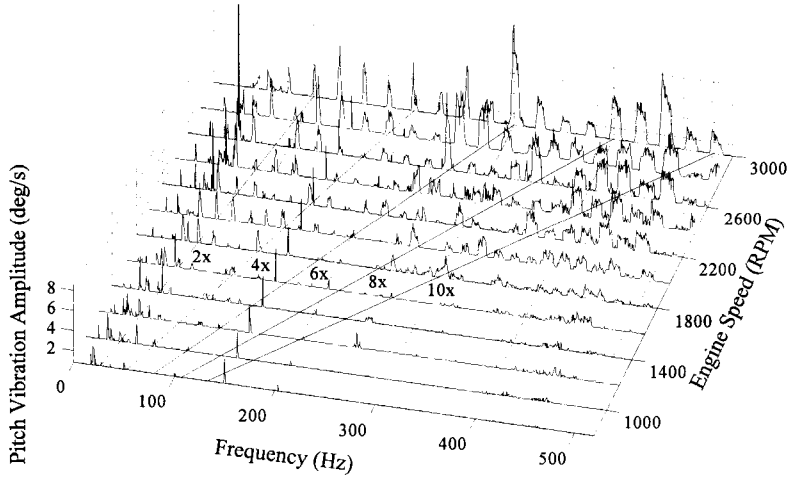
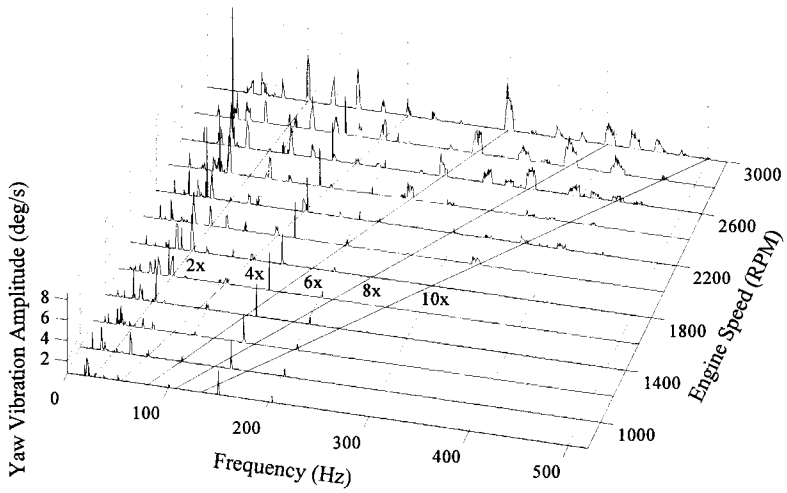


Figure 4. The pitch and yaw measurement: beam pattern on the target



**Figure 5. Resolved yaw and pitch vibration**

*This page intentionally left blank*



# Automated procedures for vibration monitoring of large rotating machinery in power plants

L GREGORI, R PROVASI, and G A ZANETTA  
CESI S.p.A, Milano, Italy

## SYNOPSIS

The paper is devoted to on-load vibration monitoring of large turbogenerator sets. It is first discussed how the practical definition of the reference period is a most important issue and procedures devised for the automatic set up and qualification of the reference model are proposed.

The integrated use of several fault indicators to increase alarm reliability is then suggested. The problem of false alarm generation is also dealt with. Results of application of the proposed techniques to large experimental data sets are summarized.

A short mention is given about preliminary tests with multiple linear regression and neural networks applications.

## 1 INTRODUCTION

The use of computer systems for vibration monitoring of large rotating machinery in power plants has become for many years a common practice and, by now, the new plants are almost always equipped with complete instrumentation sets and new vibration monitoring systems.

These systems were mainly born for diagnostic purposes and have been traditionally used to continuously collect data, so as to provide the vibration specialist with a reliable and comprehensive set of information whenever a major problem was pointed out by the plant staff.

In the last few years, there has been an increasing request to use vibration analysis as an integrating tool in order to implement predictive maintenance policies. This last result would constitute a definite pay-off for the introduction of monitoring systems.

At the same time, it has become increasingly easier and cheaper to transfer huge quantities of data from different plant stations to a central location, so as to concentrate analysis capabilities and requirements for specialised resources. That calls for the need of dealing with very large amounts of incoming data, that should be appropriately and timely analysed as a routine operation.

Therefore, full exploitation of the potential benefits of monitoring systems in such an organization calls for an early, reliable and automatic detection of deviations from the normal

vibrational behaviour. However it can be recognized that this is not yet a consolidated result, in spite of the many claims to this purpose.

A number of approaches to this problem have been proposed, with different criteria and levels of complexity. Whatever is the chosen solution, all of them require the definition of a reference model for the vibration response of the machine. Most times, this process has to be repeated from time to time in order to adapt to the inherent changes of the machine behaviour. For the remote monitoring of a number of machines, this can become a repeated and tedious task, with possibly unreliable results.

The present paper is mainly devoted to illustrate some criteria and procedures that allow for the automatic definition and validation of the reference model, with particular attention to the data collected during on-load conditions.

Another key point for the effective application of the monitoring systems is to avoid the generation of too many false alarms, while preserving the timeliness of true alarms. The comparison of the output provided by different indicators can be a valuable tool for qualifying the generated alarms. In the paper different approaches for the early detection of faulty conditions are discussed and the application to large data sets obtained from real machines is illustrated.

## 2 STATEMENT OF THE PROBLEM

In the traditional approach, which is still the most popular one in the older plants, vibration monitoring is only intended for the protection of the machine and the system simply monitors the total vibration and provide alarms or automatic shut-down when established thresholds are exceeded. The instrumentation on which this approach is based is essential, some times even not very reliable and most often it is not sufficient for diagnostic purposes.

Generally, the computerized systems are installed in connection with more complete instrumentation sets and, of course, incorporate the above mentioned protection tasks. Moreover they perform the on-line frequency analysis of the vibration signals and, therefore, are suitable for a far more precise surveillance of the machine, based on vector monitoring of the harmonic components of the vibration.

It is useful here to recall that, in view of switching to predictive maintenance, the final goal of the condition monitoring is to identify a malfunction at an early stage when vibration changes are small and, most times, slowly increasing with time. On a turboset shaft-line, this behaviour is typically associated with mechanical wear, support damage, loss of electrical insulation, progressive uneven cooling of generator bars, small rubs, alignment changes, cracks, etc... . Other problems like strong instabilities, which have very short time rises, are detected as well by more traditional monitoring techniques.

The valuable information is actually buried in a huge quantity of data, produced by the continuous flux of information from the plant, and possible deviations from normal behaviour are very often mixed with intrinsic variations due to plant operation. Therefore the original data are tedious and difficult to interrogate.

Substantially two approaches were proposed by many authors to deal with this problem. The first approach works directly on the vibration components and it is based on the violation of acceptance regions, defined by statistical techniques (see references [1]÷[5]); the second one applies similar concepts to the residual errors, obtained as difference between the measured vibration values and the expected ones, predicted by a suitable model of the vibration response (see references [3] and [6]÷[8]).

The main problem with both approaches is that they necessarily require the definition of a reference model with respect to which one has to compare the current vibration response.

This problem is scarcely ever addressed in the published literature and, at our knowledge, also in the commercial condition monitoring systems. It is generally assumed that a specialist examines manually a suitable set of data for any machine of interest and works out the requested model each time.

A policy of remote monitoring of a number of machines from central headquarters implies the repeated application of such process and that results clearly in a cumbersome and tedious task, which requires anyway a high degree of knowledge and care from the operator in order to arrive at reliable results. That explains why these approaches have been so far an academic exercise rather than an industrial practice.

Therefore an effort has been made to devise procedures that help to automatically obtain and to qualify the reference model at the request of the operator, in a sort of push-button mode, while retaining the possibility of inspection and judgement of the quality of the model obtained.

Consequently the same procedures are suitable for being repeatedly applied whenever necessary on the same machine, so as to allow for the upgrading of the reference model over the time and for an easier implementation of the model adaptivity.

The second main problem is connected with the generation of false alarms. Precision and promptness associated with improved monitoring approaches can conflict with the reliability of the responses. If it is impossible to absolutely avoid any false alarm generation, it is nonetheless necessary to try and reduce them to an acceptable number.

The solutions adopted were the introduction of some damping mechanism and the integrated use of alternative alarm indicators so as to corroborate a given alarm status.

The proposed methods were first developed in the MATLAB® environment for a proof of concept and they are now being implemented in the software of the proprietary monitoring system SMAV (Advanced Vibration Monitoring System).

### **3 DEFINITION OF THE REFERENCE MODEL**

A reference model is a structured set of information derived from suitable processing of vibrations and operational quantities (load, currents, temperatures, pressures, etc...), where the harmonic components of the vibrations are expected to assume vector values in a definite range as a function of the operation state.

When setting up a reference model, a number of decisions must be taken, concerning the quantities to be used, the range of operation on which the model is applicable, the minimum length of the reference period, the adequacy of the data and accuracy obtainable with the model.

These items are in fact essential for the correct application of any method, but they are seldom answered unambiguously, if even addressed.

The turbogenerator sets on which computerised monitoring systems were installed are equipped with four vibration transducers at each bearing. In principle, any kind of monitored vibration can be considered, but, in order to preserve simplicity and reasonable dimensions of the model, it was decided to consider only vibrations obtained from the proximity probes, that in general provide, as single transducers, the most reliable and meaningful measure of the shaft-line vibration.

Moreover only ten operational quantities at most were retained for the analysis of correlation with the vibrations in steam turbogenerator sets and a smaller number for gas turbine generators. This choice is due to the fact that many quantities are strongly correlated between each other and therefore they only duplicate the same information.

It has then been recognized that a single model cannot be applied over the entire range of operation of a turbogenerator set; perhaps this limitation can only be overcome in the residual error analysis, by the use of neural networks: tests on the subject are in progress.

Instead, it can be strongly argued which should be the leading operational quantity. Most time the active power is the best one, but in many cases it is evident that for generator vibrations the excitation current would be a more appropriate choice. In spite of that and at the expense of a better quality achievable, it was decided to adopt in any case the load as the main operational quantity in order to simplify implementation and to warrant a coherent structure of the reference model.

The entire load range can be divided in a maximum number of 8 sub-ranges for any size of machine from 50 to 660 MW. Each sub-range can further be split in a maximum of four different ranges as a function of the excitation current. Finally the other operational quantities are associated to the model only when they are correlated to each vibration of interest; in this case, their range of variation further defines the limits of validity for any new measurement.

The next step was to determine the regions of load. An original algorithm was developed that automatically determines these regions, satisfying a number of conditions: each region is such that the variance of the relevant data should be minimum with respect to the variance over the entire load range; each region should collect data relevant as much as possible steady state conditions; the number of regions should be kept to a minimum; at least 5% of the total data considered must be contained in a single region and all the defined regions should gather at least 85% of the data.

This procedure was applied to seven steam turbogenerator sets and to three gas turbogenerators. In all cases the requirements were satisfied. In Fig. 3.1 the results obtained on two distinct steam turbogenerators, characterized by different operation histories, are illustrated.

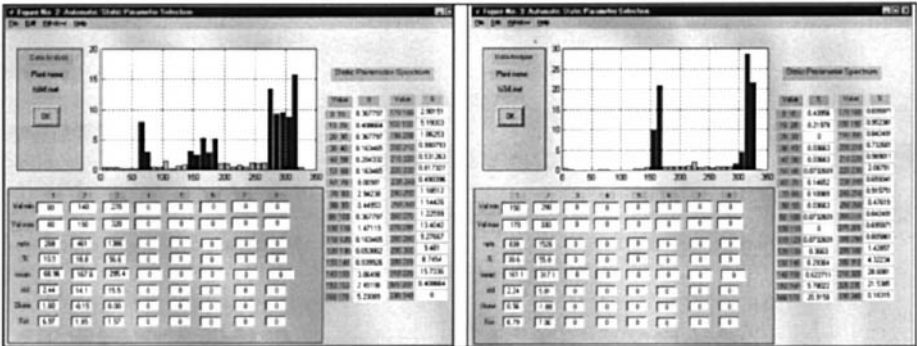


**Fig. 3.1 - Load range definition on two steam turbogenerator sets**

Keeping in mind the goal of this kind of monitoring, it is still important to stress the fact that, it is not necessary to cover all the time period at load; on the contrary it is preferable to avoid monitoring thermal transients of the machine when the vibrations are scarcely repeatable. To this purpose were also introduced time delays after start-up and major load changes, that turned out to be particularly useful with gas turbogenerators.

After definition of the ranges of load it is then possible to inspect three aspects of the data: sufficiency, adequacy and quality.

The recommendations of the minimum length for data collection in the reference period are strongly variable both in the literature and in the opinion of different specialists, usually ranging from a minimum of few weeks up to three or more months. Of course it is desirable to keep this length as short as possible, while covering the most common operation conditions.

In order to manage automatically this very important parameter, it was decided to set a 15 days initial acquisition period, after which the sufficiency of the data is tested from a statistical point of view with the following formula [9], that applies to mono-variate normal distributions:

$$n = \frac{\sigma^2}{\mu^2} \frac{Z_{\alpha/2}^2}{d^2} \tag{3.1}$$

That is to say, the minimum number  $n$  of data is a function of the normalized variance  $\sigma/\mu$ , of the significance level  $\alpha$  of the test and of the required precision  $d$ . The test is performed on each vibration harmonic for the principal components of the real and imaginary parts as long as their mean value is greater than a given threshold.

Moreover at least the 85% of the total monitoring period must be covered by the data in the resulting load regions discussed above. The experience with all the data analysed so far showed that the minimum period of 15 days is most time sufficient and it is seldom requested more than one month.

If these conditions are satisfied it is then possible to qualify the adequacy of the data. This is accomplished by the test of stationarity, applying the so called ‘rank correlation test’ [10] on a random sample of the whole set of data belonging to any load region. The sensitivity of the test can be adjusted by the associated level of significance.

In this respect, it is clear that is important not to have significant trends in the data used for the reference model. It must be said that this test is very sensitive and must be carefully tuned to an engineering level of acceptance.

If one of the previous test is not satisfied, the monitoring of a particular vibration is not enabled, the data acquisition for the definition of the reference period is continued and the previous test repeated. The reference model can be updated periodically in the initial period.

An additional check of normality is devoted to give an estimate of the accuracy of the results obtainable from the subsequent monitoring. The check is performed on a random sample of the whole set of data, by means of the Kolmogorov-Smirnov (K-S) test [11], applied to the principal components of the real and imaginary parts. Typical results are shown in Fig. 3.2, where the index of deviation of the K-S test is checked against the threshold value.

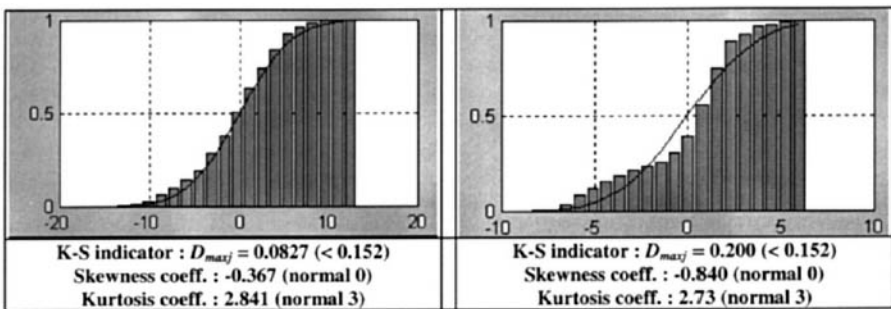


Fig. 3.2 - Examples of cumulative distribution and Kolmogorov Smirnov test

The coefficients of skewness and kurtosis are also reported, but they give more ambiguous results.

It must be observed that very often the data are not normal. In spite of that the percent of data outside the acceptance regions was found to be in general very close to those expected for the normal distributions, for a given level of significance. So that the test of normality has no consequences for the acceptance of the reference period, but it is only used for the operator's inspection.

#### 4 INDICATORS OF FAULT CONDITIONS

In order to enable the system making a cross-check among different indicators of alarm, more than a single approach was studied, so as to associate a probability to any alert or alarm condition.

The most popular approach is the vector monitoring of the harmonic components based on the acceptance regions. The form of these regions in the polar plane is different among various authors: circles [4], circular sectors [5] or ellipses ([2] and [3]) are usually proposed. In fact the ellipses are the more natural choice and they are in any case the closest to the definition in force for normal distributions. Violation of the ellipses is simply computed by the Mahalanobis distance [12]:

$$(x - \mu)' \Sigma^{-1} (x - \mu) \leq c^2 \quad (4.1)$$

The value of  $c$ , or equivalently the dimensions of the ellipses, are given by the level of significance associated to the test. Recommended values are such that the number of points outside the acceptance region for a normal bivariate distribution in the absence of faults would be in the range of 95÷99%. In a large number of tests, this indicator performed very well. In principle it can be applied to any new vibration measurement.

A second indicator was derived from the  $T^2$  test of the hypothesis, used to measure the deviation of the mean value of the vibration harmonics. In a different version, this test was proposed in reference [2]. In the rigorous statistics, the  $T^2$  test is applied to two samples of approximately equal length to check their belongings to the same normal population and it should follow the F statistics. In a number of tests, it was verified that it would be almost always violated in the correct formulation.

Therefore the indicator devised, that we still call  $T^2$ , has a similar formulation, but the threshold values are estimated empirically by assigning a tolerance on the mean value deviation and considering the covariance matrix of the entire population of data in a load range during the reference period. The formula used is:

$$\frac{n_1 n_2 (\mu_1 - \mu_2)' S^{-1} (\mu_1 - \mu_2)}{n_1 + n_2} \leq T^2 \quad (4.2)$$

The final reference value is then calibrated by comparing against the threshold value the results obtained for a number of different samples chosen at random among the data of the reference period. The value of  $n_1$  and  $n_2$  is set equal to 15 and during the monitoring period the buffer is continuously updated with the last entry. The current values are compared to the mean value of the reference period and the pooled variance matrix is used, assigning the same weight to reference and current data.

The tests performed showed that this index has a good sensitivity and promptness.

A typical graphic output for inspection of the specialist is given in Fig. 4.1.

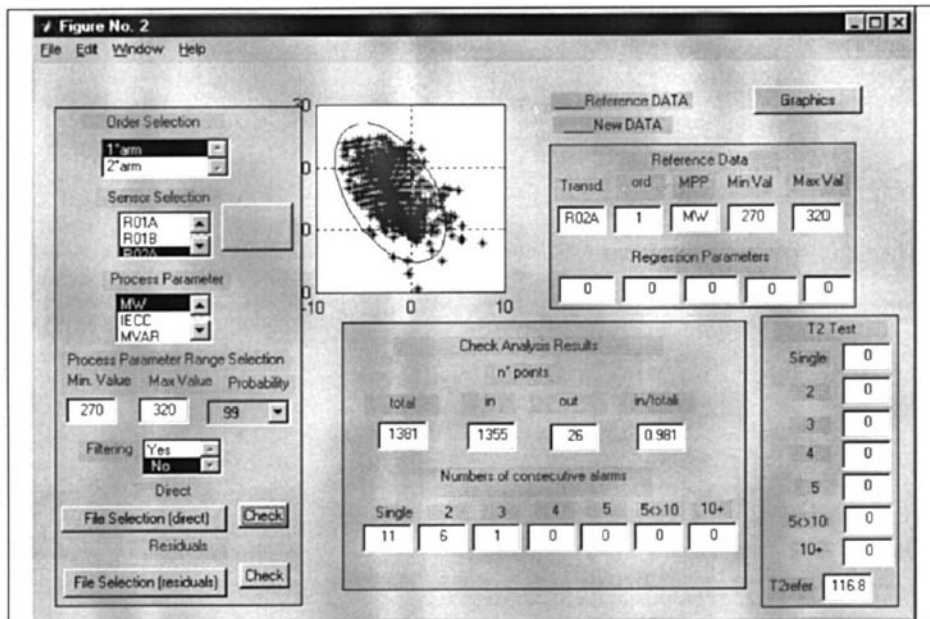


**Fig. 4.1 – Typical graphic output for visual inspection of results with acceptance regions and  $T^2$  tests. No faults in the data examined.**

The third indicator is a measure of a coherent evolution from a given reference pattern of the deformation shape of the whole shaft line or of part of it. The correlation of the vectors of the vibration deviations is computed in the sense of the Modal Assurance Criterion (MAC) and the Modal Scale Factor (MSF) is computed as well. If the deviations are random, the MAC tends to zero; if they are systematic, as in case of a definite fault, the MAC tends to unit and the MSF is meaningful with phase angle around zero values.

A similar approach was presented by Sanderson [13]. In that case the reference deformation vector was set-up with the vibration of the last acquisition. This approach is very effective for off-line inspection of stored data, but in practice it restrains the on-line monitoring to a short period and it requires each time a large number of computations.

A different mode of computation was devised, such that the reference vector is obtained once and for all from the data of the reference period and the two vectors of deviations from this reference are always computed over the last acquisitions. Moreover, not only the MAC and MSF values are considered in order to activate the alarm indicator, but also the product of their standard deviations, which stabilizes to very low values in comparison to those obtained on data in the reference period.

This last indicator also gives satisfactory results, even when the fault affects only a very limited number of bearings (i.e. 1 or 2 out of 7), but it is somewhat less prompt than the previous ones.

In Fig. 4.2 are compared test results obtained by the three indicators discussed above in the exam of vibration data containing a continuous growth and phase rotations. It can be

observed that the acceptance region violation and the  $T^2$  test give very clear results and are very prompt, while the analysis of the product of the standard deviations of the MAC and MSF coefficients is a bit more confused in the initial stage of the fault development.

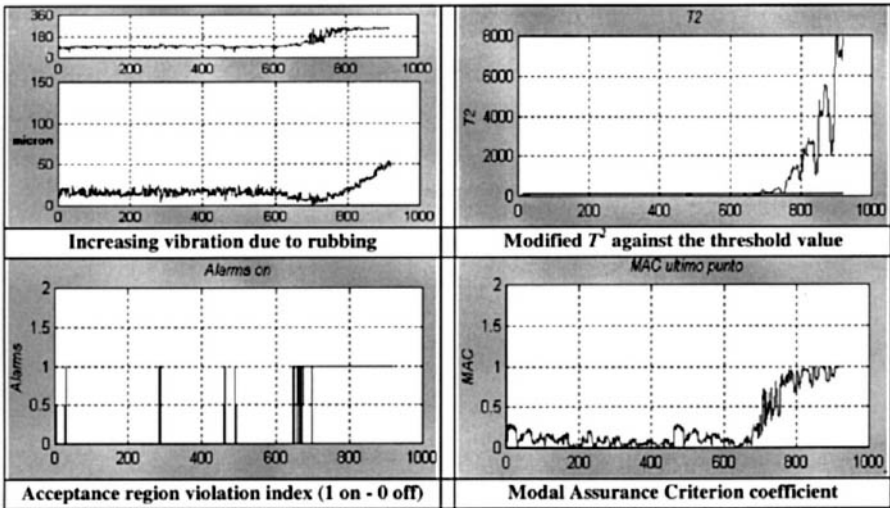


**Fig. 4.2 - Response of different indicators to a developing fault**

The cross check of these indicators can be itself a tool for reducing the number of false alarms, but it was preferred not to process them with an exclusive (AND) logic.

So that the reduction of false alarms was rather achieved by means of coherence in time of alarm conditions and consistency among different sensors.

Coherence in time means that when true alarm conditions are met, it is likely that they hold for some time and do not appear for a single acquisition, if not in a very early stage of fault development. Consistency among sensors means that a mechanical fault in general affects more than one bearing or at least, depending on the instrumentation installed, more than one sensor on a single bearing.

On the other hand, reduction of false alarms could be detrimental for their promptness and a reasonable trade-off must be accepted. The monitoring system SMAV performs an acquisition every two seconds and stores data every two minutes; the advanced alarms are applied to stored data.

From a series of tests, it was found that it was difficult, if not impossible, to produce less than 0.15% of false alarms on data which are supposed not to contain any fault, even for very long time delays. It was also observed that, requiring coherence of the alarm state for 6 to 10 consecutive acquisitions and consistency for at least two sensors, the rate of false alarms was in general less than 0.2%. Thus a maximum delay of 10 acquisitions was decided, i.e. a time delay of 20 minutes. The system can automatically choose the least possible value in the range indicated above, by processing the data relevant to the reference period. Anyway, the operator can force a greater value.



## 5 INTERPOLATION TECHNIQUES AND RESIDUAL ERROR ANALYSIS

An additional, rather than alternative, approach is then represented by the residual error analysis. The goal here is to model explicitly the vibration response of the shaft-line as a functions of the operating state of the machine, since it is in general verified that vibrations are well correlated with some of the operational quantities, so as to obtain as small as possible differences (residual errors) between measured and predicted vibrations.

The advantages with respect to direct processing of the measured vibrations by the methods discussed above, is the possibility of widen the load regions for which a single model is valid and the fact that the residuals are expected to have improved statistical properties, because most part of the deterministic contents was subtracted.

If one suppose to have a good model for residual errors computation, they can then be further processed by traditional approaches, like the one of the acceptance regions.

Tests of two interpolation techniques are in progress at present: the more traditional multiple regression technique([2], [3]) and the neural networks approach ([7], [8]).

Besides the fact that they can be a benchmark for each other, the multiple regression model also holds an engineering meaning and provides a diagnostic potential, while hopefully the neural networks can extend the range of application of the model, they can deal with non-linearities and are expected to be less sensitive to sensor failures. Also in this case, the effort is to specify procedures for setting-up the model that can be automatically applied by the system.

In fact the tests for multiple regression model adequacy [14] are cumbersome to implement and they do not always give clear responses. As such they are not most suitable for automatic application. A possible solution is perhaps the application of the canonical correlation analysis, which allows for the automatic determination of the best regression coefficients, but no definite conclusions can be drawn from the tests carried out so far.

Feed forward neural networks were first applied with a single hidden layer, a back propagation learning algorithm and sigmoidal activation functions. Preliminary encouraging results were obtained, with a  $1.5 \pm 2\%$  mean residual error and a maximum error in general not higher than 15%. The studies in progress are now particularly investigating the precision obtainable versus the precision actually needed and the usefulness of further pre-processing of input data. Indications are that the number of perceptrons in the hidden layer can be kept to a reasonable maximum number, thus allowing for affordable learning times and implementation of procedures for the automatic set-up of the model.

Of course the network can only learn what it has been presented and it could be very sensitive to the fact that during the reference period some operating conditions could not be met. Therefore, the expectation of enlarging the load regions must take into account this problem and a selection of input data during the monitoring period must be done accordingly.

It can be mentioned that an alternative approach, with use of the radial basis functions, did not give the expected results because of the uncontrolled growth of the number of centres requested for convergence.

## 6 CONCLUSIONS

The paper has been mainly focused on the problem of the definition of the reference model to be used in connection with on-load vibration monitoring of large turbogenerator sets.

A number of techniques were developed that allow for the full definition and qualification of the reference period by means of procedures that can be applied automatically and repeatedly by the system, in case at some expense of a better quality obtainable by a data analysis performed by a specialist on any particular situation. This is deemed to be an important step in promoting a more systematic application and full exploitation of the potential of

condition monitoring system and a necessary achievement for massive data processing and remote control of many turbogenerator units.

It was then proposed to monitor different alarm indicators in order to increase the overall reliability of the alarm condition. Besides the more traditional acceptance region technique, two other indices were originally elaborated starting from previous proposals. The reduction of the number of false alarm is discussed as well.

The proposed methods have been extensively tested with good success on a number of experimental data sets picked up on large steam and gas turbogenerator units and they are now being implemented for on-line testing on a proprietary system.

Finally a short mention was made of preliminary tests performed with multiple regression techniques and neural networks techniques for residual errors computation as an additional integrating approach to condition monitoring. The results obtained so far are encouraging and possible lines of further refinement have been envisaged.

## REFERENCES

- [1] G.D'Ans, J.De Raedt, P.Opendacker /An Advanced Vibration Monitoring System for Large Turbosets/ 10th Int. AIM Conf. on Power Stations (1989)
- [2] D.N.Futter, G.Hewitt, I.W.Mayes /Techniques for Remote Monitoring and Processing of Large Quantities of On-line Vibration Data/ IMechE, 5th Int.Conf. on Vibrations in Rotating Machinery, Sept. 7÷10, 1992, Bath (UK)
- [3] G.Diana, A.Vania, A.Vallini, G.A.Zanetta /Diagnostic Techniques in Condition Monitoring/ CISM/IFTToMM Symposium Diagnostics of Rotating Machines in Power Plants, Oct. 27÷29, 1993, Udine (I)
- [4] F.Herz /The Vibroview System-A Modern Concept of Condition-based Vibration Monitoring of Big Turbogenerators/ CISM/IFTToMM Symposium Diagnostics of Rotating Machines in Power Plants, Oct. 27÷29, 1993, Udine (I)
- [5] J.Courrech /New Industry Standard Technology Applied to Condition Monitoring in Power Industry/ CISM/IFTToMM Symposium Diagnostics of Rotating Machines in Power Plants, Oct. 27÷29, 1993, Udine (I)
- [6] F.Léonard, C.Poirier /Application de la Statistique et du Krigeage à la Surveillance de Groupes de Production Hydro-électrique/ 2nd Int. Symposium Acoustical and Vibratory Surveillance Methods and Diagnostic Techniques, Oct. 10÷12, 1995, Senlis(F)
- [7] I.W.Mayes /Use of Neural Networks for On-line Vibration Monitoring/ Proc. IMechE, A.J.Power Energy (UK), vol.208, n.A4(1994), pp267÷274.
- [8] R.Parenti, et alii /Steam Turbine Vibration Diagnostic System Based on Neural Hologram/ Power-Gen'98 Conf., June 9÷11, 1998, Milan(I)
- [9] B.Williams /A Sampler of Sampling/ John Wiley & Sons, New York, 1978
- [10] M.Kendall, A.Stuart /The Advanced Theory of Statistics/ Vol.3, Design and Analysis and Time Series, 3rd Edition, Charles Griffin &Company Ltd., 1976
- [11] A.O.Allen /Probability, Statistics and Queueing Theory/ Academic Press, 1978
- [12] B.F.J.Manly /Multivariate Statistical Methods/ Chapman & Hall, 1991
- [13] A.F.P.Sanderson /The Vibration Behaviour of a Large Steam Turbine Generator During Crack Propagation through the Generator Rotor/ IMechE, 5th Int.Conf. on Vibrations in Rotating Machinery, Sept. 7÷10, 1992, Bath (UK)
- [14] W.W.Hines, D.C.Montgomery /Probability and Statistics in Engineering and Management Science/ 3rd Edition, John Wiley & Sons, 1990

# Processing of blade monitoring system data

**M BALDA**

Institute of Thermomechanics, Academy of Sciences of The Czech Republic, Pilsen, Czech Republic

## 1 INTRODUCTION

The total reliability of a nuclear power plant requires the same for its single parts. Rotating blades of a turbine belong to the most loaded parts of nuclear power plant equipment. This is the reason why considerable attention is paid to blade vibration during an operation of the turbine. For the purpose, special monitoring systems have been developed for following behaviour of blades in service conditions. The monitoring system should give messages when a danger of a fatigue damage occurs. It takes place in moments, when dynamic stresses in critical places of blades exceed a safe level.

## 2 MEASUREMENTS

New monitoring systems for blade vibrations are based on an exact time measurements (1), (2). Clock pulses of a high constant frequency  $f_c$  are counted into a counter, the contents of which are stored at the moments when tips of blades are passing sensors attached to a turbine stator. The stored sequence of the counts is a typical nonstationary time series. The nonstationarity originated by a rotation is superposed on useful signals of blade tip deflections from their equilibrium positions. Figure 1 shows a typical set of measured data in three stages of their preprocessing. There was only one sensor in the stator of the turbine, the rotor of which was running by 3000 RPM, giving the effective sampling frequency  $f_s = 50$  Hz. One measurement period of the duration 2 seconds performed through one sensor gave 100 samples per blade.

In the Figure 1a and 1b, there are samples of all signals taken from 47 blades and one datum drawn after subtracting a linear trend caused by an average rotor speed. It is seen that the

blade signals the thick line in the Figure 1a are still nonstationary. The thin line drawn a distance higher is the smoothed average of all blade signals. The strongly oscillating signal belongs to the datum, and corresponds the torsional vibration of a rotor.

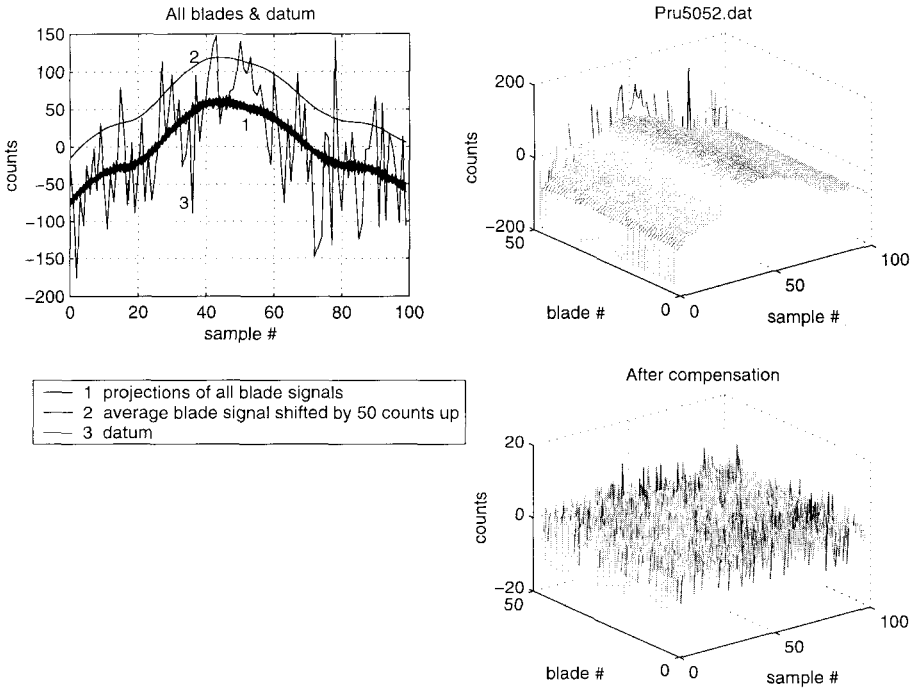


**Figure 1: Measured signals of blades and a datum**

### 3 SIGNAL RECONSTRUCTION

Instantaneous blade tip deflections may be obtained by the above mentioned preprocessing and scaling of the stored numbers of counts. A very important problem is raised by a low frequency sampling of the blade signals with respect to natural frequencies of blades. The information on frequency components of the sampled signals may give the Fourier transform.

#### 3.1 Fourier analysis of sampled signals

Sampling the signal  $h(t)$  of blade tip deflections by a sampling frequency  $f_s = 1/T$ , where  $T$  is the sampling period, corresponds to the multiplication of  $h(t)$  by the Dirac comb

$$\delta_T(t) = \sum_{k=-\infty}^{\infty} \delta(t - kT), \quad (1)$$

as a periodic series of Dirac pulses shifted mutually by  $T$  in time. The operation generates a time series, a sampled function

$$h_T(t) = h(t) \delta_T(t) = \sum_{k=-\infty}^{\infty} h(kT) \delta(t - kT) \quad (2)$$

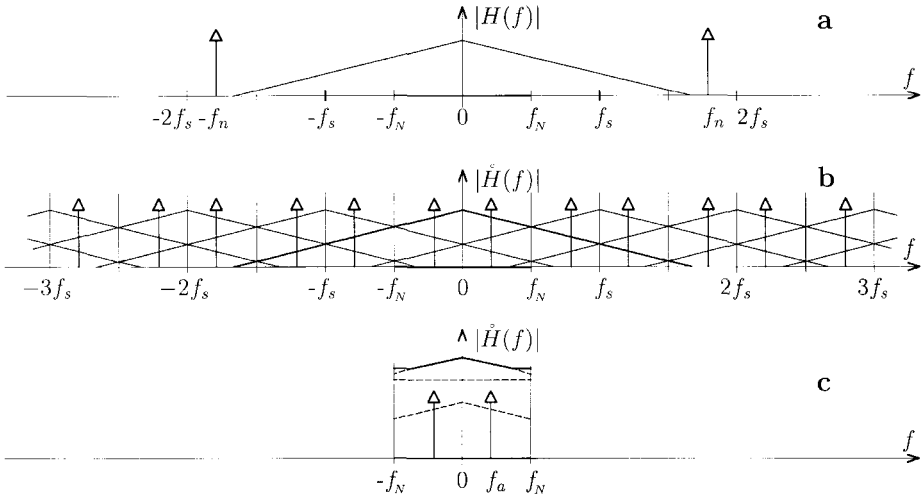


**Figure 2: Aliasing produced by a low sampling frequency  $f_s = 2f_N$**

Since the Fourier transform (FT) of the Dirac comb

$$F\{\delta_T(t)\} = \frac{1}{T} \delta_{f_s}(f) \quad (3)$$

is a (scaled) Dirac comb in the frequency domain with the repetition period  $f_s = 1/T$ , the Fourier transform of the sampled signal is

$$\begin{aligned} F\{h_T(t)\} &= \int_{-\infty}^{\infty} h(t) \delta_T(t) e^{-j2\pi ft} dt = \int_{-\infty}^{\infty} h(t) \sum_{n=-\infty}^{\infty} \delta(t - nT) e^{-j2\pi ft} dt = \\ &= \frac{1}{T} H(f) * \delta_{f_s}(f) = H_{f_s}(f) \end{aligned} \quad (4)$$

The formula expresses a convolution of the Fourier transforms  $H(f)$  of the original function  $h(t)$  and  $\delta_{f_s}(f)$  of the Dirac comb  $\delta_T(t)$  in the frequency domain. It is seen from equation (3) that the Fourier transform of the sampled signal is an infinite sum of all copies of the Fourier transform of the original function shifted by multiples of the sampling frequency  $f_s$ . In order to avoid any interference of the side frequency bands with the basic one in the

interval  $(-f_N, f_N)$ , where  $f_N = f_s / 2$  is so called Nyquist frequency, the sampling frequency  $f_s$  should be chosen at least as a double the highest frequency  $f_h$  contained in the signal:

$$f_s \geq 2f_h \tag{5}$$

In the example from the Figure 2a,  $f_h = f_n$ . The formula (5) expresses the well-known Shannon sampling theorem. The convolution in formula (4) introduces very serious problem in signal processing. If the signal were undersampled, what means, if its highest frequency contained in the signal were higher than  $f_N$ , the frequency components outside the basic frequency range  $(-f_N, f_N)$  would be moved to another frequency into that basic band. This phenomenon, called “aliasing” or “folding”, is well demonstrated in the Figure 2. The low sampling frequency  $f_s$  causes a repetition of the original FT (from Figure 2a) into side bands (Figure 2b), and a summing of overlapping contributions of all bands (Figure 2c). The particular frequency component  $f_n$  is projected into the basic band to another, aliased frequency  $f_a$ , which may be evaluated using the following formula

$$f_a = f_n - f_s \text{round}\left(\frac{f_n}{f_s}\right) = f_n - f_s k \tag{6}$$

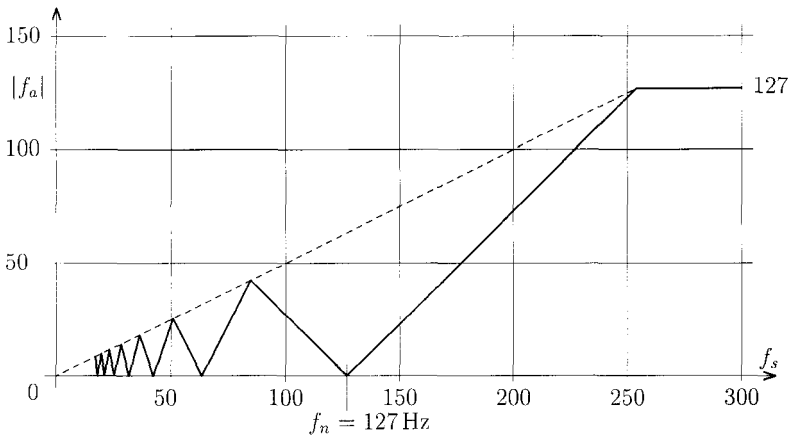


**Figure 3: Aliased frequency  $f_a$  as a function of a sampling frequency  $f_s$ .**

The Figure 3 shows the example of aliasing the frequency  $f_n = 127$  Hz, when sampled by an arbitrary sampling frequency  $f_s$ . The attainable peak aliased frequencies  $f_{ax}$  and corresponding sampling frequencies  $f_{sx}$  are

$$f_{ax} = \frac{1}{2k+1} f_n, \quad \text{and} \quad f_{sx} = \frac{2}{2k+1} f_n \quad \text{respectively.} \tag{7}$$

The signal becomes unobservable, when  $f_s = f_n / n$ , with natural  $n$ , for which  $f_a = 0$ . In this case, a particular frequency component occurs at zero frequency of an aliased spectrum.

### 3.2 Reconstruction of vibrating blade signals

A signal may not be reconstructed if the sampling frequency does not comply with the sampling theorem. This fact would disable, in general, any attempt to estimate a fatigue life of rotating blades, if the signals were undersampled. In that case, there would be only sparse information at disposal on peaks of stresses, which cause the fatigue damage and its cumulation. Fortunately, there is a way available, how to support an estimation of the residual life of blades. The monitored turbine disc with blades is not a black box for an observer. The monitored disc is well known from pre-operation investigations during its development. This means that estimates of the resonance frequencies  $\tilde{f}_n$  are known quite well in forward from numerical and experimental analyses. The rotational speed and the number of sensors distributed uniformly along the stator circumference determine the sampling period  $f_s$ . The estimates of aliased frequencies corresponding the forecasted resonant frequencies of blades in the Fourier transform of slowly sampled signals will be

$$\tilde{f}_a = \tilde{f}_n - f_s \text{round} \left( \frac{\tilde{f}_n}{f_s} \right) = \tilde{f}_n - f_s \tilde{k} \quad (8)$$

It is rather easy to find peaks in the Fourier transform, which are within a distance of  $\mu$  elementary bands on both sides from the estimated aliased frequencies due to Equation (8). The found peak frequencies may be recalculated to  $f_n$  using formula (6), where  $\tilde{k}$  is used instead of  $k$ . The reconstruction will then be done in the following steps:

- Choose an appropriate fictive sampling frequency  $\alpha f_s > 2f_n$ , where  $f_h$  is the highest natural frequency to be identified.
- Build a new reconstructed Fourier spectrum  $H_{k f_s}(f)$  in the interval  $\alpha(-f_N, f_N)/2$  by moving the parts of the aliased spectrum to places belonging to the frequencies  $f_n$ . Those parts consist of the peak complemented by  $\nu$  adhering frequency components from its both sides. An attention should be paid on the way, how the aliased spectrum was originated, as far as the order and phases of components are concerned.
- Spread a rest of the aliased Fourier spectrum over the  $H_{k f_s}(f)$  due to the user requirements.
- Apply the inverse FT to the reconstructed spectrum to obtain a reconstructed signal of the blade tip deflection

$$h_{T/k}(t) = \text{F}^{-1} \{ H_{k f_s}(f) \} \quad (9)$$

It is necessary to stress that the described method of the signal reconstruction gives only one approximation out of many others. All approximations are fitting the sequence of original signal samples exactly, if all frequency components of the aliased Fourier spectrum have been properly transferred into the reconstructed one. In that case, the reconstruction yields an acceptable signal for the damage estimation. Methods that are more accurate might be developed, however, they are all much more complicated and as such time consuming.

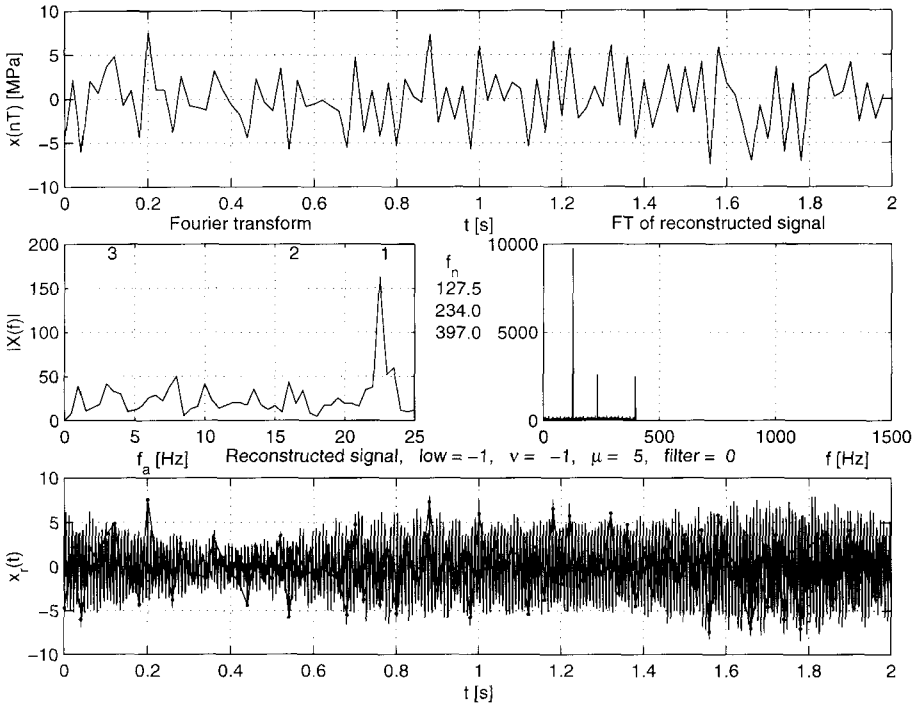


**Figure 4: Slowly sampled signal, its FT, reconstructed FT, and reconstructed signal of a real blade**

#### 4 DAMAGE ESTIMATION

An estimation of a damage of blades due to vibration is a delicate complex problem. There are the following reasons for such a statement:

- Blade tip deflections are composed out of all frequency components of the spectrum.
- Every mode of vibration has its own critical places, where extreme stress occurs. In general, they are mutually different.
- The individual modes need not generate uniaxial stress in the critical points.
- Even in the case of one dominant component of principal stress, the damage may be estimated by many different formulae giving different resulting damage.
- The stress varies at random in time and owing to conditions of operation.
- Material properties are known with a large variance.

Let us suppose the stress in critical places of a blade are almost uniaxial. A damage of a blade material is dependent on the area of hysteretic loops in the stress-deformation plot. The area is proportional to an energy spent for plastic deformations, which are a measure of the damage.



The Figure 5 shows how important is the knowledge of hysteresis loops of a complex signal. Heights of the loops may be found by a decomposition of the random stress signal into the full cycles by a procedure, which has been named by its authors a “rain flow” method (5). In the middle of seventieth, the author of this contribution has found the way, how to decompose the random process into full cycles in real time of measurements. The standard method has been single-channel oriented.

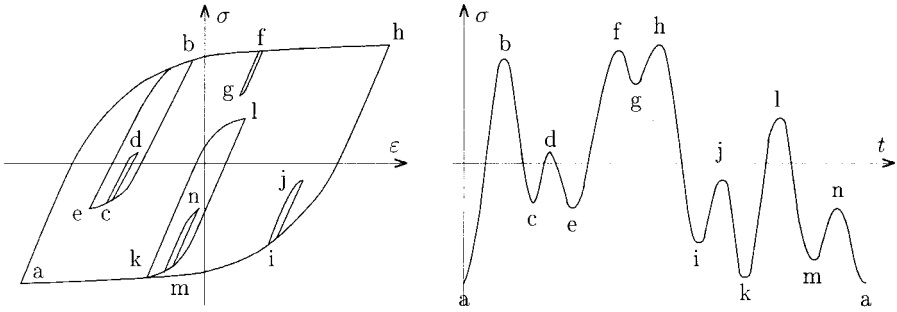


**Figure 5: Random stress and corresponding hysteric loops**

The general single-channel rain flow method is based on the application of a special memory called the stack, where incoming local extremes of a random process are stored until the extreme on the top of the stack (TOS) creates the full cycle with an extreme just below TOS. That pair of extremes creating a full cycle is then removed from the stack and counted on the proper place of 2D histogram, a matrix of full cycle counts. Then, the TOS is tested again for an existence of a full cycle till there is any. After all, the new extreme is put on TOS, and the whole procedure is repeated. A long-term using of the rain flow method for random stress decompositions has revealed cases, in which a multi-channel rain flow method would be necessary in practice. An optimization of structures exposed to random loading, and an estimation of a damage of vibrating blades belong to such tasks. This has been the reason why the multi-channel rain flow method has been developed.

The new method changes a bit the processing of full cycles, and calculates a relative damage of every blade instead of counting histograms, because the monitoring system should give information on the damage level in any time. For the purpose, a partial relative damage is evaluated as soon as the full cycle occurs. In spite of an existence of plenty of hypothesis for an estimation of the damage caused by a single cycle, the Palmgren-Miner law of linear damage cumulation is the most simple and popular. Therefore, the relative damage of the  $i$ -th full cycle of the amplitude  $s_{ai}$  and mean value  $s_{mi}$  is evaluated using the formula

$$d_i = \frac{1}{N_{cmi}} \left( \frac{s_{ai}}{s_{cmi}} \right)^{w_m}, \quad (10)$$

where  $s_{cm}$  is a fatigue limit,  $N_{cm}$  a number of harmonic cycles up to the breakdown with amplitudes  $s_a = s_{cm}$ , and  $w_m$  an exponent of the S-N curve. The subscript  $m$  denotes that those

quantities depend on the mean stress  $s_m$ . The cumulative relative damage of the  $j$ -th blade is estimated as a sum of all relative damages in the given critical place as

$$D_j = \sum_i d_{ij}, \quad (11)$$

where  $D_j$  should not exceed a constant  $k_d$  determined by a machine producer. Should the Palmgren-Miner law held perfectly,  $k_d$  would approach unity. The residual time of life of a bladed disc is determined through the blade showing the shortest life or the greatest relative damage.

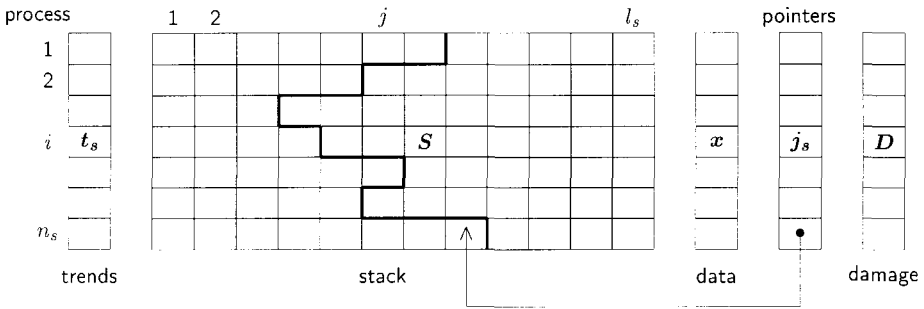


**Figure 6: Memory requirements for a decomposition of  $n_s$  signals**

The main idea of the multi-channel rain flow method compared with the single-channel one remained unchanged. Owing to this fact, there should be as many parallel stacks as a number of observed objects (blades)  $n_s$ . They constitute a stack matrix  $S \in R^{n_s \times l_s}$ , the rows of which are stacks belonging to individual blades. The number of columns  $l_s$  of the matrix  $S$  should be sufficient for storing extremes, which have not built full cycles yet. Next to it, several vectors, all of the length  $n_s$ , are necessary. Since the full cycles may occur on the blades in different times, a vector  $j_s$  of pointers to tops of the stacks should exist. A vector  $t_s$  contains zeros or ones expressing whether the particular signal just tends to minimum or maximum respectively.  $D$  might be vector or matrix containing the cumulative relative damages  $D_j$  in critical points. There is still one vector in the Figure 6, vector  $x$ , which holds recent samples of all signals, and serves for a recognition full cycles on tops of stacks before being stored there.

## 5 CONCLUSIONS

The paper describes a new method for evaluating a relative damage accumulated in critical points of all blades of one rotating turbine disc out of sparsely sampled positions of their tips provided by a blade monitoring system. The measured signals are reconstructed with the help of information on approximate resonant frequencies by reconstructing aliased Fourier spectra.

The reconstructed signals contain as many resonant frequencies as have been applied for. The relative damage is estimated from the Palmgren-Miner law of linear cumulation of elementary damages caused by closed hysteretic loops found by means of a multi-channel rain flow method applied to the reconstructed signals.

The problems of a monitoring system itself, sensors, strategy of data acquisition and a consequent decisions in a control room of a power plant would need another space and time to be dealt with.

### **Acknowledgements**

The results presented here have been supported by the Grant Agency of The Czech Republic by projects No. 101/97/0226 and 101/99/0103. The help of doctors F. Vaněk and P. Procházka for supplying the real experimental data is acknowledged with pleasure.

### **REFERENCES**

- (1) Gloger M., Jung M.: Non-Contact Blade Vibration Information System BeSSI Proceedings CISM/IFTToMM Symp. Diagnostics of Rotating Machines in Power Plants, Udine, Italy, Springer, 1993, pp. 149-165
- (2) Daněk O., Vaněk F.: Magnetokinetic Identification Method of Rotating Blade Vibrations (In Czech). Proceedings, Conference Engineering Mechanics '98, Svratka, 1998, pp. 97-100
- (3) Balda M.: An estimation of the residual life of blades. Proceedings, Colloquium Dynamics of Machines '99, IT ASCR, Prague, 1999, pp. 11-18
- (4) Balda M.: Prediction of Damage Cumulation in Vibrating Rotors. Proceedings, IToMM Fifth International Conference on Rotor Dynamics, Darmstadt, 1998, pp. 101-112
- (5) Matsuishi M., Endo T.: Fatigue of metals subjected to varying stress. Kyushu District meeting of Japan Society of Mechanical Engineers, Japan, March 1968

© 2000, Miroslav Balda

*This page intentionally left blank*

## Theoretical Considerations

*This page intentionally left blank*

# Rotordynamic interaction of a centrifugal pump impeller in an axial diffuser

**E TORBERGSEN**

Frank Mohn Flatøy AS, Frekhaug, Norway

**M F WHITE**

Department of Marine Engineering, Norwegian University of Science and Technology, Trondheim, Norway

## Abstract

This article describes a study of the rotordynamic impeller/diffuser interaction forces acting on a centrifugal impeller with an axial diffuser, and compares results with other published works.

An experimental facility including a forced whirling mechanism has been designed and built, based on a full scale radial impeller in an axial diffuser. The experimental results for the normal and tangential forces on a whirling impeller were in good qualitative agreement with those published for different designs. A rotordynamically destabilizing area for positive whirl speed ratios  $<0.3$  was detected. Significant direct added-mass was observed and low negative direct stiffness comparable with the results published for vaneless diffuser pumps was found. A cross-coupled mass term was only detected for off-design flow. The rotordynamic interaction was difficult to quantify at off-design near the onset for rotating stall in the diffuser. **Keywords:** Centrifugal pumps, impeller/diffuser interactions, rotordynamic forces, forced whirling

## Background

Fluid dynamic forces are an important design consideration for high performance turbomachinery, due to the search for higher power densities and stable rotordynamic design. In a centrifugal pump with volute or diffuser guide vanes, the impeller will see varying forces acting from the fluid because of rotor/stator interactions. They can arise from several locations in the impeller area. Research has been divided into three main areas, as follows:

1. Wear ring seals
2. Back and front shroud clearance
3. Impeller/diffuser clearance

Wear-ring seal effects in pumps are perhaps the best understood phenomena of the above mentioned forces and several authors, [1] [2] and [3], have studied these forces both theoretically and experimentally. In recent years several indications suggest that the impeller shroud clearance effects can dominate the dynamic forces. It has been shown that the shroud forces can have significant influence on the rotordynamic stability, [4]. A test apparatus for study of shroud leakage clearance and a forced whirling mechanism has been built, [5]. Results of these studies report destabilizing tangential forces for a range of whirl frequency ratios. Theoretical approaches have been presented using a bulk flow

model, [6], and Computational Fluid Dynamics, CFD, tools with turbulence modelling, [7].

Impeller/diffuser clearance forces have been shown to contribute significantly to the dynamic behaviour of a centrifugal pump. These forces are usually divided into motion dependent and pure excitational forces, [8]. The pure excitational forced vibrations can be significant, especially at part load due to complex flow phenomena, such as severe separation, stall and recirculation. Interaction between part load diffuser recirculation and balance piston flow is also reported, [9].

The unsteady motion dependent forces are usually expressed in terms of hydrodynamic force matrices which contain stiffness, damping and inertia effects. Several research studies have reported development of these hydrodynamic matrices, both theoretical and experimental. However, the geometry and design dependency makes it very difficult to automatically apply the results to new designs. One of the first simple two-dimensional models for dynamic coefficients of an impeller/volute system are published in [10]. It was based on potential flow theory with singularities. A quasi-one-dimensional model including unsteadiness in both the impeller and volute flows is presented in [11] and [12]. The forces were compared with experimental results for small whirl frequency ratios and gave good agreement, though the cross-coupled stiffness differs at several flow coefficients. Results for a whirling impeller in a volute showed destabilizing tangential forces for some whirl orbits and operation conditions, [13]. The hydrodynamic force matrix was also shown to be very sensitive to the flow coefficient. The same principle is used in a vaned diffuser, [14], where slightly lower values of dynamic stiffnesses were measured, especially the cross-coupled stiffness.

The objective of the present article was to describe the fluid-induced rotordynamic forces acting on a centrifugal pump impeller rotating in an axial diffuser. The diffuser guide vanes change the combined radial, axial and tangential motion of the fluid to a pure axial velocity. This type of design has not been analysed in literature with respect to fluid-induced forces. Such designs are often used in submerged pumps which might have limitations in the outer diameter of the pump casing. These types of pumps may have several impeller stages and are often integrated with electric motors. Typical applications for submerged pumps are sea water lift pumps for oil platforms and fluid storage caverns.

## Theoretical Studies

The fluid forces on a whirling impeller in a diffuser are shown in Figure 1. The total lateral forces,  $F_x(t)$  and  $F_y(t)$ , in the stationary frame of reference, and the normal and tangential forces,  $F_n(t)$  and  $F_t(t)$ , in the rotational, whirling frame of reference, can be expressed as a function of the displacement vector:

$$\mathbf{e}(t) = \begin{Bmatrix} X(t) \\ Y(t) \end{Bmatrix} \quad (1)$$

where X and Y represent the coordinates of the impeller centre measured from the centre of the diffuser.

If the displacement is sufficiently small, a linear model can be assumed, [15]. A mathematical expression of the total lateral fluid forces, including the pure excitational



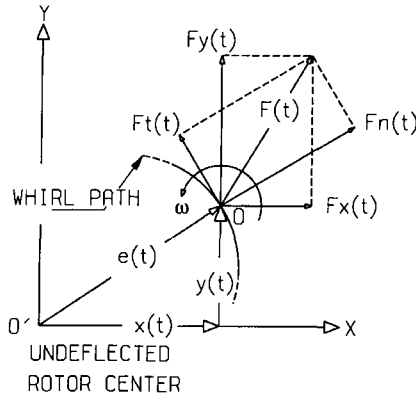


Figure 1: Diagram of the forces acting on a whirling impeller in the plane of vibration.

forces on the impeller, can then be given in the stationary frame of reference as follows:

$$\begin{Bmatrix} F_x(t) \\ F_y(t) \end{Bmatrix} = \begin{Bmatrix} F_{0x}(t) \\ F_{0y}(t) \end{Bmatrix} + \begin{bmatrix} A_{xx} & A_{xy} \\ A_{yx} & A_{yy} \end{bmatrix} \begin{Bmatrix} X(t) \\ Y(t) \end{Bmatrix} \quad (2)$$

The first part of the vector components on the right side of the equation,  $F_{0x}(t)$  and  $F_{0y}(t)$ , represents the pure excitational forces which again can be divided into a steady and an unsteady part, [13]. The steady part can be caused by unbalanced static pressure distributions, which can occur in single volute diffusers, and also gravity and buoyancy. They are commonly referred to as radial thrust and are calculated as the time average of the forces. This part will have a minimum at design flow and should be independent of any whirl motion. This is confirmed from tests by Jery, [13]. The unsteady part is typically caused by flow disturbances such as rotating stall and impeller recirculation. It also contains rotating loads, such as hydraulic unbalance, often caused by difference in the sizes of the impeller channels.

The transfer matrix  $[A]$  relates the lateral force to the shaft displacement for both direct and cross-coupled interaction. It is dependent on several parameters, but it is common to specify it as a time averaged (usually averaged over a whirl period) function dependent on impeller/diffuser geometry, whirl speed  $\Omega$ , and flow coefficient,  $\phi$ . The whirl speed is often expressed in terms of the whirl/shaft speed ratio, that is,  $\Omega/\omega$ . For the case of a circular whirl orbit with shaft angular speed  $\omega$ , the impeller motion can be represented as harmonic functions of time,  $X(t) = e \cos(\Omega t)$  and  $Y(t) = e \sin(\Omega t)$ , where  $e$  is the whirl eccentricity and  $\Omega$  the whirl speed (rad/s).

When studying the forces in the rotating frame of reference, components in terms of whirl averaged normal and tangential forces can then be given in terms of the matrix components as follows:

$$F_n = 1/2(A_{xx} + A_{yy})e \quad (3)$$

$$F_t = 1/2(-A_{xy} + A_{yx})e \quad (4)$$

where  $F_n$  is positive outwards and  $F_t$  is positive in the direction of a forward whirl orbit. A positive normal force tends to increase the displacement of the impeller. A positive  $F_t$  will have a self-exciting effect on a forward whirling impeller, that is, in the same direction as the rotation and can initiate dynamic problems often known as self-excited vibrations. The driving agent for this is the positive tangential force which tends to amplify the whirl orbit motion and it is therefore important to determine the frequency range of the destabilizing tangential force. This effect has been widely studied in the rotor/bearing and rotor/seal cases and here the fluid circumferential average velocity ratio has been shown to be the key-factor for the tangential driving force, [16] and [17].

If the  $F_n$  and  $F_t$  vary quadratically with  $\Omega/\omega$ , the  $A$ -matrix can be expressed in terms of stiffness, damping and inertia coefficients. This is the case around design flow for impellers but can be a rough approximation at off-design. For a diffuser pump, the off-diagonal elements can often be set equal in magnitude but opposite in sign, as confirmed by Jery, [13] and we get the following (neglecting pure excitational forces) :

$$-\begin{Bmatrix} \bar{F}_x \\ \bar{F}_y \end{Bmatrix} = \begin{bmatrix} \bar{K} & \bar{k} \\ -\bar{k} & \bar{K} \end{bmatrix} \begin{Bmatrix} x \\ y \end{Bmatrix} + \begin{bmatrix} \bar{C} & \bar{c} \\ -\bar{c} & \bar{C} \end{bmatrix} \begin{Bmatrix} \dot{x} \\ \dot{y} \end{Bmatrix} + \begin{bmatrix} \bar{M} & \bar{m} \\ -\bar{m} & \bar{M} \end{bmatrix} \begin{Bmatrix} \ddot{x} \\ \ddot{y} \end{Bmatrix} \quad (5)$$

The equation is made dimensionless by the reference force  $F_0 = \rho\pi r_2^3 b_2 \omega^2$ . Further, using the outlet impeller radius  $r_2$

$$x = X/r_2, \quad y = Y/r_2 \quad (6)$$

Using the whirl speed ratio,  $\Omega/\omega$ , the dimensionless normal and tangential forces on the whirling impeller can now be expressed. Combining Equations 3, 4 and 5 and using the time derivatives of the position vector, the forces can be given as follows:

$$\bar{F}_n = F_n/F_0 \cdot (e/r_2) \quad (7)$$

$$\bar{F}_t = F_t/F_0 \cdot (e/r_2) \quad (8)$$

$$\bar{F}_n = -(\bar{K} + \bar{c} \cdot (\frac{\Omega}{\omega}) - \bar{M} \cdot (\frac{\Omega}{\omega})^2) \quad (9)$$

$$\bar{F}_t = (\bar{k} - \bar{C} \cdot (\frac{\Omega}{\omega}) - \bar{m} \cdot (\frac{\Omega}{\omega})^2) \quad (10)$$

The result of this discussion is that if the normal and tangential forces on the impeller are known for at least three different whirl speeds, the rotordynamic coefficients for the impeller can be found, given that the earlier discussed quadratic fit relation for  $F_n$  and  $F_t$  with respect to whirl speed is valid.

## Test Equipment

The test rig for studying dynamic fluid forces includes a 5 bladed, 3D, full scale, radial impeller in an axial diffuser with 12 vanes. It is based on a 250 kW, submerged electric sea water lift pump for applications on offshore platforms. This design was not used in the

final commercial pump due to severe off-design flow problems. The test section is shown in fig. 2. It has a forced whirling mechanism with double eccentric sleeves and bearings and an external drive mechanism. The whirl orbit radius could be varied from 0 - 1.2 mm and whirl speed from 0 to synchronous speed. The impeller diameter was 350 mm. Both the eccentric drive and the main motor was electric with frequency converters for variable speed. For synchronizing the rotating speed and whirl orbit, PLC programming was used. The operating parameters which could be used are 0 - 3000 rpm, both main shaft and eccentric drive speed (forward or reverse precession), 0 - 500 m<sup>3</sup>/h and 0 - 15 bar.

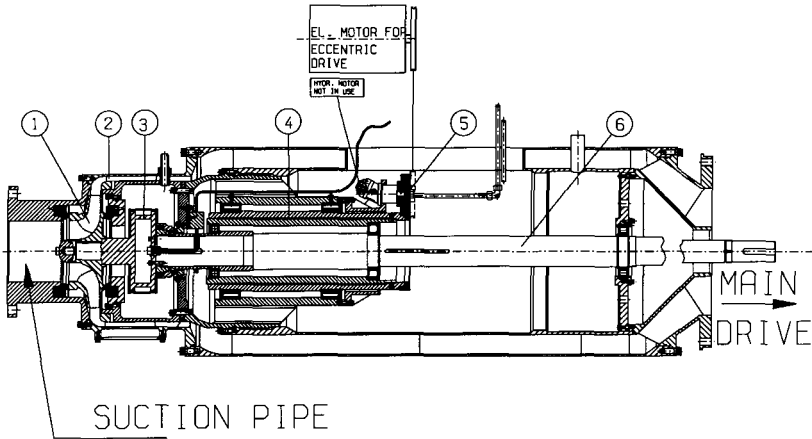


Figure 2: Forced whirling test rig for study of impeller/diffuser interaction forces (3D impeller/axial diffuser). 1. Impeller, 2. Diffuser guide vanes, 3. Dynamometer, 4. Eccentric sleeves, 5. Eccentric drive, 6. Main shaft

To prevent influence from the wear ring seals on the dynamic forces, mechanical face seals were used on both sides of the impeller. A specially designed dynamometer was used to measure the forces at the impeller shaft. It consisted of four axial bars at a large diameter to make the transverse stiffness of the dynamometer sufficient compared to the shaft stiffness. Strain gauges mounted in full bridges made the dynamometer sensitive to radial forces in perpendicular directions without undue influence from the torque and axial force. This method was also used by Brennen et al. at Caltech with their Rotor Force Test Facility [13]. The signals were transmitted from the dynamometer to the signal processing system using telemetry equipment. Impeller position was measured with contactless eddy current probes. To get a sufficiently good average of the measurements, the forces were determined using several whirl orbits, typically 30-160. Dry running tests were carried out in order to get a dynamic calibration and also subtract the dry forces from the measured impeller forces.

# Results and Discussion

In Figure 3 the normal and tangential forces for  $\phi=0.092$  are shown together with a least-square quadratic fit. The best efficiency point, BEP, for this design is  $\phi=0.105$ . Below  $\phi=0.055$  the diffuser showed a severe rotating stall. Excitational forces from the rotating stall are discussed and presented in [18] and [19]. The normal force is seen to fit quite well with the quadratic curve with a minimum point at  $\Omega/\omega \approx 0.35$ . For the negative whirl speed ratio,  $\Omega/\omega = -0.5$ , the significant high value fits into the quadratic shape. However, more whirl speeds in the negative region are needed to fully get an indication of how representative the quadratic fit really is. The tangential force for  $\phi=0.092$  shows a linear behaviour with monotonic decreasing values for increasing whirl speeds. This gives a change in sign at  $\Omega/\omega=0.3$  and the rotordynamically destabilizing region is therefore lying between 0.0 and 0.3. For flow coefficient  $\phi=0.069$ , which is near the unstable, rotating

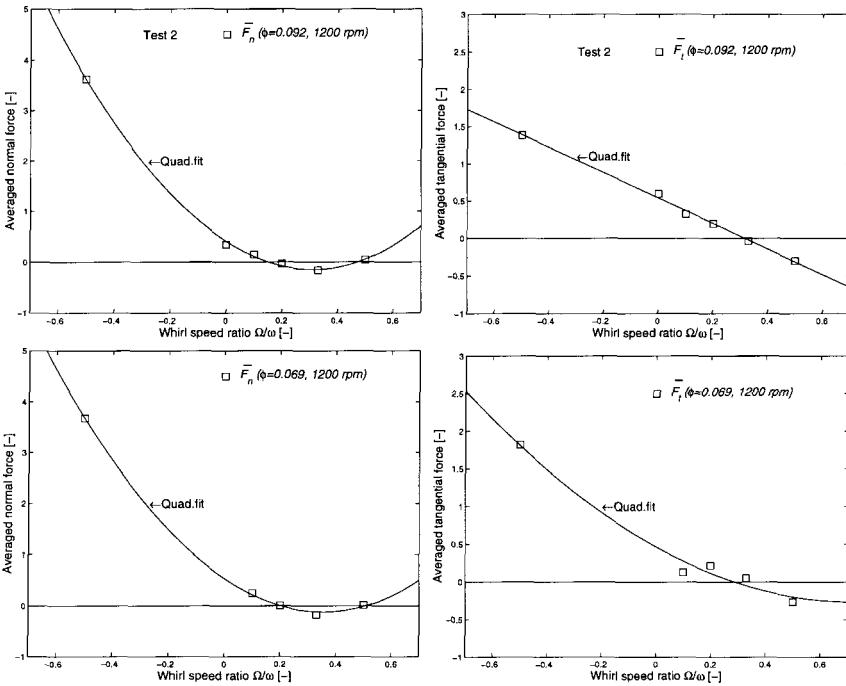


Figure 3: The dimensionless, orbit-averaged normal and tangential forces as a function of  $\Omega/\omega$ . Evaluated from measurements, 1200 rpm and  $\phi = 0.092$  (top) and  $\phi = 0.069$  (bottom). A quadratic polynomial fit is plotted (least-square).

stall region, the normal force shown in Figure 3 shows a similar behaviour as for  $\phi=0.092$ . The values of the normal force are quite similar for  $\phi=0.069$  and  $\phi=0.092$ . The tangential force for  $\phi=0.069$  shows a slightly different behaviour. A higher force at  $\Omega/\omega = -0.5$  seems

Flow $\phi$ [-]	$\Omega/\omega$	$\sigma (F_n)$	$\sigma (\bar{F}_t)$
0.092	-0.5	0.06	0.14
0.092	0.2	0.05	0.06
0.069	-0.5	0.15	0.24
0.069	0.2	0.36	0.38

Table 1: Calculated standard deviations (dimensionless, single whirl periods) for the normal and tangential forces.

to change the curve away from the linear shape observed at  $\phi=0.092$ . The change in sign from positive to negative  $\bar{F}_t$  is seen to be at the same whirl speed ratio as for  $\phi=0.092$ , that is, 0.3, giving the same destabilizing region. Despite the limited number of whirl speeds, another observation can be seen for  $\bar{F}_t$  at  $\Omega/\omega=0.1$  and 0.2, where the force is smaller at  $\Omega/\omega=0.1$  compared to  $\Omega/\omega=0.2$  and this differs from  $\phi=0.092$ . This could be an indication of an S-form of the  $\bar{F}_t$  curve, observed at off-design by Jery [13], for a volute pump. A consequence of this is that the quadratic expansion used could be inadequate when looking at flow coefficients near the unstable, rotating stall region. However, more whirl speeds should be studied to fully conclude about this.

The influence of flow on the behaviour of the whirl forces was studied for  $\Omega/\omega=0.2$  and -0.5 by using single whirl periods and calculating the standard deviation,  $\sigma$ , of the forces during several whirl periods for both flow coefficients in the second test. The standard deviations are shown in Table 1. These values show the increased unsteadiness in the flow and the difficulties in calculating the distinct whirl forces when getting close to the unstable rotating stall region. In the stall region it is not possible to quantify the rotordynamic forces by the present method because the variations for each whirl period will be too large.

## Rotordynamic Coefficients

A quadratic behaviour of the rotordynamic matrix,  $A$ , with respect to whirl speed, leads to a description of the forces in terms of stiffness, damping and inertia parts. The results in the present study showed a satisfactory quadratic fit, especially at  $\phi = 0.092$ . Using the relations derived in Equation 7 and 8, the rotordynamic coefficients can be derived from the normal and tangential forces.

In Table 2, the rotordynamic coefficients for  $\phi=0.092$  and 0.069 are shown. It can be observed that only small variations are present from the two flow coefficients. The cross-coupled mass is the only coefficient which changes significantly, from 0.0 to -1.4. The tangential force seems to be influenced by the flow, that is, from linear to quadratic when reducing the flow, and from Equation 8, it can be seen that this increases the cross-coupled mass term. However, the relatively high standard deviation for  $\bar{F}_t$  at  $\phi=0.069$  as presented in the previous section, increases the uncertainty in these results. The variation in the typical coefficients when using  $\pm\sigma$  for the normal and tangential forces at  $\Omega/\omega=-0.5$  were checked for both flow coefficients. This showed that for  $\phi = 0.069$  the direct added mass varied from 5.0 to 5.4 while the cross-coupled mass varied from -1.0 to -1.8. For  $\phi=0.092$  no significant variations were seen on the rotordynamic coefficients.

Flow $\phi$ [-]	$\phi/\phi_{BEP}$	$K$	$k$	$C$	$\bar{c}$	$M$	$\bar{m}$
0.092	0.88	-0.4	0.5	1.7	3.6	5.7	0.0
0.069	0.66	-0.5	0.5	2.0	3.7	5.2	-1.4

Table 2: Rotordynamic coefficients derived from quadratic fit, 1200 rpm.

Exp.	$\phi/\phi_{BEP}$	$K$	$k$	$C$	$\bar{c}$	$M$	$\bar{m}$
Univ. of Tokyo, vaneless diff. 6 bladed imp.	1.0	-0.42	-0.09	0.98	1.33	1.86	-0.27
Univ. of Tokyo, vaneless diff. 6 bladed imp.	0.6	-0.56	0.10	1.08	1.88	1.87	-0.32
Caltech, volute w. vaned diff. 5 bladed imp.	1.0	-2.65	1.04	3.80	8.96	6.60	-0.90
Caltech, volute w. vaned diff. 5 bladed imp.	0.65	-2.76	1.02	3.74	9.53	6.92	-1.01

Table 3: Rotordynamic coefficients for two different diffuser geometries, published by others, [20] and [21].

A comparison of these results to other impeller/diffuser designs is made in Table 3, which shows results based on experiments with similar test rigs, [20] and [21], that is, forced whirling perturbation. It should be noted that the Caltech experiments contain influences from both impeller/diffuser interactions and shroud clearance leakage flow in the same way as the present study.

## Discussion: Rotordynamic Forces

Despite the limited number of whirl speeds and lack of data from different geometric configurations, a qualitative discussion of the geometric influence can be given using both theoretical and experimental results from other designs. The general impression of the normal and tangential forces as a function of whirl speed is that they follow the same trends as reported by several authors for different impeller and diffuser geometries. Most of the published results from experiments also contain more whirl speeds than the present study in both positive and negative whirl regions.

An important parameter is the rotordynamically destabilizing region of the tangential force. This region was detected to be for whirl speed ratios  $0.0 \leq \Omega/\omega \leq 0.3$ . Despite the few flow coefficients applied in the present test, there were indications that the destabilizing region was unaffected by the flow. Consequently, this impeller/diffuser configuration seems to be less destabilizing than a typical wear-ring seal or cylindrical journal bearing, which often show a destabilizing area for  $0.0 \leq \Omega/\omega \leq 0.5$ , [15]. If strong shroud forces from a narrow shroud clearance are present, this region could be as dominating as  $0.0 \leq \Omega/\omega \leq 1.1$ , [15]. The result for the radial impeller/axial diffuser design fits into the general comparison made by Ohashi et al., [22], for published experiments for several designs, that is, the tangential force becomes destabilizing for small positive whirl speed

ratios and the shape of the normal force is parabolic with its minimum at positive whirl speed ratios.

The test carried out by Jery, [13], showed that the presence of diffuser vanes in a volute did not influence the rotordynamic forces. This leads to an assumption of limited influence from the guide vanes in the present design. The axial inlet of the vanes should make this assumption even more valid. The axial design of the diffuser guide vanes makes it difficult to define a specific impeller/diffuser clearance ratio. One possible approach is to use the distance to the outer edge of the guide vanes,  $r_3$ . This gives a clearance ratio  $r_3/r_2=1.34$ . Tsujimoto et al. have studied the influence of the clearance for a radial diffuser design theoretically assuming two-dimensional, inviscid and incompressible flow, but including the effects of impeller and diffuser losses, [23]. They found that the destabilizing whirl speed region increased with decreasing impeller/diffuser clearance. Typically results were that an infinitesimally small gap gave a destabilizing region for the tangential force for  $0.0 \leq \Omega/\omega \leq 0.5$ , while this region was reduced for increased clearances and diminished for  $r_3/r_2 > 1.5$ . When discussing only the impeller/diffuser clearance interaction the destabilizing region found in this work can be seen to be in agreement with the theoretical study by Tsujimoto. It is interesting to observe that an impeller/casing clearance ratio  $> 1.5$  is typical for a vaneless diffuser pump and the lack of destabilizing interaction predicted by Tsujimoto for this ratio, agree quite well with the low cross-coupled stiffness values measured by Ohashi for a vaneless diffuser, Table 3.

Comparing the other coefficients, the direct added mass is in good agreement with the Caltech results for volute designs which showed values from  $\approx 6-7$  (dimensionless), regardless of flow coefficient and impeller/volute configurations, [21]. The corresponding values from Ohashi et al., [14], were 1.5-2.0 for a vaneless diffuser configuration. However, the Caltech results included shroud effects. Without any volute the Caltech results showed an added mass of 4.4. Further, one of the conclusions from the dry testing in the present test was that the normal forces were underpredicted for all whirl speeds and this could influence the wet results. The inertia part is most probably higher than measured, that is, the water added mass of the impeller could be up to 25% underpredicted in the measurements.

The cross-coupled mass varied in the present study with approximately no effect at  $\phi=0.092$  to  $\bar{m}=-1.4$  at  $\phi=0.069$ . The Caltech results showed small negative values (-1.0 to 0.0) for most of the impeller/diffuser configurations, [21]. For other published results, the value of this coefficient varies significantly both in sign and values and a clear impression of the typical order of magnitude is difficult to find. It should be noted, however, that a negative sign of the cross-coupled added mass could have a destabilizing effect since it adds to the tangential force and should therefore not be neglected.

The damping coefficients, both direct and cross-coupled, are 2-3 times lower than the Caltech results for volute configurations, but in good agreement with Ohashi et al., [14], for a vaned diffuser.

Another conclusion from Ohashi et al. in [22], when comparing different published experiments, was that the large difference in measured fluid forces comes mostly from the difference of clearance space between the impeller shroud and the surrounding casing. Several articles have described the significant contribution to the rotordynamic forces which can occur from the shroud clearances. The narrower the clearance, the stronger the restrictive effect to the impeller movement. This leads to a discussion about the order of magnitude of the front shroud forces in the present study. It is useful to divide

the front region in two parts, that is, a front annular gap region from the inlet to the angled shroud and the angled shroud clearance itself. Before the tests it was assumed that the influence from the annular gap region from the inlet to the shroud, which will not be present in a real pump due to the wear-rings, did not contribute to the forces due to lower pressure and radius and a relative large clearance. However, results from Adkins, [12], indicate that despite a large clearance in this region, a contribution to the stiffness coefficients, and especially the direct component, could be present (50-75%). The minimum radial clearance was smaller and the relative axial distribution of the front annular clearance region was larger in the test carried out by Adkins. Although difficult to quantify, contribution from this region to the stiffness values should be expected in the present test as well. This leads to a conclusion of a quite small direct stiffness from the impeller diffuser clearance. A rough estimation of the added mass contribution from this region could be found by looking at a very simple added mass approach, that is, the Stokes added mass, as described in [1] and [24]. The front cylinder contributed 39% of the total added mass in this model and could be an indication of the influence of this region on the inertia forces on the impeller.

Guinzburg, [5] and [25], has measured the rotordynamic effect of an angled front shroud for different clearances and operating conditions. Using the published results from Guinzburg and the present dimensions, the rotordynamic coefficient for the shroud interaction can be estimated. This shows that only the direct added mass and cross-coupled damping would affect the rotordynamic coefficients from the measurements in the present work and still not significant, < 10%.

## Concluding Remarks

The rotordynamic forces from an experimental study have been presented in terms of whirl averaged normal and tangential forces. The main conclusions, with respect to the rotordynamic forces, were the following: A satisfactory quadratic behaviour of the normal and tangential force was detected and the quadratic fit was most satisfactory for the highest flow coefficient near BEP. The standard deviation of the whirl averaged normal and tangential forces increased significantly at the low flow case which showed that the increased flow unsteadiness affected the rotordynamic behaviour. A rotordynamically destabilizing area for positive whirl speed ratios was detected,  $0.0 \leq \Omega/\omega \leq 0.3$ , for flow coefficients near and well below the best efficiency point. The rotordynamic coefficients developed from the quadratic fit of the normal and tangential forces showed that a significant added mass term was present and independent of the flow coefficient. No cross-coupled mass term was present near design flow, but it was observed at 66% flow ( $\phi/\phi_{BEP}=0.66$ ). The direct (negative) and cross-coupled (positive) stiffness were lower than those published for volute pumps but in better agreement with those published for vaneless and vaned diffusers. The reason for the low stiffness values was assumed to be the relative high clearance between the impeller outlet and diffuser inlet/casing. The rotordynamic behaviour presented, such as the small subsynchronous destabilizing region, low direct stiffness and the significant added mass, can be assumed to be typical for a centrifugal impeller in an axial diffuser near design flow (exclusive front shroud influence) if the impeller/diffuser clearance ratio,  $r_3/r_2$ , does not vary significantly from the present design. This conclusion was based on a comparison with the results from several other designs.



# Acknowledgment

The authors wish to thank Frank Mohn Flatøy A/S, Statoil and the Research Council of Norway for supporting this work under contract number NFR 31791/211.

# References

- [1] H.F. Black. Effects of fluid-filled clearance spaces on centrifugal pump and submerged motor vibrations. In *8th Turbomachinery Symp, Texas A&M University*, 1979.
- [2] W. Diewald and R. Nordmann. Influence of different types of seal on the stability behavior of turbopumps. In *Rotordynamic Instability Problems in High Performance Turbomachinery, Texas A&M University, NASA CP-3026*, 1988.
- [3] D. Childs and J. Dressmann. Testing of turbulent seals for rotordynamic coefficients. In *Rotordynamic Instability Problems in High Performance Turbomachinery, Texas A&M University, NASA CP-2250*, 1982.
- [4] J.P. Williams and D.W. Childs. Influence of impeller shroud forces on turbopump rotor dynamics. *ASME, Journal of Vibration and Acoustics*, pages 508–515, October 1991.
- [5] A. Guinzburg, C.E. Brennen A.J. Acosta, and T.K. Caughey. Experimental results for the rotordynamic characteristics of leakage flows in centrifugal pumps. *ASME, Journal of Fluids Engineering*, pages 110–115, March 1994.
- [6] D. Childs. Fluid-structure interaction forces at pump-impeller-shroud surfaces for rotordynamic calculations. *ASME, Journal of Vibration, Acoustics, Stress, and Reliability in Design*, 111:216–225, July 1989.
- [7] T. Feng and R. Nordmann. Calculation of fluid/structure interaction at pump impeller shroud areas using finite difference techniques. In *Rotordynamic Instability Problems in High Performance Turbomachinery, Texas A&M University, NASA CP-3239*, 1993.
- [8] J. J. Verhoeven. Rotor dynamics of centrifugal pumps : a matter of fluid forces. *Shock and Vibration Digest*, (8):3–17, 1991.
- [9] J. F. Guelich. Part load flow phenomena and excitation in centrifugal pumps. In *Adv. Study Inst. on Vibration and Wear Damage in High Speed Rotating Machinery, NATO ASI Series Vol. 174*, 1989.
- [10] Jørgen Colding-Jørgensen. Effect of fluid forces on rotor stability of centrifugal compressor and pumps. In *Rotordynamic Instability Problems in High Performance Turbomachinery, Texas A&M University, NASA CP-2133*, 1980.
- [11] Douglas R. Adkins and Christopher E. Brennen. Origins of hydrodynamic forces on centrifugal pump impellers. In *Rotordynamic Instability Problems in High Performance Turbomachinery, Texas A&M University, NASA CP-2443*, 1986.
- [12] Douglas Ray Adkins. *Analyses of hydrodynamic forces on centrifugal pump impellers*. PhD thesis, California Institute of Technology, Pasadena, California, 1986.
- [13] Belgacam Jerry. *Experimental study of unsteady hydrodynamical force matrices on whirling centrifugal pump impellers*. PhD thesis, California Institute of Technology, Pasadena, California, 1987.
- [14] Hideo Ohashi, Ryoichi Hatanaka, and Akira Sakurai. Fluid force testing machine for whirling centrifugal impeller. In *JISME, The International Conference on Rotordynamics*, 1986.
- [15] Dara Childs. *Turbomachinery Rotordynamics. Phenomena, Modeling & Analysis*. John Wiley & Sons, Inc., 1993.
- [16] A. Muszynska. Experimental and analytical study on fluid whirl and fluid whip modes. In *Rotordynamic Instability Problems in High Performance Turbomachinery, Texas A&M University, NASA CP-3239*, 1993.

- [17] Agnes Muszynska. Course on rotor dynamics and vibration in turbomachinery. Von Karman Institute for Fluid Dynamics, Belgium, 1992.
- [18] E. Torbergsen and M.F. White. Diffuser rotating stall and influence on shaft excitational forces: Part 2: Numerical investigation. In *International Symposium on Computational Technologies for Fluid/Thermal/Chemical Systems with Industrial Applications, Joint ASME/JSME Meeting, San Diego, July 26-30, 1998*.
- [19] E. Torbergsen and M.F. White. Diffuser rotating stall and influence on shaft excitational forces: Part 1: Experimental investigation. In *IFTToMM, Seventh International Conference on Rotordynamics, Darmstadt, 1998*.
- [20] Hideo Ohashi and Hidenobu Shoji. Lateral fluid forces acting on a whirling centrifugal impeller in vaneless and vaned diffuser. In *Rotordynamic Instability Problems in High Performance Turbomachinery, Texas A&M University, NASA CP-2338, 1984*.
- [21] Christopher E. Brennen. *Hydrodynamics of pumps*. Oxford University Press, 1994.
- [22] H. Ohashi, A. Sakurai, and J. Nishima. Influence of impeller and diffuser geometries on the lateral fluid forces of whirling centrifugal impeller. In *Rotordynamic Instability Problems in High Performance Turbomachinery, Texas A&M University, NASA CP-3026, 1988*.
- [23] Y. Tsujimoto, A.J. Acosta, and Yoshiki Yoshida. A theoretical study of fluid forces on a centrifugal impeller rotating and whirling in a vaned diffuser. In *Rotordynamic Instability Problems in High Performance Turbomachinery, Texas A&M University, NASA CP-3026, 1988*.
- [24] R. J. Fritz. The effects of an annular fluid on the vibrations of a long rotor, part 2 - test. *ASME, Journal of Basic Engineering*, pages 930–937, 1970.
- [25] Adiel Guinzburg. *Rotordynamic Forces Generated by Discharge-to-Suction Leakage Flows in Centrifugal Pumps*. PhD thesis, California Institute of Technology, Pasadena, California, 1992.

## Nomenclature

$A_{ii}$	–Generalized force matrix	$\bar{C}, \bar{c}$	–Direct & cross-coupled damping, non-dim
$F_{0x}, F_{0y}$	–Steady impeller forces	$F_x(t), F_y(t)$	–Total impeller forces
$F_n, F_t$	–Normal and tangential force	$\bar{F}_n, \bar{F}_t$	–Normal and tangential force, non-dim.
$\bar{K}, \bar{k}$	–Direct & cross-coupled stiffness, non-dim.	$\bar{M}, \bar{m}$	–Direct & cross-coupled mass, non-dim.
$r_2$	–Impeller outlet radius	$b_2$	–Impeller outlet width
$r_3$	–Diffuser guide vanes outer radius	$e(t)$	–Displacement vector
$X(t), Y(t)$	–Impeller centre coordinates	$x, y$	–Impeller centre coordinates, non-dim.
$\Omega$	–Eccentric drive speed	$\omega$	–Rotational speed
$\rho$	–Density		

# Approaches to numerical investigation of the character and stability of forced and self-excited vibration of flexible rotors with non-linear supports

**J ZAPOMĚL**

Department of Mechanics, VŠB – Technical University of Ostrava, Czech Republic

**E MALENOVSKÝ**

Institute of Solid Bodies, Technical University of Brno, Czech Republic

## ABSTRACT

From the viewpoint of the rotor systems control it is necessary to know character of their lateral vibration to avoid operating states when the motion becomes hardly predictable. For this purpose a computer modelling method can be applied. The model rotors assumed in this paper have all essential properties of the real ones ( damping, gyroscopic effects, etc. ). Character of their steady-state vibration is studied by means of fractal geometry and theory of chaos and stability utilizing the system response on specified excitation. Application of the trigonometric collocation method was extended to systems periodically excited. New procedures for evaluation of the solution accuracy and for setting up the transition matrix for stability investigation of forced and self-excited vibration of rotors supported by fluid-film bearings have been developed. All approaches were tested and acquired experience was summarized.

## 1 INTRODUCTION

Fluid-film bearings have substantial influence on behaviour of rotor systems. From the viewpoint of control it is desirable to avoid operating states when their vibration becomes hardly predictable. It can occur even in the case of simple excitation ( i ) if the steady-state vibration has a chaotic character, ( ii ) if there are several motion states ( non-chaotic attractors ) existing simultaneously and the vibration tends to jump among them or ( iii ) if one or more parameters of the rotor system are close to a bifurcation point.

A modern and effective approach to investigation of behaviour of rotors is a computer modelling method. The model systems are assumed to have the following properties. The shaft is represented by a beam-like body that is discretized into finite elements. The discs are thin and absolutely rigid. The stationary part is flexible and is discretized into finite elements. Material damping of the shaft is viscous other kinds of damping are linear. Inertia and

gyroscopic effects of the shaft and of the discs are taken into account. The rotor is coupled with the stationary part through hydrodynamical bearings. The model systems are loaded by concentrated and distributed force or kinematic effects of constant, harmonical, periodical or polyharmonical time histories.

## 2 STEADY-STATE SOLUTION OF THE EQUATION OF MOTION

Lateral vibration of a discretized rotor system is described by the equation of motion and by the relationship for boundary conditions

$$\mathbf{M}\ddot{\mathbf{x}} + (\mathbf{B} + \eta_V \mathbf{K}_{SH} + \Omega \mathbf{G})\dot{\mathbf{x}} + (\mathbf{K} + \Omega \mathbf{K}_C)\mathbf{x} = \mathbf{f}_{st} + \mathbf{f}_A + \mathbf{f}_V + \mathbf{f}_B(\mathbf{x}, \dot{\mathbf{x}}) \quad (1)$$

$$\mathbf{x}_{BC} = \mathbf{x}_{BC}(t) \quad (2)$$

$\mathbf{M}$ ,  $\mathbf{B}$ ,  $\mathbf{K}$ ,  $\mathbf{G}$ ,  $\mathbf{K}_C$  - mass, damping, stiffness, gyroscopic, circulation matrices of the rotor system,

$\mathbf{K}_{SH}$  - stiffness matrix of the shaft,

$\mathbf{f}_{st}$ ,  $\mathbf{f}_A$ ,  $\mathbf{f}_V$ ,  $\mathbf{f}_B$  - vectors of static, applied, constrained, bearing forces,

$\mathbf{x}$ ,  $\dot{\mathbf{x}}$ ,  $\ddot{\mathbf{x}}$  - vectors of generalized displacements, velocities, accelerations,

$\mathbf{x}_{BC}$  - vector of boundary conditions,

$\Omega$ ,  $\eta_V$ ,  $t$  - angular speed of the rotor rotation, coefficient of viscous damping, time.

The hydrodynamical bearings are modelled by means of nonlinear force couplings. Elements of vector  $\mathbf{f}_B$  represent bearing forces through which the lubricant acts on the rotor journals and bearing housings. They depend on the oil pressure distribution in the bearing gap that results from solving the Reynold's equation. Relationships for determination of their magnitudes can be found e.g. in (1).

The equation of motion (1) is nonlinear. For its solution the Newmark method can be utilized but its basic algorithm must be adapted. The possible approach consists in linearization of the bearing forces in the neighbourhood of the current position. Vector  $\mathbf{f}_B$  is expanded into a Taylor series and only the absolute and the linear terms are taken into account. Then the equation of motion set up at the point of time  $t+\Delta t$  has the form

$$\mathbf{M}\ddot{\mathbf{x}}_{t+\Delta t} + (\mathbf{B} + \eta_V \mathbf{K}_{SH} + \Omega \mathbf{G})\dot{\mathbf{x}}_{t+\Delta t} + (\mathbf{K} + \Omega \mathbf{K}_C)\mathbf{x}_{t+\Delta t} = \mathbf{f}_{t+\Delta t} \quad (3)$$

$$\mathbf{f}_{t+\Delta t} \doteq \mathbf{f}_{st} + \mathbf{f}_{A,t+\Delta t} + \mathbf{f}_{V,t+\Delta t} + \mathbf{f}_{B,t} + \mathbf{D}_{B,t}(\dot{\mathbf{x}}_{t+\Delta t} - \dot{\mathbf{x}}_t) + \mathbf{D}_{K,t}(\mathbf{x}_{t+\Delta t} - \mathbf{x}_t) \quad (4)$$

$$\mathbf{D}_{B,t} = \left[ \frac{\partial \mathbf{f}_B(\mathbf{x}, \dot{\mathbf{x}})}{\partial \dot{\mathbf{x}}} \right]_{\mathbf{x}=\mathbf{x}_t, \dot{\mathbf{x}}=\dot{\mathbf{x}}_t}, \quad \mathbf{D}_{K,t} = \left[ \frac{\partial \mathbf{f}_B(\mathbf{x}, \dot{\mathbf{x}})}{\partial \mathbf{x}} \right]_{\mathbf{x}=\mathbf{x}_t, \dot{\mathbf{x}}=\dot{\mathbf{x}}_t} \quad (5)$$

$\mathbf{D}_{B,t}$ ,  $\mathbf{D}_{K,t}$  - square matrices of partial derivatives at time  $t$ .

Solution of the equation of motion (3) must satisfy the boundary conditions. Therefore it is transformed to the following form

$$\mathbf{A}_{2,t+\Delta t} \ddot{\mathbf{y}}_{t+\Delta t} + \mathbf{A}_{1,t+\Delta t} \dot{\mathbf{y}}_{t+\Delta t} + \mathbf{A}_{0,t+\Delta t} \mathbf{y}_{t+\Delta t} = \mathbf{b}_{t+\Delta t} \quad (6)$$

where  $\mathbf{A}_{0,t+\Delta t}$ ,  $\mathbf{A}_{1,t+\Delta t}$ ,  $\mathbf{A}_{2,t+\Delta t}$ ,  $\mathbf{b}_{t+\Delta t}$ ,  $\mathbf{y}_{t+\Delta t}$ ,  $\dot{\mathbf{y}}_{t+\Delta t}$ ,  $\ddot{\mathbf{y}}_{t+\Delta t}$  are obtained from matrices  $\mathbf{A}_{0,t+\Delta t}^*$ ,  $\mathbf{A}_{1,t+\Delta t}^*$ ,  $\mathbf{A}_{2,t+\Delta t}^*$  and vectors  $\mathbf{b}_{t+\Delta t}^*$ ,  $\mathbf{x}_{t+\Delta t}$ ,  $\dot{\mathbf{x}}_{t+\Delta t}$ ,  $\ddot{\mathbf{x}}_{t+\Delta t}$  by omitting their rows and columns corresponding to the degrees of freedom for which the boundary conditions are defined

$$\mathbf{A}_{2,t+\Delta t}^* = \mathbf{M} \quad (7)$$

$$\mathbf{A}_{1,t+\Delta t}^* = \mathbf{B} + \eta_V \mathbf{K}_{SH} + \Omega \mathbf{G} - \mathbf{D}_{B,t} \quad (8)$$

$$\mathbf{A}_{0,t+\Delta t}^* = \mathbf{K} + \Omega \mathbf{K}_C - \mathbf{D}_{K,t} \quad (9)$$

$$\mathbf{b}_{t+\Delta t}^* = \mathbf{f}_{st} + \mathbf{f}_{A,t+\Delta t} + \mathbf{f}_{B,t} - \mathbf{D}_{B,t} \cdot \dot{\mathbf{x}}_t - \mathbf{D}_{K,t} \cdot \mathbf{x}_t - \mathbf{A}_{1,t+\Delta t}^* \cdot \dot{\mathbf{x}}_{BC,t+\Delta t} - \mathbf{A}_{0,t+\Delta t}^* \cdot \mathbf{x}_{BC,t+\Delta t} \quad (10)$$

The mentioned modification eliminates unknown values of the vector of constraint forces  $\mathbf{f}_V$ .

In some special cases to avoid direct integration the steady-state solution of the equation of motion can be obtained by application of the trigonometric collocation method which is based on the following assumptions : (i) the steady-state response on periodic excitation is a periodic function of time, (ii) its period T is estimated as a real multiple of the period of excitation, (iii) the steady-state response can be approximated by a finite number L of terms of a Fourier series

$$\mathbf{x} = \sum_{j=0}^L \mathbf{x}_{c_j} \cdot \cos(j\omega t) + \mathbf{x}_{s_j} \cdot \sin(j\omega t) \quad (11)$$

$$\omega = \frac{2 \cdot \pi}{T} \quad (12)$$

where  $\mathbf{x}_{c_j}$  and  $\mathbf{x}_{s_j}$  are vectors of Fourier coefficients.

Solution of the equation of motion estimated in the form of ( 11 ) makes possible to include into the steady-state response harmonical components corresponding to the principle excitation frequencies resulting from expansion of the time history of loading into a Fourier series and to their multiples and mutual combinations which may also have a significant influence on behaviour of nonlinear rotors.

Vectors of applied forces  $\mathbf{f}_A$  and boundary conditions  $\mathbf{x}_{BC}$  are periodic functions of time. For the purpose of further calculation the equation of motion ( 1 ) is transformed to the form

$$\mathbf{A}_2 \cdot \ddot{\mathbf{y}} + \mathbf{A}_1 \cdot \dot{\mathbf{y}} + \mathbf{A}_0 \cdot \mathbf{y} = \mathbf{b} + \mathbf{b}_B(\mathbf{y}, \dot{\mathbf{y}}) \quad (13)$$

where  $\mathbf{A}_0$ ,  $\mathbf{A}_1$ ,  $\mathbf{A}_2$ ,  $\mathbf{b}$ ,  $\mathbf{b}_B$ ,  $\mathbf{y}$ ,  $\dot{\mathbf{y}}$ ,  $\ddot{\mathbf{y}}$  are obtained from matrices  $\mathbf{A}_0^*$ ,  $\mathbf{A}_1^*$ ,  $\mathbf{A}_2^*$  and vectors  $\mathbf{b}^*$ ,  $\mathbf{b}_B$ ,  $\mathbf{x}$ ,  $\dot{\mathbf{x}}$ ,  $\ddot{\mathbf{x}}$  by omitting their rows and columns related to the degrees of freedom for which the boundary conditions are prescribed

$$\mathbf{A}_2^* = \mathbf{M} \quad (14)$$

$$\mathbf{A}_1^* = \mathbf{B} + \eta_V \mathbf{K}_{SH} + \Omega \mathbf{G} \quad (15)$$

$$\mathbf{A}_0^* = \mathbf{K} + \Omega \cdot \mathbf{K}_C \quad (16)$$

$$\mathbf{b}^* = \mathbf{f}_{st} + \mathbf{f}_A - (\mathbf{B} + \eta_V \mathbf{K}_{SH} + \Omega \mathbf{G}) \cdot \dot{\mathbf{x}}_{BC} - (\mathbf{K} + \Omega \mathbf{K}_C) \cdot \mathbf{x}_{BC} \quad (17)$$

Estimation of the steady-state component of the solution of the modified equation of motion ( 13 ) has the form (  $\mathbf{y}_{c_j}$  ,  $\mathbf{y}_{s_j}$  are vectors of Fourier coefficients of deformation parameters for which no boundary conditions are prescribed )

$$\mathbf{y} = \sum_{j=0}^L \mathbf{y}_{c_j} \cdot \cos(j\omega t) + \mathbf{y}_{s_j} \cdot \sin(j\omega t) \quad (18)$$

The trigonometric collocation method requires to satisfy equation ( 13 ) at N collocation points

$$t_k = T \cdot \frac{k-1}{N} \quad \text{for } k = 1, 2, \dots, N \quad , N = 2 \cdot L - 1 \quad (19)$$

Substitution of expression ( 18 ) and its derivatives with respect to time into ( 13 ) for all collocation points results in a set of nonlinear algebraic equations ( 20 ).  $\mathbf{g}$  represents a vector of Fourier coefficients and  $\mathbf{r}$  is a right-hand side vector.

$$\mathbf{A} \cdot \mathbf{g} = \mathbf{r}(\mathbf{g}) \quad (20)$$

$$\mathbf{g} = [\mathbf{y}_{c0}, \mathbf{y}_{c1}, \mathbf{y}_{s1}, \mathbf{y}_{c2}, \mathbf{y}_{s2}, \dots, \mathbf{y}_{cL}, \mathbf{y}_{sL}]^T \quad (21)$$

The trigonometric collocation method provides only an approximation of the steady-state solution. Its accuracy can be studied according to satisfying the equation of motion in regions between the collocation points. Time history of the relative deviation  $d(t)$  is then defined

$$d(t) = \frac{\|\mathbf{b} + \mathbf{b}_B(\mathbf{y}, \dot{\mathbf{y}}) - \mathbf{A}_2 \cdot \ddot{\mathbf{y}} - \mathbf{A}_1 \cdot \dot{\mathbf{y}} - \mathbf{A}_0 \cdot \mathbf{y}\|}{d_{REF}} \cdot 100 \quad (22)$$

where  $d_{REF}$  is a reference value

$$d_{REF} = \frac{1}{T} \cdot \int_0^T \|\mathbf{b}(t)\| \cdot dt \quad (23)$$

### 3 INVESTIGATION OF THE CHARACTER OF THE VIBRATION

If the rotor system is loaded by force or kinematic effects of constant, polyharmonic or periodical time history, the vibration tends to one of the following attractors : rest, periodic motion, quasi-periodic motion, chaotic motion. Nonlinear mechanical systems to which rotors supported by fluid-film bearings belong are characterized by the possibility of simultaneous existence of several motion states ( chaotic or non-chaotic attractors ).

Principal information for investigation of their behaviour is provided by their response on specified loading that can be obtained numerically. Character of the vibration discussed in (3) and (4) is judged according to time histories of kinematic parameters of all or only of chosen nodes. For this purpose the following means are usually used : (i) forms of the nodes trajectories, (ii) forms of the nodes phase trajectories projected to the phase plane, (iii) Fourier spectrum of time series of displacements or velocity components of particular nodes, (iv) Poincaré maps, (v) dimension of the attractor ( e.g. correlation dimension ).

Evaluation of the correlation dimension defined e.g in ( 2 ) from time history of the nodes displacements requires to construct a set of points  $\mathbf{p}_k$  (  $k$  is an integer number ) in  $m$ -dimensional pseudo-phase space with time delay  $\tau$ . They are given as follows

$$\mathbf{p}_k = [x[t_0 + k.\tau], x[t_0 + (k + 1).\tau], \dots, x[t_0 + (k + m - 1).\tau]]^T \quad (24)$$

where  $x$  is an element of the analyzed time series and  $t_0$  is a chosen instant of time.

Correlation dimension  $d_c$  is equal to the slope of the linear part of the relationship expressing the dependence of correlation function  $C(r)$  on the radius  $r$  of an  $m$ -dimensional hypersphere. The diagram  $C(r) - r$  must be plotted in logarithmic coordinates.  $N$  is a number of  $m$ -dimensional points and  $H$  is a Heaviside function.

$$C(r) = \lim_{N \rightarrow \infty} \frac{1}{N^2} \sum_{i=1}^N \sum_{j=1}^N H(r - \|\mathbf{p}_i - \mathbf{p}_j\|) \quad (25)$$

Magnitudes of radius  $r$  must cover both the macrostructure and microstructure of the set of points  $\mathbf{p}_k$  (  $x_{\max}$  is an element of the time series having the greatest absolute value )

$$r \in (0.02.x_{\max}.\sqrt{m}; 2.x_{\max}.\sqrt{m}) \quad (26)$$

#### 4 STABILITY OF THE EQUILIBRIUM POSITION AND PERIODIC SOLUTION

Determination of the equilibrium position ( given by the vector of static deformation  $\mathbf{x}_{st}$  ) leads to solving a set of nonlinear algebraic equations

$$\mathbf{A}.\mathbf{y}_{st} = \mathbf{b} + \mathbf{b}_B(\mathbf{y}_{st}) \quad (27)$$

where  $\mathbf{A}$ ,  $\mathbf{b}$ ,  $\mathbf{b}_B$  and  $\mathbf{y}_{st}$  are obtained from matrix  $\mathbf{K} + \Omega.\mathbf{K}_C$  and vectors  $\mathbf{b}^*$ ,  $\mathbf{f}_B$ ,  $\mathbf{x}_{st}$  by omitting their rows and columns that correspond to the degrees of freedom to which the boundary conditions are referred

$$\mathbf{b}^* = \mathbf{f}_{st} - (\mathbf{K} + \Omega.\mathbf{K}_C).\mathbf{x}_{BC} \quad (28)$$

Stability of the equilibrium position is considered according to signs of real parts of the system eigenvalues. Their calculation requires to solve a quadratic eigenvalue problem

$$\det(\lambda^2.\mathbf{A}_2 + \lambda.\mathbf{A}_1 + \mathbf{A}_0) = 0 \quad (29)$$

Matrices  $\mathbf{A}_0$ ,  $\mathbf{A}_1$ ,  $\mathbf{A}_2$  are obtained from  $\mathbf{A}_0^*$ ,  $\mathbf{A}_1^*$ ,  $\mathbf{A}_2^*$  by omitting their rows and columns corresponding to the degrees of freedom for which the boundary conditions are prescribed

$$\mathbf{A}_2^* = \mathbf{M} \quad (30)$$

$$\mathbf{A}_1^* = \mathbf{B} + \eta_v \mathbf{K}_{SH} + \Omega \mathbf{G} - \mathbf{D}_{B,st} \quad (31)$$

$$\mathbf{A}_0^* = \mathbf{K} + \Omega \mathbf{K}_C - \mathbf{D}_{B,st} \quad (32)$$

Matrices of partial derivatives  $\mathbf{D}_{B,st}$ ,  $\mathbf{D}_{K,st}$  are set up for displacements corresponding to the static deformation of the rotor system and for zero vector  $\mathbf{o}$  of generalized velocities.

$$\mathbf{D}_{B,st} = \left[ \frac{\partial \mathbf{f}_B(\mathbf{x}, \dot{\mathbf{x}})}{\partial \dot{\mathbf{x}}} \right]_{\mathbf{x}=\mathbf{x}_st, \dot{\mathbf{x}}=\mathbf{0}}, \quad \mathbf{D}_{K,st} = \left[ \frac{\partial \mathbf{f}_B(\mathbf{x}, \dot{\mathbf{x}})}{\partial \mathbf{x}} \right]_{\mathbf{x}=\mathbf{x}_st, \dot{\mathbf{x}}=\mathbf{0}} \quad (33)$$

The loss of stability of the equilibrium position ( Hopf bifurcation ) produces self-excited vibration and the points of the rotor centre line start to move on closed orbits ( limit cycles ). Their forms, amplitudes and periods can be determined from the rotor system response on a small force or kinematic impulse after the initial transient components have decayed.

If the rotor system exhibits a periodic motion ( forced or self-excited vibration ), stiffness and damping parameters of the fluid-film bearings are changed periodically with the same period of  $T$ . Stability of such systems is considered using the Floquet theory. The principle problem consists in setting up the transition matrix over one period. For this purpose procedure based on application of the Newmark kinematic relationships has been developed for the case of rotors supported by fluid-film bearings. The period of  $T$  is divided into  $N$  time subintervals  $\Delta t$  and the transition matrix is then given as a product of  $N$  partial transition matrices

$$\mathbf{H}(T,0) = \mathbf{H}(T, T - \Delta t) \cdot \mathbf{H}(T - \Delta t, T - 2\Delta t) \dots \mathbf{H}(\Delta t, 0) \quad (34)$$

$$\mathbf{H}(t + \Delta t, t) = \begin{bmatrix} \frac{2}{\Delta t} \mathbf{Q}_t - \mathbf{I} & \frac{2}{\Delta t} (\mathbf{P}_t - \mathbf{I}) \\ \mathbf{Q}_t & \mathbf{P}_t \end{bmatrix} \quad (35)$$

where  $\mathbf{I}$  is an identity matrix and

$$\mathbf{P}_t = \mathbf{D}_t^{-1} \cdot \left( \frac{4}{\Delta t^2} \mathbf{A}_2 + \frac{2}{\Delta t} \mathbf{A}_{1,t+\Delta t} - \mathbf{A}_{0,t} \right) \quad (36)$$

$$\mathbf{Q}_t = \mathbf{D}_t^{-1} \cdot \left( \frac{4}{\Delta t} \mathbf{A}_2 + \mathbf{A}_{1,t+\Delta t} - \mathbf{A}_{1,t} \right) \quad (37)$$

$$\mathbf{D}_t = \frac{4}{\Delta t^2} \mathbf{A}_2 + \frac{2}{\Delta t} \mathbf{A}_{1,t+\Delta t} + \mathbf{A}_{0,t+\Delta t} \quad (38)$$

Matrices  $\mathbf{A}_2$ ,  $\mathbf{A}_{1,\tau}$ ,  $\mathbf{A}_{0,\tau}$  are obtained from  $\mathbf{A}_2^*$ ,  $\mathbf{A}_{1,\tau}^*$ ,  $\mathbf{A}_{0,\tau}^*$  by omitting their rows and columns corresponding to the degrees of freedom for which the boundary conditions are prescribed.



$\tau$  is equal to the time point  $t$  or  $t+\Delta t$  and matrices  $\mathbf{D}_{B,\tau}$ ,  $\mathbf{D}_{K,\tau}$  are defined by ( 5 )

$$\mathbf{A}_2^* = \mathbf{M} \quad (39)$$

$$\mathbf{A}_{1,\tau}^* = \mathbf{B} + \eta_v \mathbf{K}_{SH} + \Omega \mathbf{G} - \mathbf{D}_{B,\tau} \quad (40)$$

$$\mathbf{A}_{0,\tau}^* = \mathbf{K} + \Omega \mathbf{K}_C - \mathbf{D}_{K,\tau} \quad (41)$$

Calculation of the transition matrix requires to perform a large number of matrix products that can result into exceeding the greatest number with which the computer can work. Therefore it is necessary to include the normalization process into the procedure

$$\mathbf{H}^*(t + \Delta t, t) = \frac{1}{h_1} \mathbf{H}(t + \Delta t, t) \quad (42)$$

$$\mathbf{H}^*(T, 0) = \mathbf{H}^*(T, T - \Delta t) \cdot \mathbf{H}^*(T - \Delta t, T - 2\Delta t) \dots \mathbf{H}^*(\Delta t, 0) \quad (43)$$

where  $h_1$  is a positive real coefficient e.g. chosen as a greatest element of  $\mathbf{H}(t+\Delta t, t)$  in absolute value. Periodic vibration of the rotor system is stable if magnitudes of all eigenvalues of the transition matrix  $\mathbf{H}(T, 0)$  are less than 1. It occurs if condition ( 44 ) is satisfied for all eigenvalues  $\lambda^*$  of the normalized matrix  $\mathbf{H}^*(T, 0)$

$$c(\lambda) = \sum_{i=1}^N \log[h_{(i-1)\Delta t}] + \log|\lambda^*| < 0 \quad (44)$$

## 5 EXAMPLE

The described procedures were tested by means of computer simulations. Rotor system ROT1 ( fig.1 ) consists of a shaft ( SH ) carrying one disc ( D ) on its overhung end. The shaft is connected with a rigid foundation plate ( FP ) through two hydrodynamical bearings ( B1, B2 ) and rotates at constant angular speed. The rotor was lightly loaded by a concentrated force acting on it in radial direction at the disc location (  $F_y = 1000$  N,  $F_z = -1500$  N ). The shaft was represented by a beam-like body discretized into 5 finite elements ( diameter/length 80/200, 80/200, 120/200, 100/200, 80/200 mm, density  $7800 \text{ kgm}^{-3}$ , modulus of elasticity  $2.1 \cdot 10^{11} \text{ Nm}^{-2}$ , coefficient of viscous damping  $2 \cdot 10^{-7} \text{ s}$  ). Moments of inertia of the disc are  $0.12 \text{ kg.m}^2$  ( diametral ) and  $0.24 \text{ kg.m}^2$  ( polar ) and its mass is 32 kg. The overhung disc geometric ratio ( ratio between the disc radius and length of the overhung end of the shaft ) has the value of 0.3. The bearings are cylindrical, short and fully cavitated ( radius 60 mm, length 150 mm, gap 0.2 mm, dynamical viscosity  $0.004 \text{ Pa.s}$  ).

The first problem consists in judgement of stability of the equilibrium position for a specified range of rotational speeds ( 500 - 1000 rad/s ). The rotor system was lightly loaded by a radial force acting on it at the disc location. The relative eccentricities of the rotor journal centres in bearings B1 and B2 are 0.10 and 0.21. In fig.2 there is drawn a dependence of the greatest real part of the system eigenvalues on the speed of rotation. If the limit value ( 710 rad/s ) is exceeded, the bifurcation occurs and the rotor starts to exhibit self-excited vibration whose frequency is almost equal to 1/2 of the angular velocity of its rotation. The original

equilibrium position of the bearing B2 centre and trajectory of the disturbed motion referred to the speed of rotation 800 rad/s are evident from fig.3.

In the second case the rotor was excited by centrifugal force caused by the disc unbalance (eccentricity of the centre of gravity 0.5 mm). When the speed exceeds 285 rad/s, the bifurcation occurs. 1T periodic motion becomes unstable and the rotor starts to oscillate with the period of 2T (fig.5). Distribution of eigenvalues of the transition matrix corresponding to the speed of rotation 290 rad/s is drawn in fig.4 (the eigenvalue exceeding the unit circle is real and negative). Solution of 1T periodic motion was obtained by the trigonometric collocation method (1 absolute and the first 20 harmonical terms of a Fourier series). Its accuracy is evident from fig.6. 2T periodic steady-state response was calculated by means of the adapted Newmark method (time step 20  $\mu$ s).

In the third case the rotor was excited polyharmonically by a centrifugal force because of the disc unbalance (eccentricity of the centre of gravity 0.5 mm) and by harmonical oscillation of the foundation plate in vertical direction (amplitude 0,3 mm, frequency 311 rad/s). Fourier transformation of the time history of y-coordinate of the disc centre is drawn in fig.7. Correlation dimension  $d_c$  can be determined from fig.8 (dimensions  $m$  of the pseudo-phase spaces are 10, 15, 20, 25, 30). Slope of the linear part of the relationship between the correlation function  $C(r)$  and radius  $r$  is equal approximately to 2.07. It means the resuted vibration is close to the limit state separating the quasi-periodic and chaotic motions. The response was calculated by means of the adapted Newmark method (time step 10  $\mu$ s).

## 6 CONCLUSIONS AND EXPERIENCE

- The described procedures make possible to investigate character and stability of forced and self-excited vibration of rotors loaded by force or kinematics effects by means of a computer modelling method. They were tested through the way of computer simulations.
- The trigonometric collocation method can be applied for analysis of stable or lightly unstable periodic vibration of a rotor system.

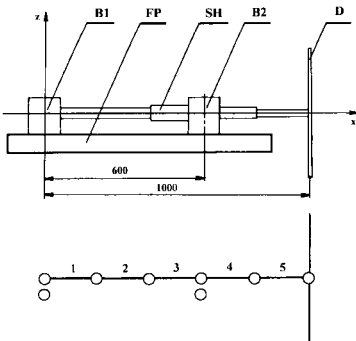


Fig.1 Scheme of rotor system ROT1

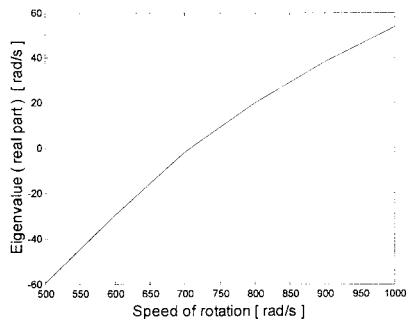
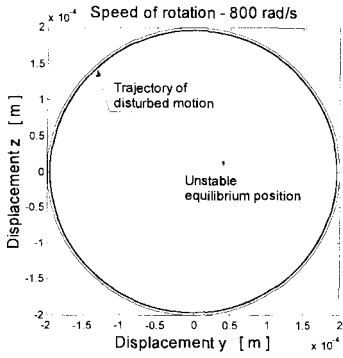
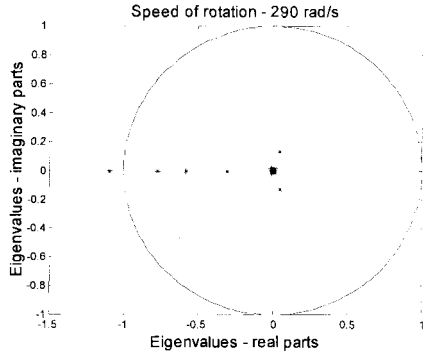


Fig.2 Greatest real parts of the eigenvalues



**Fig.3 Self-excited vibration ( bearing B2 )**



**Fig.4 Eigenvalues of the transition matrix**

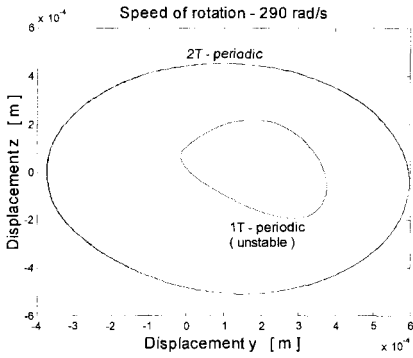


**Fig.5 Periodic attractors of the disc centre**

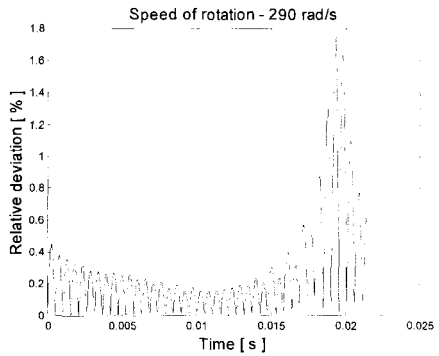


**Fig.6 Accuracy of the solution**

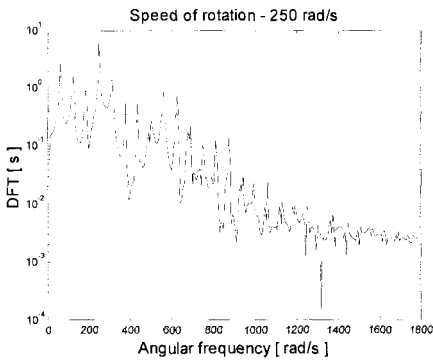


**Fig.7 Discrete Fourier transformation**

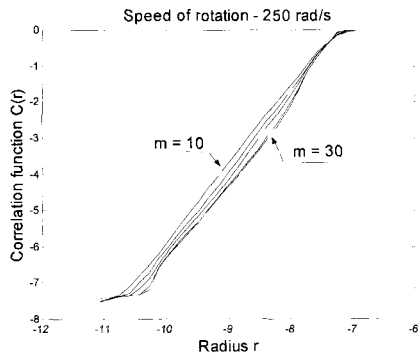


**Fig.8 Correlation function-radius relation**

- It was observed that solution of the set of nonlinear algebraic equations ( 22 ) does not converge if ( i ) the steady-state vibration is not periodic, ( ii ) its period is not estimated correctly, ( iii ) character of the steady-state response is changed during the solving process ( e.g. because of the change of the period of vibration ).
- Direct integration of the equation of motion makes possible to investigate periodic, quasi-periodic or chaotic oscillations of a rotor system including the transient period. But if there are several solutions existing simultaneously, the calculation always converges to the stable one.
- For integration of the equation of motion a Newmark method was chosen and adapted even if for solving of nonlinear problems a Runge-Kutta method is often used. The reason was good experience with its application in the field of finite elements. Modification of the Newmark method based on linearization of the vector of bearing forces in the neighbourhood of the current position is marked for good numerical stability.
- For solving sets of nonlinear algebraic equations ( 20 ), ( 27 ) the Newton-Raphson and the modified Newton-Raphson methods were applied. The bearing forces are functions only of those kinematic parameters that determine position and velocity of the rotor journal and bearing housing centres. Therefore linear and nonlinear equations of the sets can be separated and solution of the nonlinear part can be carried out independently. These manipulations considerably decrease order of the nonlinear task.
- Calculation of the transition matrix  $\mathbf{H}$  using relationship ( 43 ) requires to apply a small time increment  $\Delta t$ .
- Accuracy of determination of the correlation dimension  $d_c$  depends on the dimension of the constructed pseudo-phase space  $m$ . That's why it is desirable to perform calculation of  $d_c$  repeatedly for increasing magnitude of  $m$  until its value becomes constant.

## ACKNOWLEDGEMENT

This research work has been supported by the Grant Agency of the Czech Republic ( grant no. 101/99/1327 ) and by the Ministry of Education of the Czech Republic ( research project CEZ:J17/98:2724019 ). Their help is gratefully acknowledged.

## REFERENCES

- ( 1 ) Vance J.M.: Rotordynamics of Turbomachinery, John Wiley & Sons, Inc., 1988
- ( 2 ) Moon C.F.: Chaotic Vibrations, An introduction for Applied Scientists and Engineers, John Wiley & Sons, New York, 1987
- ( 3 ) Brown R.D., Addison P.S. and Chang A.H.C. : "Chaos in the Unbalance Response of Journal Bearings", Nonlinear Dynamics ( Kluwer ) Vol 5 1994 pp 412-432
- ( 4 ) Adiletta et al "Chaotic Motions of a Rigid Rotor in Short Journal Bearings", Nonlinear Dynamics ( Kluwer ) Vol 10 1996 pp 251-269

# Chaotic vibrations and internal resonance phenomena in a rotor system (twice the major critical speed)

T INOUE, Y ISHIDA, and T MURAYAMA

Department of Electronic-Mechanical Engineering, Nagoya-University, Japan

## ABSTRACT

Critical speeds of some nonlinear resonances are near each other in rotor systems where the effect of gyroscopic moment is small. In such systems, in the vicinity of twice the major critical speed, two types of almost periodic motions occur due to the effect of the 1:(-1) type internal resonance. One is related to a subharmonic resonance and the other is related to a combination resonance, respectively. In this paper, these two types of almost periodic motions and chaotic motions bifurcated from them are investigated.

## 1. INTRODUCTION

In the analysis of rotating machinery, we often use a 4-degree-of-freedom (4DOF) rotor system shown in the left figure in Fig. 1. In this system, when the disk is located at the center of the shaft, its angles ( $\theta_x, \theta_y$ ) and displacements ( $x, y$ ) do not couple with each other, and equations of motions governing each motion are independent. The Jeffcott rotor, which is widely used as the most simple model in the vibration analyses of linear rotor systems, is the 2 DOF deflection motion model representing the motion of the 1st mode of 4DOF model with a disk at the midspan of the shaft. In the Jeffcott rotor, there is no coupling between the deflections in the  $x$  - and  $y$  - directions. Because of the easiness of treatment, this model is also used in the analyses of nonlinear resonances <sup>(1) (2)</sup>. In this model, the forward natural

frequency  $p_f$  and the backward natural frequency  $p_b$  are independent to the rotational speed  $\omega$  and satisfy the relation  $p_f:p_b = 1:(-1)$ , because no gyroscopic moment operates.

The 2DOF inclination model, shown in the center of Fig. 1, is the simplest model taking gyroscopic moment into consideration. This model represents the motion of the 2nd mode of 4DOF model with a disk at the midspan of the shaft. In this model, the inclinations in the  $x$ - and  $y$ - directions couple with each other through gyroscopic terms. The right figure in Fig. 1 shows a natural frequency diagram of this 2DOF inclination model. Due to the effect of gyroscopic moment, natural frequencies  $p_f$  and  $p_b$  change as a function of the rotational speed. In this model, when the ratio between the polar and the diametrical moments of inertia of the rotor becomes small, the effect of gyroscopic moment becomes small, and as a result, natural frequencies almost satisfy  $p_f:p_b = 1:(-1)$ , and some critical speeds of nonlinear resonance are close to each other.

In a multi-degree-of-freedom nonlinear system, if natural frequencies satisfy a simple integral ratio, some distinctive phenomena called the internal resonance phenomena may occur. In this paper, for example, when the internal resonance phenomena occur under the condition  $p_i:p_j = m:n$ , we call it  $m:n$  type internal resonance. Since Sethna reported internal resonance phenomena <sup>(3)</sup>, many researchers have investigated various kinds of physical systems with internal resonance <sup>(4)</sup>. Recently, some researchers found chaotic motions due to internal resonance <sup>(5)</sup> in some rectilinear systems.

In a previous paper <sup>(6)</sup>, we considered the rotor systems with weak nonlinearities, and investigated phenomena with  $1:(-1)$  type internal resonance in the vicinity of twice the major critical speed in a case that  $p_f:p_b = 1:(-1)$  holds approximately. We clarified the

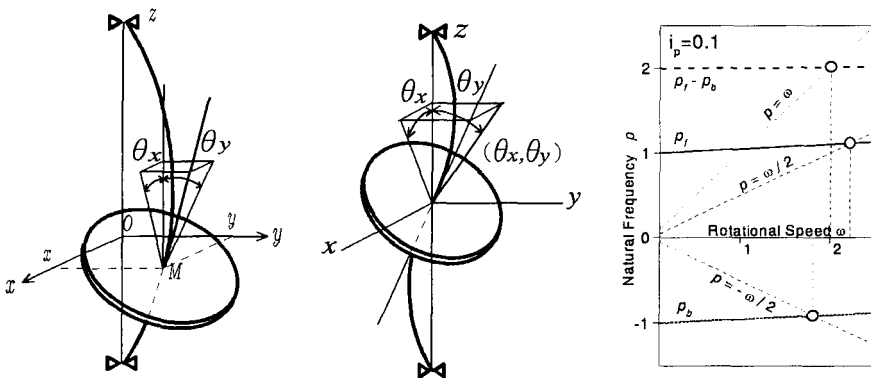


Fig. 1 Analytical Model and Natural Frequencies

dynamical characteristics, such as the change of resonance curves shape, occurrence of a new stable branch, and occurrence of almost periodic motions due to the influence of internal resonance. In those cases, the almost periodic motions occur only in the case that the effect of gyroscopic moment is small but not zero, that is, the discrepancies among critical speeds are small but not zero.

In this paper, we considered a rotor system with weak nonlinearities and small effect of gyroscopic moment, and investigated almost periodic motions, and chaotic vibrations bifurcated from them.

## 2. EQUATIONS OF MOTION AND THEORETICAL ANALYSIS

### 2.1. Equations of Motion and Nonlinear Terms

The equations of motion of the 2DOF-inclination motion model in Fig.1 are given as follows in dimensionless form:

$$\left. \begin{aligned} \ddot{\theta}_x + i_p \omega \dot{\theta}_y + c \dot{\theta}_x + \theta_x + N_{\theta_x} &= (1 - i_p) \tau \omega^2 \cos \omega t, \\ \ddot{\theta}_y - i_p \omega \dot{\theta}_x + c \dot{\theta}_y + \theta_y + N_{\theta_y} &= (1 - i_p) \tau \omega^2 \sin \omega t, \end{aligned} \right\} \quad (1)$$

where  $i_p$  is the ratio between the polar and the diametrical moments of inertia of the rotor,  $c$  is the damping coefficient,  $N_x$  and  $N_y$  are the nonlinear terms in the restoring forces in the  $x$ - and  $y$ - directions,  $\tau$  is the dynamic unbalance of the rotor,  $t$  is time. As shown in Fig. 1, the rates of changes of the natural frequencies  $p_f$  and  $p_b$  for the rotational speed  $\omega$  depend on the value of the parameter  $i_p$  governing the gyroscopic moment.

The expression of nonlinear terms  $N_x$  and  $N_y$  are derived from the potential energy  $V$  of the system as follows,  $V = V_0 + V_N$ ,  $N_x = \partial V_N / \partial \theta_x$ ,  $N_y = \partial V_N / \partial \theta_y$ . Here,  $V_0$  and  $V_N$  are potential energies corresponding to the linear and the nonlinear restoring forces, respectively. Potential energy  $V_0$  consists of second power terms. If we consider that  $N_x$  and  $N_y$  consist of second and third power terms of  $\theta_x$  and  $\theta_y$ ,  $V_N$  is represented by third and fourth power terms. In the rotor system where the rotor performs a whirling motion around the bearing centerline, the polar coordinate  $(\theta, \varphi)$  expression is more suitable than the rectangular coordinate expression. By the transformations  $\theta_x = \theta \cos \varphi$ ,  $\theta_y = \theta \sin \varphi$ , we have  $V_N$  as follows:

$$\left. \begin{aligned} V_N &= (\varepsilon_c^{(1)} \cos \varphi + \varepsilon_s^{(1)} \sin \varphi + \varepsilon_c^{(3)} \cos 3 \varphi + \varepsilon_s^{(3)} \sin 3 \varphi) \\ &+ (\beta^{(0)} + \beta_c^{(2)} \cos 2 \varphi + \beta_s^{(2)} \sin 2 \varphi + \beta_c^{(4)} \cos 4 \varphi + \beta_s^{(4)} \sin 4 \varphi). \end{aligned} \right\} \quad (2)$$

In terms of the direction angle  $\varphi$ , we can divide nonlinear forces  $N_x$  and  $N_y$  into components whose potential energies have regular shapes of distribution. The notation  $N(n)$  represents the nonlinear component whose magnitude of potential energy changes  $n$  times while  $\varphi$  changes from 0 to  $2\pi$  keeping  $\theta$  constant. Distribution of components  $N(n)$  ( $n = 1, \dots, 4$ ) are shown in Fig. 2. The notations  $\varepsilon_c^{(1)}, \dots, \varepsilon_s^{(3)}$  are the coefficients of nonlinear components  $N(1)$  and  $N(3)$ , and the notations  $\beta^{(0)}, \beta_c^{(2)}, \dots, \beta_s^{(4)}$  are the coefficients of nonlinear components  $N(0), N(2)$  and  $N(4)$ . Component  $N(0)$  is the isotropic nonlinear component, and components  $N(n)$  ( $n = 1, 2, 3, \dots$ ) are anisotropic nonlinear components.

In practical systems, the components with complex potential distribution, such as  $N(3)$  and  $N(4)$ , rarely appear. When the system is well assembled, the isotropic nonlinear component  $N(0)$  appears predominantly. However, when there is a discrepancy between the centerlines of the bearings due to misalignment, the anisotropic nonlinear component  $N(1)$  appears in addition to  $N(0)$ . In this paper, we consider a system with only the components  $N(0)$  and  $N(1)$ . In this case, we can put  $\varepsilon_c^{(1)} = \varepsilon^{(1)}$  and  $\varepsilon_s^{(1)} = 0$  by rotating the coordinate axes, without losing generality, because the anisotropic nonlinear component of this system is only  $N(1)$ .

## 2.2 Derivation of the Equations of Approximate Solutions

In the rotor systems with small  $i_p$ , that is the effect of gyroscopic moment, because the natural frequencies hold  $p_f : p_b = 1 : (-1)$  approximately, critical speeds of three kinds of nonlinear resonances shown below are close to each other at twice the major critical speed.

- (1) Forward subharmonic resonance of order 1/2  $[2p_f]$  : occurs
- (2) Backward subharmonic resonance of order 1/2  $[-2p_b]$  : does not occur
- (3) Combination resonance  $[p_f - p_b]$  : occurs

The occurrences shown here are the results of our previous investigation<sup>(7)</sup> for a rotor system with nonlinear components  $N(0)$  and  $N(1)$  and with no internal resonance.

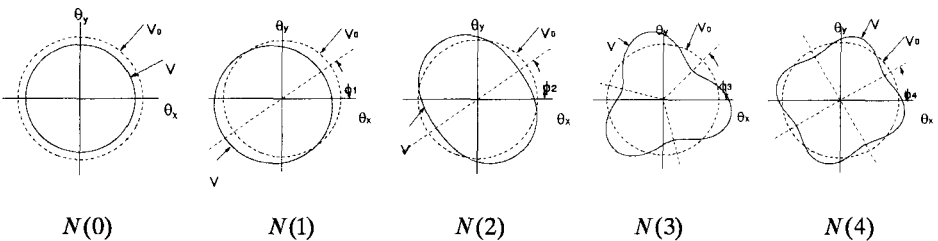


Fig. 2 Nonlinear Terms



In the system where the critical speeds are close each other, we expect that two vibration components with frequencies  $(1/2)\omega$  and  $-(1/2)\omega$  occur simultaneously by the influence of internal resonance. Therefore, we assume the solutions in the accuracy of  $O(\varepsilon)$  as follows:

$$\left. \begin{aligned} \theta_x &= R_f \cos((1/2)\omega t + \delta_f) + R_b \cos(-(1/2)\omega t + \delta_b) + P \cos(\omega t + \beta) + A_x, \\ \theta_y &= R_f \sin((1/2)\omega t + \delta_f) + R_b \sin(-(1/2)\omega t + \delta_b) + P \sin(\omega t + \beta) + A_y, \end{aligned} \right\} \quad (3)$$

Substitution of Eq. (3) into Eq. (1) and comparison of the coefficients of  $\cos \omega$ ,  $\sin \omega$  of both sides in the accuracy of  $O(\varepsilon^0)$ , respectively, yields the following equations concerning the amplitudes  $P$ , and the phase angles  $\beta$ :

$$P = \frac{(1-i_p)\tau\omega^2}{1+i_p\omega^2-\omega^2} = \frac{F}{G(\omega)}, \quad \beta = -\pi. \quad (4)$$

Comparison of the coefficients of  $\cos(1/2)\omega$ ,  $\sin(1/2)\omega$ , and constant terms of both sides in the accuracy of  $O(\varepsilon)$ , respectively, yields the following equations concerning the amplitudes  $R_f, R_b$ , the phase angles  $\delta_f, \delta_b$ , and the constant terms  $A_x$  and  $A_y$ :

$$\left. \begin{aligned} A_f \dot{R}_f &= -(1/2)c\omega R_f \\ &+ 2\varepsilon^{(1)} \{-PR_f \sin 2\delta_f - PR_b \sin(\delta_f - \delta_b) + R_b A_x \sin(\delta_f + \delta_b) - R_b A_y \cos(\delta_f + \delta_b)\} \\ &+ 4\beta^{(0)} \{(A_x^2 - A_y^2)R_b \sin(\delta_f + \delta_b) - 2A_x A_y R_b \cos(\delta_f + \delta_b) \\ &+ 2PR_f (A_y \cos 2\delta_f - A_x \sin 2\delta_f) - 2PR_b (A_x \sin(\delta_f - \delta_b) + A_y \cos(\delta_f - \delta_b))\}, \\ A_f R_f \dot{\delta}_f &= G_f R_f + 2\varepsilon^{(1)} \{-PR_f \cos 2\delta_f - PR_b \cos(\delta_f - \delta_b) \\ &+ 2A_x R_f + A_x R_b \cos(\delta_f + \delta_b) + A_y R_b \sin(\delta_f + \delta_b)\} \\ &+ 4\beta^{(0)} \{R_f (R_f^2 + 2R_b^2 + 2P^2 + 2A_x^2 + 2A_y^2) + (A_x^2 - A_y^2)R_b \cos(\delta_f + \delta_b) \\ &+ 2A_x A_y R_b \sin(\delta_f + \delta_b) - 2PR_f (A_x \cos 2\delta_f + A_y \sin 2\delta_f) \\ &+ 2PR_b (-A_x \cos(\delta_f - \delta_b) + A_y \sin(\delta_f - \delta_b))\}, \\ A_b \dot{R}_b &= (1/2)c\omega R_b + 2\varepsilon^{(1)} R_f \{P \sin(\delta_f - \delta_b) + A_x \sin(\delta_f + \delta_b) - A_y \cos(\delta_f + \delta_b)\} \\ &+ 4\beta^{(0)} R_f \{(A_x^2 - A_y^2) \sin(\delta_f + \delta_b) - 2A_x A_y \cos(\delta_f + \delta_b) \\ &+ 2P(A_x \sin(\delta_f - \delta_b) + A_y \cos(\delta_f - \delta_b))\}, \\ A_b R_b \dot{\delta}_b &= G_b R_b \\ &+ 2\varepsilon^{(1)} \{-PR_f \cos(\delta_f - \delta_b) + 2A_x R_b + A_x R_f \cos(\delta_f + \delta_b) + A_y R_f \sin(\delta_f + \delta_b)\} \\ &+ 4\beta^{(0)} \{R_b (2R_f^2 + R_b^2 + 2P^2 + 2A_x^2 + 2A_y^2) + (A_x^2 - A_y^2)R_f \cos(\delta_f + \delta_b) \\ &+ 2A_x A_y R_f \sin(\delta_f + \delta_b) + 2PR_f (A_y \sin(\delta_f - \delta_b) - A_x \cos(\delta_f - \delta_b))\}, \end{aligned} \right\} \quad (5)$$

$$\left. \begin{aligned}
 i_p \omega \dot{A}_x &= A_y + 2\varepsilon^{(1)} \{A_x A_y + R_f R_b \sin(\delta_f + \delta_b)\} \\
 &\quad + 4\beta^{(0)} \{A_y (A_x^2 + A_y^2 + 2P^2 + 2R_f^2 + 2R_b^2) - PR_f^2 \sin 2\delta_f \\
 &\quad \quad + 2R_f R_b (P \sin(\delta_f - \delta_b) + A_x \sin(\delta_f + \delta_b) - A_y \cos(\delta_f + \delta_b))\}, \\
 i_p \omega \dot{A}_y &= -A_x - \varepsilon^{(1)} \{2R_f^2 + 2R_b^2 + 2P^2 + 3A_x^2 + A_y^2 + 2R_f R_b \cos(\delta_f + \delta_b)\} \\
 &\quad - 4\beta^{(0)} \{A_x (A_x^2 + A_y^2 + 2P^2 + 2R_f^2 + 2R_b^2) - PR_f^2 \cos 2\delta_f \\
 &\quad \quad - 2R_f R_b (P \cos(\delta_f - \delta_b) - A_y \sin(\delta_f + \delta_b) - A_x \cos(\delta_f + \delta_b))\},
 \end{aligned} \right\} \quad (6)$$

where,  $A_f = (1 - i_p) \omega$ ,  $A_b = -(1 + i_p) \omega$ ,  $G_f = 1 + i_p \omega^2 / 2 - \omega^2 / 4$ , and  $G_b = 1 - i_p \omega^2 / 2 - \omega^2 / 4$ .

### 2.3 Resonance Curves and Numerical Simulation

Figure 3 shows resonance curves of a forward subharmonic resonance of order 1/2, for the case that parameter  $i_p$  is small. Routh-Hurwitz criterion is used for stability analysis.

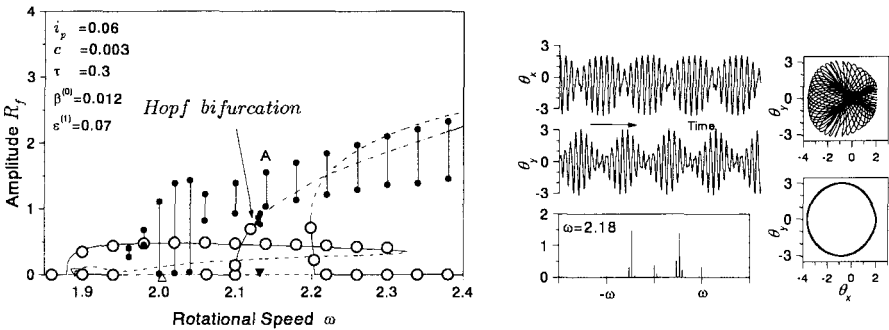


Fig. 3 Resonance Curves

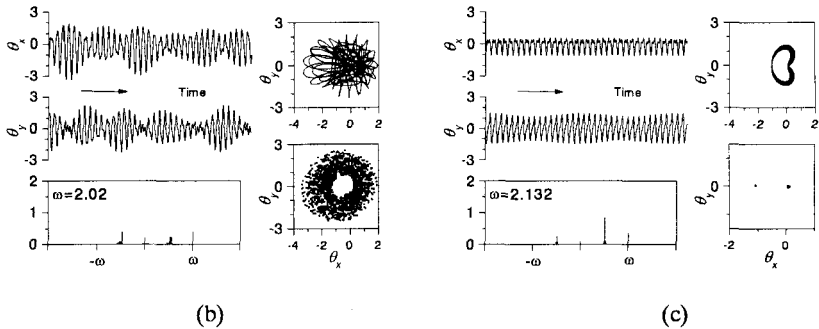


Fig. 4 Time Histories, Spectra, Orbit, and Poincaré map

In this figure, solid lines represent stable solutions, and broken lines and chain lines represent unstable solutions. Further, broken lines show the instability for the case that all of the coefficients of the characteristic equation are not positive, and chain lines show the instability for the case that all of the Hurwitz determinants are not positive. The former corresponds to the case that one of eigenvalues is positive real value, and the latter corresponds to the case that one pair of conjugate complex eigenvalues has a positive real part<sup>(8) (9)</sup>. In the latter case, Hopf bifurcation occurs where one pair of eigenvalues is a pure imaginary value. The symbol  $\bigcirc$  shows a stationary subharmonic resonance of order 1/2 and  $\bullet$  shows a maximum and a minimum amplitude of an almost periodic motion obtained in the numerical simulation. The symbols  $\blacktriangledown$ ,  $\nabla$ , and  $\triangle$  show the critical speeds of a forward and a backward subharmonic resonance of order 1/2, and combination resonance  $[p_f - p_b]$ , respectively.

In Fig. 3, two kinds of almost periodic motions are observed. One occurs in the wide range higher than the vicinity of the critical speed of combination resonance  $[p_f - p_b]$  given by  $\triangle$ . we note that the difference between maximum and minimum amplitudes shown with  $\bullet$  become large in the rotational speed range  $\omega = 2.0 - 2.5$ . The other type of almost periodic motion occurs around the chain line in the small range next to the Hopf bifurcation at  $\omega = 2.13$ . This is because the entrainment to the other almost periodic motion corresponding to the combination resonance  $[p_f - p_b]$  is strong.

We show time histories, spectra, orbit, and Poincaré map sampled for each rotation of the shaft in Fig. 4. Figure 4(a) shows them for point A in Fig. 3. In the time histories, envelopes are periodic. In the spectra, some comparatively large spectra appear on either side of the main spectra  $\omega_f \approx p_f$ , and  $\omega_b \approx p_b$ . In the Poincaré map, a closed loop appears. Figure 4(b) shows the result where the difference between maximum and minimum amplitudes is large in Fig. 3. In this figure, envelopes are not periodic, and the state points in the Poincaré map are distributed densely like as strange attractor. Figure 4(c) shows the result next to the Hopf bifurcation. Two small closed loops, which are bifurcated from the state points of subharmonic resonance of order 1/2, appear in its Poincaré map.

### 3, NUMERICAL ANALYSIS OF ALMOST PERIODIC MOTIONS AND CHAOTIC VIBRATIONS

#### 3.1, Bifurcation Diagram

A bifurcation diagram is obtained by calculating the distance between the origin and the state point in the Poincaré map sampled for each rotation of the shaft. Figure 5 shows the

bifurcation diagram and three types of Poincaré maps calculated for the parameter of Fig. 3. In the Poincaré map for  $\omega = 1.94$ , there are two state points, which means that the subharmonic resonance of order 1/2 occurs. In the bifurcation diagram, this state occurs around the critical speed of backward subharmonic resonance of order 1/2 given by  $\nabla$ , and is represented by two lines. In the Poincaré map for  $\omega = 2.18$ , a closed loop appears which means that an almost periodic motion occurs. In the bifurcation diagram, this state occurs from around the critical speed of combination resonance  $[p_f - p_b]$  given by  $\triangle$ , and is represented by distributed points. Its boundaries are clear and smooth. In the Poincaré map for  $\omega = 2.02$ , there is no closed loop and state points distribute densely like a strange attractor. In the bifurcation diagram, this state is represented by distributed points, but its boundaries are not so clear.

### 3.2 Lyapunov Exponents

Here, we study the Lyapunov exponents<sup>(10)</sup> of this 2DOF rotor system. Figure 6 shows the largest Lyapunov exponent for the parameter shown in Fig. 3. In this figure, the largest Lyapunov exponent becomes 0 in the ranges  $\omega = 1.95 - 2.0$  and  $2.04 - 2.2$  where the almost periodic motion corresponding to the combination resonance  $[p_f - p_b]$  occurs in Fig. 5. The largest Lyapunov exponent becomes a positive value in the range  $\omega = 2.0 - 2.04$  where the distribution of points becomes wide and its boundaries become unclear in Fig. 5. Hence, this proves that the chaotic motion occurs from the almost periodic motion corresponding to the combination resonance  $[p_f - p_b]$  due to the influence of internal resonance.

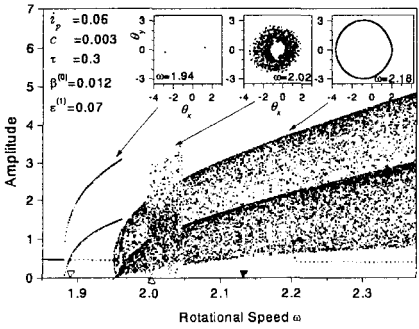


Fig. 5 Bifurcation Diagram

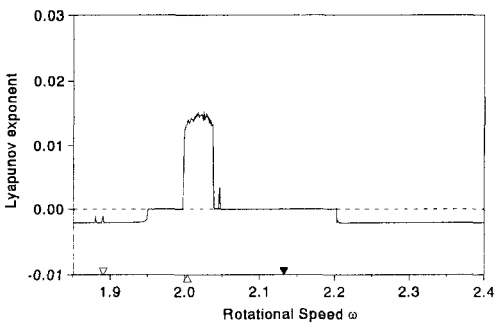


Fig. 6 Lyapunov Exponent

## 4, CONCLUSION

Concerning the nonlinear phenomena in the vicinities of twice the major critical speed of the rotor system with weak nonlinearities and small gyroscopic moment, the following results are obtained.

- (1) In the rotor system with small gyroscopic moment, the critical speeds of forward and backward subharmonic resonances of order  $1/2$  and combination resonance  $[p_f - p_b]$  locate close to each other in the vicinity of twice the major critical speed, and as a result,  $1:(-1)$  type internal resonance occurs.
- (2) Due to the effect of  $1:(-1)$  type internal resonance, Hopf bifurcation occurs in the solution of subharmonic resonance of order  $1/2$ , and an almost periodic motion occurs in the small range next to it.
- (3) Due to the effect of  $1:(-1)$  type internal resonance, an almost periodic motion corresponding to the combination resonance  $[p_f - p_b]$  occurs.
- (4) In the spectra of the almost periodic motion corresponding to the combination resonance  $[p_f - p_b]$ , some comparatively large spectra appear on either side of the main spectra  $\omega_f$  and  $\omega_b$ .
- (5) By Poincaré map, bifurcation diagram, and Lyapunov exponent, the occurrence of chaotic vibration bifurcated from the almost periodic motion corresponding to the combination resonance  $[p_f - p_b]$  due to the internal resonance is proved and its dynamical characteristics are clarified.

## REFERENCES

- (1) F.F.Ehrich, ASME J. Vib., Stress, and Reliab. in Design, Vol.110, 1988, pp.9
- (2) Y.B.Kim and S.T.Noah, Nonlinear Dynamics, Vol.1, 1990, pp.221
- (3) Sethna,P.R., Trans.ASME, Ser.E, 27-1, 1960, pp.187
- (4) Nayfeh,A.H., Balachandran,B., Appl Mech Rev vol42, no11 Part2, 1989, pp.175
- (5) Tousi,S., Bajaj,A.K., Appl.Mech., Vol.52,1985, pp446-452
- (6) Y.Ishida, T.Inoue, K.Takeuchi, IFToMM, 5th, intern. Conference on Rotordynamics, Germany, darmstadt, 1998, pp.605-616
- (7) T.Yamamoto, Y.Ishida, Ingenieur-Archiv 46, 1977, pp.125
- (8) T.Yamamoto, K.Yasuda, Bull.JSME, Vol.20, No.140 1977, pp.168
- (9) Sethna, P.R., Bajaj, A.K., Trans.ASME, J. Appl. Mech., Vol.45,(1978), pp895
- (10) Wolf,A., et. al., Physica D, 16(1985), 285-317

*This page intentionally left blank*

# A helical transformation for rotating shafts allowing a simplified experimental procedure

I BUCHER

Faculty of Mechanical Engineering, Technion, Haifa, Israel

## Abstract

Rotating shafts carrying are often playing a central role in devices and machines. Despite their importance in gas turbines and jet engines, for example, a complete model of such structures cannot be obtained via the experimental procedure of modal testing. This limitation stems from the fact that the addition of gyroscopic forces to the inertial and potential forces, normally existing in structures, gives rise to non-symmetric (non self-adjoint) differential operators. When the principal axis of stiffness of all the bearings on which the rotor rests coincide, the analysis and experimental model extraction are greatly simplified. This paper presents an idea that may be used to treat the case of non-coinciding principal axes of stiffness of the foundation. A helical transformation is proposed to "Straighten" helical modeshapes and thus simply the obtained model. This transformation may simplify the experimental procedure to a degree that a full model can be obtained despite the anisotropic nature of the supports.

## 1. Introduction

Rotating structures are more difficult to model than ordinary vibrating structures. This difficulty stems mainly from effects due to rotation. A model having a hierarchical level of complexity of rotating structures can be derived (BUCHER AND EWINS, 1999).

In the current paper we describe a simple model that still proves realistic. This model is valid for an axi-symmetric rotor mounted on nearly lossless non-isotropic supports and is suitable, for example, for a relatively slender shaft mounted on roller bearings. To this date there is no single experimental procedure for rotors that generates a complete model with one or two excitation locations. The proposed method provides the initial stages for an analytical basis that may simplify the experimental approach considerably.

It has been shown (e.g. WANG AND KIRKOPHE, 1994) that the dynamics of an isotropic rotor resting on bearings with coinciding principal axes of stiffness can be described by means of a single set of eigenvectors and eigenvalues. This is contrary to general gyroscopic systems (GÉRADIN, 1994) that require two sets of eigenvectors, right- and left-hand side ones as required by a general non-self adjoint system. The coincidence of principal axes of bearing stiffness is a unique case and indeed, many engineering structures do not possess this property. The benefits that both the analyst and the experimenter obtain from describing the dynamics of a rotating structure with a single set of vectors were discussed in (Lee, 1993; BUCHER AND EWINS, 1996). It has been shown that in some cases the decomposition of the frequency response function as based on a single set of (right-) eigenvectors is the only possibility to obtain a full model from experiments. This restriction is mostly due to the fact that rotating machines are inaccessible to external forcing devices and thus the model needs to be extracted from a fraction of the complete frequency response matrix.

This paper addresses the case of undamped (or lightly damped) anisotropic supports where a special transformation and some perturbation analysis are pursued to demonstrate the potential benefits of the proposed helical co-ordinate system abovementioned goal.

### 1.1 Mathematical formulation

This section reviews briefly the common model of linear time invariant rotor resting on general lossless supports. The dynamics of an isotropic rotating shaft is described here by the Timoshenko beam model. This model is later transformed into a helical co-ordinate system.

#### 1.1.1 Ordinary approach

It proves useful to briefly present the most common modelling conventions of undamped rotors and to discuss the mathematical properties that are associated with such models.

$$\mathbf{M}\ddot{\mathbf{q}}(t) + \mathbf{G}\dot{\mathbf{q}}(t) + \mathbf{K}\mathbf{q}(t) = \mathbf{f}(t) \quad \in \mathfrak{R}^{2n \times 1} \quad (1)$$

where

$$\mathbf{M} = \mathbf{M}^T, \quad \mathbf{K} = \mathbf{K}^T, \quad \mathbf{G} = -\mathbf{G}^T \quad (2)$$

Here,  $\mathbf{M}$  and  $\mathbf{K}$  represent the mass and stiffness matrices respectively, while  $\mathbf{G}$  is the so-called gyroscopic matrix, which is proportional to the speed of rotation (GÉRADIN, 1994).

#### 1.2 Eigenvectors: Planar and non-planar mode shapes

The frequency response of a non-damped rotor (equation (1)) can be expanded in terms of the triplets  $\lambda_r, \phi_r, l_r$ ,  $r=1..2n$  ( $\lambda_r$  being an eigenvalue,  $\phi_r, l_r$  right and left eigenvectors). The response to a sinusoidal external force vector,  $\mathbf{f}_0 e^{i\omega t}$ , can be expressed with these, as

$$\mathbf{q}(t) = \mathbf{H}(\omega) \mathbf{f}_0 e^{i\omega t} = \left( \sum_{k=1}^n \frac{-\lambda_k \phi_k l_k^T}{i\omega - \lambda_k} + \frac{-\bar{\lambda}_k \bar{\phi}_k \bar{l}_k^T}{i\omega - \bar{\lambda}_k} \right) \mathbf{f}_0 e^{i\omega t} \quad (3)$$

Here,  $\mathbf{H}(\omega)$  is the frequency response function matrix. Note that both  $\phi_r, l_r$  are required.

#### 1.3 Planar mode shapes and experimental modal analysis

Undamped rotors mounted on bearings with coinciding principal axes (a private case are isotropic bearings) of stiffness give rise to planar mode shapes (See WANG AND KIRKOPHE,



1994). It is customary to divide the response at nodes along the shaft into components in the  $xz$  and  $yz$  planes, i.e.  $\phi = \begin{pmatrix} r_x \\ r_y \end{pmatrix}$ . A planar mode shape obeys the relation,  $\phi = \begin{pmatrix} \mathbf{a} \\ i\mathbf{b} \end{pmatrix}$  where  $\mathbf{a}$  and  $\mathbf{b}$  are real vectors. A rotor mounted on this type of bearings is illustrated in figure 1,

A planar mode shape is characterised by the fact that all the points on the shaft centreline are contained in a plane rotating at the whirl speed (natural frequency), as illustrated in figure 1



**Figure 1.** A whirling mode shape (natural frequency at 242 Hz) of a rotating rotor (at 1200 Rev./min.) having isotropic supports. The thick line indicates the location of the shaft centre at  $t=0$ . Left – Animated response, Right- front view of the modeshape

#### 1.4 Non isotropic supports – non-planar mode shapes

When the foundation and the bearing are anisotropic. Figure 3 illustrates a shaft with supports having non-coinciding principal axes of stiffness.

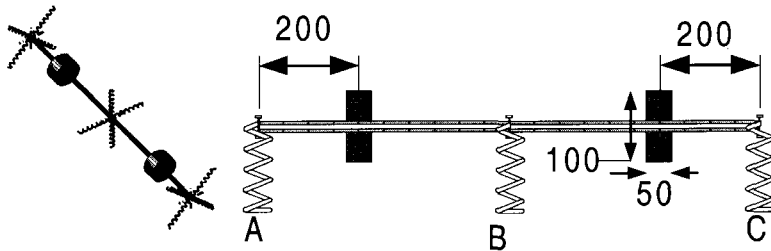


**Figure 2** Finite element model of a Rotor mounted on general (anisotropic) bearings. Left – three dimensional view showing the principal axes of stiffness (illustrated as springs).

A configuration such as depicted in figure 2 gives rise to non-planar modes as illustrated in figure 3. In this case, the centreline is no longer contained in one plane and a general eigenvector with components having an arbitrary phase is resulted.

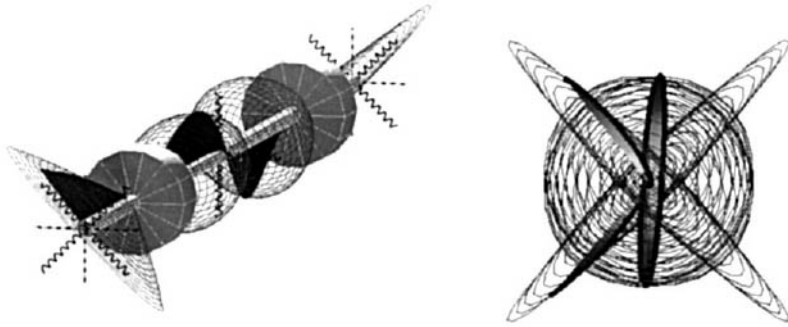


**Figure 3.** A typical mode shape of the FE model described in figure 2. The mode is computed at a Speed of  $\Omega=1200$  Rev/min and its natural frequency equals 261Hz. It can be observed that the non-isotropic bearings yield non-planar modeshapes

It is important to note (See figure 3) that the modeshapes tend to coincide with the principle axes of stiffness at the bearings. Following this observation, a special transformation, is chosen to transform such system with relatively anisotropic supports into a system with nearly de-coupled stiffness in the x and y axes.

## 2. Helical transformation and equations of motion

The main idea behind the proposed transformation is to introduce a helical co-ordinate system, which is designed to coincide with the principal axes of stiffness at every bearing.

Since the rotor (shaft and discs) is isotropic, it is shown that no additional coupling in the inertia and gyroscopic terms is introduced due to the proposed transformation.

Figure 4 illustrates an inertial co-ordinates system  $XYZ$  and a helical co-ordinates system  $xyZ$  rotate by an angle  $\psi = \beta_1 Z + \beta_0$  :

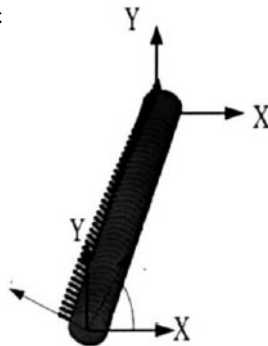


**Figure 4.** Transformed co-ordinate system along a shaft segment showing the helix angle  $\psi$

### 2.1 The structure of the equations in helical co-ordinates

A special selection of co-ordinates system (CHEN, 1995, LEE 1993) is often used in rotordynamics modelling. This selection gives rises to a simplified structure of the involved matrices in equation 1. For this representation it can be shown that a rotor mounted on supports having coinciding principal axes of stiffness, is described by (CHEN 1995):

$$\begin{bmatrix} M_0 & 0 \\ 0 & M_0 \end{bmatrix} \begin{bmatrix} \dot{q}_X \\ \dot{q}_Y \end{bmatrix} + \begin{bmatrix} 0 & G_0 \\ -G_0 & 0 \end{bmatrix} \begin{bmatrix} q_X \\ q_Y \end{bmatrix} + \begin{bmatrix} K_X & 0 \\ 0 & K_Y \end{bmatrix} \begin{bmatrix} q_X \\ q_Y \end{bmatrix} = 0 \quad (4)$$

Here we choose a helical co-ordinate system as shown in figure 5 for a single element.

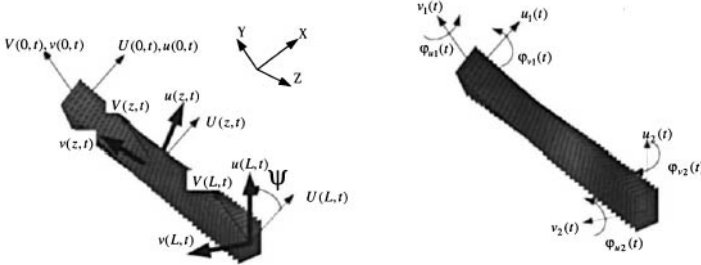


**Figure 5** The transformed degrees of freedom after undergoing a rotation an angle of  $\psi$

The displacement along the rotated helical co-ordinate system is based upon a standard representation typically used for a Timoshenko (GENTA, 1995) beam element:

$$\begin{aligned} u(z,t) &= N_1(\xi)q_u(t), & v(z,t) &= N_1(\xi)q_v(t) \\ \phi_u(z,t) &= N_2(\xi)q_u(t), & \phi_v(z,t) &= N_2(\xi)q_v(t) \end{aligned} \quad (5)$$

where  $\xi = z/L$ , also

As we wish to express the dynamics of the rotating beam in inertial co-ordinates we can transform the displacements along the helix back into the inertial co-ordinates, where linear displacements obey

$$\begin{aligned} U(z,t) &= u(z,t)\cos(\psi) - v(z,t)\sin(\psi) \\ V(z,t) &= u(z,t)\sin(\psi) + v(z,t)\cos(\psi) \end{aligned} \quad (6)$$

and the transformation of angular displacements is:

$$\begin{aligned} \Gamma_v(z,t) &= \phi_v(z,t)\cos(\psi) - \phi_u(z,t)\sin(\psi) \\ \Gamma_u(z,t) &= \phi_v(z,t)\sin(\psi) + \phi_u(z,t)\cos(\psi) \end{aligned} \quad (7)$$

### 2.2 The effect of the helical transformation on the stiffness matrix

The expressions of the potential energy following (GENTA,1995), is:

$$V = \int_0^L \frac{6EI}{\phi L^2} \left( (\Gamma_v - \partial U/\partial z)^2 + (\Gamma_u + \partial V/\partial z)^2 \right) dz + \frac{1}{2} \int_0^L EI \left( (\partial \Gamma_u/\partial z)^2 + (\partial \Gamma_v/\partial z)^2 \right) dz \quad (8)$$

and the kinetic energy (GENTA, 1995) of a beam segment

$$T = \frac{1}{2} \int_0^L \rho \left[ A \left( \frac{\partial U}{\partial t} \right)^2 + \left( \frac{\partial V}{\partial t} \right)^2 \right] + J_t \left[ \left( \frac{\partial \Gamma_U}{\partial t} \right)^2 + \left( \frac{\partial \Gamma_V}{\partial t} \right)^2 \right] dx + \frac{1}{2} \Omega \int_0^L \rho J_p \left[ \left( \frac{\partial \Gamma_U}{\partial t} \right) \Gamma_V - \left( \frac{\partial \Gamma_V}{\partial t} \right) \Gamma_U \right] dx \quad (9)$$

are substituted equations 5,6 to show that:

- 1) The kinetic energy remains unchanged due to trigonometric identities and is *independent* upon,  $\psi$ ,  $\beta_0$  and  $\beta_1$  when expressed in terms of  $u, v, \varphi_u, \varphi_v$
- 2) The potential energy remains a function of  $\beta_1$

From the bending term in equation 9 (the contribution of shear is similar but is omitted for brevity and so is the  $(z, t)$  argument), we have :

$$V_{bending} = \frac{EI}{2} \int_0^L \left[ \beta_1^2 (\varphi_u^2 + \varphi_v^2) + \frac{\partial \varphi_u^2}{\partial z} + \frac{\partial \varphi_v^2}{\partial z} + 2\beta_1 \left( \varphi_v \frac{\partial \varphi_u}{\partial z} - \varphi_u \frac{\partial \varphi_v}{\partial z} \right) \right] dz \quad (10)$$

It can be deduced that the stiffness matrix obtains the form (compare with equation 4)

$$K = \begin{pmatrix} K_u + \beta_1^2 K_0 & \beta_1 K_\Delta \\ -\beta_1 K_\Delta & K_v + \beta_1^2 K_0 \end{pmatrix}, \quad K_\Delta = -K_\Delta^T \quad (11)$$

**Proof:** the cross-terms can be expressed as (GÉRADIN, 1993) with the aid of equation 4, as:

$$K_{uv} = K_{vu}^T = \frac{\partial^2 V}{\partial q_u \partial q_v^T} = EI \beta_1 \int \left( N_2 \frac{\partial N_2^T}{\partial z} - \frac{\partial N_2}{\partial z} N_2^T \right) dz = \beta_1 K_\Delta \quad (12)$$

by transposing equation 12 it can be seen that  $K_{uv} = -K_{uv}^T \therefore$

In conclusion we may state that the helical transformation created cross coupling in the stiffness terms and that this coupling has a distinct pattern. The derivation here is independent of the nature of the shape functions being used or on the number of generalised co-ordinates, it therefore serves as a general proof for systems for which equation 9 holds.

### 2.3 Solving the Eigenvalue problem in helical co-ordinates

It has been shown (WANG AND KIRKHOPE, 1994) that the identity  $\begin{pmatrix} u \\ v \end{pmatrix} = \begin{bmatrix} I & 0 \\ 0 & iI \end{bmatrix} \begin{pmatrix} u \\ -iv \end{pmatrix}$  once substituted in equation 4 yields a symmetric eigenvalue problem with real eigenvectors. This identity is substituted into the equation of motion of the rotor in helical co-ordinates :

$$\begin{bmatrix} M_0 & 0 \\ 0 & M_0 \end{bmatrix} \begin{pmatrix} \ddot{q}_u \\ \ddot{q}_v \end{pmatrix} + \begin{bmatrix} 0 & G_0 \\ -G_0 & 0 \end{bmatrix} \begin{pmatrix} \dot{q}_u \\ \dot{q}_v \end{pmatrix} + \begin{bmatrix} K_u + \beta_1^2 K_0 & \beta_1 K_\Delta \\ -\beta_1 K_\Delta & K_v + \beta_1^2 K_0 \end{bmatrix} \begin{pmatrix} q_u \\ q_v \end{pmatrix} = \begin{pmatrix} Q_u \\ Q_v \end{pmatrix} \quad (13)$$

to yield

$$\begin{bmatrix} M_0 & 0 \\ 0 & M_0 \end{bmatrix} \begin{pmatrix} \dot{q}_u \\ -i\dot{q}_v \end{pmatrix} + i \begin{bmatrix} 0 & G_0 \\ G_0 & 0 \end{bmatrix} \begin{pmatrix} \dot{q}_u \\ -i\dot{q}_v \end{pmatrix} + \left( \begin{bmatrix} \tilde{K}_u & 0 \\ 0 & \tilde{K}_v \end{bmatrix} + i\beta_1 \begin{bmatrix} 0 & K_\Delta \\ K_\Delta & 0 \end{bmatrix} \right) \begin{pmatrix} q_u \\ -iq_v \end{pmatrix} = \begin{pmatrix} Q_u \\ -iQ_v \end{pmatrix}$$

where  $\tilde{K}_u = K_u + \beta_1^2 K_0$  (14)

Equation 14 lends itself to perturbation (around  $\beta_1 = 0$ ) analysis under the assumption that  $\beta_1$  is small. For  $\beta_1 = 0$ , the eigenvalues and a single set of eigenvectors are sufficient to fully describe the model (WANG AND KIRKHOPE, 1994). For  $\beta_1 = 0$ , the  $j^{\text{th}}$  eigenvalue/eigenvector pair is:

$$\lambda_{0j} = \omega_{0j}, \Phi_{0j} = \begin{pmatrix} a_{0j} \\ -b_{0j} \end{pmatrix}, \quad (15)$$

where there are  $n$  vectors  $a_{0j}, b_{0j}$  in the  $u, v$  directions respectively.

## 2.4 Obtaining the eigenvectors in helical co-ordinates via perturbations

To perform perturbation analysis (LANCASTER, 1985; WANG AND KIRKHOPE 1994) we need to convert equation 13 into state space where

$$\begin{bmatrix} \bar{M} & 0 \\ 0 & \bar{K} \end{bmatrix} \begin{pmatrix} -i\dot{w} \\ \dot{w} \end{pmatrix} - i \left( \begin{bmatrix} -\bar{G} & \bar{K} \\ \bar{K} & 0 \end{bmatrix} + \begin{bmatrix} 0 & i\bar{K}_\Delta \\ 0 & 0 \end{bmatrix} \right) \begin{pmatrix} -i\dot{w} \\ w \end{pmatrix} = \begin{pmatrix} -i\bar{Q} \\ 0 \end{pmatrix} \quad (16)$$

where  $w = \begin{pmatrix} u \\ -iv \end{pmatrix}$ ,  $\bar{M} = \begin{bmatrix} M_0 & 0 \\ 0 & M_0 \end{bmatrix}$ ,  $\bar{K}_\Delta = \beta_1 \begin{bmatrix} 0 & K_\Delta \\ K_\Delta & 0 \end{bmatrix}$ ,  $\bar{K} = \begin{bmatrix} \tilde{K}_u & 0 \\ 0 & \tilde{K}_v \end{bmatrix}$ ,  $\bar{G} = \begin{bmatrix} 0 & G_0 \\ G_0 & 0 \end{bmatrix}$

An unperturbed eigenvector of the form  $\Phi_{0j} = \begin{pmatrix} \omega_{0j} a_{0j} \\ b_{0j} \end{pmatrix}$  (WANG KIRKHOPE, 1994) is being used to produce the perturbed eigenvalues and eigenvectors:

$$\lambda_r = i\omega_{0j} + \lambda_{1j} + \lambda_{2j} + \dots, \quad \Phi_j = \Phi_{0j} + \Phi_{1j} + \dots \quad (17)$$

### 2.4.1 First order perturbation

The first order perturbation of the eigenvalues and eigenvectors are (LANCASTER, 1985):

$$\lambda_{1j} = \left( \begin{matrix} \omega_{0j} \Phi_{0j} \\ \Phi_{0j} \end{matrix} \right)^T \begin{bmatrix} 0 & i\bar{K}_\Delta \\ 0 & 0 \end{bmatrix} \begin{pmatrix} \omega_{0j} \Phi_{0j} \\ \Phi_{0j} \end{pmatrix} = i\omega_{0j} \beta_1 (a_{0j}^T K_\Delta b_{0j} + b_{0j}^T K_\Delta a_{0j}) \quad (18)$$

As this quantity is a scalar it can be transposed to show that

$$\lambda_{1j} = i\omega_{0j} \beta_1 (a_{0j}^T K_\Delta b_{0j} - a_{0j}^T K_\Delta b_{0j}) = 0 \quad (19)$$

**Proof:** we use equation 12 and the result that  $K_\Delta = -K_\Delta^T$  to obtain equation 19.

Remark: it is anticipated that a static transformation would not change the natural frequencies nor add dissipation.

First order eigenvector perturbation can be expressed as:

$$\phi_{1j} = i \sum_{k=1, k \neq j}^{2n} \frac{i\omega_{0k} \beta_1 (a_{0k}^T K_{\Delta} b_{0j} + b_{0k}^T K_{\Delta} a_{0j})}{\omega_{0k} - \omega_{0j}} \phi_{0k} = \beta_1 \sum_{k=1, k \neq j}^{2n} \frac{\omega_{0k} (a_{0k}^T K_{\Delta} b_{0j} + b_{0k}^T K_{\Delta} a_{0j})}{\omega_{0k} - \omega_{0k}} \phi_{0k} \quad (20)$$

Transforming the perturbed eigenvectors to the physical space we can write:

$$\phi_r = \begin{bmatrix} I & 0 \\ 0 & jI \end{bmatrix} (\phi_{0r} + \phi_{1r}) = \begin{pmatrix} a_r + \delta_r \\ -j(b_r + \gamma_r) \end{pmatrix}, \quad l_r = \begin{pmatrix} a_r + \delta_r \\ j(b_r + \gamma_r) \end{pmatrix} \quad (21)$$

Where  $\delta_r, \gamma_r$  are the perturbation terms.

As shown in BUCHER AND EWINS, 1996, the frequency response function can now be expressed as:

$$H(\omega) = \sum_{r=1}^n \frac{\omega_{0r}^2 A_r - j\omega_{0r} B_r}{\omega_{0r}^2 - \omega^2} \quad (22)$$

$$A_r = \begin{pmatrix} a_r a_r^T + \delta_r a_r^T + a_r \delta_r^T & 0 \\ 0 & b_r b_r^T + \gamma_r b_r^T + b_r \gamma_r^T \end{pmatrix}, \quad B_r = \begin{pmatrix} 0 & -a_r b_r^T - \delta_r b_r^T - a_r \gamma_r^T \\ a_r b_r^T + \delta_r b_r^T + a_r \gamma_r^T & 0 \end{pmatrix}$$

## 2.5 Exploiting the transformed co-ordinates for modal testing

The ability to choose the co-ordinate system so that it coincides with the principal axes of each bearing could yield, even when there is a large difference in the stiffness between two orthogonal directions, a nearly uncoupled stiffness matrix.

In order to demonstrate the above statement a numerical example based upon a finite element is shown. The model consists of a 1 m long shaft having an inner and outer diameter of 15 mm and 8mm respectively. Two discs are placed on the shaft. The shaft and the discs are made of steel with  $E=210$  GPa and density  $\rho=7800$  kg/m<sup>3</sup>.

Two types of supports are being used with this model. (1) Isotropic, for which the 3 bearings have the stiffness matrices, isotropic.

$$K_A = \begin{bmatrix} 1 & 0 \\ 0 & 1 \end{bmatrix} 10^6 \frac{N}{m}, \quad K_B = \begin{bmatrix} 1 & 0 \\ 0 & 1 \end{bmatrix} 10^6 \frac{N}{m}, \quad K_C = \begin{bmatrix} 1 & 0 \\ 0 & 1 \end{bmatrix} 10^6 \frac{N}{m} \quad (23)$$

(2) Anisotropic, for which the 3 bearings have the stiffness matrices

$$K_A = \begin{bmatrix} 1 & -0.5 \\ -0.5 & 1 \end{bmatrix} 10^6 \frac{N}{m}, \quad K_B = \begin{bmatrix} 1 & 0 \\ 0 & 1 \end{bmatrix} 10^6 \frac{N}{m}, \quad K_C = \begin{bmatrix} 1 & 0.5 \\ 0.5 & 1 \end{bmatrix} 10^6 \frac{N}{m} \quad (24)$$

Note that bearings A and C have their maximal stiffness at 45 and 135 degrees respectively

The two models yield modeshapes that are depicted in figure 1 and 3 respectively. Note that in the asymmetric case, the modeshapes tends to coincide with the principle axes of stiffness.

A perfectly helical modeshape will produce no cross coupling and thus  $\delta_r, \gamma_r$  will both be zero. In reality it is expected (See also figure 3) that the modeshape will not be a perfect helix and thus the perturbation terms  $\delta_r, \gamma_r$  appearing in the frequency response function (equation 21) should be estimated from measured data. An approach similar to what was proposed in BUCHER AND EWINS, 1996, 2000 could be used for this purpose. With this approach a single excitation device acting in both the  $x$  and  $y$  directions should suffice to extract the complete model from the basic modeshapes and their perturbation terms.

### 3. Conclusions and future work

In this paper the effect of undamped anisotropic supports was discussed in relation to modal analysis and modal testing. It has been shown that a helical co-ordinate system can be chosen to coincide with the principal axes of stiffness at every bearing, thus maintaining an almost de-coupled stiffness while not affecting the mass and gyroscopic matrices. This de-coupling is guaranteed for relatively small angles per unit length of the helix and tests are being conducted to find the extent of twist angles where these equations are still valid. When the cross coupling in the helical transformation is indeed small, the modeshapes can be extracted via a single bi-axial excitation device. This work serves as an initial stage in an attempt to find appropriate co-ordinate transformations allowing one to gather complete knowledge about a tested rotating shaft. It is anticipated that this approach will be further developed to adaptively change the required transformation according to the measured data and thus eliminating the cross-coupling and the non-self adjointness of rotating structures. Due to lack of space no further numerical results are presented.

### References

- [1] LIAO C.-L. AND HUANG B.-W., 1995, "Parametric resonance of a spinning pretwisted beam with time dependent spinning rate", *Journal of Sound and Vibration*, 180(1), 47-65
- [2] WIJEYEWICKREMA A. C. AND KEER L. M., 1995, "Critical speeds and buckling loads of a pretwisted rotor", *Journal of Sound and Vibration*, 179(1), 109-129
- [3] WANG AND KIRKHOPE, 1994, "New eigensolutions and modal analysis for gyroscopic/rotor systems, part 2: perturbation analysis for damped systems", *Journal of Sound and Vibration*, 175(2), 171-183
- [4] CHEN W. R. AND KEER L. M., 1993, "Transverse vibration of a rotating twisted Timoshenko beam under axial loading", *Journal of Vibration and Acoustics* 115, 285-294
- [5] CHEN W. J. 1995, "Concise equations for rotor dynamics analysis", DE Vol. 84 2, ASME Design engineering conferences Volume 3 Part B, 951-956
- [6] LEE C. W., 1993 *Vibration analysis of rotors*, Kluwer academic publishers, London
- [7] GENTA G., *Vibration of structures and machines*, 1995
- [8] LANCASTER P. AND TIMENETSKY M., 1985, *The theory of matrices*, Academic press, Orlando Florida
- [9] GERADIN M. AND RIXEN D., 1994, *Mechanical Vibrations: Theory and application to structural dynamics*, Wiley
- [10] BUCHER I. AND EWINS D. J., 1996 "Modal testing of rotating structures: difficulties, assumptions and practical approach", IMechE sixth international conference on Vibrations in rotating machinery, Oxford UK, September
- [11] BUCHER I. AND EWINS D. J., 2000 "Modal testing of rotating structures a survey and some new results", accepted for publication in A special issue of the Royal Society, philosophical transactions: Mathematical, physical and engineering science

*This page intentionally left blank*



# On the dynamics of windmilling in aero-engines

**G von GROLL and D J EWINS**

Department of Mechanical Engineering, Imperial College of Science Technology and Medicine,  
London, UK

## ABSTRACT

The relatively new problem of ‘windmilling imbalance’ in aero-engines is investigated. It falls into the class of rotor/stator rub problems, and thus features many nonlinear effects known from other rub-related phenomena. A simple four-degree-of-freedom model is derived and the results from its analysis compared with measurements conducted on a small-scale test rig. Amplitude jumps and sub- & super-harmonic vibration components were observed. Especially the sub-harmonic components are believed to provide a means to potentially excite the low frequency components of an aircraft, and this needs to be included in the aircraft structural fatigue integrity and cabin environmental assessments.

## 1 INTRODUCTION

It is a certification requirement of aero-engines to demonstrate blade containment and rotor dynamic integrity in the unlikely event of loss of a fan blade during operation. In such an event, the engine would be shut down, but the shaft would continue to rotate due to the incoming airflow. Out-of-balance forces caused by a missing fan blade provide a source of excitation for the whole engine-wing-aircraft structural assembly. This condition is referred to as ‘windmilling imbalance’ (FAA, 1999).

Rotor clearances which pertain to normal operation could now be overcome by vibrating components, thus leading to the rotor rubbing against the stator which, in turn, can potentially cause a rich mixture of effects associated with contact/impact-related phenomena. These effects manifest themselves in the occurrence of multiple solutions for steady-state response scenarios, including amplitude jumps during rotor acceleration and deceleration, and vibration responses at different/multiple frequencies of the exciting unbalance force.

The studies presented here form part of an effort to define a complete understanding of the contributing mechanisms of the post-fan-blade-off windmill dynamics and to efficiently perform windmilling analysis for large-scale engine models. The FAA, in collaboration with industry, is developing a certification procedure requiring engine and airframe man-

manufacturers to prove by analysis or test that an aeroplane under windmilling conditions is still safe to fly. It is part of the understanding required for the analysis to find out what loads are involved and to what level low-frequency vibration modes of the airframe can be excited.

## 2 RELATED RESEARCH

Windmilling is related to many other rotor/stator interaction problems discussed in the literature. The majority of numerical studies deal with a modified Jeffcott rotor, a two degree-of-freedom system either with clearance in the bearings or with the rotor touching a (flexibly-suspended) rigid stator, and only a few studies have analysed representatively complex multi-degree-of-freedom systems. Most studies do not attribute the stator with its own dynamic behaviour, *i.e.* the stator is assumed to have negligible mass. However, such a system is already capable of rich bifurcational and chaotic behaviour (Kleczyka *et al.*, 1992), even with all the simplifications stated above, so that analysing a realistic system with realistic mass and stiffness characteristics is a difficult task indeed.

In systems with rub or bearing clearance, the system stiffness changes with respect to the state of contact or non-contact, and while the stiffnesses associated with the individual states may well have a linear characteristic, the global behaviour is non-linear. It is typical for this class of system with non-linear stiffness to exhibit the well-known 'amplitude jump' behaviour (discussed later, Figures 2 and 4). Ehrich & O'Connor (1967) and Crandall (1987) studied the behaviour of a Jeffcott rotor system with bearing clearances analytically, Isaksson (1994) extended the analysis to the investigation of the influence of stator-offset to the turning points and stability of the solution branches. Ishida *et al.* (1997) have discussed non-stationary oscillations of such a system during acceleration through critical speeds. Markert & Wegener (1995) discussed rotors in retainer bearings and include the stator mass in their model when solving the equations via time integration for both transient and steady-state simulations.

Another commonly-observed type of behaviour is the presence of sub- and super-harmonic vibration. It is found in the papers cited below that a simple Jeffcott rotor with bearing clearances or a clearance between rotor and stator is a sufficiently complex analytical model to explain the existence of sub- and super-synchronous rotor vibration. An essential condition for these non-synchronous components to build up is that the system stiffness must be non-symmetric when seen from the static equilibrium position (Choi & Noah, 1988; Ehrich, 1989). This can be caused by a side force, *e.g.* gravity, or an eccentricity in the rotor/bearing assembly. Childs (1982) assumed the non-linearities to be small and performed a perturbation analysis after Linstedt & Poincaré, which yielded an expression with a higher harmonic forcing function, thereby explaining the existence of sub-harmonic  $\Omega/3$  as well as  $\Omega/2$ . Theoretically, the perturbation analysis can be carried further by including perturbations of higher orders, which in turn would explain a richer vibration spectrum. However, such a task is cumbersome so that nowadays available numerical methods are used to carry the analysis further. Choi & Noah (1987) made use of the harmonic balance method to extract sub- and super-harmonic components in the vibration spectrum. The rotor orbit was not derived analytically, but transformed into the frequency domain whose harmonics are then balanced. Kim *et al.* (1991) used this technique to solve a multi-degree-of-freedom system, using impedance matrix reduction to retain only the non-linear co-ordinates. The limitation of the harmonic balance method is that it can only capture harmonic components. Any frequencies which are not pure sub- or

super-harmonics of the excitation (as can be the case e.g. with full annular rub, or chaotic vibration), will be not be found. As a remedy for the shortcomings of the harmonic balance analysis, Sundararajan & Noah (1997) proposed a time-domain shooting algorithm which is adapted for non-autonomous systems.

It may be noted that papers dealing with dead-band clearance in bearings do not deal with rub, and thus no impact dynamics are included in the their models. However, such impact problems pose a challenge in that they typically worsen the conditioning for numerical analysis. Goldman & Muszynska (1993) used a piece-wise, continuous, local stiffness and damping during contact. In the subsequent analysis the local stator stiffness was assumed to be much higher than the stiffness of the shaft centerline radial deflection, which is valid for rigid stator bodies. This allows the displacements and frequencies to be expressed as truncated power series with higher order terms of only second degree. The authors divided rub into two parts: the “chattering regime”, which is caused by relatively elastic impacts, where the rotor bounces off the stator with enough energy to hit the stator again at a different location, and so on, and the “normal force controlled regime”, where the rotor loses sufficient energy during the impact to stay in continuous contact with the stator. Ghauri *et al.* (1996) studied numerically and experimentally the transient dynamics of a system with a step change in unbalance. A corresponding change in rotating inertia (e.g. when simulating blade loss) was neglected. The impact was modelled as classical rigid body impact with infinitesimal small duration, inhibiting the simulation from accounting for changes in rotor displacement during contact, as is possible e.g. in the model of Goldman & Muszynska (1993). Fumagalli & Schweitzer (1996) focused on the onset of whirl motion due to impact. Using a sophisticated test rig with magnetic bearings, experimental data were produced as well as a theoretical impact model. This impact model builds on the Hertz theory of static, normal contact between linear elastic spheres. The derived spring/damper characteristic of the impact is non-linear and the coefficient of restitution is speed-dependent.

As indicated by this short overview, there are numerous ways of simulating the problem at hand. In order to gain some confidence in the simulated results, measurements on a small-scale test rig were conducted and verified that the physical behaviour is adequately described and that no phenomena occurring in the measurements are omitted in the simulation.

### 3 MODELLING ROTOR/STATOR INTERACTION

#### 3.1 Kinematics

A simple and (in the literature) widely-used rotor/stator interaction system is the Jeffcott rotor with a stator ring suspended on springs, as shown below in Figure 1. For the purpose of numerical simulation, a small contact penetration of the rotor and stator rings is allowed. The contact stiffness in this penetration region is being set to orders of magnitude higher than the rotor shaft or stator suspension stiffness, so that the penetration depth is orders of magnitude smaller than rotor and stator deflections. The contact depth  $\delta$  is defined as

$$\delta(t) = \begin{cases} r_r + \epsilon_r e^{i\Omega t} - r_s - \epsilon_s - h e^{i\psi} & \text{if } |r_r + \epsilon_r e^{i\Omega t} - r_s - \epsilon_s| > h, \\ 0 & \text{otherwise} \end{cases} \quad (1)$$

where  $\Omega$  is the speed of shaft rotation,  $r_r, r_s$  are the rotor and stator displacements in the complex plane,  $\epsilon_r, \epsilon_s$  the geometric eccentricities of rotor and stator centre, and  $h$  is the gap size. These geometric parameters are depicted in Figure 1.

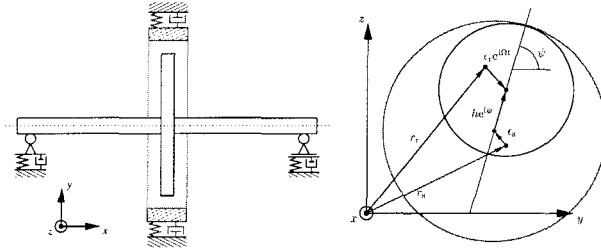


Figure 1: A Jeffcott rotor with stator

### 3.2 Equations of Motion

The equations of motion for a Jeffcott rotor interacting with a linear stator structure are:

$$m_r \ddot{r}_r + c_r \dot{r}_r + k_r r_r = -f_c + \Omega^2 m_r \epsilon_m e^{i\Omega t} \quad (2)$$

$$m_s \ddot{r}_s + c_s \dot{r}_s + k_s r_s = f_c \quad (3)$$

where  $f_c$  is the contact force between rotor and stator. In practice, there are many different contact models to choose from. One might use just a linear spring, add damping, or revert to a more realistic non-linear model. For simplicity, a linear, undamped, contact with a stiffness coefficient  $k_c$  will be used here:

$$f_c = k_c \delta \quad (4)$$

Introducing the parameters

$$\begin{aligned} \omega_r^2 &= \frac{k_r}{m_r} & \omega_s^2 &= \frac{k_s}{m_r} \equiv \gamma_s \omega_r^2 & \zeta_r &= \frac{\omega_r c_r}{2k_r} & \zeta_s &= \frac{\omega_s c_s}{2k_s} \\ \gamma_m &= \frac{m_s}{m_r} & \gamma_s &= \frac{k_s}{k_r} & \gamma_c &= \frac{k_c}{k_r} \end{aligned}$$

and substituting into equations (2) and (3) yields

$$\ddot{r}_r + 2\zeta_r \omega_r \dot{r}_r + \omega_r^2 r_r = -\omega_r^2 \gamma_c \delta + \Omega^2 \epsilon_m e^{i\Omega t} \quad (5)$$

$$\gamma_m \ddot{r}_s + 2\zeta_s \omega_s \dot{r}_s + \omega_s^2 r_s = \omega_r^2 \gamma_c \delta \quad (6)$$

Note that the stator parameters are normalised with respect to rotor parameters ( $m_r$  or  $k_r$ ). This hybrid approach is chosen to remain compatible with other papers in literature which do not consider the stator mass  $m_s$ , e.g. Ehrich (1969); Zhang (1988); Isaksson (1994); Markert & Wegener (1995). In this case one simply sets  $\gamma_m = 0$ .

Equations (2) and (3) can be solved with standard numerical techniques such as time-domain shooting methods, or by converting the task of finding periodic solutions to a boundary value problem, or in the frequency domain by the harmonic balance method. In the windmilling context, it is the steady-state response to the out-of-balance excitation forces which is of concern, rather than a particular transient event.

## 4 NUMERICAL RESULTS

For the special case of full annular rub with  $\epsilon_r, \epsilon_s = 0$  and isotropic rotor supports, the equations of motion become quasi-static for pure forward or backward whirl. At a given speed, the steady-state conditions of rotor whirl are such that the radial deflection of the rotor is constant. The only frequency component in the unbalance response spectrum is thus the engine-order speed,  $\Omega$ . This simple case is used here to illustrate the stability and continuation study. If not noted differently, the following values are used for the simulation:  $\omega_r = 1$ ,  $\gamma_m = 0.1$ ,  $\gamma_s = 2$ ,  $\zeta_r = 0.05$ ,  $\zeta_s = 0.07$ ,  $h = 3$ ,  $\gamma_c = 100$ . In Figure 2a the magnitudes of the rotor and stator responses  $r_r, r_s$  are plotted versus the rotor speed of rotation,  $\Omega$ . One can see that, for the parameters used, at speeds  $\Omega < 0.9$  the rotor unbalance response is too low to overcome the clearance (dashed line) and the rotor and stator are not in contact (stator response zero). At speeds  $0.9 < \Omega < 1.4$  rotor and stator *are* in contact (non-zero stator response), albeit the overhung part of the curve represents an unstable solution. At speeds  $\Omega > 1.4$ , well above the natural frequency of the rotor (normalised to  $\omega_r = 1$ ), the super-critically running rotor loses contact with the stator.

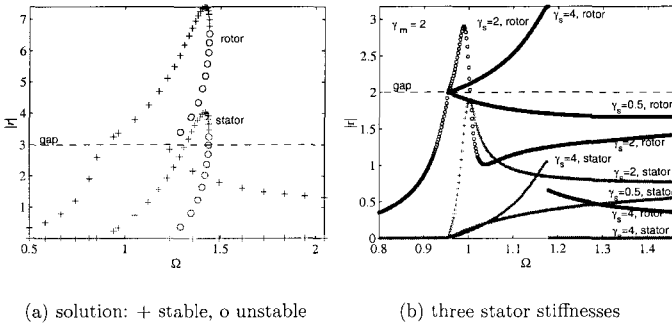


Figure 2: steady-state (constant speed) rotor and stator response over speed range

Another interesting observation is that for a stator with a natural frequency lower than the rotor, rotor and stator do not lose contact at higher speeds. In Figure 2b the rotor (o) and stator (+) responses are plotted for a range of stator stiffnesses,  $\gamma_s = 0.5, 2, 4$ , gap  $h = 2$  and  $\gamma_m = 2$ . Following the curve for a stiff stator,  $\gamma_s = 4$ , from lower speeds to higher ones, one sees the jump phenomenon occurring (unstable part of solution not plotted) and afterwards rotor and stator are out of contact. Not so for the other values  $\gamma_s = 0.5, 2$ , where there is no abrupt jump occurring and rotor and stator remain in contact over the entire range of higher speeds.

Figure 3 shows a second solution branch (of the system  $\gamma_m = 0.1$ ,  $\gamma_s = 2$ ) at  $\Omega > 6$ , which is not seen in the 1 DOF Duffing type oscillator that displays only the overhung behaviour in Figure 2. The motion in this second branch is ‘inverted’ in the sense that the stator, although it has twice the mass of the rotor in this example, is orbiting around the rotor much like a hola-hoop.

Specifying an eccentricity of the stator ring  $\epsilon_s \neq 0$  causes the rotor/stator contact to become intermittent in some speed intervals and gives rise to sub- and super-harmonic vibration components. Under these circumstances, the system has speed regimes where

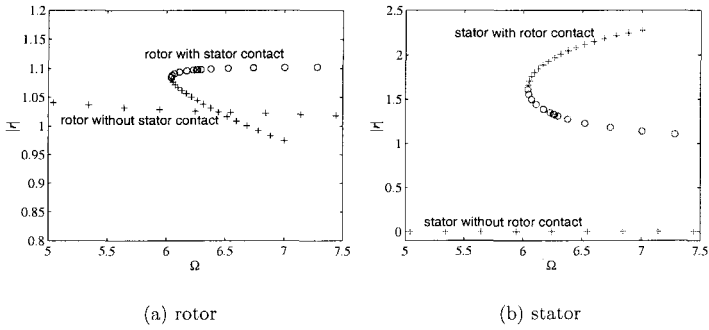


Figure 3: Second solution branch at  $\Omega > 6$ . solution: + stable, o unstable

the rotor is rubbing along the stator only over parts of the orbit, causing sub- and super-harmonics to emerge. Even a full annular rub would consist of higher harmonics (but no sub-harmonics). Figure 4 shows the time trace and spectral content of the vibrational behaviour during a slow run-up and run-down. The time traces show the magnitude of the rotor displacement, the horizontal line at  $|r| = 2$  indicates the gap between rotor and stator and, as a comparison, the response of a Jeffcott rotor without a stator is also given. The Z-mod plots show a dominant first engine-order component but also higher and sub-harmonic components. The sign of the frequency component indicates forward whirl (+) and backward whirl (-) directions. The DC component during rotor-stator contact results from the stator eccentricity, which is also responsible for the build up of sub-harmonic vibration components in the speed range  $2 < \Omega/\omega_r < 3$ .

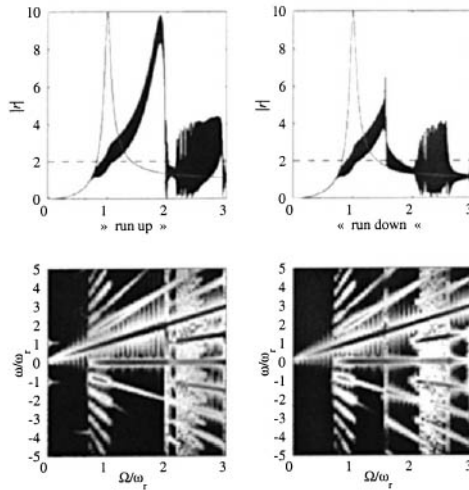


Figure 4: Sub- and Super-harmonics,  $\epsilon_s = 1 e^{i\Omega t}$

## 5 EXPERIMENTS

A rig has been built to investigate the rotor/stator contact mechanism in the wind-milling context, to map out a range of physical behaviour, and to verify the results from numerical simulations, including validation that there are no phenomena that are not predicted numerically. A photograph of the rig is shown in Figure 5. The measurements presented here can be characterised by the following main issues: (i) speed range over which rotor/stator contact is sustainable, and (ii) frequency spectrum of vibration.

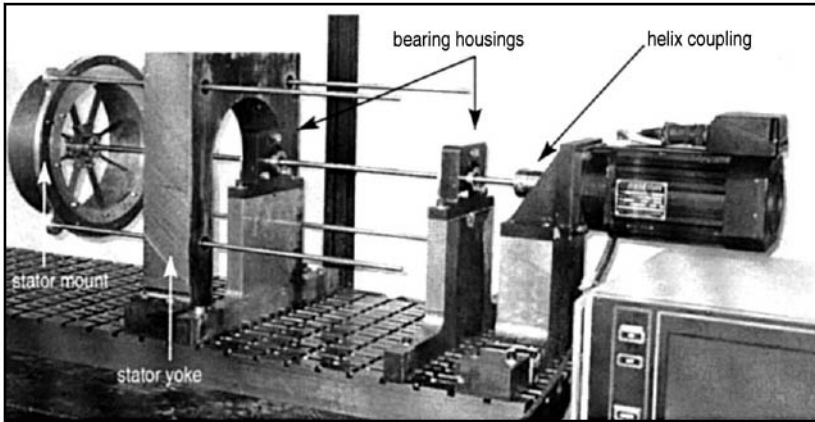


Figure 5: rotor and stator assembly in overhung configuration

Various measurements were conducted with different natural frequencies for rotor and stator. The contact behaviour described in the numerical simulation section generally matched the observed behaviour well. When  $\omega_s > \omega_r$ , rotor and stator dropped out of contact at higher speeds. For  $\omega_s < \omega_r$  rotor and stator continue to stay in contact for as long as it was considered safe to increase the speed (1800 rpm). None of these orbit plots are shown here due to constraints on space.

The following plots (Figures 6–7) show the orbits and the frequency spectra of the rotor/stator system with  $\omega_s < \omega_r$  at a series of constant speeds. The measured time histories each have a length of over 300 shaft revolutions and the frequency spectra have a resolution of 0.064Hz. The data were truncated by a few points so that each time record contained an exact integer number of revolutions, thus minimising leakage and avoiding the need to use windows in the signal processing.

Figure 6 shows a Lissajous figure with 11 main periodic components, Figure 7 looks more like random motion. However, if a stroboscopic sampling is superimposed on such a plot, so as to highlight every data point occurring at, say, the 1/rev signal (plotted as lighter dots), one can clearly see different patterns emerging, the 11 clusters in Figure 6, and tracing out ellipses in Figure 7.

With each orbit, the frequency spectrum is plotted over a range of 40dB. The sharpness of the peaks gives a good indication that the main vibration response frequencies are indeed multiples of the shaft speed, justifying the decision not to use windows in the processing as there were no significant leakage problems. Each of these frequency plots has a different grid spacing of dotted lines which attempts to match the dominant fre-

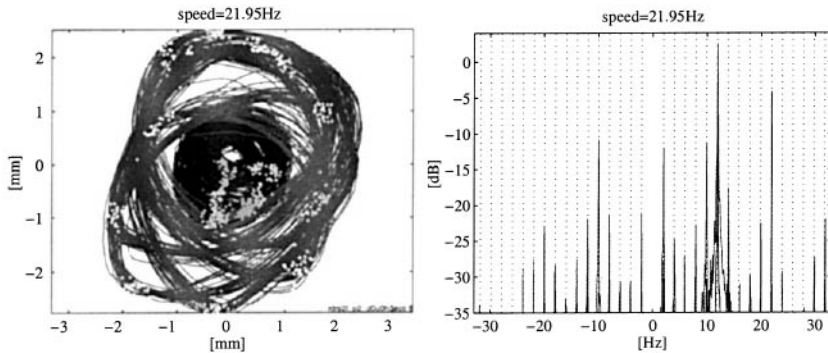


Figure 6: periodic orbit at  $\frac{1}{11}$  shaft speed

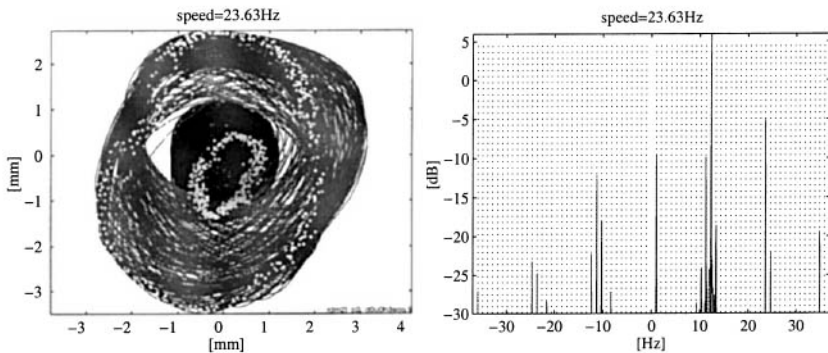


Figure 7: quasi-periodic orbit at  $\approx \frac{1}{23}$  shaft speed

quency components. In Figure 6 the dominant frequency is the resonance frequency of the combined rotor/stator system at  $\omega_{rs} \approx 12.00$  Hz and a shaft speed of  $\Omega = 21.95$  Hz. The ratio of these two frequencies is  $\omega_{rs}/\Omega \approx 6/11$ , resulting in a frequency spacing of  $\Delta\omega = \Omega/11$ . Strong components occur at  $i\Delta\omega$  with  $i = 1, 2, \dots, 7, 11, 16$ . The data for both Figures 6 and 7 are summarised in table 1.

Table 1:  $\gamma_m = 2$ ,  $\gamma_s = 0.5$ ,  $h = 2.0$  mm,  $\epsilon_s = 1.0$  mm

Figure	$\Omega$ [Hz]	$\omega_{rs}$ [Hz]	$\approx \frac{\omega_{rs}}{\Omega}$	$i$ (see text)
6	21.95	12.00	$\frac{6}{11}$	1, 2, ..., 7, 11, 16
7	23.63	12.33	$\frac{12}{23}$	1, 11, 12, 13, 23, 24, 34

The dominant frequency component around 12Hz is the frequency of the combined rotor/stator system which, of course, varies with magnitude of deflection as the system is non-linear. At the given speeds, this natural frequency of the combined rotor/stator system always seems to be strongly excited, sometimes being a stronger component in



the spectrum than the shaft speed component  $1\Omega$ . The other frequency components can also be linked: (i) the number of 1/rev clusters in the orbit plots (only Figure 6 is fairly distinct) yields the frequency grid, and (ii) the ratio of resonance frequency over speed of rotation can be approximated by a ratio of integer numbers, where the denominator is equal to fraction of shaft speed that makes up the frequency grid.

The mechanism that seems to be at work here might be relevant to a windmilling scenario, in that even very low sub-harmonics can potentially feature strongly in the response spectrum. Figures 6 and 7 show components at  $\Omega/11$  and  $\Omega/23$ , respectively, that are only 4–7 dB lower than the  $1\Omega$  component. This could potentially provide a mechanism by which a lower mode of the wing-aeroplane structure is excited although the windmill speed of the rotor is much higher.

## 6 SUMMARY

Amplitude jumps, which are familiar from the Duffing equation, are occurring in the simulation and measurements and are caused by the bi-linear system stiffness. Sub-harmonic vibration components, again in simulation as well as in measurements, are attributed to misalignment or a constant side force, both of which manifest themselves in geometric eccentricity in static equilibrium.

At certain ratios of rotor/stator mass, both rotor and stator stay in continuous contact irrespective of the speed of rotation. This effect is influenced by the relationship between the rotor and stator natural frequencies. The measured behaviour from the test rig is generally in line with the simulation results. Soft/stiff stator support conditions have an influence on whether system stays in contact at higher speeds.

The response at shaft speed  $\Omega$  was the dominant frequency component in most cases. Geometric eccentricity of rotor and stator rings generally causes other components to appear. Super-harmonics were always observed, sometimes as high as  $9\Omega$  within 40dB range of the strongest harmonic. Strong sub-harmonics were sometimes measured as low as  $\Omega/32$  within 40dB.

Accordingly, a possible mechanism for high intensity, low frequency vibration could be such a sub-harmonic coinciding with a low frequency mode of the aircraft. The sharpness of the peaks indicates a generally periodic behaviour.

The rich vibration spectrum poses a numerical challenge for frequency-domain analysis methods such as harmonic balance. Further work is thus carried out to establish which numerical solution method (shooting, boundary value, harmonic balance), or most likely which combination thereof, poses a reasonable approach for large degree-of-freedom full engine models.

## Acknowledgement

The authors are grateful to Rolls-Royce plc. for providing financial and technical support for this project and for giving permission to publish this work.

## References

- Dara W Childs. Fractional-frequency rotor motion due to nonsymmetric clearance effects. *Transactions of the ASME, Journal of Engineering for Power*, 104(3), 536–541, July 1982.
- Yeon-Sun Choi and Sherif T Noah. Nonlinear steady-state response of a rotor support

- system. *Journal of Vibration, Acoustics, Stress, and Reliability in Design*, 109(1), 255–261, 1987.
- Yeon-Sun Choi and Sherif T Noah. Forced periodic vibration of unsymmetric piecewise-linear systems. *Journal of Sound and Vibration*, 121(1), 117–126, 1988.
- S H Crandall. Nonlinearities in rotor dynamics. In *Proceedings of the eleventh international conference on nonlinear oscillations*, 44–56, Budapest, 1987. Janos Bolyai Mathematical Society.
- F F Ehrich and J J O'Connor. Stator whirl with rotors in bearing clearance. *Transactions of the ASME, Journal of Engineering for Power*, 381–390, August 1967.
- Fredric F Ehrich. The dynamics stability of rotor-stator radial rubs in rotating machinery. *ASME transactions: Journal of Engineering for Industry*, 1025–1028, November 1969.
- Fredric F Ehrich. A state-of-the-art survey in rotordynamics — nonlinear and self-excited vibration phenomena. In *Proceedings of the Second International Symposium on Transport Phenomena, Dynamics, and Design of Rotating Machinery*, volume Part II, 3–25, Honolulu, April 1989.
- FAA draft advisory circular: Transport airplane directorate propulsion Mega AC 25-XX. Federal Aviation Administration, Sept 1999. Subsection E-1.
- M Fumagalli and G Schweitzer. Measurements on a rotor contacting its housing. In *Sixth International Conference on Vibrations in Rotating Machinery*, 779–788, Oxford, September 1996. Institution of Mechanical Engineers.
- M K K Ghauri, C H Fox, and E J Williams. Transient response and contact due to sudden imbalance in a flexible rotor-casing system with support asymmetry. In *Sixth International Conference on Vibrations in Rotating Machinery*, 383–394, Oxford, September 1996. Institution of Mechanical Engineers.
- Paul Goldman and Agnes Muszynska. Chaotic behaviour of rotor/stator systems with rubs. *ASME Paper*, 93-GT-387, 1993.
- John L Isaksson. On the dynamics of a rotor interacting with non-rotating parts. Licentiate's thesis, Linköping University, 1994.
- Y Ishida, K Yasuda, and S Murakami. Nonstationary oscillation of a rotating shaft with nonlinear spring characteristics during acceleration through a major critical speed (a discussion by the asymptotic method and the complex-FFT method). *Transactions of the ASME, Journal of Vibration and Acoustics*, 119(1), 31–36, 1997.
- Y B Kim, S T Noah, and Y-S Choi. Periodic response of multi disk rotors with bearing clearances. *Journal of Sound and Vibration*, 144(3), 381–395, 1991.
- M Kleczka, E Kreuzer, and W Schiehlen. Local and global stability of a piecewise linear oscillator. In J M T Thompson and W Schiehlen, editors, *Nonlinear dynamics of engineering systems*, 533–546. The Royal Society, 1992.
- Richard Markert and Georg Wegener. Dynamik von elastischen Rotoren in Fanglagern. In *Schwingungen in Rotierenden Maschinen*, volume III. Vieweg, 1995.
- P Sundararajan and S T Noah. Dynamics of forced nonlinear systems using shooting / arc-length continuation method — application to rotor systems. *Transactions of the ASME, Journal of Vibration and Acoustics*, 119, 9–20, 1997.
- W Zhang. Dynamic instability of multi-degree-of-freedom flexible rotor systems due to full annular rub. In *Fourth International Conference on Vibrations in Rotating Machinery*. Institution of Mechanical Engineers, 1988.

# Levitron – an example of a purely permanent magnetic bearing of a rotor

**R GASCH**

Institut für Luft- und Raumfahrt, Technical University of Berlin, Germany

**M LANG**

Institut für Grenzflächenforschung und Vakuumphysik, Forschungszentrum Jülich, Germany

## **Abstract**

*Purely permanent magnetic supported levitation of a rigid body is impossible - is an often heard interpretation of Earnshaws Theorem (1842). However since the beginning of the nineties a spinning top has been offered in toy shops, which is able to rotate for minutes without any contact over a permanent magnetic base plate. The interaction of the six degrees of freedom of this fast top with the magnetic field is discussed in detail in this paper with the classical methods of rotor dynamics. Surprisingly, linearised differential equations suffice to describe the stable zone of rotational speeds.*

## **1. INTRODUCTION**

Levitron is the trade name of a fascinating toy. A top, which consists of a permanent magnet, rotates over a magnetic square base. Figure 1 illustrates this device. To begin, the top is spun on a plastic plate that covers the base. Using the plastic plate, the spinning top is lifted slowly to the floating position. The top floats at this point for a few minutes. Due to air resistance, the speed gradually decreases to below a threshold velocity, and the top tumbles down.

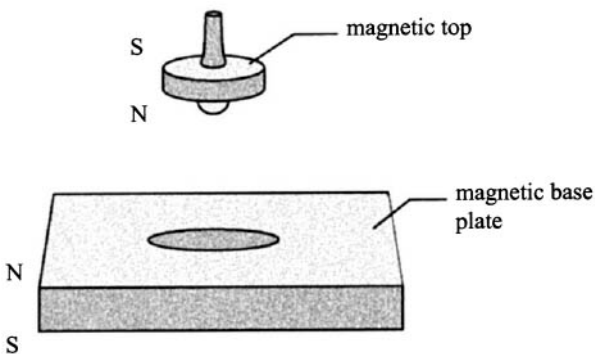


**Figure 1**

**Levitron - toy**

The levitating top is not only a fascinating toy, it raises some theoretical questions. Up to the present, purely permanent magnetic supported levitation of a rigid body seemed to be impossible [1]. Several papers have been published, which try to explain the phenomenon [2,3,4,5]. These publications [2,3] use analogies to particle physics. They explain that particles with a spin and a magnetic dipole moment (atoms, neutrons) may be stored in so called magnetic traps [6]. The explanations use the ideas of adiabatic invariant and dynamic potential, which are not common in engineering science. Instead, we use the classical methods of rotor dynamics to construct the equations of motion with the six degrees of freedom for the fast top. The stiffnesses are dependent on the magnetic forces. It can be shown that this simple model is sufficient to confirm the experiments in [3] and determine the stable speed range which is from 917 rpm to 1835 rpm.

Earnshaw's Theorem states that the sum of the stiffnesses for a particle suspended in a permanent magnetic field must be equal to zero:

$$s_x + s_y + s_z = 0 \tag{1}$$

Therefore, scientists at first believed a device like the hovering top was impossible. At least one of the three stiffnesses must be negative; that means static instability. Indeed, radial passive permanent magnetic bearing rotors need a journal bearing (gas centrifuge in Almelo/NL), or an active electro magnetic bearing to enable stability in the axial direction (System FZ-Jülich [8]). The Earnshaw Theorem alone, however, cannot account for the behaviour of the Levitron toy. The Earnshaw Theorem applies to a particle with three degrees of freedom only, the hovering top has six degrees of freedom and the 6x6 stiffness matrix is not complete with three coefficients only. Indeed, the gyroscopic effect and the coupling coefficients of the stiffness matrix of translation and tilting both effect the stable speed range.

## 2. FUNDAMENTAL STRUCTURE OF EQUATION OF MOTION

The differential equation of motion in matrix form:

$$\mathbf{M} \cdot \ddot{\mathbf{x}} + \mathbf{G} \cdot \dot{\mathbf{x}} + \mathbf{S}_{PM} \cdot \mathbf{x} = 0 \tag{2}$$

with  $\mathbf{M}$  - mass matrix       $\mathbf{G}$  - gyro matrix       $\mathbf{S}_{PM}$  - stiffness matrix  
 $\mathbf{x}$  - vector of 6 DOF's

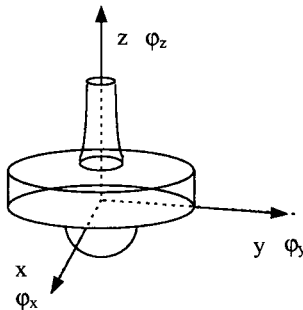


**Figure 2** Co-ordinate system for the equations of motion

Based on the co-ordinate system of figure 2, the equation of motion of a fast top in all six degrees of freedom:

$$\begin{pmatrix} m & 0 & 0 & 0 & 0 & 0 \\ 0 & m & 0 & 0 & 0 & 0 \\ 0 & 0 & m & 0 & 0 & 0 \\ 0 & 0 & 0 & \Theta_a & 0 & 0 \\ 0 & 0 & 0 & 0 & \Theta_a & 0 \\ 0 & 0 & 0 & 0 & 0 & \Theta_p \end{pmatrix} \begin{pmatrix} \ddot{x} \\ \ddot{y} \\ \ddot{z} \\ \ddot{\phi}_x \\ \ddot{\phi}_y \\ \ddot{\phi}_z \end{pmatrix} + \begin{pmatrix} 0 & 0 & 0 & 0 & 0 & 0 \\ 0 & 0 & 0 & 0 & 0 & 0 \\ 0 & 0 & 0 & 0 & 0 & 0 \\ 0 & 0 & 0 & 0 & \Omega \Theta_p & 0 \\ 0 & 0 & 0 & -\Omega \Theta_p & 0 & 0 \\ 0 & 0 & 0 & 0 & 0 & 0 \end{pmatrix} \begin{pmatrix} \dot{x} \\ \dot{y} \\ \dot{z} \\ \dot{\phi}_x \\ \dot{\phi}_y \\ \dot{\phi}_z \end{pmatrix} + \begin{pmatrix} ? & ? & ? & ? & ? & ? \\ ? & ? & ? & ? & ? & ? \\ ? & ? & ? & ? & ? & ? \\ ? & ? & ? & ? & ? & ? \\ ? & ? & ? & ? & ? & ? \\ ? & ? & ? & ? & ? & ? \end{pmatrix} \begin{pmatrix} x \\ y \\ z \\ \phi_x \\ \phi_y \\ \phi_z \end{pmatrix} = 0 \quad (3)$$

with the rotational speed  $\Omega = \dot{\phi}_z$ , mass  $m$  and the axial and polar moments of inertia  $\Theta_a$ ,  $\Theta_p$  respectively, is given by equation 3. The structure of the mass and the gyroscopic matrix is taken from [9]. The up to now unknown structure (question marks in equation 3) of the stiffness matrix will be discussed in the following section.

### 3. CONSIDERATION OF STRUCTURE OF THE STIFFNESS MATRIX

The stiffness matrix  $S_{PM}$  reflects the influence of the magnetic forces on the hovering top. We get the stiffness matrix by means of the derivatives of the forces and torques (six degrees of freedom) at the working point.

$$\mathbf{F}(\mathbf{x}) = \begin{pmatrix} F_x \\ F_y \\ F_z \\ M_x \\ M_y \\ M_z \end{pmatrix} \quad \text{with} \quad \mathbf{x} = \begin{pmatrix} x \\ y \\ z \\ \phi_x \\ \phi_y \\ \phi_z \end{pmatrix} \quad (4)$$

If we assume small displacements  $\Delta \mathbf{x}$ , the forces  $\mathbf{F}(\mathbf{x})$  can be developed in a Taylor series for the working position  $\mathbf{x}_0$  of the hovering top:

$$\mathbf{F}(\mathbf{x}) = \mathbf{F}_0 + \frac{\partial \mathbf{F}_0}{\partial \mathbf{x}} \Delta \mathbf{x} + \dots \quad (5)$$

The first derivatives in the Taylor series represent the stiffnesses. The Taylor series can be truncated after the first term, because we are only interested in the stiffnesses. Due to the six forces and the six displacements this results in a 6 x 6 matrix. Because of the conservative nature of the magnetic field we can reveal some of the structure of this matrix in advance. The model used to explain the matrix is shown in figure 3. The base magnet in figure 3 has a circular shape instead of a square shape like in the real device (figure 1). However as shown in [2], the operating of the top does not depend on the square or circular shape. Only for the sake of simplicity in this discussion do we prefer the round one.

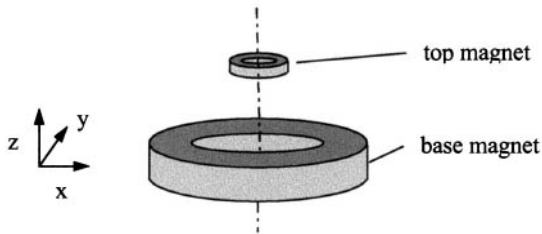


**Figure 3** Magnetic model of the levitron used for the explaining of the structure of the stiffness matrix

Basically the matrix  $S_{PM}$  must be a symmetric one because of the conservative nature of the magnetic forces:

$$s_{ij} = s_{ji} \quad (6)$$

The stiffnesses are generated by the differences of forces on small displacements or rotations on the working position, e.g. axial stiffness:

$$s_{ax} = -\frac{\Delta F_z}{\Delta z} \quad (7)$$

Some displacements do not produce any changes of forces due to this, any terms in this rotary symmetric device (fig. 3) have to be zero:

1. Rotation  $\Delta\phi_z$  does not result in any changes, therefore column 6 (row 6) contains only zeros
2. At a deviation  $\Delta z$  on the z-axis only the axial force changes. The radial forces and the tilt moment do not change.
3. With a displacement in the radial direction (figure 4), there is no force perpendicular to the direction of motion and no moment in the direction of motion. Figure 4 shows a displacement in the direction of the x-axis. The Force  $F_y$  and the moment  $M_{\phi_x}$  must be zero. The same idea can be applied to displacements in the y-direction.
4. With rotation on the lateral axis (e.g. x-axis) there is no moment in the direction of the perpendicular lateral axis, furthermore the force in the direction of the rotation axis is unaffected. E.g.  $M_{\phi_y}$  and  $F_x$  are unaffected at rotation about  $\phi_x$ -axis.

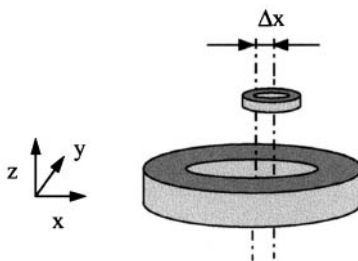


**Figure 4** Displacement in direction of the x-axis

Altogether only four independent stiffness numbers remain in the matrix. In addition to the axial stiffness we find:

the radial stiffness: 
$$s_r = -\frac{\Delta F_x}{\Delta x}, \quad (8)$$

the tilt stiffness 
$$s_{\varphi\varphi} = -\frac{\Delta M_x}{\Delta \varphi_x}, \quad (9)$$

and the coupling terms 
$$s_{\varphi r} = -\frac{\Delta F_y}{\Delta \varphi_x}. \quad (10)$$

The stiffness matrix takes the following form:

$$\mathbf{S}_{PM} = \begin{pmatrix} s_r & 0 & 0 & 0 & s_{\varphi r} & 0 \\ 0 & s_r & 0 & -s_{\varphi r} & 0 & 0 \\ 0 & 0 & s_{ax} & 0 & 0 & 0 \\ 0 & -s_{\varphi r} & 0 & s_{\varphi\varphi} & 0 & 0 \\ s_{\varphi r} & 0 & 0 & 0 & s_{\varphi\varphi} & 0 \\ 0 & 0 & 0 & 0 & 0 & 0 \end{pmatrix} \quad (11)$$

Insert this Matrix into equation 3, and it is apparent:

- That the axial degree of freedom is completely decoupled from all the other degrees of freedom.
- The rotational degree of freedom is completely free as is typical with rotation.

#### 4. NUMERICAL CALCULATION OF THE FORCES AND THE STIFFNESS MATRIX

A numerical force calculation was developed, to obtain forces and torques between the permanent magnets in all six degrees of freedom. This algorithm is explained in more detail in [10]. The procedure used in the algorithm describes magnets as bodies with surface currents on the lateral area (figure 3) and a relative permeability of  $\mu = 1$ . The program is able to calculate the forces and torques between annular magnets with magnetization in axial direction. The magnets can be in any position each other.

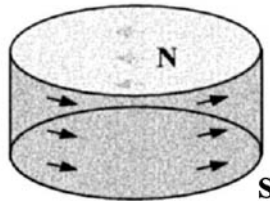


**Figure 5** Surface current at the lateral area

The field calculation uses the Biot - Savart law which describe the connection of currents with magnetic fields. For permanent magnets with surface currents it has the following form:

$$\mathbf{B}(\mathbf{r}_2) = \frac{\mu_0}{4\pi} \int \frac{\mathbf{A}_s(\mathbf{r}_1) \times \mathbf{r}}{|\mathbf{r}|^3} dA \quad \text{with } \mathbf{r} = \mathbf{r}_2 - \mathbf{r}_1 \quad (12)$$

where is  $\mathbf{B}$  the magnetic flux density at the point  $\mathbf{r}_2$ ,  $\mathbf{A}_s$  is the surface current at the point  $\mathbf{r}_1$ . The integral reaches about the whole lateral surface of the magnet (see figure 6).

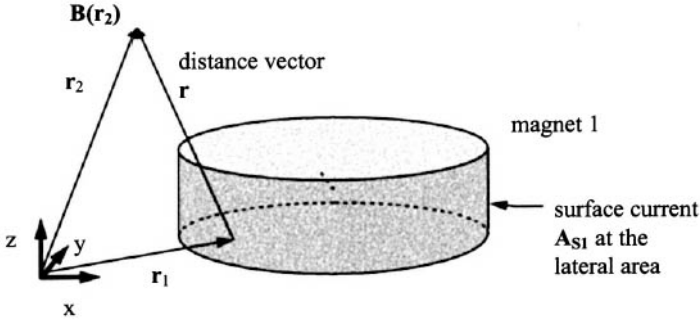


**Figure 6** Position and meaning of the different vectors.

#### 4.1 Determination of the surface current

The surface current  $\mathbf{A}_s$  is obtained from the remanence  $B_r$ :

$$\mathbf{A}_s = \frac{B_r}{\mu_0} \quad (13)$$

This equation is valid only if the magnet is homogeneous magnetized and the relative permeability is equal to  $\mu_r = 1$ . These conditions are applicable for modern permanent magnets (e.g. NdFeB  $\mu_r=1.07$ ).

#### 4.2 Force calculation by the magnetic field

The interaction of the surface current with an external field (second magnet) yield in stresses on the lateral area of the magnet (see eq.14).

$$\boldsymbol{\sigma} = \mathbf{A}_s \times \mathbf{B} \quad (14)$$

Equation (14) is the Lorentz law in the special case of surface currents. The forces and torques are obtained by surface integration of the stress:

$$\text{Forces} \quad \mathbf{F}_2 = \int \boldsymbol{\sigma} dA_2 \quad (15)$$

$$\text{Torques} \quad \mathbf{M}_2 = \int (\boldsymbol{\sigma} \times \mathbf{x}_m) dA_2 \quad (16)$$

where the vector  $\mathbf{x}_m$  is any reference point for the torque calculation.



### 4.3 Description of the numerical calculation procedure

The calculation of the forces by the field equation required two integrations:

1. calculation of the field of the magnet (equation 12)
2. force and torque calculation respectively (equations 15 and 16).

For the numerical calculation the integrals are replaced by sum. For that reason the surface current discretized in small parts  $\Delta A$  - like shown in figure 7.

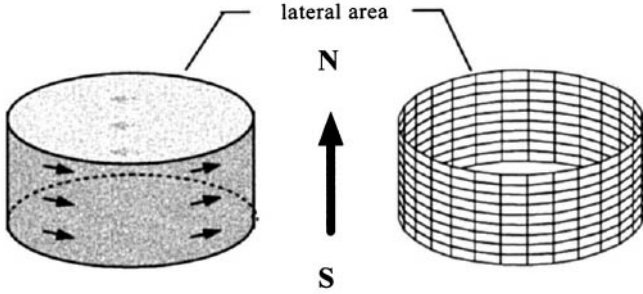


**Figure 7** Discretization into small parts  $\Delta A$

One single surface element  $\Delta A_1$  with the surface current  $\mathbf{A}_{S1}$  of the magnet 1 yield the magnetic flux density  $\Delta \mathbf{B}$  at the point  $\mathbf{r}_2$ :

$$\Delta \mathbf{B}(\mathbf{r}_2) = \frac{\mu_0}{4\pi} \cdot \frac{\mathbf{A}_{S1}(\mathbf{r}_1) \times \mathbf{r}}{|\mathbf{r}^3|} \Delta A_1 \quad (17)$$

By the summation over all the surface elements of the first magnet we get the field at one surface element of the second magnet:

$$\mathbf{B}(\mathbf{r}_2) = \frac{\mu_0}{4\pi} \cdot \sum_{m=1}^{m_{\max}} \sum_{n=1}^{n_{\max}} \frac{\mathbf{A}_{S1}(\mathbf{r}_1) \times \mathbf{r}}{|\mathbf{r}^3|} \cdot \Delta A_1 \quad (18)$$

Using this field we can find the force at this surface element  $\Delta A_2$  by modifying eq. 14:

$$\Delta \mathbf{F}(\mathbf{r}_2) = [\mathbf{A}_{S2}(\mathbf{r}_2) \times \mathbf{B}(\mathbf{r}_2)] \cdot \Delta A_2 \quad (19)$$

The summation over all the surface elements of the magnet yield forces and torques:

Forces 
$$\mathbf{F} = \sum_{k=1}^{k_{\max}} \sum_{l=1}^{l_{\max}} \Delta \mathbf{F}(k,l) \quad (20)$$

Torques 
$$\mathbf{M} = \sum_{k=1}^{k_{\max}} \sum_{l=1}^{l_{\max}} (\Delta \mathbf{F}(k,l) \times \mathbf{x}_m) \quad (21)$$

## 5. UP-DATING THE MODEL BY MEASUREMENTS AND THE CALCULATION OF THE STIFFNESS MATRIX

We measured the vertical force  $F_z$  to obtain an understanding of the stability conditions. The top was moved across the vertical axis. The axis in figure 5 show the movement that was carried out.

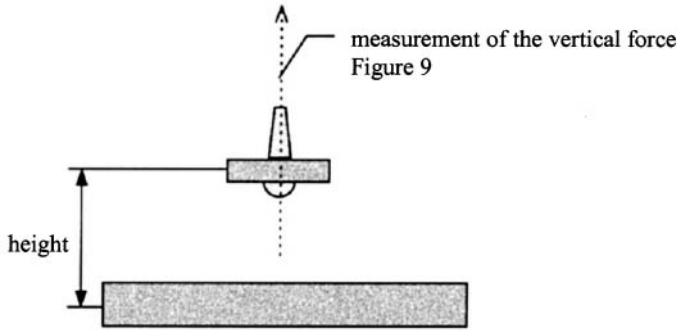


**Figure 8** Movement of the top for measurement of the vertical forces.

For measurement of the vertical force the base plate was placed on a balance and the top was fixed to a special device which was able to measure vertical movement. A graph of the vertical force versus height is shown in figure 9.

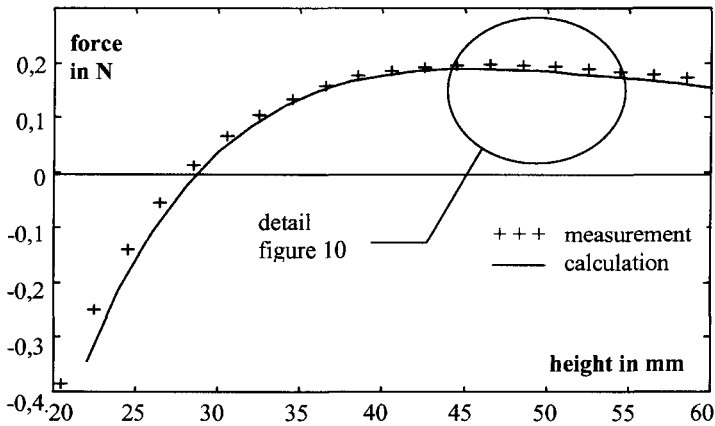


**Figure 9** Vertical force versus height. Comparison between the measurement and calculation.

The second curve in figure 9 shows the calculated values which were calculated with the described program.

Dimensions of the magnets:

-base magnet

edge length: 101 mm  
 inner radius: 8 mm  
 height: 13 mm  
 surface current: 320 kA/m

-top magnet

outer radius: 14.75 mm  
 inner radius: 5.0 mm  
 height: 5.0 mm  
 surface current: 320 kA/m

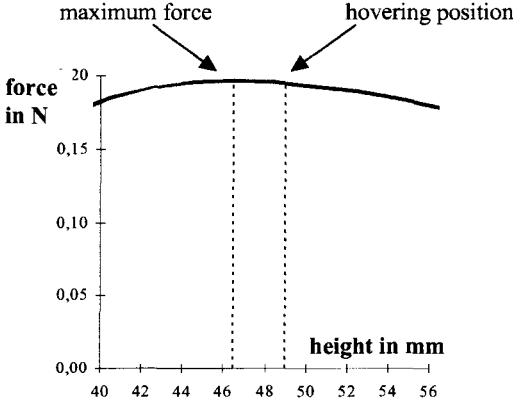


**Figure 10** Detail of the vertical force depicted in figure 9.

Positive values mean repelling forces and negative values mean attractive forces accordingly. The height on the abscissa is measured from the center of the base plate to the center of the top magnet. The hovering position was measured at a height of approximately 49 mm. This position is just beyond the maximum of the repelling force which is 46.5 mm. According to equation 7 we get a (small) positive axial stiffness  $s_{ax}$  that means stability in this direction. Because of the Earnshaw Theorem (eq.1) the radial motion is expected to be unstable due to:

$$s_r = -\frac{1}{2} s_{ax} \tag{22}$$

With the above mentioned input data we get the following stiffness matrix for the hovering top by numerical calculation:

$$S_{PM} = \begin{pmatrix} -0.43 \text{ N/m} & 0 & 0 & 0 & 0.11 \text{ N/rad} & 0 \\ 0 & -0.43 \text{ N/m} & 0 & -0.11 \text{ N/rad} & 0 & 0 \\ 0 & 0 & 0.82 \text{ N/m} & 0 & 0 & 0 \\ 0 & -0.11 \text{ N} & 0 & -8.6 \cdot 10^{-3} \text{ Nm/rad} & 0 & 0 \\ 0.11 \text{ N} & 0 & 0 & 0 & -8.6 \cdot 10^{-3} \text{ Nm/rad} & 0 \\ 0 & 0 & 0 & 0 & 0 & 0 \end{pmatrix} \tag{23}$$

## 6. SOLUTION OF THE DIFFERENTIAL EQUATION SYSTEM

In the following we focus attention mainly on the radial degrees of freedom. Because of the rotational symmetry we can reduce equation of motion by introducing complex degrees of freedom. With

$$\bar{r} = x + jy \quad \varphi = \varphi_x + j\varphi_y \quad (24)$$

we get

$$\begin{pmatrix} m & 0 \\ 0 & \theta_a \end{pmatrix} \cdot \begin{pmatrix} \ddot{\bar{r}} \\ \ddot{\varphi} \end{pmatrix} + \begin{pmatrix} 0 & 0 \\ 0 & -j\theta_p\Omega \end{pmatrix} \cdot \begin{pmatrix} \dot{\bar{r}} \\ \dot{\varphi} \end{pmatrix} + \begin{pmatrix} s_r & -js_{\varphi r} \\ js_{\varphi r} & s_{\varphi\varphi} \end{pmatrix} \cdot \begin{pmatrix} \bar{r} \\ \varphi \end{pmatrix} = 0 \quad (25)$$

Using equation (25) and the numbers we obtained from equation (23), we can find the homogeneous solution of the differential equation system. The homogeneous linear equation system results from

$$0 = \begin{pmatrix} m \cdot \lambda_v^2 + s_r & -js_{\varphi r} \\ js_{\varphi r} & \theta_a \lambda_v^2 - j\Omega\theta_p \lambda_v + s_{\varphi\varphi} \end{pmatrix} \cdot \begin{pmatrix} \bar{r} \\ \varphi \end{pmatrix} \quad (26)$$

Whose characteristic equation is:

$$m \cdot \theta_a \cdot \lambda_v^4 - j \cdot m \cdot \Omega \cdot \theta_p \lambda_v^3 + (s_{\varphi\varphi} \cdot m + s_r \theta_a) \lambda_v^2 - j \cdot \Omega \cdot \theta_p \cdot s_r \lambda_v + (s_r \cdot s_{\varphi\varphi} - s_{\varphi r}^2) = 0 \quad (27)$$

The solution gives four eigenvalues  $\lambda_v$ , which are a function of the rotational speed. Figure 11 shows the wandering of the eigenvalues as function of speed (root locus). The solution used the following data:

top mass	$m = 20 \cdot 10^{-3} \text{ kg}$
moments of inertia	axial $\theta_a = 1,32 \cdot 10^{-6} \text{ kgm}^2$
	polar $\theta_p = 2,2 \cdot 10^{-6} \text{ kgm}^2$
stiffnesses	$s_r = -0,43 \text{ N/m}$
	$s_{\varphi\varphi} = -8,6 \cdot 10^{-3} \text{ Nm/rad}$
	$s_{\varphi r} = 0,11 \text{ N/rad}$

Inertia values were taken from [3].

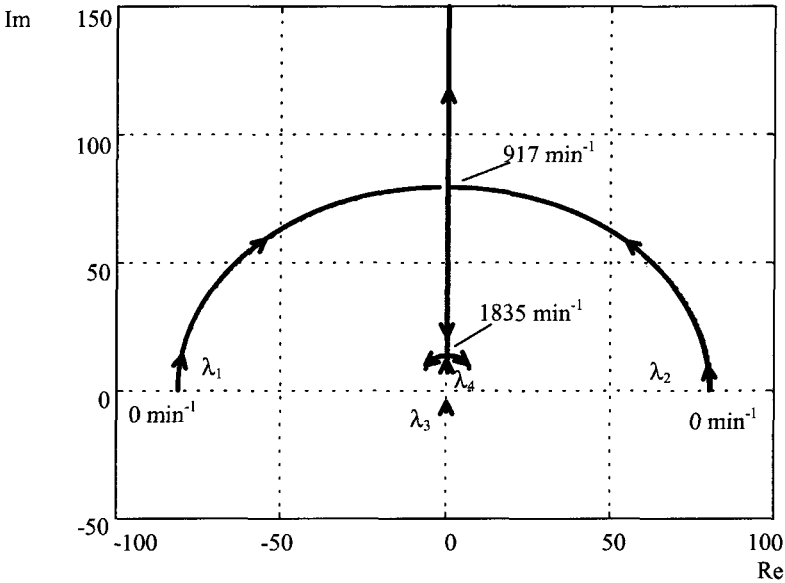


**Figure 11** Trace of the eigenvalues  $\lambda_v$  as function of speed.

The labelling of the eigenvalues are near the start point (0 rpm). All of the eigenvalues are purely imaginary in the speed range from 917 rpm to 1835 rpm. That means the system is stable in that rotational speed range, but undamped. Outside this range, there is one eigenvalue in the right plane which causes instability. These results have been compared to experimental results of [3]. They show good agreement for the lower limiting speed. The upper limit of the stable area found by measurement is somewhat than our numerical result (254 rad/s versus 192 rad/s).

**Table 1** Comparison of the calculation results with the data of [3]

	lower limit in rad/s	upper limit in rad/s
measurement of [3]	114	254
linear theory of [3]	98	227
own calculation	96	192

To get a better understanding of the locus of the eigenvalues in the complex plain of figure 10, the translation was decoupled from the rotation in equation (25) by setting  $s_{qr} = 0$ . The lateral motion is now independent of the speed. Only the rotational eigenvalues are now speed dependent.

Figure 12 shows the root locus of the eigenvalues without this coupling ( $s_{qr} = 0$ ).

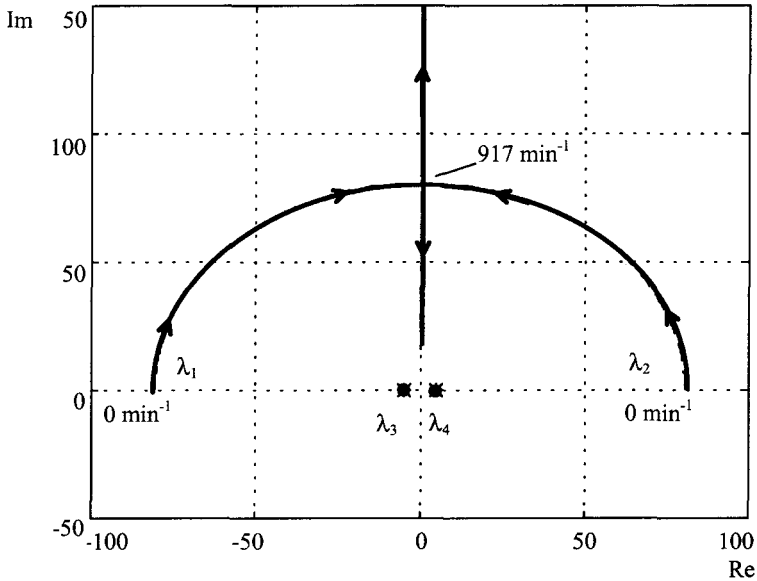


**Figure 12 Trace of the eigenvalues without the coupling of rotational and translational degrees of freedom.**

Both of the curves show the well understood stabilization effect of a gyro. Above a certain speed the eigenvalues are purely imaginary and the top is stable against tilting. This speed is the same as the lower speed limit in figure 11. It shows that the lower speed limit of the Levitron in fig. 11 is dependent on the tilting stability of the top. Both of the points on the real axis in figure 12 represent the negative radial stiffness of the lateral degrees of freedom. Without the coupling terms  $s_{qr}$  the radial stiffness is independent of the speed and the system is unstable. This means the coupling terms are very significant. They pull (fig. 11) the eigenvalues to the imaginary axis and allow a stable speed range. The upper limit is conditioned by the growing stiffness of the top against tilting moments. This leads to the lateral instability with high rotational speed.

## 7. CONCLUSIONS

The functioning of the hovering top can be explained by means of classical rotor dynamics. The Levitron is treated as a fast top and the stiffness matrix is determined by the magnetic forces. By general considerations the non zero coefficients of the stiffness matrix can be determined. Then these coefficients are found by numerical force calculation as well as by measurement. The extensive numerical calculation of the stiffness matrix is better explained in [10]. To have stability in the radial plane the existence of the coupling terms  $s_{qr}$  are important. The stable speed range shown by the homogeneous solution of the differential equation is in

good accordance to the experimental results. The hovering top is an example of a purely passive stabilized permanent magnetic rotor system.

## 8. REFERENCES

- [1] SCHWEITZER, G.; Magnetlager: Grundlagen, Eigenschaften und Anwendungen berührungsfreier elektromagnetischer Lager  
Springer - Verlag, Berlin 1993
- [2] BERRY, M.V.; The Levitron™: an adiabatic trap for spins  
Proceedings of the Royal Society, Series A, Vol 452, S. 1207-1220  
London, 1996
- [3] SIMON, M.; Spin stabilized magnetic levitation  
American Journal of Physics, Vol. 65, April 1997  
<http://www.physics.ucla.edu/marty/levitron/index.html>
- [4] JONES, T. B.; WASHIZU, M.; GANS, R.; Simple theory for the Levitron  
Journal Applied Physics, Vol 82, S 883-888, 1997
- [5] JONES, T. B.; WASHIZU, M.; GANS, R.; Dynamics of the Levitron  
Journal Physics D: Applied Physics Vol 38, S. 671-679, 1998
- [6] PAUL, W.; Electromagnetic trap for charged and neutral particles  
Review of Modern Physics, Vol. 62, No. 3, July 1990
- [7] EARNSHAW, S.; On the Nature of the Molecular Forces which regulate the Constitution of the Luminiferous Ether  
Transaction of the Cambridge Philosophical Society, Vol. VII, Part I, S.97-112  
London, 1842
- [8] FREMEREY, J.; Berührungslose permanentmagnetische Lager  
Sonderdruck aus Themenband Luftlagerungen, Hrsg. W.J. Bartz  
expert - Verlag, Renningen - Malsheim, 1993
- [9] GASCH, R.; PFÜTZNER, H.; Rotordynamik  
Springer - Verlag, Berlin, 1975
- [10] LANG, M.; GASCH, R.; Ermittlung der Steifigkeitsmatrizen von einfachen permanentmagnetischen Lagern für Rotoren;  
Electrical Engineering (Archiv für Elektrotechnik) Bd.81 (1999); Nr. 6, S.385-393

*This page intentionally left blank*



# Modelling the dynamic behaviour of a coupled rotor-foundation system by the mechanical impedance technique

P BONELLO and M J BRENNAN

Institute of Sound and Vibration Research, University of Southampton, UK

## ABSTRACT

Rotating machinery is usually placed on foundation structures that are flexible over the operational speed range and thus influence the dynamics of the coupled system. The mechanical impedance method offers a computationally efficient means of developing simple, but sufficiently accurate analytical linear models of such systems, for most practical purposes. In this paper a composite linear model of a super-critical rotor supported on a foundation through ball-bearings is developed using the mechanical impedance technique. Experimental results are presented to validate the model. Gyroscopic effects, although included in the model, were not investigated experimentally due to the limitations of the test rig.

## NOTATION

$A$	cross-sectional area of shaft/beam segment
$E$	Young's Modulus
$F_{fp}, F'_{fp}$	complex amplitudes of force at bearing pedestal no. $p$ in $x, y$ directions
$G$	shear modulus
$i$	rotor station number ( $i=1...M$ )
$I$	second moment of area of shaft element section
$\bar{k}_{bxi}, \bar{k}_{bvi}$	complex stiffnesses in $x$ and $y$ directions of bearing at rotor station no. $i$
$\bar{k}_{fxh}, \bar{k}_{fyh}$	complex stiffnesses in $x$ and $y$ direction of foundation isolation mounting at foundation station no. $h$
$L$	length of shaft/beam segment
$m$	mass per unit length
$M_{1n}, M'_{1n}$	complex amplitudes of bending moment at left hand (LH) end of shaft

	segment $n$ in $xz, yz$ planes
$M_{2n}, M'_{2n}$	complex amplitudes of bending moment at right hand (RH) end of shaft segment $n$ in $xz, yz$ planes
$n$	shaft segment number ( $n=1\dots M-1$ )
$p$	bearing pedestal number ( $p=1\dots N$ )
$Q_{1n}, Q'_{1n}$	complex amplitudes of shear force at LH end of shaft segment $n$ in $x, y$ directions
$Q_{2n}, Q'_{2n}$	complex amplitudes of shear force at RH end of shaft segment $n$ in $x, y$ directions
$r_o$	radius of gyration of shaft element section about a diameter
$h$	foundation station number ( $h=1\dots R$ )
$T$	transpose
$V_{jp}, V'_{jp}$	complex amplitudes of linear velocity of foundation in $x, y$ directions at bearing pedestal no. $p$
$V_i, V'_i$	complex amplitudes of linear velocity at rotor station no. $i$ in $x, y$ directions
$V_{1n}, V'_{1n}$	complex amplitudes of linear velocity at LH end of shaft segment $n$ in $x, y$ directions
$V_{2n}, V'_{2n}$	complex amplitudes of linear velocity at RH end of shaft segment $n$ in $x, y$ directions
$x, y$	linear deflections at a general position $z$ at time $t$ in $x$ and $y$ directions
$\alpha$	shear coefficient
$\rho$	material density
$\Omega_i, \Omega'_i$	complex amplitudes of angular velocity at rotor station no. $i$ in $xz, yz$ planes
$\Omega_{1n}, \Omega'_{1n}$	complex amplitudes of angular velocities at LH end of shaft segment $n$ in $xz, yz$ planes
$\Omega_{2n}, \Omega'_{2n}$	complex amplitudes of angular velocities at RH end of shaft segment $n$ in $xz, yz$ planes

## 1 INTRODUCTION

Rotating machinery in power plants and industry is generally supported on foundation structures that are flexible over the operational speed range and thus contribute to the dynamics of the coupled system. The mechanical impedance method offers a computationally efficient means of developing simple, but sufficiently accurate analytical linear models of coupled rotor-foundation systems. This method deals with steady state frequency response descriptions for linear mechanical components. A component is defined as having terminals that identify the position and direction of all external forces applied to the component and the corresponding resulting velocities [1]. It is described by a single matrix that incorporates mass, stiffness, damping and gyroscopic terms. Similar matrix assembly techniques to those used in the Finite Element (FE) method can be used in the mechanical impedance method. However, unlike FE matrices, the exact dynamic shape of the element is used in the derivation of its mechanical impedance matrix [2] rather than the quasi-static approximation used in FE. Hence, provided the element is uniform its size is unrestricted with no effect on accuracy. This leads to a much smaller number of degrees of freedom compared to the FE method. Consequently the mechanical impedance technique offers the suitability of FE methods to model coupled rotor-bearing-foundation systems with the

advantage of computational efficiency. Apart from being readily adaptable to include foundation effects, an additional advantage of the mechanical impedance technique over the otherwise computationally efficient Transfer Matrix method [1] is that it is formulated in terms of measurable quantities, namely frequency response functions. Hence, such a methodology is particularly useful when trying to modify a system that has already been built, where it would be quicker and easier to measure the foundation dynamics rather than to model it.

Although the mechanical impedance method is generally well documented [1], [2] its application to rotor dynamics problems is relatively unexplored. Reiger *et al.* [3] applied the analogous dynamic stiffness technique to a general rotor-bearing system in order to find its unbalance response, critical speeds and instability threshold speeds. Similar work was done more recently by Raffa *et al* [4] with respect to unbalance response. However, in both these works foundation flexibility was not included. The aim of this paper is to develop an analytical model based on the mechanical impedance technique to predict the unbalance response of a general multi-span coupled rotor-bearing-foundation system and validate it on a small scale test-rig.

## 2 MODEL DEVELOPMENT

### 2.1 General description

The simplified general model is shown in Figure 1 where the  $z$  axis is along the shaft, the  $xz$  plane is horizontal and the  $yz$  plane is vertical. This system can be conveniently divided into the rotor-bearing subsystem and the foundation subsystem. The rotor-bearing subsystem has  $M$  stations that are joined by shaft elements which are modelled as beam segments which can rotate about their longitudinal axis and bend in both  $xz$  and  $yz$  planes. A rotor station  $i$  is defined as a location along the rotor where there is either a bearing, a disc, or a change in cross-section. Any out-of-balance is assumed to be concentrated at the discs and internal damping in the shaft is neglected. The shaft segments can be modelled either as rotating Euler-Bernoulli or Timoshenko beams bending in two planes depending on the speed of interest and the size of the shaft. Each bearing (excluding the housing) is modelled as a pair of uncoupled complex (damped) springs in the  $x$  and  $y$  directions. Such a model is admissible for rolling element bearings. The foundation subsystem consists of the bearing housings (pedestals), foundation structure and isolation system. Thus the bearing pedestals are considered to be integral with the foundation, which follows the approach taken by Kramer [5]. The foundation impedance matrix can be determined either analytically by the mechanical impedance technique or alternative techniques such as FE, or empirically. The empirical approach involves measurement of the foundation subsystem impedance. With both approaches the impedance matrix of the foundation subsystem is determined independently from the rotor-bearing subsystem and subsequently integrated into the impedance matrix of the complete rotor-bearing-foundation assembly. Because the unbalance response is of interest, *synchronous* harmonic motion is assumed.

### 2.2 Model of the coupled system

The shaft element is shown in Figure 2. The relationship between the force and velocity vectors and the impedance matrix of the  $n$ -th shaft element is given by:

$$\mathbf{f}_n = \mathbf{Z}_n \mathbf{v}_n \quad (1)$$

where  $\mathbf{f}_n = [Q_{1n} \quad Q'_{1n} \quad M_{1n} \quad M'_{1n} \quad Q_{2n} \quad Q'_{2n} \quad M_{2n} \quad M'_{2n}]^T$ ,

$\mathbf{v}_n = [V_{1n} \quad V'_{1n} \quad \Omega_{1n} \quad \Omega'_{1n} \quad V_{2n} \quad V'_{2n} \quad \Omega_{2n} \quad \Omega'_{2n}]^T$  and  $\mathbf{Z}_n$  is the  $8 \times 8$  impedance matrix of the shaft element. An Euler-Bernoulli beam model is appropriate for low speed flexible shafts and a Timoshenko beam model is appropriate for high speed, larger diameter shafts. Because the polar moment of inertia is neglected in the Euler-Bernoulli shaft element, the vibrations in the two planes of bending are uncoupled. In this case the impedance matrix of the shaft element can be determined by simply expanding the impedance matrix of an Euler-Bernoulli beam bending in one plane [6] to include both planes of bending [7]. With a Timoshenko shaft element the inclusion of the polar moment of inertia results in the coupling of the two planes of bending due to the gyroscopic terms as can be seen from the pair of equations relating to vibration in the  $xz$  and  $yz$  planes of such an element [7]:

$$EI \frac{\partial^4 x}{\partial z^4} - m\omega_0^2 \left\{ 1 + \frac{EI}{\alpha AG r_0^2} \right\} \frac{\partial^4 x}{\partial z^2 \partial t^2} + m \frac{\partial^2 x}{\partial t^2} + \frac{m^2 r_0^2}{\alpha AG} \frac{\partial^4 x}{\partial t^4} - 2m\omega_0^2 \omega \frac{\partial^3 y}{\partial t \partial z^2} + \frac{2m^2 r_0^2 \omega}{\alpha AG} \frac{\partial^3 y}{\partial t^3} = 0 \quad (2a)$$

$$EI \frac{\partial^4 y}{\partial z^4} - m\omega_0^2 \left\{ 1 + \frac{EI}{\alpha AG r_0^2} \right\} \frac{\partial^4 y}{\partial z^2 \partial t^2} + m \frac{\partial^2 y}{\partial t^2} + \frac{m^2 r_0^2}{\alpha AG} \frac{\partial^4 y}{\partial t^4} + 2m\omega_0^2 \omega \frac{\partial^3 x}{\partial t \partial z^2} - \frac{2m^2 r_0^2 \omega}{\alpha AG} \frac{\partial^3 x}{\partial t^3} = 0 \quad (2b)$$

The last two terms on the left-hand side of equations (2) are the gyroscopic terms. The impedance matrix in this case is thus complicated and is obtained by solving the above equations for synchronous steady state harmonic motion and the insertion of the linear/angular velocity and force/moment boundary conditions [7].

The impedance matrices of consecutive shaft elements are assembled in a manner similar to FE [8], by using continuity of linear and angular velocities at each shaft station. For a total of  $M$  rotor stations, the assembled rotor-bearing subsystem matrix,  $\mathbf{Z}_r$ , is of order  $4M \times 4M$  where

$$\mathbf{f}_r = \mathbf{Z}_r \mathbf{v}_r \quad (3)$$

and  $\mathbf{v}_r = [V_1 \quad V'_1 \quad \Omega_1 \quad \Omega'_1 \quad \dots \quad V_M \quad V'_M \quad \Omega_M \quad \Omega'_M]^T$ .  $\mathbf{f}_r$  is the column vector of forces external to the rotor-bearing subsystem including the effects of out-of-balance and foundation movement. Additional matrices are added at the appropriate locations of the intersecting regions of the shaft element matrices to allow for the presence of discs or bearings at the rotor stations. The disc matrices contain the impedances due to disc mass and moments of inertia (polar and transverse). The  $2 \times 2$  diagonal bearing matrices contain the bearing impedance terms  $z_{bxi} = \bar{k}_{bxi} / j\omega$ ,  $z_{byi} = \bar{k}_{byi} / j\omega$ .

Since the force inputs from the rotor-bearing subsystem to the foundation assembly are located at the bearings, which are assumed to exert no restraining moment, the foundation impedance matrix can be expressed as a  $2N \times 2N$  matrix  $\mathbf{Z}_f$  where:

$$\mathbf{f}_f = \mathbf{Z}_f \mathbf{v}_f \quad (4)$$

where  $\mathbf{f}_f = [F_{f1} \ F'_{f1} \ \dots \ F_{fN} \ F'_{fN}]^T$  is the vector of forces at the bearing pedestals, and  $\mathbf{v}_f = [V_{f1} \ V'_{f1} \ \dots \ V_{fN} \ V'_{fN}]^T$  is the vector of velocities at the  $N$  bearing pedestals. Note that no external moments and angular velocities are included in the above formulation since the former are assumed to be zero and the latter are not required. If  $\mathbf{Z}_f$  is determined analytically using the mechanical impedance technique similar matrix assembly techniques to those described for the rotor-bearing subsystem can be used.

The  $2N \times 1$  foundation forcing vector  $\mathbf{f}_f$  in equation (4) contains the forces exerted by the bearings on the foundation *i.e.*

$$\mathbf{f}_f = [-z_{bx1}(V_{f1} - V_1) \ -z_{by1}(V'_{f1} - V'_1) \ \dots \ -z_{bxN}(V_{fN} - V_N) \ -z_{byN}(V'_{fN} - V'_N)]^T \quad (5)$$

Hence the equation (4) can be written as:

$$\mathbf{f}'_f = \mathbf{Z}'_f \mathbf{v}_f \quad (6)$$

where  $\mathbf{f}'_f = [z_{bx1}V_1 \ z_{by1}V'_1 \ \dots \ z_{bxN}V_N \ z_{byN}V'_N]^T$  and,  $\mathbf{Z}'_f = \mathbf{Z}_f + \Lambda_f$  where  $\Lambda_f$  is a  $2N \times 2N$  diagonal matrix of bearing impedances given by:

$$\Lambda_f = \text{diag}(z_{bx1}, z_{by1}, \dots, z_{bxN}, z_{byN}) \quad (7)$$

The final step in assembling the overall impedance matrix  $\mathbf{Z}$  of the coupled rotor-bearing-foundation assembly is the integration of the system of equations given by equation (3) for the rotor-bearing subsystem and equation (6) for the bearing-foundation subsystem. The final result is found to be:

$$\mathbf{f} = \mathbf{Z} \mathbf{v} \quad (8)$$

where  $\mathbf{v} = [V_1 \ V'_1 \ \Omega_1 \ \Omega'_1 \ \dots \ V_M \ V'_M \ \Omega_M \ \Omega'_M \ V_{f1} \ V'_{f1} \ \dots \ V_{fN} \ V'_{fN}]^T$  and

$$\mathbf{Z} = \begin{bmatrix} \mathbf{Z}_r & \mathbf{Z}_g \\ \mathbf{Z}_r^T & \mathbf{Z}'_f \end{bmatrix} \quad (9)$$

$\mathbf{Z}$  is of order  $(4M + 2N) \times (4M + 2N)$  and  $\mathbf{Z}_r$  and  $\mathbf{Z}'_f$  are the assembled rotor-bearing and bearing-foundation matrices given in equations (3) and (6) respectively.  $\mathbf{Z}_g$  is a  $4M \times 2N$  matrix which contains zeros everywhere except at entries which are filled in according to the following algorithm: if the  $p$ -th bearing ( $p = 1 \dots N$ ) is at the  $i$ -th rotor station then insert the  $2 \times 2$  diagonal matrix

$$-\text{diag}(z_{bxi}, z_{byi})$$

at the  $\{1+4(i-1)\} \dots \{2+4(i-1)\}$ -th rows,  $\{4M+1+2(p-1)\} \dots \{4M+2+2(p-1)\}$ -th columns of  $\mathbf{Z}$ .  $\mathbf{f}$  is a column vector of forces external to the complete rotor-bearing-foundation system, of length  $(4M+2N)$ . It contains only the  $x, y$  unbalance forces at the disc stations at rows  $\{1+4(i-1)\}, \{2+4(i-1)\}$  respectively for a disc at rotor station  $i$ . Elsewhere it is filled with zeros. This assumes there are no shear force and bending moments in the two planes of bending at the ends of the rotor.

### 2.3 Unbalance response

Once  $\mathbf{Z}$  and  $\mathbf{f}$  in equation (8) have been determined for each speed,  $\mathbf{Z}$  can be inverted to give  $\mathbf{v}$  and hence the deflection vector  $\mathbf{u} = \mathbf{v} / j\omega$ . Thus the unbalance response at each rotor station and bearing pedestal can be obtained. Moreover for any speed, once  $\mathbf{u}$  has been determined, the complex amplitudes  $X, Y$  of the deflections at any *arbitrary* location P along the rotor can be determined *exactly* [7]. The shaft orbit at P and the sense of whirl can be determined from knowledge of  $X$  and  $Y$ . These displacements are *absolute* values. The relative displacement between positions P on the rotor and Q on the foundation, which would be measured by proximity probes, is given by  $X_r = X_p - X_q, Y_r = Y_p - Y_q$  where  $X_p, Y_p, X_q, Y_q$  are absolute values. If P and Q are not located at a bearing station a “dummy” bearing assembly of zero bearing stiffness and damping and zero pedestal mass can be inserted between P and Q.

## 3 MODEL VALIDATION

### 3.1 Experimental work

The test rig used for the experimental verification of the coupled rotor-bearing-foundation system model is shown in Figure 3. It consisted of a mild steel 10mm diameter shaft mounted on three nominally identical double row self-aligning ball bearings housed in three mild steel bearing pedestals BP1, BP2 and BP3. The shaft carried a 30 mm diameter steel disc W, into which known unbalance masses could be screwed. The shaft was connected to the motor M via a flexible coupling. The aluminium alloy foundation consisted of a right-angled “V” section beam with three feet F1, F2, F3 attached. The whole assembly was supported on a thick layer of foam.

The model developed in the previous section was used to solve two model problems, over a rotational speed range of 1500-12000 rpm. The first problem (Problem I) was to find the absolute unbalance response at the bearing pedestals BP1, BP2, BP3 and at positions  $P_1 \dots P_6$  along the rotor using an empirical foundation impedance matrix (*hybrid model* approach). The second problem (Problem II) was to determine the unbalance response of the points  $P_3$  and  $P_5$  on the rotor relative to the foundation using an analytical foundation impedance matrix, derived by the mechanical impedance technique (*analytical model* approach). In the both problems the simulation made use of single, speed independent estimates for bearing stiffness (2MN/m) and loss factor (0.2) for both the  $x$  and  $y$  directions obtained by simple static tests, and which hence neglect any effect of ball bearing rotation [8]. For Problem I the foundation impedance matrix was measured using impact hammer excitation. Measurements were performed separately for the vertical and horizontal planes. For these tests the rotor assembly was removed but the bearings were retained in their pedestals as their mass was

negligible compared with the mass of the foundation. For Problem II the foundation subsystem was modelled as a floating Timoshenko beam with attached rigid bodies. The mass and moment of inertia of each body (including the motor) were assumed to be concentrated at the axial position of the centre of mass of the body. Dummy bearings were added between P<sub>3</sub> and Q<sub>3</sub> and between P<sub>5</sub> and Q<sub>5</sub>. The simulations are compared with experimental results in section 4.

Time constraints did not allow for the quantification of the residual unbalance due to geometric inaccuracies in the disc and the lack of straightness of the machined shaft. Hammer tests were therefore conducted on the *stationary* rig, enabling verification of the predicted unbalance response curves for the two model problems over the speed range. Using an impact hammer on the disc W in the  $x$  direction, the transfer acceleration between W and location P on the system,  $a_{pWx} = A_x/F_x$  could be measured, where  $A_x$  is the acceleration at P due to the force  $F_x$ . Now in rotation,  $F_x = U\omega^2$  and hence  $a_{pWx} = A_x/U\omega^2 = -X/U$  where  $X = -A_x/\omega^2$  is the displacement at P in the  $x$  direction due to the unbalance  $U$  at W. Similarly in the  $y$  direction the transfer acceleration is found to be  $a_{pWy} = -Y/Ue^{-j0.5\pi}$ . Hence it is seen that the magnitudes of the frequency response functions  $a_{pWx}$  and  $a_{pWy}$  respectively give the displacement responses at P in the  $x$  and  $y$  directions for unit unbalance at the disc. The use of hammer tests on the stationary test rig to determine the unbalance response of the rotating system is justified provided that (a) the behaviour of the ball bearings is unaffected by rotation, and (b) the vibrations in the  $x$  and  $y$  directions during rotation are uncoupled *i.e.* the gyroscopic effects due to the polar moment of inertia of the disc and the shaft are negligible. Subject to these conditions, the measured resonance frequencies of the stationary system can be considered as the critical speeds of the rotating system. Assumption (b) is justified by noting that the polar moment of inertia of the disc, at  $0.5660 \times 10^{-3} \text{kgm}^2$ , and the distributed polar moment of inertia of the shaft are negligible. As regards assumption (a), it is observed in [8] that ball-bearings exhibit non-linearities in rotation. Hence the static hammer tests are adequate to verify all aspects of the model relevant to this particular case study except the assumption of linear behaviour of the bearings in rotation.

As regards the rotating rig, the instantaneous displacements in the  $x$  and  $y$  directions at P<sub>3</sub> for 18 different speeds in the range 1500-6000 rpm were measured using proximity probes P1 and P2 mounted in the respective directions at point P<sub>3</sub>. The sampling frequency was 4096 Hz and the record length 0.125s. Orbits were constructed from these  $x$  and  $y$  displacements showing the motion of the shaft at P<sub>3</sub> during an interval of 0.125s.

## 4 RESULTS AND DISCUSSION

Figures 4(a)-(d) show the simulation results of the first problem for the *absolute* unbalance response at rotor position P<sub>3</sub> and at bearing pedestal BP2. The hammer test measurements are overlaid on the same axes. It can be seen that there is good agreement between predictions and measurement. The model predictions for the first two critical speeds 7025rpm, 10191rpm compare well with the measured values of 7161rpm and 10010rpm. The second critical speed is evident only in the  $x$  response and corresponds to a frequency of 167 Hz which was found to be the first torsional mode of the foundation.

Figures 5(a),(b) show the simulation results of the second problem for the *relative* motion at  $P_3$  predicted using an analytical foundation impedance matrix. The hammer test measurements are overlaid on the same axes. There is good agreement between the predicted and measured relative response in the  $y$  direction, but not as good agreement in the  $x$  direction, in the region between the critical speeds. The reason for this is that the analytical model for the foundation ignores torsion effects. It can be seen that for both simulation and measurement the relative responses in the  $x$  and  $y$  directions are practically equal in magnitude at all speeds. They were also found to be in quadrature at all speeds which means that the shaft orbits should be *circular*, subject to the condition that the ball bearings remain linear in rotation.

Figures 5(c),(d) give the  $x, y$  responses at point  $P_3$ , as measured on the rotating rig from the proximity probes. The analytical model prediction is overlaid on the same axes. It is observed that the measured response is invariably greater than that predicted, which suggests that there is a high degree of unknown residual unbalance. It is also observed that for speeds greater than around 4250rpm the slope of an imaginary curve through the measurement points roughly follows the slope of the theoretical curve, which indicates that the model is valid for these speeds. For speeds less than around 4250rpm the slope of the curve through these points does not follow the slope of the theoretical curve. In fact, the measured orbits showed that a transition from non-linearity to linearity occurs as the speed increases from 3500 to 4500 rpm and that this transition is characterised by a stage of chaos at 4000 rpm. Such chaotic behaviour of ball bearings in rotation is described in [9]. For speeds above 4500 rpm the non-linearities disappear and the measured orbits are nearly perfect circles, as predicted.

## 5 CONCLUSIONS

A mechanical impedance model of a coupled rotor-bearing-foundation system has been developed and partially validated in this paper. The correlation between predictions and measurement was found to be reasonably good. An error in the analytical model prediction for the  $x$  response due to neglect of torsional motion of the foundation was found to be of significance for speeds between the first and second critical speeds. Gyroscopic effects were negligible in the test rig used and hence for the study reported here stationary testing using an impact hammer verified all aspects of the model developed except the assumption of linear behaviour of the ball bearings under rotating conditions. Measurements on the rotating rig showed that at low speeds non-linearities were evident in the test rig. However, these non-linearities disappeared at high speeds and circular orbits, as predicted by the model were measured.

## REFERENCES

1. S. RUBIN 1967 *The Journal of the Acoustical Society of America* **41**, 1171-1179. Mechanical Impedance and Transmission Matrix Concepts.
2. V.H. NEUBERT 1987 *Mechanical Impedance: Modelling/Analysis of Structures*. Naval Sea Systems Command, Code NSEA-55N.
3. N.F. REIGER, C.B. THOMAS and W.W. WALTER 1976 *Vibrations in Rotating*



*Machinery, IMechE Conference Publications 1976-9, C187/76, 187-193. Dynamic Stiffness Matrix Approach for Rotor-Bearing Analysis.*

4. F.A. RAFFA, F. VATTA 1996 *Transactions of the ASME*, **118**, 332-339. Dynamic Stiffness Methods for Linear Rotor-Bearing Systems.
5. E. KRAMER 1980 *Vibrations in Rotating Machinery, IMechE Conference Publications 1980-4, C300/80, 333-338. Computation of the Coupled Rotor-Machine Foundation.*
6. R.H. LYON 1990 *Machinery Noise and Diagnostics*. Butterworths.
7. P. BONELLO 1998 *M.Sc. Thesis, University of Southampton. Predicting the Vibration Response of A Multi-Span Coupled Rotor-Bearing-Foundation System by the Mechanical Impedance Technique.*
8. E. KRAMER 1993 *Dynamics of Rotors and Foundations*. Springer Verlag.
9. H. TAMURA, E.H. GAD, A. SUEOKA 1986 *IFTToMM Conf.: Rotordynamics, Tokyo, 553-560. Computer Study of Radial Vibrations in a Rotor/Ball Bearing System.*

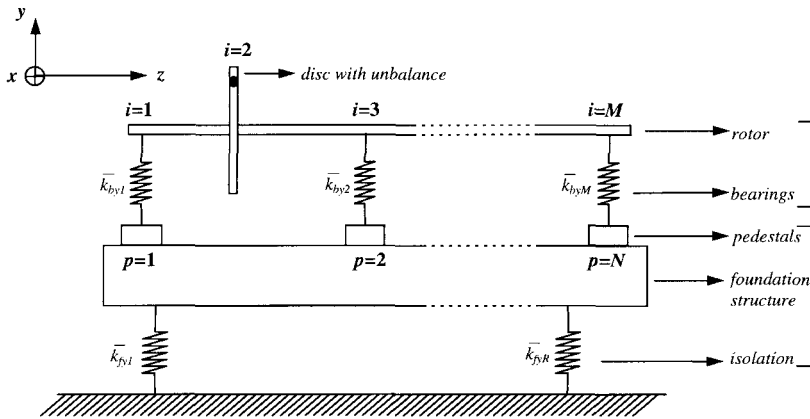


**Figure 1 Model adopted for multi-span coupled rotor-bearing-foundation system**

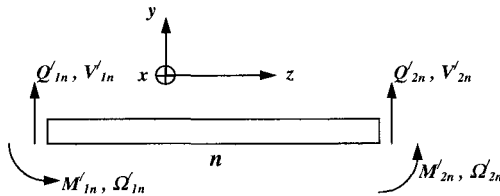


**Figure 2 Shaft element notation**

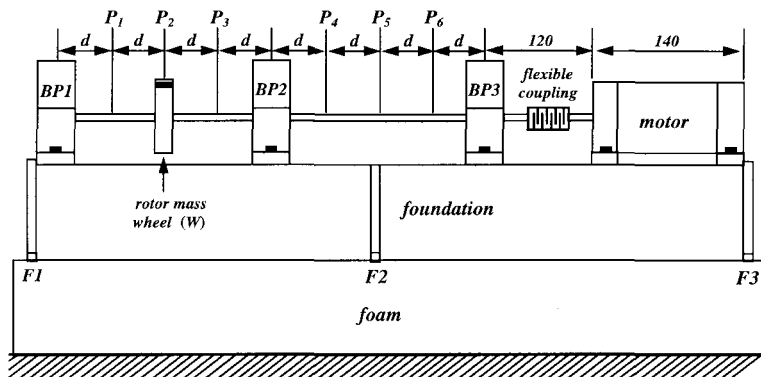


Figure 3 Test rig (all dimensions in mm,  $d=61.25\text{mm}$ )

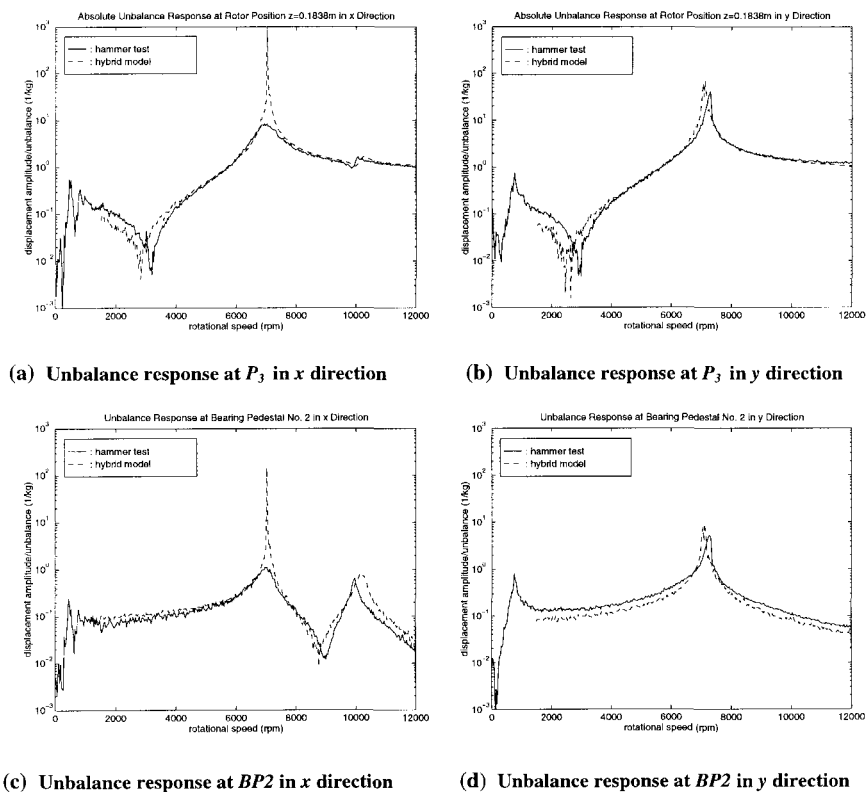
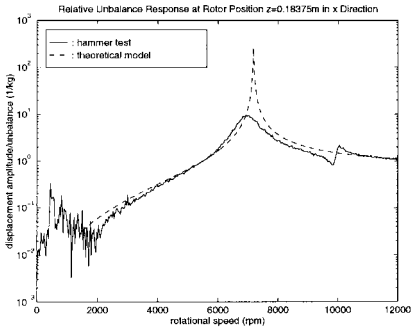
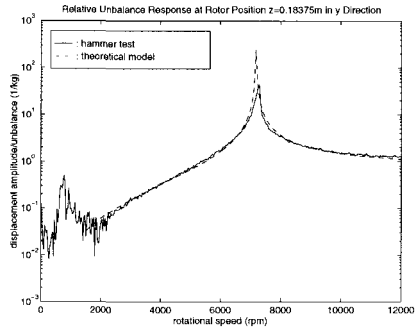


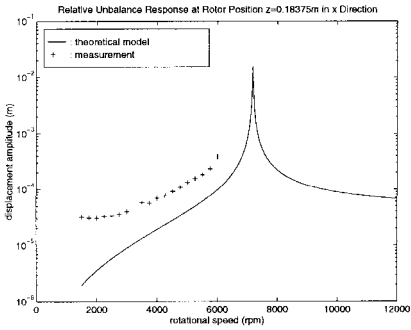
Figure 4 Absolute unbalance response in  $x$  and  $y$  directions at point  $P_3$  and bearing pedestal No.2 ( $BP2$ ): predictions from hybrid model compared with measurement (hammer test)



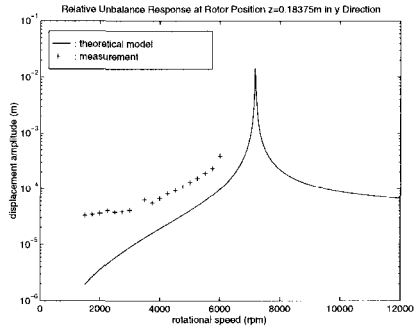
(a) Unbalance response in x direction



(b) Unbalance response in y direction



(a) Unbalance response in x direction



(b) Unbalance response in y direction

**Figure 5** Relative unbalance response in *x* and *y* directions at point  $P_3$ : analytical model predictions compared with hammer test measurement ((a), (b)), and with proximator measurement ((c), (d))

*This page intentionally left blank*

# Authors' Index

## A

Adams, M L ..... 301–310  
Adams, M L ..... 301–310  
Aenis, M ..... 3–20  
Afshari, F ..... 301–310  
Ahaus, G ..... 259–268  
Ahmed, I L M ..... 235–248  
Ahrens, J ..... 259–268  
Allaire, P E ..... 141–148, 149–164  
Antoni, J ..... 525–534  
Aoyama, E ..... 223–232  
Azuma, T ..... 361–370

## B

Bachschmid, N ..... 249–258, 449–458,  
..... 571–580  
Balbahadur, A C ..... 427–436  
Balda, M ..... 667–676  
Bannister, R H ..... 121–130  
Bell, J R ..... 645–656  
Berlioz, A ..... 131–140  
Bettella, M ..... 603–618  
Bonello, P ..... 745–756  
Bozet, J-L ..... 439–448  
Breneur, C ..... 561–570  
Brennan, M J ..... 745–756  
Bucher, I ..... 711–720  
Burrows, C R ..... 371–380

## C

Charreyron, M ..... 131–140  
Choi, D-H ..... 499–508  
Choi, S P ..... 181–186  
Choi, Y-S ..... 281–290  
Cole, M O T ..... 371–380

## D

Datta, P K ..... 235–248  
Deng, X ..... 291–300  
Dufour, R ..... 131–140

## E

Edwards, S ..... 31–42, 323–334  
El Badaoui, M ..... 525–534  
El-Hakim, M ..... 349–360

El-Shafei, A ..... 349–360  
Ewins, D J ..... 65–76, 721–730

## F

Feng, N S ..... 415–426  
Foiles, W C ..... 141–148, 149–164  
Fox, C H J ..... 547–560  
Friswell, M I ..... 31–42, 323–334  
Fujiwara, H ..... 361–370

## G

Gasch, R ..... 291–300, 731–744  
Ghiocel, D M ..... 77–90  
Goat, C A ..... 459–470  
Graham, J P ..... 167–180  
Gregori, L ..... 657–666  
Gunter, E J ..... 141–148, 149–164  
Gupta, K ..... 45–54

## H

Ha, H C ..... 181–186  
Hahn, E J ..... 415–426  
Hellmann, D-H ..... 213–222  
Herbert, R G ..... 93–100  
Herzog, R ..... 361–370  
Hirogaki, T ..... 223–232  
Hiß, F ..... 485–498  
Holmes, R ..... 509–522

## I

Inoue, T ..... 701–710  
Irretier, H ..... 335–346  
Ishida, Y ..... 701–710

## K

Kanemitsu, Y ..... 361–370  
Keogh, P S ..... 371–380  
Khan, A F ..... 547–560  
Kim, C-H ..... 499–508  
Kirk, R G ..... 21–30, 427–436  
Knopf, E ..... 3–20, 381–390  
Kreuzinger-Janik, T ..... 335–346  
Kwanka, K ..... 485–498  
Kwon, K-S ..... 535–544

**L**

Lang, M.....	731–744
Larsson, B.....	269–278
Lee, C-W.....	535–544
Lee, N-S.....	499–508
Lee, Y-B.....	499–508
Lees, A W.....	31–42, 323–334
Leung, P S.....	235–248
Levesley, M C.....	509–522
Liebich, R.....	291–300
Liew, A.....	415–426

**M**

Mahfoudh, J.....	561–570
Malenovský, E.....	691–700
Markert, R.....	581–590
Matsushita, O.....	361–370
McCloskey, T H.....	619–632
Memmott, E A.....	187–198
Mérot, P.....	439–448
Murayama, T.....	701–710

**N**

Nakata, Y.....	223–232
Namura, K.....	55–64
Nordmann, R.....	3–20, 381–390, 485–498

**O**

Okubo, H.....	361–370
---------------	---------

**P**

Park, C H.....	181–186
Pennacchi, P.....	249–258, 571–580
Petrov, E P.....	65–76
Pietsch, O.....	591–602
Pizzigoni, B.....	449–458
Platz, R.....	581–590
Play, D.....	561–570
Poysat, P.....	439–448
Preciado, E.....	121–130
Provasi, R.....	657–666

**R**

Ramakrishnan, C V.....	45–54
Rao, J S.....	45–54
Reimche, W.....	591–602
Rieger, N F.....	77–90

Roemer, M J.....	619–632
Rothberg, S J.....	645–656

**S**

Saito, E.....	55–64
Schneider, H.....	101–108
Seidler, M.....	581–590
Seok, K-Y.....	499–508
Sève, F.....	131–140
Sharp, R S.....	603–618
Singh, A K.....	45–54
Smalley, A J.....	619–632
Smith, S P.....	109–120
Sobotzik, J.....	485–498
Springer, H.....	393–402
Stegemann, D.....	591–602
Storteig, E.....	201–212
Straßburger, S.....	3–20
Südmersen, U.....	591–602
Suzuki, K.....	403–414, 473–484

**T**

Tanaka, M.....	403–414, 473–484
Tanzi, E.....	449–458
Taura, H.....	403–414
Torbergsen, E.....	679–690
Trautmann, C.....	213–222

**U**

Uenishi, Y.....	223–232
Ulbrich, H.....	259–268

**V**

Vania, A.....	313–322
Venini, P.....	249–258
Volkovas, V.....	633–644
von Groll, G.....	721–730

**W**

Wardle, F P.....	459–470
White, M F.....	201–212, 679–690
Williams, E J.....	547–560

**Z**

Zanetta, G A.....	657–666
Zapomèl, J.....	691–700